David Tomás Sánchez Martínez
Lourdes García Rodríguez
(coordinadores)

Proceedings of the 7th International Seminar on

ORC Power Systems

Editorial Universidad de Sevilla

Proceedings of the 7th International Seminar on

ORC Power Systems

David Tomás Sánchez Martínez
Lourdes García Rodríguez
(coordinadores)

Proceedings of the 7th International Seminar on

ORC Power Systems

(ORC2023)

4th to 6th
SEPTEMBER
SEVILLE 2023

EUS EDITORIAL
UNIVERSIDAD DE SEVILLA

Sevilla, 2024

Colección Actas
Núm.: 91

Comité editorial de
la Editorial Universidad de Sevilla:

Araceli López Serena
(Directora)
Elena Leal Abad
(Subdirectora)

Concepción Barrero Rodríguez
Rafael Fernández Chacón
María Gracia García Martín
María del Pópulo Pablo-Romero Gil-Delgado
Manuel Padilla Cruz
Marta Palenque
María Eugenia Petit-Breuilh Sepúlveda
Marina Ramos Serrano
José-Leonardo Ruiz Sánchez
Antonio Tejedor Cabrera

Review chairs of the 7th Internation Seminar on ORC Power Systems

Prof. Christoph Wieland (University of Duisburg-Essen) - *Review Chair*
Prof. Sotirios Karellas (National Technical University of Athens) - *Review Co-Chair*
Prof. Teemu Turunen-Saaresti (LUT University) - *Review Co-Chair*
Dr. Diego-César Alarcón-Padilla (Plataforma Solar de Almería - CIEMAT) - *Review Co-Chair*
Dr. Francesco Crespi (Universidad de Sevilla) - *Review Co-Chair*

Esta obra se distribuye con la licencia
Creative Commons Atribución-NoComercial-SinDerivadas 4.0 Internacional (CC BY-NC-ND 4.0)

Usted es libre de:
Compartir — copiar y redistribuir el material en cualquier medio o formato
La licenciante no puede revocar estas libertades en tanto usted siga los términos de la licencia
Bajo los siguientes términos:
Atribución — Usted debe dar crédito de manera adecuada, brindar un enlace a la licencia, e indicar si se han realizado cambios .
Puede hacerlo en cualquier forma razonable, pero no de forma tal que sugiera que usted o su uso tienen el apoyo de la licenciante.
NoComercial — Usted no puede hacer uso del material con propósitos comerciales .
SinDerivadas — Si remezcla, transforma o crea a partir del material, no podrá distribuir el material modificado.
No hay restricciones adicionales — No puede aplicar términos legales ni medidas tecnológicas
que restrinjan legalmente a otras a hacer cualquier uso permitido por la licencia.

© Editorial Universidad de Sevilla 2024
c/ Porvenir, 27 - 41013 Sevilla.
Tlfs.: 954 487 447; 954 487 451; Fax: 954 487 443
Correo electrónico: info-eus@us.es
Web: https://editorial.us.es

© David Tomás Sánchez Martínez y Lourdes García Rodríguez
(coordinadores)

© De los textos, los autores 2024

ISBN 978-84-472-2745-7
DOI: https://dx.doi.org/10.12795/9788447227457

Diseño de cubierta y maquetación: los autores

INDEX OF CONTRIBUTIONS

ID3 - Additive manufacturing for fast prototyping of a velocity compounded radial re-entry turbine
Authors: Dominik Stümpfl, Karel Ráž, Philipp Streit, Andreas P. Weiß 13

ID4 - Thermodynamic concept of a novel recuperative two-phase power cycle process
Authors: Benedikt G. Bederna, Riley B. Barta, Christiane S. Thomas. 23

ID7 - Performance analysis of a 1.5 MW Organic Rankine Cycle in a Carnot battery system for grid balancing services
Authors: Robin Tassenoy, Hannes Van De Velde, Kenny Couvreur, Michel De Paepe, Steven Lecompte 33

ID8 - Calibration of multi-hole probes for measurements in compressible organic vapor flows
Authors: Leander Hake, Stephan Sundermeier, Stefan Aus Der Wiesche, Maximilian Passmann 43

ID9 - pocketORC: A browser-based calculator for teaching organic Rankine cycle power systems
Authors: Martin White 53

ID10 - Evaluation of existing supercritical heat transfer correlations for designing the vapor generator in low-temperature transcritical Organic Rankine Cycle systems
Authors: Jera Van Nieuwenhuyse, Anastasios Skiadopoulos, Dimitris Manolakos, Steven Lecompte, Michel De Paepe 61

ID12 - A novel combined cooling and power cycle integrated ejector refrigeration and composition adjustment for stationary engine waste heat recovery
Authors: Xiaocun Sun, Lingfeng Shi, Hua Tian, Gequn Shu 71

ID14 - Design and construction of a reversible ORC test rig for geothermal CHP applications
Authors: Florian Kaufmann, Christopher Schifflechner, Christoph Wieland, Hartmut Spliethoff 81

ID15 - Robust and fast meanline methodology for radial inflow turbines with non-ideal gases for system level optimisation of organic Rankine cycles
Authors: Carola Freytag, Eva Alvarez-Regueiro, Pablo Ale-Martos, Esperanza Barrera-Medrano, Ricardo Martinez-Botas. 91

ID16 - Shape optimization of a sCO2 centrifugal compressor stage
Authors: Alessandro Romei, Paolo Gaetani, Giacomo Persico 101

ID17 - Optimizing the performance of a hybrid solar-biomass micro-CHP system with a TFC engine as the prime mover for domestic applications
Authors: Anastasios Skiadopoulos, Xander Van Heule, Steven Lecompte, Michel De Paepe, Dimitrios Manolakos 109

ID19 – Systematic and multi-criteria optimisation of subcritical thermally integrated Carnot batteries (TI-PTES) in an extended domain
Authors: Antoine Laterre, Olivier Dumont, Vincent Lemort, Francesco Contino 119

ID20 - ORC technology used in a heat removal system for an advanced nuclear power plant
Authors: Guillaume Lhermet, Benoit Payebien, Nicolas Tauveron, Nadia Caney, Franck Morin 130

ID22 - Assessment of trilateral Organic Rankine Cycle for solar applications with innovative turboexpander concept
Authors: Alessandro Romei, Andrea Giostri, Andrea Spinelli. 140

ID25 - Evaluation of the performance of an axial one-stage 10kW turbogenerator through experimental testing
Authors: Piotr Klimaszewski, Piotr Klonowicz, Lukasz Witanowski, Tomasz Suchocki, Piotr Lampart, Eugeniusz Ihnatowicz, Lukasz Antczak, Dawid Zaniewski, Lukasz Jedrzejewski 149

ID26 - Investigation of the turbulence level and the vortex shedding in a turbine cascade working with an organic vapor at subsonic Mach numbers
Authors: Leander Hake, Stephan Sundermeier, Stefan Aus Der Wiesche, Camille Matar, Paola Cinnella, Xavier Gloerfelt 159

ID27 - A novel approach to district heating: using a two-phase expander in a reversible heat pump-Organic Rankine Cycle system
Authors: Sindu Daniarta, Attila R. Imre, Piotr Kolasinski 169

ID28 - Optimization of a partially evaporating Organic Rankine Cycle with thermal non-equilibrium expansion
Authors: Xander Van Heule, Tasos Skiadopoulos, Dimitris Manolakos, Michel De Paepe, Steven Lecompte 176

ID29 - Cost-effective option of cold energy utilization in pharmaceutical industry
Authors: Sindu Daniarta, Dawid Sowa, Ádám Havas, Attila R. Imre, Piotr Kolasinski 184

ID30 - Numerical investigation of a transonic dense gas flow over an idealized blade vane configuration
Authors: Aurelien Bienner, Xavier Gloerfelt, Paola Cinnella, Leander Hake, Stefan Aus Der Wiesche 193

ID31 - Comprehensive analysis of ORC-VCC system for air conditioning from low-temperature waste heat
Authors: Lukasz Witanowski 203

ID33 - Pareto front analysis for the design and the working fluid selection in ORC-based pumped thermal energy storage technology in both pure electric and cogenerative applications
Authors: Marco Astolfi, Dario Alfani, Andrea Giostri 214

ID36 - Evaluating the waste heat sources in a very large crude carrier and the potential integration of Organic Rankine Cycle configurations
Authors: Amalia Stainchaouer, Christopher Schifflechner, Christoph Wieland, Hartmut Spliethoff 224

ID37 - Investigating R1234ze and R1234yf as replacements to R134a in waste heat recovery ORC applications
Authors: James Bull, James Buick, Jovana Radulovic 234

ID38 - Performance and economic assessment of a thermally integrated reversible HP/ORC Carnot battery applied to data centers
Authors: Chiara Poletto, Andrea De Pascale, Saverio Ottaviano, Olivier Dumont, Maria Alessandra Ancona, Michele Bianchi 244

ID39 - Evaluation of the performance of multiple supercritical CO2 power cycles in Waste Heat Recovery applications
Authors: Hicham Chibli, Matthew Read, Abdulnaser Sayma 254

ID40 - Design and modeling of a demonstration-scale ORC cycle for the Liquid Air Combined Cycle
Authors: Owen Pryor, William Conlon, Aaron Rimpel, Milton Venetos 264

ID41 - Guidelines and optimization criteria of a machine learning-based methodology for mixture design in ORC systems
Authors: Valerio Mariani, Saverio Ottaviano, Andrea De Pascale, Giulio Cazzoli, Lisa Branchini, Gian Marco Bianchi 273

ID45 - Potential of trigenerative Waste Heat Recovery CO2-mixture transcritical power plants for increasing the sustainability of district heating and cooling networks
Authors: Mattia Baiguini, Michele Doninelli, Ettore Morosini, Dario Alfani, Gioele Di Marcoberardino, Paolo Giulio Iora, GiampaoloManzolini, Constante Mario Invernizzi, Marco Astolfi 282

ID46 - Thermodynamic analysis of a novel pumped thermal energy storage system with waste heat integration
Authors: Meiyan Zhang, Lingfeng Shi, Peng Hu, Gang Pei, Gequn Shu 294

ID48 - Pressure profile optimisation of a nozzle for wet-to-dry expansion
Authors: Pawel Ogrodniczak, Abdulnaser Sayma, Martin T. White 304

ID51 - Thermodynamic modification of CO2-based combined cooling and power cycle with ejector
Authors: Yonghao Zhang, Lingfeng Shi, Gequn Shu 313

ID53 - Selection of suitable working fluid and storage material for ORC coupled with Thermal Energy Storage
Authors: Dawid Sowa, Sindu Daniarta, Piotr Kolasinski 323

ID54 - Influence of dopant fluorination on the heat transfer behaviour of CO2-based mixtures in transcritical power cycles
Authors: Michele Doninelli, Gioele Di Marcoberardino, Costante Mario Invernizzi, Paolo Giulio Iora 333

ID57 - On air-cooled condensers for ORC systems operating with zeotropic mixtures
Authors: Lorenzo Galieti, Carlo De Servi, Dario Alfani, Paolo Silva, Paola Bombarda, Piero Colonna 344

ID58 - Experiments on supersonic ORC nozzles in linear cascade configuration
Authors: Marco Oliveti, Marco Manfredi, Giacomo Persico, Andrea Spinelli, Paolo Gaetani, Vincenzo Dossena 354

ID59 - Numerical analysis of aerodynamics and performance of a radial-inflow micro-ORC turbine
Authors: Fatemeh Ardaneh, Marta Zocca, Antti Uusitalo, Teemu Turunen-Saaresti 363

ID61 - ORC system using R1233zd(E) for waste heat recovery from the upstream process
Authors: Meng Soon Chiong, Bemgba Nyakuma, Nur Izwanne Mahyon, Srithar Rajoo, Eva Alvarez-Regueiro, Maria Esperanza Barrera-Medrano, Ricardo F. Martinez-Botas, Yossapong Laoonual 373

ID63 - Experimental investigation of a small-scale reversible high temperature heat pump – Organic Rankine Cycle system for industrial Waste Heat Recovery
Authors: Rahul Velanparambil Ravindran, Donal Cotter, Christopher Wilson, Ming Jun Huang, Neil Hewitt. 381

ID64 - Technical comparison and evaluation of a Pumped Thermal Energy Storage with two different designs
Authors: Márcio Santos, Jorge André, Ricardo Mendes, José Ribeiro. 391

ID68 - The potential of CO2-Plume Geothermal (CPG) Systems for CO2 component manufacturers: opportunities and development needs
Authors: Christopher Schifflechner, Jasper De Reus, Hartmut Spliethoff, Martin O. Saar, Sebastian Schuster, Dieter Brillert 400

ID69 - Development of a generalised low-order model for twin-screw compressors
Authors: Florian Kaufmann, Ludwig Irrgang, Christopher Schifflechner, Hartmut Spliethoff. 410

ID71 - Decision-making matrix for the selection of mixture in ORC applications
Authors: William Combaluzier, Nicolas Tauveron, Michel Beaughon, Aldo Serafino. 420

ID72 - Reversible heat pump-ORC pilot plant – Experimental results and fluid charge optimization
Authors: Maximilian Weitzer, Sebastian Kolb, Dominik Müller, Jürgen Karl 430

ID73 - Performance of Organic Rankine Cycle system in combination with residual municipal solid waste gasification: a simulation analysis
Authors: Luca Cioccolanti, Giovanni Biancini, Ramin Moradi, Luca Del Zotto, Matteo Moglie 439

ID74 - Enhancing knowledge of engineering students at all levels on organic rankine cycle systems for their application in the built environment
Authors: Luca Cioccolanti, Ramin Moradi, Ermira Abdullah, Syamimi Saadon, Mohamad Yusof Idroas, Teoh Yew Heng, Kwanchai Kraitong 449

ID75 - Studying carbon dioxide and acetone mixtures in a single-stage absorption-compression cycle for heating and cooling applications
Authors: Jesús Gómez-Hernández, Ali Kholghi, Mercedes De Vega, Javier Villa, Ronan Grimes 458

ID77 - Valorising thermal composite recycling processes using Organic Rankine Cycles for combined heat and power applications
Authors: Ramin Moradi, Liu Yang 466

ID80 – Prediction of the ideal maximum operational temperature of hydrocarbon and HFCs as working fluids of Organic Rankine Cycle power plants based on transition state theory
Authors: Wei Yu, Chao Liu, Xijie Ban, Zhirong Li, Tianlong Yan 476

ID82 - Comparison of different evaporator topologies for industrial heat pumps
Authors: Sanjay Vermani, Nitish Anand, Johan Van Bael, Evgueni Touliankine, Aldo Serafino, Carlo De Servi. 486

ID83 - On the plant improvement of Solar-driven ORC based power unit for domestic microcogeneration
Authors: Fabio Fatigati, Marco Di Bartolomeo, Arianna Coletta, Diego Vittorini, Giammarco Di Giovine, Davide Di Battista, Roberto Cipollone 496

ID84 - Mapping the techno-economic potential of next-generation CSP plants running on transcritical CO2-based power cycles
Authors: Pablo Rodríguez-deArriba, Francesco Crespi, Sara Pace, David Sánchez 505

ID86 - Achieving 45% micro gas turbine efficiency through hybridization with Organic Rankine Cycles
Authors: Antonio Escamilla, David Sánchez Martínez, Lourdes García-Rodríguez 515

ID88 - Operational optimisation of the main heat rejection unit of CSP plants based on carbon dioxide mixtures
Authors: Francesco Crespi, Pablo Rodríguez-deArriba, Lourdes García-Rodríguez, David Sánchez. 525

ID89 - Mechanical design and rotor-dynamic analysis of the ORCHID turbine
Authors: Matteo Majer, Steven Chatterton, Ludovico Dassi, Alessio Secchiaroli, Edoardo Gheller, Carlo De Servi, Paolo Pennacchi, Piero Colonna, Matteo Pini 535

ID91 - Thermodynamic feasibility of a pumped thermal energy storage driven by ocean temperature gradient
Authors: Alessandra Ghilardi, Andrea Baccioli, Guido Francesco Frate, Lorenzo Ferrari 545

ID92 - Exergy-based methods for heat pumps
Authors: Mathias Hofmann, Jonas Freißmann, Malte Fritz, Jeremias H. Alexe, Francesco Witte, George Tsatsaronis 553

ID93 - Reduced order modelling of optimized heat exchangers for maximum mass-specific performance of Airborne ORC Waste Heat Recovery units
Authors: Fabio Beltrame, Dabo Krempus , Piero Colonna, Carlo De Servi. 563

ID97 - Basic design of an ORC demonstrator system for implementation in an Iron & Steel plant through the DECAGONE project
Authors: Magnus Windfeldt, Han Deng, Trond Andresen, Christopher Schifflechner 574

ID98 - Analytical estimation of the presence of non-condensable gases in the condensate tank of an Organic Rankine Cycle
Authors: Radheesh Dhanasegaran, Antti Uusitalo, Juha Honkatukia, Teemu turunen-Saaresti 584

ID101 - Advanced control of compressor inlet temperature in supercritical CO2 Brayton cycle
Authors: Rui Wang, Xuan Wang, Hua Tian, Gequn Shu. 596

ID103 - Potential for surplus-heat-to-power conversion in current and future aluminium production processes with off-gas recycling
Authors: Jonas Bueie, Magnus Windfeldt, Trond Andresen. 605

ID104 - Investigating the application range of ORC power plants for the exploitation of two-phase geothermal resources
Authors: Tristan Merbecks, Claudio Pietra, Paola Bombarda, Martin O. Saar, Paolo Silva, Dario Alfani. 615

ID109 - Cold Energy Recovery in LNG plants with Organic Rankine Cycle
Authors: Gabriele Marchiori, Marta Giudici, Giorgia Ruffato, Marco Astolfi 626

ID110 - Numerical investigation of organic vapor flow effects on a micro-scale radial turbocompressor
Authors: Andrés Sebastián, Rubén Abbas, Manuel Valdés 636

ID112 - Design, modeling and simulation of an experimental Rankine PTES system
Authors: Mario Petrollese, Giorgio Cau, Matteo Marchionni, Marcello Lorenzo Marroccu, Rosa Merchan 645

ID113 - Small-scale turbopumps for Waste Heat Recovery applications based on an Organic Rankine Cycles, modeling, analytical and experimental investigation
Authors: Sajjad Zakeralhoseini, Jürg Schiffmann 655

ID116 - Double-stage ORC system based on various temperature waste heat sources of the negative CO2 power plant
Authors: Kamil Stasiak, Pawel Ziólkowski, Dariusz Mikielewicz 665

ID117 - Optimization of organic Rankine cycle in ocean thermal energy conversion based on NSGA-II
Authors: Zheng Hu, Jiufa Chen, Bing Guo, Chengbin Zhang 679

ID118 - TES4Trig: Development of a demonstrator for the production of electricity, heating and cooling based on an Organic Rankine and an Ejector Cooling Cycle driven by high-temperature parabolic trough collectors with thermal energy storage
Authors: Konstantinos Braimakis, Dimitrios Tziritas, George Stavrakakis, Julio Terrón Gutiérrez, Siddhart Dutta, Christos Xynos, Panagiotis Zervas, Sotirios Karellas 689

ID119 - Simulation and operation of a CSP that works with a HRB Cycle
Authors: Antonio J. Subires, Antonio Rovira 701

ID123 - Towards a green energy community: integration of micro-ORCs combined with renewable energy technologies in buildings
Authors: Diego Antonio Rodríguez Pastor, Víctor Manuel Soltero Sánchez, Elisa Carvajal Trujillo, José Antonio Becerra, Ricardo Chacartegui 713

ID129 - Assessment of high temperature heat pump layouts equipped with a bladeless turboexpander
Authors: Matteo Passalacqua, Simone Maccarini, Stefano Barberis, Alberto Traverso 723

ID133 - Selection of the optimal working fluid in an Organic Rankine Cycle for Waste Heat Recovery through multi-objective optimization and decision making
Authors: Bipul Krishna Saha, El Mouatez Billah Messini, Syed J. Hoque, B Aneesh Bhat, Pramod Kumar 733

ID139 - Dual condensing pressure ORC for cryogenic energy storage
Authors: William M. Conlon, Milton J. Venetos 743

ID141 - Optimum coupling of thermal energy storage and power cycles for Carnot batteries
Authors: Salvatore Guccione, Rafael Guedez 751

ID142 - Aerodynamic design and numerical analysis of a counter-rotating centrifugal compressor
Authors: Cheikh Brahim Abed, Arthur Leroux 761

ORC SEVILLE 2023
7th International Seminar on O.R.C. Power Systems

© 2024 Editorial Universidad de Sevilla. Este es un artículo de acceso abierto distribuido bajo los términos de la licencia de uso y distribución Creative Commons (BY-NC-ND 4.0)

DOI: https://dx.doi.org/10.12795/9788447227457_3

ADDITIVE MANUFACTURING FOR FAST PROTOTYPING OF A VELOCITY COMPOUNDED RADIAL RE-ENTRY TURBINE

Dominik Stümpfl[1,*], Karel Ráž[2], Philipp Streit[1], Andreas P. Weiß[1]

[1] *East-Bavarian Technical University of Applied Sciences Amberg-Weiden, Center of Excellence for Cogeneration Technologies, Amberg, Germany*
[2] *University of West Bohemia, Regional Technological Institute, Pilsen, Czech Republic*

*Corresponding Author: d.stuempfl@oth-aw.de

ABSTRACT

In order to achieve a drastic reduction in CO_2 emissions to limit global warming, it must be possible to globally cover the electricity demand from renewable sources. However, the fluctuating availability of solar and wind energy will nevertheless make it necessary to complement the renewables by thermal power plants. Additionally using e.g., the potentials of waste, biomass or waste heat from industrial processes locally in Organic Rankine Cycle (ORC) power plants is a promising approach to finally achieve a stable and sustainable electricity supply. In the present work, therefore, different variants of a radial, velocity compounded re-entry cantilever turbine (Elektra turbine) are investigated regarding their potential for such applications. The paper concentrates on the fast prototyping of an existing 5 kW air turbine demonstrator, recently developed by the authors, by using the possibilities of additive manufacturing with plastic materials to substitute essential parts of the flow geometry. In this context the approach to implement the plastic parts in the turbine is explained. Experimentally determined efficiency parameters of various 3D-printed deflection channel modifications and a printed plastic wheel made of PA12GB are presented, discussed, and compared to the fully milled metal turbine. This results in a quantification of the additional losses due to the higher inaccuracies and roughness of the printed parts, which can be taken into account in further investigations. Furthermore, the various problems and hurdles that must be observed when using 3D-printed plastic parts in high-speed turbomachines are highlighted. With regard to the rotor wheel, the authors conclude that the use of additively manufactured plastic wheels is only feasible with increased preliminary testing. The time required for this is usually not in proportion to the manufacturing time and costs saved. For the stator parts however, 3D-printing turned out to be a reasonable approach.

1 INTRODUCTION

A worldwide shift away from fossil fuels like coal and oil is imperative to address the climate change. In this context, more and more politicians, industry and households recognize the value of renewable energy sources and of a distributed electricity and heat generation that can be adapted to demand, as this ensures sustainable and independent security of supply. Apart from wind and solar energy, that due to strong fluctuations cannot provide all the necessary electricity supply, thermal power plants will still play an important role in the future. However, these future thermal power plants will rely on renewable energy sources like for example, geothermal sources, biomass or waste heat in general. The latter are available decentralized, for example in industrial plants or households, and in small power units. To make these distributed sources usable, thermal power plants that operate in the range of a few megawatts, a few 100 kilowatts or even less than 100 kW_{el} are required. For this purpose Organic Rankine Cycle (ORC) plants based on turbines as expander are suitable (Weiß, 2015). As the energy sources are available in various forms and in different quantities, turbines for these plants must be easily adaptable to different applications and profitable in terms of specific costs. For such small outputs, however, the components of large steam power plants (10 - 1000 MW) cannot be just easily scaled

down, which is why alternative energy conversion machines must be used or developed for this purpose (Weiß *et al.*, 2020). In this context the present work deals with the experimental investigation of a radial, velocity compounded re-entry turbine, the so-called Elektra turbine, patented as “Elastic Fluid Turbine” by (Kolb, 1907).

In the opinion of the authors, this type of turbine seems promising for an application in small-scale ORC power plants as the requirements and framework conditions have changed compared to recent decades. At the beginning of the 20th century, velocity compounded re-entry turbines, like the Elektra, were widespread and were produced in Europe by various companies (Meuth, 1910). As early as (Stodola, 1905), among others, presented results of a 30 kW Elektra turbine with a rotational speed of about 3,000 rpm. These simple turbines were used as direct drives for fans and pumps on ships and their exhaust steam could be reused for preheating in the ship's steam propulsion system. Accordingly, the efficiency of these turbines was not crucial. Due to the increasing demand for energy and the resulting emergence of ever larger, centralized steam power plants, the Elektra has been nearly forgotten since the 1960s.

The aim of our research team is primarily to improve the isentropic expansion efficiency of a 5 kW Elektra turbine demonstrator operated with compressed air by optimizing the flow-mechanically effective geometries. For this purpose, the geometry of an Elektra turbine already designed, manufactured and investigated in earlier studies of the authors (Weiß *et al.*, 2020; Weiß *et al.*, 2022) is adapted for the use of additive manufactured plastic flow guiding geometries in order to enable a fast and easy prototyping and quickly identify further potentials for improvement on the laboratory's own compressed air test bench.

The Elektra turbine belongs to the genus of impulse turbines. With the help of Figure 1, the essential components and the functional principle of the Elektra turbine are explained. It is characterized by the fact that the energy of the gaseous working medium, flowing into the turbine at (a), is almost completely converted from high pressure into high velocity in a supersonic nozzle (Laval nozzle (c)). The resulting kinetic energy is then converted into mechanical work in only one impeller by radially passing through it several times from both sides. Therefore, the flow is alternately reversed and guided back through several deflection channels (d, e, f). The turbine shown works with four-wheel passes and thereby with four velocity stages. This concept is called velocity compounding.

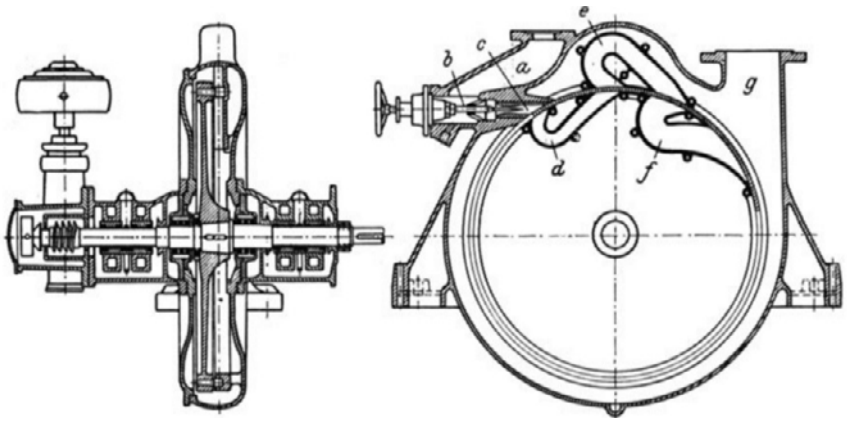

Figure 1: Exemplary structure of an Elektra turbine; a turbine inlet; b nozzle needle; c nozzle; d, e, f deflection channels; g turbine outlet (Pfleiderer and Petermann, 1991)

In order to have space for several deflection channels, the turbine is partially admitted. That means only a small area of the impeller in relation to the circumference is directly impinged by the nozzle. Also, the coverage by the other wheel passages is relatively small. This is possible because the pressure is already completely converted into velocity in the nozzle, which means that there is no more pressure drop over the rotating blades. The wheel diameter can thus be increased, without the need to reduce the blade heights too much, according to the requirements. This is only limited by the available installation space, whereby very low rotational speeds can be implemented. (Zietemann, 1930)

The Elektra concept is right now no longer state of the art and has no more fields of application. However, the authors want to prove that this kind of turbine has potential to contribute to a distributed

electricity generation in the power range of a few kilowatts. Initial results of a numerical and an experimental investigation of the Elektra, discussed and further developed in this paper, were already published in (Weiß *et al.*, 2020). Also the Laboratory of Turbomachines at the Eastern Bavarian Technical University of Applied Sciences Regensburg collaborates with our team in developing a new, advanced Elektra turbine (Janischowsky *et al.*, 2022).

The Elektra has some outstanding properties that make its use in modern small-scale power plants appear sensible. Since the specific acquisition costs [€/kW] are much more important than the achievable efficiency in the power range < 100 kW_{el}, the Elektra turbine is predestined for such applications (Zietemann, 1930). The waste heat from the turbine can still be used on site for heating or cooling purposes, which is why the low efficiency of the Elektra does not have to be a serious disadvantage (Weiß *et al.*, 2020). Depending on the number of velocity stages, rotational speeds of 3,000 rpm or lower can be implemented with the Elektra concept. This makes it possible to apply commercially available standard generators (1,500 – 6,000 rpm). Until now, turbines generally require an expensive high-speed generator and frequency converter, which contribute about 2/3 to the specific cost of the entire turbogenerator (1,000 – 1,500 €/kW_{el}). (Weiß *et al.*, 2022)

Of course, volumetric expanders like scroll, screw or rotary vane expanders can easily be implemented with a rotational speed of 3,000 rpm and similar expansion efficiencies like an Elektra turbine. However, the basic architectures of positive displacement expanders are more complicated. Screw expanders consist of two rotors i.e., they need four bearings and a clutch to the generator. Rotary vane expanders are equipped with sliding vanes which generate friction and suffer from high wear – also a clutch is needed. The single Elektra wheel can be mounted directly on the generator shaft. This is also possible for a scroll expander. However, like for the other volumetric expanders, the built in volume ratio (<< 10) of scroll expanders limits their application to rather low temperature ratios in ORC. Furthermore, all positive displacement expanders need lubrication which spoils the organic working fluid. All these disadvantages do not apply to a turbine. (Weiß, 2015)

However, the question of whether an Elektra turbine can be implemented that directly drives a standard generator and at the same time achieves a still acceptable isentropic expansion efficiency must be clarified. The early Elektra turbines achieved efficiencies well below 50% at outputs of around 30 kW (Stodola, 1905; Meuth, 1910). In this context, the question also arises at what power levels these requirements can be met. The Elektra can only be used sensibly in a power range < 100 kW_{el}. The smaller the nominal power required, the more the advantages of the Elektra concept over standard turbines come into play. (Weiß *et al.*, 2022)

With the methods of computational fluid dynamics (CFD), computer-aided investigation options and improved manufacturing processes available today, it should be possible to develop significantly better turbines than it was the case in the first half of the 20th century. In addition, additive manufacturing in combination with plastic materials offers enhanced possibilities for the development of modern Elektra turbines. Therefore, it is used in this work to test various versions of an Elektra turbine on the test stand.

2 MATERIALS AND METHODS

The investigation of the Elektra turbine presented in this publication directly follows on from the findings in (Weiß *et al.*, 2022) and (Weiß *et al.*, 2020) and continues this work. Accordingly, this investigation also follows the same design process as presented in (Weiß *et al.*, 2022). The difference to previous studies is that the hurdles for manufacturing and experimental testing have been reduced due to the use of additive manufacturing.

2.1 Elektra Design Tools

In the scope of the Elektra investigation, different design tools were used, which were already described in detail in (Weiß *et al.*, 2022) and will therefore only be listed. The design process of the Elektra turbine under investigation began with the predetermination of the geometry parameters using an in-house one-dimensional turbine design tool (1DTDT), which enables a rapid calculation of the geometry data, power output and turbine efficiency for various turbine types. Table 1 illustrates the most important characteristics of the investigated Elektra turbine, which also served as input data for the 1DTDT.

Table 1: Input data for the 1DTDT with values for the Elektra turbine (Weiß *et al.*, 2022)

Input data	Unit	Elektra turbine
Working fluid	-	pressurized air
Total inlet pressure	kPa	1,000
Total inlet temperature	K	≈ 293
Required mass flow rate	kg/s	0.065
Static exit pressure	kPa	≈ 100
Wheel diameter	m	0.08
Rotational speed (Design Point)	rpm	29,000

The 1DTDT provides essential parameters of the turbine flow geometry, like e.g., number of blades, blade angles and channel heights that were elaborated into a complete test turbine. For the numerical optimization, simulations of the flow in the turbine were carried out using CFD. These enabled a fast investigation of various flow geometries before some promising variants were manufactured and measured on the test bench. After identifying optimization potentials, the turbine geometry was adjusted in the CAD program or directly in the CFD environment and iteratively improved. The tool of choice was the Fine™/Turbo package from Cadence. As the numerical optimization using 3D CFD simulations is not the primary topic of this paper the interested reader is referred to (Weiß *et al.*, 2020; Weiß *et al.*, 2022) for more details on the simulations and mesh design.

2.2 Printing Materials and Methods

The focus of this work lies on the implementation and experimental investigation of several 3D-printed plastic deflection channels and wheels. The aim is to establish a process to enable rapid measurement of different printed geometries and an iterative improvement of the turbine efficiency in experiments. Additive manufacturing is a new technology that finds its way in ever more fields of applications. Especially in turbomachines, there are various potentials to establish 3D-printed parts in the development phase as well as in the final product. The demanding operational conditions, like e.g., high temperatures and pressures and demanding safety standards make an application of printed parts challenging, especially when using plastics (Novotny *et al.*, 2019). However there are investigations done in this field (Hernandez-Carrillo *et al.*, 2017; Spale *et al.*, 2021) and 3D-printed metal parts are already being used in turbomachinery, e.g., for non-safety-relevant parts of aircraft engines.

This work was carried out in cooperation with the Regional Technological Institute (RTI) at the University of West Bohemia in Pilsen, which has many years of experience and technical production possibilities in the field of adaptive manufacturing with plastics and metals. Based on this experience, the material PA12GB (40% glass bead filled polyamid) was chosen. PA12GB combines good material properties in terms of tensile strength and machinability, and with the printer used (Hewlett Packard Jet Fusion 4200), high accuracy can be achieved at reasonable cost. This printer has an effective build volume of 380x284x380 mm with a maximal building speed of 4115 cm^3 per hour. It is creating the final part by a multi-agent printing process from a plastic powder. Main advantage is the isotropic behavior of the material and speed of production. Furthermore, no supporting structures are necessary, so the post processing is limited to a minimum. Table 2 shows some essential specifications of the material from the manufacturer's data sheet.

Table 2: Technical specifications of PA12GB (HP Development Company, 2017)

Measurement	Value	Method
Powder melting point	186 °C	ASTM D3418
Density of printed parts	1.3 g/cm³	ASTM D792
Tensile strength, max load, XYZ	30 MPa	ASTM D638
Tensile modulus, XY	2800 MPa	ASTM D638
Tensile modulus, Z	2900 MPa	ASTM D638
Elongation at break, XYZ	6.5 %	ASTM D638
Izod impact notched (@ 3.2 mm, 23°C), XYZ	2.7 KJ/m²	ASTM D256 Test Method A

Heat deflection temperature (@ 0.45 MPa), Z	173 °C	ASTM D648 Test Method A
Heat deflection temperature (@ 1.82 MPa), Z	121 °C	ASTM D648 Test Method A

2.3 Elektra Turbine Design and Methods of Experimental Investigation

The compressed-air Elektra turbine studied here serves as a technology demonstrator on which the development process and tools can be tested and validated, so that they can subsequently be used for the design of larger Elektra turbines in ORC. For this reason, speeds suitable for standard generators (1,500 – 6,000 rpm) have not yet been targeted. This would require four velocity stages and a significantly larger wheel diameter. The turbine investigated in this paper represents the first design of an Elektra turbine of the authors, which is why, for the sake of simplicity, an Elektra with only two wheel passages was investigated. Furthermore, the turbine variants were designed to be tested on the compressed air test stand of the "Turbomachinery" laboratory at the Technical University Amberg-Weiden. Therefore, power and size had to be chosen according to the capacities of the test stand.

Figure 2 b) shows the flow paths of the Elektra version presented in (Weiß *et al.*, 2022). Three nozzles, with an offset of 120° to each other and with an inlet flow angle of 23.07° direct the working medium towards the wheel at supersonic speed. The flow is diverted through three channels, passes the wheel a second time and then flows into the surroundings via three separate outlet areas. The impeller diameter is quite small in relation to the nozzle and channel width. This allows the turbine to be kept compact. However, this also leads to limitations in the dimensioning of the deflection channel. Therefore, they are equipped with splitter blades to improve the guidance of the flow in the channels.

In order to investigate new geometries of the deflection channel faster and easier, a modular structure of the stator was implemented. In addition, the printed wheels could not be mounted directly on the shaft. The different properties of the materials would not guarantee an equal shaft-hub connection compared to the original aluminum wheel and thus the occurring torque cannot be transmitted. For this reason, the wheel is mounted to the shaft via an aluminum adapter on which it can be easily screwed (see Figure 2 a)).

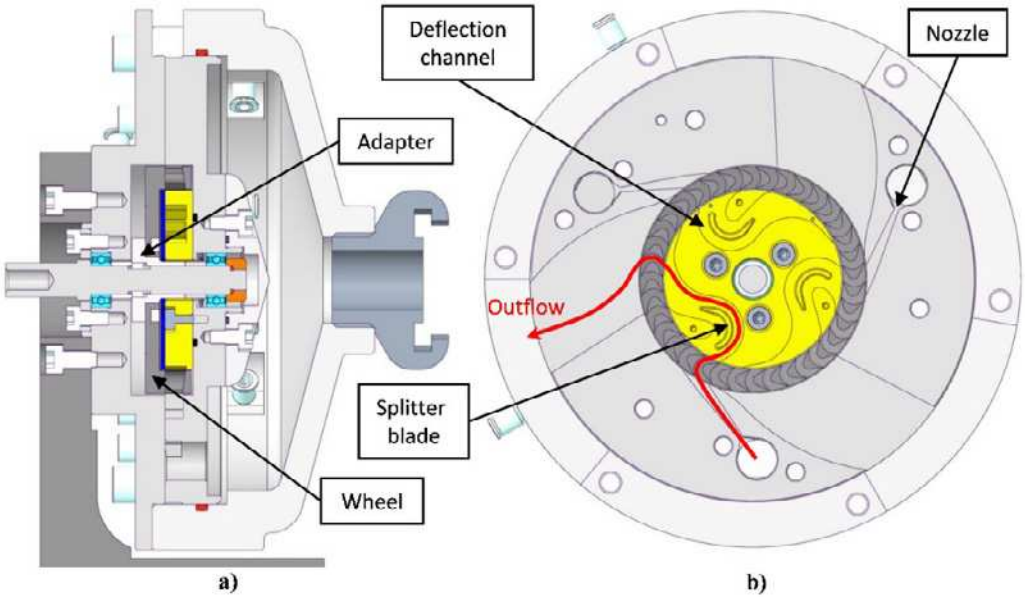

Figure 2: Sectional views of the examined Elektra turbine

Several Elektra versions, also equipped with an additively manufactured metal wheel, were already investigated experimentally on the compressed air test stand. In order not to go beyond the scope of this paper, this will not be discussed in detail. For more information on these versions and the test stand the interested reader is referred to (Weiß *et al.*, 2022). From the evaluation of the measured values obtained for mechanical power, pressures at the inlet and outlet of the turbine, temperature as well as mass flow rate through the turbine, conclusions can be drawn about the total-to-static isentropic expansion efficiency of the turbine configuration.

3 RESULTS

Four different modifications have been experimentally investigated starting from the best performing version (*Version 1*) presented in (Weiß *et al.*, 2022), that is characterized by a milled aluminum wheel and a milled aluminum deflection channel with splitter blades of 1.5 mm thickness. *Version 1* is used as a reference. *Version 2a, 2b* and *2c* have exactly the same flow geometry like *Version 1*, that is shown in Figure 2 b). Differences are the thickness of the splitter blade that is varied from 0.5 – 1.5 mm and the used material, which is PA12GB for the defelction channel. *Version 3* additionally has a printed wheel made of PA12GB in combination with the printed deflection channel with 1.5 mm splitter blades. Figure 3 shows the milled aluminum wheel (Figure 3 a)) and the printed plastic wheel (Figure 3 b)) in comparison for a better understanding of the differences. The printed deflection channels are not graphically displayed, because they have a fixed cover on both sides which means that pictures of it do not add any valuable information. The versions are listed again below with their characteristic distinguishing features:

- *Version 2a*: *Version 1* with printed deflection channel and splitter blade (1.5 mm)
- *Version 2b*: *Version 1* with printed deflection channel and splitter blade (1.0 mm)
- *Version 2c*: *Version 1* with printed deflection channel and splitter blade (0.5 mm)
- *Version 3*: *Version 1* with printed wheel/deflection channel with splitter blade (1.5 mm)

Figure 3: Comparison of: a) milled aluminum wheel (*Version 2 a, 2b and 2c*) and b) 3D printed plastic wheel (*Version 3*)

3.1 FEM and Modal Analysis of Critical Structures

In order to ensure the usability of PA12GB at speeds of up to 30,000 rpm before the first experimental investigations, finite element method (FEM) simulations of the wheel (Figure 4) and the shaft-hub connection (Figure 5), as well as a modal analysis of the wheel were carried out by the RTI. For the investigations, the software Siemens NX version 2000 with build 3701 was used. The used solver was NX Nastran with solution option solver 101 and solver 103.

The maximum stresses in the wheel are approx. 31 MPa. However, these only occur sporadically at points where no radii were applied in the CAD model. In general, the stresses are well below the load limit of 30 MPa, which makes it possible to use the wheel without any problems. This was also confirmed with a burst test that was carried out on a specially created test set-up, on which the wheel including adapter and shaft was operated at 30,000 rpm outside the turbine in order to avoid damage to the stationary parts. The maximum displacement is approx. 0.29 mm in radial direction, what is in an acceptable range as the gap between rotor and stator is 0.5 mm. In addition to that, a modal analysis of the wheel was carried out. It resulted in a 1. Eigen frequency of the wheel at 837 Hz, which is far away from 500 Hz (30,000 rpm). Furthermore, the designed connection between shaft and hub (adapter with mounted printed wheel) was investigated concerning stress and displacement. Therefore, it was loaded with a torque of 2.5 Nm resulting from former experimental investigations. The maximal stress within the aluminum adapter was 81.76 MPa and 5.02 MPa within the 3D printed wheel (see Figure 5). Both values are significantly below the materials strength limits.

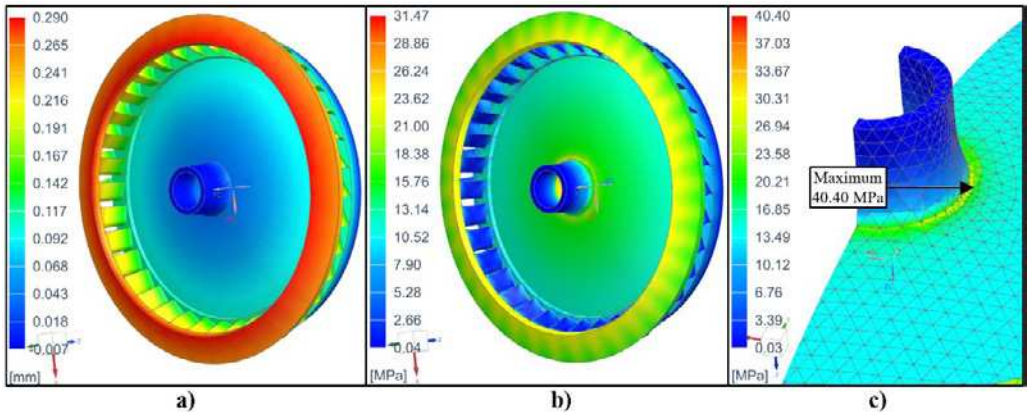

Figure 4: FEM-Simulation results of the rotating plastic wheel at 30,000 rpm: a) Displacement – Nodal Radial; b) Stress Element – Nodal Averaged, Von-Mises; c) Maximal Stress before averaging

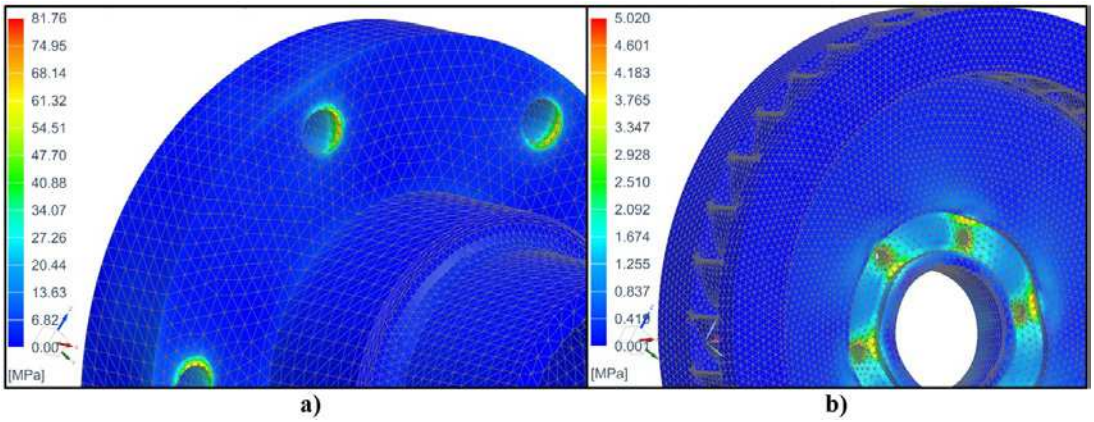

Figure 5: FEM-simulation results of shaft-wheel connection: a) Stress-Element in the adapter – Nodal Averaged, Von-Mises; b) Stress-Element in the wheel –Nodal Averaged, Von-Mises

Apart from that, the different splitter blade thicknesses were checked regarding stresses due to pressure differences in the deflection channel. Therefore, they were loaded with static pressure data from the CFD-simulation. For the printed parts, a cover and therefore a fixed connection between hub and splitter blades is applied. For that reason, no problems regarding the stress in the splitter blades were detected even with only 0.5 mm blade thickness.

3.2 Experimental Investigation

The three printed deflection channels with different splitter blade thicknesses (*Version 2a*, *2b* and *2c*) as well as the printed plastic wheel combined with a printed deflection channel (*Version 3*) were tested on the compressed air test stand. Figure 6 shows the resulting total-to-static isentropic efficiencies as a function of the applied pressure ratios (PR; turbine inlet to outlet) for a constant rotational speed of 30,000 rpm. The maximum measurement deviation of the isentropic efficiency is graphically displayed as an error indicator. The results of *Version 1* (milled aluminum wheel and milled deflection channel with 1.5 mm splitter blades) serve as reference to quantify the deviations between milled metal and printed plastic parts, which were expected due to different surface qualities.

It is obvious, that the rougher surface of the printed deflection channels results in a reduction of the efficiency. In case of the 1.5 mm splitter blade channel (*Version 1*) this deviation to *Version 2a* rises with rising PR starting from no deviation below PR = 6 (deviation within the measuring tolerance) up to approx. 3 $\%_p$ at higher PR's. Surprisingly the reduction of the splitter blade thickness did not reduce the pressure losses. The splitter blade has nearly no influence (comparing *Version 2a*, *2b* and *2c*) on the efficiency for PR > 9. Below that point the deflection channel with 1.5 mm splitter blades (*Version 2a*) still achieves the best efficiencies.

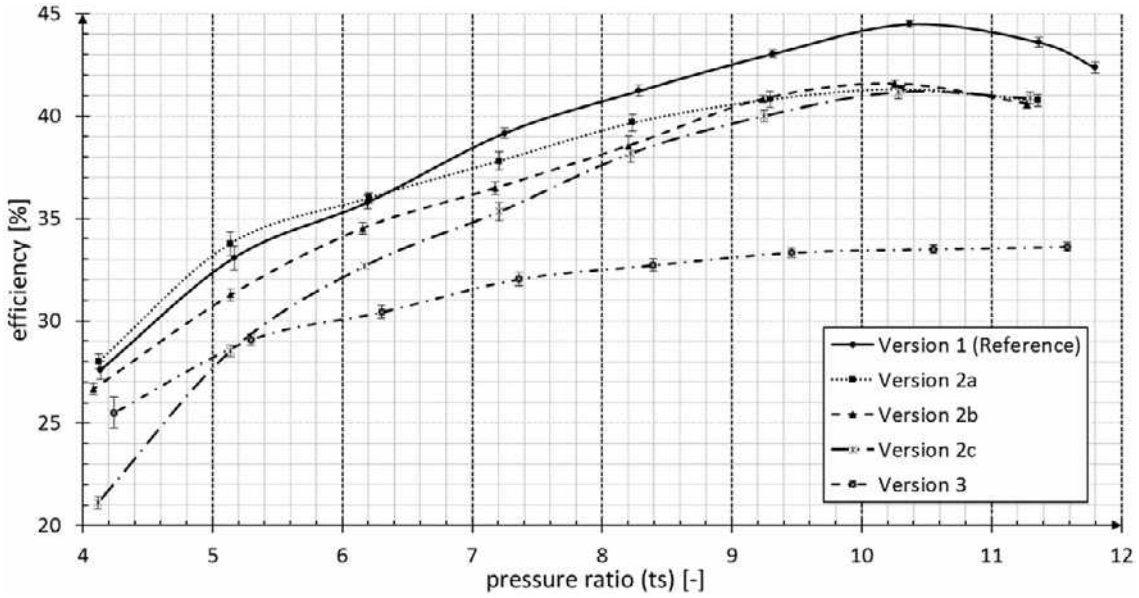

Figure 6: Measured total-to-static isentropic efficiency over PR for different Elektra versions

The flow geometries of the 3D-printed parts made of PA12GB, that could not be reworked after printing, have an average roughness of Ra = 7.8 µm. The relevant surfaces of the aluminum wheel are in a range of Ra = 1.8 µm and the milled channel achieves approx. Ra = 0.4 µm. Figure 7 a) and b) show the surface texture of the 3D printed wheel. The milled aluminum wheel, which was additionally glass bead blasted, shows a much more even surface (Figure 7 c) and d)).

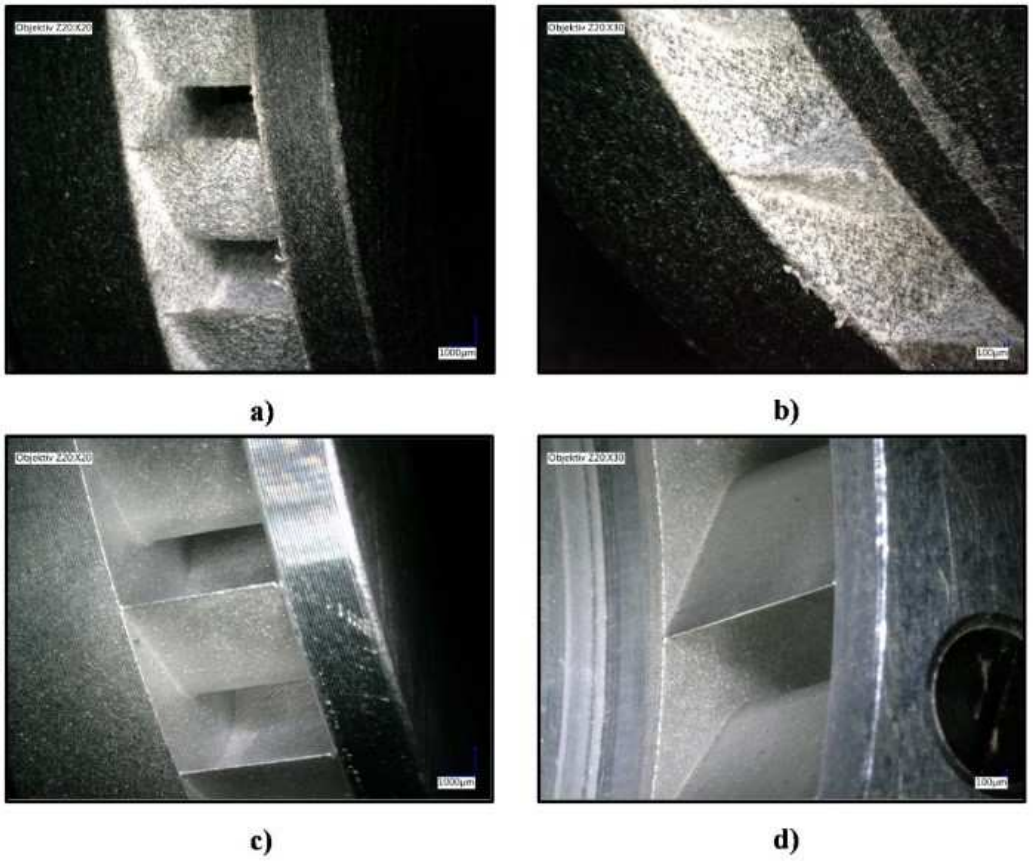

Figure 7: Surface texture of: a) Printed rotor overview; b) Printed rotor detailed view; c) Milled rotor overview; d) Milled rotor detailed view

The testing of the printed wheel (*Version 3*) caused various problems with a view to balancing. Reworking of the material is quite challenging as the plastic tends to smudge if the machining temperature gets too high. The reworking of some surfaces is nevertheless necessary to ensure the required form and position tolerances for a smooth running of the wheel. Furthermore, a tumbling of the wheel due to insufficient plan areas was detected during balancing. Additional balancing of the shaft was required to counteract this. Finally, the remaining static and dynamic imbalances could be reduced to a sufficient balancing grade, to run the printed wheel at 30,000 rpm. Higher rotational speeds could not be tested as the wheel might have been damaged. Nevertheless, the original plastic wheel geometry could be measured in the scope of this work (*Version 3*). Thus, the additional losses compared to the aluminum version can also be quantified here, which are approx. 3.5 $\%_p$ at PR = 4.4 compared to *Version 2a*. They constantly increase up to more than 7 $\%_p$ at higher PR's.

4 DISCUSSION

Additional losses of printed deflection channels due to the inaccuracies and rougher surfaces of the printed parts occur as expected and can now be quantified and factored into testing of further channel designs. The reduction of the splitter blade thickness didn't show the desired effect of increasing the efficiency compared to *Version 2a*. Reasons for that could be different surface qualities of the printed parts depending on position and location in the printer, which might compensate the advantages of reduced pressure losses by thinner blades. For further improvements of the efficiency the geometry changes must be more significant. The use of the printed plastic wheel resulted in a drastic reduction of the efficiency, which can now be calculated into further investigations and might be acceptable if manufacturing is significantly quicker and cheaper. However, it turned out that the unavoidable reworking and balancing of the printed plastic wheels is quite challenging. First, the less isotropic structure of the printed plastic wheel implies more imbalances compared to a milled metal wheel. Second, the fit between the printed plastic wheel and the necessary aluminum hub is crucial. If it is not tight, balancing is not sustainable or even not possible at all. However, the plastic tends to yield to internal stresses caused by the fits to the adapter, which means that the required fits cannot be maintained exactly. Additionally, the axial runout and the tolerances of the abutment surfaces must have the same quality as metal wheels, which is difficult to achieve by reworking. This causes a tumbling of the wheel and therefore a touching of the housing wall mainly in axial direction.

21

5 CONCLUSIONS

The investigation of the Elektra turbine using additive manufacturing to speed up the design process brought forth some interesting findings. Especially the testing of new deflection channels can now be carried out significantly faster and more cost-effective compared to milled metal parts. However, one must take into account the additional friction losses due to the rougher surface of printed PA12GB that can vary in a certain range. Further tests are required to fully capture these influences. Nevertheless, a further investigation of different stator geometries seems meaningful. However, for rotating parts at these high speeds the "fast" prototyping using additive manufacturing with plastics caused lots of unexpected problems. The time required to achieve a functional turbine structure and to record all the variables influencing the behavior of the wheel is disproportionate to the costs and time saved by fast and inexpensive additive manufacturing. In the opinion of the authors, the investigation of wheel prototypes for high-speed turbines is therefore not sensible. At the actual speeds of 1,500 – 6,000 rpm intended for the Elektra, on the other hand, the use of plastic wheels would be quite interesting. Here, the balancing of a printed plastic wheel should no longer cause problems. However, in a final application, to evaporate the working fluid in an ORC, often requires temperatures at or above the melting temperature of most plastics. This might again lead to problems when using plastic wheels. Regarding the use of the Elektra in modern ORC plants in the power range <100 kW_{el} the authors state, that the limited power and size of the investigated turbine make it difficult to further increase the efficiency of the small 5 kW Elektra demonstrator. In the future, the focus will therefore lie on the development of Elektra turbines that are suitable for use in ORC systems and operate at the targeted rotational speeds. A commonly manufactured metal 7.5 kW Elektra turbine (wheel diameter Ø D = 255

mm) that operates at 3,000 rpm in a woodchip fired combined heat and power ORC plant (working fluid hexamethyldisiloxan) is currently under testing. The results will be published as soon as available.

NOMENCLATURE

CO_2	Carbon dioxide	(–)
ORC	Organic rankine cycle	(–)
3D	Three-dimensional	(–)
CFD	Computational fluid dynamics	(–)
1DTDT	1D turbine design tool	(–)
CAD	Computer aided design	(–)
PA12GB	Polyamid 12 glass bead filled	(–)
FEM	Finite element method	(–)
PR	Pressure ratio (total-to-static)	(–)
Ra	Mean roughness	(µm)

Subscript

el	electric
p	points

REFERENCES

Hernandez-Carrillo, I., Wood, C.J., Liu, H., 2017, Advanced materials for the impeller in an ORC radial microturbine, *Energy Procedia*, vol. 129: p. 1047-1054.

HP Development Company L. P., 2017, Datasheet PA12GB, Online available: https://cimquest-inc.com/resource-center/HP/Materials/HP-PA12GB-Datasheet.pdf (accessed 23 May 2023).

Janischowsky, F., Stümpfl, D., Streit, P., Weiß, A.P., Lesser, A., 2022, CFD Simulation and Flow Study of a Velocity Compounded Radial Re-Entry Turbine - Elektra, *MATEC Web Conf.*, vol. 367, no. 12.: p. 1-11.

Kolb, O., 1907, Elastic Fluid Turbine, U.S. Patent 842,211.

Meuth, H., 1910, The Elektra Steam Turbine, *J. Am. Soc. Nav. Eng. inc.*, vol. 22: p. 402–416.

Novotný, V., Špale, J., Stunova, B.B., Kolovratnik, M., Vitvarova, M., Zikmund, P., 2019, 3D Printing in Turbomachinery: Overview of Technologies, Applications and Possibilities for Industry 4.0, *ASME Turbo Expo Conf. Proc.*, vol. 6: p. 1-9.

Pfleiderer, C., Petermann, H., 1991, *Strömungsmaschinen*, Springer, Berlin, 597 p.

Špale, J., Novotný, V., Mares, V., Weiß, A.P., 2021, 3D printed radial impulse cantilever micro-turboexpander for preliminary air testing, *AIP Conf. Pro*., vol. 2323, no. 70002: p. 1-10.

Stodola, A., 1905, *Die Dampfturbinen*. Springer, Berlin, 460 p.

Weiß, A.P., 2015, Volumetric expander versus turbine - which is the better choice for small ORC plants? *ASME ORC Conf. Proc.*, vol. 3, no. 22: p. 1-10.

Weiß, A.P., Streit, P., Popp, T., Shoemaker, P., Hildebrandt, T., Novotný, V., Špale, J., 2020, Uncommon turbine architectures for distributed power generation - development of a small velocity compounded radial re-entry turbine, *Arch. Thermodyn.* vol. 41: p. 235-253.

Weiß, A.P., Stümpfl, D., Streit, P., Shoemaker, P., Hildebrandt, T., 2022, Numerical and Experimental Investigation of a Velocity Compounded Radial Re-Entry Turbine for Small-Scale Waste Heat Recovery, *Energies*, vol. 15, no. 245: p. 1-22.

Zietemann, C., 1930, *Berechnung und Konstruktion der Dampfturbinen: Für das Studium und die Praxis*, Springer, Berlin. 469 pp.

ACKNOWLEDGEMENT

The authors like to thank the "*Technology- and Science Network Upper Palatinate*" (*TWO*) for the funding in the project "*UnoTur*" (*Unorthodox Turbines*). Furthermore, the authors like to thank for the funding by the Bavarian-Czech-Academic-Agency (BTHA) in the project "*TurPri*" (*Printed Turbines*).

ORC SEVILLE 2023
7th International Seminar on O.R.C. Power Systems

© 2024 Editorial Universidad de Sevilla. Este es un artículo de acceso abierto distribuido bajo los términos de la licencia de uso y distribución Creative Commons (BY-NC-ND 4.0)

DOI: https://dx.doi.org/10.12795/9788447227457_4

THERMODYNAMIC CONCEPT OF A NOVEL RECUPERATIVE TWO-PHASE POWER CYCLE

Bederna, Benedikt G. [1,*], Barta, Riley B.[1], Thomas, Christiane[1]

[1] *Technische Universität Dresden,*
Bitzer-Professur für Kälte-, Kryo- und Kompressorentechnik,
01062 Dresden, Deutschland

*Corresponding Author: benedikt.bederna@tu-dresden.de

ABSTRACT

The transformation of renewable or waste heat into mechanical power by the Organic Rankine Cycle (ORC) has become established as a robust and cost-effective technology. However, it must be considered that these applications normally come with a limited temperature difference between the source and the sink, which is why the maximal achievable thermal efficiency is already low in comparison with conventional power plants. In addition, this Carnot efficiency is not achievable by real ORC systems. The reasons for this are not only irreversible components or the necessary temperature differences for heat absorption or rejection, but also the need of preheating the working fluid, which is an immanent characteristic of the Rankine process itself. Thus, the mean temperature of heat absorption differs from that of a Carnot process, resulting in a limited second law efficiency. This publication describes a novel thermodynamic power cycle with the aim of completely avoiding preheating losses, which is called the Recuperative Two-Phase Power Cycle (PC-RTPC). Regarding the state changes, the process resembles the concept of the Ericsson cycle. Deviating from it, the working fluid undergoes a phase change, which implies significant advantages compared to a process using a gaseous working fluid. This is made possible by a non-linear zeotropic mixture composed of a main and an ancillary working fluid. The key element is an internal heat exchanger, which separates the two temperature levels of the source and the sink, while on its low-pressure side a condensation takes place. The primary technical challenge is an expansion into the two-phase region. For the basic cycle, which is intended to convert latent heat sources, an isothermal expansion is required. For the conversion of the sensible heat source this challenge could be avoided. This work illustrates the concept of such a cycle by a theoretical investigation and an exemplary working fluid selection for a latent heat source of 100 °C. The endoreversible cycle with an isothermal expansion is able to reach a second law efficiency of 85.8% applied to the source and sink temperatures.

1 INTRODUCTION

The transformation of renewable or waste heat into mechanical power by the Organic Rankine Cycle (ORC) has become established as a robust and cost-effective technology. Nowadays, it is used for a range of applications, however, the currently unused technical potential is still much larger. A dominating obstacle for its usage is that the majority of applications offer only limited temperature differences between the source and the sink. That is why the maximal achievable thermal efficiency is already low in comparison with conventional power plants. In addition, this Carnot efficiency is not reachable by real ORC plants, and the second law efficiencies are normally even lower than those of conventional power plants. This results in a double negative effect that the circumstance of small temperature differences and the technology itself lead to poor thermal efficiencies, and thus to insufficient economic feasibility in many cases. Therefore, the only option to raise the thermal efficiency is to increase the second law efficiency, because the external temperature levels are normally not adjustable. This publication describes the power cycle version (PC) of a novel thermodynamic cycle, which is called the Recuperative Two-Phase Cycle (RTPC) and offers potentially a higher second law

efficiency. The heat pump version of this cycle has been already presented (Bederna et al., 2023). In section 2, the underlying concept is derived from a loss analysis of a basic Organic Rankine Cycle and the concept is defined from the state of the arte. Furthermore, different ideal variants of the cycle to convert latent or sensible heat sources are presented. In section 3 an exemplary cycle is designed to convert a latent heat source of 100 °C using a latent sink of 15 °C.

2 CONCEPTION OF THE RECUPERATIVE TWO-PHASE POWER CYCLE

2.1 Loss Analysis of the Organic Rankine Cycle

If an increase of the second law efficiency is intended, a precise knowledge of the reasons for exergy destruction is needed. Therefore, an exergetic analysis of the cycle, the components and the interaction between the cycle and the source and sink is essential. A classification of the loss sources is helpful because certain sources of losses are avoidable, while others are inevitable. A first classification distinguishes endogenous losses and exogenous losses. Endogenous irreversibilities occur due to irreversibilities in the components, in particular due to friction, heat losses or leakage. They can only be influenced by higher component quality, to a limited extent. Exogenous losses describe a derivation from the ideal cycle and are additionally subdivided into three types in this publication. To illustrate these subtypes, an endoreversible basic ORC using the working fluid isobutane (R-600a) for an application with a temperature difference of 95 K between a latent heat source and latent heat sink is illustrated in Figure 1 (a). The visualization of the fluid data is exported from REFPROP (Lemmon et al., 2018), slightly modified and extended by the cycle. In Figure 1 (b) the detail of the cycle is enlarged.

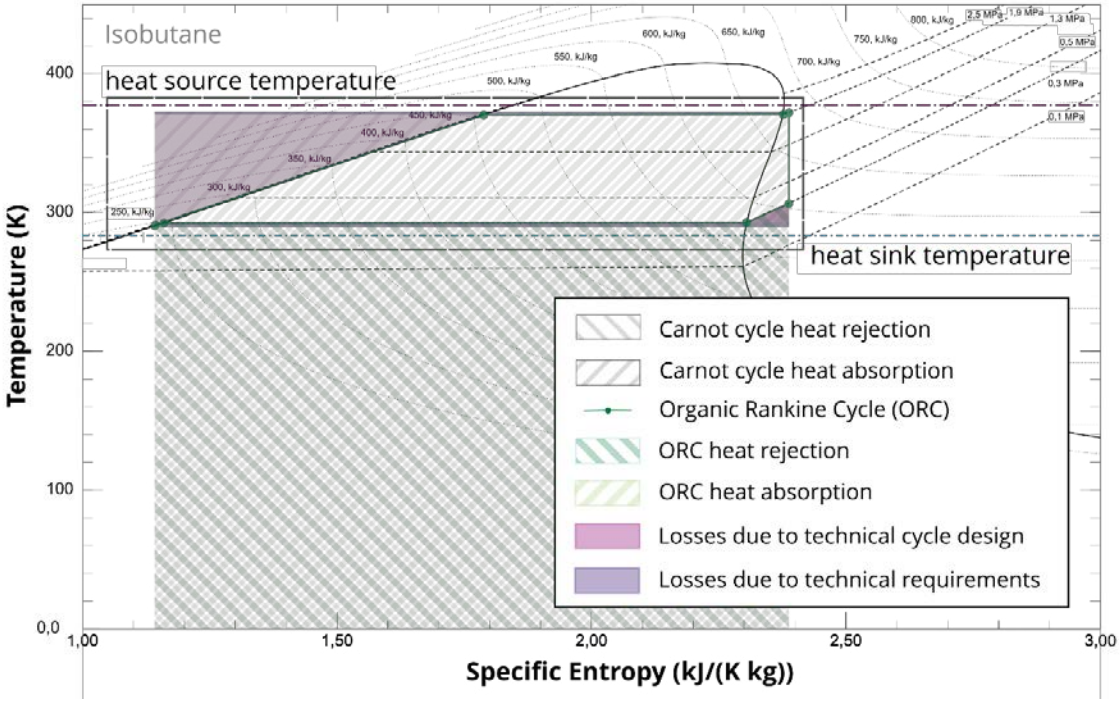

(a) T, s diagram illustrating the importance of each loss source

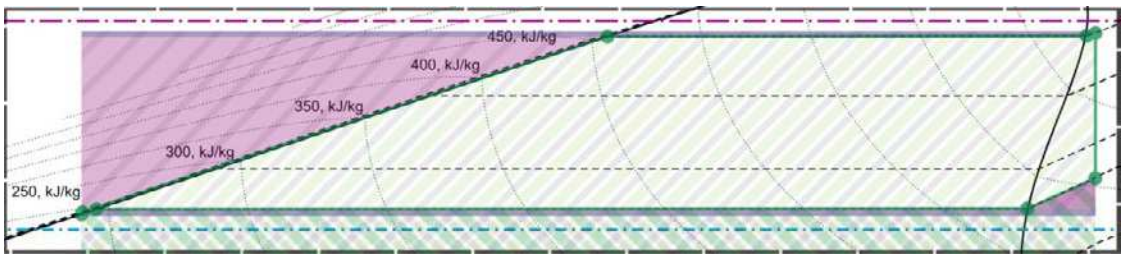

(b) Detail of the cycle

Figure 1: Visualization of exergetic losses of an endoreversible ORC

First, unavoidable exergetic losses occur due to a necessary temperature difference for the heat transfer between the cycle, the heat source and the heat sink. Only a higher heat transfer coefficient or a larger heat exchanger surface area can reduce these losses, thus the reduction potential is limited. The second subtype are losses caused by technical requirements and these are marked by the dark purple color in Figure 1. Superheating could be needed to prevent turbines from being damaged by liquid slugging. Subcooling to avoid cavitation in the feeding-pump can also be such a technical requirement which leads to a higher temperature difference in the heat exchangers. Potential reduction of this disadvantage is offered by a two-phase expansion or a geodetic suction pressure enhancement instead of subcooling at the inlet of the pump. The last subtype includes the deviations of the changes of state of the real from the ideal cycle. Thereby these losses will be called cycle-related and are marked in light purple in Figure 1. An endoreversible Organic Rankine Cycle is composed of an isochoric pressure rise, an isobaric heat absorption, an isentropic expansion and an isobaric heat rejection. Therefore, a deviation from the Carnot cycle occurs when the isobars of an ORC are not equal to isotherms. Additionally, an isochoric pressure rise is slightly different from an isentropic pressure rise. It is visible in Figure 1 that the derivation of the preheating temperature from the ideal heat absorption temperature of the Carnot cycle has the dominating effect, while the difference due to the isochoric pressure rise is negligible. A widespread approach to reduce this preheating losses in Rankine steam cycles is the regenerative feed preheating, which is achieved by injecting partially depressurized steam. For an ORC, this is normally not implemented due to the high number of pumps and increased technical complexity. Further cycle-related exergy destruction can result from the superheated working fluid after the expansion process. In this case, a recuperator can be introduced to preheat the liquid by the superheated exhaust gas. This approach can nearly eliminate the expansion losses, but the preheating losses are only reducible to a limited extent. Generally, preheating losses can only be avoided in ORC systems when an additional sensible heat source with an adequate temperature profile for preheating is available.

2.2 Organic Rankine Cycle with an Isothermal Expansion

For configurations with only one heat source, it is an option to decrease the preheating losses by an increased recuperation effect due to a non-adiabatic expansion process. Optimally, the heat supply during the expansion is high enough to ensure an isothermal expansion (Figure 2). Thereby, the exhaust gas temperature after the expansion process (point 5) is still the same as before (point 4).

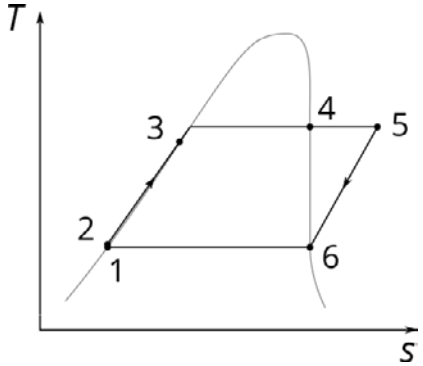

Figure 2: Concept of an Organic Rankine Cycle with an isothermal expansion

This concept was presented for the first time by Woodland et al. (2010) for ORCs, where it was proposed to flood volumetric expanders with hot oil to ensure a sufficient heat supply for a near-isothermal expansion. Igobo and Davies (2014) presented a review on low-temperature power cycles with quasi-isothermal expansion and concluded that there are two main methods to realize the heat supply in volumetric expanders. The first method is surface heating, which is more used for reciprocating piston machine, and the second is liquid flooding, which is investigated more in rotary expanders. It was summarized that the challenges for liquid flooding are high pressure drops and losses due to viscosity, while for the expander surface heating the speed must be lower to enable the heat transfer. Based on this, Igobo (2015) performed experimental tests with a reciprocating piston expander with heated surfaces and could prove an isothermal expansion for piston speeds below $0.2\ m \cdot min^{-1}$. Ziviani et al. (2018) investigated theoretically the concept of the oil flooding in ORC and predicted a performance enhancement of approximately 8 % for the fluid R-1233zd(E). Furthermore, an experimental test rig

for such a cycle was built. However, the theoretical predictions could not be demonstrated in the ensuing tests because the optional pressure levels could not be adjusted, resonance occurred in the oil line and the friction in the expander and the oil pump were higher than expected (Li et al., 2021). In summary, several technical challenges and a fundamental thermodynamic disadvantage can be identified in the context of this approach. The realization of the isothermal expansion itself presents a significant challenge. For the liquid flooding, losses due to viscosity and friction have to be taken into account and with heated surfaces, the heat transfer is not high enough to ensure a reasonable rotational speed. Furthermore, it has to be mentioned that also the recuperator causes disadvantages, especially due to the superheated vapor state of the fluid on the low-pressure side. Thus, the internal heat transfer is low and the specific volume is high, which is why large surface areas and internal volumes are required. Thermodynamically, with this approach it is not possible to avoid completely the preheating losses, even if the expansion is isothermally conducted. This is due to the higher heat capacity of the liquid in comparison to the superheated gas. In Figure 2, this is indicated by a slightly lower temperature of state point 3 compared to point 5. The new concept of the Recuperative Two-Phase Cycle, and in particular its power cycle form (PC-RTPC) aims to avoid these technical and thermodynamic disadvantages.

2.3 Ideal Recuperative Two-Phase Power Cycle (PC-RTPC)

The target of the new cycle is to avoid superheated vapor states and operates in the two-phase region, instead. This increases the heat transfer in the recuperator but also in the expansion process and equalizes the heat capacity flows in the recuperator. In **Figure 3**, a comparison of different internal recuperation processes is made. The heat capacity flow of the high-pressurize liquid $\dot{C}_{p,liq}$ is the same in all configurations. In comparisons with the basic ORC, shown in Figure 3(a), the isothermal expansion, shown in Figure 3(b), increases the preheating effect in the liquid by a higher vapor inlet temperature but does not change the vapor capacity flow $\dot{C}_{p,vap}$. To maximize the recuperation, and thus, to minimize the preheating losses, the capacity flows of both sides must be equalized, as shown in Figure 3(c). This enabled in the RTPC concept by partial condensation on the low-pressure side with simultaneous temperature change.

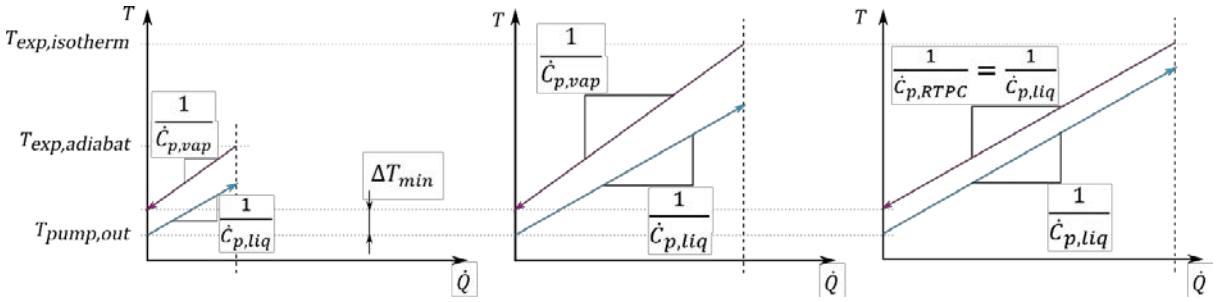

(a) Conventional ORC (b) ORC with isothermal expansion (c) Recuperative Two-Phase Power Cycle

Figure 3: Comparison of characteristics of internal recuperation

When the high-pressure and the low-pressure isobar of the ideal recuperation process are combined with isotherms, the shape of the Ericsson cycle appears. The ideal Ericsson cycle contains four changes of state: isobaric heat absorption, isothermal compression, isobaric heat rejection, and an isothermal expansion, and is able to achieve the Carnot efficiency, as well. The conventional technical implementation of the Ericsson cycle is carried out with a gaseous working fluid. Nevertheless, gaseous working fluids have significant disadvantages in terms of volumetric power density and heat transfer compared to working fluids that undergo a phase change process. The RTPC can also approximate the shape of an Ericsson cycle and avoid both disadvantages (Figure 4). Its key approach is to perform the cycle only with liquid or two-phase fluid by means of a mixture with highly nonlinear temperature glide in the two-phase region (Bederna and Hesse, 2021). All the changes of state associated with the PC-RTPC-EC are listed in Table 1.

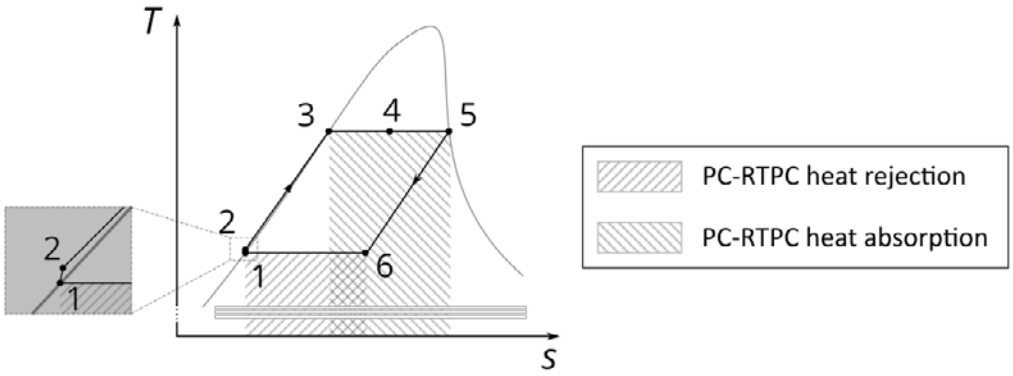

Figure 4: Ideal Recuperative Two-Phase Power Cycle realizing the Ericsson Cycle (PC-RTPC-EC)

It can be seen in Figure 1 that the isochoric pressure rise (1→2) does not cause a relevant temperature rise, why the shape is nearly identical with the Ericsson cycle. Thus, it can be assumed for the ideal Recuperative Two-Phase Power Cycle in Ericsson cycle shape (PC-RTPC-EC) that the efficiency is similar to the Carnot efficiency ($\eta_{PC-RTPC-EC,ideal} \approx \eta_{Carnot}$). This cycle concept could be used to convert latent heat sources by latent or slightly gliding sinks, such as the environment.

Table 1: Changes of state of the endoreversible Recuperative Two-Phase Power Cycle to realize the Ericsson cycle (PC-RTPC-EC)

1 → 2	isochoric	pressure rise	adiabatic	liquid
2 → 3	isobaric	preheating	heat recuperation	liquid
3 → 4	isobaric and isotherm	evaporation	heat absorption	two-phase
4 → 5	isotherm	expansion	heat absorption	two-phase
5 → 6	isobaric	condensation	heat recuperation	two-phase
6 → 1	isobaric and isotherm	condensation	heat rejection	two-phase

If the heat source does not correspond to a latent heat reservoir, but instead a stream should be cooled down, the cycle configuration can be adapted to this. For this purpose, the isothermal expansion is replaced by two or more stages of an isobaric heat absorption (3a→4a and 3b→4b) followed by an isentropic expansion (3a→4a and 3b→4b) (Figure 5).

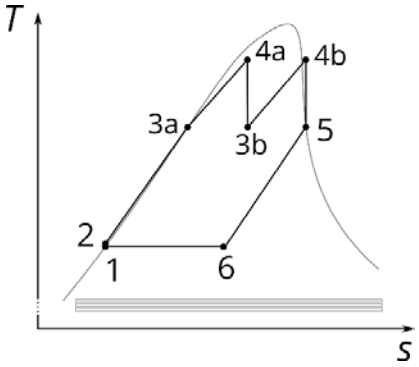

Figure 5: Ideal Recuperative Two-Phase Power Cycle with two stages realizing a trilateral cycle

Depending on the working fluid used and the temperature levels, the change of state 4b → 5 is within or outside the two-phase region. All other expansion processes always imply expansion of two-phase fluid. It should be emphasized that, in this configuration, the technically challenging isothermal expansion can be avoided. It should also be noted, however, that the characteristics of the working fluids do not permit the use of any temperature difference on the source side. In principle, the number of stages must increase for smaller temperature differences between the state points 3 and 4.

2.4 Realizing Recuperative Two-Phase Power Cycles

In order to realize an RTPC, specific zeotropic mixtures are needed as a working fluid. These mixtures consist of a main and at least one auxiliary fluid. In order to achieve the necessary inhomogeneous temperature glide characteristics, the different fluid components have to have very different normal boiling points and critical temperatures, and the composition fractions must also be very unequal. It is intended that the temperature glide of the mixture corresponds to the temperature difference between the high and low temperature levels of the cycle. By selecting the main fluid and the auxiliary fluid with the highest critical temperatures, the pressure level and the temperature difference can be roughly set. With regard to the low-pressure level, the largest part of the evaporation should be isothermal, while in the range of high vapor quality the entire temperature glide should occur linearly. Unfortunately, real fluids cannot exactly achieve this required discontinuous curve. To get an idea of this behavior, the exemplary mixture of 98 mol% n-butane (main fluid) and 2 mol% dodecane (auxiliary fluid) and ideally required isobars are shown in Figure 6.

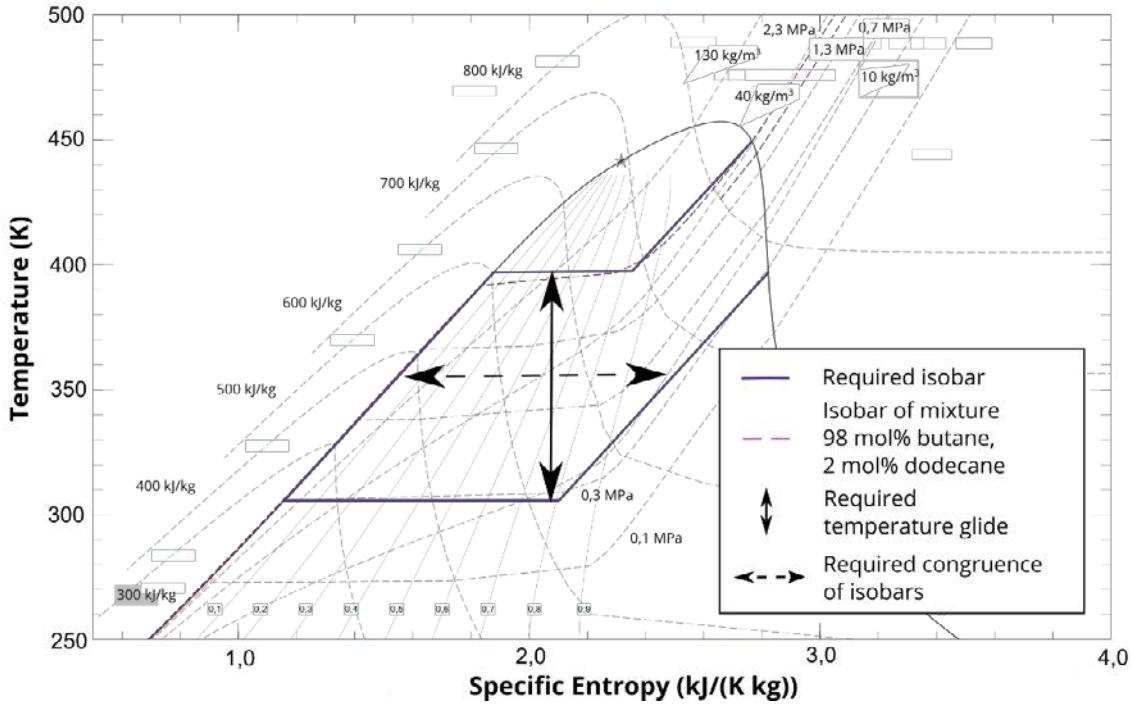

Figure 6: Real mixture data (REFPROP 10) in comparison with the required isobars of an RTPC

To match the capacity flows in the recuperator, the temperature slope of the liquid isobars must correspond to the temperature slope in the second part of the evaporation. The characteristics of the isobars in the two-phase region are mainly influenced by the ratio of the fluid components. Additional auxiliary fluids can be used to linearize the temperature glide. The exact optimization of the mixture fluid is a complex challenge due to the high number of possible mixture combinations. Additionally, the strong influence between the process parameters, the mixture components and the composition has to be adjusted simultaneously. Apart from the fluid selection, the RTPC presents several challenges associated with the technical realization. Zeotropic mixtures, especially with a large temperature glide, cause a composition shift within the process (Zhou et al., 2017). This shift can change the local fluid properties and thus corrupt the compatibility of the fluid streams in the recuperator, which can lead to unexpected exergy losses. In addition, it is known from zeotropic mixtures that the different phase change behavior can inhibit heat transfer (Weith et al., 2014). For the realization of a PC-RTPC-EC, a near-isothermal expansion is necessary, which is the main technical challenge. In comparison with approaches discussed in section 2.2, the RTPC has the advantage of a phase change in the working chamber, which is why significantly higher internal heat transfer coefficient can be assumed. Therefore, the RTPC could enable new opportunities in the context of the isothermal compression in volumetric machines. Apart from this, a multi-stage approach would be conceivable. Nevertheless, these stages have to occur in the two-phase region.

3 DESIGN OF THE POWER CYCLE REALIZING THE ERICSSON CYCLE

3.1 Basic Calculations

The state point calculation of an ideal endoreversible PC-RTPC-EC with a latent source and sink and minimal temperature differences differ from the analytical calculation approaches of ORCs (Figure 7).

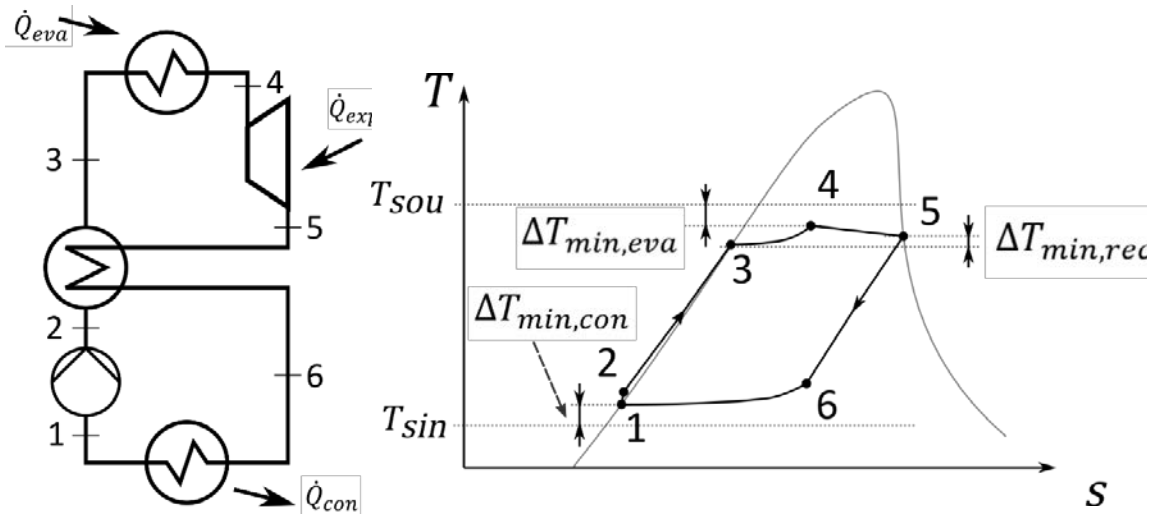

(a) Cycle configuration (b) T, s diagram

Figure 7: Calculation of an endoreversible PC-RTPC-EC

First, the minimal cycle temperature T_1 is defined by Eq. (1) and this temperature defines the low-pressure level. With that pressure the Temperature T_5 is set considering the state of the dew line.

$$T_1 = T_{sin} + \Delta T_{min,con} \tag{1}$$

The maximal temperature in the cycle T_4 is defined by source temperature T_{sou} and the minimal temperature in the evaporator and expander (Eq. (2)) and the evaporation inlet temperature T_3 is defined for by the minimal temperature difference in the recuperator according to Eq. (3).

$$T_4 = T_{sou} - \Delta T_{min,eva} \tag{2}$$

$$T_3 = T_5 - \Delta T_{min,rec} \tag{3}$$

The high-pressure level is calculated based on T_3 for a saturated liquid. Furthermore, the Temperature T_6 is determined while through the energy balance in the recuperator (Eq. (4)).

$$h_3 - h_2 = h_5 - h_6 \tag{4}$$

For the description of the quasi-isothermal compression, Eq. (5) and Eq. (6) can be used.

$$\dot{q}_{exp} = (T_4 + T_5)/2 \cdot (s_5 - s_4) \tag{5}$$

$$w_{exp} = h_5 - h_4 - \dot{q}_{exp} \tag{6}$$

For the analysis of the entire cycle, Eq. (7), which defines the thermal efficiency η_{th} by the specific net power output and the specific heat flows, and Eq. (8) of the second law efficiency η_{II} can be applied.

$$\eta_{th,HP-RTPC-EC} = \left(w_{exp} - h_2 - h_1\right) \cdot \left(\dot{q}_{exp} + h_4 - h_3\right)^{-1} \tag{7}$$

$$\eta_{II,PC-RTPC-EC} = \eta_{th,HP-RTPC-EC} \cdot {\eta_{Carnot}}^{-1} \tag{8}$$

3.2 Case Study of the Conversion of a Latent Low-temperature heat Source

For a preliminary evaluation of the possible thermodynamic potential of this cycle for the conversion of latent low-temperature sources an endoreversible RTPC is calculated and compared with the presented qualitative evaluation of Rankine power cycles. For this, the assumption is made that an isothermal expansion in the two-phase region is feasible. Although this is not realistic regarding the currently used compressors, it could be achieved at a very slow expansion velocity in a leakage-free machine. Above, it represents the thermodynamic limiting case. A latent heat source of 100 °C and a sink of 15 °C following ambient conditions are defined. Thus, the appropriated cycle configuration is the PC-RTPC-EC, approximating the shape of the ideal Ericsson cycle. It demands an isothermal expansion. The mixture selection is done manually out of alkanes and alkenes using the fluid data of REFPROP 10. First, butane is chosen as main fluid due to its suitable pressure level during condensation at the given sink temperature. Decane is the appropriate auxiliary fluid of butane to ensure the required temperature lift, as illustrated in Figure 7.

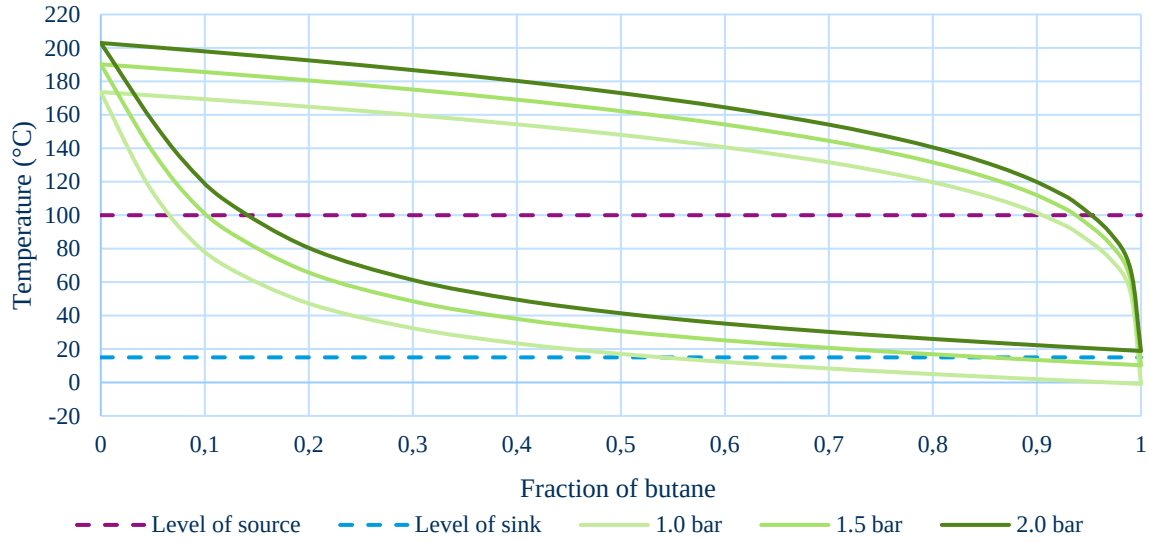

Figure 7: T, x diagram of a butane decane mixture (REFPROP 10)

The PC-RTPC-EC is calculated based on the Eq. (2) to Eq. (8). All minimal temperature differences are set to 3 K. Furthermore it is defined, that the half of the heat provided by the source is transferred by the evaporator. Different from an endoreversible calculation a pump efficiency of 80 % is set. For this case, an optimal mixture composition of 96.1 mol% butane and 3.9 mol% decane can be identified. With the resulting low-pressure level of 1.9 bar and the high-pressure level of 12.1 bar a second law efficiency of 85.8 % can be achieved. Figure 8 (a) shows the entire cycle with an expander inlet vapor quality of 0.7. In Figure 8 (b) the temperature characteristic in the recuperator is displayed.

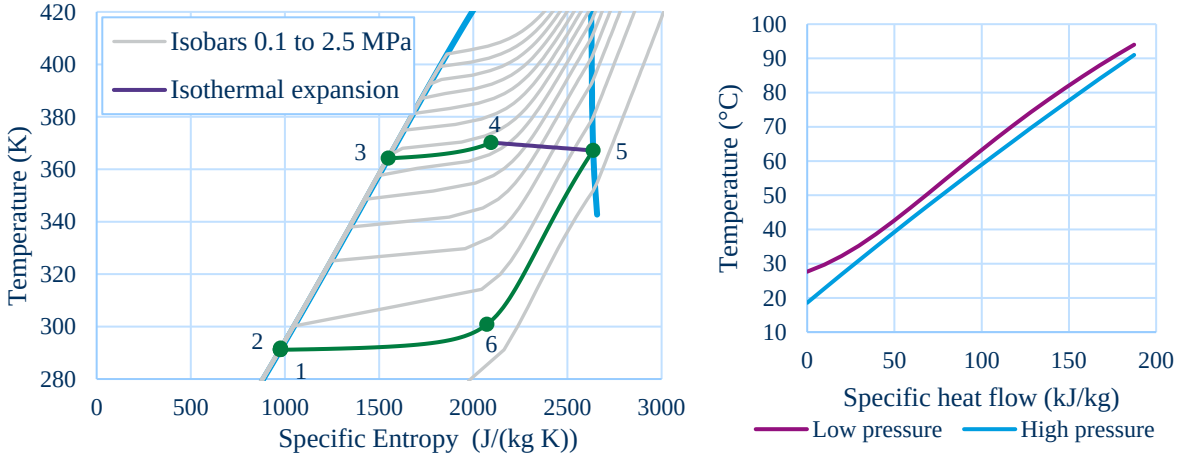

(a) T,s - diagram of the cycle (b) T,q - diagram of the recuperator

Figure 8: Recuperative Two-Phase Power Cycle in Ericsson shape with a working fluid mixture of 96.1 mol% butane and 3.9 mol% decane and an isothermal expansion

It becomes clear that with the use of this real mixture a derivation from the ideal Ericsson cycle arises due to the non-ideal isothermal evaporation (3 → 4) and condensation (6 → 1), as well as due to the temperature difference in the recuperator. In Figure 9, the results of an exergy analysis are presented. First of all, it has to be emphasized that the preheating losses, which dominate the endoreversible Rankine cycle described above, are eliminated. Due to the defined pump efficiency, endogenious losses of 0.5 % occurs. The non-avoidable exogenious exergy destructions of the first subtype (due to the necessary minimal temperature differences for the heat transfer) amount 6.4 %. Losses due to technical requirements, described as the second subtype, are not present, because a two-phase expansion is allowed and the required subcooling in the pump is currently neglected. Further losses are those due to the cycle design (third subtype). In the case of the RTPC, these are mainly caused by the difference between the required isothermal heat transfer and the real mixture behavior in the evaporator and condenser (4.6 %) as well as the introduction of a recuperation process in comparison with the Carnot cycle (2.4 %). While a minimal temperature difference in the recuperator is mandatory and not avoidable, in Figure 8 (b) it becomes clear that the glide during the recuperation process on the low-pressure side is not linear, resulting in a varying temperature difference, which must be considered as an additional exergetic loss. A better mixture components and compositions selection by an optimization approach could be a key to reduce this type of losses beyond the current state. For example, it would be possible to consider other fluid pairs with even more differing thermodynamic behavior (e.g. alkane + cycloalkanes) or to add further auxiliary fluids to linearize the temperature glide during the recuperation. In this study, the losses due to the nearly-isothermal expansion are very low. Nevertheless, the expansion process represents the main uncertainty to transfer the current results and derive the potential of a realistic RTPC-EC.

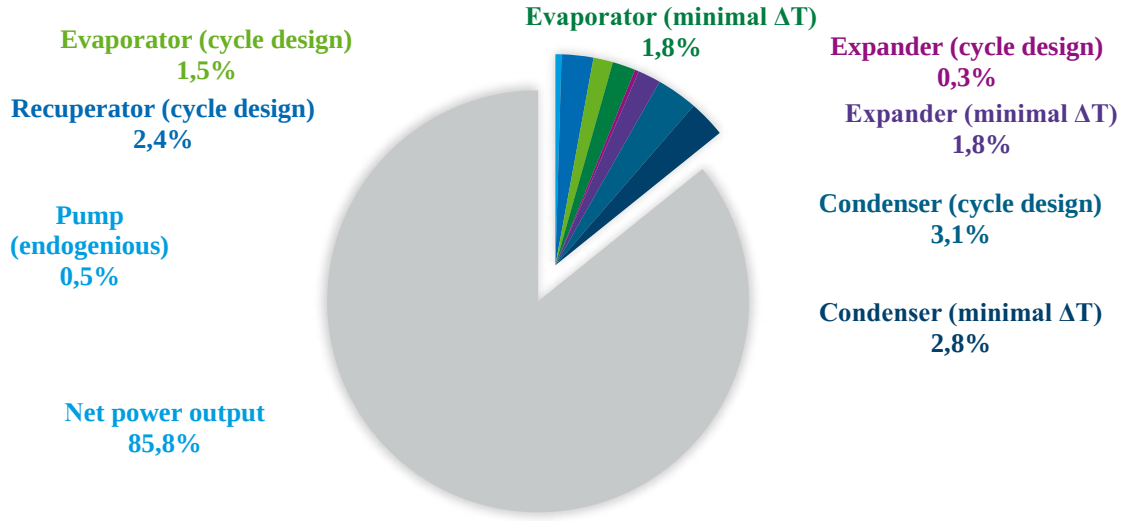

Figure 9: Relative net power output and exergy destruction in the components (heat source = 100 %)

The temperature profile of the cycle inside the evaporator and the expander is not isotherm. In the case of a sensible heat source with a slightly gliding temperature profile, this would correlate much better with the cycle shape. Thus, the second law efficiency would be even higher due to reduced cycle design losses during the heat absorption.

4 CONCLUSIONS

The main conclusions of this publication can be summarized as the following:

- The power cycle version of the novel thermodynamic Recuperative Two-Phase Cycle (PC-RTPC) has been presented. It aims to avoid the normally dominating preheating losses in ORCs by an extended internal recuperation, which is made possible by a condensation on the low-pressure side of the recuperator. Thereby, the ideal, thermodynamic version of this cycle (without any temperature differences and losses) can reach the Carnot efficiency.
- Technically, the process can be realized by an inhomogeneous zeotropic mixture composed out of fluids with very different normal boiling temperatures, according to the sink and the source.

- Different cycle versions are possible to convert latent heat sources or sensible sources with a limited minimal temperature. For sensible heat sources, a near-isothermal expansion is avoided.
- The thermodynamic potential was demonstrated by a first calculation of an endoreversible cycle in the shape of an Ericsson cycle converting a latent heat source of 100 °C by a sink of 15 °C and a second law efficiency of 85.8% was achieved. However, the maximum thermodynamically achievable second law efficiency is unknown, due to the lack of an optimization.
- Currently, there are still questions regarding the technical feasibility. On the one hand, the real behavior of the mixture under flow conditions is unknown, but it has a significant impact on the recuperation process. On the other hand, the technical realization of a practicable isothermal expansion, as it would be necessary for the conversion of isothermal heat sources, is debatable.

In order to further validate the cycle concept, two directions will be taken as the next working steps. First, an optimization procedure for identifying ideal mixtures will be set up. Second, the behavior of a real mixture with the inhomogeneous temperature glide characteristic shall be observed experimentally. For this purpose, a test rig is already being set up to investigate the recuperation process. In addition, the influence of a composition shift of the circulating mixture within the whole cycle can be determined.

NOMENCLATURE

$\dot{C}_p$	Heat capacity flow	(kW·K^{-1})	s	specific entropy	(kJ·(K ·kg)$^{-1}$)
η	Efficiency	(-)	T	temperature	(K)
h	specific enthalpy	(kJ·kg^{-1})	ΔT	temperature difference	(K)
$\dot{q}$	Specific heat flow	(kW·kg^{-1})	w	specific work	(kJ · kg^{-1})

Subscript

con	condenser	liq	liquid	rec	recuperator	th	thermal
eva	ecaporator	min	minimum	sin	sink	vap	vapor
exp	expander	out	outlet	sou	source	II	second law

REFERENCES

Bederna, B. G., Hesse, U., 2021. Vorrichtung und Verfahren zum Durchführen von Kreisprozessen, DE102021114326A1.

Bederna, B. G., Barta, R. B., Thomas, Ch., 2023, Thermodynamic Concept of a Novel Recuperative Two-Phase Heat Pump Cycle, *26th Int. Congress of Refrigeration*, August 21st-25th, 2023, Paris.

Igobo, O. N., Davies, P. A., 2014, Review of low-temperature vapour power cycle engines with quasi-isothermal expansion. *Energy*, 70, 22-34.

Igobo, O. N., 2015, Low-temperature Isothermal Rankine cycle for Desalination, Diss. Aston Uni.

Lemmon, E. W., Bell, I. H., Huber, M. L., McLinden, M. O., 2018, NIST Standard Reference Database 23, Version 10.0, NIST, Standard Reference Data Program.

Li, X., Lecompte, S., Van Nieuwenhuyse, J., Couvreur, K., Tian, H., Shu, G., De Paepe, M., Markides, C. N., 2021, Experimental investigation of an organic Rankine cycle with liquid-flooded expansion and R1233zd (E) as working fluid. *Energy Conversion and Management*, 234.

Woodland, B. J., Groll, E. A., Braun, J, E., Horton, W. T, 2010, Performance Benefits for Organic Rankine Cycles with Flooded Expansion and Internal Regeneration. *Int. Refrigeration and Air Conditioning Conference*. Paper 1134.

Weith, T., Heberle, F., Preißinger, M., Brüggemann, D., 2014, Performance of siloxane mixtures in a high-temperature Organic Rankine Cycle considering the heat transfer characteristics during evaporation. *Energies*, 7.

Ziviani, D., Groll, E. A., Braun, J. E., De Paepe, M., van den Broek, M., 2018, Analysis of an ORC with liquid-flooded expansion and internal regeneration (ORCLFE). *Energy*, 144.

Zhou, Y., Zhang, F., Yu, L., 2017, The discussion of composition shift in organic Rankine cycle using zeotropic mixtures. *Energy Conversion and Management*, 140.

ORC SEVILLE 2023
7th International Seminar on O.R.C. Power Systems

© 2024 Editorial Universidad de Sevilla. Este es un artículo de acceso abierto distribuido bajo los términos de la licencia de uso y distribución Creative Commons (BY-NC-ND 4.0)

DOI: https://dx.doi.org/10.12795/9788447227457_7

Performance analysis of a 1.5 MW organic Rankine cycle in a Carnot battery system for grid balancing services

Robin Tassenoy[1,*], Hannes Van De Velde[1], Kenny Couvreur[1], Michel De Paepe[1,2], Steven Lecompte[1,2]

[1]*Ghent University, Department of ElectroMechanical, Systems and Metal Engineering, Ghent, BE*
[2] *FlandersMake@UGENT, Core lab EEDT-MP, Leuven, BE*

*Corresponding Author: Robin.Tassenoy@UGent.be

ABSTRACT

Due to the increasing share of variable renewable energies in the energy mix, large-scale (>1 MW), long duration (>4 h) energy storage systems are becoming essential to ensure secure and stable energy supply. Carnot batteries, a combination of a power-to-heat, a thermal storage and a heat-to-power system, could provide a possible solution. Organic Rankine cycles have been considered as power-to-heat technology for Carnot batteries. However, it is not clear which grid services these organic Rankine cycles could deliver. To answer this question, a 1.5 MW organic Rankine cycle, suitable for integration in a Carnot battery, was modelled dynamically in Modelica. Dynamic finite volume heat exchanger models were used, while the operation of the pump and turbine was considered quasi-steady state due to their low time constant compared to the heat exchangers. The storage tanks were assumed perfectly mixed and modelled by time-varying boundary conditions. Furthermore, a control strategy driven by the requirements of the electrical grid was proposed. The dynamic model simulates and evaluates the organic Rankine cycles' response to the qualification test profiles for grid balancing services. It was found the organic Rankine cycle can deliver a 1 MW capacity for downward and upward secondary and tertiary reserve. Delivery of a 0.5 MW symmetric capacity for primary reserve is currently not possible due to the required full activation time. Nevertheless, the results indicate that the delivery of secondary and tertiary grid balancing services with the organic Rankine cycle could be an additional revenue stream to increase the financial feasibility of Carnot battery systems and it is thus worthwhile to investigate its potential financial benefits.

1 INTRODUCTION

1.1 Carnot batteries

Large deployment of variable renewable energies (VRE) challenges the stability of the electrical grid due to their intermittency. Energy storage can mitigate this problem by power and voltage smoothing, energy management, frequency regulation, peak shaving, load levelling, seasonal storage and standby generation during a fault (Argyrou et al., 2018). Therefore, energy storage is considered one of the main drivers to provide the flexibility needed to decarbonize the electricity grid.

The Carnot battery, a combination of a power-to-heat system, a thermal energy storage system (TES) and a heat-to-power system, is an emerging electrical energy storage concept that may provide additional flexibility to the grid. One of the Carnot battery's subsets is pumped thermal energy storage (PTES), in which an electrically driven heat pump is used to deliver heat to a hot store and/or extract heat from a cold store (McTigue et al., 2022). Organic Rankine cycles (ORCs) have been considered as heat-to-power system for Carnot batteries. Most studies have focused on the steady-state analysis and optimization of the storage concept and the obtainable round-trip efficiencies (Dumont et al., 2020). More recently, the techno-economic optimization of PTES has gained interest as well. Vecchi et al. (Vecchi et al., 2022) reviewed the techno-economic performance of Carnot batteries and discussed their

applications at energy system scale. They showed Carnot batteries have been considered mainly for load-shifting and arbitraging services and concluded that these services alone may not be sufficient to recover the investment cost of the technology, highlighting the importance of a portfolio of grid services to provide different revenue streams.

1.2 Grid balancing services

Within the portfolio of grid services, providing grid flexibility is highly promising as the need intensifies due to the large deployment of VRE (Heggarty et al., 2019). Grid flexibility is usually defined as the possibility of modifying generation and/or consumption patterns in reaction to an external signal (e.g. price) to contribute to the power system stability in a cost-effective manner. At the transmission grid level, flexibility is linked to grid balancing services offered to transmission system operators (TSOs) (Villar et al., 2018). These services match the instantaneous electricity production and demand, which is essential to ensure stable grid operation. According to their time scale, three balancing products can be distinguished: primary or frequency containment reserve (FCR), secondary or automatically activated frequency restoration reserve (aFRR) and tertiary or manually activated frequency restoration reserve (mFRR). An overview of the main service characteristics is presented in Table 1.

Table 1: Characteristics of balancing services in the European electricity grid

Balancing service	Direction	Full activation time (FAT)	Min. delivery time	Min. bid size	Ref.
FCR	symmetric	30 s	15 min	1 MW	(Elia, 2019)
aFRR	up / down	7.5 min (to 5 min)	15 min	1 MW	(Elia, 2022a)
mFRR	up / down	15 min	15 min	1 MW	(Elia, 2022b)

1.3 Dynamic modelling ORC-based PTES with respect to grid balancing services

34

From the discussion above, it is clear that PTES dynamics are essential for the delivery of grid balancing services. However, there is a lack of research on these dynamic characteristics which makes it difficult to predict, regulate and optimize the performance of PTES in actual operation processes (Lu et al., 2022). While this knowledge gap has partially been addressed for Brayton-based PTES recently (Lu et al., 2022), literature discussing the dynamic behavior of ORC-based PTES is scarce.

Dynamic simulations of Rankine-based PTES are mostly focused on compressed heat energy storage systems, characterized by the use of latent thermal energy storage systems (Tafone et al., 2023). However, in these studies the ORC as a whole is modelled quasi-steady state. The dynamics of the ORC are thus completely neglected. To the best of the authors' knowledge, no study involving detailed dynamic modelling of a full Rankine-based grid-scale PTES is currently available.

Detailed dynamic simulation of large-scale ORC systems has been performed primarily in the context of waste heat recovery (Imran et al., 2020). Imran et al. (2020) stressed that profound understanding of the ORC dynamics is important for the development of controllers for ORC systems that encounter highly transient heat sources. Therefore, the ORC dynamics will also play a crucial role when evaluating the suitability of ORCs in PTES for grid balancing services, given the strict requirements on power response time and controllability, and the need to maintain suitable temperatures in the TES.

1.4 Scope of this study

No study discussing the dynamic response of a grid-scale Rankine-based PTES to grid requirements has been found. While the dynamic modelling and control of large-scale ORCs has been studied for waste heat recovery applications, similar studies have not been performed driven by the requirements for grid balancing services. In particular, there are no studies addressing this in the context of grid-scale Carnot batteries where, next to the strict requirements on power response time and controllability, also suitable TES temperatures need to be maintained. This study aims at making a first step towards

assessing Rankine-based PTES for delivery of grid balancing services by focusing on the ORC subsystem. A dynamic model of a 1.5 MW ORC suitable for implementation in PTES was constructed. Then, a suitable control strategy was developed to follow the desired power production, while maintaining correct TES temperatures. Finally, the technical potential to deliver grid balancing services was assessed by validation of the controlled system against the prequalification tests of the European grid.

2 METHODOLOGY

2.1 Carnot battery lay-out and heat pump boundary conditions

This work focusses on the dynamic modelling of an ORC to be implemented in a Carnot battery. These PTES systems usually consist of a vapor compression heat pump, a TES and an ORC, as shown in Figure 1. This topology has been chosen over an alternative configuration using a single thermal machine as compressor (during charging) and expander (during discharging) or sharing heat exchangers between both operation modes. Although such systems have a lower investment cost, they are currently less mature and limited to smaller system sizes (Dumont et al., 2020).

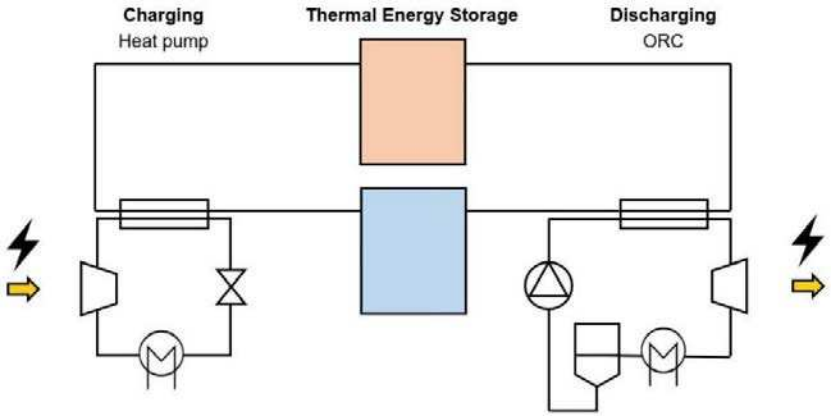

Figure 1: Schematic representation of a Rankine-based, thermally integrated Carnot battery

Rankine-based PTES typically takes advantage of a low-grade heat source to boost the electric round-trip efficiency of the system (Frate et al., 2017). Apart from low grade geothermal heat and solar thermal energy, heat sources of suitable thermal capacity and temperature level can be found mostly in the industrial sector. Balancing the heat availability and efficiency improvement of the PTES, a residual heat source of 65 °C was assumed for heat pump integration (Marina et al., 2021). As typical temperature lifts of heat pumps range from 40 to 80 °C (Arpagaus et al., 2018), the TES temperatures have been chosen to fit this range. Sensible liquid heat storage is often applied as it is reliable, mature and cost-efficient. A two-tank configuration guarantees almost constant charge and discharge profiles and was therefore selected instead of a single tank solution, despite the cost of doubling the storage volume (Frate et al., 2017). Pressurized water tanks were opted for as they are cheap, have low environmental impact and are suitable for the temperature range of interest (Dumont et al., 2020). It was assumed the water enters the ORC evaporator at 120 °C, while it returns to the cold tank at 95 °C. The ORC heat sink was assumed to be water with a constant inlet temperature of 15 °C. R1233zd(E) was selected as working fluid from a list of refrigerants suitable for ORCs in the intended operating range (De Paepe et al., 2019), considering thermodynamic and environmental performance.

As shown in Figure 1, the basic ORC system considered in this work has five main components: the pump, evaporator, turbine, condenser and liquid receiver. Although more complex topologies with higher efficiencies have been proposed in literature (Lecompte et al., 2015), the additional components increase the thermal inertia of the system and are thus expected to slow down the system's dynamic response. Therefore, the basic system was assessed first. If this topology proves suitable to deliver grid balancing services, more complex topologies can be addressed in future work.

2.2 Nominal operating conditions

A steady-state ORC model was developed in Python 3.7.9 to determine the nominal operating conditions of the different components. The fluid properties of R1233zd(E) were retrieved from REFPROP (Eric W. Lemmon, 2018). An overview of the main modelling assumptions and resulting nominal conditions is given in Table 2.

Table 2: Nominal operating conditions: modelling assumptions and results

Assumed parameter	Value	Unit	Output parameter	Value	Unit
$T_{water,ev,in}$	120	°C	$p_{evaporator}$	10.4	bar
$T_{water,ev,out}$	95	°C	$p_{condenser}$	1.7	bar
$T_{water,cond,in}$	15	°C	$pressure\ ratio$	6.29	-
$PP_{evaporator}$	5	°C	$\dot{m}_{water,ev}$	109.83	kg/s
$PP_{condensor}$	5	°C	$\dot{m}_{water,cond}$	179.81	kg/s
$SH_{evaporator}$	5	°C	$\dot{m}_{refrigerant}$	47.59	kg/s
$SC_{condenser}$	3	°C	$\dot{Q}_{evaporator}$	11.4	MW
$\eta_{is,pump}$	70	-	$\dot{Q}_{condenser}$	9.9	MW
$\eta_{is,turbine}$	87.23	-	η_{cycle}	12.8	%
$P_{el,turbine}$	1.5	MW			

2.3 Component selection and modelling

Based on the results of the steady-state cycle calculation, suitable components were selected. A dynamic ORC model was built in the object-oriented modelling language Modelica (The Modelica Association, 2023), using the simulation software Dymola 2022 (AB, 2021) and the TIL-library (TLK Thermo GmbH & IfT 2020). The component models of this library were used, and extended when necessary. Fluid properties were calculated using REFPROP (Eric W. Lemmon, 2018).

36

Plate heat exchangers (PHE) were selected for both the evaporator and condenser because they are relatively cheap, compact and have a modular design (Imran et al., 2020). Funke (Funke, 2022) produces gasketed PHE with capacities up to 30 MW and volume flow rates up to 4500 m³/h. The stainless steel FP 405 and FP 41 gasketed PHE were selected as evaporator and condenser. The PHE were modelled using the finite volume (FV) model available in the TIL-library, assuming countercurrent flow. The suitability of FV-models for dynamic simulation of evaporators and condensers has extensively been demonstrated (Imran et al., 2020). Moreover, the PHE-model of the TIL-library was successfully used to simulate dynamic behavior of PHE before (Meesenburg et al., 2020). The plate dimensions of the Funke heat exchangers were used as model input. The inside geometry of the heat exchangers was not made public by the manufacturer. Therefore, the inside geometry proposed by Lee et al. (Lee et al., 2018) and Zhang et al. (Zhang et al., 2019) were used for the evaporator and condenser respectively. The pressure drop correlation proposed by Zhang et al. (Zhang et al., 2019) was used in the condenser. The pressure drop correlation by Lee et al. (Lee et al., 2018) was initially used in the evaporator. Using this correlation required a very high number of calculation cells in the heat exchanger to avoid numerical fluctuations. Therefore, the refrigerant pressure drop correlation in the evaporator was simplified and assumed quadratic to the mass flow (Meesenburg et al., 2020). Although this simplification slightly affects the numerical values of the resulting evaporator pressure, it does not directly affects the heat exchanger dynamics. As the current study focusses on this dynamic response, this simplification was found to be acceptable. For the refrigerant side, following heat transfer correlations have been added to the TIL-library: Chisholm and Wanniarachchi (García-Cascales et al., 2007) for single-phase flow, Desideri et al. (Desideri et al., 2017) for evaporation and Zhang et al. (Zhang et al., 2019) for condensation. Heat transfer at the water side was modelled by the VDI Plate alpha correlation (Holger, 2010) available in the TIL-library.

Both the pump and expander were modelled quasi-steady state, which means part-load performance was taken into account and an immediate response of the components was assumed. These assumptions are commonly made when dynamically modelling ORCs (Imran et al., 2020). A variable turbopump was modelled by the *pump2ndOrder* – model of the TIL-library with nominal pressure difference equal to 10.5 bar and nominal volume flow rate equal to 328.2 m³/h at a nominal rotational speed of 48.3 Hz. The *EffExpander*-model from the TIL-library was extended to a performance map based model. Performance maps detailing the relation between refrigerant mass flow rate and turbine isentropic efficiency, pressure ratio and rotational speed were used to determine the turbine operating point. Currently, the turbine was modelled based on the performance map of a two-stage axial turbine NASA-CR-168289 (Timko, 1984). This high-pressure turbine is typically used in aeronautic applications. If more appropriate data for refrigerant turbines becomes available, this data can be implemented in the performance map based model. In this study the original map was rescaled using dynamic similitude to the nominal operating conditions, which was considered acceptable as the current study focusses on the dynamic performance.

A liquid receiver was added to absorb the working fluid fluctuations during operation and ensure liquid state at the pump inlet (Andritos et al., 2016). The receiver was modelled using the TIL-model. The sensible storage was not modelled in detail. Instead, a two-tank system with two perfectly mixed tanks was assumed. The water temperature at the inlet of the evaporator was thus assumed constant. A boundary model was used to impose a constant inlet temperature and pressure, while the water mass flow could be regulated.

2.4 Control strategy

The control system should make sure the ORC quickly delivers the required power production, while maximizing operational efficiency and maintaining correct TES temperatures. Therefore, three inputs were controlled using PI-controllers: the pump rotational speed, the turbine rotational speed and the water mass flow rate in the evaporator. Variable speed control of the pump is an effective way of controlling the refrigerant mass flow and consequently, the expander power. As the operating point is determined by the intersection of the pump- and expander characteristic, the expander speed was varied as function of the pressure ratio to maximize the turbine efficiency. Finally, the water mass flow in the evaporator was adapted by the PI-controller to maintain a cold storage supply temperature of 95 °C. All PI-constants were determined by analyzing the corresponding system step response in Python 3.7.9. The resulting PI-constants are summarized in Table 3.

Table 3: PI-control parameters

Controller	**k [-]**	k_i $[s^{-1}]$
Pump	1.55e-6	4.16e-6
Turbine	1343	1680
Water mass flow	1.16	4.44

2.5 Test conditions for grid balancing services

The Belgian TSO, Elia, provides prequalification tests for all balancing services discussed in Table 1. The power profiles evaluate the full activation time (FAT), the maximum power delivery, the duration of the service and the power deviation. The delivery of FCR is always symmetric and the capacity should react linearly to the frequency deviation of the grid. aFRR and mFRR on the other hand can deliver down- or up regulation separately, or do both. It should be noted that Elia sets the minimum capacity bid at 1 MW, but it is allowed to split this capacity over multiple assets. The main criterium is that the requested power uptake or production (within predefined accuracy) is reached within the prescribed FAT. In this study, the combination of down- and up regulation was not tested as it follows from the separate tests. The ORC was tested for a 1 MW capacity for mFRR and aFRR in the downward and upward direction and for a 0.5 MW symmetric FCR capacity. The prequalification tests also aim at verifying that the service can be delivered for a sufficiently long time. For Carnot batteries, this duration

is closely related with the capacity and state-of-charge of the TES. Here, focus was given to the reaction time and it was assumed the TES was sized adequately, fulfilling the duration requirement.

3 RESULTS AND DISCUSSION

3.1 Steady – state model validation

A direct validation of the different component models to experimental data is not possible, as this data is not available. Instead, the component sizing and modelling are partly validated by comparison of the steady-state results to the steady-state python calculation. The dynamic model (and implemented control) are tested by simulating the steady-state system response to constant controller setpoints. An overview of the assumed boundary conditions, controller setpoints and corresponding simulation results is given in Table 4. The deviation can be explained by the model strategy. While the thermodynamic states are fixed directly in the Python model, they follow from the physical component characteristics and choice of controlled parameters in the Modelica model. A one-on-one match is thus not to be expected. Nevertheless, the good correspondence between the results indicates proper sizing and modelling of the different components. Moreover, the controllers reach the desired setpoints illustrating the effectiveness of the implemented control method.

Table 4: Steady-state model validation: boundary conditions and simulation results

Assumed parameter	Value	Unit	Output variable	Value	Unit
$T_{water,ev,in}$	120	°C	$T_{water,ev,out}$	95	°C
$T_{water,cond,in}$	15	°C	$P_{el,turbine}$	1.5	MW
$T_{water,ev,out,set}$	95	°C	$p_{evaporator}$	9.2	bar
$P_{el,turbine,set}$	1.5	MW	$p_{condenser}$	1.6	bar
$\dot{m}_{water,cond,in}$	180	kg/s	$pressure\ ratio$	5.7	[-]
Output variable	**Value**	**Unit**	$\dot{Q}_{evaporator}$	12.2	MW
$\dot{m}_{water,ev}$	115.4	kg/s	$\dot{Q}_{condenser}$	10.7	MW
$\dot{m}_{refrigerant}$	47.4	kg/s	η_{cycle}	12.3	%

3.2 Ramping test

All grid balancing services require a sufficiently low FAT, implying the full offered capacity should be activated within this time period. The required FATs are summarized in Table 1. The prequalification test of FCR and aFRR includes a ramping test, in which the desired power is ramped between the capacity limits over the full allowable FAT. The maximum allowable deviation during the ramp is prescribed. For mFRR, the ramp itself is not prescribed. The prequalification test just requires activation within 15 minutes. Therefore, a ramp of 10 minutes was applied and the maximum power deviation after 15 minutes from the start of the activation was verified. In Figure 2, the result of the ramping test for the delivery of a 0.5 MW FCR capacity is shown. The ramping tests for a 1 MW aFRR and mFRR are analogous but ramp between 0.5 and 1.5 MW instead of the symmetric capacity shown for FCR. A summary of the simulated deviations and the allowable tolerance is given in Table 5. As can be seen, the power response for mFRR and aFRR is suitable, while the power deviation exceeds the allowable margin for FCR. In Figure 2, it can be seen that the power production slightly lags the desired setpoint. This deviation is more pronounced in the upward direction than in the downward direction. In both cases, the actual ramping rate is too slow to remain within the allowable tolerance of 10 %.

Table 5: Results of the ramping tests

Service	Maximum measured deviation [%]	Allowable tolerance [%]
mFRR down / up	0	/
aFRR (down and up)	1.5	7.5
FCR	19.2	10

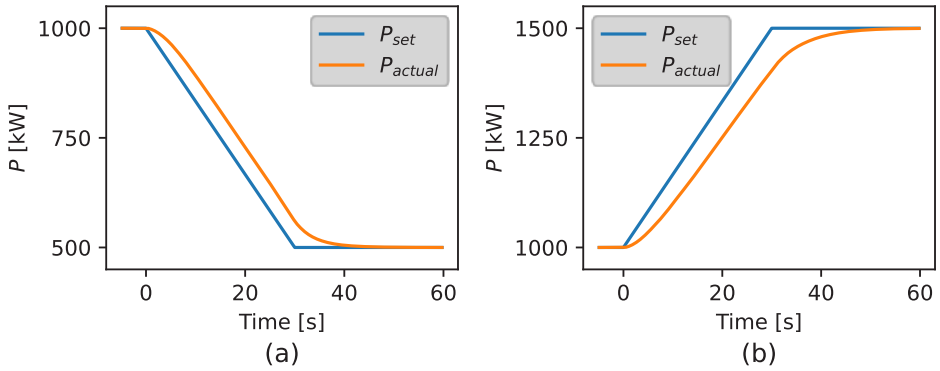

Figure 2: Ramping test for 0.5 MW symmetric FCR capacity: (a) downward and (b) upward ramp

During this modulation, the return temperature to the cold TES tank should remain correct to conclude the Carnot battery satisfies the FAT criterium of the grid services. In Figure 3, the variation of the water temperature at the outlet of the evaporator is shown for the downward and upward FCR ramp, respectively. For the downward ramp, the maximum absolute temperature deviation equals 0.08 °C. The maximum deviation during the upward step is even smaller and equals 0.05 °C. As expected, the largest temperature deviations occur during the fastest ramps. The maximum deviations during the aFRR and mFRR tests are even smaller. Moreover, the deviations are of short duration. Therefore, the return temperatures are acceptable for all steps.

The FAT requirement is thus fulfilled for a 1 MW mFRR and aFRR capacity in the downward and upward direction. The FAT requirement for FCR is not fulfilled due to limitations on the system's maximum ramping rate.

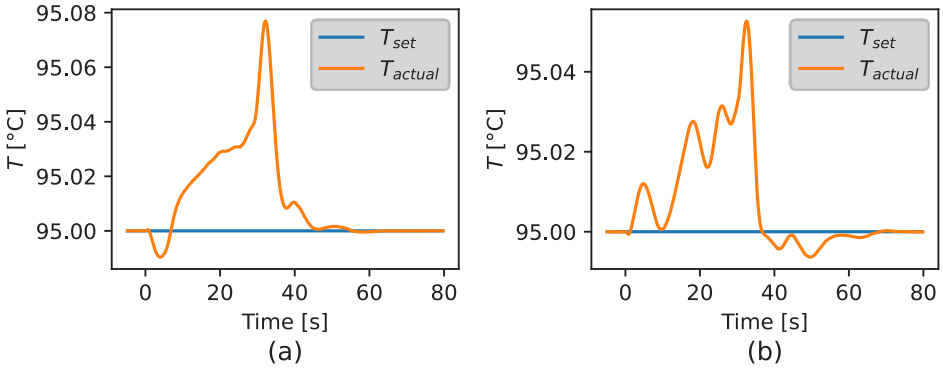

Figure 3: Water temperature at the evaporator outlet during the ramping test for 0.5 MW symmetric FCR capacity: (a) downward and (b) upward ramp

3.3 Tertiary reserve

Next to the duration requirement, the delivery of tertiary reserve is only determined by the FAT requirement discussed in Section 3.1. The ORC can thus deliver a 1 MW mFRR capacity in both the downward and upward direction.

3.4 Secondary reserve

As discussed in Section 3.1, the ORC meets the FAT requirement for aFRR. Next to this requirement, the ORC should be able to follow a synthetic load pattern within a margin of 7.5 %. A maximum of 30 deviations outside this margin is allowed. The aFRR load-following test is illustrated in Figure 4. The average absolute deviation is 0.86 and 0.78 % for the downward and upward product respectively. The maximum absolute deviation of the upward product is 1.50 %, which is below the allowed margin. The downward test shows some unexpected peaks, which are due to numerical reasons. Significantly increasing the number of calculation cells in the evaporator eliminates these numerical fluctuations.

However, as this also significantly increases calculation time, this has been verified for the downward part of the load-following test only and the full test (including the numerical fluctuations) is shown here. Numerical fluctuations occur at four separate moments. The 7.5 % margin is exceeded at only two of these (20 timesteps on a total of 18457), which is within the 30 allowed deviations. During the test, the maximum absolute deviations of the water temperature at the evaporator outlet are 1.25 and 0.02 °C for the downward and upward test. The ORC thus qualifies for an aFRR capacity of 1 MW in both directions.

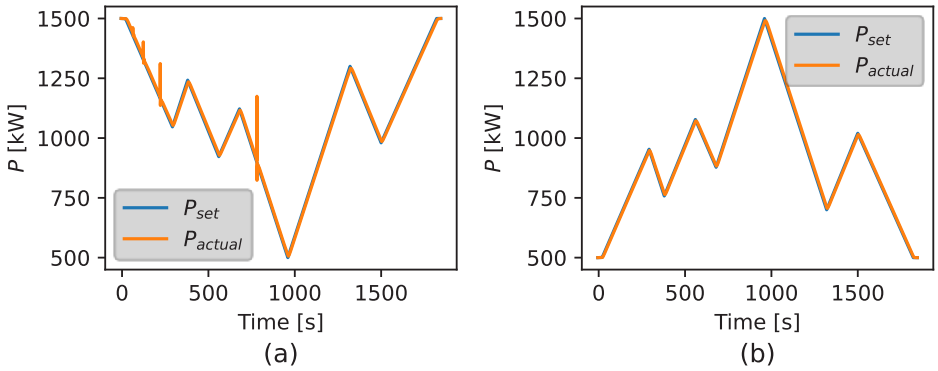

Figure 4: Load-following test for the (a) downward and (b) upward aFRR-product

3.5 Primary reserve

As discussed in Section 3.1 the FAT requirement for FCR is currently not met, due to the maximum ramping rate found with the current control mechanism. Besides this FAT criterium, the system should pass a linearity check by reacting suitably to step changes of one fourth of the contracted capacity. The required FCR capacity should be delivered within a 10 % tolerance margin 12.5 s after the step. The maximum relative deviation values per step are summarized in Table 6. All deviations are within the allowable tolerance. The maximum absolute deviation of the water temperature at the evaporator outlet over the whole ramping interval is 1.24 and 0.22 °C for the stepwise decrease and increase in turbine power output. Although the linearity check is fulfilled, the system currently thus not qualifies for a 0.5 MW symmetric FCR capacity due to the FAT requirement.

Table 6: Overview of power deviations in FCR prequalification test

	Downward FCR		Upward FCR	
Step	**P_{set} [kW]**	**Max deviation [%]**	**P_{set} [kW]**	**Max deviation [%]**
1	875	0.85	1125	6.55
2	750	1.91	1250	3.98
3	625	1.21	1375	3.30
4	500	1.01	1500	3.48

4 CONCLUSIONS

The possibility to deliver grid balancing services with large-scale ORCs in Rankine-based Carnot batteries was investigated. Therefore, a Rankine-based 1.5 MW ORC, suitable for implementation in a Carnot battery using two-tank liquid storage, was modelled dynamically in Modelica. Afterwards, a suitable system control strategy was developed and the system was evaluated according to the prequalification tests for grid balancing services in the European grid. Under the assumption of quasi-steady state thermal machine modelling and ideal behavior of the sensible storage tanks, the system can deliver a capacity of 1 MW for aFRR and mFRR, both in the downward and upward direction. A symmetric capacity of 0.5 MW for FCR is currently not possible due to limitations on the maximum ramping rate of the system. Further research on dynamic ORC control to improve the system's maximum ramping rate would thus be valuable. The results indicate that the delivery of secondary and tertiary balancing services with the ORC could be another revenue stream to increase the financial

feasibility of Carnot battery systems and it is thus worthwhile to investigate the potential financial benefits. In future work, the dynamic model will be extended to a full dynamic Carnot battery model including detailed modelling of the TES and heat pump cycle, hence further investigating optimal system scheduling within the energy system.

NOMENCLATURE

η	efficiency	
aFRR	automatically activated frequency restoration reserve / secondary reserve	(-)
FAT	full activation time	(s)
FCR	frequency containment reserve / primary reserve	(-)
$\dot{m}$	mass flow rate	(kg/s)
mFRR	manually activated frequency restoration reserve / tertiary reserve	(-)
ORC	organic Rankine cycle	(-)
p	pressure	
P	power	
PHE	plate heat exchanger	
PP	pinch point	
PTES	pumped thermal energy storage	(-)
$\dot{Q}$	heat transfer rate	(-)
SC	subooling	(K)
SH	superheat	(K)
T	temperature	
TES	thermal energy storage	(-)
TSO	transmission system operator	(-)
VRE	variable renewable energies	(-)

Subscript

cond	condenser
el	electrical
ev	evaporator
in	inlet
is	isentropic
out	outlet
set	setpoint

REFERENCES

AB, D. S. 2021. Dymola - Dynamic Modelling Laboratory - Full User Manual. In

Andritos, G., Desideri, A., Gantiez, C., Lemort, V., & Quoilin, S. 2016. Steady state and dynamic modelling of a 1 MWel commercial waste heat recovery ORC power plant *29th International conference on Efficiency, Cost, Optimisation, Simulation and Environmental Impact of Energy Systems*, Slovenia.

Argyrou, M. C., Christodoulides, P., & Kalogirou, S. A., 2018, Energy storage for electricity generation and related processes: Technologies appraisal and grid scale applications, *Renewable and Sustainable Energy Reviews*, *94*: p. 804-821.

Arpagaus, C., Bless, F., Uhlmann, M., Schiffmann, J., & Bertsch, S. S., 2018, High temperature heat pumps: Market overview, state of the art, research status, refrigerants, and application potentials, *Energy*, *152*: p. 985-1010.

De Paepe, M., Lecompte, S., & Pillai, A. 2019. CHESTER D3.4 - Detailed design of the ORC laboratory prototype.

Desideri, A., Zhang, J., Kærn, M. R., Ommen, T. S., Wronski, J., Lemort, V., & Haglind, F., 2017, An experimental analysis of flow boiling and pressure drop in a brazed plate heat exchanger for organic Rankine cycle power systems, *International Journal of Heat and Mass Transfer*, *113*: p. 6-21.

Dumont, O., Frate, G. F., Pillai, A., Lecompte, S., De paepe, M., & Lemort, V., 2020, Carnot battery technology: A state-of-the-art review, *Journal of Energy Storage*, *32*: 101756.

Elia. 2019. FCR service design note.

Elia. 2022a. Automatic Frequency Restoration Process (aFRR/R2). Retrieved 06/11/2022 from https://www.elia.be/en/electricity-market-and-system/system-services/keeping-the-balance/afrr

Elia. 2022b. Balancing services: mFRR - design note.

Eric W. Lemmon, I. H. B., Marcia L. Huber, Mark O. McLinden. 2018. REFPROP Documentation, Release 10.0.

Frate, G. F., Antonelli, M., & Desideri, U., 2017, A novel Pumped Thermal Electricity Storage (PTES) system with thermal integration, *Applied Thermal Engineering*, *121*: p. 1051-1058.

Funke. 2022. PLATE HEAT EXCHANGERS - Variety and top product quality.

García-Cascales, J. R., Vera-García, F., Corberán-Salvador, J. M., & Gonzálvez-Maciá, J., 2007, Assessment of boiling and condensation heat transfer correlations in the modelling of plate heat exchangers, *International Journal of Refrigeration*, *30*(6): p. 1029-1041.

Heggarty, T., Bourmaud, J.-Y., Girard, R., & Kariniotakis, G., 2019, Multi-temporal assessment of power system flexibility requirement, *Applied Energy*, *238*: p. 1327-1336.

Holger, M. 2010. Pressure Drop and Heat Transfer in Plate Heat Exchangers.

Imran, M., Pili, R., Usman, M., & Haglind, F., 2020, Dynamic modeling and control strategies of organic Rankine cycle systems: Methods and challenges, *Applied Energy*, *276*: 115537.

Lecompte, S., Huisseune, H., van den Broek, M., Vanslambrouck, B., & De Paepe, M., 2015, Review of organic Rankine cycle (ORC) architectures for waste heat recovery, *Renewable and Sustainable Energy Reviews*, *47*: p. 448-461.

Lee, D., Kim, D., Park, S., Lim, J., & Kim, Y., 2018, Evaporation heat transfer coefficient and pressure drop of R-1233zd(E) in a brazed plate heat exchanger, *Applied Thermal Engineering*, *130*: p. 1147-1155.

Lu, C., Shi, X., He, Q., Liu, Y., An, X., Cui, S., & Du, D., 2022, Dynamic modeling and numerical investigation of novel pumped thermal electricity storage system during startup process, *Journal of Energy Storage*, *55*: 105409.

Marina, A., Spoelstra, S., Zondag, H. A., & Wemmers, A. K., 2021, An estimation of the European industrial heat pump market potential, *Renewable and Sustainable Energy Reviews*, *139*: 110545.

McTigue, J. D., Farres-Antunez, P., J, K. S., Markides, C. N., & White, A. J., 2022, Techno-economic analysis of recuperated Joule-Brayton pumped thermal energy storage, *Energy Conversion and Management*, *252*: 115016.

Meesenburg, W., Markussen, W. B., Ommen, T., & Elmegaard, B., 2020, Optimizing control of two-stage ammonia heat pump for fast regulation of power uptake, *Applied Energy*, *271*: 115126.

Tafone, A., Pili, R., Pihl Andersen, M., & Romagnoli, A., 2023, Dynamic modelling of a compressed heat energy storage (CHEST) system integrated with a cascaded phase change materials thermal energy storage, *Applied Thermal Engineering*, *226*: 120256.

The Modelica Association. 2023. https://modelica.org/index.html

Timko, L. P. 1984. Energy efficient engine: high pressure turbine component test performance report (NASA contractor report; 162829, Issue.

TLK Thermo GmbH & IfT 2020. TIL 3.7 – Model library for thermal components and systems. In

Vecchi, A., Knobloch, K., Liang, T., Kildahl, H., Sciacovelli, A., Engelbrecht, K., Li, Y., & Ding, Y., 2022, Carnot Battery development: A review on system performance, applications and commercial state-of-the-art, *Journal of Energy Storage*, *55*: 105782.

Villar, J., Bessa, R., & Matos, M., 2018, Flexibility products and markets: Literature review, *Electric Power Systems Research*, *154*: p. 329-340.

Zhang, J., Kærn, M. R., Ommen, T., Elmegaard, B., & Haglind, F., 2019, Condensation heat transfer and pressure drop characteristics of R134a, R1234ze(E), R245fa and R1233zd(E) in a plate heat exchanger, *International Journal of Heat and Mass Transfer*, *128*: p. 136-149.

ORC SEVILLE 2023
7th International Seminar on O.R.C. Power Systems

© 2024 Editorial Universidad de Sevilla. Este es un artículo de acceso abierto distribuido bajo los términos de la licencia de uso y distribución Creative Commons (BY-NC-ND 4.0)

DOI: https://dx.doi.org/10.12795/9788447227457_8

Calibration of multi-hole probes for measurements in compressible organic vapor flows

Leander Hake[1,*], Stephan Sundermeier[1], Stefan aus der Wiesche[1], Maximilian Passmann[2]

[1] *Muenster University of Applied Sciences, Stegerwaldstr. 39, 48565 Steinfurt, Germany*
[2] *Ruhr-Universität Bochum, Universitätsstr. 150, 44801 Bochum, Germany*

*Corresponding Author: leander.hake@fh-muenster.de

ABSTRACT

Multi-hole probes are necessary devices to measure flow characteristics and losses in turbomachinery. The present contribution reports the first experience with calibrating and using multi-hole probes in high-speed flows of the organic vapor Novec 649 at elevated pressure and temperature levels. It is found that the classical scheme, established for perfect gas applications, must be extended by an additional quantity reflecting the impact of the initial thermodynamic state on the pressure signals and the data reduction. The practical use and operational issues of three- and five-hole probes for ORC-turbomachinery research are discussed based on the new results. A promising hybrid experimental-numerical calibration approach significantly reduces the tremendous calibration effort.

1 INTRODUCTION

Multi-hole probes for measuring flow angles and Mach numbers have long been used in turbomachinery applications working with perfect gas. Although powerful optical or thermal flow measurement techniques are now available, pneumatic probes are still the only approach for determining losses in turbomachinery. Whereas the calibration of multi-hole probes and the data reduction is relatively straightforward in incompressible flow (see, for instance, Hall and Povey (2017)), substantial efforts are required for compressible flows. The significant increase in calibration efforts is caused by the need to include the Mach number M as a relevant similarity number for compressible flows. Main et al. (1996) used a pseudo-Mach number coefficient C_M as an additional dimensionless parameter in addition to the pitch, yaw, and total pressure coefficients. Johanson et al. (2001) proposed a calibration scheme based on probe sectors, and Bachner et al. (2022) considered probes with base pressure holes for transonic flow applications. Due to the decreasing sensitivity regarding the pseudo-Mach number coefficient, this flow regime is particularly challenging.

To utilize multi-hole probes for investigations of the flow through cascades for organic Rankine cycle (ORC) turbines, some specific challenges must be considered. Firstly, the potential problem of condensation of the organic vapor requires special attention for pneumatic measurement systems, see Conti et al. (2022). Furthermore, the complex thermodynamic behavior of the isentropic flow relations always requires additional efforts in data reduction for organic vapors, as Schollmeier and aus der Wiesche (2022) discussed for Pitot probes.

In addition to the well-known challenges for multi-hole probe calibration in compressible flows of perfect gases, a completely new problem enters when non-ideal compressible fluid dynamics (NICFD) are considered. In NICFD, the pressure ratios and multi-hole probe coefficient behavior depend on the inlet or initial total state of the fluid. Whereas universal isentropic relations exist for a perfect gas utilizing the isentropic exponent γ, these relations become functions of the initial thermodynamic state in the case of non-ideal gas dynamics. Considering a van der Waals model, Tsien (1946) predicted this specific NICFD feature, and Spinelli et al. (2018) reported evidence for this phenomenon in experiments with expanding flows of siloxane in a Laval nozzle. For compressible flows, the data reduction process of pneumatic probes rests largely on isentropic relations. Thus, the probe calibration maps or calibration

spaces for multi-hole probes applied to organic vapor flows have to consider, in principle, the initial thermodynamic state. They are not generally independent of initial thermodynamic states, as in the case of a perfect gas. No information is available in the literature on how relevant this specific NICFD phenomenon would be for multi-hole probe data reduction. It might be argued that this NICFD feature might not affect all flow quantities similarly. For instance, the flow angle determination might be less influenced by the initial thermodynamic state as the static pressure measurement.

So far, only Pitot probes, and not multi-hole probes, have been employed for organic vapor flows (e.g., Baumgärtner (2020), Reinker et al. (2021), Conti et al. (2022), aus der Wiesche (2023)). Therefore, more information about calibrating and applying multi-hole probes in compressible organic vapor flows is needed. Their use is essential for determining ORC turbine cascade loss and investigating complex flow phenomena.

2 FUNDAMENTALS OF MULTI-HOLE PROBES

The fundamentals of multi-hole probes can be illustrated by considering a typical five-hole probe schematically shown in Figure 1 with its hole numbering (the reader will quickly transfer the following relations to three-hole probes). Figure 1 also shows the two probe designs investigated in this study.

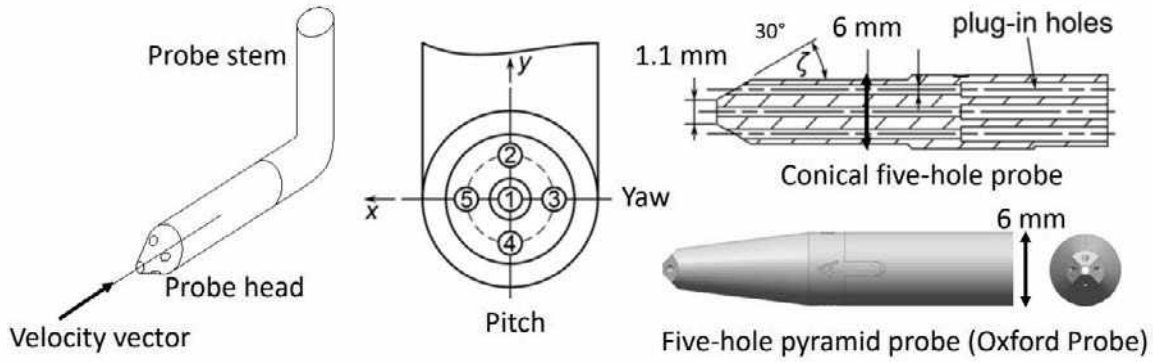

Figure 1: Schematic of a five-hole probe, hole numbering convention, and the study's probe designs

Adopting the definition used by Passmann et al. (2021), the pitch and yaw, and total pressure coefficients are

$$C_\alpha = \frac{p_2 - p_4}{p^*_{dyn}} \quad \text{and} \quad C_\beta = \frac{p_5 - p_3}{p^*_{dyn}} \quad \text{and} \quad C_{pt} = \frac{p_t - p_1}{p^*_{dyn}} \tag{1}$$

with the pseudo-dynamic pressure $p^*_{dyn} = p_1 - p_{avg}$ and $p_{avg} = (p_2 + p_3 + p_4 + p_5)/4$. Here, p^*_{dyn} is called a pseudo-dynamic pressure since p_1 and p_{avg} are close to the total and static pressures for flow-aligned probes ($\alpha = \beta = 0$) but deviate significantly if the flow is at incidence. It should be noted that alternative definitions for p_{avg} are sometimes used as discussed by Hall and Povey (2017).

To account for compressibility effects, a Mach number coefficient (sometimes called the pseudo-Mach number for the same reasons) is used according to Main et al. (1996)

$$C_M = \sqrt{\frac{2}{\gamma - 1}\left(\left(\frac{p_1}{p^*_{dyn}}\right)^{\frac{\gamma-1}{\gamma}} - 1\right)}. \tag{2}$$

In the case of organic vapor, the choice of the value of the isentropic exponent γ is, in principle, not free of difficulties (see Schollmeier and aus der Wiesche (2022)). However, C_M only represents a calculation quantity, not the actual Mach number. In this study, the Mach number coefficient (2) is evaluated using the specific heat ratio γ at the actual stagnation state of the working fluid.

The pressure distribution measured at the probe tip determines the calibration coefficients. Dimensional analysis shows that for the compressible flow of a perfect gas, a probe flow quantity is a function of the angles α and β, the Reynolds number *Re*, the Mach number *M*, and the isentropic

exponent γ. The Reynolds number dependency vanishes for sufficiently high probe Reynold numbers (Passmann et al. (2021a)). This condition is typically fulfilled in high-speed flows of organic vapors. However, an additional dimensional similarity number X is necessary to account for real gas effects in non-ideal compressible flows (see aus der Wiesche and Reinker (2022). Thus, for a five-hole probe, the three-dimensional calibration space $\{\alpha, \beta, M\}$ must be extended to a four-dimensional hyperspace $\{\alpha, \beta, M, X\}$ in the case of organic vapor flows. The need to introduce this additional similarity number X is directly related to the problem of the impact of the initial thermodynamic state, as discussed above. So far, no standard for X has been established, although sometimes the compressibility factor Z or the fundamental derivative of gas dynamics Γ are considered additional similarity quantities. Without an appropriate definition of X, the calibration of multi-hole probes has to account for the stagnation temperature T_t and pressure p_t (i.e., the temperature and pressure in the settling chamber of the wind tunnel). The stagnation conditions represent the initial thermodynamic state in the present wind tunnel experiments. The subject of the present study is to investigate how relevant the inlet state is for an actual multi-hole probe calibration for organic vapors.

3 EXPERIMENTAL AND NUMERICAL METHOD

The experimental study was conducted in the closed-loop organic vapor wind tunnel facility CLOWT calibration test section at Muenster University of Applied Sciences. General technical details about CLOWT are provided by Reinker et al. (2021, 2021a) and Hake et al. (2022). Figure 2 shows the wind tunnel schematically (without an electrical heating system and thermal insulation) and the calibration test section in more detail. The working fluid was Novec 649 by 3M. Selected thermodynamic properties of Novec 649 are listed in Table 1.

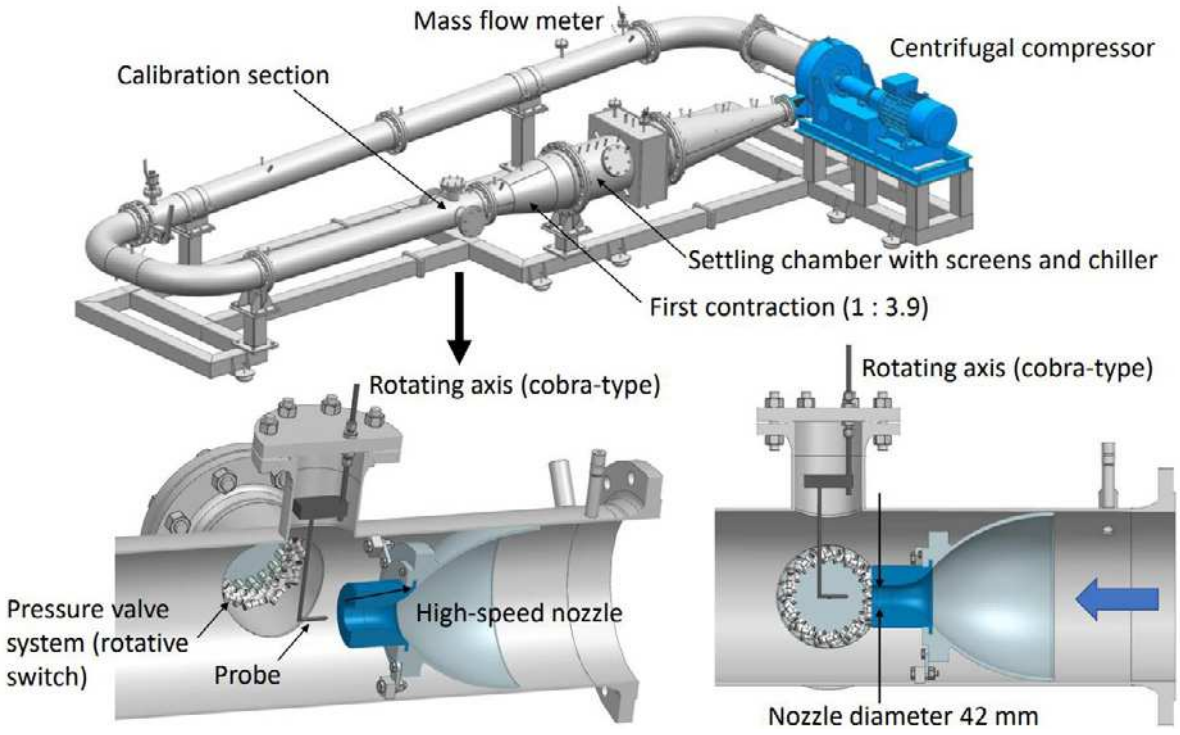

Figure 2: Test facility CLOWT and details of the calibration test section

Table 1: Thermodynamic properties of Novec 649 (after REFPROP by NIST)

Chemical Formula	Molecular Mass	Critical Pressure	Critical Temperature
$CF_3CF_2C(O)CF(CF_3)_2$	316 g/mol	1.88 MPa	442 K

The multi-hole probes were calibrated inside the calibration chamber's free jet (diameter 42 mm). The yaw angle β of the probes could be continuously varied by a cobra-type mechanism shown in Figure 2. The pitch angle α was fixed during a yaw-angle variation. The organic vapor was driven by a centrifugal compressor with variable running speed, controlling the calibration Mach number M. The total or stagnation pressure p_t and the total temperature T_t were recorded in the settling chamber. The vapor flow was accelerated to transonic speeds in a two-stage contraction zone. The static pressure p was measured at the exit of the high-speed nozzle and in the calibration chamber. In an initial set of measurements, the inflow turbulence level was determined by hot-wire anemometry to be Tu = 0.2 % up to 1.0 % at higher Mach numbers.

Before the multi-hole probe calibration, Pitot probe measurements were carried out in the free jet to verify the assumption of an isentropic nozzle expansion. The approach described by Reinker et al. (2021) and Hake et al. (2022) was employed for all pressure measurements to prevent potential measurement errors due to condensation. In this approach, all pressure lines were placed inside the heated wind tunnel, and a rotative mechanism switched the valves to the pressure transducer (see Figure 2). During the calibration, the total temperature was controlled by the chiller and the electrical heating system. The mass flow rate was measured independently in the return of the wind tunnel enabling an accurate determination of the Mach number. The amount of mass filled in the closed wind tunnel determined the density level and hence the Reynolds number Re.

The present study considers two probe designs shown in Figure 1 (right). The conical five-hole probe had the advantage that its body obeyed cylindrical symmetry, making the numerical calibration viable (see the following section and Passmann et al. (2021). In addition, the so-called Oxford Probe design (Hall and Povey (2017)) was considered, too. The Oxford Probe design is based on a truncated pyramid body with flow separation and probe sensitivity advantages. Using this pyramid body, the behavior of an original five-hole probe and a three-hole probe was investigated in the experiments with Novec 649 at two different operation conditions listed in Table 2. The two experimental cases (HD and LD, see Table 2) are shown as black dots in the T,s-diagram of Figure 3.a, too. The probe Reynolds numbers $Re = \rho U d/\mu$ with the probe diameter d and inflow velocity U was of order $Re = 5 \times 10^4$ up to 8×10^5 (with an uncertainty level of 2 – 5 %). For such a high probe Reynolds number level, the sensitivity against Reynolds number can be neglected, as Passmann et al. (2021a) discussed. Using a Laval nozzle, a maximum Mach number level of M = 1.2 could be achieved in CLOWT, but severe probe stem vibrations occurred for Mach numbers above 0.86. To avoid a destruction of the probe, the calibration was hence restricted to a maximum Mach number of about M = 0.84.

Considering precision and bias errors, the total uncertainty levels listed in Table 3 were achieved for the relevant quantities (see also Reinker et al. (2021a)). Due to the temperature control system, the temperature drift was of order 10^{-3} K/s for a constant compressor running speed, but slightly different temperature levels T_t occurred for different running speeds. Hence, the nominal total temperature levels for the calibration cases, see Table 2) were not precisely achieved for all running speeds during the experimental campaign, and systematic temperature level deviations of order 1 K existed. The nominal total specific enthalpy was nearly identical for the two experimental cases listed in Table 2 (h_t = 391.5 kJ/kg and 390.0 kJ/kg, respectively).

Table 2: Nominal operation conditions for the experimental probe calibration with Novec 649

Case	Density ρ_t	Pressure p_t	Temperature T_t	Compressibility Factor Z	Fundamental derivative Γ
High-density HD	26.9 kg/m^3	2.44 bar	378 K	0.91	0.93
Low-density LD	16.2 kg/m^3	1.51 bar	375 K	0.95	0.97

Table 3: Experimental measurement uncertainty levels (typical values)

Pressure $\Delta p/p$	Temperature $\Delta T/T$	Mach Number $\Delta M/M$	Angle $\Delta\beta$	Coefficients $\Delta C/C$
0.6 % up to 1.0 %	$\leq$ 0.1 %	1.0 % up to 4.0 %	$\leq$ 1°	$\leq$ 3 %

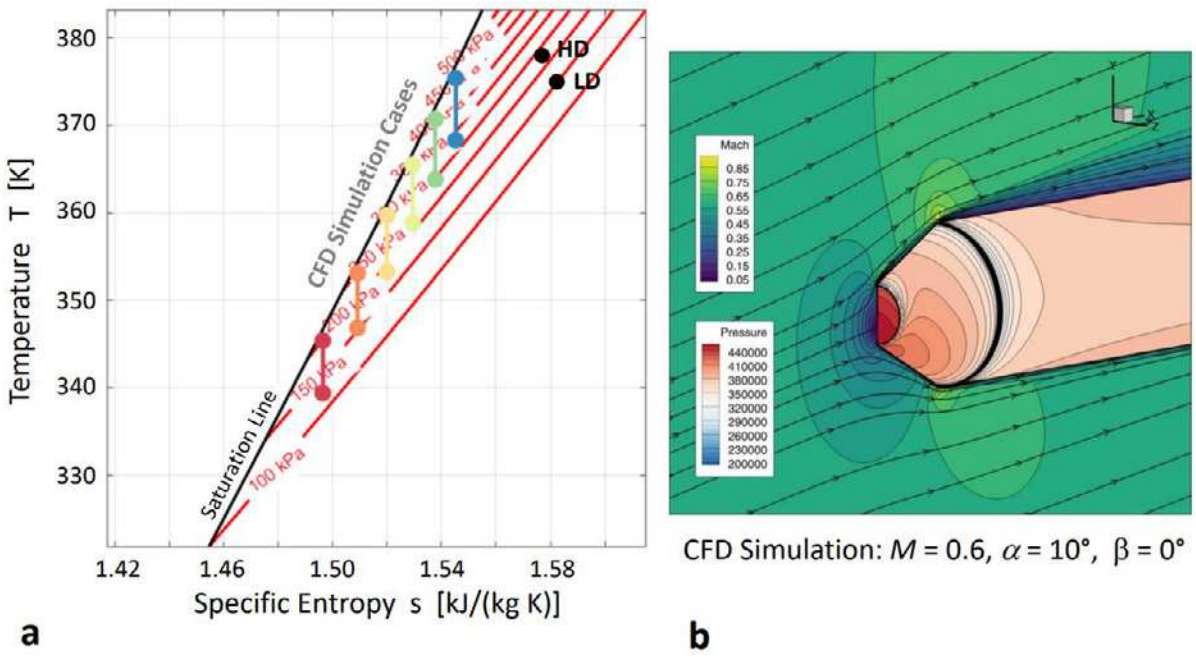

Figure 3: Calibration of multi-hole probes for Novec 649: **a** Simulated and experimentally investigated cases in the *T*,*s*-diagram; **b** simulated pressure and Mach number distribution for a case

In addition to the experimental calibration, the conical five-hole probe was the subject of a numerical calibration. Passmann et al. (2021) describe this approach in detail for air for the same probe design. In the present study, the flow of Novec 649 at several operation points, shown as colored symbols in Figure 3.a was simulated using the open-source CFD code SU2 (version 7.5.1). The k-ω-SST turbulence model and the PRSV cubic equation of state were employed for the CFD simulations. An example of the computed Mach number and surface pressure distributions is shown in Figure 3.b. Considering the locations of the probe pressure holes, the calibration coefficients, see equations (1) and (2), were obtained using the computed surface pressure distribution. The exact geometrical modeling of the actual probe head is essential for the reliability of this numerical approach. Details about this item and the meshing can be found in Passmann et al. (2021).

47

4 RESULTS AND DISCUSSION

This section presents and briefly discusses the results of the numerical and experimental calibration of the multi-hole probes. Special attention is spent on potential deviations from the calibration coefficients and maps (i.e., calibration spaces) obtained for perfect gases in organic vapor flow applications.

4.1 Aligned Probes (Nulling Mode)

For aligned probes working in the so-called nulling mode, the lateral pressure values (hole 2 up to hole 5, Figure 1) are identical. Consequently, the yaw and the pitch coefficients vanish, and only the Mach number coefficient C_M and the total pressure coefficient C_{pt} remain as relevant probe quantities.

The Mach number coefficients C_M for aligned probes are plotted against the Mach number M in Figure 4. Although two different probe designs, shown in Figure 1, were used in the experiments and the CFD simulations, their general behavior was similar. As expected, the Mach number coefficient sensitivity vanished for $M \rightarrow 1$ (the gradient of C_M decreased for $M \rightarrow 1$). This is a fundamental problem of this kind of probe in the transonic flow regime (see Main et al. (1996) or Bachner et al. (2022)).

Interestingly, the numerically computed calibration curves for different stagnation conditions did not exactly collapse to a single curve in Figure 4 (right). In the case of a perfect gas, the Mach number coefficient would not depend on the stagnation state. In the case of Novec 649, a slight but systematic difference can be noticed for the two simulated cases shown in Figure 4 (right).

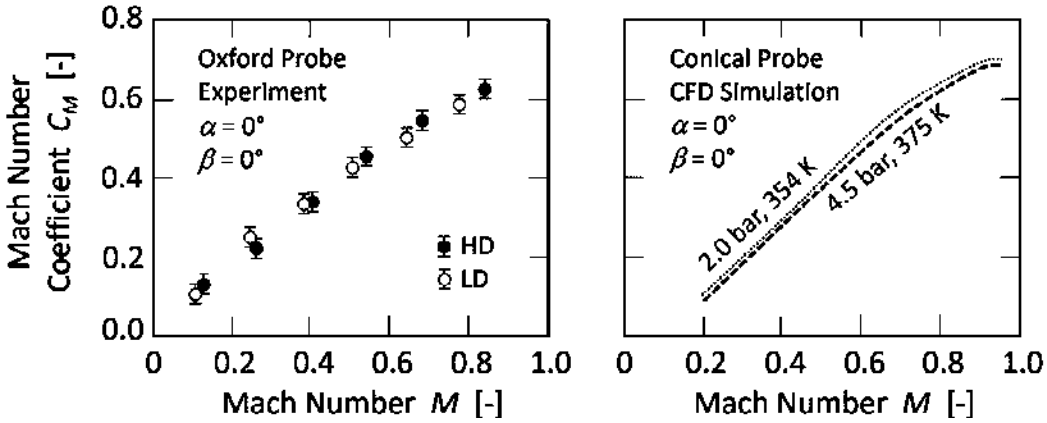

Figure 4: Mach number coefficient against Mach number for aligned probes in a flow of Novec 649

The total specific enthalpy values for the two CFD cases were h_t = 369.4 kJ/kg and 385.17 kJ/kg, respectively. Their compressibility values were Z = 0.9084 and 0.8189, respectively. For the experimental calibration data, Figure 4 (left), the nominal specific enthalpy was nearly identical for the HD and LD cases. Still, the actual values scattered for different Mach numbers due to the static temperature deviations of order 1 K, as explained in section 3. Hence, the impact of the initial stagnation state on the experimental result cannot be identified in Figure 4 (left). The error bars and the temperature scattering were too high for a definite conclusion. Hence, it was decided to conduct a detailed study at a constant running speed and nominal temperature levels to explore this NICFD issue (see the following subsection).

4.2 Three-Hole Probes (Non-Nulling Mode)

Considering non-zero yaw angles β and keeping the pitch angle α to zero, the probes become effectively three-hole probes. Then, the yaw angle, Mach number, and total pressure coefficients are the three relevant parameters for three-hole probes.

Regarding the impact of stagnation states on the calibration, a detailed study at constant compressor running speed and fixed Mach number was conducted for the two cases HD and LD, under their nominal thermodynamic conditions listed in Table 2. The outcome of the experimental and numerical calibrations at fixed Mach numbers are shown in Figure 5. Due to the different density levels, the actual Mach numbers were not identical for the HD and LD cases. Since the Mach number coefficient C_M depends on the Mach number M, the LD original data were corrected using the C_M,M-curve of Figure 4 (left). Figure 5 (left) shows the original and corrected data (in red) for the LD case at the same Mach number as for the HD case.

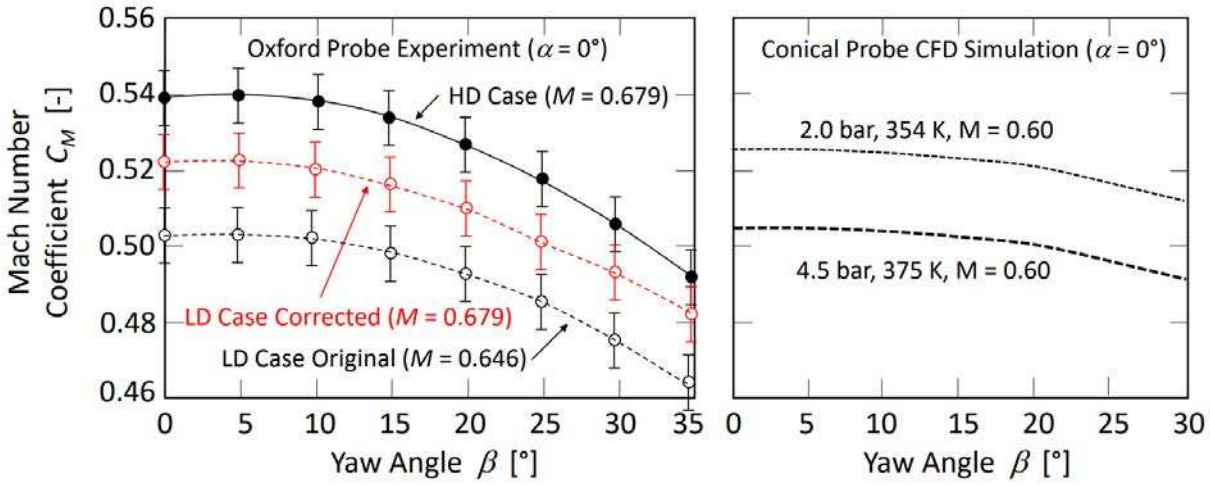

Figure 5: Mach number coefficient against yaw angle in a flow of Novec 649 at fixed Mach number

An impact of the initial thermodynamic state on the Mach number coefficient C_M of about 5 % was observed for the corrected experimental data in Figure 5 (left). In the case of the original data, the difference would be even more considerable. However, since the Mach number dependency was significant, only the corrected LD data (red symbols in Figure 5, left) and the HD data (black symbols) should be compared. The same qualitative behavior and a similar deviation for the Mach number coefficient C_M were also observed in the CFD simulation cases, as shown in Figure 5 (right). In the CFD study, the Mach number was kept the same for the two simulated cases, and no correction was required.

The behavior of the yaw angle and total pressure coefficients is illustrated in Figure 6 for both probes. No systematic influence of the initial thermodynamic state was observed for these quantities. In the case of the CFD simulations, the two cases led to identical results, and hence the two CFD curves collapsed in Figure 6.

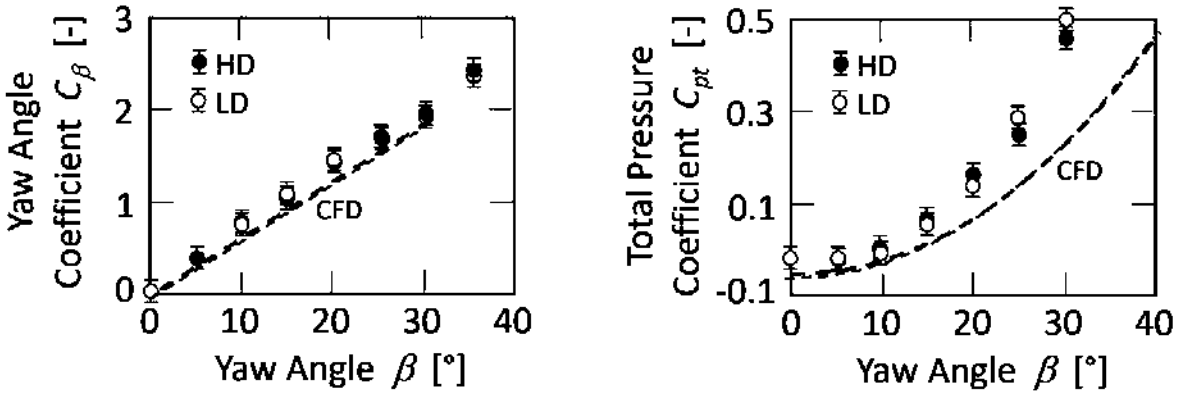

Figure 6: Yaw angle and total pressure coefficients against yaw angle at fixed Mach number

49

The CFD simulations covered the operation points shown in Figure 3; no significant differences were observed for the behavior of the yaw angle and total pressure coefficients as functions of the yaw angle β. The general behavior for the yaw angle and total pressure coefficients was similar for the pyramid and the conical probe. However, a systematic difference can be seen in the total pressure coefficient between the experimental data and the CFD simulations caused by the different probe heads. A good sensitivity was found for the yaw angle coefficient C_β, corresponding to the incompressible flow regime (Hall and Povey (2017)). The observed linear relation between C_β and β and the insensitivity against stagnation states are highly advantageous for flow angle measurement applications. The total pressure coefficient C_{pt} was insensitive against minor yaw angle variations for an aligned probe ($\beta \rightarrow 0$). This is a well-known feature of Pitot probes. For higher yaw angles, the total pressure coefficient C_{pt} exhibited a nonlinear functional dependency on β. Then, the actual probe head design becomes relevant, and a design-specific calibration is needed.

4.3 Practical Considerations for Five-Hole Probe Calibration and Use

The required efforts for a full experimental calibration of a five-hole probe for transonic flow measurements in an organic vapor are substantial, as illustrated by the following example: Following Main et al. (1996), data should be acquired at almost 10,000 individual combinations of pitch angle, yaw angle, and Mach number to calibrate a four-hole probe in the compressible flow of a perfect gas. This large number of points must be significantly increased to cover the impact of the thermodynamic state on the calibration. As a result, a four-dimensional calibration hyperspace must be covered. Furthermore, the calibration facility must be able to operate at the same thermodynamic conditions as planned for the later flow measurements. While it is not impossible to fulfill these requirements, it would be highly time-consuming and costly, severely restricting the use of multi-hole probes in compressible organic vapor flows. Based on these considerations, the following two strategies might offer a more sensible practical approach.

Firstly, the calibration efforts for a three-hole probe are within an acceptable range because the yaw angle and the total pressure coefficients are insensitive against initial states, see Figure 6. The impact of the initial states on the Mach number coefficient is of order 5 %, see Figure 5. It is recommended to use three-hole probes as a standard tool for flow angle determination and restrict the use of five-hole probes to particular studies. The five-hole probe should be used primarily in the nulling mode to limit the calibration efforts. But even then, the probes' size and required turning mechanism would create severe issues for experimental setups.

Secondly, the experimental calibration efforts can be significantly reduced by the numerical calibration method, as proposed by Passmann et al. (2021). Then, the experiments are only required for validation purposes, and a much lower number of data points is needed. This approach works particularly well for probes with a high degree of symmetry (i.e., cylindrical body shape or conical probe heads). Thus, this probe design is recommended for organic vapor flow measurements with five-hole probes in the non-nulling mode.

Artificial neuronal networks or machine learning methods for calibrating multi-hole probes might offer an attractive approach (see, for instance, Rediniotis and Vijayagopal (1999)). However, such an approach cannot avoid the fundamental non-ideal compressible flow dynamical issues and the need to gather a substantial amount of probe calibration data.

5 CONCLUSIONS

The following conclusions can be drawn from the experimental and numerical study of the behavior of multi-hole probes in organic vapor flows.

Dimensional analysis shows theoretically that the three-dimensional calibration space must be extended to a four-dimensional hyperspace for five-hole probes for organic vapor flows. In this case study, the initial thermodynamic state affected only the Mach number coefficient, not the angle or total pressure coefficients. This observation demonstrates that non-ideal compressible fluid dynamics must be accounted for in accurate ORC lab experiments and data reduction procedures. Since the Mach number coefficient C_M is involved in obtaining the static pressure p, this quantity needs special attention in the organic vapor flow field and turbine cascade loss measurements.

50

It was found that three-hole probes behaved well and offered good sensitivity regarding the flow angle determination. Since the calibration workload is at an acceptable level, the use of these devices can be recommended. Furthermore, three-hole probes can be manufactured and miniaturized easier than five-hole probes, supporting their practical use.

Due to their substantial calibration efforts, it is hard to recommend the five-hole probe as a standard tool for transonic flow measurements in organic vapors. The use of this device should be considered in the nulling mode or combination with reliable numerical calibration studies. But even then, the interaction of the relatively large probes with the flow and potential blockage issues might introduce substantial challenges.

NOMENCLATURE

C_α	pitch angle coefficient (see equation (1))	-
C_β	yaw angle coefficient (see equation (1))	-
C_M	Mach number coefficient (see equation (2))	-
C_{pt}	total pressure coefficient (see equation (1))	-
d	probe diameter	m
h	specific enthalpy	J/kg
M	Mach number	-
p	pressure	Pa
p^*_{dyn}	pseudo-dynamic pressure	Pa
Re	Reynolds number	-
s	specific entropy	J/(kg K)
T	temperature	K
Tu	turbulence intensity	-

U	velocity	m/s
X	thermodynamic similarity variable	-
Z	compressibility factor	-

Greek symbols

α	pitch angle (see Figure 1)	°
β	yaw angle (see Figure 1)	°
γ	isentropic exponent	-
Γ	fundamental derivative of gas dynamics	-
μ	dynamic viscosity	Pa s
ρ	density	kg/m3

Subscript

avg	average
t	total or stagnation state
1, 2, …	hole numbering (see Figure 1)

REFERENCES

aus der Wiesche, S., Reinker, F., 2022, Dimensional analysis and performance laws for organic vapor flow turbomachinery, ***Energy***, vol. 257, p. 124635

aus der Wiesche, S., 2023, Experimental Investigation Techniques for Non-Ideal Compressible Fluid Dynamics, ***Int. J. Turbomach. Propuls. Power***, vol. 8(2), p. 11

Bachner, J. R., Pahs, A., Weggler, P., Kocian, F., Rößling, M., 2022, Calibration of pneumatic multi-hole probes for transonic turbomachinery flows, ***CEAS Aeronautical J.***, vol. 13, p. 891-903

Baumgärtner, D., 2020, Real gas effects in ORC turbines, Doctoral thesis, University of Cambridge, Cambridge, England

Conti, C. C., Fusetti, A., Spinelli, A., Gaetani, P., Guardone, A., 2022, Pneumatic system for pressure probe measurements in transient flows of non-ideal vapors subject to line condensation, ***Measurement***, vol. 192, p. 110802

Hake, L., Reinker, F., Wagner, R., aus der Wiesche, S., Schatz, M., 2022, The Profile Loss of Additive Manufactured Blades for Organic Rankine Cycle Turbines, ***Int. J. Turbomach. Propuls. Power***, vol. 7(1), 11

Hall, B. F., Povey, T., 2017, The Oxford Probe: An Open Access Five-Hole Probe for Aerodynamic Measurements, ***Meas. Sci. Technol***., vol. 28(3), p. 035004

Johansen, E. S., Rediniotis, O. K., Jones, G., 2001, The Compressible Calibration of Miniature Multi-Hole Probes, ***ASME J. Fluids Eng***., vol. 123, p. 128-138

Main, A. J., Day, C. R. B., Lock, G. D., Oldfield, M. L. G., 1996, Calibration of a four-hole pyramid probe and area traverse measurements in a short-duration transonic turbine cascade tunnel, ***Exp. Fluids***, vol. 21, p. 302-311

Passmann, M., aus der Wiesche, S., Joos, F., 2021, Numerical Calibration of Three-Dimensional Printed Five-Hole Probes for the Transonic Flow Regime, ***ASME J. Fluids Eng***., vol. 143, p. 051501

Passmann, M., aus der Wiesche, S., Povey, T., Bergmann, D., 2021a, Effect of Reynolds Number on Five-Hole Probe Performance: Experimental Study of the Open-Access Oxford Probe, ***ASME J. Turbomach***., vol. 143, p. 091003.

Reinker, F., Wagner, R., Passmann, M., Hake, L., aus der Wiesche, S., 2021, Performance of a Rotatable Cylinder Pitot Probe in High Subsonic Non-Ideal Gas Flows, in: ***Proceedings of the 3rd International Seminar on Non-Ideal Compressible Fluid Dynamics for Propulsion and Power***, Springer, Berlin

Rediniotis, O. K., Vijayagopal, R., 1999, Miniature multihole pressure probes and their neural-network-based calibration, ***AIAA J.*** , vol. 37 (6), p. 666–674

Reinker, F., Wagner, R., Hake, L, aus der Wiesche, S., 2021a, High subsonic flow of an organic vapor past a circular cylinder, ***Exp. Fluids***, vol. 62, p. 54

Schollmeier, J.-N., aus der Wiesche, S., 2022, A user-friendly pitot probe data reduction routine for non-ideal gas flow applications, *Energy*, vol. 261, part A, p. 125143

Spinelli, A., Cammi, G., Gallarini, S., Zocca, M., Cozzi, F., Gaetani, P., Dossena, V., Guardone, A., 2018, Experimental evidence of non-ideal compressible effects in expanding flow of a high molecular complexity vapor, *Exp. Fluids*, vol. 59, p. 126

Tsien, H. S., 1946, One-dimensional flows of a gas characterized by van der Waal's equation of state, *J. Math. Phys.*, vol. 25, p. 301–324

ACKNOWLEDGEMENTS

This study was conducted within the Franco-German research project REGAL-ORC funded by ANR and DFG. The support of the lab engineer, Mustafa Kuzgunoglu-Hennecke, during the experiments, is highly appreciated.

ORC SEVILLE 2023
7th International Seminar on O.R.C. Power Systems

© 2024 Editorial Universidad de Sevilla. Este es un artículo de acceso abierto distribuido bajo los términos de la licencia de uso y distribución Creative Commons (BY-NC-ND 4.0)

DOI: https://dx.doi.org/10.12795/9788447227457_9

pocketORC: A BROWSER-BASED CALCULATOR FOR TEACHING ORGANIC RANKINE CYCLE POWER SYSTEMS

Martin T White

Thermo-Fluid Mechanics Research Centre, School of Engineering and Informatics, University of Sussex, Falmer, Brighton, UK

Corresponding Author: martin.white@sussex.ac.uk

ABSTRACT

This paper presents a steady-state design model for an organic Rankine cycle (ORC) power plant that is completely web-browser based and does not rely on any external libraries (e.g., for the computation of thermodynamic properties). This means the tool can be easily accessed by students via any electronic device with a web browser and used as a teaching aid to teach basic principles relating to ORC power systems. Therefore, ORC power cycles can be introduced interactively without requiring any programming knowledge or the distribution and installation of source files. This allows ORC power systems to be introduced earlier in the curriculum, and to a wider variety of students, than might otherwise be possible. The current version of the model combines the Peng-Robinson equation of state with a thermodynamic model of a recuperated ORC system and discretised heat exchanger sizing models. The model is written in the Python programming language and the PyScript framework is used to call Python code directly from HTML. The user can vary cycle variables such as the condensation temperature, pressure ratio, degree of superheat, recuperator effectiveness and heat-source temperature drop via the graphical-user interface which returns key indicators of cycle performance such as thermal efficiency and power output amongst others. The tool enables single-point calculation and parametric studies of a single variable and includes introductory self-paced lessons. This allows students to develop an understanding of the influence of different cycle variables on cycle performance. This paper provides an overview of the tool and its capabilities, alongside discussing its potential role as a teaching aid to support the introduction of ORC power systems into the curriculum.

1 INTRODUCTION

Over recent decades there has been a growing interest in the organic Rankine cycle (ORC) as a suitable power cycle for the conversion of low-temperature heat into power. Specifically, the ability of the cycle to convert low temperature heat from renewable sources, such as solar thermal and geothermal, alongside industrial waste heat, into power means the cycle could be an integral part of future clean energy infrastructure. Alongside this, there is a growing acknowledgement about the importance of heat pumps in the electrification and decarbonisation of heat production, and ORC systems and heat pumps share several similarities in terms of the underlying scientific fundamentals.

As such, there is a clear need for engineers and energy professionals who develop an understanding of these technologies during their education who then have the skills necessary to work with these technologies in their professional careers. Unfortunately, the complex thermodynamic nature of organic fluids means it can be difficult to fully address the underlying physics within traditional teaching activities. For example, a traditional Brayton cycle can be easily modelled using a simple system of equations that can be formulated based on the ideal gas law. This means a relatively simple system of equations can be easily solved by students, and trends in performance parameters, such as efficiency, with key cycle variables can be readily established. In comparison, for an ORC system, or indeed a

steam Rankine cycle, the more complex thermodynamic behavior means such activities can only be carried out if tabular thermodynamic properties are provided, and a rather tedious analysis procedure adopted. This may typically mean that when carrying out hand calculations in class only single-point calculations can be done, whilst trends can be shown to students but not easily replicated.

The challenge of introducing these cycles operating with more complex thermodynamic fluids into the curriculum can be aided with the use of computational modelling tools. This could include using standard software such as Excel with a suitable add-in or using more specialist open-source or commercial software. Within the ORC community there have been a number of open-source tools that have been developed for ORC power cycles in mind, which includes, amongst others, CoolProp (Bell et al., 2014) for predicting fluid properties, ThermoCycle (Quoilin et al., 2014) and ThermoPower (Casella & Leva, 2003) for dynamic modelling in Modelica, the ORC modeling kit (Dickes et al., 2016) for steady state simulation, and NiceProp (Giuffre & Pini, 2022) for characterising the non-ideal gas dynamics of organic fluids. However, many of these tools are perhaps aimed more at other researchers, alongside post-graduate students that may be completing MSc or PhD research projects in the area. They also require downloading and installing source code, and therefore a degree of fluency in programming. As such, these tools may not be that suitable for undergraduate students, or indeed post-graduate students who may have an interest in renewable and sustainable energy technologies and are enrolled onto taught courses related to energy policy, economics or business management. These students stand to benefit by learning about ORC systems, but may lack familiarity or confidence in computational modelling or programming. Of course, example models could be setup in commercial modelling software, such as Simulink or Aspen as examples, but this requires a certain level of literacy with those tools, alongside timetabled computer labs where students have access to licensed software.

This paper introduces a new steady-state modelling tool for ORC power systems, named pocketORC, that operates straight from the web browser and relies purely on data entry via a web form. This means topics related to the design and simulation of ORC power systems can be introduced in the curriculum, and students can carry out cycle simulations in real time using any electronic device with access to the internet. As such, the effect of the working fluid, and trends in key performance parameters with different cycle variables can be easily assessed in real time. This paper is structured in three parts. Firstly, an overview of the tool is provided in Section 2, which includes details on how the tool has been developed and a summary of its capabilities. This is followed by an overview of the underlying mathematical modelling in Section 3. In the third part of this paper, examples of how this tool could be used to introduce ORC power systems into the curriculum are discussed.

54

The tool can be accessed via the following link: https://martintwhite.github.io/pocketORC/.

2 OVERVIEW AND IMPLEMENTATION

pocketORC is a steady-state simulation tool for ORC systems that is based on in-house Python scripts that have been developed by the author for predicting the thermodynamic properties of organic fluids and for simulating ORC power systems. The inputs required to run the pocketORC tool, alongside the outputs generated via the tool, are integrated within a graphical-user interface written in HTML. To call the Python scripts directly from HTML, the recently developed open-source PyScript framework (Anaconda, 2022) is employed. This enables the Python scripts to be uploaded onto the web server and to be run directly from the browser. As such, no installation of any local files is necessary.

An overview of the capabilities of the model is provided in Figure 1. For several fixed inputs that define the intended heat source and heat sink, alongside component parameters, the user can vary the working fluid and six different cycle variables to vary the performance of the system. The outputs of the model include the power output, mass-flow rate, first- and second-law efficiencies alongside the pinch points and UA requirements of the heat exchangers. These are reported in tabular form, alongside a temperature-entropy diagram of the resulting cycle. The tool can simulate a range of different cycle variants, including simple subcritical cycles, recuperated cycles, transcritical cycles and trilateral or

partially evaporating cycles. Currently, three working fluids can be modelled, namely R1233zd(E), *n*-pentane and hexamethyldisiloxane (MM), although additional fluids can be easily added in the future.

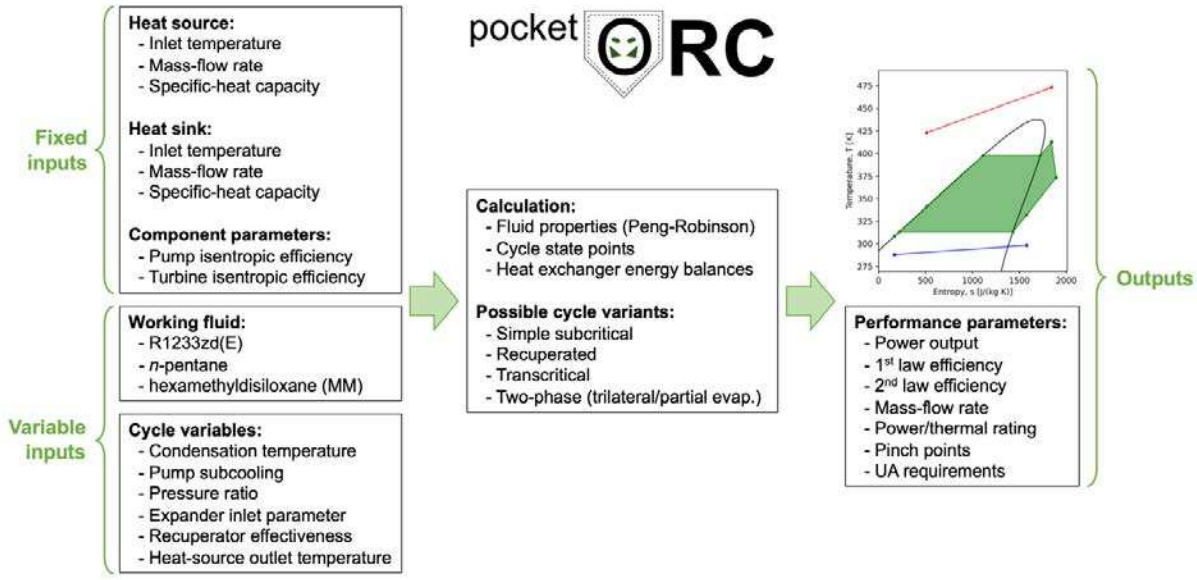

Figure 1. Overview of the modelling capabilities of pocketORC.

3 MATHEMATICAL MODELLING

This section summarises the underlying mathematical modelling that takes placed under the hood of pocketORC. To an experienced researcher working with ORC systems, it is anticipated that this theory is very familiar and therefore the precise mathematical details will not be provided here. Instead, a short summary of the approach is provided, alongside supporting justifications. A more detailed description of the underlying calculations will be made available on the website.

55

3.1 Thermodynamic properties

Thermodynamic properties of the working fluid are calculated using an in-house thermodynamic module based on the Peng-Robinson equation that has been developed by the author in a previous work (White & Sayma, 2018). Although the Peng-Robinson equation of state is not as accurate as state-of-the-art multi-parameter equations of state, such as those implemented within software packages such as CoolProp and REFPROP, the Peng-Robinson equation of state is known to provide reasonable predictions for fluid properties, particularly in the vapour-phase region. In the previous work, a maximum deviation in power output of 5.9% was found between cycle calculations completed using the Peng-Robinson equation of state and using REFPROP (White & Sayma, 2018). This level of accuracy is considered sufficient for a tool whose primary purpose is teaching. More importantly, the in-house module is simple and is uploaded to the web server as a single python script which can be run directly using PyScript. The module includes all the necessary calculations for modelling thermodynamic cycles, including the prediction of saturation properties at fixed temperature or pressure and the prediction of single-phase properties based on temperature-pressure, pressure-enthalpy, and pressure-entropy flash calculations. Working fluids are defined based on six fluid parameters, including the critical temperature, critical pressure, acentric factor, and the coefficients for a second-order polynomial describing the variation in ideal-specific heat capacity with temperature.

3.2 Thermodynamic cycle modelling

The thermodynamic cycle model is largely based on cycle modelling activities previously completed by the author (White & Sayma, 2019, White 2021). The cycle is assumed to operate under a steady-state and no heat losses or pressure drops are considered. The model can be used to simulate different cycle architectures, including recuperated and transcritical cycles, alongside cycles operating with two-

phase expansion. The heat source and heat sink are both modelled as fluid streams with a fixed specific-heat capacity, where the inlet temperature, mass-flow rate and specific-heat capacity of each stream are model inputs. The pump and turbine are modelled with a fixed isentropic efficiency. All heat exchangers are modelled as counter-flow heat exchangers using a discretised approach to determine the fluid temperature profiles. The log-mean temperature difference is then used to determine the total UA value (i.e., product of overall heat transfer coefficient U and heat exchanger surface area A) for each heat-transfer region, namely preheating, evaporation, superheating, precooling, condensation, subcooling and recuperation.

For a fixed heat source and heat sink, alongside fixed isentropic pump and turbine efficiencies, there are six variables that can be used to adjust the performance of the cycle. These are: the condensation temperature; the degree of subcooling at the pump inlet; the pressure ratio; the expander inlet parameter; the recuperator effectiveness; and the heat-source outlet temperature. All of these have standard definitions, except for the expander inlet parameter, x, which is used to enable cycles with single- and two-phase expansion to be modelled using a single parameter (White, 2021). If $x < 1$, then x defines the expander inlet vapour quality, otherwise it determines the expander inlet temperature from:

$$T = T_{\mathrm{ev}} + (x - 1)(T_{\mathrm{hi}} - T_{\mathrm{ev}}) \quad (1)$$

where T is the expander inlet temperature, T_{ev} is the evaporation temperature and T_{hi} is the heat-source inlet temperature. Thus, by allowing x to range between 1 and 2 it is possible to move the expander inlet condition from being saturated vapour (x = 1) to an expander inlet temperature that equals the heat-source inlet temperature (x = 2).

For a given set inputs, the model returns first- and second-law efficiency, the working-fluid mass-flow rate, the power rating or thermal load of each component, alongside the pinch-point temperature difference and UA value for each heat exchange process.

56

4 USAGE AS A TEACHING TOOL

4.1 Single-point performance calculation and parametric studies

In the first instance, pocketORC can be used as a single point calculator, in which, for a given set of fixed parameters and inputs, the tool calculates the performance of the cycle. The output of this calculation is a table that reports the key performance indicators alongside a temperature-entropy diagram of the cycle with the heat-source and heat-sink temperature profiles superimposed. Thus, based on an understanding of how different cycle variables influence performance, it is possible to carry out a manual iterative process in which the cycle can be optimised for a defined heat source and heat sink. In this capacity, pocketORC is a useful tool for any ORC practitioner looking to get an idea of the achievable performance from an ORC operating within a given application. A typical output from a single-point calculation completed using pocketORC is shown in Figure 2.

The second feature of pocketORC is the ability to carry out single-variable parametric studies. Any one of the six cycle variables can be selected as the parametric variable and a minimum and maximum value can be specified. Using those inputs, pocketORC creates an array of 10 input values ranging from the minimum to the maximum with a constant step and reports the variation in cycle performance parameters in the form of a table. The resulting data can be readily copied and pasted into a spreadsheet or similar program for further post processing if necessary. A typical output from a parametric study completed using pocketORC is shown in Figure 3.

4.2 Introductory lessons into ORC technology

Alongside the single-point and parametric calculators, pocketORC also includes lessons that are available on the website and which students can work through at their own pace. These lessons combine a qualitative explanation of important concepts with interactive plots which are again written in Python and interfaced with the website via PyScript. The aim of these lessons is not to delve into detail

regarding the underlying mathematical calculations, but instead to build up a working model of an ORC power system. Through this, the key cycle variables and fixed parameters considered within the calculator are introduced. It is assumed that before starting these lessons, the student already has some familiarity with important concepts such as thermodynamic state variables (i.e., temperature, pressure, density, enthalpy, entropy) and the general operating principle of a closed-loop power cycle, such as the steam Rankine cycle.

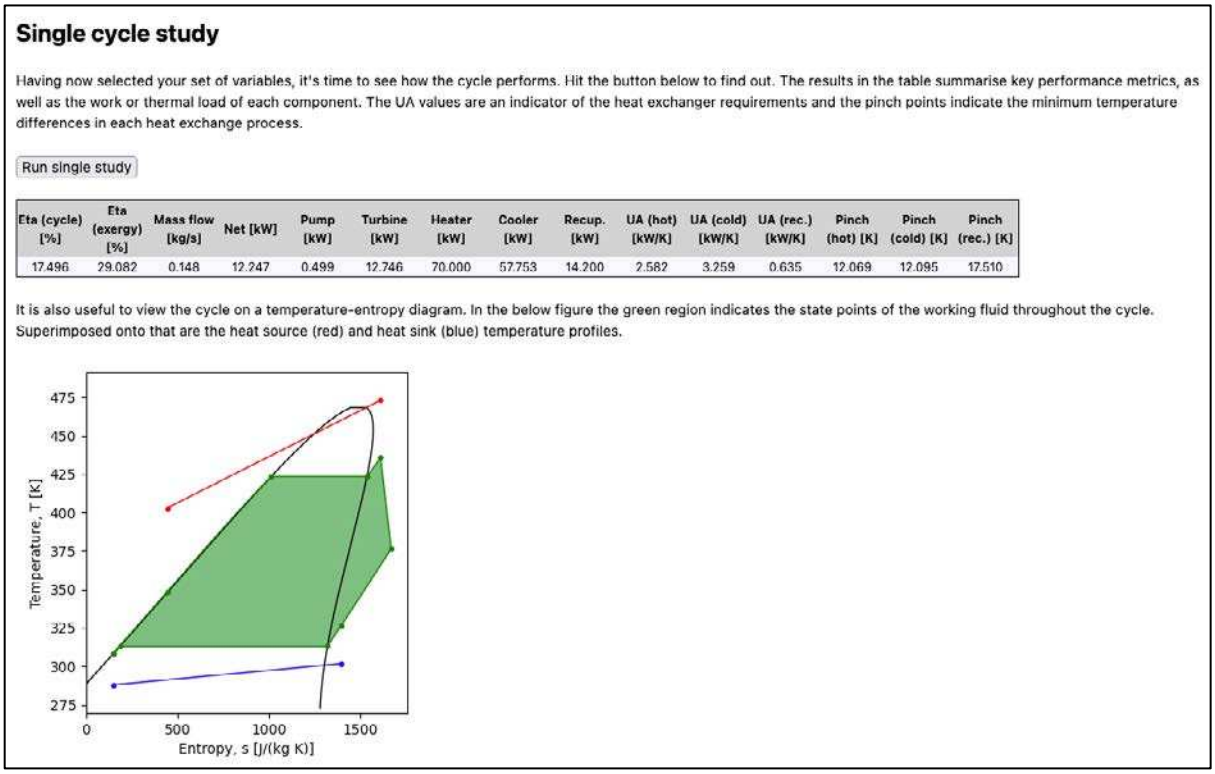

Single cycle study

Having now selected your set of variables, it's time to see how the cycle performs. Hit the button below to find out. The results in the table summarise key performance metrics, as well as the work or thermal load of each component. The UA values are an indicator of the heat exchanger requirements and the pinch points indicate the minimum temperature differences in each heat exchange process.

Run single study

Eta (cycle) [%]	Eta (exergy) [%]	Mass flow [kg/s]	Net [kW]	Pump [kW]	Turbine [kW]	Heater [kW]	Cooler [kW]	Recup. [kW]	UA (hot) [kW/K]	UA (cold) [kW/K]	UA (rec.) [kW/K]	Pinch (hot) [K]	Pinch (cold) [K]	Pinch (rec.) [K]
17.496	29.082	0.148	12.247	0.499	12.746	70.000	57.753	14.200	2.582	3.259	0.635	12.069	12.095	17.510

It is also useful to view the cycle on a temperature-entropy diagram. In the below figure the green region indicates the state points of the working fluid throughout the cycle. Superimposed onto that are the heat source (red) and heat sink (blue) temperature profiles.

Figure 2. Example output from pocketORC for a single-point performance calculation.

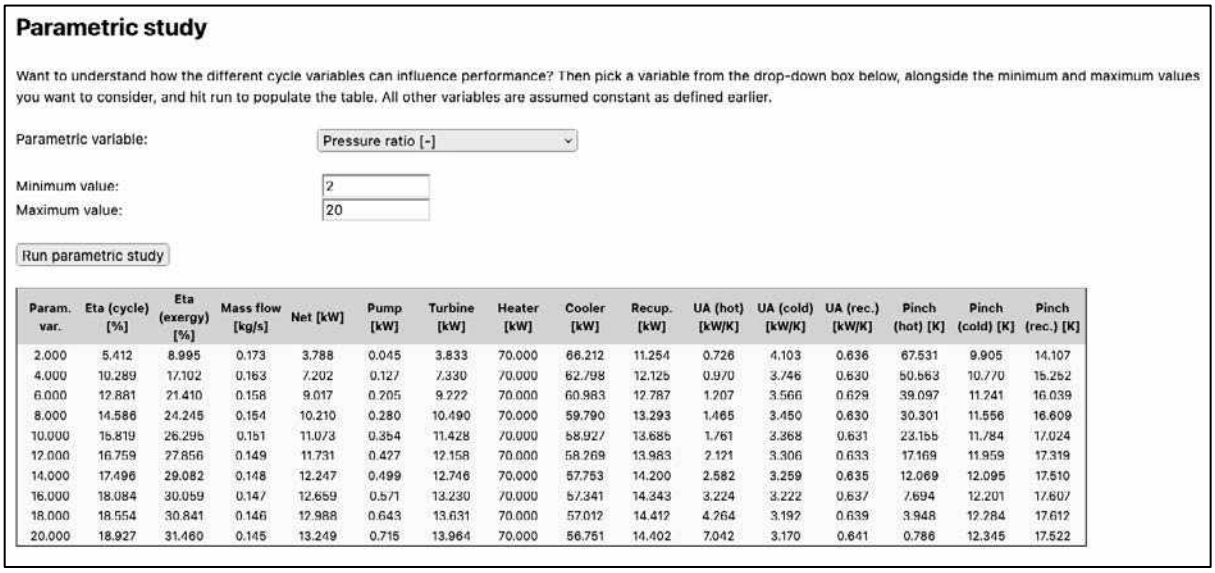

Parametric study

Want to understand how the different cycle variables can influence performance? Then pick a variable from the drop-down box below, alongside the minimum and maximum values you want to consider, and hit run to populate the table. All other variables are assumed constant as defined earlier.

Parametric variable: Pressure ratio [-]

Minimum value: 2

Maximum value: 20

Run parametric study

Param. var.	Eta (cycle) [%]	Eta (exergy) [%]	Mass flow [kg/s]	Net [kW]	Pump [kW]	Turbine [kW]	Heater [kW]	Cooler [kW]	Recup. [kW]	UA (hot) [kW/K]	UA (cold) [kW/K]	UA (rec.) [kW/K]	Pinch (hot) [K]	Pinch (cold) [K]	Pinch (rec.) [K]
2.000	5.412	8.995	0.173	3.788	0.045	3.833	70.000	66.212	11.254	0.726	4.103	0.636	67.531	9.905	14.107
4.000	10.289	17.102	0.163	7.202	0.127	7.330	70.000	62.798	12.125	0.970	3.746	0.630	60.563	10.770	15.252
6.000	12.881	21.410	0.158	9.017	0.205	9.222	70.000	60.983	12.787	1.207	3.566	0.629	39.097	11.241	16.039
8.000	14.586	24.245	0.154	10.210	0.280	10.490	70.000	59.790	13.293	1.465	3.450	0.630	30.301	11.556	16.609
10.000	15.819	26.295	0.151	11.073	0.354	11.428	70.000	58.927	13.685	1.761	3.368	0.631	23.155	11.784	17.024
12.000	16.759	27.856	0.149	11.731	0.427	12.158	70.000	58.269	13.983	2.121	3.306	0.633	17.169	11.959	17.319
14.000	17.496	29.082	0.148	12.247	0.499	12.746	70.000	57.753	14.200	2.582	3.259	0.635	12.069	12.095	17.510
16.000	18.084	30.059	0.147	12.659	0.571	13.230	70.000	57.341	14.343	3.224	3.222	0.637	7.694	12.201	17.607
18.000	18.554	30.841	0.146	12.988	0.643	13.631	70.000	57.012	14.412	4.264	3.192	0.639	3.948	12.284	17.612
20.000	18.927	31.460	0.145	13.249	0.715	13.964	70.000	56.751	14.402	7.042	3.170	0.641	0.786	12.345	17.522

Figure 3. Example output from pocketORC for a parametric study considering pressure ratio.

The lesson structure for pocketORC is provided in Table 1, which summarises the topic of each lesson and the parameters introduced. Examples of the interactive plots generated within the first three lessons are provided in Figure 4. For example, the content of Lesson 1 focusses on introducing the first two variables which control the evaporation and condensation processes, namely the condensation

temperature and pressure ratio, and the corresponding interactive plot enables the user to see these in the temperature-entropy plane (Fig. 4(a)). This is extended to the variables controlling the pump and expander inlet conditions in Lesson 2, as shown in Fig. 4(b). At this point an ideal cycle with isentropic compression and expansion processes can be defined and the cycle efficiency can be evaluated, which is the first topic of Lesson 3 (Fig. 4(c)). This is extended to real cycles, before recuperation, heat exchanger energy balances and alternative cycles are introduced in Lessons 4, 5 and 6 respectively.

Table 1: Summary of the lesson structure for pocketORC.

#	Title	Topics covered	Parameters introduced
1	Saturated properties	• Saturation properties • Evaporation and condensation	• Condensation temperature • Pressure ratio
2	Single-phase properties	• Subcooled and superheated properties • Pump and expander inlet conditions	• Degree of pump subcooling • Degree of expander superheating
3	Ideal and real cycles	• Ideal cycle • Real cycle	• Cycle efficiency • Pump isentropic efficiency • Expander isentropic efficiency
4	Recuperation	• Recuperated cycles	• Recuperator effectiveness
5	Heat exchangers	• Heat source modelling • Heat sink modelling	• Heat source inlet temperature, outlet temperature, mass-flow rate • Heat sink inlet temperature, outlet temperature, mass-flow rate • Net power output
6	Alternative cycles	• Transcritical cycles • Two-phase expansion	• Expander inlet parameter

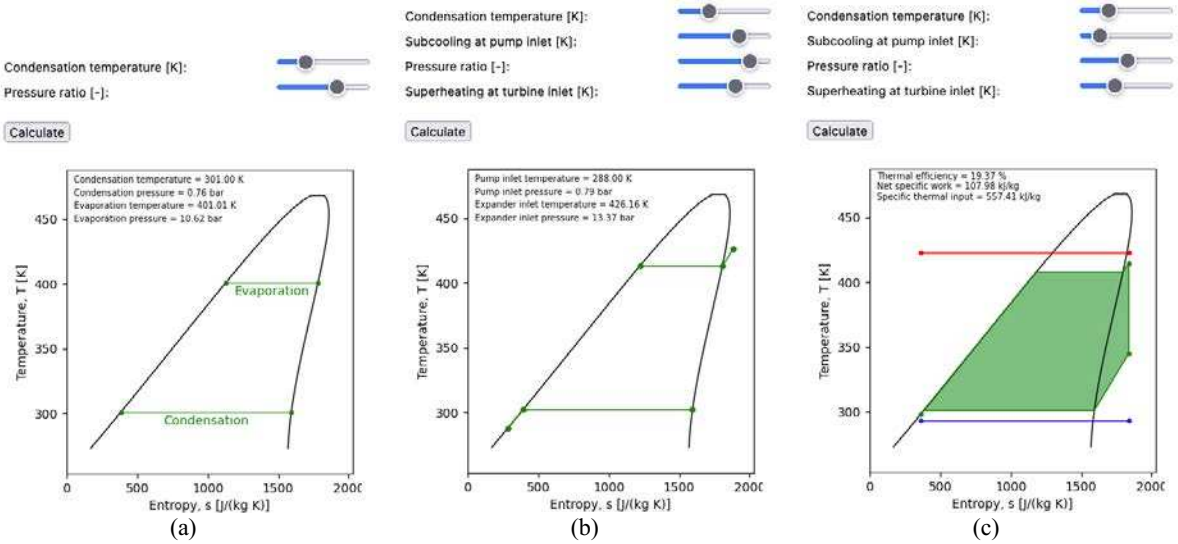

Figure 4. Example interactive plots created within Lessons 1, 2 and 3 of pocketORC.

4.3 Wider integration within the curriculum

It is intended that the available lessons, and the pocketORC calculator itself, provide a useful set of tools to introduce ORC power systems into the curriculum. Whilst these can be used as a self-paced introduction into ORC systems, several additional teaching activities can also be envisioned.

In the first instance, the tool can be used to set students an open design exercise, which could involve designing an ORC system for a particular application. In this scenario, a specific application could be introduced (i.e., geothermal, solar-thermal, waste-heat recovery) and defined in terms of an available heat source and heat sink. The students are then tasked with designing an optimal system for that application. This could be left open-ended with students free to establish optimal values for all six variables for a given working fluid, or the scope could be narrowed by fixing the heat source outlet temperature, considering simple cycles without recuperation, and providing recommendations for the degree of subcooling. Thus, simple parametric studies concerning the remaining three cycle variables can be completed by the students.

More widely, an ORC system comprises of several engineering components which themselves are introduced within the curriculum. More specifically, ORC systems are reliant on pump and turbines, alongside heat exchangers, which are components introduced within taught modules on turbomachinery and heat transfer respectively. Thus, pocketORC can be used as an aid to introduce the design of these components for ORC power cycles. In this capacity, pocketORC can be used by students to define the boundary conditions that are used in the subsequent design of these components. For example, at the time of writing the author is planning on introducing a project relating to the design of an air-cooled condenser for ORC power plants within a master's level module focused on heat transfer applications. Another possibility would be to ask the students to take the system-level analysis beyond the calculations completed within the tool. This could include evaluating a particular ORC system design from a techno-economic perspective, which would involve translating the outputs from pocketORC, such as the component power ratings or heat exchanger UA values, into estimated costs based on published cost correlations. In this capacity, ORC technology can be introduced to students from a broader energy background who may be interested in these economic factors.

59

Finally, it is worth noting the similarities in the analysis of an ORC and that of a heat pump system. Thus, the infrastructure used to build pocketORC could be easily extended to introduce a similar calculator for heat pump systems. This extension is currently planned for later in the year. This could open the possibility of introducing heat pump systems in a similar fashion to ORC systems, which could ultimately allow students to compare different technical options for a given heat source. For example, for a given waste heat stream students could be asked to evaluate and compare the performance of an ORC or heat pump system and then select the most viable option.

5 CONCLUSIONS

The wider implementation of ORC power systems requires energy professionals that have the necessary technical skills to design, simulate and evaluate the feasibility of the technology in different application areas. Principally, this knowledge should be developed within the taught curriculum of engineering and related courses. However, the high degree of scientific literacy, and potentially computing literacy, required to design and simulate ORC power cycles can hinder the extent to which the topic can be introduced in taught courses. With this is mind, this paper has introduced a new web-browser based calculator for ORC power systems that is suitable for a wider student audience. It is intended that the calculator, alongside the supporting self-paced lessons, can aid with the introduction of ORC technology at an earlier stage within the curriculum and provide a useful tool for ORC practitioners alike. Alongside providing an overview of the tool and its implementation, this paper has summarised its capabilities and put forward a vision of how it could be used as an additional teaching aid. This includes supporting open design exercises, designing power cycle components, and potentially helping to benchmark the technology against other technologies from a techno-economic perspective.

NOMENCLATURE

A	heat exchanger area	(m^2)
T	expander inlet temperature	(K)
T_{ev}	evaporation temperature	(K)
T_{hi}	heat-source inlet temperature	(K)
U	overall heat transfer coefficient	(W/m^2 K)
x	expander inlet parameter	(-)

REFERENCES

Anaconda Inc., 2022, PyScript. Online: https://docs.pyscript.net/latest/index.html [Last accessed: 29/03/2023]

Bell, I.H., Wronski, J., Quoilin, S., Lemort, V., 2014, Pure and pseudo-pure fluid thermophysical property evaluation and the open-source thermophysical property library CoolProp, *Ind. Eng. Chem. Res.,* 53, 6, 2498—2508.

Casella, F., Leva, A., 2003, Modelica open library for power plant simulation: design and experimental validation, *Proceedings of the 2003 Modelica Conference*, 3-4th November, Linköping, Sweden, pp. 41-50.

Dickes, R., Ziviani, D., de Paepe, M., van den Broek, M., Quoilin, S., Lemort, V., 2016, ORCmKit: an open-source library for organic Rankine cycle modelling and analysis, *Proceedings of ECOS 2016 – The 29th International Conference on Efficiency, Cost, Optimization, Simulation and Environmental Impact of Energy Systems*, 19-23th June, Portorož, Slovenia.

Giuffre, A., Pini, M., 2022, NiceProp: An interactive Python-based education tool for non-ideal compressible fluid dynamics, *SoftwareX*, 17, 100897.

Quoilin, S., Desideri, A., Wronski, J., Bell, I., Lemort, V., 2014, ThermoCycle: A Modelica library for the simulation of thermodynamic systems, *Proceedings of the 10th International Modelica Conference*, 10-12th March, Lund, Sweden.

White, M.T., Sayma, A.I, 2018, A generalised assessment of working fluids and radial turbines for non-recuperated subcritical organic Rankine cycles, *Energies*, 11(4), 800.

White, M.T., Sayma, A.I., 2019, Simultaneous cycle optimization and fluid selection for ORC systems accounting for the effect of the operating conditions on turbine efficiency, Front. Energy Res., 7, 50.

White, M.T., 2021, Cycle and turbine optimisation for an ORC operating with two-phase expansion, *Appl. Therm. Eng.*, 192, 11682.

ACKNOWLEDGEMENT

The author would like to acknowledge all of those that took the time to test out the pocketORC tool and provide valuable feedback during its creation.

60

ORC SEVILLE 2023
7th International Seminar on O.R.C. Power Systems

© 2024 Editorial Universidad de Sevilla. Este es un artículo de acceso abierto distribuido bajo los términos de la licencia de uso y distribución Creative Commons (BY-NC-ND 4.0)

DOI: https://dx.doi.org/10.12795/9788447227457_10

Evaluation of existing supercritical heat transfer correlations for designing the vapor generator in low-temperature transcritical organic Rankine cycle systems

Jera Van Nieuwenhuyse[1,*], Anastasios Skiadopoulos[2], Dimitris Manolakos[2], Steven Lecompte[1], Michel De Paepe[1]

[1] *Ghent University, Sint-Pietersnieuwstraat 41, 9000 Ghent, Belgium*
[2] *Agricultural University of Athens, Iera Odos 75, 11855 Athens, Greece*

*Corresponding Author: jera.vannieuwenhuyse@ugent.be

ABSTRACT

Transcritical operation of organic Rankine cycle systems for low-temperature heat conversion has gained interest over the last decades due to its performance. Compared to subcritical operation increased, thermal efficiency and higher power output is expected. The design of the supercritical vapor generator in these systems is key to the overall design and operation of the system. Over the years, several supercritical heat transfer correlations have been developed. However, the practical applicability of these correlations has rarely been evaluated. In this work, the performance of several supercritical heat transfer correlations is evaluated based on measurements on a helical coil heat exchanger. This heat exchanger was previously designed and custom-built to work under supercritical conditions and is installed in a small-scale transcritical ORC engine coupled with concentrating photovoltaic thermal collectors. The ORC has a nominal capacity of 3 kWel and the maximum temperature of the heat source (water) is 90°C. R404A was selected as the working fluid, which has a critical temperature and pressure of 72°C and 37.3 bar, respectively. The helical coil heat exchanger is made out of a 66 m long coiled tube with an inner diameter of 0.0257 m. The coil diameter is equal to 0.6 m and the heat exchanger has a nominal capacity of 41 kWth. The prediction capability of several supercritical heat transfer correlations is examined by comparing the measured performance of the helical coil heat exchanger from field tests to the results of simulations based on the (piece-wise) ε-NTU method. Based on this comparison, a best performing correlation is put forward.

1 INTRODUCTION

The performance and efficiency of an organic Rankine cycle (ORC) system can be improved by operating under transcritical conditions. That is why transcritical ORCs, where heat transfer to the high pressure working fluid takes place under supercritical conditions, have gained interest over the last decades. By operating under supercritical conditions, heat transfer losses can be reduced and cooling of the heat source can be increased in the high pressure side heat exchanger (Schuster *et al.*, 2010). The design of this supercritical heat exchanger, called the vapor generator, is key in the overall design and operation of the system. Heat exchangers in general make up a large part of the total exergy loss of a system (Liang *et al.*, 2019), so designing it well is important. As the vapor generator also accounts for the largest cost of a transcritical ORC, which can be up to 43% (Lecompte *et al.*, 2015), it is beneficial to limit the oversizing of this component to avoid unnecessary costs. Therefore, the supercritical heat transfer correlations, which are used in the design, should be reliable. Over the years, several supercritical heat transfer correlations have been developed for refrigerants (Van Nieuwenhuyse *et al.*, 2022). However, the practical applicability of these correlations has rarely been evaluated based on the performance of an actual supercritical heat exchanger. Therefore, this work will look into this performance by comparing results from a modeled heat exchanger to experimental results from a heat

exchanger incorporated in an experimental test rig. The method used is based on the method of Kaya *et al.* (2018) who did a similar investigation for several two-phase heat transfer correlations.

2 DESCRIPTION OF TEST RIG AND EXPERIMENTAL CAMPAIGN

2.1 Transcritical ORC test rig

The heat exchanger under investigation is part of a small-scale transcritical ORC test rig, with a nominal capacity of 3 kWel and is located in Athens, Greece (37°59'09"N, 23°42'21"E). A schematic diagram of the test rig is given in Figure 1. The ORC is connected to a solar field, consisting of 10 concentrating photovoltaic thermal collectors, with a total nominal heat capacity of 41 kWth. The collectors are equipped with a single-axis solar tracking system and rotate horizontally about an East-West tracking axis. An electric heater (total capacity of 48 kWel) is installed in the circuit to serve as a backup for when the solar irradiation is insufficient to reach test conditions. Water, with a maximum temperature of 90°C, is used as the heat transfer fluid in the circuit connected to the solar connectors. The helical coil heat exchanger is installed in between the water circuit and the ORC circuit and uses R404A as the working fluid. The critical temperature and critical pressure of this fluid are 72°C and 37.3 bar, respectively. A scroll type expander is used, which was modified from a commercial scroll compressor with a volume ratio of 2.8 and a swept volume of 127.1 cm^3, and the refrigerant pump is a triplex diaphragm pump. The rotational speed of the expander and pump is regulated by frequency inverters. The condenser is an evaporative condenser, but when the ORC is not operating, an air chiller is used to dissipate the heat coming from the collectors. The vapor generator is explained in more detail in the next section.

Measurement equipment is installed at different locations in the setup. The most important measurements for the current investigation are pressure and temperature measurements at the in- and outlet of the supercritical heat exchanger and volume flow rate measurements, both on refrigerant and water side. Temperatures were measured with an accuracy of 0.1K, pressures with 0.35 bar (low pressure side) or 0.6 bar (high pressure side). The volume flow rate of the water was measured with an ultrasonic flow meter (accuracy of 1%). The volume flow rate of the refrigerant was calculated using the pump's characteristic (linear correlation between volume flow rate and speed) and the accuracy was estimated at 2% (Kosmadakis *et al.*, 2016).

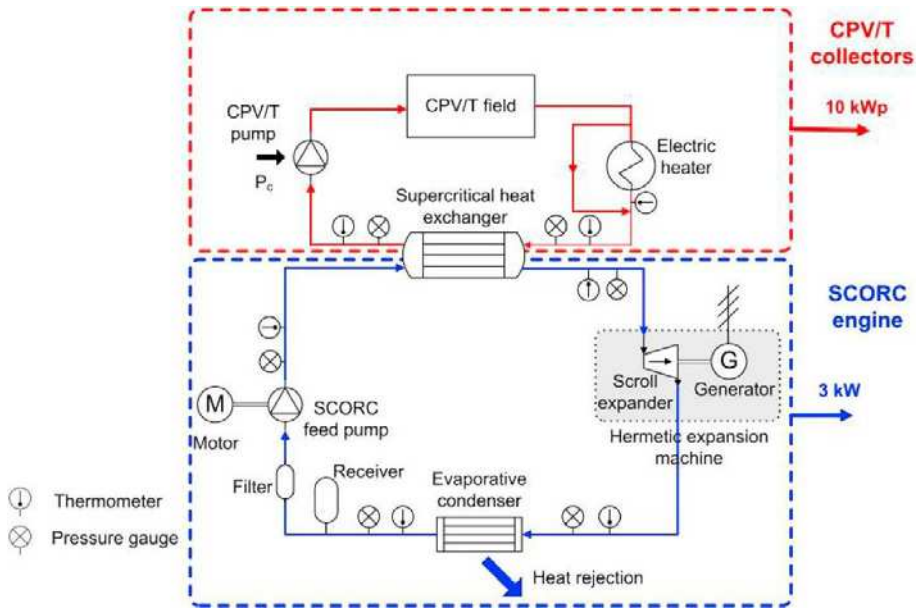

Figure 1: Schematic diagram of the transcritical ORC test rig (Kosmadakis *et al.*, 2016).

2.2 Helical coil heat exchanger layout

The vapor generator of this transcritical ORC was developed for this test rig and supercritical operation specifically (Lazova *et al.*, 2016), and is of the helical coil type with a capacity of 41 kWth. The refrigerant flows upwards in the coil which is placed in an annulus, while the heat transfer fluid (i.e. water) flows downwards in the annulus. Figure 2 shows an illustration of the cross-section of the heat exchanger design. Table 1 gives an overview of the corresponding dimensions.

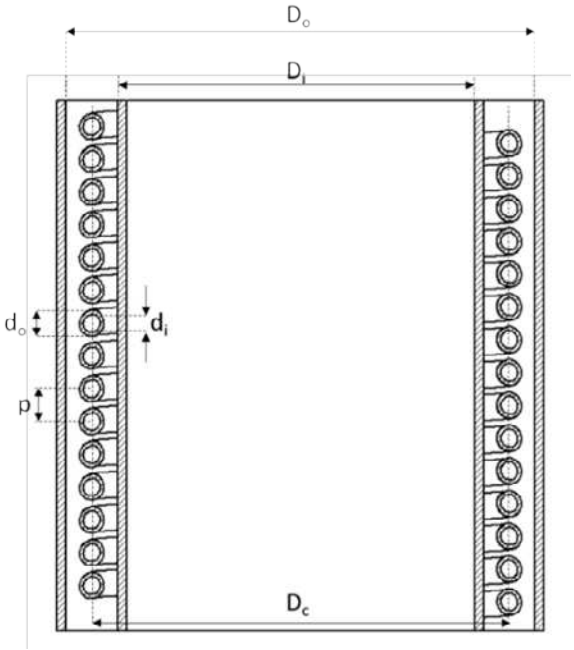

Figure 2: Cross-section of helical coil heat exchanger design.

Table 1: Dimensions of helical coil heat exchanger.

Dimension	Value [m]
Tube inner diameter d_i	0.0257
Tube outer diameter d_o	0.0377
Inner shell diameter D_i	0.526
Outer shell diameter D_o	0.674
Coil diameter D_c	0.6
Pitch p	1.25 d_o
Helical coil tube length L_t	66

2.3 Experimental campaign

In order to reach transcritical conditions (i.e. both temperature and pressure at the outlet of the supercritical heat exchanger on the refrigerant side are above its critical values), measurements were performed on clear and sunny days spread over July, August and September 2021. Solar irradiation under these conditions was maximum at around 1,000 W/m^2. Under these conditions, supercritical pressures could be obtained (for high ORC pump speed and low expander speed), but the temperature at the outlet of the supercritical heat exchanger remained below the critical value. Therefore, the back-up electrical heater was employed almost constantly during the measurements. When starting up, the pressure of the water in the solar collector's circuit was checked and increased if necessary (to reach a pressure of around 3 bar). Next, the evaporative cooler was turned on (and the air-chiller was disabled). The frequency of the water pump was set to 50 Hz. Then, the solar collectors were powered by activating the solar tracking system. When the water cooling down the collectors reached a temperature between 60 to 65°C, the ORC was started. The ORC pump first ran at a low frequency of 10 Hz. Gradually,

pressure and temperature in the system increased and pump frequency was increased in a stepwise manner. When the pump frequency was at 20 Hz, the expander was put into operation as well, with a start-up frequency of 10 Hz.

A total of 43 (quasi) steady-state operating points were measured during the experimental campaign, of which 39 were performed under transcritical operating conditions. The refrigerant heat exchanger inlet temperatures ranged from 30.3 to 45.4°C, outlet temperatures from 76.1 to 91.8°C, average pressures from 37.5 to 42.8 bar and mass flow rates from 0.27 to 0.4 kg/s. For the water, inlet temperatures ranged from 81.7 to 94.2°C, outlet temperatures from 76.4 to 88.0°C, average pressures from 3.4 to 4.7 bar and mass flow rates from 2.5 to 2.9 kg/s. Post-processing of the measurements was done with the EES software and Python (version 3.6). A heat balance of the supercritical heat exchanger was calculated in order to estimate the heat losses of the heat exchanger (see Equation (1)). In this equation, $\dot{Q}_{hx,hf}$ is the heat transferred to the ORC in the supercritical heat exchanger on the heating fluid's side. $\dot{Q}_{hx,r}$ is the heat transferred to the ORC in the supercritical heat exchanger calculated on the refrigerant side.

$$dE_{hx,rel} = \frac{\dot{Q}_{hx,hf} - \dot{Q}_{hx,r}}{\frac{\dot{Q}_{hx,hf} + \dot{Q}_{hx,r}}{2}} \quad (1)$$

On average, the heat balance closed within 23.2%. These large deviations in heat balance can be explained by the high heat losses that occur in the heat exchanger. The maximum heat losses that occurred were in the range of 22 kWth. This issue was already highlighted in the work of Golonis *et al.* (2021) and is due to the large uninsulated surface of the supercritical heat exchanger.

3 SIMULATIONS BASED ON ε-NTU METHOD

3.1 Modeling of helical coil heat exchanger

The performance of the heat exchanger was modeled by applying a piece-wise ε-NTU method. Even though, on the global heat exchanger scale, the orientation of the water and refrigerant flow is counterflow (water flows down, refrigerant up), the flow is better approximated by cross-flow on a small-scale level (Kaya *et al.*, 2018). The parameters displayed in Table 1 are used as input to the model. This is complimented with information on the mass flow rates, pressures and inlet temperatures of R404A and water. As the focus of the current work is on the heat transfer, the pressure drop over the heat exchanger is not taken into account into the simulations, and the average pressure is taken as input. For each of the performed simulations, the outlet temperatures of R404A and water are calculated, based on the aforementioned inputs. The total helical coil tube length is divided into parts of equal lengths (L_j) and for every simulation element j, the amount of heat exchanged is calculated with the ε-NTU method based on the overall heat transfer coefficient (U_j, see Equation (2)) between water and R404A for that simulation element. Based on this calculated heat exchange, input temperatures for the next simulation element are calculated. In total, 100 simulation elements were selected as increasing this number from 50 to 100 only resulted in a maximum relative deviation in simulated refrigerant outlet temperature of 0.4%. Therefore, increasing the number of elements even more would not result in more accurate simulations but would increase runtime of the simulations significantly.

$$U_j A_j = \left[\frac{1}{h_{r,j}} \frac{d_o}{d_i} + R_f \frac{d_o}{d_i} + \frac{d_o \ln\left(\frac{d_o}{d_i}\right)}{2\lambda_s} + R_f + \frac{1}{h_{hf,j}} \right]^{-1} * A_j \; with \; A_j = \pi d_o L_j \quad (2)$$

In the Equation 2, R_f represents the fouling resistance ($0.176*10^{-6}$ m^2K/W (Kakaç *et al.*, 2012)), λ_s the thermal conductivity of the steel tube (45 W/mK) and h_r and h_{hf} the convection coefficient of the refrigerant and heating fluid (i.e. water), respectively. The properties of R404A and water are calculated with CoolProp v6.3. The shell side convection coefficient h_{hf} is calculated using the calculation method of Patil *et al.* (1982). For the refrigerant side convection coefficient h_r, different correlations are applied in order to find the best suited one for the current conditions. More information on the selected

correlations is provided in the next section. In order to compensate for the fact that the refrigerant flow is helical, the following correction factor (developed by Schmidt (1967)) is applied to the refrigerant side heat transfer coefficient:

$$F_{helical} = 1 + 3.6\left(1 - \frac{d_i}{D_c}\right)\left(\frac{d_i}{D_c}\right)^{0.8} \quad (3)$$

This correction factor was also applied by Lazova *et al.* (2016) in the design of the helical coil heat exchanger under consideration in the current work. As the geometry of the heat exchanger falls within the application range of the correlation, it was deemed suited for the current investigation.

The convection coefficients are dependent on the inlet and outlet temperatures of the two fluids of that simulation element. The inlet refrigerant temperature and outlet heating fluid temperature for the *j*-th simulation element are equal to the outlet refrigerant temperature and inlet heating fluid temperature from the (*j*-1)-th simulation. The outlet refrigerant temperature and inlet heating fluid temperature of the *j*-th element need to be determined iteratively. The simulation is started at the bottom of the heat exchanger, so at the refrigerant inlet and heating fluid outlet. The inlet refrigerant temperature is known, and an initial guess has to be made for the heating fluid outlet temperature. After simulating the 100 elements, the actual heating fluid inlet temperature (at the top of the heat exchanger) is compared to the simulated one. If the difference is too big, the initial guess of the heating fluid outlet temperature at the bottom of the heat exchanger is updated and the simulation is run again. The simulation is stopped when the relative difference between the actual heating fluid inlet temperature at the top of the heat exchanger and the simulated temperature is smaller than 0.1%.

The heat losses were not directly modeled, but are taken into account by comparing the measurements to the simulations for the refrigerant side. Comparison based on the heating fluid side would not make sense as in reality the heating fluid side temperatures will always be lower than the simulated ones due to the heat losses. Normally, the actual temperatures of the heating fluid side will thus be different from the simulated ones throughout the heat exchanger. However, this does not have a significant influence on the results of the simulations as the temperature change on the heating fluid side is small (maximum of 6.8°C over the entire heat exchanger), and the properties and thus convection coefficient on the heating fluid side (i.e. water) do not really change for a small change in temperature.

65

The same type of model has been applied and validated in the work of Kaya *et al.* (2018) for comparing measurements to simulations under subcritical conditions.

3.2 Applied supercritical heat transfer correlations

As mentioned before, the goal of the current work is to evaluate the performance of several supercritical heat transfer correlations. An overview of the selected correlations, together with the intended application range and fluid is given in Table 2. p_{rel} represents the tested pressures relative to the critical pressure of the corresponding fluid, G is the mass flux under consideration expressed in kg/m^{2}s, q the heat flux in kW/m^2 and d_i the inner diameter expressed in mm. The first correlation is the well-known Dittus-Boelter correlation. This correlation is the only one from the selected correlations that is not specifically developed for supercritical flows. It is included in the current study to serve as a reference for subcritical conditions and see if there is a significant improvement in prediction when correlations developed for supercritical flow are applied. The Dittus-Boelter correlation is valid for $0.6 \leq Pr_b \leq 160$, $Re_b \geq 10^4$ and $L/d_i \geq 10$. The correlations of Petukhov *et al.* (1963), Mokry *et al.* (2011) and Garimella (2006) are selected as these correlations were used in the design stage of the current helical coil heat exchanger (Lazova *et al.*, 2016). The correlation of Garimella (2006) and Garimella *et al.* (2015) were developed for cooling heat transfer. However, as they are based on data of the same refrigerant as the current study, they are still interesting to compare to the other correlations. Yu *et al.* (2013) developed a correlation based on data of a large diameter tube of 26 mm, which is very close to the tube in the current investigation (i.e. 25.7 mm). In the work of Yu *et al.* (2013), two correlations were developed for horizontal flow, one for the top of the tube and one for the bottom. These will be depicted as Yt and Yb, respectively.

Based on the simulations explained in Section 3.1, a refrigerant outlet temperature is calculated for each of the tabulated correlations (used to determine the heat transfer coefficient on the refrigerant side). When this outlet temperature is closest to the actual outlet temperature of the corresponding measurement, the correlation is considered as best fitting.

Table 2: Heat transfer correlations for supercritical flow.

Correlation	Symbol	Fluid	p_{rel}	G	q	d_i
Dittus and Boelter (1985)	DB	Water	subcritical	n/a	n/a	n/a
Petukhov *et al.* (1963)	P	CO_2	n/a	n/a	n/a	n/a
Garimella (2006)	Ga	R404A/R410A	1-1.2	200-800	n/a	6.2-9.4
Garimella *et al.* (2015)	Gb	R404A/R410A	1-1.2	200-800	n/a	0.76-9.4
Mokry *et al.* (2011)	M	Water	1.09	200-1500	≤1250	10
Yu *et al.* (2013)	Yt & Yb	Water	1.04-1.13	300-700	200-400	26

4 RESULTS AND DISCUSSION

In total, 39 measurements were performed under supercritical conditions. In Figure 3, the results for the 3rd measurement are displayed, where the correlations' average deviation between simulated refrigerant outlet temperature and the actual outlet temperature is minimal (i.e. 0.6°C). For this measurement, the prediction based on all the correlations is good, and the maximum deviation between simulations and measurements, which is for the Dittus and Boelter (1985) correlation, is only 0.8°C. The best prediction is made by Yu *et al.* (2013) for the bottom of the tube with a difference of only 0.3°C. Very different results are observed for the 13th measurement (see Figure 4). The difference in experimental conditions between the 3rd and 13th measurement are the set frequencies of the pump and expander. For the 3rd measurement, these are 50 Hz and 5 Hz, respectively. For the 13th measurement, these are 60 Hz and 17.5 Hz. This results in a higher mass flow rate for the latter (from 0.33 kg/s to 0.38 kg/s) and a decrease in average refrigerant pressure (from 40.9 to 38.2 bar, which is a lot closer to the critical pressure of 37.3 bar). For the 13th measurement, none of the correlations can predict the outlet temperature very accurately, and the average deviation amounts to 5.4°C. The Petukhov *et al.* (2015) correlation performs the worst, with an underprediction of the outlet temperature with 6.2°C. Again, the prediction of Yu *et al.* (2013) is best, but still underestimates the actual temperature with 4.4°C. In general, over all the measurements, the Yu *et al.* (2013) correlation for the bottom of the tube is best, with an average deviation of 2.6°C, followed by the one from Garimella (2006) with an average deviation of 3°C. The one from Petukhov *et al.* (2015) is worst, with an average deviation of 3.8°C.

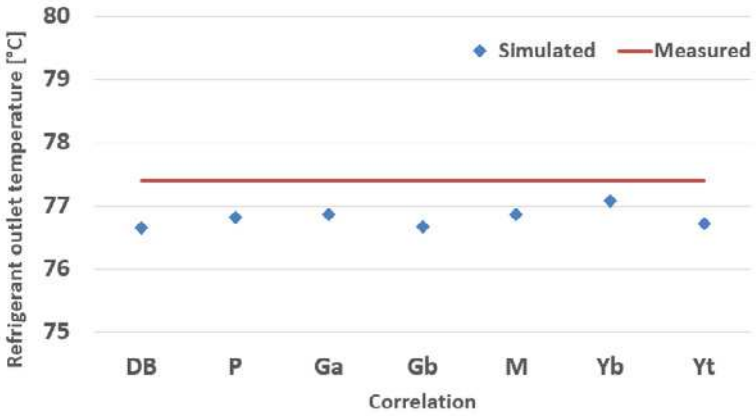

Figure 3: Simulated refrigerant outlet temperatures for 3rd measurement.

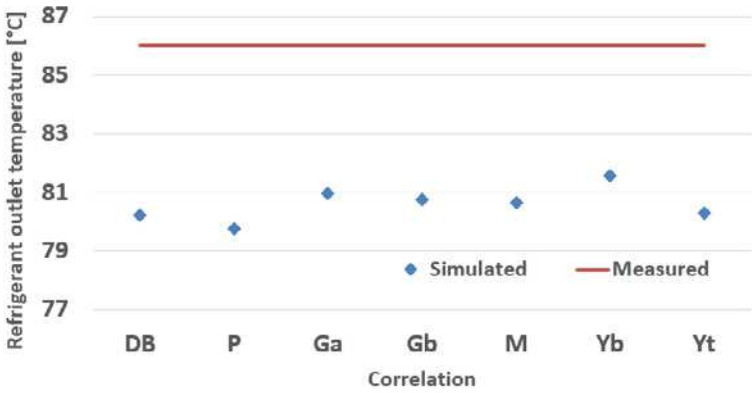

Figure 4: Simulated refrigerant outlet temperatures for 13th measurement.

Similarly, comparison can also be done based on the heat transfer rate. Overall, all the correlations underestimate the actual heat transfer in the heat exchanger. On average, over all the measurements and correlations, the heat transfer rate is underpredicted by 9.5%. The Yu *et al.* (2013) correlation for the bottom of the tube performs best with an average deviation of 7.5%, followed by the one from Garimella (2006) with 8.8%. The Dittus and Boelter (1985) correlation performs worst with an average deviation of 10.6%.

The results shown above indicate that the heat exchanger would be oversized when using the correlations from Table 2 in the sizing. This is illustrated in the following. In Figure 5, the average predicted length of the helical coil tube, based on all the measurements, for every correlation is displayed, together with the actual length of 66 m. On average, the oversizing is equal to 18.9 m. The prediction of Yu *et al.* (2013) for the bottom of the tube is best, but still 14.5 m above the actual tube length of 66 m. Part of the reason for this large oversizing is that in the current results no pinch point temperature difference was defined in the simulations and the actual heat exchanger is also oversized. Therefore, at the outlet of the heat exchanger, the temperature difference between refrigerant and water is very small, both in the simulations and reality. However, in the simulations the heat exchanger is elongated even further in order to realize the total heat transfer rate even though due to the small temperature difference this extra 'piece' of heat exchanger does not contribute much. In Figure 6, results are shown when a pinch point temperature difference (dT_{pp}) of 5°C is applied. With incorporating this pinch point temperature, the minimum temperature difference between the refrigerant and heating fluid, which will take place at the outlet of the helical coil tube, is limited to 5°C. In this work, the simulations are performed from the inlet of the tube, and from the moment this threshold is reached, the simulations are stopped. Under these conditions, the average oversizing is 9.1 m and 97% of the actual measured heat transfer rate can be delivered. The prediction by the subcritical correlation of Dittus and Boelter (1985) is worst, however, closely followed by the Petukhov *et al.* (2015) correlation. There is also a visible difference in the prediction of the two correlations from Garimella (Garimella *et al.* (2015) and Garimella (2006)). The best performing correlation of the two (i.e. Garimella (2006)) does not incorporate data on the very small diameter tube of 0.76 mm, which could be an explanation why the prediction is better for the current heat exchanger.

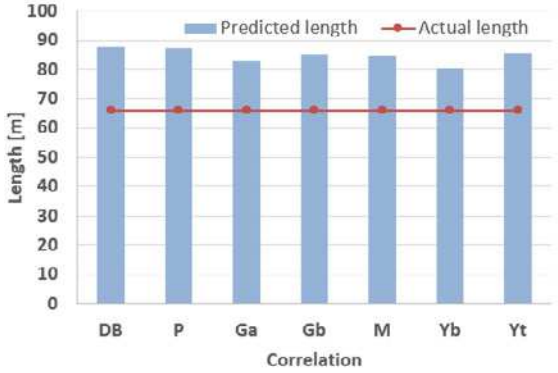

Figure 5: Average predicted length of helical coil tube.

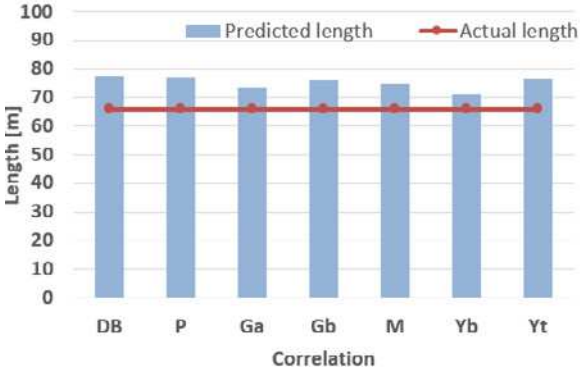

Figure 6: Average predicted length of helical coil tube for a dT_{pp} of 5°C.

In Figure 7, the heat transfer coefficient of refrigerant is illustrated for every correlation (averaged over the 100 simulation elements) and for every measurement. The average prediction of all the correlations together is also displayed. Here, it is clear why the predictions from the Yu *et al.* (2013) correlation (for the bottom), followed by the correlation of Garimella (2006), are best (following from Figure 6). Compared to the predictions of the other correlations and the average prediction of the correlations, the refrigerant side heat transfer coefficient is a lot higher. This results in a higher overall heat transfer coefficient (Equation (2)) between refrigerant and heating fluid, and thus in a smaller required element length L_j, leading to less oversizing of the entire tube length.

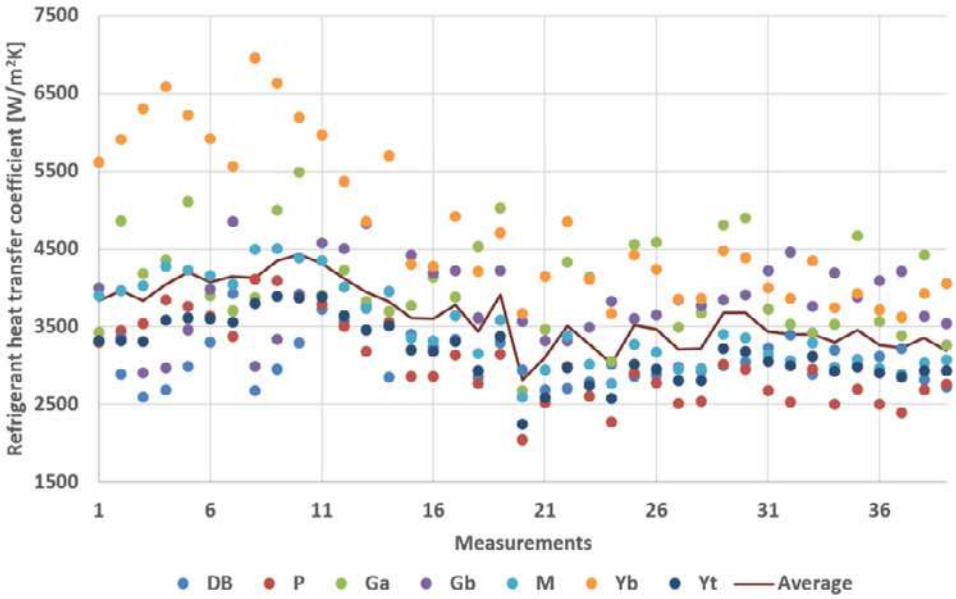

Figure 7: Average refrigerant side heat transfer coefficient for all 39 measurements.

CONCLUSION

In this work, the performance of several supercritical correlations is evaluated by comparing piece-wise simulation results to field tests performed on a helical coil heat exchanger designed to work under supercritical conditions. The measurements are used as input to the model, and based on the correlations, the refrigerant outlet temperature and the total heat transfer rate can be determined. By comparing these results to the actual measurements, a best performing correlation can be put forward.

- All correlations underpredict the refrigerant outlet temperature. The Yu *et al.* (2013) correlation for the bottom of the tube, which is based on large diameter tube data, is best, with an average

deviation of 2.6°C, the one from Petukhov *et al.* (2015) is worst, with an average deviation of 3.8°C.

- For the total heat transfer rate in the heat exchanger, the average underestimation is 9.5%. The correlation of Yu *et al.* (2013) for the bottom has the smallest average deviation of 7.5% and the correlation of Dittus and Boelter (1985) has the largest average deviation of 10.6%.
- In sizing the heat exchanger, the correlation from Yu *et al.* (2013), developed for the bottom of the tube and, performs best. The correlation of Dittus and Boelter (1985) performs the worst, closely followed by the correlation of Petukhov *et al.* (1963).
- For the correlations developed by Garimella (Garimella *et al.* (2015) and Garimella (2006)), Garimella (2006) does not incorporate data on the very small diameter tube of 0.76 mm, and performs best. This indicates that correlations developed for larger diameter tubes are required in order to make a reliable design.

The correlations can perform adequately when predicting refrigerant outlet temperatures. It is however important to simulate different working conditions (varying mass flow rates of refrigerant and heating fluid, varying pressures, varying inlet temperatures, etc.) as the prediction capability can vary for different conditions. However, when using the correlations to size the heat exchanger, all the correlations significantly overpredict the actual required length. The importance of applying a pinch point temperature is illustrated as this already improves the prediction.

NOMENCLATURE

Δ	difference	(/)	U	overall heat transfer coefficient (W/m^{2}K)
λ	thermal conductivity	(W/mK)	b	bulk
A	heat transfer area	(m^2)	c	coil
d	tube diameter	(m)	el	electrical
D	shell diameter	(m)	f	fouling
dE	error on energy balance	(/)	hf	heating fluid
F	correction factor	(/)	hx	heat exchanger
G	mass flux	(kg/m^{2}s)	i	inner
L	length	(m)	j	number of simulation element
p	pitch	(m)	o	outer
Pr	Prandtl number	(/)	pp	pinch point
q	heat flux	(W/m^2)	r	refrigerant
$\dot{Q}$	heat transfer rate	(W)	rel	relative
R	thermal resistance	(m^{2}K/W)	s	steel
Re	Reynolds number	(/)	t	total
T	temperature	(K)	th	thermal

REFERENCES

Dittus, F., & Boelter, L., 1985, Heat transfer in automobile radiators of the tubular type, *Int. Commun. Heat Mass Transfer*, vol. 12(1), 3-22.

Garimella, S., 2006, High condensing temperature heat transfer performance of low critical temperature refrigerants, *Air-Conditioning and Refrigeration Technology Institute.*

Garimella, S., Mitra, B., Andresen, U.C., Jiang, Y., & Fronk, B.M., 2015, Heat transfer and pressure drop during supercritical cooling of HFC refrigerant blends, *International Journal of Heat and Mass Transfer*, vol. 91, 477-493.

Kakac, S., Liu, H., & Pramuanjaroenkij, A., 2012, *Heat exchangers: selection, rating, and thermal design*, CRC press, third edition.

Kaya, A., Lazova, M., Kosmadakis, G., Lecompte, S., & De Paepe, M., 2018, Evaluation of existing heat transfer correlations in designing helical coil evaporators for low-temperature organic Rankine cycles via inverse design approach, *Heat Transfer Engineering*, vol. 40, 1137-1152.

Kosmadakis, G., Landelle, A., Lazova, M., Manolakos, D., Kaya, A., Huisseune, H., … & Papadakis, G., 2016, Experimental testing of low-temperature organic Rankine cycle (ORC) engine coupled with concentrating PV/thermal collectors: Laboratory and field tests, *Energy*, vol. 117, 222-236.

Lazova, M., Huisseune, H., Kaya, A., Lecompte, S., Kosmadakis, G., & De Paepe, M., 2016, Performance evaluation of a helical coil heat exchanger working under supercritical conditions in a solar organic Rankine cycle installation, *Energies*, vol. 9(6), 432.

Lecompte, S., Lemmens, S., Huisseune, H., Van den Broek, M., & De Paepe, M., 2015, Multi-objective thermo-economic optimization strategy for ORCs applied to subcritical and transcritical cycles for waste heat recovery, *Energies*, vol. 8(4), 2714-2741.

Liang, Y., Bian, X., Qian, W., Pan, M., Ban, Z., & Yu, Z., 2019, Theoretical analysis of a regenerative supercritical carbon dioxide Brayton cycle/organic Rankine cycle dual loop for waste heat recovery of a diesel/natural gas dual-fuel engine, *Energy Conversion and Management*, vol. 197, 111845.

Mokry, S., Pioro, I., Farah, A., King, K., Gupta, S., Peiman, W., & Kirillov, P., 2011, Development of supercritical water heat-transfer correlation for vertical bare tubes, *Nucl. Eng. Des.*, vol. 241, 1126-1136.

Patil, R.K., Shende, B.W., & Ghosh, P.K., 1982, Designing a helical-coil heat exchanger, *Chemical Engineering*, vol. 89(25), 85-88.

Petukhov, B.S., Krasnoshchekov, E.A., Protopopov, V.S., 1961, An investigation of heat transfer to fluids flowing in pipes under supercritical conditions. *International Developments in Heat Transfer*, 1961 International Heat Transfer Conference, ASME, University of Colorado, Boulder, CO, USA, January 8-12, Part III, Paper 67, 569-578.

Schmidt, E.F., 1967, Wärmeübergang und druckverlust in rohrschlangen, *Chemie Ingenieur Technik*, vol. 39(13), 781-789.

Van Nieuwenhuyse, J., Lecompte, S., & De Paepe, M., 2022, Current status of the thermohydraulic behavior of supercritical refrigerants: a review, *Applied Thermal Engineering*, vol. 218, 119201.

Yu, S., Li, H., Lei, X., Feng, Y., Zhang, Y., He, H., & Wang, T., 2013, Experimental investigation on heat transfer characteristics of supercritical pressure water in a horizontal tube, *Experimental Thermal and Fluid Science*, vol. 50, 213-221.

70

ACKNOWLEDGEMENT

The work presented in this paper was funded by an FWO – Flanders grant (1SA3720N) for strategic basic research of the Research Foundation Flanders. This financial support is gratefully acknowledged. I would also like to thank Tom Catternan and Marnix Van Belleghem for their work on the design and construction of the helical coil heat exchanger.

7th International Seminar on ORC Power Systems, September 4 – 6, 2023, Seville, Spain

ORC SEVILLE 2023
7th International Seminar on O.R.C. Power Systems

© 2024 Editorial Universidad de Sevilla. Este es un artículo de acceso abierto distribuido bajo los términos de la licencia de uso y distribución Creative Commons (BY-NC-ND 4.0)

DOI: https://dx.doi.org/10.12795/9788447227457_12

A novel combined cooling and power cycle integrated ejector refrigeration and composition adjustment for stationary engine waste heat recovery

Xiaocun Sun[1], Lingfeng Shi[1,*], Hua Tian[2], Gequn Shu[1,2]

[1] *Department of Thermal Science and Energy Engineering, University of Science and Technology of China, Hefei, 230027, China*
[2] *State Key Laboratory of Engines, Tianjin University, 92 Weijin Road, Nankai District, Tianjin, 300072, China*

*Corresponding Author: slf@ustc.edu.cn

ABSTRACT

The combined cooling and power cycle has wide applications ascribed to the feasibility of simultaneously providing cooling and electricity. The layout comprised of vapor compression refrigeration cycle and Organic Rankine Cycle by sharing condenser is one of the most common structures. However, for this kind of structure, the high temperatures of working fluid in compressor outlet and expander outlet aggravate the condensation load and lead to the decline of system performance. This study proposes a novel combined cooling and power cycle integrated of ejector refrigeration and composition adjustment running with CO_2 mixture. Liquid separation condenser is introduced to realize composition adjustment. Working fluid with higher CO_2 mass fraction flows to power sub-cycle and evaporation process of refrigeration sub-cycle. On the other hand, working fluid with smaller CO_2 mass fraction is pumped to the inlet of ejector and heated by expansion exhaust. A stationary engine is chosen as the research objective. The co-generation system recovers waste heat of engine exhaust and coolant to provide cooling to refrigerating chamber. The results show the priority of the novel proposed co-generation system. Under the requirement of 0 ℃ chilled fluid, the basic combined cooling and power cycle could export 8 kW cooling capacity and 6.63 kW electricity, while the novel proposed system can export 4.5% more net power output with 8 kW cooling capacity output or export 18.6% higher cooling capacity with 6.63 kW electricity.

1 INTRODUCTION

Combined cooling and power cycle (CCP) has wide applications in energy conversion and utilizing processes, such as industry, distributed energy systems, and transportation, ascribed to the feasibility of simultaneously providing cooling and electricity. Thus, enhancing the performance of CCP is an effective approach to realize the target of peaking carbon dioxide emission and carbon neutrality.

The basic CCP is comprised of an Organic Rankine Cycle (ORC) and a Vapor Compression Cycle (VCC), as depicted in figure 1(a). Liang *et al.* (2021) established a lab-scale prototype of separated CCP, R245fa and R134a were selected as working fluids for ORC and VCC, experimental results showed that the system could produce 1.8 kW cooling capacity at -4 ºC with 95 ºC water as heat source and the overall heat-to-cooling efficiency was 0.18.

To improve the compactness and flexibility of CCP, coupled type is analyzed, as presented in figure 1(b). Zhang *et al.* (2022) built a CO_2-based CCP prototype to recover ICE waste heat, the prototype could operate in three modes and the test results revealed that the prototype could export 5.8 kW power at power-alone mode, 3.2 kW power and 8.0 kW refrigeration at co-generation mode as well as 9.8 kW refrigeration at cooling-alone mode. To further improve the performance of CCP, explorations focusing on structure optimization and working fluid upgrading are carried out. Ejector is introduced to decrease the irreversible loss of throttling process in VCC. Mondal and De (2017) established an ejector-based organic flash CCP for low-grade waste heat recovery and a compressor was installed between

evaporator and ejector to match the elevated condenser pressure. On the other hand, zeotropic mixture possesses the phenomenon of temperature glide in two-phase heat exchanging process due to the characteristics of vapor-liquid equilibrium, leading to better thermal match and less exergy destruction in heat exchangers. Yao *et al.* (2022) investigated the performance of coupled CCP running with a series of CO_2-based mixtures for ICE waste heat recovery, results showed that CO_2/R32 could maximally achieve 19% power increase or 80% cooling increase compared to CCP running with pure CO_2.
However, a fixed composition of mixture for coupled CCP ($x_P = x_R = x_T$), as figure 1(b) exhibits, is usually unsuitable since the operating temperature intervals of CCP are large and the features of sub-cycles are disparate. Thus, composition-adjustable CCP is proposed to realize a further enhancement of CCP performance, as figure 1(c) presents. Barkhordarian *et al.* (2017) proposed an ammonia-water CCP system integrated with ejector and rectifier, due to the adoption of rectifier, rich ammonia fluid entered the refrigeration sub-cycle and weak ammonia fluid flowed to power sub-cycle. Zhu *et al.* (2021) designed a combined cooling, heating and power cycle using R141b/R134a, refrigeration sub-cycle operated with rich volatile fluid and power sub-cycle operated with weak volatile fluid were achieved.

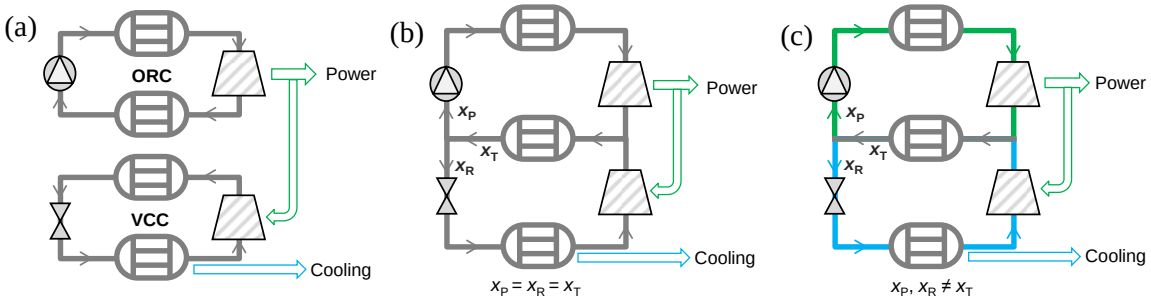

Figure 1: CCP layouts: (a) separated type; (b) coupled type; (c) composition-adjustable type.

Based on the previous discussion, ejector refrigeration and composition adjustment could both enhance the performance of CCP. From the perspective of 'mass', the above two methods are respectively corresponding to the converging and separation of streams. From the perspective of 'energy', ejector refrigeration requires heat to drive while composition adjustment prefers smaller condensation load to maintain the thermal match in condenser (Sun *et al.* 2021). However, the deep coupling of the above two methods for CCP has not been discussed. In this study, a novel CCP integrated of ejector refrigeration and composition adjustment is proposed and a detailed case study is carried out for stationary ICE power station waste heat recovery.

72

2 SYSTEM DESCRIPTION

In this section, detailed structures of the basic coupled CCP and the novel proposed improved CCP for ICE dual heat sources recovery are described. Then, the suitable zeotropic mixture for CCP is discussed. At last, the case study of CCP for stationary ICE power station waste heat recovery is implemented.

2.1 Structure of the basic coupled CCP

Figure 2(a) depicts the schematic of the basic coupled CCP proposed by Yao *et al.* (2022) and the corresponding *T-s* diagram is illustrated in figure 2(b). As shown in figure 2, liquid working fluid is obtained after condenser (11-1) and divided into two streams. One flows to power sub-cycle, subsequently, this stream is pumped to high pressure (1-2) and respectively heated by preheater (2-3), regenerator (3-6) and gas heater (6-4). Then, high temperature and pressure steam expands in turbine (4-5). The other stream does isenthalpic throttling first (1-8) and cooled the chilled fluid in evaporator (8-9). Next, it is compressed to condensation pressure (9-10) and mixed with another stream (16,10-11). Then, the converged stream is cooled in condenser (11-1). A whole circulation process completes. The advantages of the basic coupled CCP are:

- Regenerator improves the inlet temperature of turbine and reduces the condensation load.

- Zeotropic mixture possesses the superiority of CO_2 and R32, it could realize effective heat utilization of engine exhaust and coolant (CO_2) and reduce condenser intel temperature (R32).

However, there are still serval problems that need to solve:

- Heat energy of engine exhaust and coolant could not be full recovery simultaneously.
- Condenser intel temperature is still high.
- Compression work of refrigeration sub-cycle is large.

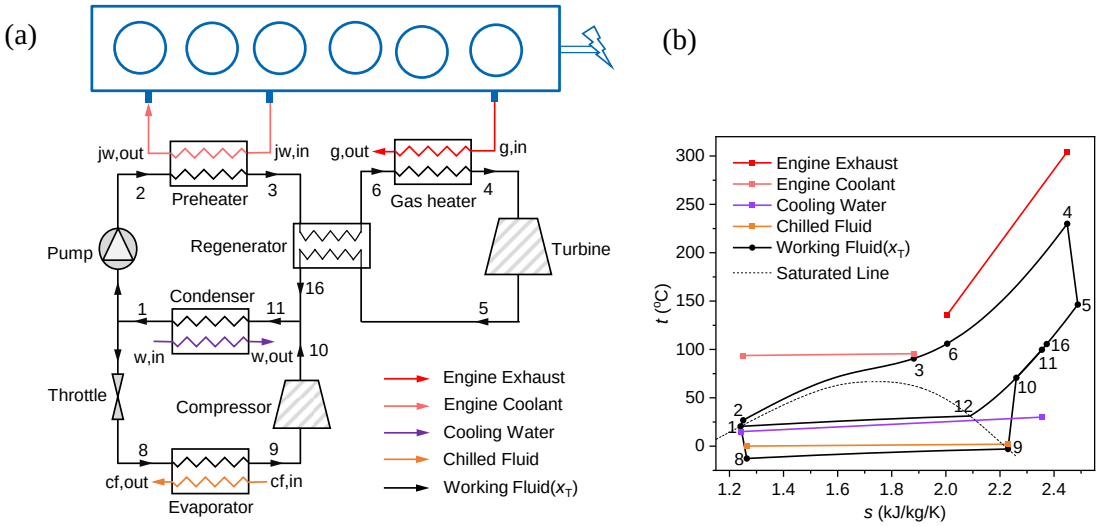

Figure 2: (a) Schematic and (b) *t-s* diagram of the basic coupled CCP.

2.2 Structure of the improved CCP

To solve the deficiency of basic coupled CCP, a novel improved CCP is proposed with the introduction of ejector refrigeration and composition adjustment, as shown in figure 3(a). The corresponding *T-s* diagram is illustrated in figure 3(b) and the four subgraphs are respectively corresponding to four compositions operating in the whole circulation process. As shown in figure 3, working fluid with composition of x_T is condensed to two-phase state in the first half of liquid separated condenser (LSC) (16-17) and separates into two streams (17-8,18). Then, working fluid with weak volatile constituent (x_1) is directly pumped to ejector (8-9), while working fluid with rich volatile constituent (x_2) is further condensed in the second half of LSC (18-1) and divides into two streams. One stream (x_2) is pumped to high pressure (1-2) and heated to high temperature by preheater (2-3) and gas heater (3-4). Then, the high temperature and pressure steam expands in turbine (4-5). The other stream (x_2) depressurizes in throttle (1-11) and exports cooling capacity in evaporator (11-12). To realize the flexible operation of ejector, an auxiliary compressor is set between evaporator and ejector (12-13) (Mondal and De 2017). After being pressured in pump2 (8-9), working fluid (x_1) divides into two streams. One stream is used to recover the heat at the outlet of ejector (R1, 9-91) and expanding exhaust (R2, 91-102), the other is used to fully utilize the unused heat of coolant (R3, 9-101). Then, these two streams converge into one flow (101,102-10) and ejects compressor exhaust (10,13-14). On the other hand, the exhaust of turbine (x_2) is cooled by another working fluid (x_1) (R2, 5-6) and joins in another stream (x_3) (6,14-15). At last, the converged stream is further cooled in R1 (15-16) and a whole circulation process completes.

The improvement of the improved CCP are:

- **Full utilization of dual waste heat sources**: regenerator is removed since the regenerative heat will improve the inlet temperature of working fluid in gas heater (3) and result in the insufficient utilization of engine exhaust. In addition, the residual heat energy of engine coolant is fully utilized to heat the primary flow of ejector in R3.
- **Better thermal match in condensation process**: the partial condensation load is utilized to preheat the primary flow of ejector (R1, R2), leading to a better thermal match in condensation process, as presented in figure 3(b).

- **Various compositions for different thermodynamic stages**: LSC is introduced to achieve composition adjustment, which could realize working fluid with rich volatile constituent operated in power sub-cycle and the evaporation process of refrigeration sub-cycle (higher evaporation pressure) as well as working fluid with weak volatile constituent operated in ejector of refrigeration sub-cycle.

It should be noted that the present proposed structure is a specific construction for ICE waste heat recovery. For a more universal application scene, similarly, an improved CCP could be designed by the method that realizes various compositions operated in different thermodynamic stages and using condensation load and unutilized heat of source to heat ejector.

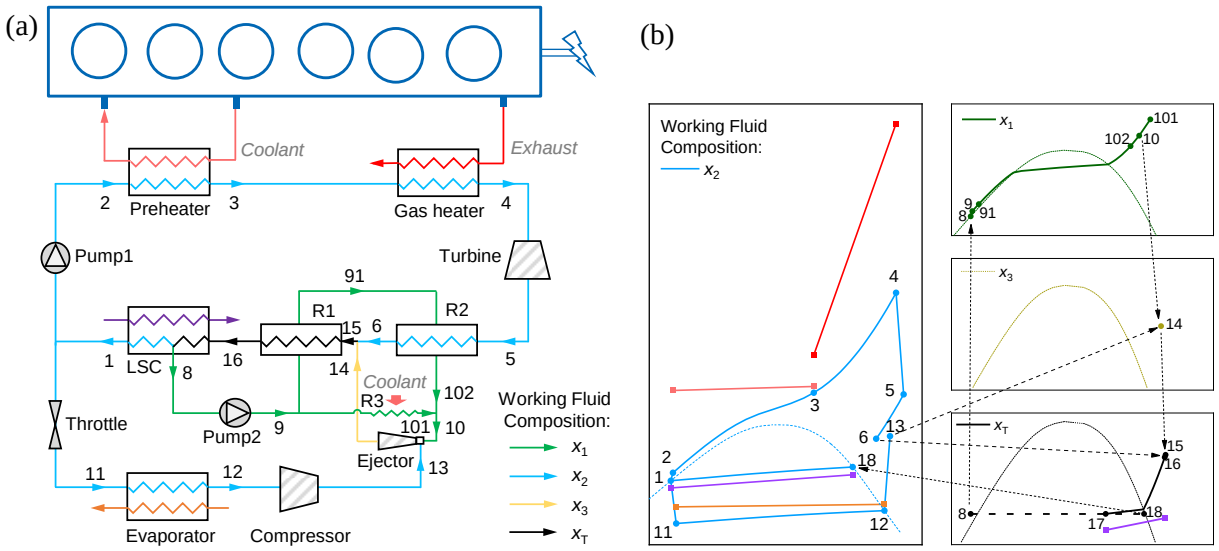

Figure 3: (a) Schematic and (b) *t-s* diagram of the improved CCP.

74

2.3 Case study

For an isolated factory, such as a foodstuff factory, as shown in figure 4(a), it usually needs ICE power station to produce electricity. Part of the electricity is used to drive the equipment and the other is used to drive the refrigeration unit to export cooling to refrigerating chamber. The huge energy contained in engine exhaust and engine coolant is directly discharged to ambience and wasted. To enhance the comprehensive performance of ICE, the coupled CCP and the improved CCP discussed above are applied, as figure 4(b) presents. On the one hand, the ICE waste heat is recovered to produce cooling and electricity. On the other hand, the supplied cooling by CCP could reduce the electricity consumed in refrigeration unit. To evaluate the performance of the new proposed CCP, a diesel ICE is selected as objective (Sun *et al.* 2021). The boundary conditions and operating parameters of CCP are enumerated in Table 1.

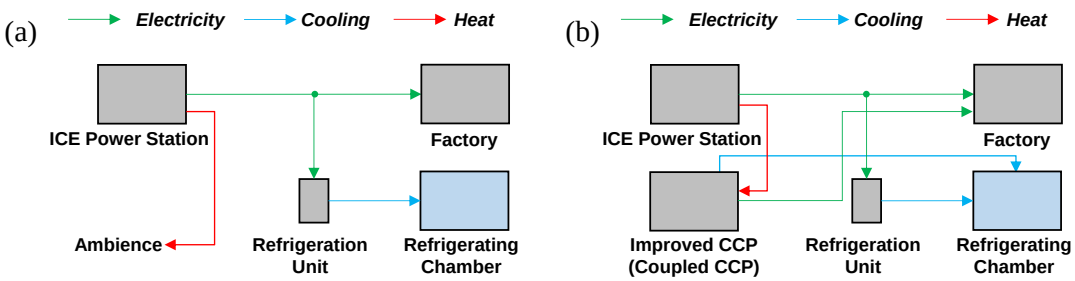

Figure 4: (a) The original isolated system; (b) The improved system combined with CCP.

Table 1: Boundary conditions and operating parameters of CCP

Term	Value
Heat sink	
Exhaust mass flow rate	0.164 kg/s
Exhaust temperature	304.4 °C
Coolant mass flow rate	4.25 kg/s
Coolant temperature	95.6-92.6 °C
Heat sink	
Cooling water inlet temperature	15 °C
Cooling water temperature rise	15 °C
Refrigeration conditions	
Cooling capacity	8 kW
Chilled fluid temperature	2-0 °C
Constraint conditions	
Pinch point of preheater, R3, LSC, evaporator	5 °C
Pinch point of R1, R2	15 °C
Pinch point of gas heater	30 °C
Pump isentropic efficiency	0.7
Turbine isentropic efficiency	0.8
Compressor isentropic efficiency	0.8
Mechanical efficiency	0.98
Generator efficiency	0.98

2.4 Fluid Selection

For ICE dual heat sources, CO_2 could realize good thermal match in heating process due to the character of specific heat in supercritical region (Yao *et al.* 2022). Therefore, CO_2 is usually selected as the optimal working fluid for ICE waste heat recovery. However, CO_2 is hard to be condensed under ambient temperature since the critical temperature is only 31 °C. In addition, the efficiency of heat to power for pure CO_2 is small. Therefore, CO_2-based mixture is proposed as the substitution of pure CO_2. Yao *et al.* (2022) investigated the performance of coupled CCP running with a series of CO_2-based mixtures for ICE waste heat recovery, results showed that CO_2/R32 could realize the best performance compared with pure CO_2, CO_2/R161, CO_2/R152a, CO_2/R134a, CO_2/R1234yf and CO_2/propane. Thus, in this study, CO_2/R32 is selected as working fluid. The properties of CO_2 and R32 are enumerated in Table 2.

75

Besides the remarkable thermodynamic performance, CO_2/R32 possesses excellent physical properties:

- **Environmental-friendly**: more proportion of CO_2, lower GWP of the mixture.
- **Safe**: CO_2 could efficiently cut down the flammability of refrigerants (Shi *et al*. 2021).
- **Thermostable**: the pyrolysis temperature of pure R32 and CO_2/R32 (mol 0.3/0.7) is more than 270 °C (Xin et al. 2022) while the wall temperature is around 260 °C according to heat transfer.

Table 2: Physical, environmental, and safety data of CO_2 and R32.

Substance	Molecular mass	t_b	t_c	P_c	ODP	DWP	Safety date
	g/mol	°C	°C	MPa			ASHRAE 34 Safety group
CO_2	44.01	-78.4	31	7.38	0	1	A1
R32	52.02	-51.7	78.1	5.78	0	716	A2L

3 METHODOLOGY

For simplicity of calculation, the following assumptions are made:

- The improved CCP is operated under steady state.
- Pressure drop and heat transfer destruction in pipes and heat exchangers are neglected.
- Energy loss in mixing and separation processes is neglected.
- Working fluid in the outlets of evaporator and condenser (LSC) is saturated.

- Pump, turbine and compressor work with fixed isentropic efficiencies.

In this study, ejector is simulated using one-dimensional model, the specific modeling refers to Zhao *et al.* (2023) and the isentropic efficiencies of the nozzle, mixing section and diffuser section are 0.9, 0.85 and 0.85, respectively.

Energy balance equations of all components are obtained based on the first law of thermodynamics and all heat exchangers are calculated by pinch point method, the details could refer to Yao *et al.* (2022).

As shown in figure 3, working fluid (x_T) is cooled to two-phase state by cooling water first in LSC (16-17), then the liquid phase (x_1) is artificially separated (17-8) and pumped to ejector (8-9), while the vapor phase (x_2) continues to be cooled by cooling water (18-1). The condensation pressure (P_{cond}) is acquired by iteration to satisfy that the minimum temperature difference between working fluid and cooling water is not less than the given pinch point of LSC (Sun *et al.* 2021).

For R1, the temperature of point 91 (t_{91}) is assumed the same as point 9 (t_9) first. After the calculation of ejector, the value of temperature at point 15 (t_{15}) is obtained. If t_{15} is larger than the sum of pinch point of R1 and t_{91}, regeneration in R1 happens and a small temperature increment is added to t_{91}. And this repetitive computation breaks up until t_{15} is less than the sum of pinch point of R1 and t_{91}. For R3, the maximum mass flow rate of coolant is limited by the result of preheater in power sub-cycle.

After satisfying the requirement of refrigeration conditions, the net power output (W_{net}) is selected as the evaluation index, given in Equation (1). In this study, maximum W_{net} is acquired through the method of exhaustion, and the independent controlling variables are obtained according to the optimization program. The program is implemented in MATLAB R2021a and the properties of working fluid are acquired by REFPROP 10.0a.

$$W_{\mathrm{net}} = W_{\mathrm{turb}} \cdot \eta_{\mathrm{gen}} - W_{\mathrm{pump1}}/\eta_{\mathrm{m}} - W_{\mathrm{pump2}}/\eta_{\mathrm{m}} - W_{\mathrm{comp}}/\eta_{\mathrm{m}} \quad (1)$$

4 RESULTS

4.1 Performance of the basic coupled CCP

There are three independent controlling variables of the basic coupled CCP namely CO_2 mass fraction (x_T), turbine inlet temperature ($t_{turb,in}$) and turbine inlet pressure ($P_{turb,in}$). Figure 5 demonstrates the performance of basic coupled CCP with the variation of $t_{turb,in}$ and x_T under the optimization of $P_{turb,in}$.

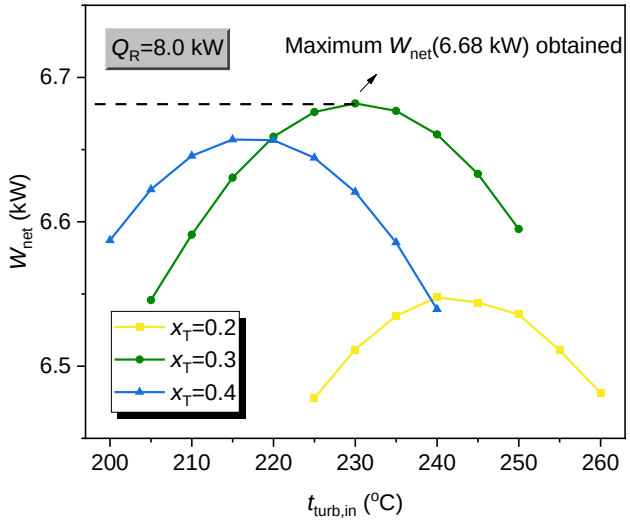

Figure 5: System performance of basic coupled CCP with variation of x_T and $t_{turb,in}$.

For a fixed x_T, the value of net power output (W_{net}) increases with $t_{turb,in}$ first and decreases then. Since the series connection of preheater and gas heater, the ideal mass flow rates to fully recover engine coolant and exhaust are interferential. A small $t_{turb,in}$ could realize full utilization of engine coolant while

the utilization rate of engine exhaust is not guaranteed. For a large $t_{turb,in}$, the inverse situation will appear. Therefore, there always exists an optimal value of $t_{turb,in}$ to realize the maximum W_{net}.
For different x_T, the performance of W_{net} depends on the performance of thermal match in condenser since a better thermal match will lead a lower condensation pressure (Sun *et al.* 2021). As depicted in figure 2(b), when x_T = 0.3, thermal match in condenser performs well and temperature difference between working fluid and cooling water in most heat transfer processes approaches to pinch point. For x_T = 0.2 and x_T = 0.4, temperature glide changes and thermal match between working fluid and cooling water deteriorates, as a result, system performance declines.

4.2 Performance of the improved CCP

Since the optimal CO_2 mass fraction of mixture (x_T) equals 0.3 for the basic coupled CCP, the same value is set for the improved CCP. Thus, there are four independent controlling variables left namely primary flow pressure of ejector (P_{10}), normalized pressure index of ejector second flow (n), turbine inlet temperature ($t_{turb,in}$) and turbine inlet pressure ($P_{turb,in}$). To improve ejector performance, an auxiliary compressor is arranged between compressor and ejector. The index n represents the pressure boost amplitude and $n \geq 1$, as presented in equation (2), n =1 ($P_{13} = P_{evap}$) represents the compressor does not work.

$$P_{13} = P_{cond}^{1-\frac{1}{n}} \cdot P_{evap}^{\frac{1}{n}};\ n = \frac{\ln(P_{13}/P_{cond})}{\ln(P_{evap}/P_{cond})} \tag{2}$$

Compared to basic coupled CCP, the governing variables of refrigeration sub-cycle in improved CCP are two more. Therefore, the cooling capacity (Q_R) of improved CCP possesses a wider regulation range. Figure 6 illustrates seven optimal results of improved CCP and all of them perform better than basic coupled CCP. Conditions A to G refer to different proportions of Q_R and W_{net}. The values of governing variables are listed in Table 3. As shown in figure 6, Q_R increases with the decrease of W_{net} from condition A to G. The maximum promotion of W_{net} is 4.5% obtained in condition A and the maximum promotion of Q_R is 18.6% obtained in condition G. Beyond the superior output capacity, the improved CCP has a better flexibility in capacity adjustment than basic coupled CCP.

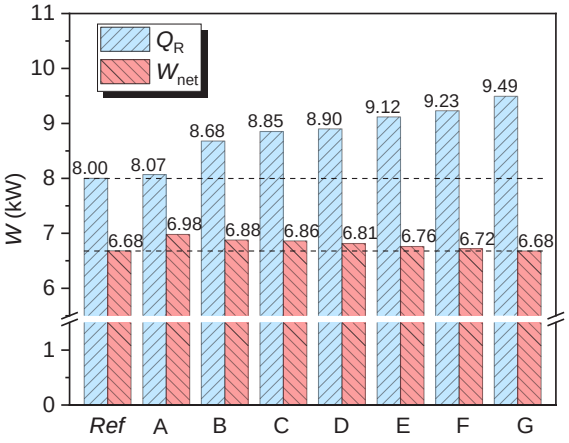

Figure 6: Optimal performance of basic coupled CCP (*Ref*) and improved CCP (A-G).

Table 3: Values of the governing variables for improved CCP

Condition	A	B	C	D	E	F	G
P_{10}/P_{cri}	0.85	0.85	0.80	0.80	0.75	0.80	0.75
n	4.4	4.2	5.0	5.0	5.0	4.4	5.2
$t_{turb,in}$(°C)	170	170	170	172	178	178	178
$P_{turb,in}$ (MPa)	9.1	9.1	9.1	9.1	9.1	9.1	9.1

P_{cri} means the critical pressure of zeotropic mixture with CO_2 mass fraction of x_1.

4.3 Effect of ejector refrigeration and composition adjustment

In this section, the effects of ejector refrigeration and composition adjustment on the improved CCP are investigated. For condition C as an example, the detailed operating parameters of the improved CCP are analyzed.

As figure 7 depicts, for the basic coupled CCP, heat utilization rate of exhaust (U_g) equals 0.914 since the installation of regenerator increases working fluid temperature at the inlet of gas heater and results in the insufficient utilization of exhaust. For the improved CCP, due to the removal of this regenerator, U_g equals 0.997. Although the optimal value of $t_{turb,in}$ for improved CCP decreases, which means the energy conversion efficiency declines, the heat imparted to CCP increases and the mass flow rate of working fluid in power sub-cycle ($m_{f,P}$) correspondingly rises. As shown in figure 7, the improvement rate is around 40% (from 0.16 kg/s to 0.22 kg/s).

Since the regenerator is removed, turbine exhaust vapor increases. To recover this part of heat energy and the residual heat of engine coolant, ejector refrigeration is introduced. As drawn in figure 7, for the improved CCP, heat utilization rate of coolant (U_{jw}) equals 1, and working fluid temperature at the inlet of condenser is 53 °C, which is 47 °C smaller than basic coupled CCP. As figure 2&3 exhibit, thermal match of condensation process in the improved CCP performs better than the basic coupled CCP.

Due to the high critical pressure of CO_2, the ejector would perform worse if CO_2 mass fraction becomes larger. Therefore, composition adjustment is introduced to realize a less CO_2 mass fraction in the primary flow of ejector. Besides, composition adjustment could realize higher CO_2 mass fraction in power sub-cycle, which could realize excellent heat recovery of dual heat sources for engine. In addition, composition adjustment could realize higher evaporation pressure in refrigeration sub-cycle, as depicted in figure 7, the evaporation pressure improves 4.5% (from 1.036 MPa to 1.082 MPa) and COP_m of refrigeration sub-cycle calculated by equation (3) improves 4.6% (from 4.80 to 5.02). It should be noticed that the introduction of LSC will increase the condensation pressure. However, the improvement of condensation process due to ejector refrigeration repairs the rise of condensation pressure.

78

$$COP_m = Q_R/(W_{pump2}/\eta_m + W_{comp}/\eta_m) \quad (3)$$

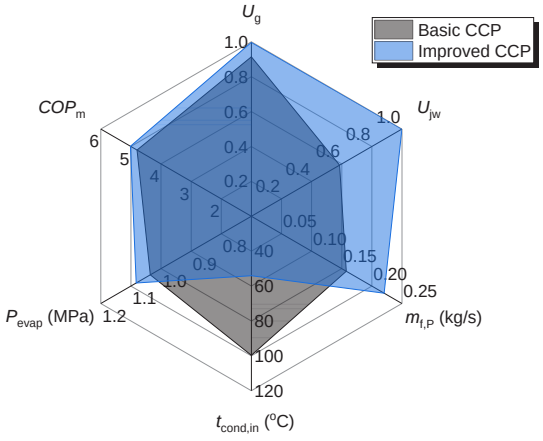

Figure 7: Parameter comparison between the basic coupled CCP and the improved CCP.

5 CONCLUSIONS

In this study, a novel improved CCP integrated of ejector refrigeration and composition adjustment is proposed, thermodynamic performance is analyzed and compared with the basic coupled CCP. The main conclusions are drawn as follows:

- The improved CCP has more flexible adjustability in capacity adjustment than the basic coupled CCP. Compared to the basic coupled CCP, the improved CCP can export 4.5% more net power output with the same cooling capacity output or export 18.6% higher cooling capacity with the same net power output.
- Ejector refrigeration could realize 100% recovery of dual heat sources and a smaller inlet temperature of condenser which means a better thermal match in condensation process.
- The introductions of composition adjustment and ejector supplement each other. Composition adjustment could realize lower CO_2 mass fraction of primary flow and higher inlet pressure of secondary flow for ejector, while ejector could repair the rise of condensation pressure brought by LSC.

NOMENCLATURE

Acronyms

COP	coefficient of performance
ICE	internal combustion engine
LSC	liquid separation condenser
R1/R2/R3	regenerator1/2/3

Symbol

m	mass flow rate	(kg/s)
t	temperature	(°C)
P	pressure	(MPa)
Q	heat/cooling capacity	(kW)
U	utilization rate	
W	power	(kW)
x	mass fraction	(MPa)

Subscript

g	engine exhaust
gen	generator
in	inlet
jw	engine coolant
m	mechanical
R	refrigeration sub-cycle
P	power sub-cycle

REFERENCES

Barkhordarian, O., Behbahaninia, A., Bahrampoury. R., 2017, A novel ammonia-water combined power and refrigeration cycle with two different cooling temperature levels, *Energy*, vol. 120: p. 816-826.

Liang Y., Mckeown A., Yu Z., Alshammari S., 2021, Experimental study on a heat driven refrigeration system based on combined organic Rankine and vapour compression cycles, *ENERG CONVERS MANAGE*, vol. 234, no. 113953.

Mondal S., De S., 2017, Ejector based organic flash combined power and refrigeration cycle (EBOFCP&RC) e A scheme for low grade waste heat recovery, *Energy*, vol. 134: p. 638-648.

Shi W., Pan L., Jin S., Dong Y., Li T., Zhao J., Wei X., 2021, Combustion Characteristic and Mechanism of a Mixture Working Fluid C3H8/CO2, *J THERM SCI*, vol. 30, no.5: p. 1768-1779.

Sun X., Shi L., Tian H., Wang X., Zhang Y., Shu G., 2021, A novel composition tunable combined cooling and power cycle using CO2-based binary zeotropic mixture, *ENERG CONVERS MANAGE*, vol. 244, no. 114419.

Xin L., Liu J., Liu C., Yu W., Liu Y., Wu C., 2022, Insight into the pyrolysis of R32 and R32/CO_2 as working fluid for organic Rankine cycle, *J ANAL APPL PYROL*, vol. 167, no. 105672.

Yao, Y., Shi, L., Tian, H., Wang, X., Sun, X., Zhang, Y., Wu, Z., Sun, R., Shu, G., 2022, Combined cooling and power cycle for engine waste heat recovery using CO2-based mixtures, *Energy*, vol. 240, no. 122471.

Zhang Y., Shi L.,1, Tian H., Li L., Wang X., Huang G., Shu G., 2022, Experimental investigation on CO2-based combined cooling and power cycle, *ENERG CONVERS MANAGE*, vol. 256, no. 115342.

Zhao, D., Xu, W., Zhao, R., Deng, S., Zhao, L., 2023, Thermodynamic analysis of the combined organic flash and ejector refrigeration cycle using zeotropic mixtures, *Appl Therm Eng*, vol. 219, no. 119605.

Zhu Y., Li W., Wang Y., Li H., Li S., 2021, Thermodynamic analysis and parametric optimization of ejector heat pump integrated with organic Rankine cycle combined cooling, heating and power system using zeotropic mixtures, *Appl Therm Eng*, vol. 194, no. 117097.

ACKNOWLEDGEMENT

The authors gratefully acknowledge the financial support from Students' Innovation and Entrepreneurship Foundation of USTC (CY2022G35).

ORC SEVILLE 2023
7th International Seminar on O.R.C. Power Systems

© 2024 Editorial Universidad de Sevilla. Este es un artículo de acceso abierto distribuido bajo los términos de la licencia de uso y distribución Creative Commons (BY-NC-ND 4.0)

DOI: https://dx.doi.org/10.12795/9788447227457_14

DESIGN AND CONSTRUCTION OF A REVERSIBLE ORC TEST RIG FOR GEOTHERMAL CHP APPLICATIONS

Florian Kaufmann[1,*], Christopher Schifflechner[1], Christoph Wieland[1,2], Hartmut Spliethoff[1]

[1] *Technical University of Munich, Chair of Energy Systems, Boltzmannstraße 15, Garching, Germany*
[2] *University of Duisburg-Essen, Chair of Energy Process Engineering and Energy Systems, Leimkugelstraße 10, Essen, Germany*

*Corresponding Author: florian.k.kaufmann@tum.de

ABSTRACT

In recent years, reversible Organic Rankine Cycles (ORC) have gained interest in academia and industry for their ability to supply heat or electricity flexibly. While many publications focus on their application in Carnot batteries or domestic systems, geothermal applications got less attention. In geothermal combined heat and power plants, reversible ORCs offer the possibility to generate electricity in times of low heat demand and supply additional heat to a district heating network (DHN) in peak load times. In previous work, the authors showed that this increases plant utilisation and reduces the load of commonly used peak-load gas boilers. This work presents the design and construction of a fully reversible ORC test rig capable of flexible operation as ORC or high-temperature heat pump (HTHP). It extends the state of the art by design and construction of a test rig for experimental validation of a previously untested cycle layout for geothermal applications. The test rig is supplied by a 200 kW hot water heating circuit as a heat source and uses a fully reversible 20 kW twin-screw machine. A closed loop intermediate cooling circuit allows simulating a DHN with varying temperature levels and mass flows during HTHP operation. This paper provides insights into the design methodology and the test rig's intended operating range and performance. Thus, the paper provides valuable insights for the research community regarding conceptual and experimental activities on reversible ORC systems. Moreover, an in-depth description of the constructed test rig, its components and instrumentation and finally the preliminary control concepts are given. Commissioning and first experimental results are expected in the year 2023.

1 INTRODUCTION

Reversible Organic Rankine Cycle (ORC) systems have gained significant attention in academia and industry within the last ten years. While there is no clear definition of a reversible ORC (rORC) in literature with respect to plant layout, such systems are generally capable of operating either as an ORC or as a high-temperature heat pump (HTHP). While an ORC uses low-temperature heat from various sources (e.g. geothermal, waste heat or solar) to generate electricity, an HTHP upgrades otherwise unused heat like ambient or low-temperature waste heat to a useful temperature level while consuming electricity. Multiple applications have been proposed for rORC systems. One of the first was their use for flexible heat and electricity generation in residential applications, more specifically in a Net-Zero-Energy-Building, proposed by Dumont et al. (2015). In their work, the authors experimentally determined an ORC cycle efficiency of 4.2 % (at 3.7 kW power output) and a heat pump COP of 3.1, respectively. They moreover highlight the importance of component selection and associated problems (i.e. with high pressure losses) for reversible systems. Based on that concept, Quoilin et al. (2016) confirmed the technology's ability to produce significant amounts of electricity (next to its primary task of space heating) by means of annual simulations. After optimising some constructional and operational system parameters, the authors report a yearly electricity production of 3500 kWh by the ORC. In a simulative study, Kosmadakis and Panagioti (2019) show the potential for increased profits of a rORC

compared to mono-functional plants in an industrial context despite their higher initial cost. Their results indicate decreasing economic viability of reversible configurations (compared to heat delivery by a gas boiler) with increasing heat pump capacity. Steinmann et al. (2019) present various application scenarios for rORCs serving as a sector-coupling technology to decarbonize the heat and electricity supply. In a similar context, Urbanucci et al. (2019) highlight the ecological and economic advantages of an rORC compared to conventional (fossil) backup technologies for peak load times. In their study, carbon dioxide emissions were reduced by 11 % while the annual cost of the considered micro-CHP trigeneration system dropped by 7 %. The recently most investigated application of rORCs is their use in pumped thermal electricity storages (PTES). Frate et al. (2017) introduce a thermally integrated PTES relying on a rORC and investigate the effect of different heat source temperatures and working fluids. In accordance with other studies, they recommend R1233zd(E) as the most promising working fluid achieving a maximum roundtrip efficiency of 1.3 with thermal integration of a heat source at 110°C. Staub et al. (2018) consider the effect of different process topologies on the roundtrip efficiency of PTES systems. Their results indicate roundtrip efficiencies of around 0.5 when the heat source temperature is limited to 80°C and realistic component constraints are considered. While Dumont et al. (2015) first validated the reversible use of scroll machines as compressors and expanders, this was recently also achieved by Steger et al. (2021) for twin-screw machines in a PTES test rig yielding efficiencies of 1-4 % in ORC mode and COPs of 4-6 in heat pump mode. This dual use of a rORC's core component is a major achievement for improving the economic viability of rORC plants. However, several authors point out that the efficiency of reversibly used compressors significantly decreases in at least one operational mode due to the different process conditions calling for optimisation in system design and machine integration (Frate et al., 2017; Staub et al., 2018; Dumont and Lemort, 2019).

A promising application for rORCs is their use in geothermal combined heat and power plants previously analysed by Kaufmann et al. (2022). Here, the primary task of the geothermal well is heat supply to a district heating network (DHN). Excess heat in times of low heat demand is used to generate electricity with the ORC. During peak load times, when the geothermal heat is not sufficient for the DHN, the plant operates in HTHP mode and takes load from a fossil peak load boiler. The results indicate a minor economic benefit of the reversible configuration but highlight the dependency on gas and electricity prices. The plant layout including the main cycle components for ORC and HTHP are depicted in Figure 1.

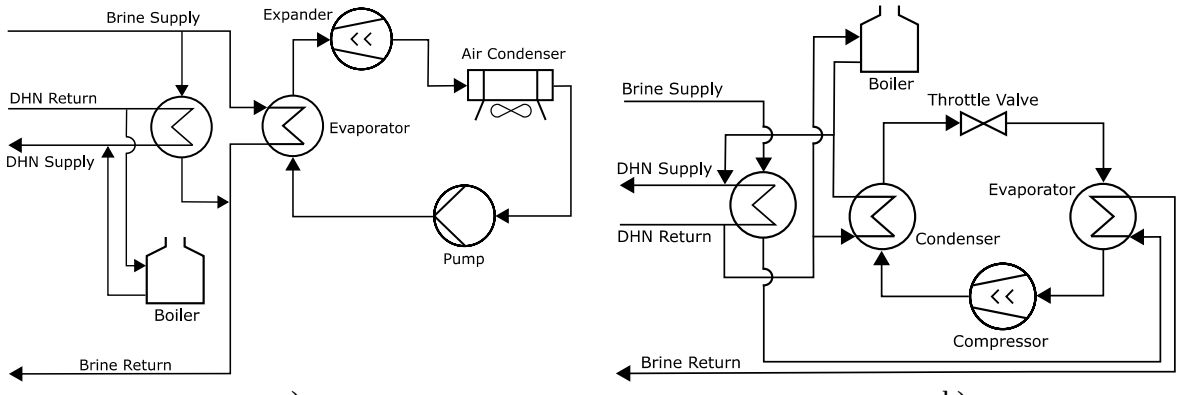

Figure 1: Plant layout for a reversible ORC integrated into a geothermal CHP plant with ORC (a) and HTHP (b) operation

No experimental studies have been conducted on the proposed plant concept so far. Hence, this work extends the state of the art by presenting the design and construction of a fully reversible ORC test rig suitable for concept validation. The overarching goals in the design process are a reduction in plant cost, maximum plant flexibility as well as high part-load efficiencies in both operating modes with a special focus on the ideal integration of the reversible compressor.

2 CYCLE DESIGN METHODOLOGY

2.1 Practical and Economic Boundary Conditions

The determining constraint in the design process is the identification of a suitable reversible compressor. The goal of economic viability strongly indicates the reversible use of one machine, since the compressor or expander is one of the most expensive components in ORCs or HTHPs, respectively. Considering the available sizes of twin-screw and scroll machines and keeping later large-scale applications in mind, the use of a twin-screw machine is the preferred option. This ensures meaningful results for a potential scale-up of the technology. The limited budget for the test rig further required the twin-screw machine to be as small as possible. These constraints as well as a small number of suitable suppliers led to the decision for a *Bitzer OSK5361-K* compressor, which was modified for reversible operation by the manufacturer. An existing 200 kW_{el} heating circuit built for a previous test rig by Eyerer et al. (2020) is used as a heat source for the planned test rig. Its capability to deliver hot water at temperatures up to 140°C and mass flow rates of up to 2 kg/s (depending on the heating duty) is another boundary condition for the design. The last external boundary condition is the cooling water temperature, which shows seasonal variations between 20°C and 30°C.

2.2 Thermodynamic Design Procedure

The general thermodynamic design is based on cycle simulations of the ORC and HTHP conducted in *Matlab* (The MathWorks Inc., 2021). The required fluid properties are obtained from *Refprop 10* (Lemmon et al., 2018). Based on consistent recommendations in the scientific literature, the eco-friendly HCFO refrigerant R1233zd(E) is used in the test rig. Some basic assumptions and simplifications are used in the thermodynamic design of ORC and HTHP alike. Pressure losses between the main cycle components (c.f. Figure 1) are neglected, which is justified by the a-priori unknown piping and instrumentation layout. The same applies to the heat exchangers, as their design is unknown during the thermodynamic design phase. Moreover, heat losses are neglected and a good insulation of the test rig is assumed. No detailed component models are used to calculate the heat exchanger characteristics. The evaporator, condenser and ORC-subcooler are calculated based on energy balances considering a pinch point of 5°C in the heat exchangers. This simplification is justified by the high uncertainty associated with correlations for heat transfer coefficients of R1233zd(E) and detailed models for plate heat exchangers in general. Almost all manufacturers consider their specific plate design proprietary knowledge, making the use of detailed component models practically impossible in a design phase. Therefore, the used heat exchangers were later designed by the manufacturers based on the maximum duties and flowrates. This ensures a sufficient heat exchange area and should hence avoid limitations at operational points with smaller heat duties. An electromechanical efficiency of 95% is considered for the main motor driving the compressor as well as the pump motor. Since a reluctance motor is used, this efficiency is realistic for the main drive in its design point. For the pump itself, an isentropic efficiency of 80 % was assumed, which is high compared to commercial products. While a pump efficiency deviating from the design value will reduce the experimental net cycle efficiency, it doesn't influence the fluid's outlet temperature in a magnitude that would be relevant at this design stage.

The allowed rotational speed of the reversible compressor is a major limitation for the operational field of the test rig. For the chosen machine, the manufacturer gives upper and lower limits of 4200 rpm and 500 rpm, respectively. In order to account for this, a semi-empirical model for the compressor and expander is used in the design process. The compressor is modelled according to the method proposed by Giuffrida (2016), while the expander model is based on the publication by Dawo et al. (2021). The models account for heat transfer inside the machine, heat and friction losses, internal leakages as well as losses due to over- and under-compression/expansion. The models take the applied pressure ratio, the inlet enthalpy and the inlet mass flow as input parameters and return the machine speed, the shaft power as well as the outlet enthalpy.

For the ORC design, a mesh grid is created using heating water flowrates between 0.2 kg/s and 1.2 kg/s as well as heating water temperatures of 100°C, 120°C and 140°C. The resulting combinations of

flowrate and temperature are used as input parameters for the ORC calculation together with a cooling water inlet temperature of 20°C and a cooling water temperature lift of 20°C. A superheating of 10°C after the evaporator as well as a subcooling of 5°C after the subcooler are considered for the working fluid consistently. A numerical optimization algorithm is then applied to determine the working fluid mass flow and evaporation pressure resulting in the maximum shaft power output at the expander under the given boundary conditions. The machine speed limitations as well as the heat exchanger pinch points are used as constraints for the optimization algorithm.

For the HTHP design, three different temperature levels in the simulated DHN with a lift of 20°C are considered: 50°C to 70°C, 70°C to 90°C and 90°C to 110°C. For each of those temperature levels in the DHN the following design procedure is conducted. First, a mesh grid is created using heat source flowrates between 0.2 kg/s and 3 kg/s as well as DHN flowrates between 0.1 kg/s and 1.6 kg/s. The resulting combinations of heat source and heat sink flowrate as well as the DHN temperature levels are used as input parameters for the HTHP calculation. The heat source for the HTHP in a real plant is the geothermal brine before reinjection (c.f. Figure 1). Assuming a pinch point of 5°C between geothermal brine and DHN water in the DHN heat exchanger, the heat source temperature for the heat pump is set to 55°C, 75°C and 95°C for the respective DHN temperature levels. Again, a numerical optimization algorithm is applied to determine the working fluid mass flow and evaporation pressure. The condensation temperature of the working fluid is set to the upper DHN temperature plus 5°C, removing the condensation pressure as a degree of freedom. The main constraint for the algorithm is to match the required amount of heat for the DHN in the condenser. Analogously to the ORC design, the machine speed limits and a pinch point of 5°C in the evaporator are further constraints.

The design procedure is summarised in form of a flowchart in the subsequent Figure 2.

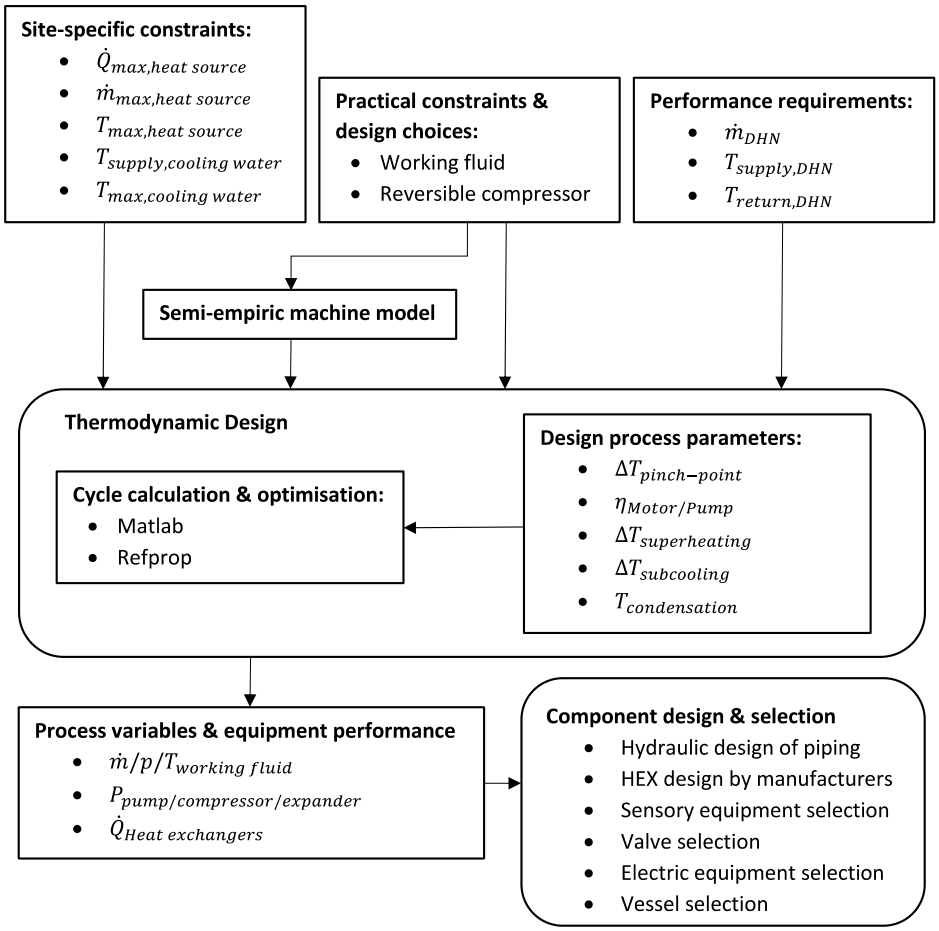

Figure 2: Flow scheme for the applied design procedure during test rig design

The round-edged boxes in Figure 2 represent a procedure conducted in the design process while the sharp-edged rectangles indicate data and information in- and outputs. Figure 3 shows the design values for the thermal efficiency of the ORC and the COP of the HTHP in subfigures a) and b), respectively. The colour scale from blue (low values) over green to yellow (high values) indicates operational areas of similar thermal efficiency or COP. Not all values from the previously described calculation method are depicted in the figure. This results from a preliminary screening of the results. For the HTHP, all result points where the heat demand of the DHN could not be matched due to compressor speed are removed from subfigure b). Moreover, a 22 kW motor was initially intended for the test rig and hence all operating points with a compressor shaft power exceeding this value were not further considered and removed from subfigure b). In a similar fashion, all heat source conditions that exceed the 200 kW heating capacity of the heating circuit were not further considered in the ORC design and are hence removed from subfigure a).

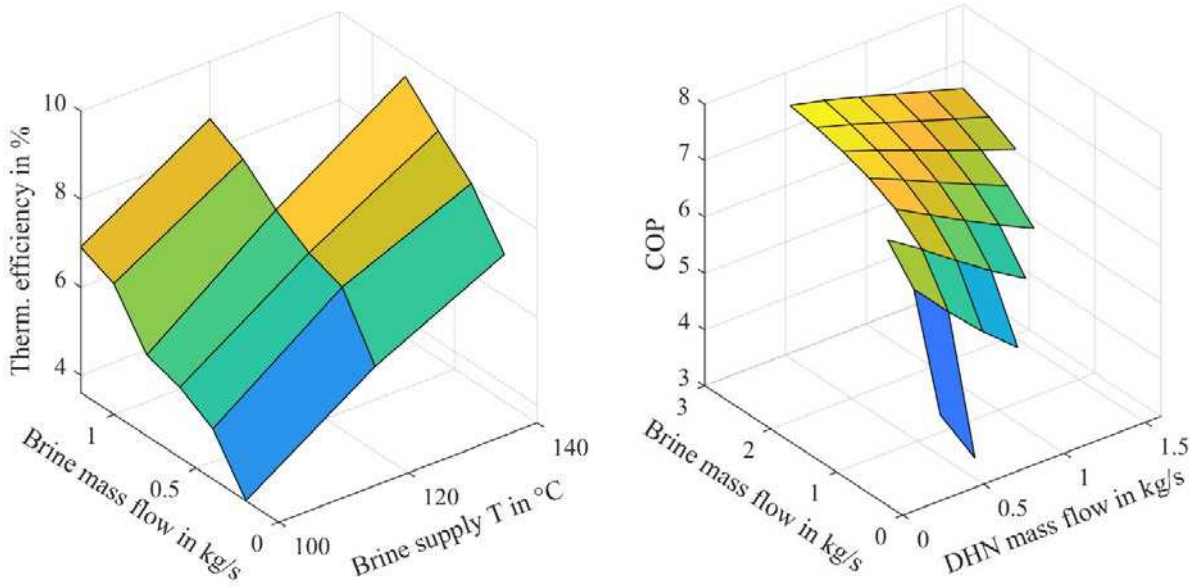

a) b)

Figure 3: Design thermal efficiency of the ORC (a) and COP of the HTHP (b)

As indicated in Figure 3, thermal efficiencies between 4% and 9% in ORC mode as well as COPs between 3 and 7.5 HTHP mode are expected. However, since losses were neglected in the thermodynamic design procedure, lower values should arise during plant operation. The thermodynamic design yields the relevant flowrates and fluid properties relevant for further component design and selection.

2.3 Piping Design Procedure

With the flowrates, fluid states and fluid properties available between the individual cycle components, the hydraulic design is possible. In order to avoid high pressure losses, fluid velocities in the piping should be within a certain range. For gasses, the target velocity should be 10-30 m/s while a value of 1-3 m/s for liquids is recommended (VDI-Wärmeatlas, 2002). Due to the flexibility in construction, the low risk for leakages and the relatively cheap prices, soldered copper pipes are used for the working fluid piping. These pipes are available at certain discrete sizes. A suitable piping size is selected for each piping segment, ensuring the fluid velocities to remain within the previously mentioned limits for all design points. The piping of the heating circuit and the intermediate cooling circuit is constructed from steel pipes using compression fittings for easy assembly. Here, the suitable pipe sizes are also determined from the previously obtained flowrate requirements.

3 TEST RIG CONSTRUCTION

Figure 4 shows a simplified P&ID of the constructed test rig in order to visualize the most important components and their connection. The design and specifications of the individual components are subsequently discussed in detail. Not all components of the final test rig are depicted in Figure 4 for the sake of clarity, but the relevant missing components will be described in the subsequent sections as well.

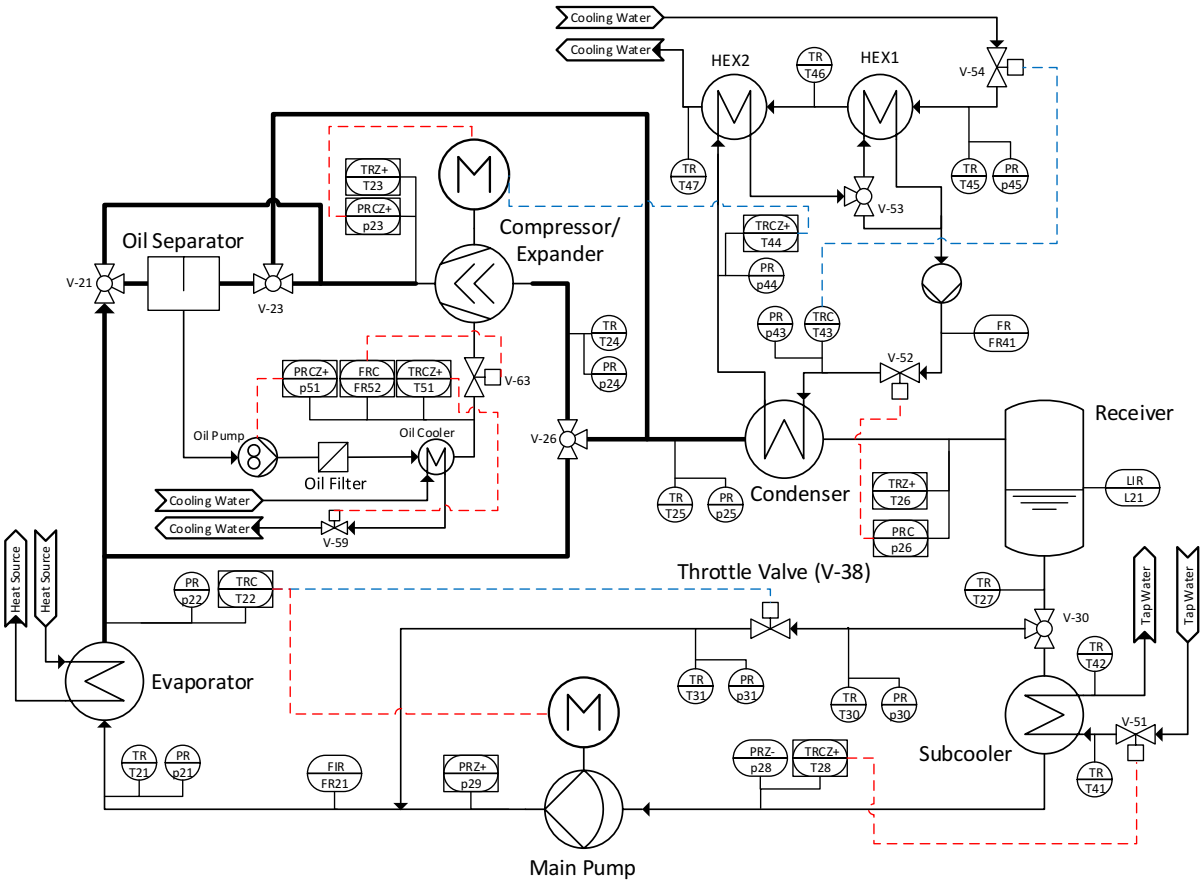

Figure 4: Simplified P&ID of the constructed reversible ORC test rig without the heating circuit. Main control loops for ORC (red) and HTHP (blue) operation.

For this reason, the component and sensor numbering does not necessarily follow ascending order. In Figure 4, a thick line indicates vapour-only piping whereas liquid or two-phase piping is indicated by regular line thickness. For the sensory equipment labels in Figure 4, the abbreviations according to DIN EN 62424 were used. In this context the label's first letters F, P and T represent the process variables flow, pressure and temperature, respectively. The subsequent letters C, R and Z+ indicate the control of the respective process variable, its registration or a binary switching function with respect to an upper boundary value, respectively. A picture of the most recent constructional state of the test rig including its dimensions is given in Figure 5 at the end of this section. It visualizes the fact that the test rig was designed and built with the intent to achieve reasonable compactness due to spatial restrictions.

3.1 Heating Circuit

As mentioned before, the heating circuit was previously constructed for an ORC test rig at the Chair of Energy Systems of TUM. Here, only the most important specifications of the heating circuit will be summarized and the interested reader is referred to the detailed description by Eyerer et al. (2020). The heating circuit consists of a closed loop filled with water as heating medium. The water is heated by a 200 kW electrical resistance heater whose power is adjusted via pulse width modulation, generating the

required inlet temperature at the evaporator. The maximum temperature of the heating circuit is 140°C which aligns well with commonly observed wellhead temperatures of geothermal wells in southern Bavaria. The flowrate in the heating circuit is adjustable by a speed-controlled centrifugal pump and a bypass valve around the evaporator. While the pump can deliver up to 4.7 L/s of water to the evaporator, the actual obtainable flowrate in the heating circuit is strongly limited by the heating power of the resistance heater and hence depends on the temperature lift over the heater.

3.2 Cooling Circuit

The cooling circuit consists of a closed water loop, connecting the condenser in the working fluid circuit to the in-house cooling water line. The necessity for this intermediate circuit arises from the need to simulate a DHN. The in-house cooling water supply temperature varies between 20°C and 30°C while the maximum allowed reflux temperature is 60°C. Hence, an intermediate circuit is required to simulate elevated temperatures at the cold side of the condenser in HTHP mode. In HTHP mode only HEX2 (c.f. Figure 4) is in operation while the 3-way ball valve (V-53) in the cooling circuit is used to include HEX1 as well during ORC operation. For elevated temperatures in the intermediate cooling circuit (e.g. a temperature lift of 90°C to 110°C), the heat transfer area between the cooling water house line and the intermediate circuit has to be limited in order to avoid cooling water reflux temperatures above 60°C. Accordingly, only a small heat exchanger is used in HTHP mode, while a larger heat exchange area is desirable in ORC. A larger area leads to a smaller temperature approach between the cooling water and the intermediate circuit, effectively lowering the condensation temperature in the ORC and increasing its power output. The heat exchangers HEX1 (HEXONIC LB31-80H-5/4") and HEX2 (SWEP B12Lx30) are brazed plate heat exchangers. A fixed speed centrifugal pump (Wilo Yonos Maxo plus 30/0,5-12) with a maximum flowrate of around 3 kg/s circulates the water in the intermediate circuit. A linear regulating valve (V-52, ESBE VLA121) at the pump head is used to control the flowrate in the circuit. The same valve type is used in the cooling water supply line to adjust the flowrate (V-54). Further, a membrane expansion vessel (Reflex S8, not depicted in Figure 4) is integrated into the intermediate circuit to compensate the water's thermal expansion and maintain an elevated pressure in the circuit. An inductive flow sensor (KROHNE OPTIFLUX 4050) is used to measure and control the water flowrate in the circuit. In addition, several PT100 class A temperature sensors and pressure transmitters (JUMO Midas) are integrated in the cooling water line and intermediate circuit for monitoring and control purposes.

87

3.3 Working Fluid Circuit

The working fluid circuit uses manual 3-way ball valves (V-21, V-23, V-26 and V-30) to switch between ORC and HTHP operation. For both operation modes, the cycle starts with saturated working fluid, which is stored in a 30 L receiver vessel (A-Cold V8.AC.30.2). The receiver buffers fluctuations in the system's working fluid charge and allows for effective drainage of liquid from the condenser, increasing its effectiveness. Moreover, it acts as a vapour barrier towards the pump, avoiding dry running of the pump. A guided radar level sensor (KROHNE OPTIFLEX 1300C) monitors the liquid level in the receiver. In ORC mode, the working fluid is subcooled in a brazed plate heat exchanger (SWEP B8THx30) before entering the main pump (Verder Hydra-Cell G10 EKCEHFEMC) used to circulate the working fluid and increase its pressure. A 1.5 kW_{nom} induction motor (ecoDrives FCPA 100 L6/PHE) drives the pump at variable speed, allowing for simple pump speed and hence flowrate controll. The degree of subcooling (to avoid pump cavitation) is controlled with a linear valve (V-51, ESBE VLA121) on the water side of the subcooler. In order to ensure sufficient subcooling in summer, the subcooler is connected to the tap water instead of the cooling water line. A filter dryer (Danfoss DCR 0487(s) with a 48-DM core) is integrated into the piping between subcooler and pump. It is bypassed during regular operation and only used to remove moisture and particles after the initial commissioning of the test rig. In HTHP mode, the pump is bypassed and the working fluid is directed to an electronic expansion valve (SIEMENS MVL661.20-2.5), which throttles the working fluid into the two-phase region. A Coriolis flow meter (KROHNE OPTIMASS 1400C S25) measures the working fluid mass flowrate before the evaporator in both operation modes. In the evaporator (SWEP V200THx80, brazed plate type), the working fluid is evaporated and slightly superheated. In ORC mode, the working is then directed to a high performance oil-separator-collector (ESK Schultze BOS2-

R-35F) where the lubrication oil (Fuchs KMÖ B320SX) is separated from the vapour phase, which is consecutively passed into the expander. As previously mentioned, the expander is a modified twin-screw compressor (Bitzer OSK5361-K) originating from the refrigeration sector. The compressor has a built-in volume ratio of 3.1 and a swept volume of 0.678 L per rotation. The expander drives a 30 kW_{nom} synchronous reluctance motor (ABB M3BL 2000MLA 4) in generative mode. In comparison to conventionally used induction machines, reluctance machines are characterized by very high part-load efficiencies with respect to torque and rotational speed. This will significantly benefit the test-rig's overall efficiency, as the electrical machines will be operated in very low part-load for some of the design points. During HTHP operation, the vapour from the evaporator is directly routed to the compressor, which is driven by the previously mentioned motor. In both operation modes, an inverter can adapt the motor speed, allowing for effective load control. The compressed high-temperature vapour is then passed through the oil-separator before being put into the condenser (SWEP B200THx70, brazed plate type) where it liquefies and drains into the receiver. Analogously, the working fluid vapour after the expander in ORC mode is fully condensed in the condenser and drains into the receiver, closing the cycle. The rather complex piping around the oil-separator and compressor stems from the mono-directional flow requirement of the oil-separator. As indicated in Figure 4, a multitude of PT100 class A temperature sensors and pressure transmitters (BD Sensors 17.620G) enable a close monitoring of the fluid states before and after most major components.

3.4 Oil System

The oil separated from the working fluid vapour is collected in the oil-separator and fed into the test rig's oil system. Sufficient lubrication of the compressor (or expander) bearings and rotor profiles is the primary purpose of the oil system. The oil ensures proper functionality and longevity of the bearings. Moreover, it reduces friction losses of the rotors and seals the individual compression or expansion chambers by reducing leakage pathways inside the machine. After the separator, an oil pump (Verder VERDERGEAR VGS200) is used in ORC mode to compensate for pressure losses in the oil system and ensure a sufficient flowrate towards the machine. In HTHP mode, the pump can be bypassed due to the pressure gradient produced by the compressor. Subsequently an oil filter (Filtration Group Pi 2005, filter type Pi 3105 PS10) is passed to remove potentially harmful particles. Another brazed plate heat exchanger (SWEP BH3x50) is used to cool down the oil before its injection onto the bearings. It is connected to the in-house cooling water line on the cold side and the water flowrate can be controlled by the linear regulating valve V-59 (ESBE VLA121). The total oil flowrate is measured by a Coriolis mass flow meter (RHEONIK RHM 06) and controlled by the regulating valve V-63 (Emerson EX5-U21).

88

3.5 Preliminary Control Strategy

The test rig's two functionalities increase the complexity of the required control system compared to a mono-functional plant. The main control loops for both operation modes are depicted as dashed lines in Figure 4. The red lines show the ORC control loops while blue is used for the HTHP mode. For both operation modes the available heat source flow and temperature are considered as boundary conditions (c.f. Section 2.2) and are not part of the control strategy. In ORC mode the superheating after the evaporator (T22) is controlled by adapting the pump speed and hence the refrigerant mass flow rate. The evaporation pressure (p23) is controlled by the expander speed, which is possible due to the use of a volumetric expansion machine. The condensation pressure (p26) is controlled by adapting the mass flow rate in the cooling circuit using V-52. This determines the heat extracted from the main cycle and hence the condensation pressure for a given mass flow rate. Finally, the subcooling before the pump is controlled by an adaption of the tap water mass flow rate in the subcooler using V-51. In HTHP mode, the flowrate in the cooling circuit is set as a boundary condition. The water-side condenser inlet temperature (T43) is controlled by the cooling water flowrate in the house line via V-54. The respective outlet temperature (T44) is controlled by the compressor speed. The compressor speed influences both the refrigerant flowrate and the condensation pressure making a careful design of this control loop critical. The superheating after the evaporator (T22) is controlled by the throttle valve V-38, which also has an impact on the overall process conditions. It becomes clear that the process parameters in HTHP mode are interdependent making a stable control more complex in this operation mode. The control

loops for the oil system (as described in Section 3.4 already) are only indicated for ORC operation in Figure 4 but are valid for HTHP operation as well.

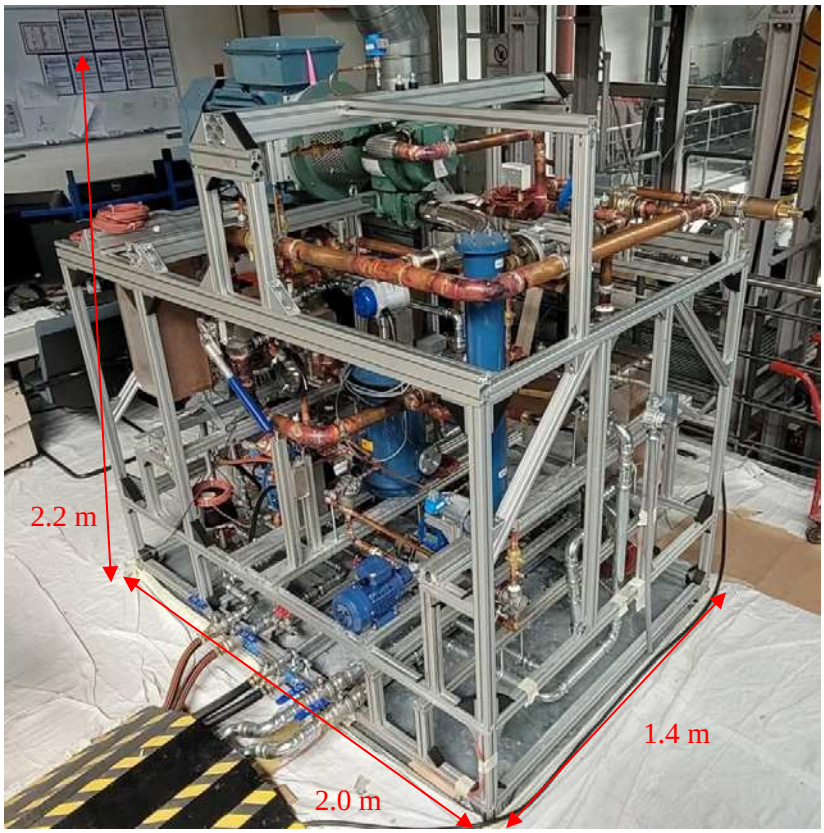

89

Figure 5: Most recent constructional state of the reversible ORC test rig including dimensions

4 CONCLUSION AND OUTLOOK

This work presents the design and construction of a fully reversible ORC test rig that can also be operated as a HTHP. It is intended for the experimental validation of a previously untested cycle layout for geothermal applications. The test rig is supplied by a 200 kW hot water heating circuit as a heat source and uses a fully reversible 20 kW twin-screw machine as compressor and expander. A closed loop intermediate cooling circuit allows simulating a DHN with varying temperature levels and mass flows during HTHP operation. This paper provides insights on the design methodology as well as the intended operating range and performance of the test rig. Moreover, an in-depth description of the constructed test rig, its components and instrumentation are given. Finally, a brief overview of the intended control strategy and associated difficulties is given. Commissioning and first experimental results are expected in late fall 2023. After commissioning, the test rig will be experimentally characterized by replicating the boundary conditions described in Section 2.2. The obtained efficiencies and COP values will allow conclusions on the quality and flexibility of the proposed design. This allows deducting measures to improve the general design and part-load efficiency. Moreover, optimised control strategies for reversible ORCs will be derived from the test rig. Finally, the obtained experimental data can be used to validate component models for key components of reversible plants such as heat exchangers and especially reversible twin-screw machines.

REFERENCES

Dawo, F., Eyerer, S., Pili, R., Wieland, C., Spliethoff, H., 2021, Experimental investigation, model validation and application of twin-screw expanders with different built-in volume ratios, *Applied Energy* 282, 116139.

Dumont, O., Lemort, V., 2019. Thermo-technical approach to characterize the performance of a reversible heat pump/organic Rankine cycle power system depending on its operational conditions, in: *Proceedings of ECOS 2019*. The 32nd International Conference on Efficiency, Cost, Optimization, Simulation and Environmental Impact of Energy Systems, Wroclaw, Poland. June 23-28.

Dumont, O., Quoilin, S., Lemort, V., 2015, Experimental investigation of a reversible heat pump/organic Rankine cycle unit designed to be coupled with a passive house to get a Net Zero Energy Building, *International Journal of Refrigeration* 54, 190–203.

Eyerer, S., Dawo, F., Wieland, C., Spliethoff, H., 2020, Advanced ORC architecture for geothermal combined heat and power generation. *Energy* 205, 117967.

Frate, G.F., Antonelli, M., Desideri, U., 2017, A novel Pumped Thermal Electricity Storage (PTES) system with thermal integration, *Applied Thermal Engineering* 121, 1051–1058.

Giuffrida, A., 2016, A semi-empirical method for assessing the performance of an open-drive screw refrigeration compressor, *Applied Thermal Engineering* 93, 813–823.

Kaufmann, F., Schifflechner, C., Wieland, C., Spliethoff, H., 2022, Techno-Economic Evaluation of reversible Organic Rankine Cycles in geothermal combined Heat and Power Plants, in: *Proceedings of ECOS 2022*: The 35th International Conference on Efficiency, Cost, Optimization, Simulation and Environmental Impact of Energy Systems, Technical University of Denmark.

Kosmadakis, G., Neofytou, P., 2019, Potential and Cost Effectiveness of a Reversible High-Temperature Heat Pump/ORC Unit for the Exploitation of Industrial Waste Heat, in: *Proceedings of the 5th International Seminar on ORC Power Systems*, 5th International Seminar on ORC Power Systems, Athens, Greece. September 9-11.

Lemmon, E.W., Bell, I.H., Huber, M.L., McLinden, M.O., 2018, NIST Standard Reference Database 23: Reference Fluid Thermodynamic and Transport Properties-REFPROP: Standard Reference Data Program. National Institute of Standards and Technology, Gaithersburg, United States.

Quoilin, S., Dumont, O., Harley Hansen, K., Lemort, V., 2016, Design, Modeling, and Performance Optimization of a Reversible Heat Pump/Organic Rankine Cycle System for Domestic Application, *Journal of Engineering for Gas Turbines and Power* 138 (1).

Staub, S., Bazan, P., Braimakis, K., Müller, D., Regensburger, C., Scharrer, D., Schmitt, B., Steger, D., German, R., Karellas, S., Pruckner, M., Schlücker, E., Will, S., Karl, J., 2018, Reversible Heat Pump–Organic Rankine Cycle Systems for the Storage of Renewable Electricity, *Energies* 11 (6), 1352.

Steger, D., Karl, J., Schlücker, E., 2021, Launch and first experimental results of a reversible heat pump-ORC pilot plant as Carnot Battery, in: *Technical University of Munich (Ed.), Proceedings of the 6th International Seminar on ORC Power Systems.*

Steinmann, W.-D., Bauer, D., Jockenhöfer, H., Johnson, M., 2019, Pumped thermal energy storage (PTES) as smart sector-coupling technology for heat and electricity, *Energy* 183, 185–190.

The MathWorks Inc., 2021. MATLAB, Natick, Massachusetts, United States.

Urbanucci, L., Testi, D., Bruno, J.C., 2019, Integration of Reversible Heat Pumps in Trigeneration Systems for Low-Temperature Renewable District Heating and Cooling Microgrids, *Applied Sciences* 9.

VDI-Wärmeatlas, 2002. VDI-Wärmeatlas: Berechnungsblätter für den Wärmeübergang, 9th ed. Springer-Verlag Berlin Heidelberg GmbH, Heidelberg.

ACKNOWLEDGEMENT

Funding from the Bavarian State Ministry of Education, Science and the Arts in the framework of the project Geothermal-Alliance Bavaria is gratefully acknowledged.

ORC SEVILLE 2023
7th International Seminar on O.R.C. Power Systems

© 2024 Editorial Universidad de Sevilla. Este es un artículo de acceso abierto distribuido bajo los términos de la licencia de uso y distribución Creative Commons (BY-NC-ND 4.0)

DOI: https://dx.doi.org/10.12795/9788447227457_15
Paper ID #15, page 1 of 10

Robust and Fast Meanline Methodology for Radial Inflow Turbines with Non-ideal Gases for System Level Optimisation of Organic Rankine Cycles

Carola Freytag*, Eva Alvarez-Regueiro, Pablo Ale Martos, Esperanza Barrera-Medrano, Ricardo Martinez-Botas

** Imperial College London*

Exhibition Road, SW7 2AZ, London

United Kingdom

*Corresponding Author: c.freytag20@imperial.ac.uk

ABSTRACT

Waste heat recovery aims to increase the overall system efficiency and thus, reduce emissions. One technology commonly considered is the Organic Rankine Cycle (ORC) which uses a refrigerant as the working fluid. For an efficient operation of the ORC, the different components, e.g., the turbine, need to be optimised considering the entire system. This paper investigates the capability of meanline modelling for nozzled turbines to model the non-ideal gas effects of different refrigerants. For optimal implementation at a system level, it is important to have sufficient accuracy and low computational cost. The meanline model was compared with CFD for three different working fluids. A 3D parametric model was generated, and a numerical experiment was performed using Latin Hypercube Sampling. Seven meanline design parameters were investigated over a broad design space to show the influence of each respective one on turbine performance. Subsequently, the meanline model was calibrated against a subset of geometries and compared to the entire data sample. The average error stayed below 5%, which is sufficiently accurate for preliminary-stage calculations.

1 INTRODUCTION

The development of new, zero-emission propulsion systems for heavy-duty vehicles is necessary to meet the emission restrictions to NetZero by 2050 imposed by the governments. Additionally, it is also required to incorporate existing or in-development technological solutions capable of meeting the new limited emissions target during the decarbonization journey. The Organic Rankine Cycle (ORC) System is an innovative technology poised to be attractive for mobility/heavy-duty applications, where other, less polluting powertrains than conventional ICE systems are not able to meet the torque demand under certain operating conditions. Leveraging the principles of the Rankine Cycle, the ORC system enables the efficient conversion of waste heat into usable energy, making it a viable solution for enhancing the emissions for the transitions of these machines to a NetZero scenario.

The ORC system utilizes organic fluids with low boiling points to extract heat energy from exhaust gases, engine coolant, or other waste heat sources. This heat is then converted into mechanical energy, which can be used to power auxiliary systems, reduce reliance on conventional fuels, and improve overall energy efficiency. Thereby, the recovery of heat from exhaust gases of internal combustion engines (ICE) could mean a significant option for reducing emissions and fuel consumption in the heavy-duty sector. This approach has been widely investigated in literature (Maizza & Maizza, 2001; Teng et al., 2007) and different cycle configurations have been proposed (Nemati et al., 2017; Yu et al., 2016). Among the options studied, the Rankine cycle operated with organic fluids (Organic Rankine Cycle – ORC) is a promising solution (Sun et al., 2017) for two reasons:

i. It provides good thermal efficiency over a wide range of operating temperatures, suitable for integration with engines used in heavy vehicles in the transport sector.

ii. The organic fluids used have low global warming and ozone depletion potentials (Desideri et al., 2016; Eyerer et al., 2016; C. M. Invernizzi et al., 2016).

The implementation of waste heat recovery via ORC-based power units for heavy-duty solutions has been studied under different configurations on conventional/unconventional power train systems. Some of these solutions using the ORC system for the recovery of residual thermal energy to the exhaust allow the thermal efficiency of the power production unit to be increased to values of more than 40% (C. Invernizzi et al., 2007; Noriega et al., 2020).

To increase system efficiency, the turbine must be appropriately designed, based on the application under study and potential constraints. The initial turbine design is commonly delivered using low-order models (0D-1D), following the meanline modelling approach. This approach assumes that the flow behaviour through the turbine can be represented by the flow through all stations of the turbine from the volute inlet to the rotor exit along the "meanline" path, being this the streamline at mid-span. Meanline modelling is computationally cost-effective, thus allowing the assessment of a broad range of design possibilities, however, it usually requires calibration against experimental data on similar designs and operating conditions. Baines (Whitfield & Baines, 1990) developed a meanline model commonly used in the most recent research on radial turbines. Originally formulated using the ideal gas equation with air as a working fluid, this model has been adapted by other authors to implement the equation of state for the real gas behaviour of refrigerants normally present in an ORC system (Rahbar et al., 2015). One of the key aspects when using the meanline modelling approach is the calibration of the loss coefficients used to model losses occurring in each station. There is limited data available for radial turbines operating with organic fluids in literature (Da Lio et al., 2017; Desideri et al., 2016; Eyerer et al., 2016).

To address this lack of available data and provide a universal tool in the preliminary stage of a radial turbine in an ORC application, this work aims to calibrate the meanline model for a radial turbine using CFD performance data from a range of geometries by applying different refrigerants, such as R1233zd(E), R1234ze(Z) and Benzene. In the first step, a sensitivity analysis is conducted for the different meanline design parameters, and this analysis gives insights into which key parameters should be investigated in the preliminary design stages. Subsequently, the data is used to calibrate a meanline model to capture the overall performance of the turbine under different organic fluids. A comparison is made between CFD and meanline modelling to verify the applicability of the design methodology for a range of fluids. Thus, a robust methodology is developed which can be embedded into the system-level assessment of ORC applications without the need for time-consuming CFD simulations.

92

2 1D MODELLING APPROACH

The meanline approach used in this assessment was developed in Python and adapted from the work conducted by (Hohenberg et al., 2021). The model was further extended during the current study focusing on two main areas of development: firstly, the model was extended to consider an additional turbine station – the nozzle. Secondly, the model was adapted to consider the properties of different refrigerants, and non-ideal gas effects were included in the model by *look-up* tables instead of ideal gas equations (Bell et al., 2013).

Meanline modelling describes the flow through a turbine based on 1D equations for continuity, momentum and energy solved at mean height between two stations. To account for losses, semi-empirical enthalpy loss models are introduced based on physical processes in the turbine. Losses in the stator part are accounted for by assuming a pressure loss and swirl loss coefficient (Japikse & Baines, 1997). The main losses in the rotor are as follows: passage loss due to friction on the wall (Wasserbauer & Glassman, 1975), incidence loss due to flow incidence at the rotor leading edge (Futral & Wasserbauer, 1965) and tip clearance loss due to secondary flows at the rotor tip clearance (Spraker, 1987). A blockage factor is included in all stations to account for the blockage effects in the mass flow produced by the geometry. All these loss models need to be calibrated against experimental/ computational data to allow for an accurate prediction of the turbine performance. Figure 1 summarizes

the meanline approach, which allows for prediction of total-to-static isentropic efficiency η_{t-s} and mass flow $\dot{m}$ based on a given pressure ratio, PR, and rotational speed, N. Additionally, the implemented loss models are given for which the loss coefficients need to be calibrated against experimental or numerical data.

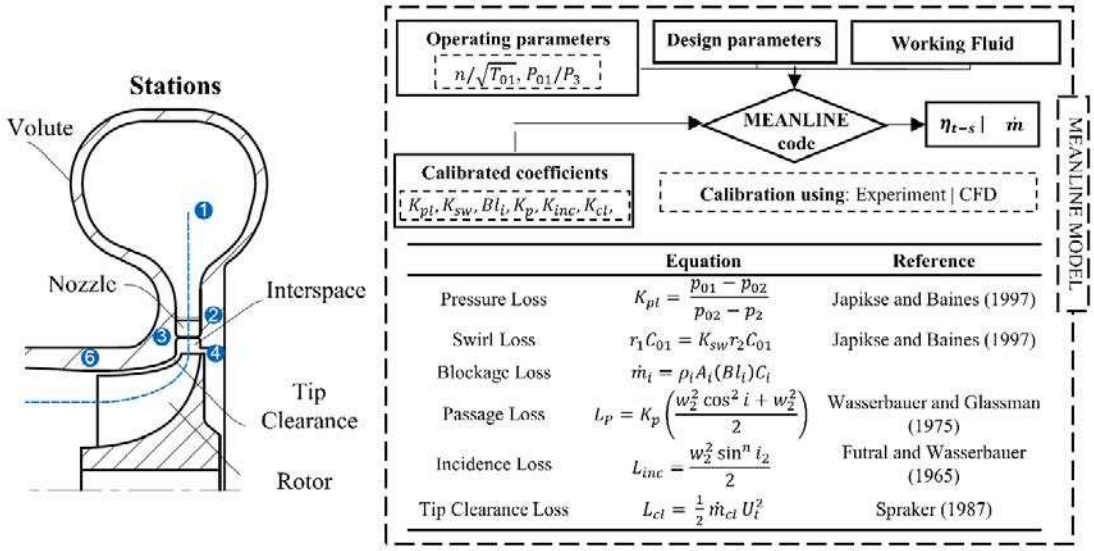

Figure 1. Meridional section of a radial turbine showing the meanline stage (left) and meanline modelling approach (right)

3 WORKING FLUID SELECTION

93

For the selection of working fluids to be investigated, a simple ORC configuration consisting of a pump, evaporator, turbine and condenser (Figure 2) was modelled by basic thermodynamic equations. No pressure drop was considered through the piping connecting the elements nor through the heat exchangers, and constant isentropic efficiency of 75% was assumed across the turbomachinery elements.

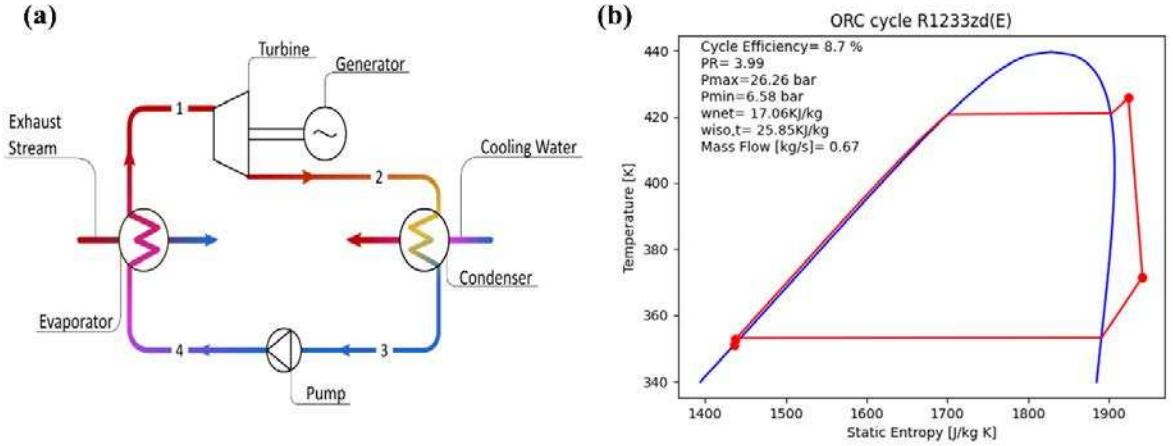

Figure 2. ORC diagram (a) and resulting h-s Diagram for R1233zd(E) (b)

The application consisted of exhaust gases from a heavy-duty engine which takes the ORC fluid to a maximum temperature of 430 K, while the minimum temperature was set to 350 K, based on the cooling limitations of the application reported in the literature (Lang et al., 2013; Robertson, 2019). The evaporating pressure were calculated as the saturation pressure at the maximum temperature minus a superheating of 5 K if the temperature was below the critical temperature. If the maximum temperature of the cycle was above the critical temperature, the evaporating pressure was taken as the saturation

pressure at the critical temperature minus 2 K. The condensing pressure was set as the saturation pressure at the minimum temperature of the cycle plus 2 K subcooling. This way, using different working fluids leads to varying pressure ratios across the turbine. The efficiency of the ORC cycle was evaluated as the ratio between the net-specific work and the evaporating heat. An example of the h-s diagram and cycle properties for, R1233zd(E) is shown in Figure 2 (b). After a preliminary analysis using different fluids, R1233zd(E), R1234ze(Z) and Benzene showed the highest cycle efficiency and were selected to investigate the turbine design. A summary of the ORC efficiency using different working fluids is shown in Table 1:

Table 1. ORC efficiency using different working fluids.

Fluid	**R245fa**	**R1233zd(E)**	**R1234ze(Z)**	**R1234ze(E)**	**Benzene**	**D4**	**D5**
$\boldsymbol{\eta_{ORC}}$ **[%]**	8.19	8.7	8.23	4.11	10.3	7.9	7.7

R1233zd(E) and R1234ze(Z) are 3rd generation refrigerants, substitutes of the widely used R245fa, with very similar thermophysical properties, but zero global warming potential, GWP, and ozone depletion potential, ODP (Eyerer et al., 2019; Yang et al., 2019). Benzene is an aromatic hydrocarbon with a higher critical temperature and pressure than the other two and a low environmental footprint too, but higher levels of toxicity and flammability. Table 2 summarizes the boundary conditions of the turbine depending on the fluid subsequently used to calculate the aerodynamic performance of the different turbine designs.

Table 2. Turbine boundary conditions based on the ORC system for the fluids of study.

Fluid	**R1233zd(E)**	**R1234ze(Z)**	**Benzene**
$\boldsymbol{PR}$ **[-]**	4	3.9	5.5
$\boldsymbol{P_{evap}}$**[bar]**	26.3	33.7	5.6
$\boldsymbol{P_{cond}}$**[bar]**	6.6	8.6	1.0

94

4 NUMERICAL SETUP

A 3D model developed in the parametric CAE platform CAESES (FRIENSHIP SYSTEMS, n.d.) was used to analyse the influence of geometric parameters on the turbine performance for the three different working fluids. For this purpose, Latin Hypercube Sampling (LHS) was conducted and the CFD data generated was used both for the sensitivity analysis of key design parameters as well as verification for the meanline model.

The parametric model consisting of both a nozzle and a rotor was initially introduced by (Alvarez-Regueiro et al., 2022). Both vanes and blades are defined through the parametrisation of the meridional profile as well as camberline and blade surface thickness distribution. In Figure 3(a) a representation of the rotor profile is given along with the defining parameters. The rotor is radial-fibred and thus, one definition of the camber line is sufficient to describe the full blade. The nozzle meridional profile is defined by the rotor blade height as well as the inlet and the outlet radii which are a function of the rotor inlet diameter. The geometry has a constant number of vanes (13) and blades (11). Finally, the geometry is defined and flow domains (cf. Figure 3 (a), right) can be exported for CFD simulations.

Simulations were conducted ANSYS CFX with mesh generation using Turbo-Grid. The numerical setup shown in Figure 3 (b), is a single-passage RANS model with SST turbulence model. To calculate the thermophysical properties of each working fluid, Peng-Robinson equation of state was used. Mesh studies were conducted for all three fluids, with the maximum average $y_{+,ave,Nozzle} = 24$ at the nozzle and $y_{+,ave,Rotor} = 17$ at the rotor for R1234ze(Z). As can be seen in Figure 3(b), turbine efficiency is insensitive to the applied mesh size and based on this study a mesh was selected containing of 2.2 million elements, resulting in a computational time of less than 24 core hours per simulation.

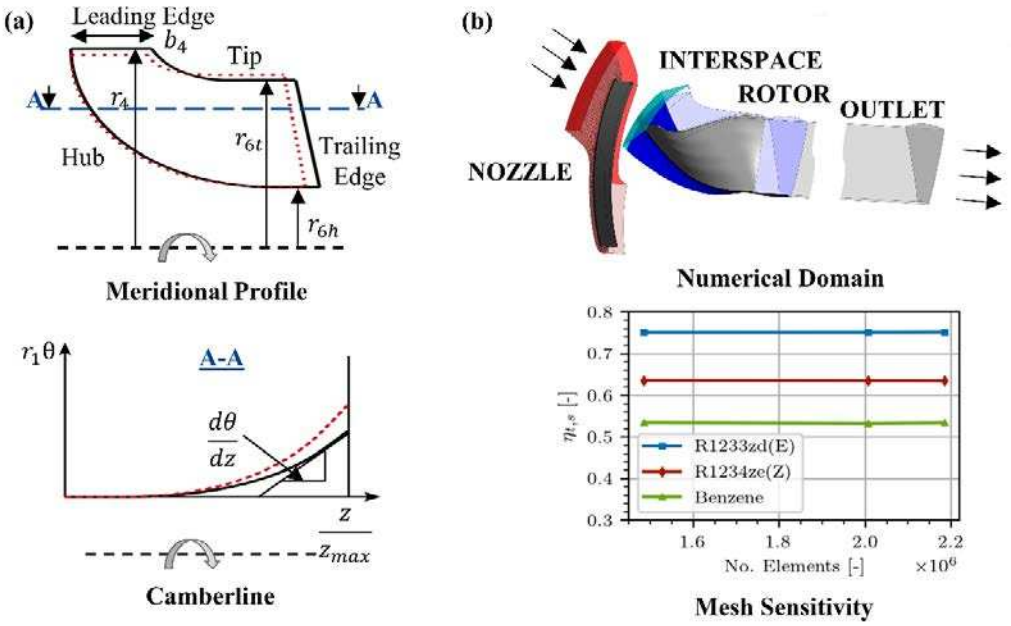

Figure 3. Meridional blade and camberline parametrisation of the rotor (a) and numerical setup (b)

A frozen rotor model was applied as it proved to be more robust than the stage interface: for a sample of 100 designs, 93% converged using frozen rotor compared to 56% using stage interface. The mean absolute deviation between both models was 0.44% in relative deviation for mass flow and 1% in percentage points for efficiency.

5 RESULTS

95

5.1 Design of Experiment

Six geometrical meanline parameters as well as the rotational speed, N, were selected given their influence on the turbine performance. An overview of those parameters is given in Table 3 with both baseline value and lower/ upper boundaries of the sample. All over parameters are kept constant during all simulations. Latin Hypercube Sampling (LHS) was performed with 500 samples for each working fluid with a convergence rate of approximately 80%. For each working fluid, the design vectors were kept the same, thus, only the fluid itself and respective boundary conditions were changed.

Table 3. Design parameters: baseline value and design space for sampling

Design Parameter	Baseline Value	Design Space
$r_4\ [mm]$	24	[22.0 – 32.0]
$r_{6s}/r_4\ [-]$	0.82	[0.78 – 0.85]
$r_{6h}/r_4\ [-]$	0.24	[0.18 – 0.27]
$\alpha_4\ [deg]$	77	[73.0 – 80.0]
$b_4\ [mm]$	5	[2.00 – 8.00]
$\beta_6[deg]$	-63	[-72 – -55]
$N\ [krpm]$	50	[30.0 – 90.0]

To assess the results of the sensitivity analysis, Figure 4 (left) presents the resulting mass flow, $\dot{m}$, against rotational speed. The mass flow is normalized by the respective mean value $\dot{m}_{mean}$ of the dataset, with values of $2.07\frac{kg}{s}$ $(\mathrm{R1233zd}(E))$, $2.32\frac{kg}{s}$ (R1234ze(Z)) and $0.33\frac{kg}{s}$ (Benzene). Next to the data points, a trend line (curve fitting) is implemented which is also presented for the remaining design parameters in Figure 4 (right). It can be noted that the overall mass flow for R1233zd(E) and R1234ze(Z) are at similar levels. Simulations conducted with Benzene will result in lower mean mass flow explained by the overall lower inlet pressure and density. Furthermore, it can be noticed that all

the exit angle β_6 and the radius ratios r_{6s}/r_4 and r_{6h}/r_4 have negligible effect on the resulting MFP, whereas there is a nearly linear positive correlation with both the rotor inlet diameter and blade height. Additionally, the nozzle inlet angle α_2 and the mass flow share a negative relationship.

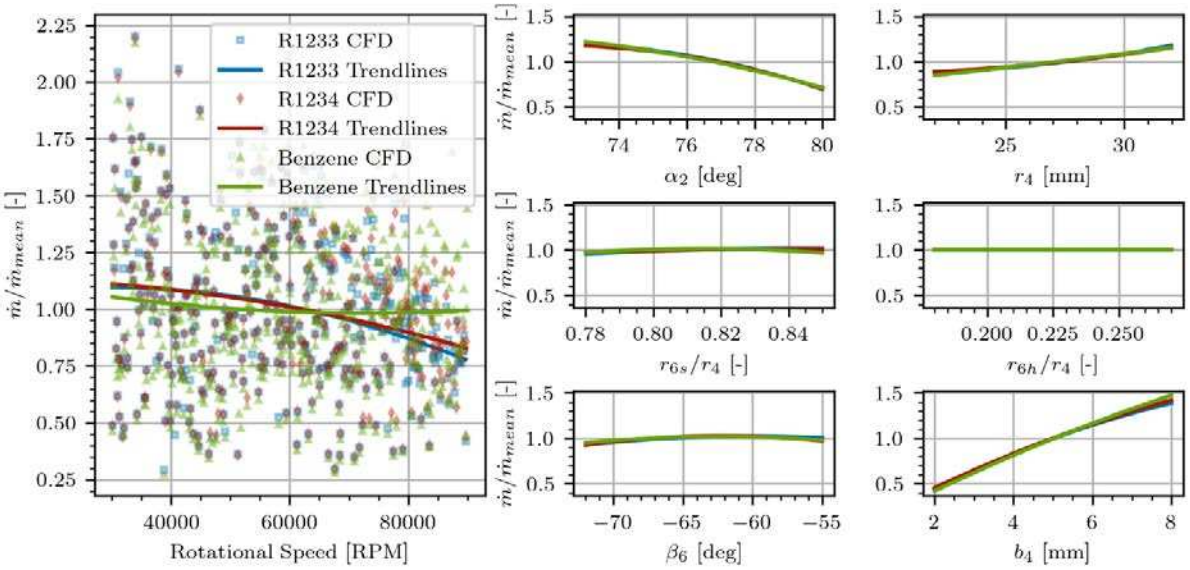

Figure 4. Mass flow sensitivity of each design parameter for the three different fluids

All of the above can be explained by the mass flow equation Eq. (1) at the nozzle inlet. The key driver of mass flow difference between the three working fluids is the density level of the fluid while alteration of geometrical parameters results in modification of effective area A_{ref}.

$$\dot{m} = A_{ref} * C_m * \rho = 2\pi r_2 * b_2 * C_2 * \cos(\alpha_2) * \rho_2 \qquad (1)$$

96

The results of the sensitivity analysis for the second performance parameter of interest, the isentropic efficiency η_{t-s}, is presented in Figure 5. Again, R1233zd(E) and R1234ze(Z) show very similar trends, whereby R1234ze(Z) seem to result in slightly higher performance than R1233zd(E) when applied on the same turbine. The peak efficiency of the turbine operating with Benzene is also slightly lower than for both refrigerants.

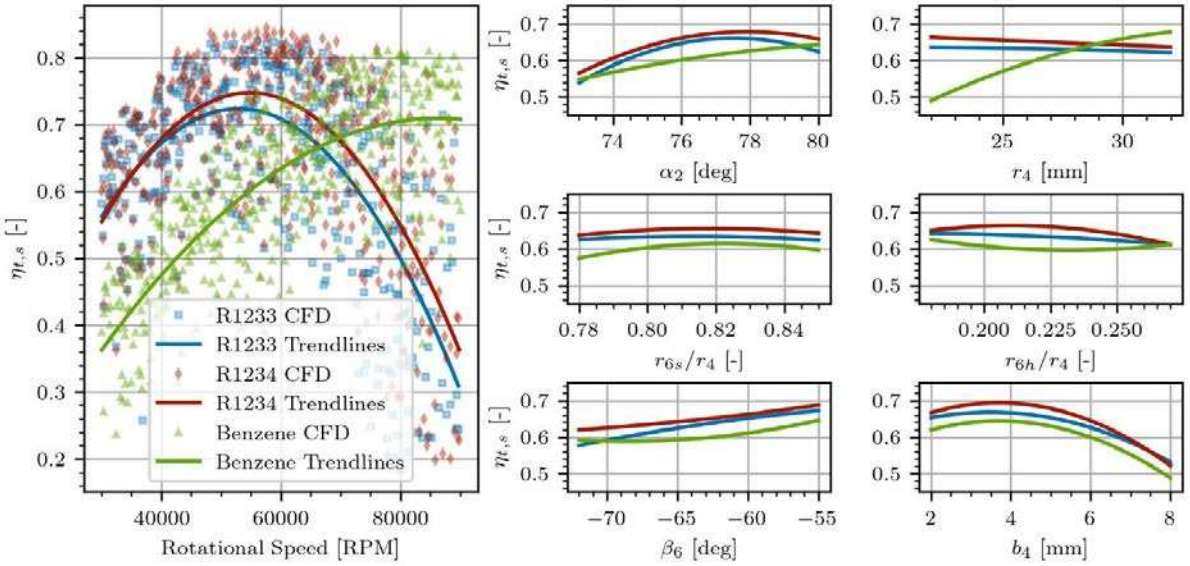

Figure 5. Efficiency sensitivity of each design parameter for the three different fluids

Interestingly, all geometrical parameters show similar influences on the performance of the respective turbine, apart from the rotor inlet radius r_4 and rotational speed N. It is obvious, that while the optimum efficiency for R1233zd(E) and R1234ze(Z) is around 55 kRPM, the optimum for Benzene is just reached at the upper limit for 90 kRPM. This can be explained by the difference in PR boundary conditions between the fluids. Benzene turbine has a higher PR, around 5.5 at a higher rotational speed to achieve high efficiency in the expansion process.

In terms of blade inlet radius, no clear correlation is found for the two refrigerants while there seems to be a clear increase in performance towards higher radii for Benzene. This can be analysed by looking at the isentropic velocity ratio $\frac{U}{C_{is}}$, shown in Eq. (2):

$$\frac{U}{C_{is}} = \frac{2\pi r_2 N}{\sqrt{2\Delta h_{0is}}}, \qquad with\ \frac{C_{is}^2}{2} = \Delta h_{0is} = \frac{\gamma R T_{01}}{\gamma - 1}\left[1 - \frac{1}{PR}^{\frac{\gamma-1}{\gamma}}\right] \tag{2}$$

In the case of radial inflow turbines, the peak efficiency theoretically falls on a value of approximately 0.7. Given the higher pressure ratio needed across the turbine when running with Benzene, either r_4 or N need to be increased for a similar velocity ratio. For all nozzle inlet angle α_2, radius ratio r_{6s}/r_4, and rotor inlet blade height b_4 the turbine performs best at similar values, especially for the latter parameter, a clear optimum can be found. Overall, it can be concluded through the sensitivity analysis of the geometrical design parameters that a geometry optimized for a specific working fluid should perform similarly for the other fluids if the rotational speed is modified for the different loads.

5.2 Verification of Meanline model

As mentioned in previous sections, meanline modelling approaches based on semi-empirical loss models need to be calibrated for a given application. Thus, the CFD model described in Section 4 was used to calibrate the loss coefficients of the model for each working fluid, respectively. For this purpose, a genetic algorithm is used minimising the RRMSE of both predicted meanline and CFD efficiency and mass flow values, given a specific range of each loss coefficient. A small LHS consisting of 20 samples in total was performed for the calibration, varying between the minimum and maximum of each design parameter.

A total of 1000 iterations were performed for each calibration resulting in a ***Pareto*** front between prediction accuracy for both prediction parameters at which the prediction of one parameter cannot be further improved without reducing the accuracy of the other, as shown in Figure 6(a). The selected set of loss coefficients thus forms a compromise between mass flow and efficiency accuracy. Both the parameter ranges and the resulting loss coefficients are given in Table 4. The calibrations for R1233zd(E) and R1234ze(Z) find similar coefficients, whereas the one for Benzene results in a higher pressure loss coefficient for the nozzle $K_{pl,N}$ as well as passage loss coefficient at the rotor K_p.

Table 4. Loss coefficient ranges and results from calibration

Parameter	Range	R1233zd(E)	R1234ze(Z)	Benzene
Bl_2, Bl_4, Bl_6	[0.8 – 1.0]	0.80, 0.93, 0.83	0.87, 0.94, 0.80	0.80, 0.99, 0.91
$K_{pl,N}$	[0.0 – 0.3]	0.09	0.07	0.28
K_{inc}	[0.6 – 1.4]	0.72	0.64	0.91
K_p	[0.0 – 0.4]	0.08	0.03	0.27
K_{cl}	[1.0 – 2.0]	1.13	1.48	1.01

The Sampling performed in Section 5.1 was subsequently used for verification of the different models and resulting deviations from CFD for both efficiency and mass flow, see Figure 6(b), together with the corresponding mean and standard deviation. For all three fluids, the mean error is close to zero, with

a standard deviation of approximately 5%, proving a good agreement between CFD and the proposed meanline methodology.

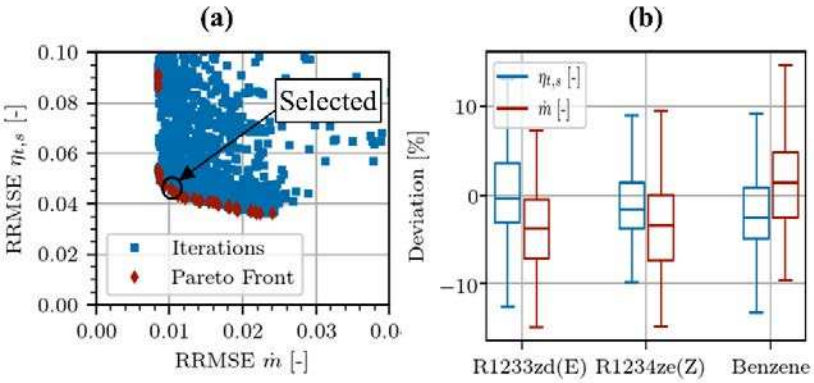

	$\Delta\eta_{t-s}$ Mean, Std	$\Delta\dot{m}$ Mean, Std
R1232zd(E)	-3.88 [%], 4.56 [%]	0.13 [%], 5.43 [%]
R1234zc(Z)	-3.47 [%], 5.37 [%]	-1.09 [%], 4.64 [%]
Benzene	1.21 [%], 4.86 [%]	-1.75 [%], 4.65 [%]

Figure 6. Pareto front for R1233zd(E) calibration (a), error distribution compared to LHS (b) and resulting Mean and Standard deviation (c)

Lastly, a sensitivity study for the different design parameters similar to Figure 5 was performed for the meanline approach, resulting in similar influences on the selected design space. As an example, Figure 7 compares the impact of rotational speed on turbine efficiency which shows a good comparison between 1D and 3D approaches.

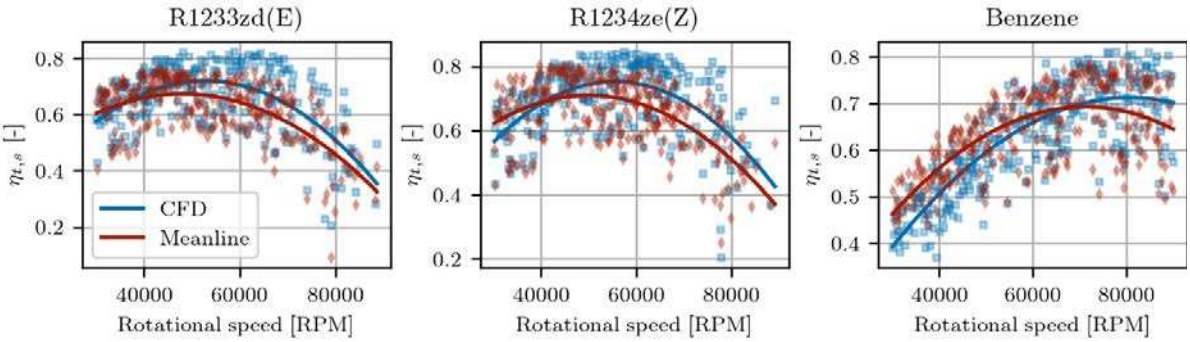

Figure 7. Influence of rotational speed on the efficiency for the three different fluids, both CFD and meanline

6 CONCLUSION

The research conducted aimed to investigate the accuracy of the meanline modelling approach when considering the non-ideal gas effects of different refrigerants in turbine performance prediction. Three different working fluids were selected. A sensitivity analysis was performed for a broad range of design parameters using a 3D parametric CFD model. Subsequently, calibration was performed for each working fluid using a small data subset of this investigation.

For the two refrigerants R1233zd(E) and R1234ze(Z), the results of the calibration proved to be similar whereas the calibration coefficient for the last working fluid, Benzene, deviated significantly. A comparison between CFD and meanline modelling results was carried out to assess the accuracy of the meanline performance prediction. Results showed that the 1D modelling approach is sufficiently accurate and capable of capturing the real-gas effect on the turbine performance parameters when compared to reference data given an average error within 5%. Therefore, the proposed meanline methodology seems to be suitable to allow a preliminary design analysis of main geometrical parameters when integrated on the system level, and, therefore, can help overcome the computational effort of CFD simulations in the preliminary stage.

NOMENCLATURE

A	Area	(m^2)
b	Blade height	(mm)
Bl	Blockage factor	(-)
C	Absolute velocity	(m s^{-1})
C_p	Heat capacity	(J kg^{-1} K^{-1})
CFD	Computational fluid dynamics	
GWP	Global Warming Potential	(-)
Δh_{0is}	Isentropic enthalpy drop	(J kg^{-1})
i	Incidence angle	(°)
K	Loss coefficient	(-)
LHS	Latin Hypercube Sampling	
L	Loss	(kJ kg^{-1})
$\dot{m}$	Mass flow rate	(kg s^{-1})
n	Rotational speed	(rps)
N	Rotational speed	(rpm)
ORC	Organic Rankine Cycle	
ODP	Ozone Depletion Potential	(-)
P	Pressure	(Pa)
PR	Pressure ratio	(-)
r	Radius	(mm)
RRMSE	Relative mean square error	(-)
T	Temperature	(K)
U_t	Blade tip speed	(m s^{-1})
W	Relative velocity	(m s^{-1})
y_+	Y plus	(-)
z	Axial position	(mm)
Z_{max}	Rotor length	(mm)

Greek Letters

α_2	Nozzle vane angle	(°)
β_6	Rotor blade angle	(°)
γ	Adiabatic coefficient	(-)
θ	Circumferential angle	(°)
ρ	Density	(kg m^{-3})
η_{t-s}	Total-to-static efficiency	(-)
η_{ORC}	Cycle efficiency	(-)

Subscripts

0	Stagnation conditions
1	Volute inlet
2	Nozzle inlet
3	Nozzle outlet
4	Rotor inlet
6	Rotor outlet
evap	Evaporating
cond	Condensing
inc	Incidence
is	Isentropic
p	Passage loss
pl	Pressure loss
sw	Swirl loss
tc	Tip clearance loss
LE	Leading edge
TE	Trailing edge

REFERENCES

Alvarez-Regueiro, E., Yang, B., Barrera-Medrano, E., Martinez-Botas, R., & Rajoo, S. (2022). Optimization of an organic Rankine cycle radial turbine using a reduced-order model coupled with computational fluid dynamics. *Journal of Engineering for Gas Turbines and Power*, *144*(10).

Bell, I. H., Quoilin, S., Wronski, J., & Lemort, V. (2013). Coolprop: An open-source reference-quality thermophysical property library. *ASME ORC 2nd International Seminar on ORC Power Systems.*

Da Lio, L., Manente, G., & Lazzaretto, A. (2017). A mean-line model to predict the design efficiency of radial inflow turbines in organic Rankine cycle (ORC) systems. *Applied Energy*, *205*, 187–209.

Desideri, A., Gusev, S., van den Broek, M., Lemort, V., & Quoilin, S. (2016). Experimental comparison of organic fluids for low temperature ORC (organic Rankine cycle) systems for waste heat recovery applications. *Energy*, *97*, 460–469.

Eyerer, S., Dawo, F., Kaindl, J., Wieland, C., & Spliethoff, H. (2019). Experimental investigation of modern ORC working fluids R1224yd(Z) and R1233zd(E) as replacements for R245fa. *Applied Energy*, *240*, 946–963.

Eyerer, S., Wieland, C., Vandersickel, A., & Spliethoff, H. (2016). Experimental study of an ORC (Organic Rankine Cycle) and analysis of R1233zd-E as a drop-in replacement for R245fa for low temperature heat utilization. *Energy*, *103*, 660–671.

FRIENSHIP SYSTEMS. (n.d.). *Computer aided engineering system empowering simulation, CAESES* (v. 4.4.2). https://www.caeses.com.

Futral, S. M., & Wasserbauer, C. A. (1965). Off-design performance prediction with experimental verification for a radial-inflow turbine. *National Aeronautics and Space Administration, NASA TN D-2621*.

Hohenberg, K., Martinez-Botas, R., Łuczyński, P., Freytag, C., & Wirsum, M. (2021). Numerical and experimental investigation of a low order radial turbine model for engine-level optimization of turbocharger design. *Journal of Engineering for Gas Turbines and Power*, *143*(10).

Invernizzi, C., Iora, P., & Silva, P. (2007). Bottoming micro-Rankine cycles for micro-gas turbines. *Applied Thermal Engineering*, *27*(1), 100–110.

Invernizzi, C. M., Iora, P., Preißinger, M., & Manzolini, G. (2016). HFOs as substitute for R-134a as working fluids in ORC power plants: A thermodynamic assessment and thermal stability analysis. *Applied Thermal Engineering*, *103*, 790–797.

Japikse, D., & Baines, N. C. (1997). *Introduction to turbomachinery*. Concepts ETI, Inc.

Lang, W., Colonna, P., & Almbauer, R. (2013). Assessment of waste heat recovery from a heavy-duty truck engine by means of an ORC turbogenerator. *Journal of Engineering for Gas Turbines and Power*, *135*(4).

Maizza, V., & Maizza, A. (2001). Unconventional working fluids in organic Rankine-cycles for waste energy recovery systems. *Applied Thermal Engineering*, *21*(3), 381–390.

Nemati, A., Nami, H., Ranjbar, F., & Yari, M. (2017). A comparative thermodynamic analysis of ORC and Kalina cycles for waste heat recovery: A case study for CGAM cogeneration system. *Case Studies in Thermal Engineering*, *9*, 1–13.

Noriega, S. B., De Servi, C., & Colonna, P. (2020). Hybrid electric powertrain for long-haul trucks and buses: preliminary analysis of a new concept based on a combined cycle power plant. *Journal of the Global Power and Propulsion Society*, *4*, 63–79.

Rahbar, K., Mahmoud, S., Al-Dadah, R. K., & Moazami, N. (2015). Parametric analysis and optimization of a small-scale radial turbine for Organic Rankine Cycle. *Energy*, *83*, 696–711.

Robertson, M. C. (2019). *Thermofluid optimisation of turboexpanders for mobile organic Rankine cycle systems* [PhD Thesis]. Imperial College London.

Spraker, W. A. (1987). Contour clearance losses in radial inflow turbines for turbochargers. *ASME Paper*, *87-ICE-52*.

Sun, W., Yue, X., & Wang, Y. (2017). Exergy efficiency analysis of ORC (Organic Rankine Cycle) and ORC-based combined cycles driven by low-temperature waste heat. *Energy Conversion and Management*, *135*, 63–73.

Teng, H., Regner, G., & Cowland, C. (2007, April 16). *Waste heat recovery of heavy-duty diesel engines by organic Rankine cycle part II: working fluids for WHR-ORC*.

Verbruggen, F. J. R., Hoekstra, A., & Hofman, T. (2018). Evaluation of the state-of-the-art of full-electric medium and heavy-duty trucks. *31st International Electric Vehicle Symposium and Exhibition, EVS 2018 and International Electric Vehicle Technology Conference 2018, EVTeC 2018*.

Wasserbauer, C. A., & Glassman, A. J. (1975). FORTRAN program for predicting off-design performance of radial-inflow turbines. *National Aeronautics and Space Administration, NASA TN D-8063*.

Whitfield, A., & Baines, N. C. (1990). *Design of radial turbomachines*. John Wiley and Sons Inc.

Yang, J., Ye, Z., Yu, B., Ouyang, H., & Chen, J. (2019). Simultaneous experimental comparison of low-GWP refrigerants as drop-in replacements to R245fa for Organic Rankine cycle application: R1234ze(Z), R1233zd(E), and R1336mzz(E). *Energy*, *173*, 721–731.

Yu, G., Shu, G., Tian, H., Huo, Y., & Zhu, W. (2016). Experimental investigations on a cascaded steam-/organic-Rankine-cycle (RC/ORC) system for waste heat recovery (WHR) from diesel engine. *Energy Conversion and Management*, *129*, 43–51.

100

ORC SEVILLE 2023
7th International Seminar on O.R.C. Power Systems

© 2024 Editorial Universidad de Sevilla. Este es un artículo de acceso abierto distribuido bajo los términos de la licencia de uso y distribución Creative Commons (BY-NC-ND 4.0)

DOI: https://dx.doi.org/10.12795/9788447227457_16

SHAPE OPTIMIZATION OF A sCO_2 CENTRIFUGAL COMPRESSOR STAGE

Alessandro Romei*, Paolo Gaetani, Giacomo Persico

Laboratory of Fluid Machines,
Department of Energy, Politecnico di Milano,
Via Lambruschini 4a, 20156 Milano, Italy
*Corresponding Author: alessandro.romei@polimi.it

ABSTRACT

The design of a centrifugal compressor for supercritical carbon dioxide (sCO_2) power cycle must account for non-ideal gas effects and the possible occurrence of two-phase flows. Shape optimization techniques combined with computational fluid-dynamic (CFD) simulations can produce optimized designs while inherently coping with the peculiar flow characteristics near the thermodynamic critical point.

This work presents the first shape-optimization attempt of such non-conventional compressors. The compressor stage includes the impeller and the vaneless diffuser and starts the compression close to the critical point. The impeller blade angle distributions and meridional channel are parameterized with Bezier control points, which grant a local shape control within the optimization routine. The pinch of the vaneless diffuser is optimized as well. The validated CFD solver accounts for both non-ideal effects and two-phase homogeneous flows under the assumption of thermodynamic equilibrium and barotropic fluid. The constrained optimization problem is solved with genetic algorithms. To reduce the computational cost, surrogates for the objective function and constraints are trained over a limited number of CFD results. The surrogate accuracy is improved throughout the optimization process by adding optimal stage geometries to the initial training samples.

The optimized geometry shows an appreciable efficiency increase (0.7 percentage points) while delivering the design pressure ratio. Although performing better in the design condition, the operating range of the compressor is altered by optimization. This finding leaves the door open for future optimizations that include both design and off-design operating points in the definition of the objective function and constraints.

1 INTRODUCTION

The use of carbon dioxide operating in thermodynamic supercritical conditions (sCO_2) as working fluid in closed gas cycles offers the opportunity to exploit multiple classes of hot sources alternative to fossil fuels, ranging from nuclear energy to concentrated solar power and waste heat from industrial processes, owing to the expected higher efficiency and smaller plant footprint with respect to conventional configurations such as steam or organic Rankine cycles. Moreover, sCO_2 power systems also benefit from compactness, thanks to the high density of the working fluid, which ultimately offers the opportunity for effective control of the dynamics of the plant.

A key component of sCO_2 power systems is the main compressor, which is usually centrifugal due to the typical low volumetric flow rates and operates close to the thermodynamic critical point. The corresponding compression process allows for a significant reduction of the work required thanks to the liquid-like properties of CO_2 in these thermodynamic conditions. However, the large departure from the ideal-gas thermodynamics (Pecnik et al., 2012; Baltadjiev et al., 2015; Ameli et al., 2018), as well

as the potential occurrence of two-phase flows (Lettieri et al., 2015; Hosangadi et al., 2019; Persico et al., 2021), pose challenges in the aerodynamic design of impeller blade and meridional channel. The set-up of reliable design tools that comply with the above non-ideal effects is crucial to accelerate the development and the success of the entire technology.

Most of the studies available in the literature analyze the aerodynamics and thermodynamics of the flow within the machine or discuss the validation of computational tools for compressor flow analysis. However, few works (see, for example, Pelton et al., 2017) focus on the design process of such non-conventional machines. In the present study, we propose automatic shape optimizations as a means to design sCO_2 centrifugal compressors. Leveraging a validated computational fluid-dynamic (CFD) solver, which provides an accurate representation of thermophysical fluid properties and accounts for the onset of two-phase flows, shape optimization has the potential to unveil new design paradigms for sCO_2 compressor stages.

2 BASELINE GEOMETRY

The baseline machine is a single-stage centrifugal compressor that was designed from scratch for the inlet total conditions of $P_{01} = 85\ bar$ and $T_{01} = 305\ K$ and has to provide an outlet pressure of $250\ bar$. The compressor stage includes a shrouded impeller and a vaneless diffuser. The main design parameters are: $\phi_{01} = 0.04$, $\phi_2 = 0.20$, $M_u = 0.70$, and $\lambda = 0.625$. The impeller has 8 main blades and 8 splitter blades resulting from blade loading considerations. The meridional channel, the blade angle distribution, and the thickness distribution for the main impeller blades are reported in Figure 1. The splitter blade is obtained by cutting the blade angle distributions at a specified normalized meridional coordinate $\tilde{m}$ and applying the same thickness distribution as the main blade. The splitter for the baseline geometry starts from $\tilde{m} = 0.2$.

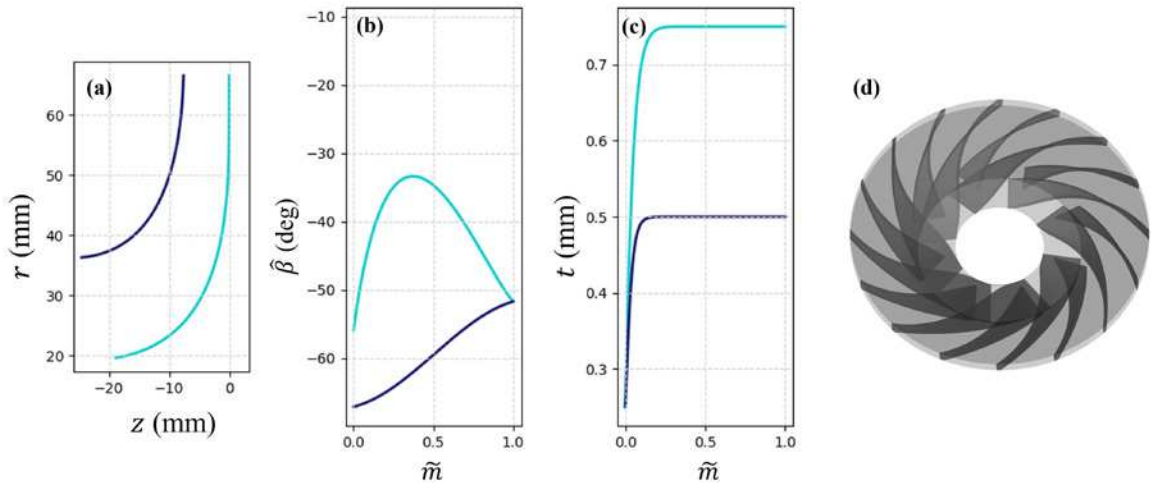

Figure 1: Baseline impeller geometry. (a) meridional view. (b) blade angle distribution. (c) thickness distribution. (d) three-dimensional view.

The performance estimates are determined based on steady RANS simulations. The RANS equations are solved with the Ansys-CFX finite-volume flow solver, using high-order numerical schemes for both inviscid and viscous fluxes. Turbulence effects are introduced by resorting to the $k - \omega$ SST model assuming a fully turbulent flow.

A specific feature of the present model refers to the representation of the non-ideal thermodynamics of the fluid. This is crucial for the proper modeling of turbomachinery operating with sCO_2, whereby the proximity to the critical point originates a large departure from ideal-gas behavior. In particular, the thermodynamic description of the fluid is modeled here by resorting to the Span-Wagner equation of

state. However, the challenges of simulating the flow in technically-relevant sCO_2 compressors are also related to two-phase flows: the proximity of the inlet compressor state to saturation might indeed trigger phase change processes that need to be taken into account in the simulation model. In this work, we make use of a barotropic model, which belongs to the class of homogeneous equilibrium models (HEM), in which the thermo-physical properties (density and dynamic viscosity) of the fluid are assumed only depending on pressure. The barotropic relationships $\rho = \rho(P)$ and $\mu = \mu(P)$ are generated along the isentrope at the impeller inlet section for each thermodynamic state. The barotropic model was first proposed for application to sCO_2 compressors by the same authors (Persico et al., 2021), and it was subsequentially validated against experimental data of a MW-scale sCO_2 centrifugal compressor prototype by Toni et al. (2022).

The computational mesh was generated with Ansys-Turbogrid. To reduce the computational cost per simulation, which is critical in shape optimization tasks, periodic boundary conditions are exploited. Therefore, the computational domain includes a single-blade passage containing the main blade, the splitter blade, and the vaneless diffuser. Other components, such as the volute and the sealings, are omitted to limit the computational cost. After a grid-dependence analysis, a mesh composed of 1.7 million cells was adopted. The resulting grid convergence index for the total-to-total efficiency η_{TT} is 0.3%.

Calculations were performed assigning the total state at the inlet. The flow rate was imposed at the outflow, except close to choked-flow conditions, for which an average static pressure was assigned. No-slip boundary conditions were imposed on the solid walls. As the flow domain is rotating with the impeller, a counter-rotating velocity was assigned at the endwalls of the vaneless diffuser. Considering the high Reynolds number ($\sim 10^8$) as a consequence of the low kinematic viscosity of carbon dioxide in supercritical conditions, the assumption of hydraulically smooth surfaces is not appropriate and, hence, wall roughness ($k_s = 5\ \mu m$) and corresponding wall functions are specified.

The CFD simulation returns a $\eta_{TT} = 92.2\%$, $\lambda = 0.625$, and an outlet total pressure of $266\ bar$. This value of total pressure is sufficient to meet the cycle target of 250 bar while accounting for the losses in additional components (e.g., volute) and the dissipation of the residual kinetic energy. 103

3 SHAPE OPTIMIZATION

3.1 Shape parameterization

To perform the shape optimization, the baseline geometry needs to be parameterized with a finite number of control points, which becomes the design variables. This task is accomplished by parameterizing the meridional channel and the blade angle distribution with Bezier control points as in Figure 2. Four control points are used to reproduce the meridional hub contour $\{M_{hj}\}$, the meridional shroud contour $\{M_{sj}\}$, the hub blade angle distribution $\{B_{hj}\}$, and the shroud blade angle distribution $\{B_{sj}\}$, with $j = 1, \dots, 4$. Not all these design parameters are independent: (i) the trailing edge is cut at the same radial coordinate, therefore the last control point of the hub contour follows the displacement of M_{s4}, and (ii) the outlet blade angle does not change along the span, hence a single control point B_4 is considered for both the hub and the shroud distribution. The thickness distribution is not modified throughout the optimization not to compromise the mechanical integrity of the impeller. In general, the splitter blade may follow a different blade angle distribution with respect to the main blade; however, to reduce the number of design variables, the splitter follows the main blade distributions, and the only design parameter is the meridional coordinate at which the main blade is cut (S). Finally, a front-pinch is considered for the vaneless diffuser, and the diffuser pinch (ζ) and the radial coordinate at which the straight part begins (δ) can be both objects of the optimization. The vaneless diffuser extends up to $R_3 = 1.6\ R_2$.

Overall, 17 design variables are considered for the shape optimization problem, of which 7 are related to the meridional channel, 7 control the blade angle distribution, 2 parameterize the vaneless diffuser, and 1 is for the splitter. Table 1 reports the design space for each of these design variables.

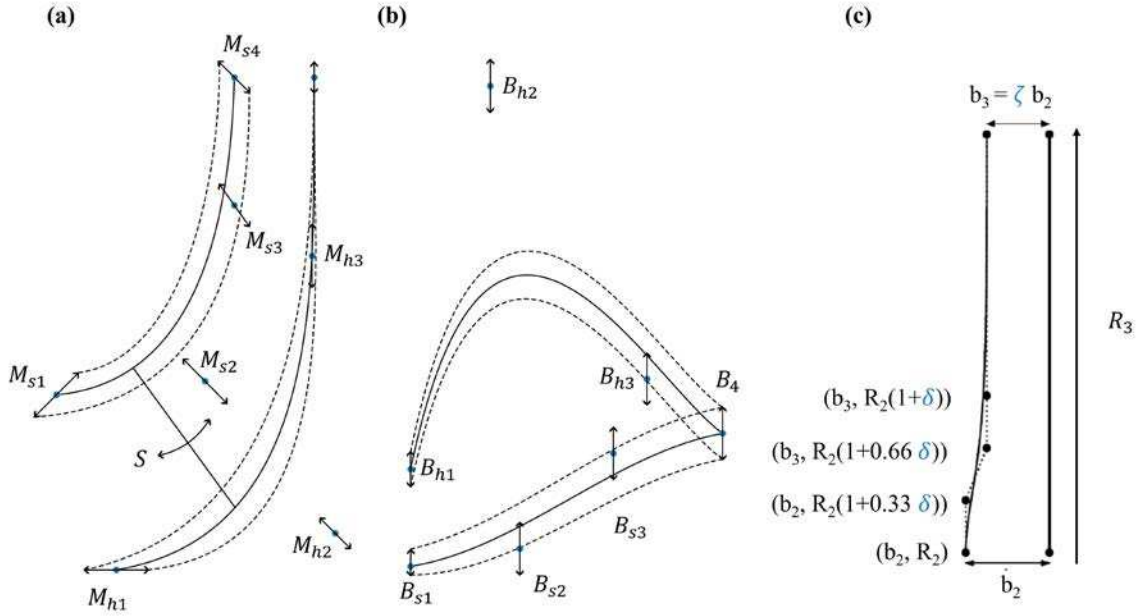

Figure 2: Centrifugal compressor stage parameterization. (a) meridional channel. (b) blade angle distribution. (c) vaneless diffuser.

Table 1: Design space identified by 17 design variables.

	M_{h1}	M_{h2}	M_{h3}	M_{s1}	M_{s2}	M_{s3}	M_{s4}	S	
Max	3.0 mm	2.0 mm	3.0 mm	3.0 mm	3.0 mm	2.0 mm	2.0 mm	0.45	
Min	-3.0 mm	-2.0 mm	-3.0 mm	-3.0 mm	-3.0 mm	-2.0 mm	-2.0 mm	0.15	
	B_{h1}	B_{h2}	B_{h3}	B_{s1}	B_{s2}	B_{s3}	B_4	δ	ζ
Max	2.0 deg	3.0 deg	3.0 deg	2.0 deg	3.0 deg	3.0 deg	3.0 deg	0.20	1.00
Min	-2.0 deg	-3.0 deg	-3.0 deg	-1.0 deg	-3.0 deg	-3.0 deg	-3.0 deg	0.10	0.60

104

3.2 Surrogate-assisted evolutionary strategy

The optimization problem aims at maximizing the total-total efficiency η_{TT} of the stage. Moreover, three constraints are considered, involving the work coefficient λ, the absolute flow angle α_3 at $1.2R_2$, and the mass imbalance $\dot{m}_{imb}$ of the solution. The first two constraints follow aerodynamic consideration. The work coefficient is constrained because the optimal compressor has to provide the required pressure ratio. The absolute flow angle cannot exceed 67 deg (measured from the meridional direction) to keep a safe margin from the onset of instabilities in the vaneless diffuser thus guaranteeing a wide operating range. The last constraint about the mass imbalance is included explicitly in the optimization routine to discard solutions that are characterized by a bad convergence. Therefore, the optimization problem reads as:

$$\max \quad \eta_{TT} \tag{1.1}$$
$$s.t. \quad 0.62 \leq \lambda \leq 0.63 \tag{1.2}$$
$$60\ deg \leq \alpha_3 \leq 67\ deg \tag{1.3}$$
$$|\dot{m}_{imb}| \leq 0.1\% \tag{1.4}$$

The constrained optimization problem is solved with the genetic algorithm (GA). As the GA requires many evaluations to converge, a surrogate strategy is adopted to reduce the computational cost, leveraging the surrogate-assisted strategy implemented in the in-house optimizer FORMA (Persico et al., 2019).

Figure 3 summarizes the optimization workflow. At first, 170 stage geometries are generated within the prescribed design space with Latin hypercube sampling. The objective function and the constraints are calculated with CFD simulations as detailed in section 2. The mesh is regenerated each time using the grid-convergent set-up described before. Four distinct Kriging, one for each objective function/constraint, are introduced as surrogates of the CFD simulation. The employed Kriging models have up to second-order monomials of the input variables as the mean trend and incorporate a Gaussian correlation function. The Kriging hyperparameters are determined by maximum likelihood estimation.

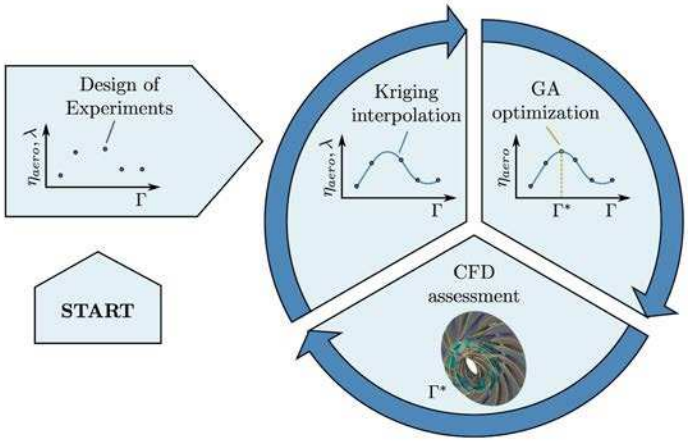

Figure 3: Flow chart summarizing the surrogate-assisted shape optimization strategy.

Once the four Kriging predictors are obtained, the GA optimization is executed on surrogate responses. The so-identified optimal stage geometry is assessed with CFD, and new Kriging predictors are re-generated on all simulated cases, namely the initial design of experiments plus the simulated optimal geometries selected by the surrogate optimization. In this way, the surrogate reliability progressively increases by adding geometries close to the expected optimal region. The optimization procedure is repeated until convergence, i.e. the surrogate optimization converges to the same optimal geometry of the previous iteration.

105

3.3 Optimal geometry

The convergence history of the optimization is shown in Figure 4. It reports the convergence after the first surrogate training on the design of experiments obtained with Latin hypercube sampling. In the initial design pool, there are no geometries that can outperform the baseline while satisfying all the constraints. Looking at the convergence history, the mass imbalance does not affect the convergence process. Except for a few solutions, most of the simulations have negligible values of mass imbalance between the inlet and the outlet section. Meeting the targets for λ and α_3 is more critical, especially the latter. Apparently, the best efficiency is obtained for absolute flow leaving the impeller with a more tangential direction. The optimal solutions are found close to the upper limit of the α_3-constraint (67 deg). The increase in the absolute flow angle will have a detrimental effect on the machine operation at low flow rates (left limit of the operating curve). As a result, the optimal compressor stage shows a $\eta_{TT} = 92.9\%$, with an increase of 0.7 percentage points from the baseline value, while satisfying the imposed aerodynamics constraint, namely $\lambda = 0.629$ and $\alpha_3 = 66.7\ deg$.

Figure 5 compares the baseline and the optimal impeller geometries. The main changes in the meridional channel are localized at the hub, whose curvature is slightly increased. Then, the backswept of the blade is reduced, shifting the entire shroud blade angle distribution to more meridional values. Moreover, the splitter length is increased to further reduce the aerodynamic loading in the front part of the blade, which has been increased as a consequence of the higher work coefficient. At the same time the splitter length does not increase the blockage in the impeller inlet area to prevent the onset of choking. It is interesting to note that the optimization has changed the front part of the shroud blade profile, which is typically the most critical region where most of the diffusion occurs. In this region,

there is also a two-phase supersonic pocket, as highlighted in Figure 6 by the sudden increase in the Mach number. This two-phase region is slightly increased for the optimal stage because of the positive incidence that results from a more meridional inlet blade angle. However, in this way, the flow detachement on the blade suction side is considerably reduced, motivating the path followed by the optimization to increase the total-total efficiency.

The complete list of optimal design variables is reported in Table 2. From this table, it can also be observed that the optimal stage has a vaneless diffuser with a pinched section that extends up to 1.18 R_2 and reduces the outlet blade height by almost 20%. Interestingly, the optimal values for some variables are found at the extreme boundary of the associated design space, suggesting that there may be space for further improvement by enlarging the design space. In particular, the shroud blade angle distribution would shift to a more meridional direction.

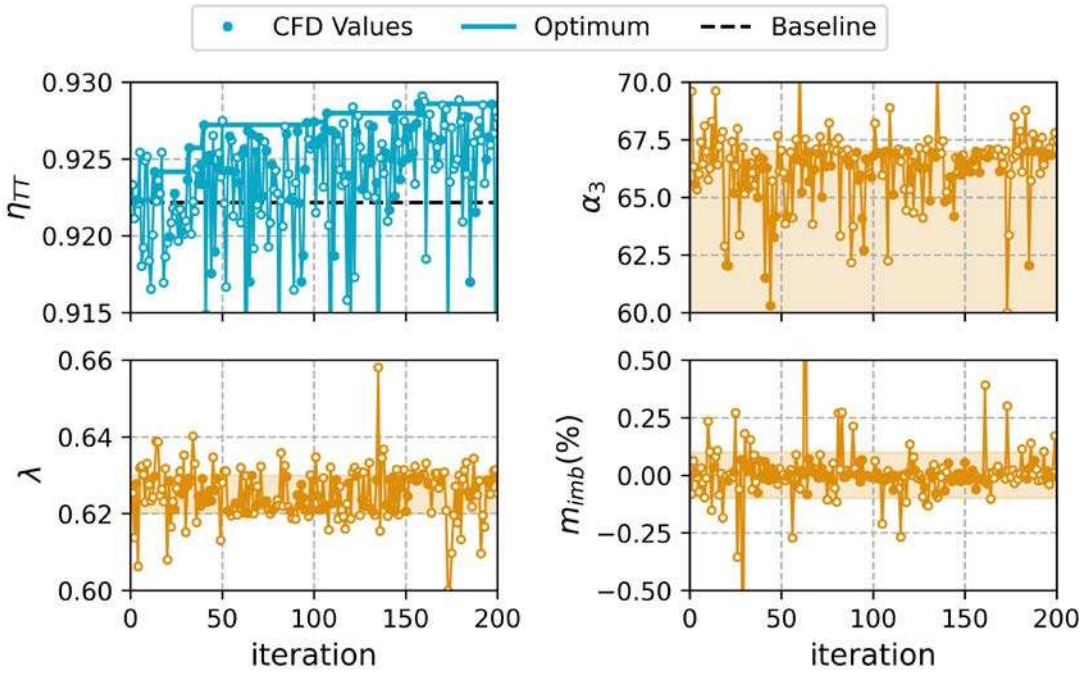

Figure 4: Convergence history. The filled mark indicates a geometry that satisfies all constraints. The void mark indicates a geometry for which at least one constraint is not satisfied.

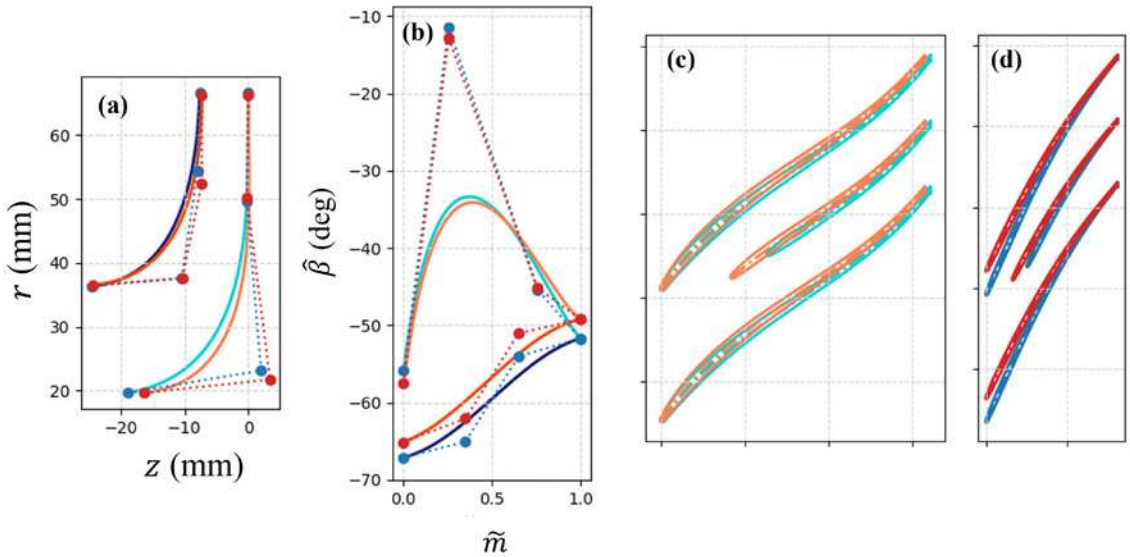

Figure 5: Baseline (cyan/blue) and Optimal (red/orange) impeller geometries. (a) meridional view. (b) blade angle distribution. (c) blade-to-blade view at hub. (d) blade-to-blade view at tip.

Table 2: Optimal design variables. Variables marked with * means that the optimal solution is found at the boundary of the associated design space.

	M_{h1}	M_{h2}*	M_{h3}	M_{s1}	M_{s2}	M_{s3}	M_{s4}	S	
Opt	2.6 mm	2.0 mm	0.6 mm	0.3 mm	-0.1 mm	-1.9 mm	-0.5 mm	0.16	
	B_{h1}	B_{h2}	B_{h3}	B_{s1}*	B_{s2}*	B_{s3}*	B_4	δ	ζ
Opt	-1.6 deg	-1.3 deg	2.5 deg	2 deg	3 deg	3 deg	2.5 deg	0.18	0.79

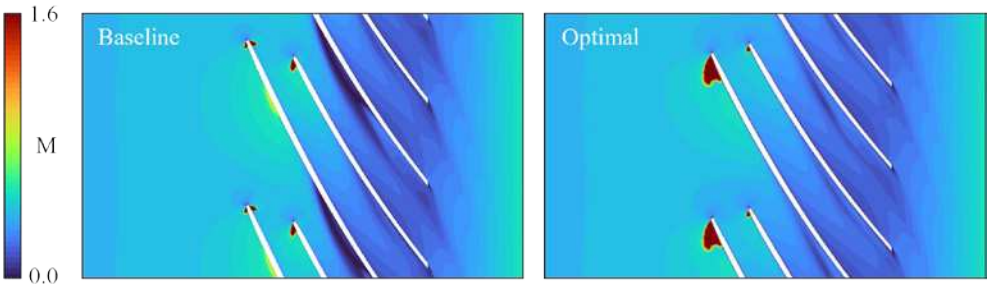

Figure 6: Mach number fields at tip section (90% blade height) for baseline and optimal stages.

As the last analysis, it is worth investigating the variation in the operating range after the optimization. The performance map across the flow range at the nominal rotational speed is reported in Figure 7. Both the right and the left limits are changed as a result of the optimization.

On the one hand, the left limit, which identifies the minimum mass flow rate without incurring compressor instability, is moved towards a higher flow rate in the optimized case by almost 10%. This increase in minimum flow rate can be explained in light of the higher work coefficient, which requires a larger flow diffusion. It is worth highlighting that the identification of the left limit with RANS simulations is not accurate, as the instabilities are inherently time-dependent phenomena and also depend on the machine-plant interaction. For the present analysis, the limit was set based on numerical consideration, i.e. when the simulation is not able to converge to a steady solution (oscillations in torque larger than 2%).

On the other hand, the right limit, which identifies the maximum mass flow rate before choked-flow conditions, is increased by 8%. As discussed in previous works (Persico et al. 2021; Toni et al., 2022), sCO_2 compressors are prone to an anticipated choking due to the sudden drop in the speed of sound for the two-phase flow mixture The choked-flow conditions occur similarly between the baseline and the optimal. The larger swallowing capacity of the compressor is a result of the larger flow passage area at the throat given by the hub curvature increase.

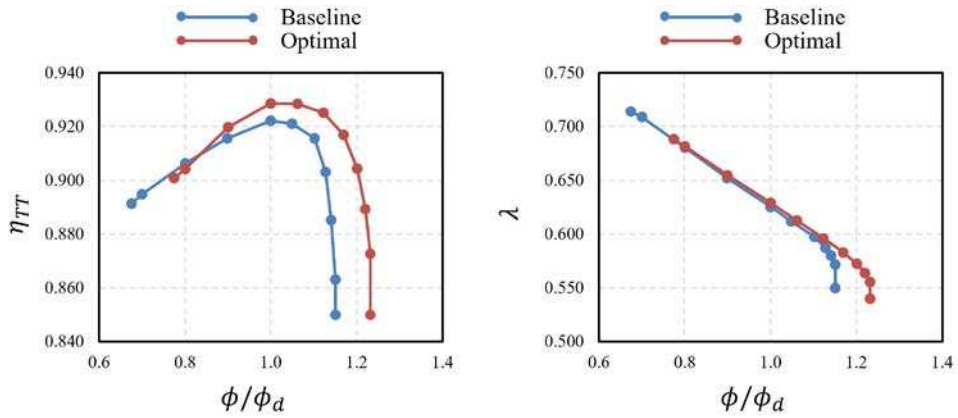

Figure 7: Efficiency (left) and work coefficient (right) curves over the flow range for baseline and optimized stage geometries.

4 CONCLUSION

This work discusses a first shape-optimization attempt for sCO_2 centrifugal compressor stage. The baseline stage is a single stage that provides an overall pressure ratio of about 3 starting from the upstream total conditions $P_{01} = 85\ bar$ and $T_{01} = 305\ K$. The baseline shape is parametrized with a number of Bezier curves for the meridional contours and the blade angle distributions. The geometrical parameterization also includes the length and the extent of the vaneless diffuser pinch and the initial splitter meridional location for a total of 17 design variables.

The shape optimization method is applied to optimize the baseline total-total efficiency while constraining the work coefficient and the absolute flow angle at the impeller outlet. The optimization converges to a new compressor shape that is more efficient (+0.7 percentage points in total-total efficiency) and satisfies the imposed constraints. As a side effect, the operating range of the compressor changes, with a reduction in the surge margin and an increase in the right limit. This finding leaves the door open for future optimizations that include both design and off-design operating points in the definition of the objective function and constraints.

REFERENCES

Ameli, A., Afzalifar, A., Turunen-Saaresti, T., and Backman, J., 2019, "Centrifugal compressor design for near-critical point Applications". J Eng Gas Turbines Power 141 (3).

Baltadjiev, N. D., Lettieri, C., and Spakovszky, Z. S., 2015. "An Investigation of Real Gas Effects in Supercritical CO_2 Centrifugal Compressors". J. Turbomach 137(9), 09.

Hosangadi, A., Liu, Z., Weathers, T., Ahuja, V., and Busby, J., 2019, "Modeling multiphase effects in CO_2 compressors at subcritical inlet conditions". J Eng Gas Turbines Power 2019;141(8):081005.

Lettieri, C., Yang, D., and Spakovszky, Z., 2015. "An Investigation of Condensation Effects in Supercritical Carbon Dioxide Compressors". J Eng Gas Turbines Power 137(8).

Pecnik, R., Rinaldi, E., and Colonna, P., 2012, "Computational fluid dynamics of a radial compressor operating with supercritical CO_2", J Eng Gas Turbines Power 134 (12).

Pelton, R., Jung, S., Allison, T., and Smith, N., 2018. "Design of a wide-range centrifugal compressor stage for supercritical CO_2 power cycles". J Eng Gas Turbines Power 140(9), 092602.

Persico, G., Gaetani, P., Romei, A., Toni, L., Bellobuono, E.F., and Valente, R., 2020, "Implications of phase change on the aerodynamics of centrifugal compressors for supercritical carbon dioxide applications". J Eng Gas Turbines Power 143 (4).

Persico, G., Rodriguez-Fernandez, P., and Romei, A., 2020, "High-fidelity shape optimization of non-conventional turbomachinery by surrogate evolutionary strategies". J. Turbomach. 141(8), 081010.

Toni, L., Bellobuono, E. F., Valente, R., Persico, G., Romei, A., and Gaetani, P., 2022. "Computational and Experimental Assessment of a MW-Scale Supercritical CO_2 Compressor Operating in Multiple Near-Critical Conditions". J Eng Gas Turbines Power 144(10), 101015.

ACKNOWLEDGEMENT

The shape optimization workflow applied to centrifugal compressors has been developed in the framework of the CO2OLHEAT project, which has received funding from the European Union's Horizon 2020 research and innovation programme under grant agreement N° 101022831.

ORC SEVILLE 2023
7th International Seminar on O.R.C. Power Systems

© 2024 Editorial Universidad de Sevilla. Este es un artículo de acceso abierto distribuido bajo los términos de la licencia de uso y distribución Creative Commons (BY-NC-ND 4.0)

DOI: https://dx.doi.org/10.12795/9788447227457_17
Paper ID #17, page 1 of 10

Optimizing the performance of a hybrid Solar-Biomass micro-CHP system with a TFC engine as the prime mover for domestic applications

Anastasios Skiadopoulos[1,*], Xander van Heule[2], Steven Lecompte[2], Michel De Paepe[2], Dimitrios Manolakos

[1] *Agricultural University of Athens, Department of Natural Resources and Agricultural Engineering, Athens, Attica, Greece*
[2] *Ghent University, Department of Electromechanical, Systems and Metal Engineering, Ghent, Belgium*

*Corresponding Author: tskiado@aua.gr

ABSTRACT

The annual performance of a hybrid micro-Cogeneration of Heat and Power (CHP) system driven by solar energy and biomass with a Trilateral Flash Cycle (TFC) engine as the prime mover is simulated and optimized in this work. The system is sized to meet the Space Heating (SH) demand of a typical multi-family building in Athens, Greece. Particular attention is paid to the challenging two-phase expansion phenomenon, the factor mainly affecting the efficiency of the TFC, under off-design and partial load conditions. Under optimized operating conditions, the average annual CHP efficiency, TFC thermal efficiency, and solar energy conversion efficiency were estimated to be 89.2%, 8.4%, and 4.3%, respectively. The TFC can cover 18% of the building's SH demand and 40% of its electricity demand, with the Levelized Cost of Electricity (LCOE) and Levelized Cost of Heat (LCOH) in the range of 0.21~0.28 €/kWh$_{el}$, and 0.065~0.087 €/kWh$_{th}$, respectively. Furthermore, PayBack Periods (PBP), between 15 and 25 years, can be anticipated, when current market energy prices are considered.

1 INTRODUCTION

CHP is a well-established alternative to the standard practice of segregated electricity and heat production, because of increased primary energy conversion efficiency, and lower GreenHouse Gas (GHG) emissions. Micro-CHP units typically have a nominal electric capacity lower than 50 kW$_{el}$. They are particularly suitable for the domestic sector, a major energy consumer and GHG emitter in the EU. Micro-CHP systems driven by Renewable Energy Sources (RES), and hybridized by combining intermittent and stable RES, can play a significant role in increasing the energy efficiency of buildings, while reducing substantially their carbon footprint.

In regions with low to middle latitudes, it is of particular interest to study the sustainability of hybrid micro-CHP systems driven by solar energy and biomass (currently the RES with the highest share in the EU). Biomass Boilers (BB) for residences typically operate at top temperatures of about 90~95ºC. On the other hand, several types of solar thermal collectors have been developed, capable to provide heat at temperatures up to 400ºC, but, for residential applications, the temperature of the heat source is limited to a maximum of 120~130ºC. At such temperature ranges of the heat source, an efficient heat-to-power technological solution is the utilization of a bottoming power cycle (Padinger, Aigenbauer, and Schmidl 2019).

Among the commonly applied bottoming power cycles, the Organic Rankine Cycle (ORC) has certain advantages, such as the low maintenance cost, nearly unsupervised operation, and flexibility in the design (Tchanche *et al.* 2011), that render it a promising solution for residential micro-CHP. However, in an ORC, the potential of the heat source is not optimally exploited, because of the increased exergy losses during the evaporation of the WF in the evaporator (Schuster *et al.* 2010). The temperature of the finite heat source drops as the WF evaporates isothermally, leading to reduced attainable evaporating

pressure, and, consequently, generated power. This sub-optimal match between the heat source and the WF at the evaporator of an ORC can be overcome if the evaporation of the WF is omitted, transforming the power cycle into a triangle (Schuster *et al.* 2010).

A promising alternative to the ORC power cycle is the TFC, originally conceptualized for optimal heat recovery in geothermal applications (Smith 1993). In the TFC, the WF enters the suction port of the expansion machine in the saturated liquid state (or two-phase mixture in the generalization of the concept), where two-phase expansion, also known as flashing, occurs, and power is generated. Several theoretical studies comparing the TFC and the ORC for various heat sources (e.g. see (Fischer 2011)) have been published. They highlight the potential of the TFC as a high-efficiency alternative to the ORC. However, the technological maturity of the TFC is low because flashing is a complex non-equilibrium phenomenon, and the efficiency of expanders in the two-phase region is not sufficiently mapped. Only a handful of experimental works in flashing have been undertaken (Öhman and Lundqvist 2013; Smith, Stošić, and Aldis 1996), all indicating that the efficiency of two-phase expansion improves as the quality of the WF at the suction port of the expander increases.

The purpose of this work is to numerically assess the performance of a novel hybrid micro-CHP system in Athens, Greece, driven by solar energy and biomass, and a TFC engine as the prime mover. The unit consists of a BB, an array of Evacuated Tube Collectors (ETC), a TFC engine, with a twin-screw expander as the expansion machine, and a Thermal Energy Storage (TES) tank. It operates in heat-driven mode, and it is sized to meet the SH demand of an average-sized multi-family building. An integrated numerical tool is developed in Matlab to calculate the energy output of the micro-CHP system on an annual basis, with an hourly time step. A novel feature of this work is that the efficiency of two-phase expansion under off-design operating conditions is carefully monitored, by applying a dedicated thermodynamic low-order model (Skiadopoulos *et al.* 2021). Optimization simulations are performed pinpointing the operating conditions that maximize total efficiency on an annual basis. This study concludes with a preliminary economic analysis to assist in an initial assessment of the modeled system's competitiveness.

2 MODEL RESIDENCE

The model residence is a multi-family house in Athens, Greece, consisting of ten average-sized multi-family apartments, with a total floor area of 920 m^2, a shape factor equal to 1.1, and 10% openings coverage on its faces. The heating period is assumed to start on October 15 and end on April 15. The U values for the building's structural elements, extracted from the EU Buildings Database, are assumed to be average values of the buildings' inventory in Greece. The SH demand of the building is calculated on an hourly basis for the heating period, assuming a desired internal temperature of 20ºC and an operating temperature threshold of 15ºC for the heating system. Typical meteorological Year (TMY) data for Athens are taken from the PVGIS database. The annual electricity demand for the building is calculated utilizing average electricity consumption data for households in Greece, and it is assumed that the annual electricity demand is distributed uniformly throughout the year. The energy demand data for the model residence are listed in Table 1, where $\dot{Q}_{sh,max}$, $Q_{th,an}$, and $P_{el,an}$ are the maximum hourly SH demand, the total annual heating demand, and the total annual electricity demand of the building, respectively.

Table 1: Energy demand of model residence

$\dot{Q}_{sh,max}$ [kW$_{th}$]	$Q_{th,an}$ [MWh$_{th}$]	$P_{el,an}$ [MWh$_{el}$]
83.56	132.79	34.22

3 MICRO-CHP SYSTEM

Description

The layout of the modeled micro-CHP system is presented in Figure 1. Two different modes of operation are selected, i.e. a CHP mode, and a TFC mode. In CHP mode, the TFC operates when there is sufficient solar irradiance (over 400 W/m^2 for this work), and the condenser of the engine, with water as the Cooling Fluid (CF), charges the TES, which provides heat to the building. The BB acts as an

auxiliary heat source when the capacity of the TES is not sufficient. In TFC mode, only the TFC operates, and heat is dissipated in an air-cooled condenser.
When the system operates in CHP mode, the temperature of the Heat Transfer Fluid (HTF) at the system evaporator is in the range of 100~120ºC, whereas in the summer period, the respective range is 80~120ºC. Water pressurized at 4 bar, to avoid partial evaporation in the solar collectors' circuit, is selected as the HTF. The generated electricity from the TFC would, in an actual building, be, by priority, utilized to cover its energy demand, and the surplus could be sold to the power grid or stored locally. However, in this work, it is assumed that the generated electricity is used only to cover the building's demand, averaged on a monthly and annual basis, since an electricity demand profile, that would allow calculating the actual hourly surplus or deficit, is not available.

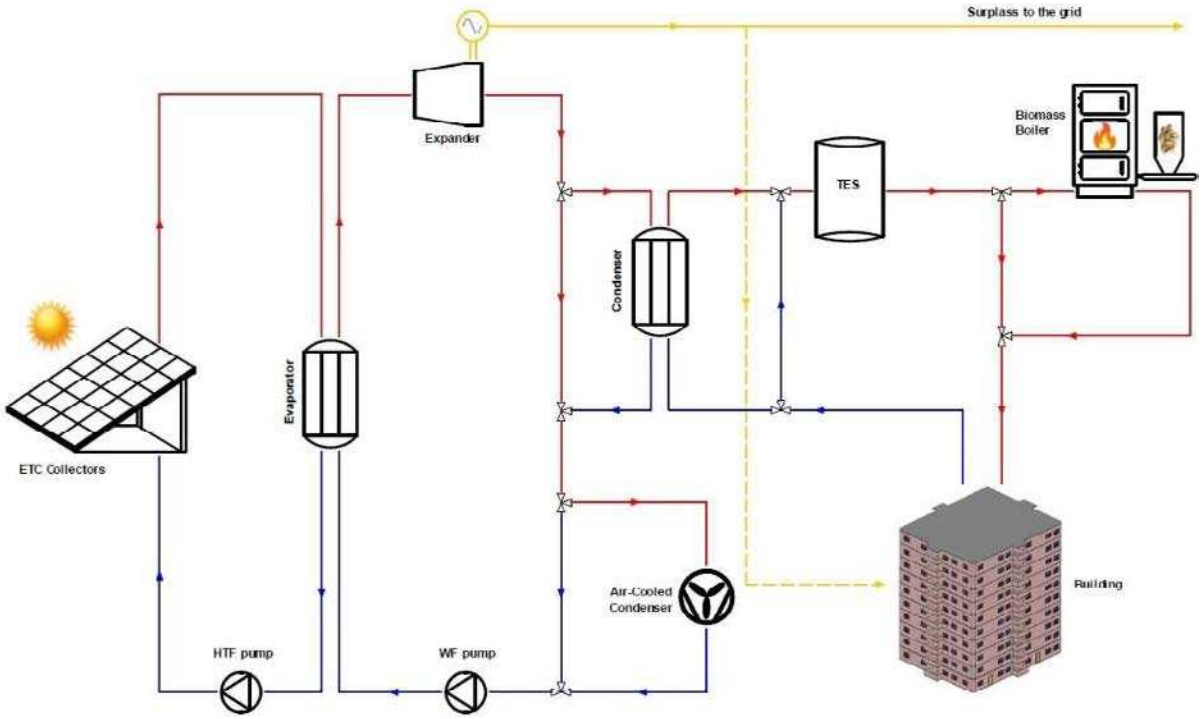

Figure 1: Layout of the hybrid micro-CHP system.

Components' sizing
The Thermomax DF 100 30 ETCs, developed by Thermomax Ltd., are selected as the solar field of the system. The area A_{col} of the collectors is equal to 180 m^2, indirectly estimated by calculating the necessary heat duty $\dot{Q}_{htf}$ (an equation for the calculation of the collectors' heat duty is given in Section 4) from the solar field at an average temperature of the HTF equal to 120ºC, ambient temperature T_{amb} equal to 20ºC, and solar irradiance normal on the ETCs 1000 W/m^2, while assuming a target thermal efficiency n_{th} equal to 10% for the TFC, and a heat duty $\dot{Q}_{con}$ at the condenser equal to $\dot{Q}_{sh,max}$. At these operating conditions, the nominal electric capacity P_{tfc} of the TFC becomes equal to 10 kW$_{el}$.
The minimum and maximum allowed temperatures of water in the TES are assumed to be 45 and 50ºC, respectively. The necessary volume V_{TES} of the TES is 15 m^3, estimated assuming that the heat capacity of the TES should meet $\dot{Q}_{sh,max}$ within one hour. Finally, the nominal capacity $\dot{Q}_{BB,nom}$ of the BB is equal to 90 kW$_{th}$, sufficient to meet $\dot{Q}_{sh,max}$.

4 MODELING

Solar Field
The parameters of the ETCs are listed in Table 2, with η_o the optical efficiency at normal incidence, and a_1, a_2 the first and second order losses coefficient, respectively. The inclination angle

β is selected to maximize the solar irradiance normal on the collectors at the studied location on an annual basis.

Table 2: Solar field parameters

η_o [-]	a_1 [W/m²-K]	a_2 [W/m²-K²]	β [º]
0.832	1.14	0.0144	32

Under steady-state operation of the ETCs, the heat transfer rate $\dot{Q}_{ev}$ from the ETCs to the HTF is given by Equation (1), where G_t is the total irradiance on the collectors. Moreover, $\dot{m}_{htf}$ and $c_{p,ht}$ are the mass flow rate and the specific heat, under constant pressure, of the HTF, respectively. Finally, $T_{htf,out}$ and $T_{htf,in}$ are the temperatures of the HTF flowing in and out of the ETCs, respectively.

$$\dot{Q}_{ev} = A_{col} \cdot [G_t \cdot \eta_o - a_1 \cdot (T_m - T_{amb}) - a_2 \cdot (T_m - T_{amb})^2] = \\ = \dot{m}_{htf} \cdot c_{p,htf}\left(T_{htf,out} - T_{htf,in}\right) \quad (1)$$

The efficiency η_{col} of the ETCs is given by Equation (2).

$$\eta_{col} = \eta_o - a_1 \cdot (T_m - T_{amb})/G_t - a_2 \cdot (T_m - T_{amb})^2/G_t = \dot{Q}_{ev}/(A_{col} \cdot G_t) \quad (2)$$

TFC

Assuming negligible heat losses at the evaporator, $\dot{Q}_{ev}$ will also be equal to the heat transfer rate from the HTF to the WF. This assumption is expressed by Equation (3), where $\dot{m}_{wf}$ is the mass flow rate of the WF, while $h_{ev,in}$ and $h_{ev,out}$ are its specific enthalpies at the inlet and outlet of the evaporator, respectively.

$$\dot{Q}_{ev} = \dot{m}_{wf} \cdot \left(h_{ev,out} - h_{ev,in}\right) \quad (3)$$

The condensation temperature T_{con} of the WF is given by Equation (4), where $T_{cf,out}$ is the temperature of the CF at the outlet of the evaporator, and PP_{con} the pinch-point temperature difference at the condenser. When the CF is Air, $T_{cf,out}$ is equal to $T_{amb} + \Delta T_{CF}$, with ΔT_{CF} denoting the allowed temperature rise of the CF. When the TFC operates in CHP mode, $T_{cf,out}$ is equal to the temperature T_{TES} of water in the TES at the beginning of the timestep. The determination of T_{con} leads directly to the calculation of the condensation pressure p_{con}.

$$T_{con} = T_{cf,out} + PP_{con} \quad (4)$$

The coupling between the TFC and the ETCs at the evaporator is accomplished by the pinch point temperature difference PP_{ev} in an iterative manner. Specifically, Equations (3),(5), and (6) are solved iteratively until convergence, with $\dot{m}_{wf}$, and the evaporation pressure p_{ev}, the iteration variables for a given quality $x_{ex,in}$ of the WF at the suction port of the expander. In Equation (5) $T_{htf,pr}$ is the temperature of the HTF at the end of preheating. In Equation (6), $\dot{Q}_{pr}$ denotes the heat transfer rate to the WF during preheating.

$$T_{htf,pr} = T_{sat,wf}(p_{ev}) + PP_{ev} \quad (5)$$

$$\dot{Q}_{pr} = \dot{m}_{wf} \cdot \left(h_{l,sat}(p_{ev}) - h_2\right) = \dot{m}_{htf} \cdot c_{p,htf} \cdot \left(T_{htf,pr} - T_{htf,in}\right) \quad (6)$$

Having calculated $\dot{m}_{wf}$ and p_{ev}, the thermodynamic low-order model simulating two-phase expansion (Skiadopoulos *et al.* 2021) in the twin-screw expander is applied to calculate the specific enthalpy $h_{con,in}$ of the WF at the expander's discharge. The power $\dot{w}_{ex}$ generated by the expander is given by Equation (7), where $\eta_{ex,is}$ is the isentropic efficiency of the expander, and $h_{con,in,is}$ is the WF's specific enthalpy corresponding to an isentropic expansion to p_{con}.

$$\dot{w}_{ex} = \dot{m}_{wf} \cdot \left(h_{ev,out} - h_{con,in}\right) = \dot{m}_{wf} \cdot \eta_{ex,is} \cdot \left(h_{ev,out} - h_{con,in,is}\right) \quad (7)$$

The required power $\dot{w}_{pu,tfc}$ from the TFC pump is given by Equation (8), where $\eta_{pu,is}$ is the pump's isentropic efficiency, and $h_{ev,in,is}$ the specific enthalpy of the WF corresponding to an isentropic pumping to p_{ev}.

$$\dot{w}_{pu,tfc} = \dot{m}_{wf} \cdot \left(h_{ev,in} - h_{con,out}\right) = \dot{m}_{wf} \cdot \left(h_{ev,in,is} - h_{con,out}\right)/\eta_{pu,is} \quad (8)$$

The heat rate $\dot{Q}_{con}$ at the condenser is given by Equation (9), with $h_{con,out}$ the specific enthalpy of the WF at the outlet of the condenser.

$$\dot{Q}_{con} = \dot{m}_{wf} \cdot \left(h_{con,out} - h_{con,in}\right) \quad (9)$$

The thermal efficiency η_{th} of the TFC is calculated by Equation (10), where $\dot{w}_{pu,htf}$ denotes the power absorbed by the HTF pump.

$$\eta_{th} = \dot{w}_{net}/\dot{Q}_{ev} = \left(\dot{w}_{ex} - \dot{w}_{pu,tfc} - \dot{w}_{pu,htf}\right)/\dot{Q}_{ev} \quad (10)$$

Table 3: Modeling parameters of the TFC cycle

PP_{ev} [ºC]	PP_{con} [ºC]	$\eta_{pu,is}$ [-]	WF [-]	CF [-]	$\eta_{pu,htf}$ [-]	ΔT_{sub} [ºC]	ΔT_{CF} [ºC]
5	5	0.75	R245fa	Water & Air	0.70	5	10

The values of the TFC modeling parameters are compiled in Table 3. The values of the parameters are typical in power cycle modeling, and a sensitivity analysis, beyond the purpose of this work, should be undertaken to highlight their effect on the performance of the TFC. ΔT_{sub} and $\eta_{pu,ht}$ are the total efficiency of the HTF pump, and the WF sub-cooling at the pump suction, respectively.

TES

The energy balance of the TES is expressed by Equation (11), where ΔT_{TES} is the temperature difference of water in the TES, and $\dot{Q}_{sh,TES}$ the heat rate from the TES to the building for SH purposes. Moreover, Δt_{CHP} is the time step for the simulations of the micro-CHP system, equal to 1 hr. Finally, $m_{H_2O,TES}$ and $c_{p,H_2O,TES}$ are the total mass and the specific heat of water in the TES, respectively.

$$m_{H_2O,TES} \cdot c_{p,H_2O,TES} \cdot (\Delta T_{TES}/\Delta t_{CHP}) = \dot{Q}_{con} - \dot{Q}_{sh,TES} \quad (11)$$

It must be noted that thermal losses from the TES to the ambient are neglected for this work.

CHP

The total SH demand $\dot{Q}_{sh}$ of the building within Δt_{CHP} is calculated by Equation (12), where $\dot{Q}_{sh,BB}$ is the heat rate from the BB.

$$\dot{Q}_{sh} = \dot{Q}_{sh,TES} + \dot{Q}_{sh,BB} \quad (12)$$

By priority, $\dot{Q}_{sh}$ is covered by the TES. If its heat capacity is not sufficient at the beginning of the timestep, the BB acts as an auxiliary heat source.

Performance indices

The total solar energy conversion efficiency is given by Equation (13),

$$\eta_{tot,sol} = \eta_{col} \cdot \eta_{th} = \dot{w}_{net}/(A_{col} \cdot G_t) \quad (13)$$

whereas the CHP efficiency η_{CHP} is calculated by Equation (14), where η_{BB} is the efficiency of the BB, taken equal to 85% in this work.

$$\eta_{CHP} = \frac{\dot{w}_{net} + \dot{Q}_{con}}{\dot{Q}_{ev} + \dot{Q}_{sh,BB}/\eta_{BB}} \quad (14)$$

Economic analysis

The capital investment C_{inv} is calculated by Equation (15),

$$C_{inv} = sc_{tfc} \cdot P_{tfc} + sc_{col} \cdot A_{col} + sc_{BB} \cdot \dot{Q}_{BB,nom} + C_{TES} \quad (15)$$

where sc_{tfc}, sc_{col}, and sc_{BB} are the specific investment costs for the TFC, the ETCs, and the BB, respectively. Moreover, C_{TES} is the investment cost for the TES, given by Equation (16) (González-Pino *et al.* 2020).

$$C_{TES} = 29.968 \cdot V_{TES}^{0.6382} \quad (16)$$

The $LCOE$ and $LCOH$, and PBP, given by Equations (17), (18), and (19), respectively, indices are utilized for a preliminary economics analysis. In Equations (17), (18), and (19) cw_{el} and cw_{th} represent the contribution of electricity and heat to the total cost of the micro-CHP system over its lifetime N_{lt}. Also, e_{el} and e_{he} denote the price of electricity and heating, respectively, for households in Greece. Moreover, E_{tot} and Q_{tot} are the total electricity and heat produced annually by the unit (considered constant over N_{lt}). Finally, C_{fuel} is the total cost of biomass for the operation of the system in a year, M the, constant, annual maintenance cost, and r is the interest rate. The values of the economic analysis parameters are listed in Table 4.

$$LCOE = cw_{el} \cdot \left(C_{inv} + \sum_{i=1}^{N_{lt}} \frac{M + C_{fuel}}{(1+i)^r} \right) \Bigg/ \sum_{i=1}^{N_{lt}} E_{tot} \quad (17)$$

$$LCOH = cw_{th} \cdot \left(C_{inv} + \sum_{i=1}^{N_{lt}} \frac{M + C_{fuel}}{(1+i)^r} \right) \Big/ \sum_{i=1}^{N_{lt}} Q_{tot} \quad (18)$$

$$PBP = \frac{C_{inv}}{E_{tot} \cdot e_{el} + Q_{tot} \cdot e_{he} - \left(M + C_{fuel}\right)} \quad (19)$$

Table 4: Parameters of the economic analysis

sc_{tfc} [€/kW$_{el}$]	sc_{col} [€/m^2]	sc_{BB} [€/kW$_{th}$]	N_{lt} [yr]	r [%]	M [€]	cw_{el} [-]	cw_{th}[-]
2000~4000	200~400	900~1200	20	5	$0.01 \cdot C_{inv}$	0.25	0.75

5 RESULTS & DISCUSSION

The hybrid micro-CHP system's governing equations, along with the ones of the thermodynamic low-order two-phase expansion model (Skiadopoulos *et al.* 2021), are integrated into a numerical model in the software environment of Matlab (R2022b). Three operational degrees of freedom are identified, i.e. T_m, $x_{ex,in}$ and $\dot{m}_{htf}$, by inspecting the governing equations. The target of the simulations is to maximize total efficiency at the current timestep, and not the optimization of the TFC sub-system. This implies that the TFC will operate at off-design and partial load conditions for long periods during the year. As a result, another primary target of this study is accomplished, which is the monitoring of the efficiency of the TFC under varying operating conditions. The performance optimization of the hybrid micro-CHP system is performed within Matlab, by applying a native genetic optimization algorithm, with T_m, $x_{ex,in}$ and $\dot{m}_{htf}$ constituting the optimization parameters. When the system operates in CHP mode, the target is to maximize η_{CHP}, otherwise, the target of the simulations is to maximize $\eta_{tot,sol}$.

TFC **114**

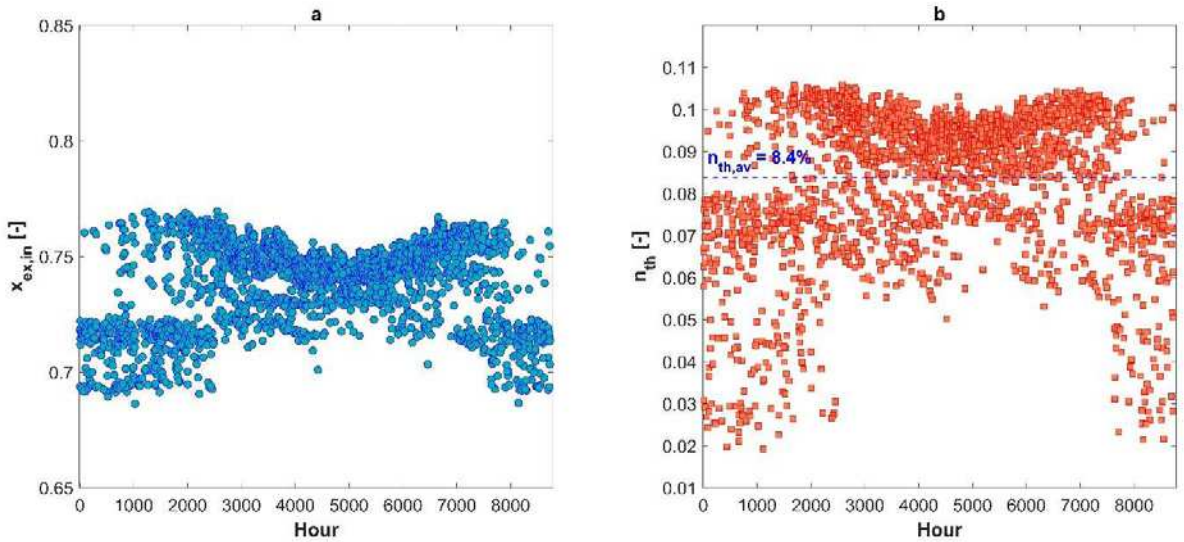

Figure 2: a) Optimal $x_{ex,in}$ and b) η_{th} of the TFC over the year.

The optimal values of $x_{ex,in}$, and the obtained η_{th} of the TFC throughout the year are presented in Figure 2. Higher values of $x_{ex,in}$ maximize the efficiency of the TFC, because $\eta_{ex,is}$ improves as the amount of vapor at the suction port of the expander increases. Concerning η_{th}, values as high as 10.5% can be achieved, with an annual average $\eta_{th,av}$ equal to 8.4%. The estimated values for $\eta_{th,av}$ and maximum η_{th} are within the range documented in the literature (7.5-13%) for micro-CHP systems with the ORC as the prime mover (González *et al.* 2015). However, a concrete conclusion concerning the competitiveness of the TFC against the ORC for micro-CHP systems will be reached when the two technologies are compared under the same operating conditions.

Micro-CHP Performance

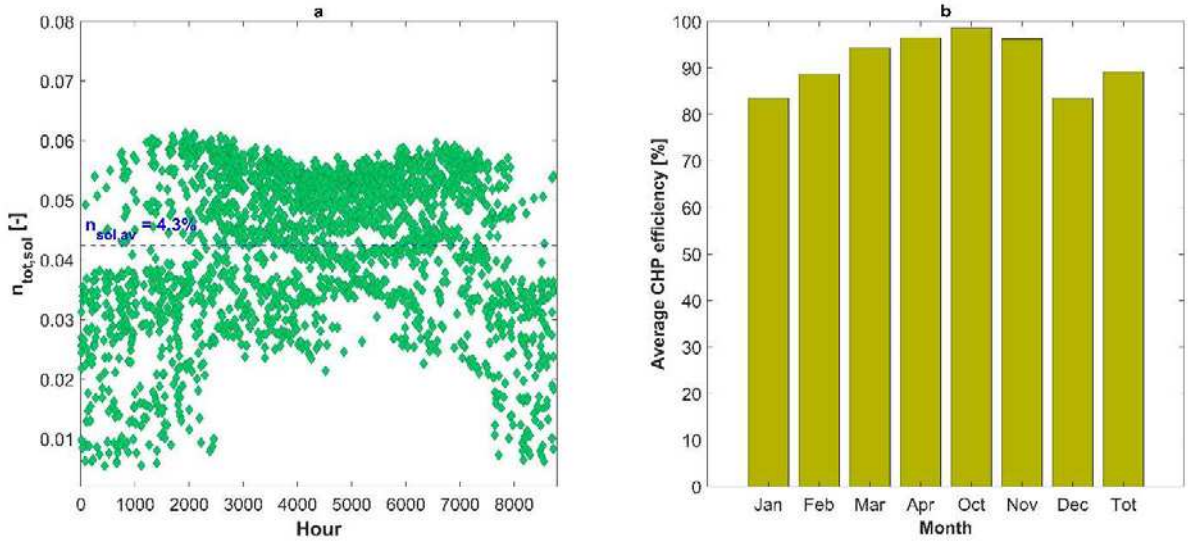

Figure 3: a) $\eta_{tot,sol}$ over the year, and b) Average monthly and annual η_{CHP}.

The TFC and BB will operate in Athens for 2344 and 2495 hours, respectively. The values of $\eta_{tot,sol}$ throughout the year, along with the average monthly and annual η_{CHP} are presented in Figure 3. The Solar-TFC subsystem of the micro-CHP can achieve an annual average value for $\eta_{tot,sol}$ equal to 4.3%, higher than the one estimated (3%) for a small-scale Solar-ORC system in Athens with similar architecture (Soulis *et al.* 2022). The average η_{CHP} over the heating period is equal to 89.2%, with higher values observed as the BB's contribution is decreased. The η_{CHP} values estimated herein are substantially higher than the ones reported for micro-CHP systems driven by an ORC (60-80%) (González *et al.* 2015). However, it must be mentioned that no heat losses toward the ambient, or pressure losses in the hydraulic circuits have been considered in the present work.

The monthly and annual contributions of the TFC and BB in the coverage of the building's SH demand, along with the contribution of the TFC in the electricity demand, are presented in Figure 4. The TFC can cover approximately 18% of the SH demand and 40% of the electricity demand over the year, highlighting the added value coming from the flexibility to operate the unit in TFC mode.

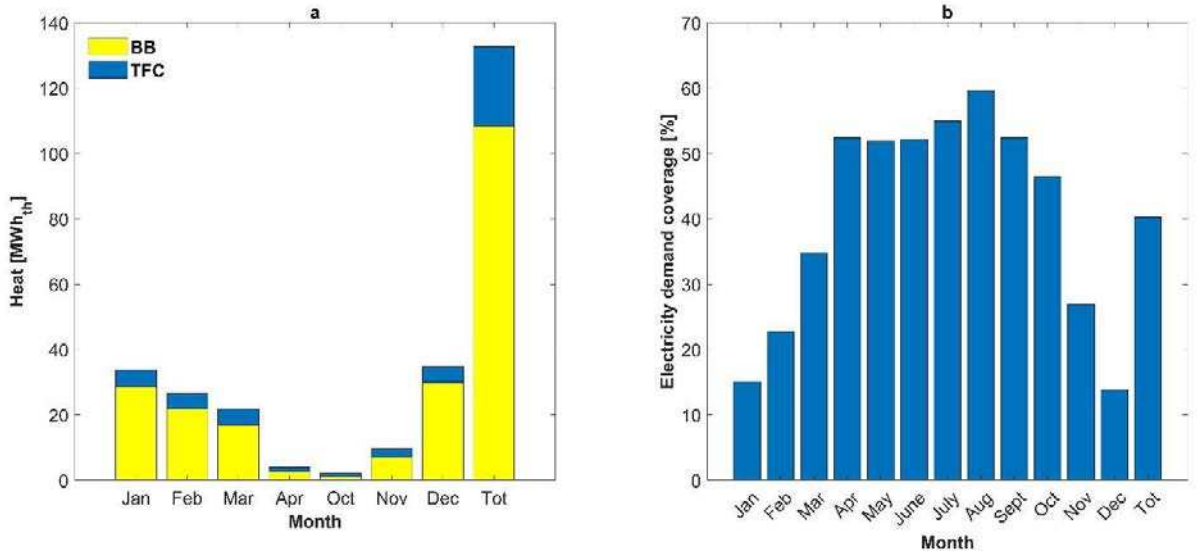

Figure 4: Monthly and annual contribution of a) the TFC and the BB in the coverage of the SH demand, and b) the TFC in electricity demand coverage of the building.

Economic assessment

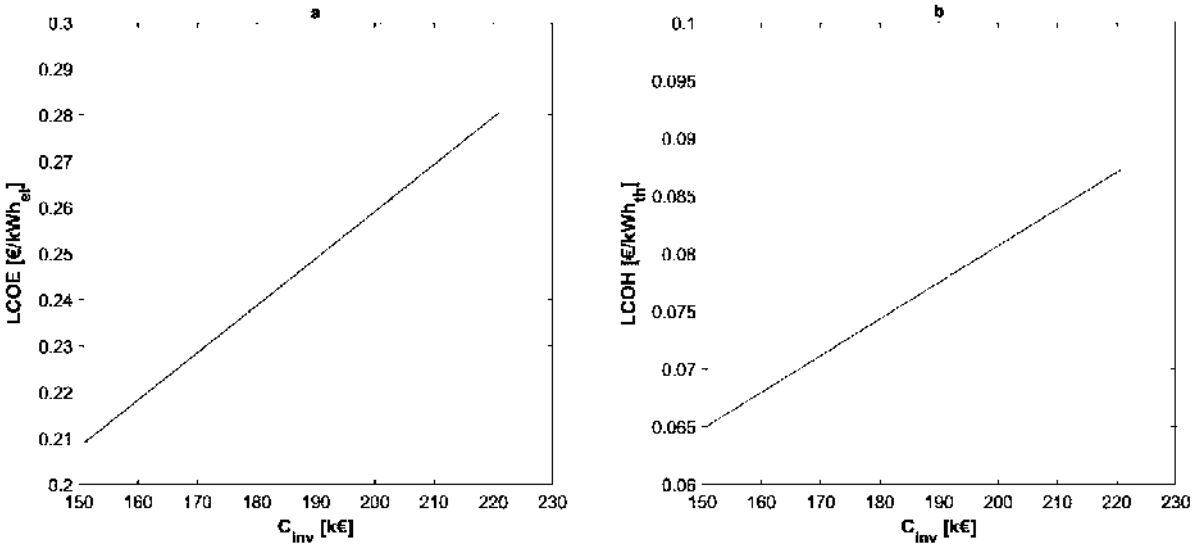

Figure 5: a) $LCOE$, and b) $LCOH$ as a function of C_{inv}.

A parametric economic assessment of the micro-CHP system is performed, with C_{inv} the parameter. For this purpose, the upper and lower limits of C_{inv} are calculated, based on the ranges of sc_{tfc}, sc_{col}, and sc_{BB} in Table 4. For the estimation of C_{fuel}, wood pellets, with a lower heating value of 4.9 kWh/kg, and an average market price of 0.22€/kg, are considered. It is reckoned that approximately 22 tons of wood pellets are required to operate the micro-CHP system annually. It must be stressed that in a more elaborate economic analysis, the effect of the type and market price of biofuel must be considered.

The values of $LCOE$ and $LCOH$ as a function of C_{inv} are plotted in Figure 5. Competitive values for heating and electricity are estimated, considering their current market prices in the EU, and the uncertainty in the price and availability of fossil fuels. These values can be further diminished by decreasing the specific investment costs of the equipment and by introducing financial incentives to assist the penetration of RES in the energy mix.

116

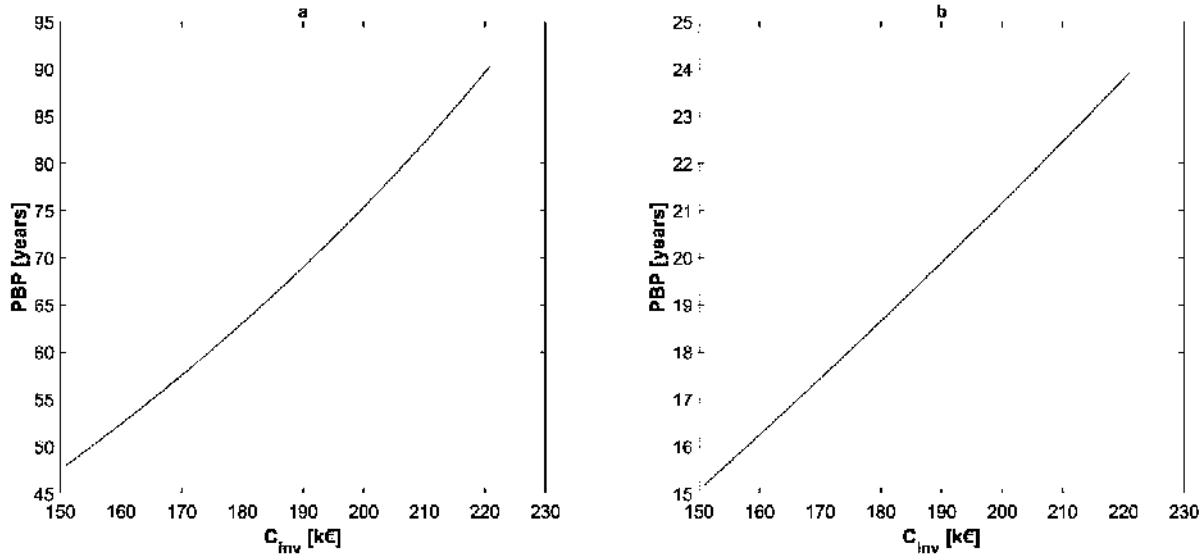

Figure 6: PBP for a) EU-27 average e_{el} and e_{he} prices in 2nd half of 2021, and b) EU-27 average e_{el} and e_{he} prices in 2nd half of 2022, as a function of C_{inv}.

For the estimation of PBP, it is assumed that e_{he} is equal to the price of natural gas that would be used for SH in the model residence if the micro-CHP unit was not installed. On the other hand, e_{el} is equal to the electricity price of the power grid. Two different cases are examined for e_{el} and e_{he} to illustrate the sensitivity of PBP on market prices of energy. In the first scenario, e_{el} and e_{he} are equal to the

average price of electricity and natural gas for the EU-27 in the second half of 2021 (e_{el}= 0.13 €/kWh$_{el}$ and e_{he}= 0.06 €/kWh$_{th}$), whereas, in the second scenario, the respective values for the second half of 2022 are considered (e_{el}= 0.24 €/kWh$_{el}$ and e_{he}= 0.10 €/kWh$_{th}$). PBP as a function of C_{inv} for the two examined cases is plotted in Figure 6. Favorable values are obtained for PBP when the current energy market prices are considered. However, if these prices drop substantially in the future, the economic viability of the modeled micro-CHP unit will be based on the reduction of C_{inv} and the concurrent quest for more economical biofuels.

6 CONCLUSIONS

In the present work, the annual performance of a hybrid micro-CHP system with a TFC engine as the prime mover was simulated. The system is driven by solar energy and biomass, and it was sized to meet the annual SH demand of an average-sized multi-family building in Athens, Greece. Optimization simulations were undertaken to maximize the primary energy conversion efficiency throughout the year for all the selected operational modes.

The numerical experiments indicated that the hybrid unit can achieve an average CHP efficiency of 89.2% over the heating period, with higher values observed as the contribution of solar energy to the building's energy mix increases. The TFC can cover 18% of the building's annual SH demand, and 40% of the annual electricity demand. The average annual solar energy conversion efficiency of the Solar-TFC subsystem reaches 4.3%, whereas the average annual, and maximum thermal efficiency of the TFC are 8.4% and 10.5%, respectively. In the simulations, particular attention was paid to the flashing phenomenon in the TFC expander, the main phenomenon affecting the TFC thermal efficiency, under varying operating conditions. It was pointed out that higher vapor qualities at the onset of two-phase expansion ensure optimal operation of the two-phase expander. Competitive values, compared to current market energy prices, of $LCOE$ (0.21~0.28 €/kWh$_{el}$) and $LCOH$ (0.065~0.087 €/kWh$_{th}$) were estimated. On the other hand, the PBP values are more favorable when current prices of electricity and heating for households are considered.

Concluding, it must be stressed that the presented herein model needs to be appended so that it can also model an ORC, to perform a detailed comparison between the TFC and the ORC as bottoming cycles for the modeled hybrid micro-CHP unit. This will be accomplished when the developed expander model is calibrated to model expansion in the dry vapor region as well. Also, different layouts, operational modes, and types of solar collectors must be examined, and the environmental impact of the unit has to be assessed.

REFERENCES

Fischer, Johann. 2011. "Comparison of Trilateral Cycles and Organic Rankine Cycles." *Energy* 36(10):6208–19. doi: 10.1016/J.ENERGY.2011.07.041.

González-Pino, I., E. Pérez-Iribarren, A. Campos-Celador, and J. Terés-Zubiaga. 2020. "Analysis of the Integration of Micro-Cogeneration Units in Space Heating and Domestic Hot Water Plants." *Energy* 200:117584. doi: 10.1016/J.ENERGY.2020.117584.

González, Arnau, Jordi Roger Riba, Rita Puig, and Pere Navarro. 2015. "Review of Micro- and Small-Scale Technologies to Produce Electricity and Heat from Mediterranean Forests' Wood Chips." *Renewable and Sustainable Energy Reviews* 43:143–55. doi: 10.1016/J.RSER.2014.11.013.

Öhman, Henrik, and Per Lundqvist. 2013. "Experimental Investigation of a Lysholm Turbine Operating with Superheated, Saturated and 2-Phase Inlet Conditions." Pp. 1211–18 in *Applied Thermal Engineering*. Vol. 50. Pergamon.

Padinger, Reinhard, Stefan Aigenbauer, and Christoph Schmidl. 2019. "Best Practise Report on Decentralized Biomass Fired CHP Plants and Status of Biomass Fired Small-and Micro Scale CHP Technologies."

Schuster, A., S. Karellas, and R. Aumann. 2010. "Efficiency Optimization Potential in Supercritical Organic Rankine Cycles." *Energy* 35(2):1033–39. doi: 10.1016/J.ENERGY.2009.06.019.

Skiadopoulos, Anastasios, Xander van Heule, George Kosmadakis, Dimitrios Manolakos, Michel de Paepe, and Steven Lecompte. 2021. "Thermodynamic Low-Order Model for the Simulation of

Two-Phase Expansion within a TFC Unit." in *Proceedings of the 6th International Seminar on ORC Power Systems*, edited by T. U. of Munich. Technical University of Munich.

Smith, I. K. 1993. "Development of the Trilateral Flash Cycle System: Part 1: Fundamental Considerations." *Proceedings of the Institution of Mechanical Engineers, Part A: Journal of Power and Energy* 207(3):179–94. doi: 10.1243/PIME_PROC_1993_207_032_02.

Smith, I. K., N. Stošić, and C. A. Aldis. 1996. "Development of the Trilateral Flash Cycle System. Part 3: The Design of High-Efficiency Two-Phase Screw Expanders." *Proceedings of the Institution of Mechanical Engineers, Part A: Journal of Power and Energy* 210(1):75–92. doi: 10.1243/pime_proc_1996_210_010_02.

Soulis, Konstantinos X., Dimitris Manolakos, Erika Ntavou, and George Kosmadakis. 2022. "A Geospatial Analysis Approach for the Operational Assessment of Solar ORC Systems. Case Study: Performance Evaluation of a Two-Stage Solar ORC Engine in Greece." *Renewable Energy* 181:116–28. doi: 10.1016/J.RENENE.2021.09.046.

Tchanche, Bertrand F., Gr Lambrinos, A. Frangoudakis, and G. Papadakis. 2011. "Low-Grade Heat Conversion into Power Using Organic Rankine Cycles - A Review of Various Applications." *Renewable and Sustainable Energy Reviews* 15(8):3963–79. doi: 10.1016/J.RSER.2011.07.024.

ACKNOWLEDGEMENT

The research work was supported by the Hellenic Foundation for Research and Innovation (H.F.R.I.) under the "First Call for H.F.R.I. Research Projects to support Faculty members and Researchers and the procurement of high-cost research equipment grant" (Project Number: 1087, Acronym: SOL-art).

ORC SEVILLE 2023
7th International Seminar on O.R.C. Power Systems

© 2024 Editorial Universidad de Sevilla. Este es un artículo de acceso abierto distribuido bajo los términos de la licencia de uso y distribución Creative Commons (BY-NC-ND 4.0)

DOI: https://dx.doi.org/10.12795/9788447227457_19

SYSTEMATIC AND MULTI-CRITERIA OPTIMISATION OF SUBCRITICAL THERMALLY INTEGRATED CARNOT BATTERIES (TI-PTES) IN AN EXTENDED DOMAIN

Antoine Laterre[1,2,*], Olivier Dumont[2], Vincent Lemort[2], Francesco Contino[1]

[1] *Thermodynamics and Fluid Mechanics, Institute of Mechanics, Materials and Civil Engineering, Université catholique de Louvain, Place du Levant 2, 1348 Louvain-la-Neuve, Belgium*
[2] *Thermodynamics Laboratory, Aerospace and Mechanical Engineering Department, University of Liège, Allée de la Découverte 17, 4000 Liège, Belgium*

*Corresponding Author: antoine.laterre@uclouvain.be

ABSTRACT

Thermally integrated pumped thermal energy storage (TI-PTES) is a flexibility option to recover low-grade heat (i.e. < 100°C) and to provide overnight storage. Common criteria when optimising such system are the power-to-power efficiency (i.e. electricity recovery), the total exergy efficiency (i.e. combined heat and electricity recovery) and the energy density (i.e. storage size). However, these objectives are generally conflicting and multi-criteria optimisation is therefore required to discuss the trade-offs. Design guidelines have been proposed for some specific case studies but are still lacking for the remaining wide range of possible integration scenarios. This work therefore presents a systematic multi-criteria analysis of a TI-PTES consisting of a high temperature vapor compression heat pump, a sensible heat thermal storage and an organic Rankine cycle, in an extended integration domain (i.e. heat source from −25 to 100°C, sink from −25 to 50°C). The single objective optimisation reveals that the design trends are not uniform and that the tipping points are located where the difference between the source and sink temperatures is less than 30 K. The multi-criteria analysis shows that there is a region of the domain where the criteria do not conflict. The results also highlight that density and exergy efficiency are much less conflicting with each other than they are with power-to-power efficiency.

1 INTRODUCTION

Next to sobriety measures, improving the efficiency of energy systems and supporting the integration of renewables are key elements of the energy transition. This includes the deployment of flexibility options, such as energy storage, as well as reducing the amount of energy lost in conversion from one form to another. In this regard, it has been estimated that in 2012, 52 % of the primary energy consumed worldwide was actually lost as so-called recoverable waste heat (Forman *et al.*, 2016). Despite its reduced exergy (i.e. 63 % of this waste energy had a temperature below 100°C, which is corresponds to only 21 % of the total waste heat exergy content), the challenges of energy transition cannot waste any piece of the enormous volume of energy consumed every year.

There exist several routes for waste heat recovery, such as exergy upgrade with high temperature vapor compression heat pumps (HT-VCHP) and conversion to electricity with organic Rankine cycles (ORC). However, there is not always an on-site thermal demand, and the waste heat can have too low exergy potential to be directly converted into electricity. In such case, thermally integrated pumped thermal energy storage (TI-PTES, or Carnot batteries) could be another option (Frate *et al.*, 2017). Indeed, TI-PTES can increase the efficiency of renewable energy systems through waste heat recovery, while providing the necessary flexibility (i.e. energy storage).

Since its first mentions (Mercangöz *et al.*, 2012; Steinmann, 2014) and actual first characterisation (Frate *et al.*, 2017), the concept has attracted growing interest and several implementations have been proposed. The most common is the basic hot TI-PTES layout (see Fig. 1), consisting in a subcritical HT-VCHP, a two-tank sensible thermal energy storage (TES) and a subcritical ORC.

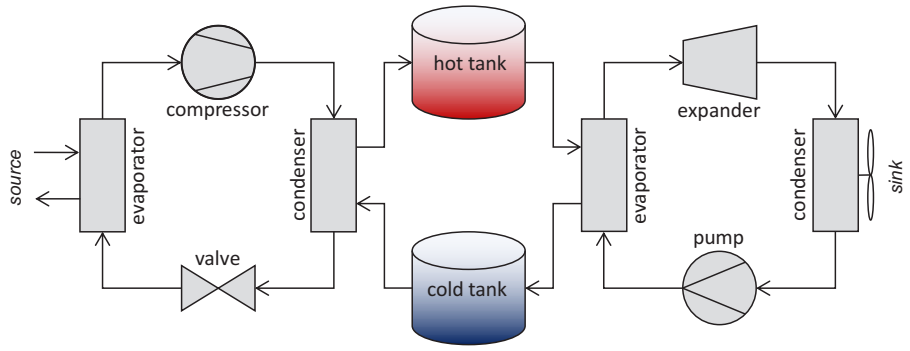

Figure 1: Cycle layout of the basic hot TI-PTES. Note that the circulating pumps are not considered.

When optimising the thermodynamic cycle of these storage systems, typical criteria are to maximise the power-to-power efficiency η_{P2P} (i.e. efficiency of electricity recovery), the total exergy efficiency η_{II} (i.e. efficiency of combined heat and electricity recovery) and the electrical energy density ρ_{el} (i.e. storage size). However, as pointed out by Frate *et al.* (2020a), these three objectives can be conflicting. This implies that it is not possible to design a TI-PTES system that maximises these criteria simultaneously, and that trade-offs must therefore be discussed. Recently, it has been suggested to formalise this conflicting nature by referring to it as the *Carnot battery trilemma* (Weitzer *et al.*, 2022a).

For now, many studies have optimised the thermodynamic design of TI-PTES and proposed cycle modifications to enhance some performance indicators, like η_{P2P} (e.g. internal regenerators (Frate *et al.*, 2020a), organic flash cycles (Weitzer *et al.*, 2022b), zeotropic mixtures (Lu *et al.*, 2022), …). On the other hand, far fewer have focused on optimising and mapping the performance of TI-PTES with respect to the *Carnot battery trilemma* in the entire thermal integration domain (i.e. combination of possible source and sink temperatures). As an illustration, the current domain exploration for TI-PTES with sensible TES is represented in Fig. 2. It can be observed that the region with source temperatures below 60°C has been particularly little explored. This can be attributed in part to the fact that, due to Carnot efficiency, η_{P2P} is lower in that region of the domain (i.e. usually below 50 %), whereas as TI-PTES has often been considered primarily as an electrical storage option, this performance may have seemed rather poor. However, when looking at TI-PTES as a flexible waste heat recovery option, there is no indication that η_{P2P} should override η_{II}. Moreover, a significant share (i.e. 45 %) of the low temperature waste heat to be recovered (i.e. $<$ 200°C) is precisely below 60°C, as shown by Marina *et al.* (2021).

A direct consequence of this poor investigation of the integration domain is that it is currently not possible to provide theoretical maximum performance and design guidelines for TI-PTES across the entire domain, and with regard to the three criteria of the *Carnot battery trilemma*.

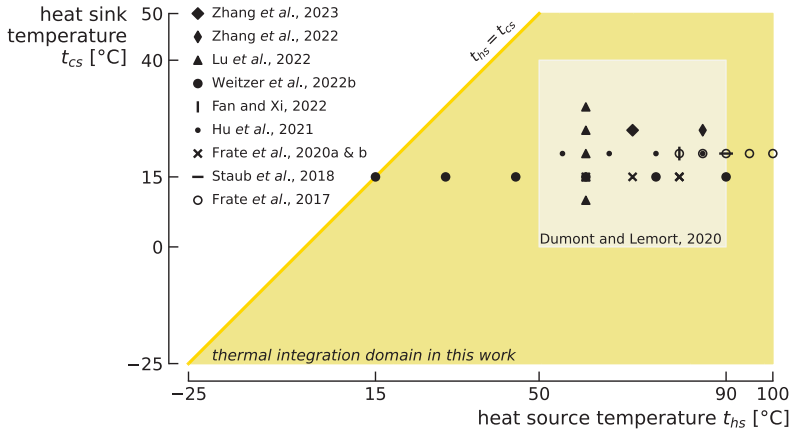

Figure 2: Current exploration of the thermal integration domain for TI-PTES with sensible TES. Note that most authors have not studied the *Carnot battery trilemma* in its entirety.

The goal of this work is therefore to investigate and characterise the *Carnot battery trilemma* in the entire integration domain, with ambient temperatures ranging from -25 to $50°C$ to cover the majority of climates that can be encountered (i.e. from polar to dry). More precisely, an optimisation of the basic hot TI-PTES cycle is first conducted to maximise separately each objective of the *trilemma*. The idea is to map the maximum theoretical performance that could be reached and to formulate design guidelines according to the desired objectives. The results are used to assess whether the guidelines can be generalised to the whole domain or whether they need to be adapted in each region. A specificity of the method is to simultaneously optimise the thermodynamic cycle and the choice of working fluids, to fully embrace the potential synergies between them. Then, a multi-criteria optimisation is proposed to characterise the *trilemma* in the entire domain. Based on the results, implementation constraints are discussed, and design recommendations and cycle improvements are finally proposed.

2 METHODOLOGY

2.1 System description

The system investigated in this work is the basic hot TI-PTES. The latter consists in a subcritical HT-VCHP, a two-tank pressurized water TES and a subcritical air-cooled ORC (see Fig. 1). Although enhanced cycles give better performance, the basic configuration is adopted as the aim of this study is to provide generic design guidelines. Based on the obtained results, cycle improvements are suggested in the last section. The two-tank architecture is preferred to a single tank as it provides a constant thermal profile regardless of the state of charge and storage duration (i.e. no diffusion losses due to a thermocline). However, assuming a perfect thermocline, the results obtained here can extrapolate to the single tank case (Frate *et al.*, 2020a).

The thermodynamic performance of the system is assessed using an in-house `Python` model[1]. The corresponding model parameters are summarised in Table 1. `CoolProp` is used to access the fluids properties (Bell *et al.*, 2014). In the model, the evaporation and condensation pressures are obtained with a pinch analysis. Also note that the thermal storage losses are neglected (i.e. overnight storage). Finally, the heat source and sink are treated as dry atmospheric air (i.e. only sensible heat is considered).

2.2 Optimisation problem

The *Carnot battery trilemma* consists of the trade-off between the power-to-power efficiency η_{P2P}, the exergy efficiency η_{II}, and the energy density ρ_{el}. These performance indicators are therefore adopted for the single objective and multi-criteria optimisations. They are defined as

$$\eta_{P2P} = \frac{W_{orc}}{W_{hp}} \quad (1) \qquad \eta_{II} = \frac{W_{orc}}{W_{hp}+Ex_{hs}} \quad (2) \qquad \rho_{el} = \frac{h_{st,ht}-h_{st,lt}}{v_{st,ht}+v_{st,lt}} \cdot \eta_{orc} \quad (3)$$

where W_{orc} and W_{hp} are the ORC and HT-VCHP net power output and input respectively, and Ex_{hs} is the exergy of the heat source. The reference state used for the latter's definition corresponds to the heat sink temperature, so $t_{hs} = t_{cs}$ yields $\eta_{II} = \eta_{P2P}$. The density is defined as the ratio between the difference in specific enthalpy of the tanks and their specific volumes, multiplied by the ORC efficiency.

To optimise the performance of TI-PTES, a set of eight design variables are used. The hot tank storage temperature $t_{st,ht}$, the heat source glide $\Delta T_{hs,gl}$ and the storage temperature spread $\Delta T_{st,sp}$ (i.e. the temperature difference between the hot and cold tanks) have already been identified as key parameters influencing η_{P2P}, η_{II} and ρ_{el} respectively (Dumont and Lemort, 2020; Frate *et al.*, 2020a; Weitzer *et al.*, 2022b). Note that it is here assumed that the heat source can be treated as free waste heat (i.e. $\Delta T_{hs,gl}$ has no constrained value and is therefore used as a design variable). We also include the liquid subcooling $\Delta T_{hp,sc}$ in the HT-VCHP as well as the vapor superheat $\Delta T_{hp/orc,sh}$ in the HT-VCHP and in the ORC. Indeed, these parameters can take different optimum values depending on the thermal profiles and working fluids (Frate *et al.*, 2020a; Maraver *et al.*, 2014). The constraints associated with these variables are reported in Table 1.

[1] The code can be provided upon request.

Table 1: Model parameters and constraints for the TI-PTES optimisation.

Name	Symbol	Value	Name	Symbol	Value
Heat source temperature	t_{hs}	-25 to 100°C	Heat sink temperature	t_{cs}	-25 to 50°C
Heat source temp. glide	$\Delta T_{hs,gl}$	*design var.*	Heat sink temp. glide	$\Delta T_{cs,gl}$	10 K [(b)]
HP vapor superheat	$\Delta T_{hp,sh}$	*design var.*	ORC vapor superheat	$\Delta T_{orc,sh}$	*design var.*
HP liquid subcooling	$\Delta T_{hp,sc}$	*design var.*	ORC liquid subcooling	$\Delta T_{orc,sc}$	3 K [(c)]
Min. HP temperature lift	$\Delta T_{hp,min}$	5 K [(a)]	Min. ORC temp. drop	$\Delta T_{orc,min}$	5 K [(a)]
HP working fluid	$fluid_{hp}$	*design var.*	ORC working fluid	$fluid_{orc}$	*design var.*
Compressor efficiency	$\eta_{is,comp}$	0.75 [(a)]	Expander efficiency	$\eta_{is,exp}$	0.75 [(a)]
Max. compress. exit temp.	$t_{comp,max}$	180°C [(b)]	Pump efficiency	$\eta_{is,pmp}$	0.50 [(a)]
Min. HP/ORC superheat	$\Delta T_{sh,min}$	3 K [(c)]	Min. HP subcooling	$\Delta T_{sc,min}$	3 K [(c)]
Hot tank storage temp.	$t_{st,ht}$	*design var.*	Storage temp. spread	$\Delta T_{st,sp}$	*design var.*
Max. storage temperature	$t_{st,ht,max}$	150°C [(c)]	Storage pressure	p_{st}	7.5 bar
Min. storage temperature	$t_{st,lt,min}$	$t_{hs} - \Delta T_{hs,gl}$	Min. HP/ORC pressure	$p_{hp/orc,min}$	0.5 bar [(b)]
Pinch point in exchangers	ΔT_{pp}	3 K [(a,b)]	Pressure losses	Δp	0.0 bar [(b,c)]

[(a)] Dumont and Lemort, 2020 [(b)] Frate *et al.*, 2020a [(c)] Weitzer *et al.*, 2022a

Finally, an innovation of the method proposed here is to simultaneously optimise the thermodynamic cycle and the selection of working fluids in the HT-VCHP and ORC, to fully embrace the potential synergies between them. A set of 31 working fluids are used. These were selected from the list of those available in `CoolProp` because they have a zero ODP, a low GWP and because their critical point is compatible with the range of temperatures investigated in this work (i.e. thermal domain and storage temperatures). These fluids are available in Table A1 in Appendix.

To map the performance of TI-PTES, the integration domain is discretised with a 5 K resolution into 296 cells. Both single objective and multi-criteria optimisations are then carried out using NSGA-II (Deb *et al.*, 2002) through the `RHEIA` framework (Coppitters *et al.*, 2022). In order to guarantee a sufficient domain exploration, the population size is set to 500 and the mutation probability to 50 %. Note that this probability is very high, which leaves room for improvement in future work. Since no formal convergence criteria exists in NSGA-II, the minimum number of generations is set to 800. However, in many of the cells, much more generations have been run to get satisfactory results.

122

3 RESULTS

3.1 Single objective optimisation

The three optimisations have been conducted separately in the extended integration domain to maximise η_{P2P}, η_{II}, and ρ_{el}, respectively. The obtained mappings are depicted in Fig. 3. They are represented as a payoff table to illustrate the conflict between the different objectives of the *trilemma*. The corresponding design variables are depicted in Fig. 5. For the sake of brevity, the optimum vapor superheat and liquid subcooling in the HT-VCHP and ORC, as well as the optimum selection of working fluids, are not reported in this paper. They will be discussed in future work.

Results for optimised η_{P2P}

The power-to-power efficiency increases with the difference between the source and sink temperatures ΔT_{hs-cs} from about 25 % when $\Delta T_{hs-cs} = 0$ K to about 320 % when $\Delta T_{hs-cs} = 125$ K. However, because of a design shift, the growth is not continuous (i.e. the tipping point is $\Delta T_{hs-cs} = 30$ K). Indeed, for $\Delta T_{hs-cs} > 30$ K, $t_{st,ht}$ is minimised (i.e. the heat pump lift is always 5 K, its minimum value), so the coefficient of performance of the heat pump is maximised. Instead, for $\Delta T_{hs-cs} \leq 30$ K, $t_{st,ht}$ gradually increases with decreasing ΔT_{hs-cs}. The existence of this tipping point, which had already been detected by Weitzer *et al.* (2022b) and Jockenhöfer *et al.* (2018), can be explained with η_{P2P}^{Carnot}, the Carnot efficiency of TI-PTES (i.e. the thermodynamic limit). Considering the irreversibilities at the heat exchanges, which can be modelled as the temperature difference ΔT between the fluids, the latter

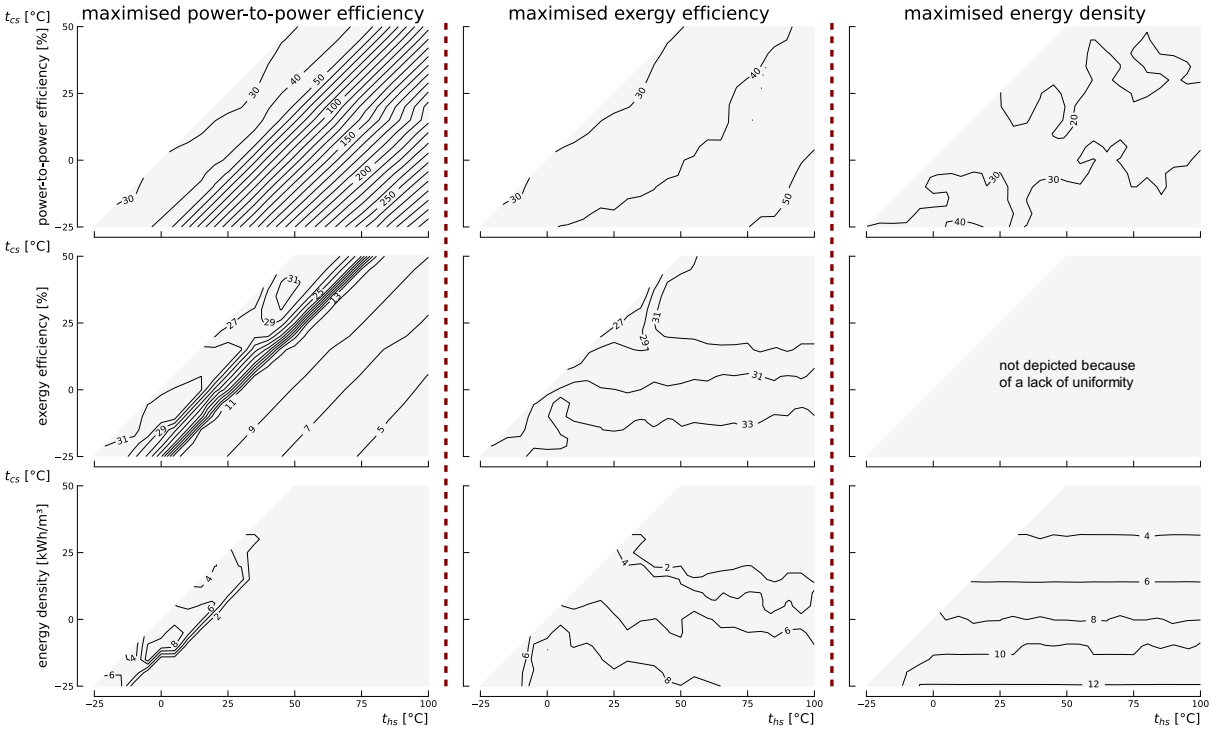

Figure 3: Payoff table with η_{P2P} (1st row), η_{II} (2nd row) and ρ_{el} (3rd row) for the configurations maximising η_{P2P} (1st column), η_{II} (2nd column) and ρ_{el} (3rd column) respectively. Some contour lines have been smoothed to eliminate local convergence issues (model artefacts).

is defined as

$$\eta_{P2P}^{Carnot} = COP_{HT-VCHP}^{Carnot} \cdot \eta_{ORC}^{Carnot} = \frac{(t_{st,ht}+\Delta T)(t_{st,ht}-t_{cs}-2\cdot\Delta T)}{(t_{st,ht}-\Delta T)(t_{st,ht}-t_{hs}+2\cdot\Delta T)} \quad , \qquad (4)$$

and it is depicted in Fig. 4 for different $t_{st,ht}$, ΔT and ΔT_{hs-cs}. When ΔT_{hs-cs} is below the tipping point (i.e. < 30 K), the exergy losses at the ORC cannot be sufficiently compensated by the high COP, thus $t_{st,ht}$ must be increased to reduce these losses, so that the resulting η_{P2P} is improved (see Fig. 4a). Please note, however, that this analysis with the Carnot efficiency is somewhat incomplete since it suggests maximising $t_{st,ht}$ to maximise η_{P2P}, while an optimal $t_{st,ht}$ actually exists, as observed in Fig. 5 (i.e. there exist optimum trade-offs between $COP_{HT-VCHP}$ and η_{orc}).

It can also be shown that the greater the irreversibilities in heat transfers (i.e. the greater ΔT), the higher the tipping point. Note that the particular case $\Delta T = 0$ (i.e. no irreversibilities) does not allow detection of the tipping point, and therefore leads to incorrect conclusions about the optimum $t_{st,ht}$ (see Fig. 4b).

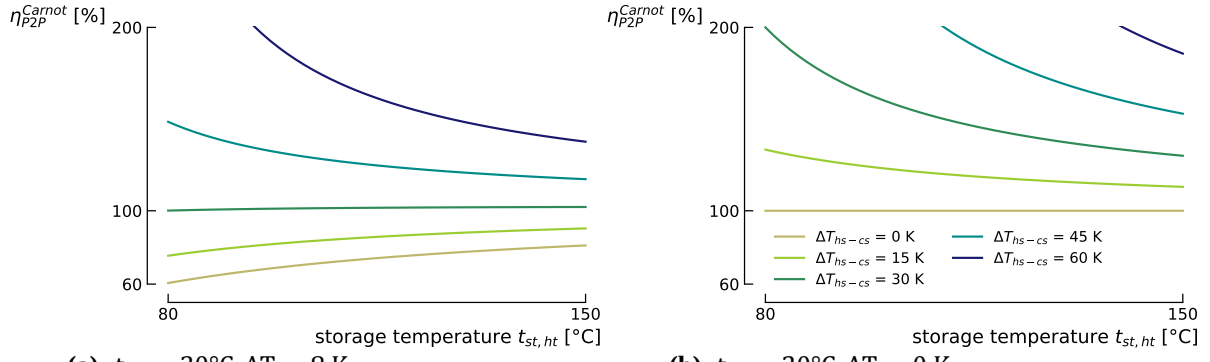

(a) $t_{cs} = 20°C, \Delta T = 8$ K **(b)** $t_{cs} = 20°C, \Delta T = 0$ K

Figure 4: Carnot efficiency of TI-PTES with and without consideration of heat transfer irreversibilities. The latter are represented through ΔT, the temperature difference between the fluids.

Ultimately, these results illustrate that, when ΔT_{hs-cs} is above the tipping point, the search for the maximum η_{P2P} leads to a TI-PTES degenerated into a TES + ORC (i.e. the heat pump lift is minimised), which makes it a waste heat recovery option, but no longer a true electrical storage system.

Regarding the other two design variables, since maximising η_{P2P} involves getting as close as possible to ideal Carnot cycles, $\Delta T_{st,sp}$ and $\Delta T_{hs,gl}$ are minimised on the largest part of the domain to limit the exergy losses at the heat transfers. However, there exists a narrow region (i.e. $\Delta T_{hs-cs} < 20$ K and $t_{hs} \leq 25°C$) where $t_{st,ht}$ is maximised and $\Delta T_{st,sp}$ takes much higher values: there, the relative storage spread, which is defined as

$$\Delta T_{st,sp}^{rel} = \frac{\Delta T_{st,sp}}{t_{st,ht} - t_{hs}} \quad , \qquad (5)$$

is approximately 60 %. Interestingly, this leads to increased η_{II} and ρ_{el}, what relaxes the *Carnot battery trilemma*, as this will be further discussed in the multicriteria analysis.

Results for optimised η_{II}

The exergy efficiency drops with t_{cs} from about 35 % when $t_{cs} = -25°C$ to about 30 % when $t_{cs} = 15°C$, mainly due to the reduction in W_{orc}. In that region of the domain, $t_{st,ht}$ is always maximised (i.e. maximisation of W_{orc} to the cost of increased W_{hp}) and $\Delta T_{st,sp}$ is between 60 and 100 K (i.e. relative decrease in W_{hp} due to increased cooling effect, thanks to larger subcooling at the condenser). This result is partly in contrast with that of Frate *et al.* (2020a) who, for equivalent design variables, also recommended maximising $t_{st,ht}$ but minimising $\Delta T_{st,sp}$. Sensitivity analyses will be conducted in future works to better understand the role of $\Delta T_{st,sp}$ w.r.t. the imposed design constraints.

When $t_{cs} > 15°C$, η_{II} slightly re-increases and stabilises around 32 % because of a design shift: $t_{st,ht}$ and $\Delta T_{st,sp}$ are reduced to about 130°C (especially for lower ΔT_{hs-cs}) and 10 K respectively. The reason for this shift will be further explored in future works but could be due to a limited fluid availability when $t_{cs} < 15°C$ (i.e. high critical point required while respecting the minimum pressure constraint).

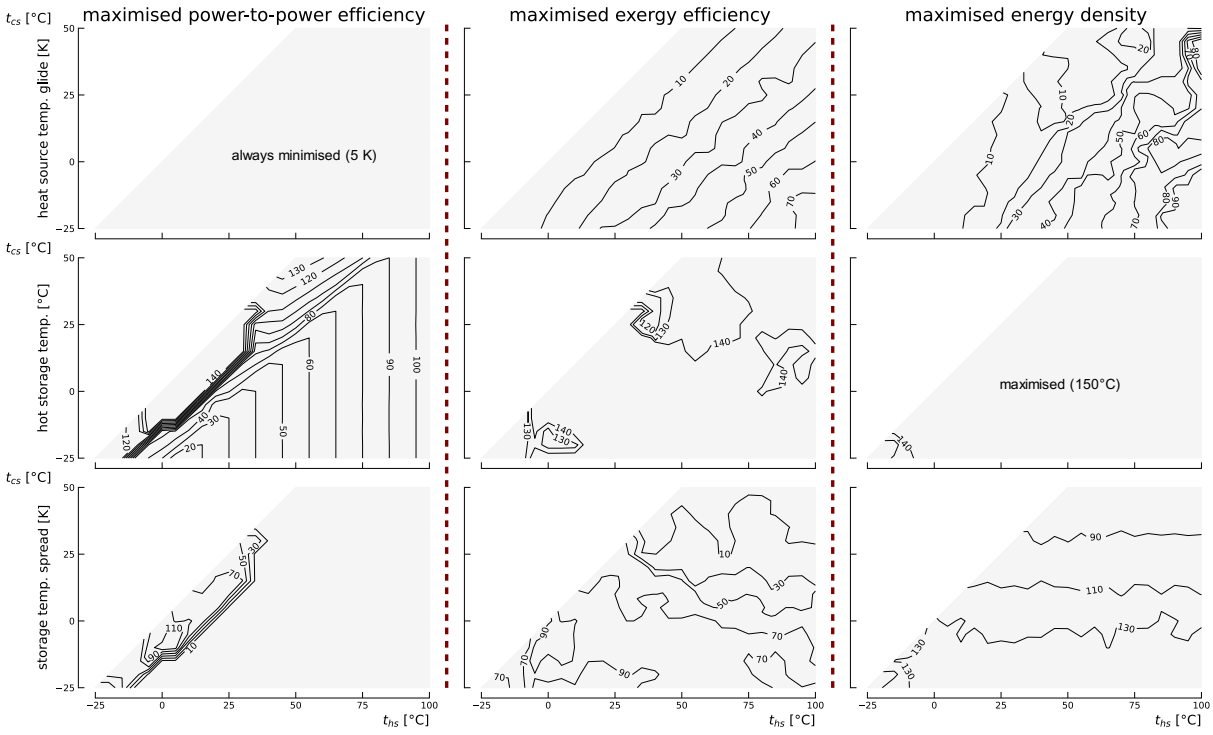

Figure 5: Set of design variables with the most significant influence on the *Carnot battery trilemma*: $\Delta T_{hs,gl}$ (1st row), $t_{st,ht}$ (2nd row) and $\Delta T_{st,sp}$ (3rd row). Some contour lines have been smoothed to eliminate local convergence issues (model artefacts).

The other key parameter influencing η_{II} is $\Delta T_{hs,gl}$. A high $\Delta T_{hs,gl}$ leads to an effective waste heat utilisation but reduces $COP_{HT-VCHP}$ as the evaporation temperature is decreased. A trade-off must therefore be found. A relevant result of this study is that the relative heat source glide, defined as

$$\Delta T_{hs,gl}^{rel} = \frac{\Delta T_{hs,gl}}{\Delta T_{hs-cs}} \quad , \qquad (6)$$

must always be comprised between 55 and 60 % in order to maximise η_{II}.
Let's finally observe that η_{II} is always superior for TI-PTES than in other power-to-x-to-power systems, which hardly exceed 25 % (Dias *et al.*, 2020). Note that this does not consider the waste heat that is lost when the TI-PTES is not charging.

Results for optimised ρ_{el}
The optimum electrical energy density results of a trade-off between the thermal density (i.e. the higher $\Delta T_{st,sp}$, the higher the thermal density) and η_{orc} (i.e. the higher $\Delta T_{st,sp}$, the lower η_{orc}). As it can be observed in Fig. 3, because η_{orc} is a function of t_{cs}, ρ_{el} linearly decreases with increasing t_{cs}. It ranges from 12.1 kWh/m^3 when $t_{cs} = -25$°C to 2.5 kWh/m^3 when $t_{cs} = 50$°C. Note that a thermal storage in a single tank with an ideal thermocline could double these values, as one of the two tanks would be removed.
The optimum storage spread linearly varies from around 145 K when $t_{cs} = -25$°C to 72 K when $t_{cs} = 50$°C. To reach such spreads and to maximise η_{orc}, $t_{st,ht}$ is always maximised. Moreover, as a rule of thumb, it can be shown that for designs maximising the density, $t_{st,ht} - t_{cs} - \Delta T_{st,sp} \approx 27$ K.
Note that although $\Delta T_{hs,gl}$ takes a certain trend with ΔT_{hs-cs}, there is still a lack of convergence. This is due to the fact that this parameter does not have a direct influence on ρ_{el}, but it must have a sufficient value for $t_{st,lt}$ to be higher than $t_{hs} - \Delta T_{hs,gl}$ (see constraint in Table 1).

Finally, in a general way for all the results, it is observed that when $t_{hs} \leq -20$°C, the optimised designs are not in total agreement with what has been described above (i.e. they have lower $t_{st,ht}$ and $\Delta T_{st,sp}$). This is due to the constraint on $p_{hp/orc,min}$, which imposes to choose fluids with lower critical points, as they have higher saturation pressures at lower temperatures, and to the subcritical regime constraint.

3.2 Multi-criteria analyses

The Pareto fronts obtained with the multi-criteria analyses are shown for two locations of the domain in Fig. 6. These fronts are used to draw qualitative trends exclusively, the quantitative results being specific to each position in the integration domain. To quantify the conflict between the three objectives, a criterion has been established using the best and worst performance as follows:

$$i_{conflict} = \sqrt{\frac{\left(\frac{\eta_{P2P}^{max} - \eta_{P2P}^{min}}{\eta_{P2P}^{max}}\right)^2 + \left(\frac{\eta_{II}^{max} - \eta_{II}^{min}}{\eta_{II}^{max}}\right)^2 + \left(\frac{\rho_{el}^{max} - \rho_{el}^{min}}{\rho_{el}^{max}}\right)^2}{3}} \quad . \qquad (7)$$

The thresholds to discriminate the different areas on the map are set arbitrarily. When $i_{conflict} \leq 15$ %, the conflict is said to be slight. For 15 % $< i_{conflict} \leq 50$ %, it is medium. Above, it is high. Fig. 6a shows that the criteria are only slightly conflicting for $t_{hs} = 25$°C and $t_{cs} = 15$°C. Indeed, the relative difference between the best and worst performance is only 1.9 % for η_{P2P}, 1.7 % for η_{II} and 3.2 % for ρ_{el}. In general, this result can be extended to the whole region of the domain where $t_{hs} \leq 25$°C and $\Delta T_{hs-cs} < 20$ K, as the relative difference between the best and worst performance of each criterion does not usually exceed 15 % (see light grey zone in Fig. 6).
In contrast, Fig. 6b shows that the *trilemma* is much more intense for $t_{hs} = 55$°C and $t_{cs} = 15$°C. The front between η_{P2P} and η_{II} is linear, and it results mainly of a simultaneous trade-off between $\Delta T_{hs,gl}$, $t_{st,ht}$ and $\Delta T_{st,sp}$, which in line with the observations drawn in the previous section. The steep front between ρ_{el} and η_{P2P} illustrates well the very binary nature of the problem: it is not really possible to obtain a satisfactory trade-off between the two criteria, as one tends to clearly degrade the other. Indeed,

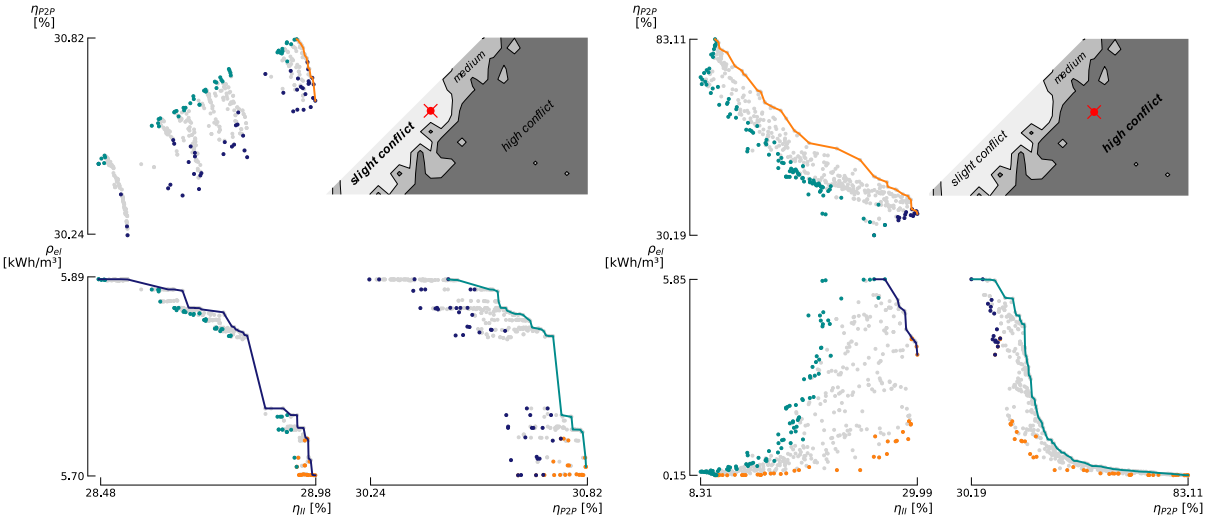

(a) 25°C heat source and 15°C heat sink ($\Delta T_{hs-cs} = 10$ K)

(b) 55°C heat source and 15°C heat sink ($\Delta T_{hs-cs} = 40$ K)

Figure 6: 3D Pareto fronts of the *Carnot battery trilemma* for two locations in the integration domain. The map of the domain shows the conflict between the three criteria.

the maximisation of η_{P2P} requires minimising $\Delta T_{hs,gl}$, $t_{st,ht}$ and $\Delta T_{st,sp}$ whereas opposite trends are observed for ρ_{el}. Finally, it can be noted that ρ_{el} and η_{II} are much less conflicting with each other than with η_{P2P}. This is largely due to the fact that they both maximise $t_{st,ht}$ over most of the domain, and that they do not minimise $\Delta T_{st,sp}$ and $\Delta T_{hs,gl}$.

4 CONCLUSION AND DISCUSSIONS

This work focused on the analysis of the *Carnot battery trilemma* over the entire thermal integration domain. The objectives were to map the theoretical performance that TI-PTES could reach, to formulate design guidelines and to study the conflict between η_{P2P}, η_{II} and ρ_{el}.
It was found that, when optimised, η_{P2P} is a function of ΔT_{hs-cs}, and that η_{II} and ρ_{el} are functions of t_{cs} only. Moreover, it has been shown that, for each objective, general design guidelines can be established. Yet, it has also been demonstrated that, for the considered set of design constraints, these guidelines are not uniform across the domain and that the existence of tipping points lead to the formation of sub-regions. This applies in particular to $t_{st,ht}$ and $\Delta T_{st,sp}$ when optimising η_{P2P} and η_{II}.
The multi-criteria analysis also revealed the existence of a region where the three objectives are almost not conflicting. This means that the *trilemma* does not have the same intensity over the whole thermal domain. In general, the main source of conflict is the value of $t_{st,ht}$, which must be minimised to maximise η_{P2P} and maximised to maximise η_{II} and ρ_{el}.

According to the results obtained, improvements could be made to the basic TI-PTES. Firstly, when the HT-VCHP lift is very high, the required compression ratio can exceed 30. This suggests the use of multistage or cascaded heat pumps. Then, for designs involving large $\Delta T_{st,sp}$, two cases can be encountered. In the first, the evaporation point in the ORC is relatively low compared to the critical point, with a possible vapor superheat (e.g. maximisation of η_{II}). In such case, the use of an internal regenerator could be interesting. Nevertheless, this consideration depends on the choice of the fluid and deserves further investigation. In the second case, the ORC operates very close to the critical point, with a potentially large superheat. This highlights that the use of transcritical ORCs could be relevant in such configurations. Finally, the presence of important glides should push towards further investigation of the use of zeotropic mixtures. Some of these points will be addressed in future work, together with more detailed analyses of the designs, including the choice of fluids, and the role of liquid subcooling and vapor superheat.

NOMENCLATURE

Abbreviations

COP	coefficient of performance	ORC	organic Rankine cycle
GWP	global warming potential	TES	thermal energy storage
HT-VCHP	high temperature vapor compression heat pump	TI-PTES	thermally integrated pumped thermal energy storage
ODP	ozone depletion potential		

Greek and Latin letters

ΔT	temperature difference, K	p	pressure, bar
Δp	pressure loss, bar	ρ	density, kWh/m^3
η	efficiency, %	t	temperature, °C
h	specific enthalpy, J/kg/K	v	specific volume, m^3/kg

Sub- and superscript

cs	cold sink	II	exergy
el	electrical	lt	low temperature
gl	temperature glide	P2P	power-to-power
hp	heat pump	pp	pinch point
hs	hot source	rel	relative
$hs - cs$	source – sink temperature	sp	spread
ht	high temperature	st	storage

REFERENCES

Bell, I.H., Wronski, J., Quoilin, S., Lemort, V., 2014. Pure and pseudo-pure fluid thermophysical property evaluation and the open-source thermophysical property library CoolProp. *Industrial & engineering chemistry research* 53, 2498–2508.

Coppitters, D., Tsirikoglou, P., Paepe, W.D., Kyprianidis, K., Kalfas, A., Contino, F., 2022. RHEIA: Robust design optimization of renewable Hydrogen and dErIved energy cArrier systems. *Journal of Open Source Software* 7, 4370.

Deb, K., Pratap, A., Agarwal, S., Meyarivan, T., 2002. A fast and elitist multiobjective genetic algorithm: NSGA-II. *IEEE transactions on evolutionary computation* 6, 182–197.

Dias, V., Pochet, M., Contino, F., Jeanmart, H., 2020. Energy and economic costs of chemical storage. *Frontiers in Mechanical Engineering* 6, 21.

Dumont, O., Lemort, V., 2020. Mapping of performance of pumped thermal energy storage (Carnot battery) using waste heat recovery. *Energy* 211, 118963.

Fan, R., Xi, H., 2022. Energy, exergy, economic (3E) analysis, optimization and comparison of different Carnot battery systems for energy storage. *Energy Conversion and Management* 252, 115037.

Forman, C., Muritala, I.K., Pardemann, R., Meyer, B., 2016. Estimating the global waste heat potential. *Renewable and Sustainable Energy Reviews* 57, 1568–1579.

Frate, G.F., Antonelli, M., Desideri, U., 2017. A novel Pumped Thermal Electricity Storage (PTES) system with thermal integration. *Applied Thermal Engineering* 121, 1051–1058.

Frate, G.F., Ferrari, L., Desideri, U., 2020a. Multi-criteria investigation of a pumped thermal electricity storage (PTES) system with thermal integration and sensible heat storage. *Energy Conversion and Management* 208, 112530.

Frate, G.F., Ferrari, L., Desideri, U., 2020b. Multi-Criteria Economic Analysis of a Pumped Thermal Electricity Storage (PTES) With Thermal Integration. *Front. Energy Res.* 8, 53.

Hu, S., Yang, Z., Li, J., Duan, Y., 2021. Thermo-economic analysis of the pumped thermal energy storage with thermal integration in different application scenarios. *Energy Conversion and Management* 236, 114072.

Jockenhöfer, H., Steinmann, W.-D., Bauer, D., 2018. Detailed numerical investigation of a pumped thermal energy storage with low temperature heat integration. *Energy* 145, 665–676.

Lu, P., Luo, X., Wang, J., Chen, J., Liang, Y., Yang, Z., He, J., Wang, C., Chen, Y., 2022. Thermodynamic analysis and evaluation of a novel composition adjustable Carnot battery under variable operating scenarios. *Energy Conversion and Management* 269, 116117.

Maraver, D., Royo, J., Lemort, V., Quoilin, S., 2014. Systematic optimization of subcritical and transcritical organic Rankine cycles (ORCs) constrained by technical parameters in multiple applications. *Applied Energy* 117, 11–29.

Marina, A., Spoelstra, S., Zondag, H.A., Wemmers, A.K., 2021. An estimation of the European industrial heat pump market potential. *Renewable and Sustainable Energy Reviews* 139, 110545.

Mercangöz, M., Hemrle, J., Kaufmann, L., Z'Graggen, A., Ohler, C., 2012. Electrothermal energy storage with transcritical CO2 cycles. *Energy* 45, 407–415.

Smith, C., Nicholls, Z.R.J., Armour, K., Collins, W., Forster, P., Meinshausen, M., Palmer, M.D., Watanabe, M., 2021. The Earth's Energy Budget, Climate Feedbacks, and Climate Sensitivity Supplementary Material. Climate Change 2021: The Physical Science Basis. Contribution of Working Group I to the Sixth Assessment Report of the Intergovernmental Panel on Climate Change.

Steinmann, W.D., 2014. The CHEST (Compressed Heat Energy STorage) concept for facility scale thermo mechanical energy storage. *Energy* 69, 543–552.

Weitzer, M., Müller, D., Karl, J., 2022a. Two-phase expansion processes in heat pump – ORC systems (Carnot batteries) with volumetric machines for enhanced off-design efficiency. *Renewable Energy* 199, 720–732.

Weitzer, M., Müller, D., Steger, D., Charalampidis, A., Karellas, S., Karl, J., 2022b. Organic flash cycles in Rankine-based Carnot batteries with large storage temperature spreads. *Energy Conversion and Management* 255, 115323.

Zhang, M., Shi, L., Hu, P., Pei, G., Shu, G., 2023. Carnot battery system integrated with low-grade waste heat recovery: Toward high energy storage efficiency. *Journal of Energy Storage* 57, 106234.

Zhang, Y., Xu, L., Li, J., Zhang, L., Yuan, Z., 2022. Technical and economic evaluation, comparison and optimization of a Carnot battery with two different layouts. *Journal of Energy Storage* 55, 105583.

128

ACKNOWLEDGEMENTS

The first author acknowledges the support of Fonds de la Recherche Scientifique - FNRS [40014566 FRIA-B1]. The computational resources have been provided by the Consortium des Équipements de Calcul Intensif (CÉCI), funded by the Fonds de la Recherche Scientifique de Belgique (F.R.S.-FNRS) under Grant No. 2.5020.11 and by the Walloon Region.

APPENDIX

Table A1: Technical and physical properties of the investigated working fluids (data from `CoolProp 6.4.1` (Bell *et al.*, 2014)).

Fluid	Category	T_{crit} [°C]	p_{crit} [bar]	$p_{sat,15°C}$ [bar]	GWP_{100}	ASHRAE 34[b]	Type	No.
R1270 (Propene)	HC	91.1	45.6	8.9	3.1	A3	wet	1
R1234yf	HFO	94.7	33.8	5.1	0.501[a]	A2L	dry	2
R290 (n-Propane)	HC	96.7	42.5	7.3	0.02[a]	A3	wet	3
R161	HFC	102.1	50.1	7.0	4.84[a]	N/A	wet	4
R1243zf		103.8	35.2	4.4	0.261[a]	N/A	isentropic	5
R1234ze(E)	HFO	109.4	36.3	3.6	1.37[a]	N/A	isentropic	6
R152a	HFC	113.3	45.2	4.4	164[a]	A2	wet	7
R13I1		123.3	39.5	3.7	0.4	A1	wet	8
RC270 (cyclo-Propane)	HC	125.2	55.8	5.5	N/A	N/A	wet	9
RE170 (dimethyl-Ether)	HC	127.2	53.4	4.4	1.0	N/A	wet	10
R717 (Ammonia)		132.2	113.3	7.3	N/A	B2L	wet	11
R600a (iso-Butane)	HC	134.7	36.3	2.6	N/A	A3	dry	12
1-Butene	HC	146.1	40.1	2.2	N/A	N/A	dry	13
R1234ze(Z)	HFO	150.1	35.3	1.2	0.315[a]	A2L	isentropic	14
R600 (n-Butane)	HC	152.0	38.0	1.8	0.006[a]	A3	dry	15
trans-2-Butene	HC	155.5	40.3	1.7	N/A	N/A	dry	16
Neopentane	HC	160.6	32.0	1.2	N/A	N/A	dry	17
R1233zd(E)	HCFO	166.5	36.2	0.9	3.88[a]	A1	dry	18
Novec649		168.7	18.7	0.3	N/A	N/A	dry	19
R601a (iso-Pentane)	HC	187.2	33.8	0.6	N/A	A3	dry	20
R601 (n-Pentane)	HC	196.5	33.7	0.5	N/A	A3	dry	21
R602 (n-Hexane)	HC	234.7	30.4	0.1	3.1	N/A	dry	22
Acetone		235.0	47.0	0.2	0.5	N/A	isentropic	23
cyclo-Pentane	HC	238.6	45.7	0.3	N/A	N/A	dry	24
Methanol		239.4	82.2	0.1	2.8	N/A	wet	25
R603 (n-Heptane)	HC	267.0	27.4	<0.1	N/A	N/A	dry	26
cyclo-Hexane	HC	280.5	40.8	<0.1	N/A	N/A	dry	27
Benzene	HC	288.9	48.9	<0.1	N/A	N/A	dry	28
MDM	Siloxane	290.9	14.1	<0.1	N/A	N/A	dry	29
Toluene	HC	318.6	41.3	<0.1	3.3	N/A	dry	30
ethyl-Benzene	HC	344.0	36.2	<0.1	N/A	N/A	dry	31

[a] Value from Table 7.SM.7 of IPCC 6th Assessment Report (Smith *et al.*, 2021)
[b] ASHRAE Standard 34-2022, "Designation and Safety Classification of Refrigerants"

129

ORC SEVILLE 2023
7th International Seminar on O.R.C. Power Systems

© 2024 Editorial Universidad de Sevilla. Este es un artículo de acceso abierto distribuido bajo los términos de la licencia de uso y distribución Creative Commons (BY-NC-ND 4.0)

DOI: https://dx.doi.org/10.12795/9788447227457_20

ORC technology used in a Heat Removal System for Advanced Nuclear Power Plants

Guillaume Lhermet [1, 2], Benoit Payebien [2], Nicolas Tauveron [2, *], Nadia Caney [2] and Franck Morin [1]

[1] *CEA, DES, IRESNE, DER, SESI, LCOS, F-13108 Saint Paul Lez Durance, France*
[2] *Université Grenoble Alpes, F-38000 Grenoble, France*

*Corresponding Author: *nicolas.tauveron@cea.fr*

ABSTRACT

This work concerns the design of a specific passive system for an advanced pressurized water reactor (PWR). The system studied is based firstly on passive safety condensers, which are increasingly used in the design of advanced nuclear power plants. These condensers are typically immersed in large water tanks that serve as a heat sink. They are located at a sufficient height to ensure a natural two-phase circulation mode. Such a heat removal system can be used for a relatively long period depending on the size of the tank.

The present research is based on using a fraction of the energy stored in this volume of boiling water as a heat source for an organic Rankine cycle via an immersed heat exchanger. The electrical energy produced will power various critical components, complementing existing systems.

Three unusual issues challenge the use of an ORC in this context: the nature of the hot source (boiling pool water), the low temperature of the hot source (100°C), and the requirement for system reliability and robustness. Apart from these three challenges, the usual constraints associated with ORC systems still exist: maximizing energy performance, using an environmentally friendly fluid and minimizing space requirements.

An experimental test bench with a boiling water pool and an ORC with submerged evaporator was built to address the main questions. The first set of results shows the nominal operation of the coupling between the boiling water pool and the ORC when Novec649™ is used as working fluid. The reliability of the system is then studied through the investigation of the immersed evaporator and the implementation of a theoretical model. The theoretical model of the system will be used to scale the system.

130

1 Introduction

With approximately 450 nuclear power plants (NPP), nuclear power generates approximately 10% of global electricity [1], [2]. Three major nuclear accidents occurred in the last five decades: Three Mile Island (1979), Chernobyl (1986), and Fukushima Daiishi (2011) [3]–[5]. The experience feedback of these accidents is taken into account in the design of the new generation NPPs (generation III and beyond) with a view to improving safety. The state of the art of these accidents is incorporated into new generation NPPs (generation III and beyond) to improve safety systems for nuclear new builds. As a result, a safety enhancement program has been developed, with a focus on passive safety systems for new-generation NPPs, able to handle with highly severe conditions resulting in a long period of loss of offsite power inducing a global loss of heat sink event. These systems can function during station blackout (SBO).

Passive systems, like the passive residual heat removal system (PRHRS), derive their effectiveness from the lack of rotating machinery (such as pumps or diesel engines). These systems only rely on natural forces, such as natural convection, to transfer the residual heat from the core to the cold source (water or air). The use of passive systems simplifies plant systems, as well as their operation and maintenance [6].

Some new generation NPPs already include PRHRS [7]. This PRHRS can be connect directly to the primary loop as on the AP1000 [8] or the CAP1400 [9]. Indeed, a PRHR transfers the residual heat from the core to the in-containment refuelling water storage tank (IRWST) through a heat exchanger (HX). To ensure natural convection, the IRWST is located above the reactor. Another existing solution is to connect the PRHRS through the secondary loop in order to cool the steam generator (SG) which removes the decay heat from the primary loop, as existing on the HPR1000 [10] or the CPR1000 [11]. This system is named secondary side passive residual heat removal system (SSPRHRS). Because the SSPRHRS is connected to the secondary side, the PRHR HX acts as a safety condenser (SACO).

Moreover, while passive cooling systems are effective and dependable, they should not be the only focus. Thus, another safety concern raised by various safety authorities is the installation of an emergency power supply in addition to the existing power supplies [12]. Then, one concept is to use the water tank as a hot source for a thermodynamic cycle such as a Stirling engine or an Organic Rankine Cycle (ORC). The electricity generated by the cycle will provide electricity for its own use (pump) as well as a production surplus [13], [14]. The Figure 1 illustrates the coupling of a PRHRS and an ORC.

ORC is a thermal-driven power cycle that generates electricity by using a heat source and a low-boiling-point fluid as the working fluid [15], [16]. ORC has been identified as one of the best thermal engines for producing electricity with a low heat source (150 °C) [17]. The majority of the heat sources used are geothermal, with approximately 3 GW of cumulative installed capacity in 2020, with power output ranging from a few kW to several dozen MW [18].

A tubular evaporator immersed in the boiling water tank enhances the coupling between the ORC and the boiling water tank. Natural convection is used to transfer heat from the boiling water to the tubes outer walls. Additionally, mini-channel type tubes have been selected to enable heat transfer over a maximum surface area while maintaining acceptable heat transfer coefficients inside the tubes. This kind of tube is widely used to dissipate heat in confined spaces [19].

Thus, despite the fact that ORC are a well-established system, their use in nuclear safety necessitates a focus on their reliability. Indeed, the ORC must be capable of producing electricity on any situation (extreme climatic conditions, aging of components etc.) continuously. In addition, the innovative design of the heat exchanger also necessitates an experimental investigation of the heat transfer coefficients inside and outside the tubes in order to scale it up for a full-scale application. This article will concentrate on these two research directions.

131

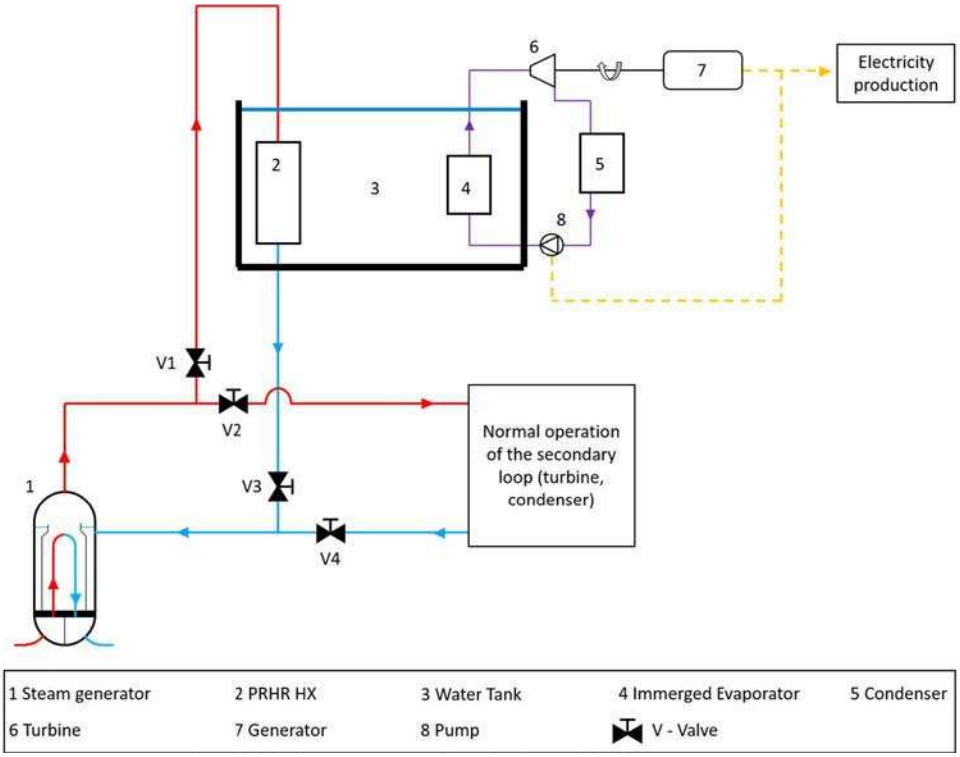

Figure 1 : PRHRS and ORC coupling - simplified diagram

2 Experimental test bench

2.1 The experimental ORC

The experimental test bench is composed of two main parts:

- The ORC composed of an immersed evaporator.
- The boiling water tank, which is supposed to replace the SACO pool, composed of heating rods, which are supposed to replace the operation of the passive SACO.

The test bench objective is to operate as a small-scale demonstrator and, through the results obtained, to enable scale transposition. At the volumetric pump inlet, the working fluid is liquid. The volumetric pump raises the working fluid pressure to a high level. The fluid is evaporated in the boiling water tank using an immersed evaporator. This vapour is then expanded in a partial admission axial micro-turbine with a maximum power of about 1 kW. A generator transforms the mechanical power produced by this expansion into electricity. The low-pressure vapor is cooled by a plate condenser, which uses an active external water circuit as a cold source, before it is sent back to the pump.

The system lubrication is provided by the working fluid itself. An external circuit designed specifically for the generator keeps it cool. A small centrifugal pump is placed just before the volumetric pump to slightly increase the pressure and avoid cavitation. A tank, located between the condenser and the centrifugal pump, ensures a sufficient net positive suction head (NPSH) at the centrifugal pump inlet. An additional system comprised of a heat exchanger and a bypass system allows for the investigation of a wide range of cold source temperatures. The use of a pump in combination with a needle valve allows for the investigation of a wide range of mass flow rates and pressures.

The boiling water tank has a capacity of 1.5 m3. It includes ten 20 kW heating rods. Every heating rod has a heat flux density of 10.1 W/cm^2, which is roughly the same order of size as a SACO [20]. The power in the pool varies between 0 kW and 100 kW (five heating rods maximum). The maximum power ratio between heating rods and immersed exchanger is approximately five.

Temperature sensor rods are used to measure the temperature gradient in the tank. The positioning of the rods in the water tank is described in Figure 2. A level sensor system linked to an automatic valve controls the amount of water in the tank.

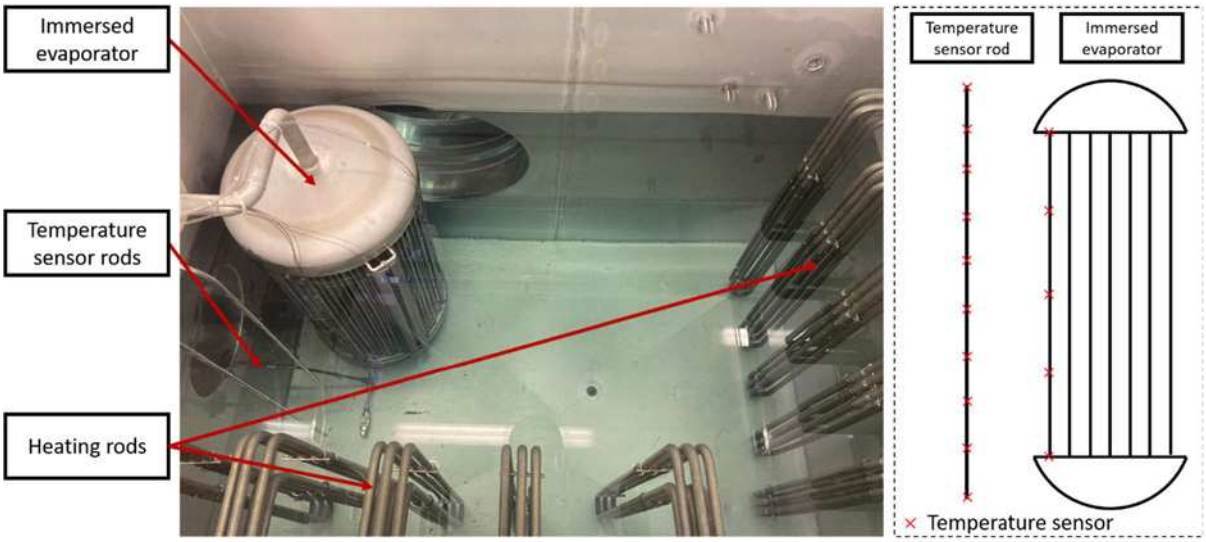

Figure 2 : Boiling water tank

2.2 Measurement

The characteristics of the measuring equipment used for measurement and data acquisition are listed in Table 1.

The working fluid, the water tank and cold source loops are equipped with Type-T thermocouples to measure the temperatures between the various components. Figure 2 shows the temperature sensors at the evaporator exterior tube wall. The working fluid circuit is instrumented with absolute pressure sensors (APS) at the turbine inlet and outlet to measure the two pressure stages within the plant. The volume flow measurements of the cold circuit are made with electromagnetic flow meters (EFMs) while the fluid flow is measured with a Coriolis-type mass flow rate meter. The gross power produced at the turbine is measured with a power meter.

Table 1: Measurement characteristics

Variable	Equipment	Range	Uncertainty
Electrical power	Wattmeter	0–3250 W	± 0.3%
Volume flow (cold source)	EFM	0–2500 L/h	± 0.33%
Mass flow rate (working fluid)	Coriolis	50–500 kg/h	± 0.30%
Temperature	Thermocouple Type-T	−200–200 °C	± 0.1 °C
Pressure	APS	0–7 bar	± 1%

3 Working fluid

The working fluid used in this work is the Novec649^{TM}. This fluid is neither toxic nor flammable [21]. Furthermore, Novec649^{TM} is exempt from the Kyoto and Paris agreements on refrigerant working fluids due to its environmental characteristics (ozone depletion potential (ODP) = 0 and global warming potential (GWP) = 1) (Table 2) [22], [23]. Moreover, Novec649^{TM} is a dry fluid ($\partial T/\partial s > 0$) which avoid any risk of erosion on the turbine. A other interest lies in its moderate high pressure.

The thermodynamic properties of the Novec649^{TM}, come from EES (engineering equation solver) software [24].

Table 2: Novec649^{TM} properties

Properties	Novec649™
Fluid type	Dry
Fluid class	Fluoroketone
Formula	$CF_3CF_2C(O)CF(CF_3)_2$
Critical temperature (°C)	169
Critical pressure (bar)	18.7
Normal glide	0
ODP	0
GWP	1
Flammability	No
Toxicity	Null

4 Global ORC results

The experimental test bench initial results allowed for the determination of the ORC nominal operating point. The cycle T-s diagram is shown in Figure 3.

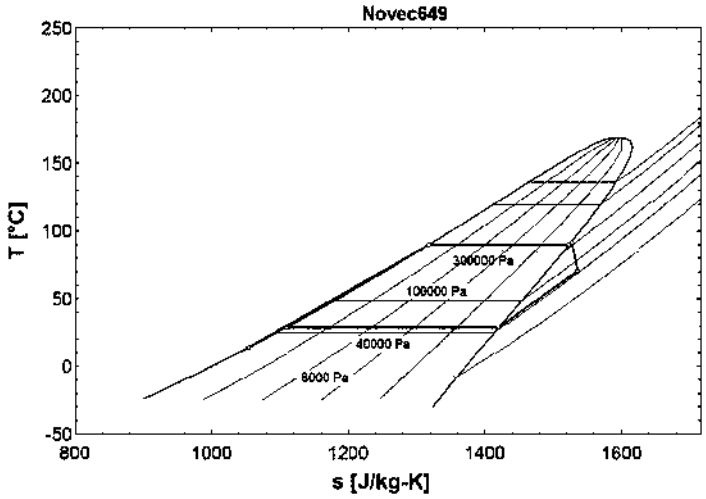

Figure 3 : Novec649^{TM} T-s Diagram

The ORC overall efficiency during nominal operation is around 2%. Because of moderate hot source temperature, overall efficiency is low. Furthermore, due to the ORC small size, partial admission machine has been chosen, leading to an isentropic turbine efficiency of 50%. Detailed elements on turbine type and efficiency can be found in a recent article [25]. Projected full scale machine (i.e. without partial admission) would lead to an isentropic turbine efficiency of nearly 75%.

The low efficiency value of the global system is not a central problem as the amount of recoverable hot source is significantly higher than the amount of hot source required for the cycle to operate properly in real operation (~150 kW), where the hot source is the residual power of a nuclear reactor core (30 MW). Furthermore, the size of the turbo machine will be larger during scaling up, which will increase turbine and system efficiencies.

134

Table 3 : Nominal point

Specification	Unit	Data
Electrical power	Watts	138
Overall efficiency	%	2
Turbo generator efficiency	%	16
Pressure rate	[-]	7.4
Temperature of hot source	°C	≈100
Cold source temperature	°C	13

The experimental ORC can generate about 140 Watts of electrical power under nominal operation. According to the initial calculations, the ORC will need to be able to generate about 10 kW of power at scale 1. Thus, theoretical models of the ORC components under the EES software are realized in order to scale up the ORC.

The present analysis is focused on the submerged evaporator model. An axial turbine model in nominal and degraded conditions (partial evaporation condition at turbine inlet) was realized and experimentally validated in a recent article [25]. A condenser model in normal and off-normal conditions (cold source temperature variation) was realized and experimentally validated in a separate paper.

5 Immersed evaporator

The ORC immersed evaporator was designed to validate experimentally inside and outside heat transfer coefficients. The validation of these models will support a scale transposition via the conservation of some dimensionless numbers (Re; Ra).

The size of the experimental immersed evaporator is summarized in the

Table 4.

Table 4 : Experimental immersed evaporator design.

Specification	Unit	Data
Length in height	[mm]	800
Distance between heat transfer tube	[mm]	18
Outside tube diameter	[mm]	3.17
Tube thickness	[mm]	0.89
Number of tubes	[-]	551
Total exchanger diameter	[mm]	406.4

5.1 Natural convection

Since the tubular evaporator is submerged in a tank of water, the heat transfer is processed by natural convection. Since the Rayleigh number (eq (1)) value at the wall is around 10^5, the flow is laminar. In this context, two correlations have been examined.

$$Ra = Gr.Pr \tag{1}$$

$$Gr = \frac{\rho^2 g\beta(T_{water} - T_{wall})d^3}{\lambda\mu^2} \tag{2}$$

The Churchill and Chu (1975) correlation, used in the MARS code for vertical surfaces with Gr.Pr> 0.1 [26], [27].

$$Nu_d = \left\{ 0.825 + 0.387Ra^{\frac{1}{6}} / \left[1 + \left(\frac{0.492}{Pr} \right)^{\frac{9}{16}} \right]^{\frac{8}{27}} \right\}^2 \tag{3}$$

For laminar flow on vertical surfaces, the Ostrach laminar theory (1953) has been used [28], [29].

$$Nu_d = 0.555Ra^{\frac{1}{4}} \tag{4}$$

Figure 4 shows the comparison between the theoretical and experimental convective heat transfer coefficients. It has been noted that Ostrach (1953) correlation calculates a convective heat transfer coefficient for the entire test in a +/- 30% range. Additionally, the estimated convective exchange coefficient values are of an order of magnitude consistent with the literature [30]. Thus, this correlation has been selected for the next step.

Other natural convection models have been tested, based on a revised Ra* [31], [32]. The results presentations required a more detailed paper.

5.2 Inside tubes

Bibliography concerning working fluid evaporation correlation is very limited due to the facts that Novec649™ is a relatively recent working fluid used in ORC systems and that the Reynolds number inside the tubes is small (due to the small mass flow rate).

In single phase, the Nusselt number of the fluid is calculated using eq (5), which is a classic correlation in single-phase laminar flow $Re_{lo} < 2300$.

$$Nu_{sp} = 4.36 \tag{5}$$

A previous study on a plate evaporator demonstrated that the Gullapalli correlation was adapted for for low Reynolds in Novec649™ in two-phase conditions [33], [34].

$$Nu_{tp-Gullapalli} = 1.926.Bo_{eq}^{0.3}.\left[(1-x)+x.\left(\frac{\rho_l}{\rho_v}\right)^{0.5}\right].Re_l^{0.5}.Pr_l^{\frac{1}{3}} \quad (6)$$

The Gullapalli correlation estimates the two-phase heat transfer coefficient with an approximate value of 400 W/m².K. The results are coherent with low Reynolds numbers results of the literature [35]. However, the Gullapalli correlation overestimates the value of the heat transfer rate; it would be interesting to correct this value using a corrective coefficient.

However, the goal of this model is to predict a shift in scale for an exchanger size. The accuracy in exchanged power that this model can provide is therefore crucial. The size of the components at scale 1 will then reflect this accuracy. Then, as we can see on the Figure 5 this model predicts the global heat transfer between the theoretical model results and the correlated ones within 5%.

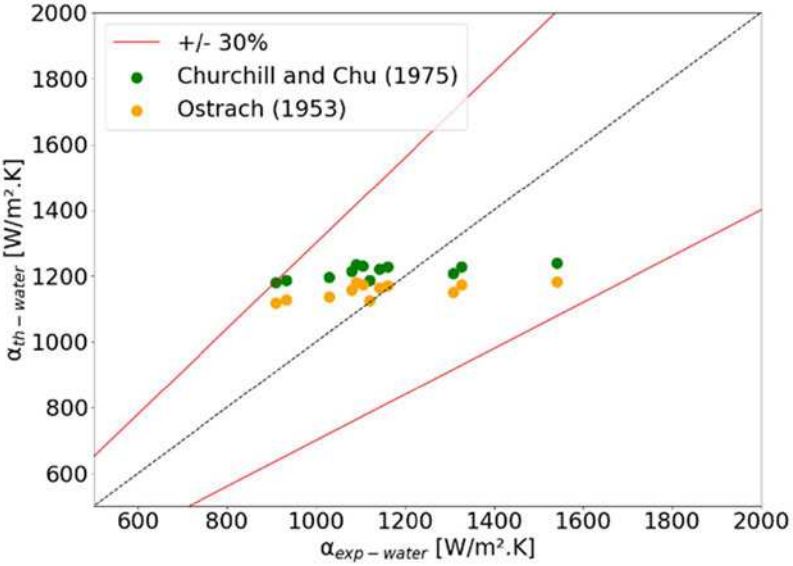

Figure 4 : Experimental and correlated natural convection heat transfer coefficients comparison

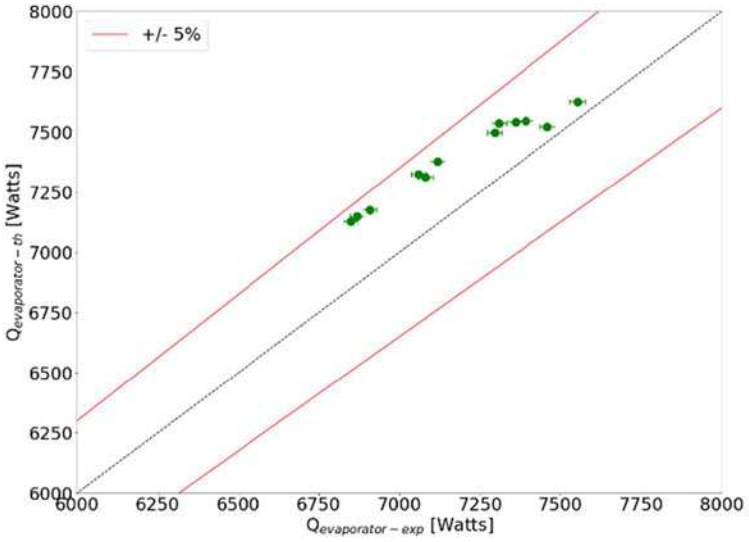

Figure 5 : Comparison of the experimental and correlated global power exchanged in the evaporator

6 CONCLUSIONS

To conclude, this study has shown by experiments that it is possible to recover low grade heat through an immersed heat exchanger and convert it to electricity.

An evaporator model has been developped, using the Ostrach [28], [29] correlation in natural convection and the Gullapalli [33], [34] correlation inside the tubes. This model predicts the global heat transfer between the theoretical model results and the correlated ones within 5%. This model, coupling through a global ORC system description enable the quantification of electricity production in various conditions.

The experimental study is still in progress in order to investigate off nominal situations and other ORC fluids performances.

ACKNOWLEDGMENTS

The authors would like to express their gratitude to the Atomic Energy and Alternative Energies Commission (CEA) and Electricité de France (EDF).

NOMENCLATURE

Symbols		
d	tube diameter	(m)
g	acceleration of gravity	(m/s²)
T	temperature	(K)
x	vapour quality	(-)
Greek letters		
α	heat transfer coefficient	(W/m².K)
β	coefficient of thermal expansion	(K^{-1})
λ	thermal conductivity	(W/m.K)
μ	dynamic viscosity	(Pa.s)
ρ	density	(kg/m^3)

Subscripts	
d	diameter
eq	equivalent
exp	experimental
l	liquid
sp	single-phase
th	theoretical
tp	two-phase
v	vapor

GLOSSARY

EES	engineering equation solver
GWP	global warming potential
HX	heat exchanger
IRWST	in-containment refuelling water storage tank
NPSH	net positive suction head
NPP	nuclear power plants

ODP	ozone depletion potential
ORC	organic Rankine cycle
PRHRS	passive residual heat removal system
SACO	safety condenser
SBO	station blackouts
SG	steam generator
SSPRHRS	secondary side passive residual heat removal system

References

[1] 'Nuclear Power Today | Nuclear Energy - World Nuclear Association'. https://www.world-nuclear.org/information-library/current-and-future-generation/nuclear-power-in-the-world-today.aspx (accessed Nov. 28, 2022).

[2] '95/06080 Energy, electricity and nuclear power estimates for the period up to 2015', *Fuel Energy Abstr.*, vol. 36, no. 6, p. 430, Nov. 1995, doi: 10.1016/0140-6701(95)95132-6.

[3] G. R. Skillman and J. L. Rempe, 'The Three Mile Island Unit 2 Accident', in *Encyclopedia of Nuclear Energy*, E. Greenspan, Ed., Oxford: Elsevier, 2021, pp. 17–29. doi: 10.1016/B978-0-12-409548-9.12146-3.

[4] A. R. Sich, 'The Chernobyl Nuclear Power Plant Unit-4 Accident', in *Encyclopedia of Nuclear Energy*, E. Greenspan, Ed., Oxford: Elsevier, 2021, pp. 30–52. doi: 10.1016/B978-0-12-819725-7.00080-5.

[5] Internationale Atomenergie-Organisation, Ed., *The Fukushima Daiichi accident*. in STI/PUB. Vienna, Austria: International Atomic Energy Agency, 2015.

[6] T. L. Schulz, 'Westinghouse AP1000 advanced passive plant', *Nucl. Eng. Des.*, vol. 236, no. 14, pp. 1547–1557, Aug. 2006, doi: 10.1016/j.nucengdes.2006.03.049.

[7] J. Li *et al.*, 'Experimental investigation on the heat removal capacity of secondary side passive residual heat removal system for an integrated reactor', *Appl. Therm. Eng.*, vol. 204, p. 117973, Mar. 2022, doi: 10.1016/j.applthermaleng.2021.117973.

[8] S. Estévez-Albuja, G. Jiménez, and C. Vázquez-Rodríguez, 'AP1000 IRWST numerical analysis with GOTHIC', *Nucl. Eng. Des.*, vol. 372, p. 110991, Feb. 2021, doi: 10.1016/j.nucengdes.2020.110991.

[9] Y. Q. Li *et al.*, 'Analyses of ACME integral test results on CAP1400 small-break loss-of-coolant-accident transient', *Prog. Nucl. Energy*, vol. 88, pp. 375–397, Apr. 2016, doi: 10.1016/j.pnucene.2016.01.012.

[10] D. C. Sun, Y. Li, Z. Xi, Y. F. Zan, P. Z. Li, and W. B. Zhuo, 'Experimental evaluation of safety performance of emergency passive residual heat removal system in HPR1000', *Nucl. Eng. Des.*, vol. 318, pp. 54–60, Jul. 2017, doi: 10.1016/j.nucengdes.2017.04.003.

[11] M. Wang, H. Zhao, Y. Zhang, G. Su, W. Tian, and S. Qiu, 'Research on the designed emergency passive residual heat removal system during the station blackout scenario for CPR1000', *Ann. Nucl. Energy*, vol. 45, pp. 86–93, Jul. 2012, doi: 10.1016/j.anucene.2012.03.004.

[12] *Éléments de sûreté nucléaire - Les réacteurs de recherche*. EDP Sciences, 2019. doi: 10.1051/978-2-7598-2301-7.

[13] K. P. Singh, H. Sound, I. Rampall, C. Hill, and J. Rajkumar, 'Autonomous self-powered system for removing thermal energy from pools of liquid heated by radioactive materials and method of the same', p. 14.

[14] E. Tatli, J. G. Belechak, B. Lu, C. Stansbury, C. Guler, and M. J. Ostrosky, 'Power generation from decay heat for spent nuclear fuel pool cooling and monitoring', p. 7.

[15] M. Astolfi, '3 - Technical options for Organic Rankine Cycle systems', in *Organic Rankine Cycle (ORC) Power Systems*, E. Macchi and M. Astolfi, Eds., Woodhead Publishing, 2017, pp. 67–89. doi: 10.1016/B978-0-08-100510-1.00003-X.

[16] J. B. Obi, 'State of Art on ORC Applications for Waste Heat Recovery and Micro-cogeneration for Installations up to 100kWe', *Energy Procedia*, vol. 82, pp. 994–1001, Dec. 2015, doi: 10.1016/j.egypro.2015.11.857.

[17] N. Tauveron, S. Colasson, and J.-A. Gruss, 'Available systems for the conversion of waste heat to electricity', presented at the ASME International Mechanical Engineering Congress and Exposition, Proceedings (IMECE), 2014. doi: 10.1115/IMECE2014-37984.
[18] C. Wieland, F. Dawo, C. Schifflechner, and M. Astolfi, 'Market report on organic rankine cycle power systems: recent developments and outlook', p. 10, 2021.
[19] S.-M. Kim and I. Mudawar, 'Universal approach to predicting saturated flow boiling heat transfer in mini/micro-channels – Part II. Two-phase heat transfer coefficient', *Int. J. Heat Mass Transf.*, vol. 64, pp. 1239–1256, Sep. 2013, doi: 10.1016/j.ijheatmasstransfer.2013.04.014.
[20] B.-U. Bae, B.-J. Yun, S. Kim, and K. H. Kang, 'Design of condensation heat exchanger for the PAFS (Passive Auxiliary Feedwater System) of APR+ (Advanced Power Reactor Plus)', *Ann. Nucl. Energy*, vol. 46, pp. 134–143, Aug. 2012, doi: 10.1016/j.anucene.2012.03.029.
[21] '3m-novec-engineered-fluid-649.pdf'. Accessed: Jan. 07, 2022. [Online]. Available: https://multimedia.3m.com/mws/media/569865O/3m-novec-engineered-fluid-649.pdf
[22] *Proposal for a REGULATION OF THE EUROPEAN PARLIAMENT AND OF THE COUNCIL on fluorinated greenhouse gases*. 2012. Accessed: May 30, 2022. [Online]. Available: https://eur-lex.europa.eu/legal-content/EN/ALL/?uri=celex%3A52012PC0643
[23] 'United Nations Climate Change, Kyoto Protocol Reference Manual on Accounting of Emissions and Assigned Amounts, 2008'. Accessed: Jan. 06, 2022. [Online]. Available: https://unfccc.int/resource/docs/publications/08_unfccc_kp_ref_manual.pdf
[24] 'EES: Engineering Equation Solver | F-Chart Software : Engineering Software'. https://fchartsoftware.com/ees/ (accessed Jul. 12, 2021).
[25] G. Lhermet, N. Tauveron, N. Caney, Q. Blondel, and F. Morin, 'A Recent Advance on Partial Evaporating Organic Rankine Cycle: Experimental Results on an Axial Turbine', *Energies*, vol. 15, no. 20, Art. no. 20, Jan. 2022, doi: 10.3390/en15207559.
[26] S. W. Churchill and H. H. S. Chu, 'Correlating equations for laminar and turbulent free convection from a vertical plate', *Int. J. Heat Mass Transf.*, vol. 18, no. 11, pp. 1323–1329, Nov. 1975, doi: 10.1016/0017-9310(75)90243-4.
[27] J.-J. Jeong, K. S. Ha, B. D. Chung, and W. J. Lee, 'Development of a multi-dimensional thermal-hydraulic system code, MARS 1.3.1', *Ann. Nucl. Energy*, vol. 26, no. 18, pp. 1611–1642, Dec. 1999, doi: 10.1016/S0306-4549(99)00039-0.
[28] S. Ostrach, 'An analysis of laminar free-convection flow and heat transfer about a flat plate paralled to the direction of the generating body force'. Jan. 01, 1953. Accessed: Apr. 05, 2023. [Online]. Available: https://ntrs.nasa.gov/citations/19930092147
[29] C. Y. Warner and V. S. Arpaci, 'An experimental investigation of turbulent natural convection in air at low pressure along a vertical heated flat plate', *Int. J. Heat Mass Transf.*, vol. 11, no. 3, pp. 397–406, Mar. 1968, doi: 10.1016/0017-9310(68)90084-7.
[30] Q. Men, X. Wang, X. Zhou, and X. Meng, 'Heat Transfer Analysis of Passive Residual Heat Removal Heat Exchanger under Natural Convection Condition in Tank', *Sci. Technol. Nucl. Install.*, vol. 2014, p. e279791, Nov. 2014, doi: 10.1155/2014/279791.
[31] J. Xu, X. Xie, M. Ding, C. Yan, and G. Fan, 'A one-dimensional code of double-coupled passive residual heat removal system for the swimming pool-type low-temperature heating reactor', *Nucl. Eng. Des.*, vol. 374, p. 111070, Apr. 2021, doi: 10.1016/j.nucengdes.2021.111070.
[32] D. Lu, Y. Zhang, X. Fu, Z. Wang, Q. Cao, and Y. Yang, 'Experimental investigation on natural convection heat transfer characteristics of C-shape heating rods bundle used in PRHR HX', *Ann. Nucl. Energy*, vol. 98, pp. 226–238, Dec. 2016, doi: 10.1016/j.anucene.2016.08.009.
[33] Q. Blondel, N. Tauveron, G. Lhermet, and N. Caney, 'Zeotropic mixtures study in plate heat exchangers and ORC systems', *Appl. Therm. Eng.*, vol. 219, p. 119418, Jan. 2023, doi: 10.1016/j.applthermaleng.2022.119418.
[34] V. S. Gullapalli, 'Estimation of Thermal and Hydraulic Characteristics of Compact Brazed Plate Heat Exchangers'.
[35] P. Horák, M. Formánek, T. Fečer, and J. Plášek, 'Evaporation of refrigerant R134a, R404A and R407C with low mass flux in smooth vertical tube', *Int. J. Heat Mass Transf.*, vol. 181, p. 121845, Dec. 2021, doi: 10.1016/j.ijheatmasstransfer.2021.121845.

ORC SEVILLE 2023
7th International Seminar on O.R.C. Power Systems

© 2024 Editorial Universidad de Sevilla. Este es un artículo de acceso abierto distribuido bajo los términos de la licencia de uso y distribución Creative Commons (BY-NC-ND 4.0)

DOI: https://dx.doi.org/10.12795/9788447227457_22

ASSESSMENT OF TRILATERAL ORGANIC RANKINE CYCLE FOR SOLAR APPLICATIONS WITH INNOVATIVE TURBOEXPANDER CONCEPT

Alessandro Romei*, Andrea Giostri, Andrea Spinelli

Department of Energy, Politecnico di Milano,
Via Lambruschini 4a, 20156 Milano, Italy
*Corresponding Author: alessandro.romei@polimi.it

ABSTRACT

Low-temperature solar collectors coupled with thermal energy storage can enable stable and carbon-free energy production. The key issue is to efficiently convert solar energy into electricity without resorting to complex architecture that may hinder the technical and economic feasibility of the entire system. In this work, we propose a fully integrated organic Rankine cycle (ORC) with the solar field and energy storage, targeting 200 kW. The system consists of a single circuit of the selected organic fluid that passes through the solar collectors, the thermocline thermal energy storage, and the ORC unit. The organic fluid remains liquid inside the solar field and the thermal energy storage, leading to a trilateral thermodynamic cycle. Leveraging the thermodynamic behavior of molecularly complex fluids, the radial-inflow turbine expands from saturated liquid to superheated vapor. Following the idea of White (App. Therm. Eng., 192 (2021), 116852), the nozzle cascade expands the two-phase flow mixtures and delivers superheated vapor to the rotating cascade. In this way, the rotor processes dry organic vapors without incurring mechanical damage or suffering from additional losses due to two-phase interactions. Three maximum temperatures are investigated, and each of them entails a different fluid selection to have the liquid-to-vapor expansion through the stator. Preliminary designs of the radial-inflow turbines are carried out by employing a meanline code, validated for single-phase organic-fluid flows, revealing that feasible designs can be obtained. Based on these results, the proposed technology appears feasible and promising on the technical ground.

1 INTRODUCTION

A number of studies have investigated the potential of trilateral (TORC) or partial evaporation organic Rankine cycles (PE-ORC), for improving the total conversion efficiency of ORC (Smith, 1993; White, 2021). The advantage of partial evaporation is related to the reduction of the isothermal heat of vaporization, allowing for a better temperature match between the heat source and the organic fluid, and resulting in higher usage of the energy available from the heat source (Fischer, 2011).

In the context of distributed concentrated-solar power (CSP) applications, the use of TORC was investigated by several authors (see, e.g., Casati et al., 2013; Perusi & Astolfi, 2019) as a solution able to guarantee an easy integration of thermal energy storage (TES) without the need of a heat transfer fluid loop, i.e. the organic fluid also passes through the solar field and is stored directly in the TES. The organic fluid must remain liquid in these components, hence the fluid is liquid before entering the expansion phase. To overcome the issue related to the two-phase expansion, Casati et al. (2013) proposed a throttling valve to accomplish a flashing process, delivering saturated vapor to the turbine.

A possible solution to avoid the throttling valve can be represented by positive-displacement machines (Smoth, 1996; Astolfi, 2015), as experimental tests proved their excellent capabilities in managing

multi-phase mixtures (Henrik & Per, 2013). Nonetheless, the achievable expansion ratio is limited by the built-in volume ratio of the machine. Multi-stage arrangements can extend the overall volume ratio, but even so, the maximum value is around 20 (Read, 2017), thus restricting the applicability of twin-screw turbines only to low-temperature applications (~ 373 K). To circumvent this limit, thus enabling the uptake of the technology for temperatures up to 523 K, turboexpanders seem the only viable solution. This collides with the lack of turbine designs capable of handling two-phase mixtures efficiently (additional loss due to two-phase interaction) and reliably (droplets impinging rotating cascades).

A remedy can be offered by the peculiar thermodynamics of molecularly complex organic fluids, for which the flashing process may lead the whole liquid fraction to evaporate into superheated vapor (Lai & Fischer, 2012). This concept, introduced by Elliott (1982) and referred to as the wet-to-dry cycle, has been recently revamped by White (2021). Leveraging such fluid characteristics, White (2021) conceived a turbomachinery (estimated efficiency > 85%) in which the nozzle cascade expands the two-phase flow and delivers superheated vapor to the rotating cascade.

In this work, the idea of White (2021) for the turbine concept is adopted to enable a TORC directly coupled with the solar field and TES, thus removing the need for the throttling valve and the flashing unit. To this aim, a number of fluids are preliminarily envisaged, and the effects on the plant and turbine design are highlighted.

2 SYSTEM DESCRIPTION

The direct solar TORC concept is based on the coupling of a CSP solar field (i.e., parabolic trough or linear Fresnel reflectors), a TES, and a two-phase direct expansion ORC. In particular, the working fluid, entering the solar field as sub-cooled liquid, is heated by the concentrated solar radiation till reaching saturated-liquid condition. Since the hot and cold fluid are both in the liquid state, it is possible to directly store thermal energy in a single-tank thermocline (i.e., packed bed with solid filler) without the need for a different storage media, thus allowing the reduction of the cost associated with a heat transfer fluid loop. The saturated liquid is directly expanded in the turbine (Exp) and the discharged superheated steam enters the regenerator (Reg) to pre-heat the working fluid before entering the solar field. Figure 1 shows the layout of the direct solar TORC considered.

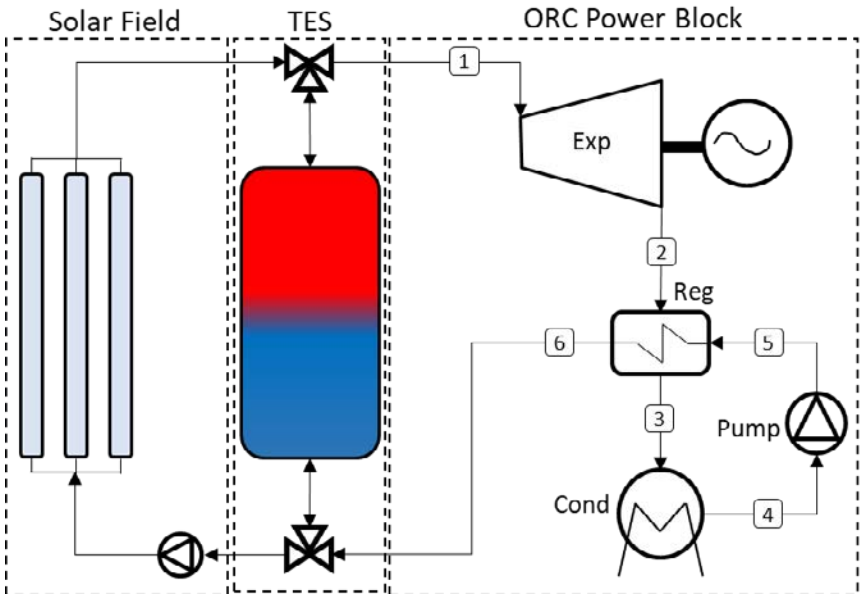

Figure 1: Plant layout. Exp: Radial-inflow turbine. Cond: Condenser. Reg: Regenerator. TES: Thermal Energy Storage.

The electric power output is set to 200 kW; in particular, small-scale CSP plants are recognized as a viable solution to foster technology development thanks to easier land availability and a reduction of bankability issues (Skumanich, 2011). As underlined by Rohani et al. (2021), limited water resources in potentially suitable locations (i.e., semi-desertic areas) point towards the adoption of an air-cooled condenser. As per the system model, the different investigated designs are based on a set of common assumptions as summarized in Table 1 (Casati et al., 2013; Perusi & Astolfi, 2019).

Table 1: Main assumptions considered for the simulation of the ORC system.

Cycle						Pressure drops		
$\dot{W}_{net}$ [kW]	η_{pump}	η_{m-e}	η_{aux}	$\Delta T_{pp,rec}[K]$	x_1	$\Delta P_{sf}[bar]$	$\Delta P/P_{in,reg}$ Liq - vap	$\Delta P/P_{in,cond}$
200.0	0.75	0.97	0.95	5.0	0	1.0	0.03 - 0.02	0.02

In this work, the aim is to assess the feasibility of the system, rather than targeting a detailed system design and optimization. It follows that the focus is on the expander as it is the sole component that is not off-the-shelf. On the contrary, the solar field and heat exchangers employed in this solution are commercially available, while the single-tank TES is a well-proven solution that has been already tested in a real operating environment (Pelay et al. 2017). Therefore, the maximum temperature is imposed as a boundary condition, and a complete model for the solar field is avoided in this preliminary feasibility study. Only cycle efficiency will be discussed, instead of sun-to-electrical (global) efficiency. For the same reason, the pressure drops in the solar collectors (ΔP_{sf}) are assumed constant. Under these assumptions, the points of the thermodynamic cycle can be determined straightforwardly as for a simple recuperative ORC.

2.1 Fluid Screening

142

A number of molecularly complex organic fluids are preliminarily considered, which can potentially enable a complete liquid vaporization within an adiabatic stator. As previously highlighted, the expansion starts from saturated liquid to avoid a two-phase mixture in the solar field and thermal energy storage system, thus enabling a relevant simplification of the plant layout. The constraint of the saturated liquid condition is the main difference from the findings of White (2021), who instead considered the inlet vapor quality as a free parameter to optimize the second-law efficiency of the cycle. As a result of this additional constraint, the number of organic fluids that can accomplish the complete vaporization in the stator is likely reduced. Moreover, as the organic fluid also passes through the solar collector, the analysis is limited to non-flammable fluids. The candidate fluids are linear siloxanes (MM, MDM), cyclic siloxanes (D4, D6), and a Novec fluid (NOVEC649).

To assess the feasibility of the candidate fluids, an isentropic expansion is considered from saturated liquid conditions corresponding to the maximum cycle temperature T_{max} up to the condensation pressure P_{cond}. Three maximum temperatures are considered: $423\,K$, $473\,K$, and $523\,K$. As the maximum temperature increases, the cycle efficiency raises as well. A higher maximum temperature, compatible with the thermal degradation of the selected organic fluid, can be obtained by increasing the concentration ratio of the solar collectors (commercial linear absorbers can reach a maximum temperature equal to 660 K). However, this would increase the CAPEX of the system. Therefore, the optimal T_{max} will result from the techno-economic optimization of these two competing effects. In this study, the aim is the technical feasibility, hence more maximum temperatures are analyzed in this phase. Regarding the minimum cycle temperature, which is the condensation temperature, it directly establishes the minimum pressure in the cycle. To avoid extreme sub atmospheric pressures, which complicate the condenser design and maintenance, the condensation temperature is taken as $T_{cond} = \max(316\,K, T_{sat}(P_{cond} = 0.03\,bar))$.

Figure 2 reveals which fluids can theoretically enable a complete liquid vaporization in the stator. The candidate fluid changes with the maximum temperature. In particular, an increase in T_{max} requires a more complex fluid with a higher critical temperature.

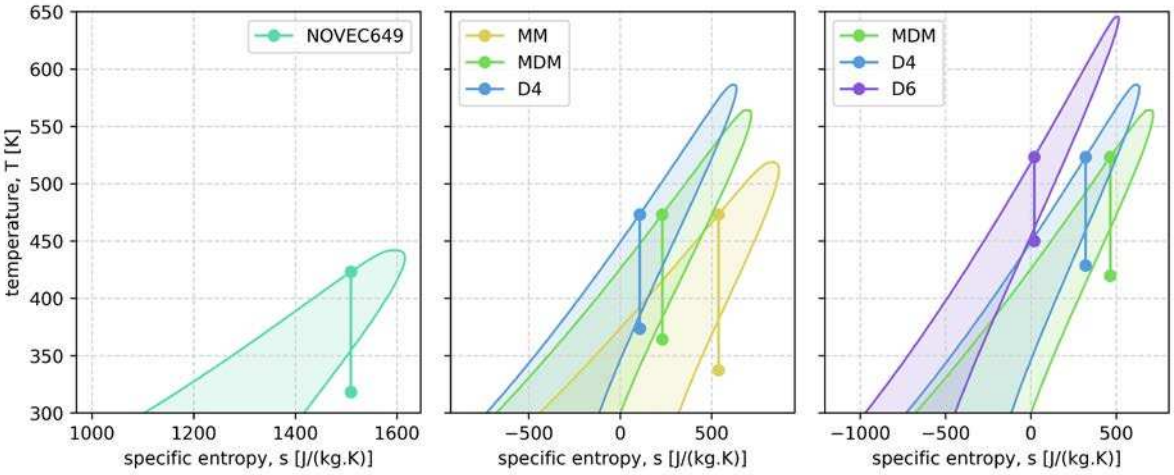

Figure 2: Candidate fluids that can enable a liquid-to-vapor expansion through an isentropic expansion from $P_{sat}(T_{max})$ to $P_{cond} = \max(P_{sat}(T_{cond} = 416\ K), 0.03\ bar)$. Left: $T_{max} = 423\ K$. Middle: $T_{max} = 473\ K$. Right: $T_{max} = 523\ K$.

3 TURBINE MODEL

The turbine performance and design are carried out with an in-house meanline code (Manfredi et al., 2021). The code was validated against the performance data of seven radial turbines, including radial-inflow turbines for ORC application, by Manfredi et al. (2021). The meanline method is based on the solution of one-dimensional continuity, energy, and momentum equations, complemented with specific correlations for losses. It includes the following components: (i) the nozzle, either of converging or converging-diverging type, (ii) the vaneless interspace, (iii) the rotor, with either radial or backswept blades at the inlet, and (iv) a downstream conical diffuser. The model retrieves the full turbine geometry, comprehensive of nozzle/rotor blade angles, clearances, blade thicknesses, cascade pitches, chords and openings, and it evaluates the average flow quantities and thermodynamic state at each turbine section (1, 3*, 3, 4, 6, 7), identified as in Figure 3.

To properly take into account the loss generation mechanisms across each component, a suitable set of empirical models was selected through a loss sensitivity analysis, whose details can be found in Manfredi et al. (2021) together with the resulting optimal set of loss correlations. In a nutshell, the following sources of loss are considered: nozzle passage loss (Glassman, 1976), nozzle trailing-edge loss (Glassman, 1976), friction in the vaneless interspace (Kastner & Bhinder, 1975), rotor passage loss (Baines, 1998), rotor trailing-edge loss (Glassman, 1976), rotor clearance loss (Spraker, 1987), windage loss in the backplate (Daily and Nece, 1960), and kinetic energy loss.

The input parameters to perform the turbine design are the inlet conditions, namely the total pressure, the total temperature, the flow angle, the mass flow rate, and the required pressure ratio. In addition to the system inputs, other design variables, which include several geometrical ratios (i.e., r_{6hub}/r_{6tip}, b_4/r_4, r_1/r_3, and cascade solidities) and a few key dimensionless parameters (flow coefficient, work coefficient), are set based on empirical best practices. The reaction degree is modified to maximize the efficiency while ensuring dry-vapor conditions at the stator outlet, taking a conservative margin from saturation to accommodate potential non-equilibrium effects. For all cases presented afterward, the reaction degree does not exceed the value of 0.3.

The method implements a strategy to handle nozzle choking conditions and three different geometries may be contemporarily investigated: subsonic converging nozzles, converging nozzles in choking conditions with post-expansion, and supersonic converging-diverging nozzles. As the two phases within the stator are considered at the thermodynamic equilibrium, the speed of sound is smaller than their single-phase counterparts, leading to supersonic flows at the stator outlet. Therefore, converging-diverging nozzles are required to handle the supersonic expansion efficiently. The post-expansion ratio in the semi-bladed channel ($3^* \mapsto 3$) is set at 0.92. Finally, the meanline method is not able to handle rotors with supersonic Mach numbers ($M_{w4} > 1$). From a technical ground, supersonic rotors bring additional design challenges and reduced turbine operability (unstarting issues and unique incidence). The turbine efficiency η_{turb}, which is employed in the cycle analysis, is the total-to-static efficiency evaluated at the diffuser outlet.

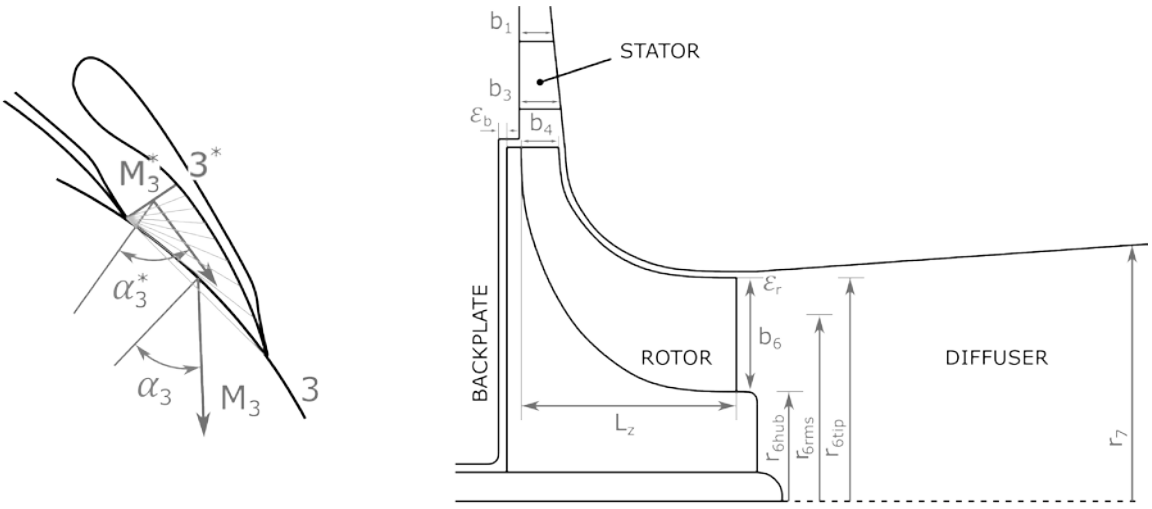

Figure 3: Details of the supersonic post expansion in the converging-diverging stator (left) and meridional channel of the turbine (right) – adapted from Manfredi et al. (2021).

4 RESULTS AND DISCUSSION

In this section, the thermodynamic cycle estimates are discussed alongside the associated turbine design. To integrate the turbine design with the cycle, a first cycle design is run with a constant turbine efficiency ($\eta_{turb} = 0.800$). This first iteration sets the boundary conditions for the turbine design. Once the meanline turbine design is obtained, as well as its isentropic efficiency, the cycle estimates are updated with the new turbine efficiency. A new design would follow due to the mass-flow rate variation to meet the target of 200 kW. However, the deviation is so small that the same turbine design can accommodate the new mass flow rate with negligible variation in efficiency.

Table 2 reports the outcomes of the integrated cycle and turbine analysis. The cycle efficiency increases with the maximum temperature, although such an increase may be hindered by the higher condensation temperature that complies with the technical constraint on the minimum pressure. Such constraint is particularly relevant for cyclic siloxanes, for which the condensation temperature is rather high ($> 348\ K$). A cogenerative exploitation may help compensate for this penalty in electric efficiency, as proposed by Casati et al. (2013).

However, at the highest temperature ($T_{max} = 523\ K$), efficient turbine designs were not found. Although some fluids (i.e., MDM, D4, and D6) can be regarded as potential fluids from a cycle

perspective, a number of design issues occur. Cyclic siloxanes require supersonic relative Mach numbers at the rotor inlet to accomplish the expansion, leading to unfeasible meanline turbine design. On the other hand, the MDM turbine can be designed with $M_{w4} < 1$, but the rotor deceleration in the absolute frame of reference is not sufficient to bring M_6 to subsonic values. This would complicate the diffuser design (converging-diverging shape), and there would be two sonic throats (nozzle and diffuser) that would drastically reduce the turbine operability.

Table 2: Main cycle and turbine parameters. Underlined fluid names indicate the most suitable fluids for the corresponding maximum temperatures. Fluids marked with * lead to not feasible turbine designs (cycle efficiency computed with $\eta_{turb} = 80.0\%$).

Fluid	P_{cond} [bar]	T_{cond} [K]	P_{max} [bar]	T_{max} [K]	η_{turb} [%]	η_{cycle} [%]
Novec649	0.88	318	13.15	423	84.7	11.7
MM	0.14	318	9.21	473	85.3	17.0
MDM	0.03	329	3.02	473	85.6	15.7
D4*	0.03	349	1.80	473	n/a	12.7
MDM*	0.03	329	7.48	523	n/a	20.7
D4*	0.03	349	4.86	523	n/a	18.1
D6*	0.03	404	1.13	523	n/a	12.0

The fluids that maximize the cycle efficiency are Novec 649 ($T_{max} = 423\ K$) and MM ($T_{max} = 473\ K$). The cycle thermodynamic transformations and the evolution of static quantities in the turbine are conveniently reported in a temperature-specific entropy ($T - s$) diagram in Figure 4. In the same figure, the meridional channels of the corresponding turbines are also reported.

As displayed in Figure 4(b), all turbine stators complete the fluid vaporization. The pressure at the stator outlet is consistently lower than the saturation pressure along the same isentrope to accommodate potential non-equilibrium effects, which can delay the complete liquid vaporization (White, 2022).

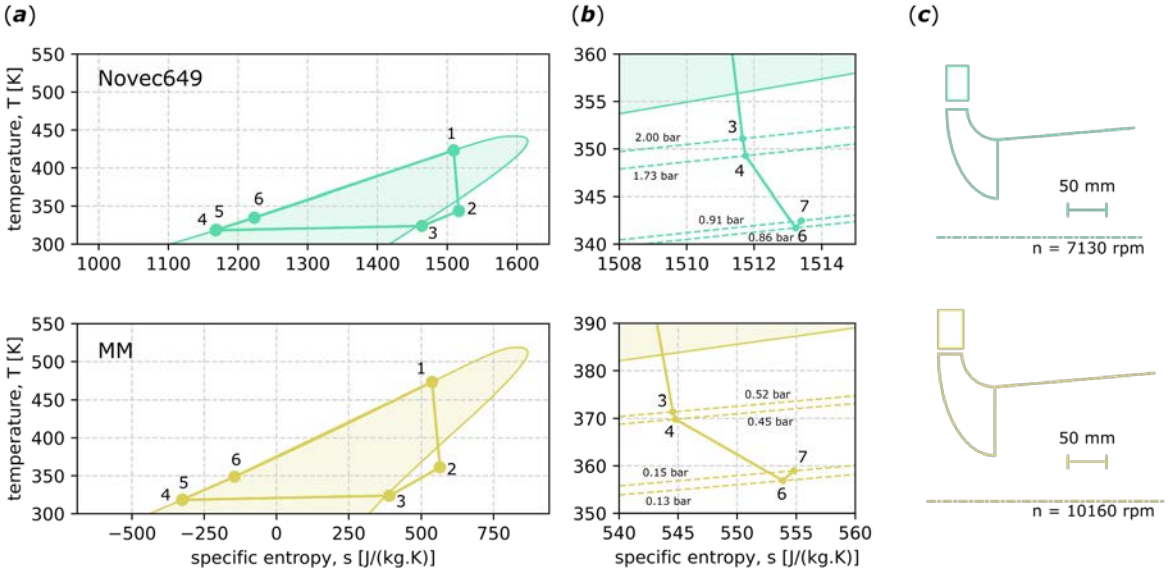

Figure 4: (a) Thermodynamic transformations of feasible TORCs for different temperature levels – see Figure 1 for point nomenclature. (b) Static thermodynamic states in the turbine – see Figure 3 for point nomenclature. (c) Meridional channel of corresponding radial-inflow turbines.

The Novec649 and MM turbine are similar in terms of dimensions. As the MM turbine has to provide a three-times larger specific work, this is accomplished by increasing the centripetal action via the

rotational speed, which raises to 10 000 rpm and is still easily achievable by means of gearboxes available in the market. The stator deals with most of the expansion, delivering an absolute supersonic flow at the rotor, which becomes subsonic in the relative frame of reference. As the two-phase mixture is considered at thermodynamic equilibrium, the two-phase speed of sound is considerably smaller than the two single-phase counterparts (less than $30\,m/s$). It follows that the expansion occurs almost entirely in the diverging part. The absolute Mach number at the stator outlet M_3 is 1.6 for Novec649 and 2.1 for MM. The absolute Mach number at the rotor outlet M_6 are 0.6 for Novec649 and 0.9 for MM, hence a classical divergent diffuser is sufficient to recover a portion of the outlet kinetic energy. To avoid excessively lengthy diffusers, a non-negligible fraction of kinetic energy is still lost, which is responsible for around 5 percentage points of efficiency loss $\Delta\eta_{loss}$, as highlighted in Figure 5.

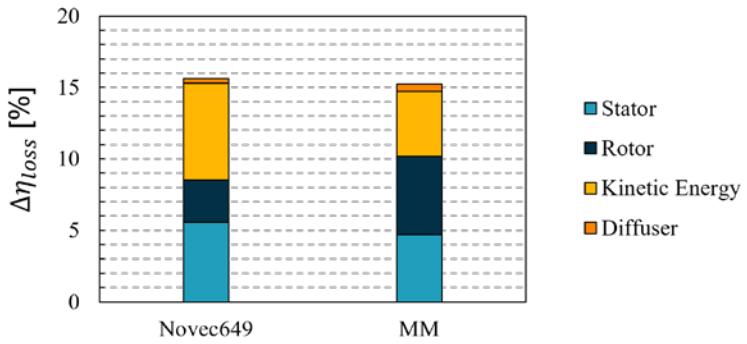

Figure 5: Loss breakdown for radial turbines that maximize cycle efficiency for the two maximum temperature levels (Novec 649 for 423 K and MM for 473 K).

5 CONCLUSIONS

This work has assessed the feasibility of a direct coupling between the organic Rankine cycle, the solar field, and thermal energy storage. The organic fluid remains in the liquid state within the solar field and the thermal energy system, ensuring a relevant technical simplification of these components and reducing the plant footprint. Instead of introducing a throttling valve to deliver dry vapor to the turbine, with a consequent efficiency penalty of the power cycle, a new radial-inflow turbine concept is conceived to handle the two-phase expansion. Leveraging the retrograde shape of the saturation curve of molecularly complex fluids, the whole two-phase expansion is processed within a converging-diverging nozzle, which delivers dry vapor to the subsequent rotor cascade. In this way, blade erosion and additional fluid-dynamic losses associated with the two-phase mixture in the rotating cascade are bypassed.

To explore the potential of this system, three maximum temperatures, namely 423K, 473K, and 523K, are considered. It is found that the optimal fluid changes with the cycle maximum temperature. For 423K, the only non-flammable organic fluid that can enable complete liquid vaporization within the stator is Novec649. Multiple fluids exist for the other two temperature levels, including linear (MM, MDM) and cyclic siloxanes (D4, D6).

Efficient turbine designs have been obtained for temperature levels of 423K and 473K, achieving turbine efficiency of ~ 85%. The optimal cycle efficiencies are 11.7% for Novec649 and 17.0% for MM, respectively, with reference to the two maximum temperatures. At $T_{max} = 473$ K, an efficient turbine has been also designed using MDM as the working fluid. However, due to a technical constraint on the minimum cycle pressure (limited to 0.03 bar), the resulting cycle efficiency is 15.7%, i.e., comparably smaller than the MM counterpart. On the contrary, all candidate fluids for the case at 523K (MDM, D4, D6) lead to unfeasible turbine designs, which would have required dealing with supersonic flows in the rotor and the diffuser as well. Therefore, the proposed concept, i.e., direct trilateral ORC with a radial turboexpander, is feasible only if the maximum temperature achieved in the solar field is smaller than 473 K.

146

Future works will be devoted to developing a model of the overall system; in particular, the effect of the main design parameters will be investigated (i.e., maximum temperature, working fluid) to identify the solution characterized by the best economic attractiveness (i.e., LCOE) taking into account technological constraints. Moreover, the detailed aerodynamic design of the turbo-expander component will be performed to confirm the encouraging, but still preliminary, results coming from the meanline analysis.

NOMENCLATURE

α	absolute flow angle
b	blade height
ε	clearance
η_{cycle}	cycle thermodynamic efficiency
η_{pump}	pump isentropic efficiency
η_{m-e}	mechanical and electrical efficiency
η_{aux}	efficiency for auxiliary consumptions
η_{turb}	turbine isentropic efficiency
M_{w4}	relative Mach number at the rotor inlet
M_6	absolute Mach number at the rotor outlet
L_z	rotor axial length
P_{cond}	condensation pressure
P_{max}	maximum cycle pressure
r	radius
s	specific entropy
T_{cond}	condensation temperature
T_{max}	maximum cycle temperature
$\Delta T_{pp,rec}$	pinch-point temperature in the regenerator
x_1	vapor quality
$\dot{W}_{net}$	electric power

REFERENCES

Astolfi (2015), “Techno-economic optimization of low temperature CSP systems based on ORC with screw expanders”, Energy Proc. 69, 1100-1112.

Baines (1998). “A meanline prediction method for radial turbine efficiency”. No. 11, Professional Engineering Publishing for the Institution of Mechanical Engineers, pp. 45–56.

Casati et al. (2013), “Thermal energy storage for solar-powered organic Rankine cycle engines”, Sol. Energy 96, 205-219.

Daily & Nece (1960). “Chamber dimension effects on induced flow and frictional resistance of enclosed rotating disks”. Journal of Fluid Engineering, 82(1), pp. 217–230.

Elliott (1982). “Theory and tests of two-phase turbines”. Tech. rep., Jet Propulsion Laboratory, California Institute of Technology, Pasadena.

Lai & Fischer (2012). “Efficiencies of power flash cycles”. Energy 44, 1017-1027.

Fischer (2011). “Comparison of trilateral cycles and organic Rankine cycles”. Energy 36, 6208-6219.

Glassman (1976). “Computer program for design analysis of radial-inflow turbines”. Tech. rep., NASA Technical Note, TN D-8164, Washington D.C., USA.

Henrik & Per (2013), “Experimental investigation of a Lysholm Turbine operating with superheated, saturated and 2-phase inlet conditions”. App. Therm. Eng. 50(1), 1211-1218.

Kastner & Bhinder (1975). “A method for predicting the performance of a centripetal gas turbine fitted with a nozzle-less volute casing”. In ASME Turbo Expo: Vol. V01BT02A003.

Manfredi et al. (2021). “A reduced-order model for the preliminary design of small-scale radial inflow turbines”. ASME Turbo Expo, paper no. GT2021-59444.

Pelay et al. (2017), “Thermal energy storage systems for concentrated solar power plants”. Renew. Sust. Energy Reviews 79, 82-100.
Perusi & Astolfi (2019), “Comparison between direct and indirect ORCs for CSP applications”, Proceedings of 5th International Seminar on ORC Power Systems, Paper ID: 58.
Read et al (2017). “Optimisation of power generation cycles using saturated liquid expansion to maximise heat recovery”. Proc. Inst. Mech. Eng., Part E: J. Proc. Mech. Eng. 231(1), 57-69.
Rohani et al. (2021). “Optimization of water management plans for CSP plants through simulation of water consumption and cost of treatment based on operational data”. Sol. Energy 223, 278-292.
Skumanich (2011), “CSP at a crossroads: The first solar electric power plants are still proving their worth after three decades, so why aren't we seeing more CSP reach the development stage?”. Renew. Energy Focus 12, 52-55.
Smith (1993). “Development of the trilateral flash cycle system: Part 1: Fundamental considerations”. Proc. Inst. Mech. Eng., Part A: J. Power Energy 207 (3), 179-194.
Smith et al. (1996). “Development of the Trilateral Flash Cycle System: Part 3: The Design of High-Efficiency Two-Phase Screw Expanders”. Proc. Inst. Mech. Eng., Part A: J. Power Energy, 207 (1), 75-93.
Spraker (1987). “Contour clearance losses in radial inflow turbines for turbochargers”. ASME Paper, 871.
White (2021). “Cycle and turbine optimisation for an ORC operating with two-phase expansion”. App. Therm. Eng. 192, 116852.
White (2022). “Investigating the wet-to-dry expansion of organic fluids for power generation”. Int. J. Heat and Mass Transfer 192, 122921.

ORC SEVILLE 2023
7th International Seminar on O.R.C. Power Systems

© 2024 Editorial Universidad de Sevilla. Este es un artículo de acceso abierto distribuido bajo los términos de la licencia de uso y distribución Creative Commons (BY-NC-ND 4.0)

DOI: https://dx.doi.org/10.12795/9788447227457_25

Evaluation of the performance of an axial one-stage 10kW turbogenerator through experimental testing

Piotr Klimaszewski[1,*], Piotr Klonowicz[1], Łukasz Witanowski[1], Tomasz Suchocki[1], Piotr Lampart[1], Eugeniusz Ihnatowicz[2], Łukasz Antczak[2], Dawid Zaniewski[2], Łukasz Jedrzejewski[2]

[1]*Institute of Fluid-Flow Machinery, Polish Academy of Sciences, Gdansk, Poland*
[2]*MARANI Sp. z o.o., Zabrze, Poland*

*Corresponding Author: pklimaszewski@imp.gda.pl

ABSTRACT

The paper describes the results of experimental research on a prototype one-stage turbo-generator with a nominal power of 10 kW and a rotational speed of 24 000 rpm. The expander at the Institute of Fluid-Flow Machinery, Polish Academy of Sciences was developed as part of the R&D project with Marani company. The unit construction consists of an overhanging rotor and shaft mounted on rolling bearings. The turbo-generator was tested on a specially constructed laboratory test stand in the first stage. Compressed air instead of refrigerant gas (R1233zd) was used. The test results converged with the parameters obtained using the RANS simulation. The convergence for the turbine mass flow was 97% of the value obtained in the CFD model, which is satisfactory. The power generated by the turbo-generator, which was compared at this stage, also achieved satisfactory convergence (95% to 97%) with the calculation model. These tests allowed determine the compliance of the adopted design assumptions and confirmed the correctness of the calculation tools used.
The next stage of work was to examine the ORC unit in operating conditions. That stage was aimed at checking the correct work of the machine with the ORC system. The turbine achieved internal efficiency calculated from temperatures at a level slightly lower than that obtained from numerical calculations (total-to-static efficiency). The efficiency was equal to about 73%, and the difference between calculated and measured values do not exceed 0.25 pp. (percentage point). The electric efficiency was about 65% and a maximum electric power output of 6.8 kW was measured.

1 INTRODUCTION

The rise in energy consumption over the past century has led to increased emissions of greenhouse gases, subsequently resulting in a rise in global temperatures. Continuing on this trajectory could yield detrimental effects, such as escalating destructive weather phenomena (Ramanathan and Feng, 2009). The industry sector was one of the first to enact climate regulations, with various sectors having unique methods for reducing CO2 emissions. Particularly in steel and aluminium production, waste heat recovery presents an ideal opportunity to boost overall process efficiency.

The Organic Rankine Cycle (ORC) technology has emerged as a promising solution to facilitate energy recovery from waste heat within the industry. ORC systems are specifically engineered to synergize with industrial apparatuses such as compressors, large engines, or various eco-friendly technologies. The fundamental components of ORC systems include a turbine, pump, condenser, and evaporator. These systems operate based on the Organic Rankine Cycle. The fluids utilized in this context differ from water and include, for instance, hydrocarbons and refrigerants. The fluid selection process was thoroughly described by (Klimaszewski *et al.*, 2019).

ORC turbine design offers a fertile ground for optimization. The rotor and stator geometry can be numerically analyzed using specialized software. Various publications address this issue. (Witanowski

et al., 2023) presented the Nelder-Mead optimization of a single-stage axial turbine in their paper. The turbine, functioning within the ORC system, utilized R7100 as the working fluid. The optimization results were promising, with the total-to-static efficiency of the new geometry increasing by about 5.5 percentage points at the design point.
An alternate approach involves optimizing the ORC turbine to operate in two distinct work modes: for parameters appearing in cogeneration and condensation mode. A multi-objective optimization for a turbine working with MM was conducted by (Witanowski *et al.*, 2023). The authors identified a flow path with improved efficiency using the Implicit Filtering algorithm. A substantial efficiency increase of 4.8 percentage points was observed in the cogeneration mode, and in the cogeneration mode turbine efficiency, it increased by about 3.1 percentage points. Another significant approach in the optimization field involves hybrid algorithms, as the blade shape optimization geometry discussed (Witanowski *et al.*, 2023).

Authors of various publications have conducted experimental tests on ORC turbines, either on a test stand or as part of an ORC system. Kang, S. H. (Kang, 2016) describes preliminary tests of an ORC turbine coupled with an ORC system. The working fluid was R245fa. A two-stage radial expander was used, with the generator directly connected to the turbine. The installation achieved a maximum electric power of 39 kW, a cycle efficiency of 9.8%, and turbine efficiency based on output equal to 58.4%. The author highlighted the potential for further efficiency improvements via the reduction of heat and pressure losses.

The article (Fu *et al.*, 2015) details an ORC system designed for an electric power output of 250 kW. The preliminary test results were quite satisfactory. The system achieved a maximum net power output of approximately 219.5 kW, a maximum thermal efficiency of 7.94%, and a turbine speed of 12,386 RPM, with an isentropic efficiency equal to 63.7%. The working fluid used was the refrigerant R245fa. The power generated by the turbine was transferred to the generator via a gearbox, with the electric generator maintaining a rotational speed of 3600 RPM.

150

The authors of the publication (Borsukiewicz-Gozdur, 2013) outlines experimental research conducted on an ORC power plant. The ORC installation was designed to operate with a geothermal heat source, with hot water temperatures ranging from 66ºC to 111ºC. The experiment also involved a hermetic turbine working with R227ea fluid as part of the ORC system. The turbine generator was designed for a rotational speed of 3000 RPM, a standard value in the power grid. The electric efficiency of the ORC system was approximately 4.88%.

2 TEST STAND

The test stand was built in the laboratory of the Institute of Fluid Flow Machinery Polish Academy of Sciences. The turbine (no. 2 in Figure 1) was mounted on the test stand. The test stand consists of a compressor connected with an air heater and flow meter (no. 1 in Figure 1), a system of valves for fluid control connected by pipelines (no. 4 in Figure 1), a generator cooling system (no. 5 in Figure 1). The measuring system includes pressure sensors and thermocouples (no. 6 in Figure 1) that elements are connected to a device for data collection. The mobile measurement instruments were used to control the machine's mechanical vibrations and the shaft's displacement.

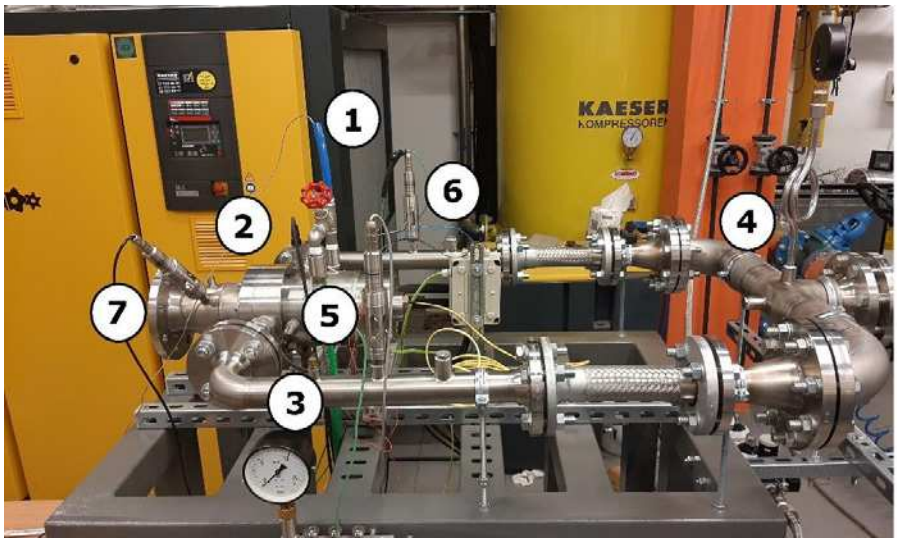

Figure 1 Turbine 10 kW on a test stand, 1-compressor, 2-turbine, 3- feed pipeline, 4 - control valves, 5 – cooling system, 6 – pressure transmitter, 7- turbine outlet.

The ORC turbine was designed to work with R1233zd, a refrigerant with low global warming and ozone deployment potential. The 10 kW turbine investigation on the test stand was carried out with substitute medium - air. The main reason for using air instead of R1233zd on the laboratory test stand was the complexity of building a system for testing with refrigerant. At this stage, the primary goal was to test the mechanical construction, specifically the vibration level in the x-axis. The test stand allows also to check of the mechanical working parameters of the turbine and check the quality of fabrication flow system elements.

151

The installation works as follows: compressed air goes by pipelines from the compressor to the heater, and hot air is divided into two streams for the left and right inlets on a turbine. The outlet is open, the air goes to atmospheric conditions. The pipeline delivering fluid to the turbine was marked as no. 3 in Figure 1, the turbine outlet was shown as no. 7 in Figure 1. The fluid flow throw machine was controlled, the parameters like temperature, pressure and mass flow were measured and analysed. The laboratory installation includes the main cycle five pressure and five temperature sensors.
The test stand also includes a separate cooling water system used for generator cooling (more details were described in the article (Zaniewski *et al*., 2023)).
The power system consists of a water resistor and an electro-energetic converter for controlling electric power parameters.

3 10 KW TURBO-GENERATOR TESTS

Tests in the laboratory consist of three phases. The first phase include a direct load of the turbogenerator, the water resistor was directly connected to the turbine generator, and the electric load was controlled by the mechanical movement of elements. When the parameters of the research were satisfied then, the next phase include the use electro-energetic device. The device connects the turbogenerator with the electric grid indirectly, allow also to control its work parameters. In the second phase electronic device was used to connect indirectly with a water resistor. In the third phase, the connection was prepared to an electro-energetic grid.
The observed parameters were static pressure on an inlet, total temperature on the inlet, the total temperature on the outlet, mass flow, rotation speed and electric power.
In that part of the investigation, parallel conduct tests of vibrations parameters were conducted (Figure 2). Necessary to define the quality of the mechanical work of a machine. All tests were achieve satisfied values and did not exceed recommend values for that kind of micro-turbines. The recommended values

are based on the standard ISO 20816 (Industrial machinery with a power rating above 15 kW and operating speeds between 120 r/min and 30 000 r/min).

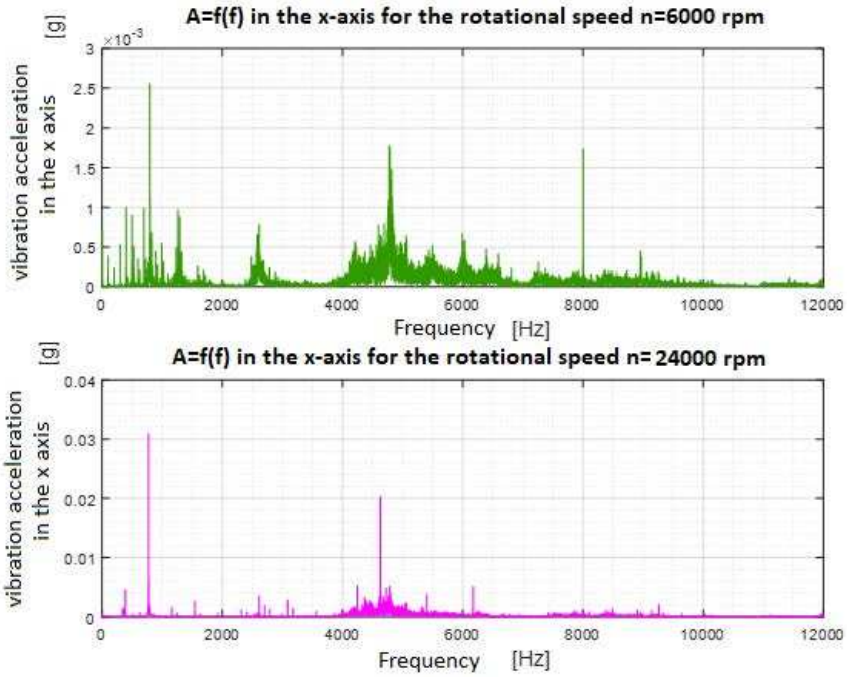

Figure 2 The amplitudes of vibration acceleration in the Y axis for the frequency spectrum up to 12000 Hz recorded for the speed of 6000 rpm (upper graph) and the nominal speed of 24000 rpm (lower graph) respectively.

152

The amplitudes of vibration acceleration in the X axis for the rotational speed of 6000 rpm and 24000 rpm are shown. The peak values achieved at nominal speed are an order of magnitude higher than at much lower rotational speeds.

4 CFD RESULTS ANALYSIS COMPARED TO EXPERIMENTAL RESULTS

The CFD calculations were used to verify experimental results. The mathematical model was solved with the use of CFD methods. Numerical methods include the body's inlet domain and the diffuser's outlet domain. The addictive losses connected with bearing and windage were also included.
The mash was present in Figure 3. The computational mesh was prepared with Ansys Turbogrid and ICEM software. The mesh domain includes a rotor and stator consisting of 26 629 378 elements and 28 430 740 nodes, the mesh is hexahedral. The area with more density mesh includes the rotor and stator, that area was the most important for calculations of fluid flow and boundary layers. The stator mesh domain includes 4 644 640 nodes and 4 227 440 elements. The rotor domain includes 10 850 840 nodes and 10 107 860 elements.

The Ansys CFX code uses the RANS equations with the k-ω SST turbulence model to describe fluid dynamics. The finite volume method with a second-order discretization scheme is used to solve these equations. The inlet boundary conditions include total pressure, total temperature, and flow direction. The outlet boundary condition is the average static pressure. The frozen rotor technique, also known as the multiple reference frame method, is used to handle the stationary stator domain and the moving rotor domain.

The total pressure on the inlet domain used for calculation was equal to 1.82 bar and the total temperature was set at 45.3°C, the turbulence was on the medium intensity (5%). The analysis performed in this study was stationary, with a constant rotor speed equal to 13,700 rpm. The

experimental and simulation results were compared and it was assumed that the fluid used in the simulation was air, modelled as an ideal gas. On the outlet domain, relative pressure was equal to 1.027 bar and the pressure profile blend was set as 0.05.

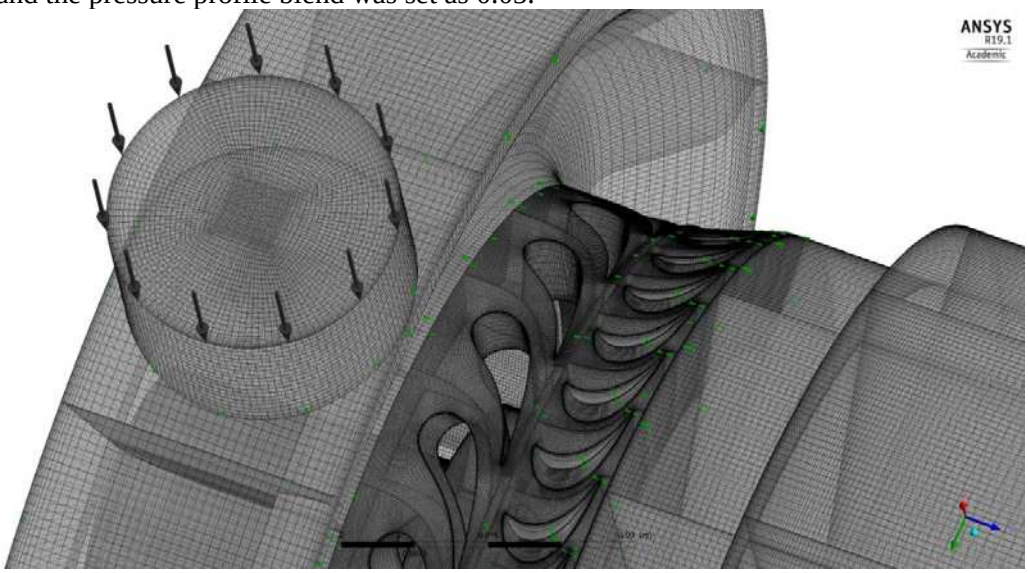

Figure 3: Computation mesh, visible an area with high density

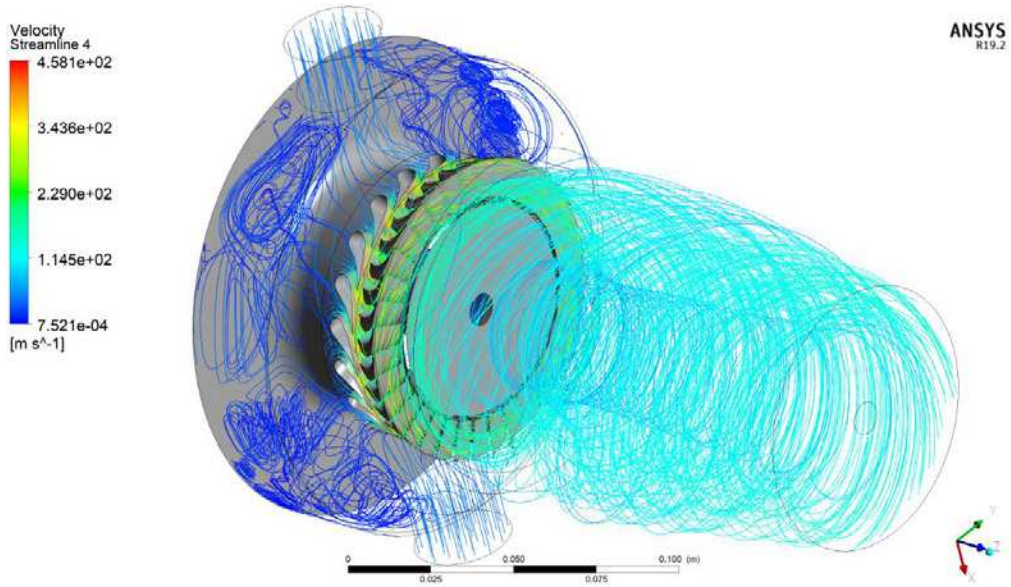

Figure 4: Streamlines for nominal works parameters.

The streamlines were presented in Figure 4. The area with higher velocity is marked by red colour. The lower speed is shown by blue colour. The flow throws the rotor and stator correctly and in line with the assumptions. The highest speed was observed at the stator outlet. The streamlined figure on the impeller area does not appear incorrect phenomenon. That means the flow system was correctly designed.
The pre-processing was conducted with the use of Ansys CFX pre-processor, and numerical calculations were conducted with the use of Ansys CFX solver.

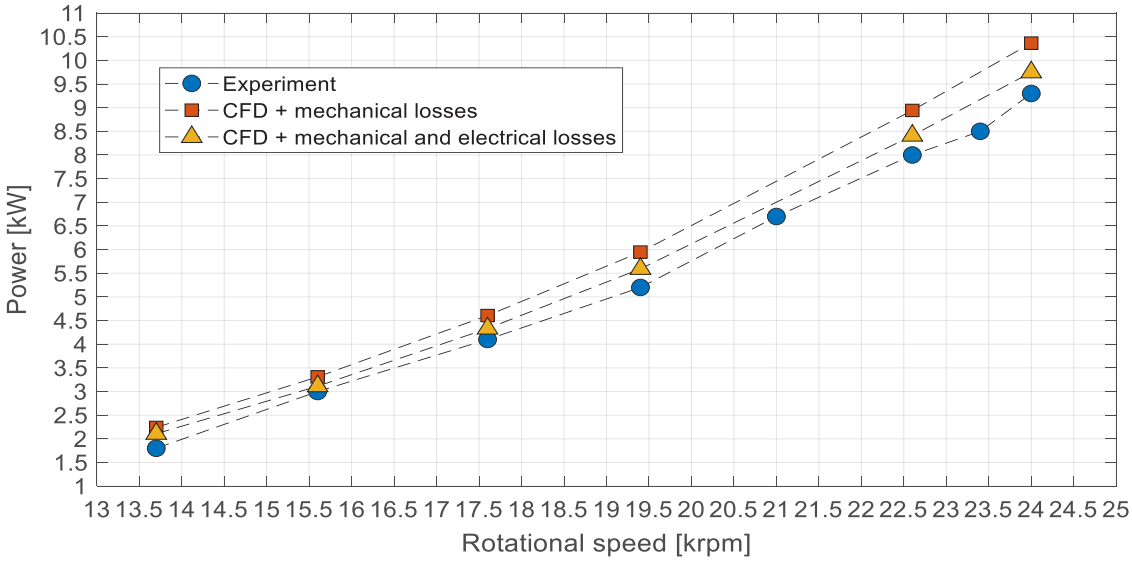

Figure 5 Electric power achieve in the experiment in the function of rotational speed comparison to functions of rotation speed for choosing numerical models.

The results of numerical calculations and experimental data were presented in Figure 5. The convergence for nominal parameters was on the satisfied level, for low values of rotation speed was equal to 97% for high 95%. The electrical efficiency of the generator was equal to 94%. The electrical efficiency value was determined based on the information provided in the technical documentation of the electric generator and energy conversion system. This value also takes into account the losses that result from the experience of the Institute of Fluid Flow Machinery team. By considering both the documented specifications and the team's expertise, a comprehensive assessment of the electrical efficiency was achieved. The red points describe the results of the experiment, the blue points show the results of CFD calculation considering losses in bearings and friction losses values, and the orange points includes also electrical losses. The achieved values of CFD calculations include the domain of the full stator domain and rotor domain.

154

5 THE RESULTS OF TURBINE TESTS ON THE ORC UNIT SYSTEM

The next stage of tests was a laboratory test of the ORC unit with conditions similar to industrial. The turbine was mounted in the ORC installation, the pipelines of the inlet and outlet were connected, and the measured devices were calibrated. The tests of the turbine were conducted on the designed, working fluid R1233zd. The tests of ORC installation were conducted in the laboratory in controlled conditions. The heat was assured by the heating system based on the gas boiler. The main object of the experiment was the turbine (Figure 6 no.1). The control of the cycle parameters was assured by the pump (Figure 6 no.2), flow meter (Figure 6 no.5), control valve (Figure 6 no.4) and heat exchanger (Figure 6 no.3). The level of vibration does not exceed safety values. Measured parameters of fluid flow in the different points of the fluid system confirmed the correction of calculation. The construction was hermetic, there are no appear leakages or other unexpected damages.

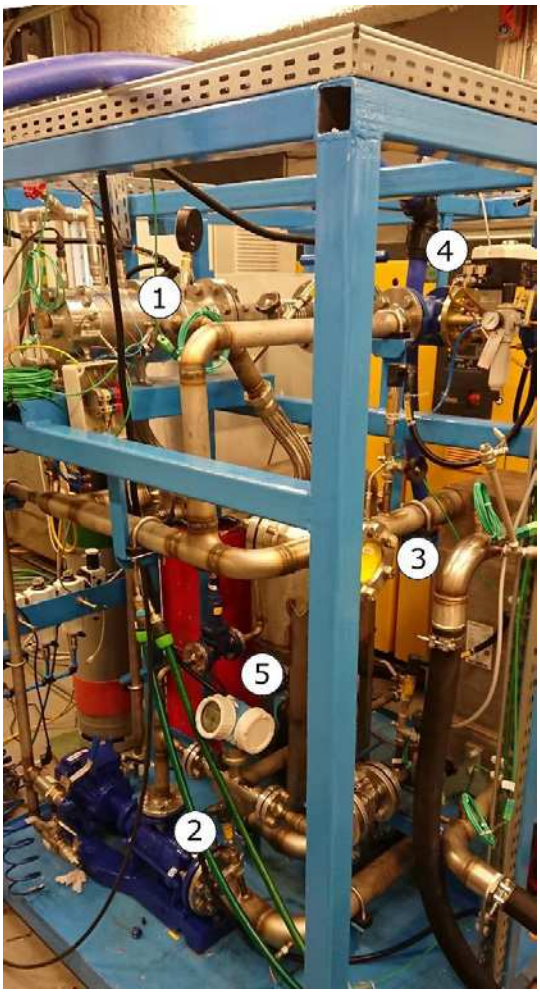

Figure 6 Turbine installed on ORC plant, 1 – turbine, 2 – feed pump, 3 – heat exchanger, 4 – control valves, 5 – flow meter.

The third stage of tests was conducted in industrial conditions. The ORC system was connected to an air compressor, and the hot compress air was a source of waste heat. The data for parameter calculation were collected based on the sensor system. Sensors, similar to the preview stage of the experiment measured different parameters on the ORC loop like temperature, pressure and mass flow. The data from sensors allow for calculating the efficiency of the turbine and ORC cycle. The efficiency was calculated with the use of different parameters, first base on temperature calculation, second base on power generated by water resistor, and third base on power achieve in electro energetic system. The first method get the best results and efficiency was the highest, the value was equal to about 72%. In that method, temperature and pressure values were used to find the enthalpy value for fluid. Then based mass flow was calculated efficiency with the use of Equation (1). The efficiency calculated by the second method achieve a value of about 60%, the third method get the worse results, and the efficiency was about 57%. The changes in efficiency in the function of time was presented in Figure 7.

$$\eta_t = \frac{h_1 - h_2}{h_1 - h_{2s}} \quad (1)$$

The efficiency of the ORC cycle was presented in Figure 8. The chart presents a change in the efficiency of the function of time. The ORC cycle efficiency achieves the highest value base on the temperature measurements. A description of the calculation method of cycle efficiency was present in Equation (2). This equation also takes into account the loss parameter, including pump energy consumption, pipe

losses, and more. The calculation base on the temperature achieves a value of 6%. The temperature of hot water, the source of heat for ORC installation, was equal to 74°C on the evaporator inlet. The temperature of cooling water, at the condenser inlet was equal to 12°C. The second efficiency taking into account the process of energy conversion and electrical losses achieved a value of about 4.6%.

$$\eta_c = \frac{\dot{m}(h_2 - h_1)}{Q_s} - P_{AX} \quad (2)$$

The peaks visible on the charts result from the unstable work of the heat source. The industrial tests get satisfactory results. The main goals were achieved.

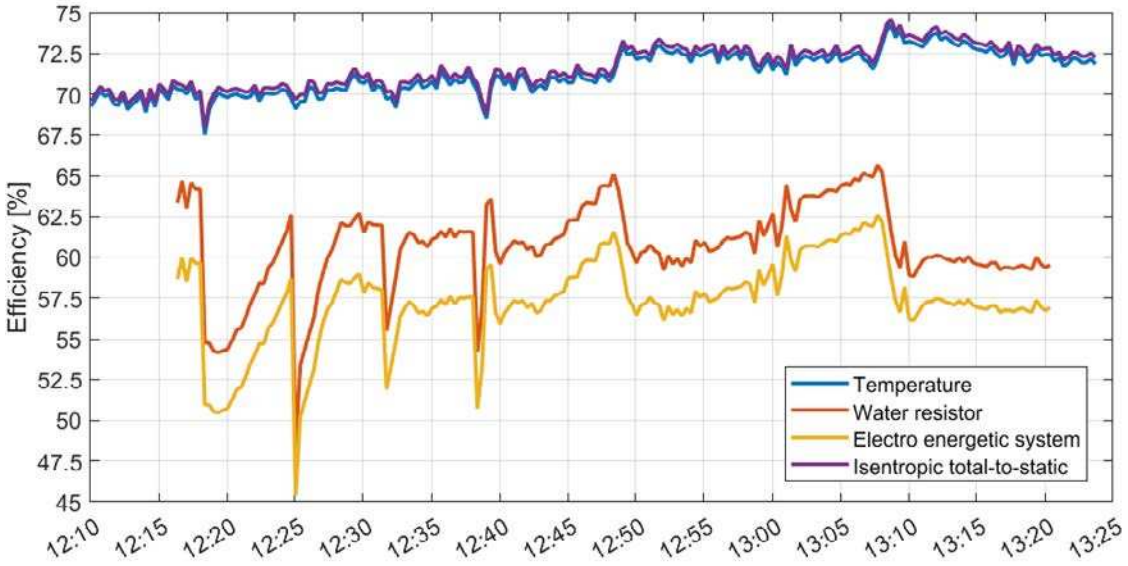

Figure 7 Efficiency of the turbine based on data from different measurement systems.

156

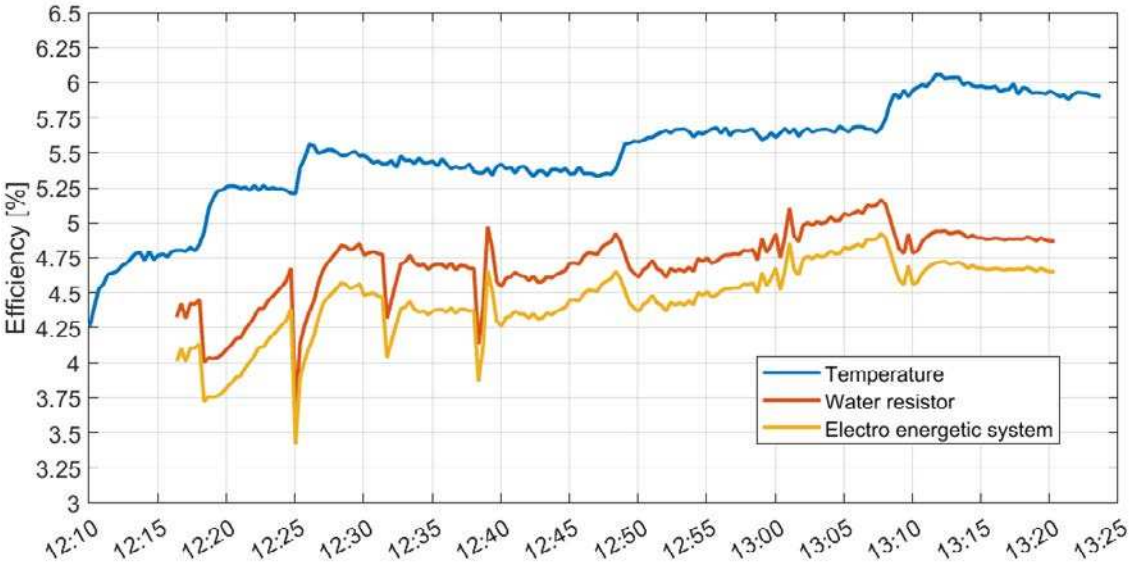

Figure 8 The ORC cycle efficiency base on different source

6 CONCLUSIONS

In this study, a three-phase experimental approach was employed to assess the performance and efficiency of a turbine incorporated into an ORC unit. This procedure involved independent turbine evaluations, laboratory tests, and full-scale industrial testing. The following conclusions summarize the key findings from the investigation.

- The experiment proceeded in three distinct stages. Initially, tests were conducted to disconnect the turbine on a dedicated test stand. Subsequently, laboratory tests were carried out to evaluate the turbine mount integrated with the ORC unit. The final phase encompassed testing the ORC unit within an industrial setting.
- The standalone turbine tests delivered satisfactory results, generating an electric power output of approximately 9 kW and achieving a rotor speed of 24,000 RPM.
- The second phase of testing proved equally successful. The primary focus was on examining the mechanical connections and operating parameters of the turbine when coupled with the ORC system under laboratory conditions. The results aligned with the predictions, with the observed data closely matching the CFD simulation values.
- The ORC unit exhibited satisfactory performance during the industrial testing phase, achieving an efficiency rating of approximately 4.6%.
- Based on the empirical data collected, it is concluded that the machine operates optimally in terms of field flow efficiency.

NOMENCLATURE

h_1	enthalpy on turbine inlet	[kJ/kg]
h_2	enthalpy on turbine outlet	[kJ/kg]
h_{2s}	isentropic enthalpy	[kJ/kg]
$\dot{m}$	mass flow	[kg/s]
P_{AX}	cycle losses	[-]
Q_s	heat source	[kJ/s]
η_c	efficiency of the cycle	[-]
η_t	efficiency of the turbine	[-]

REFERENCES

Zaniewski, D., Klimaszewski, P., Klonowicz, P., Witanowski, Ł., Lampart, P., Jędrzejewski, Ł., Suchocki, T. (2023). Organic Rankine cycle turbogenerator cooling – Optimization of the generator water jacket heat exchange surface. *Applied Thermal Engineering*, 223(January), 120041. https://doi.org/10.1016/j.applthermaleng.2023.12004

Witanowski, Ł., Ziółkowski, P., Klonowicz, P., Lampart, P. (2023). A hybrid approach to optimization of radial inflow turbine with principal component analysis. *Energy*, *272*(January). https://doi.org/10.1016/j.energy.2023.127064

Witanowski, Ł., Klonowicz, P., Lampart, P., Ziółkowski, P. (2023). Multi-objective optimization of the ORC axial turbine for a waste heat recovery system working in two modes: cogeneration and condensation. *Energy*, 264(October 2022), 126187. https://doi.org/10.1016/j.energy.2022.126187

Witanowski, Ł., Klonowicz, P., Lampart, P., Klimaszewski, P., Suchocki, T., Jędrzejewski, Ł., Zaniewski, D., Ziółkowski, P. (2023). Impact of rotor geometry optimization on the off-design ORC turbine performance. *Energy*, 265(December 2022), 126312. https://doi.org/10.1016/j.energy.2022.126312

Ramanathan, V., Feng, Y. (2009). Air pollution, greenhouse gases and climate change: Global and regional perspectives. *Atmospheric Environment*, 43(1), 37–50.

Klimaszewski, P., Zaniewski, D., Witanowski, Ł., Suchocki, T., Klonowicz, P., Lampart, P. (2019). A case study of working fluid selection for a small-scale waste heat recovery ORC system. *Archives of Thermodynamics*, *40*(3), 159–180. https://doi.org/10.24425/ather.2019.129999

Kang, S. H. (2016). Design and preliminary tests of ORC (organic Rankine cycle) with two-stage radial turbine. *Energy*, *96*, 142–154. https://doi.org/10.1016/j.energy.2015.09.040

Fu, B.-R., Lee, Y.-R., Hsieh, J.-C. (2015). Design, construction, and preliminary results of a 250-kW

organic Rankine cycle system. *Applied Thermal Engineering*, *80*, 339–346. https://doi.org/10.1016/j.applthermaleng.2015.01.077

Borsukiewicz-Gozdur, A. (2013). Experimental investigation of R227ea applied as working fluid in the ORC power plant with hermetic turbogenerator. *Applied Thermal Engineering*, *56*(1–2), 126–133. https://doi.org/10.1016/j.applthermaleng.2013.03.039

ACKNOWLEDGEMENT

This work has been founded by The National Centre for Research and Development and from The Smart Growth Operational Programme (European funds) within the project No. POIR.01.01.01-00-0512/16 carried out jointly with the Marani Company.

ORC SEVILLE 2023
7th International Seminar on O.R.C. Power Systems

© 2024 Editorial Universidad de Sevilla. Este es un artículo de acceso abierto distribuido bajo los términos de la licencia de uso y distribución Creative Commons (BY-NC-ND 4.0)

DOI: https://dx.doi.org/10.12795/9788447227457_26

Investigation of the turbulence level and the vortex shedding in a turbine cascade working with an organic vapor at subsonic Mach numbers

Leander Hake[1,*], Stephan Sundermeier[1], Stefan aus der Wiesche[1], Camille Matar[2], Paola Cinnella[2], Xavier Gloerfelt[3]

[1] *Muenster University of Applied Sciences, Steinfurt, Germany*
[2] *Sorbonne University, Paris, France*
[3] *ENSAM - Paris Tech, Paris, France*

*Corresponding Author: leander.hake@fh-muenster.de

ABSTRACT

Detailed turbulence and trailing edge vortex shedding measurements employing hot-wire anemometry and numerical simulations using a high-resolution unsteady Reynolds-averaged Navier-Stokes method were conducted for the high subsonic flow of the organic vapor Novec 649 through the VKI turbine cascade at elevated pressure and temperature level. Turbulent spectra downstream and upstream of the cascade were obtained and analyzed. The simulations indicated that acoustics waves (shed shockwaves) and locally supersonic flow occurred at the trailing edge even at a moderate isentropic exit Mach number of 0.7. Strong evidence for that loss-relevant mechanism was found in the hot-wire signals. The vortex shedding frequency depended primarily on the Reynolds number, not the Mach number.

1 INTRODUCTION

Predicting turbulence levels and vortex shedding in turbine cascades is of significant engineering relevance, especially for efficiency calculations. Although powerful computational fluid dynamics (CFD) methods have been developed to simulate the development of turbulence quantities and unsteady flow phenomena in turbomachinery, their accuracy and reliability limits are unclear. That issue is discussed in detail in a corresponding review article by Sieverding and Manna (2020). Especially for organic vapor flows, relatively little is reported regarding the turbulent flow through a turbine cascade and the development of turbulent quantities and transonic vortex shedding. Experimental data are strongly needed to validate numerical methods for these flows.

Sanz et al. (1998) conducted a numerical and experimental investigation of the wake flow downstream of a linear turbine cascade. They studied the turbulent kinetic energy distribution of airflow through the so-called VKI cascade, described by Kiock et al. (1986). In the wake of the blades, relatively high turbulent energy contents were observed. The employed turbulence models (i.e., Spalart-Allmaras and low-Reynolds-number k-ε) could predict the profile pressure distribution and other flow quantities but failed regarding the decay of the turbulent kinetic energy downstream of the cascade. The authors suggested that the periodic vortex shedding caused significant discrepancies between the measured and computed turbulent kinetic energy k from the blunt trailing edge. A steady Reynolds-averaged Navier-Stokes (RANS) approach does inherently not cover such unsteady phenomena, and unsteady RANS (URANS) methods or large-eddy-simulations (LES) or even direct numerical simulations (DNS) are required to resolve these unsteady flow features. Sanz and Scheier (2021) recently reported that the qualitative prediction of secondary flows in a transonic turbine stage was, in their own words, “good,” but their unsteady RANS simulation failed regarding turbulence production and destruction. Significant deviations of more than 100 % were reported between the measured and computed turbulent kinetic energy k at different downstream stations.

That issue also turns the attention to the anisotropy of turbulence in cascade flows. The existence of non-isotropic structures in the wake flow of low-pressure steam turbine airfoils was experimentally

indicated by Antos et al. (2018). Several experimental studies performed with air as a working fluid (e.g., Zunino et al. (1987), Gregory-Smith et al. (1988), Dossena et al. (1993), Ames and Plesniak (1995), and Volino et al. (2008)) demonstrated that high turbulent kinetic energy levels can occur in the wake of turbine blades. Melzer and Pullan (2019) presented schlieren pictures demonstrating the existence of acoustic waves (shed shockwaves) at a Mach number of about 0.65 for an idealized trailing edge configuration. It is reasonable to assume that these acoustic waves and their reflections in the cascade contribute significantly to the total turbulent kinetic energy. Since vortex shedding and acoustic wave propagation are coherent fluid motion phenomena, a clear distinction between the true turbulent kinetic energy k and recorded fluctuations is needed for a correct data interpretation and comparison with the outcome of CFD methods.

The present experimental and numerical case study was conducted to provide data for turbulent quantities for a high-subsonic organic vapor flow through a representative turbine cascade. The objective was to increase the understanding of trailing edge flows, acoustic wave propagation, and the production of turbulent kinetic energy. The experimental work is a direct continuation of recent studies regarding losses in organic Rankine cycle (ORC) turbine cascades (i.e., Hake et al. (2022, 2023)). Still, the present investigation focused on turbulence behavior and unsteady flow phenomena. The recently tested hot-wire anemometry described in Hake et al. (2022a) for high-speed organic vapor flows was utilized for this. The present numerical work aimed to study the prediction capabilities of unsteady RANS methods for high-speed organic vapor flows in more detail. Matar et al. (2023) recently demonstrated that steady RANS methods have inherent difficulties in predicting turbulent flow in the wake of a cylinder. In contrast, unsteady RANS (URANS) methods can significantly increase our qualitative understanding of turbulent compressible organic vapor flows.

2 EXPERIMENTAL AND NUMERICAL METHODS

Since reliable literature data (i.e., Sanz et al. (1998) and Melzer and Pullan (2019)) for air are available at a Mach number level of about 0.65, this study employed the same turbine cascade as Sanz et al. (1998) and considered a similar exit Mach number. Although the present study considered only high-subsonic flow and not supersonic flow, the detailed assessment of RANS methods for predicting compressible turbulence production and decay in organic vapors is an essential starting point. In this section, the experimental and numerical methods are briefly explained. Further information can be found in Hake et al. (2022, 2022a, 2023), aus der Wiesche (2023), and Matar et al. (2023).

160

2.1 Experimental Setup and Procedure

The measurements were performed using the closed-loop organic vapor wind tunnel (CLOWT) at Muenster University of Applied Sciences, shown in Figure 1. The non-toxic organic vapor Novec 649 by 3M was selected as a testing fluid. Its thermodynamic behavior represents working fluids for ORC power systems, and some general thermodynamic properties are listed in Table 1. The nominal experimental stagnation conditions (as obtained by total pressure and temperature measurements in the settling chamber of the wind tunnel), including the compressibility factor Z, isentropic exponent γ, and the fundamental derivative of gas dynamics Γ (calculated using REFPROP), are listed in Table 2.

Table 1: Thermodynamic properties of Novec 649 (after REFPROP by NIST)

Chemical Formula	Molecular Mass	Critical Pressure	Critical Temperature
$CF_3CF_2C(O)CF(CF_3)_2$	316 g/mol	18.8 bar	442 K

Table 2: Nominal stagnation conditions for the experimental study with Novec 649

Pressure p_o	Temperature T_o	Compressibility Factor Z	Isentropic Exponent γ	Fundamental Derivative Γ
2.30 bar	373 K	0.914	1.046	0.946

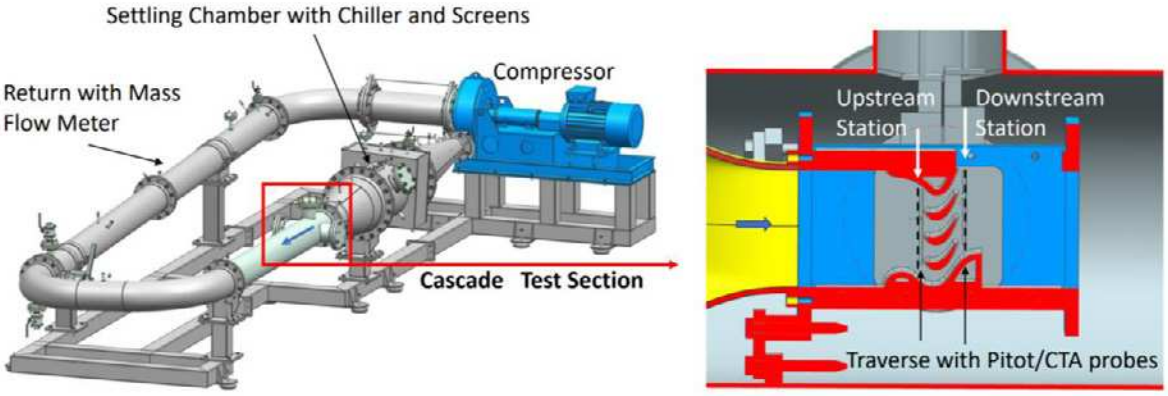

Figure 1: Wind tunnel facility CLOWT with main components and details of the cascade test section.

The airfoil profile for the cascade, established by three full blades and two half-profile pieces, see Figure 1, was the same as described by Kiock et al. (1986) and Sanz et al. (1998). Data for the test cascade are listed in Table 3. The actual roughness level was comparable with aged airfoils. At the upstream and downstream stations, see Figure 1, hot-wire probes in the constant-temperature mode (CTA) and Pitot probes were traversed in the *y*-direction. The minimal normalized distance x/c between the trailing edge and the probe head (i.e., the downstream station 2) was similar to Sanz et al. (1998) namely $x/c = 0.04$. In addition to the hot-wire and Pitot probe measurements, static pressure measurements were conducted using twenty wall pressure taps at the central blade passage under investigation. Furthermore, the vibration behavior of the downstream CTA probe and its stem was observed using a high-speed camera and optical access to the cascade through a window.

The desired exit Mach number M_2 was controlled by the variable wind tunnel compressor running speed, which was adjustable via the electric engine frequency. The maximum exit Mach number and Reynolds number were $M_2 = 0.70$ and $Re_2 = 3.2 \times 10^6$, respectively. The temperature drift rate during a single CTA sampling time (5 up to 10 s) at a single traverse location was only 10^{-3} K/s leading to nearly constant total temperature conditions. However, absolute stagnation temperature deviations from the nominal conditions listed in Table 2 of about $\Delta T_o = \pm 2$ K occurred during the total campaign.

161

Table 3: Cascade data for the present case study

Quantity	Symbol	Value
Spacing (blade pitch)	t	22.0 mm
Chord	c	30.5 mm
Axial chord	b	25.0 mm
Throat	o	8.3 mm
Span	H	50.0 mm
Trailing edge thickness	t_{TE}	1.4 mm
Relative airfoil roughness	k_s/c	4×10^{-4}
Nominal inflow/exit angles	β_1 / β_2	30° / 67.8°

The primary investigation tool was the hot-wire anemometry (HWA) in the constant-temperature mode (CTA). Single tungsten wire probes (L-shape probe design with wire diameter d = 10 µm and length l = 4 mm) were employed as described by Hake et al. (2022a, 2022b). The hot wire probes were aligned normally to the main flow direction in the center line of the cascade. The anemometer was based on a modified electric circuit and amplifier device manufactured by SVMtec (Stuttgart, Germany). The bandwidth was 20 kHz (low-pass filter), and the sampling frequency was 50 kHz. The hot wire signal was digitalized and processed by components manufactured by NI, and the data reduction and post-processing filtering were performed using MATLAB software.

The generalized King equation for the average output electrical voltage signal

$$\bar{E}^2 = A(M, T_o) + B(M, T_o)(\rho u)^{1/2} \qquad (\text{with } E = \bar{E} + E') \qquad (1)$$

has proven its reliability (Hake et al. (2022a, 2022b), de Souza and Tavoularis (1998)). The coefficients A and B in Equation (1) depend on the Mach number M and total temperature T_o. The total temperature was fixed during the experiments, and only the Mach number dependency remained. During the calibration, the mass flux ρu was varied for a given Mach number level M, and the electrical voltage output E was recorded. The calibration measurements were executed at the upstream station (for the low M levels) and downstream station (for the high M levels) of the cascade. For the calibration, the probes were placed in the center of the blade passage where nearly uniform flow conditions existed. The outcome of a previous Pitot probe test combined with static pressure taps was used to obtain the required reference calibration velocities at these locations.

The above *in situ* calibration approach avoided issues with mounting and demounting probes during the experimental campaign. However, an independent calibration study using different wire dimensions was necessary to derive the required correction scheme for obtaining quantitative results. The signal attenuation due to the finite wire length l compared to the turbulent macro length Λ and the cut-off frequency limitation made appropriate correction schemes necessary (Hake et al. (2022b). Two different correction schemes were applied, namely (i) the wire length attenuation correction proposed by Dryden et al. (1937) resting on the integral length scale Λ obtained by the autocorrelation function and (ii) the Wyngaard (1968) correction scheme assuming local isotropy. The correction due to the finite bandwidth was done by assuming a Lorentzian profile for the spectra resting on the actual macro length scale Λ (Hinze (1975)) and calculating the suppressed spectral contribution due to the actual cut-off frequency by numerical integration.

Additional wire vibrations (natural frequencies of the probe device, including wire and the stem) occurred due to the high dynamic loads in high-speed flows. The corresponding natural frequencies were calculated using relations from structural dynamics (see, for instance, Szabo (2001)). Stem vibrations could be identified optically by the high-speed camera approach.

The fluctuating part E' of CTA signals depends on density, velocity, and temperature or pressure fluctuations (de Souza and Tavoularis (1998)):

$$\frac{E\prime}{\bar{E}} = \left(S_u + (\gamma - 1)M^2 S_\rho\right)\frac{u\prime}{\bar{u}} + S_\rho \frac{p\prime}{\bar{p}} + \left(S_T - (1 - \tfrac{\gamma-1}{2}M^2)S_\rho\right)\frac{T_o\prime}{\overline{T_o}} \qquad (2)$$

The high Reynolds number and wire overheat ratio led to the identity of the sensitivity coefficients S_ρ and S_u for density and velocity, as demonstrated by Hake et al. (2022a). Hence, only mass flux $(\rho u)'$ and pressure p' fluctuations contributed to E' for a fixed total temperature T_o. As de Souza and Tavoularis (1998) discussed, the additional pressure fluctuation contribution can be substantial. The existence of acoustic waves increases the fluctuation level of the electrical HWA signal, and it is impossible to distinguish the fluctuation modes in a compressible flow employing only HWA. In the present study, a pseudo-turbulence intensity Tu^* and a pseudo-turbulent kinetic energy k^* was obtained resting on the measured fluctuating and average output signals. In the case of vanishing pressure fluctuations, these quantities would be identical to the usual turbulence intensity Tu and turbulent kinetic energy k. However, in the case of acoustic waves with their coherent fluid motion contributions, Tu and Tu^* systematically differ (with $Tu^* > Tu$). That was the case for the present investigation at higher Mach numbers. Hence, Tu's proper turbulence intensity was estimated by filtering out the coherent contributions to the total recorded power density spectrum. It is important to note that the systematic difference between Tu and Tu^* is a consequence of Equation (2) and is not directly related to non-ideal gas dynamics.

2.2 Computational Fluid Dynamics Method

Two-dimensional compressible steady and unsteady RANS simulations were carried out using the in-house MUSICAA finite-difference solver. The inviscid fluxes were discretized by means of 4th-order centered differences, whereas the 2nd-order was used for viscous fluxes. The scheme was supplemented with a 4th-order selective filter to eliminate grid-to-grid oscillations and a low-order shock-capturing term activated locally by combining Jameson's (2017) shock sensor and the Ducros et al (1999) dilatation/vorticity sensor. A four-stage Runge-Kutta algorithm was used for time integration, and high-order implicit residual smoothing (Cinnella et al. (2015)) was applied to relax stability constraints on the time step. A CFL number of 0.5 was fixed throughout the computational domain to

decrease the time-to-convergence of the steady RANS solutions, while in the URANS computations, the time step was fixed and the maximum CFL number reached in the domain was 5. Turbulence modeling was performed through the Spalart-Allmaras (SA) eddy viscosity model, modified by Crivellini et al.. The SA model does not explicitly compute the turbulence kinetic energy *k*. However, we used the same relation ($k = \mu_t \Omega/(\rho (C_\mu)^{1/2})$) as used by Sanz et al. (1998) to obtain an approximation for *k*. The Reynolds stress was then computed using the linear Boussinesq hypothesis. Because the Reynolds number level was high, the flow was fully turbulent from the front stagnation point. Since the experiments were carried out with rough blades, see Table 3, the existence of a turbulent boundary layer flow seemed to be reasonable.

The behavior of the dense gas was modeled by the equation of state of Peng-Robinson improved by Stryjek and Vera (Stryjek et al. (1986)), along with a power-law approximation of the specific heat at constant volume in the dilute gas limit. Dynamic viscosity and thermal conductivity coefficients were computed using the Chung-Lee-Starling models (Chung et al. (1988)). At the inlet, conservation of Riemann invariants and total temperature and pressure was imposed, while a simple extrapolation was performed at the outlet where the static pressure was imposed. The periodic flow was assumed in the pitch-wise direction, so only one blade passage of an infinite cascade was simulated. The computational domain extended from −2.5 to 2 projected chords in the streamwise direction. The blade passage was discretized using a multi-block structured curvilinear mesh. First, an O-block was extrapolated from the blade surface with a fixed cell growth rate of 1.05 over 150 points and then connected to H-blocks, see Figure 2 (left). Cell clustering was performed in the TE region to increase the spatial resolution of the unsteady wake, amounting to a total of 165 000 points, see Figure 2 (right), which was found to be appropriate after a grid-convergence study.

Figure 3 shows the computed isentropic Mach number distribution for Novec 649 at an exit Mach number of M_2 = 0.70 (as in the present experiments) and air at M_2 = 0.64 (as in Sanz et al. (1998)). While both RANS and URANS show similar overall trends, the trailing edge region exhibited some local differences. The qualitative agreement with the experimental data from Sanz et al. (1998) was reasonable, with maximum deviations of 7 % and 9 % located at $s/c \approx 0.4, 0.2$ on the suction and pressure sides, respectively.

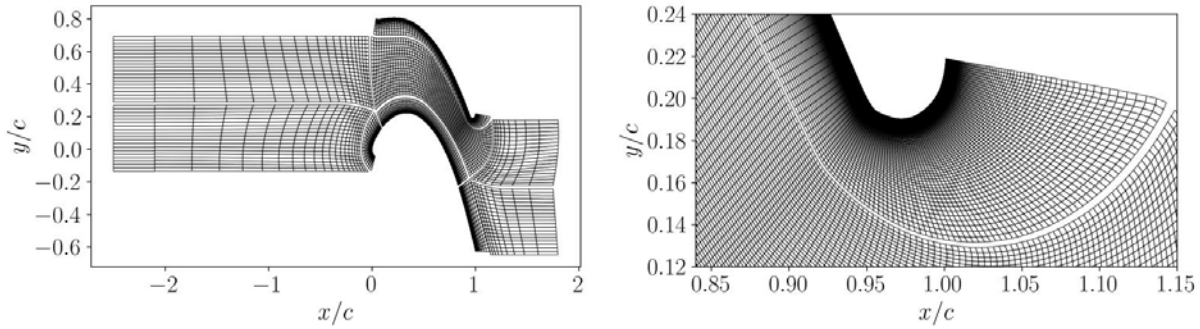

Figure 2: Computational mesh with shown every fifth line (left) and trailing edge details (right)

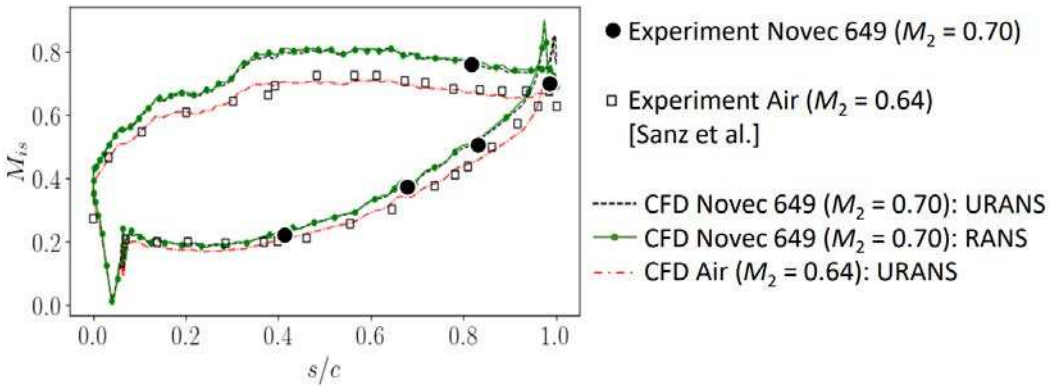

Figure 3: Computed and experimentally determined isotropic profile Mach number distribution

3 RESULTS AND DISCUSSION

3.1 Inflow Conditions

The measured inflow (pseudo) turbulence intensity *Tu** (see Section 2.2) against the inlet and exit Mach numbers M_1 and M_2 are plotted in Figure 4 (left). The data point sets correspond to the two different HWA data correction schemes (i) and (ii). However, the same qualitative behavior of the measured turbulence intensity *Tu** resulted. For low Mach numbers, the inflow fluctuation level increased linearly, but an extreme rise in the turbulence intensity *Tu** can be seen for an exit Mach number M_2 = 0.70. Filtering out the contributions assumed to be caused by coherent fluctuations, the red symbols denoted by "corrected" can be derived in Figure 4 (left). These data followed a linear trend and might be assumed as the proper inflow turbulence intensity *Tu*. The inflow power density spectra shown in Figure 4 (right) demonstrate the existence of additional natural frequency contributions. The location of the measuring point was close to the blade stagnation point (see inset of Figure 4). The spectrum for the higher exit Mach number did not exhibit an amplitude decrease with frequency. This is indicating a loss of isotropy due to the emission of pressure waves affecting the HWA signal, see Equation (2).

3.2 Trailing Edge Vortex-Shedding

The trailing edge vortex shedding was investigated using the power spectra obtained at the downstream station. Samples of spectra obtained in the wake of the trailing edge are shown in Figure 5. The shedding frequency 1x and their double 2x (CTA is not sensitive in flow direction) can be identified clearly in the power spectra for M_2 = 0.13. In the case of higher Mach numbers, the high dynamic loads caused significant vibrations of the wire and the probe stem, adding several artificial peaks to the power spectrum (noticeably also in the inflow spectra shown in Figure 4). These resonances correspond to the natural frequencies of the mechanical systems. Whereas in the case of the low Mach number, the spectrum decreases roughly with an exponent of −5/3, indicating isotropy, a nearly constant spectrum resulted for M_2 = 0.70, indicating a loss of isotropy as observed by Antos et al. (2018).

The vortex-shedding frequency f can be expressed by a non-dimensional Strouhal number $St = f t_{TE}/\bar{u}_2$ defined by the trailing edge thickness t_{TE} and the average exit velocity. The vortex shedding Strouhal numbers *St* against exit Reynolds and Mach numbers are shown in Figure 6. The data obtained by HWA for the organic vapor Novec 649 are compared with literature data obtained by Sieverding and Heinemann (1990) for air for the same cascade at different test facilities (denoted as VKI and DFVLR in Figure 6). The Reynolds number level was higher for the organic vapor than for the same Mach number in air. Hence, the range of Re_2 was larger for Novec 649, but the same range for M_2 was achieved. Plotting the Strouhal number against the Reynolds number (Figure 6, left) led roughly to an agreement with both literature data sets. The deviations at lower Reynolds numbers can be attributed to the different trailing edge shapes and turbulence conditions in the involved test facilities VKI and DFVLR. However, a significant deviation can be observed between the data set DFVLR and the Novec 649 and VKI data if one plots the Strouhal number against the exit Mach number (Figure 6, right).

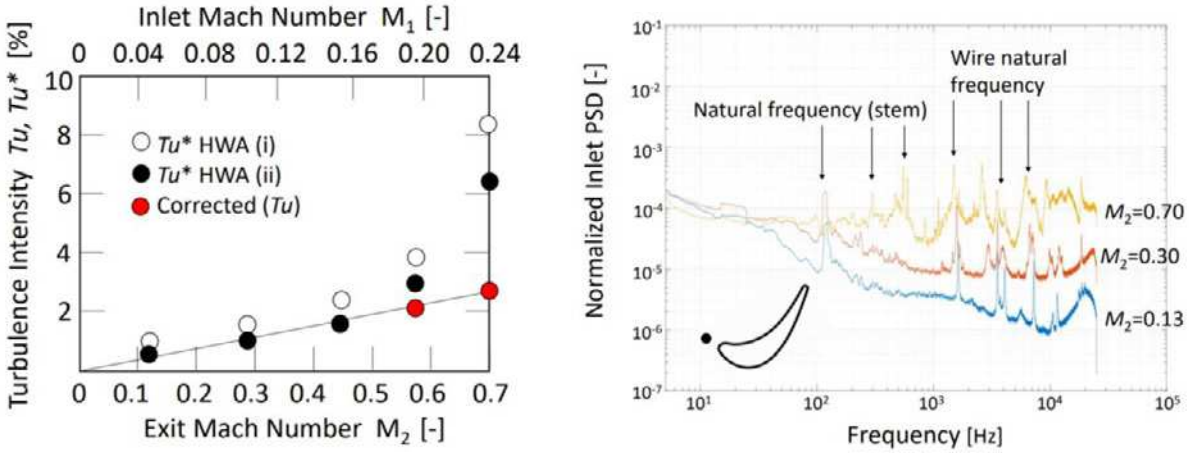

Figure 4: Inflow turbulence intensity *Tu* against M_2 (left) and inflow power spectra (right).

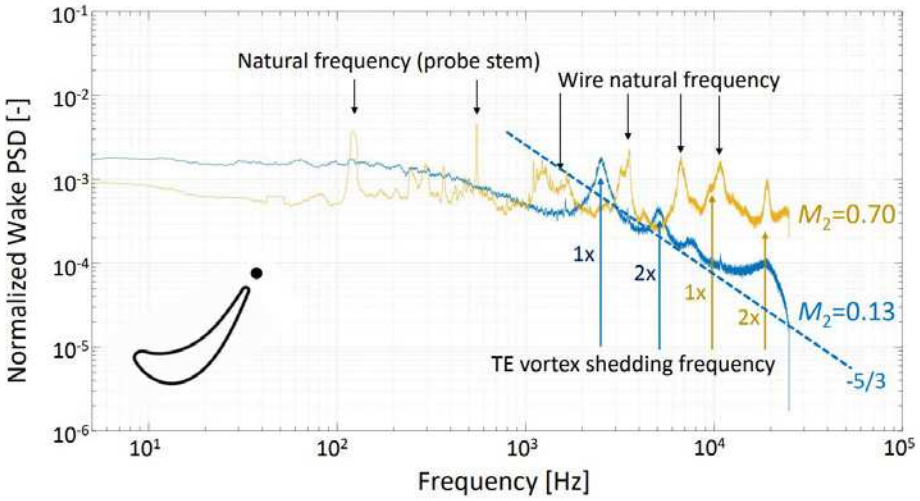

Figure 5: Power spectra obtained in the blade wake region for M_2 = 0.13 and M_2 = 0.70.

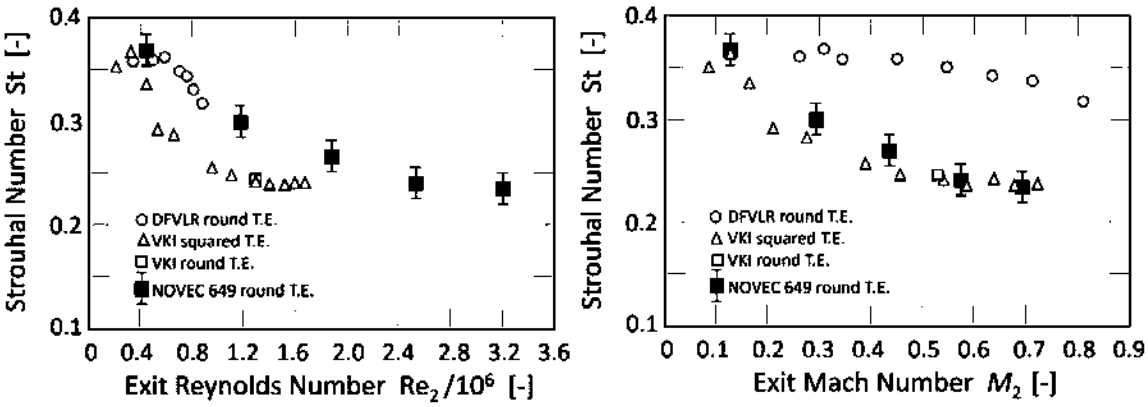

Figure 6: Vortex shedding Strouhal number against Re (left) and against Mach number (right).

Then, two clearly different branches of Strouhal numbers resulted. This can be interpreted as evidence for the hypothesis of Sieverding and Heinemann (1990) that the Reynolds number and the boundary layer flow are the primary quantities for vortex shedding and not the compressibility expressed by the Mach number. The new Novec 649 measurements supported roughly this hypothesis.

Acoustic waves can also interact with the vortex street, and for higher Mach numbers, a complex flow and loss behavior results (Melzer and Pullan (2021)). The URANS study can illustrate this. Figure 7 (left) shows a numerical-schlieren picture for Novec 649 at M_2 = 0.70, demonstrating the existence of vortex shedding and acoustics waves. Samples of numerically obtained power spectra are shown in Figure 7 (right).

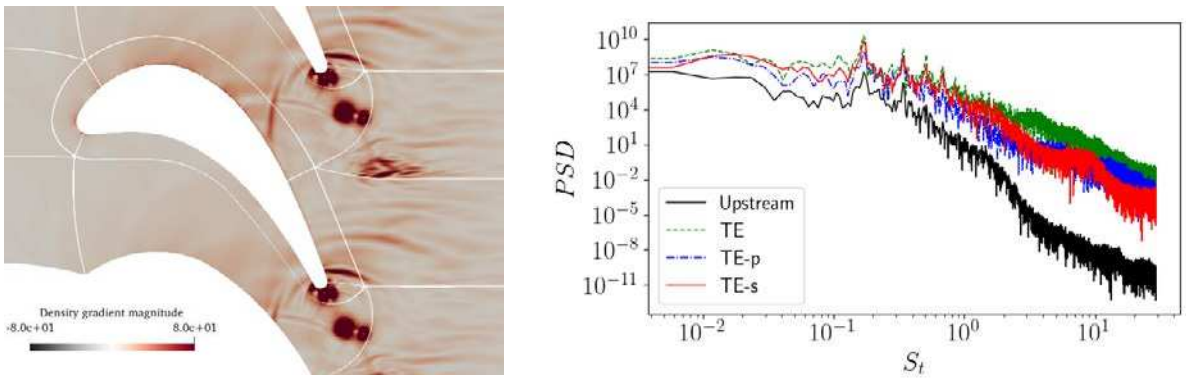

Figure 7: URANS simulations of the vortex street (left) and power spectra (right) for M_2 = 0.70.

In the computations, the pressure power density spectra (PSD) are computed at an upstream position of the blade (Upstream), just downstream of the trailing edge (TE), near the TE on the pressure (TE-p) and suction (TE-s) sides, respectively. Hence, the upstream spectrum should feature only pressure fluctuations caused by the upstream traveling acoustic waves, while the TE PSDs also capture the vortex shedding characteristic frequency. The computed peak Strouhal number was St = 0.17, identical at all positions. Its value deviated from the measured values ($St \approx 0.23$). That might indicate a shortcoming of the URANS method: as the turbulence kinetic energy content is not well resolved (see also below).

3.3 Cascade Exit Wake Flow Results

Wake flow results against the normalized traverse coordinate y/t are plotted in Figure 8. The flow data were obtained at the downstream station close to the blade trailing edge. In addition to the new Novec 649 data, the literature data for air reported by Sanz et al. (1998) are shown (in red color).

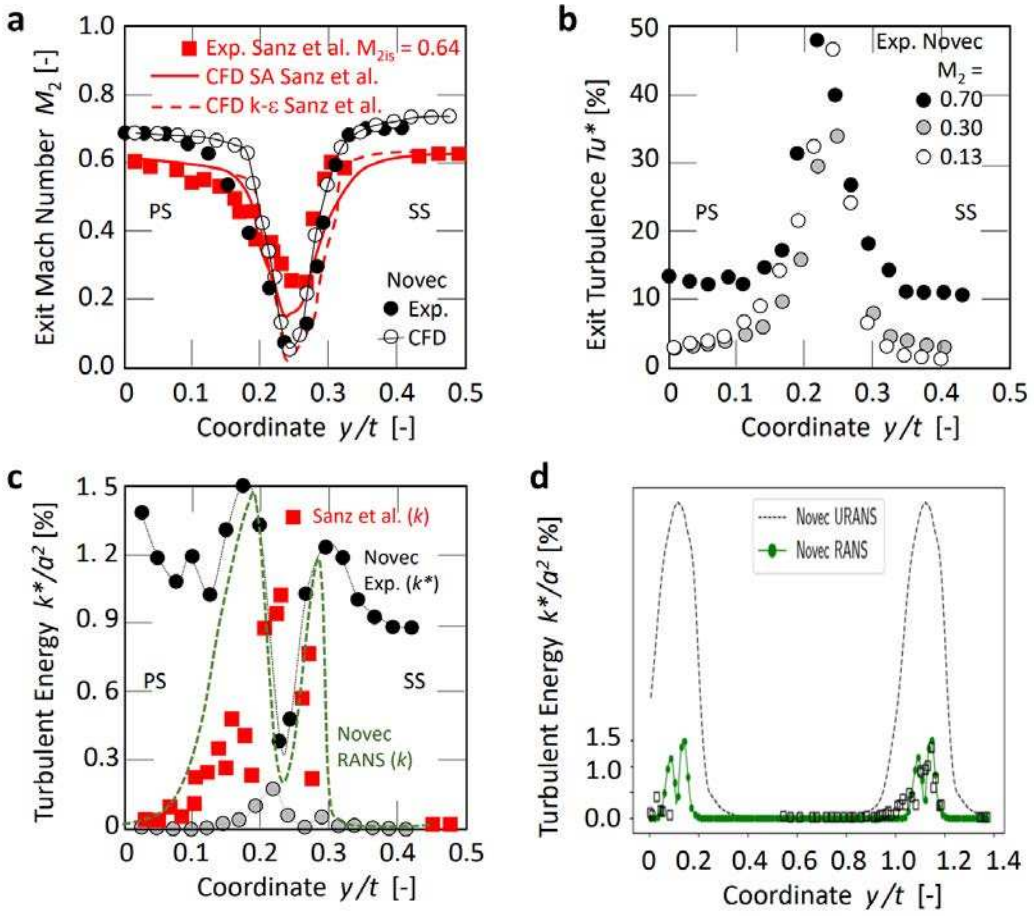

Figure 8: Wake flow profiles: **a** Mach number, **b** pseudo turbulence intensity Tu^*, **c** normalized (pseudo)-turbulent kinetic energy k^*/a^2, **d** computed (pseudo)-turbulent kinetic energy k^*/a^2

The qualitative agreement between experiment and CFD for Novec 649 regarding the exit Mach number M_2 was reasonable, Figure 8.a. The present HWA measurements for the local turbulence intensity Tu^* (Figure 8.b) exhibited the expected behavior: a significant peak at the trailing edge for all Mach numbers existed. The level for Tu^* was quite high in the wake, but it should be kept in mind that coherent fluid motion (vortex shedding and acoustic waves) contributed to the total recorded fluctuations signals. That can be seen clearly in the comparison of the normalized turbulent kinetic energy k^*/a^2 (Figure 8.c). Here, the measured turbulent kinetic energy k^* was normalized by the square of the stagnation speed of sound a. The hot-wire probe enabled a resolution of the local fluctuation minimum at the trailing edge. At the suction and the pressure side of the airfoil, the turbulent kinetic energy reached local maxima in the turbulent boundary layers, but outside of the boundary layers, the measured level for Novec 649 was very high in the case of the higher Mach number M_2 = 0.70. The asymmetry regarding the pressure

and suction side can be attributed to shockwave reflections that are only present on the pressure side (PS) of the trailing edge, with the reflection occurring from the suction surface (SS) of the adjacent blade (Melzer and Pullan (2019)). Since acoustic waves did not occur at low Mach number levels, the Novec 649 data for $M_2 = 0.3$ did not exhibit such a high fluctuation energy level in the passages away from the blades. That observation indicated that outside of the boundary layer and wake domain, the hot-wire signals must be corrected regarding the acoustic wave contributions. Regarding the turbulent kinetic energy level, Figure 8.d, the steady RANS predictions were in much better agreement with the present measurements than the URANS. URANS largely overpredicted the peak due to the large velocity fluctuations caused by the passage of each vortex, while the overall amplitude found in the RANS solution was in good agreement with the present measurements, Figure 8.d. This is essentially due to the different mean recirculating flow sizes behind the TE, which was much smaller in URANS. This tendency was already observed in the case of the wake behind a circular cylinder (Matar et al. (2023)), and is shown here in Figure 9. While two mean counter-rotating vortices extending over more than 5 % of the axial chord were observed in the RANS computations, the recirculation region only covered 2 % in the URANS and was asymmetric.

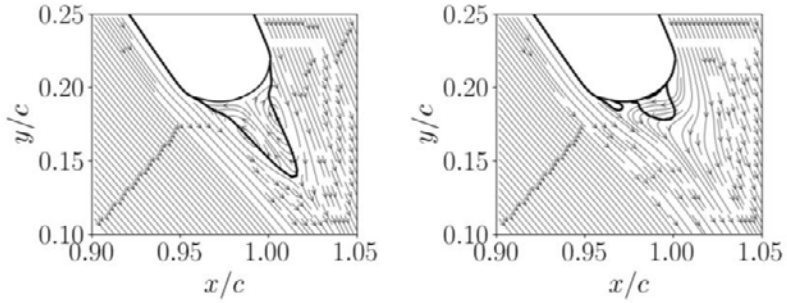

Figure 9: Streamlines (arrows) and null main flow direction velocity component iso-contour (thick black contour) indicating extent of mean recirculation region from RANS (left) and URANS (right)

167

4 CONCLUSIONS AND OUTLOOK

The main findings of the present experimental and numerical study of the high-subsonic turbulent flow of an organic vapor through a turbine cascade can be summarized as follows:

- Transonic vortex shedding inclusive acoustic waves and a loss of isotropy occurred for exit Mach numbers $M_2 > 0.5$, fully in agreement with the observations in the literature
- Vortex shedding and pressure fluctuations significantly contributed to the turbulence level and hence to the trailing edge losses at exit Mach numbers of about $M_2 = 0.7$
- High-resolution unsteady RANS (URANS) methods can qualitatively predict transient transonic vortex shedding features including acoustic waves, but the absolute levels of turbulent kinetic energy were largely overpredicted by URANS, and RANS led to a better result regarding the predicted turbulent kinetic energy in the wake
- A careful interpretation of fluctuation signals is required for a correct interpretation of hot-wire measurements and numerical simulations

The exploration of large-eddy-simulation (LES) methods for predicting transonic vortex shedding is the subject of ongoing research.

REFERENCES

aus der Wiesche, S., 2023, Experimental Investigation Techniques for Non-Ideal Compressible Fluid Dynamics, *Int. J. Turbomach. Propuls. Power*, vol. 8(2), p. 11

Ames, F. E., Plesniak, M. W., 1995, The influence of large scale, high intensity turbulence on vane aerodynamic losses, wake growth, and the exit turbulence parameters, *Proc. ASME Turbo Expo*, 5 – 8 June 1995, Houston, Texas, paper 95-GT-290

Antos, P., Uruba, V., Jonas, P., Prochazka, P., Skala, V., Hoznedl, M., Sedlak, K., 2018, Measurement of turbulence in LP part of the 1090 MW steam turbine, *Proceedings XXIV Biennial Symposium on Measuring Techniques in Turbomachinery*, 29 – 31 August 2018, Prague, Czech Republic, paper MTT2418A31

Chung, T., Ajlan, M., Lee, L., Starling, K., 1988, Generalized multiparameter correlation for nonpolar and polar fluid transport properties, *Ind. Eng. Chem. Res*., vol. 27, no. 4, p.671–679

Cinnella, P., et al., 2015, Recent Progress in High-Order Residual-Based Compact Schemes for Compressible Flow Simulations: Toward Scale-Resolving Simulations and Complex Geometries, in: *Notes on Numerical Fluid Mechanics and Multidisciplinary Design Volume 128*, pp 397-421, Springer, Berlin,

de Souza, F., Tavoularis, S., 1998, Hot-Wire Response in High-Subsonic Flow, *Proc. 37th AIAA Aerospace Sciences Meeting and Exhibition*, January 11-14, 1999, Reno, NV, paper AIAA 99-0310

Dossena, V., Perdichizzi, A., Ubaldi, M., Zunino, 1993, Turbulence measurements downstream of a turbine cascade at different incidence angles and pitch-chord ratios, *Proc. ASME Turbo Expo*, 24 – 27 May 1993, Cincinnati, Ohio, paper 93-GT-52

Dryden, H. L., Schubauer, G. B., Mock, W. C., Skramstad, H. K., 1937, Measurements of Intensity and Scale of Wind-Tunnel Turbulence and Their Relation to the Critical Reynolds Number of Spheres, NACA No. 581

Ducros, F., Ferrand, V., Nicoud, F., Weber, C., Darracq, D., Gacherieu, C., Poinsot, T., 1999, Large-Eddy Simulation of the shock/turbulence interaction, *JCP*, vol. 152(1), pp. 517–549

Gregory-Smith, D. R., Walsh, J. A., Graves, C. P., Fulton, K. P., 1988, Turbulence Measurements and Secondary Flows in a Turbine Rotor Cascade, *ASME J. Turbomachinery*, vol. 110, pp. 479-485

Hake, L., Reinker, F., Wagner, R., aus der Wiesche, S., Schatz, M., 2022, The Profile Loss of Additive Manufactured Blades for Organic Rankine Cycle Turbines, *Int. J. Turbomach. Propuls. Power*, vol. 7(1), 11

Hake, L., Sundermeier, S., Cakievski, L., Bäumer, J., aus der Wiesche, S., Matar, C., Cinnella, P., Gloerfelt, X., (2022a), Hot-Wire Anemometry in High Subsonic Organic Vapor Flows, *Proc. ASME Turbo Expo*, June 2022, Rotterdam, The Netherlands, paper GT2022-81689

Hake, L., Sundermeier, S., aus der Wiesche, S., Bienner, A., Gloerfelt, X., Matar, C., Cinnella, P., 2022b, CFD-supported data reduction of hot-wire anemometry signals for compressible organic vapor flows. *Proc. XXVI Biennial Symposium on Measuring Techniques in Turbomachinery*, September 2022, Pisa, Italy

Hake, L., Sundermeier, S., aus der Wiesche, S., 2023, Profile Loss Prediction for Organic Rankine Cycle Turbines: An Experimental Case Study, *Proc. 15th European Turbomachinery Conference*, 24 – 28 April 2023, Budapest, Hungary

Hinze, J. O., 1975, *Turbulence*, 2nd edition, McGraw-Hill, New York

Jameson, A., 2017, The origins and further development of the Jameson-Schmidt-Turkel (JST) scheme. AIAA J., vol. 55(5)

Kiock, R., Lehthaus, F., Baines, N. C., Sieverding, C. H., 1986, The Transonic Flow Through a Plane Turbine Cascade as Measured in Four European Wind Tunnels, *ASME J. Eng. Gas Turb. Power*, vol. 108, 277-284

Matar, C., Cinnella, P., Gloerfelt, X., Reinker, F., aus der Wiesche, S., 2023, Investigation of non-ideal gas flows around a circular cylinder, *Energy*, vol. 268, p. 126563

Melzer, A. P., Pullan, G., 2019, The Role of Vortex Shedding in the Trailing Edge Loss of Transonic Turbine Blades, *ASME J. Turbomachinery*, vol. 141(4), paper 041001

Sanz, W., Gehrer, A., Woisetschläger, J., Forstner, M., Artner, W., Jericha, H., 1998, Numerical and experimental investigation of the wake flow downstream of a linear turbine cascade, *Proc. ASME Turbo Expo*, 2 – 5 June 1998, Stockholm, Sweden, paper 98-GT-246

Sanz, W., Scheier, D., 2021, Unsteady Simulation of a Transonic Turbine Stage with Focus on Turbulence Prediction, *Int. J. Turbomach. Propuls. Power*, vol. 6, p. 36

Sieverding, C. H., Heinemann, H., 1990, The Influence of Boundary Layer State on Vortex Shedding From Flat Plates and Turbine Cascades, *ASME J. Turbomachinery*, vol. 112, pp. 181-187

Sieverding, C. H., Manna, M., 2020, A Review on Turbine Trailing Edge Flow, *Int. J. Turbomach. Propuls. Power*, vol. 5(2), p. 10

Stryjek, R., Vera, J. H., 1986, PRSV: An improved Peng–Robinson equation of state for pure compounds and mixtures, *The Canadian Journal of Chemical Engineering*, vol. 64, no. 2, p. 323–333

Szabo, I., 2001, *Höhere technische Mechanik*, Springer, Berlin

Volino, R. J., Kartuzova, O., Ibrahim, M. B., 2008, Experimental and computational investigations of separation and transition on a highly loaded low-pressure turbine airfoil: Part 2 – high freestream turbulence intensity, *Proc. IMECE*, October 31 – November 6, 2008, Boston, Massachusetts, paper IMECE2008-68776

Wyngaard, J. C., 1968, Measurement of small-scale turbulence structure with hot wires, *J. Scientific Instruments*, vol. 1, pp. 1105-1108

Zunino, P., Ubaldi, M., Satta, A., 1987, Measurements of secondary flows and turbulence in a turbine cascade passage, *Proc. ASME Turbo Expo*, May 31 – June 4, 1987, Anaheim, California, paper 87-GT-132

ACKNOWLEDGEMENT

This study was conducted within the Franco-German research project REGAL-ORC funded by ANR and DFG.

ORC SEVILLE 2023
7th International Seminar on O.R.C. Power Systems

© 2024 Editorial Universidad de Sevilla. Este es un artículo de acceso abierto distribuido bajo los términos de la licencia de uso y distribución Creative Commons (BY-NC-ND 4.0)

DOI: https://dx.doi.org/10.12795/9788447227457_27

A NOVEL APPROACH TO DISTRICT HEATING: USING A TWO-PHASE EXPANDER IN REVERSIBLE HEAT PUMP-ORGANIC RANKINE CYCLE SYSTEM

Sindu Daniarta[1,2,*], Attila R. Imre[2,3], Piotr Kolasiński[1]

[1] *Wrocław University of Science and Technology, Department of Thermodynamics and Renewable Energy Sources, Wrocław, Poland*
[2] *Budapest University of Technology and Economics, Department of Energy Engineering, Budapest, Hungary*
[3] *Centre for Energy Research, Department of Thermohydraulics, Budapest, Hungary*

*Corresponding Author: sindu.daniarta@pwr.edu.pl / daniarta@energia.bme.hu

ABSTRACT

A district heating system involves a central generation and distribution of heat to residential buildings through a network of insulated pipes. Heat can be generated, for example, from the combustion of fossil fuels and biomass. Since there are many environmental restrictions and the growth of heat and energy demand, several industrial waste heat and renewable energy sources, such as geothermal or solar thermal energy may be promising to be utilized for district heating purposes. However, in some districts, various low-temperature heat sources might be available; as a result, a heat pump is installed to increase the temperature to accommodate demand peak loads. The heat pump is operated only for a certain period and sometimes not used during summer. To optimize the utilization of the heat source, the district heating system may be transformed into a power generation system that can generate, for example, electricity instead of heat during the summer. This goal may be achieved by applying a reversible system. Therefore, this article discusses the novel reversible heat pump-organic Rankine cycle (RHPORC) system using a two-phase expansion system. Some working fluids were selected based on thermal properties, as well as safety and environmental issues. Some selected two-phase volumetric expanders were introduced in the novel system. In the end, the performances of the system based on the selected working fluid were compared. According to the results of a study, using RHPORC in district heating systems might save annual energy consumption by up to 50%.

1 INTRODUCTION

For more than a century, commercial district heating systems have been running at high temperatures to meet demand, and they are often fueled by fossil fuels. The fourth generation of district heating systems, in which low-temperature district heating (LTDH) uses renewable energy, may play a key role in the EU's effort to reduce the dependency on fossil fuels to heat buildings (Averfalk *et al*., 2021). In this case, low-temperature does not relate to a particular temperature range in absolute terms; instead, it refers to the set of temperatures in the district energy network or the available energy source (e.g., solar thermal, waste heat, geothermal, and so on) under consideration (Bertelsen *et al*., 2021).

Some recent articles (Buffa *et al*., 2019; Sarbu *et al*., 2022) reviewed and reported the integration of renewable energy sources for district heating systems focused on the low-temperature system where the utilization of the fifth generation of district heating and cooling (DHC) system has been introduced. Multi-low-temperature renewable energy sources operated in bivalent parallel or serial modes could also be introduced to meet the heating demands (Buday and Buday-Bódi, 2023). Nevertheless, relying on low-temperature renewable heat sources was insufficient to fulfil demand during the peak hour (Kontu *et al*., 2019; Østergaard and Andersen, 2018). As a result, a heat pump may be the most effective

means of increasing the temperature and satisfying demand. Furthermore, in the literature, a few articles (Marty *et al*., 2018; Mikielewicz *et al*., 2022; Wang *et al*., 2018) reported the performance of the LTDH system simultaneously operated with organic Rankine cycle (ORC). In that case, the ORC operates using an available surplus heat (e.g., when a load of district heating demand is low during summer). Moreover, this ORC is installed in a stand-alone system, making the investment cost more expensive and not attractive for investors. As a result, an alternative or improved design is required to enhance the LTDH system that will be introduced and described in this article.

This article aims to present a viable solution for an LTDH system using a heat pump and ORC. There is growing interest in using low-temperature heat sources from renewable sources, including solar thermal, geothermal, waste heat, biomass, and so on. The novel reversible heat pump-organic Rankine cycle (RHPORC) system employing two-phase expander is introduced as an alternative design for LTDH regarding the operation and load of heating demand. Some volumetric expanders such as screw, multi-vane, or scroll might be used to do so, even though two-phase expansion might be avoided due to a common problem (e.g., blade erosion) in turbomachinery (Daniarta and Kolasiński, 2021; Francesconi *et al*., 2022; van Heule *et al*., 2022). Moreover, this article compared the system using only a heat pump or RHPORC. A case study of LTDH was given including the assumed period time and two different working fluids to demonstrate the performance of RHPORC. In the end, the benefit of using RHPORC is described.

2 REVERSIBLE HEAT PUMP-ORGANIC RANKINE CYCLE SYSTEM AND A CASE STUDY

DHC could enable the integration of low-grade renewable heat sources like geothermal, waste heat, solar thermal energy, and so on, even while the majority of DHC systems are still powered by coal and natural gas. The International Renewable Energy Agency (IRENA) reported that the percentage of renewable energy in district heating might rise from 8% in 2017 to 77% in 2050 (IRENA, 2020). It is found that the different local heat sources available in a given area make it challenging to maintain the same operating temperatures for district heating networks. Therefore, a proper selection of low-temperature heat sources, which is suitable to meet the base demand, is required. Although many various heat sources might be available in a district, we describe only one case in this paper. For this example, the geothermal energy source is chosen to meet a load of heating demand illustrated in Figure 1, and then the heat and the temperature level are raised using the heat pump to satisfy the peak demand.

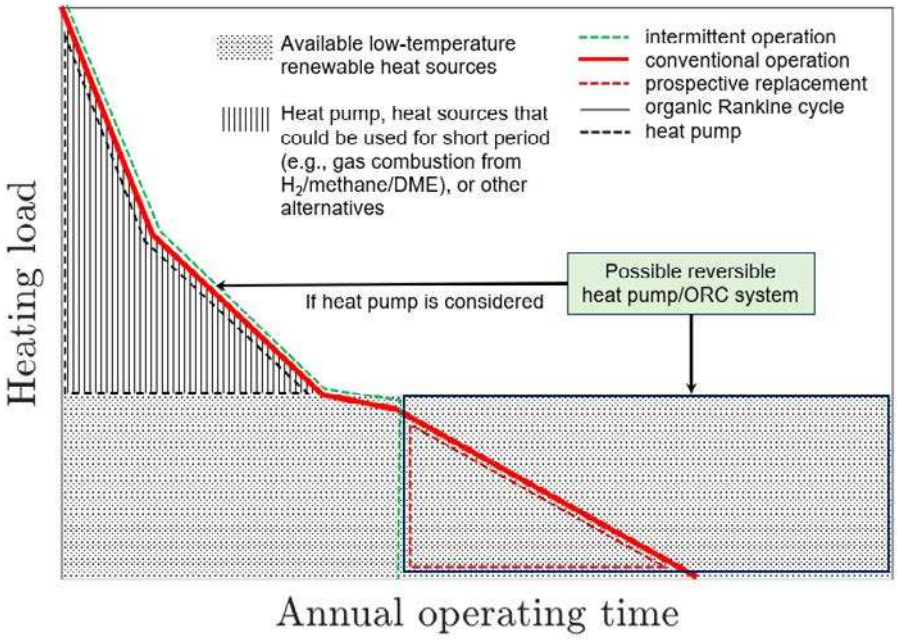

Figure 1: An illustration of an operating system for a case

To supply the base demand, the LTDH system uses geothermal at least 5,000 hours (Nuytten *et al*., 2013), assuming the system runs intermittently rather than continuously as illustrated in Figure 1. Moreover, to meet the peak demand, the heat pump must run for 3,000 hours (Kallert *et al*., 2017), and the gas combustion (H_2, methane or biogas) has to run for 2,000 hours. Given that there is no need for heating during 3,760 of the 8,760 hours in a year, geothermal energy is not utilized. Therefore, geothermal energy might also be used to produce electricity via ORC. Installing ORC with new components might require a higher financial investment. We propose designing the RHPORC system since the heat pump also plays a key role in this LTDH system and is utilized, but only occasionally, to increase its competitiveness. For further analysis, we assumed this RHPORC system operates 3,000 hours as a heat pump and 3,760 hours as ORC as illustrated in Figure 2.

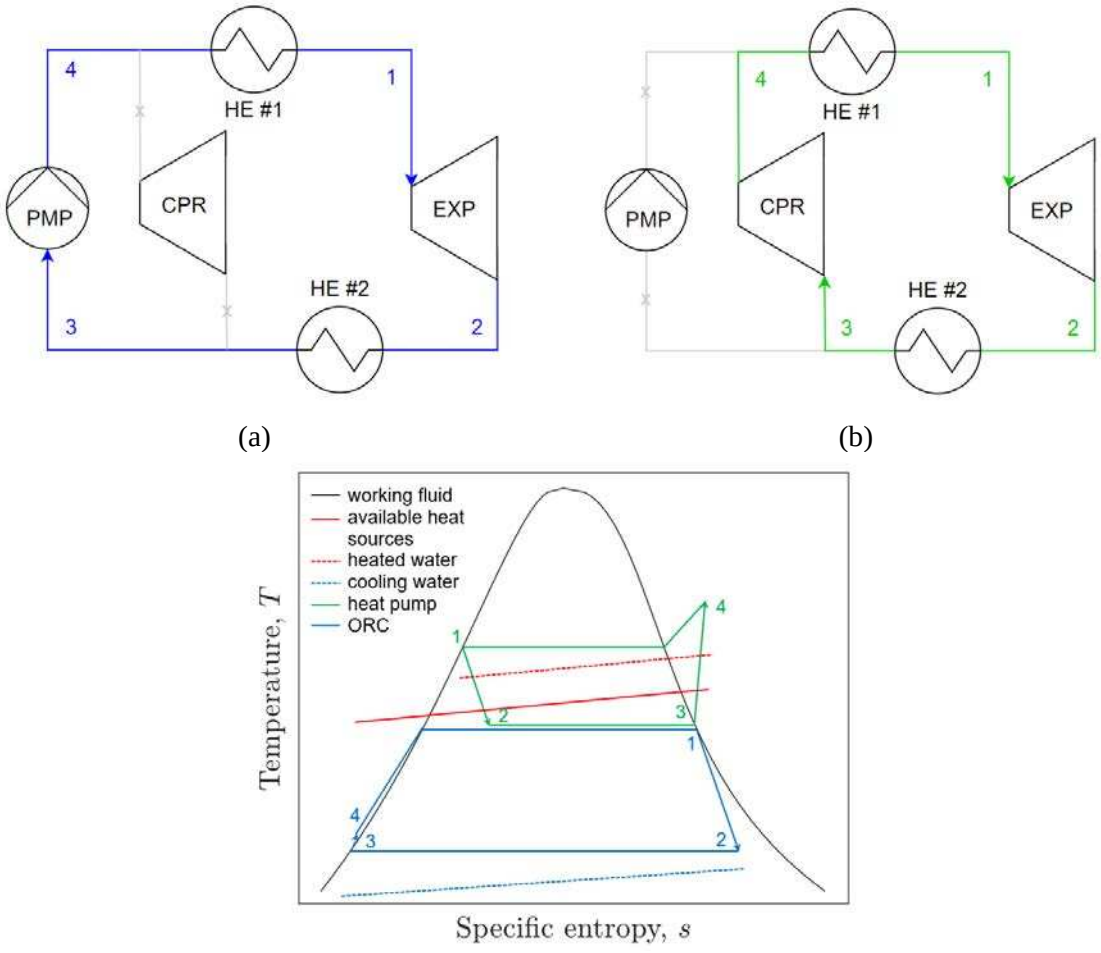

Figure 2: A novel reversible heat pump-organic Rankine cycle (RHPORC) (a) in ORC mode, (b) in heat pump mode, and (c) its thermodynamic process in *T-s* diagram, where HE, EXP, PMP, CPR describe as the heat exchanger, expander, pump, and compressor, respectively.

The RHPORC is designed using two heat exchangers (as condenser and evaporator), a pump (for ORC), a compressor (for heat pump), and an expander (for both heat pump and ORC). In a different application, the RHPORC system has been introduced (Daniarta *et al*., 2022; Francesconi *et al*., 2022; Wieland *et al*., 2023). The list of the components shown in Figure 2 is described in Table 1 along with the specific process that is expressed as a function of mass and energy balance using Equations (1) and (2), where $\dot{m}$, h, $\dot{W}$, and $\dot{Q}$ represent the mass flow rate, specific enthalpy, power, and heat transfer rate, respectively.

$$\sum \dot{m}_{\text{in}} = \sum \dot{m}_{\text{out}} \tag{1}$$

$$\dot{Q} + \sum \dot{m}_{\text{in}} h_{\text{in}} = P + \sum \dot{m}_{\text{out}} h_{\text{out}} \quad (2)$$

The described model in this study was implemented in MATLAB and simulation was performed using thermal properties data taken from REFPROP 10.0 (Lemmon *et al.*, 2018). In this case, some assumptions are taken into account as follows. Dimethyl ether (DME or RE170) and 1,1-Difluoroethane (R152a) are selected as working fluids as they have a relatively low negative environmental effect (i.e., in global warming potential and ozone depletion potential). Assuming the geothermal heat is taken at 80°C (at 300 kPa) and the water is heated up to 100°C using a heat pump, where the pinch point temperature is 5°C. Each component operates in a steady-state condition. Heat exchangers operate with constant pressure, constant overall heat transfer coefficient, and constant specific heat. The change of kinetic and potential energy of the stream in the heat exchangers is negligible. Moreover, there are no heat or pressure losses. For some rotating components, such as the compressor, pump, and expander, the isentropic efficiency is assumed at 0.8. The isentropic efficiency of the expander for heat pump mode is assumed to be 0.5. Therefore, the coefficient performance (COP) of the heat pump and the efficiency of ORC could be determined in this RHPORC.

Table 1: List of RHPORC components and specific processes referred to in Figure 2

List of component	Specific enthalpy (ORC mode) (kJ/kg)	Specific enthalpy (heat pump mode) (kJ/kg)	Mass flow rate (kg/s)	Product (kW)
HE #1	$h_{\text{ORC.1}} - h_{\text{ORC.4}}$	$h_{\text{HP.4}} - h_{\text{HP.1}}$	$\dot{m}_{\text{wf}}$	$\dot{Q}_{\text{ORC,HE1}}$, $\dot{Q}_{\text{HP,HE1}}$
Expander	$h_{\text{ORC.1}} - h_{\text{ORC.2}}$	$h_{\text{HP.1}} - h_{\text{HP.2}}$	$\dot{m}_{\text{wf}}$	$P_{\text{ORC,EXP}}$, $P_{\text{HP,EXP}}$
HE #2	$h_{\text{ORC.2}} - h_{\text{ORC.3}}$	$h_{\text{HP.3}} - h_{\text{HP.2}}$	$\dot{m}_{\text{wf}}$	$\dot{Q}_{\text{ORC,HE2}}$, $\dot{Q}_{\text{HP,HE2}}$
Pump	$h_{\text{ORC.4}} - h_{\text{ORC.3}}$	-	$\dot{m}_{\text{wf}}$	$P_{\text{ORC,PMP}}$
Compressor	-	$h_{\text{HP.4}} - h_{\text{HP.3}}$	$\dot{m}_{\text{wf}}$	$P_{\text{HP,CPR}}$

3 RESULT AND DISCUSSION

The used MATLAB configuration was taken from (Daniarta *et al.*, 2022), where the model has been validated. Moreover, the obtained simulation result is described in Figure 3 which compares the required and generated energy, and rejected heat between four different scenarios, each with a specific working fluid (DME and R152a) and specific design (RHPORC and only heat pump with throttle valve). In this study, the model did not involve a quasi-dynamic simulation of the system, only a method that assumes the system operates at the condition above mentioned. Moreover, the heating load supplied by the heat pump was assumed to be constant. The obtained mass flow rates of the heat pump and the ORC based on this simulation are 0.30 kg/s and 0.18 kg/s, respectively.

The result indicates that utilizing various working fluids may lead to varying amounts of heat being rejected; for example, the heat pump using R152a as working fluid might reject heat up to 234.45 MWh, which is 4.32 MWh more than in the case of the same configuration using DME. A heat pump using only a throttle valve (i.e., without a two-phase volumetric expander) tends to require more energy. This heat pump requires 53.66 MWh of electricity for R152a (with COP of 3.51) and 47.12 MWh for DME (with COP of 4). This energy consumption could be reduced up to 7.82 MWh (for R152a) and 5.59 MWh (for DME) by introducing the two-phase volumetric expansion (integrated with the generator) to replace the throttle valve. Moreover, the COP of the heat pump mode (RHPORC) could be 4.11 and 4.54 for R152a and DME, respectively.

The introduction of the RHPORC appears to hold promise since, as mentioned in the previous section, the heat pump might be switched into ORC operating mode to generate electricity when there is an excess of heat (during the summer). The ORC makes use of shared components like heat exchangers and expanders. As shown in Figure 2, the expander utilized in the heat pump mode is likewise used in ORC mode. The result from the mathematical modelling (presented in Figure 3) indicates that ORC employing R152a and DME may produce energy of 22.45 MWh and 22.20 MWh, respectively. Using the above-mentioned assumption, the efficiency of RHPORC in ORC mode for R152a and DME could be up to 7.39% and 7.47%, respectively. This study shows that the district heating system employing RHPORC uses less energy overall, with the total net energy usage of the system being 23.39 MWh (R152a) and 19.32 MWh (DME).

The results show that RHPORC offers a perspective in the district heating system with reasonably low annual energy consumption based on the aforementioned mathematical modelling result. Nonetheless, it is important to pay close attention to the design of the two-phase expander. As an alternative to a turbine, a volumetric rotating expander (such as a screw, multi-vane, or scroll) might be used in this RHPORC as these expanders could operate in two-phase conditions (Daniarta and Kolasiński, 2021; Francesconi *et al.*, 2022; van Heule *et al.*, 2022). Moreover, the design of a two-phase volumetric expander might be conducted based on the feature of volumetric machines operating in both heat pump and ORC mode that pressure and volumetric expansion ratio are the parameters that must be considered.

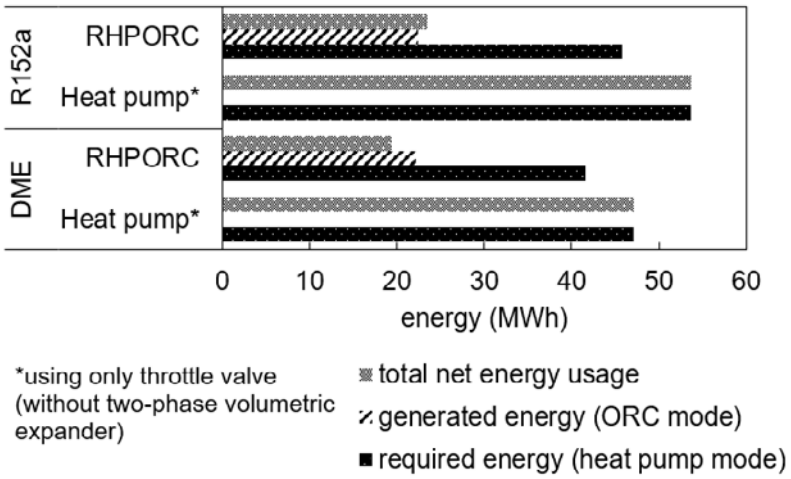

(a)

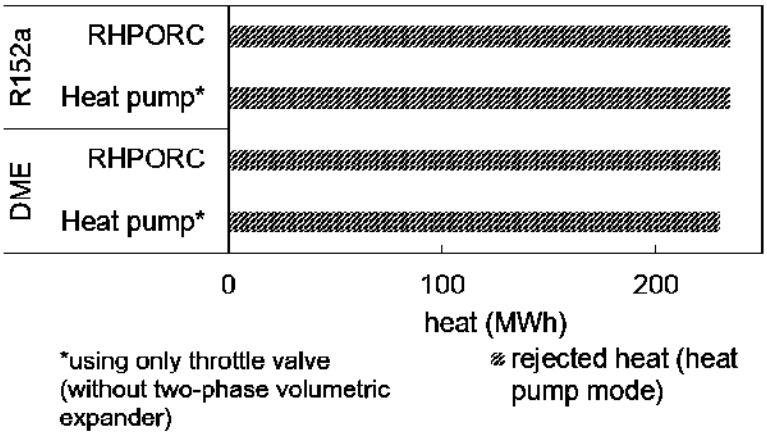

(b)

Figure 3: The obtained result in (a) required and produced energy (both heat pump and ORC mode), and (b) the rejected heat (heat pump mode)

4 CONCLUSIONS

This paper introduced the RHPORC (a reversible thermodynamic system which could be operated as a heat pump and ORC) that might be used to improve the district heating system. The study also discusses the comparison between the RHPORC system and a conventional heat pump with a throttle valve. The comparison between two different working fluid (i.e., R152a and DME) were examined. The result shows that RHPORC using DME offers better efficiency in ORC mode than in the case of the application of R152a. However, using R152a in heat pump mode might offer more rejected heat than DME. Moreover, the results of the study show that introducing RHPORC in district heating systems could reduce up to 50% of annual energy consumption, but the design of a two-phase volumetric expander needs to be considered carefully.

NOMENCLATURE

COP	the coefficient performance	(-)
h	specific enthalpy	(kJ/kg)
$\dot{m}$	mass flow rate	(kg/s)
P	power	(kW)
$\dot{Q}$	heat transfer rate	(kW)

Subscript

CPR	compressor
EXP	expander
HE1	heat exchanger 1
HE2	heat exchanger 2
HP	heat pump
PMP	pump
wf	working fluid

Abbreviations

DHC	district heating and cooling
DME	dimethyl ether
LTDH	low-temperature district heating
ORC	organic Rankine cycle
RHPORC	reversible heat pump-organic Rankine cycle

REFERENCES

Averfalk, H., Benakopoulos, T., Best, I., Dammel, F., Engel, C., Geyer, R., Gudmundsson, O., Lygnerud, K., Oltmanns, J., Nord, N., 2021, *Low-Temperature District Heating Implementation Guidebook: Final Report of IEA DHC Annex TS2. Implementation of Low-Temperature District Heating Systems*, Fraunhofer IRB Verlag, Stuttgart: 206 p.

Bertelsen, N., Mathiesen, B.V., Djørup, S.R., Schneider, N.C.A., Paardekooper, S., García, L.S., Thellufsen, J.Z., Kapetanakis, J., Angelino, L., Kiruja, J., 2021, *Integrating low-temperature renewables in district energy systems: Guidelines for policy makers*, International Renewable Energy Agency, Abu Dhabi: 122 p.

Buday, T., Buday-Bódi, E., 2023. Reduction in CO2 Emissions with Bivalent Heat Pump Systems, *Energies.*, vol. 16, no 7: p. 3209.

Buffa, S., Cozzini, M., D'Antoni, M., Baratieri, M., Fedrizzi, R., 2019, 5th generation district heating and cooling systems: A review of existing cases in Europe, *Renew. Sustain. Energy Rev*, vol. 104: pp. 504–522.

Daniarta, S., Kolasiński, P., 2021, A preliminary study of two-phase volumetric expanders and their application in ORC systems, i*n Proceedings of the 6th International Seminar on ORC Power Systems*, Technical University of Munich, Munich: id. 78.

Daniarta, S., Kolasiński, P., Imre, A.R., 2022, A Preliminary Design and Modeling Analysis of Two-Phase Volumetric Expanders for a Novel Reversible Organic Rankine-Based Cycle for Carnot Battery Technology, *Appl. Sci.*, vol. 12, no. 7: p. 3557.

Francesconi, M., Briola, S., Antonelli, M., 2022, A Review on Two-Phase Volumetric Expanders and Their Applications, *Appl. Sci.*, vol. 12, no. 20: p. 10328.

IRENA., 2020, *Global renewables outlook: Energy transformation 2050*, International Renewable Energy Agency, Abu Dhabi: 291 p.

Kallert, A., Schmidt, D., Bläse, T., 2017, Exergy-based analysis of renewable multi-generation units for small scale low temperature district heating supply, *Energy Procedia*, vol. 116: pp. 13–25.

Kontu, K., Rinne, S., Junnila, S., 2019, Introducing modern heat pumps to existing district heating systems – Global lessons from viable decarbonizing of district heating in Finland, *Energy*, vol. 166: pp. 862–870.

Lemmon, E.W., Bell, I.H., Huber, M.L., McLinden, M.O., 2018. NIST Standard Reference Database 23: Reference Fluid Thermodynamic and Transport Properties-REFPROP, Version 10.0, National Institute of Standards and Technology. Stand. Ref. Data Program, Gaithersbg.

Marty, F., Serra, S., Sochard, S., Reneaume, J.-M., 2018, Simultaneous optimization of the district heating network topology and the Organic Rankine Cycle sizing of a geothermal plant, *Energy*, vol. 159: pp. 1060–1074.

Mikielewicz, J., Ochrymiuk, T., Cenian, A., 2022, Comparison of traditional with low temperature district heating systems based on organic Rankine cycle, *Energy*, vol. 245: p. 123280.

Nuytten, T., Claessens, B., Paredis, K., Van Bael, J., Six, D., 2013, Flexibility of a combined heat and power system with thermal energy storage for district heating, *Appl. Energy*, vol. 104: pp. 583–591.

Østergaard, P.A., Andersen, A.N., 2018, Economic feasibility of booster heat pumps in heat pump-based district heating systems, *Energy*, vol. 155: pp. 921–929.

Sarbu, I., Mirza, M., Muntean, D., 2022, Integration of Renewable Energy Sources into Low-Temperature District Heating Systems: A Review, *Energies*, vol. 15, no. 18: p. 6523.

van Heule, X., De Paepe, M., Lecompte, S., 2022, Two-Phase Volumetric Expanders: A Review of the State-of-the-Art, *Energies*, vol. 15, no.14: p. 4991.

Wang, Hai, Wang, Hai-ying, Zhu, T., Gao, N., 2018, Evaluation on energy performance in a low temperature district heating system integrated with organic Rankine cycle, *J. Zhejiang Univ. A*, vol. 19: pp. 461–478.

Wieland, C., Schifflechner, C., Braimakis, K., Kaufmann, F., Dawo, F., Karellas, S., Besagni, G., Markides, C.N., 2023, Innovations for organic Rankine cycle power systems: Current trends and future perspectives. *Appl. Therm. Eng*, vol. 225: p. 120201.

ORC SEVILLE 2023
7th International Seminar on O.R.C. Power Systems

© 2024 Editorial Universidad de Sevilla. Este es un artículo de acceso abierto distribuido bajo los términos de la licencia de uso y distribución Creative Commons (BY-NC-ND 4.0)

DOI: https://dx.doi.org/10.12795/9788447227457_28

Optimization of a Partially Evaporating Organic Rankine Cycle with thermal non-equilibrium expansion.

Xander van Heule[1,2,*], Tasos Skiadopoulos[3], Dimitris Manolakos[3], Michel De Paepe[1,2], Steven Lecompte[1,2]

[1] *Ghent University, Department of Electromechanical, systems and Metal Engineering, Sint-Pietersnieuwstraat 41 Ghent, Belgium*
[2] *Flanders Make, Leuven, Belgium, FlandersMake@Ugent.be*
[3] *Agricultural University of Athens, Department of Agricultural Engineering, Iera Odos street 75 Athens, Greece*

*Corresponding Author: xander.vanheule@ugent.be

ABSTRACT

The Trilateral Flash Cycle (TFC) is an alternative to the Organic Rankine Cycle (ORC). The TFC have been shown to have greater exergy efficiencies compared to the ORC in low-grade heat-to-power conversion. This is a result of the more efficient heat transfer from the heat carrier to the working fluid, even though the TFC has inherently a lower thermal efficiency. However, these results are based on cycle modeling assuming equilibrium conditions, but the actual two-phase expansion process is a non-equilibrium process. Thermal non-equilibrium between vapour and liquid occurs during the evaporation (or flashing) of the working fluid during the two-phase expansion process. The liquid phase has a temperature greater than the corresponding pressure's saturation temperature and the equilibrium assumption overestimates the actual vapour quality. In a previous work, this non-equilibrium expansion was modeled and predicted based on the homogeneous relaxation model (HRM). In this work, the impact of the non-equilibrium process on the efficiency of the TFC is investigated and compared to the equilibrium model. The overall power recuperation is around 86% lower when including the thermal non-equilibrium nature of the expansion process. Therefore, the thermodynamic non-equilibrium losses should thus be incorporated when predicting the performance of a TFC.

176

1 INTRODUCTION

The reduction in greenhouse gas emissions, to reduce the effects of climate change, consists of a wide variety of possible actions. One such action is the reduction of the total process losses through recuperative methods. One of the most significant losses with the current global infrastructure is waste heat (Firth *et al.*, 2019, Forman *et al.*, 2016) for which there exist multiple methods to recover this lost energy. The estimated global waste heat is around 52% of the global energy input of which around 65% is low-temperature waste heat. If these waste energy streams could be efficiently harvested, it would reduce the required initial energy input as a larger share of this energy would become useful, reducing greenhouse gas emissions in the process. The largest untapped sector of waste heat was the transport sector according to Firth *et al.* (2019). Methodologies to harvest waste heat exist such as the Organic Rankine Cycle (ORC) or variants thereof. One such variant is the Trilateral Flash cycle (TFC) which does not evaporate the working fluid in the evaporator. Instead, a saturated liquid is expanded to the low pressure compared to a superheated vapour in the basic ORC. This cycle has larger net power output compared to the basic ORC (Li *et al.*, 2017, Fischer, 2011), especially with lower heat source temperatures (Woodland *et al.*, 2020). This is a result of the better temperature profile matching between the waste heat carrier and the working fluid (Lecompte *et al.*, 2015a) within the evaporator. However, these studies do assume similar isentropic efficiencies for both vapour and two-phase expanders. It is also possible to partially evaporate the working fluid within the evaporator of the cycle, this cycle is

known as the Partially Evaporating Organic Rankine Cycle (PEORC). This reduces the temperature profile matching but also decreases the volume flow rate of the cycle compared to the TFC, which can become large (Fischer, 2011). This can result in higher net power output of the cycle (Lecompte *et al.*, 2013) due to the reduction in required pumping power. This is especially the case when the pump's isentropic efficiency is low.

In literature, when cycles are studied which incorporate two-phase expansion, assumptions are made to describe this process. As mentioned, it is often based upon an isentropic efficiency, as similarly done for vapour expansion processes. Another assumption often made is the thermodynamic stability of the process. However, it has been shown that this assumption does, depending on the expander type, not have good agreement with experimental data. Currently, this assumption corresponds to experimental data for Lysholm expanders operating in two-phase conditions (Öhman and Lundqvist, 2013) but not for reciprocating expanders (Kanno and Shikazono, 2015) where the non-equilibrium effects are not negligible and represent a substantial part of the losses.

In previous work (van Heule *et al.*, 2023), the two-phase expansion within a reciprocating expander was modelled by using an adapted homogeneous relaxation model (HRM) and compared to the homogeneous equilibrium model (HEM). The HEM is based on the conservation equations with the assumption that the mixture is in thermodynamic equilibrium at all times. This implies that evaporation can happen instantaneously. The HRM is based on the HEM but without the thermal equilibrium assumption. Instead, a vapour generation rate equation is used which describes the evaporation rate based on a relaxation equation (Downar-Zapolski *et al.*, 1996). Hereby it is possible to have a mixture of saturated vapour and superheated liquid at the same chamber pressure as was also experimentally observed by Kanno and Shikazono (2015). In this work, this model is implemented within a Trilateral Flash cycle and optimized based on the cycle's net power output which is compared to an optimization with the HEM expansion.

2 METHODS

177

2.1 Modeling of thermal non-equilibrium expansion

The thermal non-equilibrium occurring within the expander chamber of a reciprocating expander was chosen to be modelled with an adapted Homogeneous Relaxation Model. This model assumes that the phases have the same pressure, as they occupy the same expansion volume, but not that the phases necessarily have the same temperature even though the expansion occurs within the two-phase region. This is a result of an evaporation equation that limits the evaporation rate through an empirical thermal relaxation time as expressed in equations (1) and (2):

$$\frac{\Gamma_g}{\rho} = -\frac{x - \bar{x}}{\Theta} \tag{1}$$

$$\Theta = \Theta_0 \cdot \epsilon^a \cdot \psi^b \tag{2}$$

, where Γ_g is the volumetric vapour generation rate, ρ the mixture density, x the actual vapour quality, $\bar{x}$ the equilibrium vapour quality, Θ the relaxation time, ϵ the void fraction and ψ the non-dimensional pressure difference defined in equations (3) and (4) depending on the operational pressure.

$$\psi = \frac{p_s - p}{p_s} \qquad if\ p < p_{\text{lim}} \tag{3}$$

$$\psi = \frac{p_s - p}{p_c - p_s} \qquad if\ p > p_{\text{lim}} \tag{4}$$

where p_s is the saturation pressure corresponding to the liquid superheat, p is the actual pressure, p_c is the critical pressure, and p_{lim} an empirical pressure threshold. The values of the numerical parameters Θ_0, a, and b in equation (2), determined experimentally by Downar-Zapolski *et al.* (1996), are respectively $6.51 * 10^{-4} s$, -0.257 and -2.24 when equation (3) is used and $3.84 * 10^{-7} s$, -0.54 and -

1.76 when equation (4) is used and the empirical pressure threshold was 10 bar. These values were based on water flowing through a diverging nozzle. This was adapted by van Heule *et al.* (2023) based on the experimental data of Kanno and Shikazono (2017) who performed expansion experiments with water in a piston moving with a trapezoidal movement profile. Based on this experimental data, the best fitting values of the numerical parameters Θ_0, a, and b are $9 * 10^{-15} s$, -0.7, and -15.7 respectively but only for the definition using equation (3) as only pressures beneath 10 bar were experimented on.

The model keeps track of the mass and internal energy of each phase separately throughout the expansion process. The actual vapour quality can easily be calculated in each time step based on the masses of each phase as expressed in equation (5), while the equilibrium vapour fraction is a function of the total internal energy of the mixture within the expansion chamber and the saturated specific internal energy values corresponding with the chamber pressure as expressed in equation (6):

$$x = \frac{m_g}{m_l + m_g} \tag{5}$$

$$\bar{x} = \frac{u - u_l}{u_g - u_l} \tag{6}$$

where m_g is the vapour mass, m_l the liquid mass, u_g and u_l the specific internal energy of saturated vapour and liquid at the working chamber respectively, and u the specific internal energy of the entire mixture. All fluid properties are obtained through the REFPROP 10 (Lemmon *et al.*, 2018) library including the metastable liquid temperature, required for p_s in equations (3) and (4), based on thespecific internal energy of the liquid phase and the working chamber pressure. The working chamber pressure in turn is obtained through the saturated vapour phase assumption of the HRM model through REFPROP.

2.2 Partial evaporating organic Rankine cycle

178

As mentioned in Section 1, the Partial Evaporating ORC (PEORC) is similar to a basic ORC but the working fluid is not fully evaporated within the evaporator. The PEORC used in this study is for a constant heat carrier flow, reciprocating expander geometry, condensing pressure, and evaporating pressure. The boundary conditions used are listed in Table 1 and Figure 1 is an example of the cycle with a vapour quality of 0.3. Point 1 on this figure is determined by the pump subcooling and the condensing pressure. Point 2 is calculated based on constant isentropic pump efficiency. Point 3, the inlet of the expander, is determined by the evaporating pressure and the initial vapour quality of the expansion. Point 4* is the state at the end of the expansion stroke and model. However, this point is not yet in equilibrium and does therefore not have a defined location within this type of temperature-entropy diagram. Here it is plotted on the location with the same density and specific internal energy. The process from point 4* to 4 on Figure 1 is an isochoric process between the metastable point 4* and thermodynamic stable point 4 at the low pressure. This thus includes both non-equilibrium losses and over- or under-expansion losses. Lastly, an isobaric heat rejection process occurs within the condensor to the predefined subcooling to close the cycle. The pinch point condition within the evaporator can occur either at the heat source exit or within the evaporator where the working fluid starts boiling. Which condition occurs depends on the vapour quality at which expansion is occurring. For low vapour qualities at the expander inlet, the pinch point will occur at the heat source outlet, while it occurs at the working fluid saturated point for higher expander vapour qualities. The cycle can dynamically switch between the two conditions depending on which assumed location indeed gives a higher temperature difference at the other location. The geometric properties of the free piston expander are also listed in Table 1 and are based on a reciprocating expander for waste heat recovery of a truck engine (Rijpkema *et al.*, 2021). The stroke and expander cycle speed can be altered based on the requirements of the mass flow rate coupled with the choice of expansion inlet quality. The intake stroke is taken as 25% of the entire expanding stroke (Glavatskaya *et al.*, 2012).

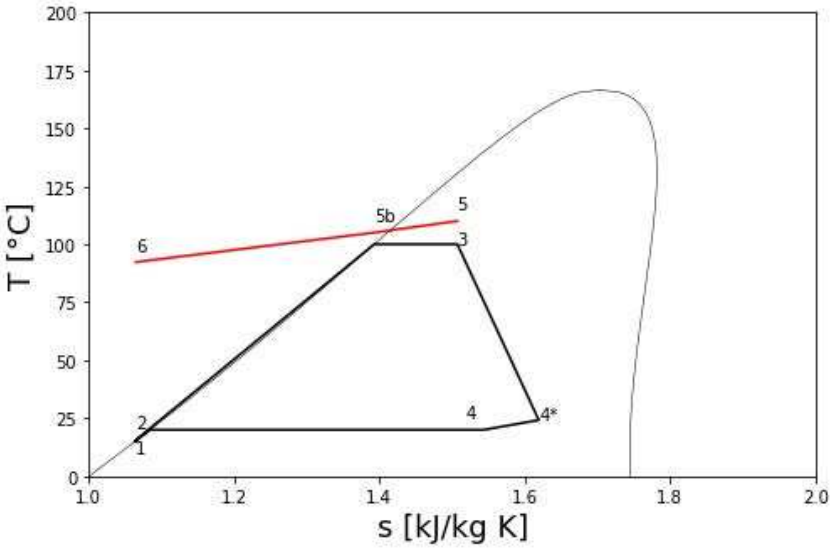

Figure 1: TS diagram of PEORC with expander inlet vapour quality equal to 0.3 where point 4* represents a metastable condition with corresponding density and specific internal energy.

Table 1: Boundary conditions of the partially evaporating Organic Rankine Cycle.

Condensing temperature	20 °C
Evaporating temperature	100 °C
Working fluid	R1233ZD(E)
Heat carrier	Air
Heat source temperature	110 °C
Heat source flow rate	0.2 kg/s
Subcooling pump	5 °C
Evaporator pinch point	5 °C
Isentropic pump efficiency	0.7
Vapour quality at expander inlet	0-1
Expander diameter	0.09 m
Expander clearance length	0.003 m
Intake stroke duration	25 %

179

In the following, the cycles will be compared based upon the net power output as defined in equations (7) to (9):

$$W_{net} = W_{exp} - W_{pump} \tag{7}$$

$$W_{pump} = \dot{m_{wf}} \cdot (h_2 - h_1) \tag{8}$$

$$W_{exp} = \frac{\int p \cdot dV}{t_{cycle}} \tag{9}$$

where W_{net} is the net power output of the cycle, W_{exp} the power delivered by the expander during the expansion stroke, W_{pump} the power required to run the pump, $\dot{m_{wf}}$ the mass flow rate of the working fluid, h_2 and h_1 the specific enthalpy at the outlet and inlet of the pump respectively, p the pressure within the working chamber, V the volume of the working chamber, and t_{cycle} the duration of one expander stroke cycle. Because the heat source is taken constant, this power is also a measure of the second law efficiency as defined in equation (10) (Lecompte *et al.*, 2015b):

$$\eta_{II} = \frac{W_{net}}{E_{hs,in}} \tag{10}$$

where η_{II} is the second law efficiency and $E_{hs,in}$ is the exergy flow within the system of the heat source. The isentropic efficiency of the expander is defined in equation (11) were h_3 is the specific enthalpy at the expander inlet (point 3 in Figure 1) and h_{4s}^* the isentropic specific enthalpy of point h_4^* in Figure 1.

$$\eta_s = \frac{W_{exp}}{\dot{m_{wf}} \cdot (h_3 - h_{4s}^*)} \tag{11}$$

3 RESULTS

3.1 Impact of vapour quality on working fluid flowrate

The choice of vapour quality at the start of expansion has a large impact on the required flow rate of the working fluid as presented in Figure 2.

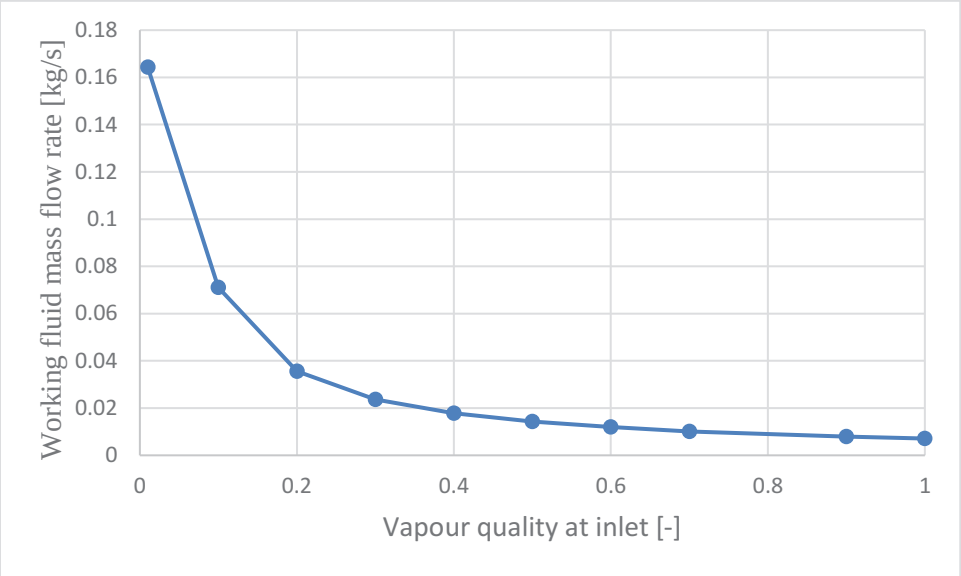

Figure 2: Required working fluid mass flow rate in function of vapour quality.

As mentioned, this phenomenon of large flow rates is a known issue with the TFC as the required pumping power drastically increases. Choosing a vapour quality already slightly higher than saturated liquid already drastically reduces the required pumping power and thus increases the net power output of the cycle. The difference in the required mass flow rate is also problematic for the chosen expander as the dimensions were predefined. One possibility would be to use multiple expanders and assume the two phase inlet condition is equally split across the different expanders. As an example, using two of these expanders for an inlet vapour quality of 0.1 increases the net power output compared to only one expander as each expander only has half the required mass flow rate resulting in less under expansion losses. However, this does not result in a higher overall net power production compared to other vapour qualities operating with one expander. Thus in the following discussion, only one expander is used irrespective of the vapour quality to find the optimal operation point.

3.2 Cycle optimization

First, the cycle from Table 1 will be optimized for the net power production, defined in Equation (7), with respect to the vapour quality at the end of the evaporator, point 3 in Figure 1. For this configuration, the optimal vapour quality is found to be 0.51 with a net power production of 477.9 W. The net power production in function of vapour quality is shown in Figure 3 where the expanders strokes per minute are optimized on each operation point. A lower vapour quality of the optimum is not beneficial to the cycle as the increase in pumping power is dominant, while an increase in vapour quality is not beneficial

due to a reduced heat transfer within the evaporator as a result from the pinch point condition, resulting in less net power production. The optimum point found matches with the speed where the expander on which the dimensions are based (Rijpkema *et al.*, 2021) has an isentropic filling factor of 1. This indicates the important impact of the expander design choice on the optimum working point of the cycle. The isentropic efficiency of the expansion (equation (11)) is also included in Figure 3. This is rather constant around the optimum design point. The impact of the dimensions of the expander on the required strokes per minute and net power is presented in Table 2. A change in the clearance length of the dead volume or the diameter has an impact on the net power but a respectively big change in optimal strokes per minute. The optimum with these other expander dimensions changes for the same cycle.

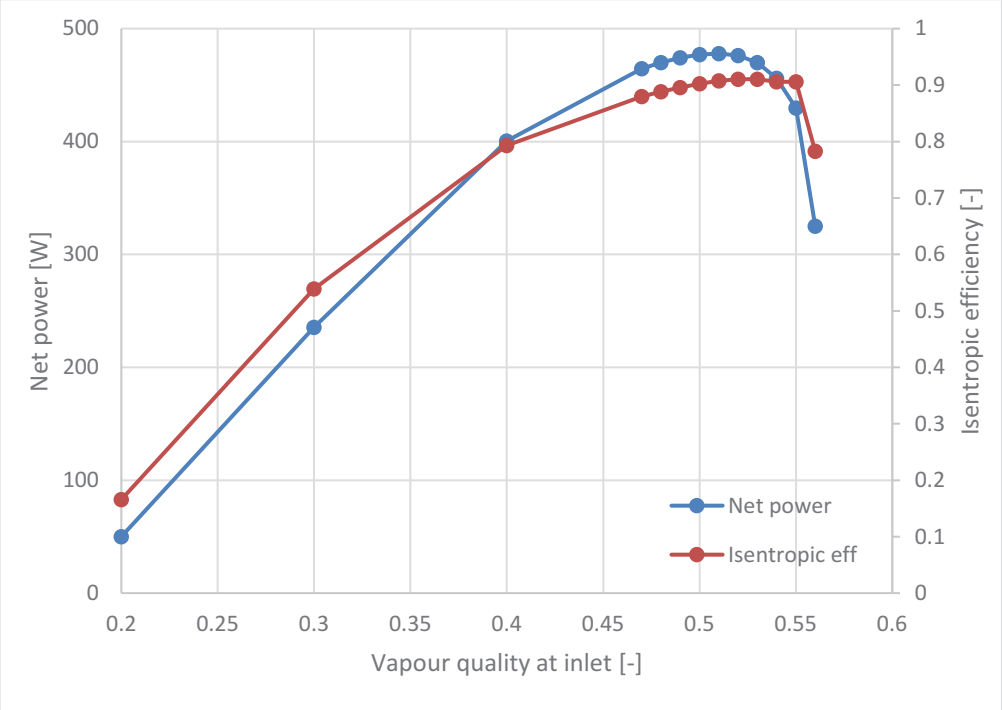

Figure 3: Net power produced of the described TFC in function of vapour quality.

Table 2: Impact of expander dimensions on cycle performance with an expander inlet vapour quality of 0.5.

Diameter [m]	Clearance length [m]	Required strokes per minute [rpm]	Net power [W]
0.09	0.003	963	477.0
0.09	0.002	1575	463.4
0.09	0.004	667	468.0
0.08	0.003	1394	429.9
0.10	0.003	634	459.1

4 DISCUSSION

The performance of the PEORC around the found optimum is compared to the same cycle, but the expansion is modeled without the HRM. It is thus assumed that equilibrium is achieved throughout the entire process at each point in time. The results are shown in Table 3. Firstly the net power with the incorporation of the homogeneous relaxation model is consistently around 86% of the net power output without the HRM which is a non-negligible amount that should be taken into account in cycle comparisons. However, this is less than the benefit gained when comparing the PEORC to a Basic ORC.

It is hereby speculated that the PEORC is still beneficial compared to the Basic ORC for low-temperature heat sources, but in a lesser extent than originally derived. The optimum for the cycle, without incorporating the non-equilibrium expansion, occurs at a slightly lower vapour quality compared to the cycle including the HRM.

Table 3: Cycle performance with HRM and HEM expansion using the same cycle time.

Vapour quality [-]	Net power HRM [W]	Net power HEM [W]
0.54	456.0	526.1
0.53	470.0	543.3
0.52	476.1	551.8
0.51	477.9	555.1
0.50	477.0	555.5
0.49	474.2	553.7
0.48	470.0	550.5

5 CONCLUSIONS

A Trilateral Flash Cycle (TFC) is modeled for a constant heat source, expander design, high pressure, and low pressure. The expansion within the TFC incorporates the thermal non-equilibrium phenomena occurring within a reciprocating expander. This is incorporated through the use of the Homogeneous Relaxation Model (HRM) where the liquid phase can be in a metastable superheated state as the evaporation occurs slower than thermodynamic stable conditions would require. The mass flow rate of the working fluid is heavily dependent on the vapour quality at the evaporator outlet, resulting in very high pumping power for low vapour qualities and thus a low net power output. On the other hand, a decrease in transferred heat within the evaporator for increasing vapour qualities also results in lower net power outputs. Thus an optimum occurs for the chosen cycle and expander. With the choices taken in this paper, the optimum was found at a vapour quality of 0.51. The performance of the chosen cycle is only around 86% of the same cycle when the non-equilibrium expansion is not incorporated within the expander model, indicating the importance of this phenomenon within the reciprocating expander.

182

In future work, the findings will be validated based on an experimental campaign on a two-phase reciprocating piston expander, which is currently under construction. Additionally, the cycle simulation could be adapted to optimize the cycle without predefining the expander dimensions. In this way, an expander can be designed to best fit a certain application.

NOMENCLATURE

ϵ	void fraction	(–)	ρ	density	(kg/m³)
Θ	relaxation time	(s)	h	specific enthalpy	(J/kg)
m	mass	(kg)	p	pressure	(Pa)
t	time	(s)	V	volume	(m³)
u	specific internal energy	(J/kg)	W	power	(W)
$\bar{x}$	equilibrium vapour quality	(–)	x	vapour quality	(–)
Γ	volumetric vapour generation rate	(kg/m³s)			

Subscript

c	critical
g	vapour phase
l	liquid phase
s	saturated
wf	working fluid

REFERENCES

Downar-Zapolski, P., Bilicki, Z., Bolle, L., Franco, J., 1996, The non-equilibrium relaxation model for one-dimensional flashing liquid flow, *Int. J. Multiph. Flow*, vol. 22, no. 3: p. 473-483.

Firth, A., Zhang, B., Yang, A., 2019, Quantification of global waste heat and its environmental effects, *Appl. Energy*, vol. 235, no. 1: p. 1314-1334.

Fischer, J., 2011, Comparison of trilateral cycles and organic Rankine cycles, *Energy*, vol. 36, no. 1: p. 6208-6219.

Forman, C., Muritala, I.K., Pardemann, R., Meyer, B., 2016, Estimating the global waste heat potential, *Renewable Sustainable Energy Rev.*, vol. 57, no. 1: p. 1568-1579.

Glavatskaya, Y., Podevin, P., Lemort, V., Shonda, O., Descombes, G., 2012, Reciprocating expander for an exhaust heat recovery rankine cycle for a passenger car application, *energies*, vol. 5: p. 1751-1765.

Kanno, H., Shikazono, N., 2015, Experimental and modeling study on adiabatic two-phase expansion in a cylinder, *Int. J. Heat Mass Transf.*, vol 86, no. 1: p. 755-763.

Lecompte, S., van den Broek, M., De Paepe, M., 2013, Thermodynamic analysis of the partially evaporating trilateral cycle, *Int. Seminar on ORC power systems*, p. 1-4.

Lecompte, S., Huisseune, H., van den Broek, M., Vanslambrouck, B., De Paepe, M., 2015a, Review of organic Rankine cycle (ORC) architectures for waste heat recovery, *Renewable Sustainable Energy Rev.*, vol. 47, no. 1: p. 448-461.

Lecompte, S., Huisseune, H., van den Broek, M., De Paepe, M., 2015b, Methodical thermodynamic analysis and regression models of organic rankine cycle architectures for waste heat recovery, *Energy*, vol. 87, no. 1: p. 60-76.

Lemmon, E.W., Bell, I.H., Huber, M.L., McLinden, M.O., 2018, NIST Standard Reference Database 23: Reference Fluid Thermodynamic and Transport Properties-REFPROP, Version 10.0, *National Institute of Standards and Technology*, Standard Reference Data Program, Gaithersburg.

Li, Z., Lu, Y., Huang, Y., Qian, G., Chen, F., Yu, X., Roskilly, A., 2017, Comparison study of Trilateral Rankine Cycle, Oraginc Flash Cycle and basic Organic Rankine Cycle for low grade heat recovery, *Energy Procedia*, vol.142, no. 1: p. 1441-1447.

Öhman, H., Lundqvist, P., 2013, Experimental investigation of a lysholm turbine operating with superheated, saturated and 2-phase inlet conditions, *Appl. Therm. Eng.*, vol. 50, no. 1: p. 1211-1218.

Rijpkema, J., Thantla, S., Fridh, J., Andersson, S.B., Munch, K., 2021, Experimental investigation and modeling of a reciprocating piston expander for waste heat recovery from a truck engine, *Appl. Therm. Eng.*, vol 186, no. 1: p. 1-15.

van Heule, X., Skiadopoulos, A., Manolakos, D., De Paepe, M., Lecompte, S., 2023, Modelling of two-phase expansion in a reciprocating expander, *Appl. Therm. Eng.*, vol. 218, no. 1: p. 1-10.

Woodland, B.J., Ziviani, D., Braun, J.E., Groll, E.A., 2020, Considerations on alternative organic Rankine Cycle congurations for low-grade waste heat recovery, *Energy*, vol. 193, no. 1: p. 1-17.

ACKNOWLEDGEMENT

I would like to thank the Research Foundation-Flanders for their financial support through FWO-Flanders grants (1SD9723N).

ORC SEVILLE 2023
7th International Seminar on O.R.C. Power Systems

© 2024 Editorial Universidad de Sevilla. Este es un artículo de acceso abierto distribuido bajo los términos de la licencia de uso y distribución Creative Commons (BY-NC-ND 4.0)

DOI: https://dx.doi.org/10.12795/9788447227457_29

COST-EFFECTIVE OPTION OF COLD ENERGY UTILIZATION IN PHARMACEUTICAL INDUSTRY

Sindu Daniarta[1,2,*], Dawid Sowa[1], Ádám Havas[2], Attila R. Imre[2,3], Piotr Kolasiński[1]

[1] *Wrocław University of Science and Technology, Department of Thermodynamics and Renewable Energy Sources, Wrocław, Poland*
[2] *Budapest University of Technology and Economics, Department of Energy Engineering, Budapest, Hungary*
[3] *Centre for Energy Research, Department of Thermohydraulics, Budapest, Hungary*

*Corresponding Author: sindu.daniarta@pwr.edu.pl / daniarta@energia.bme.hu

ABSTRACT

In pharmaceutical industries, nitrogen is used for several purposes, including inerting storage containers to prevent chemical reactions with oxygen at a temperature range of 2 to 8 °C. To meet these specifications, the regasification of liquefied nitrogen (LIN), transforming the liquefied nitrogen into gas phases at certain temperatures and pressures, is necessary. One potential solution that can be applied to increase efficiency and reduce costs while maintaining strict quality and safety standards in the pharmaceutical industry is a replacement of the conventional LIN regasification process with an organic Rankine cycle (ORC). This process could utilize cold energy from the process while using nitrogen as a cooling source and ambient air as the hot side of the thermodynamic cycle. Using the ORC system for this cold energy utilization is promising as the technology is now more developed, compact, relatively reasonable cost, and reliable. Since there are few investigations in cold energy utilization as power generation, this article discusses the techno-economic feasibility of the ORC system in the case of its application in pharmaceutical industries with a particular focus on cold energy utilization in LIN regasification. In this analysis, propane was selected as the working fluid of the ORC system as it has good criteria such as thermal properties, zero ozone depletion potential, and low global warming potential. The analysis was optimized for different heat source conditions. Several designs (with and without the direct expansion system) were developed. In the end, their techno-economic performances and cost-effectiveness were compared. The obtained results show that replacing the conventional LIN regasification in the pharmaceutical industry with an ORC system may improve the efficiency of the system and reduce power consumption. The results of the study additionally indicate that, in terms of cost-effectiveness, reusing existing components of the prior system – specifically, the nitrogen vaporizers and pump – would result in a 23.81% reduction in investment costs and a 22.00% decrease in levelized cost of energy (LCOE).

1 INTRODUCTION

According to the International Energy Agency (IEA), the demand for nitrogen will be significantly growing for several applications and industries by 2030 and 2050 (IEA, 2022). Pure nitrogen, which manufacturers obtain in liquid form, is necessary for several pharmaceutical operations that include inerting storage containers to prevent chemical reactions with oxygen at a temperature range of 2 to 8 °C. When nitrogen is utilized, it must be regasified and the temperature and pressure was set to desired condition before use. The energy required to separate nitrogen from the air and then liquefy the nitrogen is high, and often all of this energy is lost when nitrogen is regasified without proper reutilization. In regasification, heat is required to evaporate the liquefied nitrogen (LIN) to the gas phase. The regasification can be done in several approaches: by vaporizing without utilization, absorbing the cold energy directly for other purposes or even acting as a cold solution for power generation.

In literature studies, several studies were found discussing the utilization of LIN cold energy as power generation. Recent articles (Gao *et al*., 2022; Tian *et al*., 2023; Wang *et al*., 2022) reported the experimental investigation on the utilization of liquid nitrogen as a heat sink for a 1 kW small-scale organic Rankine cycle (ORC). In these studies (Gao *et al*., 2022; Tian *et al*., 2022), the performance of basic ORC was also compared to regenerative ORC and the result shows that regenerative ORC outperforms basic ORC. Moreover, several studies (Tafone *et al*., 2017; Wojcieszak, 2019) have reported the utilization of LIN cold energy via a direct expansion system as power generation in which the expander is directly used to expand the nitrogen gas. For the use of cold energy from LIN, both ORC and a direct expansion system are promising; therefore, it appears that they may be employed in the pharmaceutical industries.

Data taken from the one of pharmaceutical industries in Hungary reported that the monthly consumption of LIN, from which the average daily consumption could be inferred as the production is non-stop. In the opinion of the authors, there is still room to improve the performance of the system based on the utilization of cold energy taken from LIN. Due to the likely lack of studies related to the use of LIN regasification in this industry, therefore, in this study, the aim is to present the utilization of the cold energy taken from LIN regasification to generate electricity. An ORC and a direct expansion were considered in this application as promising solutions. The current work explores the performance and cost-effectiveness of the designed ORC and the direct expansion in the application in order to identify the cost-effective option for the improvement of the industry. The economic evaluation includes the calculation of the levelized cost of electricity (LCOE) which is a parameter for determining the economic feasibility of power generation.

2 METHODS

The thermodynamic model and the economic analysis were developed for the design of a single ORC and direct expansion system for the utilization of cold energy which is computed using computer-based simulation via MATLAB and the thermal properties data taken from REFPROP 10.0 (Lemmon *et al*., 2018). In this case, the designed power generation system from the LIN regasification is illustrated in Figure 1. Moreover, the principle of operation of this system can be described based on Figure 1.

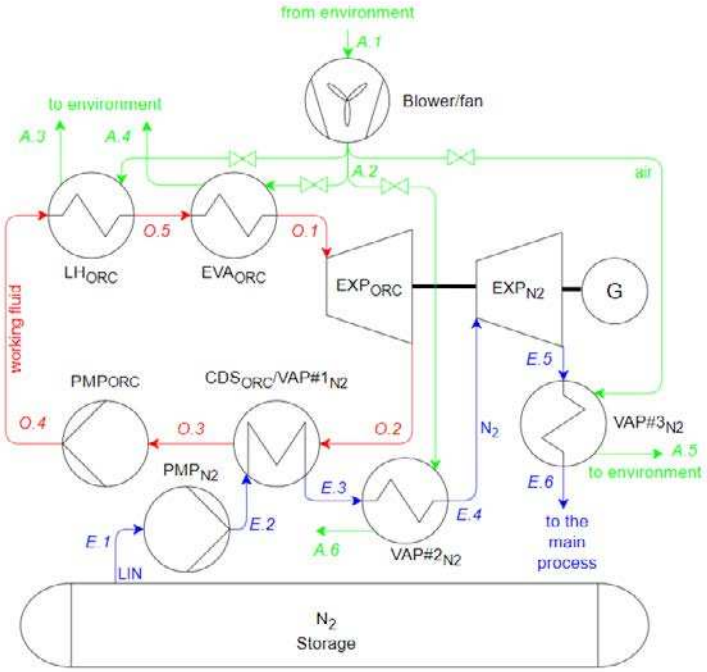

Figure 1: A flow process diagram of the designed system, where LH, EVA, EXP, G, CDS, PMP, VAP, and LIN represent liquid heater, evaporator, expander, generator, condenser, pump, vaporiser, and liquid nitrogen, respectively.

The ORC, is a system that includes an expander, heat exchangers (condenser and evaporator), a pump, and a generator, could be installed in the LIN regasification system utilizing the cold energy of LIN through the condenser. The condenser is used to condense the working fluid of ORC (from the process point O.2 to O.3), while simultaneously evaporating the LIN into the gas phase under specific temperature and pressure (see, process E.2-E.3). For the short distribution system, the LIN is pressurized up to 3 MPa (Darvishmanesh *et al*., 2011). Moreover, an additional system like a direct expansion system could be installed for LIN regasification. Vaporizing of nitrogen (see, process E.3-E.4) requires heat to increase the temperature so then it could be directly expanded (see, point E.5). Since the temperature of nitrogen is still low after the expansion, it needs further heat addition to reach desired temperature according to the requirements, that is why the vaporizer is required to be installed (see, process E.5-E.6). It is worth noting that heat sources in the process of evaporation utilize the air from the environment, so the blower/fan is required in this case.

2.1 Thermodynamic model and assumptions

In this study, the power generation is designed based on ORC utilizing cold energy as heat sinks and the air as heat sources (which is the same manner as in these articles (Habibi *et al*., 2018; Wajs *et al*., 2022)), while the direct expansion system is used to expand the cooling source (which is the similar method as in these articles (Tafone *et al*., 2017; Wojcieszak, 2019)). Mass and energy balance equations for various components illustrated in Figure 1 are described using Equations (1) and (2), where $\dot{m}$, h, $\dot{W}$, and $\dot{Q}$ represent the mass flow rate in kg/s, specific enthalpy in kJ/kg, power in kW, and heat transfer rate in kW, respectively. The LIN is pressurized to 3 MPa (Darvishmanesh *et al*., 2011) and the mass flow rate is varied based on the monthly consumption data from the factory, while the air temperature is assumed using the monthly mean temperature in Hungary taken from this data (The World Bank, 2021). Moreover, the list of components and the processes are listed in Table 1.

$$\sum \dot{m}_{\text{inlet}} = \sum \dot{m}_{\text{outlet}} \tag{1}$$

$$\dot{Q} + \sum \dot{m}_{\text{inlet}} h_{\text{inlet}} = P + \sum \dot{m}_{\text{outlet}} h_{\text{outlet}} \tag{2}$$

186

Table 1: List of components and specific processes referred to in Figure 1.

List of component	Specific enthalpy (kJ/kg)	Mass flow rate (kg/s)	Product (kW)
ORC expander	$h_{\text{O.1}} - h_{\text{O.2}}$	$\dot{m}_{\text{wf}}$	$P_{\text{ORC,EXP}}$
ORC condenser	$h_{\text{O.2}} - h_{\text{O.3}}$	$\dot{m}_{\text{wf}}$	$\dot{Q}_{\text{ORC,CDS}}$
ORC pump	$h_{\text{O.4}} - h_{\text{O.3}}$	$\dot{m}_{\text{wf}}$	$P_{\text{ORC,PMP}}$
ORC liquid heater	$h_{\text{O.5}} - h_{\text{O.4}}$	$\dot{m}_{\text{wf}}$	$\dot{Q}_{\text{ORC,LH}}$
ORC evaporator	$h_{\text{O.1}} - h_{\text{O.5}}$	$\dot{m}_{\text{wf}}$	$\dot{Q}_{\text{ORC,EVA}}$
Nitrogen pump	$h_{\text{E.2}} - h_{\text{E.1}}$	$\dot{m}_{\text{N2}}$	$P_{\text{N2,PMP}}$
Nitrogen vaporizer #1	$h_{\text{E.3}} - h_{\text{E.2}}$	$\dot{m}_{\text{N2}}$	$\dot{Q}_{\text{N2,VAP\#1}}$
Nitrogen vaporizer #2	$h_{\text{E.4}} - h_{\text{E.3}}$	$\dot{m}_{\text{N2}}$	$\dot{Q}_{\text{N2,VAP\#2}}$
Nitrogen expander	$h_{\text{E.4}} - h_{\text{E.5}}$	$\dot{m}_{\text{N2}}$	$P_{\text{N2,EXP}}$
Nitrogen vaporizer #3	$h_{\text{E.6}} - h_{\text{E.5}}$	$\dot{m}_{\text{N2}}$	$\dot{Q}_{\text{N2,VAP\#3}}$
Blower/fan	$h_{\text{A.2}} - h_{\text{A.1}}$	$\dot{m}_{\text{air}}$	$P_{\text{air,fan}}$

Some assumptions are taken into consideration as follows. Propane (R-290) is selected as a working fluid for ORC since this substance has been tested for experimental investigation (Gao *et al*., 2022; Tian *et al*., 2023; Wang *et al*., 2022). The mass flow rate of nitrogen was calculated based on the monthly consumption of LIN consistent throughout 254 working days. All components are operating in a steady-state condition. In the heat exchanger, the change of kinetic and potential energy of the stream is negligible, no heat and pressure losses occur, and it operates in constant pressure, constant overall heat transfer coefficient, and constant specific heat. The pinch temperature of the heat source and the evaporator is set at 5°C. This value also applies to condensers and nitrogen. Moreover, the isentropic

efficiency of the pump and expander is assumed at 0.8 (Astolfi *et al*., 2017; Habibi *et al*., 2018), and the efficiency of the fan is 0.6 (Walraven *et al*., 2015). The expander of ORC is operating in the two-phase conditions. Operation in these conditions is possible for some rotary volumetric expanders (Daniarta and Kolasiński, 2021; Francesconi *et al*., 2022; van Heule *et al*., 2022). In addition, the power of the fan was calculated using the function (Walraven *et al*., 2015) that can be expressed in Equation (3).

$$P_{\text{air,fan}} = \frac{\Delta p_{\text{air}} \dot{m}_{\text{air}}}{\rho_{\text{air}}} \tag{3}$$

The specific enthalpy and the mass flow rate of the components listed in Table 1 could be used to calculate the power consumption, power production, and heat transfer rate. By using these parameters, the net efficiency of the cold energy utilization could be determined as a function of net power output over the heat transfer rate input as described in Equation (4). It is worth noting that the heat transfer rate input includes the liquid heater and evaporator. Some existing components such as vaporizer #2 and vaporizer #3 (that were the modified components from the prior system), the liquid pump of nitrogen, and the blower/fan are not taken into consideration in the calculation of the efficiency.

$$\eta_{\text{system}} = \frac{P_{\text{net}}}{\dot{Q}_{\text{input}}} = \frac{P_{\text{ORC,EXP}} + P_{\text{N2,EXP}} - P_{\text{ORC,PMP}} - P_{\text{N2,PMP}} - P_{\text{air,fan}}}{\dot{Q}_{\text{ORC,LH}} + \dot{Q}_{\text{ORC,EVA}} + \dot{Q}_{\text{N2,VAP\#2}} + \dot{Q}_{\text{N2,VAP\#3}}} \tag{4}$$

2.2 Estimation and cost analysis

The investment cost is calculated based on the additional purchased components such as the ORC system (expander, condenser, pump, evaporator and liquid heater), nitrogen expander, and generator. The cost (C_p^0) for each component could be estimated based on their capacities (X), for example, the estimated cost for the rotary component is determined from the power or volumetric flow rate ($\dot{V}$), the estimated cost for stationary components (liquid heater, evaporator, and condenser) from the area of the heat exchanger (several functions of the estimated cost for selected components are described in Equation (5) and summarized in Table 2). Other components are listed in Table 3. In this case, power consumption and power production could be computed using the enthalpy change and the mass flow rate aforementioned. Moreover, the area of the heat exchanger (A) could be determined using obtained heat transfer rate ($\dot{Q}$), the logarithmic mean temperature difference (LMTD) and the overall heat transfer coefficient (U) (Habibi *et al*., 2018). Using several assumptions that are classified by (Silla, 2003), the overall heat transfer coefficient for different components of heat exchangers have been assumed. The specific value assumed for the overall heat transfer coefficient is 0.600 kW/m^{2}K for the air-cooled heat exchangers and 2.029 kW/m^{2}K for the condenser. These coefficients represent the conditions of heat transfer between a fluid and its surroundings/other fluids per unit area and per degree of temperature difference.

$$C_{\text{p}}^0 = 10^{K_1 + K_2 \log_{10}(X) + K_3 (\log_{10}(X))^2} \tag{5}$$

Table 2: List of the estimated cost function for selected components based on Equation (5).

List of components	Capacity in unit	Range of capacity	Estimated cost function		
			K_1	K_2	K_3
ORC pump and nitrogen pump in USD (Turton *et al*., 2012)	kW	1-100	3.4771	0.1350	0.1438
Generator (Pili *et al*., 2019)	kW	80-10,000	4.1055	0.0570	0.0797
An air-cooled heat exchanger (liquid heater, evaporator, vaporizer) in USD (Turton *et al*., 2012)	m^2	200-2,000	4.0336	0.0234	0.0497

Table 3: List of the estimated cost function for other components

List of components	Capacity in unit	Range of capacity	Estimated cost function
ORC expander and nitrogen expander in USD (Towler and Sinnott, 2021)	kW	100-20,000	$C^0_{\mathrm{p,EXP}} = -14 \cdot 10^3 + 1.9 \cdot 10^3 (P_{\mathrm{EXP}})^{0.75}$
Heat exchangers (condenser) in USD (Smith, 2005)	m^2	80-4,000	$C^0_{\mathrm{p,CDS}} = 32.8 \cdot 10^3 \left(\frac{A_{\mathrm{CDS}}}{80}\right)^{0.68}$
Blower/fan in EUR (Walraven *et al*., 2015)	kW	1-100	$C^0_{\mathrm{p,fan}} = 1.31 \cdot 10^4 \left(\frac{P_{\mathrm{fan}}}{50}\right)^{0.76}$

The purchase cost of the condenser was obtained in 2000, the air-cooled heat exchangers (e.g., liquid heater, evaporator, and vaporizer) and pump in 2001, the expander in 2010, and the generator and the blower/fan in 2013. Moreover, the CEPCI for 2000, 2001, 2010, and 2013 are 391.0, 397.0, 532.9, and 567.3, respectively (Mignard, 2014; Rodgers, 2022). In this study, the purchase cost of all equipment was converted from USD to EUR and the annual average exchange rate of USD to EUR in 2000, 2001, 2010, and 2013 was 1.09, 1.11, 0.75, and 0.75, respectively (Statista, 2023). Then the total purchase cost ($C_{\mathrm{p,total}}$) was calculated using CEPCI for 2022 of 813 (Rodgers, 2022) and multiplied with the bare module factor (F_{BM}) for expanding the existing system to estimate the bare module of capital cost (C_{BM}), where the bare module factor for each component is taken from the book (Turton *et al*., 2008). Furthermore, the capital cost of the bare module is multiplied by 1.18 to estimate the capital cost of the total module (C_{TM}) that includes contractor fees, auxiliary facilities, the cost of integration and installation, the cost of the project, and so on (Lemmens, 2016). These capital costs of the bare module and the total module aforementioned could be expressed as a function of the purchased cost, described as Equations (6) and (7), respectively.

188

$$C_{\mathrm{BM}} = \sum_{i=1}^{n} C_{\mathrm{p,i}} \cdot F_{\mathrm{BM}} \tag{6}$$

$$C_{\mathrm{TM}} = 1.18 \sum_{i=1}^{n} C_{\mathrm{BM,i}} \tag{7}$$

Two indicators, the specific investment costs (SIC) and levelized cost of electricity ($LCOE$), are chosen to evaluate the economic feasibility of the redesigned system. These specific investment costs and levelized cost of electricity can be expressed as functions by Equations (8) and (9). Some assumptions are taken into account in this analysis. The reference year is 2022. The annual discount rate (d) and inflation rate are 6.08% and 2.00%, respectively. The lifespan of the installed system (y) is 20 years and the operating time (t) is 254 working days. Moreover, the cost of operation and maintenance is 0.01 EUR/kWh.

$$SIC = \frac{C_{\mathrm{TM}}}{P_{\mathrm{net}}} \tag{8}$$

$$LCOE = \frac{C_{\mathrm{TM}} + \sum_{i=1}^{y} \frac{C_t}{(1+d)^i}}{\sum_{i=1}^{y} \frac{P_{\mathrm{net}} \cdot t}{(1+d)^i}} \tag{9}$$

3 RESULTS AND DISCUSSION

The obtained result demonstrates that the net power generation varies based on the ambient air temperature, with power generation in the winter being comparatively lower than in the summer. The ORC and direct expansion system may provide 8.5 kW and 39 kW of gross power in December,

respectively. The potential gross power output of an ORC and a direct expansion system in July is 24.00 kW and 67.45 kW, respectively. Consequently, the system may generate 23.72 kW of net electricity (with a system efficiency of 13.16%) in December and 50.02 kW (with a system efficiency of 15.93%) in July, depending on the power consumption of the pump and blower/fan. Figure 2 shows the trend of the fluctuating net generated power.

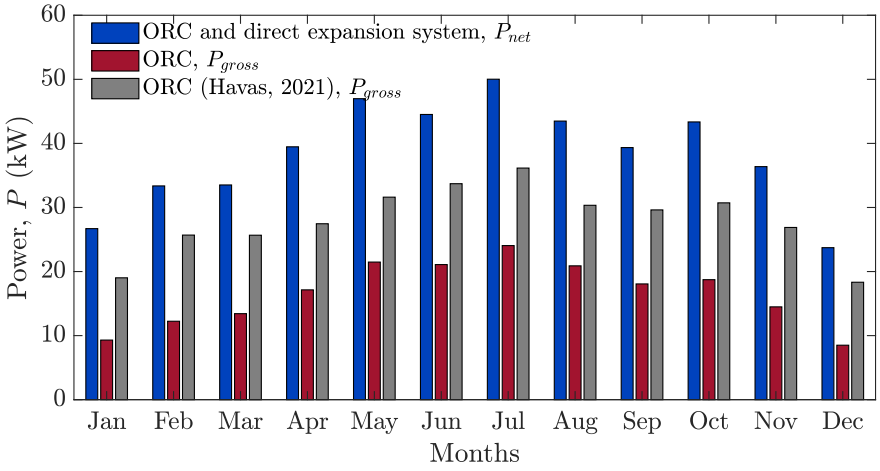

Figure 2: The monthly generated power.

In comparison, a Master thesis (Havas, 2021) reported the utilization of LIN cold energy using simplified ORC estimation. In this case, the cycle is assumed operating 5°C under ambient temperature and above LIN temperature. Although, it used ambient air as a heat source, slightly different average temperature data of ambient air were taken into consideration. Therefore, the fluctuating power generation was slightly different from this study. According to the ORC estimation (Havas, 2021), the system might generate 18.33 kW of gross electricity in December and 36.15 kW in July. The trend of both fluctuating gross ORC power based on the estimation (Havas, 2021) and this study is depicted in Figure 2. The result demonstrates that when compared to gross ORC power for this study, the mean absolute percentage error (MAPE) is 41.72%. It appears that the ORC estimation (Havas, 2021) predicts more gross power generation than expected.

189

For economic analysis, the calculation is performed based on the highest generated net power, which is shown in July (see, Figure 2). In this study, the economic analysis was performed using two different options. The first choice (i.e., Case #1) redesigns components (nitrogen pump and vaporizers) that are already in use (by reusing the existing vaporizers). Another option (i.e., Case #2) uses completely new components to replace the existing system (without reusing the existing vaporizers). These two possibilities are employed to see the cost-effective option and the difference between the choices for this utilization of LIN cold energy in the pharmaceutical business, where the difference is depicted in Figure 3 and summarized in Table 4. It shows that Case #1 might save the cost of a bare module by up to 56.52 thousand euros while reusing the nitrogen pump could cut the cost of a bare module by up to 15.25 thousand euros. In addition, case #1 offers a 23.81% capital cost reduction for the bare module.

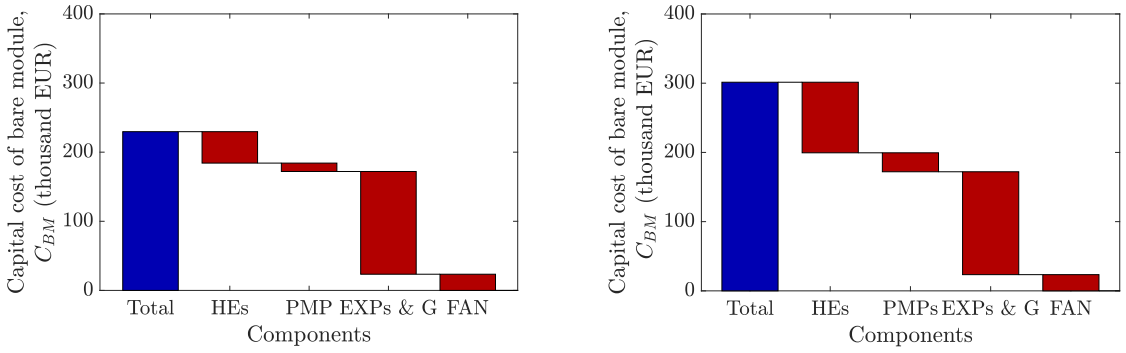

Figure 3: The capital cost of the bare module for (a) case #1 and (b) case #2.

Table 4: The obtained result of the economic analysis.

Options	C_{BM} (EUR)	C_{TM} (EUR)	SIC (EUR/kW)	$LCOE$ (EUR/kW)
Case #1	229,627.72	270,960.71	5,417.02	0.119
Case #2	301,394.12	355,645.07	7,110.03	0.153

Furthermore, the other obtained result in this study is indicated as the capital cost of the total module, investment cost, and LCOE which is summarized in Table 4. Case #2 offers an investment cost of 7.11 thousand euros per kW, and a total capital cost of 355.65 thousand euros, making its LCOE 0.034 euro/kW more expensive than Case #1. This study shows that utilization of LIN cold energy in pharmaceutical business using ORC and direct expansion in the Case #2 performs 31% investment cost more expensive than Case #1. It appears that Case #2 is less attractive compared to Case #1.

4 CONCLUSIONS

The industry is increasingly becoming more and more interested in increasing system efficiency. The potential utilization of LIN cold energy in the pharmaceutical business was discussed in this study. The result of this paper can be concluded as follows:

1. LIN cold energy can be used to generate power using an ORC and direct expansion system; taking into consideration the LIN regasification as the ORC's heat sink and expanding it to produce power.
2. The ORC estimation from (Havas, 2021) and the redesign of ORC were examined and compared.
3. The cost-effective solution for the use of LIN cold energy in pharmaceutical businesses was also discussed in this study. The outcome implies that reusing the system's existing components, such as the nitrogen vaporizers and pump (e.g., Case #1), may provide a more cost-effective solution than the suggested system making use of entirely new components (e.g., Case #2) that would save 23.81% on investment costs and 22.00% on LCOE.

190

It is worth noting that this paper highlights the potential benefits of implementing ORC and a direct expansion system on the utilization of LIN cold energy as power generation. Moreover, several areas could be also interesting to do in further work and research such as the dynamic simulation of the performance under different operating conditions as the system uses air as the heat source, testing the system in various cases scenarios, comparing the obtained simulation results with the validation through experimental study (that could be in lab scale or pilot project).

NOMENCLATURE

A	area	(m^2)	P	power	(kW)
C	cost	(EUR)	p	pressure	(Pa)
d	discount rate	(%)	ρ	density	(kg/m^3)
h	specific enthalpy	(kJ/kg)	$\dot{Q}$	heat transfer rate	(kW)
η	efficiency	(–)	SIC	specific investment cost	(EUR/kW)
K	constant	(–)	t	operating time	(hours)
$LCOE$	levelized cost of electricity	(EUR/kW)	X	capacity refers to A or P	(m^2 or kW)
$\dot{m}$	mass flow rate	(kg/s)	y	the lifespan of an installed system	(year)

Subscript

BM	bare module	p	purchase
CDS	condenser	PMP	pump
EVA	evaporator	t	operating time
EXP	expander	VAP	vaporizer
G	generator	wf	working fluid
LH	liquid heater	TM	total module

REFERENCES

Astolfi, M., Fantolini, A.M., Valenti, G., De Rinaldis, S., Inglese, L.D., Macchi, E., 2017, Cryogenic ORC To Enhance The Efficiency Of LNG Regasification Terminals, *Energy Procedia*, vol. 129: pp. 42–49.

Daniarta, S., Kolasiński, P., 2021, A preliminary study of two-phase volumetric expanders and their application in ORC systems, *in Proceedings of the 6th International Seminar on ORC Power Systems*, Technical University of Munich, Munich, id. 78.

Darvishmanesh, S., Firoozpour, L., Vanneste, J., Luis, P., Degrève, J., Van der Bruggen, B., 2011, Performance of solvent resistant nanofiltration membranes for purification of residual solvent in the pharmaceutical industry: experiments and simulation, *Green Chemistry*, vol. 13, issue 12: pp. 3476-3483.

Francesconi, M., Briola, S., Antonelli, M., 2022, A Review on Two-Phase Volumetric Expanders and Their Applications. *Appl. Sci.*, vol. 12, no. 20: p. 10328.

Gao, W., Wu, Z., Tian, Z., Zhang, Y., 2022, Experimental investigation on an R290-based organic Rankine cycle utilizing cold energy of liquid nitrogen, *Appl. Therm. Eng*., vol. 202: p. 117757.

Habibi, H., Zoghi, M., Chitsaz, A., Javaherdeh, K., Ayazpour, M., 2018, Thermo-economic analysis and optimization of combined PERC - ORC - LNG power system for diesel engine waste heat recovery, *Energy Convers. Manag*., vol. 173: pp. 613–625.

Havas, Á., 2021, *Kriogenikus rendszerek energetikai hasznosításának lehetőségei*. Master thesis, Budapest University of Technology and Economics, Budapest.

IEA, 2022. *Nitrogen demand by end use and scenario, 2020-2050*, IEA, Paris.

Lemmens, S., 2016, Cost Engineering Techniques and Their Applicability for Cost Estimation of Organic Rankine Cycle Systems, *Energies*, vol. 9, no. 7: p. 485.

Lemmon, E.W., Bell, I.H., Huber, M.L., McLinden, M.O., 2018, NIST Standard Reference Database 23: Reference Fluid Thermodynamic and Transport Properties-REFPROP, Version 10.0, National Institute of Standards and Technology. Stand. Ref. Data Program, Gaithersbg.

Mignard, D., 2014, Correlating the chemical engineering plant cost index with macro-economic indicators, *Chem. Eng. Res. Des.*, vol. 92, issue 2: pp. 285–294.

Pili, R., Romagnoli, A., Jiménez-Arreola, M., Spliethoff, H., Wieland, C., 2019, Simulation of Organic Rankine Cycle – Quasi-steady state vs dynamic approach for optimal economic performance, *Energy*, vol. 167, pp. 619–640.

Rodgers, T., 2022. *Chemical Engineering Plant Cost Index*, https://personalpages.manchester.ac.uk/staff/tom.rodgers/Interactive_graphs/CEPCI.html?reactors/ (accessed 4 April 2023).

Silla, H., 2003, *Chemical process engineering: design and economics*, CRC Press, Boca Raton: 504 p.

Smith, R., 2005. *Chemical process: design and integration*, John Wiley & Sons, West Sussex: 712 p.

Statista, 2023. *Euro (EUR) to U.S. dollar (USD) exchange rate from Jan 1999 - Apr 04, 2023*, https://www.statista.com/statistics/412794/euro-to-u-s-dollar-annual-average-exchange-rate/ (accessed 6 April 2023).

Tafone, A., Borri, E., Comodi, G., van den Broek, M., Romagnoli, A., 2017, Preliminary assessment of waste heat recovery solution (ORC) to enhance the performance of Liquid Air Energy Storage system, *Energy Procedia*, vol. 142: pp. 3609–3616.

The World Bank, 2021. *Hungary – Climatology*, https://climateknowledgeportal.worldbank.org/country/hungary/climate-data-historical (accessed 4 April 2023).

Tian, Z., Chen, X., Zhang, Y., Gao, W., Chen, W., Peng, H., 2023, Energy, conventional exergy and advanced exergy analysis of cryogenic recuperative organic rankine cycle, *Energy*, vol. 268: p. 126648.

Tian, Z., Gan, W., Qi, Z., Tian, M., Gao, W., 2022, Experimental study of organic Rankine cycle with three-fluid recuperator for cryogenic cold energy recovery, *Energy*, vol. 242: p. 122550.

Towler, G., Sinnott, R., 2021, *Chemical engineering design: principles, practice and economics of plant and process design*, Butterworth-Heinemann, Oxford: 1040 p.

Turton, R., Bailie, R.C., Whiting, W.B., Shaeiwitz, J.A., Bhattacharyya, D., 2012, *Analysis, synthesis and design of chemical processes*, Pearson Education, Michigan: 1007 p.

van Heule, X., De Paepe, M., Lecompte, S., 2022, Two-Phase Volumetric Expanders: A Review of the State-of-the-Art, *Energies*, vol. 15, no. 14: p. 4991.

Wajs, J., Mrozek, M., Fornalik-Wajs, E., 2022, Combined cold supply system for ship application based on low GWP refrigerants - Thermo-economic and ecological analyses, *Energy Convers. Manag.*, vol. 258: p. 115518.

Walraven, D., Laenen, B., D'haeseleer, W., 2015, Economic system optimization of air-cooled organic Rankine cycles powered by low-temperature geothermal heat sources, *Energy*, vol. 80: pp. 104–113.

Wang, F., Gao, W., Li, G., Tian, Z., Wang, X., 2022, Experimental study on power generation plant of a 1 kW small-scale Organic Rankine Cycle system using R290, *Energy Sci. Eng.*, vol. 10, issue 3: pp. 740–751.

Wojcieszak, P., 2019, Exergy Analysis of Liquid Nitrogen Power Cycles, *EPJ Web Conf.* vol. 201: p. 01004.

ACKNOWLEDGEMENT

Part of this study in the utilization of LIN cold energy was conducted in a Master's thesis in 2021 by Ádám Havas at the Budapest University of Technology and Economics, Hungary.

ORC SEVILLE 2023
7th International Seminar on O.R.C. Power Systems

© 2024 Editorial Universidad de Sevilla. Este es un artículo de acceso abierto distribuido bajo los términos de la licencia de uso y distribución Creative Commons (BY-NC-ND 4.0)

DOI: https://dx.doi.org/10.12795/9788447227457_30

NUMERICAL INVESTIGATION OF A TRANSONIC DENSE GAS FLOW OVER AN IDEALIZED BLADE VANE CONFIGURATION

A. Bienner[1,*], X. Gloerfelt[1], P. Cinnella[2], L. Hake[3] and S. aus der Wiesche[3]

[1] *Arts et Métiers, DynFluid Laboratory, 151 bd. de l'Hôpital, 75013 Paris, France.*
[2] *Sorbonne Univ., Jean Le Rond D'Alembert Institute, 4 place Jussieu, 75005 Paris, France.*
[3] *Muenster Univ. of Applied Sciences, Stegerwaldstr. 39, 48565 Steinfurt, Germany.*

*Corresponding author: aurelien.bienner@ensam.eu

ABSTRACT

A joint numerical and experimental investigation of an idealized blade vane configuration, representative of an ORC turbine, is undertaken using Novec649 as the working fluid. First laminar-turbulent transition over the blade is studied by means of large-eddy simulation (LES). The geometry of the leading edge is modified to avoid an incipient separation. Afterwards, RANS simulations are carried out for both air and Novec649. The dense gas flow achieves a lower pressure ratio and exit Mach number compared to air, while shock waves generated at the blade leading edge are weaker. However, the dense gas induces a lower base pressure resulting in higher losses. Qualitative and quantitative comparisons with experiments and with a wall-modeled LES are also planned.

1 INTRODUCTION

In most Organic Rankine Cycles (ORC), the working fluid, an organic compound, is compressed, heated, and then expanded in a turbine. The latter component can be critical for the cycle efficiency and it is of utmost importance to estimate the various loss mechanisms. Since ORC are intended to convert energy from relatively low-temperature sources, organic fluids are expanded in small-scale turbines, working in the transonic to supersonic regimes. At these flow speeds, the main losses in a linear cascade of turbine blades are due to shock-wave systems, laminar and turbulent boundary layers on blade walls and vortex shedding from the trailing edge (TE). Due to their molecularly complex structures, organic fluids operate in the so-called dense-gas regime, where the fundamental derivative of fluid dynamics is lower than one. A direct consequence is the decrease of the speed of sound during a compression, which would yield weaker shock waves, thus lower associated losses. On the contrary, the higher sound speed attained in the expansion fan close to the trailing edge would imply a lower base presssure, which can conversely increase the profile losses. Finally, little is known about the laminar-turbulent transition over ORC turbine blades. Designers generally assume a fully turbulent boudary-layer state but it is known that the transition will influence the viscous losses. Due to the combination of various mechanisms with a somehow contradictory influence, experimental and numerical databases are critical to improving turbine efficiency. Few facilities exist for dense gases and consist essentially in blowdown or suckdown tunnels, where only short-time statistics are possible (Baumgärtner *et al.*, 2020) A continuously running pressurized closed-loop wind tunnel (CLOWT) using Novec649, an environmentally friendly working fluid, in the high subsonic speed range, has been built at University of Muenster. Due to the high pressures and the high-density of Novec649, the experimental study of transonic linear cascade requires high compressor performance. As a consequence, the tunnel

test section has relatively small dimensions and measurements for a linear cascade are thus challenging (Hake *et al.*, 2023). One way out is to use an idealized vane configuration. Instead of an entire blade cascade, the test set-up is usually limited to a single, geometrically simple blade with side-walls designed to generate quasi-periodic flow conditions. This idea has been used to study the transonic TE flow and the associated profile losses, e.g. by Denton & Xu (1990) or Rossiter *et al.* (2023). An idealized vane configuration with low-curvature blades has been designed in the work of Passmann (2021). A picture of the CLOWT test section is shown in figure 1, where the test section height $B = 36.5$mm. The experiments were conducted with air as the working medium in the outlet Mach number range 0.8 to 1.7, and included Schlieren visualizations, blade pressure distribution and traversing probe measurements. While the profile is lacking the curvature that most turbine blade profiles exhibit, it can be used as a test case for the investigation of basic phenomena such as tip gap flows in Passmann *et al.* (2018) or loss mechanisms with a dense gas in the present study.

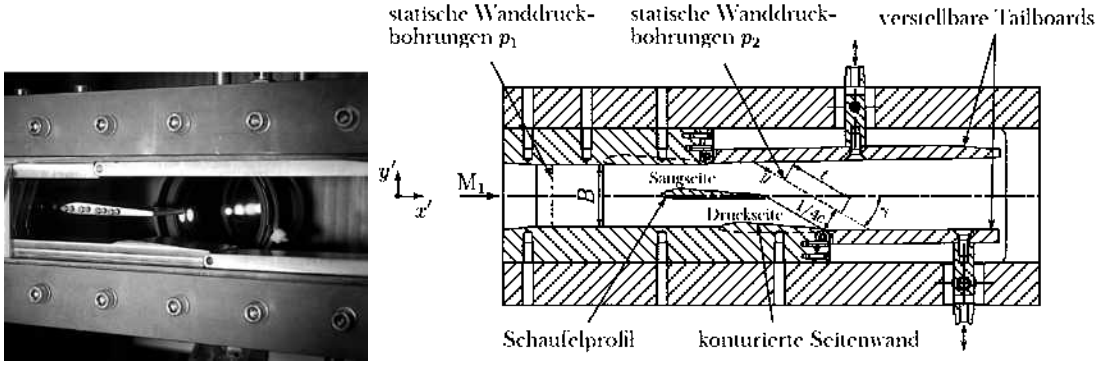

Figure 1: View (left) and sktech (right) of the experimental setup (from Passmann (2021).

Particular attention must be paid to the influence of the laminar-turbulent transition on turbine losses. Considering the high level of freestream turbulence (FST) intensity encountered in turbine environments, FST-induced transition is generally the principal mechanism of laminar-turbulent transition for turbine blades (Mayle, 1991; Sandberg & Michelassi, 2022). The Computational Fluid Dynamics (CFD) tools currently used in ORC design are based on Reynolds-averaged Navier-Stokes (RANS) models and usually ignore this phenomenon, considering that transition occurs straight downstream of blade leading edge (Romei *et al.*, 2020). To gain knowledge on FST-induced transition in dense-gas boundary layers (BL), a study was realized for a zero-pressure-gradient Novec649 BL by means of wall-resolved large eddy simulations (LES) (Bienner *et al.*, 2022*c*). It was found that, despite $M = 0.9$ in the freestream, the turbulent profiles were very close to incompressible databases due to the high specific heat of Novec649, which significantly reduces friction heating. Moreover, the large-scale FST was shown to influence not only the location of transition but also its mechanism, notably the laminar streaks size and arrangement. To investigate the effect of a finite thickness leading edge and of the favorable pressure that it induces on FST-induced transition, LES have been performed around the leading edge of our idealized turbine stator (Bienner *et al.*, 2022*b*). It was shown that transition occurs early on the blade and that the laminar-streak breakdown, which is usually the precursor of turbulent spots, is highly disrupted by large vortical structures impinging the leading edge. In the present paper, additional results on the leading edge study are presented, showing the influence of the geometry over the transition. Afterwards, the flow of Novec649 past the complete idealized blade is investigated using RANS, due to the extremely high cost of LES. A comparison with air flow in the same conditions is used to get insights into dense-gas effect on turbine efficiency. Companion experiments are scheduled for June/July 2023, and we plan to present them at the conference. High-fidelity wall-modeled LES are also planned.

194

M_{in}	c_{in} [m/s]	p_{in} [bars]	p_{in}/p_c	T_{in} [°C]	T_{in}/T_c	ρ_{in} [kg/m^3]	ρ_{in}/ρ_c	μ_{in} [Pa.s]	Γ_{in}
0.52	74	3.3	0.17	60	0.75	44.1	0.07	1.26×10^{-5}	0.8

Table 1: Thermodynamic and aerodynamic conditions at the inlet of LES domain. Subscript *in* is used for inlet quantities and subscript *c* for critical ones.

2 NUMERICAL SET-UP

The in-house code MUSICAA is used to solve the compressible Navier-Stokes equations over a curvilinear multiblock domain using generalized coordinate transformation. The fluid Novec649 is modeled with the Peng-Robinson-Stryjek-Vera equation of state (Stryjek & Vera, 1986) and the Chung-Lee-Starling model (Chung *et al.*, 1988) for transport properties. The ideal gas law and Sutherland's model are used for air flows. Concerning LES of the leading-edge region (§ 3), spatial discretization uses 10th-order centered finite differences for inviscid fluxes and 4th-order schemes for viscous fluxes, supplemented by a 10th-order selective filtering. A four-stage Runge-Kutta (RK4) algorithm is used for time integration and a fourth-order implicit residual smoothing (IRS) (Bienner *et al.*, 2022*a*) is applied to enlarge its stability limit and enable larger timesteps. Non-reflecting Tam & Dong's boundary conditions are applied at the inlet, top and outflow boundaries with imposed mean quantities from a companion RANS simulation. A sponge zone combining grid stretching and a Laplacian filter is added at the oulet. At the inlet, synthetic freestream turbulence is generated by means of Random Fourier Modes. Adiabatic no-slip conditions are applied at the wall and periodicity is enforced in the spanwise direction. More details can be found in Bienner *et al.* (2022*b*). For RANS simulations (§ 4), the Spalart-Allmaras model is used, with a turbulent viscosity prescribed at the inlet $\tilde{\nu} = 10\nu_\infty$. The RANS transport equation is discretized on a 3-point stencil, whereas 4th-order standard centered differences are used for the inviscid and viscous fluxes combined with a 4th-order Jameson-type selective filtering. As the repeated application of the filter can lead to an overdissipation for small time steps (or CFL numbers), the filtering coefficient χ is replaced by min(χ,CFL) (Edoh *et al.*, 2018), so that the shocks are sharply captured in steady computations. The RK4 algorithm is supplemented with a second-order IRS. Stagnation pressure and temperature are imposed at the inlet, based on Riemann invariants, whereas a back-pressure condition is used at the outlet. Adiabatic no-slip wall conditions are used.

195

3 INFLUENCE OF THE GEOMETRY ON LAMINAR-TURBULENT TRANSITION

To get insights into the laminar-turbulent transition for the idealized vane configuration, we performed LES on a subregion of the turbine vane centered around the suction side of the LE. Operating conditions are representative of the future experimental campaign in CLOWT facility (see table 1), corresponding to a flow of Novec649 in relatively dilute conditions. More details about the thermodynamic conditions are given in section 4.2, along with results concerning the Novec649 RANS simulation that served to initialize and to impose boundary conditions mean values in LES. The fundamental derivative of gas dynamics Γ has a value below 1 so that the flow occurs in the so-called dense-gas thermodynamic region, as used in ORC applications. In a first attempt, we used the idealized blade geometry of Passmann (2021), which was used to investigate tip gap effects on losses in the CLOWT facility (using air as the working fluid). The profile consists of simple circular arcs and straight lines. The rear parts of pressure and suction side are composed of straight lines. The suction side is inclined at an angle of 4.5° with respect to the pressure side. The chord length of the profile is set at *ch*=62 mm and a thick rounded TE shape was chosen (diameter of 2.4 mm). This leads to high Reynolds conditions, with $Re_{ch,in} = 9\times10^6$ with Novec649. The flow accelerates from $M = 0.5$ up to $M = 1.1$ at the outlet. The incoming FST has an intensity $T_u = \sqrt{(u'^2+v'^2+w'^2)/3} = 5\%$ and a Reynolds number $Re_{L_f} = 18\times10^3$, based on the turbulence integral length-scale L_f. A computational

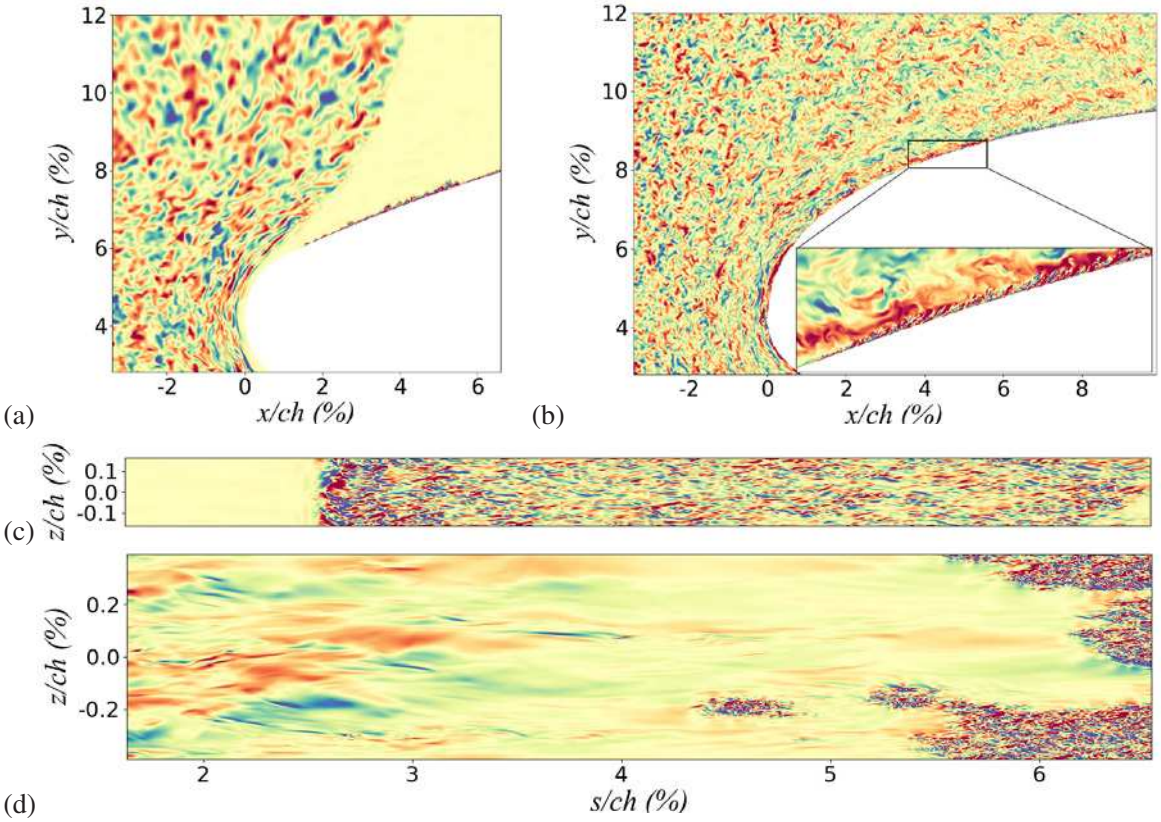

Figure 2: Snapshot of the spanwise fluctuations w' in a mid-span (a-b) and a wall-normal plane at $n^+ \sim 10$ (c-d) for the original (a-c) and smoothed (b-d) geometry. Levels: $\pm 0.05 \times c_{in}$

196

domain of 350 millions points was used, with a resolution $\Delta n_w^+ \times \Delta s^+ \times \Delta z^+ \sim 0.3 \times 25 \times 10$, where s and n denote the curvilinear abscissa along the blade and the wall-normal distance, respectively (Δn_w^+ being the resolution at the wall). Snapshots in mid-span and wall-normal planes are displayed in figures 2(a) and (c). FST has not yet impacted the leading-edge that the transition has already occurred on the suction side, meaning that the transition is not induced by the FST. The early turbulent front at $s = 1.5$ mm, which is clearly identified on the wall-normal slice, results from an incipient flow separation occuring at a curvature discontinuity resulting from the connection of two circles forming the idealized blade geometry.

In turbines, the most likely mechanism of laminar-turbulent transition is the FST-induced transition. Since we are interested in designing an idealized configuration representative of ORC turbines, a new geometry of the LE region is proposed to avoid the curvature discontinuity responsible for the laminar-separation-bubble transition. The curvature evolution is smoothed using two super-ellipses defined by $(\frac{a-x}{a})^n + (y/b)^n = 1$ (Narasimha & Prasad, 1994), where $n = 2.3$, $a/ch = 18.47\%$, $b/ch = 5.81\%$ for the suction side super-ellipse and $n = 2.4$, $a/ch = 26.70\%$, $b/ch = 4.18\%$ for the pressure side super-ellipse. Then, the suction side straight line is connected to the super-ellipse using a Bézier curve. The trailing-edge (TE) of the smoothed geometry is kept equal to the initial one. The original and smoothed nose geometries are compared in figure 3, the smoothed one being closer to the typical shape of turbine stator noses. The curvature discontinuity of the original design is visible in the right insert. Note that the pressure distribution on the blade is weakly affected. A new LES is carried out on a refined grid of 2.1 billions points, which yields a resolution $\Delta n_w^+ \times \Delta s^+ \times \Delta z^+ \sim 0.45 \times 13 \times 11$, typical of wall-resolved LES. The inlet turbulence corresponds to $T_u = 5\%$ and $Re_{L_f} = 11 \times 10^3$. Spanwise velocity snapshots in figure 2(b)-(d) show the

transitional front is no longer localized but is distributed along a transitional region where turbulent spots appear and merge to form the turbulent BL, as expected in a FST-induced transition. Further analyses of the LES results on the smoothed geometry can be found in Bienner *et al.* (2022*b*). An important conclusion is that the FST-induced transition occurs rapidly at approximately 6% of the chord, despite the favorable pressure gradient, which can delay significantly the transition location (Mayle, 1991). It also justifies the use of RANS simulations without any transition model in the following.

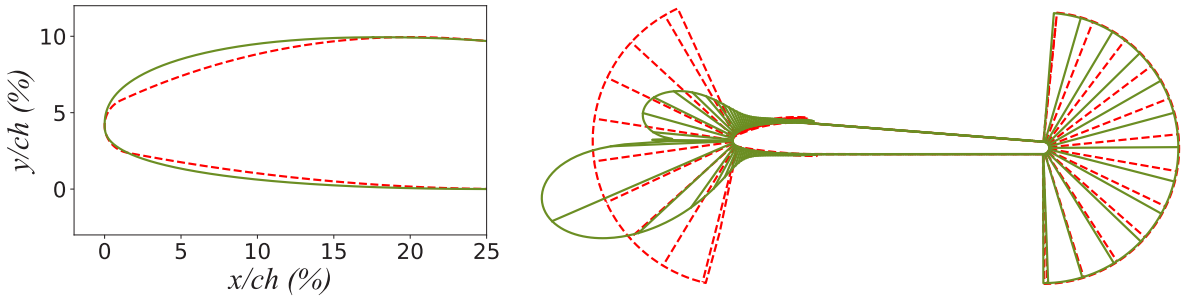

Figure 3: Comparison of the original (- - -) and smoothed (——) geometries: zoom on the LE region (left) and profile curvature (right).

4 PRELIMINARY STUDIES OF THE IDEALIZED TURBINE BLADE

4.1 Validation of the RANS strategy for air flow

To assess our RANS methodology, the experimental investigation with air in Passmann (2021) is numerically reproduced (the LE geometry is thus the original one). The 2D computational grid of 234×10^3 points has a resolution $\Delta n_w^+ \sim 1.0 - 1.2$ and $\Delta s/ch \sim 0.30\%$, with 720 points along the blade. The domain is extended 1.5 chord upstream of the LE and 2 chords downstream of the TE. At the inlet, a total pressure of $p_{0,1} = 4$ bars and a total temperature of $T_{0,1} = 308$ K are imposed. A comparison of the shock system in the TE region with an experimental Schlieren picture is proposed in figure 4. The numerical simulation correctly reproduces the fishtail shock system and the position of the oblique shock waves. Moreover, the pressure distribution along the blade in figure 4 (right) is also in good agreement with the experimental one. To check the grid convergence, RANS is also run on a finer mesh, with $\Delta s/ch \sim 0.22\%$ and 900 points along the blade. The pressure distribution perfectly matches the medium grid one, showing that mesh independency is achieved on the medium grid.

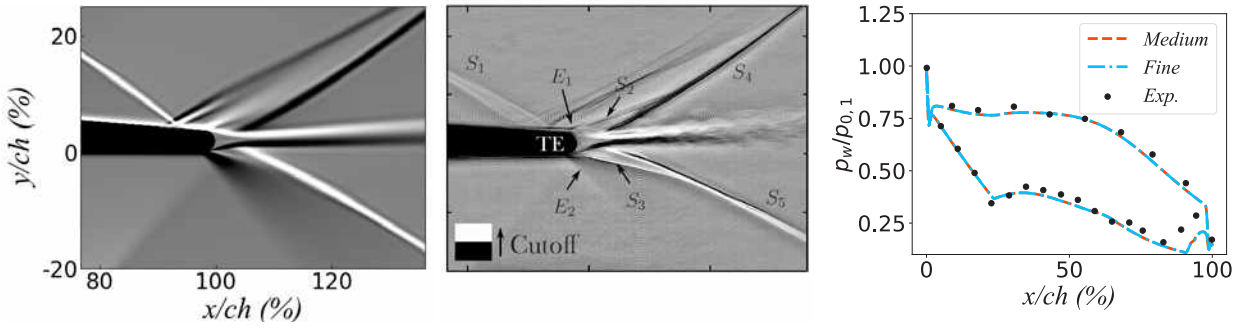

Figure 4: Schlieren visualizations of the shock system in RANS (left) and Passmann's experiment (middle). Right: pressure distribution around the blade from experiments and RANS simulations.

Case	ch $[mm]$	M_1	c_1 $[m/s]$	$p_{0,1}$ [bars]	$T_{0,1}$ $[K]$	$\rho_{0,1}$ [kg/m^3]	M_2	c_2 $[m/s]$	Re_{M_2}	π $p_{0,1}/p_2$
Novec649	61.2	0.55	76	3.8	335	55.0	1.59	87	8.5×10^6	3.7
Air	246	0.51	343	4.0	308	4.52	1.71	279	8.5×10^6	5.3

Table 2: Thermodynamic and aerodynamic conditions of RANS simulations.

4.2 Dense-gas effects

As already mentioned, the thermodynamic conditions selected for Novec649 correspond to relatively dilute conditions, with a total pressure of $p_{0,1} = 3.8$ bars and a total temperature of $T_{0,1} = 335$ K (see table 2). The inlet values are calculated one chord upstream of the LE and the exit values are evaluated along the line of measure plotted in figure 5, which corresponds to a distance of $0.25 \times ch/\cos(\gamma)$ where $\gamma = 60°$ denotes the stagger angle. The outlet Reynolds number Re_{M_2}, based on the chord and the outlet Mach number M_2, is equal to 8.5×10^6. Several regions of interest are identified in the Schlieren-like visualization of figure 5: laminar-turbulent transition (region 1), shock-wave-boundary layer interactions (region 2) and wake development (region 3).

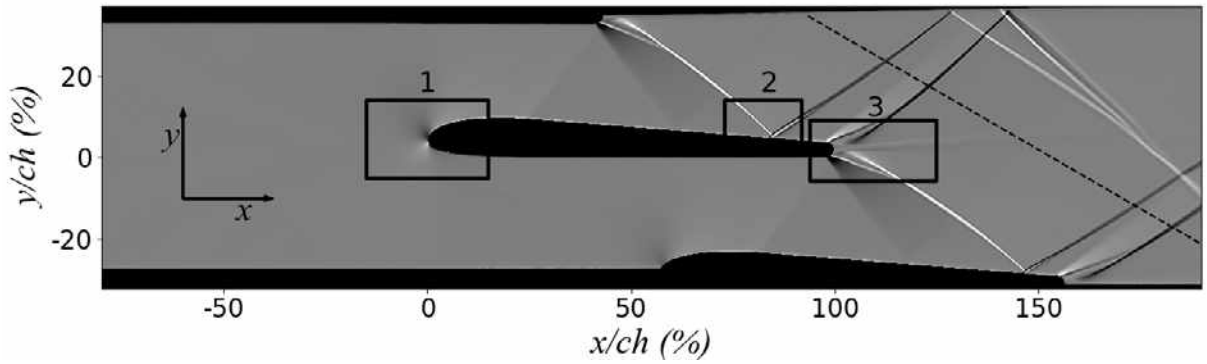

Figure 5: Schlieren-like visualization of the idealized blade vane configuration in the Novec649 2D RANS simulation (see section 4.2): density gradient in y-direction (levels $\pm10^4$). - - -: line of measure.

For comparison purposes, a simulation with air is also realized. The chord is modified to 246 mm in order to match the outlet Reynolds number of the Novec649 simulation and the newly designed nose is used (see table 2). First, we observe that the pressure ratio, $\pi = p_{0,1}/p_2$, is significantly lower in the Novec649 configuration ($\pi_{Novec649} = 3.7$) than in air ($\pi_{air} = 5.3$). To get more insights, the pressure distributions of the air and Novec simulations are compared in figure 6 (left). Concerning the air flow, the pressure distribution of the smoothed blade profile is rather similar to the one of the initial blade profile in figure 4 (right), as already mentioned in section 3. In line with the differences observed in pressure ratio, the pressure distribution levels around the blade for the Novec649 simulation are increased, which would correspond to a decrease of the isentropic Mach number. Moreover, a difference in the position of the reflected shock at the suction side is noticed. The fundamental derivative of gas dynamics $\Gamma = 1 + \frac{\rho}{c}\frac{\delta c}{\delta \rho}_s$, shown in figure 6 (right), increases from 0.8 upstream to 0.95 downstream but stays below 1.0, meaning that the flow occurs inside the dense-gas region. This results in a reverse behavior of the speed of sound compared to perfect gases, namely, $\frac{\delta c}{\delta \rho}_s < 0$ and the speed of sound increases while the flow expands. For instance, in the shock interaction region in figure 7, the speed of sound increases from 76 at the inlet to 90 at the outlet in the Novec649 flow whereas, in the air configuration, c decreases monotonically. This yields a lower Mach number increase in the Novec flow than in the air flow (see figure 8). Therefore, shock waves are weakened

in the dense gas yielding a lower pressure ratio. In particular, the higher pressure ratio across the impinging shock on the suction side in the air flow induces a larger separation bubble compared to the Novec649 flow (see figure 9). The second compression shock at the impingement, hardly noticeable in the dense gas configuration, is clearly visible in air. Due the larger separation region and the fact that the location of the shock is closer to the TE in the air flow, the BL remains separated at the TE downstream whereas it is attached in the Novec649 flow. Finally, due to the acceleration around the TE corner, the flow undergoes a supersonic expansion before separating from the TE. At the end of the recirculation region, the supersonic flow coming from the suction and pressure sides re-aligns by means of a fish-tail shaped system of shock waves. Due to the differences in the BL states and in the expansion around the TE, the opening angle of the fishtail shocks is increased with Novec649.

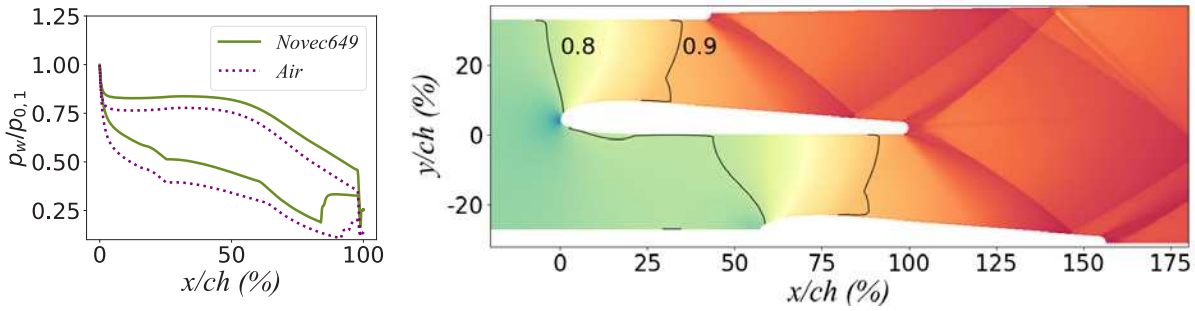

Figure 6: Left: pressure distribution of the Novec649 and air RANS simulation around the smoothed profile. Right: Γ field in the Novec649 RANS simulation (levels 0.7 to 1.0).

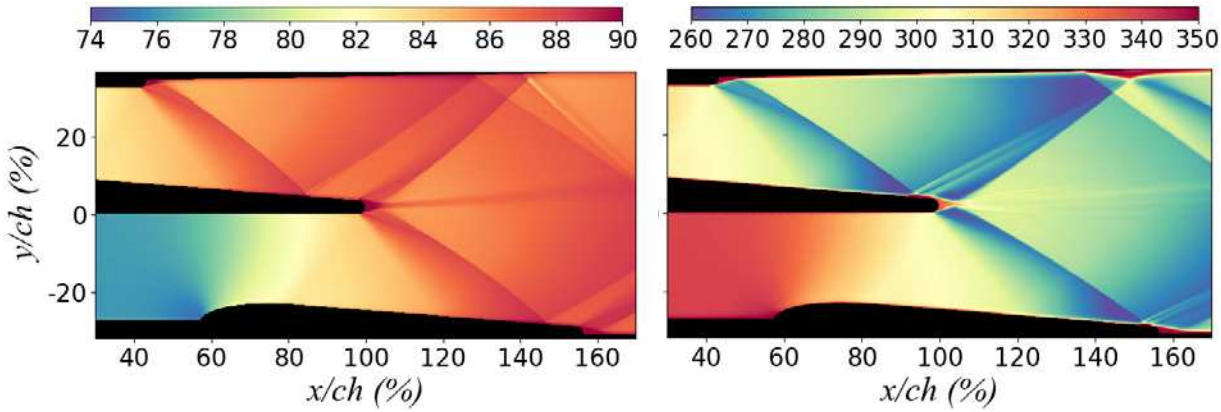

Figure 7: Sound speed c field of the Novec649 (left) and air (right) RANS simulation around the smoothed profile (levels 0.4 to 2.0).

5 CONCLUSION AND FUTURE WORK

The transonic dense gas flow over an idealized blade vane configuration has been studied by means of RANS simulations. When compared to air flow at similar Reynolds number conditions, the investigation reveals that the Novec649 flow exhibits weaker shocks due to the reverse behavior of the sound speed, ultimately leading to a lower pressure ratio between inlet and outlet. The shock topology is consequently affected, with a wider opening angle of the fishtail shocks in the Novec649 configuration. Moreover, the fact that the shock impingement in Novec649 arises more upstream of the TE with respect to air changes significantly

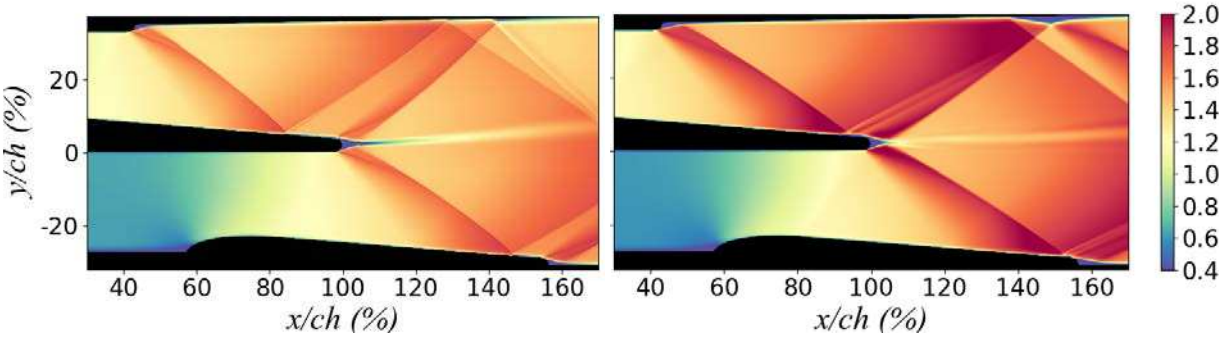

Figure 8: Mach number field of the Novec649 (left) and air (right) RANS simulation around the smoothed profile (levels 0.4 to 2.0).

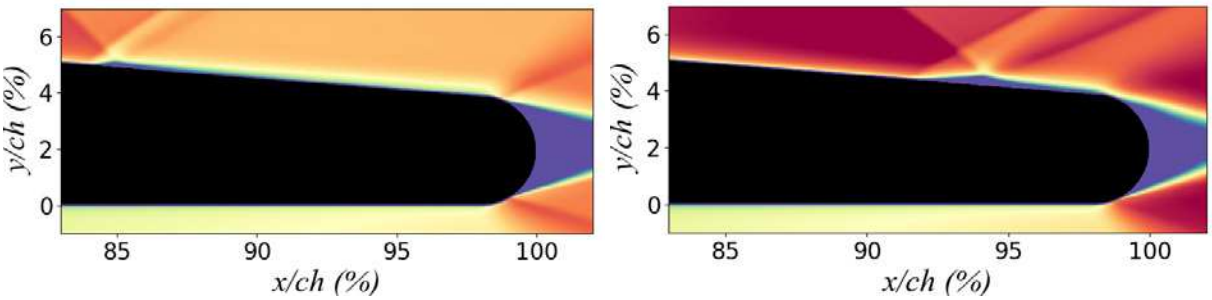

Figure 9: Mach number field of the Novec649 (left) and air (right) RANS simulation (levels 0.4 to 2.0): zoom on the shock-BL interaction and on the TE.

200

the shock-BL interaction and the BL state at the wake birth, which may affect the wake development. In particular, unsteady RANS captures the vortex shedding in the wake for the air flow whereas a steady wake is obtained in Novec649. This is a pitfall of RANS modeling, notoriously inaccurate for the prediction of several phenomena occurring in turbomachinery. For instance, RANS simulations cannot predict accurately the wake dynamics or fails in capturing shock-BL interaction dynamics, overestimating the shock strength while underestimating the size of separated region eventually occurring at the shock foot. We plan to perform high-fidelity simulations on the idealized blade configuration to investigate the complex dynamics in the wake vicinity. Due to the high Reynolds number based on the chord of the profile ($Re_{ch} \sim 10 \times 10^6$), a direct numerical simulation (DNS) or a wall-resolved LES is out of reach. Indeed, as seen in section 3, 2.1 billions points are necessary to simulate only $\sim 10\%$ of chord on the suction side, which leads to almost 40 billions in order to simulate the full blade. Therefore, the LES will be conducted with wall-model to relax the constraint on the near wall resolution but also to be able to significantly increase the timestep. Since we observed that the boundary layer becomes turbulent relatively rapidly, the use of wall-modeled LES is specially relevant to reduce the computational cost.

Even if weaker shocks are encountered with Novec649, the overall losses will not necessarily be lower. Indeed, the profile losses associated with the base pressure at the TE are expected to increase with dense gases. The wall-modeled LES will allow a proper description of the wake dynamics and thus a detailed analysis of the TE loss mechanisms. A comparison with air will be realized in order to quantify the effect of the dense gas on the turbine performance (Baumgärtner *et al.*, 2020) and on the energy separation phenomenon (Sieverding & Manna, 2020). The companion experiments will provide a quantitative and qualitative comparison with the numerical simulations, thanks to Schlieren imaging, pressure distribution around the blade

and pressure/velocity profiles in the blade wake.

ACKNOWLEDMENTS

This research has been funded by the Agence Nationale de la Recherche through the ANR-20-CE92-0019-02 project Regal-ORC. This work was granted access to the HPC resources of IDRIS and TGCC under the allocation A0132A01736 made by GENCI (Grand Equipement National de Calcul Intensif).

References

BAUMGÄRTNER, D., OTTER, J.J. & WHEELER, A.P.S. 2020 The effect of isentropic exponent on transonic turbine performance. *ASME Journal of Turbomachinery* **142** (8), 081007.

BIENNER, A., GLOERFELT, X. & CINNELLA, P. 2022*a* Assessment of a high-order implicit residual smoothing time scheme for multiblock curvilinear meshes. *11th International Conference on Computational Fluid Dynamics (ICCFD11)* 11-15 July, Maui, HI, USA .

BIENNER, A., GLOERFELT, X. & CINNELLA, P. 2022*b* Leading-edge effects in freestream turbulence induced transition in a dense gas flow. *13th Direct and Large-Eddy Simulations (DLES13)* 26-28 October, Udine, Italy .

BIENNER, A., GLOERFELT, X., CINNELLA, P., HAKE, L., AUS DER WIESCHE, S. & STREHLE, S. 2022*c* Study of bypass transition in dense-gas boundary layers. *12th International Symposium on Turbulence and Shear Flow Phenomena Conference (TSFP12)* 19-22 July, Osaka, Japan (Online) .

CHUNG, T.H., AJLAN, M., LEE, L.L. & STARLING, K.E. 1988 Generalized multiparameter correlation for nonpolar and polar fluid transport properties. *Ind. Eng. Chem.* **27** (4), 671–679.

DENTON, J.D. & XU, L. 1990 The trailing edge loss of transonic turbine blades. *ASME Journal of Turbomachinery* **112**, 277–285.

EDOH, A.K., MUNDIS, N.L., MERKLE, C.L., KARAGOZIAN, A.R. & SANKARAN, V. 2018 Comparison of artificial-dissipation and solution-filtering stabilization schemes for time-accurate simulations. *J. Comput. Phys.* **375**, 1424–1450.

HAKE, L., SUNDERMEIER, S., AUS DER WIESCHE, S., MATAR, C., CINNELLA, P. & GLOERFELT, X. 2023 Investigation of the turbulence level and the vortex shedding in a turbine cascade working with an organic vapor at subsonic Mach numbers. In *7^{th} International Seminar on ORC Power Systems (ORC2023)*. Seville, Spain.

MAYLE, R.E. 1991 The role of laminar-turbulent transition in gas turbine engines. In *Proceedings of ASME International Gas Turbine and Aeroengine Congress and Exposition*. Orlando, USA.

NARASIMHA, R. & PRASAD, S. N. 1994 Leading edge shape for flat plate boundary layer studies. *Experiments in Fluids* **17**, 358–360.

PASSMANN, M., AUS DER WIESCHE, S. & JOOS, F. 2018 An experimental and numerical study of tip-leakage flows in an idealized turbine tip gap at high Mach numbers. In *ASME Turbomachinery Technical Conference and Exposition*, , vol. GT2018-76366. Oslo, Norway.

PASSMANN, M. G. 2021 Experimentelle Untersuchungen zu transsonischen Schaufel-Spaltströmungen in Axialturbinen. PhD thesis, Münster University.

ROMEI, A., VIMERCATI, D., PERSICO, G. & GUARDONE, A. 2020 Non-ideal compressible flows in supersonic turbine cascades. *J. Fluid Mech.* **882**, A12–1–A12–26.

ROSSITER, A.D., PULLAN, G. & MELZER, A.P. 2023 The influence of boundary layer state and trailing edge wedge angle on the aerodynamic performance of transonic turbine blades. *ASME Journal of Turbomachinery* **145**, 041008.

SANDBERG, R.D. & MICHELASSI, V. 2022 Fluid dynamics of axial turbomachinery: blade and stage-level simulations and models. *Ann. Rev. Fluid Mech.* **54**, 255–285.

SIEVERDING, C. & MANNA, M. 2020 A review on turbine trailing edge flow. *International Journal of Heat and Fluid Flow* **5** (2), 1–60.

STRYJEK, R. & VERA, J.H. 1986 PRSV: An improved Peng-Robinson equation of state for pure compounds and mixtures. *The Canadian Journal of Chemical Engineering* **64** (2), 323–333.

ORC SEVILLE 2023
7th International Seminar on O.R.C. Power Systems

© 2024 Editorial Universidad de Sevilla. Este es un artículo de acceso abierto distribuido bajo los términos de la licencia de uso y distribución Creative Commons (BY-NC-ND 4.0)

DOI: https://dx.doi.org/10.12795/9788447227457_31

COMPREHENSIVE ANALYSIS OF ORC-VCC SYSTEM FOR AIR CONDITIONING FROM LOW-TEMPERATURE WASTE HEAT

Łukasz Witanowski[1,*]

[1] *Turbine Department, Institute of Fluid-Flow Machinery, Polish Academy of Sciences, ul. Fiszera 14, 80-231 Gdańsk, Poland,*
*Corresponding Author: lwitanowski@imp.gda.pl

ABSTRACT

Due to the need to reduce electricity consumption, methods of increasing the efficiency of energy use are being sought. One of the possibilities is the use of low-temperature waste heat for the production of electricity or cooling. Systems that convert heat into cold seem particularly attractive. This approach allows, above all, the removal of the generator. It eliminates the electrical part of the expander and, as a consequence, increases the efficiency of waste heat utilization, simplifies the construction of the ORC turbogenerator, and removes certain restrictions.
The paper presents an analysis of the ORC-VCC cycle using waste heat at a temperature of 95°C and heat up to 130kW. Various novel working fluids (e.g. R1224yd(Z), R1233zd(E), R1336mzz(Z)) are considered. Selected fluids are characterized by low global warming potentials. An in-house code was developed and used to calculate cycle parameters. Single and multi-objective optimization was performed, aiming at the maximization of the ORC efficiency, Net Present Value (NPV) and the Internal Rate of Return (IRR). Pareto frontiers were obtained, and a decision-making method was used to select an optimum solution. The obtained ORC efficiency was 5.25%, COP_{VCC} 0.47 and the cycle efficiency was above 27.1%.

1 INTRODUCTION

The Organic Rankine Cycle (ORC) and Vapor Compression Cycle (VCC) are two prominent thermodynamic processes employed in various industrial applications for energy conversion and refrigeration purposes, respectively (Lecompte *et al.*, 2015). Recently, the integration of these two cycles, known as the ORC-VCC system, has garnered substantial attention from researchers and industry practitioners due to its potential for increased energy efficiency and waste heat recovery. The primary benefit of the suggested technological approach lies in the integration of both the turbine and compressor stages on a singular shaft. This design effectively eliminates the need for a coupling mechanism as well as a generator for driving the turbine or compressor, thereby eradicating supplementary mechanical and electrical components. As a result, the overall system is streamlined to its most elementary configuration (Fig. 1). In summary, the generation of cooling by the VCC system is possible thanks to the harnessing of waste heat by the ORC system and the use of a turbocompressor. Furthermore, a cooling water system is necessary for heat dissipation from each of the condensers.

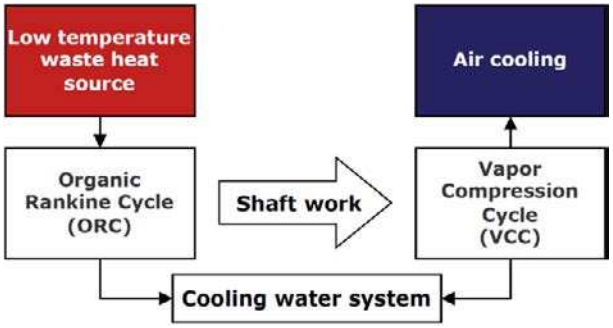

Figure 1: Conception of ORC-VCC

In the past decade, several studies have sought to investigate and optimize the performance of ORC-VCC systems. Karellas and Braimakis (2016) investigated the thermodynamic modeling and economic assessment of a micro-scale tri/cogeneration system, integrating an Organic Rankine Cycle (ORC) and a Vapor Compression Cycle (VCC) for combined heat, power, and refrigeration production. The system's performance is evaluated under various operating conditions, and its economic viability is analyzed using a case study on a Greek Island. The base case scenario yields a net electric efficiency of 2.38% and an exergy efficiency of about 7%. The system offers an Internal Rate of Return (IRR) of approximately 12% and a payback period of 7 years due to fuel oil and electricity savings. Nasir and Kim (2016) explored the thermal performance of working fluid combinations in ORC-VCC for domestic air conditioning. Among the seven fluids analyzed, Isobutane and R134a exhibited the best performance in standalone VCC and ORC-VCC, respectively. The optimal combination was R134a ORC-Isobutane VCC, which, when optimized, achieved a COP of 0.219 with dry air and 0.281 with 50% relative humidity air at the VCC evaporator inlet. The cycle's performance is analyzed by Aphornratana and Sriveerakul (2010) using a mathematical model. The research highlights the significant impact of the expander-to-compressor piston area ratio on the system's COP, with R22 outperforming R134a across all temperature ranges. Furthermore, incorporating a liquid-preheater substantially decreases generator energy input, subsequently enhancing the COP. In the work of Toujeni *et al.* (2017), authors investigate the impact of system parameters on the performance metrics of a novel combined ORC-VCC system for cogeneration of electricity and refrigeration. The study aims to introduce and assess the proposed configuration, finding that the system's feasibility and performance are contingent upon the availability of the hot source and the desired cold temperature. Optimization results demonstrate that the use of two generators improves system performance under appropriately chosen conditions. Four systems - single-fluid and dual-fluid ORC-VCC systems, and ORC-FTVIC systems utilizing single-fluid and dual-fluid - are examined, with an emphasis on performance optimization at various heat source temperatures using six different working fluids (Bao *et al.* 2020). The results reveal that the cooling capacity, COP and second law efficiency of the dual-fluid ORC-FTVIC-D system are always maximum among the four systems, but the optimum working fluid of systems will change with the variation of heat source temperature The study also finds that parameters such as the turbine inlet pressure and temperature, evaporation temperature, and intermediate vapor injection temperature significantly influence the cycle performance of the systems. Asim *et al.* (2021) showed an innovative integrated vapor compression cycle-organic Rankine cycle system (i-VCC-ORC), which recovers waste heat rejected by the condenser of a VCC. The study identifies the optimal working fluid pair as R600a-R141b, with a net COP of 3.54 and ORC thermal efficiency of 3.05%. This integrated system improves the system's COP by 12.5% compared to a standalone VCC system. The research also determines an optimal operating condition through sensitivity analysis, demonstrating the potential of the i-VCC-ORC system for electricity generation from waste heat. An investigation into a combined power and cooling system, incorporating an ORC and a VCC, demonstrated almost double the thermal efficiency in the ORC–VCC mode compared to the standalone ORC mode (Kim). Employing six different working fluids, the study revealed a significant improvement in thermal efficiency when a VCC cycle was introduced alongside the ORC cycle. Further, Kim demonstrated that the inclusion of a recuperator amplified both thermal and second-law efficiencies, achieved by reducing the load on the solar collector and condenser and harnessing residual heat from the turbine outlet. Under the explored operational conditions, R245fa was identified as the working fluid yielding the highest thermal efficiency. Seiti *et al.* (2022) investigates the use of ultra-low temperature waste heat to drive a thermo-mechanical refrigeration (TMR) system, particularly focusing on an expander-compressor unit (ECU) based design. The study examines the system's performance with various commercial refrigerants within a temperature spectrum of 50 °C to 85 °C, identifying optimal operating conditions. Results demonstrate improved system efficiency at higher heat source temperatures and enhanced cooling quality through refrigerant substitution. These findings contribute significantly to waste heat recovery practices and suggest future exploration with sustainable refrigerants. It was shown that an ORC-VCC, can significantly enhance power generation and cooling efficiency in rural areas (Aryanfar, *et al.*, 2022). By utilizing a Parabolic Trough Solar Collector (PTC) and exploring four different working fluids (R245fa, R114, R600, R142b), the study identified R245fa as the fluid with the least exergy destruction. Optimal performance was found to be dependent on specific turbine inlet

204

temperature and pressure conditions. Moreover, it was observed that the turbine inlet pressure holds substantial influence over the system's overall cost and thermal efficiency, highlighting the importance of optimization in such renewable energy systems. In order to illustrate the used working fluids and heat source and its temperature, a summary of mentioned works is presented in Table 1.

Table 1: An overview of investigations into ORC-VCC technology

Author	Heat source	Heat input	Working fluid
Aphornratana and Sriveerakul (2010)	Thermal energy at a temperature higher than 80°C	≤ 7 kW	R22, R134a
Wang *et al.* (2011)	Hot water - 190°C	≤ 10 kW	R245fa
Karellas and Braimakis (2016)	Biomass combustion, solar energy – up to 110°C	≤ 50 kW	R134a, R152a, R245fa
Nasir and Kim (2016)	Hot water – 100°C	-	R245fa, R123,R134a, R1234yf, R1234ze, Butane, Isobutane
Toujeni *et al.* (2017)	Low temperature heat sources (solar energy, biomass)	-	R600 (ORC) and Ammonia (VCC)
Kim (2022)	Thermal oil – up to 150°C	≥100 kW ≤ 250 kW	R245fa, R114, R600, R142b, R152a, R1234yf
Sleiti *et al.* (2022)	Hot water – between 48°C and 120°C	≤ 1 kW	R134a
Aryanfar *et al.* (2022)	Parabolic solar collector (PTC), Therminol VP-1	-	R245fa, R114, R600, R142b
Witanowski (2023) [This work]	Hot water - 95°C	≤ 130 kW	R1233zd(E), R1336mzz(Z), R1224yd(Z)

The article presents an analysis of the small scale ORC-VCC system for air conditioning from low temperature waste heat source. The heat source parameters were set at 95°C and 1 kg/s, guided by the obtained parameters of available waste heat sources. The cost of the installation was determined based on an estimate of the order value made with local suppliers of installation components, intended for the submitted grant application. Initially, nine objective functions are employed in the optimization process, which utilizes a hybrid genetic algorithm. In a single optimization process, optimization is conducted for three distinct working fluids. Only the fluid R1233zd(E) is applied in the Pareto optimization. The selected working fluids are characterized by a low environmental impact, as indicated by their Ozone Depletion Potential (ODP) and Global Warming Potential (GWP) values. The study analyzes the techno-economic parameters of the installation, enabling the selection of an installation characterized not only by relatively high efficiency but also largely justified from an economic perspective.

205

2 ORC-VCC model optimization methodology

2.1 System description and parameters

The schematic of thermodynamic cycle of the ORC-VCC system has been presented in Fig .1. The system is composed of and ORC subsystem (with regenerator) and a VCC subsystem. The turbine and compressor components are integrated within single structure. The expander and compressor share a common housing and are connected by a single shaft. The cycle was analyzed using only one working fluid in a given study, meaning that the working fluid in both the ORC and VCC cycles was identical. The assumptions regarding the system are presented in Table 2. The efficiencies of the machines under examination were chosen with a high safety margin in mind. For instance, the internal efficiency of a turbine was established at 80%. This value is notably lower than the efficiencies reported in the literature for low power axial (Engineer *et al.*, 2021) or low power high-speed radial-inflow turbines; (Uusitalo *et al.*, 2020, Witanowski et al., 2023).

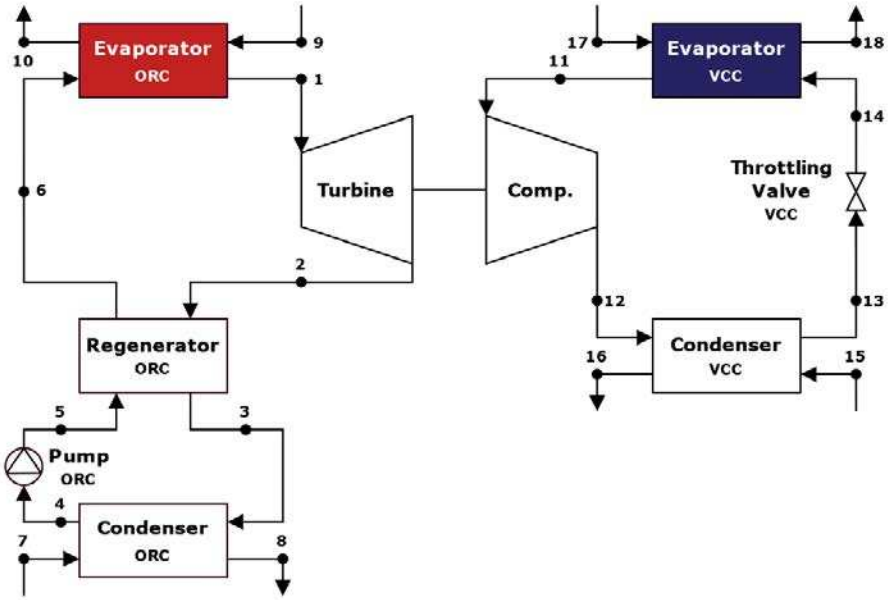

Figure 2**:** Schematic diagram of the ORC-VCC

Table 2: Efficiency and thermodynamic assumptions of the ORC-VCC system

Parameter	Symbol	Unit	Value
Chilled water temperature (cold side)	T_{18}	°C	8
Chilled water temperature (hot side)	T_{17}	°C	12
Cooling water temperature (cold side)	T_7, T_{15}	°C	15
Heat source mass flow	m_9	kg/s	1
Heat source temperature (hot side)	T_9	°C	95
Compressor efficiency (VCC)	η_c	-	80%
Pump efficiency (ORC)	η_p	-	50%
Turbine efficiency (ORC)	η_t	-	80%

206

2.2 Economic parameters

Simple Payback Time, Net Present Value (NPV) and Internal Rate of Return (IRR)were used to assess the financial viability of the investment project (2-4). Each method provides a different perspective on the potential profitability and risks associated with an investment. The analysis was carried out for European Union countries: Greece, Italy, Poland and Spain. However, in the optimization process, the value of the energy price assigned to Greece was assumed. Table 3 summarizes some assumptions for the economic evaluation of the ORC-VCC system.

$$C_i = \left(P_{comp} - P_{p_{orc}} - P_{p_{cs}}\right) * AOT * C_{ei} \quad (1)$$

$$SPBT = C_s / C_i \quad (2)$$

$$NPV = \sum_{j=1}^{t} \frac{C_{ij}}{(1+d)^j} - C_s \quad (3)$$

$$\sum_{j=1}^{t} \frac{C_{ij}}{(1+IRR)^j} = C_s \quad (4)$$

Table 3: Economic assumptions of the ORC-VCC system

Parameter		Symbol	Unit	Value
Electricity prices for non-household consumers (*Electricity Price Statistics. Eurostat Statistics Explained*, 2022)	Greece	C_{e1}	€/kWh	0.3042
	Italy	C_{e2}	€/kWh	0.2525
	Poland	C_{e3}	€/kWh	0.1555

Spain	C_{e4}	€/kWh	0.1879
Cost of ORC-VCC system (up to 35 kW_{th})	C_s	€	30000
Discount rate (NPV analysis)	d	%	5
Operation time	t	years	8
Annual operation time	AOT	h	8000

2.3 Optimization approach

A hybrid algorithm optimization which is embedded in MATLAB was used in the optimization task. The method consist of Genetic Algorithm (GA) and Pattern Search method (PA). After the termination of the GA, the best point is selected as an initial point for the Pattern Search method. This approach allows to perform a faster and more efficient local search instead of performing stochastic algorithm alone. The NPV (f_1), IRR (f_2) and cycle efficiency (f_3) are selected as the single objective function. Each function, from f_1 to f_3, was executed for three working fluids. As a result, functions f_4 to f_6 were created for fluid R1336mzz(Z), and functions f_7 to f_9 for factor R1224yd(Z). For mutli-criteria optimization (functions f_{10} to f_{12}), the process was carried out using the R1233zd(E) fluid. The mutli-criteria optimization objective functions are defined as follows:,

$$f_{10} = 0.3 \times \text{NPV} + 0.7 \times \eta_{cyc} \quad (5)$$

$$f_{11} = 0.5 \times \text{NPV} + 0.5 \times \eta_{cyc} \quad (6)$$

$$f_{12} = 0.7 \times \text{NPV} + 0.3 \times \eta_{cyc} \quad (7)$$

During the constrained optimization, 11 parameters (decision variable) related with ORC-VCC cycle calculation were modified. The changing parameters and boundaries are showed in Table 4. The boundaries are set based on preliminary calculations. Each of the changing parameters was modified and tested to prepare a wide range of possible solutions.

In the optimization process, the prices adopted were those of Greece, driven by the highest price for electricity. This approach represents an optimistic variant when considering prices in other EU countries, but in light of the decarbonization strategy, such a price could become standard throughout the EU. The adopted price influenced the minimum values achieved, and if the process was guided solely by one objective function and a limited set of solutions, it could potentially introduce bias into the results. However, the construction of multiple objective functions and the identification of the Pareto frontier effectively eliminated the impact of the adopted energy price on the optimization.

Table 4: Efficiency and thermodynamic assumptions of the ORC-VCC system

Argument	Parameter	Symbol	Unit	Lower Bounds	Upper Bounds	Best value
x_1	Evaporator pinch temperature difference (VCC)	ΔT_{vcc_ev}	K	3	10	9.82
x_2	Degree of superheating in evaporator (VCC)	ΔT_{vcc_sup}	K	3	10	5.24
x_3	Degree of subcooling in condenser (VCC)	ΔT_{vcc_sub}	K	3	10	9.28
x_4	Regenerator pinch temperature difference (ORC)	ΔT_{orc_reg}	K	3	15	13.97
x_5	Degree of superheating in evaporator (ORC)	ΔT_{orc_sup}	K	3	15	4.65
x_6	Degree of subcooling in condenser (ORC)	ΔT_{orc_sub}	K	7	15	8.38
x_7	Evaporator pinch temperature difference (ORC)	ΔT_{orc_ev}	K	3	10	5.81
x_8	Condenser pinch temperature difference (ORC)	ΔT_{orc_con}	K	3	10	4.17
x_9	Saturation temperature in evaporator (ORC)	T_{1sv}	°C	50	85	64.9
x_{10}	Saturation temperature in evaporator (ORC)	T_{4sv}	°C	25	55	41.26
x_{11}	Chilled water mass flow rate	m_{16}	kg/s	0.7	2	1.99

3 RESULTS OF OPTIMIZATION

Twelve optimization runs were carried out in the study, including nine single optimization runs and three multi-criteria runs. About 10 000 evaluation of objective function were performed. The NPV

in comparison with η_{orc}, COP_{vcc}, η_{cyc} are shown in Fig. 3 and Fig 4. The highest NPV values do not correspond to the highest efficiencies and COP obtained. The efficiency of the ORC cycle is close to 9%, the COP_{vcc} is 7, and the efficiency of the cycle is up to 50%. On the other hand, the highest NPV value was obtained at the level of 68 k€, where the efficiency orc is 5.27%, COP_{vcc} is 4.75 and the efficiency of the cycle is 27.1%. The points illustrated in the given context represent a collection of Pareto front points, denoted by red crosses. Within this set, the optimal point is determined based on the criterion of the maximum Net Present Value (NPV). In the case of waste heat recovery, the most crucial issue is often economic justification. Therefore, in this instance, the Net Present Value (NPV) indicator was used as a most important metric. The design parameters, thermodynamic preferences and economic specification of optimal cycle design are shown in Table 5 and Table 5. The mechanical power of the turbine and compressor is about 7 kW, while transferred heat in the VCC evaporator is 33.49 kW.

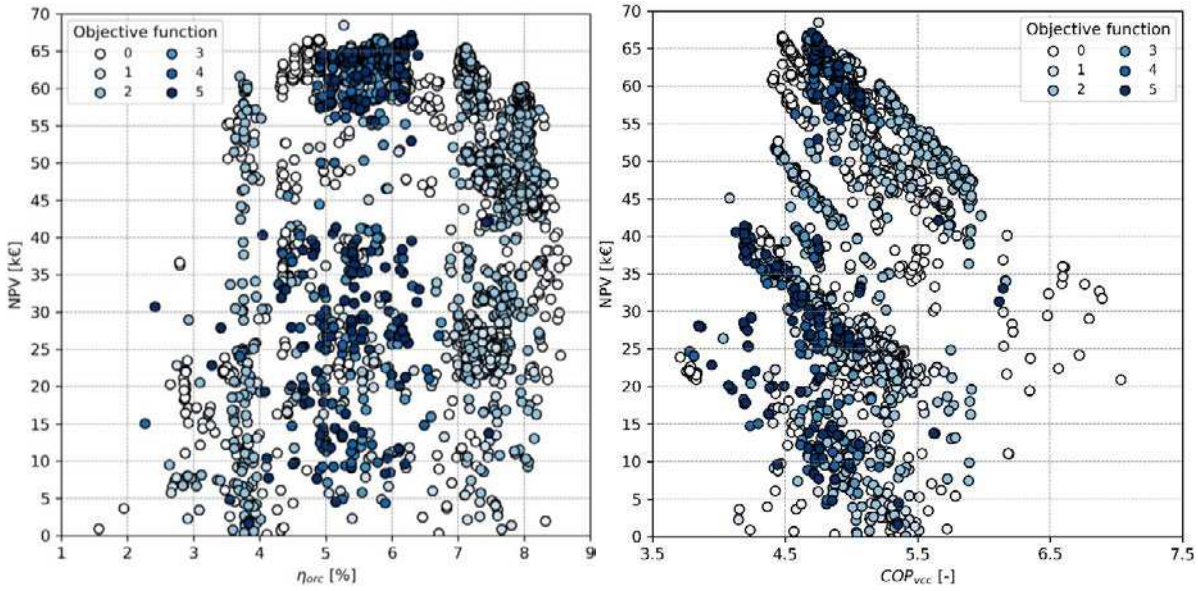

Figure 3**:** Comparison of NPV with η_{orc} (left) and COP_{vcc} (right)

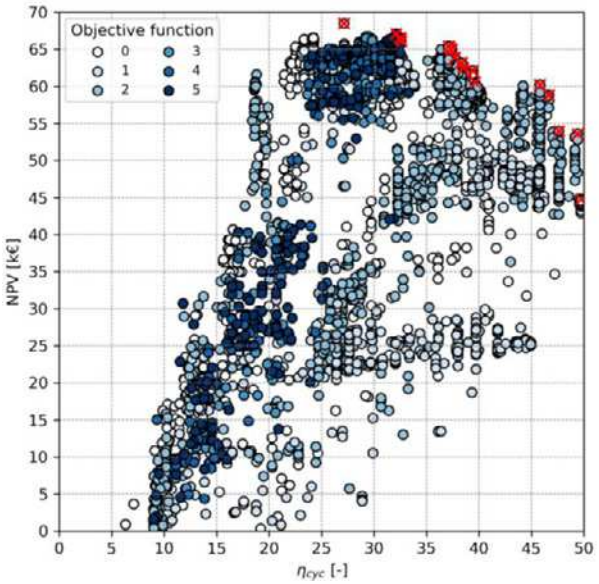

Figure 4**:** Comparison of NPV with η_{cyc}

Table 5: ORC-VCC thermodynamic points and system performance parameters

Point	T (°C)	p (kPa)	System parameters	
1	73.73	447	fluid	R1233zd(E)
2	55.06	210	P_{tur}	6.97 kW
3	48.82	210	P_{comp}	6.93 kW
4	34.61	210	P_{p_orc}	0.23 kW
5	34.85	447	P_{p_cs}	0.46 kW
6	39.19	447	Q_{e1}	123.62 kW
7, 15	15	200	Q_{r1}	3.21 kW
8, 16	31.11	200	Q_{c1}	116.88 kW
9	95	200	Q_{e2}	33.49 kW
10	65.62	200	Q_{c2}	40.43 kW
11	3.41	44	η_{cyc}	27.1 %
12	51.21	210	η_{orc}	5.27 %
13	29.97	210	COP_{vcc}	4.75
14	-1.83	44	IRR	48.65 %
17	12	200	NPV	68.47 k€
18	8	200	SPBT	1.97

Upon completion of the optimization task, it was discerned that the optimal solution closely approximates the upper boundary of parameter x_{11}, a correlation that is clearly evident in Fig. 5 and in Table 4. Consequently, an additional optimization iteration was conducted, in which the upper boundary of x_{11} was augmented to 5. Additional data results were denoted by a white square. The results confirmed that the optimal solutions were close to the original upper boundary of 2. Values greater than 2 were eliminated by the optimization process due to thermodynamic cycle relations and the lack of possible solutions. Future investigations should consider extending the upper boundary of this parameter to avoid potentially eliminating better solutions.

209

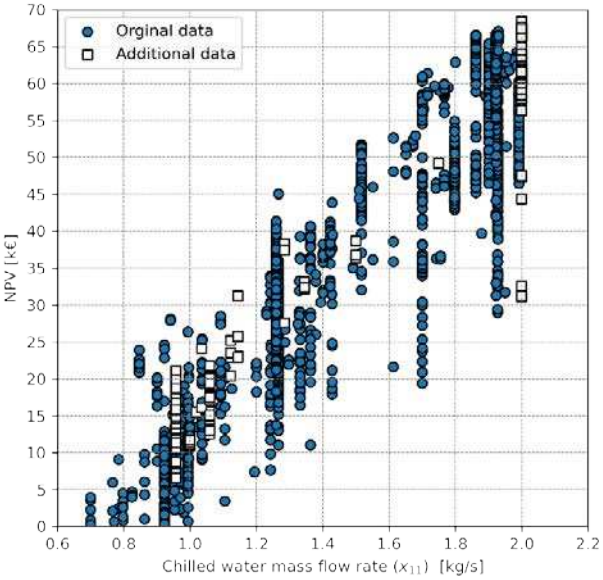

Figure 5**:** Comparison of NPV with chilled water mass flow

In order to compare the profitability of investments in selected EU countries, calculations were performed using project data obtained for the optimal variant. Greece, which was considered during the optimization, is the best compared to other countries, which is obviously related to

the highest price of electricity. The lowest NPV values of 20 000 Euros were obtained for Poland. The SBPT for this country is close to 4 years (Fig 6).

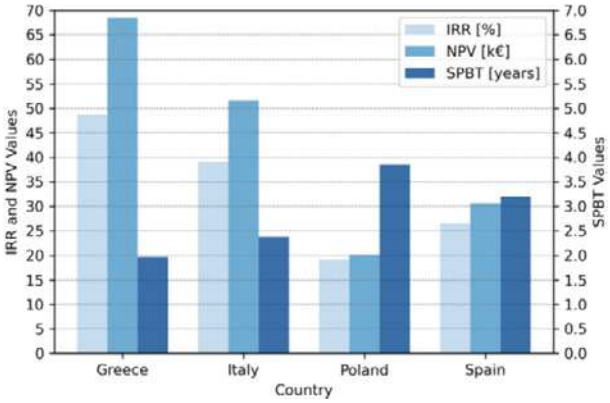

Figure 6**:** Comparison of economic indicators in selected UE countries

To determine the significance of individual of the objective function, multi-point linear regression was used. The data collected during all optimization runs were cleaned and standardized. The matrix of the significance of the individual parameters is shown in Fig. 7. The variable x_{11} has the highest value for objective functions related the most with the cost (NPV, IRR). In turn variable x_9 has the highest value for the η_{cyc} and η_{orc}. In case where COP_{vcc} was optimized x_{10} has the highest value. A common feature of all objective functions is the low significance of x_2-x_8 variables. The efficiency of the ORC-VCC system, COP, and economic coefficients are contingent upon the internal efficiency of the turbine, a variable that was not considered during the optimization process. To analyze the impact on the parameters of the optimal variant, a characterization of the influence of efficiency on the heat transfer in the VCC evaporator and the NPV index was conducted (Fig. 8). The NPV curve is typified by greater steepness, which is dictated by the escalating proportion of power required to operate auxiliary devices, subsequently impacting profit reduction. When the efficiency decreases from 80% to 60%, the NPV diminishes by 37%, whereas the power transferred in the VCC evaporator reduces by approximately 25%.

210

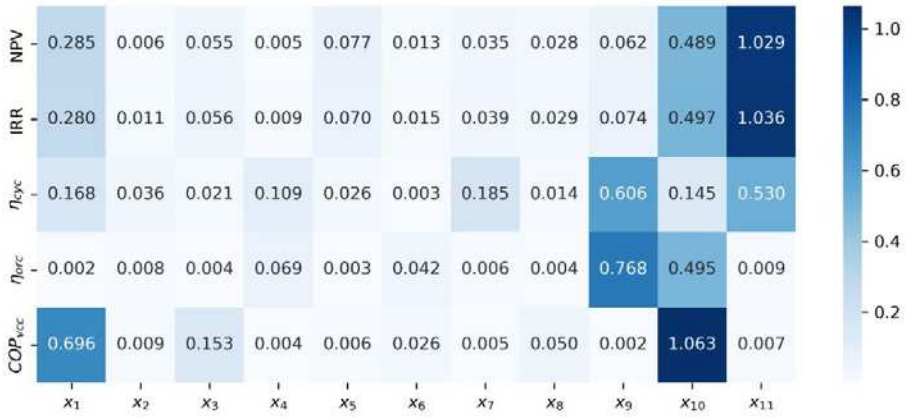

Figure 7**:** Summary of significance of the objective functions variables

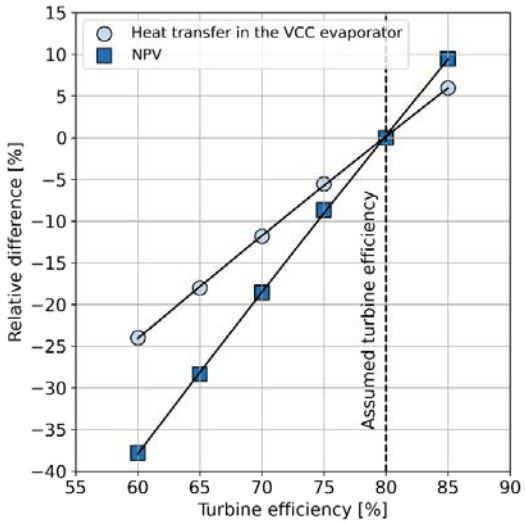

Figure 8**:** Influence of turbine efficiency on the heat transfer in the VCC evaporator and NPV

4 CONCLUSIONS

The paper presents the thermo-economic analysis of ORC-VCC system for air conditioning from low-temperature waste heat. A total of 12 optimization runs were conducted to generate an extensive and diverse array of potential solutions. Well-known economic parameters, such as NPV and IRR, alongside cycle efficiency, were selected to serve as objective functions for the optimization process. The created objective functions took into account the power required to supply the cooling system pump and the ORC circulation pump. The cost of the installation was estimated based on quotations from a Polish supplier. With this assumption, the SPBT of the investment amounted to less than two years, and the NPV was approximately 70 000 Euros. Based on these figures, it can be concluded that the aforementioned installation is economically justified.

The selected formulas for the objective functions allowed for the examination of a wide range of acceptable solutions. Considering both the Net Present Value (NPV) and the efficiency of the system appears to be an appropriate approach. NPV is closely tied to the net power generated by the system, which directly reflects the level of future revenues. Meanwhile, seeking the highest efficiency, which may not correspond to the highest NPV or power, allows for exploration in entirely new areas. In conclusion, multi-criteria or multi-functional optimization, performed sequentially for several objective functions, allows approximation towards the global optimum.

211

NOMENCLATURE

IRR	internal rate of ratio	(%)
NPV	net present value	(€)
P	power (kW)	
SPBT	simply payback time	(years)
Q	Heat transfer (kW)	
x	argument of objective function	

Subscript

comp	compressor
c1	ORC condenser
c2	VCC condenser
e1	ORC evaporator
e2	VCC evaporator
p_orc	ORC pump
p_cs	cooling system pump

r1 ORC regenerator
tur turbine

REFERENCES

Witanowski, Ł., Ziółkowski, P., Klonowicz, P., & Lampart, P. (2023). A hybrid approach to optimization of radial inflow turbine with principal component analysis, *Energy*, vol. *272*, p. 127064. https://doi.org/10.1016/j.energy.2023.127064

Wang, H., Peterson, R., Herron, T., 2011, Design study of configurations on system COP for a combined ORC (organic Rankine cycle) and VCC (vapor compression cycle). *Energy*, vol. 36, no. 8, p. 4809–4820.

Uusitalo, A., Turunen-Saaresti, T., Honkatukia, J., Dhanasegaran, R., 2020, Experimental study of small scale and high expansion ratio ORC for recovering high temperature waste heat. *Energy*, vol. 208, p. 118321.

Toujeni, N., Bouaziz, N., Kairaouani, L., 2017, Energetic investigation of a new combined ORC-VCC system for cogeneration. *Energy Procedia*, vol. 139, p. 670–675.

Sleiti, A. K., Al-Ammari, W. A., & Al-Khawaja, M., 2023, Experimental investigations on the performance of a thermo-mechanical refrigeration system utilizing ultra-low temperature waste heat sources. *Alexandria Engineering Journal*, vol. 71, p. 591–607. https://doi.org/10.1016/j.aej.2023.03.083

Nasir, M. T., Kim, K. C., 2016, Working fluids selection and parametric optimization of an Organic Rankine Cycle coupled Vapor Compression Cycle (ORC-VCC) for air conditioning using low grade heat, *Energy and Buildings*, vol. 129, p. 378–395.

Lecompte, S., Huisseune, H., van den Broek, M., Vanslambrouck, B., De Paepe, M., 2015, Review of organic Rankine cycle (ORC) architectures for waste heat recovery, *Renewable and Sustainable Energy Reviews*, vol. 47, p. 448–461.

Kim, M.-H., 2022, Energy and Exergy Analysis of Solar Organic Rankine Cycle Coupled with Vapor Compression Refrigeration Cycle. *Energies*, vol. 15, p. 5603. https://doi.org/10.3390/en15155603

Karellas, S., Braimakis, K., 2016, Energy-exergy analysis and economic investigation of a cogeneration and trigeneration ORC-VCC hybrid system utilizing biomass fuel and solar power, *Energy Conversion and Management*, vol. 107, p. 103–113.

Engineer, Y., Rezk, A., Hossain, A. K., 2021, Energy analysis and optimization of a small-scale axial flow turbine for Organic Rankine Cycle application, *International Journal of Thermofluids*, vol. 12, p. 100119.

Electricity price statistics. Eurostat statistics explained, 2022.

Bao, J., Zhang, L., Song, C., Zhang, N., Zhang, X., & He, G., 2020, Comparative study of combined organic Rankine cycle and vapor compression cycle for refrigeration: Single fluid or dual fluid? *Sustainable Energy Technologies and Assessments*, vol. 37, p. 100595. https://doi.org/10.1016/j.seta.2019.100595

Asim, M., Kashif, F., Umer, J., Alvi, J. Z., Imran, M., Khan, S., Zia, A. W., & Leung, M. K. H., 2021, Performance assessment and working fluid selection for novel integrated vapor compression cycle and organic rankine cycle for ultra low grade waste heat recovery. *Sustainability* (Switzerland), vol. 13, p. 1–17. https://doi.org/10.3390/su132111592

Aryanfar, Y., Assad, M. E. H., Khosravi, A., Atiqure, R. S. M., Sharma, S., Alcaraz, J. L. G., & Alayi, R.,2022, Energy, exergy and economic analysis of combined solar ORC-VCC power plant, *International Journal of Low-Carbon Technologies*, vol. 17, p. 196–205. https://doi.org/10.1093/ijlct/ctab099

Aphornratana, S., Sriveerakul, T., 2010, Analysis of a combined Rankine-vapour-compression refrigeration cycle, *Energy Conversion and Management*, vol. 51, no. 12, p. 2557–2564.

ACKNOWLEDGEMENT

Part of calculations were carried out at the Academic Computer Centre in Gdańsk.

ORC SEVILLE 2023
7th International Seminar on O.R.C. Power Systems

© 2024 Editorial Universidad de Sevilla. Este es un artículo de acceso abierto distribuido bajo los términos de la licencia de uso y distribución Creative Commons (BY-NC-ND 4.0)

DOI: https://dx.doi.org/10.12795/9788447227457_33

Pareto front analysis for the design and the working fluid selection in ORC-based pumped thermal energy storage technology in both pure electric and cogenerative applications

Marco Astolfi[1,*], Dario Alfani[1], Andrea Giostri[1]

[1] *Dipartimento di Energia, Politecnico di Milano, Via Lambruschini 4a, 20156, Milano (MI), Italy*

*Corresponding Author: marco.astolfi@polimi.it

ABSTRACT

Carnot Batteries are a sub-technology of Pumped Thermal Energy Storage concept where closed cycles are used in both charging and discharging phase. In charging mode, cheap off-peak electricity from the grid is used to store heat at a temperature different than the ambient one (generally higher) while in discharging mode the stored heat is exploited for power production. Carnot Batteries can be designed with different thermodynamic cycles (Brayton cycle, Steam Rankine cycle, Organic Rankine cycle) and can adopt different types of thermal energy storage technologies. For low duration storage (daily or weekly cycling) sensible or latent energy storage with phase change materials can be adopted, while for long duration storage (months, seasonal) the use of thermochemical reactions could be a valid option, as proposed by H2020 RESTORE project. Performance of Carnot Batteries is highly affected by the thermal storage temperature, the condensation temperature in discharging mode and the availability of residual heat at a temperature higher than the ambient one for boosting the heat pump coefficient of performance in charging cycle. This paper focuses on the optimal design of a reversible thermodynamic system working as a heat pump (HP) cycle in charging mode and as an organic Rankine cycle (ORC) in discharging mode. A dedicated numerical model developed in Python is employed to compare the techno-economic performances of different working fluids and select the most promising candidates. Main difficulty is related to the use of reversible heat exchangers which design impacts both on the charging and discharging operation, strongly affecting the system round trip efficiency, and requiring a discretized off-design modelling. A Pareto front of optimal round trip efficiency against total area of heat exchangers is obtained by varying the main design parameters, such as heat transfer temperature differences and heat exchangers pressure drops. Results show that for a given overall heat transfer area low critical temperature fluid are mainly penalized by poor HP performance due to high compressor specific work, while high critical temperature fluids are mostly penalized by high pressure drops caused by the low fluid density. The most promising working fluid for the present application is cyclopentane, reaching a RTE close to 35% for the pure electric configuration at its maximum RTE over total heat transfer area parameter.

1 INTRODUCTION – ENERGY STORAGE TECHNOLOGIES

In order to reach a full decarbonization of the electricity market a massive adoption of renewable energies will be required in the soon future and those technologies will need to be coupled to energy storage in order to compensate for their non-fully predictable and non-programmable power output. Energy storage technologies are numerous and cover a large range in power and capacity (namely storage duration): from few kW to multi-MW, from few seconds to seasonal storage. Some energy storage technologies are already at commercial level like flywheels, electrochemical batteries and pumped hydro energy storage, having a high penetration on the market in spite of some intrinsic limits. As a consequence, the energy market strongly needs alternative solutions that can provide energy storage in a reliable, efficient, site independent and affordable way, possibility pushing the storage duration towards long term (monthly, seasonal). Several technologies have been proposed in recent years in open literature or developed by startups and large companies to answer to these needs, leading to a variety of concepts that can be basically split in three main categories: mechanical storage, pumped thermal energy storage and chemical energy storage. Technologies based on thermodynamic systems

are numerous and they may require both the pressurization of a fluid and the storage of heat: among them adiabatic compressed air energy storage (A-CAES) (Cheung, Carriveau, & Ting, 2012), CO_2 Battery (Astolfi, Rizzi, Macchi, & Spadacini, 2021) and liquid air energy storage (LAES) are the most mature ones but they all require not only the accumulation of energy in a sensible or latent energy storage, but also the storage of the working fluid at high pressure and, in case air is not used, also at low pressure. Carnot battery technologies, on the contrary, are based on the adoption of closed thermodynamic cycles in both charging phase (heat pump for heat temperature upgrade) and discharging phase (heat exploitation with a power cycle) and thus they require only the storage of heat, potentially simplifying the system design and operation, and reducing the size for seasonal storage. Finally, Carnot batteries performance can be increased by exploiting waste heat recovery in the charging phase by increasing the evaporation temperature of the heat pump and thus the Coefficient of Performance (COP). Carnot batteries are differentiated by the selection of the thermodynamic cycle adopted for charging and discharging phase and the type of thermal energy storage adopted:

- **Thermodynamic cycle:** the use of different thermodynamic cycles is proposed in literature and on the market: (i) closed gas Brayton cycles are commercialized by Malta Inc. (Laughlin, 2017) and also studied by SWRI, (ii) Steam Rankine cycles have been proposed by H2020 CHESTER project (Steinmann, 2014), (iii) Organic Rankine Cycles (ORC) are investigated by H2020 CHESTER (Steinmann, 2014) and RESTORE projects (Alfani, Giostri, & Astolfi, 2023) while transcritical CO_2 cycles are proposed by Man Energy Solution and Echogen (Miller, 2018). Additionally, some systems architectures do not adopt a heat pump for the charging cycle preferring to directly dissipate electrical power to the HTF medium, usually air, and eventually to rocks as proposed by Siemens Gamesa (Eggers, von der Heyde, Thaele, Niemeyer, & Borowitz, 2022), Pintail power and Enel Green Power in cooperation with Brenmiller Energy.
- **Thermal storage**: thermal storage can be classified in (i) sensible heat storage, in case liquid or gas streams are heated during the charging phase and then stored directly or by releasing heat to a high heat capacity medium, like in dual media thermocline solutions (rocks, metal spheres), (ii) latent heat storage, in case the heat is used in charging phase for melting a solid or vaporizing a liquid storage medium called Phase Change Material (PCM) (ice for low temperature storage, salts and their eutectic mixtures for temperatures up to 700-800°C (Sarbu & Dorca, 2019)) and (iii) thermochemical storage, where the heat is used to support a specific chemical reaction. Latent and thermochemical energy storage are mainly proposed for thermodynamic cycles with a pure working fluid phase transition (i.e., evaporation and condensation of organic fluids or CO_2), while sensible heat is preferrable for Brayton cycles, supercritical CO_2 or non-eutectic fluid mixtures, thanks to better matching of the temperature profiles.

215

2 LITERATURE ON CARNOT BATTERIES AND SCOPE OF THE STUDY

Previous studies have already shown the potential of ORC-based PTES systems considering both decoupled and coupled cycles architectures and, in this latter case, scientific literature has mostly focused on small-size systems that allow for the adoption of volumetric machines working as compressors in charge operation and expanders during discharge. Steger et al. (Steger et al., 2020) carried out a numerical multi-objective (electrical storage capacity and power-to-power efficiency) Pareto optimization to provide insights on the design and working fluid selection of a reversible HP/ORC system coupled to a latent energy storage. In particular, the authors highlighted the relevance of the working fluid enthalpy of vaporization in the process design, as it directly affects the mass flow rate and thus it significantly influences the investment costs of the system. Studying a similar system and considering the same working fluids (cyclopentane, R1233zd(E), Novec649 and R365mfc), Eppinger et al. (Eppinger, Zigan, Karl, & Will, 2020) achieved power-to-power efficiencies above 60% for a heat source of 110°C, adopting both a sensible and latent heat storage for a pure electric system. The authors performed several parametric analyses and highlighted that, for most of the investigated cases, R1233zd(E) appeared to be the best choice thanks to the trade-off between system efficiency and environmental sustainability and safety. On the other hand, when considering also latent storages solutions, cyclopentane achieved the highest power-to-power efficiency. Limiting their analysis to reversible systems coupled to a sensible heat storage, Dumont et al. (Dumont & Lemort, 2020) developed a set of performance maps considering different combinations of working fluid, waste heat

temperatures (50-90°C), storage temperature glide (5-15°C), and ambient temperature (0-40°C). The authors identified R1233zd(e), R1234yf, R11, R236ea and R245fa as the working fluids presenting the best performances. In the framework of the H2020 CHESTER project, Jockenhöfer et al. (Jockenhöfer, Steinmann, & Bauer, 2018) investigated a decoupled system adopting butene for both the charging and discharging cycles. The results of the analysis showed that the investigated system can provide a net power ratio of 1.25 if a heat source temperature of 100°C and a heat sink temperature of 15°C are available. A similar system has been studied by Frate et al. (Frate, Antonelli, & Desideri, 2017) investigating 17 working fluid candidates but limiting the analysis to a sensible heat storage. The numerical results showed the possibility to boost the round trip efficiency (RTE) to values higher than 1 thanks to the combination with a low-grade heat source. Considering a heat source temperature of 110°C, R1233zd(E) has been identified as the optimal fluid as it allows to achieve a theoretical maximum RTE of 1.3. Finally, the H2020 RESTORE project (Alfani et al., 2023) is focusing on the design of a seasonal storage system for district heating (DH) purposes that adopts ORC-based Carnot batteries to support an endothermic (during charging process) and exothermic (during discharging process) thermochemical reaction that would allow to store energy by mean of solids salts with high energy densities, requiring low-cost storage technologies already used in food and chemical industry.

This paper aims to discuss the methodology proposed for the selection of the best working fluid(s) for Carnot battery applications adopting coupled cycles that use the same working fluid and the same heat exchangers in both operation modes as reported in Figure 1 with representative T-s diagrams. Differently to other works in literature, two different turbomachines are adopted for the compression and the expansion of the working fluid since the use of reversible volumetric machines (piston, screw or scroll) is still characterized by very uncertain information about the penalization due to volume ratio variation when passing from one to another operation mode. From one hand, the choice of using coupled cycles is well motivated by the possibility to reduce the investment cost, ensuring high annual utilization factors of main components (i.e., heat transfer equipment) and facilitate the charging and discharging operations of the thermal energy storage using both solid-to-liquid PCM and thermochemical reactors. On the other hand, using coupled cycles requires specific numerical tools to account for the heat exchangers operation in off-design mode and precisely evaluate the impact on discharge cycle performance when pressure levels and mass flow rates different from the charging cycle are adopted. In this study a subcritical heat pump (HP) and subcritical power cycle (PC), adopting an organic working fluid, are considered in order to provide the best matching between the fluid phase transition process and both latent or thermochemical thermal energy storages that can be implemented in this concept. Two different cases have been considered: (i) a electricity-only (ELE) storage system, which operates with daily or weekly cycles of charging and discharging and aims at maximizing the electrical round trip efficiency, adopting a latent thermal energy storage for heat accumulation at high temperature as proposed by H2020 CHESTER project; (ii) a cogenerative system (CHP) which main goal is dispatching large amount of thermal energy on seasonal base for district water heating through ORC condensation, while also providing dispatchability and storage of electricity as a secondary benefit; in this case a thermochemical reaction is at the base of the thermal energy storage as proposed by H2020 RESTORE project (Available online at: https://www.restore-dhc.eu/)

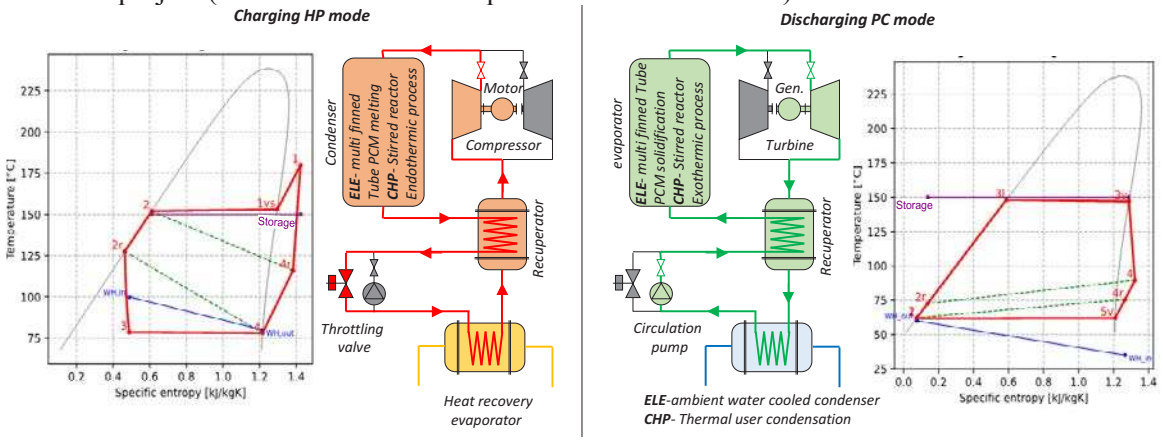

Figure 1: Coupled cycles configuration scheme adopting reversible heat exchangers and representative T-s diagrams.

3 METHODOLOGY

A numerical code is developed in Python 3.10 to compute the system overall round-trip efficiency (RTE), see Equation (1), and heat transfer area of all the heat exchangers for different combinations of working fluid and cycle operating parameters and it implements REFPROP 10 (Lemmon, Bell, Huber, & McLinden, 2018) for the computation of working fluid thermodynamic and transport properties. For the CHP case, it is possible to always obtain large thermal power released to the district heating network independently from the cycle configuration and the working fluid selected because of the rather low maximum achievable efficiency of the PC. For this reason, for both investigated cases electrical round-trip efficiency of the system, defined as the ratio between the net power released by the power cycle and the electrical power absorbed by the heat pump (according to the assumption of same charging and discharging hours), is selected as the main figure of merit to account for the system performance and to guide fluid selection. In this preliminary analysis, the additional auxiliaries consumption related to the cooling water circulation, to the waste heat or to the thermal energy storage are neglected for both the charging and discharging cycle. Thanks to this simplification the RTE is equivalent to the product between the heat pump coefficient of performance (COP_{HP}) and the power cycle electrical efficiency ($\eta_{,PC}$), as reported in Equation (1).

$$RTE = \frac{\dot{W}_{turb,el,PC} - \dot{W}_{pump,el,PC}}{\dot{W}_{comp,el,HP}} = COP_{HP} \cdot \eta_{PC} \quad (1)$$

From a general point of view, by adopting larger heat transfer surfaces it is possible to increase the system overall RTE thanks to the lower irreversibilities in the heat transfer processes, at the expenses of a higher heat exchanger investment cost that likely represent the main share of capital cost according to the high heat/electrical power ratio of the adopted thermodynamic cycles (high COP for the HP and low PC thermal efficiency). The trade-off between RTE and total heat transfer area is investigated with a Non-dominated Sorting Genetic Algorithm (NSGA) (Deb, Pratap, Agarwal, & Meyarivan, 2002) for multi-objective optimization to define the Pareto front and identify the most promising techno-economic solutions for both the ELE and the CHP cases. The optimization variables considered for this analysis are six design parameters that characterize the heat exchanger dimensions:

- The pinch point temperature differences (ΔT_{pp}) in the high-pressure (condenser in charge mode) and low-pressure (evaporator in charge mode) heat exchangers, which directly affect the heat transfer average temperature difference and thus the heat exchangers UA parameter. Once the storage temperature is assumed and the ΔT_{pp} defined, the minimum and maximum pressure of the charging cycle are also determined. The higher the ΔT_{pp}, the lower is the heat transfer area with a consequent penalization in performance because of the increased pressure difference in the HP cycle and the lower pressure ratio in the PC one. The pinch point temperature difference in the recuperator is not considered as optimization variable as it results from the specification of the compressor outlet temperature, which fixes the thermal duty of the recuperator. In a precedent study (Alfani et al., 2023) it has already been highlighted the dependency of the overall system RTE and heat transfer surfaces from the compressor outlet temperature, so in this work the outlet temperature from the compressor has been fixed at a conservative value of 180°C to limit de-superheating at compressor outlet, also considering that the actual limit of existing high-temperature heat pumps is close to 200°C (Turboden S.p.A., 2023).
- The pressure drops (Δp) on the working fluid side for all the heat exchangers of the system that affects the working fluid velocity in the tubes. Higher is a specific pressure drop, higher the heat transfer coefficient and lower the area of the heat exchanger for the same duty and average ΔT but also lower is the system performance due to additional compression ratio in charging and reduction of the expansion one in discharging.

The performance of the turbomachinery has been set constant independently of the working fluid choice, the pressure ratio and the volumetric flow rate thus assuming to design compressor and turbine as axial machines adopting a suitable number of stages and rotating at optimal speed (i.e. adopting gear box or power electronics for power output frequency control). Assumed efficiency values are 75%, 80% and 85% for the pump, the compressor and the turbine respectively.

Table 1: Heat pump cycle heat exchangers design parameters range for Pareto front analysis.

Parameter	Value
HP Evaporator pinch point temperature difference, °C	[0.5 - 10]
HP Condenser + de-superheating pinch point temperature difference, °C	[0.5 - 10]
HP Evaporator overall pressure drops working fluid side, %	[1% - 20%]
HP Condenser + de-superheating overall pressure drops working fluid side, %	[1% - 20%]
HP recuperator pressure drops working fluid low pressure side, %	[1% - 20%]
HP recuperator pressure drops working fluid high pressure side, %	[1% - 20%]

3.1 Heat exchangers preliminary sizing methodology

A realistic heat exchangers preliminary sizing is of high relevance for the study of coupled Carnot battery systems where the same heat exchangers are used in different modes (alternatively as condenser or evaporator) and at different pressure levels. Simplified methods adopting the same UA in both operation modes likely lead to misleading results as they do not take into account the changes in fluid thermophysical properties which lead to variations of fluid velocity, pressure drops and heat transfer coefficient. Heat exchanger design is carried out in the charging cycle calculation with the following methods and assuming tube diameter and tube thickness equal to 25 mm and 2 mm respectively, SS316 material and tube internal roughness equal to 10^{-3} mm:

- ***High pressure heat exchanger*:** in charging mode fluid condensation and de-superheating are carried out in the coiled tubes of the stirred reactor acting as a once-through heat exchanger for the CHP case or in the tubes of the PCM heat exchanger for the ELE case. Inlet fluid velocity is determined in order to match the assumed overall pressure drop. Number of tubes is then calculated, and the tube length and overall heat transfer area are eventually retrieved knowing the local overall heat transfer coefficient obtained by the combination of internal heat transfer coefficient (working fluid side) and the external one (stirred reactor or PCM side), plus the metal conductive resistance. Gnielinski correlation (Gnielinski, 1975) is adopted for vapor working fluid de-superheating, Cavallini correlation (Cavallini et al., 2006) is implemented for condensation (requiring an additional internal iterative procedure for the determination of the tube wall temperature). Differently, the external heat transfer coefficient is assumed constant and equal to value of 2000 W/m^{2}K for both the stirred reactor as suggested from [34] and for a solid-liquid PCM (in this case local heat transfer coefficient is much lower with values around 100 W/m^{2}K (Castell et al., 2008) but finned tubes with high external to internal area ratio can be adopted (Asgari, Javidan, Nozari, Asgari, & Ganji, 2021; Zhu, Li, & Zhu, 2022)). Pressure drops are calculated only considering the frictional contribution for vapor and two-phase flow regime.
- ***Low pressure heat exchanger*:** in charging mode the fluid evaporation is carried out in a shell and tube once-through heat exchanger and, also in this case, the number of tubes is found iteratively to match the assumed pressure drops while hot pressurized water from waste heat recovery or renewable energy flows in the shell. Liu and Winterton correlation (Liu & Winterton, 1991) is adopted for the heat transfer coefficient in flow boiling conditions (requiring an additional internal iterative procedure for the determination of the heat flux) while the external heat transfer coefficient is calculated with Zukauskas correlation (Žukauskas, 1972) by assuming a fixed longitudinal and transversal tube pitch (both equal to 1.25), a staggered tube arrangement and a fixed baffle spacing with respect to shell diameter (0.2). Working fluid pressure drops in evaporation are calculated only considering the frictional contribution. A co-current heat exchanger is adopted in order to increase the evaporation temperature and improve the COP as already discussed in (Alfani et al., 2023).
- ***Recuperator:*** a finned tube battery heat exchanger is implemented considering liquid fluid flowing in tubes and vapor flowing on the external finned surface in cross flow arrangement. The number of tubes and tube pitch calculation relies on an iterative procedure to match the pressure drops on liquid and vapor side, respectively. Gnielinski and Zukauskas correlations are used for the computation of liquid and vapor heat transfer coefficients, respectively. A fixed $A_{ext,tot}/A_{int}$ ratio equal to around 11 is adopted, as suggested in (Macchi & Astolfi, 2016).

When switching to power production mode the off-design operation of the heat exchangers is calculated fixing its geometry in order to find the cycle evaporation temperature, the condensation temperature and the recuperator outlet temperature plus all the pressure drops by adopting the correct correlation for each fluid state as reported above. The resolution scheme is reported in Figure 2.

218

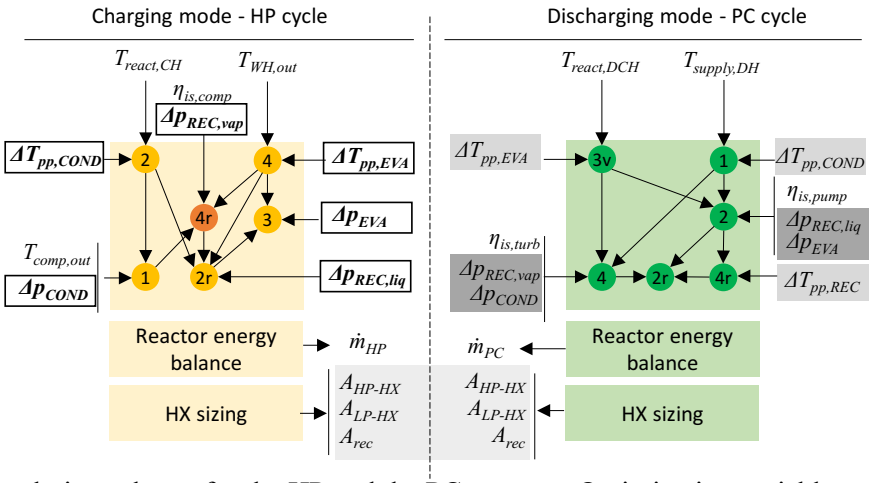

Figure 2: Resolution scheme for the HP and the PC systems. Optimization variables are in bold and white boxes on the HP cycle, closing variables used to match the heat exchangers surface are reported in light gray boxes on the PC cycle, while variables in dark gray box are iteratively calculated.

4 RESULTS

Results section is divided in two parts: the first one focuses on the analysis of the results obtained for cyclopentane with a description of the Pareto fronts and the trend of variables adopted in the analysis, the second part focuses on the comparison of cyclopentane with two other fluid candidates.

4.1 Cyclopentane analysis

The results of the multi-objective optimization are reported in Fig. 3 for both the electricity-only (ELE) configuration (Fig. 3.a) and the cogenerative (CHP) one (Fig. 3.b), considering cyclopentane as working fluid. The figure reports the tradeoff between electrical RTE (x-axis) and the total heat transfer surface of the system (y-axis): in blue it is depicted the overall population explored by the NSGA optimizer in the last generation, while in red it is possible to notice the optimal solutions on the Pareto front, i.e. the set of non-dominated solutions.

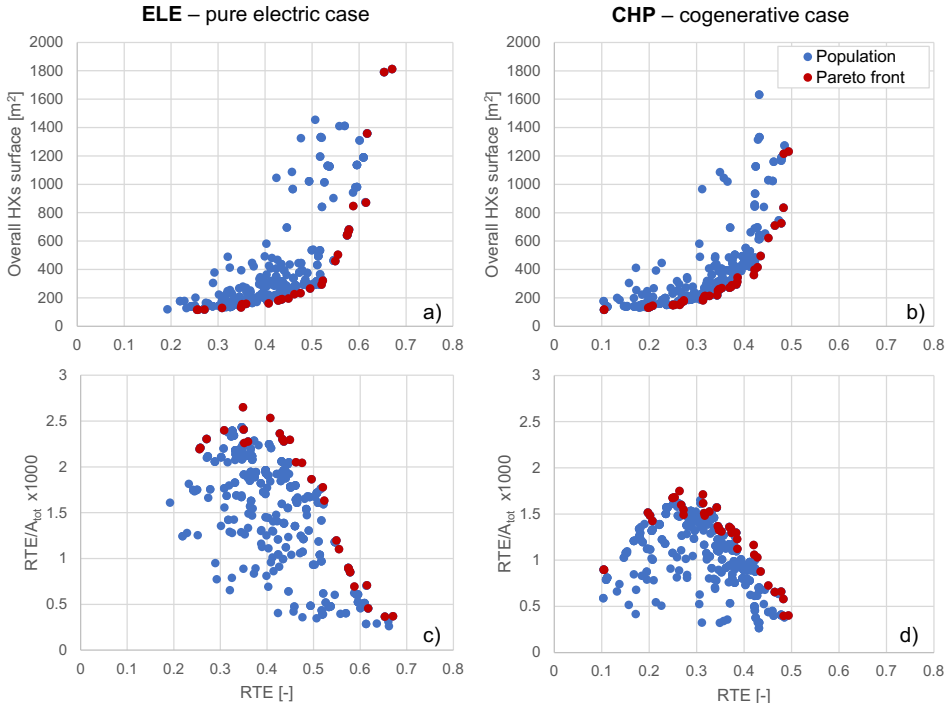

Figure 3: Pareto front of optimal solutions (red) for the electricity only (a) and cogenerative case(b). RTE/A_{tot} ratio for the electricity only (c) and cogenerative (d) cases.

As expected, the electricity only system is capable of achieving higher values of round-trip efficiency (up to close 70% that is value comparable to current Li-ion batteries and PHES) thanks to the much lower condenser pressure in the power cycle (discharging mode), which allows for a higher enthalpy drop in the turbine and thus an improved net power output of the system.
From the graph of Fig. 3.a and 3.b it is possible to notice that the trend of the overall heat transfer surface versus the electrical RTE of the system is strongly not linear: above a certain RTE threshold, an increase of the system performance can be attained only with an exponential growth of heat transfer surfaces due to the non-linear correlation between heat transfer temperature differences and heat transfer surfaces. This RTE threshold is equal to around 0.5 for the ELE configuration and to around 0.4 for the CHP system, as it is possible to notice from the evident soaring of heat exchangers surfaces above these values. It is also worth mentioning that the maximum RTE/A_{tot} (Fig. 3.c and 3.d) is not obtained by pushing the round-trip efficiency to the maximum achievable values and the optimal point is found for both cases in a region of the Pareto front characterized by rather low RTE values. In particular, the maximum RTE/A_{tot} is found between RTE values of 0.3 and 0.4 for the ELE configuration, while it is characterized by lower values (0.25-0.35) for the CHP system, as it could be expected due to the overall lower RTE values of such configuration. In addition, for the CHP system the RTE/A maximum value is lower than in the ELE case (-30%).

The trends of the Pareto optimal values for the pinch point temperature differences of the low-pressure heat exchanger (evaporator in HP mode) and of the high-pressure heat exchanger (condenser in HP mode) are depicted in Fig. 4.a and 4.b, respectively. For both system configurations the trend of these optimization variables is similar: the optimization variable which is mainly responsible for the trade-off between RTE and overall HX surface is the $\Delta T_{pp,LP}$, as this parameter linearly varies between the minimum and maximum RTE of both systems, being pushed to the lower bound only for combinations of very high RTE and HXs total surface. Similar considerations can be made for $\Delta T_{pp,HP}$, even if it possible to notice that the optimizer set its value really close to the upper bound in the low-RTE range of the Pareto front, denoting that it could be useful to slightly relax the upper bound on this variable.

These results also suggest that the assumption considered for the precedent analysis of using a pinch point temperature difference of 2°C to design the heat exchangers in the HP/charging cycle of the cogenerative system (Alfani et al., 2023) could be improved by adopting values around 5°C and 7°C for the LP HX and HP HX respectively, in order to attain the maximum RTE/A_{tot} ratio.

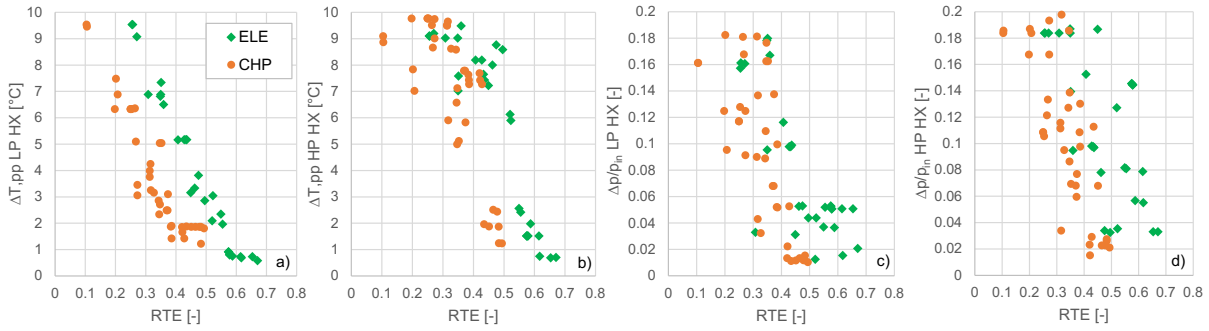

Figure 4: Trend of some of the optimization variables along the Pareto front for the electricity only (green) and cogenerative (orange) cases.

As the pressure drops affect less significantly the trade-off between system performance and overall HX surface, their trend on the Pareto front is less linear and tends to be more scattered. However, as expected, it is possible to notice that the working fluid side relative pressure drop in the low-pressure HX tends to decrease for higher RTE values. This trend can be explained considering that this pressure drop has two opposing effects on the HX surface as (i) higher fluid velocities lead to higher convective heat transfer coefficients and (ii) higher pressure drops in two-phase conditions (in this case evaporation), lead to lower average heat transfer temperature differences considering a fixed $\Delta T_{pp,LP}$. However, as the first effects is more significant than the second, the higher the LP HX pressure drop, the lower this heat exchanger surface. On the other hand, even if this variable does not affect the COP of the heat pump, as it only increases or decreases the pressure drop foreseen by the lamination valve,

it strongly influences the condensation temperature of the power cycle, significantly affecting the power output attainable in discharge mode.

In contrast, the pressure drop in the cold and low-pressure side of the recuperator (heat pump mode) also affects the COP of the charge cycle as, at fixed compressor outlet temperature and pressure, it increases the compressor pressure ratio and thus its electrical consumption. For this reason, to maximize the COP of the heat pump the optimizer tends to select the optimal values of this variable closer to the lower bound.

4.2 Fluid comparison

Figure 5 depicts the comparison in both the ELE and CHP case of cyclopentane and the other two fluids, NOVEC649 (representative of fluids with a lower critical temperature) and octane (representative of fluids with a higher critical temperature). R1233zd(E), that is a fluid highly recommended in open literature for these applications, has not been included both because of its low critical temperature, likely too close to the storage temperature, and because if may be phase out in the next years according to the REACH regulation (Williams, Panko, & Paustenbach, 2009). It is possible to highlight that octane can potentially reach RTE slightly higher than cyclopentane especially in the CHP case, but this is generally obtained with heat exchangers with an overall heat transfer area that, for the same RTE, can be up to 60% higher in the interval of RTE where the maximum of RTE/A_{tot} is located. This aspect results from the larger ratio between the latent heat of vaporization and the enthalpy variation in compression/expansion, which is a consequence of the distance between the thermodynamic cycle and the fluid critical point, which leads to lower operative pressures thus requiring higher heat transfer surfaces to achieve reasonable pressure drops in the components. Only in some ELE cases at very high heat transfer area, octane can reach the same RTE with a lower heat transfer area. Additionally, the use of octane may lead to challenges in system operation related to the leakage in of air for sub-atmospheric condensation pressures and the very high volumetric flow rates at turbine outlet: this is particularly relevant for ELE case where the condensation pressure can be low as 0.03 bar. NOVEC649 analysis leads to almost opposite considerations: the proximity of the critical point implies a reduction of heat pump performance because of the lower latent heat of condensation at high temperature, which is not compensated by the compact heat exchangers that can be designed with higher operating pressures. RTE/A_{tot} parameter is penalized and generally reaches values up to half the corresponding value achievable with cyclopentane. Maximum reachable RTE are penalized as well and cannot go over 60% in ELE case and 50% in CHP one.

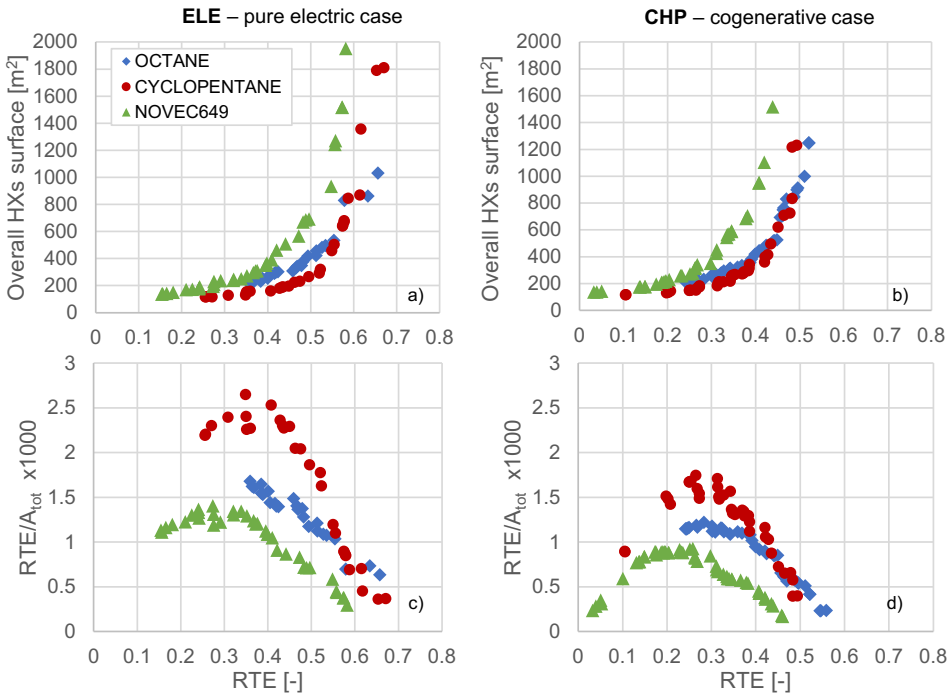

Figure 5: Comparison of the Pareto front and RTE/A_{tot} obtained with cyclopentane (red), NOVEC649 (green) and octane (blue) for both the electricity only (left) and CHP (right) cases.

5 CONCLUSIONS AND FUTURE WORKS

This work provides a numerical quantification of the performance attainable with ORC-based Carnot batteries under a realistic representation of the heat exchangers and adopting a Pareto front analysis. Two cases have been investigated with the aim of considering both pure electric (ELE) and cogenerative (CHP) applications where the ORC condensation heat is exploited by a thermal user (e.g. district heating, industrial processes like drying), as proposed by H2020 RESTORE project. Results show that cyclopentane is a promising working fluid in both cases when a waste heat integration is available in charging mode at low-mid temperature (minimum 80°C) and a reasonable temperature of the constant temperature thermal energy storage (150°C) is assumed. Round-trip efficiencies for the ELE case are around 10% higher than CHP case for the same overall heat transfer area, thanks to the lower condensation pressure and ranges between 20% for very low heat exchanger dimension up to 70% but requiring an exponential increase of the heat transfer area. Maximum RTE/A parameter, that for high heat to power ratio cycles as in this case can be considered a reasonable techno-economical figure of merit, is obtained at rather low RTE around 35% for the ELE case showing the difficulties that Carnot batteries technology may experience in getting high performance at minimum levelized cost of storage. The parameters more relevant for the analysis are the two-phase flow heat exchangers temperature differences while the pressure drops, due to the nonlinear relation with global heat transfer coefficient, have a lower impact on the overall heat transfer area and performance. Comparison of cyclopentane with respect to other fluids show that adopting a high critical temperature fluid as octane allows to potentially reach higher RTE but it also requires much larger heat transfer area because of the lower fluid density and heat transfer coefficients for average pressure drops. Differently, NOVEC649, having a lower critical temperature, can adopt smaller heat exchangers but it is penalized in cycle thermodynamic leading to a lower RTE.

Next step of this study will focus on the extension of this work towards a full techno-economic optimization where the capital cost of the system or the levelized cost of the technology will be analyzed against RTE with a Pareto front analysis.

222

REFERENCES

Alfani, D., Giostri, A., & Astolfi, M. (2023). Working Fluid Selection and Tthermodynamic Optimization of the Novel Renewable-Energy Based RESTORE Seasonal Storage Technology. In *Proceedings of ASME Turbo Expo 2023 Turbomachinery Technical Conference and Exposition GT2023 June 26-30, 2023, Boston, Massachusetts* (pp. 1–14).

Asgari, M., Javidan, M., Nozari, M., Asgari, A., & Ganji, D. D. (2021). Simulation of solidification process of phase change materials in a heat exchanger using branch-shaped fins. *Case Studies in Thermal Engineering*, *25*, 100835. https://doi.org/10.1016/j.csite.2020.100835

Astolfi, M., Rizzi, D., Macchi, E., & Spadacini, C. (2021). A Novel Energy Storage System Based on Carbon Dioxide Unique Thermodynamic Properties. https://doi.org/10.1115/GT2021-59487

Castell, A., Solé, C., Medrano, M., Roca, J., Cabeza, L. F., & García, D. (2008). Natural convection heat transfer coefficients in phase change material (PCM) modules with external vertical fins. *Applied Thermal Engineering*, *28*(13), 1676–1686. https://doi.org/10.1016/j.applthermaleng.2007.11.004

Cavallini, A., Col, D. Del, Doretti, L., Matkovic, M., Rossetto, L., Zilio, C., & Censi, G. (2006). Condensation in Horizontal Smooth Tubes: A New Heat Transfer Model for Heat Exchanger Design. *Heat Transfer Engineering*, *27*(8), 31–38. https://doi.org/10.1080/01457630600793970

Cheung, B., Carriveau, R., & Ting, D. S.-K. (2012). Storing Energy Underwater. *Mechanical Engineering*, *134*(12), 38–41. https://doi.org/10.1115/1.2012-DEC-3

Deb, K., Pratap, A., Agarwal, S., & Meyarivan, T. (2002). A fast and elitist multiobjective genetic algorithm: NSGA-II. *IEEE Transactions on Evolutionary Computation*, *6*(2), 182–197. https://doi.org/10.1109/4235.996017

Dumont, O., & Lemort, V. (2020). Mapping of performance of pumped thermal energy storage (Carnot battery) using waste heat recovery. *Energy*, *211*, 118963. https://doi.org/10.1016/j.energy.2020.118963

Eggers, J. R., von der Heyde, M., Thaele, S. H., Niemeyer, H., & Borowitz, T. (2022). Design and

performance of a long duration electric thermal energy storage demonstration plant at megawatt-scale. *Journal of Energy Storage*, *55*, 105780. https://doi.org/10.1016/j.est.2022.105780

Eppinger, B., Zigan, L., Karl, J., & Will, S. (2020). Pumped thermal energy storage with heat pump-ORC-systems: Comparison of latent and sensible thermal storages for various fluids. *Applied Energy*, *280*, 115940.

Frate, G. F., Antonelli, M., & Desideri, U. (2017). A novel Pumped Thermal Electricity Storage (PTES) system with thermal integration. *Applied Thermal Engineering*, *121*, 1051–1058. https://doi.org/10.1016/j.applthermaleng.2017.04.127

Gnielinski, V. (1975). New equations for heat and mass transfer in the turbulent flow in pipes and channels. *NASA STI/Recon Technical Report A*, *41*(1), 8–16.

Jockenhöfer, H., Steinmann, W.-D., & Bauer, D. (2018). Detailed numerical investigation of a pumped thermal energy storage with low temperature heat integration. *Energy*, *145*, 665–676. https://doi.org/10.1016/j.energy.2017.12.087

Laughlin, R. B. (2017). Pumped thermal grid storage with heat exchange. *Journal of Renewable and Sustainable Energy*, *9*(4), 044103. https://doi.org/10.1063/1.4994054

Lemmon, E. W., Bell, I. H., Huber, M. L., & McLinden, M. O. (2018). NIST standard reference database 23: reference fluid thermodynamic and transport properties-REFPROP, Version 10.0, National Institute of Standards and Technology. *Standard Reference Data Program*.

Liu, Z., & Winterton, R. H. S. (1991). A general correlation for saturated and subcooled flow boiling in tubes and annuli, based on a nucleate pool boiling equation. *International Journal of Heat and Mass Transfer*, *34*(11), 2759–2766. https://doi.org/10.1016/0017-9310(91)90234-6

Macchi, E., & Astolfi, M. (2016). *Organic Rankine Cycle (ORC) Power Systems*. Elsevier Science.

Miller, J. (2018). *Low-cost, long-duration electrical energy storage using a CO2 -based Electro Thermal Energy Storage (ETES) system. Echogen Power Systems.*

RESTORE: Renewable Energy based seasonal Storage Technology in Order to Raise Economic and environmental sustainability of DHC. Available online at: https://www.restore-dhc.eu/. (n.d.).

Sarbu, I., & Dorca, A. (2019). Review on heat transfer analysis in thermal energy storage using latent heat storage systems and phase change materials. *International Journal of Energy Research*, *43*(1), 29–64. https://doi.org/10.1002/er.4196

Steger, D., Regensburger, C., Eppinger, B., Will, S., Karl, J., & Schlücker, E. (2020). Design aspects of a reversible heat pump-Organic rankine cycle pilot plant for energy storage. *Energy*, *208*.

Steinmann, W. D. (2014). The CHEST (Compressed Heat Energy STorage) concept for facility scale thermo mechanical energy storage. *Energy*, *69*, 543–552. https://doi.org/10.1016/j.energy.2014.03.049

Turboden S.p.A. (2023). Large-scale Heat Pumps up to 200°C to Play a Crucial Role in the Path for Decarbonization of Heating Sector. *Mitsubishi Heavy Industries Technical Review*, *60*(1), 1–5.

Williams, E. S., Panko, J., & Paustenbach, D. J. (2009). The European Union's REACH regulation: A review of its history and requirements the EU REACH regulation: A review E. S. Williams et al. *Critical Reviews in Toxicology*, *39*(7), 553–575. https://doi.org/10.1080/10408440903036056

Zhu, X., Li, Y., & Zhu, Q. (2022). Heat transfer enhancement technology for fins in phase change energy storage. *Journal of Energy Storage*, *55*, 105833. https://doi.org/10.1016/j.est.2022.105833

Žukauskas, A. (1972). Heat Transfer from Tubes in Crossflow. In *Advances in heat transfer, Academic Press* (pp. 93–160). https://doi.org/10.1016/S0065-2717(08)70038-8

ACKNOWLEDGEMENT

The current work has been developed for the RESTORE project (www.restore-dhc.eu/), which has received funding from the European Union's Horizon 2020 research and innovation programme under grant agreement No. 101036766.

This study was carried out within the NEST - Network 4 Energy Sustainable Transition (D.D. 1243 02/08/2022, PE00000021) and received funding under the National Recovery and Resilience Plan (NRRP), Mission 4 Component 2 Investment 1.3, funded from the European Union - NextGenerationEU. This manuscript reflects only the authors' views and opinions, neither the European Union nor the European Commission can be considered responsible for them.

ORC SEVILLE 2023
7th International Seminar on O.R.C. Power Systems

© 2024 Editorial Universidad de Sevilla. Este es un artículo de acceso abierto distribuido bajo los términos de la licencia de uso y distribución Creative Commons (BY-NC-ND 4.0)

DOI: https://dx.doi.org/10.12795/9788447227457_36

EVALUATING THE WASTE HEAT SOURCES IN A VERY LARGE CRUDE CARRIER AND THE POTENTIAL INTEGRATION OF ORGANIC RANKINE CYCLE CONFIGURATIONS

Amalia Stainchaouer[1,*], Christopher Schifflechner[1], Christoph Wieland[1,2], Hartmut Spliethoff[1]

[1] *Technical University of Munich, Chair of Energy Systems, Boltzmannstraße 15, Garching, Germany*
[2] *University of Duisburg-Essen, Chair of Energy Process Engineering and Energy Systems, Leimkugelstraße 10, Essen, Germany*

*Corresponding Author: amalia.stainchaouer@tum.de

ABSTRACT

Decarbonizing the shipping industry is gaining increasing attention, with the Waste Heat Recovery (WHR) technologies being in the spotlight as fuel saving solutions for marine engines. Although many studies focus on assessing of recovered energy from marine main engines using Organic Rankine Cycle (ORC) systems, only a few investigations deal with the overall waste heat potential of the vessel, considering also the auxiliary diesel generator sets. In this work, the waste heat potential of the heat sources available from the main engine and the auxiliary gensets are examined as functions of the engine loads in different sailing and laden conditions by applying real long-term operational data of a case study Very Large Crude Carrier (VLCC). A direct and an indirect method, with respect to the heat balance, are followed to estimate the exhaust gas waste heat. In particular, the former method is developed using the measured temperature values, while the latter one introduces the exhaust gas mass flow rates estimated indirectly by the measured fuel oil consumption. Furthermore, two rcORC configurations are proposed to determine the achievable energy recovery by exploiting the major waste streams of the main engine and auxiliary gensets. Two methods are evaluated: (i) utilizing only the exhaust gases of the main engine to evaporate the ORC working fluid, and (ii) utilizing the exhaust gases of both main engine and auxiliary gensets. The simulations based on the real exhaust gas temperature measurements for the mean engine load during sailing indicate that the rcORC power output can be estimated equal to 530 kW, being increased up to 653 kW and 741 kW due to the diesel gensets integration, for R245fa and R1233zd(E) as the selected ORC working fluids, correspondingly.

1 INTRODUCTION

The current regulations of the International Maritime Organization (IMO) render the sustainable integration of WHR technologies essential for the greenhouse gas emissions reduction of the shipping industry. Therefore, several studies examine the alternatives to capture and reuse the low-grade waste streams of vessels' Internal Combustion Engines (ICEs) to cover the heat and electricity needs, and hence, decrease the fuel consumption of the auxiliary boilers and diesel gensets, respectively. A diesel engine's main waste heat streams are the exhaust gas, jacket cooling water and scavenge air, representing around 50 % of the fuel input heat. The dual pressure Steam Rankine Cycle (SRC) units are well-established approach for recovering waste heat in maritime applications, while the ORC systems constitute an alternative solution. ORC systems perform better than SRC configurations at low engine loads, but ORC systems can not contribute to the steam production (Andreasen *et al.*, 2017). Mondejar *et al.* (2018) reviewed the use of ORC systems in the shipping industry and compared configurations of different research works, concluding that, in order to ensure the financial sustainability of such applications in vessels, a regenerative ORC configuration using the exhaust gases of the main engine is the most suitable option.

In this context, the analysis of the waste heat source profile of ships constitutes the initial step in terms of on-board installation of WHR technologies to estimate the overall potential (Chunwee *et al*., 2022). Although the variation of the engine load in ships during the different sailing situations results in uncertainties concerning the available waste heat, there is a lack of operational data and profiles for the different types of vessels in the literature. Chunwee *et al*. (2022) developed a methodology to describe the generic ship speed profile and determined correlations of the exhaust gas temperature and mass flow rate as a function of the engine load for slow- and medium- speed engines. However, the investigation of the rest waste streams is not involved in this work. Andreasen *et al*. (2017) estimated the temperature and mass flow rate values for the three main waste streams for a container ship using for its propulsion a two-stroke MAN diesel engine of 23 MW; but there is no information regarding the voyage characteristics. Furthermore, only a few investigations examine the potential integration of the auxiliary diesel gensets exhaust gases in the WHR systems. Mondejar *et al*. (2017) focused on the use of the main engines (4 of 5.9 MW) and diesel gensets (4 of 2.8 MW) mixture in order to preheat, evaporate and superheat the regenerative ORC working fluid installed in a passenger cruise vessel. In this work, the actual measured data linked to the 1-year operation of a VLCC are used, after defining the voyage and ship characteristics, to describe its waste heat sources potential as a function of the main engine load and determine the energy flow. The exhaust gas waste stream of diesel gensets is also evaluated based on their operational profiles formed by using real records. The final step is to examine the potential power output of ORC systems integrated in this case study vessel and estimate the respective contribution of diesel gensets.

2 DESCRIPTION OF THE INVESTIGATED CASE STUDY

2.1 System description

This study investigates the one-minute measured operational data of a case study VLCC over a 1-year period, from September 2021 to August 2022, provided by partner METIS in the context of the EU-funded project ENGIMMONIA. These data are used in order to determine the potential of the waste heat sources in this case study vessel in the whole range of the performed main engine loads. Table 1 characterizes the ship, as well as the main engine and diesel generators key technical features. It is noted that the main engine is used for the vessel propulsion and the diesel gensets to cover the electricity needs. Moreover, there is also an auxiliary boiler applied for the heat demands.

Table 1: Main technical features of the ship, main engine and diesel gensets

Ship	Main engine	Diesel generators
Ship type: VLCC	Engine type: 2S-Diesel Wärtsilä	Gensets type: 4S-Diesel
Deadweight: 319,368 tons	Number of cylinders: 7	Number: 3
Overall length: 339.76 m	Turbochargers: 2	Nominal power: 1800 kW (×2), 2390 kW (×1)
Prop. diameter: 10.00 m	Piston stroke: 3.38 m	Nominal speed: 900 rpm
Prop. pitch: 6.91 m	Cylinder bore: 0.82 m	
Draft: 22.28 m	Nominal power: 31,640 kW	
Year of construction: 2011	Nominal speed: 80 rpm	

2.2 Voyage analysis

Understanding the voyage constitutes an important part of the investigation, since it provides critical information regarding the main engine operation. It is noted that the vessel was mainly travelling in the Indian Ocean, while for a period of more than 3 months, it was in the Pacific and South Atlantic Oceans. The location can be evaluated based on the latitude and longitude data points. Based on the records, Figure 1a presents all the sailing situations of the VLCC as time percentages. It is mentioned that the sailing full speed ahead status, which corresponds to 6,312 hours annually, is selected as a reference condition for this study due to the high vessel speeds, and hence, the high main engine loads that occur

in this situation. In particular, the respective minimum, mean and maximum vessel speeds are equal to 9, 22 and 37 km/h. Figure 1b depicts also the normal distributions of vessel speed for both laden and unladen conditions, with the cargo being computed indirectly using the mean ship draft and the laden condition being defined by setting a threshold in terms of cargo weight of 100,000 metric ton, according to Wieland *et al*. (2022).

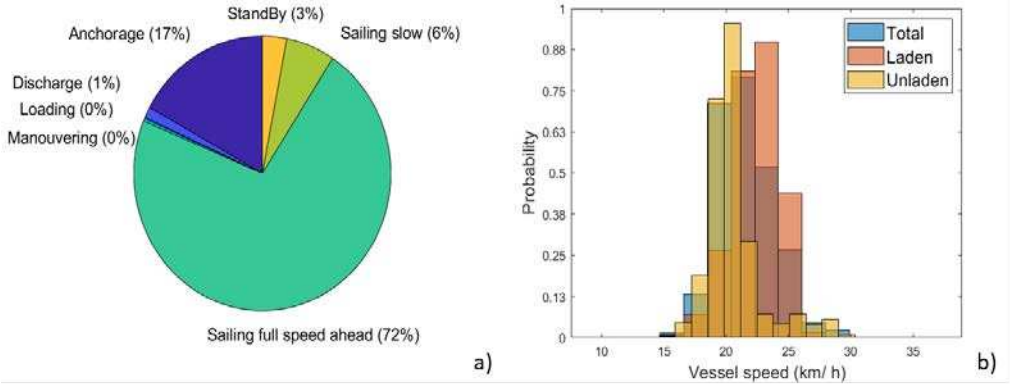

Figure 1: (a) Sailing status of the VLCC and (b) normal distributions of vessel speed for laden, unladen and for the total in sailing full speed ahead status

3 OPERATIONAL PROFILES

3.1 Main engine

The data cleaning and analysis are carried out using MATLAB® (R2021b) software. This process involves the treatment of missing values and outliers, using the filling with the next value and moving median functions for the retrieval of missing data and the remove of outliers, respectively. The operational profiles are created using the averaged data for each engine load. The discrepancies due to the errors of the measuring equipment are not included in this study. The loads of main engine are calculated by applying the measured power output values, with the mean and maximum main engine loads being equal to 36 % and 71 %, respectively, in both laden and unladen conditions, considering only the sailing full speed ahead status. Regarding the fuel input heat and the efficiency of the main engine, the given data set includes the fuel oil mass flow consumption, the fuel oil lower heating value, as well as the power output of the main engine required for the vessel propulsion. After the calculation process, the specific fuel oil consumption in the mean engine load is 173 g/kWh, while the fuel oil mass flow rate is increased from 0.33 to 0.92 kg/s as the engine load increases from 20 % to 60 %, correspondingly. As for the exhaust gases of the Main Engine (ME), the temperature values after the turbochargers are included in the data set, while the exhaust gas mass flow rates are calculated by using the fuel oil consumption and the estimated air mass flow rates, as indicated in Equation (1)-Equation (2). To determine the mass flow rate of the scavenged air, technical features of an internal combustion engine with similar operational characteristics are introduced from the online CEAS calculation tool of MAN Diesel & Turbo. The aim is to calculate the ratio of air to stoichiometric air (lambda, λ) as a function of the engine load, considering an air-fuel equivalence ratio (AFR) equal to 14.6 kg_{air}/kg_{fuel}, according to Equation (3), since the fuel chemical composition and the combustion conditions are unknown and there is no related information in the given manufacturer datasheet.

$$\dot{m}_{exg,ME} = \dot{m}_{B,ME} + \dot{m}_{air,ME} \quad (1)$$

$$\dot{m}_{air,ME} = 14.6 \cdot \lambda \cdot \dot{m}_{B,ME} \quad (2)$$

$$\lambda = a \cdot l^6 + b \cdot l^5 + c \cdot l^4 + d \cdot l^3 + e \cdot l^2 + f \cdot l^1 + g \cdot l^0 \quad (3)$$

Table 2: Coefficients for lambda estimation used CEAS calculation tool

Coefficient	Value	Coefficient	Value
a	$-1.1073 \cdot 10^{-10}$	e	$-1.6163 \cdot 10^{-02}$
b	$4.3839 \cdot 10^{-08}$	f	$1.8100 \cdot 10^{-01}$
c	$-6.6532 \cdot 10^{-06}$	g	$4.7222 \cdot 10^{-00}$
d	$4.7947 \cdot 10^{-04}$		

The exhaust gas outlet temperature of the turbochargers calculated based on the operational data presents deviations compared to the Wärtsilä manufacturer data up to 75 K due to the different operating conditions under which the manufacturer's tests were carried out (Figure 2a). It is also highlighted that manufacturer's tests are dedicated to simulate ICE's operation under one design point and cannot be compared to the continuous operation of ME integrated to the case study VLCC. The different measuring equipment and conditions can also provoke discrepancies between these recorded data. Figure 2a also shows the estimated exhaust gas mass flow rate following the already described calculation process. Moreover, the overall analysis indicates that this selection of lambda coefficient from MAN manufacturer's data has a greater influence than the smaller differences in fuel oil consumptions between the measurements and MAN manufacturer's data. Therefore, with respect to the main engine heat balance, two methodologies are proposed; (i) using the temperature values of the operational data and calculating the mass flow rate from the heat balance (Direct Method; DM), and (ii) using the mass flow rate estimated based on the given fuel oil consumption and calculating the temperature values from the heat balance (Indirect Method; IM). The data analysis shows also that the exhaust gas temperature measurements are more reliable than the fuel oil consumptions due to their higher correlations with the power output and vessel speed. Assuming an ambient temperature equal to 30 °C, since it was mainly travelling under tropical conditions, and an exhaust gas specific heat ($C_{p,exg}$) of 1.02 kJ/kgK, the waste heat in the exhaust gases of the main engine can be determined with the following formula:

$$\dot{Q}_{exg,ME} = \dot{m}_{exg,ME} \cdot C_{p,exg} \cdot \left(T_{exg,ME} - 30\ °C\right) \quad (4)$$

227

Regarding the Scavenge Air Cooler (SAC), the fresh water inlet and outlet temperatures, as well as the scavenge air outlet temperature, are included in the operational data, and thus, by considering a typical value for the fresh water mass flow rate equal to 221 kg/s, the scavenge air inlet temperature can be calculated from the heat balance in the SAC (Equation (5)). Figure 2b illustrates the scavenge air inlet temperature for both followed approaches due to the different air mass flow rate in each case and the manufacturer one.

$$\dot{Q}_{SAC,ME} = \dot{m}_{fw} \cdot C_{p,fw} \cdot \left(T_{fw,out} - T_{fw,in}\right) = \dot{m}_{air,ME} \cdot C_{p,air} \cdot \left(T_{sca,in} - T_{sca,out}\right) \quad (5)$$

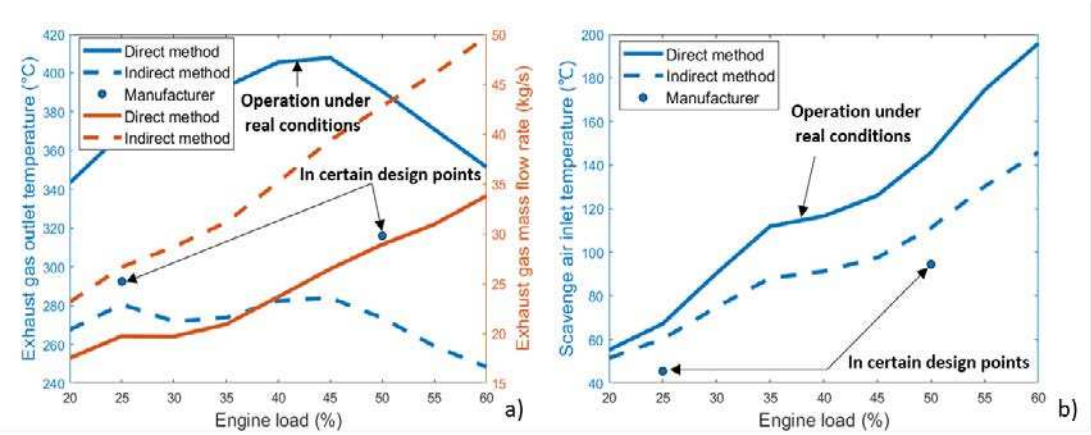

Figure 2: (a) Exhaust gas temperature and mass flow rate and (b) scavenge air inlet temperature as a function of the engine load for direct and indirect methods and from Wärtsilä manufacturer data

In the case of jacket water cooler, the manufacturer data that refer to the cooling water inlet and outlet temperatures are introduced to evaluate the respective rejected heat, since they are not recorded. Thus, the inlet and outlet temperatures are increased, as the engine load increases from 20 % to 60 %, from 61 to 69 ℃ and 64 to 76 ℃, correspondingly, while a constant mass flow rate of the cooling water equal to 55 kg/s can be assumed. The rejected heat in the jacket cooling water is computed according to the Equation (6).

$$\dot{Q}_{JWC,ME} = \dot{m}_{cw} \cdot C_{p,cw} \cdot \left(T_{cw,out} - T_{cw,in}\right) \quad (6)$$

Finally, the heat losses in the lubricating oil cooler ($\dot{Q}_{lo,ME}$) and due to the radiation ($\dot{Q}_{rad,ME}$) are considered to represent approximately 4 % of the fuel input heat in total.

3.2 Diesel gensets

Concerning the diesel gensets (DGs), their total fuel oil mass flow consumption is measured, and hence, the individual consumption for every data point can be estimated by using the recorded electrical power output of each generator and considering, in line also with the manufacturer data, that the specific fuel oil consumption is the same for the three units in the whole range of loads from 192 to 194 g/kWh. Based on the data analysis, it is found that there is no correlation between the loads of the main engine and diesel gensets, with the mean power output being varied from 1,009 to 1,180 kW for the different main engine loads. As depicted in Figure 3a, this power demand is covered either by the operation of only one genset (in a load of 66 % for gensets 1 and 2, and 50 % for genset 3) or by using two of them, working in lower part loads. According to the analysis of the diesel generator sets data, the mean exhaust gas temperature, for all the examined cases in terms of the gensets operational profiles, is 394 ℃. Following the calculation process already described for the main engine, but with a ratio of air to stoichiometric air equal to 1.9 (Mondejar *et al.*, 2017), the exhaust gas mass flow rates can be estimated (Figure 3b).

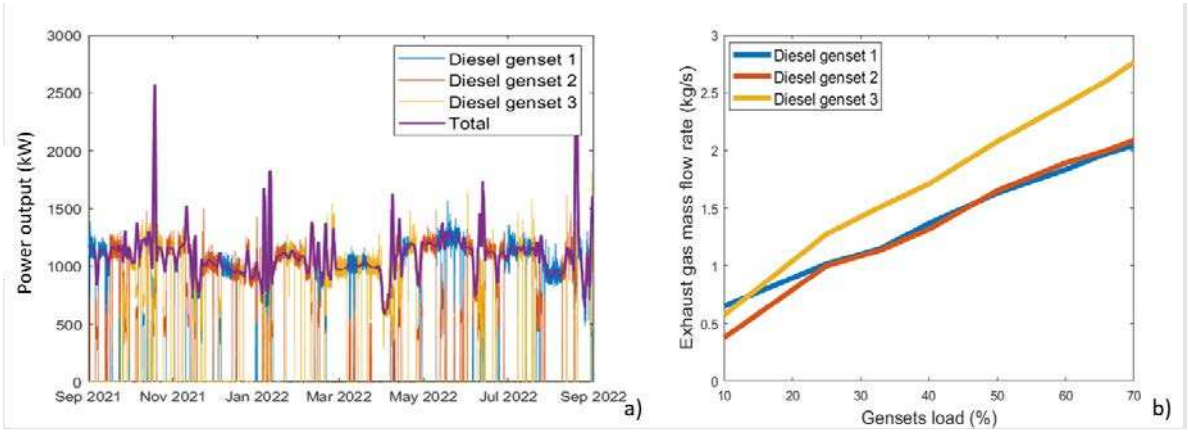

Figure 3: (a) Power output of diesel gensets during the 1-year period and (b) exhaust gases mass flow rates as a function of the generators loads

4 METHODS

4.1 VLCC waste heat potential

The calculations regarding the fuel input heat, exhaust gas waste heat, as well as the heat rejected to the scavenge air cooler, jacket cooling system, lubricating oil cooler and the heat released to the ambient as radiation, are conducted by applying the Equation (4)-(6). It should be mentioned that the main engine efficiency in the mean load has been determined to be 49 %. Therefore, the heat balance (in kW) in the main engine can be described by:

$$\dot{Q}_B = \dot{m}_B \cdot Hu = P_{prop} + \dot{Q}_{exh,ME} + \dot{Q}_{SAC,ME} + \dot{Q}_{JWC,ME} + \dot{Q}_{lo,ME} + \dot{Q}_{rad,ME} \quad (7)$$

Where $\dot{Q}_B$ is the heat of the input fuel and P_{prop} is the power needed for the propulsion included in the available data. The respective amounts of heat and the required propulsion power are presented as a function of the main engine load in Figure 4a. The validation in terms of energy balance implementation is conducted using exclusively data produced by CEAS calculation tool as inputs and comparing the output in the lubricating oil with the values given in MAN's technical datasheet. Based on Figure 4a, the waste heat percentages in the exhaust gases, SAC and JCW are 29.0 %, 13.4 % and 5.0 % for an engine load equal to 60 %. In the mean engine load, the percentage of the waste heat in the exhaust gases is increased up to 35 %, while the waste heat is decreased to 6.6 % in SAC and remains almost constant in JCW. The decrease of the SAC waste heat, with a corresponding increase in the exhaust gases waste heat, and the JCW waste heat stability as the engine load drops are also reported in Mondejar *et al*. (2018). According to Kosmadakis and Neofytou (2022), the waste heat rejected in JCW system depicts the 6 % of the fuel thermal content. In this study, the potential in JCW, given in Table 3, is equal to 1,204 kW (5.4 % of the fuel thermal content) in the mean engine load. Therefore, considering only the sailing full speed ahead status and assuming that the main engine operates in constant load of 36 %, the corresponding Sankey diagram is presented in Figure 4b.

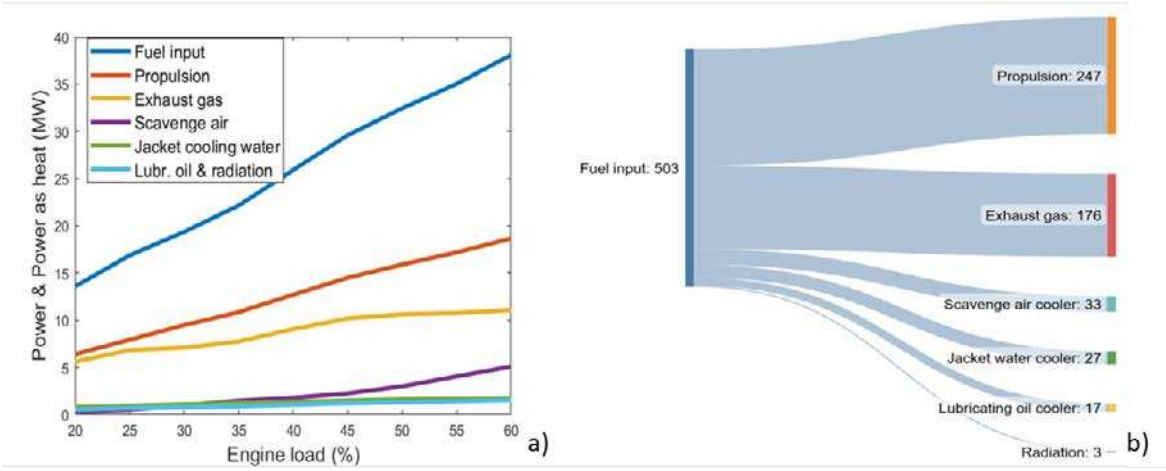

Figure 4: (a) Heat balance in main engine as a function of load and (b) Sankey diagram (in TJ) in mean engine load

The theoretical waste heat potential in the auxiliary gensets exhaust gases can be within 715-929 kW, for all possible operational situations discussed in Section 3.2. Moreover, the high temperature heat demands required for steam production in terms of heater and tanks periphery, fuel oil heating, cargo heating, etc. are considered to be covered by the auxiliary boiler and by using an Exhaust Gas Boiler (EGB). The thermal power that refers to the EGB in a VLCC can be 970 kW (Sakalis, 2018), and according to IMO 4th GHG study the auxiliary boiler power output is equal to 300 kW on sail. It is also noted that compared to the case of SRC, there is no further temperature reduction of the high temperature exhaust gases related to the steam turbine operation. In this study, it is assumed that the low temperature heat demands for the fresh water generation are covered by both SAC and JCW. Concerning the scenario of waste heat recovery from both ME and DGs exhaust gases, the mixture occurs before the EGB, according the Equation (8), where the calculation of the enthalpy when temperature is known, and vice versa, is conducted using REFPROP 9.1 library.

$$h_{mix} = \frac{(\dot{m}_{exg,ME} \cdot h_{exg,ME} + \dot{m}_{exg,DG,i} \cdot h_{exg,DG,i} + \dot{m}_{exg,DG,j} \cdot h_{exg,DG,j})}{(\dot{m}_{exg,ME} + \dot{m}_{exg,DG,i} + \dot{m}_{exg,DG,j})} \quad (8)$$

Where $i \neq j$ and can be 1,2 or 3, depending on which diesel genset is in operation. In the case that only one auxiliary generator works, its exhaust gases mass flow rate and enthalpy are $\dot{m}_{exg,DG}$ and $h_{exg,DG}$ and the Equation (8) is converted respectively. Table 3 summarizes the mass flow rate, temperature and theoretical and technical waste heat potential values of the available waste heat sources in this case study VLCC for a main engine load of 36 %, with the temperature values being computed for the EGB

outlet point. It is noted that the minimum acceptable exhaust gas temperature in order to avoid condensation of the sulfuric acids contained in the flue gas is 160 ℃ (Sakalis, 2018). This is considered in the utilization efficiency calculation necessary for the determination of technical potential. The capacity of the ORC systems is investigated for a potential integration in this VLCC in Section 4.2 and Section 5. Regarding the utilization efficiencies in JCW and SAC, the values 45 % (Kosmadakis and Neofytou, 2022) and 50 % are used, respectively.

Table 3: Mass flow rate, temperature and capacity values in mean main engine load

Heat source	Mass flow rate (kg/s)	Temperature (℃)	Theoretical potential (kW)	Technical potential (kW)
ME exhaust gases (DM)	20.9	347.4	6,766	3,994
ME & DG exhaust gases (DM)	23.1	351.9	7,585	4,522
ME exhaust gases (IM)	31.1	243.2	6,763	2,639
ME & DG exhaust gases (IM)	33.3	253.3	7,585	3,169
SAC (DM)	20.4	111.9	1,468	734
SAC (IM)	30.6	88.3	1,465	733
JCW	55.5	69.6	1,204	542

4.2 Scenarios for ORC power output estimation

The investigated waste heat source profile can be used as an input in order to estimate the potential power output and thermal efficiency of ORC systems integrated in this case study VLCC. Regarding the design of marine ORC configurations, there are many design options not only in terms of the utilized heat sources, but also concerning the included components and the working fluid. The literature survey of Mondejar *et al*. (2018) indicates that the most preferable ORC units for WHR of the exhaust gases or other high temperature sources in marine applications are rcORC configurations. In this study, a recuperative configuration that absorbs heat from the main engine or from both main engine and diesel gensets exhaust gases for the direct ORC working fluid evaporation is considered (Figure 5). The evaluation of the ORC performance indicators and thermodynamic properties is conducted using the conventional refrigerant R245fa and R1233zd(E), due to its lower global warming potential. Concerning the calculation method, the integral optimization code developed in MATLAB® and described in Pili (2021) is applied, using the net power output as the optimization function in the design mode of operation with the cost computation being disactivated, to compare the performance results of the examined ORC configurations for the two followed methodologies with respect to the main engine exhaust gases. It is also noted that, in this study, a water-cooled condenser is considered, with the power demand of the condenser water pump being neglected for the calculation of the net power. In Table 4, the main assumptions and constraints for the ORC thermal design are presented. This is followed by the equations used in the investigation of the ORC potential to calculate the performance.

230

Table 4: Key assumptions and constraints for the rcORC design

Variable	Assumed value
Exhaust gases minimum temperature	160 ℃
Evaporating minimum and maximum pressure	18.0, 29.2 bar
Pinch-point evaporator	5-100 K
Pinch-point condenser	5-20 K
Expander/Pump isentropic efficiency	70 %/ 75 %
Recuperator effectiveness	0.8
Condensing temperature	25-100 ℃

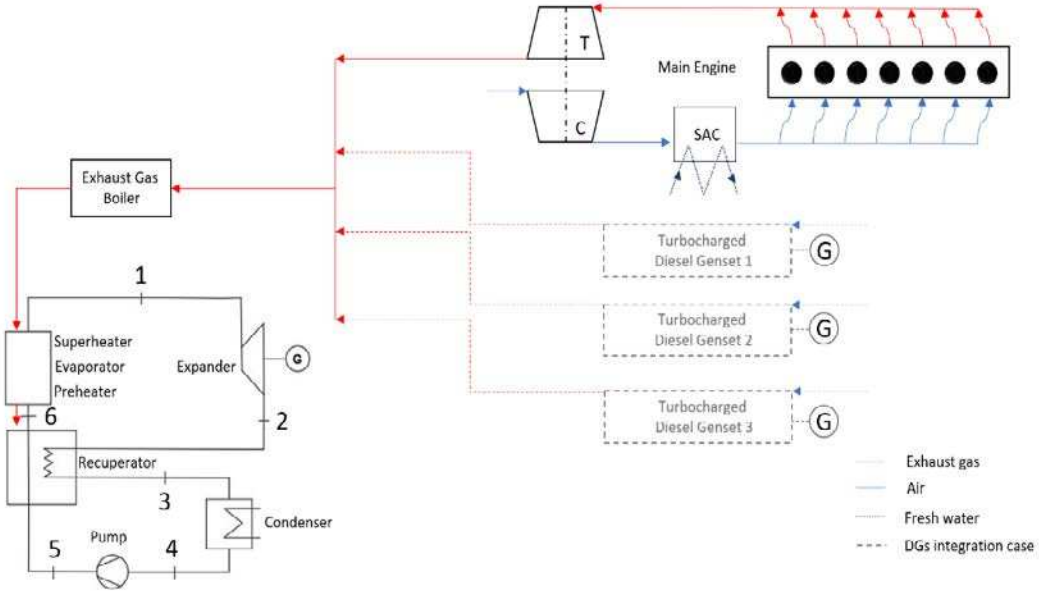

Figure 5: Schematic diagram of the whole system

The system efficiency is given by the equation:

$$\mathrm{eta_{sys}} = \mathrm{eta_{th}} \cdot \mathrm{eta_{ut}} = \frac{\mathrm{P_{el,net}}}{\dot{m}_{hs} \cdot (h_{hs,in} - h_{hs,out})} \cdot \frac{\dot{m}_{hs} \cdot (h_{hs,in} - h_{hs,out})}{\dot{m}_{hs} \cdot (h_{hs,in} - h_{hs,0})} \quad (9)$$

Where $\mathrm{eta_{th}}$ refers to the thermal efficiency of the ORC and is defined as the ratio of the generated electric net power ($\mathrm{P_{el,net}}$) to the heat input. Moreover, $\mathrm{eta_{ut}}$ stands for the utilization efficiency and expresses the percentage of the actual heat input to the theoretical amount of heat that could have been absorbed in the case of the exhaust gases outlet temperature was equal to the ambient one.

231

5 RESULTS

It can be assumed that the rcORC operates at full load under the already described conditions in Section 4.1. Therefore, considering this assumption and the assumptions, constraints and efficiencies definitions from Section 4.2, Table 5 and Table 6 summarize the simulation results for all the examined cases for working fluids R245fa and R1233zd(E), correspondingly.

Table 5: Results for rcORC thermodynamic parameters using R245fa

Variable	ME (DM)	ME & DGs (DM)	ME (IM)	ME & DGs (IM)
$\dot{m}_{wf}$ (kg/s)	16.9	19.2	10.9	12.9
p_{evap} (bar)	22.9	22.5	19.2	27.8
$T_{exp,in}$ (°C)	164.5	164.7	163.7	168.0
T_{cond} (°C)	37.8	32.1	28.0	27.9
SH (K)	36.0	36.7	44.0	28.9
$P_{el,net}$ (kW)	528.3	653.2	381.1	484.8
$\mathrm{eta_{th}}$ (%)	13.4	14.5	14.5	15.5
$\mathrm{eta_{ut}}$ (%)	57.9	59.6	39.0	41.7
$\mathrm{eta_{sys}}$ (%)	7.8	8.6	5.7	6.5

Table 6: Results for rcORC thermodynamic parameters using R1233zd(E)

Variable	ME (DM)	ME & DGs (DM)	ME (IM)	ME & DGs (IM)
$\dot{m}_{wf}$ (kg/s)	15.4	18.6	11.1	12.8
p_{evap} (bar)	22.0	24.9	20.2	28.1
$T_{exp,in}$ (°C)	179.3	178.7	179.2	185.7
T_{cond} (°C)	37.8	28.1	35.4	30.3
SH (K)	41.6	34.0	46.2	34.2
$P_{el,net}$ (kW)	531.7	740.6	389.0	515.1
eta_{th} (%)	13.3	16.4	14.8	16.5
eta_{ut} (%)	57.9	59.6	39.0	41.7
eta_{sys} (%)	7.8	9.8	5.8	6.9

Under these conditions and concerning the direct method, the evaporating pressure and the SH temperature difference is almost the same with respect to the diesel gensets integration when R245fa refrigerant is examined. However, the condensation process takes place in a lower temperature level and the working fluid mass flow rate is increased, resulting in a 24 % power output increase. In the case of R1233zd(E), the mass flow rate increase and condensation temperature drop with the simultaneous increase in evaporating pressure lead to a power increase of 39 %, when the diesel gensets are included. As for the indirect method, the maximum power output is attained when the evaporating pressure is close to the upper constraint with a lower SH temperature difference compared to the case of exploiting only the exhaust gases of the main engine for both examined refrigerants. In this case, the power output increase is equal to around 27 % and 32 % for R245fa and R1233zd(E), respectively. The comparison of the results from the two different working fluids indicates that R1233zd(E) performs better than R245fa due to the higher temperatures in the evaporator outlet point, having greater impacts on the power output than the lower SH temperature differences and differences between the condensation temperatures.

232

6 CONCLUSIONS

This study focuses on the analysis of the real long-term operational data of a case study VLCC in order to evaluate its overall waste heat potential and estimate the power output and efficiency of the proposed ORC configurations. Concerning the main engine, a direct method using the real measurements of exhaust gas temperature and an indirect one based on the estimation of the exhaust gas mass flow rates from fuel oil consumption are followed. The direct method should be considered as the most precise since it is conducted using the real measurements and the exhaust gas temperature measurements present higher correlations with the ME power output and vessel speed records than the fuel oil consumption ones, in which many uncertainties are involved. The introduction of manufacturer's data created for single design points in the calculation process for estimating the exhaust gas temperature makes also the indirect method less accurate. Furthermore, the potential of rcORC integration in this VLCC using the exhaust gases of the main engine based on the real measurement data is estimated to be equal to 530 kW. This power output can be increased by; the thermodynamic optimization of the ORC system and the exploitation of diesel gensets exhaust gases.

The following future work suggestions are drawn from this study:

- These configurations and technical modifications in ships are characterized by high complexity and cost, and hence, a techno-economic analysis is necessary to be conducted to secure the sustainability of such systems in VLCCs.
- The treatment of low temperature heat demands of a VLCC when the replacement of SRC with ORC systems should be examined, as well as the changes in the fresh water needs should be also addressed. In cases that the SAC is not used for the coverage of vessel's heat loads, the compressed scavenge air, with a temperature of 88 – 112 °C, can be used with a by-pass loop to preheat the ORC working fluid. This solution can also contribute to the decrease in the scavenge air cooling needs, leading to less required amounts of fresh water in SAC.

NOMENCLATURE

eta	efficiency (%)
h	enthalpy (kJ/kg)
l	engine load (%)
m	mass flow rate (kg/s)
p	pressure (bar)
λ	coefficient Lambda (-)
Hu	lower heating value (kJ/kg)
P	power output (kW)
Q	heat (kW)
DG	diesel gensets
DM	direct method
IM	indirect method
ME	main engine
ORC	organic Rankine cycle
SH	superheating temperature difference (K)
T	temperature (°C)
VLCC	very large crude carrier
WHR	waste heat recovery

Subscripts

cond	condensation
cw	cooling water
evap	evaporation
exg	exhaust gas
fw	fresh water
lo	lubricating oil
prop	propulsion
ut	utilization
rad	radiation
sys	system
th	thermal
wf	working fluid
B	fuel
JCW	jacket cooling water
SAC	scavenge air cooler

REFERENCES

Andreasen, J.G., Meroni, A., Haglind, F., 2017, *A Comparison of Organic and Steam Rankine Cycle Power Systems for Waste Heat Recovery on Large Ships, Energies 2017*, doi:10.3390/en10040547

Chunwee, N., Tam, I.C.K., Wetenhall, B., 2022, *Waste Heat Source Profiles for Marine Application of Organic Rankine Cycle, Journal of Marine Science and Engineering*, doi:10.3390/jmse10081122

IMO, 2020, *4th Greenhouse Gas Study* (Internet). Available from: Fourth Greenhouse Gas Study 2020 (imo.org)

Kosmadakis, G., Neofytou, P., 2022, *Reversible high-temperature heat pump/ ORC for waste heat recovery in various ships: A techno-economic assessment. Energy*, vol. 256, doi: 10.1016/j.energy.2022.124634

MAN, Diesel & Turbo, Denmark, 2014, *Waste heat recovery systems (WHRS)*. URL: https://mandieselturbo.com/docs/librariesprovider6/technical-papers/waste-heat-recovery-system.pdf

Mondejar, M. E., Ahlgren, F., Thern, M., Genrup, M., 2017, *Quasi-steady state simulation of an organic Rankine cycle for waste heat recovery in a passenger vessel. Applied Energy*, vol. 185, p.1324-1335

Mondejar, M.E., Andreasen, J.G., Pierobon, L., Larsen, U., Thern, M., Haglind, F., 2018, *A review of the use of organic Rankine cycle power systems for maritime applications. Renewable and Sustainable Energy Reviews*, vol. 91, p.126-151.

Pili, R., 2021, *Design and Off-Design of Organic Rankine Cycle Systems Recovering Fluctuating Industrial Waste Heat*, Munich, Ph.D. Dissertation, ISBN: 9783843950114.

REFPROP 9.1 Version, https://data.nist.gov/od/id/ECBCC1C130222ED9E04306570681B10740

Sakalis, G. N., 2018, *Development of a Method for Simulation and Optimization of Integrated Thermal Energy Systems of Ships*, Athens, Ph.D. Dissertation, URI: http://dspace.lib.ntua.gr/xmlui/handle/123456789/48296

Wieland, C., Faza'a, N., Schuster, A., Springer, J. P., Nowak, E., Medina, E. R., Katsikas, S., Sakalis, G., Splietthoff, H., 2022, *Energy Efficiency for Marine Application: Waste Heat Recovery Solutions and Photovoltaics in Long-Distance Shipping. Transport Research Area (TRA) Conference*, Lisbon

ACKNOWLEDGEMENT

This study has been conducted within the ENGIMMONIA project funded by the European Union's Horizon 2020 research and innovation program (grant agreement nº 955413).

ORC SEVILLE 2023
7th International Seminar on O.R.C. Power Systems

© 2024 Editorial Universidad de Sevilla. Este es un artículo de acceso abierto distribuido bajo los términos de la licencia de uso y distribución Creative Commons (BY-NC-ND 4.0)

DOI: https://dx.doi.org/10.12795/9788447227457_37

INVESTIGATING R1234ZE AND R1234YF AS REPLACEMENTS TO R134A IN WASTE HEAT RECOVERY ORC APPLICATIONS

James Bull*, James Buick, Jovana Radulovic

[1] *University Of Portsmouth, Anglesea Rd, Portsmouth PO1 3DJ*

*Corresponding Author: james.bull@port.ac.uk

ABSTRACT

The ever-growing energy demand across the globe puts significant pressure on the power generation sector to find renewable and sustainable alternatives to fossil fuels. Organic Rankine Cycle (ORC) technology can be applied to low-medium temperature heat sources to generate useful work. In this paper, an ORC cycle, powered by a medium temperature exhaust gas at 423.15 K, is modelled. Working fluids R1234ze and R1234yf were compared as replacements to R134a and considered across a variety of operating conditions comparing both the energetic and exergetic performance. Sizing of heat exchangers (evaporator and condenser) has also been undertaken. Following a comprehensive evaluation, R1234ze is recommended as a viable replacement to R134a, specifically regarding the pump and turbine performance.

1 INTRODUCTION

234

Increasing global energy demand has put significant strain on the energy sector to find alternative sources to the finite fossil fuels in order to reduce global warming and ozone depletion. Researchers have concentrated on two primary strategies to tackle these challenges: enhancing the utilization of renewable and sustainable energy sources and optimizing the efficiency of energy systems to maximize energy utilization from a source.

The five main renewable energy sources can be categorized into the following; hydropower, biomass, solar, wind and geothermal. Hydropower has the greatest benefit within energy storage systems due to large capacity and low cost, however in many cases it requires an initial resource investment to create the storage in the first place (Zhao et al., 2022). Biomass energy plays a significant role in eliminating fossil fuel use, specifically in countries with an abundance of bioresources (Vallios et al., 2009). Solar, wind and geothermal energy are all important renewable energy sources with high potential for energy generation. Li et al. (2015) compared the use of geothermal power plants against the solar and wind generation systems and identified significant advantages for the former. Specifically, geothermal power generation demonstrated greater stability in power output in higher capacity with a lower ecological effect. Bett and Thornton (2016) further supported this when analyzing the impact climate has on the wind and solar power across Britain. The results show that the seasonal variability in potential power generated for solar and wind is up to 70% and 30%, respectively, across the year.

An alternative to renewable and sustainable energy sources is that of waste heat recovery (WHR). Waste heat recovery allows the utilization of otherwise wasted heat energy from industrial processes, power generation, or other sources. By capturing and reusing this heat, energy efficiency is significantly improved. This reduces the overall energy consumption and the reliance on primary energy sources, leading to lower greenhouse gas emissions and a more sustainable use of resources (Zhang & Akiyama, 2009). Waste heat recovery possesses several advantages compared to the renewable energy sources described above. Since WHR is an integrated application to existing processes, it does not require land development or resource extraction. Additionally, WHR also exhibits a high potential utilization factor

compared to solar or wind energies (Jung et al., 2014). Various technologies can be employed to harness WHR, such as the organic Rankine cycle (ORC) (Galanis et al., 2009). The Organic Rankine Cycle (ORC) is one of the most versatile power cycle technologies implemented in a variety of low-medium temperature scenarios . While similar to the conventional Rankine cycle, the ORC utilizes refrigerants or organic substances as working fluids instead of water. This allows for the recovery of energy from low-temperature waste heat sources, facilitated by the lower boiling points of organic working fluids compared to water (Nguyen et al., 2010).

Arguably, the most important aspect of designing an ORC system is the working fluid selection. Over the years many researchers have investigated the working fluid selection against a range of operational conditions and system components (Bao & Zhao, 2013; Campos Rodríguez et al., 2013; Özcan & Ekici, 2021; Zeyghami, 2015). Specifically, one of the most used working fluids in a variety of low-medium grade ORC applications is R134a (Lai et al., 2011; Quoilin et al., 2013; Saleh et al., 2007; Shengjun et al., 2011). Environmentally speaking, although R134a has an Ozone Depletion Potential (ODP) of 0, it is a hydrofluorocarbon (HFC) with a global warming potential GWP of 1430 (Lemmon et al., 2018). This is of significant importance based on the harmful impact high GWPs has on the environment and the subsequent regulations implemented to phase out such working fluids (Schulz & Kourkoulas, 2014). Two working fluids often used to replace R134a are R1234ze and R1234yf, both of which having an ODP of 0 and GWP of 6 and 4, respectively (Lemmon et al., 2018). Yamada, Mohamad, and Kien (2012) highlighted that comparing R134a to a selection of working fluids in a basic ORC, both R1234ze and R1234yf displayed similar performance. Le et al. (2014) optimized a basic and regenerative supercritical ORC and identified R1234ze as the best working fluid for net power against R134a. Moles et al. (2017) directly compared R1234yf and R1234ze against R134a within a basic and regenerative cycle. The main findings presented indicate both fluids offer similar performance to R134a at lower evaporating temperatures. However, as the evaporating temperature increases R1234yf requires a higher pump power and produces a lower net cycle efficiency, whereas, R1234ze requires lower pump power and produces higher pump efficiency.

235

From the literature above it is clear there is a need not only to investigate ORC systems for waste heat recovery, but also to aide the expanse of research dedicated to identifying suitable replacements to R134a. Therefore, this paper aims to add to the existing working fluid evaluations of R134a replacements by comparing the performance against R1234ze and R1234yf. The working fluids are evaluated through modelling an ORC system heated by exhaust gas at 423.15 K. The comparison will include a heat exchanger sizing for the evaporator and condenser. An energetic and exergetic analysis of the ORC system will be considered to establish both the thermodynamic performance and assess the areas of energy waste between the working fluids.

2 METHODOLOGY

2.1 Organic Rankine Cycle

The ORC configuration and T-S diagram for the system setup is shown in Figure 1. The assumptions made for the cycle include no system heat losses and no pressure drop within the pipework. In order to complete the energetic and exergetic analysis, REFPROP was used to determine the required properties of the working fluids considered (Lemmon et al., 2018). The heating fluid was set as exhaust air and the cooling fluid was set as water. Table 1 demonstrates the assumed variables for the energetic and exergetic analysis.

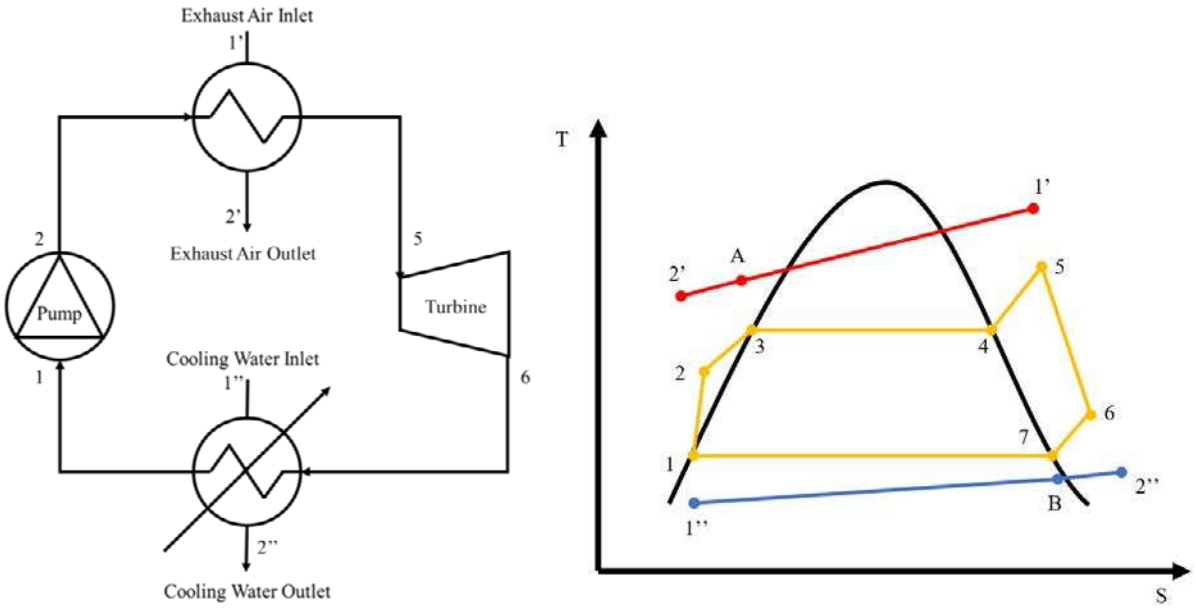

Figure 1: Organic Rankine Cycle configuration and T-S diagram

Table 1: Assumed parameters for the energetic and exergetic analysis

Variable	Value	Variable	Value
Ambient temperature	298.15 K	Condenser Pinch Point	10 K
Heating Fluid inlet Temperature	423.15 K	Pump inlet Temperature	293.15 K
Cooling Fluid inlet Temperature	278.15 K	η_{Pump}	80%
Approach Temperature	20 K	$\eta_{Turbine}$	70%
Evaporator Pinch Point	20 K		

The maximum temperature of the ORC was determined from the heating fluid inlet temperature minus the approach temperature. The maximum pressure of each working fluid was set as the saturated liquid pressure at 363.15 K. The energetic and exergetic analysis was completed using equations (1)-(10) (Cengel et al., 2011; Dincer & Rosen, 2012).

$$\eta_{Pump} = \frac{h_2 - h_1}{h_{2is} - h_1} \tag{1}$$

$$\eta_{Turbine} = \frac{h_5 - h_6}{h_5 - h_{6is}} \tag{2}$$

$$W_{Net} = W_{Turbine} - W_{Pump} = (h_5 - h_6) - (h_2 - h_1) \tag{3}$$

$$Q_{in} = h_5 - h_2 \tag{4}$$

$$\eta_{Cycle} = \frac{W_{Net}}{Q_{in}} \tag{5}$$

The exergy efficiency was evaluated using equation (6).

$$\eta_{ex} = \frac{W_{Net}}{Q_{in}\left(1 - \frac{T_0}{T_5}\right)} \tag{6}$$

And the exergy destruction for each component of the cycle was calculated using equations (7)-(10).

$$Ex_{D,E} = \dot{m}_{wf}\left((h_5 - T_0 s_5) - (h_2 - T_0 s_2)\right) + \dot{m}_{wf}(h_5 - h_2)\left(1 - \frac{T_0}{T_5}\right) \tag{7}$$

$$Ex_{D,T} = \dot{m}_{wf}\big((h_5 - T_0 s_5) - (h_6 - T_0 s_6)\big) + \dot{m}_{wf}(h_5 - h_6) \quad (8)$$

$$Ex_{D,C} = \dot{m}_{wf}\big((h_6 - T_0 s_6) - (h_1 - T_0 s_1)\big) \quad (9)$$

$$Ex_{D,P} = \dot{m}_{wf}\big((h_2 - T_0 s_2) - (h_1 - T_0 s_1)\big) + \dot{m}_{wf}(h_2 - h_1) \quad (10)$$

2.2 Heat Exchanger

There are three primary types of heat exchangers frequently used: fin and tube, plate, and shell and tube configurations. To maintain consistency in modeling the evaporator and condenser for all fluids, a shell and tube configuration is chosen. This configuration is preferred due to its versatility in accommodating various temperature ranges and fluid states between the hot and cold sides. The configuration for the shell and tube heat exchangers is that of TEMA type E, shown in Figure 2.

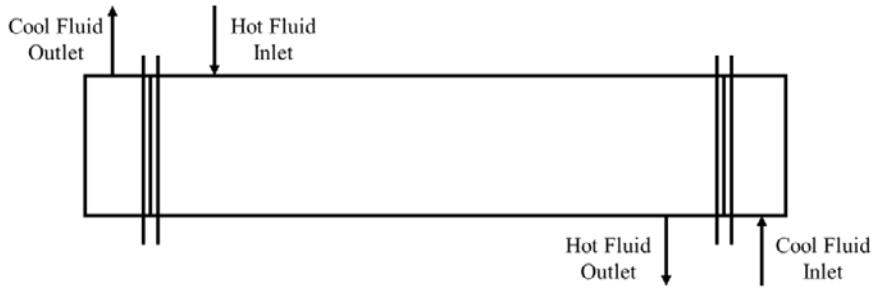

Figure 2: Shell and Tube Heat Exchanger Configuration TEMA Type E

The methodology used is off the work done by Bull et al. (2020) using the shell and tube heat exchanger design methodology from (Kakac et al., 2020; Kern, 1983). To account for the phase change of the working fluid, the evaporator calculations were split into three sections: pre-heater, phase change and super heater. The condenser calculations were split into two sections: phase change and super heater. To split the sections, the appropriate heating and cooling fluid temperatures were calculated from the corresponding working fluid phase change temperatures with the general energy balance equation shown in equation (11).

$$\dot{m}_{wf}(h_{out} - h_{in}) = \dot{m}_{hf/cf} C_{p,hf/cf}(T_{out} - T_{in}) \quad (11)$$

Where the $\dot{m}_{hf/cf}$ and $C_{p,hf/cf}$ is the mass flow rate and the specific heat capacity of the heating/cooling fluid respectively. The mass flow rate for each working fluid was fixed at the required mass flow rate for the ORC to output 10 kW of power. In order to size the heat exchanger, the shell and tubes diameters were set as 0.06 m and 0.01 m, respectively, and 1 shell pass with 2 tubes. In addition, the heat exchanger was modelling with negligible tube thickness and no fouling or baffles. For each section, average values for density, viscosity, specific heat capacity and thermal conductivity were calculated through REFPROP.

2.2.1 Pre-heat and Super heat

To calculate the heat transfer area required the log mean temperature difference was determined by equation (12).

$$\Delta T_{LMCF} = \frac{\Delta T_1 - \Delta T_2}{\ln\left(\frac{\Delta T_1}{\Delta T_2}\right)} \quad (12)$$

With correction factor (F) incorporated for the pre-heater and super-heater sections defined by equation (13) and subsequent corrected LMTD given by equation (14):

$$F = \frac{\sqrt{R^2+1}}{(R-1)} \frac{\ln\left(\frac{1-P}{1-PR}\right)}{\ln\left(\frac{\frac{2}{P}-1-R+\sqrt{R^2+1}}{\frac{2}{P}-1-R-\sqrt{R^2+1}}\right)} \quad (13)$$

$$\Delta T_{LM} = \Delta T_{LMCF} F \quad (14)$$

The overall heat transfer coefficient was determined by equation (15):

$$U = \frac{1}{\frac{1}{h_{wf}} + \frac{1}{h_{hf/cf}}} \quad (15)$$

Where the heat transfer coefficient for the working fluid side and the thermal fluid side are given by equation (16):

$$h = \frac{Nu\, k}{D} \quad (16)$$

The values for the Nusselt number were calculated using the Dittus-Boelter correlation shown in equation (17):

$$Nu = 0.023 Re^{0.8} Pr^{n} \quad (17)$$

The heating exponent, n, is 0.4 and 0.3 for the cold fluid and hot fluid respectively. The required heat transfer area is calculated using equation (18):

$$A = \frac{Q_{ht}}{U \Delta T_{LM}} \quad (18)$$

Where the heat transferred for each section is calculated using equation (19):

$$Q_{ht} = \dot{m}_{wf}(h_{out} - h_{in}) \quad (19)$$

2.2.2 Phase Change

The Shah correlation (Shah, 1979) for two-phase flow was additionally incorporated for the heat transfer coefficient in the phase change section for the evaporator and condenser using equation (20):

$$h_{lv} = h_l \left[(1-x)^{0.8} + \frac{3.8x^{0.76}(1-x)^{0.04}}{p_r^{0.38}}\right] \quad (20)$$

Where the mixture, x, was averaged to 0.5 and the reduced pressure was calculated with the critical fluid pressure using equation (21):

$$p_r = \frac{p_{crit}}{p_2} \quad (21)$$

2.2.2 Pressure Drop

The Pressure drop for the heat exchangers was calculated using equations (22) and (23):

$$\Delta p_t = \frac{2 f_t L \rho u_t^2}{D_t} \quad (22)$$

$$\Delta p_s = \frac{f_s G_s^2 D_s}{2 \rho D_e} \quad (23)$$

Where the respective friction factors are given by equations (24) and (25):

$$f_t = (1.58 \ln(Re_t) - 3.28)^{-2} \quad (24)$$

$$f_s = e^{(0.576-0.19\ln(Re_s))} \quad (25)$$

3 RESULTS

The following results include the respective adjustments to the evaporation and condensation pressure for each fluid based on the pressure drop calculated. The energetic performance characteristics is compared for each fluid and shown within Table 2. A percentage comparison of the energetic performance characteristics is shown in Table 3.

Table 2: Comparison of energetic analysis results

Fluid Name	Mass Flow (kg/s)	Net Power (kW)	Pump Power (kW)	Turbine Power (kW)	Rate of Heat In (kW)	Efficiency (%)	Back Work Ratio
R134a	0.271	8.622	0.654	9.276	71.10	12.127	0.071
R1234ze	0.285	8.503	0.548	9.051	73.49	11.571	0.061
R1234yf	0.320	8.530	0.794	9.324	76.05	11.217	0.085

Table 3: Percentage comparison of energetic analysis results against R134a

Fluid Name	Mass Flow (%)	Net Power (kW)	Pump Power (%)	Turbine Power (%)	Heat In (%)	Back Work Ratio (%)
R1234ze	5.087	-1.381	-16.229	-2.428	3.360	-14.144
R1234yf	18.155	-1.071	21.345	0.510	6.960	20.729

Based on the cycle parameters set within the methodology, R134a required the lowest mass flow rate and achieved the highest cycle efficiency of 0.271 kg/s and 12.127 %, respectively. Interestingly, R1234ze required the lowest pump power of 0.548 kW, and subsequently, generated the lowest turbine output power of 9.051 kW. However, R1234ze required 16.229 % less pump power compared to R134a in order to generate only 2.428 % less turbine power and achieve 1.381 % less net power. This result is further reflected by the back work ratio as R1234ze has the lowest with a value of 0.061, a 14.144 % drop from that of R134a. On the other hand, R1234yf displayed contrasting results, requiring the highest pump power, heat input, turbine power output, and subsequently displaying the highest back work ratio with the lowest cycle efficiency. Based on the energetic analysis conducted, despite favorable performance shown from R134a, R1234ze could be used as a suitable replacement in an ORC of this nature.

239

Table 4: A comparisons of exergetic analysis results

Fluid Name	Evaporator (kW)	Turbine (kW)	Condenser (kW)	Pump (kW)	Exergy Efficiency
R134a	29.408	21.599	61.545	1.155	46.583
R1234ze	30.290	20.989	64.616	0.967	44.430
R1234yf	31.340	21.616	67.370	1.405	43.069

Table 5: A percentage comparison of exergetic analysis results against R134a

Fluid Name	Evaporator (%)	Turbine (%)	Condenser (%)	Pump (%)
R1234ze	2.999	-2.823	4.989	-16.262
R1234yf	6.570	0.081	9.463	21.639

Table 4 demonstrates a comparison of the exergetic analysis results and Table 5 highlights the percentage comparison against R134a. Overall, R134a displayed the lowest exergy destruction for the evaporation and condenser components of the ORC. Additionally, R134a had the highest exergy efficiency of 46.583 % indicating increased reversibility of the system. Taking into consideration the exergy destruction reported at each component, R1234ze showed lower exergy destruction compared to R134a in both the turbine and pump by 2.823 % and 16.262 %, respectively. However, R1234yf not only demonstrated the lowest exergy efficiency of 43.069 %, it also had the highest exergy destruction across all components of the cycle presented. Similar to the energetic analysis, the exergetic analysis indicates that R1234ze proves to be a favorable replacement to R134a, especially when considering the fluid performance through the pump and turbine sections of the ORC.

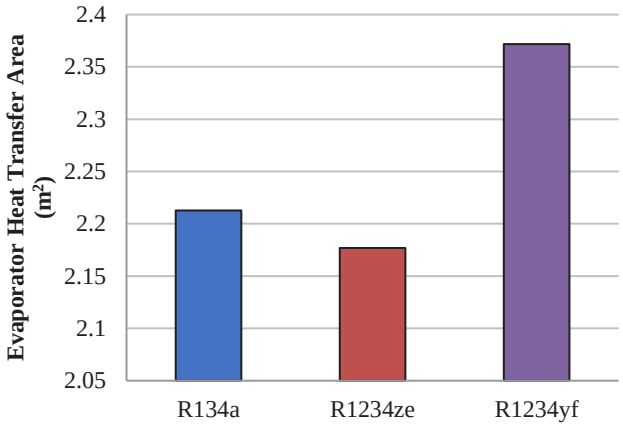

Figure 3: Evaporator heat transfer area required

Figure 3 demonstrates the heat transfer area required through the evaporator section of the ORC. The area required for R134a, R1234ze and R1234yf was calculated as 2.212 m^2, 2.177 m^2 and 2.371 m^2, respectively. Although R134a displayed the lowest mass flow rate and lowest heat in, shown in Table 2, R1234ze demonstrated the lowest area required for the heat exchanger. In contrast, R1234yf demonstrated the highest heat transfer area required. A similar correlation can be noted for the condenser heat exchanger sizing. Figure 4 presents a comparison of the heat transfer area required for the condenser section of the ORC. Overall, R1234yf has the highest area required of 31.768 m^2. Whereas R1234ze displays the lowest area of 29.347 m^2.

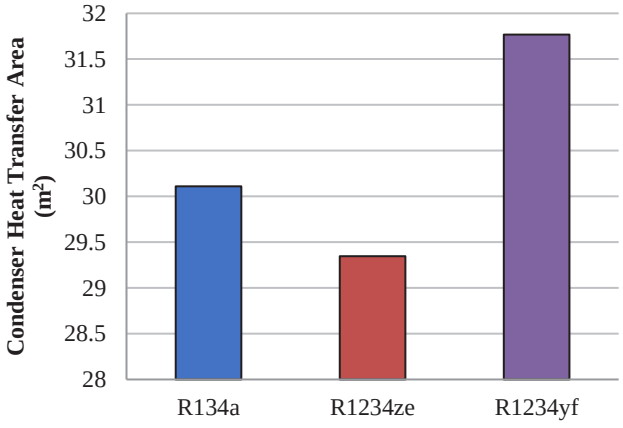

Figure 4: Condenser heat transfer area required

4 CONCLUSIONS

The results present in this study indicate the following conclusions:

- Based on the energetic analysis, although R134a displayed the best overall performance, R1234ze could be used as a suitable alternative.
- During the exergetic analysis, R1234ze proved to be a suitable replacement especially through the pump and turbine sections of the ORC.
- In both the condenser and evaporator heat exchanger sizing, R1234ze demonstrated the lowest area required.
- In all aspects evaluated within this paper, R1234yf would not be recommended as a suitable replacement to R134a.

NOMENCLATURE

T	Temperature
p	Pressure
η	Efficiency
W	Work done
h	Enthalpy
Q	Heat
Ex	Exergy
s	Entropy
$\dot{m}$	Mass Flow Rate
C_p	Specific Heat Capacity
U	Heat Transfe r Coefficient
D	Diameter
Nu	Nusselt Number
Re	Reynolds Number
Pr	Prandtl Number
A	Heat Transfer Area
ρ	Density
G	Mass Flux
f	Friction Factor
u	Velocity
L	Heat Exchanger Length
Subscript	
1,2,3,4,5,6,7	Position in ORC
is	isentropic
ex	Exergy
D	Destruction
P	Pump
E	Evaporator
T	Turbine
C	Condenser
0	Ambient Conditions
wf	Working Fluid
hf	Heating Fluid
cf	Cooling Fluid
in	Generalized Reference Inlet
out	Generalized Reference Outlet
LM	Log Mean
ht	Heat Transferred
lv	Liquid-Vapor Phase
crit	Critical Point
r	Ratio

s	Shell
t	Tube

REFERENCES

Bao, J., & Zhao, L. (2013). A review of working fluid and expander selections for organic Rankine cycle. *Renewable and Sustainable Energy Reviews*, *24*, 325–342.

Bett, P. E., & Thornton, H. E. (2016). The climatological relationships between wind and solar energy supply in Britain. *Renewable Energy*, *87*, 96–110. https://doi.org/10.1016/j.renene.2015.10.006

Bull, J., Buick, J. M., & Radulovic, J. (2020). Heat exchanger sizing for organic rankine cycle. *Energies*, *13*(14), 1–10. https://doi.org/10.3390/en13143615

Campos Rodríguez, C. E., Escobar Palacio, J. C., Venturini, O. J., Silva Lora, E. E., Cobas, V. M., Marques Dos Santos, D., Lofrano Dotto, F. R., & Gialluca, V. (2013). Exergetic and economic comparison of ORC and Kalina cycle for low temperature enhanced geothermal system in Brazil. *Applied Thermal Engineering*, *52*(1), 109–119. https://doi.org/10.1016/j.applthermaleng.2012.11.012

Cengel, Y. A., Boles, M. A., & Kano\uglu, M. (2011). *Thermodynamics: an engineering approach* (Vol. 5). McGraw-hill New York.

Dincer, I., & Rosen, M. A. (2012). *Exergy: energy, environment and sustainable development*. Newnes.

Galanis, N., Cayer, E., Roy, P., Denis, E. S., & Désilets, M. (2009). Electricity generation from low temperature sources. *Journal of Applied Fluid Mechanics*, *2*(2), 55–67. https://doi.org/10.36884/jafm.2.02.11870

Jung, H. C., Krumdieck, S., & Vranjes, T. (2014). Feasibility assessment of refinery waste heat-to-power conversion using an organic Rankine cycle. *Energy Conversion and Management*, *77*, 396–407. https://doi.org/https://doi.org/10.1016/j.enconman.2013.09.057

Kakac, S., Liu, H., & Pramuanjaroenkij, A. (2020). *Heat exchangers: selection, rating, and thermal design*. CRC press.

Kern, D. (1983). *Process Heat Transfer*. Tosho Printing Co., LTD.

Lai, N. A., Wendland, M., & Fischer, J. (2011). Working fluids for high-temperature organic Rankine cycles. *Energy*, *36*(1), 199–211. https://doi.org/10.1016/j.energy.2010.10.051

Le, V. L., Feidt, M., Kheiri, A., & Pelloux-Prayer, S. (2014). Performance optimization of low-temperature power generation by supercritical ORCs (organic Rankine cycles) using low GWP (global warming potential) working fluids. *Energy*, *67*, 513–526. https://doi.org/10.1016/j.energy.2013.12.027

Lemmon, E. W., Bell, and I. H., Huber, M. L., & McLinden, M. O. (2018). *NIST Standard Reference Database 23: Reference Fluid Thermodynamic and Transport Properties-REFPROP, Version 10.0, National Institute of Standards and Technology*. https://www.nist.gov/srd/refprop

Li, K., Bian, H., Liu, C., Zhang, D., & Yang, Y. (2015). Comparison of geothermal with solar and wind power generation systems. *Renewable and Sustainable Energy Reviews*, *42*, 1464–1474.

Moles, F., Navarro-Esbrí, J., Peris, B., Mota-Babiloni, A., & Mateu-Royo, C. (2017). R1234yf and R1234ze as alternatives to R134a in Organic Rankine Cycles for low temperature heat sources. *Energy Procedia*, *142*, 1192–1198.

Nguyen, T. Q., Slawnwhite, J. D., & Boulama, K. G. (2010). Power generation from residual industrial heat. *Energy Conversion and Management*, *51*(11), 2220–2229.

Özcan, Z., & Ekici, Ö. (2021). A novel working fluid selection and waste heat recovery by an exergoeconomic approach for a geothermally sourced ORC system. *Geothermics*, *95*(November 2020). https://doi.org/10.1016/j.geothermics.2021.102151

Quoilin, S., Van Den Broek, M., Declaye, S., Dewallef, P., & Lemort, V. (2013). Techno-economic survey of Organic Rankine Cycle (ORC) systems. *Renewable and Sustainable Energy Reviews*, *22*, 168–186. https://doi.org/https://doi.org/10.1016/j.rser.2013.01.028

Saleh, B., Koglbauer, G., Wendland, M., & Fischer, J. (2007). Working fluids for low-temperature organic Rankine cycles. *Energy*, *32*(7), 1210–1221. https://doi.org/10.1016/j.energy.2006.07.001

Schulz, M., & Kourkoulas, D. (2014). Regulation (EU) No 517/2014 of The European Parliament and of the council of 16 April 2014 on fluorinated greenhouse gases and repealing Regulation (EC)

No 842/2006. *Off. J. Eur. Union*, *2014*(517), L150.
Shah, M. M. (1979). A general correlation for heat transfer during film condensation inside pipes. *International Journal of Heat and Mass Transfer*, *22*(4), 547–556.
Shengjun, Z., Huaixin, W., & Tao, G. (2011). Performance comparison and parametric optimization of subcritical Organic Rankine Cycle (ORC) and transcritical power cycle system for low-temperature geothermal power generation. *Applied Energy*, *88*(8), 2740–2754.
Vallios, I., Tsoutsos, T., & Papadakis, G. (2009). Design of biomass district heating systems. *Biomass and Bioenergy*, *33*(4), 659–678. https://doi.org/10.1016/j.biombioe.2008.10.009
Yamada, N., Mohamad, N., & Kien, T. (2012). Study on thermal efficiency of low- to medium-temperature organic Rankine cycles using HFO−1234yf. *Renewable Energy*, *41*, 368–375.
Zeyghami, M. (2015). Performance analysis and binary working fluid selection of combined flash-binary geothermal cycle. *Energy*, *88*, 765–774. https://doi.org/10.1016/j.energy.2015.05.092
Zhang, L., & Akiyama, T. (2009). How to recuperate industrial waste heat beyond time and space. *International Journal of Exergy*, *6*(2), 214–227.
Zhao, J. F., Oh, U. J., Park, J. C., Park, E. S., Im, H. Bin, Lee, K. Y., & Choi, J. S. (2022). A Review of World-wide Advanced Pumped Storage Hydropower Technologies. *IFAC-PapersOnLine*, *55*(9), 170–174. https://doi.org/10.1016/j.ifacol.2022.07.030

ORC SEVILLE 2023
7th International Seminar on O.R.C. Power Systems

© 2024 Editorial Universidad de Sevilla. Este es un artículo de acceso abierto distribuido bajo los términos de la licencia de uso y distribución Creative Commons (BY-NC-ND 4.0)

DOI: https://dx.doi.org/10.12795/9788447227457_38

PERFORMANCE AND ECONOMIC ASSESSMENT OF A THERMALLY INTEGRATED REVERSIBLE HP/ORC CARNOT BATTERY APPLIED TO DATA CENTERS

Chiara Poletto[1,*], Andrea De Pascale[1], Saverio Ottaviano[1], Olivier Dumont[2], Maria Alessandra Ancona[1], Michele Bianchi[1]

[1] *University of Bologna, Viale del Risorgimento 2, 40136 Bologna, Italy*
[2] *University of Liège, Allée de la Découverte 17, 4000 Liège, Belgium*

*Corresponding Author: chiara.poletto3@unibo.it

ABSTRACT

Carnot batteries (CBs) are drawing increasing attention as grid-scale storage technologies, especially when the contribution of waste heat occurs, resulting in thermally integrated energy storages. In this context, since data centers (DCs) convert almost all the supplied electricity into recoverable waste heat, this work aims at investigating the convenience of integrating a reversible Organic Rankine Cycle (ORC)/Heat Pump (HP) Carnot battery with a DC fed by a photovoltaic power plant. For this purpose, a detailed semi-empirical off-design model of a CB is implemented in a rule-based control strategy to manage the ORC/HP operations in the integrated system. In case of renewable production surplus, the exceeding energy can be stored in the CB through the HP, which is thermally integrated with DC waste heat with the double advantage of operating with a higher coefficient of performance and of reducing the required cooling system power. The stored energy is reconverted through the ORC when the electric demand overcomes the renewable production. A sensitivity analysis varying the storage volume and the energy price has been performed to investigate the influence of such parameters on the integrated system performance. The thermal integration allows to reach roundtrip efficiencies around 37 %, although the very low operating temperatures. The CB intervention results to be economically convenient, especially when the average electricity price is high as it occurred during year 2022. The yearly additional gain, with a storage volume of 10 m^3, is assessed to be around 8270 €, and the simple payback period is less than 10 years.

1 INTRODUCTION

Today world's total electricity consumption is attributable for 2 % to data centers (DCs), due to the strong development of the Information Technology (IT) field (Huang *et al.*, 2019). Since almost the whole of DCs servers electricity demand is converted to thermal energy (Cho *et al.*, 2012), a significant amount of energy is required for cooling. For this reason, DCs are well suited for coupling with thermal energy recovery technologies, like organic Rankine cycle (ORC) power plants (Marshall and Duquette, 2022). Due to the very low temperatures at which the heat is typically released, almost all of the few works investigating this application, integrate the ORC with other technologies, especially heat pumps (HPs). Apart from Ebrahimi *et al.* (2017), who proposed the integration of an ORC system into a data center cooling system, Temiz and Dincer (2022) proposed an integrated system, which includes a parabolic trough-type concentrated solar plant with a Rankine cycle, a bifacial photovoltaic plant, a hydrogen storage system, and a Li-Br absorption refrigeration cycle. Marshall and Duquette (2022), instead, analyzed an ORC system assisted by a HP integrated in the cooling system. An alternative solution to address DCs waste heat (WH) is the residential thermal demand. Jang *et al.* (2022) proposed a waste heat recovery HP that recovers WH from a DC to satisfy the residential thermal demand. Hou *et al.* (2023) introduced a thermal energy storage (TES) for the optimal control of a DC WH consumer.

Based on the above literature review, it is interesting to investigate the integration of a Carnot battery (CB) in DC cooling systems. CBs belong to grid-scale storage technologies and represent a solution to limit the mismatch between the renewable energy source production and the electricity demand (Vecchi *et al.*, 2022). This solution has been proposed by Dumont (2017). The CB working principle is based on storing electric energy in the form of thermal energy through a heat pump, and to reconvert the stored thermal energy into electricity through a heat engine. Furthermore, CBs show higher performance when integrated in waste heat recovery systems (Frate *et al.*, 2020) (Dumont *et al.*, 2020).
In this context, this study aims at investigating the economic convenience of integrating a reversible (to reduce the investment cost) HP/ORC Carnot battery in the cooling system of a DC fed by a photovoltaic (PV) power plant. The DC waste heat is partially recovered through the HP when the PV production overcomes the DC demand, and stored at higher temperature in a sensible TES. When the PV production becomes lower than the DC electric demand, the stored thermal energy is used to power the ORC, reducing the electricity that must be purchased from the grid. Furthermore, in wintertime, the possibility of directing the high temperature thermal energy to a district heating (DH) network is included. Two different scenarios in terms of electricity and thermal energy prices are compared.

2 METHODOLOGY

In this section, the analyzed system is described and the control strategy is presented. Hypothesis, boundary conditions, and key performance indicators are defined.

2.1 The integrated system configuration

The integration of a reversible HP/ORC CB with a sensible TES in the cooling system of a DC, the main components and their function, and the energy flows are described below, according to the numbers in Figure 1:

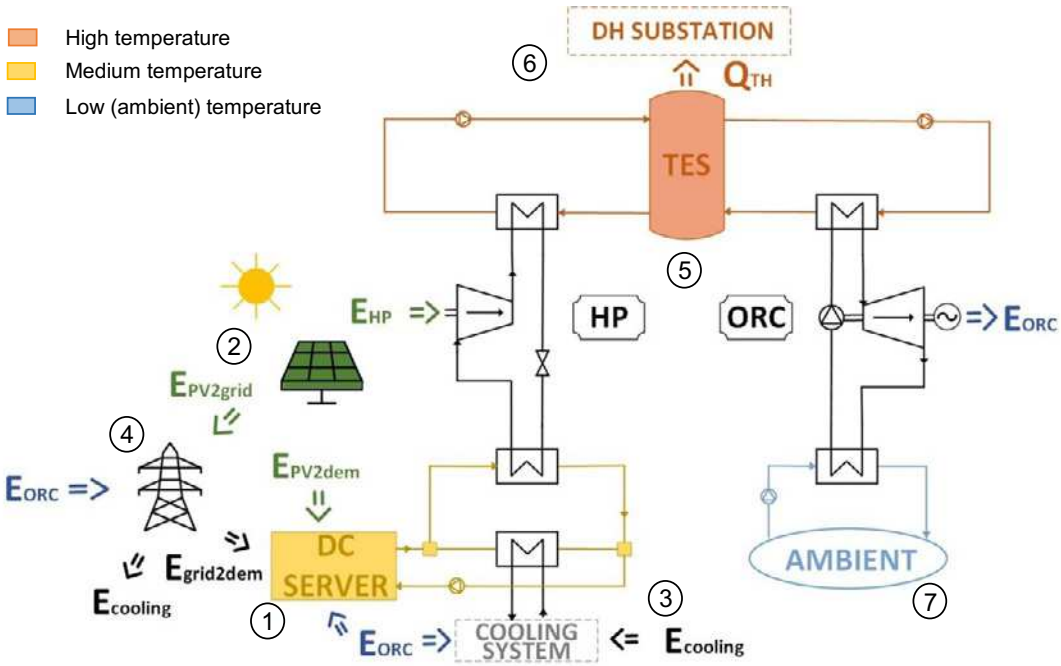

Figure 1: Integrated system configuration layout

1. An on-site DC server, which require a certain power demand, assumed constant over time.
2. An on-site solar photovoltaic power plant, which feeds the DC.
3. The DC cooling system.
4. The electric grid, which feeds the DC and the cooling system when the integrated system electricity production is not enough, and absorbs the electricity PV surplus production.

5. The reversible HP/ORC CB, which can be charged (HP mode) exploiting the PV surplus and the DC waste heat, or discharged to reconvert the heat into electricity (ORC mode) and to directly send thermal energy (thermal discharge) from the TES to a thermal user (i.e., DH).
6. A DH substation, which absorbs the thermal energy discharged by the CB.
7. The ambient, which is at the outside air temperature.

2.2 The Carnot battery model and management description

The Carnot battery scheduling management is driven by the maximization of the economic benefit provided by adding the CB to the integrated system. Indeed, the objective function (Eq. (1)) is the differential gain (ΔC) between the two configurations with and without the Carnot battery intervention.

$$\Delta C = E_{ORC} \cdot C_{el} + \Delta E_{cooling} \cdot C_{el} + Q_{TH} \cdot C_Q - E_{HP} \cdot C_{el} \quad (1)$$

The differential gain, evaluated at each time step, is equal to the sum of three positive terms minus a cost contribution. The first two positive terms are proportional to respectively the ORC energy production (E_{ORC}), and the electric energy saved from the cooling system ($\Delta E_{cooling}$) when using the HP to remove DC waste heat. These terms are multiplied by the cost of electricity (C_{el}). The third term is associated with the thermal energy sold to the thermal user (Q_{TH}), and it is proportional to the thermal energy price (C_Q). The negative contribution is related to the renewable surplus that feeds the HP (E_{HP}) in place of being sold to the grid.

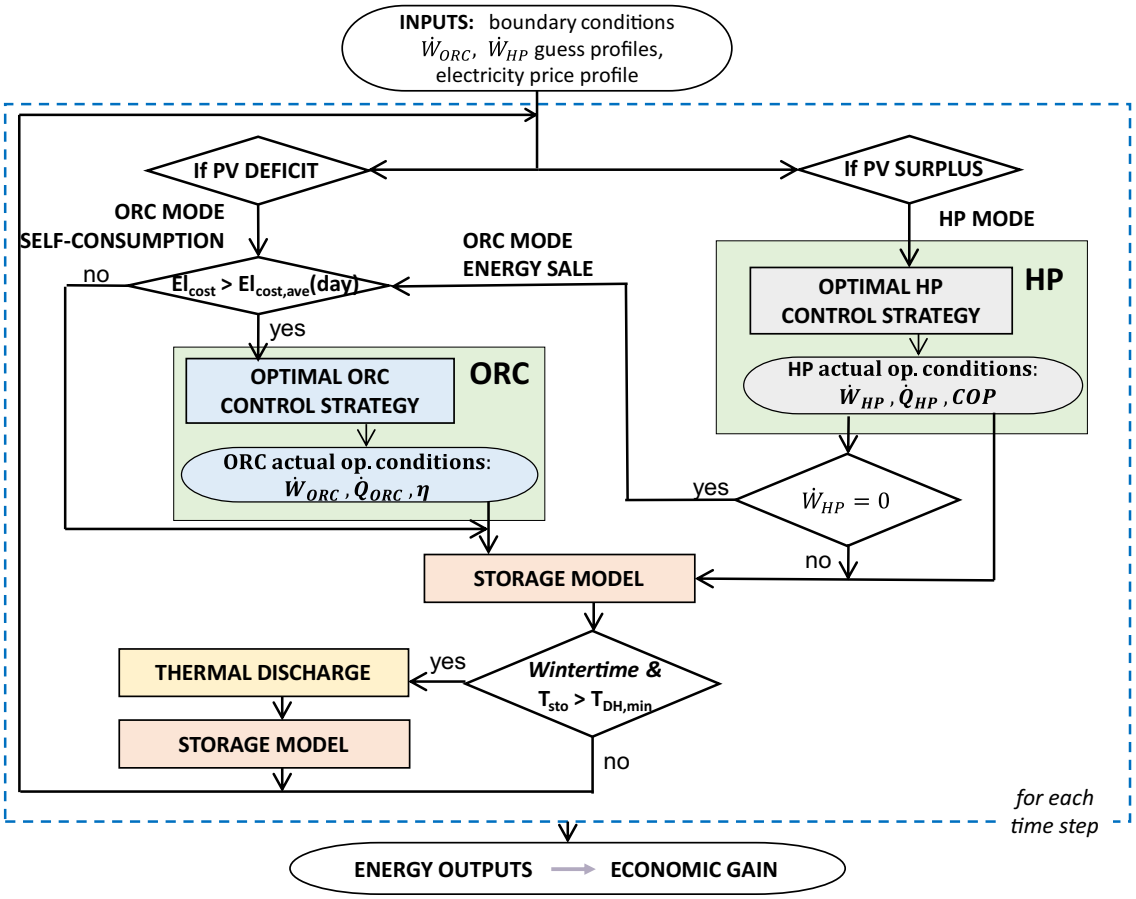

Figure 2: Carnot Battery management flowchart

The control algorithm, adopted to solve the problem, is developed according to a rule-based strategy (Figure 2). Starting from a first attempt solution, the algorithm decides to turn on/off the Carnot battery and to switch its mode (HP/ORC), according to the boundary conditions. The algorithm checks the renewable electric power availability, with reference to the DC electricity demand. In case of DC

electric demand not entirely covered by the renewable production (power deficit), the algorithm checks the actual electricity price: if it is higher than the average electricity price of that day, and the available thermal power in the CB storage is enough ($T_{storage}$ > 60 °C), then the ORC is run, discharging the TES. When the renewable production overcomes the electric demand (power surplus), the HP is run absorbing the electric surplus to charge the storage ($T_{max,storage}$ = 100 °C). If the HP is not called to work, the code checks the economic convenience of running the ORC to produce a power surplus to sell to the grid. The possibility of let the HP work in power deficit, absorbing electricity from the grid when the price is low, is not consider for the sake of a conservative approach. Then, the energy balance on the TES provides the storage updated conditions in terms of temperature and availability of thermal energy. Furthermore, it is assumed that, in winter season, the eventual extra thermal energy, available in the TES at temperature higher than $T_{DH,min}$ (80 °C), can be sold to a DH substation. Thus, a thermal discharge occurs and the storage conditions are updated.

Although the algorithm checks first the possibility of discharging the ORC and then of the thermal discharge, the priority is implicitly given to the thermal discharge. More in details, in case of renewable production surplus, the HP is run to charge the storage. Then, depending on the season, two different scenarios may take place. In wintertime, as soon as the storage has reached a temperature value of $T_{DH,min}$, the HP production is sent to the thermal user. Furthermore, until there is renewable production in surplus, the HP will continue working reducing the DC cooling load. In summertime, the HP continues running until the storage is not full. Then, the storage will be discharged through the ORC as soon as it is convenient in terms of electricity price. When the storage is discharged, the HP can start again charging the storage, reducing the DC cooling load. In case of power deficit, the storage can be discharged through the ORC to produce electricity to cover the DC demand in surplus. Actually, this last situation only happens during summertime, when the storage can be left fully charged by the HP operation. Indeed, in wintertime, the HP production, as soon as it is released in the TES, it is directly sent to the thermal user, and the storage is not kept fully charged to run the ORC.

As it will be shown in the results section, it is economically convenient to address the HP thermal production to the thermal user (when possible) rather than reconvert it into electricity, to avoid the penalization due to the low electric discharging efficiency. Furthermore, it is advisable to use the HP as much as possible to reduce the cooling load associated with the cooling system (as it represents an economic revenue), and to recover the thermal energy discharged by the DC servers.

The routine's outputs are the HP/ORC energy values included in Eq. (1), which evaluates the economic benefit of the CB intervention.

The reversible HP/ORC system (Dumont *et al.*, 2015) has been modelled following a semi-empirical approach, rescaled and validated taking as reference the prototype installed at the Thermodynamics Laboratory of the University of Liège. For the sake of brevity, it is left to the interested reader the reference prototype experimental work (Dumont *et al.*, 2021) and the study dealing with the modelling approach (Torricelli *et al.*, 2022). The sensible TES has been modelled as a one-dimensional stratified water thermal energy storage tank.

2.3 Hypothesis, boundary conditions and performance indexes

The hypothesis and boundary conditions adopted in this study are listed in Table 1. The data center electric demand is assumed as constant and equal to 200 kW, 97 % of which is converted into heat (Wahlroos *et al.*, 2018) that needs to be removed through a cooling system composed of a chiller and fans (allowed to work only when ambient air is at temperature below 15 °C) for direct free cooling. The PV production, at each time step (15 minutes), has been calculated adopting the irradiance hourly profile in Bologna (Italy) during year 2020, as the assumed ambient temperature hourly profile (*JRC Photovoltaic Geographical Information System (PVGIS) - European Commission*, 2021). The ambient temperature influences the ORC performance and the thermal losses to the environment occurring in the TES. The storage volume has been varied from 5 to 30 m^3 with a step of 5 m^3. In addition to the cost parameters listed in Table 2, the electricity price profile derives from the hourly spot market profile in Italy in 2018 and in 2022 (*GME*, 2023). Two scenarios with very different energy prices (Figure 3) have been analyzed. The thermal energy price is constant over the year and equal to 0.08 and 0.16 €/kWh respectively in years 2018 and 2022 (*Costi e tariffe del teleriscaldamento*, 2023).

Table 1: Hypothesis and boundary conditions

Data Center	
IT + lighting and other losses electric consumption (kW)	200
Electricity converted into WH (%)	97
WH Temp. (°C)	50
Cooling System	
COP chiller (-)	4
COP fans (-) (Nadjahi *et al.*, 2018)	20
Max Temp. to use fans (°C)	15
PV Solar Panels	
Area (m^2)	2000
Efficiency (%)	25
HP/ORC Nominal Power (kW)	25
TES Volume (m^3)	from 5 to 30

Table 2: Cost parameters

Cost parameters	
HP/ORC cost (€/kW)	2500
Storage cost (€)	(Shamoushaki *et al.*, 2021)
Lifetime (years)	20
Discounted rate (%)	6
Thermal energy price (€/kWh)	0.08 / 0.16

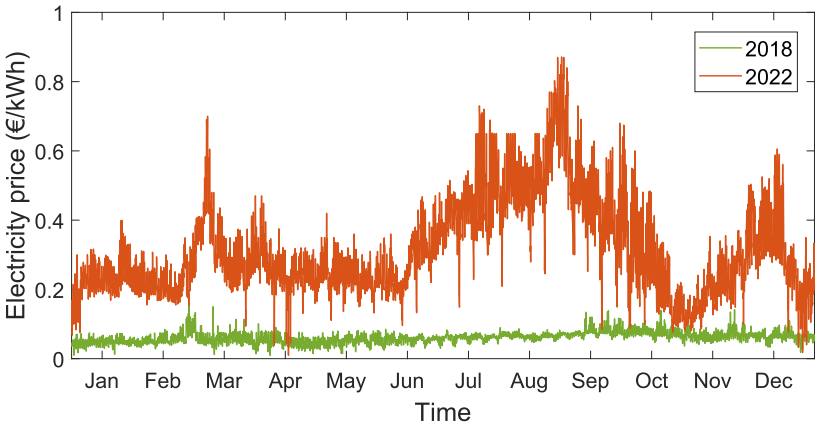

Figure 3: Yearly electricity cost profiles

The additional revenues, due to the CB integration into the system, are associated with the ORC electrical production, the thermal production, and the energy saved from the cooling system. The expenses are due to the renewable surplus consumed by the HP (operating cost) and the levelized cost of the CB (investment cost). The payback period (PB), in the forms of simple payback period (SPB) and discounted payback period (DPB), is evaluated according to Eq. (2) and (3).

$$SPB = \frac{I_{HP/ORC} + I_{storage}}{\sum \Delta C} \tag{2}$$

$$\sum_{t=1}^{DPB} \frac{\sum \Delta C}{(1+r)^t} = I_{HP/ORC} + I_{storage} \tag{3}$$

where $I_{HP/ORC}$ and $I_{storage}$ are the investment cost of the HP/ORC and storage, r is the discount rate and ΔC is the yearly economic differential gain.
The operation of the CB is evaluated through the yearly average COP/efficiency (η_{ORC}), defined respectively for the HP mode and for the ORC mode, according to Eq. (4) and (5). The overall performance is provided by the average roundtrip efficiency, η_{rt} (Eq. (6)).

$$COP = \frac{\sum Q_{HP}}{\sum E_{HP}} \tag{4}$$

(5)

$$\eta_{ORC} = \frac{\sum E_{ORC}}{\sum Q_{ORC}}$$

$$\eta_{rt} = COP \cdot \eta_{ORC} \tag{6}$$

where Q_{HP} and Q_{ORC} are the thermal energies associated with the HP and ORC operation.
The data center and cooling system performance improvement are assessed evaluating the Power Usage Effectiveness (PUE) and the Energy Reuse Effectiveness (ERE) described respectively in Eq. (7) and (8), according to Nadjahi *et al.*, (2018).

$$PUE = \frac{E_{cooling} + E_{light\&loss} + E_{IT}}{E_{IT}} \tag{7}$$

$$ERE = \frac{E_{cooling} + E_{light\&loss} + E_{IT} - E_{reuse}}{E_{IT}} \tag{8}$$

where $E_{cooling}$ is the electricity required to cool down the servers, $E_{light\&loss}$ is the electricity lost in the energy distribution system and in other infrastructures (UPS or PDU) and to light the data center, E_{IT} is the input energy of the IT equipment, and E_{reuse} is the recovered thermal energy.
Eventually, the cooling system reduction of load, due to a partial use of the HP to cool down the data center, is described by the utilization factor (UF), which is the ratio between the cooling energy of the chiller and the fans in the two scenarios with ($E_{cooling,chiller/fans}$) and without ($E_{cooling,chiller/fans,noCB}$) the CB intervention.

$$UF_{chiller/fans} = \frac{E_{cooling,chiller/fans}}{E_{cooling,chiller/fans,noCB}} \tag{9}$$

249

3 RESULTS AND DISCUSSION

This section presents and discusses the techno-economic performance of the analyzed system. In the first subsection, the economic gain obtainable with the CB intervention is shown varying the storage volume, and for two different profiles of the energy price (year 2018 and year 2022). In the second subsection, the improvement of the performance due to the integration of the CB is assessed.

3.1 Carnot battery techno-economic performance

In Figure 4 and Figure 6, the additional revenues and expenses, due to the CB integration into the system, are shown with the 2018 and 2022 energy prices. The increase of the storage volume, and thus of the energy storage capacity, allows the CB to operate longer, improving the decoupling of the DC demand and the PV production. Indeed, a significant increase of the ORC production occurs. The HP electric consumption slightly increases until a certain size of the storage volume (25 m^3), and then it remains constant because it has reached its maximum production, with reference to the renewable electricity in surplus. In other words, when the storage volume is smaller than 25 m^3, it happens that, in case of renewable surplus, the HP operation can be hindered by the storage, which is already full. When the storage volume is bigger (30 m^3), the HP operation is no more prevented by the storage size, but it depends only on the availability of renewable energy in surplus (besides the hot and cold temperatures). The significant improvement of the ORC production is obtained at the expense of the thermal production, which is reduced with the increase of the storage volume. The savings from the cooling system, when using the HP to remove DC waste heat, increase with the HP production (and with the storage volume). During year 2022 the improvement in the saving is much more visible because of the significant increase in the electricity price.
The SPB and DPB values are shown in Figure 5 and Figure 7 respectively for year 2018 and 2022. When the electricity price is low (year 2018), it results that it is not convenient to add a CB to the

system, as it would require too many years to recover the investment cost (Figure 5). On the contrary, when the electricity price increases (year 2022), the integrated system with the CB becomes an interesting solution for small sizes of the storage. The payback period significantly decreases, reaching interesting values especially for relatively compact sizes of the storage volume (Figure 7).
Table 3 provides a comparison of the performance of the CB in the two reference years and for a storage volume of 10 m^3, which is the value that maximizes the economic gain (4200 € for year 2018 and 8270 € for year 2022).

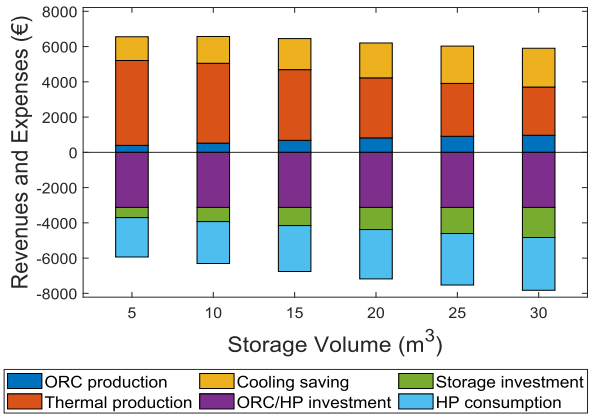

Figure 4: Economic gain due to the CB (year 2018)

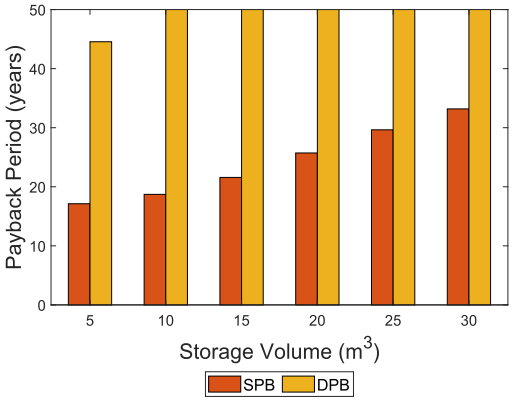

Figure 5: PB of the CB (year 2018)

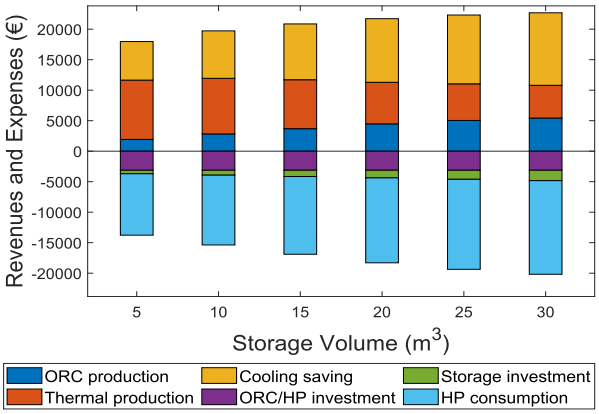

Figure 6: Economic gain due to the CB (year 2022)

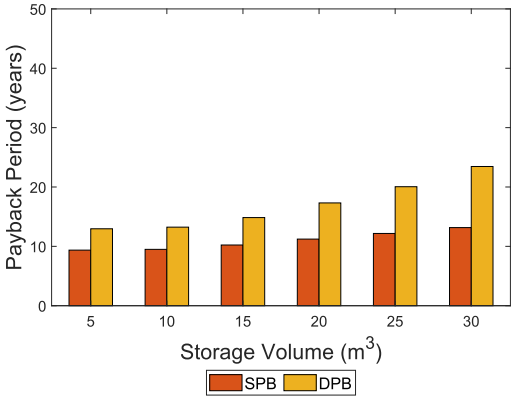

Figure 7: PB of the CB (year 2022)

Table 3: CB performance for a storage volume of 10 m^3

	Year 2018			Year 2022			PV
	HP	ORC	TH dis.	HP	ORC	TH dis.	
Annual average COP/efficiency (-)/(%)	4.88	7.64	-	4.90	7.62	-	25
Annual electrical energy (kWh)	37649	7863	-	35689	7385	-	918994
Annual thermal energy (kWh)	183658	102882	56641	175019	96960	56972	-
Annual running hours (h)	1540	1049	467	1462	998	469	4267
Annual average roundtrip efficiency (%)	37.28		-	37.34		-	-

3.2 Integrated system overall performance

The data center PUE and ERE improve with the Carnot battery intervention (Figure 8) because part of the cooling power is provided by the HP, and about 37 % of the HP electric consumption (which is not used as thermal energy) is recovered by the ORC ($\eta_{rt} \cong 37$ %, as shown in Table 3). Since the CB intervention (running hours) increases with the storage volume, the PUE and the ERE improve with the same trend. For the same reason, a storage capacity increase allows to reduce the required cooling system power (especially of the chiller that is more energy-consuming due to the lower COP) as shown through the UF in Figure 9. To conclude, the overall performance of the integrated system seems to improve with the CB intervention, regardless of the energy price.

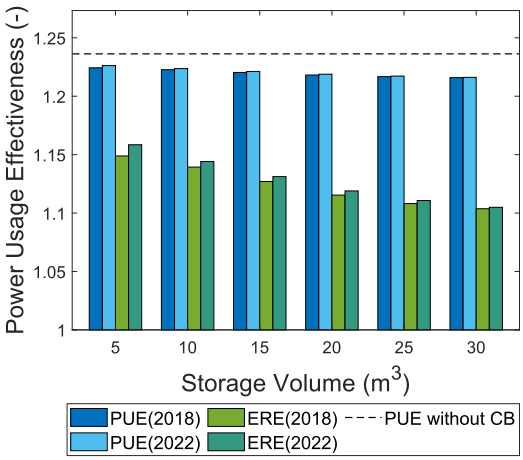

Figure 8: PUE and ERE

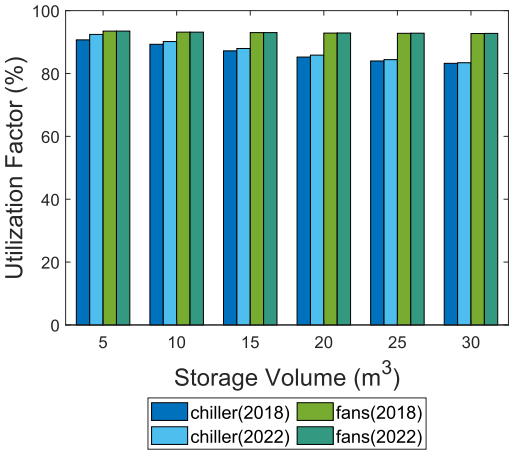

Figure 9: Utilization factor

4 CONCLUSIONS

251

This work enriches the current literature on the application of CB to DC waste heat recovery technologies, simulating the integration of a reversible HP/ORC Carnot battery in the cooling system of DC, which is fed by the electricity production of a PV power plant. When the PV panels produce a surplus of electricity, the exceeding energy can be stored in the CB through the HP, reducing also the cooling system load (and consumption). When the demand overcomes the renewable production, the stored thermal energy is used to power the ORC. Furthermore, during wintertime, the possibility of selling the stored thermal energy to the DH is included. With the aim to manage the ORC/HP operations in the integrated system, a rule-based control strategy is implemented. A sensitivity analysis varying the storage volume and the energy price has been performed to find out the best compromise for the storage size, and to investigate the influence of the storage capacity and the energy price on the integrated system. Results show that the Carnot battery integration is economically convenient (although the conservative hypothesis according to which the CB is not allowed to absorb electricity from the grid) especially when the energy price is high, as it occurred during year 2022. The yearly additional gain, with a storage volume of 10 m^3, is assessed to be about 8270 €, and the simple payback period is less than 10 years. Furthermore, the conservative hypothesis adopted for the CB operation, and the model validated over a prototype plant (not optimized) leave high room for improving the overall performance and the economic benefit. The thermal integration allows to reach roundtrip efficiencies around 37 %, although the very low operating temperatures. Since part of the cooling power is provided by the HP, and part of the HP electric consumption is recovered by the ORC, the data center PUE and ERE improve with the Carnot battery intervention.

Concerning the future developments, the possibility of buying electricity from the grid when the price is low, to run the HP, will be considered, and the system dynamic inertia will be included when changing the CB operating mode.

NOMENCLATURE

Δ	difference	(-)
η	efficiency	(%)
C	cost	(€)
CB	Carnot battery	
COP	coefficient of performance	(-)
DC	data center	
DPB	discounted payback period	(year)
E	electric energy	(kWh)
ERE	energy reuse effectiveness	(-)
I	investment cost	(€/kW)
PUE	power usage effectiveness	(-)
Q	thermal energy	(kWh)
r	discounted rate	(-)
SPB	simple payback period	(year)
UF	utilization factor	(%)

Subscripts

dem	demand
DH	district heating
el	electric
HP	heat pump
IT	information technology equipment
light&loss	other losses included lighting
noCB	without Carnot battery
ORC	organic Rankine cycle
PV	photovoltaic
Q	thermal energy
reuse	recovered energy
rt	roundtrip
sto/storage	thermal energy storage
TH	thermal user

REFERENCES

Cho, J., Lim, T. and Kim, B.S. (2012) 'Viability of datacenter cooling systems for energy efficiency in temperate or subtropical regions: Case study', *Energy and Buildings*, 55, pp. 189–197. Available at: https://doi.org/10.1016/j.enbuild.2012.08.012.

Costi e tariffe del teleriscaldamento in Emilia Romagna (2023). Available at: https://www.ilteleriscaldamento.eu/teleriscaldamento_emilia_romagna.htm (Accessed: 21 March 2023).

Dumont, O. (2017) *Investigation of a heat pump reversible into an organic Rankine cycle and its application in the building sector*. PhD Dissertation.

Dumont, O. *et al.* (2020) 'Carnot battery technology: A state-of-the-art review', *Journal of Energy Storage*, 32, p. 101756. Available at: https://doi.org/10.1016/j.est.2020.101756.

Dumont, O., Charalampidis, A. and Lemort, V. (2021) 'Experimental Investigation Of A Thermally Integrated Carnot Battery Using A Reversible Heat Pump/Organic Rankine Cycle', *International Refrigeration and Air Conditioning Conference* [Preprint]. Available at: https://docs.lib.purdue.edu/iracc/2085.

Dumont, O., Quoilin, S. and Lemort, V. (2015) 'Experimental investigation of a reversible heat pump/organic Rankine cycle unit designed to be coupled with a passive house to get a Net Zero

Energy Building', *International Journal of Refrigeration*, 54, pp. 190–203. Available at: https://doi.org/10.1016/j.ijrefrig.2015.03.008.
Ebrahimi, K., Jones, G.F. and Fleischer, A.S. (2017) 'The viability of ultra low temperature waste heat recovery using organic Rankine cycle in dual loop data center applications', *Applied Thermal Engineering*, 126, pp. 393–406. Available at: https://doi.org/10.1016/j.applthermaleng.2017.07.001.
Frate, G.F., Ferrari, L. and Desideri, U. (2020) 'Multi-criteria investigation of a pumped thermal electricity storage (PTES) system with thermal integration and sensible heat storage', *Energy Conversion and Management*, 208, p. 112530. Available at: https://doi.org/10.1016/j.enconman.2020.112530.
GME - Gestore dei Mercati Energetici SpA (2023). Available at: https://www.mercatoelettrico.org/It/Tools/Accessodati.aspx?ReturnUrl=%2fIt%2fdownload%2fDatiStorici.aspx (Accessed: 21 March 2023).
Hou, J. *et al.* (2023) 'Model predictive control for a university heat prosumer with data centre waste heat and thermal energy storage', *Energy*, 267, p. 126579. Available at: https://doi.org/10.1016/j.energy.2022.126579.
Huang, Q. *et al.* (2019) 'Development and composition of a data center heat recovery system and evaluation of annual operation performance', *Energy*, 189(C). Available at: https://ideas.repec.org/a/eee/energy/v189y2019ics036054421931895x.html (Accessed: 16 March 2022).
Jang, Y. *et al.* (2022) 'Performance characteristics of a waste-heat recovery water-source heat pump system designed for data centers and residential area in the heating dominated region', *Journal of Building Engineering*, 62, p. 105416. Available at: https://doi.org/10.1016/j.jobe.2022.105416.
JRC Photovoltaic Geographical Information System (PVGIS) - European Commission (2021). Available at: https://re.jrc.ec.europa.eu/pvg_tools/it/#MR (Accessed: 17 December 2021).
Marshall, Z.M. and Duquette, J. (2022) 'A techno-economic evaluation of low global warming potential heat pump assisted organic Rankine cycle systems for data center waste heat recovery', *Energy*, 242, p. 122528. Available at: https://doi.org/10.1016/j.energy.2021.122528.
Nadjahi, C., Louahlia, H. and Masson, S. (2018) 'A review of thermal management and innovative cooling strategies for data center', *Sustain. Comput. Informatics Syst.* [Preprint]. Available at: https://doi.org/10.1016/J.SUSCOM.2018.05.002.
Shamoushaki, M. *et al.* (2021) 'Development of Cost Correlations for the Economic Assessment of Power Plant Equipment', *Energies*, 14(9), p. 2665. Available at: https://doi.org/10.3390/en14092665.
Temiz, M. and Dincer, I. (2022) 'A newly developed solar-based cogeneration system with energy storage and heat recovery for sustainable data centers: Energy and exergy analyses', *Sustainable Energy Technologies and Assessments*, 52, p. 102145. Available at: https://doi.org/10.1016/j.seta.2022.102145.
Torricelli, N. *et al.* (2022) 'Optimal Management of Reversible Heat Pump/Organic Rankine Cycle Carnot Batteries', *Journal of Engineering for Gas Turbines and Power*, 145(4). Available at: https://doi.org/10.1115/1.4055708.
Vecchi, A. *et al.* (2022) 'Carnot Battery development: A review on system performance, applications and commercial state-of-the-art', *Journal of Energy Storage*, 55, p. 105782. Available at: https://doi.org/10.1016/j.est.2022.105782.
Wahlroos, M. *et al.* (2018) 'Future views on waste heat utilization – Case of data centers in Northern Europe', *Renewable and Sustainable Energy Reviews*, 82, pp. 1749–1764. Available at: https://doi.org/10.1016/j.rser.2017.10.058.

ORC SEVILLE 2023
7th International Seminar on O.R.C. Power Systems

© 2024 Editorial Universidad de Sevilla. Este es un artículo de acceso abierto distribuido bajo los términos de la licencia de uso y distribución Creative Commons (BY-NC-ND 4.0)

DOI: https://dx.doi.org/10.12795/9788447227457_39

EVALUATION OF THE PERFORMANCE OF MULTIPLE SUPERCRITICAL CO2 POWER CYCLES IN WASTE HEAT RECOVERY APPLICATIONS

Hicham A. Chibli*, Matthew Read, Abdulnaser Sayma

Thermo-Fluids Research Centre, School of Science and Technology, City, University of London, Northampton Square, London, EC1V 0HB, United Kingdom

*Corresponding Author: hicham.chibli@city.ac.uk

ABSTRACT

This paper aims to systematically evaluate the common supercritical carbon dioxide power cycles that are suitable for low to high grade waste heat recovery applications, with source temperatures ranging from 450 to 850 ℃. A number of cycles varying from the simple to the fully cascaded split cycles are investigated against a predefined waste heat source for multiple temperatures and flow rates with a target power net yield of the order of 1 MWe. The conditions at the inlet to the main compressor in the sCO_2 loop are also varied to quantify the role of the environmental heat sink in effective heat recovery. The sCO_2 cycle parameters including the mass flowrate and split ratio as well as the effectiveness of the individual heat exchangers are optimized for multiple pressure ratios. Additionally, a detailed exergy analysis is conducted to identify the sources of entropy generation in the various components and enable a detailed comparison of the various cycle configurations reviewed. Improving the quality of the heat source from 450 to 850 ℃ yielded ~30% increase in cycle performance, while degrading the heat sink quality from 15 to 35 ℃ reduced the net output power by ~30%. The cascaded and split cycles were determined to achieve the highest performance across all conditions considered.

1 INTRODUCTION

The ever-rising cost of fossil fuels and increasing demand for power generation, have incentivized the implementation of bottoming cycles to extract an improved overall system performance. The elevated density and heat capacity of sCO_2 compared to air allow for an increased efficiency at a reduced footprint, without the limitations of a condensing steam cycle. Consequently, interest in designing and building power cycles that use sCO_2 as a working fluid surged in the last few decades. Feher (1968) pioneered the research in this field, when he proposed a pseudo-supercritical cycle that alleviates the shortcomings of the readily popular Rankine and Brayton cycles. While the former features heat addition and removal at constant temperatures, leading to an improved cycle efficiency, it suffered from a limited temperature range and excessive wetness formation in the low pressure turbine stages. The Brayton cycle allows a wider range of working temperatures, and better use of heat recuperation technologies, at the cost of notably exaggerated compression work intrinsic to the gaseous nature of air. Feher recognized that the abundance, chemical stability and inert nature of CO_2, in addition to its low critical pressure and temperature and high density all contribute to its suitability for use in modern power cycles. Angelino (1968) independently researched the use of CO_2 in recuperated transcritical power cycles to achieve the low compression work of condensing steam cycles, while taking advantage of the elevated turbine inlet temperatures of closed Brayton cycles. Additionally, he identified the recovered heat from the low to high pressure side of the cycle as the largest source of internal irreversibility and devised a series of modifications involving flow splitting to reduce losses and improve performance.

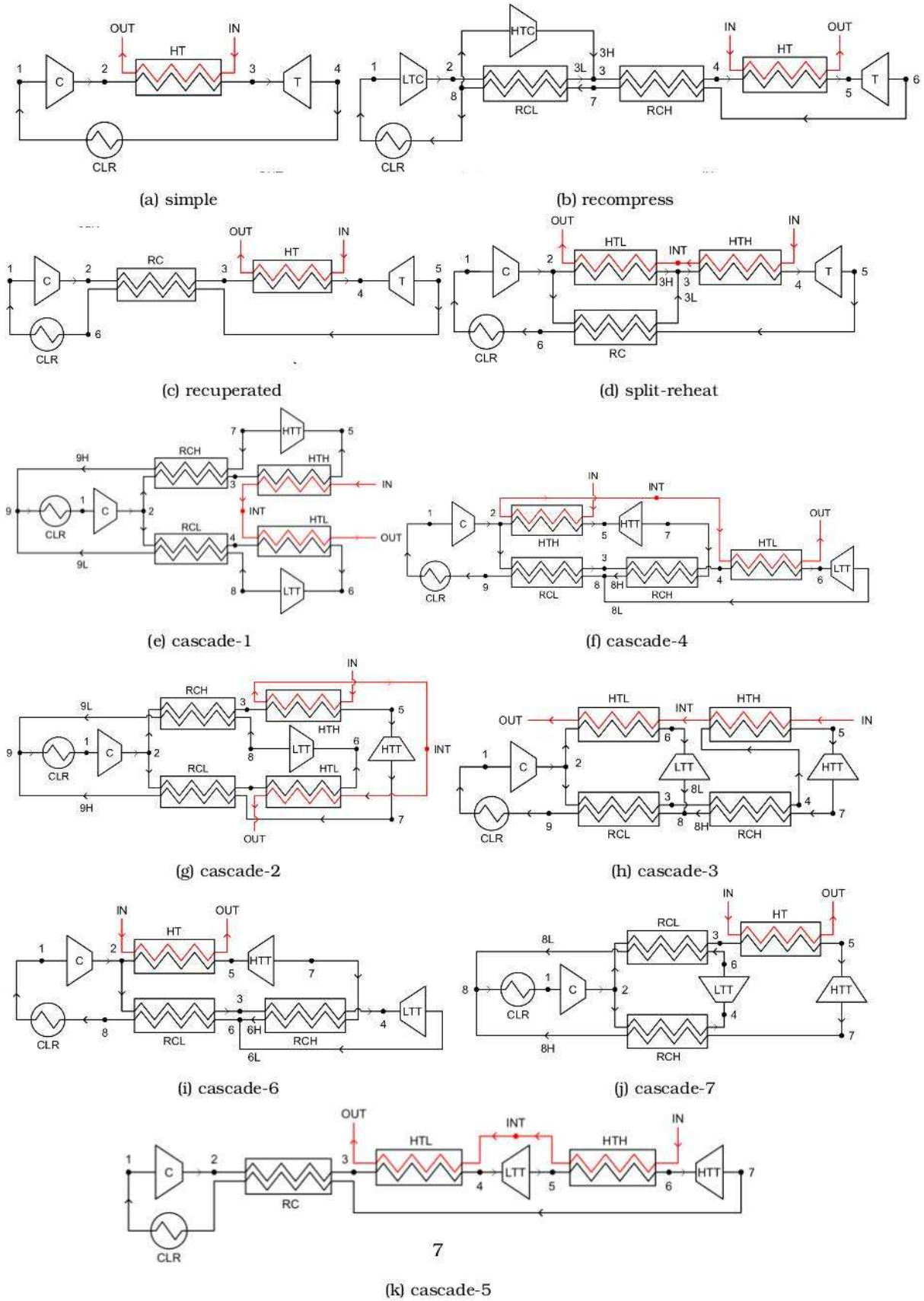

Figure 1: Schematics of the various waste heat recovery cycles considered in this study

Numerous studies have since been conducted, especially in the last decade to evaluate the implementation of sCO_2 cycles in applications ranging from nuclear and concentrated solar power to waste heat recovery. Ahn et al. (2015) reviewed the current status of research and development in Gen IV nuclear reactors, where the application of sCO_2 cycles offers several advantages over conventional water-cooled technology. Increasing the turbine inlet temperatures from the current 300 °C to 500 – 900 °C, while maintaining low compression work, at reduced size turbine stages owing to the low specific volume of sCO_2, leads to significant efficiency improvements. The authors also reviewed 12 sCO_2 cycle configurations for efficiency and heat transfer area requirements and concluded that the recompression cycle constitutes the best candidate for nuclear power applications. Additionally, they reviewed the experimental sCO_2 facilities in 5 key locations in USA, Japan and S. Korea, focusing mostly on the mechanical design aspects including bearing stability, thrust mitigation and vibrations. Crespi et al. (2017) reviewed all the published research in the field of sCO_2 power cycles up to date. The authors categorized the different investigative approaches including concepts, applications, and layouts, into a modular classification system using standard building blocks of standalone cycle components. The latter are intuitively utilized to construct more complex cycles and qualitatively evaluate and compare them. An effective quantitative comparison, however, was not provided. Since these cycles were evaluated under widely varying conditions and component parameters, as declared in their respective sources, the resulting heterogenous performance data was not suitable for systemic review.

Table 1: Summary of cases analyzed in this study with their respective conditions

Heat Source Conditions		**Cycle Base Temperature [°C]**	**P_{min} / P_{max} [bar]**	**Reference Figure**
Temperature [°C]	**Flowrate [kg/sec]**			
450	9.00	25	74/122-250	2a
650	5.75	25	74/122-250	2b
850	4.06	25	74/122-250	2c/3a
850	4.06	35	74/122-250	3b
850	4.06	45	74/122-250	3c

256

Moroz et al. (2015) investigated the application of sCO_2 in a bottoming cycle for a gas turbine, using the recuperated, recompression and precompression cycle configurations. The recuperated cycle was deemed the most suitable. Kim et al (2017) evaluated the performance of the recuperated, split-reheat and cascaded transcritical cycles in heat recovery from gas turbine. For the conditions considered in this study, the split-reheat cycle achieved the best overall performance at reduced cost and complexity. Khadse et al. (2018) completed a thermodynamic optimization of the recuperated and recompression configurations for exhaust heat recovery from a next generation heavy duty simple cycle gas turbine and favored the recompression arrangement for the chosen exhaust gas mass flow rate and temperature. Wang et al. (2021) completed a thermo-economic optimization study of multiple waste heat recovery sCO_2 cycles comprised of the recuperated, split-reheat and cascaded configurations and selected the split-reheat arrangement as the best candidate due to its balanced overall performance and reduced design and operational complexity.

2 SETUP AND ANALYSIS

The supercritical CO2 cycles considered in this study include the simple cycle (base case), the recuperated cycle, the split-reheat cycle, the recompression cycle (2 stage compression) in addition to multiple variations of the cascaded cycle (2 stage expansion). The schematics of these cycles are shown in Figure 1, with high and low temperature components and streams annotated accordingly. *MATLAB* models were prepared that allow simulating the performance of these cycles using the thermodynamic database *CoolProp* that employs the Span-Wagner Polar EOS formulation (Bell and Jäger, 2016 and Span and Wagner, 1996). The turbomachinery stages were modeled with a specified isentropic efficiency, $\eta_{is} = 75\%$ for the compressor and $\eta_{is} = 85\%$ for the turbine. The counter flow type heat exchangers were discretized to maintain a set pinch temperature $\Delta T_{min} = 10$ °C between the cold and warm streams. To simulate additional mechanical losses in the respective cycles, a 1% drop of total pressure was imposed at every heat exchanger. No heat losses to the environment were considered. The minimum pressure in the cycle was maintained right at the critical point to avoid a phase change during the heat rejection process, whereas the maximum pressure was varied to accommodate both the design and performance of turbomachinery stages, not to exceed 250 bar as a reasonable limit of material properties and manufacturability. The minimum and maximum temperatures of the working fluid are dictated by the availability of a suitable heat sink and source. The former is a function of the cooler pinch temperature and cooling fluid temperature, while the latter is the function of the waste heat source temperature and the heat exchange process. To understand the effect of the cooling requirements, which vary geographically, multiple cycle base (minimum) temperatures were considered, that correspond to heat sink temperatures of 15, 25 and 35 °C. Three qualities of waste heat source were evaluated in this study: high (850 °C), medium (650 °C) and low (450 °C) with air as working fluid. In order to maintain equivalent source conditions, the mass flow of hot air was adjusted to yield a constant source rate of exergy at a nominal net cycle output power of 1 MWe. A summary of the cases analyzed in this work is provided in Table 1.

2.1 Energy and Exergy Balance

The conditions within these cycles are optimized to achieve a maximum net power output. This is reflected through the system efficiency which is the product of the cycle efficiency and the heat recovery efficiency of the cycle, as detailed in Wang et al. (2021):

$$\eta_{sys} = \eta_{cycle} \times \eta_{heat} \tag{1}$$

Where the system and cycle efficiencies are expressed as follows:

$$\eta_{cycle} = \frac{\dot{W}_{net}}{\dot{Q}_{cycle}} \text{ and } \eta_{heat} = \frac{\dot{Q}_{cycle}}{\dot{Q}_{max}} \tag{2}$$

The maximum rate of heat available from the source is defined relevant to the ambient conditions as:

$$\dot{Q}_{max} = \dot{m}_{air} (h_{in} - h_0)_{air} \tag{3}$$

The power transfer and exergy loss rate are calculated across the turbine and compressor stages using:

$$\dot{W}_{turbo} = \dot{m}_{CO2} (h_{in} - h_{out}) \text{ and } \dot{L}_{turbo} = -T_0 \dot{m}_{CO2} (s_{in} - s_{out}) \tag{4}$$

Similarly, the heat transfer and exergy loss rates through the heater and recuperator can be determined as follows:

$$\dot{Q}_{heater} = \dot{m}_{air} (h_{in} - h_{out})_{air} = \dot{m}_{CO2} (h_{out} - h_{in})_{CO2} \tag{5}$$

$$\dot{L}_{heater} = -T_0 (\dot{m}_{air} (s_{in} - s_{out})_{air} + \dot{m}_{CO2} (s_{in} - s_{out})_{CO2}) \tag{6}$$

$$\dot{Q}_{recuperator} = \dot{m}_{CO2}\,(h_{in} - h_{out})_{warm} = \dot{m}_{CO2}\,(h_{out} - h_{in})_{cold} \quad (7)$$

$$\dot{L}_{recuperator} = -T_0(\,\dot{m}_{CO2}\,(s_{in} - s_{out})_{warm} + \dot{m}_{CO2}\,(s_{in} - s_{out})_{cold}) \quad (8)$$

Since the energy transferred to the cooling fluid is assumed lost to the environment, all the exergy removed out of the sCO_2 stream is treated as destroyed in the cooler for this analysis:

$$\dot{L}_{cooler} = \dot{m}_{CO2}\,((h_{in} - h_{out}) - T_0\;(s_{in} - s_{out}))_{CO2} \quad (9)$$

Some of the cycles involve splitting the working fluid flow to achieve better matching of the heat capacities of the warm and cold streams in the heat exchangers. This leads to additional losses when the split streams of dissimilar temperatures are merged back together at the constant pressure. This is captured as shown below:

$$\dot{L}_{mixing} = -T_0\,(\dot{m}_{in,1}s_{in,1} + \dot{m}_{in,2}s_{in,2} - \dot{m}_{out}s_{out})_{CO2} \quad (10)$$

2.2 Cycle Optimization Procedure

The *MATLAB* Global Optimization package using the parallelized *MultiStart* scheme is employed to maximize the net power output of the waste heat recovery power cycles. The heat source temperature and mass flowrate are fixed for each run, as well as the cycle base temperature and pressure and pressure ratio, while the mass flowrate of sCO_2 and the flow split ratio when applicable, are adjusted to identify the optimum performance parameters. The heat transfer effectiveness in the heaters and recuperators are also varied with the stipulation that the specified respective pinch temperature never exceeds the minimum temperature difference between the cold and warm streams along the length of the heat exchanger. The size of the pool of start points of problem variables was increased successively for each run to establish the convergence of the solver to a valid global optimum that satisfies the specified constraints.

258

2.3 Comparative Cycle Analysis

The various waste heat recovery cycles are simulated over a range of pressure ratios for different heat source temperatures and shown in Figure 2. As detailed earlier, the waste heat source availability is fixed for all cases by adjusting the hot air mass flowrate. All the cycles benefit from the higher heat source *quality* as evident in the significant performance improvements. However, the more complex cycles that allow flow splitting are more capable of taking advantage of the higher available source temperatures, with the simple cycle achieving the most modest gains. Cascade-3 configuration which allows the high temperature turbine stream double recuperation before being energized from the heat source achieves the best performance over the range of source temperatures. The performance advantages of this cycle in comparison to the other cascaded cycles seem to diminish at low pressure ratios, with the trend being more evident for a lower heat source temperature. It is notable that the solver systemically converges to eliminate the low temperature heater in cascade-4 cycle by assigning a zero effectiveness to the same, rendering the latter identical to cascade-6 cycle. The same results are noted for cascade-2 and cascade-7 cycles. It is to be noted that despite no effective heat transfer in the low temperature heater for both cycles, the pressure drop in the same is still calculated, leading to a measurable drop in the availability of the sCO_2 stream, and a slight downshift of the performance curves.

The split-reheat cycle performs significantly better than the more complex cascaded cycles for a low heat source temperature, with the exception of the cascade-3 configuration. At higher heat source temperatures, the performance of cascade-4/cascade-6 matches the split-reheat cycle, however the latter continues to deliver a higher net power output than the other cascaded setups. These results are quite inconsistent with those from the classical topping cycle performance analysis, that studies the performance relative to the turbine inlet temperature variations, without correcting the results to allow quantifying the heat recovery from the waste heat source. A similar observation is made for the recuperated cycle that matches the performance of the non-split cascade-5 cycle. The solver converges to eliminate the high temperature heater, and the cascaded turbine stages effectively perform as a single

expansion stage. It should be clarified that the pressure drop in the high temperature heater, as well as the specification of isentropic efficiency in the distinct turbine stages, result is a slight variation in performance compared to the recuperated cycle. Once more, these observations are unintuitive when contrasted with the isolated cycle performance analysis of sCO_2 power cycles.

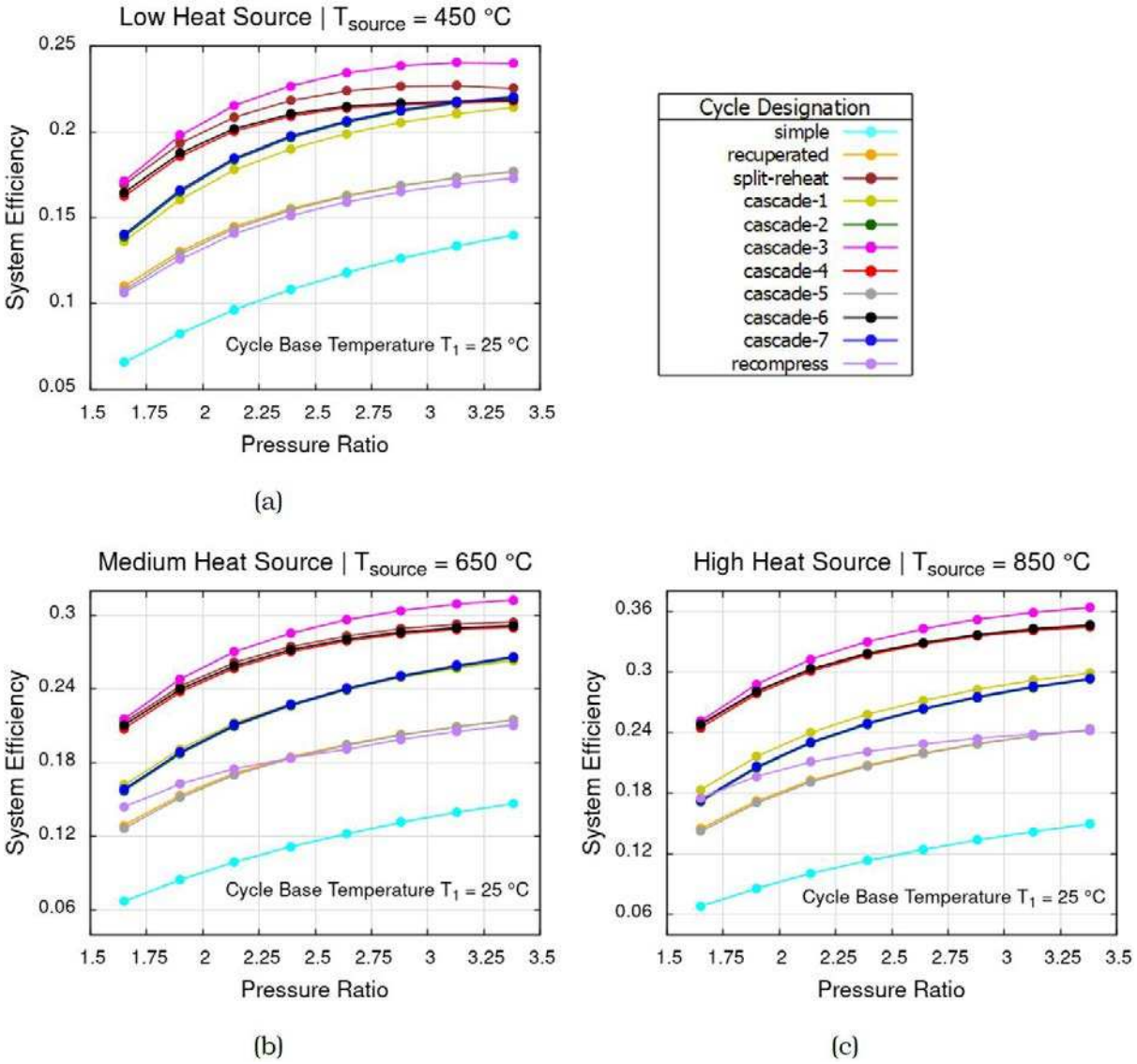

Figure 2: System performance as a function of pressure ratio for the various waste heat recovery cycles evaluated at heat source temperatures of a) 450, b) 650 and c) 850 °C with a cycle base temperature of 25 °C and pressure of 74 bar

To further qualify these findings, the exergy destruction rate in the various cycle components is computed and presented in Table 2 for each cycle at different heat source temperatures. The loss sources are categorized according to the nature of energy transfer to fall into turbomachinery (work transfer), heat exchangers (heat transfer) and stream mixing junctions (isobaric mixing, no energy transfer) groups. Since the energy/exergy transferred through the cooler is removed from the sCO_2 stream, it is grouped separately. The net work output rate of the cycle and the residual exergy rate in the heat source discharge stream (heater outlet) are also presented, all normalized by the available reversible work rate in the heat source (heater inlet).

Table 2: Exergy transfer rate breakdown as percentage of the reversible available work of the heat source stream evaluated at cycle base temperature of 25 °C and pressure of 74 bar and pressure ratio of 3.38 for heat source temperatures of 450, 650 and 850 °C

Cycle Component	Exergy Destruction Rate [%]				Work Out Rate [%]	Exergy Out Rate [%]
	Turbomachinery	Heat Exchangers	Mixing	Heat Sink		
Heat Source temperature = 450 ˚C						
simple cycle	4.6	7.5	0.0	32.1	24.9	30.9
recuperated cycle	7.1	13.7	0.0	5.7	31.4	42.0
split-reheat cycle	9.8	11.3	0.0	8.2	40.1	30.6
cascade-1 cycle	9.0	12.8	0.0	7.4	38.1	32.7
cascade-2 cycle	8.3	11.0	0.0	6.7	39.1	34.9
cascade-3 cycle	9.4	9.1	0.0	8.2	42.7	30.6
cascade-4 cycle	8.9	12.4	0.0	9.4	38.7	30.6
cascade-5 cycle	6.8	14.3	0.0	5.7	31.5	41.7
cascade-6 cycle	8.9	11.9	0.0	9.4	38.9	30.9
cascade-7 cycle	8.3	10.5	0.0	6.7	39.3	35.2
recompress cycle	7.1	14.0	0.1	5.7	30.8	42.3
Heat Source temperature = 650 ˚C						
simple cycle	3.4	9.5	0.0	42.4	24.9	19.7
recuperated cycle	6.9	19.6	0.0	5.5	36.3	31.7
split-reheat cycle	9.1	14.1	0.0	7.3	49.9	19.5
cascade-1 cycle	7.7	16.9	0.0	6.2	44.6	24.6
cascade-2 cycle	6.9	14.5	0.0	5.5	45.0	28.1
cascade-3 cycle	8.8	11.5	0.0	7.2	53.0	19.5
cascade-4 cycle	9.0	14.8	0.0	7.5	49.2	19.5
cascade-5 cycle	6.6	20.1	0.0	5.5	36.4	31.4
cascade-6 cycle	9.0	14.4	0.0	7.4	49.4	19.7
cascade-7 cycle	6.9	14.2	0.0	5.5	45.1	28.3
recompress cycle	6.9	19.9	0.1	5.5	35.7	32.0
Heat Source temperature = 850 ˚C						
simple cycle	3.3	17.7	0.0	41.0	24.0	13.9
recuperated cycle	6.4	22.9	0.0	5.1	39.0	26.6
split-reheat cycle	8.3	16.0	0.0	6.6	55.3	13.8
cascade-1 cycle	7.2	20.3	0.0	5.7	48.0	18.9
cascade-2 cycle	6.5	18.6	0.0	5.1	47.0	22.8
cascade-3 cycle	8.0	13.4	0.0	6.4	58.5	13.8
cascade-4 cycle	8.2	16.0	0.0	6.6	55.4	13.8
cascade-5 cycle	6.2	23.3	0.0	5.1	39.0	26.4
cascade-6 cycle	8.2	15.6	0.0	6.6	55.6	14.0
cascade-7 cycle	6.5	18.4	0.0	5.1	47.1	23.0
recompress cycle	9.5	14.4	0.0	4.3	38.9	32.9

260

As predicted the simple cycle yields the highest losses in the cooler section, as the energy from the warm turbine exhaust stream is not recovered; the recuperated cycle in contrast, exhibits the lowest losses in the cooling process due to utilizing the residual energy in the turbine exhaust stream to improve the cycle efficiency. Nonetheless the sharp variations in the heat capacity of the recuperator cold and warm streams, mainly due to the thermodynamic properties of sCO_2 in the vicinity of the critical point, lead to the most elevated heat exchanger losses in the recuperated cycle. By splitting the flow in some of the more complex cycles, a better match of the heat capacity is achieved by the virtue of different mass flowrates of the cold and warm streams in the recuperators. As such, heat transfer occurs between fluids of less dissimilar temperatures, leading to a reduction of exergy destruction in the process. Cascade-3 cycle registers the lowest share of irreversibility creation in the heat exchanger group, consistent with the highest performance discussed earlier. All the cycles show an increase in the heat exchanger losses as the heat source temperature rises, since the temperature gradient between the cold stream, governed by fixed compressor discharge conditions and the hot air stream becomes more prevalent.

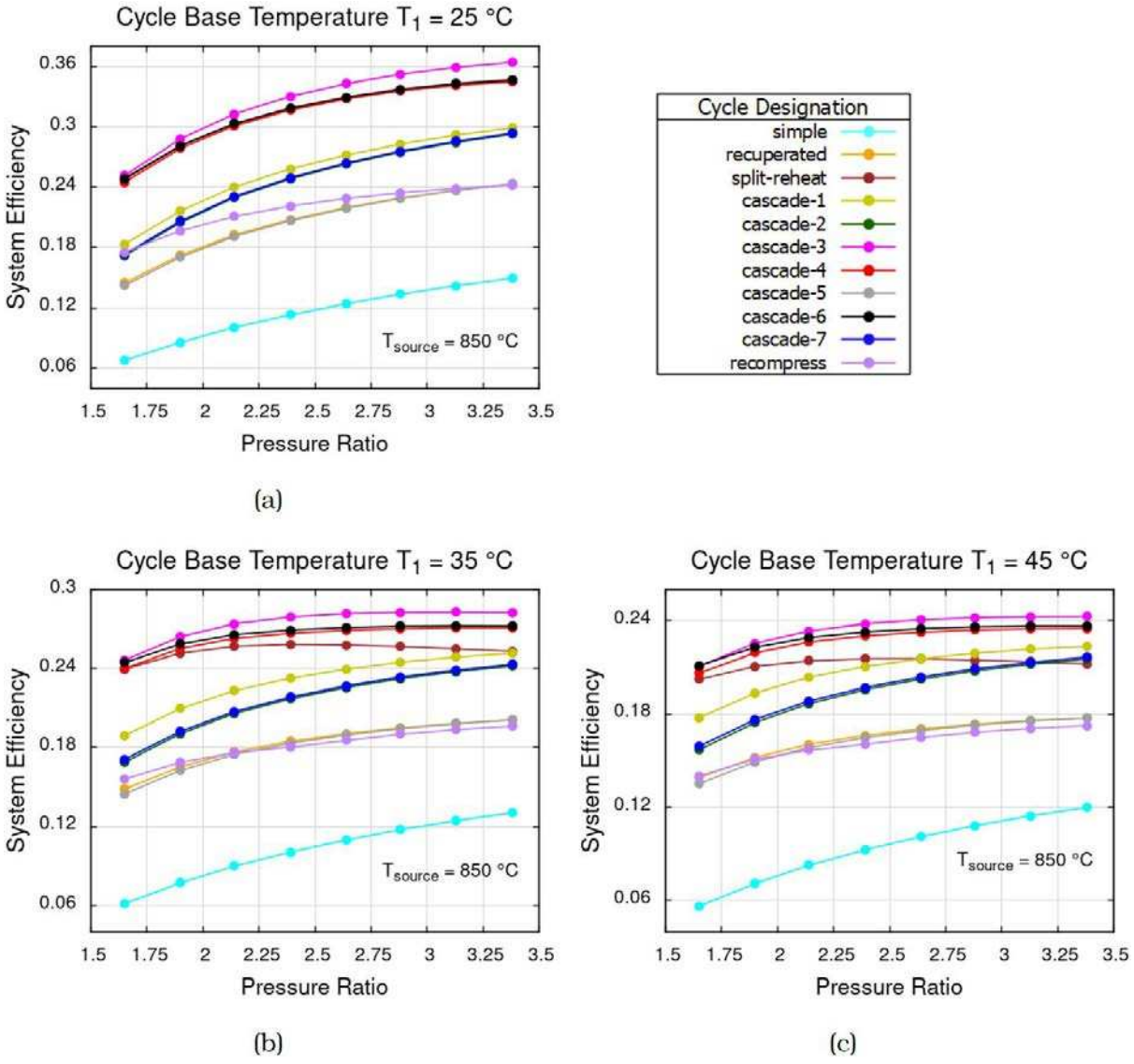

Figure 3: System performance as a function of pressure ratio for the various waste heat recovery cycles evaluated at cycle base temperatures of a) 25, b) 35 and c) 45 °C and base pressure of 74 bar with a heat source temperature of 850 °C

The results displayed in Figure 3 showcase the role of the available heat sink on the effectiveness of waste heat recovery in sCO_2 cycles. The cooling fluid temperature dictates the cycle base temperature through heat transfer across a temperature gradient, modelled in this study as a fixed pinch temperature $\Delta T_{min} = 10$ °C. A significant drop in cycle performance is noted as the base temperature increases from 25 to 45 °C, notably for the cascaded cycles with ~30% reduction in net power output. As the compressor inlet temperature increases, the fluid heat recovery capacity is reduced, together with the ability of flow splitting to reduce the exergy losses in the recuperator sections by achieving better stream matching. This is particularly evident with the split-reheat cycle that no longer outperforms the more complex cascaded cycles that can take advantage of double expansion stages to extract energy from low and high quality streams. The lack of recuperation of the simple cycle configuration causes a less detrimental effect on the performance as the base temperature is elevated.

3 CONCLUSIONS

A number of sCO_2 power cycles were investigated for waste heat recovery applications. These include the simple, recuperated, split-reheat, recompression in addition to several variations of cascaded cycles with distinct flow splitting arrangements. The roles of the heat source and sink availability in the effective cycle energy recovery were reviewed. Increasing the heat source temperature from 450 to 850 °C led to ~30% improvement in performance, while increasing the cycle base temperature from 25 to 45 °C reduced the net output power by ~30%. Detailed analysis of the energy and exergy transfer was conducted to identify the individual cycle characteristics. The cascade-3 cycle was determined to achieve the highest performance across all conditions, while the less complex split-reheat configuration mostly outperformed the rest. The recompression and non-split cascaded cycles offered no performance advantage over the basic recuperated arrangement. However, merely optimizing the cycle for thermodynamic performance is not adequate to determine the suitability of a specific cycle configuration for a given set of requirements. Extending the effort to include an economical component of such optimization is quintessential especially in the current energy market. The authors plan to address this topic in future studies.

262

NOMENCLATURE

h	specific enthalpy	(kJ/kg)
$\dot{L}$	rate of exergy loss	(kW)
$\dot{m}$	mass flowrate	(kg/sec)
P	pressure	(bar)
$\dot{Q}$	heat transfer rate	(kW)
s	specific entropy	(kJ/kg/K)
sCO_2	supercritical CO_2	
T	temperature	(°C)
$\dot{W}$	power	(kW)

Greek

η	efficiency

Schematics Abbreviations

C	compressor
CLR	cooler
HT	heater
HTC	high temperature compressor
HTH	heater high
HTL	heater low
HTT	high temperature turbine
IN	waste heat source inlet

7th International Seminar on ORC Power Systems, September 4 – 6, 2023, Seville, Spain

INT	waste heat source internal
LTC	low temperature compressor
LTT	low temperature turbine
OUT	waste heat source outlet
RC	recuperator
RCH	recuperator high
RCL	recuperator low
T	turbine
*x*H	high temperature stream
*x*L	low temperature stream

Subscript

0	ambient conditions
cycle	closed cycle attribute
heat	heat recovery attribute
is	isentropic
source	waste heat source
sys	system

REFERENCES

Li, B., Wang, S., Wang, K., Song, L., 2021, Comparative investigation on the supercritical carbon dioxide power cycle for waste heat recovery of gas turbine, *J. Energy Conversion and Management*, vol. 228, p. 1-12.

Khadse, A., Blanchette, L., Kapat, J., Vasu, S., Hossain, J., and Donazzolo, A., 2018, Optimization of Supercritical CO2 Brayton Cycle for Simple Cycle Gas Turbines Exhaust Heat Recovery Using Genetic Algorithm, *ASME. J. Energy Resour. Technol.*, vol. 140, p. 1-8.

Crespi, F., Gavagnin, G., Sánchez, D., 2017, Supercritical Carbon Dioxide Cycles for Power Generation: A Review, *J. Applied Energy*, vol. 195, p. 152-183.

Kim, Y.M., Sohn, J.L., Yoon, E.S., 2017, Supercritical CO_2 Rankine cycles for waste heat recovery from gas turbine, *J. Energy*, vol. 118, p. 893-905.

Bell, I., Jäger, A., 2016, Helmholtz Energy Transformations of Common Cubic Equations of State for Use with Pure Fluids and Mixtures, *J. Res. NIST*, vol. 121, p. 238-263.

Ahn, Y., Jun Bae, S., Kim, M., Cho, S.K., 2015, Review of Supercritical CO_2 Power Cycle Technology and Current Status of Research and Development, *J. Nuclear Engineering and Technology*, vol. 47, p. 647-661.

Moroz L., Pagur P., Rudenko O., Burlaka M., Joly C., 2015, Evaluation for scalability of a combined cycle using gas and bottoming sCO_2 turbines, *Proceedings of the ASME 2015 Power Conference collocated with the ASME 2015 9th International Conference on Energy Sustainability, the ASME 2015 13th International Conference on Fuel Cell Science, Engineering and Technology, and the ASME 2015 Nuclear Forum*, ASME 2015 Power Conference, San Diego, USA: p. 1-10.

Span, R., Wanger, W., 1996, A New Equation of State for Carbon Dioxide Covering the Fluid Region from the Triple Point Temperature to 1100 K at Pressures up to 800 MPa., *J. Phys. Chem. Ref. Data*, vol. 25, p. 1509-1596.

Angelino, A., 1968, Carbon Dioxide Condensation Cycles for Power Production, *J. Engineering for Power*, vol. 90, p. 287-295.

Feher, E.G., 1968, The Supercritical Thermodynamic Power Cycle, *J. Energy Conversion*, vol. 8, p. 85-90.

ACKNOWLEDGEMENT

This work is part of the Industrial Waste Heat Recovery Using Supercritical Carbon Dioxide Cycles (SCOTWOHR) research project funded by UKRI EPSRC (EP/V001752/1).

ORC SEVILLE 2023
7th International Seminar on O.R.C. Power Systems

© 2024 Editorial Universidad de Sevilla. Este es un artículo de acceso abierto distribuido bajo los términos de la licencia de uso y distribución Creative Commons (BY-NC-ND 4.0)

DOI: https://dx.doi.org/10.12795/9788447227457_40

Design and Modeling of a Demonstration-scale ORC Cycle for the Liquid Air Combined Cycle

Owen M. Pryor[1]*, William M. Conlon[2], Aaron M. Rimpel[1], Milton J. Venetos[2]

[1] *Southwest Research Institute, 6220 Culebra Rd, San Antonio TX 78238*
[2] *Pintail Power LLC, complete address*

*Corresponding Author: owen.pryor@swri.org

ABSTRACT

Energy storage is becoming an increasing focus for the future energy markets. One potential hybrid system for ling duration energy storage is the Liquid Air Combined Cycle (LACC). The LACC utilizes excess renewable energy to liquefy and store air during the charge cycle. During its discharge cycle, the system uses the exhaust heat from a conventional combustion turbine and an ORC bottoming cycle to vaporize and superheat the stored air that has been pressurized, which is subsequently expanded to atmosphere through a turbine. During the development of the cycle, it has been identified that the main technologies to advance the cycle are the ORC bottoming cycle machinery and the coupled operation between the liquified air subsystem and the ORC subsystem. This paper presents modeling and simulation of the LACC that involves ORC conditions that fall outside the operating regime of more common applications. Due to the low temperatures of liquified air, the ORC system operates on the order of -70°C for the pump, and the turbine has a pressure ratio around 40. The conceptual design of a demonstration system has been developed that focuses on these challenges in order to advance the overall system.

1 INTRODUCTION

In order to combat climate change and greenhouse gas emissions, the world needs to develop new technologies around decarbonization. Through the Paris Climate Agreement, over 140 countries have pledged to limit the increase in global temperatures to less than 2°C (Paris Climate Agreement, 2015). The United States has further pledged to decarbonize the energy industry by 2035 (Psaki, 2021). The best way to accomplish these goals is to electrify systems, vehicles homes utilizing clean energy which has been estimated to increase global energy demand by 116% by 2040 (Merfield, 2022).

One solution to combat climate change is to increase the share of renewable energy that is used by the grid while at the same time increasing the reliability of the grid and accounting for the increased energy demand that a decarbonized world would require. There are two main challenges that need to be overcome with the reliance on renewable energy. The first is the time-dependent volatility of the energy source. Wind and solar power outputs vary by the minute, hour and season due to diurnal effects, weather patterns and season with the changes in delivered energy on similar orders of magnitude as the designed output. The second challenge is the mismatch between the peak of available energy and energy demand. The two solutions to these challenges are either to oversize the renewable energy generation and curtail the energy when not needed or to store the energy.

Energy storage is the concept of storing energy at times when the supply is high and discharge the energy during periods of high demand. Energy storage comes in a variety of technologies depending on the energy stored, time of discharge and the challenge that it is addressing (Allison et al., 2020). The proposed solution that this paper is discussing is the Liquid Air Combined Cycle (LACC).

Liquid Air Combined Cycle (LACC) is a Long-duration Energy Storage (LDES) system intended for managing variability of renewable resources at large-scale, of the order of a Gigawatt of power and tens to hundreds of Gigawatt-hours of energy to permit discharge durations in the range of days to weeks (Conlon et al., 2022). The LACC system is comprised of three major sub-systems for charging, storage and discharging. The charging sub-system employs customary cryogenic refrigeration equipment, driven by electricity, to liquefy air for storage at atmospheric pressure and approximately -195°C. The storage sub-system uses insulated storage tanks, similar to those used to store Liquefied Natural Gas (LNG) at approximately -178°C. The discharge sub-system is a hybrid turbomachinery cascade with a fuel-burning gas turbine high-temperature topping cycle, an intermediate temperature pressurized air cycle that expands regasified air, and a low-temperature Organic Rankine Cycle (ORC), which condenses against pressurized liquid air.

Except for the ORC and the air turbine expander, all LACC components are at high Technology Readiness Level (TRL). Low temperature ORC systems have largely focused on low-grade heat sources around a 100-150°C with extremely small temperature deltas between the source and sink (Jankowski and Borsukiewicz, 2019). Most of these systems are still designed with sink temperatures at or close to ambient (Kosmadakis and Neofytou, 2020; Xu et al., 2022). Some studies have been performed on ORC systems using liquefied natural gas (LNG) as the sink. LNG has a temperature of around -162°C which is similar to the -194°C for liquefying air. Sun et al (2020) determined that several ORC fluids could be utilized with a cold heat sink but were forced to limit the ORC condensing temperature to -80°C (ethane) for the different fluids explored. Our research has similar sink temperatures but has a much higher source temperature and therefore a higher pressure ratio compared to cycles previously studied in the literature.

Two demonstration systems have been identified to address the unique challenges of the system. The first system addresses the unique control challenges of the LACC system between the multiple fluids at a reduced scale of around 13.5 MW. The second focuses on the development of the ORC machinery components using liquid nitrogen to condense the process fluid and electric heaters to provide the heat to the system.

265

2 LIQUID AIR COMBINED CYCLE

The LACC is a hybrid LDES technology intended for managing the variability of renewable resources on a range of scales by providing large-scale (10+ GWh) and long-duration (days to weeks) storage. Figure 1 illustrates the conceptual design of the commercial-scale LACC, which uses two ambient air streams at different times for cryogenic liquefaction during charging and as combustion air during discharging. The system would consume electric power to drive refrigeration during charging and consumes fuel and liquefied air during discharging. Discharge power would be produced by a turbomachinery cascade that resembles CAES: a conventional combustion turbine whose exhaust heat is captured for heating pressurized air to power an air turbine. Pressurized liquid air is re-gasified using heat rejected from an Organic Rankine Cycle (ORC), which extracts additional energy from the combustion turbine exhaust gas. A cooling loop maintains gas turbine performance on hot days. Table 1 describes the major equipment and their corresponding functions.

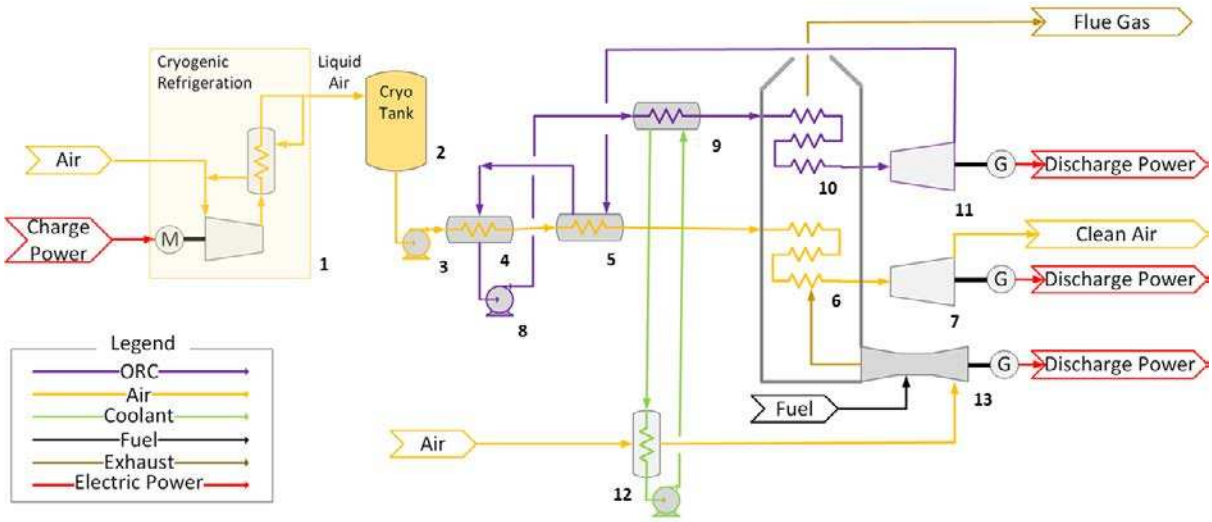

Figure 1: Liquid Air Combined Cycle™ System

Table 1: Unit Operations of the LACC System

ID#	Major Equipment	Description
1	Cryogenic refrigerator	During charging, a cryogenic refrigeration system uses low-cost or excess renewable energy to cool air to the liquid state.
2	Liq. air storage tank	Liquid air is stored at atmospheric pressure in an insulated tank permitting long-term storage of weeks or months.
3	Liq. air cryopump	A conventional cryopump, such as used for LNG send-out, pressurizes liquid air from the storage tank.
4	Air vaporizer	The pressurized liquid air absorbs heat rejected during condensation of the ORC working fluid and is transformed to pressurized vapor.
5	Air preheater	The pressurized regasified air is further heated by cooling the ORC working fluid prior to its condensation.
6	Exhaust gas heater	The pressurized air is then heated to high temperature using exhaust gas from a gas turbine.
7	Air turbine	Pressurized hot air flows through a turbine generator, similar to a steam turbine, to produce power. The clean, dry air is exhausted to atmosphere.
8	ORC pump	Liquid refrigerant is pumped to pressure.
9	ORC preheater	Further heating is obtained by heat transfer from the coolant loop that provides gas turbine inlet air chilling.
10	Exhaust gas heater	The refrigerant is evaporated and superheated by gas turbine exhaust.
11	ORC turbine	The pressurized hot refrigerant produces power in a turbine and exhausts as low-pressure refrigerant.
12	Inlet air cooler	Ambient air is cooled, increasing the air density to allow the gas turbine to operate at its maximum power point and maximize the exhaust heat available for extracting stored energy.
13	Gas turbine	A gas turbine can provide the exhaust heat used to drive the discharge cycle. By controlling the inlet air temperature via the cooling loop, this turbine can always operate at optimum conditions to maximize the cycle efficiency and power output.

266

Most of the major components described represent components that are currently commercially available. To advance the LACC technology, the authors believe that two different demonstration systems need to be developed. The first system would involve demonstrating the full system at a demonstration-scale to add confidence in the technology. The second is to advance the ORC components that have not been previously demonstrated at these conditions.

3 LACC DEMONSTRATION SYSTEM

The demonstration system has been designed to highlight the unique challenges of the technology and increase the confidence in the system. Table 2 shows the major cycle state points for the system. Figure 2 shows the modifications to the system required. The system has been reduced in size for approximately 13.7 MW of total power output. Most of the major equipment was downsized with minimum changes to the system. The major changes of note are:

- A reduction of the turbine inlet temperature (TIT) for the air turbine (7).
- An decrease of the flue gas exhaust temperature.
- An increase in the temperature that the vaporized air leaves the first heat exchanger (4).
- Liquid nitrogen would be used instead of liquid air

Only addition was the use of a heat transfer fluid for the ORC. This decision was made after discussions with vendors concerned about the possible interactions of ethane with the exhaust. The addition of the intermediate heat transfer fluid reduces the volume and mass of ORC refrigerant, allows the ORC system to be more compact, and eliminates leakage of flammable ethane refrigerant into the flue gas, reducing the area subject to Class I Div. 2 hazard classification. Previous versions of the commercial scale applications utilized a recuperator to maximize the heat recovery of the ORC bottoming cycle but was removed due to the small size compared to other heat exchangers. The elimination of pressure drop through the recuperator allowed the ORC condensing pressure to be reduced, which offset the performance loss while also reducing CAPEX of the discharge train.

267

Table 2: Cycle Conditions of the LACC System Demonstration.
Parenthesis denote the process equipment associated with the state point

Location	Temperature [°C]	Pressure [MPa]	Enthalpy [kJ/kg]	Density [kg/m^3]	Fluid
Liquid air storage (2)	-198	0.10	-127	816	Nitrogen
Liq. pump exit (3)	-196	7.09	-117	824	Nitrogen
Air inlet to exhaust gas heater (5)	112	6.81	393	**58**	Nitrogen
Air turbine inlet (6)	525	6.71	848	28	Nitrogen
Air turbine outlet (7)	20	0.10	304	1.1	Nitrogen
ORC pump inlet (8)	-81	0.16	19	534	Ethane
ORC pump outlet (8)	-72	16.8	58	540	Ethane
ORC transfer to HX fluid inlet (10)	15	16.6	285	429	Ethane
ORC turbine inlet (11)	340	16.5	1355	100	Ethane
ORC turbine outlet (11)	140	0.32	895	2.8	Ethane
Gas turbine inlet (14)	25	0.10	309	1.1	Nitrogen
Gas turbine outlet (14)	562	0.10	886	0.4	Nitrogen
Flue gas exit	100	0.10	387	0.9	Nitrogen

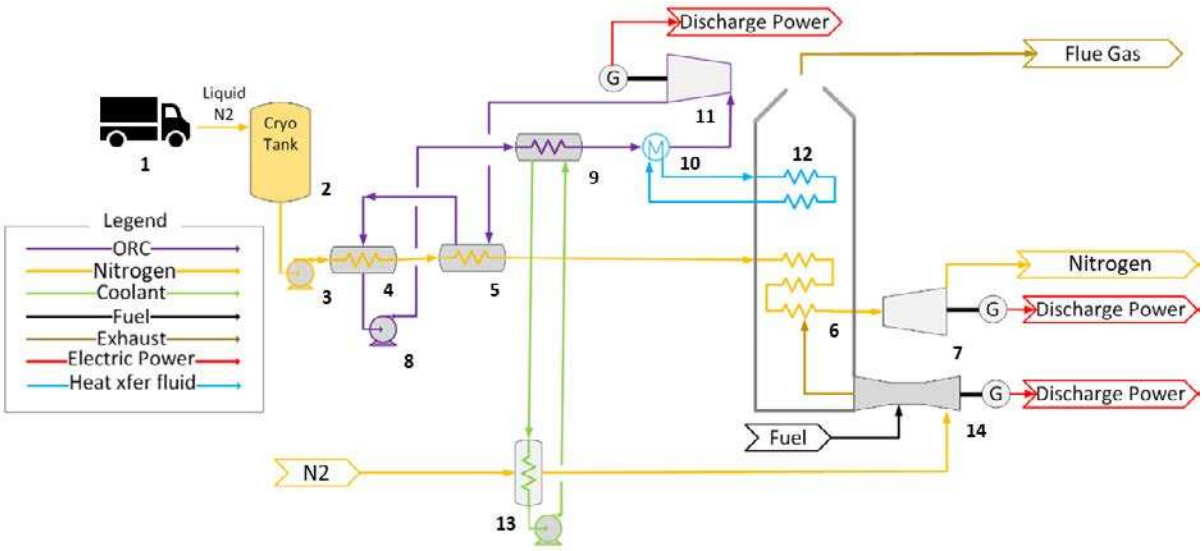

Figure 2: Demonstration of the LACC Technology

The performance of the demonstration systems was estimated using the Ebsilon Professional modelling software (STEAG, 2021). A comparison of the major results between the commercial scale and demonstration scale systems are shown in Table 3. The goals of this demonstration system are to show the first application of the technology, demonstrate the control system and transient operation and understand the major component interactions with each other while reducing the complexity of the system by removing the charge system and focusing on the discharge train which is at a lower TRL.

Table 3: Performance of the LACC System Demonstration

Parameter	Commercial Scale	Demonstration Scale
Net Power [kW]	117,319	13,530
Gas Turbine Power [kW]	62,000	6,500
Air Turbine Power [KW]	40,810	5,337
ORC Turbine Power [kW]	17,911	2,614
Net Fuel Rate [kJ/kWh (HHV)]	5,068	5,484
Liquid Air Flow Rate [tons/h]	260	36.3
Specific Air Consumption [kg/kWh]	2.25	2.68
Specific Cost [$/kWh]	1,250	3,000

The commercial scale system has been envisioned to compete against other large-scale energy storage systems. As such the system was designed to utilize the available, commercial equipment. It would be able to store 10s of GW of energy to be discharged as needed. While most of the components for the LACC technology are fully mature, the overall system has never been tested. The demonstration system is designed at about one-tenth of the commercial reference plant would be based on Solar Turbines Taurus 65. This smaller gas turbine would reduce the maximum temperature (gas turbine exhaust) by around 40°C. This reduction means that a smaller portion of the power is provided by the gas turbine (51% of gross power for commercial-scale, 45% of gross power for the demonstration-scale). It is also less efficient by comparing the specific air consumption, the amount of air that is consumed by a kWh of discharged energy.

The demonstration system was not designed to be a commercially available product but to fully demonstrate the technology gaps of the LACC technology. Since the liquefaction cycles studied for the LACC have both been commercially proven, the goal was to examine what were the limiting factors to advance the technology. The key risk factors that were identified were the operability, controls and transient operation of the discharge system. As such, the demonstration loop has been designed with the same cycle configuration as the commercial-scale system design. This system would be geared for

simulating real world markets. Start-up and shutdown times of the turbomachinery could be better analyzed and the interactions between the various loops as the discharge train starts and stops in response to energy demands.

An assessment was performed to understand the availablility of components for both the commercial- and demonstration-scale systems. In this analysis, it was identified that several components were not available at either scale. The first is the turbine for the liquid air loop. The air turbine would need to undergo a pressure ratio of 67 in order to expand back down to atmospheric conditions which are not currently available commercially. This technology development is currently underway in similar CAES systems (Giovannelli, 2020; He, 2021). The evaluation also revealed that the ORC turbomachinery did were outside of standard applications of the technology due to the low temperatures at the pump inlet and the turbine exit. Further concerns also revealed that the pressure ratio of the ORC fell outside of standard cryogenic technology ranges as well. This evaluation led the team to design a second loop focused on demonstration the ORC machinery.

4 ORC COMPONENT VALIDATION LOOP

A second loop was designed to advance the ORC equipment. The component validation will focus on the discharge cycle and validate the two main components below TRL 5. As such, a demonstration of this technology is shown in Figure 3. Components are denoted by the letters in the figure and state points denoted by the numbers. Table 4 shows the cycle points for the validation loop.

Instead of using gas turbine inlet air and exhaust as the heat sources, electric heaters will control the temperature of a thermal fluid in order to provide the requisite ORC temperatures before the turbine. Liquid nitrogen would be purchased from an external source for storage in a bullet tank adjacent to the loop. A cryopump would pressurize the air for feeding the two heat exchangers D and E, with regasified nitrogen discharged to atmosphere.

269

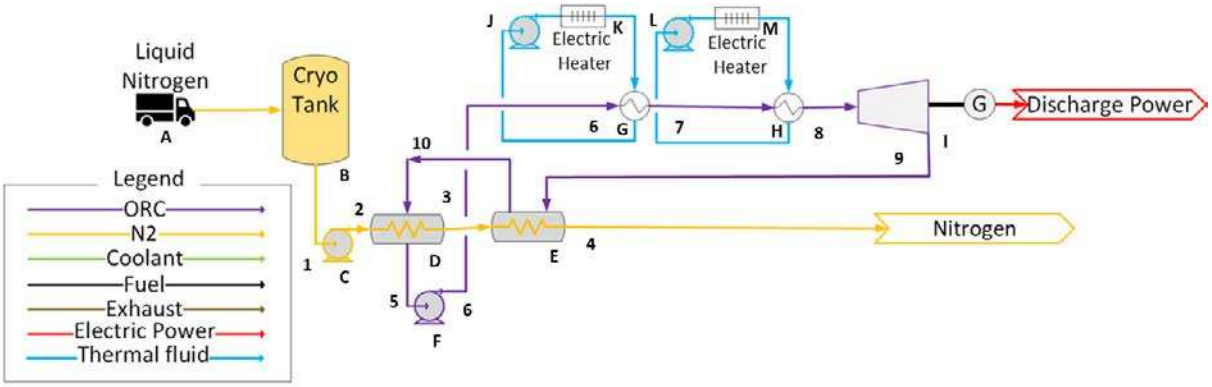

Figure 3: ORC Component Validation Loop

Table 4: Cycle Conditions of the ORC Validation System.

State Point	Temperature [°C]	Pressure [MPa]	Enthalpy [kJ/kg]	Density [kg/m^3]	Fluid
1	-198	0.10	-127	816	Nitrogen
2	-196	7.09	-117	824	Nitrogen
3	-78	6.95	166	140	Nitrogen
4	112	6.81	393	58	Nitrogen
5	-81	0.16	19	534	Ethane
6	-72	16.8	58	540	Ethane
7	15	16.6	285	429	Ethane
8	340	16.5	1355	100	Ethane
9	140	0.32	895	2.8	Ethane
10	-72	0.24	41	522	Ethane

The machinery size of the component validation loop is based on the demonstration system and the expected architecture of the commercial scale application. The commercial scale system falls between the typical sizes for axial vs. radial expanders based on Balje correlations (Balje, 1962). Other considerations that were included aimed at limiting the surface speed, rotational speed, and enthalpy drop per stage as discussed in Bidkar et al. (Bidkar et al., 2016). These assumptions included limiting the rotational speed of the machine to less than 30,000 rpm, the enthalpy drop per stage less than 75,000 N-m/kg and a specific speed between 10 to 300. Based on these assumptions, the axial turbine is described below in Table 5. This turbine has a high stage count and very small shaft diameter in order to account for the pressure ratio of 50 and to meet the requirements described above. This falls outside of standard design practices and would need to be further studied before testing the component.

Table 5: ORC turbine sizing for the component validation test.

Parameter	Value
Inlet conditions	340°C 16.5 MPa
Outlet conditions	140°C 0.32 MPa
Rotational speed	28,000 rpm
Stage count	8
Shaft diameter	0.06 m
Enthalpy drop per stage	66,500 N-m/kg
Specific speed	21.76
Power output	2,500 kW
Efficiency	88%

Previous research had been performed in Pryor et al. (Pryor et al. 2022) to understand the sizing of the commercial scale machines. Comparatively, the machine here is significantly faster with a much smaller diameter. One concern with the modeling is that it assumes a high efficiency for the demonstration system which may not be possible for such a small machine. The specific speed of the system was set to 21.76 for the sizing calculations while the peak efficiency is typically found between 30-100 based on the correlations.

The ORC pump also needs further validation for the given conditions. The main concern with the pump is the extremely high-pressure ratios for the system. These are outside of the current area of available ORC equipment. While cryogenic pumps are available that can reach these pressures, the flow rate is

about 1/20th of the required flow rate and designed for different fluids (LCO_2, LOX, LNG, etc.). Other options for cryogenic pumps include the technology used in the RS-25 for the space shuttle. The RS-25 oxidizer pump had a flow rate over 11 kg/s but only had a pressure rise of 0.7 MPa (McLaughlin, 1998). This shows that while each of the main conditions can be met independently, the combination of flow rate and pressure rise is unavailable commercially.

5 CONCLUSIONS

A pathway for the LACC technology development has been created to bring the LACC technology to commercial readiness. Two different validation systems were created to target the areas requiring further development.

The first was a demonstration of the overall technology. This system was reduced to around 15% of the flow rates of the system and produce around 13% of the power compared to the commercial-scale conceptual design. The goals of the demonstrator are to understand how the discharge train would respond to real-world energy markets that would require a highly transient operation. This would demonstrate that the LACC system is able to effectively respond to the highly volatile energy markets predicted to dominate the future. This reduction has been shown to cause around a 20% drop in performance as measured by the specific air consumption of the system.

The second system was created to advance the TRL of the ORC components. The two major ORC machines need to be developed, the turbine and the ORC pump. Conceptual sizing of the ORC turbine shows that while the component-validation turbine design is possible using axial machinery, the turbine design would fall outside of the standard practices due to the extremely high speeds required.

To further develop the LACC concept, future work would need to be performed for both systems described in this paper. A detailed design of the LACC turbine would need to be performed to address the design challenges described in the paper including a rotor dynamic, casing and thermo-mechanical assessment. Once the ORC components have been validated, the larger demonstration loop could undergo further development to advance the LACC technology.

271

NOMENCLATURE

CAES	Compressed Air Energy Storage
LACC	Liquid Air Combined Cycle
LCO_2	Liquefied Carbon Dioxide
LDES	Long Duration Energy Storage
LNG	Liquefied Natural Gas
LOX	Liquefied Oxygen
ORC	Organic Rankine Cycle
TIT	Turbine Inlet Temperature
TRL	Technology Readiness Level

REFERENCES

Allison, T.C., Smith, N.R., Rimpel, A.M., and Brun, K., 2020, Overview of Machinery-Based Grid-Scale Energy Storage Technologies, Proceedings of Turbomachinery and Pump Symposium, *Texas A&M University*, Virtual.

Balje, O., 1962, *A Study on Design Criteria and Matching Turbomachines: Part A – Similarity Relatives and Design Criteria of Turbines*, Trans. ASME Series A.

Bidkar, R.A., Mann, A., Singh, R., Sevincer, E., Cich, S., Day, M., Kulhanek, C.D., Thatte, A., Peter, A., Hofer, D. and Moore, J., 2016, Conceptual designs of 50MWe and 450MWe supercritical CO2 turbomachinery trains for power generation from coal. Part 1: Cycle and Turbine, *Proceedings of the 5th International Symposium on Supercritical CO_2 Power Cycles*.

Conlon, W. M., Venetos, M. J., Hume, S., 2022, Liquid Air Combined Cycle, Turbo Expo: Power for Land, Sea, and Air, Vol. 86014, *American Society of Mechanical Engineers*.

Giovannelli, A., Tamasi, L. and Salvini, C., 2020, Performance analysis of industrial steam turbines used as air expander in Compressed Air Energy Storage (CAES) systems, *Energy Reports*, 6, pp.341-346.

He, Y., Chen, H., Xu, Y. and Deng, J., 2021, Thermodynamic research on compressed air energy storage system with turbines under sliding pressure operation, *Energy*, 222, p.119978.

Jankowski, M. and Borsukiewicz, A., 2019. Multi-objective approach for determination of optimal operating parameters in low-temperature ORC power plant. *Energy Conversion and Management*, 200, p.112075.

Kosmadakis, G. and Neofytou, P., 2020, Investigating the performance and cost effects of nanorefrigerants in a low-temperature ORC unit for waste heat recovery, *Energy*, 204, p.117966.

McLaughlin, B., 1998, Space Shuttle Main Engine Orientation, Space Transportation System Training Data, BC98-04, *Rocketdyne*.

Merfield, D., 2022, Energy Transition: transformational change to build a sustainable future, *ARPA-e Energy Innovation Summit 2022*.

Paris Agreement to the United Nations Framework Convention on Climate Change, Dec. 12, 2015, T.I.A.S. No. 16-1104.

Pryor, O., Rimpel, A., Conlon, W., 2022, Organic Rankine Cycle Turbine and Heat Exchanger Sizing for Liquid Air Combined Cycle, *Proceedings of ASME Turbo Expo 2022*, ASME.

Psaki, J., 2021, FACT SHEET: President Biden Sets 2030 Greenhouse Gas Pollution Reduction Target Aimed at Creating Good-Paying Union Jobs and Securing U.S. Leadership on Clean Energy Technologies, White House Press Briefing, April 22, 2021.

STEAG Energy Services,2020, Ebsilon Professional 15.01.

Sun, Z., Wu, Z., Zhao, Q., Liu, X. and Lin, K., 2020, Thermodynamic improvements of LNG cold exergy power generation system by using supercritical ORC with unconventional condenser, *Energy Conversion and Management*, 223, p.113263.

Xu, X., Zhang, L., Zhang, H., Ma, J. and Sambatmaryde, K., 2022. Investigation of an artificial cold source with variable temperature for ORC test rig. *Case Studies in Thermal Engineering*, 37, p.102234.

272

ACKNOWLEDGEMENT

This material is based upon work supported by the Department of Energy DE-FE0032002.

Disclaimer: “This report was prepared as an account of work sponsored by an agency of the United States Government. Neither the United States Government nor any agency thereof, nor any of their employees, makes any warranty, express or implied, or assumes any legal liability or responsibility for the accuracy, completeness, or usefulness of any information, apparatus, product, or process disclosed, or represents that its use would not infringe privately owned rights. Reference herein to any specific commercial product, process, or service by trade name, trademark, manufacturer, or otherwise does not necessarily constitute or imply its endorsement, recommendation, or favoring by the United States Government or any agency thereof. The views and opinions of authors expressed herein do not necessarily state or reflect those of the United States Government or any agency thereof.”

ORC SEVILLE 2023
7th International Seminar on O.R.C. Power Systems

© 2024 Editorial Universidad de Sevilla. Este es un artículo de acceso abierto distribuido bajo los términos de la licencia de uso y distribución Creative Commons (BY-NC-ND 4.0)

DOI: https://dx.doi.org/10.12795/9788447227457_41

Guidelines and optimization criteria of a machine learning-based methodology for mixture design in ORC systems

Valerio Mariani, Saverio Ottaviano*, Andrea De Pascale, Giulio Cazzoli, Lisa Branchini, Gian Marco Bianchi

Department of Industrial Engineering, University of Bologna, viale del Risorgimento 2, Bologna

*Corresponding Author: saverio.ottaviano2@unibo.it

ABSTRACT

Working fluid selection in organic Rankine cycles (ORC) is a critical issue in the system design for specific applications. In most cases, pure fluids are employed as working medium, and the choice among commercial products is fundamentally based on the heat source temperature level, on fluid cost and safety requirements. Mixtures of organic fluids present some interesting features. First of all, zeotropic blends can help reducing the irreversibility associated to the isothermal heat transfer of pure working fluids in the evaporator and in the condenser, with potential improvement of the overall conversion efficiency from heat sources with finite capacity. Moreover, the possibility of using fluids with relatively high global warming potential, blended with low-GWP fluids, allows reducing the equivalent carbon emissions (according to the European F-gas regulation), helping the full transition to cleaner compounds. However, there is a lack of organic mixtures specifically optimized for ORC systems, particularly because different applications require fluids with different properties, and the available solution may not be the optimal for the specific case. Due to the large number of molecules available to be combined, the use of numerical algorithms is mandatory to accomplish the mixture formulation task (type, number and amount of each component). In this work, an optimization tool based on a Bayesian statistical inference methodology is implemented and tested, to define the composition of mixtures of different groups of organic fluids (HFC, HFO, HC). The algorithm adopts a mixed exploration-exploitation searching strategy on a solution domain made by the different pure molecules commonly employed. The tool is programmed to fulfil the maximization of an objective function, built from a set of key physical properties and performance indexes of the mixture. The choice of the properties accounted in the optimization (with relative weight) is discussed, and the algorithm is applied to a case study to demonstrate its capability to define a low-GWP blend replacing HFC 134a, maintaining and possibly enhancing the performance.

1 INTRODUCTION

The use of mixtures of working fluids in organic Rankine cycle is gaining attention due to some favourable characteristics. Mixtures can be used for achieving target values of thermodynamic properties, or for reducing undesired properties of pure molecules, such as high Global Warming Potential (GWP) or flammability. For zeotropic mixtures, the continuous variation of temperature during the phase change may enhance the temperature match between working fluid and heat source, reducing exergy losses and increasing the power output (Angelino and Colonna di Paliano, 1998; Bamorovat and Kim, 2017). Moreover, the need for replacement of currently used high-GWP fluids may occur by mixing such fluids with low-GWP molecules, especially during the transition to clean fluids. Fluids with good thermo-physical properties but high value of GWP can be blended with low-GWP fluids to reduce the resulting environmental impact and maintain good thermodynamic properties. Many studies have been published on the optimization of the working fluid in ORC applications, some of them also including binary mixtures. In the most common approach for working fluid choice, a group of fluids is identified based on predefined criteria, and then the optimal substance is obtained by means

of a parametric optimization procedure (Freeman *et al.*, 2017). More complex analyses on pure working fluids have been conducted, for example, by Papadopoulos *et al.* (2010); Lampe *et al.* (2014); Cignitti *et al.* (2017); Schilling *et al.* (2021), where a computer-aided fluid selection is integrated in the design of the ORC plant. Integrated design has been less applied to the case of mixture. Some examples are the works by Schilling *et al.* (2021) and by White *et al.* (2018), which extended the computer-aided approach to blends optimization to carry out the thermodynamic and thermo-economic analyses, considering simple non-recuperated subcritical ORC systems.

Due to the large number of independent variables affecting the working fluid performance, together with the highly non-linear behaviour of some of those, classical optimization techniques may face failure. In the current state of the art, different approaches have been adopted to design the proper mixture to employ as working fluid in refrigeration and waste heat recovery applications. Systematic analyses based on iterative routines, constraints from experience and simulation results have shown the potential to fulfil very specific tasks properly in short time (Tang *et al.*, 2022; Sleiti and Al-Ammari, 2022). Some Authors, instead, proposed the use of heuristic techniques aiming at a generally valid method able to perform mixture design without stringent boundaries, e.g., Papadopulos *et al.* (2010) with combined Computer Aided Molecular Design (CAMD) and Simulated Annealing, and Li and Gluesenkamp (2021), with the Particle Swarming Optimization (PSO) technique. Heuristic methods have been widely reviewed and adopted in the current state of the art to attack different engineering optimization tasks (Nazari-Heris *et al.*, 2018), due to their problem simplification power, low computation effort, fast search while ensuring a 'enough good' solution. However, those methods lack the ability of finding the global optimum solution and do not provide clear measures of the result quality among all the possible options. It must be considered that the ORC mixture composition design features a wide solution domain (large as the number of possible pure fluids to employ), and high complexity of the optimization function, related to the highly multi-objective nature of the problem (Babatunde and Sunday, 2018). Therefore, ensuring the best composition under given constraints and returning the confidence are key features, thus, alternatives to heuristics should be investigated as well. In this framework, probabilistic techniques are attractive to accomplish the task. However, in the current literature, the use of such methods for ORC working fluid design is scarcely investigated. In particular, Bayesian optimization has the ability to map the solution domain in an efficient manner, thanks to the combined use of a probabilistic surrogate model and a proper acquisition function, which infers according to the Bayes theorem (Stigler, 1982).

274

This work deals with the development of an optimization tool, based on Bayesian inference and aimed at guiding the identification of low-GWP optimized mixtures for ORC applications. The searching algorithm is a modified version of the original work by some of the Authors (Mariani *et al.*, 2021). A set of representative pure fluids as potential mixture components, and a set of constraints have been selected in line with practical observations and the results of an extensive literature review. To demonstrate the methodology capabilities, the code has been run with the aim of replacing R134a with a new azeotropic mixture which mimics its characteristics, while reducing the GWP below 750. This work aims at providing a flexible and user-friendly approach to define optimal ORC mixtures, but it can be applied to any mixture selection procedure for preliminary screening.

2 METHODOLOGY

2.1 Mixture optimization algorithm

The implemented algorithm searches, among the possible mixture compositions, the global maximum of a user-designed objective function according to the general approach described in Mariani *et al.* (2021). In particular, in this study the solution domain is given by the mass fraction of each pure fluid. The searching procedure starts with a Gaussian Process (GP) used as probabilistic surrogate model to determine the belief on the objective function shape over the domain. In the second step, the Upper Confidence Bound (UCB) exploration-exploitation mixed strategy is applied by means of the acquisition function A (Eq. (1)), in which X in the evaluation point, M is the predictive mean, K is the covariance matrix, θ is the exploitation-exploration split hyperparameter, tuned at 0.5. The algorithm has been set in order to perform 50 random initial evaluations, and then 200 evaluations according to the abovementioned strategy.

$$A(X) = M(X) + \theta \cdot K(X) \quad (1)$$

The optimization tool was developed in *Python* 3.0 by means of the *bayes_opt* (https://github.com/bayesian-optimization/BayesianOptimization) open library. The tool is required to define the composition of a mixture, having GWP below 750, able to replace R134a as a working fluid in an ORC cycle for given values of vaporization temperature (75 °C) and condensation temperature (30 °C). Such values have been selected based on the design conditions of the test bench at University of Bologna, which is a micro-ORC for low temperature heat recovery, suitable for renewable thermal sources such as geothermal and solar thermal energy, or for low grade waste heat recovery (Bianchi *et al.*, 2022). The solution domain has been defined by ten different pure fluids comprising: the hydro-fluoro-carbons (HFCs) R134a, R32, R245fa, R227ea, R152a; the hydro-carbons (HCs) propane, i-butane; the hydro-fluoro-olefins (HFOs) R1234yf, R1234ze; the hydro-cloro-fluoro-carbon (HCFC) R142b. The number of fluids selected for the blend optimization is a trade-off between results accuracy and acceptable simulation time. The ten base fluids have been selected among commercial solutions by means of a preliminary screening, mainly based on the value of the critical temperature, keeping in mind that the target is to obtain a surrogate of R134a ($T_C \cong 101$ °C). Another criterion was to include pure fluids from different chemical families. Critical temperatures of the selected fluids are in the interval between 78.4 °C (R32) and 154 °C (R245fa and R1234ze). Due to limitations related to the numerical method, the maximum domain size for each simulation is of 20 fluids. To further increase the total searching domain, multiple runs can be conducted in parallel and/or in sequence.

Once the solution domain has been defined, at each optimization step the performance of the formulated mixtures is evaluated by means of a group of user-defined indicators, which are compared to those of the reference fluid, the R134a. The key indicators, here called 'optimization targets', are: molecular weight (MW) and critical temperature (T_C), both depending only on the fluid (trivial properties); dynamic viscosity (μ), latent heat of vaporization (HoV), liquid and vapor density (ρ_L, ρ_V), liquid and vapor heat capacity (c_L, c_V), and the temperature glide (ΔTG), all evaluated at a fixed pressure; the Jacob number (*Ja*) (Kuo *et al.*, 2011). The latter, defined in Eq. (2), represents a rough thermodynamic estimation of the ORC potential performance provided by the fluid working with T_{vap} and T_{cond} as vaporization and condensation temperatures. Kuo *et al.* (2011) demonstrated that *Ja* is related to the thermal efficiency with inverse proportion. In Eq. (2), the specific heat $\overline{c_p}$ is computed as the average between the specific heat of the saturated vapor at T_{vap} and T_{cond}, while HoV is referred to the heat of vaporization at T_{vap}. The temperature glide is defined as the difference between the saturation temperatures of vapor (T_V) and liquid (T_L) at constant pressure (Eq. (3)) and determines whether the mixture is zeotropic or azeotropic.

275

$$Ja = \frac{\overline{c_p} \cdot (T_{vap} - T_{cond})}{HoV} \quad (2)$$

$$\Delta TG = (T_V - T_L)_{p=const} \quad (3)$$

This set of properties and parameters has been selected due to their strong bonds with thermodynamic performance and operating issues. For instance, the value of the viscosity affects the volumetric efficiency of the positive displacement machines, as lower viscosity leads in general to higher leakages (Bianchi *et al.*, 2020). In the case of retrofit of an existing ORC system, the replacement of a pure fluid with a mixture characterized by a substantially different value of μ should be accompanied by measures to reduce the leakages in pump and expander. Such measures can be the substitution of the lubricant oil or the modification of the working temperature (to adjust the viscosity), or even the change of one or both the displacement machines with more sealed ones (in case the viscosity difference is high). The density has a direct effect on the fluid mass flow rate and power output, as both decrease with lower values of ρ if the volume flow rate remains the same. The heat of vaporization represents the largest contribution to the heat transferred in the evaporator, hence its variation may causes the change of the mass flow rate if the thermal power input is assumed constant. This is more true in case of recuperated ORC systems, in which an important part of the economization is provided in the recuperator. Finally, the specific heat influence in general both the transferred thermal power and the specific work.

These optimization targets have been combined to design the objective function reported in Eq. (4), in the manner that the optimum mixture lies on a weighted Pareto frontier with the minimum Euclidean distance from the reference fluid. In Eq. (4), φ is the generic optimization target, W is the weight assigned to each optimization target, which can be adjusted in order to change its relevance against the others. The higher is the weight value, the larger is the impact of the optimization target on the final value of the objective function. Thus, higher weight values can be assigned to the properties that are discovered to be difficult to match by the optimizer. Increasing the weight of some optimization targets, may result in worsening of the match of the other optimization parameters with lower weight values. To obtain adequate values of the weights, preliminary runs were performed by setting each weight equal to 1.0. Results revealed that density and heat of vaporization were affected by the larger errors against those of R134a. The successive step consisted in a series of optimization runs, launched increasing progressively the weights of density and heat of vaporization by 0.1. After the preliminary analysis, weights have been tuned to the following values: i) 2.0 for the liquid density; ii) 1.5 for the Jacob non-dimensional number; iii) 1.2 for the heat of vaporization; iv) 1.0 for the remaining optimization targets. Such values have shown the best balance on the absolute relative errors of the optimization targets.

$$F = 100 - \frac{1}{\sqrt{\sum_i W_i}} \cdot \sqrt{\sum_i W_i \cdot \left(\frac{\varphi_{i,R134a} - \varphi_i}{\varphi_i}\right)^2} \tag{4}$$

Eventually, two different arbitrary screening criteria, here called ‘light constraints’, must be fulfilled, namely the solution is discarded if the associated GWP is higher than 750 or if the associated temperature glide is higher than 2.0 K, i.e. if the mixture is zeotropic. As for the optimization targets and the related weights, the screening values can be changed according to the specific objective. For the sake of clarity, the workflow of the described algorithm is reported in Figure 1.

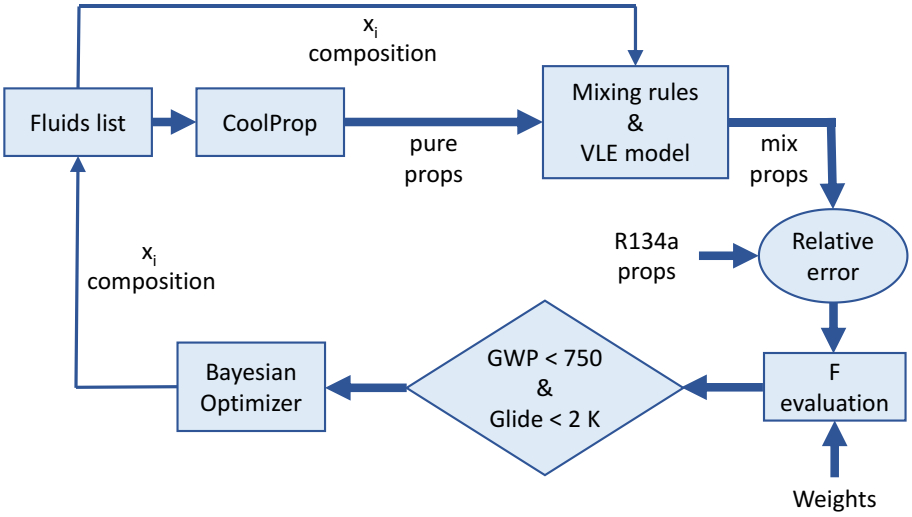

Figure 1: Workflow of the present mixture formulation and optimization algorithm.

2.2 Mixing rules definition

In order to assess the iterative solutions proposed by the algorithm, methods to estimate both the optimization targets and the light constraints are needed. It must be underlined that the optimization tool is required to perform several iterations, thus, the mixing rules called during the evaluation step should be as simple as possible in order to limit the computation effort. In this work, molecular weight, critical temperature, latent heat of vaporization, density values, heat capacity values, GWP, have been approached as additive quantities, meaning that they are calculated as a weighted average. In particular: i) the mixture critical temperature is calculated as moles weighted average; ii) the mixture latent heat of vaporization, heat capacity, and GWP values are calculated as mass weighted averages; iii) the mixture molecular weight, and density values are calculated as mass weighted inverse averages. Concerning the dynamic viscosity, the moles weighted logarithmic average according to the classical

Grunberg-Nissan correlation (Grunberg and Nissan, 1949) was applied. A simplified version of the original formula was implemented by neglecting the components' cross-term in order to limit to the minimum the use of fitting parameters with arbitrary values.
Once the mixing rules have been defined, the fractions of the single components are provided by the optimizer according to the mixture option under evaluation, whilst the property of those pure components are calculated by calling the *CoolProp* open library (Bell *et al.,* 2014). For the computation of the so-called non-trivial properties, *CoolProp* must be provided with the reference thermodynamics conditions as input. In this work, heat of vaporization, viscosity, and density values are considered at the respective saturated states (liquid or vapor) for the temperature value T that corresponds to the non-dimensional temperature $T^* = T/T_C = 0.7$ (with T and T_C expressed in °C). The value of $T^* = 0.7$ was chosen arbitrarily, as representative of average normalized temperature at which the vaporization process takes place in ORC systems. Instead, the heat capacity values were calculated at saturated states (liquid or vapor) and ambient pressure. It must be pointed out that the expression of the Jacob non-dimensional number (Eq. (2)) involves c_V, HoV, T_{vap}, T_{cond}, thus, it does not require a specific mixing rule, since it has been calculated directly by using the c_V and the HoV of the mixture. Regarding the temperature glide of the new mixture options, since the Vapor-Liquid Equilibrium (VLE) properties are not additive, a dedicated sub model has been implemented to predict the dew point temperature and the bubble point temperature. These two temperature values are calculated according to the pure thermodynamics model presented in Mariani *et al.* (2021). Since the phase equilibrium sub-model is not the focus of the present paper, only the main features will be mentioned, avoiding the extended description of the equations, which can be found in Mariani *et al.* (2021). The bubble point temperature and the dew point temperature problems are numerically solved by means of a system of equations comprising the VLE for each component as a non-ideal fluid, the Soave-Kwong-Redlich cubic equation of state, and the phase mass equilibrium.

2.3 Mixing rules validation

In order to address the optimization tool towards the global best solution, it is important to ensure a high degree of accuracy in estimating the properties used as optimization targets. For the validation procedure, 53 commercial refrigerant mixtures (with known properties) have been taken from the online database W-Refrigerant (https://w-refrigerant.com). Those mixtures are made by different combinations of CFCs (Chloro-Fluoro-Carbons), PFCs (Per-Fluoro-Chemicals), HCFCs, HFCs, HCs, HFOs. For each mixture, the properties resulting from the mixing rules have been compared with those calculated with the commercial software REFPROP 10.0 (Lemmon et al., 2018), which has been assumed as validation benchmark. For the sake of brevity, the validation results are summarized in Table (1), by means of the Root Mean Squared Error (RSME) and the coefficient of determination (R^2). Table 1 shows that the implemented mixing rules have excellent performances in predicting heat capacity of the considered fluid mixtures, with low RSME values and nearly perfect correlation coefficients ($R^2 \approx 1$). The agreement with REFPROPR values for the optimization targets T_C, ρ, HoV is nice as well, whilst the accuracy in predicting μ and ΔTG is slightly lower but still falling in an acceptable confidence.

277

Table 1: Root Mean Squared Error (RSME) and coefficient of determination (R^2) for each optimization target. Metrics are calculated considering the values from REFPROP 10.0 as a reference.

Optimization target	RSME	R^2
T_C (K)	5.3	0.9141
μ (mPa·s) @T^* = 0.7, Q = 0	5.6 x 10^{-4}	0.8982
ρ (kg/m^3) @T^* = 0.7, Q = 0	5.3	0.9500
HoV (kJ/kg) @T^* = 0.7, Q = 0	10.1	0.9516
c_V (kJ/kg/K) @p = 1 bar, Q = 1	5.2 x 10^{-3}	0.9995
c_L (kJ/kg/K) @p = 1 bar, Q = 0	1.1 x 10^{-2}	0.9980
ΔTG (K) @ p = 1 bar	1.4	0.8814

An in-depth analysis of the data has revealed that the prediction performance loss depends on few mixtures: i) binary mixtures with PFCs (e.g., R508a, R508b, R509a); ii) ternary mixtures of PFCs with HCs (e.g., R403a, R403b, R413a); iii) mixtures containing intermediate quantity of CFC (<40%) (e.g., R500). It must be underlined that due to the high GWP associated to PFCs and the non-zero ODP (Ozone Depletion Potential) of CFCs, those groups will be not included in the optimization routine. Therefore, one can say that this group-dependent prediction derating does not affect the overall reliability of the mixing rules.

3 RESULTS

The focus of this work is the application of the probabilistic Bayesian optimization methodology, with the specific purpose of designing a blend of organic fluids able to mimic the thermodynamic performance of R134a in ORC plants. At the end of the run of 250 iterations, the optimization tool has formulated 50 random, and 200 guided solutions. Among all the resulting mixtures, only 193 fulfil the light constraints of GWP and ΔTG. High-GWP blends are those characterized by a large fraction of R134a, while a glide higher than 2 K is obtained by mixing fluids with large difference of critical temperatures, resulting in zeotropic behaviour. Among the 193 available solutions, the objective function score rises from a minimum of 55 to a maximum of 70.4. In order to focus the analysis to the most relevant solutions, a subset including only the highest fifteen percentile (i.e. mixtures with score from 59.5 up to the maximum) has been selected and is shown in Figure 2.

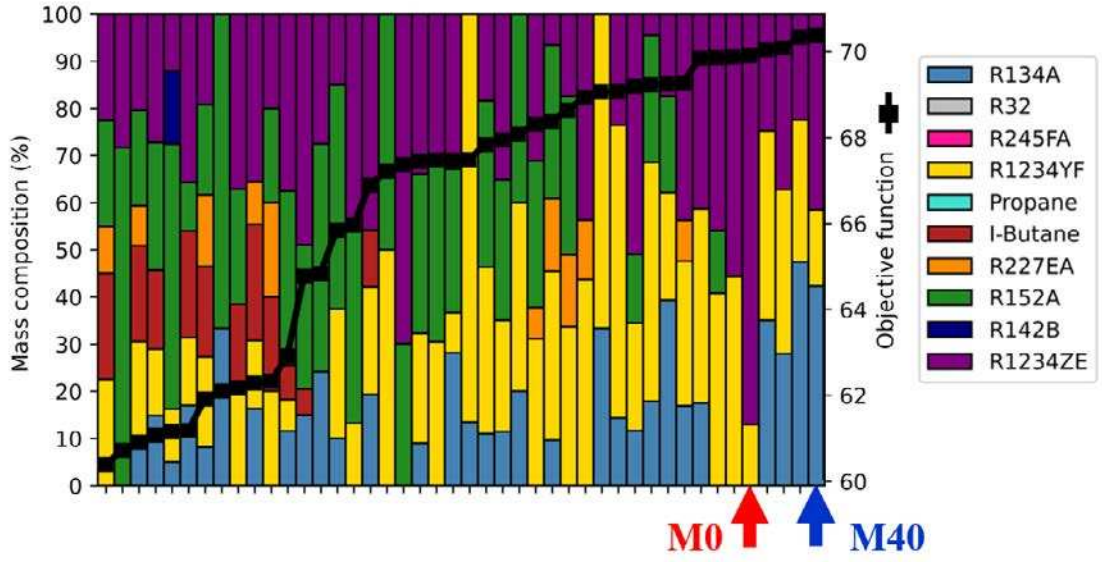

Figure 2: Composition of the mixture solutions proposed as surrogate for R134a (left-hand axis), and the corresponding objective function score (black line, right-hand axis).

Each bar of the graph is a mixture solution, composed of the pure fluids according to the colours in the legend. The mixtures have been ordered according to the value of the objective function, which is shown with the black curve with squared markers referred to the right-hand axis. Figure 2 shows three of the initial components in the database (namely R245fa, R32, and propane) are not employed in any of the best mixtures, whilst the fluid R142b is in one single mixture with score around 61. The absence of the refrigerants R245fa, R32 and R142b is likely due to their high GWP (1030, 675 and 2310, respectively). Moreover, the composition analysis reveals that mixtures including HCs show in general lower scores. Focusing on the high score side of the bar chart, it is visible that the best options are characterized by large amount of HFOs (R1234ze, R1234yf), which are also the fluids that guarantee lowest value of GWP, close to zero.

Two solutions have been underlined in Figure 2: i) the optimum mixture (M40), with the highest score of 70.4, is a ternary mixture of R134a (42.3%), R1234yf (16.2%) and R1234ze (41.5%); ii) the mixture named M0, namely the best R134a-free option, is a binary mixture of R1234yf (13%) and R1234ze

278

(87%) with a 69.9 value of the objective function. The radar chart in Figure 3 shows the comparison between R134a and the two mixtures M40 and M0. The properties reporting the symbol * are normalized against those of R134a.

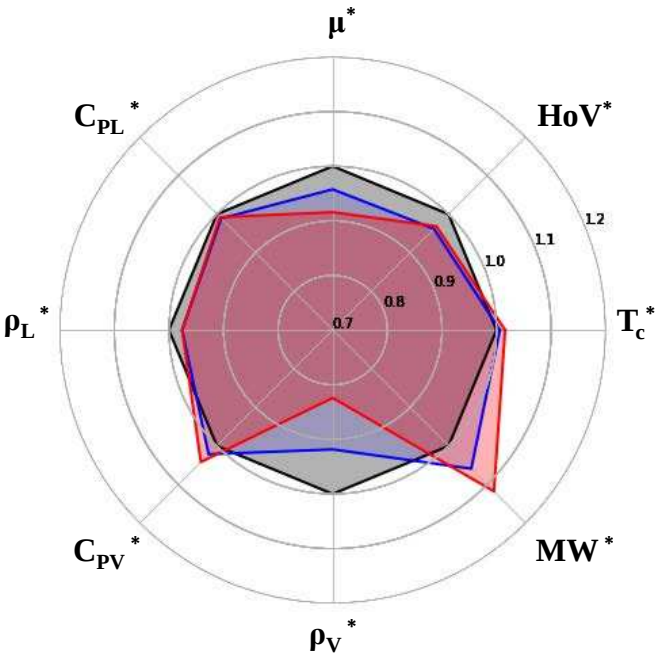

Property	R134a	M40	M0
μ (mPa·s)	0.1052	0.1008	0.0964
HoV (kJ/kg)	123.2	119.3	118.5
T_C (K)	374.2	380.6	376.5
MW (g/mol)	102	108	114
ρ_V (kg/m^3)	118.0	97.3	108.4
C_{PV} (kJ/kg/K)	0.79	0.82	0.81
ρ_L (kg/m^3)	991.6	967.7	967.7
C_{PL} (kJ/kg/K)	1.28	1.27	1.26

Figure 3: Radar chart of the optimization targets normalized against R134a (φ/φ_{R134a}) for the highest score mixture M40 (blue), and the best R134a-free mixture M0 (red) in comparison with R134a (black). Punctual values are also provided in the table.

279

In Figure 3 it is visible that the optimum mixture (M40) can match the properties of R134a with a degree of accuracy between the 98% and the 95%, except for the vapour phase density, which is underestimated of around the 10%. The GWP of the M40 mixture is 608, and the Jacob number is 0.37. The mixture M0 behaves as the M40 mixture in terms of heat of vaporization, critical temperature, heat capacity, liquid density, viscosity, whilst a slight reduction of the match can be seen for molecular weight (10% increase) and vapour density (20% decrease). The values of GWP and Jacob number for the M0 mixture are 5.7 and 0.37, respectively.

Regarding the discrepancy of the values of some properties between optimal mixtures and target, some issues should be considered, especially in case of retrofitting of an existing ORC system originally operated with R134a. For example, the lower HoV value of both optimal solutions compared to R134a, together with the lower values of vapour density, suggest that the resulting volume flow rate would be slightly higher in both pump and expander, in order to recover the same thermal input from the heat source. However, in this example, the modest differences compared to R134a should not modify significantly the system performance in case of retrofit, and also the required modifications to the existing equipment should be limited.

In conclusion, the HFOs binary mixture M0 designed by the proposed tool can be an attractive alternative as a working fluid for the retrofit of ORC plants in place of R134a. Indeed, according to the match in Figure 3, the M0 can be operated without significant adjustments on piping, pump etc., while taking advantage of the GWP 99+% reduction and the lack of R134a. However, it must be considered that the Jacob number of both mixtures is larger than that of R134a (0.35), suggesting that a slight penalization of the thermodynamic efficiency is expected, if the mixture works in a cycle with the selected values of hot and cold temperature.

Main next developments will be dedicated, in addition to a general improvement of the mixing rules, to the introduction of the mixture flammability among the properties considered in the optimization, and the integration in the algorithm of a simplified model of the ORC system, with the aim of providing a stronger validation of the method capabilities.

Furthermore, the algorithm can be used to address the design of an overall 'best replacing mixture', by setting up the accomplishment of plant-related targets (e.g., net power output, best efficiency) as well as environmental and safety constraints (e.g., low GWP, low flammability). Under this framework, significant changes should be applied: i) definition of a new objective function based on general plant-related parameters instead of fluid properties; ii) reviewing the list of pure components; iii) include a model of an ORC test bench in order to test the formulated mixture as working fluid runtime, then, evaluate the next composition based on the performance of the virtual plant. It must be considered that at each iteration of the optimizer, the ORC model would perform a number of sub-iterations for solving the operating cycle. As a result, in order to limit the computation time (which would increase from tens of seconds up to hours), the user should put more care in determining the maximum epochs, the exploration-exploitation split, providing the code with guidelines about the pure fluids that must be used with larger amount.

4 CONCLUSIONS

This paper deals with the implementation and testing of an optimization algorithm able to design working fluid mixtures for ORC systems. The algorithm employs a probabilistic Bayesian methodology to create blends of organic fluids. The scope of the optimization routine is to maximize a multi-objective function, which includes a set of properties and performance indexes that are considered representative of the fluid behaviour during operations. After the tuning and validation of the mixing rules implemented in the algorithm, the tool was run with the purpose of designing a low-GWP surrogate mixture for R134a, considering an application characterized by vaporization temperature of 75 °C and condensation temperature of 30 °C. The tool has designed 193 mixtures, with a score varying between 55 and 70.4. The solution with the highest value of the optimization function is a ternary mixture of R134a (42%), R1234yf (16%) and R1234ze (42%), with GWP value around 600. The best solution without any trace of R134a is a binary mixture of two HFOs (R1234yf, R1234ze), with almost null GWP (5.7).

The strength of the proposed tool lies in its simplicity, low numerical effort and good performance in mixture design. Moreover, it is based on open-source software (Python and CoolProp) and can be applied to any mixture selection procedure for preliminary screening. Future developments will be aimed at improving the algorithm performance, in terms of accuracy of the mixing rules and definition of more convenient indexes to estimate the real performance of the fluid at the specified working conditions.

280

REFERENCES

Angelino, G., Colonna di Paliano, P., 1998, Multicomponent Working Fluids For Organic Rankine Cycles (ORCs), Energy, vol. 23, p. 449–463. https://doi.org/10.1016/S0360-5442(98)00009-7

Babatunde, A.F., Sunday, O.O., 2018, A Review of Working Fluids for Organic Rankine Cycle (ORC) Applications, The 2nd International Conference on Engineering for Sustainable World, IOP Conf. Ser. https://doi.org/10.1088/1757-899X/413/1/012019

Bamorovat Abadi, G., Kim, K.C., 2017, Investigation of organic Rankine cycles with zeotropic mixtures as a working fluid: Advantages and issues. Renewable Sustainable Energy Rev., vol. 73, p. 1000–1013. https://doi.org/10.1016/j.rser.2017.02.020

Bell, I.H., Wronski, J., Quoilin, S., Lemort, V., 2014, Pure and Pseudo-pure Fluid Thermophysical Property Evaluation and the Open-Source Thermophysical Property Library CoolProp, Ind. Eng. Chem. Res., vol. 53, p. 2498–2508. https://doi.org/10.1021/ie4033999

Bianchi, M., Branchini, L., De Pascale, A., Melino, F., Ottaviano, S., Peretto, A., Torricelli, N., 2020. Replacement of R134a with low-GWP fluids in a kW-size reciprocating piston expander: Performance prediction and design optimization. Energy 206, 118174. https://doi.org/10.1016/j.energy.2020.118174

Bianchi, M., Branchini, L., De Pascale, A., Melino, F., Ottaviano, S., Peretto, A., Torricelli, N., 2022. Performance and total warming impact assessment of pure fluids and mixtures replacing HFCs in

micro-ORC energy systems. Applied Thermal Engineering 203, 117888. https://doi.org/10.1016/j.applthermaleng.2021.117888

Cignitti, S., Andreasen, J.G., Haglind, F., Woodley, J.M., Abildskov, J., 2017, Integrated working fluid-thermodynamic cycle design of organic Rankine cycle power systems for waste heat recovery, Appl. Energy, vol. 203, p. 442–453. https://doi.org/10.1016/j.apenergy.2017.06.031

Freeman, J., Hellgardt, K., Markides, C.N., 2017, Working fluid selection and electrical performance optimisation of a domestic solar-ORC combined heat and power system for year-round operation in the UK, Appl. Energy, vol. 186, p. 291–303. https://doi.org/10.1016/j.apenergy.2016.04.041

Grunberg, L., Nissan, A. H., 1949, Mixture Law for Viscosity, Nature, vol. 164, p. 799-800. https://doi.org/10.1038/164799b0

Kuo, C., Hsu, S., Chang, K., Wang, C., 2011, Analysis of a 50 kW organic Rankine cycle system, Energy, vol. 36, p. 5877-5885, https://doi.org/10.1016/j.energy.2011.08.035

Lampe, M., Stavrou, M., Bücker, H.M., Gross, J., Bardow, A., 2014, Simultaneous Optimization of Working Fluid and Process for Organic Rankine Cycles Using PC-SAFT, Ind. Eng. Chem. Res., vol. 53, p. 8821–8830. https://doi.org/10.1021/ie5006542

Lemmon, E.W., Bell, I.H., Huber, M.L., McLinden, M.O. NIST Standard Reference Database 23: Reference Fluid Thermodynamic and Transport Properties-REFPROP, Version 10.0, National Institute of Standards and Technology, Standard Reference Data Program, Gaithersburg, 2018.

Li, Z., Shen, B., Gluesenkamp, K.R., 2021. Multi-objective optimization of low-GWP mixture composition and heat exchanger circuitry configuration for improved system performance and reduced refrigerant flammability. Int. J. Refrig., vol. 126, p. 133–142. https://doi.org/10.1016/j.ijrefrig.2021.01.003

Mariani, V., Pulga, L., Bianchi, G.M., Falfari, S., Forte, C., 2021, Machine Learning-Based Identification Strategy of Fuel Surrogates for the CFD Simulation of Stratified Operations in Low Temperature Combustion Modes, Energies, 14. https://doi.org/10.3390/en14154623

Nazari-Heris, M., Mohammadi-Ivatloo, B., Gharehpetian, G.B., 2018, A comprehensive review of heuristic optimization algorithms for optimal combined heat and power dispatch from economic and environmental perspectives, Renewable Sustainable Energy Rev., vol. 81, p. 2128–2143. https://doi.org/10.1016/j.rser.2017.06.024

Papadopoulos, A.I., Stijepovic, M., Linke, P., 2010, On the systematic design and selection of optimal working fluids for Organic Rankine Cycles, Appl. Therm. Eng., vol. 30, p. 760–769. https://doi.org/10.1016/j.applthermaleng.2009.12.006

Schilling, J., Entrup, M., Hopp, M., Gross, J., Bardow, A., 2021, Towards optimal mixtures of working fluids: Integrated design of processes and mixtures for Organic Rankine Cycles, Renewable Sustainable Energy Rev., vol. 135. https://doi.org/10.1016/j.rser.2020.110179

Sleiti, A.K., Al-Ammari, W.A., 2022, Systematic thermodynamic approach for designing mixed refrigerants used in hydrogen precooling process, Int. J. Hydrog. Energy, vol. 47, p. 20915–20931. https://doi.org/10.1016/j.ijhydene.2022.04.233

Stigler, S. M., 1982, Thomas Bayes's Bayesian Inference, J. R. Stat. Soc. Ser. A Stato. Soc., vol. 145, p. 250-258, https://doi.org/10.2307/2981538

Tang, J., Kang, L., Liu, Y., 2022, An Effective Method for Working Fluid Design of Organic Rankine Cycle, Processes, vol. 10. https://doi.org/10.3390/pr10091857

White, M.T., Oyewunmi, O.A., Chatzopoulou, M.A., Pantaleo, A.M., Haslam, A.J., Markides, C.N., 2018, Computer-aided working-fluid design, thermodynamic optimisation and thermoeconomic assessment of ORC systems for waste-heat recovery, Energy, vol. 161, p. 1181–1198. https://doi.org/10.1016/j.energy.2018.07.098

ORC SEVILLE 2023
7th International Seminar on O.R.C. Power Systems

© 2024 Editorial Universidad de Sevilla. Este es un artículo de acceso abierto distribuido bajo los términos de la licencia de uso y distribución Creative Commons (BY-NC-ND 4.0)

DOI: https://dx.doi.org/10.12795/9788447227457_45

POTENTIAL OF TRIGENERATIVE WASTE HEAT RECOVERY CO_2-MIXTURE TRANSCRITICAL POWER PLANTS FOR INCREASING THE SUSTAINABILITY OF DISTRICT HEATING AND COOLING NETWORKS

Mattia Baiguini[1,2]*, Michele Doninelli[1], Ettore Morosini[3], Dario Alfani[3], Gioele Di Marcoberardino[1], Paolo Giulio Iora[1], Giampaolo Manzolini[3], Costante Mario Invernizzi[1], Marco Astolfi[3]

[1] *Università degli studi di Brescia, Dipartimento di ingegneria meccanica e industriale, Via Branze 38, 25123 Brescia, Italy*
[2] *Scuola Universitaria Superiore IUSS Pavia, Piazza Vittoria 15, Pavia, 27100, Italy*
[3] *Politecnico di Milano, Dipartimento di energia, Via Lambruschini 4a, 20156 Milano, Italy*

*Corresponding Author: mattia.baiguini@iusspavia.it

ABSTRACT

The waste heat released by high-temperature processes can be exploited by power cycle designed for full electric or combined heat and power applications, with the potential to cover even the cooling demand in a trigenerative perspective. The use of CO_2-based mixtures as working fluids for power cycles can be a promising solution for power production. These systems present a rejected heat in a temperature range (50–180 °C) that allows, depending on the needs, an effective coupling with a district heating and cooling network. This work investigates the potential of trigenerative system adopting CO_2-based power cycles which exploit the residual thermal power of the exhaust gases of a small-scale gas turbine. First, the performances of lithium bromide absorption chiller are investigated for various heat source levels, adopting different configuration. Then, various designs of CO_2-based power cycles are simulated focusing on the coupling with both the district heating and the chiller. A sensitivity analysis on the cycle minimum temperature is presented, evidencing that CO_2 mixtures can achieve remarkable net electric efficiency values even at high cycle minimum temperatures, marking a significant difference with respect to CO_2 cycles. Considering the yearly demand of district heating and cooling, keeping the electric output at design value, the economic profitability of the investment is characterized presenting the LCOE of the retrofitted solution, considered comparable with actual selling prices.

1 INTRODUCTION

The demand and production of thermal power for space heating and cooling applications rose significantly in the last decades: the International Energy Agency (IEA) reports that from 1990 to 2016 the space cooling demand has tripled, and it is mainly provided by air conditioning systems, consuming 2000 TWh of electricity per years worldwide (IEA, 2018). On the other hand, the agency highlights that fossil fuels account for the 64% of the primary energy used for space heating, with natural gas covering 42% of the share (at around 760 billion Nm^3 in 2021) (IEA, 2022). In this scenario polygeneration plants are crucial not only to achieve high overall efficiency, but also to save primary energy and provide flexible operations. Organic Rankine Cycles (ORC) are nowadays the most used technology for waste heat recovery from high temperature industrial process and from small gas turbine (below 500°C). (Macchi & Astolfi, 2017). In recent years, pure CO_2 (carbon dioxide) and CO_2 mixtures power cycles have been proposed as an alternative technology to ORC (and steam cycle in large size applications) thanks to the higher fluid thermal stability and the compactness of turbomachinery. These systems have been recently investigated in several European H2020 funded projects like SCARABEUS, DESOLINATION, CO_2OLHEAT, SCO2FLEX and SOLARSCO2OL. A previous work (Morosini et al., 2023) underlined the advantages of coupling CO_2-based power cycles with a high (180°C) and a low temperature (100°C) thermal user, in a cogenerative perspective. These results indicate a potentially

exploitable source to produce chilled water too, thus adopting both district heating and cooling networks.

The concept of trigeneration and polygeneration, using a pure CO_2 based power block, is well known in the literature (Bellos et al., 2022). These systems typically consider electricity, hot and cold water and hydrogen as useful outputs providing an economic analysis on the specific case study. This work aims at investigating the trigeneration potential of pure and mixture CO_2-based power cycles for heat recovery applications. For this purpose, the absorption chiller (AC) is modelled to estimate the coefficient of performance (COP) of the component at various conditions. Then, different configurations of CO_2-based power cycles are investigated, aiming at an effective coupling with both the DHC networks. In particular, the revamping of a plant operating with small-scale gas turbines is explored. The heat rejected from the CO_2 power block together with the heat recovered from low temperature exhaust gases is used to produce pressurized hot water for the district heating (DH) during winter season and chilled water for the district cooling (DC) during summer season. Finally a techno – economic analysis is carried-out comparing the original and proposed system layouts in order to minimize the differential electricity production cost. Aspen Plus® V12 (*Aspen Plus* n.d.) is selected as modeling software for all the analyses.

2 ABSORPTION CHILLER

An absorption chiller produces cold thermal power (typically chilled water) exploiting a low-medium temperature heat source, adopting a thermodynamic cycle with a mixture of a refrigerant and an adsorbent (Somers et al., 2011). In this work both single effect AC (SEAC) and double effect AC (DEAC) are investigated using H_2O-LiBr (lithium bromide) mixture as working fluid.

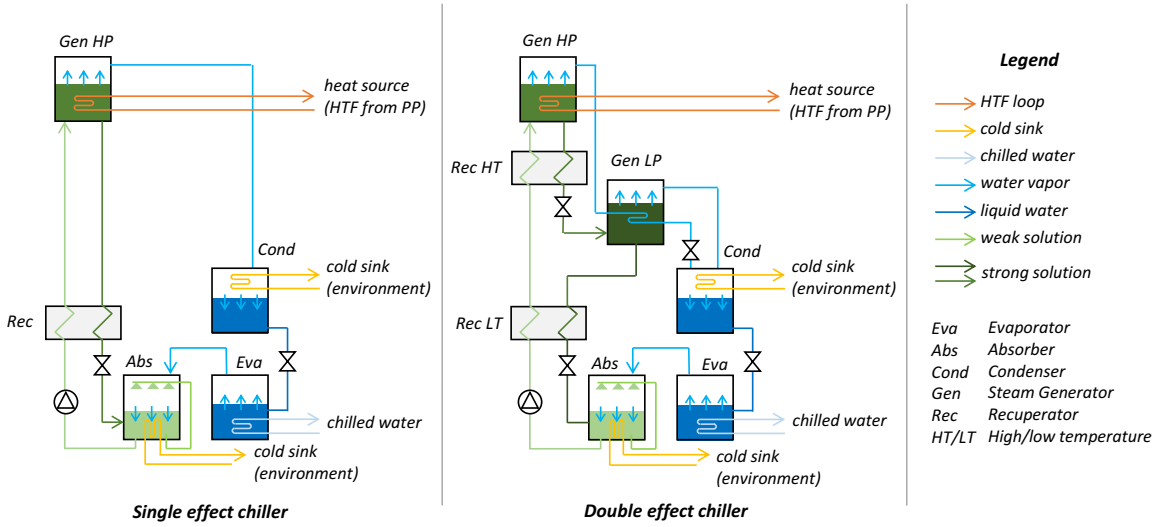

Figure 1: Absorption chiller layout: single effect (left) and double effect (right).

Typically, SEAC works at lower pressures (up to 10 kPa) in the vapor generator and exploits heat source temperatures lower than 100°C, leading to COP values of around 0.7. Meanwhile, DEAC and multi effect AC work at higher pressure levels (up to 100 kPa), heat source temperature up to 160°C–180°C, generally resulting in COP above 1 (Somers et al., 2011). In a SEAC (Figure 2 left), the pumped mixture is pre-heated in a recuperator and then heated by the hot source in the generator, up to a partial evaporation, depending on temperature and pressure. The LiBr-rich flow (strong solution) is conveyed to the recuperator, depressurized and fed to the absorber. The generated vapour is first condensed using ambient air as cold sink and expanded down to the evaporation pressure. The pressure levels are set by saturation conditions at the temperature T_{cond} and T_{eva}. In the evaporator, cold thermal power is produced typically by cooling down chilled water. The refrigerant enters the adsorber where is mixed with the strong solution, cooled down and send to the pump. In the DEAC solution (Figure 2, right), a layout with two generators in series at different pressure levels is adopted since this layout allowed the

employment of only one pump is adopted (Farshi et al., 2012). As shown in Figure 2 the strong solution exits from the high-pressure generator and it is expanded to an intermediate pressure, corresponding to condensation pressure. Then the evaporated water and strong solution flow into the components previously presented. The advantage of the double effect is to separate more water from the solution, thus increasing the cooling capacity and COP. The H_2O-LiBr mixture is modelled with the ELECNRTL pre-defined package in ASPEN Plus, as suggested in literature (Somers et al., 2011). The boundary conditions and assumptions, which are consisted with other works (Somers et al., 2011) (Farshi et al., 2012), for the simulation of the AC are reported in Table 1.

Table 1: Simulation boundary conditions and assumptions for the absorption chiller

Chiller Parameter	
Condensation conditions, T_{cond}/P_{cond}	40 °C / 7.38 kPa
Evaporation conditions, T_{eva}/P_{eva}	3 °C / 0.75 kPa
LiBr concentration (massic)	55%
Minimum approach temperature difference in the generators	5 °C
Pitch point temperature difference in the generators	5 °C
Temperature approach for DC-AC	3 °C

The thermal power is provided by pressurized water that works as heat transfer fluid (HTF). The analysis consists in identify the COP, defined in Eq. (1) as the ratio between the cooling capacity $\dot{Q}_{CC}$ and the thermal input $\dot{Q}_{HTF}$, for various conditions of the HTF, neglecting the electric consumption of the pump (Osta-Omar & Micallef, 2016).

$$COP = \frac{\dot{Q}_{CC}}{\dot{Q}_{HTF}} \tag{1}$$

An optimization analysis is carried out on the maximum pressure of the double effect cycle to find the best value of COP for each HTF maximum temperature ($T_{HTF,in}$) and HTF temperature difference (ΔT_{HTF}), compatible with system constraints. In fact, according to the Dühring chart, crystallization phenomena occurs when the mass concentration of LiBr is above 65% (Salehi et al., 2019). For this reason, the maximum pressure level must be compatible with this threshold to prevent pipes and components clogging. The resulting trends of the COP for both configurations are reported in Figure 2.

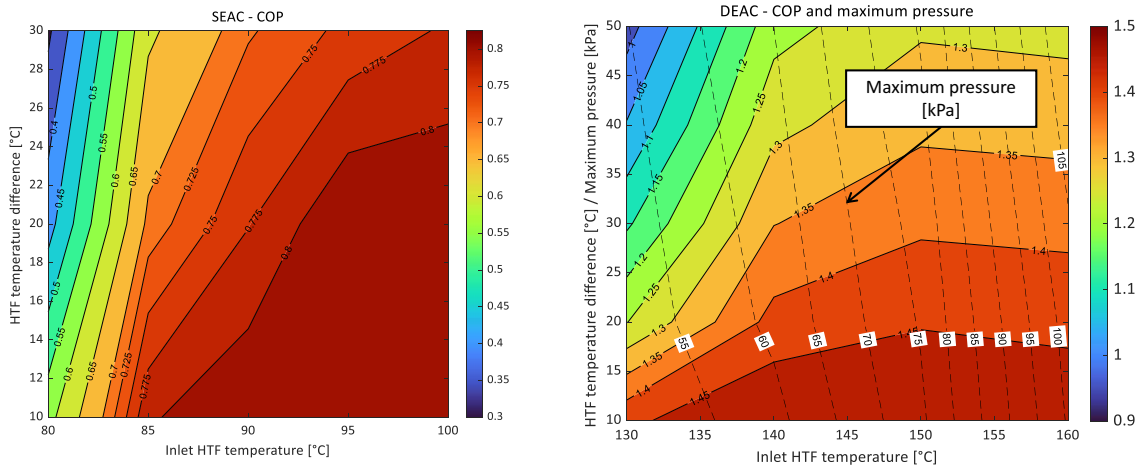

Figure 2: Absorption chiller COP: single effect (left) and double effect (right)

For both categories of AC, higher COP are computed at high $T_{HTF,in}$ and low ΔT_{HTF} (close to isothermal hot source), with a flat response over a certain value of $T_{HTF,in}$, equal to 95°C and 150°C for the SEAC and DEAC, respectively. As in the SEAC the pressure level is fixed by the condensation condition, increasing the $T_{HTF,in}$ corresponds to a higher vapor fraction leading to a higher cooling capacity. Situations in which the ΔT_{HTF} is low also correspond to conditions in which the internal regeneration of the AC is greatest. Therefore, at high $T_{HTF,in}$ the COP is favoured by greater steam production and,

at the same time, by less $\dot{Q}_{HTF}$ introduction at low ΔT_{HTF}. In the DEAC, every case is optimised maximising the COP and varying the maximum pressure, so this effect is not evident and it is possible to achieve a COP in the range between 1.25 and 1.45 even with relatively low $T_{HTF,in}$ and large ΔT_{HTF}. In the DEAC the optimum high pressure varies from 50 kPa to 105 kPa and for each case, the limit is set due the reaching of the crystallization constraint.

3 CASE STUDY

An existing trigeneration power plant, located in the city of Milan (A2A, 2023), is selected as case study. In Table 2 the components and the power balance of the system are listed. The electric power is produced by two Taurus 60S-7801 5MWe gas turbines by Solar Turbine (Taurus 60, n.d) each one powered by natural gas with an input thermal power of 17 MW. The expander outlet temperature is 510°C and the flue gas mass flow rate is 43.22 kg/s. In this study, the heat recovery units and the compressors chiller are replaced by a trigenerative CO_2 based power cycle for additional electricity production.

Table 2: Trigeneration power plant components

Components	Power
Gas turbines	10 MWe
Heat recovery steam generator	16 MWth
Compressor chillers	7.5 MWth

3.1 CO_2 power cycles

For the power cycles analysis, the stack temperature is set to 120°C leading to an available thermal power ($\dot{Q}_{fg}$) of 18.33 MW from both turbines at full load. The flue gas directly releases heat to the working fluid with a minimum temperature approach of 30°C in the primary heat exchanger (PHE) thus avoiding the use of a high temperature HTF loop. The cascade cycle is selected for this application as suggested by a previous work (Morosini et al., 2023) and it is here proposed in two different architectures (Figure 3) differing in one recuperator with the aim to consider three different design criteria: maximization of thermal recovery (MTR) namely ensure a complete exploitation of the heat source from the power plant, maximization of the power production (MPP) and maximization electric efficiency (MEE). Each cycle is investigated with both pure CO_2 in supercritical cycle and mixture of CO2 and dopant in transcritical cycle.

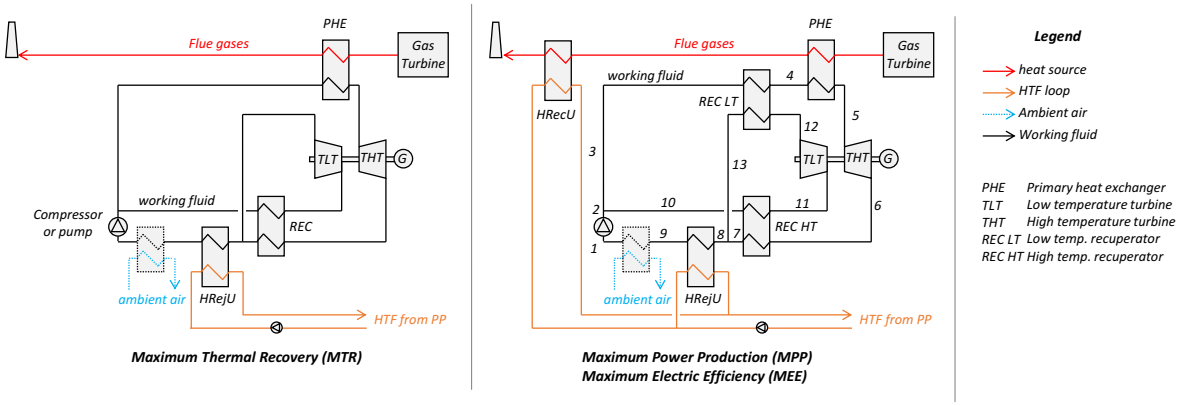

Figure 3: Cascade Cycle. MTR configuration (left), MPP/MEE (right)

MTR cycle adopts only one recuperator to exploit the heat available from high temperature turbine exhaust for heating the fluid expanded by the low temperature turbine. As result the heat introduction process starts right after the compressor (pure CO_2 cycle) or the pump (CO_2 mixtures), allowing for a complete cooling of the heat source in the power cycle heat introduction process and leading to a heat

source recovery factor ($\chi = \dot{Q}_{PHE}/\dot{Q}_{fg}$) equal to 1. The heat rejected by the cycle is recovered in the HRejU unit by heating up a HTF loop (Figure 3). On the contrary MPP and MEE cycles adopt an additional recuperator that allows to preheat the high temperature working fluid loop fluid before the heat introduction by cooling down the hot working fluid released by the low temperature turbine. In this case, the internal heat recovery is improved allowing to increase the cycle thermodynamic efficiency at the expense of the heat source recovery factor. As a result, the heat source is not totally exploited and thus after the power plant utilization it can still release heat to the HTF loop in the HrecU unit (Figure 3). A sensitivity analysis is carried out on the minimum cycle temperature ($T_{min,cy}$) between 50°C and 70°C considering ambient air as cold sink when the plant is not working in cogenerative mode or when a fraction of the rejected thermal power cannot be used for HTF heating. For each design criteria (MTR, MPP, MEE), for each minimum temperature and for both pure CO_2 and blended CO_2, the power plant (for a total number of 30 cases) is optimized with the aim to maximized the electric power for MTR (while guaranteeing $\chi = 1$) and MPP architectures and to maximize electric efficiency for MEE one. The following design parameters are varied to identify the optimal design: i) minimum pressure which impacts on the dopant molar fraction for working fluid blends, ii) split fraction after the pump and iii) maximum cycle temperature. Table 3 reports the assumed values for the analysis: turbomachinery efficiencies refer to small-scale applications, while a maximum pressure (250 bar) is necessary in order to do not penalize the performance (Alfani et al., 2021) (Morosini et al., 2023) .

Table 3: Power block parameters

Cycle Parameter	
Cycle maximum pressure	250 bar
PHE minimum temperature approach	30 °C
Recuperators pinch point (MITA)	10 °C
Pressure drops (PHE/HRecU and HRejU)	3/1 bar
Pressure drops recuperator (HP/LP)	1/2 bar
Isentropic efficiency (expander/compression)	85/80 %
Generator/Motor efficiency, $\eta_{g/m}$	97/97 %

Table 4 provides the properties for the chosen working fluids. Hexafluorobenzene (C_6F_6) is the selected dopant because its high thermal stability (up to 600°C) and the mixture is modelled with the Peng Robinson EoS (Di Marcoberardino et al., 2022). Differently, CO_2 is modelled with the Span and Wagner EoS (Span & Wagner, 1996).

Table 4: Pure fluids and mixture properties

Fluids	**Molar weight [kg/kmol]**	**T_{cr} [°C]**	**P_{cr} [bar]**	**Binary interaction parameter [-]**
CO_2	44.01	31.06	73.83	$k_{ij} = 0.16297 - 0.0003951 \cdot T\ [K]$
C_6F_6	186.06	243.58	32.73	

3.2 District heating and cooling system

The water for DH is supplied at 95°C and has a return temperature of 60°C (Mise, 2020) and the provided temperature range for the chilled water is from 6°C to 12°C (AIRU - Annual Report, 2022). An intermediate loop (IL) of heat transfer fluid is implemented to avoid direct heat transfer between the power plant working fluid and both the district hating water or the absorption chiller mixture, as proposed in Figure 3. The temperature limits of the IL must be compatible with the source and utilization range; therefore, the selected IL range is defined once the temperature range of working fluid and gases are computed. A minimum temperature approach of 10°C is always considered in each heat exchanger.

3.3 Key Performance Indicators

The performance of the power plant is evaluated trough the electrical efficiency η_{el} and the differential levelized cost of electricity (LCOE). The first is defined in Eq. (2).

$$\eta_{el} = \frac{\sum \dot{W}_{TURB} \cdot \eta_{g/m} - \dot{W}_{pump/comp}/\eta_{g/m}}{\dot{Q}_{PHE}} = \frac{\dot{W}_{el}}{\dot{Q}_{PHE}} \quad (2)$$

From the economical point of view, the goal is finding the layout and the design parameters that minimize the differential LCOE related to the installation of the CO_2 based power plant with respect to a reference case where the electric power is produced only with the gas turbines and the hot and cold thermal power are produced from a total exploitation of the exhaust gases sensible content ($\dot{Q}_{fg}$), and the second, representing the solution proposed in this work. Therefore, the yearly differential cost considers the annualized investment cost of the power block ($Capex$), the operating costs ($O\&M$) and the profit loss related to the reduced fraction of hot and cold thermal power with respect to the reference scenario because of electrical power production. LCOE is expressed as follow:

$$LCOE = \frac{Capex \cdot CRF + O\&M + \Delta E_{hot} \cdot LCOH + \Delta E_{cold} \cdot LCOC}{8760 \cdot u_{el} \cdot \dot{W}_{el}} \quad (3)$$

The $Capex$, corresponding to the sum of the equipment and Balance of Plant (BoP) costs, is calculated according to Weiland et al (Weiland et al., 2019), and the correlation of Wright et al (Wright et al., 2016) only for the gas-CO_2 PHE. The specific $O\&M$ is 30 \$/kW and the BoP cost are the 30% of the total equipment cost (Marchionni et al., 2018). $LCOH$ is the Levelized Cost Of Heating and it is equal to 80 \$/MWh (Næss-Schmidt et al., 2021), while the Levelized Cost Of Cooling (LCOC) is calculated by using the correlations and assumptions proposed by Correa et al (Correa-Jullian et al., 2019): assuming a COP of 1.3, LCOC is equal to 40 \$/MWh. The utilization factor u is 91% (corresponding to 8000h/year) while heat for DH is required for 41% of the running hours (15 weeks/year) and heat for the absorption chiller 24% of the running hours (9 weeks/year). The capital recovery factor (CRF) is 7.8%. ΔE_{hot} and ΔE_{cold} are the reduction of thermal energy and cooling energy with respect to the reference case.

287

4 RESULTS AND DISCUSSION

4.1 Considerations on Cycle optimization

For the MTR and MPP conditions (pure CO_2), optimal cycle minimum pressure is rather constant while reducing the cycle maximum temperature has two opposing effects: from one hand it allows to increase the heat input to the cycle by reducing the recuperator outlet temperature, while, on the other hand, it implies a reduction of cycle efficiency. However, the two effects are nearly balanced and the power output varies by less than 1.5% in the cycle maximum temperature optimal range between 440°C and 480°C. For MEE the highest cycle efficiency corresponds to a turbine inlet temperature of 480°C (compatible with the minimum temperature approach in PHE). Results reported in this paper refer only to the optimal cases and nominal conditions.

4.2 Power Cycle Performance

Figure 4 depicts the trend of electric efficiency and power output for all the cycle combination varying the cycle minimum temperature.

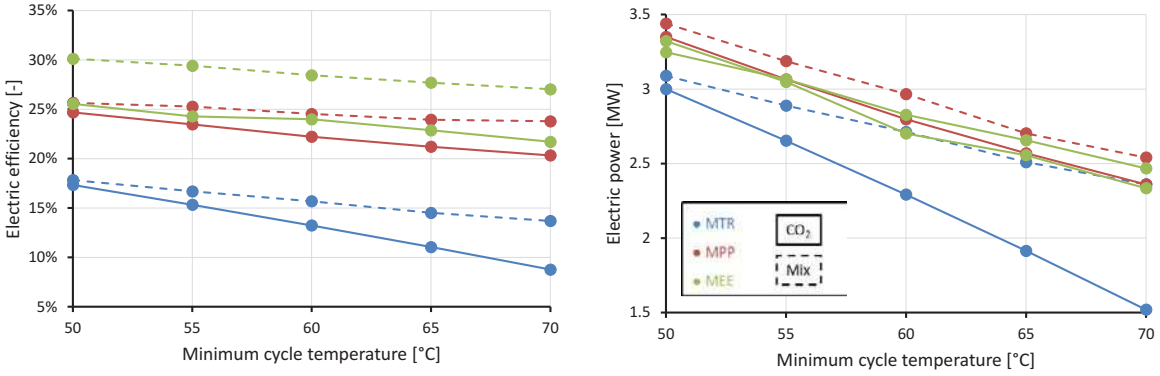

Figure 4: Electric efficiency (left) and electric generation (right)

Increasing the $T_{min,cy}$ implies a penalization of the cycle performance due to the increase of fluid specific volume (for pure CO_2 cycles) and reduction of the pressure ratio (blended CO_2) but the effect is more marked for the pure CO_2 cases since transcritical cycles always benefit by a fluid pressurization in liquid state that is less affected by change in the working fluid volumetric behavior. Among the different cycles configuration, the MTR cycle with CO_2 is the most penalized one since the need of ensuring a complete heat source cooling in the PHE which results in a limitation of the cycle pressure ratio and leads to cycle minimum pressures higher than the optimal one: all these effects are exacerbated when the cycle minimum temperature increases. While the use of pure CO_2 always leads to the lowest efficiency and power production it is interesting to note that the MTR cycle with CO_2 mixture for high cycle minimum temperature can get a power output close to the other cycles because the lower efficiency is compensated by and higher recovery factor with respect to both MPP and MEE configurations. The complete cascade cycle featuring also the second recuperator in both MPP and MEE cases outperform the MTR thanks to a more effective regeneration. In the MEE case, the TIT (Turbine Inlet Temperature) is set to the maximum value of 480°C, compatible with the constraint on the minimum pinch temperature at the PHE, justifying the highest electric efficiency. At the same TIT, the mixture has higher thermodynamic efficiency (around +3%) thanks to more balanced heat capacities within the recuperators. However pure CO_2 takes advantage of the lower PHE inlet temperature due to an unbalanced recuperator, experiencing higher electrical output. This effect is true only at low cycle minimum temperature, while at high temperatures an evident efficiency drops of pure CO_2 compared to the mixture can be noticed due to the increase of the compressibility factor. As regards the MPP strategy, which represents the trade-off between the heat source cooling grade and the cycle efficiency, the mixture outperforms pure CO_2 even if the optimal TIT is around 10°C lower to provide a more effective heat source cooling, without involving a substantial cycle efficiency penalization. In fact, pure CO_2 suffers both the distance from the critical point and the unbalanced recuperators, while the mixture keeps the benefits of liquid compression and balanced heat capacities by varying the composition.

288

4.3 Hot and cold power nominal availabilities

Thermal power is released by the system to the IL through the HRecU and HRejU units that completes the flue gas cooling down to stack temperature and collects the useful heat released by the cycle respectively. The amount of heat collected by each unit depends on the specific cycle layout, the optimization strategy, and minimum cycle temperature, as shown in Figure 5 for 50°C and 70°C cycle minimum temperature cases. Moreover Figure 6 summarizes the resulting annual produced energy. In the MTR configuration, the entire thermal duty of the sensible heat source is provided to the cycle through the PHE and exploited with a relatively-low cycle efficiency compared to the other layouts considered (Figure 3), but the amount of rejected thermal power from the HRejU unit is considerable as represented in Figure 5. The good temperature level (above 180°C of the rejected heat) provided by the MTR configuration allows the exploitation of the total duty for DH and DC purposes, depending on

the seasonal need. Above 100°C the HRejU is used in a DEAC, while the fraction below 100°C in a SEAC, with COP evaluated according to the maps in Figure 2.

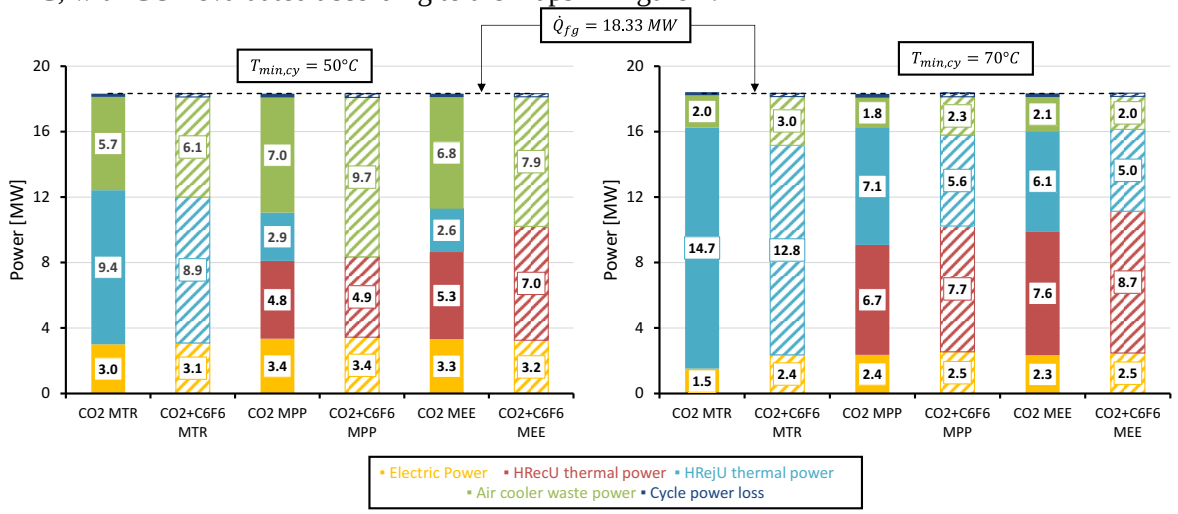

Figure 5: Power balance for $T_{min,cy} = 50°C$ (left) and $T_{min,cy} = 70°C$ (right) in winter season.

On the other hand, the MEE and MPP configurations present a good fraction of thermal power available also from the HRecU at high temperatures (above 220°C), that can be entirely used for DH and DC through a DEAC. As regards the HRejU unit of these configurations, the thermal duty available for DH purposes strongly depends on the cycle minimum temperature since the required temperature range for the intermediate HTF is 70-100°C. Due to this limitation, an air cooler is always necessary to dissipate the residual thermal power. Instead, in summer season, the terminal temperatures of the HTF loop can be adjusted to exploit the entire rejected duty in a SEAC, with an associated COP depending on the specific temperature range and the air cooler is not required. As highlighted in Figure 6, the best annual energy production is reached with the mixture in MEE strategy at 70°C minimum temperature, mainly due to better thermodynamic efficiency compared to CO_2 and higher valuable heat at the HrecU for DC and DH.

289

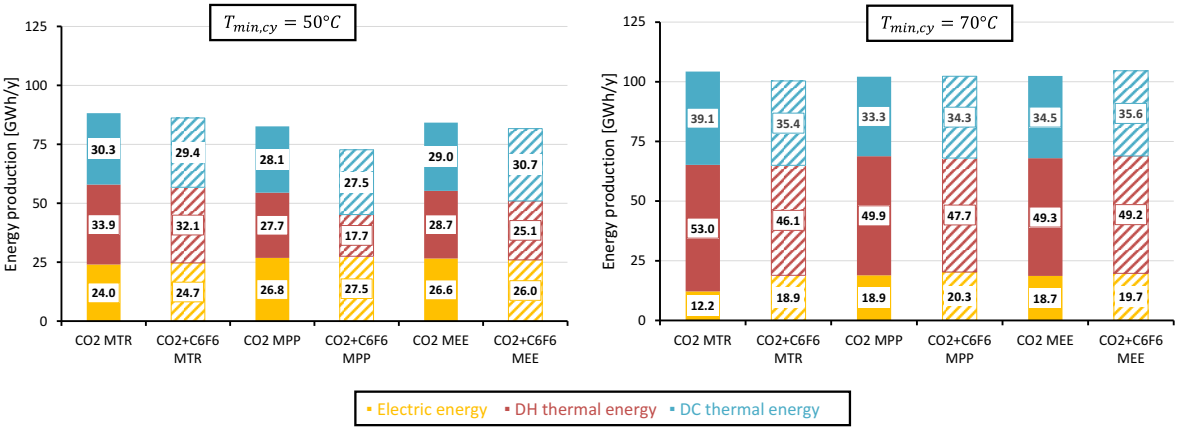

Figure 6: Annual energy production for $T_{min,cy} = 50°C$ (left) and $T_{min,cy} = 70°C$ (right).

4.4 Differential LCOE

Previous results suggests that the cycles operating with a minimum cycle temperature of 70°C are reasonably the most promising ones since they allow to heat rejection to the environment during both summer and winter season, thus only this case is considered in this preliminary economic analysis. Figure 7 shows the resulting differential LCOEof the different cases, as expressed in Eq. (3), highlighting the $Capex$ and $O\&M$ costs and the costs relating to the missed selling of heat and cold. Considering the annual energy balance depicted in Figure 6 (right), the higher electricity output

produced by the mixture based cycles, with respect to the cycle operating with pure fluid, lead to a reduction of the LCOE. On the other hand, the CO_2 MTR case of is characterized by the minimum ΔE_{hot} and ΔE_{cold} because of the highest annual thermal production. Nevertheless, the annual electric production mainly affects the differential LCOE. Considering only electricity as output, all the analyzed cases are economically viable compared to different Italian electric gross prices (PUN – Prezzo Unico Nazionale) (GME, 2023), however the cases that has a lower electric energy generation are the most penalized.

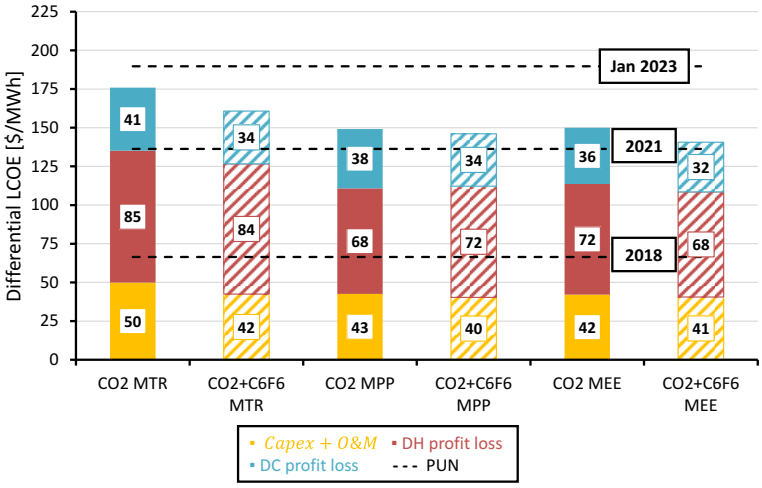

Figure 7: Differential LCOE for $T_{min,cy} = 70°C$ cases compared to the Italian PUN.

MPP configuration has the lowest specific power cycle cost ranging from 3736 $/kW for the mixture to 4723 $/kW for CO_2 since the larger power production is not obtained with a substantial increase of equipment cost with respect to the MEE case. MTR case is on the contrary the most penalized one since it does not maximize power production and uses large heat exchangers to provide complete heat source coolingleading to a cost of 176 $/MWh. Also accounting for profit losses due to the missed selling of heating and cooling due to power production the LCOE strongly increases leading to final values that are up to three times higher than the LCOE due to only $Capex$ and $O\&M$ costs. MEE case with mixture has the lowest differential LCOE with values around 140 $/MWh. The studied trigeneration plant is economically feasible for PUN related to the recent years where the geopolitical circumstances lead to a very variable natural gas price and the relative PUN. On the contrary, adopting lower PUN prices related to a more stable global situation the installation of a cogenerative power plant would require incentives or the application of carbon tax to fossil fuel use to be economically competitive as generally true for any cogenerative power system.

290

5 CONCLUSIONS

In this paper, a theoretical revamp of a trigeneration plant is presented. By first analyzing the H_2O-LiBr absorber, it is possible to quantify the COP at different heat source condition. Then, simulations were carried out on a heat recuperative plant with different designs using CO_2 and a CO_2 mixture as working fluids. The maximum thermal recovery configuration in the PHE has higher thermal energy production comparing MPP and MEE, however on the economic aspect, the MTR presents a high differential LCOE due to the lowest electric energy production. The MPP strategy ensures high electric production and it proves to be the ideal approach when only energy production is considered as useful outcomes. However, for trigenerative scopes, the MEE configuration presents a good compromise between outputs and investment cost. The mixture of CO_2 and C_6F_6 is preferrable with respect to pure CO_2.

NOMENCLATURE

Acronyms

AC	Absorption Chiller
BoP	Balance of Plant
Capex	Capital Expenditure
COP	Coefficient Of Performance
CRF	Capital Recovery Factor
DC	District Cooling
DEAC	Double Effect Absorption Chiller
DH	District Heating
ELECNRTL	Electrolyte-NRTL
HRecU	Heat Recovery Unit
HRejU	Heat Rejection Unit
HTF	Heat Transfer Fluid
IL	Intermediate Loop
IEA	International Energy Agency
MITA	Minimum Internal Temperature Approach
MPP	Maximum Power Production
MEE	Maximum Electric Efficiency
MTR	Maximum Thermal Recovery
O&M	Operation & Maintenance
PHE	Primary Heat Exchanger
PUN	Prezzo Unico Nazionale
SEAC	Single Effect Absorption Chiller
TIT	Turbine Inlet Temperature

Roman and Greek letter

P	Pressure	bar/kPa
$\dot{Q}$	Thermal power	MW
T	Temperature	°C
$\dot{W}$	Mechanical Power	MW
ΔT	Temperature difference	°C
η	Efficiency	(-)
χ	Recovery factor	(-)

Chemical formula

CO_2	Carbon Dioxide
C_6F_6	Hexafluorobenzene
H_2O	Water
$LiBr$	Lithium Bromide

Subscript

comp	compressor
cond	condensation
cy	cycle
el	electric
eva	evaporation
fg	flue gases
g	generator
m	motor
min	minimum
pump	pump
turb	turbine

APPENDIX A

Table 5: Streams thermodynamic properties for the best economic case for pure fluid and mixture. For the mixture case the dopant fraction is 19%.

	CO_2 + C_6F_6 MEE Case				CO_2 MPP Case			
Stream	**Flow [kg/s]**	**T [°C]**	**P [bar]**	**Vapor Frac. [-]**	**Flow [kg/s]**	**T [°C]**	**P [bar]**	**Vapor Frac. [-]**
1	66.1	70	93.5	0	72.7	70	118	1
2	66.1	93.9	254	0	72.7	129.8	254	1
3	35.7	93.9	254	0	38.5	129.8	254	1
4	35.7	278.5	253	1	38.5	236.8	253	1
5	35.7	480	250	1	38.5	470	250	1
6	35.7	412.8	97.9	1	38.5	390.3	122	1
7	35.7	118.6	96.9	0.71	38.5	139.8	120	1
8	66.1	114.3	95.9	0.67	72.7	139.8	120	1
9	66.1	80	94.9	0.28	72.7	80	119	1
10	30.4	93.2	254	0	34.2	129.8	254	1
11	30.4	400.8	253	1	34.2	379.3	253	1
12	30.4	334.4	96.9	1	34.2	303.3	122	1
13	30.4	109.6	95.5	0.64	34.2	139.8	120	1

REFERENCE

- International Energy Agency, I. (n.d.). *The Future of Cooling Opportunities for energy-efficient air conditioning Together Secure Sustainable*. Retrieved March 7, 2023, from www.iea.org/t&c/

AIRU-the Italian District Heating Association-promotes and spreads the application and innovation of energy installations in district heating systems. (n.d.). www.ecoline.it

Alfani, D., Binotti, M., Macchi, E., Silva, P., & Astolfi, M. (2021). sCO2 power plants for waste heat recovery: design optimization and part-load operation strategies. *Applied Thermal Engineering*, *195*, 117013. https://doi.org/10.1016/J.APPLTHERMALENG.2021.117013

Aspen Plus | Leading Process Simulation Software | AspenTech. (n.d.). Retrieved April 11, 2023, from https://www.aspentech.com/en/products/engineering/aspen-plus

Bellos, E., Said, Z., Lykas, P., & Tzivanidis, C. (2022). A review of polygeneration systems with CO2 working fluid. *Thermal Science and Engineering Progress*, *34*, 101435. https://doi.org/https://doi.org/10.1016/j.tsep.2022.101435

Correa-Jullian, C., Crespo, A., Cortés, F., & Ibarra, M. (2019). *Simulation of a Solar Fired Absorption System for a Case Study in the Dairy Industry*. 1–10. https://doi.org/10.18086/EUROSUN2018.04.16

Di Marcoberardino, G., Morosini, E., Di Bona, D., Chiesa, P., Invernizzi, C., Iora, P., & Manzolini, G. (2022). Experimental characterisation of CO2 + C6F6 mixture: thermal stability and vapour liquid equilibrium test for its application in transcritical power cycle. *Applied Thermal Engineering*, 118520. https://doi.org/10.1016/j.applthermaleng.2022.118520

Farshi, L. G., Seyed Mahmoudi, S. M., Rosen, M. A., & Yari, M. (2012). *Use of low grade heat sources in combined ejector-double effect absorption refrigeration systems*. https://doi.org/10.1177/0957650912446902

IEA. (2022). *Heating*. https://www.iea.org/reports/heating

Macchi, E., & Astolfi, M. (2017). *Organic Rankine Cycle (ORC) Power Systems - 1st Edition* (1st Editio). https://doi.org/https://doi.org/10.1016/C2014-0-04239-6

Marchionni, M., Bianchi, G., & Tassou, S. A. (2018). Techno-economic assessment of Joule-Brayton cycle architectures for heat to power conversion from high-grade heat sources using CO2 in the supercritical state. *Energy*, *148*, 1140–1152. https://doi.org/10.1016/J.ENERGY.2018.02.005

MISE. (2020). *Progetto modifica della Centrale di teleriscaldamento di Milano Bicocca, localizzata nel Comune di Milano - Info - Valutazioni e Autorizzazioni Ambientali - VAS - VIA - AIA*. https://va.mite.gov.it/it-IT/Oggetti/Info/7576

Morosini, E., Doninelli, M., Alfani, D., Astolfi, M., Di Marcoberardino, G., & Manzolini, G. (2023). Analysis of the potential of CO2 based mixtures to improve the efficiency of cogenerative waste heat recovery power plants. *5th European SCO2 Conference for Energy Systems: March 14-16, 2023, Prague, Czech*

Republic, 169–178. https://doi.org/10.17185/DUEPUBLICO/77287

Næss-Schmidt, S., Jensen, H. N., & Jasper, L. (2021). *District heating tariffs in Europe. Comparison of tariffs and regulation in Europe*. *April*, 1–36. https://open.overheid.nl/repository/ronl-ec66e0006b7e0acc22629091d63b448a4af5b0c3/1/pdf/heating-tariffs-in-europe.pdf

Osta-Omar, S. M., & Micallef, C. (2016). Mathematical Model of a Lithium-Bromide/Water Absorption Refrigeration System Equipped with an Adiabatic Absorber. *Computation 2016, Vol. 4, Page 44*, *4*(4), 44. https://doi.org/10.3390/COMPUTATION4040044

Salehi, S., Yari, M., Mahmoudi, S. M. S., & Farshi, L. G. (2019). Investigation of crystallization risk in different types of absorption LiBr/H2O heat transformers. *Thermal Science and Engineering Progress*, *10*, 48–58. https://doi.org/10.1016/J.TSEP.2019.01.013

Somers, C., Mortazavi, A., Hwang, Y., Radermacher, R., Rodgers, P., & Al-Hashimi, S. (2011). Modeling water/lithium bromide absorption chillers in ASPEN Plus. *Applied Energy*, *88*(11), 4197–4205. https://doi.org/10.1016/J.APENERGY.2011.05.018

Span, R., & Wagner, W. (1996). A new equation of state for carbon dioxide covering the fluid region from the triple-point temperature to 1100 K at pressures up to 800 MPa. *Journal of Physical and Chemical Reference Data*, *25*(6), 1509–1596. https://doi.org/10.1063/1.555991

Weiland, N. T., Lance, B. W., & Pidaparti, S. R. (2019). SCO2 power cycle component cost correlations from DOE data spanning multiple scales and applications. *Proceedings of the ASME Turbo Expo*, *9*. https://doi.org/10.1115/GT2019-90493

Wright, S., … C. D.-F. I. S., & 2016, undefined. (2016). Thermo-economic analysis of four sCO2 waste heat recovery power systems. *Sco2symposium.Com*. http://sco2symposium.com/papers2016/SystemModeling/059paper.pdf

ACKNOWLEDGEMENT

This publication was produced while attending the PhD programme in *PhD in Sustainable Development And Climate Change* at the University School for Advanced Studies IUSS Pavia, Cycle XXXVIII, with the support of a scholarship financed by the Ministerial Decree no. 351 of 9th April 2022, based on the NRRP - funded by the European Union - NextGenerationEU. (web site phd-sdc.it).

This study was carried out within the *NEST - Network 4 Energy Sustainable Transition* (D.D. 1243 02/08/2022, PE00000021) and received funding under the National Recovery and Resilience Plan (NRRP), Mission 4 Component 2 Investment 1.3, funded from the European Union - NextGenerationEU. This manuscript reflects only the authors' views and opinions, neither the European Union nor the European Commission can be considered responsible for them.

ORC SEVILLE 2023
7th International Seminar on O.R.C. Power Systems

© 2024 Editorial Universidad de Sevilla. Este es un artículo de acceso abierto distribuido bajo los términos de la licencia de uso y distribución Creative Commons (BY-NC-ND 4.0)

DOI: https://dx.doi.org/10.12795/9788447227457_46

Thermodynamic analysis of a novel pumped thermal energy storage system with waste heat integration

Meiyan Zhang, Lingfeng Shi*, Peng Hu, Gang Pei, Gequn Shu

Department of Thermal Science and Energy Engineering, University of Science and Technology of China, Hefei 230027, China

*Corresponding Author: slf@ustc.edu.cn

ABSTRACT

Pumped thermal energy storage (PTES) system is a large-scale electricity storage technique, and the thermally integrated PTES system has been brought forward to raise the energy storage efficiency and extend feasible ways to utilize the low-grade waste heat (<100 °C). The solutions to raise the power-to-power efficiency of the thermally integrated PTES system have aroused much attention worldwide. This paper presents an innovative thermally integrated PTES system, in which the two-stage heat pump with an economizer is incorporated into the PTES system. Despite utilizing the waste heat at charge time, the low-grade waste heat is also poured into the discharging process innovatively. The simulation model of the thermally integrated PTES system is established in the software MATLAB, and the physical properties of the substances are acquired from the software Refprop 10. The parameters of the PTES system are displayed and the power-to-power efficiency of the PTES system is investigated under various thermal storage temperatures. The results indicate that the power-to-power efficiency increases first and then declines as the low heat storage temperature rises when the high heat storage temperature is deemed. However, the energy storage density of the system dwindles with the increment of low heat storage temperature. The rise of the component efficiency contributes to the improvement of the power-to-power efficiency obviously, which can reach 87.3% as the isentropic efficiencies are 90%. The exergy destruction in the heat exchangers and mechanical components occupy a large proportion of the overall exergy destruction, which infers that the modification of the heat transferring and expansion/ compression processes are viable for performance enhancement.

294

1 INTRODUCTION

Carbon dioxide (CO_2) emissions pose a great threat to the global environment as a culprit of global warming (Deng et al., 2023). United Nations Framework Convention on Climate Change (UNFCCC) established an international environmental treaty to limit the increase in global mean temperature relative to pre-industrial times to less than 2 °C (JebabliLahiani & Mefteh-Wali, 2023). As the world's largest CO_2 emitter, China has actively undertaken the responsibility for net-zero emission, pledging to peak carbon dioxide by 2030 and achieve carbon neutrality by 2060 (Jiang & Xia, 2023). With the continuous rising of the market share of renewable energy, especially solar energy, and wind energy, the mismatches between renewable energy supplies and load demands result in challenges for integrating renewable resources into the existing power grids (Liu et al., 2020). In consequence, the energy storage system should be implemented for peak shaving, load balancing, and improving the flexibility and resiliency of the power grid (KazemiTabatabaei & Moslemi, 2023; Yong, Wu, Zhou, Tao, & Chen, 2023).

The energy storage technique has aroused much attention in recent years, which can be classified into physical energy storage, electrochemical energy storage, and so on. Pumped thermal energy storage (PTES) is a branch of the physical energy storage technology (Dumont et al., 2020) and has been recognized as a promising energy storage technique with large potential, owing to the advantages of unlimited by geographical locations, high energy storage density (up to 16.86 kWh/m^3) (FrateFerrari & Desideri, 2020) and small installation footprint (Vecchi et al., 2022). The conventional low-temperature

PTES system faces the problem of relatively low round-trip efficiency as compared to other large-scale storage technologies (Zhang, Shi, Hu, Pei, & Shu, 2023). Therefore, the thermally integrated PTES system has been brought forward to improve the power-to-power efficiency, in which the low-grade waste heat from many fields (for instance, industrial waste heat, solar energy) is delivered to the charging process of the PTES system and works as the low-temperature heat source of the heat pump (HP). Many scholars have devoted much work to investigating the performances of the PTES system with heat integration from the views of selecting and matching superior working fluids in different processes (Hassan et al., 2020), evaluating thermal storage medium (Eppinger, Zigan, Karl, & Will, 2020) and searching efficient system configurations.

As the charging process and the discharging process of the thermally integrated PTES system lie in a different range of working temperatures, the configurations should be designed separately to attain high energy utilization efficiency. As can be discovered from the published literature, most studies carried out the research based on the basic structure of the charging and discharging process (Fan & Xi, 2022; FrateFerrari & Desideri, 2020; Kurşun & Ökten, 2022), namely the recuperated/ non-recuperated HP and the recuperated/ non-recuperated ORC. Weitzer et al. compared the performances of various PTES systems that based on ORC and organic flash cycle (OFC) (Weitzer et al., 2022), the results indicate that the OFC with two-phase expander outperforms the ORC for large thermal storage temperature spreads and the off-design performance of the two-phase expansion has also been evaluated (WeitzerMüller & Karl, 2022). What's more, the PTES system with OFC as the discharging process was also evaluated by (Tian & Xi, 2022) and (Wang et al., 2022), and the analyses show that the PTES system with the OFC is worse than that of the PTES system caused by the large exergy destruction in the pressure reducing valve. Apart from utilizing the low-grade waste heat in the charging process, (Zhang et al., 2023) presented an advanced thermally integrated PTES system, in which the waste heat is also conveyed to the discharging process to warm the working fluid. The evaluation results explain that the power-to-power efficiency can be promoted by 18.4% in contrast to the conventional PTES system as the thermal storage temperature is 130 °C.

Although a volume of research has focused on searching various kinds of PTES system configurations to improve power-to-power efficiency, the concerning study should also be carried out deeply to dig out new effective configurations for the thermally integrated system. Against this backdrop, this paper proposed a novel thermally PTES system, in which both the charging process and the discharging process are updated with new configurations. To be specific, the charging process includes parallel compression and an economizer with the intent of reducing the energy destruction in the pressure-reducing valve. In the discharging process, the waste heat is applied to assist the heating process of the working fluid into the expander. Furthermore, the proposed thermally integrated PTES system is evaluated under various internal parameters. In section 2, the proposed thermally integrated PTES system is put forward. In section 3, the basic assumptions for model construction and thermodynamic indicators are presented. In section 4, the parameters analysis and exergy evaluation results are shown. In section 5, the main conclusions of the paper are drawn.

2 SYSTEM DESCRIPTION

To improve the energy storage efficiency of the thermally integrated PTES system, a novel PTES system with heat integration has been proposed to exploit the energy utilization potential of the low-grade waste heat, as displayed in Figure 1. Moreover, the T-S diagram of the proposed PTES system is also depicted in Figure 1. As can be discovered from the figure, the PTES system can be divided into three subsystems, namely the charging process (HP), the heat storage system, and the discharging process (ORC). Different from the traditional thermally integrated PTES system, the advanced PTES system adopts the parallel compression HP at the charge time. Apart from working as the low-temperature heat source of the HP, the low-grade waste heat has been also delivered to the ORC to preheat the working fluid at the inlet of the evaporator at the discharge time. In the charging process, the compressed working fluid from the two compressors is mixed and heat the heat storage medium in the condenser. Moreover, the working fluid out of the condenser splits into two streams, one of them is decompressed by valve 1, and the other stream flows into the economizer to release its heat energy. The liquid working fluid from the economizer goes into the recuperator for further temperature reduction and then reduces its pressure through valve 2 to absorb the waste heat in the evaporator. When there is

an electricity demand for the local area, the high-temperature heat storage medium heats the working fluid at the inlet of the expander, and the stream expands and drives the expander for power production. Furthermore, the working fluid condensed by the cooling water is warmed in the recuperator and the additional heater successively before entering the evaporator.

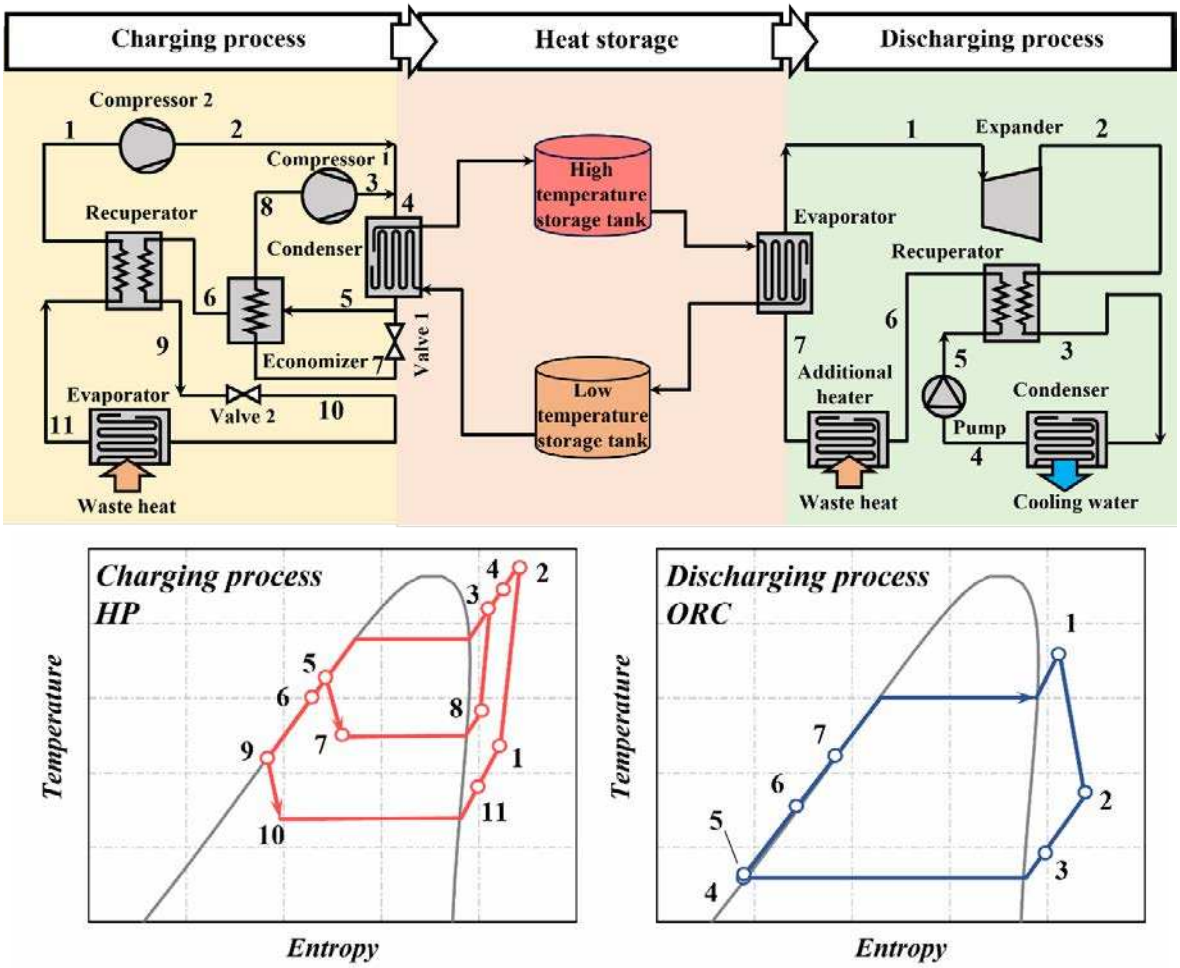

Figure 1: System configuration T-S diagram of the novel thermally integrated PTES system

3 METHODOLOGY

3.1 Basic assumptions

The software MATLAB is a mathematical calculation-based programming software widely used in many fields, which has been implemented to simulate the proposed PTES system in this work. The physical properties of the substances (organic working fluid and pressurized water) utilized in this paper is acquired from the software Refprop 10. The basic parameters of the novel PTES system are summarized in Table 1. The working fluid in the charging and discharging process affects the performance of the PTES system directly, which should be chosen carefully to achieve the best performance of the system. However, the selection of the working fluid is not in the scope of this study, and the working fluid applied in the HP and ORC is the R1233zd(E) for its advantages of safety properties and good performance. Under the consideration of the physical properties, safety, and economic feasibility, the thermal storage medium is selected as pressurized water. To compare the performance of the PTES system under different working conditions, the surplus power poured into the charging process is deemed as 1000 kW. The temperature differences of the phase change heat exchanger and the single-phase heat exchanger are chosen as 2 °C and 5 °C, respectively. Moreover, the isentropic efficiencies of the pump, the compressor, and the expander are 85%, and the efficiencies of the motor and the generator are also 98%. The thermal storage efficiency of the heat storage tank strongly depends on the construction material and the external conditions and should be determined by

the real experiment. For the simplicity of the theoretical research, the heat storage efficiency is assumed as 100% in this study.

Table 1: Basic parameters of the novel PTES system

Item	Unit	Value
Surplus power poured at the charge time	kW	1000
Temperature of the cooling water	°C	20
Temperature difference of the phase change heat exchanger	°C	2
Temperature difference of the single change heat exchanger	°C	5
Waste heat inlet temperature	°C	80
Waste heat outlet temperature	°C	60
Compressor efficiency	-	85%
Pump efficiency	-	85%
Motor efficiency	-	98%
Expander efficiency	-	85%
Generator efficiency	-	98%
Thermal storage efficiency	-	100%
Working fluid of the PTES system	-	R1233zd(E)

3.2 Thermodynamic modelling

Energy storage efficiency is a crucial performance indicator of the energy storage system. As low-grade waste heat (<100 °C) is widely distributed in various scenarios, for instance, industrial waste heat, solar energy, and geothermal energy, the waste heat utilized in the advanced PTES system is recognized as sufficient and free of charge. Therefore, the energy storage efficiency of the thermally integrated PTES system, namely the power-to-power efficiency, is defined as the ratio of the power output at the discharge time to the surplus power into the PTES system at the charge time.

$$\eta_{\mathrm{PTP}} = \frac{Power_{\mathrm{dischar}}}{Power_{\mathrm{char}}} \tag{1}$$

where $Power_{\mathrm{dischar}}$ is the electric power output of the PTES system at discharge time, kWh; $Power_{\mathrm{char}}$ is the electric power input of the PTES system at charge time, kWh.

During the charging process of the PTES system, the heat energy released from the condenser in the HP is stored in the high-temperature storage tank, and then the energy is delivered to the evaporator in the ORC for power production. The relationship between energy storage efficiency and the charging and discharging processes can be derived as below:

$$\eta_{\mathrm{PTP}} = COP * \eta_{\mathrm{st}} * \eta_{\mathrm{ORC}} \tag{2}$$

where the COP is the coefficient of the HP, the η_{ORC} is the efficiency of the discharging process, the η_{st} is the thermal storage efficiency of the heat storage tanks.

The energy storage density (ESD, kWh/m^3) is also an important indicator for the energy storage system, which is formulated as:

$$ESD = Power_{\mathrm{dischar}} / V_{\mathrm{tank}} \tag{3}$$

where the V_{tank} is the total volume of the high-temperature and low-temperature heat storage tanks, m^3.

Furthermore, the second law of thermodynamics has been also applied to evaluate the energy transmission process of the PTES system and thereby discover the energy-saving potential of the thermally integrated system. The exergy destruction in each component (for instance, the heat exchanger, the compressor, and the expander) can be described as Equation (3), which is formulated as the difference between the total exergy inflows and total outflows. The dead state of the exergy analysis is set to be 20 °C and 101.325 kPa.

$$EX_{\mathrm{des,i}} = \sum EX_{\mathrm{inflow,i}} - \sum EX_{\mathrm{outflow,i}} \tag{4}$$

4 RESULTS AND DISCUSSION

4.1 Parameter analysis

The parameters of the proposed PTES system are demonstrated in Table 2, in which the main thermophysical properties at each state point are shown. The temperatures of the high-temperature and low-temperature storage tanks are selected as 130 °C and 90 °C. Apparently, the power-to-power efficiency of the new PTES system can achieve 78.89% when the waste heat inlet temperature is 80 °C.

Table 2: Parameters of the novel PTES system at the high and low heat storage temperatures are 130 °C and 90 °C

State point	Pressure (MPa)	Temperature (°C)	Mass flow rate (kg/s)	Power (kW)
Charging process of PTES system				
1	0.37	81.5	25.22	-
2	1.81	143.5	25.22	-
3	1.81	129.3	1.16	-
4	1.81	142.8	26.38	-
5	1.81	92.1	25.22	-
6	1.81	87.0	25.22	-
7	0.74	85.0	1.16	-
8	0.74	90.0	1.16	-
9	1.81	74.0	25.22	-
10	0.37	58.0	25.22	-
11	0.37	63.0	25.22	-
Power input	-	-	-	1000
Discharging process of PTES system				
1	0.93	94.7	28.38	-
2	0.15	45.1	28.38	-
3	0.15	36.1	28.38	-
4	0.15	30.0	28.38	-
5	0.93	30.4	28.38	-
6	0.93	36.6	28.38	-
7	0.93	75.0	28.38	-
Power output	-	-	-	788.9

The thermal storage system is a crucial subsystem of the PTES system, and the heat storage temperature pair of the heat storage system influences the COP and the ORC efficiency as the boundary conditions. Hence, the variations of the performance indicators of the charging and the discharging process along with the heat storage temperatures are investigated and the results are shown in Figure 2. In the performance evaluation process, the temperature difference of the heat storage tanks should be larger than 10 °C. It should be noted that the COP of the HP declines when the low heat storage temperature increases, whereas the efficiency of the ORC goes up under the condition that the high heat storage temperature is deemed.

With the rising of the low heat storage temperature, the power-to-power efficiency firstly augments and then dwindles along with the increment of the low-temperature heat storage temperature when the high heat storage temperature is higher than 110 °C. This is mainly because the presence of the power-to-power efficiency of the thermally integrated PTES system is a competition between the performances of the HP and ORC, and the importance of the charging process on the whole system performance is becoming more predominant as the low storage temperature goes up. What's more, the power-to-power efficiency declines with the increment of the high heat storage temperature, and the performance of the charging process has a huge impact on the overall efficiency. Under the condition that the heat storage temperatures are 140 and 110, the power-to-power efficiency is calculated to be 79.2%.

The power-to-power efficiency of the PTES system reaches its highest value when the temperatures of the high-temperature storage tank and low-temperature storage tank are 110 °C and 100 °C, respectively. However, the energy storage density can only attain 0.94 kWh/m^3, which is relatively low as compared to other energy storage techniques. Figure 3 depicts the energy storage

density of the proposed PTES system under various heat storage temperature pairs. It is obvious that the energy storage density increases along with the temperature difference of the heat storage tanks. Taking into consideration the variation trend of the power-to-power efficiency under different heat storage temperatures, the heat storage temperatures of the tanks should be selected carefully to fulfill the requirements of high power-to-power efficiency and energy storage density. When the high heat storage temperature is 140 °C, the power-to-power efficiency and energy storage density have the opposite trends as the low heat storage temperature is lower than 110 °C. The selection of the low heat storage temperature to be 110 °C seems to be a rational option considering the balances of the two indicators, and a temperature higher than 110 °C is not worth choosing for the poor performances in the two aspects.

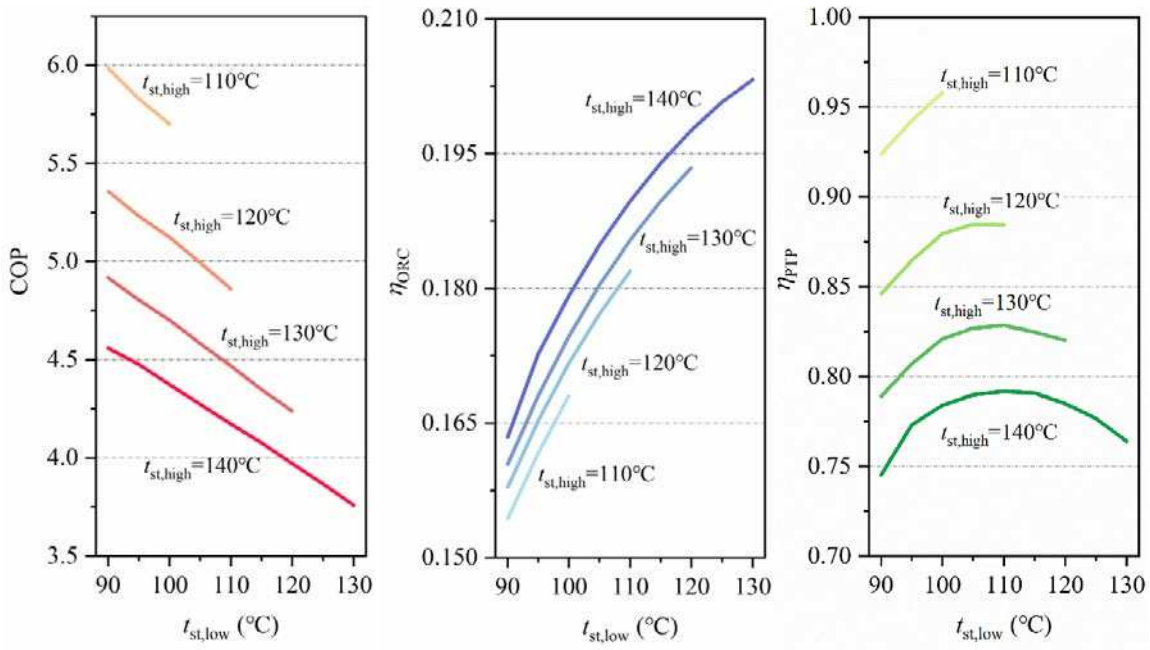

(a) COP of charging process (b) η_{ORC} of discharging process (c) η_{PTP}

Figure 2: Performance indicators of the charging and discharging process under different thermal storage temperatures

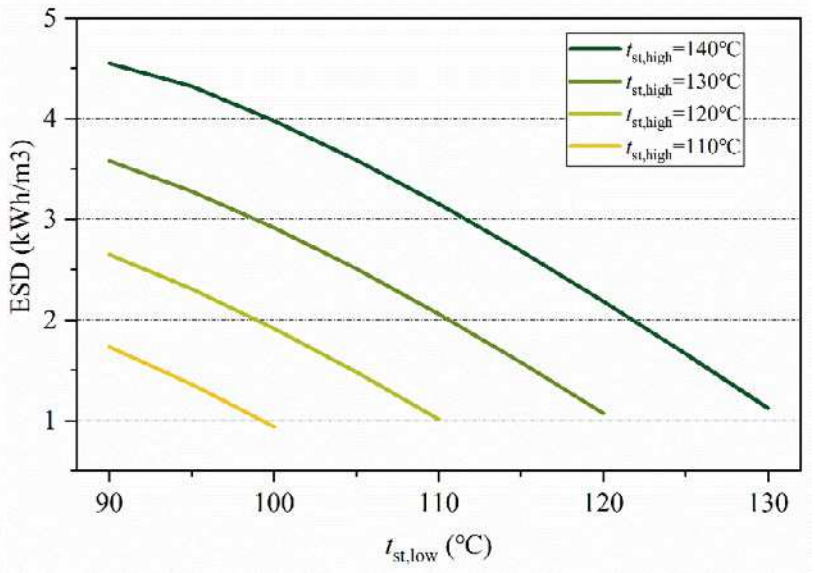

Figure 3: Energy storage density of the PTES system under different heat storage temperatures

The mechanical components, namely the compressor, the expander, and the pump, are significant equipment in the PTES system. Generally, improving the efficiencies of the mechanical components has been proven to be a viable measure to promote the power-to-power efficiency of the thermally integrated PTES system by many scholars. However, the quantitive research on the isentropic efficiencies of the compressor and the expander on the performance of the thermally integrated PTES system should be evaluated thoroughly. The variations of the power-to-power efficiency with various isentropic efficiencies are demonstrated in Figure 4, and the efficiencies vary from 60% to 90%. The performances of the PTES system are evaluated under the condition that the high and low heat storage temperatures are 140 °C and 110 °C. The power-to-power efficiency increases along with the isentropic efficiencies, and it can be discovered that the energy storage efficiency of the PTES system reaches the largest value (87.3%) when the compressor efficiency and the expander efficiency are 90%. Whereas the power-to-power efficiency can only attain 43.4% as the isentropic efficiencies are 60%. Moreover, the same amount of isentropic efficiency increment in the expander seems to be more beneficial to the performance of the proposed PTES system than that of the compressor.

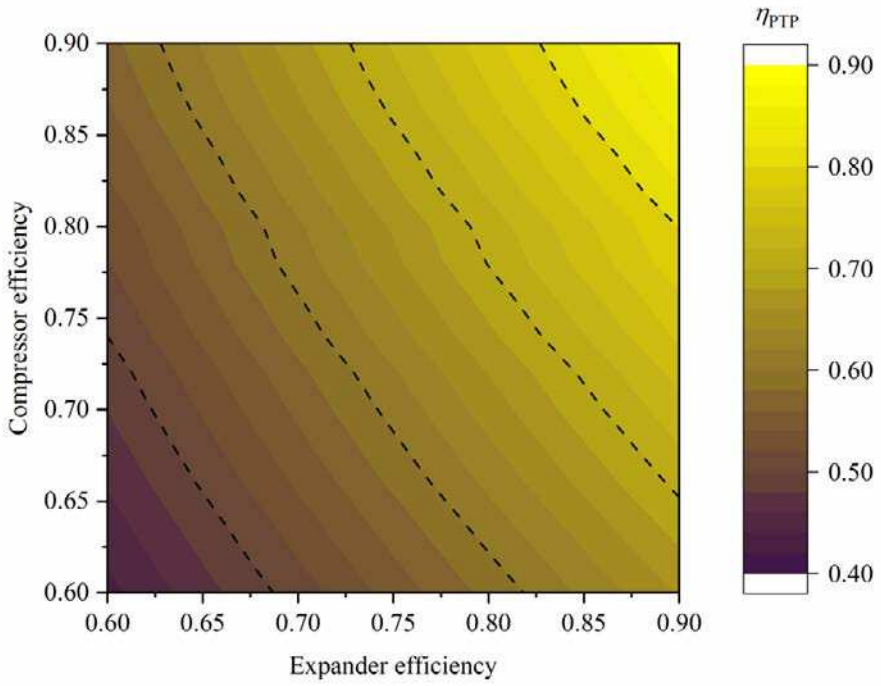

Figure 4: Variations of power-to-power efficiency under different compressor efficiency and expander efficiency

4.2 Exergy analysis

The exergy evaluation method is developed based on the second law of thermodynamics and has been widely implemented to investigate the energy-saving potential of various energy systems in many fields. The exergy flow diagram of the novel PTES system is depicted in Figure 5, in which the exergy inflows, exergy outflows, and exergy destruction in the main equipment are displayed. It should be mentioned that the exergy flows were calculated and diagrammed under the condition that the high and low heat storage temperatures are 140 °C and 110 °C, respectively. To be specific, in the charging process of the PTES system, a total power input of 1000 kW is conveyed to the compressors in the HP. What's more, the working fluid in the evaporator absorbs 464.54 kW exergy from the low-grade waste heat, and then the gas working fluid (525.51 kW) flows into the recuperator for temperature enhancement. During the charge time, the heat exchangers possess the largest part of the total exergy destruction (54.62%), and the sum of the exergy losses in the compressors is 118.77 kW (32.52%). And the exergy destructions happened in the mixer and the valves are 1.44 kW and 45.52 kW.

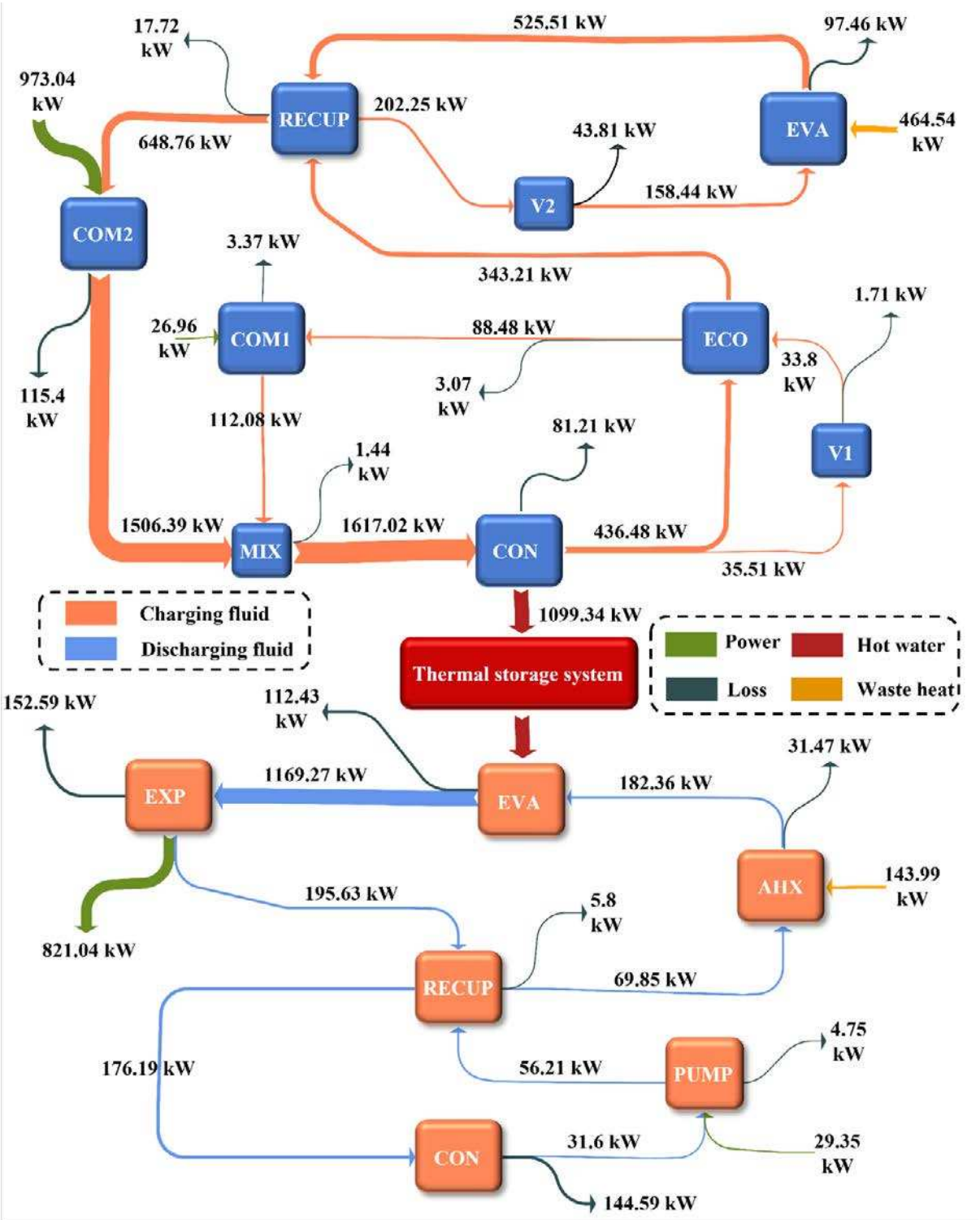

Figure 5: Exergy flow diagram of the novel PTES system (the high and low thermal storage temperatures are 140 °C and 110 °C)

The heat storage system stored the exergy of 1099.34 kW after the charging process in the HP. The expander can produce electricity of 821.04 kW when there is a demand for power, and the power output of the ORC is 791.69 kW after deducting the power requirement of the pump. While in the discharging process of the novel PTES system, the total exergy losses in the heat exchangers (the evaporator, condenser, regenerator, and the additional heater) are 294.30 kW. Furthermore, the exergy destructed in the expander and the generator takes a proportion of 33.79% of the overall exergy loss in the ORC. To sum up, the total exergy loss of the novel PTES system is calculated to be 816.84 kW.

The heat exchangers have the largest part of the overall exergy loss, and the exergy destruction that happened in the mechanical components is second to it. The analysis results indicate that modifying the heat exchange processes of the heat exchangers and improving the efficiencies of the mechanical components should be the dominant measures for the efficiency-boosting of the PTES system. Furthermore, the reduction of the exergy destruction in the heat transferring process, namely the heat transfer area of the heat exchangers, would augment the investment cost of the PTES system. Therefore, the minimum temperature difference of the heat exchangers ought to be selected based on the PTES overall performance and the economic indicators.

1 CONCLUSIONS

In this paper, a novel thermally integrated PTES system has been proposed to improve the power-to-power efficiency of the system and exploit the energy utilization potential of low-grade waste heat. In order to evaluate the performance of the PTES system under various working conditions, the parameter analysis has been carried out to show the variations of the power-to-power efficiency with different heat storage temperatures and the isentropic efficiencies of the compressor and the expander. Furthermore, the exergy flow diagram of the novel PTES system was also diagrammed to point out the direction of boosting the energy storage efficiency of the PTES system with heat integration.

- In the charging process of the advanced PTES system, parallel compression with an economizer is employed to increase the amount of waste heat utilization. Moreover, an additional heater is added to the ORC to boost power production at the discharge time.
- With the increment of the low heat storage temperature, the COP declines and the ORC efficiency increases under certain high storage temperatures. And the power-to-power efficiency can attain the highest value when the temperatures of the high heat storage tank and low heat storage tank are 110 °C and 100 °C. However, the energy storage density is relatively low as the temperature differences of the tanks are small.
- The isentropic efficiencies of the compressor and the expander affect the performance of the PTES system directly. The rise of the component efficiency contributes to the improvement of the power-to-power efficiency, which can reach 87.3% as the isentropic efficiencies are 90%.
- The exergy evaluation results show that the exergy destruction that happened in the heat exchangers is the mechanical components that are the most important parts of the overall system. The findings imply that modifying the heat-transferring process and improving the isentropic efficiencies of the mechanical component would be effective measures for performance enhancement.

According to the analysis results above, the heat storage temperatures of the tanks ought to be chosen carefully to sustain the requirements of high power-to-power efficiency and energy storage density. More possible measures for raising the two indicators simultaneously should be developed, for instance, optimizing the heat storage method and searching for more effective configurations. This is also a direction of future research.

NOMENCLATURE

Abbreviations			
AHX	additional heater	HP	heat pump
COM	compressor	ORC	organic Rankine cycle
CON	condenser	PTES	pumped thermal energy storage
ECO	economizer	RECUP	recuperator
ESD	Energy storage density	V	valve
EXP	expander		
Symbols			
COP	coefficient of performance	*power*	electric power (kWh)
ESD	energy storage density (kWh/m^3)	*V*	volume (m^3)
EX	exergy flow (kW)	η	efficiency
Subscripts			
char	charging process	ORC	organic Rankine cycle
dischar	discharging process	st	storage
PTP	power-to-power	tank	heat storage tank

REFERENCES

Deng, X., Chen, W., Zhou, Q., Zheng, Y., Li, H., & Liao, S., et al. (2023). Exploring spatiotemporal pattern and agglomeration of road CO2 emissions in Guangdong, China. *Science of The Total Environment, 871*, 162134.

Dumont, O., Frate, G. F., Pillai, A., Lecompte, S., De Paepe, M., & Lemort, V. (2020). Carnot battery technology: A state-of-the-art review. *Journal of Energy Storage, 32*, 101756.

Eppinger, B., Zigan, L., Karl, J., & Will, S. (2020). Pumped thermal energy storage with heat pump-ORC-systems: Comparison of latent and sensible thermal storages for various fluids. *Applied Energy, 280*, 115940.

Fan, R., & Xi, H. (2022). Exergoeconomic optimization and working fluid comparison of low-temperature Carnot battery systems for energy storage. *Journal of Energy Storage, 51*, 104453.

Frate, G. F., Ferrari, L., & Desideri, U. (2020). Multi-criteria investigation of a pumped thermal electricity storage (PTES) system with thermal integration and sensible heat storage. *Energy Conversion and Management, 208*, 112530.

Hassan, A. H., O Donoghue, L., Sánchez-Canales, V., Corberán, J. M., Payá, J., & Jockenhöfer, H. (2020). Thermodynamic analysis of high-temperature pumped thermal energy storage systems: Refrigerant selection, performance and limitations. *Energy Reports, 6*, 147-159.

Jebabli, I., Lahiani, A., & Mefteh-Wali, S. (2023). Quantile connectedness between CO2 emissions and economic growth in G7 countries. *Resources Policy, 81*, 103348.

Jiang, B., & Xia, D. (2023). Toward carbon neutrality in China: A national wide carbon flow tracing and the CO2 emission control strategies for CO2-intensive industries. *Science of The Total Environment, 879*, 163009.

Kazemi, M., Tabatabaei, S. S., & Moslemi, N. (2023). A novel public-private partnership to increase the penetration of energy storage systems in distribution level. *Journal of Energy Storage, 62*, 106851.

Kurşun, B., & Ökten, K. (2022). Comprehensive energy, exergy, and economic analysis of the scenario of supplementing pumped thermal energy storage (PTES) with a concentrated photovoltaic thermal system. *Energy Conversion and Management, 260*, 115592.

Liu, L., Wang, Z., Wang, Y., Wang, J., Chang, R., & He, G., et al. (2020). Optimizing wind/solar combinations at finer scales to mitigate renewable energy variability in China. *Renewable and Sustainable Energy Reviews, 132*, 110151.

Tian, W., & Xi, H. (2022). Comparative analysis and optimization of pumped thermal energy storage systems based on different power cycles. *Energy Conversion and Management, 259*, 115581.

Vecchi, A., Knobloch, K., Liang, T., Kildahl, H., Sciacovelli, A., & Engelbrecht, K., et al. (2022). Carnot Battery development: A review on system performance, applications and commercial state-of-the-art. *Journal of Energy Storage, 55*, 105782.

Wang, P., Li, Q., Liu, C., Wang, R., Luo, Z., & Zou, P., et al. (2022). Comparative analysis of system performance of thermally integrated pumped thermal energy storage systems based on organic flash cycle and organic Rankine cycle. *Energy Conversion and Management, 273*, 116416.

Weitzer, M., Müller, D., Steger, D., Charalampidis, A., Karellas, S., & Karl, J. (2022). Organic flash cycles in Rankine-based Carnot batteries with large storage temperature spreads. *Energy Conversion and Management, 255*, 115323.

Weitzer, M., Müller, D., & Karl, J. (2022). Two-phase expansion processes in heat pump – ORC systems (Carnot batteries) with volumetric machines for enhanced off-design efficiency. *Renewable Energy, 199*, 720-732.

Yong, X., Wu, Y., Zhou, J., Tao, Y., & Chen, W. (2023). Prospects and barriers analysis framework for the development of energy storage sharing. *Sustainable Cities and Society, 89*, 104368.

Zhang, M., Shi, L., Hu, P., Pei, G., & Shu, G. (2023). Carnot battery system integrated with low-grade waste heat recovery: Toward high energy storage efficiency. *Journal of Energy Storage, 57*, 106234.

ACKNOWLEDGEMENT

This work was supported by the Youth Innovation Promotion Association CAS (Grant No. 2022463), the USTC Institute for Carbon Neutrality and Joint research center for multi-energy complementation and conversion.

ORC SEVILLE 2023
7th International Seminar on O.R.C. Power Systems

© 2024 Editorial Universidad de Sevilla. Este es un artículo de acceso abierto distribuido bajo los términos de la licencia de uso y distribución Creative Commons (BY-NC-ND 4.0)

DOI: https://dx.doi.org/10.12795/9788447227457_48

Pressure profile optimisation of a nozzle for wet-to-dry expansion

Pawel Ogrodniczak[1,*], Abdulnaser Sayma[1], Martin T. White[1,2]

[1] *City, University of London, Northampton Square, London EC1V 0HB, United Kingdom*
[2] *University of Sussex, Falmer, Brighton BN1 9RH, United Kingdom*

*Corresponding Author: pawel.ogrodniczak@city.ac.uk

ABSTRACT

Wet-to-dry expansion within the nozzle guide vane of an ORC turbine has been proposed as a means to improve the power output of ORC systems for waste-heat recovery (< 250 °C). However, given the rapid fluid acceleration in the stator, the phases can develop significant velocity and temperature disparity due to the density difference and finite rate of interphase heat transfer. Since these factors can significantly affect the phase-change process, wet-to-dry nozzle design techniques must account for non-equilibrium effects. The first part of this paper aims to further validate a previously developed quasi-1D inviscid nozzle design tool that accounts for non-equilibrium effects. The interphase mass, momentum and energy exchange models have been updated using correlations better tailored to evaporating droplet flows, while the drag equation and vapour mass fraction definition have been updated. The validation is performed using non-equilibrium CFD simulations, which, unlike the design model, account for lateral flow variations, viscous and turbulence effects, and secondary momentum forces. The results showed that these effects delay the evaporation, with CFD-predicted outlet vapour mass fraction being about 10 to 15% smaller than predicted by the quasi-1D tool. However, the overall flow behaviour and phase-change pattern were in satisfactory agreement, justifying the use of the design tool for 1D optimisation. In the second part of the paper, the quasi-1D tool is coupled to a gradient-based optimiser to optimise the nozzle pressure profile and enhance evaporation of siloxane MM for expansions with inlet pressure ranging from 450 to 650 kPa, and inlet quality of 0.3. The design variables are the control points of a Bezier curve that defines the shape of the intended nozzle pressure profile. CFD simulations of the optimised geometries indicate a 5.5 to 6.6% increase in the outlet vapour mass fraction, which was raised from 84.9, 88.2 and 90.7% to 90.4, 94.8 and 97.2% for the 450, 550 and 650 kPa inlet pressures respectively. More abrupt expansion in the optimised nozzles resulted in the development of a shock and led to nozzle efficiency deterioration compared to the baseline. This emphasises the need for multi-objective optimisation, which will be conducted in future studies.

1 INTRODUCTION

In an effort to improve the performance of ORC systems, researchers have proposed several novel cycle architectures (Wieland et al., 2023). Among the proposed alternatives, the so-called wet-to-dry cycle could be capable of generating up to 30% more power than the basic single-phase ORC in the temperature range between 150 and 250 °C (White, 2021). In the wet-to-dry cycle, a two-phase working fluid can completely vapourise during expansion, in the process referred to as flash boiling. This offers greater flexibility in terms of expander selection than other two-phase cycles; turbomachines could be employed provided that complete mixture evaporation occurs in the stator, thus avoiding possible concerns related to erosion in the rotor. Turbomachines offer higher expansion ratios than volumetric expanders, enabling application of the wet-to-dry cycle at temperatures above 150 °C. Moreover, having a turbine that could accept two-phase inlet conditions could be an advantage in the off-design operation of ORC systems (Lhermet et al., 2022).

The successful design of a wet-to-dry turbine depends on the capability of the stator to facilitate complete mixture evaporation to avoid liquid droplets entering the rotor. Preliminary numerical studies, using simplified equilibrium models, indicate a radial turbine stator can be designed that can facilitate the wet-to-dry transition (White, 2021). Further investigations have demonstrated that more realistic flow modelling

techniques that account for mechanical and thermal non-equilibrium between the liquid and vapour phases are required when assessing the evaporation process under conditions relevant to the wet-to-dry cycle (White, 2022). Later investigations focused on non-equilibrium CFD simulations in a simple converging-diverging nozzle, demonstrating that full evaporation may be difficult to achieve in a nozzle with low inlet pressures (Ogrodniczak & White, 2023), although low pressures are more attractive from the standpoint of maximising cycle performance (White, 2021). However, these previous investigations assumed a fixed nozzle pressure distribution and did not consider any form of geometry optimisation.

This study aims to optimise the pressure profile in a converging-diverging nozzle, having a straight centerline (non-deflecting nozzle), seeking to maximise evaporation rate of two-phase siloxane MM. To this end, a previously developed quasi-1D non-equilibrium two-phase nozzle design tool was employed (White 2022). The design tool has been updated to make it more suitable for evaporating droplet flows and then verified using non-equilibrium CFD simulations. It is important to note that the tool assumes a quasi-1D inviscid flow, which means that neither lateral phase separation nor viscosity effects could be considered during optimisation. Phase separation (e.g. liquid film forming in the vicinity of the nozzle wall) could reduce the available contact area between the phases, which in turn leads to reduced interphase heat and mass transfers, and lower evaporation rates. Moreover, in the context of two-phase turbines, phase separation in the stator would be associated with flow non-uniformities at the rotor inlet and possible erosion issues. As for the effect of viscosity, it is mainly responsible for entropy generation; thus, the quasi-1D inviscid model cannot simultaneously estimate the vapourisation rate and nozzle performance. Although the above effects are not considered at the optimisation stage, the optimised geometries are simulated using two-dimensional CFD, which accounts for the phase lateral separation as well as the effects of viscosity and turbulence, serving a means of validation and providing an expanded analysis. The results reveal the influence of the pressure profile and nozzle shape on the evaporation rate, nozzle performance and flow behaviour.

2 QUASI-1D NOZZLE DESIGN TOOL VALIDATION

2.1 Two-fluid Model

This section provides an overview of the two-fluid model that is employed in both the quasi-1D nozzle design tool and the CFD simulations. It also highlights the modifications that have been introduced in this study to tailor the model to evaporating droplet flows. For more detailed information, an interested reader is referred to our previous work (White 2022; Ogrodniczak & White, 2022, 2023).

Flash boiling in the nozzle is simulated using the two-fluid model, also known as the six-equation model. The two-fluid model employs the Eulerian-Eulerian framework to analyse the two-phase flow, which means that both phases are treated as interpenetrating continua, with separate conservation equations:

$$\frac{\partial(\alpha\,\rho)_\beta}{\partial \mathrm{t}} + \nabla\cdot\left(\alpha\,\rho\,\vec{\mathrm{U}}\right)_\beta = \dot{m}_{ex} \tag{1}$$

$$\frac{\partial\left(\alpha\,\rho\,\vec{\mathrm{U}}\right)_\beta}{\partial \mathrm{t}} + \nabla\cdot\left(\alpha\,\rho\,\vec{\mathrm{U}}\,\vec{\mathrm{U}}\right)_\beta = -\alpha_\beta\,\Delta P + \nabla\cdot\tau_\beta + \dot{m}_{ex}\,\vec{\mathrm{U}}_{ex} + M_{ex} \tag{2}$$

$$\frac{\partial(\alpha\,\rho\,h_{tot})_\beta}{\partial \mathrm{t}} + \nabla\cdot\left(\alpha\,\rho\,\vec{\mathrm{U}}\,h_{tot}\right)_\beta = -\alpha_\beta\frac{\partial P}{\partial t} + \nabla\cdot(\alpha\,\lambda\,\Delta T)_\beta + \nabla\cdot\left(\vec{\mathrm{U}}\,\tau\right)_\beta + \dot{m}_{ex}\,h_{ex} + \dot{q}_{ex} \tag{3}$$

where β is the phase index, α the volume fraction, ρ the density, $\vec{U}$ the velocity vector, P the pressure (assumed identical in both phases), τ the stress tensor, while h_{tot}, T and λ are specific total enthalpy, temperature and thermal conductivity. The volume fraction conservation equation is also solved, which states that the sum of phase volume fractions equals unity. The phases interact by exchanging mass, momentum and energy. The interphase mass exchange is denoted by $\dot{m}_{ex}$, and the products $\dot{m}_{ex}\,\vec{U}_{ex}$ and $\dot{m}_{ex}\,h_{ex}$ represent the interphase exchange of momentum and energy associated with the mass transfer. The additional momentum and energy exchange terms are the interfacial forces and heat-exchange, which are denoted as M_{ex} and $\dot{q}_{ex}$ respectively. The phase change is assumed to be solely the result of interphase heat transfer, which is evaluated by means of a two-resistance model. The two-resistance model assumes an

interface between the phases, which is at local saturation temperature. Vapour and liquid exchange heat with the interface, and the sum of heat exchanged across the interface determines the interphase mass transfer:

$$\dot{m}_{ex} = \frac{\dot{q}_{ex}}{h_L - h_V} = \frac{\mathfrak{H}_L A_{int}(T_{int} - T_L) + \mathfrak{H}_V A_{int}(T_{int} - T_V)}{h_L - h_V} \tag{4}$$

where, A_{int} is the interfacial area concentration, $\mathfrak{H}$ is the heat-transfer coefficient, while h is the specific enthalpy; subscripts L and V denote liquid and vapour phases respectively. To determine the mass transfer, the interfacial area and heat-transfer coefficients are required. The interfacial area is the surface area of the droplets per unit volume (i.e., $A_{int} = 6\alpha_L/D_d$). The droplet mean diameter, D_d, is estimated using the definition of the Weber number We, which relates the disruptive aerodynamic force that acts to fragment the droplet to the surface tension force that resists that fragmentation:

$$We = \frac{\rho_V \, D_d \, |u_V - u_L|^2}{\sigma} \tag{5}$$

where σ is the surface tension. Experimental results indicate that as long as the ratio $\mu_L/\rho_L D_d \sigma$ stays below 0.1 (μ_L is the liquid dynamic viscosity), which is satisfied in all investigated cases, droplet breakup is expected for $We > 11$, in both subsonic and supersonic flow regimes (Guildenbecher, 2009; Gobyzov, 2020). Hence, the maximum stable droplet size can be determined; since no droplet coalescence is simulated, the droplet size decreases or remains constant with increasing streamwise position.

The heat-transfer coefficient on the continuous (vapour) side is evaluated with the Ranz-Marshall (1952) correlation, derived from experimental tests on a water droplet evaporating in a hot air stream. It is more challenging to estimate the heat-transfer coefficient between the droplet and the interface. In previous studies, the authors assumed a constant Nusselt number of 6, which comes from heat-transfer analysis in a solid sphere. Nevertheless, the heat transfer will likely be enhanced in a droplet due to effects such as internal circulation. To predict the heat transfer rate more accurately, a correlation applied in RELAP5/MOD3 (NRC, 1995), a code designed for transient simulation of light water reactor coolant systems, was adapted in this work. The correlation is based on Brown's (1948) work on condensation of water droplets:

$$Nu_L = 2 + 7 \times \min\left(1 + \frac{c_{p,L} \max(0, |T_{sat} - T_L|)}{h_{LV}}, 8\right) \tag{6}$$

where Nu_L is the liquid Nusselt number, $c_{p,L}$ is the liquid specific heat capacity at constant pressure, h_{LV} is the latent heat of vapourisation, while T_{sat} is the saturation temperature. This correlation was originally obtained for droplets suspended in a hotter medium. However, the authors assume that similar heat-transfer coefficients can be expected for droplet cooling, and the correlation serves as the current best-estimate.

In the case of the droplet flow, there are three major momentum exchange mechanisms: drag, lift and turbulent dispersion effects, with the first having the highest impact. The drag coefficient is estimated using the Ishii-Zuber (1979) correlation, which was also used in previous simulations. However, the formulations used for the lift and turbulent dispersion forces have been updated in the current work. To evaluate the lift force, the Legendre & Magnaude (1998) is applied, which is more suited to small fluid particles. The previously applied turbulent dispersion model was more suitable for bubbly flow; since liquid droplets are significantly denser than vapour, they are not so easily caught in vapour turbulent eddies. This was accounted for by setting a turbulent dispersion coefficient that depends on the turbulent Stokes number: $c_{TD} = e^{-0.5St_t}$, where c_{TD} is the dispersion coefficient, while St_t is the turbulent Stokes number. In case the droplet relaxation time is much higher than the turbulent eddy lifetime, the droplets will be weakly affected by the eddies. Hence, the turbulent dispersion tends to zero as the turbulent Stokes number increases. Lastly, a suitable equation of state was employed to predict fluid's properties and close the system of equations.

2.2 Quasi-1D Nozzle Design Tool

Two-phase expansion under conditions relevant to the wet-to-dry cycle entails rapid acceleration to supersonic velocities, which leads to significant velocity slip and thermal non-equilibrium that affects the phase change process. Previously, the authors developed a quasi-1D non-equilibrium nozzle design tool, capable of accounting for the non-equilibrium effects. The design tool is based on a simplified version of the two-fluid model described in the preceding section. The flow is assumed to be quasi-1D and inviscid, varying only in the longitudinal direction. Consequently, lift and turbulent dispersion forces are not included.

The nozzle design routine is initiated with the selection of the working fluid and boundary conditions, which include the inlet total pressure and vapour quality alongside inlet velocity. Since the nozzle is intended as a turbine stator integrated with the wet-to-dry cycle, the cycle condensation temperature and the turbine degree of reaction are used to define the nozzle outlet pressure. Previous numerical studies indicate that siloxane MM is a promising candidate for the wet-to-dry cycle, which is why it was selected for the current investigation. The previous results also indicate that a complete wet-to-dry transition can be difficult to achieve when expanding from pressures lower than 750 kPa. On the other hand, the wet-to-dry cycle provides a higher advantage over the single-phase expansion at low pressures. This study aims to undertake optimisation to enhance the evaporation rate at low pressures and consequently enable the design of wet-to-dry turbine at lower pressures. Therefore, three relatively low inlet pressures were considered, namely, 450, 550 and 650 kPa. These pressure levels could correspond to heat source inlet temperature in the approximate range of 170 to 190 °C; temperatures levels where wet-to-dry cycle may provide substantial power output increase (White, 2021). Inlet quality and degree of reaction were set to 0.3 and 0.4 respectively, while the cycle condensation temperature was fixed at 40 °C. The three expansion cases are reported in Fig.1, which shows the ideal isentropic process. Although expanding from lower inlet qualities could offer a further increase in the power output, preliminary turbine design studies have shown that it would require a lower degree of reaction, which could have a detrimental effect on the turbine efficiency (White, 2021). The mass flow rate is set to 0.12 kg/s, which translates to a turbine isentropic power of around 100 to 120 kW under the investigated operating conditions. This power output is estimated assuming that the turbine has sixteen stator vanes; each nozzle representing one stator vane. This power rating could correspond to a small-scale system designed for waste-heat recovery from low-temperature sources. To fully define the nozzle geometry, two geometrical parameters, the ratios of nozzle length to throat height (L/o_{th}), and nozzle width to throat height (b/o_{th}) were set to 30 and 3 respectively (values set in line with former studies).

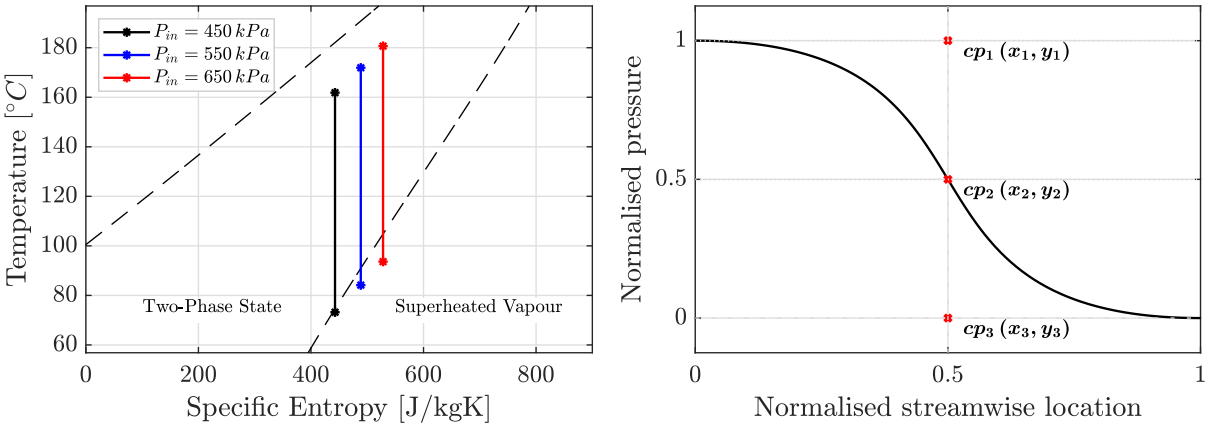

Figure 1: Three investigated expansion cases under isentropic flow assumption (left); normalised baseline pressure profile (right); the red asterisks (*) show the location of the Bezier curve control points.

The quasi-1D tool follows an inverse design approach, where the pressure profile is pre-defined and Eqs. 1-3 are solved to converge on the imposed pressure distribution. NIST REFPROP 10.0 (Lemmon et al., 2018) is employed to evaluate the thermodynamic properties of siloxane MM. Figure 1 illustrates the design pressure profile, which was constructed using a Bezier curve with three control points, cp_1, cp_2 and cp_3, explicitly shown with red markers on the plot. The profile shown is identical to the profile used in all previous investigations and will be referred to as the baseline profile. In this profile, the Bezier control points are

positioned such that the pressure gradient approaches zero at the inlet and outlet of the nozzle. Moreover, the pressure at the middle of the nozzle is set to the average of the inlet and outlet pressures.

2.3 Quasi-1D Tool Validation

Before proceeding with the optimisation, the quasi-1D tool has been validated using CFD. Although the validation has already been performed by the authors (Ogrodniczak & White, 2022), several modifications have since been made. Firstly, as highlighted in Section 2.2. the liquid side heat-transfer coefficient, alongside the lift and turbulent dispersion forces, have been updated. A correction to the drag force equation in the quasi-1D tool, which previously caused a discrepancy in the velocity slip, has also been added; the velocity slip directly affects the maximum diameter, which in turn impacts the evaporation rate. Finally, the vapour thermodynamic quality was previously used to measure evaporation rate. However, in the presence of significant non-equilibrium effects, it may be more appropriate to use the vapour mass fraction calculated based on the ratio of vapour to total mass flow rates (i.e., $\dot{m}_V/(\dot{m}_L + \dot{m}_V)$).
The nozzle geometries generated by the tool are assessed through steady-state two-dimensional simulations performed in ANSYS CFX (2021 R1), that accounts for the effects of viscosity and turbulence. REFPROP 10.0 was used to construct look-up tables for the thermo-physical properties of siloxane MM. The maximum droplet diameter formulation was not directly implemented in the CFD. Instead, the streamwise droplet diameter profile extracted from the quasi-1D tool was imposed through a user-defined expression. Direct implementation of Eq. 5 in the CFD solver caused numerical instabilities and hindered convergence. This could be due to excessive droplet size variation in the transverse direction caused by phase separation. As for the grid structure, the authors relied on the previous validation study in determining the appropriate mesh resolution. Nonetheless, it should be mentioned that the grid was improved by constructing a fully structured hexahedral mesh, eliminating low-quality distorted elements. For more details on the numerical setup, the reader is referred to Ogrodniczak & White (2022). Figure 2 presents the updated validation study results.

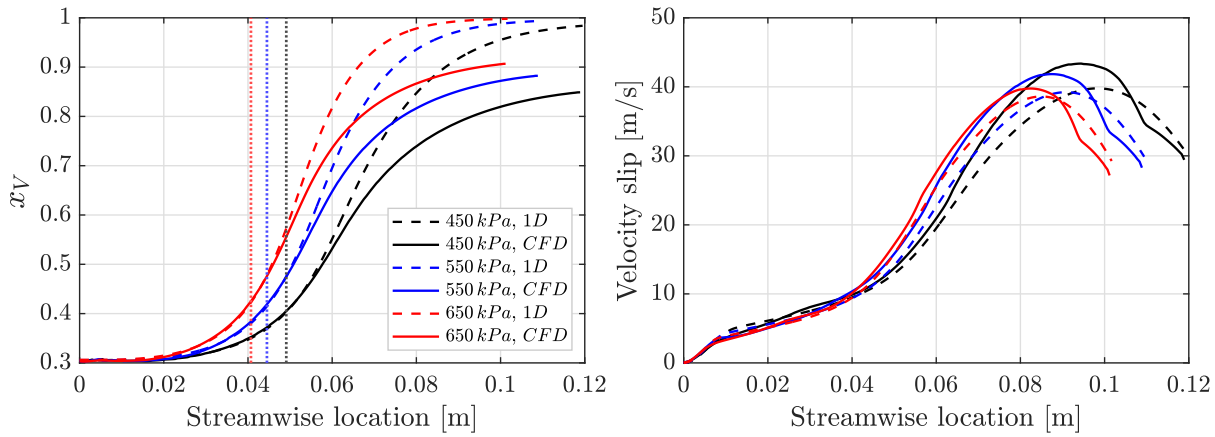

Figure 2: Comparison of average streamwise variation of vapour mass fraction (left) and velocity slip (right) between the quasi-1D tool and CFD; the dotted lines represent the throat location.

Figure 2 illustrates the average streamwise variation of vapour mass fraction x_V. The quasi-1D tool predicts near-dry conditions at the nozzle outlet with x_V ranging from 0.984 to 0.998. Most of the phase change occurs shortly past the throat in the diverging nozzle section. The curve then flattens as the flow approaches the outlet. This trend is similar for each of the three expansions; however, the higher the pressure the quicker the evaporation and the higher the outlet vapour quality. Although the CFD predicts a visibly lower evaporation rate compared to the quasi-1D tool, the phase-change pattern looks very similar in both cases. The discrepancy in x_V gradually increases in the diverging section, reaching the maximum of around 0.10–0.15 at the outlet. In summary, the lateral phase separation, viscosity, and turbulence effects are likely to delay the evaporation and lead to increased liquid content in the nozzle outflow.

In the previous study, the velocity slip estimated by the quasi-1D tool was significantly smaller than the CFD predictions. With the corrected drag formulation, the velocity slip difference is reduced from a maximum of 38 m/s to less than 5 m/s (Fig. 2). Overall, the slip predicted by the quasi-1D tool is now much higher, which

translates to smaller droplet size in the nozzle diverging section and higher evaporation rates (Eqs. 4-6). Despite the quantitative differences between the design tool and the CFD, the overall phase change pattern is conserved. Therefore, it seems rational to assume that enhancing the evaporation rate in the quasi-1D tool will translate to enhanced evaporation in the CFD. This justifies using the quasi-1D tool for optimisation.

3 PRESSURE PROFILE OPTIMISATION

3.1 Optimisation Setup

As apparent from Fig. 2, achieving complete mixture evaporation at pressures below 650 kPa is challenging. This study aims to enhance evaporation by optimising the nozzle pressure distribution to assess whether complete evaporation could be achieved in low-pressure expansions. A nonlinear constrained optimisation is setup using the gradient-based *fmincon* optimiser available within MATLAB. Since it was found that multiple pressure profiles resulted in complete evaporation, the objective function was defined as:

$$f(\mathbf{x}) = \mathrm{x}_{\mathrm{V,max}} \frac{L_N}{L \,@\, x_{V,\mathrm{max}}} \tag{7}$$

where $\mathrm{x}_{\mathrm{V,max}}$ is either 1 in case of full evaporation or the maximum vapour mass fraction achieved, L_N is the nozzle length, and $L \,@\, x_{V,\mathrm{max}}$ is the streamwise distance at which the mixture turns to dry vapour or reaches the maximum x_V. Maximising $f(\mathbf{x})$ ensures that a pressure profile is found that ensures the quickest wet-to-dry transition. The design variables are the coordinates of the three Bezier control points shown in Fig. 1. Although it was initially planned to include the geometrical ratios, L/o_{th} and b/o_{th} as design variables, both parameters were found to have little effect on the evaporation rate. To avoid flow discontinuities, the zero-gradient condition is maintained at the inlet and outlet, which implies that the y-coordinate of the control points cp_1 and cp_3 is fixed at 1 and 0 respectively. Hence, there are four design variables in total, which include the x-coordinates of all three control points, and the y-coordinate of the middle control point cp_2. Each design variable can take any value between 0 and 1 in terms of the normalized coordinates (see Fig. 1). However, the resulting profile has to satisfy two conditions (optimisation constraints). First, the pressure gradient dp/dx has to remain negative throughout the expansion, i.e. the pressure had to continually decrease. The other constraint was related to the maximum magnitude of the pressure gradient $|dp/dx|$, which could not exceed 25 (expressed in terms of normalised coordinates). It was found that pressure profiles with $|dp/dx| > 25$ resulted in excessive nozzle curvature. This in turn led to very abrupt expansions associated with flow separation. To avoid ending up at a local minimum, the optimiser was run using 100 randomly generated starting points within the design space.

3.2 Optimisation results

Figure 3 presents the comparison between the baseline and optimised pressure profiles. In each case, the optimum pressure profile reaches the maximum allowable gradient of 25. The profiles for 550 and 650 kPa expansions look almost identical, with most of the expansion happening closer to the inlet. This seems logical as the breakup occurs quicker, with the remaining of the expansion occurring with smaller droplets. It is unclear why the pressure drop occurs further downstream for the 450 kPa expansion. The main reason why the optimiser strove to maximise the pressure gradient and bring about a more rapid expansion is that it promotes a more severe droplet fragmentation and leads to smaller droplet diameters in the diverging section of the nozzle. The post-breakup droplet diameter in nozzles designed with the baseline profile varied between 10.4 and 13.2 μm. This reduced to around 4.34 to 5.57 μm in the optimised nozzles. The smaller the droplet size the larger the interfacial area for a given liquid volume fraction; this in turn directly enhances the rate of interfacial heat transfer rate and consequently interphase mass transfer. According to the quasi-1D tool, the optimised geometry provides dry outlet conditions in each case and wet-to-dry transition took place further upstream of the outlet compared to the baseline profile (compare dashed line in Fig. 2 and Fig. 3). In order to test whether the enhanced evaporation rate was merely the result of reduced droplet size, the design was repeated for the baseline and optimised profiles using a constant droplet diameter of 15 μm. Even though the droplet diameter remained constant, the evaporation was enhanced, which indicates there are other mechanisms involved in raising the evaporation rate when the pressure gradient is increased.

Although the quasi-1D results look promising, the evaporation may be reduced by the two-dimensional, viscosity and turbulence effects as apparent from Fig. 2. Figure 3 shows the comparison between quasi-1D and CFD predictions of average streamwise x_V for the optimised pressure profiles. First, comparing Fig. 3 to Fig. 2, it can be easily noticed that like in the baseline cases, the evaporation rate estimated by CFD is reduced in comparison with the quasi-1D tool prediction, while the overall trends are conserved. Comparing the CFD results of the baseline and optimised geometries (Fig. 4), a visible and consistent improvement in the outlet vapour mass fraction can be observed, which amounts to around 0.055 to 0.066. The outlet x_V increases from 0.849, 0.882 and 0.907 to 0.904, 0.948 and 0.972 for the 450, 550 and 650 kPa expansions respectively. Although full evaporation was not achieved in any of the investigated cases, the liquid mass fraction at the outlet of the optimised nozzle design for the expansion from 650 kPa dropped below 3%, which is promising. Considering the gradient of the x_V curve near the outlet, it appears that further increase in the outlet x_V could be achieved by elongating the nozzle.

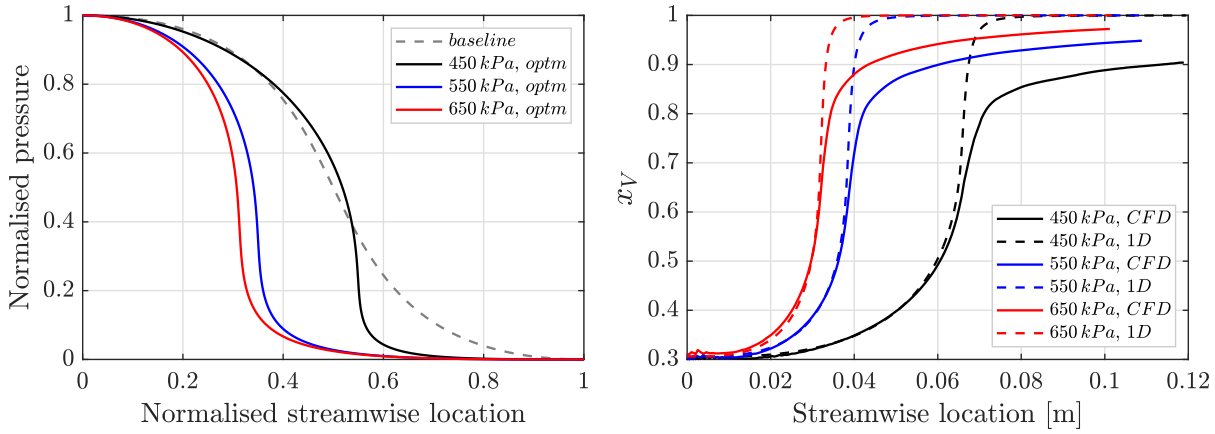

Figure 3: Optimised pressure profiles (left); Comparison of average streamwise variation of vapour mass fraction x_V predicted by the quasi-1D tool and CFD in the optimised geometries.

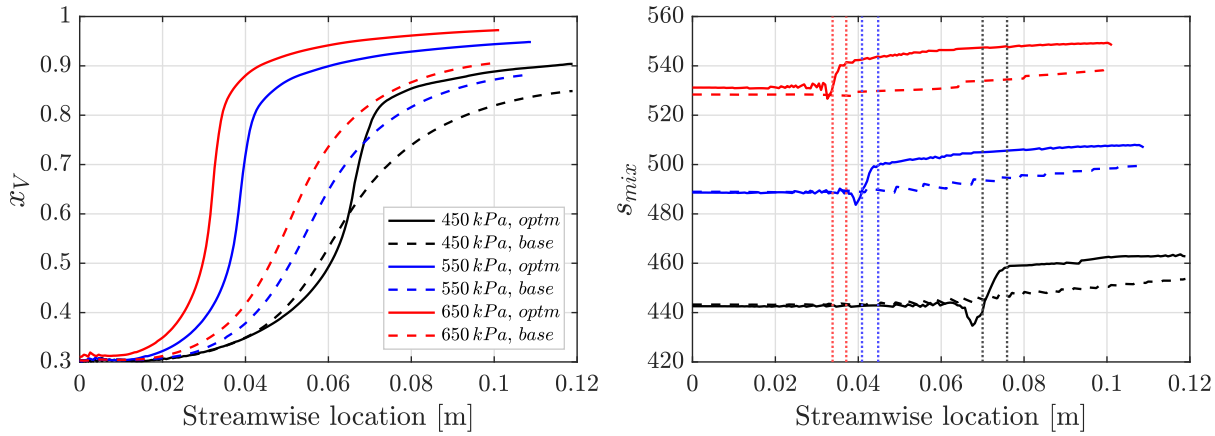

Figure 4: Comparison of CFD predictions of average streamwise variation of a) vapour mass fraction and b) mass-flow average entropy for the baseline (*base*) and optimized (*optm*) pressure profiles; dotted lines represent the nozzle sections with the most sudden entropy increase.

The influence of the pressure profile on the nozzle efficiency and flow uniformity is also important. Figure 4 reports the average streamwise variation of mass-flow averaged entropy (s_{mix}). Generally, the more rapid pressure change that results in the optimised case has a negative effect on the nozzle performance as the total entropy generated increases. One can note a small kink in the entropy curves, showing a local decrease in total entropy in the throat area, which would not happen in any real process. However, as entropy immediately rises after, it is thought that overall the results remain valid. To provide a more explicit measure of nozzle performance, nozzle efficiency was calculated, based on the ratio of actual to isentropic kinetic

energy rise. The efficiency of the baseline nozzles was 80.97, 82.76 and 84.39% for the 450, 550 and 650 kPa expansion respectively. The efficiency dropped to 72.37, 78.43 and 82.11% for the optimised geometries, which is in line with the total entropy curves (Fig. 4).

Figure 5 shows 2D vapour mass fraction contours, which reveal the flow's spatial uniformity, shedding more light on flow behaviour and the cause for the sudden rise in generated entropy. What appears to be common in each case, is the phase separation in the diverging section of the nozzle. This is due to much higher liquid density and high relaxation times; the droplets cannot immediately adjust to the changing geometry in an accelerating flow field. For that reason, the liquid tends to remain in the centre of the nozzle past the throat, while the vicinity of the wall is occupied by the vapour phase. The flow-field looks very similar in each baseline geometry. Comparing the baseline and optimised nozzles, the phase separation in the diverging section seems to be alleviated in the optimised geometries. Nevertheless, an oblique shock appears to form in the optimised nozzles shortly downstream of the throat, which eventually causes entropy generation and performance loss. The dotted lines from Fig. 4 also shown on the contours, indicate where the sudden entropy generation occurs in the nozzle. It can be observed that the location of the sudden rise in s_{mix} can be linked to the onset of the shock. Looking at the optimised geometries, the most abrupt flow area change occurs for the 450 kPa expansion, the area change gradually decreases as the inlet pressure is raised. This is also the reason why the shock is stronger for the 450 kPa expansion, resulting in a more pronounced efficiency loss; over 8% lower efficiency compared with slightly over 2% loss for the 650 kPa expansion. In summary, the optimised geometry can provide higher outlet vapour mass fraction and reduces the extent of lateral phase separation in the diverging section. However, more abrupt expansion can induce shocks and consequently performance losses. The influence of the multidimensional and viscosity effects on the nozzle performance highlights the limitation of the 1D optimisation, which can only be applied to maximise the evaporation rate. CFD-based nozzle shape optimisation could be applied to perform multi-objective optimisation, aimed at enhancing the evaporation rate while maintaining high nozzle efficiency. It is also important to note that all the investigated nozzles have a straight centerline. For a curved deflecting nozzle, one could expect that phase separation would be enhanced due to lateral gradients. Most likely, liquid phase would concentrate on the pressure side of the nozzle, creating a characteristic liquid film as found by Rane & He (2020). Such phase separation would lead to a reduced interfacial area A_{int}, which in turn lowers the interphase mass exchange rate and delays the evaporation (see Eq. 4). The phase separation could also decrease the uniformity of flow delivered by the nozzle. In summary, the design of a curved (deflecting) nozzle that would facilitate complete mixture evaporation and uniform outlet flow conditions is likely to be more challenging.

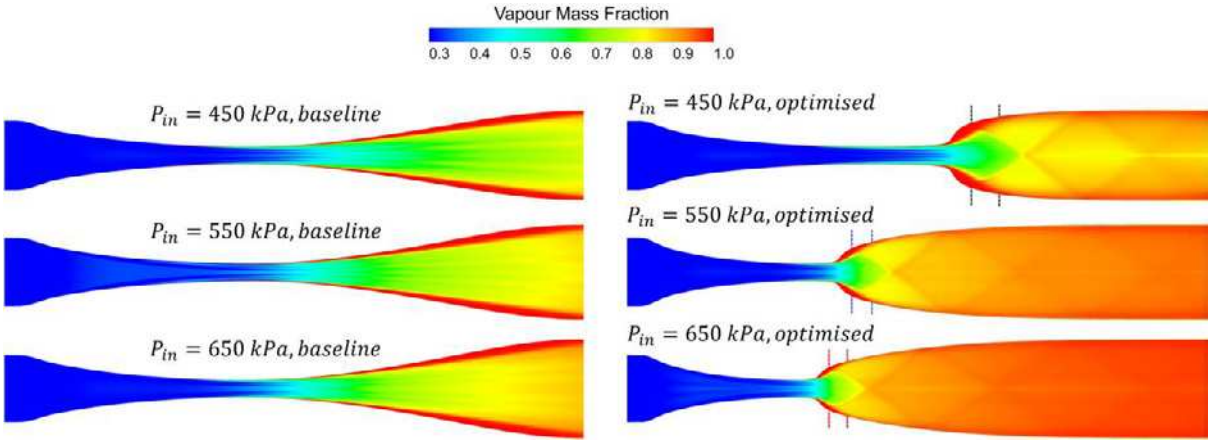

Figure 5: Two-dimensional contours of vapour mass fraction in the baseline and optimised geometries; dotted lines correspond to the location of the most sudden entropy increase.

4 CONCLUSIONS

Pressure profile optimisation was conducted in this study, using a CFD-validated quasi-1D non-equilibrium design tool, capable of generating nozzle geometries for the wet-to-dry expansion of organic vapours. Three expansions with inlet pressure ranging from 450 to 650 kPa and constant inlet vapour quality of 0.3 were

investigated for the siloxane MM. It was found that the quasi-1D nozzle design tool is capable of predicting the phase-change pattern, but the assumption of inviscid quasi-1D flow and the omission of viscous and turbulence effects leads to an overprediction in the evaporation rate. However, since the phase-change pattern predicted by the quasi-1D tool is similar to the CFD predictions, the tool was still deemed suitable for performing 1D optimisation. Optimised geometries were simulated using a CFD model that accounted for viscosity, turbulence and two-dimensional effects. It was found that the optimised nozzles resulted in a rapid expansion that enhanced the evaporation rate. The CFD simulations conducted on the geometries generated using the optimised pressure profile achieved between 5.5 to 6.6% higher vapour mass fraction at the outlet, which reached 90.4, 94.8 and 97.2% for the expansions from 450, 550 and 650 kPa respectively. Although complete evaporation was achieved in none of the cases, reaching near-dry conditions for inlet pressures in the order of 650 kPa seems promising. Evaluation of the flow-field revealed that the abrupt expansion in the optimised geometries was associated with the formation of an oblique shock downstream of the throat, which in turn contributed to elevated entropy generation. The nozzle efficiencies for the optimised geometries were approximately 2 to 8% lower compared to the baseline geometries, with more pronounced loss at low pressures. This highlights the limitation of the 1D optimisation and emphasises the need for multi-objective CFD-based shape optimisation to maximise outlet vapour mass fraction whilst minimising performance loss.

REFERENCES

Brown, G., 1948, "*Heat transmission by condensation of steam on a spray of water drops"*, PhD thesis, University of London (Imperial College of Science and Technology).

Gobyzov, O. A., M. N. Ryabov, and A. V. Bilsky, 2020, "Study of Deformation and Breakup of Submillimeter Droplets' Spray in a Supersonic Nozzle Flow", *Applied Sciences*, 10(18), p. 6149.

Guildenbecher, D. R., Lopez-Rivera, C., and Sojka, P. E., 2009, "Secondary atomization", *Experiments in Fluids*, 46(3), pp. 371–402.

Ishii, M. and N. Zuber, 1979, "Drag coefficient and relative velocity in bubbly, droplet or particulate flows", *AIChE Journal*. 25(5), pp. 843–855.

Legendre, D. and Jacques M., 1998, "The lift force on a spherical bubble in a viscous linear shear flow", *Journal of Fluid Mechanics*, 368, pp. 81–126.

Lhermet, G., Tauveron, N., Caney, N., Blondel, Q., Morin, F., 2022, "A Recent Advance on Partial Evaporating Organic Rankine Cycle: Experimental Results on an Axial Turbine", *Energies*, 15(20), p. 7559.

Lemmon, E. W. et al. (2018). NIST Standard Reference Database 23: Reference Fluid Thermodynamic and Transport Properties-REFPROP, Version 10.0, National Institute of Standards and Technology.

NRC - US Nuclear Regulatory Commission, 1995, "RELAP5/MOD3 Code Manual. Volume 4: Models and correlations", Tech. rep, Idaho National Engineering Laboratory.

Ogrodniczak, P. and White, M.T., 2022, "Numerical validation of a two-phase nozzle design tool based on the two-fluid model applied to wet-to-dry expansion of organic fluids", *4th International Seminar on Non-Ideal Compressible Fluid Dynamics for Propulsion and Power*, 3-4th November, London, UK.

Ogrodniczak, P. and White, M.T., "Non-equilibrium CFD simulation of the wet-to-dry expansion of the siloxane MM in a converging-diverging nozzle", *Applied Thermal Engineering*, [Under review].

Rane, S. and He L., 2020, "CFD analysis of flashing flow in two-phase geothermal turbine design", *Journal of Computational Design and Engineering*, 7(2), pp. 238–250.

Ranz, W. E. and W. R. Marshall Jr., 1952, "Evaporation from Drops: Part 1", *Chemical Engineering Progress*, 48(3), pp. 141–146.

White, Martin T., 2021, "Cycle and turbine optimisation for an ORC operating with two-phase expansion", *Applied Thermal Engineering*, 192, p. 116852.

White, Martin T., 2022, "Investigating the wet-to-dry expansion of organic fluids for power generation", *International Journal of Heat and Mass Transfer*, 192, p. 122921.

Wieland, C., Schifflechner, C., Braimakis, K., Kaufmann, F., Dawo, F., Karellas, S., Besagni, G., Markides, C.N., 2023, "Innovations for organic Rankine cycle power systems: Current trends and future perspectives", *Applied Thermal Engineering*, 225, p. 120201.

ORC SEVILLE 2023
7th International Seminar on O.R.C. Power Systems

© 2024 Editorial Universidad de Sevilla. Este es un artículo de acceso abierto distribuido bajo los términos de la licencia de uso y distribución Creative Commons (BY-NC-ND 4.0)

DOI: https://dx.doi.org/10.12795/9788447227457_51

Thermodynamic modification of CO_2-based combined cooling and power cycle with ejector

Yonghao Zhang[1], Lingfeng Shi[1,*], Gequn Shu[1]

[1]*Department of Thermal Science and Energy Engineering, University of Science and Technology of China, Hefei 230027, China*
*Corresponding Author: slf@ustc.edu.cn

ABSTRACT

CO_2-based combined cooling and power cycle (CCP) has received increasing attentions especially in scenarios with diversified energy desires for its excellent natural properties. In this paper, an ejector is introduced into a conventional CCP system to reduce exergy loss in refrigeration throttling. A refrigerated truck is selected as the typical application scenario. And the simulated results indicate that approximately 28% of the expansion work during throttling can be recovered by the ejector, concurrently saving 0.3kW and 0.7kW compression work with respect to 10.8kW and 6.5kW cooling load under the freezing and refrigeration conditions. To extend the application of CCP system in more general scenarios, the ejector based CCP system is further modified to suit single heat source conditions. Two modified ejector based CCP systems namely ME-CCP-I and ME-CCP-II are proposed to recover waste energy from the compressor discharge. The adaptations to various heat source and refrigerating temperature are comprehensively studied. And the results demonstrate the ME-CCP-II system will be more suitable for air-conditioning scenarios while the ME-CCP-I system is advanced in freezing scenarios. In addition, recovering waste energy from the compressor discharge contributes great to the total energy efficiency of the CCP system as well as the heat transfer in regeneration process. With the mass split ratio increased from 0.1 to 0.9, the total energy efficiency of the ME-CCP-I system can raise from 0.27 to 0.64 and the relative enhancement is ranging from 1.26% to 11.86% versus the baseline system. Meanwhile, the ME-CCP-I system can reduce 48.6% irreversible loss in the heat regeneration process versus the baseline one when the same amount of exhausted energy after expansion is recovered.

313

1 INTRODUCTION

With a global phase-down of hydrofluorocarbons (HFCs) after an October 2016 meeting of the parties to the Montreal Protocol(UNEP Ozone Secretariat., 2016), the substitute of high-GWP refrigerants has been the spotlight in energy and chemical industry. Carbon dioxide (CO_2), as one of the representative natural refrigerants and once widely used refrigerant in the early twentieth century (Lorentzen and Pettersen, 1993), has again arrested interests in the field due to its outstanding properties in both thermodynamics and ecology (Bianchi et al., 2021). Thereupon, CO_2 based power and refrigeration technologies have rapidly boomed, which is widely applied in solar thermal power system (White et al., 2021), electric vehicle heat pump (Song et al., 2022), supermarket refrigeration system (Dilshad et al., 2020) and etc.

In scenarios with multiple energy desires, the cogeneration systems are generally more attractive for its sufficient efficiency, include the combined heating and power (CHP) system, combined cooling and power (CCP) system, and combined cooling, heating and power (CCHP) system. In the last years, plenty of researchers have devoted to the theoretical constructions and modifications on CO_2-based CCP systems (Wang *et al.*, 2012; Hou *et al.*, 2018; Manjunath *et al.*, 2018;Pan *et al.*, 2020; Zhao *et al.*, 2022). According to the coupled methods of the power subcycle and refrigeration subcycle, the CCP system can be simply classed into indirect type and direct type, wherein the latter directly shares a thermodynamic process of the two subcycles and thus more compact layouts with better exergoeconomic can achieve (Hou *et al.*, 2018). In our previous studies (Zhang et al., 2022a, 2022b),

the experimental prototype of direct type CO_2-based CCP system was developed and tested. The prototype integrated a transcritical CO_2 Rankine cycle and a reverse Carnot cycle (i.e. vapor compression refrigeration cycle, VRC) via the conjunct condenser and reservoir. The tested results indicate that switching the combined cycle from simultaneous cooling and power mode to power-alone mode or cooling-alone mode will either improve the power output or refrigeration output, concurrently ameliorating the effectiveness of heat transfer in the coupling condenser. Nevertheless, the VRC system with CO_2 commonly suffers lower efficiency due to the considerable exergy loss during throttling. In this context, ejector is approved an efficient solution to realize available work recovery in the throttling. Actually, approximately 8% to 27% improvement in COP could achieve in a transcritical ejector expansion refrigeration cycle (ERC), as reported by Banasiak *et al.*(2012), Elbel and Hrnjak (2008), Lawrence and Elbel (2019), Lee *et al.*(2014), Lucas and Koehler (2012), Minetto *et al.*(2013), Nakagawa *et al.*(2011).

As there is few attention paid to the direct type CCP system with ejector, the ejector is firstly introduced in the CCP system to enhanced COP of the conventional subcritical VRC subcycle in this paper. On the basis, another gap in the conventional CCP system is also considered, that is the available heat recovery from the refrigeration side. For typical CO_2 power cycles, the mismatch of heat capacity in the regenerator is the primary reason that results in the pinch point in heat transfer and performance deterioration (Luu et al., 2017). Shu *et al.*(2016) proposed a preheat-recuperative CO_2 Rankine cycle in engine waste heat recovery, wherein the engine coolant is employed as the preheat source. The crest span of specific heat capacity C_p of the CO_2 is accommodated well with the coolant and it simultaneously reforms the heat capacity allocation in the regenerator, which contributes to remarkable performance enhancement. In general scenarios with single heat source, waste heat from the compressor discharge in refrigeration subcycle is a possible preheat source. Hence, a further modification is conducted on the aforementioned ejector-assisted CCP system and two potential layouts derived from the scheme are investigated in the second case of the paper. Conclusively, the relevant results may offer some instructive references to future studies and applications of the CO_2-based CCP system.

2 METHODS AND MODELS

314

2.1 Description of CCP system

Fig.1 illustrated the schematic diagrams of the typical CCP system (Fig.1(a)) and its modified schemes with ejector(Fig.1(b-d)). The corresponding T-s diagrams are presented in Fig.2. In this paper, the basal CCP system (Figure.1(a), namely B-CCP) is firstly compared with the preliminarily modified CCP system with ejector (Figure.1(b), namely E-CCP). The power subcycle and refrigeration subcycle are integrated via the sharing condenser. And thus diverse outputs can be conveniently achieved by regulating the mass splitting in the condenser outlet. In the preliminary modification, the ejector is introduced to reduce the irreversible loss during throttling. Compared with the B-CCP system, the suction pressure of compressor in E-CCP system is quite enhanced so as to reduce the compression work. A refrigerated truck with two refrigeration requirements (i.e. refrigerating condition with evaporating temperature of 0℃ and freezing condition with evaporating temperature of -20℃) is selected as the research objective, which is consistent with our previous work (Zhang et al., 2020). Both of the exhaust gas and the coolant from the engine are recovered to drive the CCP system. The refrigerated truck is equipped with a 246kW diesel engine and the refrigeration load is 10.8kW and 6.5kW in refrigerating condition and freezing condition, respectively. The specifications of the exhaust gas and coolant from the engine are listed as followings:

- Inlet temperature and mass flow rate of exhaust gas: $T_{eg,in}$ =470.7℃ and m_g=1372.3kg/h.
- Inlet temperature, returned temperature, and mass flow rate of engine coolant: $T_{jw,in}$ =85℃, $T_{jw,re}$ =78.4℃, Q_{jw}=16.8m^3/h.

When turn to the common scenarios with single accessible heat source, the E-CCP system is further modified as ME-CCP-I system (Figure.1(c)) and ME-CCP-II system (Figure.1(d)). In this case, the outflow from pump is firstly preheated by compressor discharge. The particular difference is that in ME-CCP-II system, the back pressure of the expander is the suction pressure of compressor rather than the condensing pressure, which indicates the over-expansion in expander. In CO_2 transcritical power cycle, a proper over-expansion in expander is beneficial to thermal efficiency as suggested by Zhao et

al.(2020). And therefore the scheme is also taken into consideration in this work to investigate its adaptation to the CCP system. Meanwhile, an additional precooler is needful to reduce the work consumption in compressor in the ME-CCP-II system.

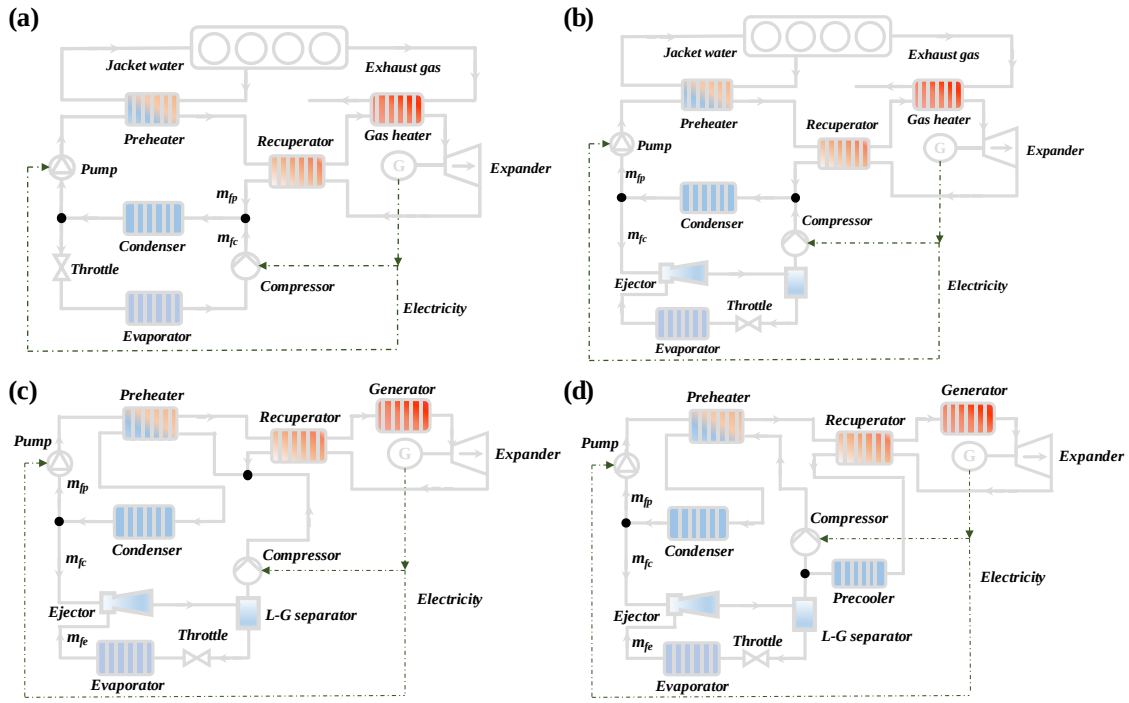

Figure.1: Schematic diagrams of the typical CCP system and the modified schemes with ejector: (a) Basal CCP system, namely B-CCP, (b) Ejector-assisted CCP system, namely E-CCP, (c) Modified ejector-assisted CCP system without over-expansion in power subcycle, namely ME-CCP-I, and (d) Modified ejector-assisted CCP system with over-expansion in power subcycle, namely ME-CCP-II.

315

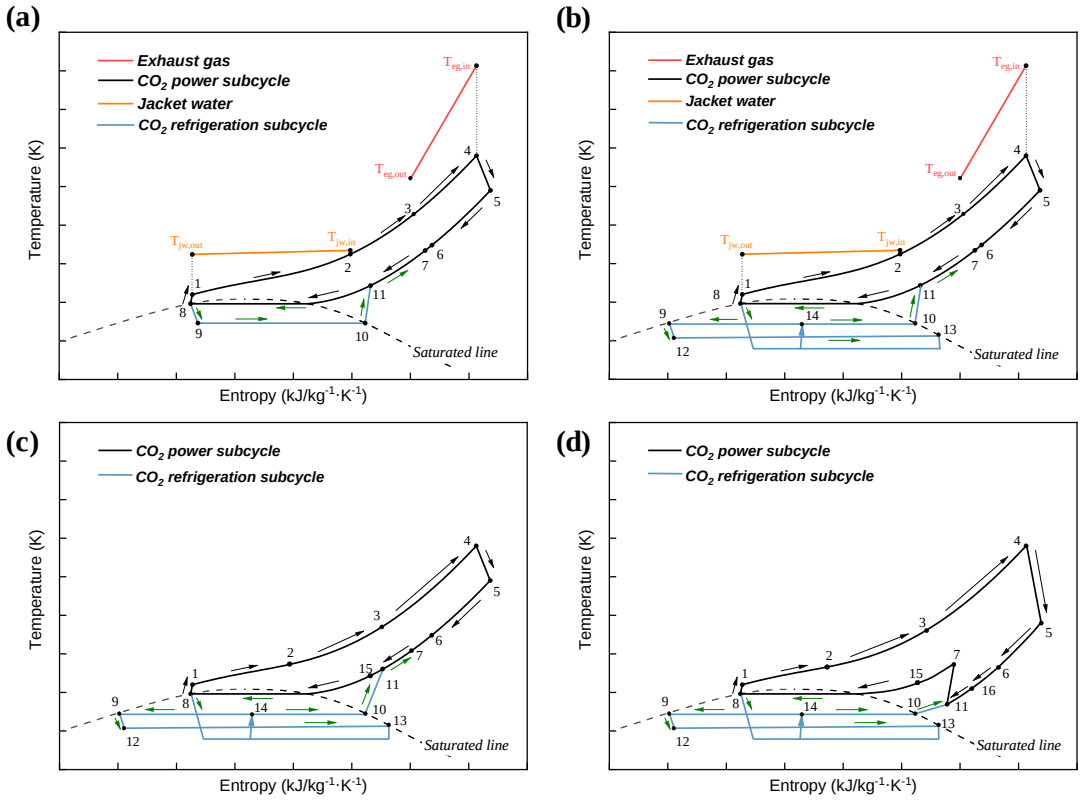

Figure.2: T-s diagrams of the typical CCP system and the modified schemes with ejector: (a) B-CCP system, (b) E-CCP system, (c) ME-CCP-I system, and (d) ME-CCP-II system.

2.2 Modeling of CCP system

To simulate the performance of the above systems, some necessary assumptions are made as followings:

- The systems perform in steady state condition, and pressure drop and heat loss in the components are negligible.
- Isentropic efficiencies are adopted to simulate the expander, compressor and pump, and the throttling process is regarded isenthalpic.
- The working fluids from evaporator outlet, condenser outlet and liquid-gas separator are saturated.
- Pinch temperature in the condenser, precooler, preheater, recuperator, and gas heater are settled at 5℃, 5℃, 5℃, 10℃ and 30℃ to guarantee efficient heat transfer.
- The condensing temperature should be less than 30℃ to ensure condensing of the CO_2, which is set 25℃ in this work.
- Inner flow in the ejector is steady and one-dimensional, and the internal irreversibility of ejector is described by nozzle efficiency ($\eta_n = 0.9$), mixing efficiency($\eta_m = 0.85$)and diffuser efficiency($\eta_d = 0.85$).

Based on the energy conversion and conservation, the quasi one-dimensional thermodynamic models of the CCP systems are built in MATLAB platform. The equations of each component and efficiencies of the machines are briefly summarized in **Table 1**. The properties of CO_2 are accessible in NIST database by invoking the REFPROP program. For the ejector, a constant-pressure mixing theory (Keenan *et al*., 1950) is adopted to simulate the inner process in the two-phase ejector. An averaged relative discrepancy between the simulated and experimental results is 2.48% as conducted in our previous study (Zhang et al., 2020), that ensures the validation of the simulation.

In the first case with a refrigerated truck as objective, the pinch point temperature difference method is applied to acquire the mass flow in power subcycle (Shu et al., 2016), while the mass flow in refrigeration subcycle is determined by the refrigeration load. While in the second case, the heat source is turned to common scenarios, where the temperature of heat source is an independent variable and its impact on system performance is one of the discussed scope. To simplify the simulation, the inlet temperature of the expander is used to reflect heat source conditions and the mass flow rate in the power subcycle is allocated as 1kg/s, i.e. $m_{fp} = 1\text{kg/s}$. However, the mass flow in refrigeration subcycle is still depend on the refrigeration load. The mass split ratio in condenser outlet is defined as $SR = m_{fc}/m_{fp}$, and the mass flow rate of working fluid running through the evaporator can therewith be calculated by entrainment ratio of the ejector: $m_{fe} = m_{fc} \cdot \mu$. As there are diverse energy outputs in the CCP system, the net power output ($W_{net} = W_{exp} - W_{pump} - W_{com}$) with same refrigeration capacity and the total energy efficiency of the CCP system (defined $\eta_{en} = \frac{Q_{eva}+W_{net}}{Q_{absorb}}$) are used to evaluate the performance of different schemes. All of E-CCP system, ME-CCPI, and ME-CCPII systems are allocated with the identical SR to ensure the same refrigeration load. And its impact on systematic performance is also taken into account.

316

On the other hand, to investigate the potential amelioration on heat regeneration process in these systems, the exergy analysis in heat transfer is also conducted. The exergy of working fluid at the specific state point is calculated by Equation (1), wherein the T_0, h_0, s_0 is the referenced environmental temperature, enthalpy and entropy at thermodynamic equilibrium state. The EUD (energy-utilization diagram) methodology (Jin et al., 2004) is adopted to graphically present the endogenous exergy destruction in the corresponding section based on A (energy level) and ΔH (energy transformation quantity) diagram. Herein, the energy level A is defined by Equation (2), and the ΔE_x and ΔS represent the exergy change and the entropy change, respectively. For the specific energy transformation process, the energy and exergy of the donor and receptor can be signified by paired curves. And the area between the curves become equal to the exergy destruction during the process.

$$ex_i = h_i - h_0 - T_0(s_i - s_0) \quad (1)$$

$$A = \frac{\Delta E_x}{\Delta H} = 1 - \frac{T_0 \Delta S}{\Delta H} \quad (2)$$

Table 1: Energy balance equations of the key components

Component	Equation
Expander	$W_{exp} = (h_4 - h_{5,s})\eta_{exp}$, η_{exp}=0.8 (Hou et al., 2018)
Gas heater/Generator	$Q_{gh} = m_{fp}(h_4 - h_3) = m_g(h_{g,in} - h_{g,out})$
Recuperator	$Q_{re} = m_{fp}(h_3 - h_2) = m_{fp}(h_5 - h_6)$
Preheater	$Q_{pre} = m_{fp}(h_2 - h_1) = m_{jw}(h_{jw,in} - h_{jw,out})$ or $Q_{pre} = m_{fp}(h_2 - h_1) = (m_{fp} + m_{fc})(h_7 - h_{15})$
Precooler	$Q_{prec} = m_{fp}(h_5 - h_{16})$
Condenser	$Q_{cond} = (m_{fp} + m_{fc})(h_{11} - h_8)$ or $Q_{cond} = (m_{fp} + m_{fc})(h_{15} - h_8)$
Evaporator	$Q_{eva} = m_{fc}(h_{10} - h_9)$ or $Q_{eva} = m_{fe}(h_{13} - h_{12})$
Pump	$W_{pump} = m_{fp}(h_{1,s} - h_8)/\eta_{pump}$, η_{pump} = 0.75 (Zhao *et al*.2020)
Compressor	$W_{com} = m_{fc}(h_{11,s} - h_{10})/\eta_{com}$ or $W_{com} = m_{fc}(h_{7,s} - h_{11})/\eta_{com}$; η_{com}=1.003-0.121·P_r (Liao et al., 2000)
Throttle	$m_{fc}h_8 = m_{fe}h_9$ or $m_{fe}h_9 = m_{fe}h_{12}$
LG-separator	$(m_{fc} + m_{fe})h_{14} = m_{fc}h_{10} + m_{fe}h_9$
Ejector	$m_{fc}h_8 + m_{fe}h_{13} = (m_{fc} + m_{fe})h_{14}$, entrainment ratio $\mu = {m_{fe}}/{m_{fc}}$

3 RESULTS AND DISCUSSIONS

317

3.1 Case 1: Effectiveness verification of ejector in CCP system (B-CCP vs. E-CCP)

The simulated results of the B-CCP and E-CCP systems are listed in Table 2. To achieve the maximum net power, the inlet temperature and pressure of expander are optimized with PSO algorithm. Obviously, the refrigeration COP (which is defined as: Q_{eva}/W_{com})is definitely enhanced with the help of the ejector, which is improved by 29.2% and 15.9% under freezing and refrigeration condition, respectively. The performance of the ejector is represented by the ejector efficiency η_{eje}, which is calculated by Equation (3), defined as the ratio of the recovered expansion work by the ejector to the maximum potential expansion work(Elbel and Hrnjak, 2008). Herein, approximately 28% of the expansion work during throttling can be recovered by the ejector, subsequently the compressor ratio is reduced by 14.7% and 7.0%. Although the absolute enhancement in net power output is just 0.7kW and 0.3kW under the two conditions, it accounts for 20.6% and 14.3% of the compression work. Hence, it indicates sufficient potential in energy saving with a larger refrigeration load. Furthermore, according to the results, the ejector will perform better in scenarios with lower evaporating temperature because of the lager pressure difference in throttle.

$$\eta_{eje} = \mu\frac{(h(P_{LG}, s_{sf}) - h_{sf})}{h_{pf} - h(P_{LG}, s_{pf})} \tag{3}$$

Table 2: Performance index of B-CCP and E-CCP system

	Freezing condition			Refrigeration condition		
	B-CCP	E-CCP	RV(%)	B-CCP	E-CCP	RV(%)
Net power output (kW)	31.6	32.4	+2.5	32.9	33.2	+0.9
Refrigeration COP (-)	1.92	2.48	+29.2	5.21	6.04	+15.9
Compressor work(kW)	3.4	2.7	-20.6	2.1	1.8	-14.3
Compressor ratio(-)	3.27	2.79	-14.7	1.85	1.72	-7.0
Ejector efficiency η_{eje}(%)	/	28.6	/	/	28.8	/

3.2 Case 2: Adaptation analysis of ME-CCP-I and ME-CCP-II

In this section, the original scheme without compressor discharge heat recovery (i.e. E-CCP system without preheater) is included as the baseline system. The performance index of the three CCP schemes with respect to different expander inlet temperature and evaporating temperature is firstly discussed. For consideration with the refrigeration span, an evaporating temperature from -20℃ to 10℃ is appropriate for freezing, refrigeration and air conditioning. While for the expander inlet temperature, T_g from 200℃ to 300℃ is possible to cover most of the heat source like solar energy, bioenergy, and industrial waste heat, etc. The expander inlet pressure of each system is optimized to achieve the maximal W_{net} and it is restricted within 20MPa in account of the state of the art . As for the refrigeration subcycle, the mass split ratio is set as 0.2 in the baseline condition.

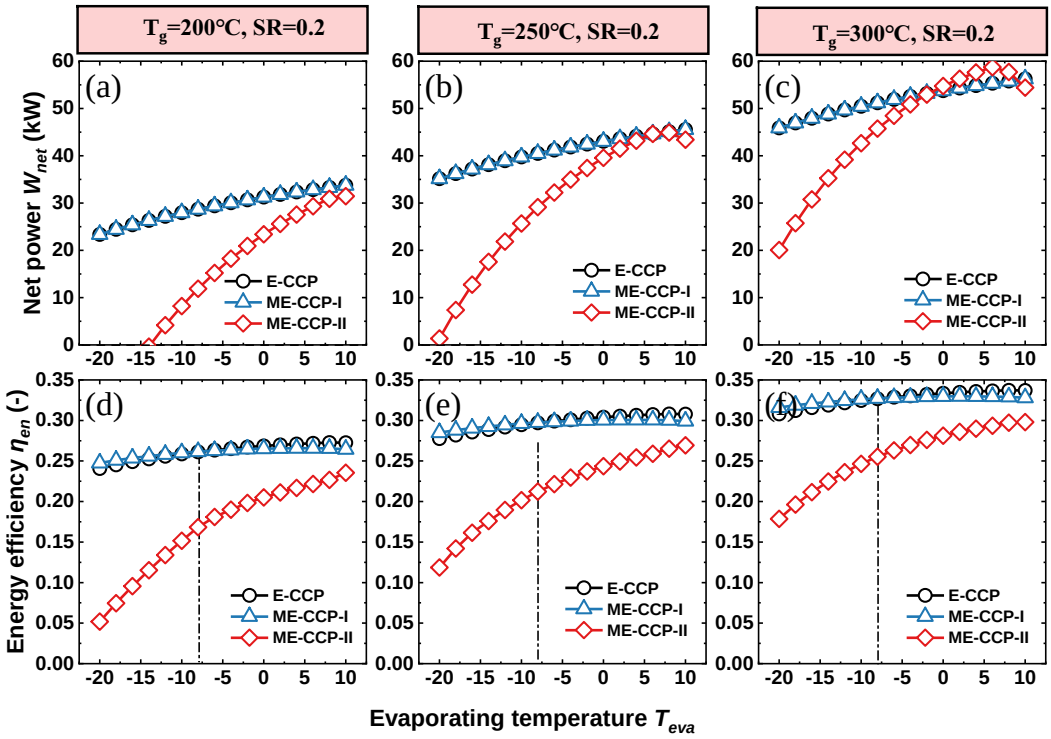

Figure 3: Performance comparison with respect to various heat source and evaporating temperature.

As is can be seen in Figure 3, the E-CCP system and ME-CCP-I system demonstrate identical changes in net power with respect to evaporating temperature and it has no concern with the heat source temperature. Overall, the net power output in these two system performs much better than the ME-CCP-II system when the expander inlet temperature is equal to 200℃ and 250℃. As for the ME-CCP-II system, an extra overexpansion ratio imposes great energy consumption in the compressor and thus it will be more suitable for air conditioning scenarios. Simultaneously, a higher grade heat source makes greater sense to the ME-CCP-II system as well. As presented in Figure 3(c), the ME-CCP-II system excels the ME-CCP-I with evaporating temperature ranging from 0℃ to 8℃ at T_g=300℃ condition. For instance, when the evaporating temperature is equal to 6℃, the ME-CCP-II can offer 58.7kW mechanical power output with 30.0kW refrigeration load, which is improved by 6.15% versus the ME-CCP-I and E-CCP systems (which is 55.3kW in the condition). However, the ME-CCP-II system has a poor performance on total energy efficiency in all of the simulated conditions, which is resulted from the reduced heat regeneration in recuperator.

For the ME-CCP-I system, only if the evaporating temperature is lower than -8℃, the ME-CCP-I system will present better energy efficiency than the baseline system. Hence, it will be more suitable for freezing scenarios. This is predictable because once the temperature of compressor discharge is higher than the pumped outflow will the preheater work. Meanwhile, the enhancement is also related to the mass split ratio, that is the refrigeration load. Figure 4 presents the variations of total energy efficiency of the ME-CCP-I and baseline E-CCP system with respect to varying mass split ratio when

T_g=300℃ and T_{eva}=-20℃. With the mass split ratio increased from o.1 to 0.9, the total energy efficiency of the ME-CCP-I system can raise from 0.27 to 0.64 and the relative enhancement is ranging from 1.26% to 11.86% versus the E-CCP system.

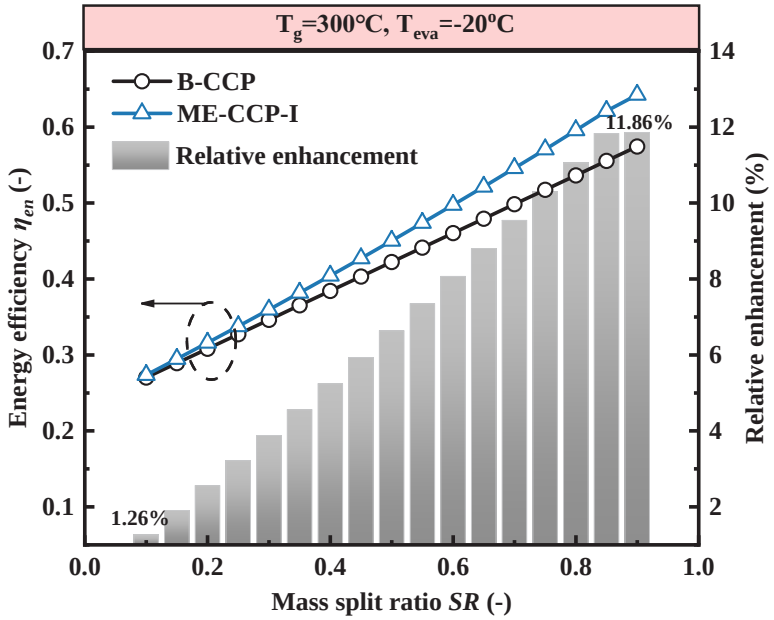

Figure 4: Variation of energy efficiency with respect to mass split ratio: T_g=300℃ and T_{eva}=-20℃.

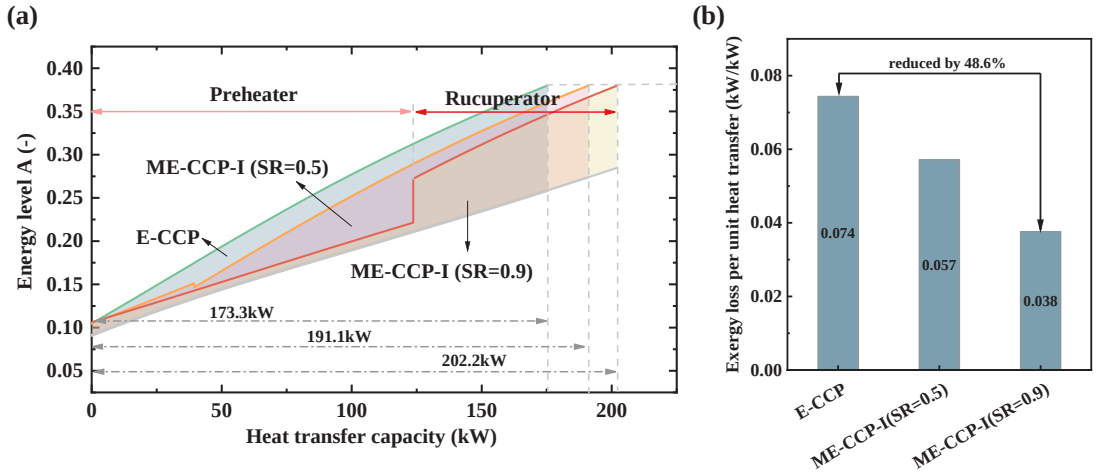

Figure 5: Heat transfer and exergy destruction in preheater and recuperator : T_g=300℃ and T_{eva}=-20℃.

Figure 5 presents the energy utilization diagram in the preheater and recuperator of the ME-CCP-I system and E-CCP system with different mass split ratio. Therein, the grey solid curve represents the low-temperature fluid between the pump outlet and generator inlet, while the green, orange and red curves indicate the high-temperature fluid that performs as the regenerating heat source, with *SR* equal to 0, 0.5, and 0.9 respectively. The shaded area between the two heat transfer fluids signifies the exergy destruction during the heat transfer process and the horizontal axis indicates the actual heat transfer capacity in the exchanger. Obviously, preheat in the preheater can definitely ameliorate temperature match during the heat regeneration process, and improve the ultimate temperature of the high-pressure fluid at the recuperator outlet. As there is no preheater in the baseline E-CCP system, it can be equivalent to the condition with SR=0 in the ME-CCP-I system. Therefore, with the SR increased from 0 to 0.9, the available heat regeneration is enhanced from 173.3kW to 202.2kW, and the exergy loss during the regenerating process is simultaneously reduced from 13.0kW to 7.61kW. To concurrently reveal the variations of exergy loss and heat transfer capacity in the case, a dimensionless exergy loss over per

unit heat transfer capacity is presented in Figure 5(b), which is calculated by Equation (4). For the E-CCP system, a high $ex_{d,Q}$ with 0.074 is obtained without heat recovery from the compressor discharge. While for the ME-CCP-I system, the values are just 0.057 and 0.038 when the SR is equal to 0.5 and 0.9, respectively. Hence, ME-CCP-I system can reduce 48.6% irreversible loss in the heat regeneration process versus the E-CCP system when the same amount of exhausted energy after expansion is recovered.

$$ex_{d,Q} = \frac{Ex_{d,tot}}{Q_{tot}} \tag{4}$$

4 CONCLUSIONS

In this paper, a thermodynamic modification on CO_2-based combined cooling and power cycle with ejector is conducted. A refrigerated truck is firstly selected as the typical application scenario to verify the effectiveness of the ejector and then further modification on the baseline ejector-based CCP system is performed to extend its application to more general scenarios with single heat source. The impacts of heat source, refrigerating temperature, and mass split ratio on adaptation of the modified systems are comprehensively investigated. Conclusively, the relevant results may offer some instructive references to future studies and applications of the CO_2-based CCP system, and the main conclusions are listed as followings:

- Approximately 28% of the expansion work during throttling can be recovered by the ejector, concurrently saving 0.3kW and 0.7kW compression work with respect to 10.8kW and 6.5kW cooling load under the freezing and refrigeration conditions.
- The ME-CCP-II system will be more suitable for air-conditioning scenarios while the ME-CCP-I system is advanced in freezing scenarios.
- Recovering waste energy from the compressor discharge contributes great to the total energy efficiency of the CCP system as well as the heat transfer in regeneration process. With the mass split ratio increased from 0.1 to 0.9, the total energy efficiency of the ME-CCP-I system can raise from 0.27 to 0.64 and the relative enhancement is ranging from 1.26% to 11.86% versus the baseline system. Moreover, the ME-CCP-I system can reduce 48.6% irreversible loss in the heat regeneration process versus the baseline system when the same amount of exhausted energy after expansion is recovered.

320

NOMENCLATURE

CCP	Combine cooling and power cycle
COP	Coefficient of performance
RV	Relative variation
h	Specific enthalpy
ex	Specific exergy
s	Specific entropy

Subscript

com	Compressor
cond	Condenser
d	Destruction
eje	Ejector
eva	Evaporating
exp	Expander
fc	Mass flow rate in compressor
fe	Mass flow rate in refrigeration side
fp	Mass flow rate in power side
gh	Gas heater or generator
i	Specific state point in the cycle
in	Inlet

jw	Jacket water
out	Outlet
pre	Preheater
pump	Pump
tot	Total

REFERENCES

Banasiak, K., Hafner, A., Andresen, T., 2012. Experimental and numerical investigation of the influence of the two-phase ejector geometry on the performance of the R744 heat pump. Int. J. Refrig. 35, 1617–1625. https://doi.org/10.1016/J.IJREFRIG.2012.04.012

Bianchi, G., Besagni, G., Tassou, S.A., Markides, C.N., 2021. Overview and outlook of research and innovation in energy systems with carbon dioxide as the working fluid. Appl. Therm. Eng. 195, 117180. https://doi.org/10.1016/J.APPLTHERMALENG.2021.117180

Dilshad, S., Kalair, A.R., Khan, N., 2020. Review of carbon dioxide (CO2) based heating and cooling technologies: Past, present, and future outlook. Int. J. Energy Res. 44, 1408–1463. https://doi.org/10.1002/er.5024

Elbel, S., Hrnjak, P., 2008. Experimental validation of a prototype ejector designed to reduce throttling losses encountered in transcritical R744 system operation. Int. J. Refrig. 31, 411–422. https://doi.org/10.1016/j.ijrefrig.2007.07.013

Hou, S., Zhang, F., Yu, L., Cao, S., Zhou, Y., Wu, Y., Hou, L., 2018. Optimization of a combined cooling, heating and power system using CO2 as main working fluid driven by gas turbine waste heat. Energy Convers. Manag. 178, 235–249. https://doi.org/10.1016/j.enconman.2018.09.072

Jin, H., Zhao, H., Liu, Z., Cai, R., 2004. A novel EFHAT system and exergy analysis with energy utilization diagram. Energy 29, 1983–1991. https://doi.org/10.1016/j.energy.2004.03.009

KEENAN, J.H., NEUMANN, E.P., LUSTWERK, F., 1950. AN INVESTIGATION OF EJECTOR DESIGN BY ANALYSIS AND EXPERIMENT. J. Appl. Mech. ASME 17, 299–309.

Lawrence, N., Elbel, S., 2019. Experimental investigation on control methods and strategies for off-design operation of the transcritical R744 two-phase ejector cycle. Int. J. Refrig. 106, 570–582. https://doi.org/10.1016/j.ijrefrig.2019.04.020

Lee, J.S., Kim, Min Soo, Kim, Mo Se, 2014. Studies on the performance of a CO2 air conditioning system using an ejector as an expansion device. Int. J. Refrig. 38, 140–152. https://doi.org/10.1016/J.IJREFRIG.2013.08.019

Liao, S.M., Zhao, T.S., Jakobsen, A., 2000. A correlation of optimal heat rejection pressures in transcritical carbon dioxide cycles. Appl. Therm. Eng. 20, 831–841. https://doi.org/10.1016/S1359-4311(99)00070-8

Lorentzen, G., Pettersen, J., 1993. A new, efficient and environmentally benign system for car air-conditioning. Int. J. Refrig. 16, 4–12. https://doi.org/10.1016/0140-7007(93)90014-Y

Lucas, C., Koehler, J., 2012. Experimental investigation of the COP improvement of a refrigeration cycle by use of an ejector. Int. J. Refrig. 35, 1595–1603. https://doi.org/10.1016/j.ijrefrig.2012.05.010

Luu, M.T., Milani, D., McNaughton, R., Abbas, A., 2017. Analysis for flexible operation of supercritical CO2 Brayton cycle integrated with solar thermal systems. Energy 124, 752–771. https://doi.org/10.1016/j.energy.2017.02.040

Manjunath, K., Sharma, O.P., Tyagi, S.K., Kaushik, S.C., 2018. Thermodynamic analysis of a supercritical/transcritical CO2 based waste heat recovery cycle for shipboard power and cooling applications. Energy Convers. Manag. 155, 262–275. https://doi.org/10.1016/j.enconman.2017.10.097

Minetto, S., Brignoli, R., Banasiak, K., Hafner, A., Zilio, C., 2013. Performance assessment of an off-the-shelf R744 heat pump equipped with an ejector. Appl. Therm. Eng. 59, 568–575. https://doi.org/10.1016/J.APPLTHERMALENG.2013.06.032

Nakagawa, M., Marasigan, A.R., Matsukawa, T., 2011. Experimental analysis on the effect of internal heat exchanger in transcritical CO2 refrigeration cycle with two-phase ejector. Int. J. Refrig. 34, 1577–1586. https://doi.org/10.1016/j.ijrefrig.2010.03.007

Pan, M., Bian, X., Zhu, Y., Liang, Y., Lu, F., Xiao, G., 2020. Thermodynamic analysis of a combined supercritical CO 2 and ejector expansion refrigeration cycle for engine waste heat recovery. Energy Convers. Manag. 224, 113373. https://doi.org/10.1016/j.enconman.2020.113373

Shu, G., Shi, L., Tian, H., Li, X., Huang, G., Chang, L., 2016. An improved CO2-based transcritical Rankine cycle (CTRC) used for engine waste heat recovery. Appl. Energy 176, 171–182. https://doi.org/10.1016/j.apenergy.2016.05.053

Song, Y., Cui, C., Yin, X., Cao, F., 2022. Advanced development and application of transcritical CO2 refrigeration and heat pump technology—A review. Energy Reports 8, 7840–7869. https://doi.org/10.1016/J.EGYR.2022.05.233

UNEP Ozone Secretariat, n.d. No Title, in: In Twenty-Eighth Meeting of the Parties to the Montreal Protocol on Substances That Deplete the Ozone Layer (Kigali, Rwanda, 2016); Document UNEP/OzL.Pro.28/CRP/10, United Nations Environment Programme, 2016.

Wang, J., Zhao, P., Niu, X., Dai, Y., 2012. Parametric analysis of a new combined cooling, heating and power system with transcritical CO2 driven by solar energy. Appl. Energy 94, 58–64. https://doi.org/10.1016/j.apenergy.2012.01.007

White, M.T., Bianchi, G., Chai, L., Tassou, S.A., Sayma, A.I., 2021. Review of supercritical CO2 technologies and systems for power generation. Appl. Therm. Eng. 185, 116447. https://doi.org/10.1016/J.APPLTHERMALENG.2020.116447

Zhang, Y., Shi, L., Tian, H., Li, L., Wang, X., Huang, G., Shu, G., 2022a. Experimental investigation on CO2-based combined cooling and power cycle. Energy Convers. Manag. 256, 115342. https://doi.org/10.1016/j.enconman.2022.115342

Zhang, Y., Shi, L., Tian, H., Li, L., Wang, X., Sun, X., 2022b. Experiment on CO2-based combined cooling and power cycle : A multi-mode operating investigation. Appl. Energy 313, 118884. https://doi.org/10.1016/j.apenergy.2022.118884

Zhang, Y., Shu, G., Tian, H., Shi, L., Sun, X., 2020. Modified CO2-based combined cooling and power cycle with multi-mode and adjustable ability. Energy Convers. Manag. 226, 113485. https://doi.org/10.1016/j.enconman.2020.113485

Zhao, D., Han, C., Cho, W., Zhao, L., Kim, Y., 2022. Directly combining a power cycle and refrigeration cycle: Method and case study. Energy 259, 125017. https://doi.org/10.1016/J.ENERGY.2022.125017

Zhao, D., Zhao, R., Deng, S., Zhao, L., Chen, M., 2020. Transcritical carbon dioxide power cycle for waste heat recovery: A roadmap analysis from ideal cycle to real cycle with case implementation. Energy Convers. Manag. 226, 113578. https://doi.org/10.1016/J.ENCONMAN.2020.113578

ACKNOWLEDGEMENT

The authors gratefully acknowledge the financial support from the National Key R&D Program of China (Grant No. 2022YFE0100100).

ORC SEVILLE 2023
7th International Seminar on O.R.C. Power Systems

© 2024 Editorial Universidad de Sevilla. Este es un artículo de acceso abierto distribuido bajo los términos de la licencia de uso y distribución Creative Commons (BY-NC-ND 4.0)

DOI: https://dx.doi.org/10.12795/9788447227457_53

SELECTION OF SUITABLE WORKING FLUID AND STORAGE MATERIAL FOR ORC COUPLED WITH THERMAL ENERGY STORAGE

Dawid Sowa[1,*], Sindu Daniarta[1,2], Piotr Kolasiński[1]

[1] *Wrocław University of Science and Technology, Department of Thermodynamics and Renewable Energy Sources, Wrocław, Poland*

[2] *Budapest University of Technology and Economics, Department of Energy Engineering, Budapest, Hungary*

* Corresponding Author: dawid.sowa@pwr.edu.pl

ABSTRACT

Some low-temperature energy sources (e.g., waste or solar heat) tend to be intermittent, and the heat supply from such sources may fluctuate over time. This kind of heat could be utilized using organic Rankine cycle (ORC) to generate electricity. Moreover, the increase in their reliability may be possible thanks to the application of thermal energy storage (TES), in which surplus thermal energy may be accumulated in the storage material. This energy can then be used in these periods of time when the heat source is not available or its output is limited. In this way, energy generation may be levelled. In some cases, a wide range of operating conditions and a variety of working fluids that are used in ORC systems mean that the choice of TES material may be difficult, since there are several types of TES materials, and each analysed case can give different material selections. Because of that, optimizing TES that is connected to the ORC system can be an interesting scientific challenge. Therefore, the aim of this study is to present the selection of proper working fluid-TES material pairs for different working conditions applied to a model of the ORC system coupled with TES. Various configurations of the ORC-TES system were investigated, taking into account differences between latent and sensible TES, and both for simple and recuperated cycles. The results obtained show that the combination of ORC with TES is promising for application in intermittent and fluctuating heat sources.

1. INTRODUCTION

Some of the energy sources that are in use have intermittent characteristics. This means that their parameters, like temperature and flow rate, are not constant and fluctuate over time. These energy sources include renewable energy sources, such as solar energy, as well as recovered waste heat from industrial processes or vehicles. The amplitude and duration of these changes vary, from relatively slow changes in the day-night cycle related to solar radiation to very fast changes in the internal combustion engines applied in vehicles, which may be caused by road conditions. To utilize this kind of intermittent and fluctuating heat source, an organic Rankine cycle (ORC) might be one of the promising technologies since it offers a wider range of operating temperatures. Moreover, the ORC system would typically have a certain point of maximum efficiency (Ahmed *et al.*, 2021; Ahmed and Imre, 2023; Daniarta *et al.*, 2021) for which it was designed. As the conditions shift away from the design point, the efficiency deteriorates. That means that if it harvests energy from fluctuating energy sources, it may operate in unfavourable operating conditions for a significant period of time.

In designing and operating the ORC, efficiency is not the only concern. If the operating conditions move sufficiently from the allowed operating range, it may be necessary to turn off the system from operation

to prevent damage. This may be caused by the too high temperature of the heat source, which in turn could cause excess pressure of the working fluid, or its thermal decomposition. Having a relatively low temperature of the heat source might potentially lead to partial evaporation of the working fluid and then it might lead to increase droplets in the expander. In particular, for a turbine, operating in two-phase conditions is often avoided as it might result in expander damage. As an alternative, a promising way of levelling intermittent energy sources is by storing their thermal energy in the storage material. Thermal energy storages (TES), also called heat storages, vary in size, thermal power, operating temperature and type of storage material used. Different modes of operation are possible for TES. A smaller thermal energy storage would be sufficient to provide buffering of fluctuations, reducing peaks and valleys, while a larger thermal energy storage could be used to shift energy production to the time periods characterized by the highest energy demand (Daniarta and Kolasiński, 2021). With fluctuations reduced, the system can work near the design point for longer time periods, and in some cases, the size of the expander can be reduced, since it does not have to handle periodically increased input (Li et al., 2021).

Depending on the type of material used for thermal energy storage, thermal energy storage can be classified into:

- Sensible thermal energy storage (STES)—in which thermal energy is stored by changing the temperature of the storage material, such as hot water, sand, or rocks. As more energy is stored in the STES, the temperature of the material increases.
- Latent heat thermal energy storage (LTES)—in which thermal energy is absorbed and released by using phase change of the material (called phase change material - PCM), such as kinds of paraffin. The storage density of LTES is higher than the STES.
- Thermochemical energy storage (TCES)—in which reversible chemical reactions are used to provide even higher storage density than LTES. One of the reactions used is water adsorption in zeolites.

These technologies differ not only in operating principles but also in storage capacity, power, storage period, the time needed to charge and discharge them, efficiency and cost (Sarbu and Sebarchievici, 2018).

A recent review reported that TES could be connected with ORC systems for different purposes, either directly or indirectly (Daniarta et al., 2023). In a direct system, the working fluid flows through TES, whereas in an indirect, an additional medium is used to transfer the heat. Only a few modeling simulation and experimental investigation were found in the study of literature. A prior study (Kolasiński and Daniarta, 2021) reported simulation results of sizing TES for the ORC system. However, only simple ORC with selected TES material was examined. Therefore, to extend the study, in this paper, a modelling analysis was carried out for ORC systems powered by thermal energy storage considering recuperated systems, which can be the state of the art of this paper. A comparison between different working fluids and storage materials was described. Both sensible and latent heat storage materials were analysed. Their efficiency, and thermal energy storage size (i.e., the amount of the storage material required) were evaluated. For simplification, only direct systems, without intermediate working fluids, were considered.

2. MODEL OF THE SYSTEM

Two types of ORC systems, which are simple and recuperated ORCs, are considered in the present analysis. The design of both systems is presented in Figure 1. The simple system, which is composed of four main components: evaporator (which for the purpose of this analysis can be subdivided into preheater, evaporator and in some cases superheater), expander, condenser (which for the purpose of this analysis can be subdivided into precooler and condenser), and pump.

Furthermore, recuperated ORC as the second type of the considered system in this analysis, has an additional component (see Figure 1) in which an internal heat exchanger is used to recover heat from

the working fluid flowing from the outlet of the expander and use it to heat up the liquid working fluid at the inlet to the evaporator. This configuration is more commonly applied for ORC systems using complex (dry) working fluids, because of the higher thermal power at the outlet of the expander (Astolfi, 2017).

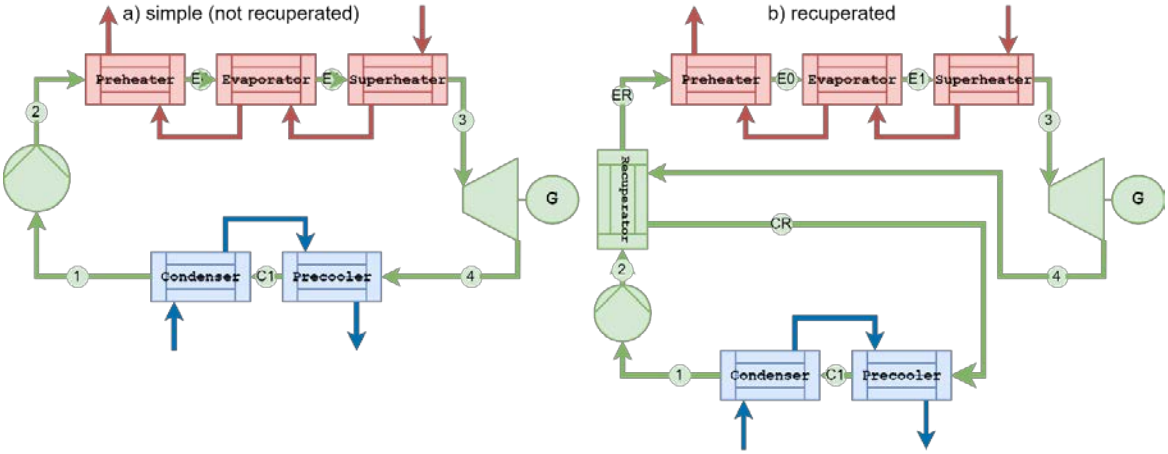

Figure 1: Design of a) simple and b) recuperated ORCs

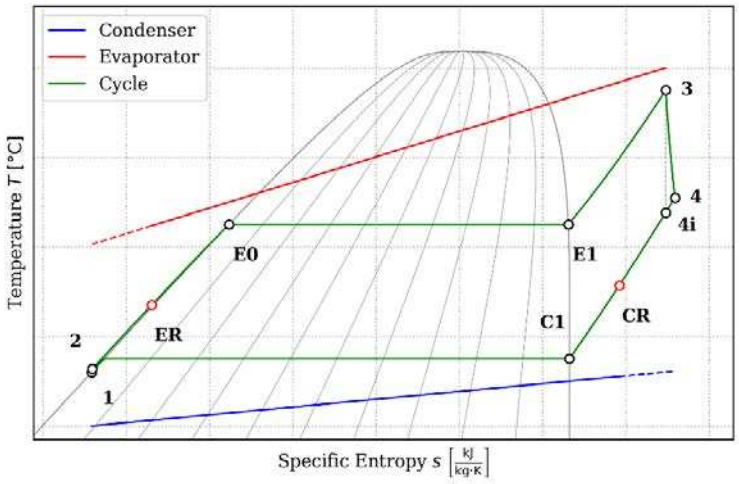

Figure 2: Simple and recuperated ORC on T-s diagram

Cycle diagrams for both of them are similar in the temperature-entropy diagram shown in Figure 2, with the exception of two additional characteristic state points for the recuperated system.

In this study, the modeling simulation was developed using several assumptions, as follows:

- Isentropic efficiencies of the expander and pump (η_{exp} and η_P) are constant and equal to 0.8 and 0.7 respectively,
- There is no superheating (i.e., thermodynamic properties of working fluid in point E1 and 3 are the same),
- Subcooling temperature (ΔT_{sub}) is constant, and equal to 3,
- Temperature differences between mediums (pinch point temperature) (ΔT) are constant and equal to 5,
- Condensation temperature (T_C) is constant and equal to 30 °C,
- Heat losses to the environment, as well as pressure drops in heat exchangers and pipelines, are assumed to be negligible,
- Heat is supplied to the cycle directly from the TES,

- In recuperated cycle, the ΔT_{low} (temperature difference between point 2 and CR, as described in Equation (4)) is set for half of the temperature difference between C1 and 4.

Several different working fluids with low global warming potential (GWP) and low ozone depletion potential (ODP) were selected in this study due to limited negative environmental effects. For instance, some HFOs and hydrocarbons are chosen including Novec649, R1233zd, R1234yf, R1234ze(E), R1234ze(Z), R1243zf, Neopentane, Isobutane, Isobutene, Isopentane, n-Pentane and n-Propane. The thermal properties of the working fluids were taken from the CoolProp library (Bell et al., 2014). Moreover, various TES materials and their properties were taken from the articles (Daniarta et al., 2022; Kolasiński and Daniarta, 2021) such as Monel, stainless steel 446, sandstone, granite, chrome brick, concrete, chamotte brick, silicon carbide, magnesite brick and rapeseed, soybean, sunflower, cotton, and jatropha oils. Variations of specific heat capacity of the selected sensible TES materials vs. temperature based on that data are depicted in Figure 3.

In calculations, for latent TES, it is assumed that the discharge process happens entirely in isothermal conditions during the phase change. Moreover, for sensible TES, the discharge is proceeded in non-isothermal conditions. In further analysis, it was assumed that the starting temperature is 20 °C lower than the critical temperature of the working fluid, or equal to the maximum temperature of the TES material (as presented in Figure 3), or 180 °C, whichever is smaller. Under these conditions, the highest calculated pressure was 27 bars (n-Propane), which can be handled using commercially available heat exchangers. Discharge is assumed to continue as long as the expansion ratio (i.e., pressure ratio between expanders inlet and outlet) is equal at least to 2 and the temperature of storage material is at least 50 °C.

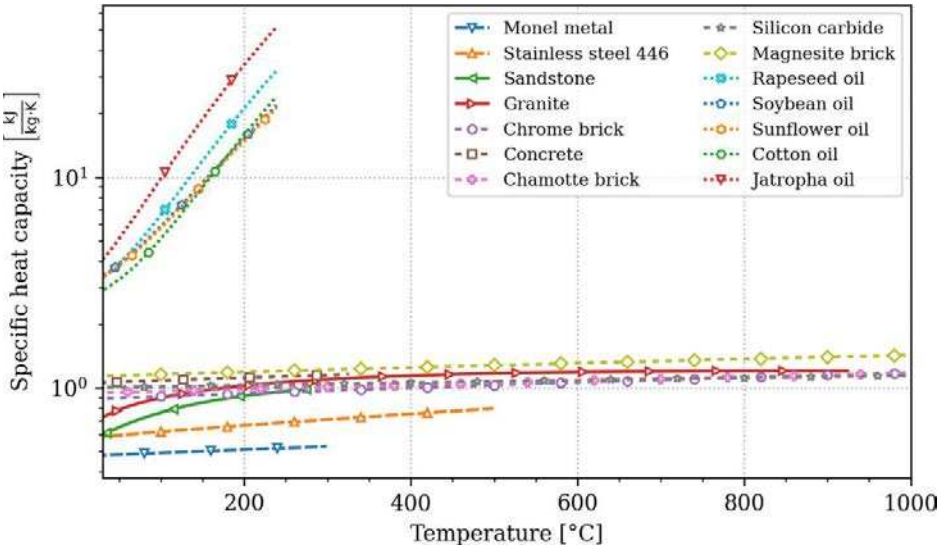

Figure 3: Variation of specific heat capacity vs. temperature of different sensible TES materials, where the data is taken from (Kolasiński and Daniarta, 2021)

3. MATHEMATICAL MODEL AND RESULTS

Based on the above-mentioned assumptions, the thermal properties of the working fluid in characteristic points of the system can be calculated. Using them it is possible to determine other assessment parameters, such as heat input, the net output power and the net efficiency of the ORC system expressed in Equations (1) – (3).

$$\dot{Q}_{\mathrm{in}} = \dot{m}_{\mathrm{f}} \cdot \Delta h_{\mathrm{in}} = \dot{m}_{\mathrm{f}} \cdot (h_3 - h_2) \tag{1}$$

$$W_{\mathrm{net}} = W_{\mathrm{exp}} - W_{\mathrm{pump}} = \dot{m}_{\mathrm{f}} \cdot \left(\Delta h_{\mathrm{exp}} - \Delta h_{\mathrm{pump}}\right) = \dot{m}_{\mathrm{f}} \cdot [(h_3 - h_4) - (h_2 - h_1)] \tag{2}$$

$$\eta_{net} = \frac{W_{net}}{\dot{Q}_{in}} \tag{3}$$

Recuperated ORC can be described in a way similar to the simple ORC, while two additional points can be determined if a parameter ΔT_{low} is introduced by Equation (4). This parameter describes the low-end temperature difference, that is, between the points CR (gas flowing out from the recuperator into the condenser) and 2 (liquid flowing out from the pump into the recuperator).

$$T_{CR} = T_2 + \Delta T_{low} \tag{4}$$

The specific enthalpy of the working fluid for the second of the added points can be calculated from the energy balance of the heat exchanger that is described in Equation (5).

$$\dot{m}_F \cdot (h_4 - h_{CR}) = \dot{m}_f (h_{ER} - h_2) \tag{5}$$

Furthermore, the net power of the ORC system and efficiency can be calculated in the same way as the simple ORC using Equations (2) and (3), however, because of the introduction of the recuperator, $\dot{Q}_{in}$ is smaller, and efficiency is higher (see, Equation (6)).

$$\dot{Q}_{in} = \dot{m}_f \cdot (h_3 - h_{ER}) \tag{6}$$

The amount of heat that can be stored in TES depends on the mass of the TES material, the temperature difference between charged and discharged conditions, and the specific heat capacity of the TES material, as given in Equation (7).

$$Q_{TES} = c_p(T_{sm})\Big|_{T_{charged}}^{T_{discharged}} \cdot \left(T_{charged} - T_{discharged}\right) \cdot m_{sm} \tag{7}$$

As the temperature of the thermal energy storage material changes, so does its specific heat capacity. Based on the experimental data, the function $c_p(T_{sm})$ can be approximated by a polynomial equation, which in general form is given by Equation (8).

$$c_p(T_{sm}) = c_0 + c_1 \cdot T + c_2 \cdot T^2 + \cdots + c_n T^n \tag{8}$$

327

For the PCMs used in the latent TES, assuming that the TES is fully charged when the material is completely melted, and fully discharged, when the material is completely solidified, the whole process is isothermal. Two parameters such as melting temperature and melting enthalpy are sufficient to determine stored heat. In this case, melting temperature describes the temperature at which the process takes place. In addition, melting enthalpy describes specific heat stored by the phase change. Therefore, for LTES, Equation (7) can be expressed as a function of melting enthalpy that is described in Equation (9).

$$Q_{LTES} = m_{sm} \cdot \Delta h_{melting} \tag{9}$$

One of the aims in the selection of the TES material is to minimize the required mass to store the heat so that the space requirements and cost of TES could be minimized. In the previous work (Kolasiński and Daniarta, 2021), a dimensionless parameter ζ_{sm} for sizing of the heat storage was introduced, which is defined as a ratio of the mass of the thermal energy storage material needed to store heat, to the mass of the working fluid, as given by Equation (10).

$$\zeta_{sm} = \frac{m_{sm}}{m_f} = \frac{\Delta h_{HE}}{c_p(T_{sm})\Big|_{T_{charged}}^{T_{discharged}} \cdot \left(T_{charged} - T_{discharged}\right)} \tag{10}$$

For latent TES, it can be simplified to the form given by Equation (11).

$$\zeta_{sm} = \frac{m_{sm}}{m_f} = \frac{\Delta h_{HE}}{\Delta h_{melting}} \tag{11}$$

This parameter can be calculated separately for the precooler ($\zeta_{precooler}$) and evaporator ($\zeta_{evaporator}$), or as the total for both of them (ζ_{total}).

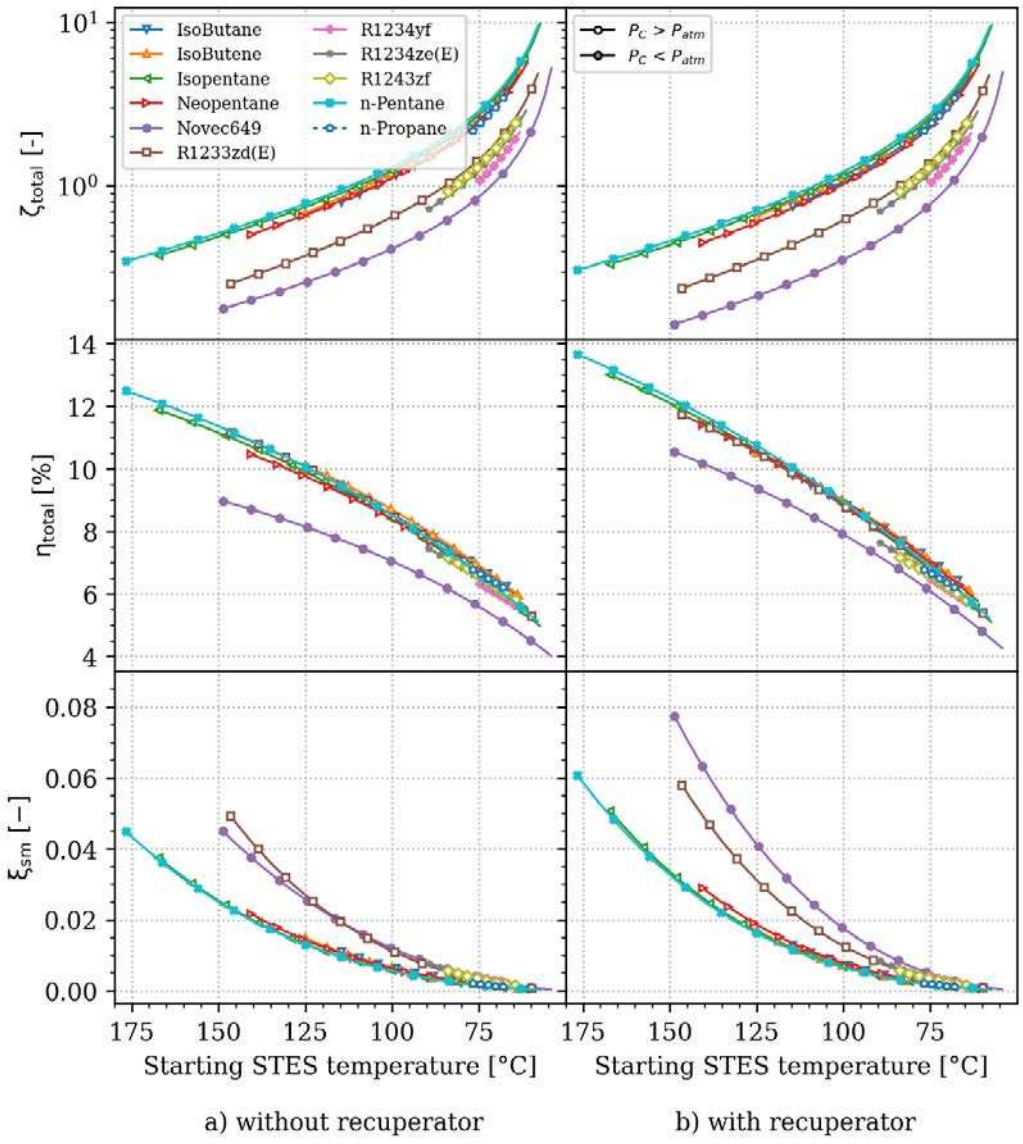

Figure 4: Variation of assessment parameters of ORC with TES vs starting STES temperature, for jatropha oil and working fluids with low GWP and no ODP.

The mass of the storage material, that is needed to implement TES, is not the only parameter that should be evaluated. The efficiency of different ORCs with different working fluids also needs to be evaluated. The total efficiency of the discharge could be defined as a ratio of work generated by the ORC during the discharge, to the heat input during that time, as shown in Equation (12).

$$\eta_{total} = \frac{\int_{t,charged}^{t,discharged} W_{net} \cdot dt}{Q_{TES}} \tag{12}$$

For LTES, since the temperature of the thermal energy storage material is constant, the ORC system can work in steady-state conditions, and net power output during the discharge would remain constant. In this case, η_{total} would be equal to η_{net}.

For sensible heat, as the STES is discharging, the temperature decreases, which lowers the pressure ratio in the cycle, and by extension the power output and efficiency. The discharging process is limited by the minimum pressure difference for which the expander can operate properly. For that type of TES

material, the transient discharge process can be approximated by a series of quasi-steady-state processes as follows:

1. The discharge process is divided into n steps so that during each, the same amount of heat accumulated in TES is used,
2. For each step, the temperature of the LTES is found based on Equation (7),
3. For that temperature, working fluid parameters for characteristic state points are determined, and
4. For these points, the assessment parameters of the cycle are calculated.

By carrying out these calculations for all the working fluid and storage material pairs, the efficiencies of ORC systems and needed amounts of TES materials can be compared. As an example, the results obtained for the jatropha oil are presented in Figure 4. Jatropha oil was selected because of its high specific heat capacity, as seen in Figure 3. As can be seen, the obtained results indicate that Novec649 seems to be a good choice for the working fluid in the analysed case, if minimizing the amount of the storage material in relation to the amount of the working fluid (ζ_{total}) is the only objective. For Jatropha oil-based STES, which operates between 100 °C and 50 °C, it has a 36% lower value than the next best fluid (R1233zd(E)). However, the total efficiency for Novec649 (η_{total} - also presented in Figure 4) is very low. On the other hand, n-pentane which shows very high η_{total}, got very high value of (ζ_{total}). This is true for both non-recuperated and recuperated cycles.

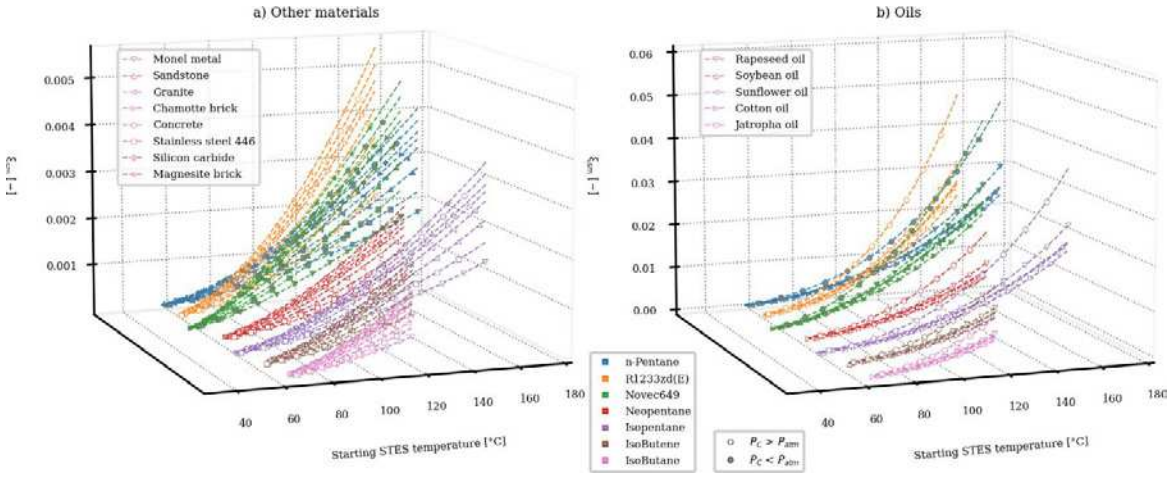

Figure 5: ξ_{sm} of ORC with TES vs starting STES temperature, for different sensible storage materials and working fluids with low GWP and no ODP.

In order to combine ζ_{total} and η_{total}, a new parameter ξ_{sm} can be introduced, which can be defined as a ratio of total efficiency to the nth power, to the parameter ζ_{total} as given by Equation (13). The purpose of exponent n is to give more weight to the efficiency of the cycle, and in this case, a value of 2 was assumed. The relative importance of efficiency and the amount of storage material depends on the specific case. For volume-constrained applications, the weight of ζ_{total} is higher.

$$\xi_{sm} = \frac{(\eta_{total})^n}{\zeta_{total}} = \frac{(\eta_{total})^2}{\zeta_{total}} \tag{13}$$

For the non-recuperated cycle obtained ξ_{sm} values show best results from around 105 °C for R1233zd(E). R1233zd(E) requires significantly less storage material than n-pentane and gives very similar efficiency. R1234ze(Z) and Novec649 both give similar values, like R1233zd(E) for lower temperatures. The worst value of ξ_{sm} was obtained for n-pentane.

The subplots on the right side of Figure 4 show the same values calculated for the recuperated cycle. Unsurprisingly, recuperation largely improves both ξ_{sm} and η_{total} for Novec649, and other dry working fluids. It has very little influence on ζ_{total}, so, the difference in ξ_{sm} between non-recuperated and recuperated cycles, are almost entirely results of changed η_{total}. Because of that, if recuperation is used, Novec649 obtains much better values.

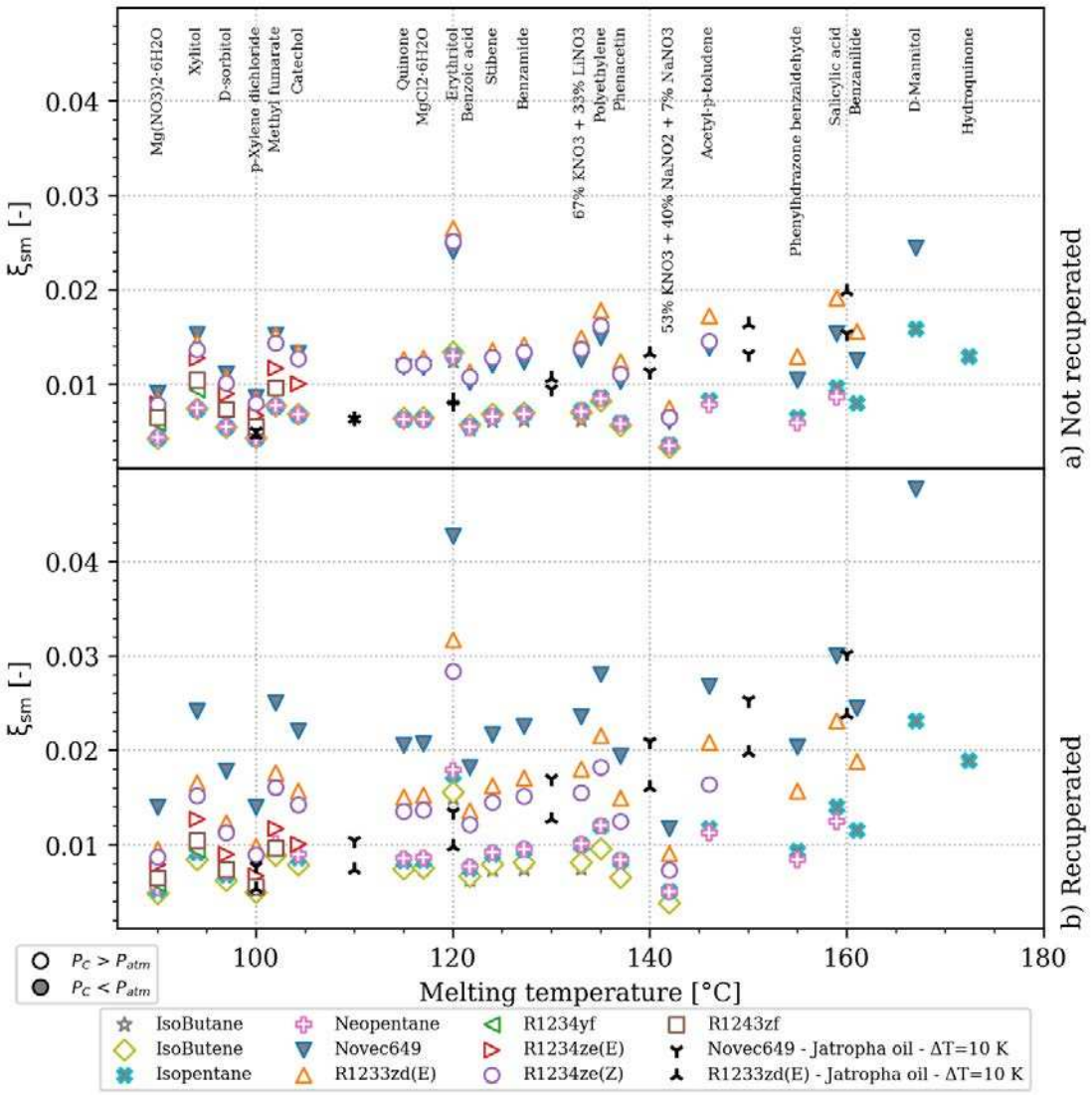

Figure 6: Variation of assessment parameter ξ_{sm} of ORC with TES vs. starting melting temperature of PCM for different materials and working fluids with low GWP and no ODP. PCM parameters are taken from (Daniarta et al., 2022). For comparison, also presented are values for two working fluids (Novec649 and R1233zd(E)) with sensible storage material (Jatropha oil) with the temperature difference between during the discharge 10 K.

In Figure 5, values calculated for the rest of the storage materials, with non-recuperated ORC, were presented. They were separated between oils and other materials since oil has an order of magnitude higher specific heat capacity. As can be seen, the results are similar to those shown in Figure 4. R1233zd(E), R1234ze(Z), and Novec 649 give very good results.

In Figure 6, ξ_{sm} values calculated for latent storage materials are presented, as a function of their melting temperature. By comparing the results, with Figure 5, it can be noticed, that while PCMs

perform significantly better than solid sensible storage materials, vegetable oils can reach the same order of magnitude as PCMs. Unlike PCMs, however, they do not give the advantage of stable temperature output, and by extension, stable operating conditions. As can be seen, however, even with temperature difference limited to 10 K, they perform comparable to PCMs. Additionally, oils give the possibility of using them at the same time as heat transfer fluids in CSP (concentrated solar power) and other applications (Nitedem et al., 2017), simplifying the construction of the heat exchanger.

In regards to heat exchangers it is worth mentioning that not all types of heat exchangers are compatible or suitable for use with TES due to pressure, design, construction, and other parameters (Daniarta et al., 2023).

4. SUMMARY AND CONCLUSIONS

This paper presents the results of modeling analysis of ORC and TES power systems performed for different working fluid and TES material pairs. Both sensible and latent working fluids were considered, as well as the effects of recuperation. Some remarks can be concluded as follows:

- Working fluid and TES material pairs were evaluated based on the amount of storage material needed to accumulate heat for a given amount of the working fluid. Additionally, the total efficiency of the TES discharge process was calculated. To combine the two criteria, an additional parameter ξ_{sm} was introduced, defined as a ratio of square total efficiency, to the ζ_{sm} (ratio of the storage material mass to the working fluid mass).
- For analyzed working fluids, in the simple, non-recuperated configuration, the best value was obtained for R1233zd(E) above 105°C, while the worst was obtained for n-pentane. Presented results may be applied for working fluid and thermal energy storage material selection for ORC systems which are utilizing TES as heat sources. The recuperation has very little effect on ζ_{total}, it improves however the total efficiency, particularly of dry working fluids, like Novec 649, and, because of that improves their ξ_{sm}. For that reason, Novec 649 performed better than other fluids in this variant. It should be pointed out however, that recuperation requires an additional heat exchanger, which decreases benefits from the reduced amount of the storage material needed, both in terms of the volume and in terms of cost, which effects were not estimated in this study. Additionally, to obtain 30 °C condensation temperature Novec 649, would require vacuum in condenser, and would therefore be better suited for applications with higher heat sink temperature.
- Generally, R1233zd(E) can be regarded as a good choice for applications with TES, thanks to both high efficiency and low amount of storage material needed.
- It also was shown, that, thanks to their large specific heat capacity, vegetable oils and especially jatropha oil, can perform comparably to some PCM materials. They can even outperform them if a large temperature drop during discharge is allowed.
- The further works of the authors on the presented topic will be focused on experimental validation of the obtained results.

NOMENCLATURE

c_p	specific heat capacity	$(\frac{kJ}{kg \cdot K})$	$\dot{Q}$	heat flux	(kW)
h	specific enthalpy	$(\frac{kJ}{kg})$	T	temperature	(K)
			W	power	(kW)
$\dot{m}$	mass flow	$(\frac{kg}{s})$	η	efficiency	(−)
Q	heat	(kJ)	ζ_{sm}/ξ_{sm}	parameters for sizing TES	(−)

Subscript

sub	subcooling	1	point after condenser
f	working fluid	2	point after pump
sm	storage material	3	point after evaporator
in	input	4	point after expander
out	output	CR	low-pressure side recuperator outlet
TES	thermal energy storage	ER	high-pressure side recuperator outlet
exp	expander		
pump	pump		
net	netto		

REFERENCES

Ahmed, A. M. and Imre, A. R. 2023. Investigation of thermal efficiency for subcritical ORC and TFC using super dry working fluids, *Energy Science & Engineering*, vol. 11, no. 2, 711–26

Ahmed, A. M., Kondor, L., and Imre, A. R. 2021. Thermodynamic Efficiency Maximum of Simple Organic Rankine Cycles, *Energies*, vol. 14, no. 2, 307

Astolfi, M. 2017. Technical options for Organic Rankine Cycle systems, pp. 67–89, in Macchi, E. and Astolfi, M. (eds.), *Organic Rankine Cycle (ORC) Power Systems*, Cambridge, Woodhead Publishing

Bell, I. H., Wronski, J., Quoilin, S., and Lemort, V. 2014. Pure and pseudo-pure fluid thermophysical property evaluation and the open-source thermophysical property library CoolProp, *Industrial & Engineering Chemistry Research*, vol. 53, no. 6, 2498–2508

Daniarta, S. and Kolasiński, P. 2021. Features and characteristics of low-grade heat storage for organic Rankine cycle, in *Proceedings of the 6th International Seminar on ORC Power Systems*

Daniarta, S., Kolasiński, P., and Imre, A. R. 2021. Thermodynamic efficiency of trilateral flash cycle, organic Rankine cycle and partially evaporated organic Rankine cycle, *Energy Conversion and Management*, vol. 249, 114731

Daniarta, S., Nemś, M., and Kolasiński, P. 2023. A review on thermal energy storage applicable for low- and medium-temperature organic Rankine cycle, *Energy*, vol. 278, 127931

Daniarta, S., Nemś, M., Kolasiński, P., and Pomorski, M. 2022. Sizing the Thermal Energy Storage Device Utilizing Phase Change Material (PCM) for Low-Temperature Organic Rankine Cycle Systems Employing Selected Hydrocarbons, *Energies*, vol. 15, no. 3, 956

Kolasiński, P. and Daniarta, S. 2021. Sizing the thermal energy storage (TES) device for organic Rankine cycle (ORC) power systems, *MATEC Web of Conferences*, vol. 345, 00018

Li, X., Xu, B., Tian, H., and Shu, G. 2021. Towards a novel holistic design of organic Rankine cycle (ORC) systems operating under heat source fluctuations and intermittency, *Renewable & Sustainable Energy Reviews*, vol. 147, 111207

Nitedem, E. S., N'Tsoukpoe, K., Ouédraogo, I., Coulibaly, Y., and Py, X. 2017. Jatropha curcas crude oil as heat transfer fluid or thermal energy storage material for concentrating solar power plants, *Energy for Sustainable Development*, vol. 40, 59–67

Sarbu, I. and Sebarchievici, C. 2018. A Comprehensive Review of Thermal Energy Storage, *Sustainability*, vol. 10, no. 1, 191

ORC SEVILLE 2023
7th International Seminar on O.R.C. Power Systems

© 2024 Editorial Universidad de Sevilla. Este es un artículo de acceso abierto distribuido bajo los términos de la licencia de uso y distribución Creative Commons (BY-NC-ND 4.0)

DOI: https://dx.doi.org/10.12795/9788447227457_54

INFLUENCE OF DOPANT FLUORINATION ON THE HEAT TRANSFER BEHAVIOUR OF CO_2-BASED MIXTURES IN TRANSCRITICAL POWER CYCLES

Michele Doninelli*, Gioele Di Marcoberardino, Costante Mario Invernizzi, Paolo Giulio Iora

Università degli Studi di Brescia, Dipartimento di ingegneria meccanica e industriale, Via Branze 38, 25123 Brescia, Italy

*Corresponding Author: m.doninelli002@unibs.it

ABSTRACT

CO_2-based mixtures are recognized to be an effective working fluid to overcome the limitations of pure sCO_2 cycles for power production in high-temperature environments. Based on the temperature level of the heat source, several dopants, characterized by high critical temperature, can be adopted for blending CO_2. As thermal stability is one of main concern in the working fluids selection, fluorinated compounds have been considered in the recent years as potential solution due to high C-F chemical bond energy. However, the available thermodynamic and transport properties of CO_2 mixtures with fluorinated hydrocarbons are relatively scarce, thus further experimental and theoretical investigations are necessary to properly design the power cycle components.
The CO_2-based mixtures are considered in this work for high-temperature heat recovery to assess the influence of fluorine atoms substitution to hydrogen atoms both on cycle efficiency and heat exchangers size. Benzene (C_6H_6) and two fluorinated derivatives (fluorobenzene C_6H_5F, hexafluorobenzene C_6F_6) are considered here to assess the influence of the presence of fluorine atoms in the molecule of the dopant on the transport properties of the CO_2-mixtures and their heat transfer behaviour. These three halogenated aromatic dopants possess good thermal stability related with the benzene ring structure and could be potentially exploited for medium-high temperature level applications (350-550°C) such as waste heat recovery and concentrated solar power.
Specific models for transport properties implemented in Matlab codes are optimized for the considered mixtures with a novel approach, and the design of the PCHE recuperator has been carried out. It turns out that the use of fluorobenzene as CO_2 dopant in medium-high temperature heat recovery can be a good solution in terms of heat exchangers sizes, efficiency, cost, and environmental characteristics (GWP and toxicity).

1 INTRODUCTION

CO_2-mixtures are recently studied as a valid alternative to sCO_2 as working fluid for closed power cycles to turn the supercritical recompressed cycle into a transcritical cycle even at high ambient temperatures, by enhancing the working fluid critical temperature with the addition of a proper amount of selected dopants.
The main fields of application of CO_2 mixtures are Concentrated Solar Power (CSP), with the aim at reducing the Levelized Cost of Electricity (LCOE), (see for instance the H2020 projects Scarabeus and Desolination), but also waste heat recovery (WHR) applications for the combined heat and power production (Morosini et al., 2023) or electricity and desalinated water production (Michele Doninelli et al., 2023), as well as for trigeneration. The dopant selection to be mixed with CO_2 is a critical aspect to be properly evaluated for the specific application, where the main drivers are the critical temperature and the thermal stability. Since CO_2-based cycles could potentially be competitive in WHR applications where the heat source is higher than 400°C (Astolfi et al., 2017), it is necessary that the dopant overcomes the actual limits of thermal stability of the fluids typically employed in Organic Rankine Cycles. In this scenario, fluorinated dopants such as C_6F_6 (Di Marcoberardino et al., 2022), C_4F_{10} and

C_6F_{14} (Di Marcoberardino et al., 2020) have been proposed, since perfluorocarbons possess good thermal stability thanks to the combination of high energy of the C-F chemical bond and high electronegativity of fluorine atoms.
However, it should be noted that the presence of fluorine atoms has also an impact on the viscosity, thermal conductivity, and density. From previous studies, the viscosity of fluorinated compounds resulted to be considerably higher than their hydrocarbon homologues (Freire et al., 2008), while the thermal conductivity decreases with the number of fluorine atoms (Irving & Jamieson, 1975). Three dopants are here considered to investigate the impact of fluorination on the heat exchangers: benzene (C_6H_6), fluorobenzene (C_6H_5F), hexafluorobenzene (C_6F_6). In particular, fluorobenzene is proposed for the first time as potentially applicable dopant in WHR applications. In fact, the expected thermal stability is high due to the aromatic stability of benzene structure, although reasonably lower than C_6F_6 which was proved to be thermally stable at 550-600°C in Inconel 625 (Di Marcoberardino et al., 2022). Additional advantages of fluorobenzene is a lower cost and global warming potential (GWP) compared to C_6F_6 and a much lower toxicity compared to benzene. In fact, the radiative efficiency (RE) of fluorobenzene is reported to be 0.07 (Hodnebrog et al., 2020), compared to 0.15 of C_6F_6. The medium-high flammability of the three dopants is comparable, but it is a minor drawback in mixtures with high-CO_2 content.
The Friction-Theory model for viscosity (Quiñones-Cisneros et al., 2001) and thermal conductivity (Quiñones-Cisneros et al., 2021) are tuned based on the experimental data of the pure components and used to predict the transport properties of the mixtures for a realistic Printed Circuit Heat Exchanger (PCHE) recuperator design. The objectives of this work are a detailed description of the heat transfer behaviour of the selected CO_2 blends, the influence of fluorination on both cycle efficiency and thermal properties, the introduction of fluorobenzene as interesting CO_2 dopant for WHR applications.

2 FINE-TUNING OF TRANSPORT PROPERTIES OF THE INVESTIGATED BLENDS

334

The dynamic viscosity and thermal conductivity are fluid properties related to momentum and heat transfer and are key properties for the determination of the heat transfer coefficients. The prediction of transport properties of mixtures is difficult due to non-ideal behaviour. Almost all the methods available to estimate the transport properties of dense pure fluids and mixtures are empirical or semi-theoretical (Poling & Prausnitz, 2001).
The generic transport property π is calculated as a sum of a "zero-density" property π_0 and a "residual property" $\Delta\pi$:

$$\pi(T,p) = \pi_0(T) + \Delta\pi(T,p) \quad (1)$$

The zero-density term can be calculated with methods that are derived from the rigorous kinetic theory of gases, whilst almost all the methods available to describe the residual property are empirical or semi-theoretical (Poling & Prausnitz, 2001), with the corresponding-state (CS) based methods being the most applied. The zero-density viscosity and thermal conductivity of the mixture are computed here with the Wilke (Wilke, 1950) and the Wassiljewa-Mason-Saxena (Mason & Saxena, 1959) equations, respectively, with the zero-density properties of the pure components obtained with the Chung model (Chung et al., 1988)(Chung et al., 1984). About the residual term, when the two components in the mixture are very different in size and shape, the CS approach tends to fail since the reference fluid cannot be "conformal" with both the components in the mixture. As highlighted in a previous work (M. Doninelli & Di Marcoberardino, 2023), the transport properties of CO_2 complex mixtures are potentially better described with the use of the relatively recent friction-theory models (Quiñones-Cisneros et al., 2000)(Quiñones-Cisneros et al., 2021), which relies on an equation of state to describe the residual transport property of the mixture. The f-theory models can provide good results for mixtures even if the optimization is carried out only on pure component experimental data: no binary interaction parameters are involved in the model.

2.1 Friction Theory model for viscosity and thermal conductivity

The residual dynamic viscosity of the mixture has been calculated with the viscosity model developed by Quiñones-Cisneros et al. (Quiñones-Cisneros et al., 2001), as in the following quadratic relation:

$$\Delta\eta(T,p) = k_a p_a + k_r p_r + k_{rr} {p_r}^2 \quad (2)$$

where k_a, k_r, k_{rr} are friction factors, obtained with mixing rules, related to the attractive (subscript "a") and repulsive (subscript "r) pressure terms. In the general one-parameter model, the pure-component friction factors are obtained only as function of a critical characteristic viscosity $\eta_{c,i}$:

$$k_{j,i} = \frac{\eta_{c,i}\ \hat{k}_{j,i}}{P_{c,i}} \quad (3)$$

while the reduced coefficient $\hat{k}_{j,i}$ depends only on the EoS selected for the calculation of the attractive (p_a) and repulsive (p_r) pressure terms - see Table 2 of (Quiñones-Cisneros et al., 2001). The critical characteristic viscosity formally represents the viscosity of the fluid at the critical point, but it is in fact the only adjustable parameter of the model, which is based on corresponding states behaviour, and can be tuned on available experimental data once selected the thermodynamic model to obtain attractive and repulsive pressures. Thus, only one parameter has to be regressed based on experimental data available for the pure fluid, which is beneficial especially for fluids with scarce experimental viscosities. A one-parameter model for thermal conductivity is still lacking, so the model presented in (Quiñones-Cisneros et al., 2021) has been used with a second-order truncation:

$$\Delta\lambda = \lambda_c + \phi_{a,1} s_a + \phi_{a,2} {s_a}^2 + \phi_{r,1} s_r + \phi_{r,2} {s_r}^2 \quad (4)$$

where the attractive and repulsive residual entropy of the mixture has been computed with the PR EoS. The friction coefficients $\phi_{j,i}$ and the critical enhancement term λ_c contain nine coefficients (a_i, b_i, A_0, B_0, ϕ_c) that must be regressed for each pure compound on available experimental data in dense conditions (residual term). Then, mixing rules are applied to have mixture's friction coefficients.

335

2.2 Friction Theory models optimization for the fluids of interest

Friction coefficients for thermal conductivity are already available in (Quiñones-Cisneros et al., 2021) for many compounds including CO_2. In this work, the coefficients of benzene, fluorobenzene and hexafluorobenzene are regressed in Matlab environment by using Levenberg-Marquardt algorithm and presented in Table 1. As innovative outcome of this work, a temperature-dependent critical characteristic viscosity is found to best reproduce the experimental data: the simplicity of the one-parameter model has been compensated by a temperature dependence to improve the accuracy. The critical characteristic viscosity of the pure dopant (Eq. 3) has been expressed in the form of the Uyehara and Watson (Uyehara, OA and Watson, 1944) equation with a temperature dependent factor k(T) fitted on experimental data (validity range of the factor [280-700 K]):

$$\eta_c = k(T) \cdot MM^{\frac{1}{2}} \cdot P_c^{\frac{2}{3}} \cdot {T_c}^{-\frac{1}{6}} \quad (5)$$

This approach has been tested on pure benzene, where the mean percentage error decreases from 5.77% (constant temperature parameter) to 1.94% in comparison with the reference correlation for the viscosity of benzene (Avgeri et al., 2014), in the 320-650 K and 1-200 bar range. In case of hexafluorobenzene and fluorobenzene a substantial improvement is observed too. The expressions for the factor k(T), which best reproduce the critical characteristic viscosity of the three dopants, are reported in Tables 2. The well-known constant value of characteristic critical viscosity for pure CO_2 (376.872 μP) has been used (Quiñones-Cisneros et al., 2001).

Table 1: optimised parameters for f-theory thermal conductivity model.

	Thermal Conductivity Model								
	a_0	a_1	a_2	b_0	b_1	b_2	A_0	B_0	Φ_c
CO_2	0.3868	35.6309	15.9827	3.6295	2.6629	-2.6629	0.2274	0.3120	-0.6579
C_6H_6	-3.2476	2.8255	0.9565	0.2035	2.4728	0	0.0010	0.0022	0.001
C_6H_5F	-4.3332	0.1001	-0.8412	5.5838	1.7321	-1.8845	0.0272	0.2826	-0.05
C_6F_6	0.9287	5.5583	-1.8031	0.0344	0.0022	0	0.0142	0.0018	0.0408

Table 2: optimised k(T) factor for Eq. (5) – viscosity model.

	Viscosity model – k(T) coefficient optimised
C_6H_6	$k(T[K]) = -0.0000000293\ T^3 + 0.0000688326\ T^2 - 0.0526172200\ T + 20.6066312478$
C_6H_5F	$k(T[K]) = -0.0000000216\ T^3 + 0.0000493068\ T^2 - 0.0360406074\ T + 16.2908833076$
C_6F_6	$k(T[K]) = -0.0000001877\ T^3 + 0.0003181158\ T^2 - 0.1770737101\ T + 42.4647664823$

The comparison for thermal conductivity is reported in Figure 1. The liquid field is characterized by high intermolecular interactions, and the comparison shows the capability of the models to describe the departure from ideal gas conditions.

336

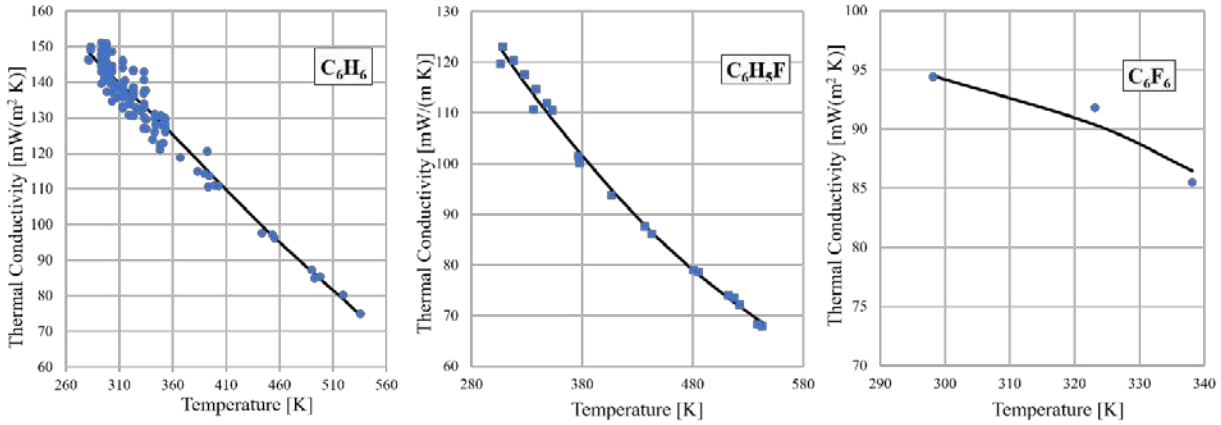

***Figure 1**. Experimental liquid thermal conductivity (dots) vs optimised model (solid lines).*

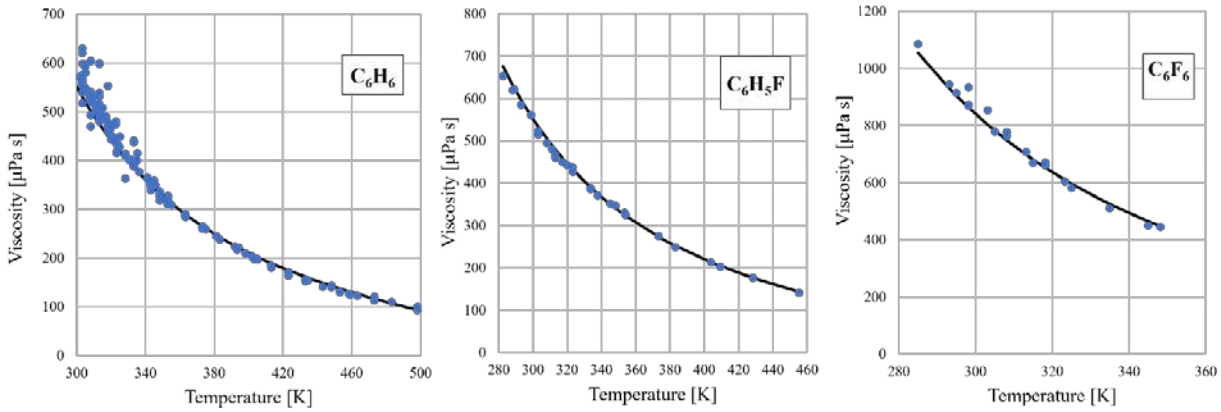

***Figure 2**. Experimental liquid dynamic viscosity (dots) vs optimised model (solid lines).*

Only three liquid thermal conductivity data at ambient pressure available for C_6F_6 from (Irving & Jamieson, 1975), while the rest of liquid viscosities and thermal conductivities presented in Figure 1 and 2 are saturated liquid data available from the NIST database available in Aspen Plus environment. Notably, the dynamic viscosity increases with fluorine content while the thermal conductivity decreases at the same reduced conditions. The increase in the viscosity of fluorinated dopants, compared to their hydrocarbon homologues, relies in the stronger intermolecular interactions in fluorinated compounds (which is reflected also in smaller vapour pressures of the pure dopants and bubble pressure for the mixtures). In general, highly viscous fluids possess also large thermal conductivities. However, it is generally known that for non-polar fluids the dimensionless ratio $M\lambda / R\eta$ is approximately constant value between 2-3 (Poling & Prausnitz, 2001), which means that the thermal conductivity is inversely proportional to the molar mass, that is larger for C_6F_6 (186.96 g/mol) compared to C_6H_6 (78.11 g/mol).

3 CASE STUDY: HIGH-TEMPERATUER HEAT RECOVERY

337

The considered case study is the exploitation of available heat from the exhaust gases of a commercial 12.9 MW_{el} gas turbine, representative of a high-temperature heat source. The adoption of a CO_2-based power cycle in the high-temperature heat recovery market represents a competitive alternative to the state-of-the-art ORCs, which are limited below 350°C due to thermal stability limit. From a study of (Papapetrou et al., 2018), around the 40% of the total waste heat potential in EU is available in the range 500-1000°C, then it is necessary to improve the efficiency of the technologies employed for the conversion of such waste heat to reduce the impact of fossil fuels consumption. For this reason, it is relevant to identify innovative working fluids that could be applied in high-temperature applications.
Fluorobenzene has been considered for the first time as potential CO_2 dopant, and the relevance of this dopant relies on the capability of this mixture to compromise on GWP, ODP, toxicity, cost, thermal stability, availability, compared to more fluorinated dopants typically considered in the literature.
The heat is recovered from the flue gases by the CO_2-based power cycle in the upper temperature range (with direct heat transfer) to produce additional electric power, and by a heat transfer fluid (HTF) in the lower temperature range for cogeneration purposes. The simple recuperated layout is selected even if it cannot guarantee a good degree of cooling of the sensible heat source if compared to other layouts (Morosini et al., 2023). However, the fraction of available heat that is introduced into the primary heat exchanger (PHE) is converted with high thermodynamic efficiency and the rest of heat can be exploited in to produce useful heat at a good thermal level in cogenerative mode. This case could be representative of cogeneration for district heating or for industries that requires valuable heat in the temperature range 100-200°C to satisfy processes like distillation, evaporation, sterilization, vulcanization, etc. About the 20% of the primary energy demand for industrial heating is within the 100-200°C temperature range. For this reasons, the proposed technology could be an important step towards the decarbonization. In this study, both the dopant molar fraction and the turbine inlet temperature (TIT) are optimised to achieve the maximum electrical output, but the optimal cycle configuration can be adjusted to satisfy the specific thermal and electrical demand.

3.1 Power Cycles and Heat Source Description

The exhaust gases have been simulated with molar fractions that are representative of a typical composition of gas turbine exhausts (Scholes et al., 2016), and the temperature level (555°C) and mass flow rate (40 kg/s) are representative of a commercially available 12.9 MW_{el} gas turbine: considering a stack temperature of 120°C, the total available thermal duty is 19.81 MW_{th}.
The power cycle assumptions are in Table 3, where both the mixture's composition and the TIT have been optimized on the total heat recovery efficiency, i.e., the electric output of the cycle has been maximized. An 89% molar content of CO_2 results to be the optimal composition for the mixtures with both C_6F_6 and C_6H_5F. In case of C_6H_6, for the sake of comparison it is considered a 89% composition too even in the optimum results to be 88% since the output differences are negligible (3.51 MW_{el} and 3.514 MW_{el} respectively). The cycle minimum pressure is the bubble pressure of the mixture (87.1 bar for CO_2+C_6H_6, 85.1 bar for CO_2+C_6H_5F ,84.4 bar for CO_2+C_6F_6) at the considered minimum cycle temperature (50°C). The simulations are carried out in Aspen Plus V12 with the Peng Robinson EoS and optimized binary interaction parameters (BIP) K_{ij} regressed on vapour-liquid equilibrium (VLE) data where available (for CO_2+C_6H_6 k_{ij}=0.0774 available in Aspen database, for CO_2+C_6F_6 $k_{ij}(T)$= 0.16297-0.0003951·T[K] from (Di Marcoberardino et al., 2022)). A BIP equal to zero is used for the CO_2+C_6H_5F since there are no VLE data available.

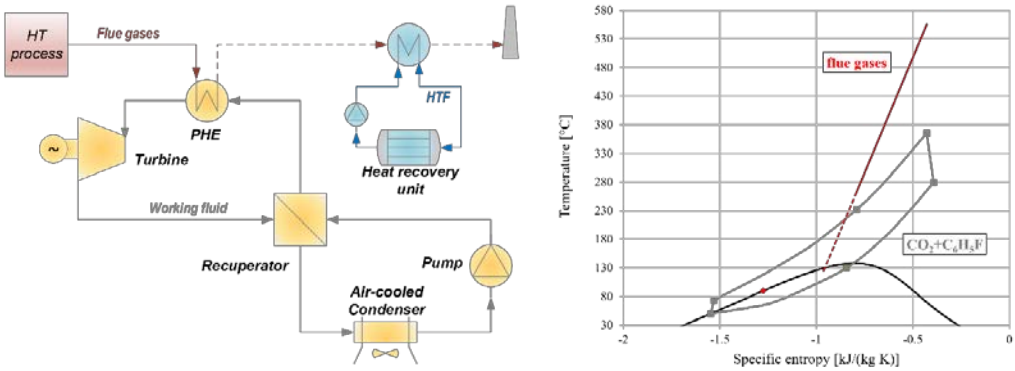

***Figure 3**. System layout for cogeneration scope (left) and T-s diagram (right).*

The assumptions on the simple recuperated power block are summarized in Table 3.

Table 3: power cycle operating conditions.

Parameter	Value
TIT	365°C
Cycle minimum temperature	50°C
Cycle maximum pressure	250 bar
Dopant molar fraction	11%
PHE approach temperature	30°C
Recuperator MITA	10°C
Pump/Expander isentropic efficiency	80/85%
Pressure drops (PHE/HRU)	3/1 bar
Pressure drops recuperator (HP/LP)	0.3/1 bar
Generator/Motor efficiency	97/97%

3.2 Heat recovery results

The results of the cogenerative case-study are represented in Table 4. Since the electrical power production has been maximized, the main key performance index of the system is the electrical efficiency defined as:

$$\eta_{el} = \frac{\dot{W}_{net}}{\dot{Q}_{available,flue\ gases}} \quad (6)$$

Table 4: Cogeneration results.

Parameter	CO_2+C_6H_6	CO_2 + C_6H_5F	CO_2 + C_6F_6
Mass flow rate [kg/s]	64.4	65.5	75.5
Net electric power $\dot{W}_{net}$ [MW]	3.51	3.51	3.35
Electrical efficiency η_{el} [%]	17.7	17.7	16.9
Flue gases PHE outlet T [°C]	261.4	261.8	265.6

4 RECUPERATOR DESIGN COMPARISON

The printed circuit heat exchanger (PCHE) technology has been selected for the design of the recuperator at such high pressures (up to 250 bar) since the manufacturing process (diffusion bonding) gives to the material its parental strength and allows for good compactness. Conventional straight semi-circular channels with 2 mm width are considered, a roughness of 0.1 μm and the metal block made of SS316. A local balance approach has been used to compute the local area required since the thermodynamic and transport properties varies along the heat exchanger. In the one-phase field, the well-known Gnielinski correlation (1976, (Gnielinski, 1975)) is used for the calculation of the heat transfer coefficient while the Darcy friction factor calculated with the correlation of Chen (1979, (Chen, 1979)) is used for the pressure drop. The Cavallini-based model of Deng et al. (2019, (Deng et al., 2019)) has been used for the heat transfer coefficient in the two-phase field since it has been validated by Illyes et al.(Illyés et al., 2022) for a condensing CO_2-rich mixture. The Del Col model (2013, (Del Col et al., 2013)) was therefore considered to compute the two-phase pressure drops.
The T-Q diagram of the recuperator for the CO_2+C_6H_6 is represented in Figure 4, with the local global heat transfer coefficient (solid lines) and the temperature difference (dashed lines) along the heat exchangers for the three dopants.

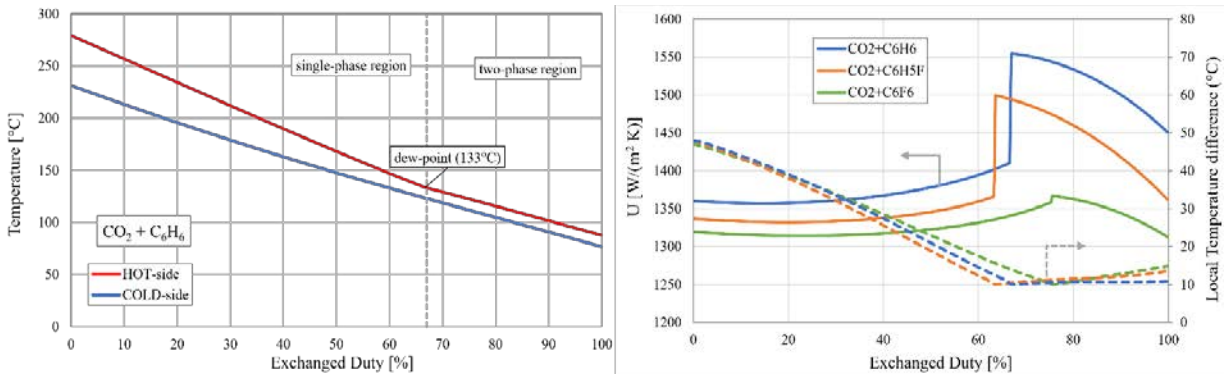

***Figure 4**. T-Q diagram (left) and local U and LMTD for the three mixtures (right).*

The results of the design of the PCHE recuperator for the considered mixture under the same MITA (10°C), hot-side pressure drop (1 bar), and with almost the same thermal duty is reported in Table 5.

Table 5: PCHE recuperator design results (89% CO_2, ΔP_{hot}=1 bar).

Parameter	CO_2+C_6H_6	CO_2 + C_6H_5F	CO_2 + C_6F_6
M_{cycle} [kg/s]	65.45	65.49	75.51
G [kg/(m^2 s)]	635	626	700
Thermal duty exchanged [MW]	19.74	20.23	19.87
LMTD [°C]	17.24	17.42	19.39
Length [m]	2.36	2.42	2.17

Number of channels hot/cold [-]	65’615	66’596	51’574
Heat transfer area (hot/cold side) [m^2]	794.7	828.51	767.1

For C_6F_6, the mass flux to achieve the thermal duty at the constrained pressure drop increase with fluorine content due to higher mass density compared to C_6H_6, and this is reflected in the lower number of plates (frontal area) required to accommodate the total mass flow. At almost the same dynamic viscosity (Figure 5) in the single-phase field, the fluorine content in C_6F_6 promotes higher Reynolds numbers that are compensated by the lower thermal conductivity of fluorinated dopant, and the resulting overall heat transfer coefficient is inferior to the hydrocarbon dopant (Figure 4). The effect of more unbalanced heat capacities (high local temperature differences) of CO_2+C_6F_6 is that the channels are shorter (see Table 5) and the total area required for the CO_2+C_6F_6 mixture is 3.6% lower than the CO_2+C_6H_6 mixture. In other words, the worsening of the heat transfer behaviour that is evident in the global heat transfer coefficient is counterbalanced by the higher LMTD, at the same MITA, and the most fluorinated dopant provides the most compactness but the lowest cycle efficiency.
In case of C_6H_5F, the density gain is not so relevant as for C_6F_6, while the lower thermal conductivity (Figure 5) entails a slight reduction of the heat transfer coefficients, resulting in a total heat transfer area only 4.25% higher than the benzene case.

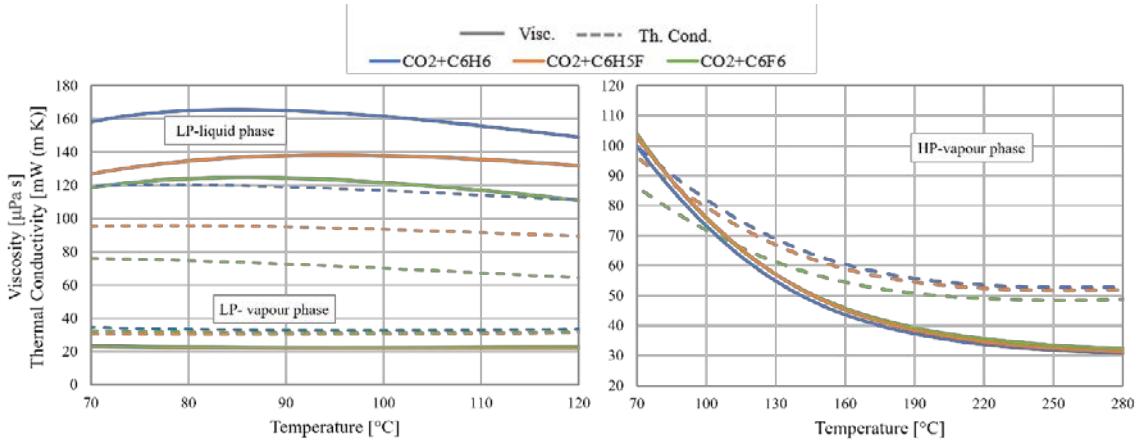

Figure 5. Thermal conductivity and viscosity in the HP supercritical side and two-phase field.

As the viscosity is a molar-based property, at the same molar content (89% CO_2) the influence of the dopant is limited in the high-pressure side. Deviations in dynamic viscosity are relevant in the two-phase field where the first liquid droplet of the CO_2+benzene, in equilibrium with its vapour phase, is at high dopant molar content (64%) compared to the fluorinated mixtures (47%): the molar content of the viscous dopant in the liquid phase is considerably higher, even if the dopant itself (benzene) is less viscous than the fluorinated dopants.
The thermal conductivity is more mass fraction-based (for that reason the mixing rules applied are based on the mass fractions (Quiñones-Cisneros et al., 2021)), and the influence of heavier fluorine atoms is evident at the same molar content, even at 89% molar CO_2. The penalization of the global heat transfer coefficient (Figure 4) in fluorinated dopants is mainly due to lower thermal conductivity. However, for CO_2+C_6F_6, this is compensated by a higher local temperature difference at the same MITA, at almost equal thermal duty exchanged, which leads to a more compact heat exchanger but lower cycle efficiency. In case of CO_2+C_6H_5F, the heat transfer behaviour is only partially deteriorated by fluorination, and the LMTD (Table 5) is similar to CO_2+C_6H_6 leading to a slightly larger heat exchanger, nevertheless keeping a good cycle efficiency.

5 CONCLUSIONS

In this paper, benzene and two fluorinated derivates were investigated as CO_2 dopants in high-temperature heat recovery application to evaluate the impact of fluorination on cycle efficiency and on heat exchangers by sizing the PCHE recuperator. Proper transport properties models have been tuned, with an innovative approach, based on experimental data to carry out a realistic heat exchanger design.

For the first time, the adjustable parameter of the one-parameter friction theory model for viscosity has been tuned with a temperature-dependent approach, to compensate for the incapability of the equation of state to describe the severe increase of intermolecular forces in the liquid dense phase region, at low temperatures, with clear benefits in the properties prediction.

The thermal conductivity drop (also associated with the increase of the viscosity) of fluorinated compounds is reflected in a decline of the global heat transfer coefficient (-8.3% for C_6F_6 compared to C_6H_6), which is compensated by more unbalanced heat capacities (higher local temperature differences) in the recuperator. In case of C_6F_6, the divergence of the heat capacities in single-phase and VLE regions leads to higher local temperature differences and a slightly more compact heat exchanger, though with a negative effect on the cycle efficiency. This work provides insights on the heat transfer behaviour of CO_2 mixtures within the internal heat recovery process, which is the key factor that determines the cycle efficiency.

Fluorobenzene C_6H_5F is proposed for the first time as potential CO_2 dopant. Its adoption results to be an interesting solution for heat recovery and solar applications in the medium-high temperature range since it guarantees high efficiency similar to that of benzene (+1% compared to C_6F_6) with a slight penalization in the heat transfer behaviour due to the fluorine atom, relatively-low GWP and low cost (compared to C_6F_6), low toxicity (compared to C_6H_6), zero ODP. Future works will be intended to fill the gap on experimental VLE data of the CO_2+C_6H_5F mixture and to assess its thermal stability limit.

NOMENCLATURE

Acronyms

BIP	Binary Interaction Parameter
CS	Corresponding States
LCOE	Levelized Cost of Electricity
LMTD	Logarithmic mean temperature difference
LP	Low pressure
HP	High Pressure
MITA	Minimum Internal Temperature Approach
ODP	Ozone Depletion Potential
PHE	Primary Heat Exchanger
PCHE	Printed Circuit Heat Exchanger
TIT	Turbine Inlet Temperature
VLE	Vapour-Liquid Equilibrium
WHR	Waste Heat Recovery

Roman and Greek letter

G	Mass Flux	kg/(m^2 s)
M	Mass Flow Rate	kg/s
MM	Molar Mass	kg/mol
P	Pressure	bar
T	Temperature	°C
U	Overall Heat Transfer Coefficient	W/(m^2 K)]
$\dot{Q}$	Thermal power	MW
$\dot{W}$	Mechanical Power	MW
ΔT	Temperature difference	°C
η	Dynamic viscosity	Pa s
λ	Thermal Conductivity	W/(m K)

Subscript

a	attractive
c	critical
i,j	species
r	repulsive
th	thermal
0	zero-density conditions

REFERENCES

Astolfi, M., Lasala, S., & Macchi, E. (2017). Selection Maps for ORC and CO2 Systems for Low-Medium Temperature Heat Sources. *Energy Procedia*, *129*, 971–978. https://doi.org/10.1016/j.egypro.2017.09.217

Avgeri, S., Assael, M. J., Huber, M. L., & Perkins, R. A. (2014). Reference Correlation of the Viscosity of Benzene from the Triple Point to 675 K and up to 300 MPa. *Journal of Physical and Chemical Reference Data*, *43*(3). https://doi.org/10.1063/1.4892935

Chen, N. H. (1979). An Explicit Equation for Friction Factor in Pipe. *Industrial &*

Engineering Chemistry Fundamentals, *18*(3), 296–297. https://doi.org/10.1021/i160071a019

Chung, T. H., Ajlan, M., Lee, L. L., & Starling, K. E. (1988). Generalized multiparameter correlation for nonpolar and polar fluid transport properties. *Industrial \& Engineering Chemistry Research*, *27*(4), 671–679. https://doi.org/10.1021/ie00076a024

Chung, T. H., Lee, L. L., & Starting, K. E. (1984). Applications of Kinetic Gas Theories and Multiparameter Correlation for Prediction of Dilute Gas Viscosity and Thermal Conductivity. *Industrial and Engineering Chemistry Fundamentals*, *23*(1), 8–13. https://doi.org/10.1021/i100013a002

Del Col, D., Bisetto, A., Bortolato, M., Torresin, D., & Rossetto, L. (2013). Experiments and updated model for two phase frictional pressure drop inside minichannels. *International Journal of Heat and Mass Transfer*, *67*, 326–337. https://doi.org/10.1016/j.ijheatmasstransfer.2013.07.093

Deng, H., Rossato, M., Fernandino, M., & Del Col, D. (2019). A new simplified model for condensation heat transfer of zeotropic mixtures inside horizontal tubes. *Applied Thermal Engineering*, *153*(December 2018), 779–790. https://doi.org/10.1016/j.applthermaleng.2019.02.128

Di Marcoberardino, G., Invernizzi, C. M., Iora, P., Ayub, A., Di Bona, D., Chiesa, P., Binotti, M., & Manzolini, G. (2020). Experimental and analytical procedure for the characterization of innovative working fluids for power plants applications. *Applied Thermal Engineering*, *178*, 115513. https://doi.org/10.1016/j.applthermaleng.2020.115513

Di Marcoberardino, G., Morosini, E., Di Bona, D., Chiesa, P., Invernizzi, C., Iora, P., & Manzolini, G. (2022). Experimental characterisation of CO2 + C6F6 mixture: thermal stability and vapour liquid equilibrium test for its application in transcritical power cycle. *Applied Thermal Engineering*, 118520. https://doi.org/10.1016/j.applthermaleng.2022.118520

Doninelli, M., & Di Marcoberardino, G. (2023). On the design of recuperator for transcritical cycle adopting CO2-based mixture as working fluid: a focus on transport properties prediction - under review. *Applied Thermal Engineering*.

Doninelli, Michele, Morosini, E., Gentile, G., Putelli, L., Di Marcoberardino, G., Binotti, M., & Manzolini, G. (2023). Thermal desalination from rejected heat of a transcritical cycle working with a CO2-based mixture in CSP application: a focus on the MED technology. *Sustainable Energy Technologies and Assessments*.

Freire, M. G., Ferreira, A. G. M., Fonseca, I. M. A., Marrucho, I. M., & Coutinho, J. A. P. (2008). Viscosities of liquid fluorocompounds. *Journal of Chemical and Engineering Data*, *53*(2), 538–542. https://doi.org/10.1021/je700632z

Gnielinski, V. (1975). New equations for heat and mass transfer in the turbulent flow in pipes and channels. *NASA STI/Recon Technical Report A*, *41*(1), 8–16.

Hodnebrog, Aamaas, B., Fuglestvedt, J. S., Marston, G., Myhre, G., Nielsen, C. J., Sandstad, M., Shine, K. P., & Wallington, T. J. (2020). Updated Global Warming Potentials and Radiative Efficiencies of Halocarbons and Other Weak Atmospheric Absorbers. In *Reviews of Geophysics* (Vol. 58, Issue 3). https://doi.org/10.1029/2019RG000691

Illyés, V., Morosini, E., Doninelli, M., David, P.-L., Guerif, X., Werner, A., Di Marcoberardino, G., & Manzolini, G. (2022). *Design of an Air-Cooled Condenser for CO2-Based Mixtures: Model Development, Validation and Heat Exchange Gain with Internal Microfins*. 1–11. https://doi.org/10.1115/gt2022-82438

Irving, J. B., & Jamieson, D. T. (1975). Thermal conductivity of 13 fluorocarbon liquids. *Journal of Fluorine Chemistry*, *5*(5), 449–456. https://doi.org/https://doi.org/10.1016/S0022-1139(00)82503-8

Mason, E. A., & Saxena, S. C. (1959). Thermal Conductivity of Multicomponent Gas Mixtures. II. *The Journal of Chemical Physics*, *31*(2), 511–514. https://doi.org/10.1063/1.1730386

Morosini, E., Doninelli, M., Alfani, D., Astolfi, M., Di Marcoberardino, G., & Manzolini, G. (2023). Analysis of the potential of CO2 based mixtures to improve the efficiency of cogenerative waste heat recovery power plants. *The 5th European SCO2 Conference for Energy Systems*.

Papapetrou, M., Kosmadakis, G., Cipollina, A., La Commare, U., & Micale, G. (2018). Industrial waste heat: Estimation of the technically available resource in the EU per industrial sector, temperature level and country. *Applied Thermal Engineering*, *138*(July 2017), 207–216. https://doi.org/10.1016/j.applthermaleng.2018.04.043

Poling, B. E., & Prausnitz, J. M. (2001). The Properties of Gases and Liquids. In *Solutions*.

Quiñones-Cisneros, S. E., Pollak, S., & Schmidt, K. A. G. (2021). Friction Theory Model for Thermal Conductivity. *Journal of Chemical and Engineering Data*, *66*(11), 4215–4227. https://doi.org/10.1021/acs.jced.1c00400

Quiñones-Cisneros, S. E., Zéberg-Mikkelsen, C. K., & Stenby, E. H. (2000). The friction theory (f-theory) for viscosity modeling. *Fluid Phase Equilibria*, *169*, 249–276.

Quiñones-Cisneros, S. E., Zéberg-Mikkelsen, C. K., & Stenby, E. H. (2001). One parameter friction theory models for viscosity. *Fluid Phase Equilibria*, *178*(1–2), 1–16. https://doi.org/10.1016/S0378-3812(00)00474-X

Scholes, C., Ho, M., & Wiley, D. (2016). Membrane-Cryogenic Post-Combustion Carbon Capture of Flue Gases from NGCC. *Technologies*, *4*(2), 14. https://doi.org/10.3390/technologies4020014

Uyehara, OA and Watson, K. (1944). A universal viscosity correlation. *National Petroleum News*, *36*, 714–722.

Wilke, C. R. (1950). A viscosity equation for gas mixtures. *The Journal of Chemical Physics*, *18*(4), 517–519. https://doi.org/10.1063/1.1747673

ORC SEVILLE 2023
7th International Seminar on O.R.C. Power Systems

© 2024 Editorial Universidad de Sevilla. Este es un artículo de acceso abierto distribuido bajo los términos de la licencia de uso y distribución Creative Commons (BY-NC-ND 4.0)

DOI: https://dx.doi.org/10.12795/9788447227457_57

ON AIR-COOLED CONDENSERS FOR ORC SYSTEMS OPERATING WITH ZEOTROPIC MIXTURES

Lorenzo Galieti[1]*, Carlo De Servi[1,3], Dario Alfani[2], Paolo Silva[2]
Paola Bombarda[2], Piero Colonna[1]

[1]*Propulsion and Power, Delft University of Technology, Delft, The Netherlands*
[2] *Dipartimento di Energia, Politecnico di Milano, Milano, Italy*
[3] *VITO, Thermal Energy Systems, Mol, Belgium*

*Corresponding Author: l.galieti@tudelft.nl

ABSTRACT

The use of mixtures as working fluids of ORC systems is being intensively investigated because of the better temperature profile matching achievable in the heat exchangers, resulting in lower thermodynamic irreversibilities and increased efficiency. The gains are expected to be higher for low-temperature air-cooled power plants, where the ratio between the auxiliary power consumption associated to the cooling of the working fluid and the net power output of the ORC plant is higher. For instance, a temperature glide in the condenser may enable a reduction in the fan consumption at the cost of an increased heat transfer area, and possibly a decrease in the minimum temperature of the thermodynamic cycle. This solution is expected to be attractive for geothermal applications: since the drilling of the geothermal well is by far the dominant cost, the additional investment for the condenser can be more easily compensated by the increased revenues related to the greater electrical power output.

This study focuses on the modelling and sizing of an air-cooled condenser for geothermal ORC power plants operating with working fluid binary mixtures. A detailed fin and tube air cooled condenser model is developed and integrated with an in-house tool for the simulation of ORC systems. Working fluid thermodynamic properties are computed with the PCP-SAFT equation of state (EoS). The tool is used to investigate the effect of the condenser design assumptions on the geothermal plant maximum power output for an optimal working fluid mixture, whose composition is determined by optimizing the PCP-SAFT parameters. The outcome is a pseudo-fluid mixture that represents the ideal working fluid for the given thermal source.

The results indicate that the adoption of mixtures allows the air-cooler consumption and generally the minimum cycle temperature to be decreased, leading to an increased plant efficiency. In addition, design guidelines for the condenser are derived, based on the tradeoff between component size and plant efficiency. Finally, the optimization results show that if the onset of the mixture condensation occurs in the recuperator, it might be possible to reduce the fan consumption and size of the condenser simultaneously, albeit at the expense of an increased complexity of the regenerator design.

1 INTRODUCTION

Mixtures are a promising option for ORC systems exploiting low temperature thermal sources. In those systems, the impact on the plant power output of the condenser auxiliary power consumption as well as that of the higher condensing temperatures is high and can be reduced by exploiting the temperature glide of mixtures. This improves the matching between the temperature profiles of the working fluid

and the power plant thermal sink, thus reducing the heat transfer irreversibilities. The benefit consists of net power gains ranging from 4% (Trapp and Colonna, 2013) to over 10% (Heberle et al, 2011) when compared to ORC systems operating with pure fluids and the same pinch point temperature difference in the condenser. At the same time, the reduced mean temperature difference achievable with the mixture glide leads to a larger condenser heat transfer area, which may further increase due to the degradation of the mixture heat transfer coefficient with respect to pure fluids, as observed in different experimental campaigns (Radermacher and Hwang, 2005). For this reason, the thermodynamic advantages related to the adoption of mixtures as working fluid of ORC systems might not necessarily guarantee an economic benefit.

More recent works evaluated the economic benefit of zeotropic mixtures in geothermal applications by means of thermo-economic optimizations. For instance, Andreasen (Andreasen et al, 2021) compared the performance of mixtures of propane, i-butane, i-pentane and R1234yf to that of their pure components. They found that a R1234yf/i-butane mixture can achieve 5% higher net present values than R1234yf, which was the best pure fluid candidate among the selected ones. A similar result was obtained by Heberle (Heberle and Brüggemann, 2015) who reported a decrease in electricity generation cost of 4-10% compared to the most cost-efficient pure component. However, given the limited set of fluids considered in both works, it is not possible to generalize the results of these studies.

The choice of the mixture components is challenging due to the considerable number of combinations which can be achieved even from a limited set of pure components. This problem can be addressed by using Continuous Molecular Targeting (CoMT) methods, where the EoS parameters that describe the mixture components are relaxed to continuous variables and optimized together with the ORC process parameters. In this way, the computationally demanding mixed integer optimization problem representing the selection of the mixture components is simplified to a continuous one with a larger number of optimization variables. The outcome of the simplified problem is an optimal pseudo-mixture (or pure pseudo-fluid) enabling the ORC system to achieve the maximum possible performance, and whose properties must be subsequently approximated with existing fluids. An alternative method that avoids treating the EoS parameters as optimization variables is that proposed by Schilling (Schilling et al, 2021): by using the Group Contribution PCP-SAFT (Sauer et al, 2014), the authors directly optimized the molecular structure of the working fluids in the mixture, thus taking into account an extremely large number of mixture candidates, albeit with components having a structure limited to certain molecular groups. When considering liquid wastewater at 150 ºC as heat source, Schilling et al. identified a combination of propene/propionaldehyde (94%/6%) as the optimal mixture and reported a limited (3%) decrease in Specific Investment Cost (SIC) compared to the optimal pure fluid, i.e. propene. At the same time, the SIC obtained for the optimal pseudo-mixture and that of the optimal pure pseudo-fluid resulted to be equal. It may be then argued that the better thermo-economic performance observed for the propene/propionaldehyde mixture is only due to the additional degrees of freedom in ORC system design introduced by the possibility of tuning the mixture composition.

345

The aim of this work is to evaluate the increase in performance achievable by using zeotropic mixtures in geothermal applications with respect to that obtained in the case of pure working fluids as a function of the pinch point temperature difference assumed for the air-cooled condenser design. To this purpose, a detailed fin and tube air-cooled condenser model is developed and integrated with an in-house tool for the simulation of ORC systems. To the authors' knowledge, even though air cooling is by far the most common solution in geothermal binary plants (Di Pippo, 2016), the works documented so far in the literature on ORC mixtures for such applications consider water-cooled condensers. These not only are more compact than the air-cooled ones, but the corresponding power consumption can be neglected as well.

2 METHODOLOGY

2.1 Power Plant

This study considers an air-cooled recuperated ORC system for geothermal applications. Two cases are investigated: in the first one, the geothermal brine temperature at the outlet of the power plant is unconstrained; in the second case, it is limited to 100 ºC, exemplifying a combined heat and power

(CHP) application with a serial plant layout, or equivalently a conventional all-electric power plant configuration exploiting a high salinity brine. Note that there are other possible CHP plant configurations, but the serial one is the most suitable in case of a limitation on the brine leaving temperature.

The thermodynamic cycle calculation procedure is similar to that adopted in (Krempus et al, 2021). In particular:

1. Pinch-point temperature difference is fixed in each heat exchanger.
2. Turbomachinery isentropic efficiencies are fixed.
3. All the pressure drops except the one on the air side of the condenser are prescribed.

Table 1 indicates the general cycle specifications: the thermal source of the plant is geothermal brine at 150 ºC. This is modelled as pure water, as it is assumed to be coming out as liquid from the geothermal well. Notice that neither the brine composition (provided that the specific heat capacity remains constant) nor the mass flow rate affect the estimation of the plant thermodynamic performance. Their effect is limited to the sizing of the cycle components and the power plant capacity. The pinch-point temperature difference and pressure drop in the heat exchangers, as well as the turbomachinery thermodynamic efficiencies are fixed in accordance with (Krempus et al, 2021). The only relevant difference with respect to the work documented in (Krempus et al, 2021) is related to the condenser pinch-point temperature difference, which is varied in the present study from a maximum of 10 ºC to a minimum theoretical value of 0.5 ºC. Moreover, in contrast to (Krempus et al, 2021), cycle maximum temperature and condensation pressure were not constrained: the first one because of the relatively low temperature of the geothermal source, which is unlikely to cause any thermal decomposition of the working fluid, while the second one was left unconstrained to allow for a larger design space exploration. Finally, the condenser is sized as a fin and tube heat exchanger, by using the procedure described in section 2.3.

The power output is chosen as objective function of the optimal design problem. This is reasonable for geothermal applications because, as already mentioned, the exploration and drilling of the geothermal wells are much more expensive than the ORC power block (Astolfi et al, 2013). Optimal cycle parameters and mixture composition are found using the genetic algorithm provided by the optimization suite Pymoo (Blank and Deb, 2020).

346

Table 1: Thermodynamic cycle specifications

Parameter	Value	Parameter	Value	Parameter	Value	Parameter	Value
$T_{\mathrm{HRVG_{H_{in}}}}$	150 ºC	$\Delta T_{\mathrm{pp_{Reg}}}$	10 ºC	$\Delta T_{\mathrm{pp_{HRVG}}}$	10 ºC	η_{turbine}	90%
$P_{\mathrm{HRVG_{H_{in}}}}$	40 bar	$\Delta P_{\mathrm{Reg_H}}$	0.025 bar	$\Delta T_{\mathrm{pp_{Cond}}}$	0.5-10 ºC	η_{fan}	65%
$\Delta P_{\mathrm{HRVG_H}}$	0.05 bar	$\Delta P_{\mathrm{Reg_C}}$	$0.025p_{\max}$	$\Delta P_{\mathrm{Cond_H}}$	0.025 bar	T_{amb}	30 ºC
$\Delta P_{\mathrm{HRVG_C}}$	$0.025P_{\max}$	η_{pump}	80%				

2.2 Thermodynamic property modeling

The PCP-SAFT EoS (Gross and Sadowski, 2001) as implemented in (Colonna et al, 2019) is adopted to predict the thermodynamic properties of the working fluids, both in the case of pure compounds and mixtures. Only non-polar molecules were considered in this study. These can be modelled using three EoS parameters, namely segment number, diameter and energy parameter. Moreover, because of the lack of experimental data, all mixture binary interaction parameters are set to zero.

The ideal gas specific heat and molecular weight of the pure pseudo-fluids are calculated directly from the PCP-SAFT parameters using a QSPR method (Stavrou, 2017). Additional constraints are applied to the PCP-SAFT parameters to avoid unfeasible pseudo-fluids, see (Stavrou, 2017) for more details. The molar fractions and PCP-SAFT parameters of the working fluid components are optimized together with the cycle parameters. The bounds of the overall optimization space are reported in Table 2.

Table 2: Bounds of the optimization variables.

Cycle	Min	Max	Fluid	Min	Max
T_{max}	90 ºC	140 ºC	M	2 (-)	6.5 (-)
$P_{max,R}$	0.5	0.8	σ	2 (Å)	4.5 (Å)
T_{min}	$30 + \Delta T_{\mathrm{ppCond}}$	60 ºC	ε_K	150 (K)	300 (K)
			c	0.01	0.5

2.3 Air Cooled Condenser model

The air-cooled condenser is of the fin and tube heat exchanger type, see the example shown in Figure 1. The air flows through a series of finned tube rows, while the condensing fluid flows inside the tubes, following a serpentine path that depends on the tube arrangement. This study exclusively considers arrangements with one row for each pass, as in the example reported in Figure 2.

Table 3 reports the main geometrical features of the tube banks. The tubes feature classical circular fins, whose characteristic dimensions are selected based on (Serth, 2014). The effect of the number of passes was also considered by repeating the optimization study for different values of this variable.

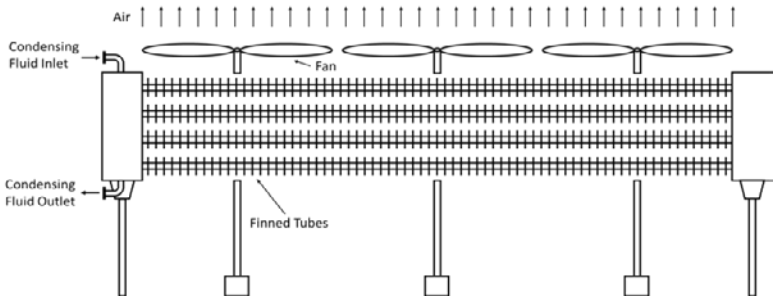

Figure 1: Configuration of an air-cooled fin and tube condenser

The model handles both superheated and saturated working fluid states. It takes the working fluid mass flow rate, inlet and outlet enthalpies, as well as the heat exchanger design pinch-point as inputs. The outputs are the heat exchange area, frontal area, design air velocity, the air side pressure drop and the fan power.

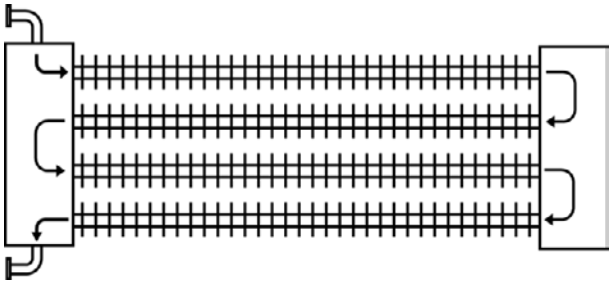

Figure 2: Configuration with one row per pass

Table 3: Tube bank characteristic dimensions

Parameter	Value
D_{Ext}	25.5 mm
D_{Fin}	56 mm
$Tube\ Pitch$	60 mm
$Tube\ Length$	9 m
N_{Passes}	3-6

Table 4 provides a summary of the principal correlations used by the model. Note that the adopted version of the PCP-SAFT is unable to directly compute the transport properties of the pseudo-fluids from the EoS parameters, unlike the molecular weight and ideal gas specific heat. For this reason, the de-superheating and condensing heat transfer coefficients are set to 200 at 1500 W/m^2K, respectively. Based on a preliminary condenser design exploration, these values were found to be characteristic of medium-sized condensers. Significant deviations may be expected for very large or very small

condensers due to the very low or high flow velocities involved in these cases. However, such a simplification does not introduce significant inaccuracies in the model for two reasons: the first is that the air heat transfer coefficient was usually found to be 2-3 times lower than that of the condensing fluid, even when considering the effect of the fins. The second is that the working fluid is only slightly superheated at the entrance of the condenser, because of the presence of the regenerator upstream. The rejected sensible heat is then rather small if compared to the total heat load of the heat exchanger. In most of the analyzed test cases, the error on the heat exchanger area was found to be less than 5%. The exceptions are usually in the case of condensers operating with mixtures showing a high glide (on the order of 20ºC or more) and, consequently, exhibiting a considerable degradation of the heat transfer coefficient.

The validation of the model was performed by sizing the condenser for representative working fluids and operating conditions using the model, and then comparing the estimated performance with the predictions generated by the commercial software Aspen Plus. Table 5 summarizes the main process parameters of one of the validation cases.

Table 4: Main correlations of the model.

Parameter	Source
h_{air}	VDI-GVC, 2010
F	VDI-GVC, 2010
ΔP_{air}	$Serth,$ 2014
h_{cond}	Deng et al, 2019
h_{desup}	Dittus-Boelter Corr.

Table 5: Validation case with Aspen Plus.

Parameter	Model	Software
$h_{air}\ (W/m^2K)$	744	730
$\Delta P_{air}\ (Pa)$	91	95
$\dot{Q}\ (MW)$	3.20	3.18
$A\ (m^2)$	1016	1018

348

3 RESULTS

3.1 Scenario 1: no constrain on the temperature of the leaving brine

Figure 3 exemplifies the T-s diagram obtained for an optimal pseudo-binary mixture. The glide in the condenser is perfectly linear and matches the air temperature profile. On the contrary, the evaporator operates at a high reduced pressure, with a limited temperature glide and the fluid exiting as saturated vapor, as commonly observed in ORC systems.

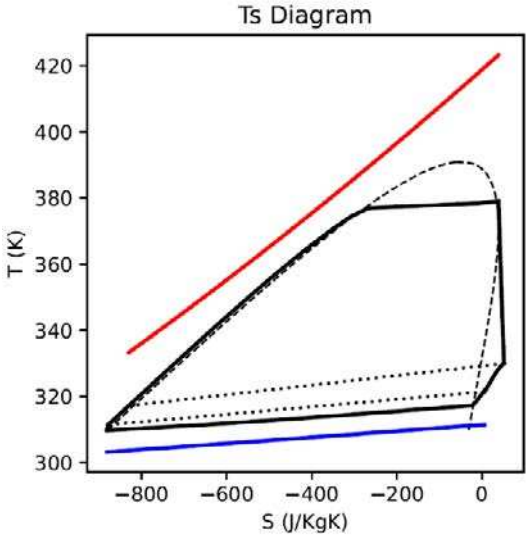

Figure 3: T-s diagram of the optimal pseudo-binary mixture for a condenser with 4 passes and a pinch-point of 8 ºC

Given the large variation of the heat source temperature, the optimal mixture glide in the evaporator is arguably significantly higher than the optimal one in the condenser. Even if the EoS parameters are relaxed to continuous values, it is essentially impossible to find a mixture whose difference in boiling point of the components allows for a glide varying from about 10 degrees during condensation to several tens of degrees in the evaporator Furthermore, large glides during evaporation would correspond to fluids with broader saturation domes and operating at lower reduced evaporation pressures, which may be below the limits imposed on this variable. Finally, it should be noted that such a high glide would also result in a substantial reduction of the mixture heat transfer coefficient, as this phenomenon is driven by the difference in boiling temperature of the mixture components.

Figure 4 compares the second law efficiency of the ORC system operating with the optimal pseudo-mixtures and that found for the optimal pseudo-fluids, as a function of the condenser pinch temperature difference and heat transfer area. For a given pinch-point temperature difference, the optimal pseudo-mixtures show a higher performance, confirming their superior thermodynamic potential. However, if this comparison is performed with respect to the condenser heat exchange area, it can be seen from Figure 4b that pure fluids and mixtures have comparable second-law efficiencies. Similar conclusions might be deduced from the results reported by Schilling et al. for water cooled power plants (Schilling et al, 2021).

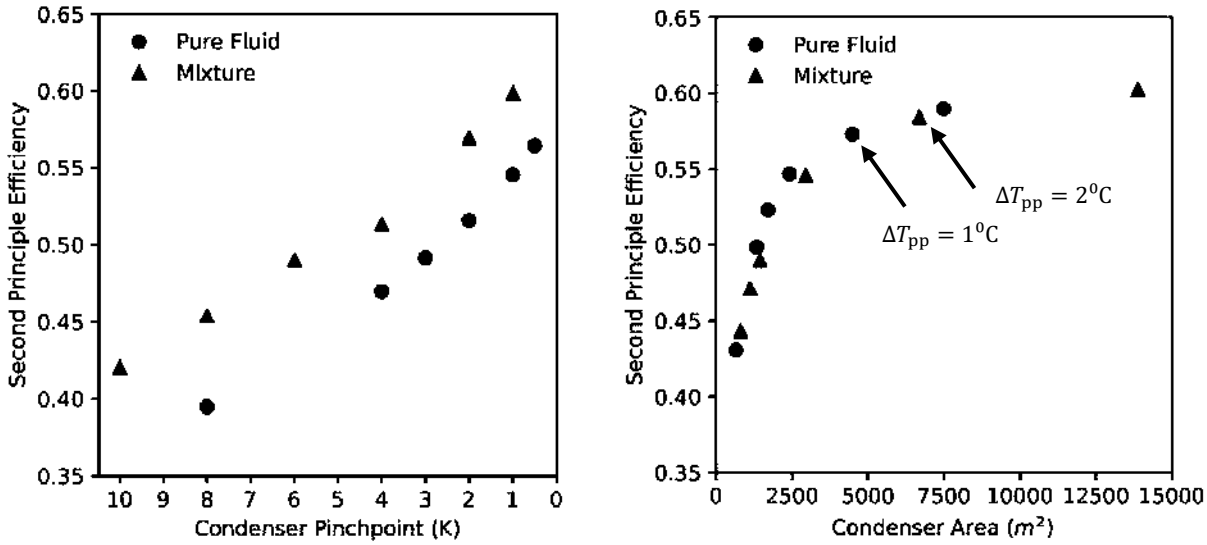

a) As a function of the pinch-point **b) As a function of the condenser area**

Figure 4: Comparison of the second law efficiency of the ORC systems operating with the optimal pseudo-mixtures and pseudo-fluids for a condenser with 3 passes and an unconstrained temperature of the leaving brine

At the same time, it should be noted that the pure fluid ORC systems achieving the highest efficiencies exhibit very low condenser pinch-point temperature differences (1 and 0.5 ºC), which may not be achievable in a real component. For instance, effects such as thermal conduction along the tubes, the difference between static and total temperature, or flow maldistribution in the tube bundle may reduce the actual heat transfer rate under low temperature differences. This can limit the efficiency improvement attainable by increasing the condenser area in the case of pure fluids. On the contrary, with mixtures, a higher pinch-point temperature difference is attained also in the case of large heat transfer areas, thus resulting in a feasible and more operable condenser. For this reason, in geothermal applications, where the driving cost is represented by the exploration and drilling of the geothermal wells, it may be profitable to decrease the logarithmic temperature difference both by exploiting working fluid mixtures temperature glide and adopting relatively low pinch points values.

Concerning the number of passes, they do not seem to significantly affect the results. This can be better understood by observing Figure 5: the glides of the resulting optimal mixtures are relatively mild. Increasing the number of passes does not increase the effective logarithmic temperature difference and,

thus, does not yield significant reductions in the required heat exchange area. It can also be seen that the glide of the optimal mixtures follows almost a linear trend as a function of the prescribed condenser minimum temperature difference. Given all the complex interaction between the components, fluid and cycle parameters, understanding the reason of this trend requires additional investigations.

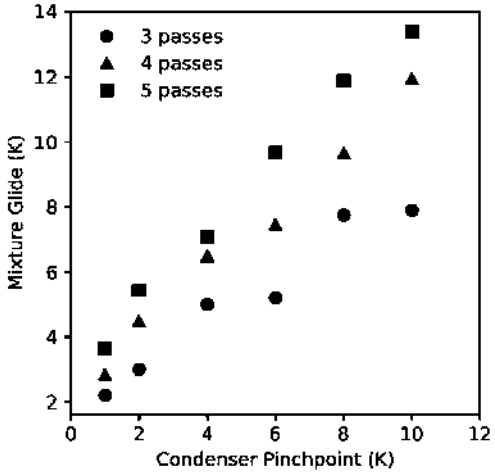

Figure 5: Condensation glide of the pseudo-mixtures as a function of the condenser pinch-point, for an unconstrained temperature of the leaving brine

3.2 Scenario 2: Constrained temperature of the leaving brine

In general, the considerations made in the previous section still apply when the brine outlet temperature is constrained to a minimum value of 100 ºC, as it can be seen in Figure 6.

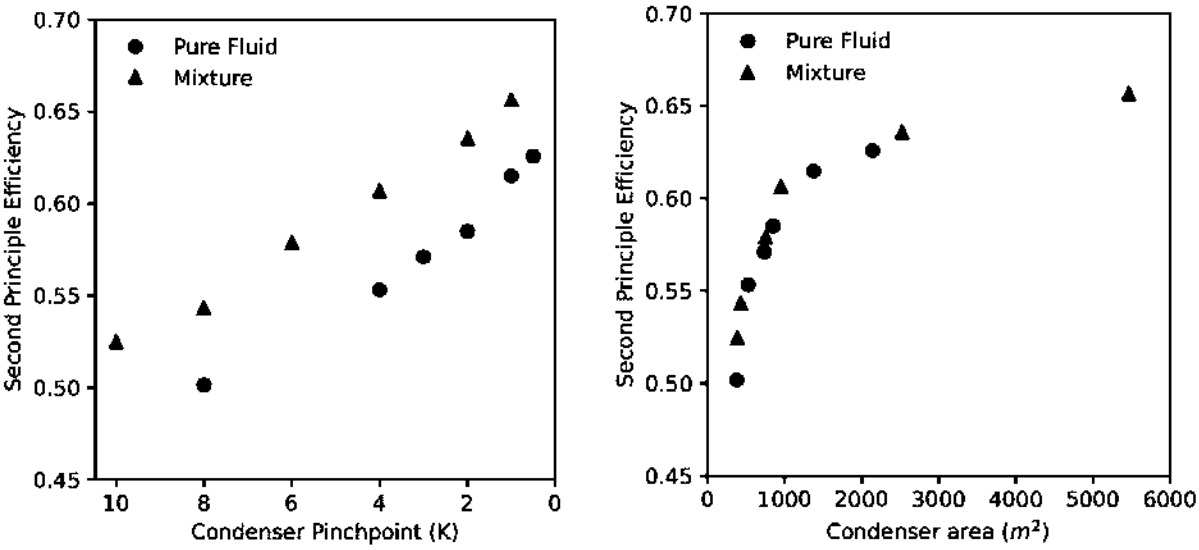

a) As a function of the pinch-point **b) As a function of the condenser area**

Figure 6: Comparison of second law efficiency of pseudo-pure fluids and pseudo-mixtures for a minimum brine leaving temperature of 100 ºC

As the brine temperature is now constrained to a high value, regeneration plays a much more important role in the thermodynamic cycle. For this reason, the optimization problem may have two different optima, as shown in Figure 7: one features a pseudo-mixture with a linear glide, while the other another pseudo-mixture that partially condenses in the regenerator, so as to maximize the recuperated thermal energy. This is an unexplored option in ORC technology and could prove useful to reduce the total heat

exchange area of the power plant by taking advantage of the higher heat transfer coefficient of the liquid working fluid. However, such a gain might be partially offset by the degradation of the mixture heat transfer coefficient, which in this case is expected to be quite significant.

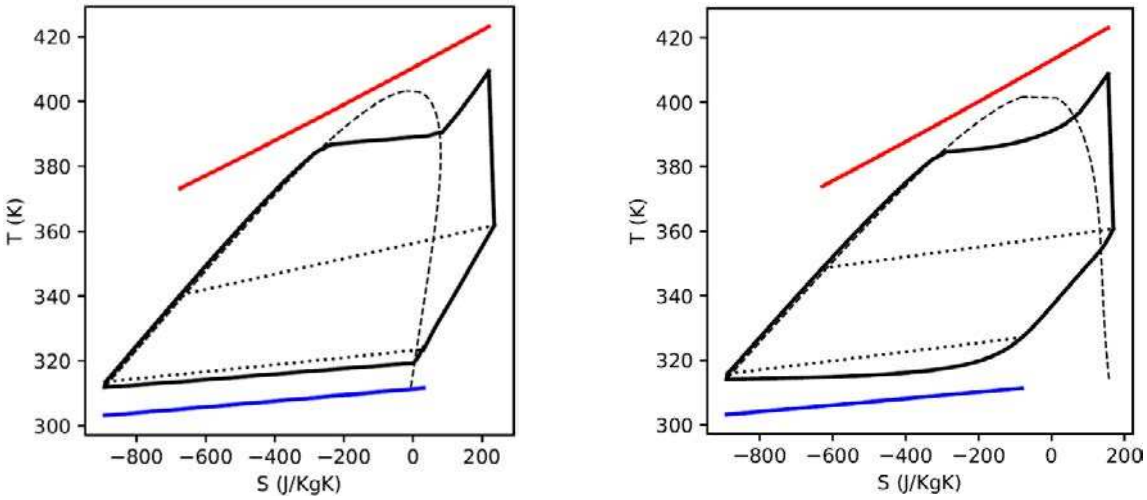

a) Condenser with a linear glide **b) Regenerator with partial condensation**

Figure 7: Possible thermodynamic cycles with mixtures for a minimum brine leaving temperature of 100 ºC

4 CONCLUSIONS

The use of mixtures as working fluids for air-cooled geothermal ORC power plants was investigated by means of an in-house tool for steady-state thermodynamic cycle computations and optimization, integrating a preliminary design model of the condenser. The predictive capabilities of the PCP-SAFT EoS were exploited to identify the optimal working fluids for the application by optimizing the parameters of the EoS. Notably, the identified pseudo-pure compounds or pseudo-mixtures set the maximum possible performance of the ORC system for the prescribed design specifications. The main findings of the study are:

351

- For a prescribed pinch-point temperature difference in the condenser, the ORC systems operating with binary mixtures exhibit better performance than those with pure fluids, confirming the expected thermodynamic advantages.
- The identified pseudo-mixtures and pure fluids exhibit an equivalent performance as a function of the condenser heat transfer area. However, for a prescribed ORC system power output, mixtures allow for condensers with higher pinch-point temperature differences. As temperature differences lower than 1 ºC are arguably not attainable, mixtures are then expected to allow for higher actual efficiencies.
- Because of the relatively low glide of the optimal mixtures, increasing the number of passes does not yield any significant improvement of the effective mean logarithmic temperature difference and, consequently, does not reduce the surface area of the condenser. Thus, a large number of passes is generally not recommended, if not to respect other design constraints.
- Given that generally the cost of exploration and realization of the wells is by far the dominant one, in geothermal applications it could be worthwhile to further increase the plant power output by using mixtures and, at the same time, adopting relatively low pinch-point temperature differences in the condenser.
- When the brine leaving temperature is constrained, such as in CHP applications, allowing a partial condensation of the mixture in the regenerator could be an interesting option to reduce the size of the condenser and improve the efficiency of the power plant.

NOMENCLATURE

m	Segment number (PCP-SAFT)	**Subscript**	
σ	Segment diameter (PCP-SAFT)	pp	Pinch-point
ε_K	Segment energy parameter (PCP-SAFT)	HRVG	Heat recovery vapor generator
c	Molar concentration	Reg	Regenerator
F	Logarithmic temperature difference correction factor	R	Reduced quantity with respect to the critical one
η	Isentropic Efficiency	Ext	External
h	Heat Transfer Coefficient	H	Hot Side
D	Diameter	C	Cold Side
N_{Passes}	Number of tube passes		

ACKNOWLEDGEMENT

This project has received funding from the European Union's Horizon 2020 research and innovation program under the Marie Skłodowska-Curie grant agreement No 956965. The authors also gratefully acknowledge the support of Umberto Merlo and Stefano Filippini from LU-VE S.p.A within the Easy-Go project.

This study was also carried out within the *NEST - Network 4 Energy Sustainable Transition* (D.D. 1243 02/08/2022, PE00000021) and received funding under the National Recovery and Resilience Plan (NRRP), Mission 4 Component 2 Investment 1.3, funded from the European Union - NextGenerationEU.

This manuscript reflects only the authors' views and opinions, neither the European Union nor the European Commission can be considered responsible for them.

352

REFERENCES

Andreasen, J. G., Baldasso, E., Kærn, M. R., Weith, T., Heberle, F., Brüggemann, D., & Haglind, F. (2021). Techno-economic feasibility analysis of zeotropic mixtures and pure fluids for organic Rankine cycle systems. *Applied Thermal Engineering*, *192*. https://doi.org/10.1016/j.applthermaleng.2021.116791

Astolfi, M., Romano, M. C., Bombarda, P., & Macchi, E. (2014). Binary ORC (Organic Rankine Cycles) power plants for the exploitation of medium-low temperature geothermal sources - Part B: Techno-economic optimization. *Energy*, *66*, 435–446. https://doi.org/10.1016/j.energy.2013.11.057

Blank, J., & Deb, K. (2020). *Pymoo: Multi-Objective Optimization in Python*.

Colonna, P., Van Der Stelt, T., & Guardone, A. (2019). *FluidProp (Version 3.1): A program for the estimation of thermophysical properties of fluids*.

Deng, H., Rossato, M., Fernandino, M., & Del Col, D. (2019). A new simplified model for condensation heat transfer of zeotropic mixtures inside horizontal tubes. *Applied Thermal Engineering*, *153*, 779–790. https://doi.org/10.1016/j.applthermaleng.2019.02.128

Di Pippo, R. (2005). *Geothermal Power Plants*. Elsevier. ISBN: 978-1-85617-474-9. https://doi.org/10.1016/B978-1-85617-474-9.X5029-8

Gross, J., & Sadowski, G. (2001). Perturbed-chain SAFT: An equation of state based on a perturbation theory for chain molecules. *Industrial and Engineering Chemistry Research*, *40*(4), 1244–1260. https://doi.org/10.1021/ie0003887

Heberle, F., & Brüggemann, D. (2015). Thermo-economic evaluation of organic rankine cycles for geothermal power generation using zeotropic mixtures. *Energies*, *8*(3), 2097–2124. https://doi.org/10.3390/en8032097

Heberle, F., Preißinger, M., & Brüggemann, D. (2012). Zeotropic mixtures as working fluids in Organic Rankine Cycles for low-enthalpy geothermal resources. *Renewable Energy*, *37*(1), 364–370. https://doi.org/10.1016/j.renene.2011.06.044

Krempus, D., Bahamonde, S., Van Der Stelt, T., De Servi, C. M., Klink, W., Colonna, P., (2021). On mixtures as working fluids for air-cooled ORC bottoming power plants of gas turbines, 6th International Seminar on ORC Power Systems, Paper ID: 68

Sauer, E., Stavrou, M., & Gross, J. (2014). Comparison between a homo- and a heterosegmented group contribution approach based on the perturbed-chain polar statistical associating fluid theory equation of state. *Industrial and Engineering Chemistry Research*, *53*(38), 14854–14864. https://doi.org /10.1021/ie502203w

Schilling, J., Entrup, M., Hopp, M., Gross, J., & Bardow, A. (2021). Towards optimal mixtures of working fluids:Integrated design of processes and mixtures for Organic Rankine Cycles. *Renewable and Sustainable Energy Reviews*, *135, 110179*. https://doi.org/10.1016/j.rser.2020.110179

Serth, R. (2014). *Process Heat Transfer*. Elsevier. https://doi.org/10.1016/C2011-0-07242-3

Stavrou, M. (2017). *Integrated process and solvent design for CO2 capture using Continuous Molecular Targeting-Computer Aided Molecular Design (CoMT-CAMD)*. https://doi.org/10.4233/uuid:b44de3d4-25dd-453c-988c-07fca027a612

Trapp, C., & Colonna, P. (2013). Efficiency improvement in precombustion Co2 removal units with a waste-heat recovery ORC power plant. *Journal of Engineering for Gas Turbines and Power*, *135*(4). https://doi.org /10.1115/1.4023121

VDI-GVC. (2010). VDI Heat Atlas. In *VDI Heat Atlas*. Springer Berlin Heidelberg. ISBN: 978-3-540-77876-9. https://doi.org/10.1007/978-3-540-77877-6

ORC SEVILLE 2023
7th International Seminar on O.R.C. Power Systems

© 2024 Editorial Universidad de Sevilla. Este es un artículo de acceso abierto distribuido bajo los términos de la licencia de uso y distribución Creative Commons (BY-NC-ND 4.0)

DOI: https://dx.doi.org/10.12795/9788447227457_58

Experiments on Supersonic ORC Nozzles in Linear Cascade Configuration

Marco Oliveti, Marco Manfredi, Giacomo Persico, Andrea Spinelli*, Paolo Gaetani, Vincenzo Dossena

Politecnico di Milano, Department of Energy, 20156, Milano, Italy

* Corresponding Author: andrea.spinelli@polimi.it

ABSTRACT

In organic Rankine cycles (ORCs), the turbo-expander represents a critical component due to the major impact of its efficiency on working fluid selection, cycle layout and overall plant performance and profitability. Also, its design is complicated by large expansion ratios, by the demand of operational flexibility and by the thermo-physical characteristics of the working fluid and non-ideal gas effects. This typically leads to turbines with low number of stages and transonic/supersonic flow regimes. For these reasons, the ORC turbine design relies on advanced aerodynamic models and high-fidelity tools based on computational fluid dynamics (CFD). The verification of high-fidelity tools requires accurate fluid thermodynamic models and experimental data concerning canonical flows, since experiments on non-ideal flows within ORC turbine cascades are still missing in the literature. To fill this gap, a novel experiment has been designed at Politecnico di Milano on an ORC supersonic linear cascade, aimed at characterizing the flow field within the bladed and semi-bladed portion of the channels, at the trailing edge where shock/fan systems arise, and downstream the cascade, by retrieving the pitch-wise total pressure loss distribution. This paper reports the outcomes of an experimental campaign focused on the expansion of hexamathyldisiloxane (MM) within the cascade. Initial commissioning tests were performed using nitrogen at different pressure levels. Finally, the experimental data gathered during a campaign carried out with MM in non-ideal conditions are presented and compared with CFD simulations, allowing to assess real gas effects on the trailing edge shock pattern and pressure distribution through the cascade.

1. INTRODUCTION

In the last decades, ORCs experienced a remarkably increasing appeal, since, in a context of limited resources, it is crucial to exploit efficient technologies for power generation from low/medium enthalpy grade sources. The use of organic fluids instead of water for the Rankine cycle leads to considerable advantages, such as reduced specific enthalpy drops and single-phase expansions, which make this technology one of the most attractive for low-to-medium temperature sources (Colonna et al., 2015). However, complex fluid flows establish within the turbo-expander due to the strong non-ideal behaviour of the working fluids in proximity of the liquid-vapor saturation curve, where the expansion generally takes place. Moreover, the expanders are often designed with a low number of stages, which result in high pressure ratio cascades which leads to transonic and supersonic flows, characterized by complex shock wave patters.

Therefore, the fluid dynamic design of an ORC expander, typically an axial or radial turbine, requires a major attention, also considering that the efficiency of the expander has a crucial impact on the cycle performance and therefore on its overall profitability (Macchi, 2017). In order to successfully design an ORC turbine, several low-fidelity tools were conceived, mainly based on a mean-line method able to compute the thermodynamics and the geometry of each stage at blade mid-span. These methods have proven their value in traditional turbomachinery, where several experimental campaigns where carried out to validate the reliability of the correlations exploited for the losses prediction. The lack of experimental data on ORC turbines in the open literature, though, has often forced to settle for a validation

of mean-line models results through high-fidelity CFD simulations. However, the effectiveness of the latter with organic fluids operating at low compressibility factors is in general established on the use of the state of the art fluid models, while a systematical comparison between simulations and experimental results is still missing. The only experiments documented in literature on the flow of organic fluids are, in fact, providing results for nearly isentropic nozzle expansions or flow around wedge profiles and bluff bodies (Zocca et al., 2019; Reinker et al., 2021). Further data were then provided in (Baumgärtner et al., 2020), which reports a study on an annular turbine cascade but still requiring a numerical estimation of the total pressure downstream the blades.

In order to cover the described literature gap and to attempt a first validation of the CFD simulations results, an experiment was conceived at Politecnico di Milano with the aim of analyzing the flow field across a supersonic turbine linear cascade representative of ORC applications. This paper briefly covers the design of experiment in Section 2. After that, Section 3 reports the main results of the experimental campaign, with a rigorous analysis of the flow field and a comparison between experimental data and CFD simulation results.

2. DESIGN OF THE EXPERIMENT

The campaign was designed to take place within the Test Rig for Organic VApors (TROVA) (Spinelli et al., 2013), a blowdown wind tunnel conceived to work with organic fluids flowing across a stationary test section that replaces the expander. In this specific context, a converging-diverging geometry was selected to represent a supersonic turbine linear cascade for ORC applications, illustrated in Figure 1. A thorough description of the design of the whole test section and of the related instrumentation is pro-

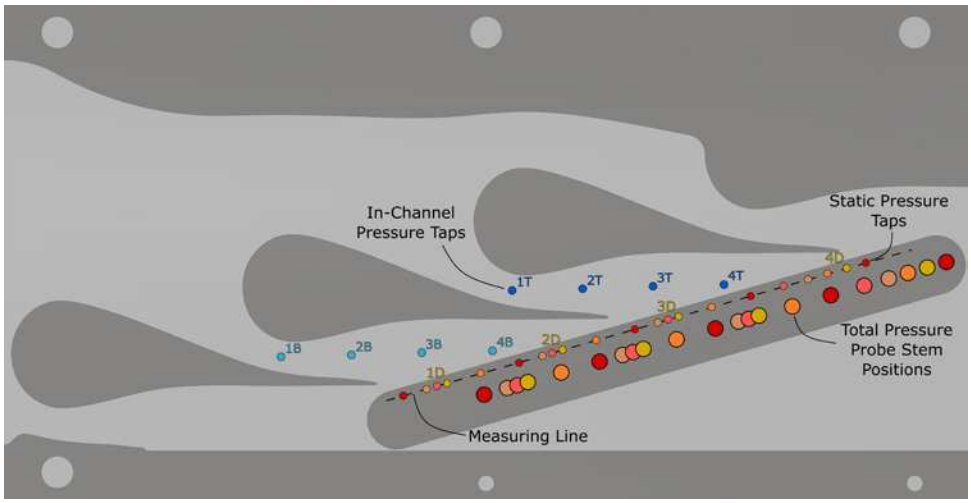

Figure 1: Test section configuration. The static pressure taps are numbered according to their location on the top channel (T), bottom channel (B) or downstream measuring line (D). The circles on the measuring line coincide with the probe head locations

vided in Manfredi et al. (2023), while here are resumed only the main features, essential to point out the cascade characteristics and allow a better understanding of the results outlined in the next sections.

The experiments were designed to be carried out with hexamethyldisiloxane (MM) as working fluid, which is typically considered for medium to high temperature ORC applications and it is particularly convenient for the current investigation, since it exhibits an highly non-ideal thermodynamic behaviour at temperature levels well below the thermal stability limit. As highlighted in Section 1, the main interest of this work is to investigate the flow field of expansions occurring in the non-ideal region. For this reason, the design conditions were fixed at p_{Td} = 25 bar and T_{Td} = 261.5°C, leading to a corresponding compressibility factor of Z_{Td} = 0.31. These conditions were exploited for the whole geometry optimization and as boundary conditions for CFD validations. Nonetheless, as specified later in Section 3, experiments will be mostly carried out at lower pressures, still allowing an assessment of the flow

field at fairly low values of Z, while reducing at the same time issues related to the limited Schlieren measurement range (Conti et al., 2017) and to the test section sealing.
As reported in Figure 1, the linear cascade features three blades and two side-walls, implementing two main central channels, where all the measurements are performed, and two lateral ones. The geometric pitch is of 45 mm and the stagger angle is $\gamma = 75°$. Both inlet and outlet are perfectly axial, meaning that the flow deflection is null, resembling the small deflection of radial machine vanes. The test section, however, aims to be representative also of axial turbines; in fact, the original profile was extracted from Romei et al. (2020), where the flow turning through the cascade is 75°. Here, a null deflection is equivalent to operate the blade with a 75° incidence at the inlet. To withstand such extreme boundary condition and avoid flow detachment, the blade shape was modified, assessing its performance with a CFD validation. The equivalence of the resulting flow field to the one characterizing typical turbine cascades is also proven by the blade pressure distributions reported in Manfredi et al. (2023). The profile was then optimized with the in-house tool FORMA (Persico et al., 2019) to minimize entropy generation. The result is a profile featuring a large curvature radius at the leading edge, which makes it tolerant to significant incidence angle variations while still keeping identical post-throat flow fields and therefore achieving very similar performances, as most of the entropy generation occurs in the supersonic region.
As far as the sidewalls are concerned, they were carefully designed to ensure that periodicity was attained, despite the reduced number of available channels. The lower side-wall is obtained simply by reproducing the pressure side of the blade from the throat to the trailing edge and carving the profile with a sufficiently large curvature radius to avoid any flow detachment at the inlet section. The upper side-wall was instead derived by merging the suction side of the blade to the flow streamline extracted from the numerical simulations previously performed on the optimized blade geometry. Such streamline is depicted in Figure 2 and it can be compared to the upper-wall shape in Figure 1, where the addition of a large fillet is present at the inlet section to avoid separation.

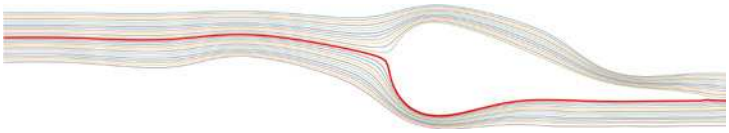

Figure 2: Flow streamline selected for sidewall design

Once the cascade and the sidewalls were defined, a 2D CFD simulation of the flow across the complete test section was carried out to investigate the obtained periodicity. The simulation was performed in design conditions and periodicity was assessed by extracting several quantities, such as entropy and Mach number, from the measuring line and verifying that the peaks of their auto-correlations where spaced by a pitch distance. The auto-correlation assessment pointed out a very good periodicity, as reported in the related plot observable in (Manfredi et al., 2022), concluding the cascade design.
In order to experimentally investigate the flow, several measuring techniques were implemented. Inlet conditions, changing over time due to the blowdown nature of the facility, are measured in a plenum upstream the test section, where the flow can be considered uniform and characterized by a very low kinetic energy. Here a flush-mounted pressure transducer and two termocouples (J and K type) are placed to measure respectively total pressure and temperature. Furthermore, four pressure taps (dark and light blue dots in Figure 1) are inserted in both central channels. They are equispaced between the throat section and the blade trailing edge locus and allow to evaluate the pressure distribution along the expansion, to verify the in-channel periodicity and to assess the agreement with CFD simulations results.
Since one of the main scopes of this work is the direct measurement of the cascade performances through the evaluations of losses, downstream the blades a tailored insert was designed to measure both static and total pressure. The former is measured by pressure taps, equivalent to the ones located inside the two main channels. The latter, instead, is obtained by the insertion of a L-shaped total pressure probe accurately designed to achieve a satisfying resolution and sufficient stiffness to avoid unwanted bending of the stem. Each static pressure taps (of 0.3 mm diameter) is connected to a locally mounted absolute

transducer, while the total pressure probe is connected through pneumatic lines to a remote differential transducer. The need of measuring both static and total pressures is due to the inevitable generation of a bowed shock in front of the probe head, due to the supersonic incoming flow. The probe measures, therefore, a post-shock total pressure, but, coupling this information with the static pressure from the relative tap, it is possible to retrieve the pre-shock total pressure solving the balance equations across the shock wave (Manfredi et al., 2023). In order to achieve a distribution of the losses across the two main channels, 21 measuring points (machined on five different inserts) were located along the two pitches, not uniformly spaced to enhance resolution in the wakes, as can be appreciated from Figure 1, where different circle colors designate taps belonging to different inserts.
Lastly, optical visualizations are carried out through a double-passage Schlieren device that allows to observe the flow-field density gradient. This measuring technique is of paramount importance as it allows to study the complex shock pattern established during the test allowing a direct comparison with the flow field obtained through CFD simulations.

3. EXPERIMENTAL CAMPAIGN

This paper covers the first portion of the experimental campaign described in the Section 2, namely the validation of the test concept by exploring the cascade flow field through optical visualizations and static pressure measurements, focusing on the analysis of test repeatability, periodicity and consistency with CFD simulations results. Therefore, the total pressure probe was not inserted and traversed in the frame of this campaign and losses across the cascade were not measured; this is, however, the subject of upcoming tests. Before beginning the experiments carried out with MM, for which the cascade was originally designed, few preliminary tests were performed using nitrogen as working fluid. The aim of these tests, which are way faster to be executed as the plant is filled with nitrogen at ambient temperature, is to asses the experiments results repeatability and check the instrumentation and the acquisition system. Moreover, a first comparison with CFD calculations is relevant as well, since the simulations results with nitrogen in ideal gas conditions can be considered the most reliable ones. Here, we will focus on repeated test carried out with an initial inlet total pressure of 8 bar.
Starting with a repeatability analysis on two exemplary tests, in Figure 3 the signals acquired from the 8 in-channels taps are plotted as ratios between the measured static pressure and the upstream total pressure (p_{T0}), highlighting their evolution as function of p_{T0}; notice that, since the total pressure is decreasing during the test due to the emptying of the feeding reservoir, the plots have to be read from right to left. The taps are numbered from the upstream to downstream and divided between upper and lower

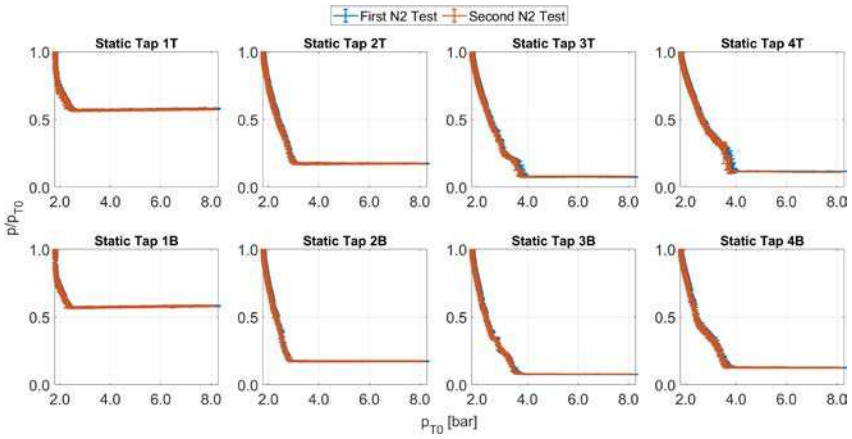

Figure 3: Nitrogen test repeatability analysis. In-channel pressure ratio p/p_{T0} vs upstream total pressure p_{T0}

channel, as specified in Figure 1. As can be clearly appreciated, the two tests generate overlapped results at every measuring point, ensuring an excellent experiment repeatability. In addition, the plots show a perfectly flat trend during the test, which is expected when using nitrogen, since outlet Mach and

therefore pressure ratios are only function of the area ratio and the specific heat ratio γ, which is constant for a perfect gas. The steep pressure ratio slope at low values of p_{T0} represents the final portion of the test when the downstream backpressure approaches the upstream total pressure, producing a series of normal shocks entering the cascade channels. Figure 4 illustrates a comparison between the expected flow field obtained from CFD simulation, represented though a contour of the density gradient, and the actual flow field extracted from the Schlieren visualization at the timestep corresponding to p_{T0} = 7 bar. The simulation was performed with a 2D domain, representative of the blade midspan flow field, and the

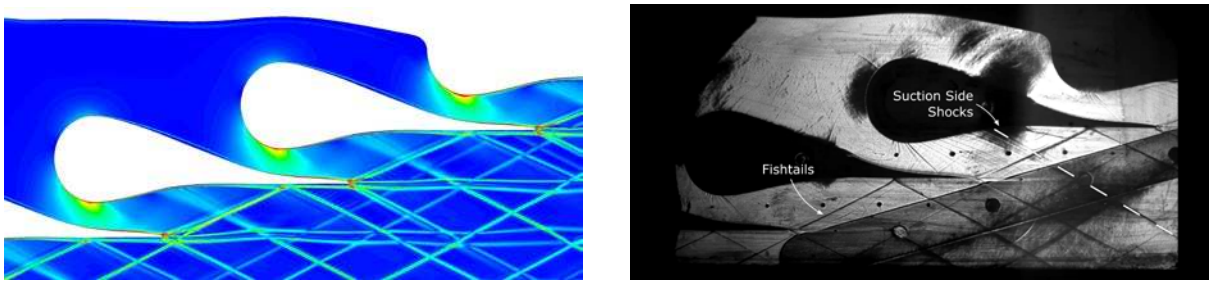

(a) CFD simulation - Density gradient contour **(b)** Schlieren visualization of the flow field

Figure 4: Flow field comparison between CFD simulation and Schlieren visualization with p_{T0} = 7 bar

mesh was defined through Ansys ICEM, creating a multi-block structured grid featuring approximately 345k cells and a dense o-grid region around the blades and the sidewalls to reach $y^+ \leq 1$, so to achieve a near-wall boundary layer resolution in combination to the selected k-ω SST turbulence model. Due to the nature of the experiment, the level of inflow turbulence was set as low as 1%. The influence of this value on the simulations results, however, is extremely limited, as the Reynolds number is around 10 million, making the flow fully turbulent from the beginning of the blowdown process. Moreover, a no slip boundary condition was imposed to all the walls, which were treated as perfectly smooth without specifying a level of roughness. This is justified by the fact that the endwalls have an irrelevant value of R_a, as the front wall is made of quartz glass, while a lapping process is required on the back wall to achieve a reflection of the light source needed for Schlieren visualizations. Blades and sidewalls are, instead, characterized by a maximum R_a of 0.2 μm, whose only influence would be on the evaluation of the total pressure losses, which is not addressed in the current experiments. The illustrated flow field is characterized by a complex pattern of shocks distinguishable into two main types, namely the blades fishtails originating from the trailing edges and the oblique shocks starting from the suction side of each blade in the region between pressure taps 2 and 3, where the profile curvature changes concavity. Then, since the flow is constrained by either blades or sidewalls, the shocks are reflected and interfere with each other, creating the displayed structures. The comparison between the CFD and the experimental

358

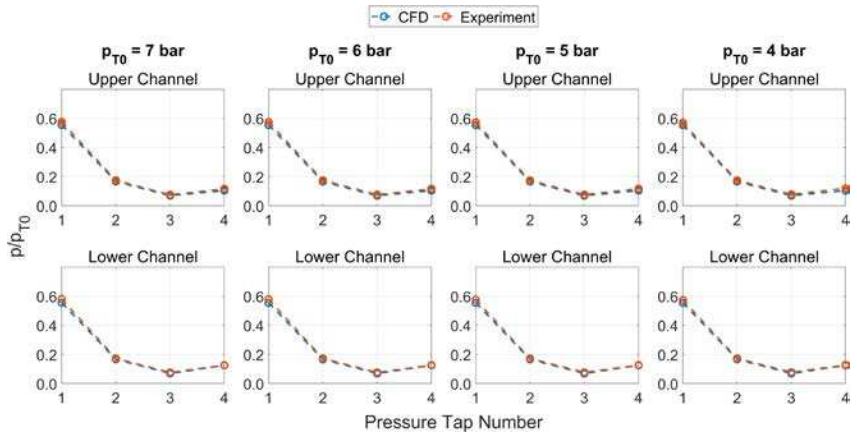

Figure 5: In-channel pressure ratio comparison with CFD - N2 tests

flow field shows an excellent agreement as both the blades fishtails opening angles and the slope of the shockwaves originating from the suction sides are concerned, while small disagreement is present on the reflected shocks, possibly due to a non-perfect numerical prediction of the boundary layer development. This qualitative analysis is confirmed by Figure 5, where the pressure ratios of the in-channel signals are compared to the same quantity extracted from CFD simulation at different values of p_{T0}, always reporting and excellent agreement. It is relevant to underline that, even if a careful assessment of the measurements uncertainties was carried out through the calibration of the instrumentation, the error bars are not reported here, as their amplitude would not be clearly appreciable. However, as an order of magnitude, the value of the error of the pressure ratios is always below 0.6%.

After these encouraging results obtained with nitrogen, a set of experiments using MM as working fluid was carried out. Here, in addition to tests where only the in-channel pressures were measured assessing the cascade periodicity and the test repeatability, experiments were also carried out acquiring the static pressures along the downstream measuring line and specifically at the four positions marked with yellow circles in Figure 1. As far as the thermodynamic conditions are concerned, the initial upstream total pressure was fixed at 13 bar, with a total temperature of 235°C, reaching $Z_{T0} = 0.65$ and a value of the fundamental derivative of gas dynamics of $\Gamma = 0.619$. Focusing on the experiments carried out acquiring

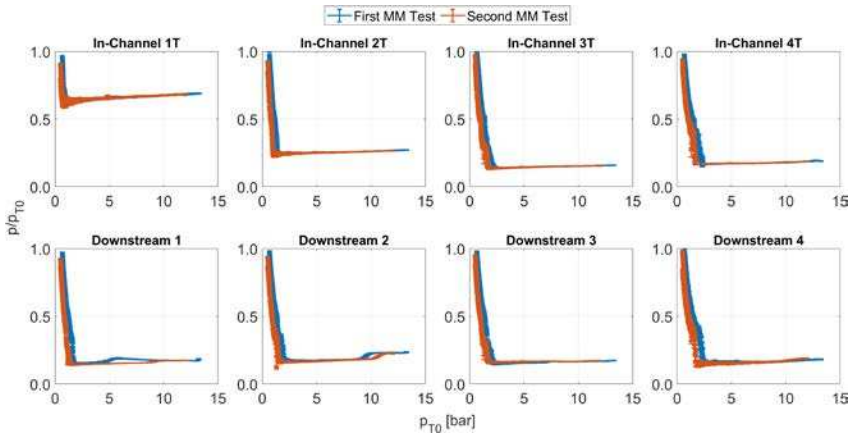

Figure 6: MM test repeatability analysis - Upper blade channel and downstream measuring line

also the downstream pressures, Figure 6 shows, for two exemplary test repetitions, the pressure ratio distribution as function of the upstream p_{T0} along the upper channel taps and the four measuring points downstream the cascade, numbered, with reference to Figure 1, from bottom to top. It can be easily appreciated that also with MM as working fluid, a very good repeatability is attained, especially within the blade channels and in the third and fourth downstream measurement points. The pressure ratios are, correctly, no more constant throughout the blowdown process, since, in non-ideal conditions, the Mach number is also a function of the stagnation conditions and increases as the test proceeds, resulting in a progressive reduction of the fishtail slope and a decreasing trend of p/p_{T0}. The variation from this trend that can be spotted in the first two downstream measuring points (Downstream 1 and 2 in Figure 6), is motivated by the presence of several shockwaves that, after being reflected by the lower sidewall, lie near the pressure taps, increasing the acquired pressure. Along the process p_{T0} decreases and the fishtails angles are reduced, therefore the shocks moves away from the tap location, which suddenly detects a pressure reduction. Such evolution of the flow field can be observed in Figures 7a and 7b, where two frames from the Schlieren visulizations when $p_{T0} = 10$ bar and $p_{T0} = 4$ bar are reported. The four pressure taps downstream the cascade are highlighted in yellow, while white dashed lines are superimposed over two shock reflections to better depict the flow field differences in two distinct moments of the experiment and the effect of the shockwaves on the pressures acquired by the measuring points closer to the lower sidewall. This phenomenon explains the peculiar trends reported in Figure 6, and also indicates a non perfect repeatability, as the specific shock pattern and boundary layer evolution are highly sensitive to operating conditions. Nonetheless, the experimental data show a very good agreement with CFD

359

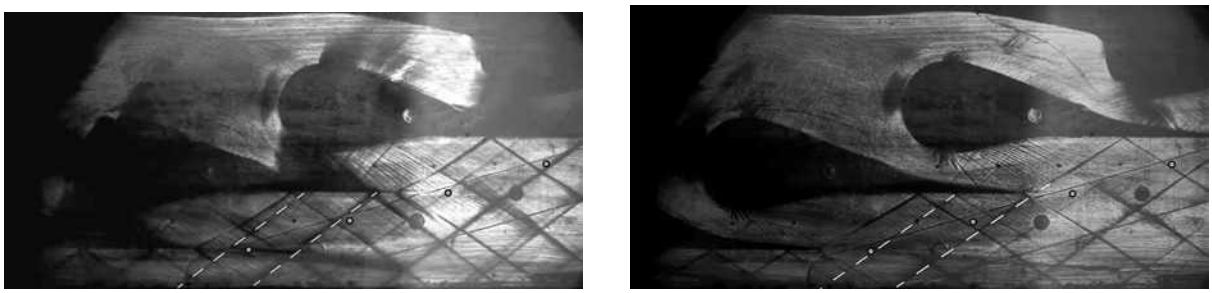

(a) p_{T0} = 10 bar **(b)** p_{T0} = 4 bar

Figure 7: Schlieren visulizations of the flow field with MM

simulation results. The latter were, as for nitrogen tests, performed through a 2D analysis representative of the midspan section, implementing, via Look-up Tables, state-of-the-art model for MM (Thol et al., 2016), to correctly reproduce the non-ideal thermodynamics of the gas. Figure 8 reports the comparison between the in-channel pressure ratios obtained through experiments and numerical simulations at four different upstream conditions. As can be noticed, the plots corroborate the results discussed so far,

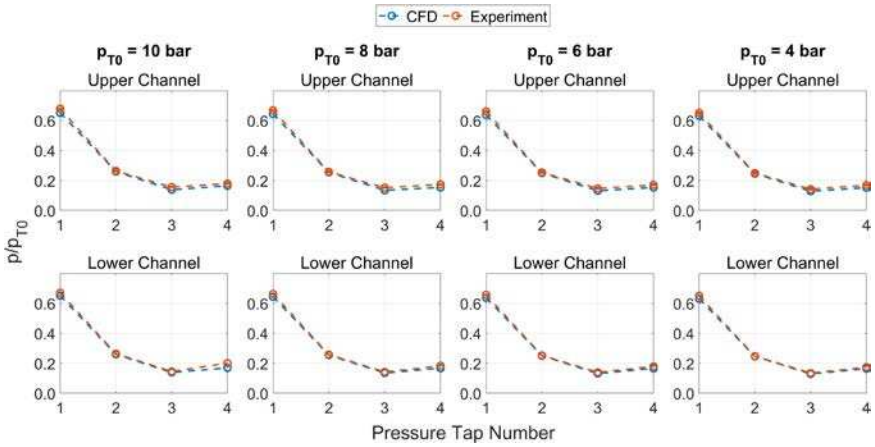

Figure 8: In-channel pressure ratio comparison with CFD - MM tests

showing a very accurate CFD prediction of the experimental data, with the only exception of the fourth pressure tap in the lower channel, that, as observable in Figure 7, is affected by the shock reflection from the lower wall at high upstream total pressures. A similar comparison is also reported in Figure 9,

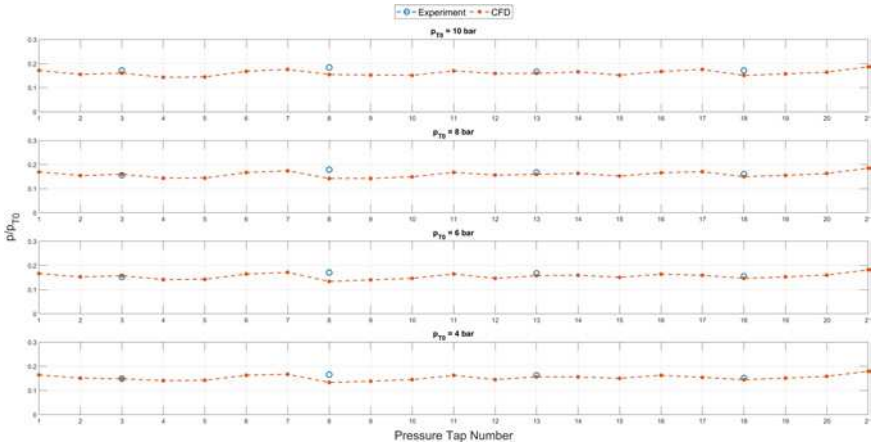

Figure 9: MM tests - Downstream line compared to CFD simulations results

where the pressures acquired in the four downstream taps are compared to the ones expected from CFD simulations.

4. CONCLUSIONS

This paper introduced the first part of an innovative experimental campaign on a supersonic turbine linear cascade for ORC applications, operating with the siloxane MM. A blowdown wind tunnel was exploited as test facility and the test section was carefully designed to include both the cascade and the measuring system. The latter was conceived to acquire the upstream total conditions, to evaluate the static pressure evolution through the blade channels and to compute the total pressure losses across the cascade measuring both downstream static and total pressures. Moreover, for a deeper investigation of the flow field, Schlieren visualizations were performed during each experiment. The design process and the test results assessment were tackled through an extensive exploitation of CFD simulations, which were mostly performed on a 2D domain representative of the midspan section, exploiting state of the art models to characterize the thermodynamics of MM. The aim of the experiments presented in the current paper was to fully characterize the flow field across the cascade, comparing experimental data with CFD simulations results, while leaving the measurement of the cascade losses to the upcoming second part of the investigation. A set of preliminary tests were performed with nitrogen, to assess the instrumentation and carry out a first analysis through experiments which are less time consuming and comparable with simulations based on the ideal gas thermodynamics. Excellent results were found in terms of test repeatability and the comparison between the measured and the CFD simulated flow field showed very good agreement, through both in-channel pressure acquisitions and density gradient visualizations. The main experiments were then carried out with MM as working fluid, exploring expansions processes characterized by initial values of Z_{T0} as low as 0.65. Outcomes similar to the nitrogen test ones were achieved, confirming the excellent test repeatability and the good prediction of the flow field through CFD simulations. One of the main issues highlighted is the effect on the downstream measured quantities of the complex shock pattern that arises from the reflection of shockwaves on the lower sidewall. To reduce the complexity of the flow field, some analysis are currently taking place, considering re-design of the sidewall. In conclusion, the results here reported are considered fully satisfactory and establish a solid basis on which a full campaign for cascade loss characterization is being currently built.

361

REFERENCES

David Baumgärtner, John J Otter, and Andrew PS Wheeler. The effect of isentropic exponent on transonic turbine performance. *Journal of Turbomachinery*, 142(8), 2020.

Piero Colonna, Emiliano Casati, Carsten Trapp, Tiemo Mathijssen, Jaakko Larjola, Teemu Turunen-Saaresti, and Antti Uusitalo. Organic Rankine Cycle Power Systems: From the Concept to Current Technology, Applications, and an Outlook to the Future. *Journal of Engineering for Gas Turbines and Power*, 137(10), 10 2015.

Camilla Conti, Andrea Spinelli, Giorgia Cammi, Marta Zocca, Fabio Cozzi, and Alberto Guardone. Schlieren visualizations of non-ideal compressible fluid flows. 13th International Conference on Heat Transfer, Fluid Mechanics and Thermodynamics. Portoroz, Slovenia, Jul 2017.

Ennio Macchi. Theoretical basis of the organic Rankine cycle. In *Organic Rankine Cycle (ORC) Power Systems*. Woodhead Publishing, Jan 2017.

Marco Manfredi, Giacomo Persico, Andrea Spinelli, Paolo Gaetani, and Vincenzo Dossena. Loss measurement strategy in ORC supersonic blade cascades. In *Proceedings of the* 4^{th} *international seminar on non-ideal compressible fluid dynamics for propulsion and power - NICFD 2022*, ERCOFTAC Series. Springer, 2022.

Marco Manfredi, Giacomo Persico, Andrea Spinelli, Paolo Gaetani, and Vincenzo Dossena. Design and commissioning of experiments for supersonic ORC nozzles in linear cascade configuration. *Applied Thermal Engineering*, 224, 2023.

Giacomo Persico, Pablo Rodriguez-Fernandez, and Alessandro Romei. High-Fidelity Shape Optimization of Non-Conventional Turbomachinery by Surrogate Evolutionary Strategies. *Journal of Turbo-*

machinery, 141(8), 04 2019.

Felix Reinker, Robert Wagner, Leander Hake, and Stefan aus der Wiesche. High subsonic flow of an organic vapor past a circular cylinder. *Experiments in Fluids*, 62(3):54, March 2021.

Alessandro Romei, Davide Vimercati, Giacomo Persico, and Alberto Guardone. Non-ideal compressible flows in supersonic turbine cascades. *Journal of Fluid Mechanics*, 882:A12, 2020.

Andrea Spinelli, Matteo Pini, Vincenzo Dossena, Paolo Gaetani, and Francesco Casella. Design, Simulation, and Construction of a Test Rig for Organic Vapors. *Journal of Engineering for Gas Turbines and Power*, 135(4), 03 2013.

Monika Thol, Frithjof H Dubberke, Gabor Rutkai, Thorsten Windmann, Andreas Köster, Roland Span, and Jadran Vrabec. Fundamental equation of state correlation for hexamethyldisiloxane based on experimental and molecular simulation data. *Fluid Phase Equilibria*, 418:133–151, 2016.

Marta Zocca, Alberto Guardone, Giorgia Cammi, Fabio Cozzi, and Andrea Spinelli. Experimental observation of oblique shock waves in steady non-ideal flows. *Experiments in Fluids*, 60, 05 2019.

ORC SEVILLE 2023
7th International Seminar on O.R.C. Power Systems

© 2024 Editorial Universidad de Sevilla. Este es un artículo de acceso abierto distribuido bajo los términos de la licencia de uso y distribución Creative Commons (BY-NC-ND 4.0)

DOI: https://dx.doi.org/10.12795/9788447227457_59
Paper ID #59, page 1 of 10

Numerical Analysis of Aerodynamics and Performance of a Radial-Inflow Micro-ORC Turbine

Fatemeh Ardaneh[1,2*], Marta Zocca[1], Antti Uusitalo[1], Teemu Turunen-Saaresti[1]

[1] *LUT University, School of Energy Systems, P.O. Box 20, 53851 Lappeenranta, Finland*
[2] *Turku University of Applied Sciences, Computational Engineering and Analysis Research Group, Engineering and Business, Technology Industry, Joukahaisenkatu 3, 20520 Turku, Finland*

* Corresponding Author: Fatemeh.Ardaneh@lut.fi

ABSTRACT

Organic Rankine Cycle (ORC) has proven to be an effective way to recover waste heat. The performance of ORC systems is profoundly affected by turbine selection, which is one of the most critical components. In this study, a numerical aerodynamic analysis of a micro-ORC turbine is carried out as an effort towards the formulation of a reduced order model (ROM) of the turbine for the dynamic simulation of the complete ORC system. The studied turbine is the radial-inflow turbine of the waste heat recovery micro-ORC test rig at the Laboratory of Fluid Dynamics, LUT University. The performance of the turbine, which features a highly supersonic flow at the stator outlet, is evaluated through steady-state CFD simulations of the complete turbine geometry using linear siloxane MDM (Octamethyltrisiloxane $C_8H_{24}O_2Si_3$) as working fluid. Results are discussed and compared with experimental data. Turbine efficiency is studied numerically at varying rotational speeds (25000-31000 rpm). A significant fluctuation in the flow angle at the stator is observed at low rotational speeds, while it decreases at higher speeds. At increasing rotational speed, the analysis shows a corresponding increase in the discharged flow rate, and the turbine efficiency up to 0.2061 kg/s and 79.3, respectively. Moreover, the flow features through the turbine nozzle ring and rotor blades are examined and discussed for selected operating conditions.

1. INTRODUCTION

Organic Rankine cycle (ORC) power systems with low capacity and high temperature are increasingly investigated due to the potential for large markets for distributed renewable energy conversions and mobile/stationary heat recovery (Colonna et al., 2015). As rotary volumetric machines are limited in their maximum pressure ratio, a kinetic type of turbines are often favored for reaching high conversion efficiency and high expansion ratios, that are required especially in high temperature ORC applications (Zhao et al., 2019). Radial-inflow turbine can be considered as a feasible choice because of its compactness, high power density, and high flow coefficient. High expansion efficiency, on the other hand, is particularly challenging (De Servi et al., 2019). In order to achieve high expansion efficiency, machines must have a supersonic radial stator and a normal radial-inflow rotor, both of which are difficult to design because of their small size and significant real gas effects along the expansion (Colonna et al., 2006).

Both numerical and experimental methods have been used in various publications to investigate ORC turbine geometry, performance, real gas effects, and flow characteristics. Design and experimental study of ORC and radial turbines to improve efficiency are always an interesting subject for researchers. The study by Weiß et al. (2018) examined two micro-turbines for small ORC plants, an axial impulse turbine and a radial cantilever. This study shows that these turbines are efficient expanders for ORC plants. However, the radial cantilever is generally more efficient than the axial impulse equivalent. Also, the working fluid selection greatly affects the thermodynamics, performance, and size of the ORC machinery (Wang et al., 2011). The design and performance prediction of supersonic radial vanes that are used

in small-scale ORC turbines for high temperatures was conducted using numerical methods in recent works related to high-temperature small-scale radial-inflow ORC turbines (Li et al., 2022). A CFD simulation by Fiaschi et al. (2016), was used to develop the geometry design of radial ORC expanders from a 0D into a 3D design. In this study, the results of these two approaches were found to be in agreement.

Based on the literature review of radial-inflow micro-ORC turbines, most of the research efforts have been concentrated on designing the turbine and finding more efficient working fluids. There is a lack of discussion and analysis of detailed turbine flow characteristics, mainly, flow angle fluctuations, in both components (rotor and stator). It is also less discussed when it comes to loss issues. Regarding these discussions, there are only a few studies where small-scale and high-expansion-ratio ORC turbines are investigated experimentally. This study addresses this opening issue for the radial-inflow turbine of the waste heat recovery micro-ORC test rig at the Laboratory of Fluid Dynamics, LUT University. This study compares experimental results with steady-state numerical simulations of the introduced turbine. The investigated conditions were selected based on the available experimental data with four different rotational speeds. In addition, the simulations are carried out at the turbine design condition. The difference between numerical and experimental data is investigated with focus on the details of the flow characteristics at different rotational speeds (and pressure ratio) and their effect on the performance of the micro-ORC turbine. The micro-ORC test facility utilizes high-temperature exhaust gas heat of the diesel generator and the working fluid is siloxane MDM (Octamethyltrisiloxane $C_8H_{24}O_2Si_3$) (Turunen-Saaresti et al., 2017).

It should be noted that previous research has been done already with the experimental setup in recent years. By analyzing the preliminary radial turbine design calculations, Uusitalo et al. (2013) found that larger turbine wheels with higher outlet blade heights and lower rotational speed can be designed with molecularly complex fluids, which can be beneficial for small-scale ORC units. Uusitalo et al. (2014) designed a small-scale ORC turbine stator for the experimental radial turbine. This supersonic design took into account flow characteristics and shock waves through convergent-divergent nozzles. In addition, a CFD analysis on the magnitude of expansion losses and their effect on the performance of radial turbines is presented by Uusitalo and Zocca (2023).

364

2. METHODOLOGY

The experimental setup and CFD model are introduced. Also, the case study is presented to discuss the reason for choosing the numerical model presented in the result section. In the current work, the average of the experimental data at each rotational speed is calculated and compared with the steady-state numerical simulations. To compare in detail, the results of pressure, Mach number, relative velocity, and flow angle are investigated for both stator and rotor components. The investigated flow angles are the angle of absolute and relative velocity, shown in Figure 1.

2.1 Description of the experimental setup

The experimental data have been obtained from the micro-ORC test setup at LUT. The experimental ORC system recovers high temperature exhaust gas heat from a 150-200 kW scale diesel engine. The ORC is equipped with a supersonic radial turbine, permanent magnet generator, and a partial admission type of feed pump assembled on the same shaft with a nominal rotational speed of 31 000 rpm. The turbogenerator is hermetically sealed and the bearings are lubricated by using liquid MDM. The low pressure working fluid vapor is used for generator cooling. In the experiments, the rotational speed of the turbogenerator can be controlled via a frequency converter, which allows to adjust the turbine operation at different off-design conditions. It is worth noting that as the main feed pump of the system is assembled on the turbogenerator shaft, the rotational speed directly affects the turbine inlet pressure and working fluid mass flow rate. Several test runs have been carried out with the experimental system and the performance of the turbine has been investigated under conditions which are close to the system design conditions. In addition, the operation has been experimentally investigated at several off-design

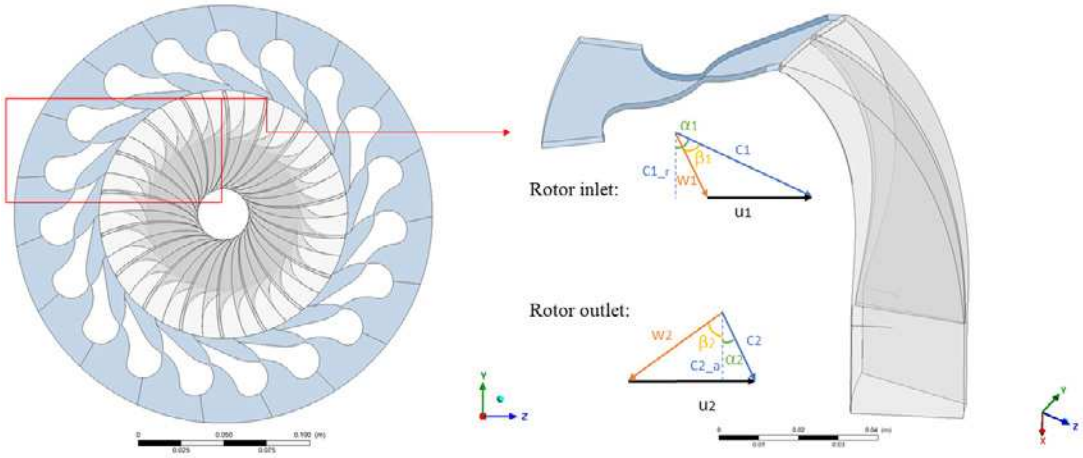

Figure 1: Top view of the LUT micro-ORC turbine (left). Geometry of the computational domain (one passage) and velocity triangles at rotor inlet and outlet (right).

Table 1: Design conditions of the LUT micro-ORC turbine (left). Reference turbine operating conditions from experimental runs (right). The conditions at 31 000 rpm are the design point.

Turbine power	12 kW
Turbine efficiency	76 %
Fluid mass flow rate	0.2 kg/s
Rotor diameter	144 mm
Blade height at the rotor inlet	2 mm
Mach number at the stator outlet	2.2
Specific speed, Flow coefficient	0.5, 0.4

N [rpm]	T1 [^{o}C]	p1 [bar]	T2 [^{o}C]	p2 [bar]
25298	252.3	6.515	219.9	0.094
27057	252.8	6.653	216.6	0.099
28835	255	6.713	219.2	0.098
30623	251.2	6.879	213	0.098
31000	***265***	***7.900***	-	***0.070***

365

points. The turbine measurements include the pressure and temperature measurements at the inlet and outlet, as well as mass flow measurement. The fluid thermodynamic properties, such as density and enthalpy have been defined by using the measured temperature and pressure data. The mass flow rate of MDM has been measured by using an oval gear meter, measuring the liquid working fluid flow rate entering the evaporator. The main design parameters of the investigated turbine and measured operation conditions are presented in Table 1. The experimental setup, experimental results and measurement uncertainties are discussed and analyzed in detail in Uusitalo et al. (2020).

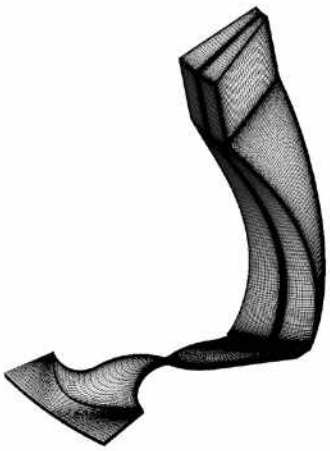

Figure 2: Numerical grid

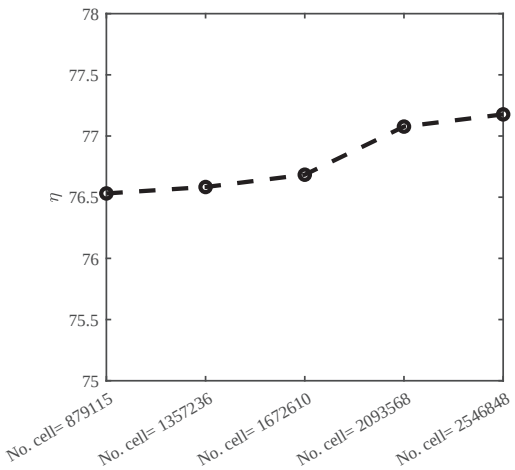

Figure 3: Grid independence study based on the turbine efficiency.

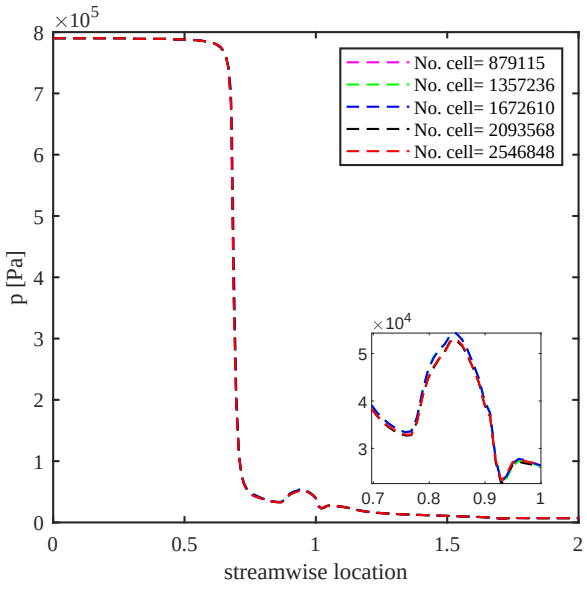

Figure 4: Grid independence study based on the area average of static pressure from inlet to outlet of the turbine. Streamwise locations 0-1 represent the stator. Streamwise locations 1-2 represent the rotor.

2.2 Computational Fluid Dynamic analysis methods

Simulations were performed using Ansys CFX, and structured grids were generated using Pointwise. An exemplary grid is shown in Figure 2. A finite-volume-based method for the solution of the RANS equations using the k–ω SST turbulence model (Menter, 1993; Menter et al., 2003) is used in steady-state simulations. Simulations were conducted using a stator flow channel and a rotor flow channel modeled with periodic boundary conditions, representing blade row periodicity. Both the frozen-rotor and the mixing-plane approaches (ANSYS, 2019) were used to model the interface between the stator and the rotor, namely the non-rotating domain and the rotating domain. As the boundary conditions for the simulations, temperature and pressure were set as the inlet conditions, and the outlet boundary condition was static pressure. The boundary conditions applied in the CFD simulations are reported in Table 1 for all the studied operating points. Convergence residuals and simulated mass imbalance were used to monitor the convergence of the simulations.

366

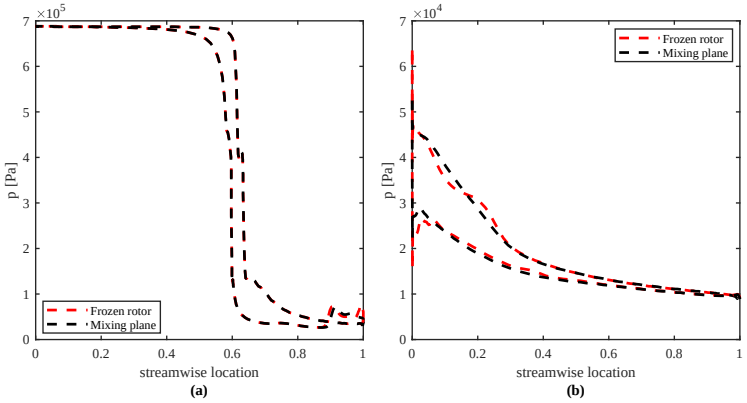

Figure 5: Comparison of frozen rotor and mixing plane model. Turbine blade loading (Span=0.5) at N=30624rpm. (a) Stator, (b) Rotor.

Table 2: Grid independence study. The grid of case 4 is the one used throughout the numerical study.

Case No.	Number of cells	η	Deviation of η with respect to case 4 (%)
1	879115	76.5	0.71
2	1357236	76.5	0.64
3	1672610	76.6	0.51
4	2093568	77.0	-
5	2546848	77.1	-0.13

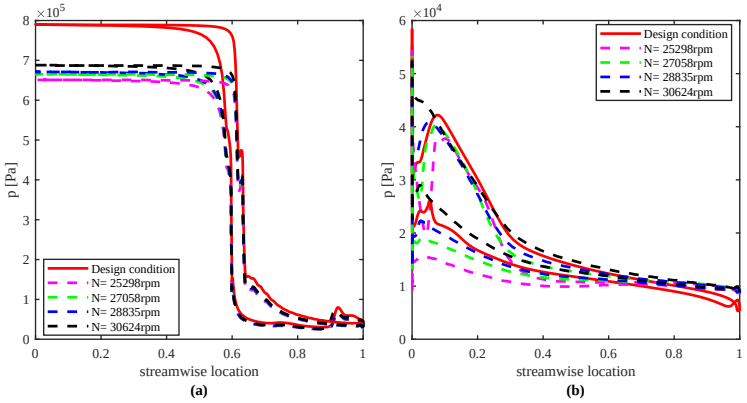

Figure 6: Turbine blade loading (Span=0.5). (a) Stator, (b) Rotor

A grid independence study was performed for the turbine in design conditions using the frozen rotor model and five grid resolutions. Results are presented in Figure 3, 4 and in Table 2. Generally, the results of all cases are similar with high accuracy, but the most significant differences in the flow structure are occurring at the stator trailing edge, where shock waves are present. As it can be seen from Figure 4, such differences are observed up to the grid resolution of case 4, since results of case 4 and 5 overlap. The grid resolution of case 4 with fewer cells is selected for the rest of the simulations. The overall efficiency of the turbine obtained in each case is presented in Table 2. CFD simulations are performed using both the frozen rotor and the mixing plane models in the stator-rotor interface in order to compare the results between these two approaches. In this section, an example of the results of these models at rotational speed equal to 30624 rpm is presented. Figure 5a-b shows the turbine blade loading on both stator and rotor components. The results of these simulations demonstrate the similarity between the two models. Due to this result, the grid study done with the frozen rotor model can be considered acceptable for the mixing plane model. In addition, it is sufficient to analyze the results of one model. Consequently, the results of section 3 are limited to the mixing plane model.

367

3. RESULTS AND DISCUSSIONS

The turbine stator and rotor blade loading are presented in Figure 6a-b. Pressure and Mach number from stator inlet to rotor outlet are presented in Figure 7a-b. The trends of pressure and Mach number along the expansion are similar in all the studied operating conditions, as shown in Figures 6 and 7 . The pressure decreases and the Mach number increases rapidly near the throat section of the stator. The most notable differences between the different cases occur near the stator outlet, which is the flow area where shock waves are present. This difference can be observed in the divergent section of the stator nozzle, as shown in Figure 6a. Note that the streamwise location on the figure is the dimensionless distance from the inlet to the outlet. In addition, there are some differences in the rotor pressures and Mach numbers between the cases, as are shown in Figure 6b and 7b. The pressure is lower when rotational speed is lower, however the design rotational speed seems to be exception. It is worth noting that the rotor outlet Mach number is significantly higher in the design condition when compared to the other cases. This is mainly because a lower turbine outlet pressure was used in the turbine design, when compared to the

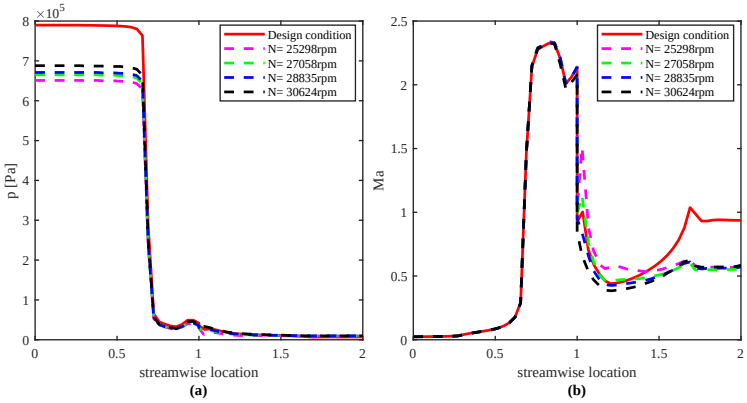

Figure 7: Area average of (a) pressure and (b) Mach number from inlet to outlet of the turbine. Streamwise locations 0-1 represent the stator. Streamwise locations 1-2 represent the rotor.

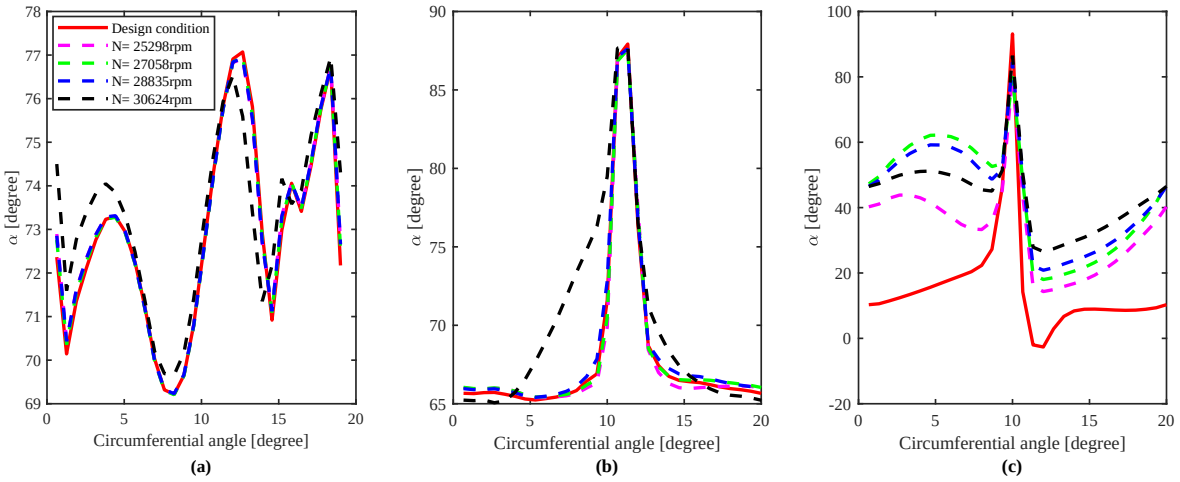

Figure 8: Flow angle distribution at: (a) Stator trailing edge(Span=0.5, streamwise=0.947), (b) Rotor leading edge(Span=0.5, streamwise=1), (c) Rotor trailing edge (Span=0.5, streamwise=1.72).

turbine outlet pressure reached in the experiments. This leads to higher density and lower velocities in the simulation cases that are based on the experimentally defined values. The flow angle at the stator outlet was investigated, and the results are presented in Figure 8a, as it has significant effect on the rotor inlet flow angle which is affected by the shock wave pattern at the stator outlet. There are higher fluctuations of the flow angle at lower rotational speeds with respect to the higher speeds. This non-uniform flow can lead to increased losses in off-design conditions. As it is expected and shown in Figure 8a, based on the non-uniform flow at the stator outlet, shock waves occur before the flow passes through the rotor. Because of the use of the mixing plane approach (ANSYS, 2019), the shock waves are not affecting the flow angle at the rotor inlet and the pattern of rotor inlet flow angle is generally similar for all the cases, as shown in Figure 8b. Table 3 presents the average value of the flow angle at the inlet and outlet of the rotor. From Figure 8c and Table 3, it can be observed that the averaged absolute flow angle of rotor is not significantly changing between the different cases. It can also be observed that the flow angle at rotor discharge is relatively high, which has an impact on the turbine efficiency as fully axial discharge flow typically maximizes the efficiency of a radial turbine. The high flow angle at the rotor discharge is mainly explained by the high turbine outlet pressure, as well as by the changes in the rotational speed. Figure 9a-b display the streamlines coloured by magnitude of relative velocity at the rotor for 25.3 krpm and 30.6 krpm cases. The Mach number distribution is shown for the same

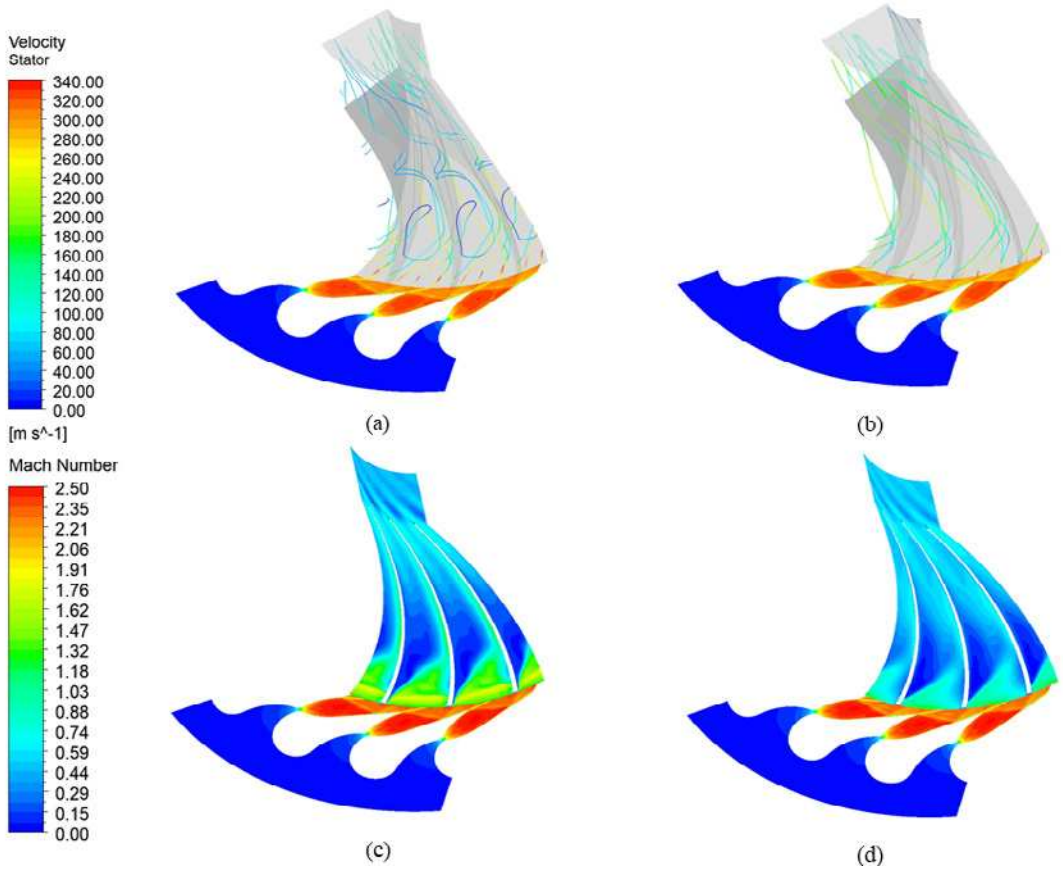

Figure 9: Streamlines coloured by velocity magnitude and Mach number contours in turbine at two different rotational speed: (a) Relative velocity at N=25298rpm, (b) Relative velocity at N=30624rpm, (c) Mach number at N=25298rpm, (d) Mach number at N=30624rpm.

369

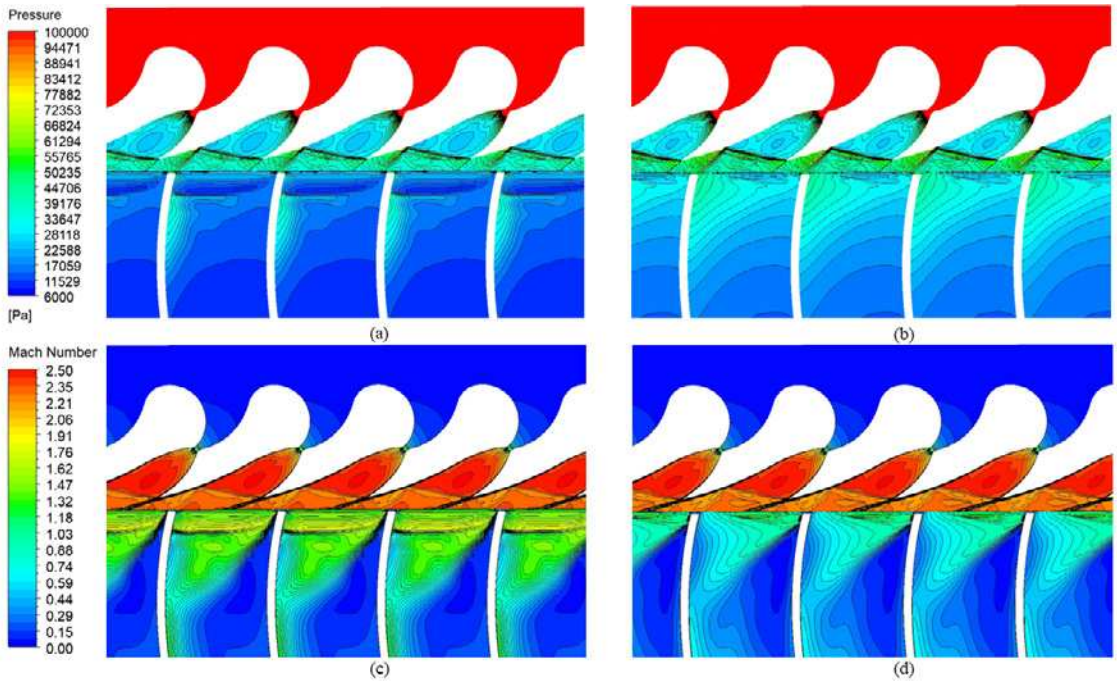

Figure 10: Pressure and Mach number contours in the turbine at two different rotational speeds: (a) Pressure distribution at N=25298rpm, (b) Pressure distribution at N=30624rpm, (c) Mach number at N=25298rpm, (d) Mach number at N=30624rpm.

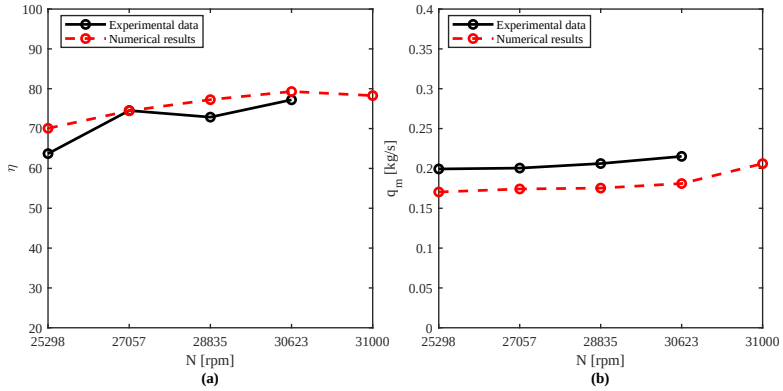

Figure 11: Turbine performance at varying rotational speed: (a) Efficiency, (b) Mass flow rate.

cases in Figure 9c-d. A clear flow separation region can be observed with the case having the lowest rotational speed near the rotor leading edge, whereas a clear flow separation region cannot be observed with the higher rotational speed. This can be explained by the increased incidence with lower rotational speeds, causing flow separation in the rotor and reducing efficiency. A non-uniform flow pattern can be observed in Figure 9c-d at the stator outlet and rotor inlet section caused mainly by the shock waves. More detailed pressure and Mach number distributions at the stator and at the rotor inlet section are shown in Figure 10a-d. Figure 10a-b present the pressure contours in the stator and at the leading edge of the rotor blade. The pressure contours at two different rotational speeds, at the interface between these two components, does not have significant differences. However, in the Mach number contours, the differences between the two cases are more noticeable. The flow is clearly supersonic at the rotor inlet with lower rotational speed and a shock-like pattern is seen, as shown in Figure 10c-d.

Table 3: Turbine power and flow angle of absolute velocity at rotor inlet and outlet

N [rpm]	$\alpha 1$ [degree]	$\alpha 2$ [degree]	P [W]
25298	70.9	36.7	7981
27057	70.8	39.7	8582
28835	70.8	40.5	9071
30623	72.1	42.5	9489
31000	***70.6***	***16.5***	***12034***

Table 4: Total efficiency and mass flow rate of the turbine and their difference with respect to the experimental data.

N [rpm]	Exp. η	CFD η	Δ (%)	Exp. q_m	CFD q_m	Δ (%)
25298	63.7	70.0	9.98	0.199	0.170	-14.5
27057	74.5	74.4	-0.08	0.200	0.174	-13.07
28835	72.8	77.2	6.02	0.206	0.175	-14.94
30623	77.2	79.3	2.70	0.215	0.181	-15.85
31000	-	***78.3***	-	-	***0.2061***	-

Figure 11 and Table 4 present the performance of the turbine as resulting from experiments and numerical simulations. The difference of numerical results with respect to the experimental data is also shown in Table 4. Numerical results generally follow the experimentally defined turbine efficiency trend and the efficiency is reduced as the rotational speed is reduced. As it is shown in Figure 11a, there is a decrease in efficiency measured at rotational speed of 28835 rpm while it was not observed in numerical results. It is expected that this is caused by the uncertainty of experimental data. Uncertainties and fluctuations related to the experimental system are discussed more in detail in Uusitalo et al. (2020). Because the temperature drop over the turbine is rather small with MDM, despite the high expansion ratio, even a small deviation in outlet temperature can have a significant effect on the results. Another reason for the difference between the numerical and experimental results is the use of the average of the measurement data at each rotational speed range. The difference between the numerical results and the measurements is more noticeable on the mass flow rate than on the efficiency, as shown in Figure 11b. In addition to measurement uncertainties, the high pressure difference between the inlet and outlet of the stator might lead to some leakage over the stator blade in the experiments, which can partly explain the difference between the measured and simulated mass flows. This is not considered in the numerical simulation, as

in the simulations the flow is only going through the stator throat. In the design condition, even though the mass flow rate is higher than the other rotational speeds, the efficiency is lower than at the rotational speed of 30623 rpm. This is mainly due to the fact that at the turbine design conditions, the turbine expansion ratio is greater than in the experimentally investigated operating conditions, which increases the flow velocities and expansion losses, thus reducing efficiency. As the inlet pressure is higher in design conditions, the fluid has higher density at the stator throat, resulting in a higher mass flow rate.

4. CONCLUSIONS

Four different operating conditions were used to evaluate the performance of a radial-inflow micro-ORC turbine using MDM as the working fluid. Numerical simulations were used to analyze the turbine's flow characteristics and performance. The simulation results were compared to experimental measurements. In general, the numerical results and the experimental results have acceptable agreement, predicting similar trends for both the efficiency and the mass flow rate at different operating conditions. At low rotational speeds, significant fluctuations in the flow angle at the stator outlet were observed and a clear flow separation region was predicted to occur in the rotor, due to the high incidence angle at the rotor leading edge. At higher rotational speeds, the mass flow rate, power output and efficiency were increased. In addition, the flow fluctuations at the stator outlet were reduced. It was also observed that the numerical simulations had some deviations in the mass flow rate when compared to measured values. These deviations can be caused for example by leakage flow over the stator blade or by manufacturing tolerances in the stator throat. As a future work, the experimental setup will be updated to provide more detailed measurements of the turbine and to reduce uncertainties related to the measured values. In addition, shock wave stator-rotor interactions could be further investigated with unsteady simulation in the future.

NOMENCLATURE

c	Absolute flow velocity	(m/s)
c_a	Axial component of the absolute velocity	(m/s)
c_r	Radial component of the absolute velocity	(m/s)
Ma	Mach number	(-)
N	Rotational speed	(rpm)
P	Power	(W)
p	Pressure	(Pa, bar)
q_m	Mass flow rate	(kg/s)
T	Temperature	(^{o}C)
w	Relative velocity	(m/s)
α	Flow angle	(degree)
β	Relative flow angle	(degree)
Δ	Deviation with respect to experimental results	(%)
η	Efficiency	(-)
Subscript		
1	Inlet	
2	Outlet	

371

REFERENCES

ANSYS, I. (2019). Cfx-solver theory guide r19. 2.

Colonna, P., Casati, E., Trapp, C., Mathijssen, T., Larjola, J., Turunen-Saaresti, T., and Uusitalo, A. (2015). Organic Rankine Cycle Power Systems: From the Concept to Current Technology, Applications, and an Outlook to the Future. *Journal of Engineering for Gas Turbines and Power*, 137(10). 100801.

Colonna, P., Nannan, N., Guardone, A., and Lemmon, E. (2006). Multiparameter equations of state for selected siloxanes. *Fluid Phase Equilibria*, 244(2):193–211.

De Servi, C. M., Burigana, M., Pini, M., and Colonna, P. (2019). Design Method and Performance Prediction for Radial-Inflow Turbines of High-Temperature Mini-Organic Rankine Cycle Power Systems. *Journal of Engineering for Gas Turbines and Power*, 141(9). 091021.

Fiaschi, D., Innocenti, G., Manfrida, G., and Maraschiello, F. (2016). Design of micro radial turboexpanders for orc power cycles: From 0d to 3d. *Applied Thermal Engineering*, 99:402–410.

Li, C., Guo, Z., Guo, H., Bao, X., and Zhou, L. (2022). Influences of main design parameters on the aerodynamic performance of a micro-radial inflow turbine. *AIP Advances*, 12(10):105012.

Menter, F. R. (1993). Zonal two equation kw turbulence models for aerodynamic flows. In *23rd fluid dynamics, plasmadynamics*.

Menter, F. R., Kuntz, M., and Langtry, R. (2003). Ten years of industrial experience with the sst turbulence model. *Turbulence, heat and mass transfer*, 4(1):625–632.

Turunen-Saaresti, T., Uusitalo, A., and Honkatukia, J. (2017). Design and testing of high temperature micro-orc test stand using siloxane as working fluid. In *Journal of Physics: Conference Series*, volume 821, page 012024. IOP Publishing.

Uusitalo, A., Turunen-Saaresti, T., Guardone, A., and Grönman, A. (2014). Design and flow analysis of a supersonic small scale orc turbine stator with high molecular complexity working fluid. In *Turbo Expo: Power for Land, Sea, and Air*, volume 45660, page V03BT26A004. American Society of Mechanical Engineers.

Uusitalo, A., Turunen-Saaresti, T., Honkatukia, J., Colonna, P., and Larjola, J. (2013). Siloxanes as Working Fluids for Mini-ORC Systems Based on High-Speed Turbogenerator Technology. *Journal of Engineering for Gas Turbines and Power*, 135(4). 042305.

Uusitalo, A., Turunen-Saaresti, T., Honkatukia, J., and Dhanasegaran, R. (2020). Experimental study of small scale and high expansion ratio orc for recovering high temperature waste heat. *Energy*, 208:118321.

Uusitalo, A. and Zocca, M. (2023). Design and numerical analysis of supersonic radial-inflow turbines for transcritical orc processes. *Energy Conversion and Management*, 277:116609.

Wang, E., Zhang, H., Fan, B., Ouyang, M., Zhao, Y., and Mu, Q. (2011). Study of working fluid selection of organic rankine cycle (orc) for engine waste heat recovery. *Energy*, 36(5):3406–3418.

Weiß, A. P., Popp, T., Müller, J., Hauer, J., Brüggemann, D., and Preißinger, M. (2018). Experimental characterization and comparison of an axial and a cantilever micro-turbine for small-scale organic rankine cycle. *Applied Thermal Engineering*, 140:235–244.

Zhao, Y., Liu, G., Li, L., Yang, Q., Tang, B., and Liu, Y. (2019). Expansion devices for organic rankine cycle (orc) using in low temperature heat recovery: A review. *Energy Conversion and Management*, 199:111944.

ORC SEVILLE 2023
7th International Seminar on O.R.C. Power Systems

© 2024 Editorial Universidad de Sevilla. Este es un artículo de acceso abierto distribuido bajo los términos de la licencia de uso y distribución Creative Commons (BY-NC-ND 4.0)

DOI: https://dx.doi.org/10.12795/9788447227457_61

ORC SYSTEM USING R1233ZD(E) FOR WASTE HEAT RECOVERY FROM THE UPSTREAM PROCESS

M.S. Chiong[1,2], N.I. Mahyon[1,2,*], B.B. Nyakuma[1], S. Rajoo[1,2], E. Alvarez-Regueiro[3], M.E. Barrera-Medrano[3], R.F. Martinez-Botas[3] and Y. Laoonual[4]

[1] *UTM LoCARtic, IVeSE, Universiti Teknologi Malaysia, Skudai, Johor, Malaysia.*
[2] *Faculty of Mechanical Engineering, Universiti Teknologi Malaysia, Skudai, Johor, Malaysia.*
[3] *Dept. of Mechanical Engineering, Imperial College London, London SW7 2BX, UK*
[4] *King Mongkut's University of Technology Thonburi (KMUTT), Bangkok 10140, Thailand*

*Corresponding Author: izwanne@utm.my

ABSTRACT

The upstream is an energy-intensive sector of the petroleum industry. Nearly one-third of the industry's energy is discharged as thermal losses via cooling systems or into the environment. Waste heat recovery (WHR) from upstream processes could significantly reduce current fossil energy's carbon footprint and competitiveness and stimulate the transition to carbon-neutral renewable energy sources by utilizing the free energy generated from WHR to support renewable energy production. In the WHR system, the working fluid selection is critical to the design, thermodynamic performance, operation practicality, and environmental impact of organic Rankine cycles (ORC). This study comparatively examined the ORC performance of six working fluids (easily accessible in Malaysia) for WHR from upstream processes using a thermodynamic model. Results showed that R1233zd(E) is a promising working fluid for WHR due to its zero Global Warming Potential (GWP). The single-loop ORC cycle using R1233zd(E) delivered 6.2% thermal efficiency at a 250°C temperature difference by maintaining an operating pressure ratio of 9:1. These conditions ensured a practical turbine expander design for mechanical work recovery. The WHR process reduced the overall carbon footprint of the upstream product by 6.2%.

1 INTRODUCTION

The upstream is one of the most energy-intensive sectors of the petroleum industry due to its significant energy demands. Various upstream processes and equipment in the industry discharge multiple grades of low (≤ 230°C), medium (230 to 650°C), and high (≥ 650°C) temperature waste heat (PBOG, 2013). The thermal losses from co-produced hot liquid, incineration, gas flares, prime movers, amine gas treaters, and natural gas compressors account for one-third of the energy consumed in the industry (EPA, 2015). According to analyses, the waste heat typically discharged into the environment or through cooling systems can be successfully recovered in the industry to significantly reduce the overall carbon footprint of current fossil fuel systems by lowering greenhouse gases (GHG), flue/exhaust emissions, fuel consumption, and operational costs. The utilization of WHR technologies (such as Electric Turbo-compounding (ETC), organic Rankine cycle (ORC), and Thermo-electric generators (TEG)) for power generation, process heat, and heat can stimulate the transition to carbon neutrality by supplying free energy to diversify the energy mix and making renewables a practical and competitive energy source.

The process of WHR using ORCs critically requires the selection of an appropriate working fluid that satisfies the cycle's thermodynamic performance, operational practicality, and environmental impact. Numerous working fluids (e.g., R1233zd(E), R245fa, R134a, and R410a) have been previously examined for application in ORC systems. The performance and efficiency of ORC systems are dependent on the unique properties of the selected working fluid. Therefore, this study aims to investigate the most suitable working fluid for the WHR application at the MTJA gas-holding area in

the Gulf of Thailand. This area covering 7,250 km² was created as an interim measure to exploit and equally share the proceeds of the natural resources in the seabed or continental shelf claimed by Malaysia and Thailand (MTJA, n.d.).

2 LITERATURE REVIEW

ORC systems are widely studied for WHR because of their ability to generate power from low to medium-temperature heat sources. The selection of the working fluid is a critical factor affecting ORC systems' performance and environmental impact. Several working fluids, such as R134a, R245fa, and R123, have been investigated. Muhammad *et al.* (2015) investigated low-grade WHR using an ORC system. The system yielded a maximum thermal efficiency of 5.75% and a maximum expander isentropic efficiency of 77.74% using R245fa. Shu *et al.* (2016) reported that R123 is better suited for WHR from heavy-duty diesel engines, while R245fa is more suitable for light- and medium-duty. This observation was attributed to the difference in their thermodynamic properties and limited onboard cooling capacity. An overall 2.8% improvement in the system's thermal efficiency was achieved using R123. Hijriawan *et al.* (2022) demonstrated that a maximum improvement of 3.17% in system efficiency is achievable using R134a as the working fluid. However, hydrofluorocarbons (HFCs) and hydrochlorofluorocarbon (HCFC) working fluids have high global warming potentials (GWPs), which are subject to phase-out regulations. Table 1 compares the environmental impact and thermophysical properties of the ORC working fluids.

Table 1: Environmental impact and thermophysical properties of different ORC working fluids

Working fluid	Class	GWP	ODP	Critical temperature (°C)	Critical pressure (bar)
R123 (A-Gas, n.d.)	HCFC	77	0.0015	183.7	36.6
R245fa (Honeywell, 2013b)	HFC	1,030	None	154.0	36.5
R134a (Honeywell, 2013a)	HFC	1,430	None	101.1	40.6
R410a (Honeywell, 2013c)	HFC	2,088	None	71.4	49.0
R1233zd(E) (Honeywell, 2015)	HFO	1	None	165.5	35.7
R600a (Darment, n.d.; Sinteco, 2020)	HC	3	None	135.0	36.0

GWP – Global warming potential; ODP – Ozone depletion potential; HCFC – hydrochlorofluorocarbon; HFC – hydrofluorocarbon; HFO – hydrofluoroolefin; HC – hydrocarbon.

R1233zd(E) has recently been proposed as an alternative working fluid for ORC systems due to its zero GWP and low ozone depletion potential. Several studies have demonstrated the feasibility of using R1233zd(E) in ORC systems for WHR from diesel engines and exhaust gases. Elahi *et al.* (2022) reported that R1233zd(E) showed better performance compared to R1234ze(Z), R1234ze(E), and R1234yf based on the exergy analysis of WHR using ORC. The working fluid with the higher critical temperature showed better thermal and second-law efficiencies. Rijpkema *et al.* (2021) demonstrated that 0.7% of the engine power of a heavy-duty truck could be recovered using an R1233zd(E)-operated ORC. However, Mariani *et al.* (2022) showed that an equivalent system could produce an additional 8.0% power output from a mechanical engine.

The discrepancies in thermal efficiency improvement can be due to the difference in the cycle's configuration and operating conditions. Therefore, a dedicated ORC working fluid selection study is critical for new applications. It is a relatively inexpensive analytical study that can effectively eliminate unnecessary uncertainties.

To the best of the authors' knowledge, no previous study has investigated using R1233zd(E) as a working fluid for ORC WHR from the upstream process of the petroleum industry. Therefore, this study examines the operational feasibility, thermal efficiency, and environmental impact of using R1233zd(E) in an ORC WHR system for upstream processes. In addition, its performance will be benchmarked with

other common ORC working fluids accessible in Malaysia, as given in Table 1. The T-s diagrams of the selected working fluids are shown in Figure 1.

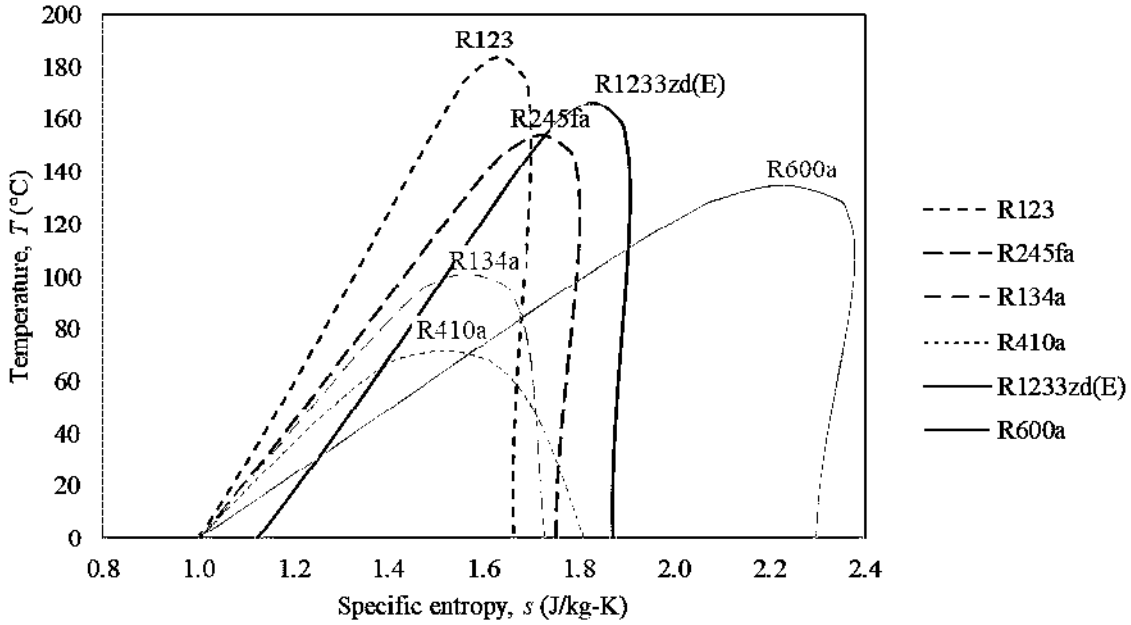

Figure 1: T-S diagram of potential ORC working fluids.

3 METHODOLOGY

The pilot-sized WHR system used in this study has a 260 kW heat source supply. As shown in Figure 2, the system consists of an ETC, ORC, and TEG. The ORC turbine inlet condition is set at 250°C and 27.0 bar (abs). A higher turbine inlet temperature associated with larger power output can simultaneously increase the cycle's thermal efficiency by enabling an economizer for internal WHR. The working fluid temperature at the condenser outlet is controlled within the range of 28.5±1.5°C due to the cooling water temperature limitation.

A thermodynamic model was developed to analyze the performance of the ORC cycle under steady-state conditions. The thermophysical properties of the working fluids were deduced from the CoolProp database (n.d.). All heat exchangers are assumed to achieve energy equilibrium and pressure drop is ranging between 3 kPa and 50 kPa. As a precautionary step, a minimum of 5°C temperature difference between fluids are maintained across all heat exchangers to avoid pinch point problem. The ORC turbine's total-static efficiency was 65%, the turbine generator efficiency was 60% and back work-to-pump efficiency was 20%, resulting in a net ORC output. The governing equations of the thermodynamic model are given as below:

Heat addition into ORC at evaporator:	$q_{in} = h_1 - h_6$	Eq. 1
Energy balance at evaporator:	$\dot{m}_{exh} c_p \left(T_{exh,in} - T_{exh,out}\right) = \dot{m}_{wf}(h_1 - h_6)$	Eq. 2
Heat rejection from ORC at condenser:	$q_{out} = h_4 - h_3$	Eq. 3
Energy balance at condenser:	$\dot{m}_{cw} c_p \left(T_{cw,in} - T_{cw,out}\right) = \dot{m}_{wf}(h_4 - h_3)$	Eq. 4
Energy balance at economizer:	$(h_6 - h_5) = (h_2 - h_3)$	Eq. 5
Pump's specific energy input (back work):	$w_{pump} = v_5(p_6 - p_5)$	Eq. 6
Gross specific work output from turbine:	$w_{turb,gross} = h_1 - h_2$	Eq. 7
Net specific work output from ORC:	$w_{out,net} = \left(w_{\text{turb},gross} \times \eta_{generator}\right) - \left(w_{pump}/\eta_{pump}\right)$	Eq. 8

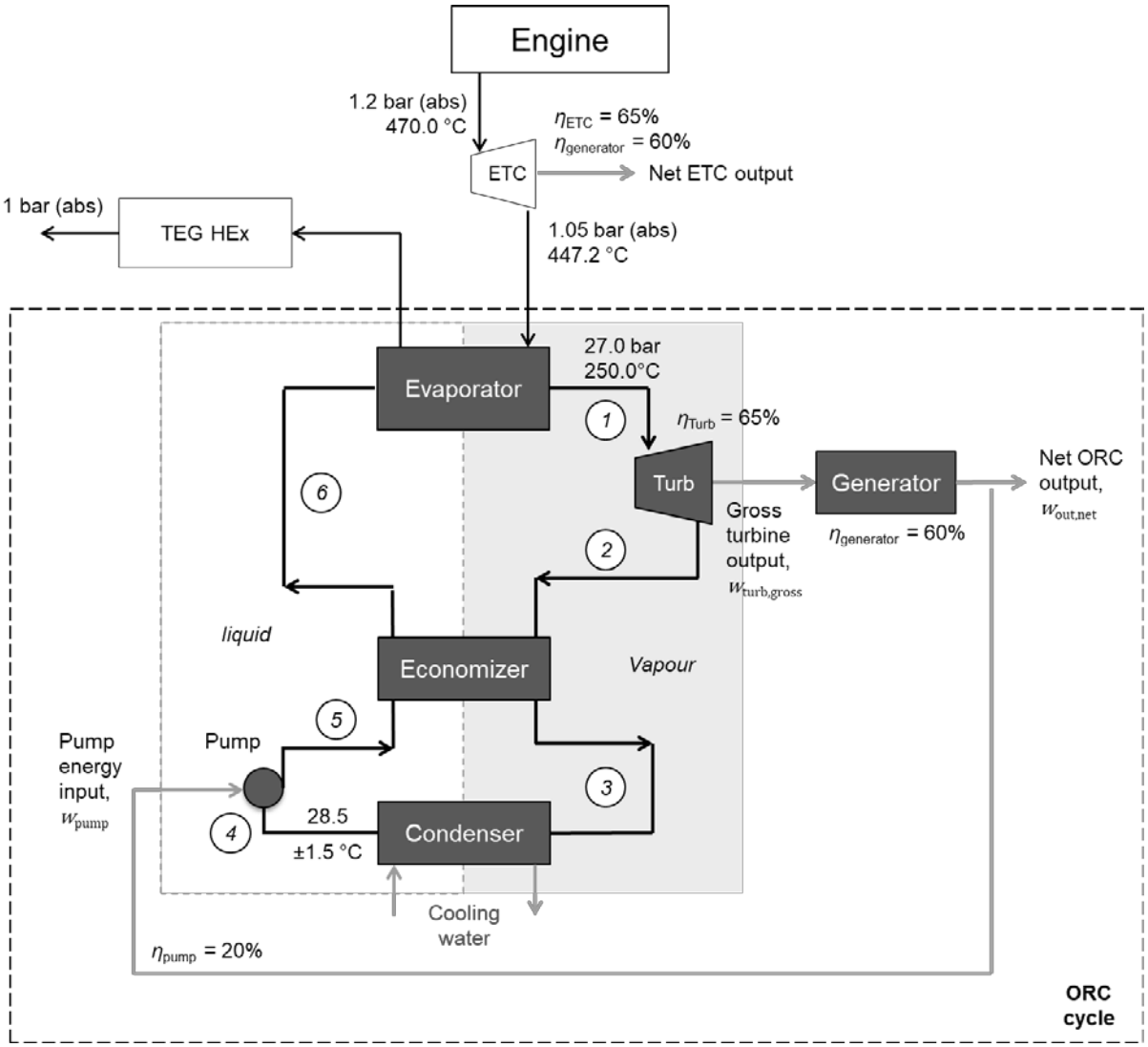

Figure 2: Schematic of the ORC cycle in the pilot-size WHR system.

Figure 1 shows the performance of the six working fluids in the ORC cycle. The choice of working fluids is based on their ease of accessible in Malaysia. The ORC turbine's expansion ratio was adjusted for some working fluids to ensure workability at the given operating conditions while maintaining the condenser outlet pressure above ambient. In the following section, the results of the working fluid analysis are presented.

4 RESULTS AND DISCUSSION

Table 2 provides an overview of the performance parameters of the six ORC working fluids. The examined performance parameters include the resultant specific output power, cycle thermal efficiency, turbine expansion ratio, and condenser outlet temperature. It is worth noting that all working fluids fulfilled the condenser outlet temperature requirements. However, the results indicate that the most efficient working fluid may not necessarily produce the highest output power. For instance, R123 exhibits the highest thermal efficiency (8.0%), but its output power is approximately 43% lower than R600a, which delivers the highest net output of 46.8 kJ/kg despite being less efficient.

Table 2: Performance parameters of the six selected ORC working fluids.

Working fluid	Net specific work output (kJ/kg)	Mass flow rate (kg/s)	Net output power (kW)	Thermal efficiency
R123	26.6	0.833	22.1	8.0%
R245fa	24.8		20.6	6.2%
R134a	16.8		14.0	2.6%
R410a	6.7		5.6	0.6%
R1233zd(E)	24.7		20.6	6.2%
R600a	46.8		39.0	4.4%

Cont'd	Expansion ratio	Thermal power input at evaporator (kW)	Evaporator inlet temperature (°C)	Condenser outlet temperature (°C)
R123	17	180.4	130	28
R245fa	9	200.1	139	27
R134a	3	275.9	75	30
R410a	1.35	336.2	40	30
R1233zd(E)	9	191.2	141	28
R600a	6	469.6	110	28

Figure 3 shows that the cycle's thermal efficiency increases almost linearly with the working fluid's critical temperature, which is consistent with the findings of Elahi *et al.* (2022). However, the increment in net specific work output is not linear, as higher critical temperature working fluids require a larger expansion ratio for the given operating conditions. For example, R123 requires an extremely high expansion ratio (23:1), as depicted in Figure 4. On the other hand, R600a requires significantly higher input (thermal) energy at the evaporator, which is evident from Figure 4. Despite its higher energy consumption, R600a delivers higher net output, and its thermal efficiency ratio adheres to global trends.

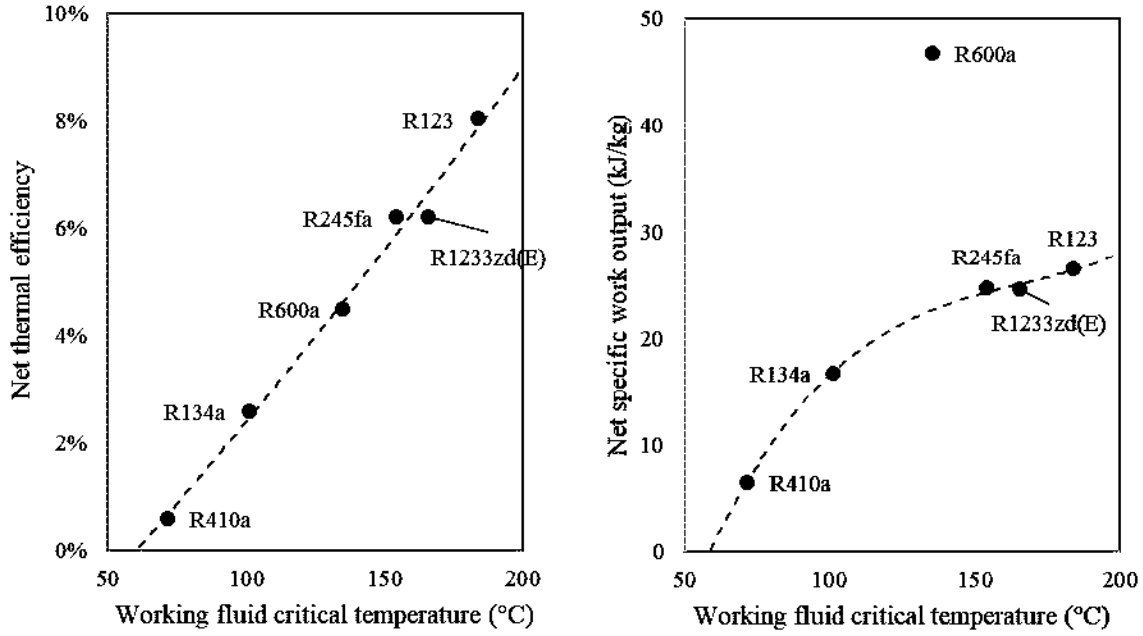

Figure 3: Cycle thermal efficiency and net output at working fluids critical temperatures.

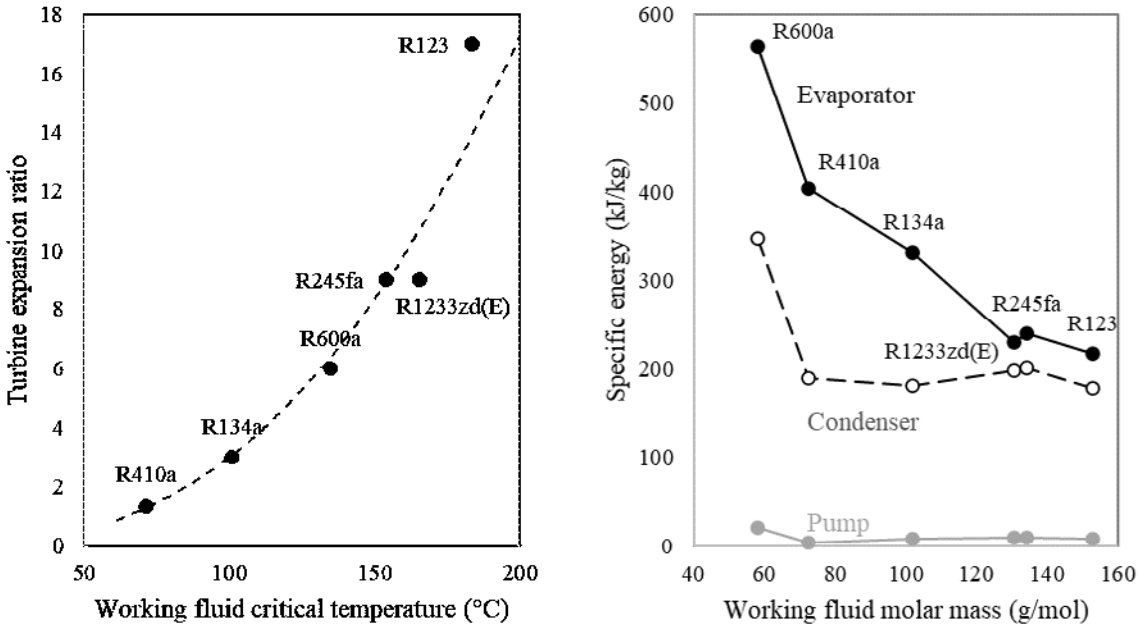

Figure 4: Cycle turbine expansion ratio and thermodynamic properties of working fluids.

The higher energy consumption of R600a is due to its thermophysical properties, such as its specific enthalpy, which is nearly double that of the other working fluids. However, this requires further investigation into the potential of larger heat exchangers to transfer significantly higher heat energy at the evaporator and condenser. Conversely, R245fa, R134a, and R410a are unsuitable due to their higher GWP, even though R245fa exhibits similar thermodynamic performance as the other preferred working fluids. Since the objective of WHR is to mitigate climate change and achieve carbon neutrality, using R245fa is counterintuitive.

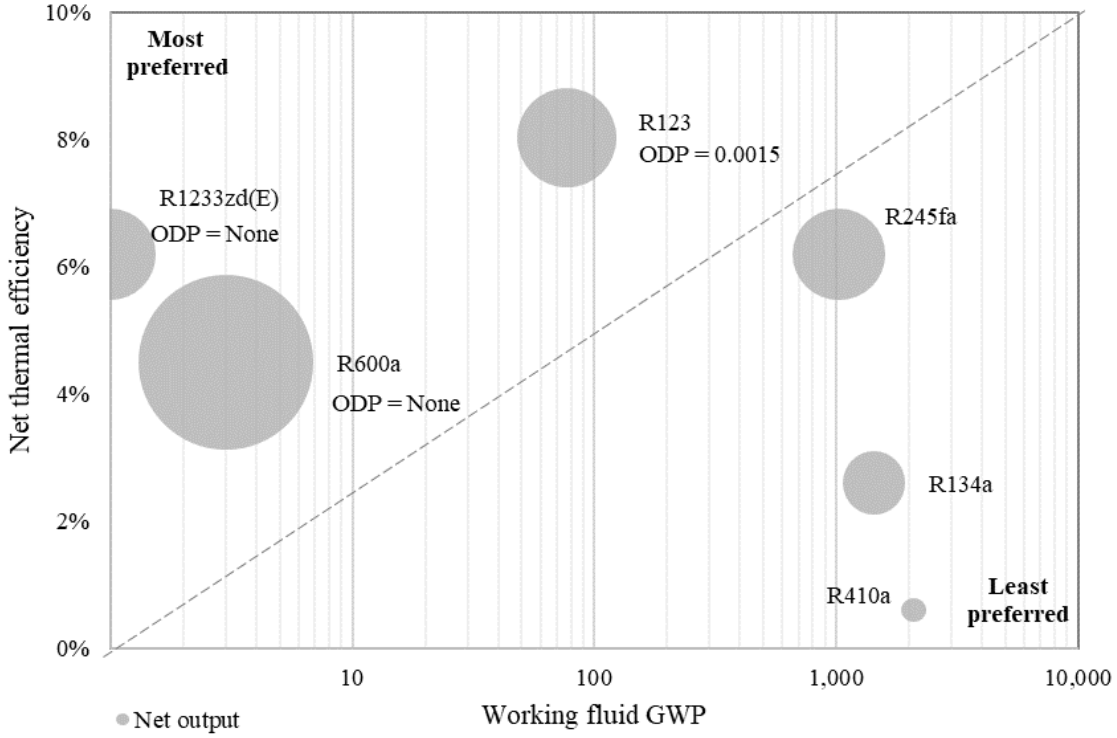

Figure 5: Cycle thermal efficiency and net output based on working fluids' critical temperature.

The cycles' thermodynamic performance and environmental impact (based on GWP) are shown in Figure 5. The most suitable working fluid should exhibit high thermal efficiency but low GWP, as located in the top left corner. Based on GWP, R1233zd(E), R600a, and R123 are the most suitable options. However, R123 has a comparatively higher GWP (77) and ODP (0.0015) than others, which is undesirable for this study. The comparison between R1233zd(E) and R600a shows that the latter only has a lower turbine expansion ratio. The formation of supersonic flow under high expansion ratios is a major challenge in ORC turbine design (Uusitalo & Zocca, 2023), which R600a could mitigate. However, R1233zd(E) has a notably higher thermal efficiency, lower environmental impact, and lower specific energy consumption at the evaporator and condenser. These benefits outweigh its only shortcoming, which indicates turbine design is critical to the ORC cycle for WHR applications.

5 CONCLUSIONS

The thermodynamic and environmental performance of six working fluids were examined for ORC-based WHR for the upstream process. The results showed that:

- R600a has the highest net output power but an inefficient cycle, while R123 has the best thermal efficiency despite a lower output power compared to R600a.
- R245fa, R134a, and R410a are undesirable due to their significantly higher GWP, although their thermodynamic performance was comparable to the preferred working fluids.
- The thermal efficiency of the ORC cycle increased linearly with the working fluid's critical temperature, but the increment in net output energy was non-linear.
- Due to its thermophysical properties, R600a required significantly higher input energy at the evaporator.
- R1233zd(E) and R600a emerged as the preferred working fluids for ORC-based WHR based on thermodynamic and environmental performance analyses.
- ORC turbine design remains a critical requirement for practical ORC-WHR applications.

379

Overall, the study provided valuable insights into selecting ORC-based WHR systems and highlighted the importance of considering thermodynamic and environmental performance factors during the process.

REFERENCES

A-Gas, n.d., R123 Technical Information Sheet. Available online: https://www.agas.com/media/4tbjckam/r123-technical-information.pdf. Last accessed: 23.03.2023.

CoolProp, n.d., What is CoolProp? Available online: http://www.coolprop.org/. Last accessed: 23.03.2023.

Darment, n.d., Refrigerant with sales cylinder R600A (0,42kg) Isobutaani. Available online: https://darment.eu/product/refrigerant-with-sales-cylinder-r600a-042kg-isobutaani/. Last accessed: 26.03.2023.

Elahi, A. E., Mahmud, T., Alam, M., Hossain, J., Biswas, B. N., 2022, Exergy analysis of organic Rankine cycle for waste heat recovery using low GWP refrigerants, *International Journal of Thermofluids*, vol. 16: p. 100243.

EPA, 2015. Waste Heat to Power Systems. Available online: https://www.epa.gov/sites/default/files/2015-07/documents/waste_heat_to_power_systems.pdf. Last accessed: 26.03.2023.

Honeywell, 2013a, (a), Genetron® 134a (R-134a). Available online: https://www.honeywell-refrigerants.com/europe/product/genetron-134a/. Last accessed: 26.03.2023.

Honeywell, 2013b, Genetron® 245fa (R-245fa). Available online: https://www.honeywell-refrigerants.com/europe/product/genetron-245fa/. Last accessed: 26.03.2023.

Honeywell, 2013c, Genetron® AZ-20 (R-410A). Available online: https://www.honeywell-refrigerants.com/europe/product/genetron-az-20/. Last accessed: 26.03.2023.

Honeywell, 2015, Solstice® zd (R-1233zd). Available online: https://www.honeywell-refrigerants.com/europe/product/solstice-zd/. Last accessed: 26.03.2023.

Mariani, A., Morrone, B., Laiso, D., Prati, M.V., Unich, A., 2022, Waste Heat Recovery in a Compression Ignition Engine for Marine Application Using a Rankine Cycle Operating with an Innovative Organic Working Fluid, *Energies*, vol. 15: p. 7912.

Muhammad, U., Imran, M., Lee., D. H., Park, B. S., 2015, design and experimental investigation of a 1 kW organic Rankine cycle system using R245fa as working fluid for low-grade waste heat recovery from steam, Energy Conversion and Management, vol. 103: p. 1089-1100.

MTJA, n.d., Malaysia-Thailand Joint Authority. Available online: https://www.mtja.org/home#AboutJDA. Last accessed: 26.03.2023.

PBOG, 2013, From Waste Heat to High Performance. Available online: https://pboilandgasmagazine.com/from-waste-heat-to-high-performance/. Last accessed 26.03.2023.

Rijpkema, J., Andersson, S. B., Munch, K., 2021, Experimental study of an organic Rankine cycle with R1233zd(E) for waste heat recovery from the coolant of a heavy-duty truck engine, *Energy Conversion and Management*, vol. 244: p. 114500.

Shu, G., Z., M., Tian, H., Hou, Y., Zhu, W., 2016, Experimental comparison of R123 and R245fa as working fluids for waste heat recovery from heavy-duty diesel engine, *energy*, vol. 115, part. 1: p. 756-769.

Sinteco, 2020, Isobutane R600a – 99.5%. Available online: https://www.sinteco-srl.com/wp-content/uploads/2020/09/R600a.pdf. Last accessed: 23.03.2023.

Uusitalo, A., Zocca, M., 2023, Design and numerical analysis of supersonic radial-inflow turbines for transcritical ORC processes, Energy Conversion and Management, vol. 277: p.116609

ACKNOWLEDGEMENT

The authors thank MTJA Research Vot 4B325 for funding this work.

LIST OF ABBREVIATIONS & SYMBOLS

Abbreviations

ETC	Electric Turbo-compounding
GHG	Greenhouse gases
GWP	Global Warming Potential
HC	Hydrocarbon
HCFC	Hydrochlorofluorocarbon
HFC	Hydrofluorocarbon
HFO	Hydrofluoroolefin
ODP	Ozone depletion potential
ORC	Organic Rankine Cycle
TEG	Thermo-electric generators
WHR	Waste heat recovery

Symbols

c_p	Constant pressure specific heat, J/kg-K
h	Specific enthalpy, J/kg
$\dot{m}$	Mass flow rate, kg/s
η	Efficiency, --
q	Specific energy, J/kg
s	Specific entropy, J/kg-K
T	Temperature, °C or K
v	Specific volume, m^3/kg

Subscripts

1	Evaporator outlet, turbine inlet
2	Turbine outlet, economizer inlet
3	Economizer outlet, condenser inlet
4	Condenser outlet, pump inlet
5	Pump outlet, economizer inlet
6	Economizer outlet, evaporator inlet
cw	Cooling water
exh	Exhaust
generator	Generator
gross	Gross output
in	Input to ORC cycle
net	Net output
out	Output from ORC cycle
pump	Pump
turb	Turbine

ORC SEVILLE 2023
7th International Seminar on O.R.C. Power Systems

© 2024 Editorial Universidad de Sevilla. Este es un artículo de acceso abierto distribuido bajo los términos de la licencia de uso y distribución Creative Commons (BY-NC-ND 4.0)

DOI: https://dx.doi.org/10.12795/9788447227457_63

Experimental Investigation of a Small-Scale Reversible High-Temperature Heat Pump – Organic Rankine Cycle System for Industrial Waste Heat Recovery

Rahul Velanparambil Ravindran*[1], Donal Cotter[1], Christopher Wilson[1], Ming Jun Huang[1], Neil Hewitt[1]

[1]Centre for Sustainable Technologies, Belfast School of Architecture and Built Environment, Ulster University, Belfast, United Kingdom, BT15 1ED

*Corresponding Author : velanparambil_ravindran-r@ulster.ac.uk

ABSTRACT

A reversible system that can function as both a high-temperature heat pump (HTHP) and an organic Rankine cycle system (ORC) can enhance the efficiency of industrial waste heat recovery. The reversible system can either upgrade waste heat to process heat (HTHP mode) or generate power (ORC mode). This paper presents the experimental investigation of a small-scale reversible HTHP-ORC system using an automotive open-drive scroll machine to operate as the compressor (HTHP) and expander (ORC) in the system. The refrigerant R1233zd(E) was selected as the working fluid for both modes of operation. Based on an analysis of the experimental results, the HTHP achieved a COP_{el} of 4.6 at 30 K temperature lift, with the scroll compressor achieving a maximum overall isentropic efficiency of 73.4%. In ORC mode, at a source temperature of 75 °C, the cycle thermal efficiency was 3.8%, and the expander overall isentropic efficiency was 43%.

Keywords: waste heat recovery, reversible HTHP-ORC system, high-temperature heat pump, organic Rankine cycle, low GWP refrigerant.

1 INTRODUCTION

The global surface temperature has risen by 1.1 ˚C, and the negative impacts due to climate change will continue to intensify (IPCC, 2022). Decarbonising the industrial sector is a key strategy adopted by the European commission to achieve carbon neutrality by 2050 (European Commission, 2021). Waste heat recovery is an effective strategy in the transition towards decarbonisation. A reversible HTHP-ORC system could be an effective waste heat recovery technology in the industrial sector to upgrade heat or generate power, thus increasing energy efficiency. Due to the configuration similarities between the heat pump and organic Rankine cycle systems, it is possible to develop a reversible system with minimal modifications. Such a system can be applied in paper, chemical, and food industries to provide process heat (HTHP) when there is a heat demand and if heating is not required the same system can be used to generate electricity (ORC). The reversible system can also be implemented as part of a district heating network ,where the upgraded heat can be used for space heating in office and commercial buildings in summer season or for power generation (winter season) (Palomba *et al.*, 2020). The potential of the reversible system has also been explored in residential (Dumont *et al.*, 2015), automobile (Cuevas *et al.*, 2019) and marine (Kosmadakis *et al.*, 2022) sectors. Other research trends include a feasibility check of the reversible system coupled to a thermal storage as a Carnot battery (Eppinger *et al.*, 2021).

This paper describes a small-scale reversible HTHP – ORC system for recovering industrial waste heat within the lower temperature band (< 100 °C). The study focuses on the experimental investigation of a lab-scale prototype of the reversible system in HTHP and ORC modes, followed by a performance analysis of the whole system (HTHP and ORC) and scroll machine (compressor and expander roles).

2 REVERSIBLE SYSTEM LAYOUT

To operate a reversible HTHP-ORC system, a few equipment modifications are required. These include a compact single volumetric scroll acting as both a compressor (HTHP) and an expander (ORC), a valve arrangement to switch the refrigerant flow between the suction and discharge sides of the scroll machine, and a pump placed in parallel with the expansion valve. The schematic diagram of the reversible system is shown in Figure 1. This layout results in a compact and cost-effective system. In this system layout, the heat exchanger roles as evaporator and condenser remain unchanged when the system switches between ORC and HTHP modes.

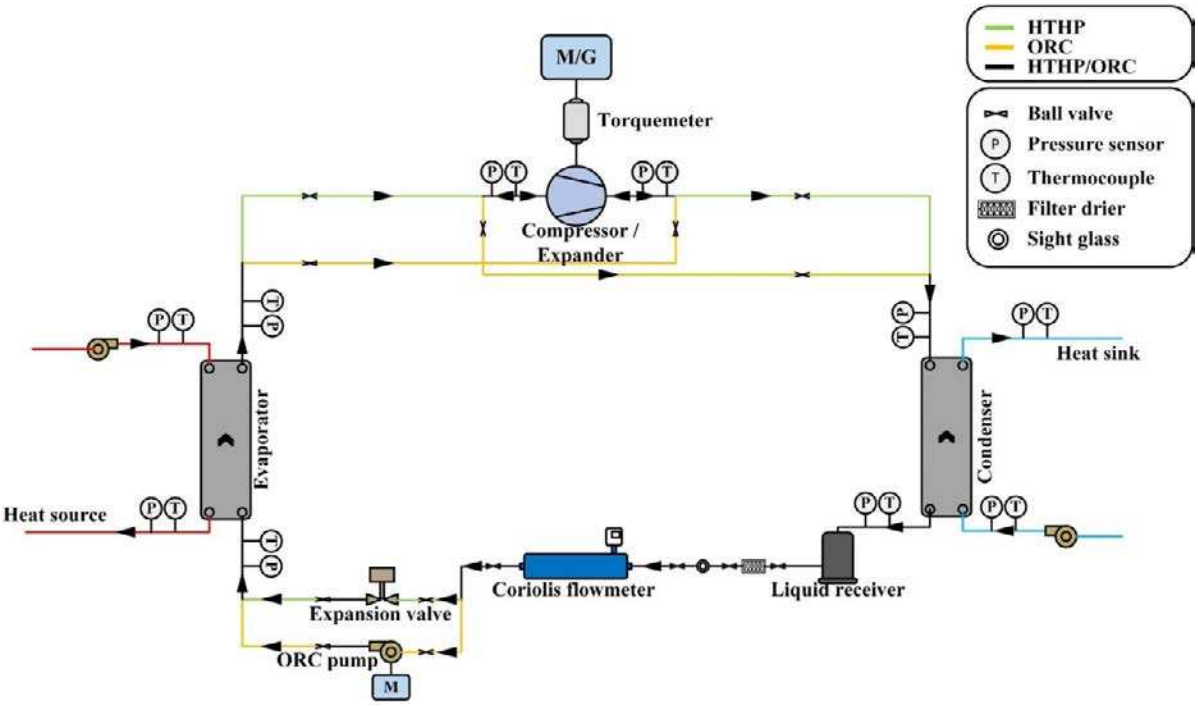

Figure 1: Schematic diagram of the reversible HTHP-ORC system

3 EXPERIMENTAL SETUP

The experimental setup of the reversible HTHP-ORC system is shown in Figure 2. A thermal balancing rig was connected to control the setpoint temperatures via secondary hydraulic circuits to the evaporator and condenser heat exchangers. A modified automotive A/C scroll compressor (Sanden TRSA09) was used for both compressor (HTHP) and expander (ORC) roles. The compressor has a swept volume of 85.7 cm^3 and a reported built-in volume ratio of 1.9. A belt drive was used for power transmission between the motor (HTHP) and the scroll machine. In ORC mode, the motor was replaced with an alternator and a rotary vane pump was chosen to pump the refrigerant. The specifications for the main system components and sensors are listed respectively in Table 1 and Table 2. The refrigerant R1233zd(E) was selected as the working fluid in both operating modes. R1233zd(E) has a very low ODP and a GWP of 3.88 (World Meteorological Organization, 2018) and is considered an effective replacement for R245fa. The selection of equipment and working fluid for the reversible system has been discussed in previous work. (Ravindran *et al.*, 2023).

Table 1: System equipment used in HTHP and ORC modes of operation.

Equipment	Model	Value
Scroll compressor/expander	Sanden TRSA09 (Model No: 3663)	Displacement (85.7 cm^3)
		Power (1.5 kW)
Motor	ETEC 3-phase induction motor (2 pole)	Power (3 kW)
	ETEC 3-phase induction motor (6 pole)	Power (0.25 kW)
Alternator	RTX alternator	12V, 65A
Inverter	Tec drive inverter	4 kW
	Tec drive inverter	0.37 kW
Evaporator	SWEP B85H (20 plates)	Heat exchange area (1.08 m^2)
Condenser	SWEP B26T (26 plates)	Heat exchange area (1.34 m^2)
Expansion valve	Danfoss (ETS 12.5)	-
Pump	Fluid-O-Tech (FPO 501)	Displacement (500 l/h)

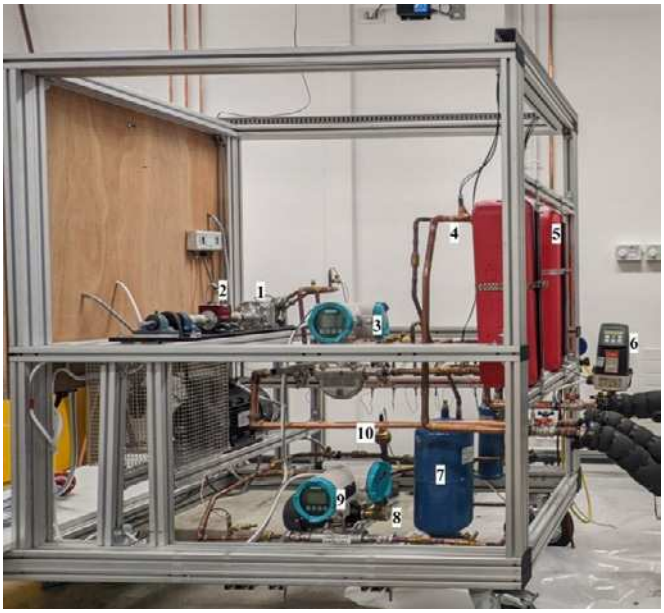

Figure 2: Experimental setup for reversible system (1). Scroll machine (2). Torque meter (3). Coriolis flow meter (sink side) (4). Condenser (5). Evaporator (6). Flow meter (source side) (7). Liquid receiver (8). ORC vane pump (9). Coriolis flow meter (refrigerant) (10). Expansion valve.

Table 2: Sensors used for measurement and data acquisition.

Sensor	Model	Variable	Range
PT100	RS PRO PT100 RTD Sensor	Temperature (˚C)	-50 – 250 °C
Pressure	Emerson PT3-30A (5 Nos)	Pressure (bar)(gauge)	0-30 bar
	ALCO PT4-50S (2 Nos)		0-50 bar
Torque meter	Sensor Technology SGR511-EB	Torque (Nm) & RPM	0-30 Nm
Flow meter	Siemens SITRANS FCS400	Mass flow rate (kg/s)	-
	Danfoss MAG 6000		-
Energy	Siemens 7KT 1665	Power (kW)	-
Data acquisition	Datalogger DT85	-	-

4 METHODOLOGY

The operating conditions for experiments in HTHP and ORC modes are presented in Table 3. The compressor was modified to operate as an expander by removing the check valve on the discharge side. In HTHP mode, motor speed controlled the refrigerant mass flow rate, whereas, in ORC mode, it was set by the rotary vane pump. Water and Therminol 66 were used as the secondary fluids for the source and sink sides, respectively, in HTHP mode; in ORC mode, normal tap water replaced Therminol 66 as the secondary fluid on the sink side. The refrigerant and water properties were taken from the REFPROP 10 database, while the Therminol 66 properties were provided by SWEP SSPG8 software. A DT85 datalogger was used for data acquisition.

Table 3: Operating conditions.

Variable	HTHP	ORC
Source inlet temperature (°C)	40 - 85	65 - 75
Sink outlet temperature (°C)	55 - 105	10
Evaporator thermal load (kW)	2.70 – 8.53	5.78 – 12.00
Condenser thermal load (kW)	3.00 - 8.82	5.69 – 11.70
Mass flow rate (kg/s)	0.0186 – 0.056	0.024 - 0.047

4.1 HTHP mode

The experiments in HTHP mode were conducted by varying the sink outlet temperature and compressor speed and maintaining the source inlet temperature setpoint constant. A total of 55 steady-state points were obtained. The compressor power can be calculated from the compressor speed and torque. The thermal power consumption of the compressor was determined from the suction and discharge enthalpies and the refrigerant mass flow rate.

$$\dot{W}_{cp,mech} = \frac{2\pi N_{cp}\tau}{60} \quad (1)$$

$$\dot{W}_{cp,therm} = \dot{m}_r * (h_{dis} - h_{su}) \quad (2)$$

The mechanical COP is defined as the ratio of heat supplied to the sink and mechanical power consumption, $\dot{W}_{mech}$.

$$COP_{mech} = \frac{\dot{Q}_{cd}}{\dot{W}_{mech}} \quad (3)$$

The COP_{el} is defined as the ratio of heat supplied to the sink and electrical power consumption, $\dot{W}_{el}$.

$$COP_{el} = \frac{\dot{Q}_{cd}}{\dot{W}_{el}} \quad (4)$$

The internal isentropic efficiency of the compressor was calculated as follows.

$$\eta_{cp,is,int} = \frac{(h_{dis,is} - h_{su})}{(h_{dis} - h_{su})} \quad (5)$$

Compressor overall isentropic efficiency was determined from refrigerant mass flow rate and suction and discharge enthalpies.

$$\eta_{cp,is,overall} = \frac{\dot{m}_r(h_{dis,is} - h_{su})}{\dot{W}_{mech}} \quad (6)$$

The volumetric efficiency of the compressor is defined as the ratio of the actual volume flow rate and the theoretical volume flow rate. The actual volume flow rate was determined from the refrigerant mass flow rate and specific volume at the suction side of the compressor.

$$\eta_{cp,vol} = \frac{\dot{m}_r v_{su}}{(\dot{V}_s N_{cp}/60)} \quad (7)$$

4.2 ORC mode

In ORC mode, the experiments were conducted by varying the source inlet temperature and the pump speed and maintaining the sink inlet temperature setpoint constant. The refrigerant mass flow rate was set by controlling the speed of the rotary vane pump. The superheat at the evaporator outlet was controlled by varying the mass flow rate.

The mechanical power produced by the expander was calculated using the expander RPM and torque. The thermal power generated was determined from the suction and discharge enthalpies and mass flow rate.

$$\dot{W}_{exp,mech} = \frac{2\pi N_{exp}\tau}{60} \quad (8)$$

$$\dot{W}_{exp,therm} = \dot{m}_r * (h_{su} - h_{dis}) \quad (9)$$

The thermal efficiency of the ORC was determined using the thermal power of the expander and pump, as well as the thermal load of the evaporator.

$$\eta_{orc,therm} = \frac{\dot{W}_{exp,therm} - \dot{W}_{pp,therm}}{\dot{Q}_{ev}} \quad (10)$$

The system overall efficiency was calculated as the ratio of net power generated to heat supplied, $\dot{Q}_{ev}$.

$$\eta_{orc,overall} = \frac{\dot{W}_{mech} - \dot{W}_{pp}}{\dot{Q}_{ev}} \quad (11)$$

The performance of the scroll expander was characterized by determining the internal isentropic and overall isentropic efficiency and filling factor.

$$\eta_{exp,is,int} = \frac{(h_{su} - h_{dis})}{(h_{su} - h_{dis,is})} \quad (12)$$

$$\eta_{exp,is,overall} = \frac{\dot{W}_{mech}}{\dot{m}_r(h_{su} - h_{dis,is})} \quad (13)$$

$$\phi_{ff} = \frac{\dot{m}_r v_{su}}{(\dot{V}_s N_{cp}/(60 * r_v))} \quad (14)$$

5 RESULTS AND DISCUSSION

5.1 HTHP mode

The scroll compressor performance was analysed through isentropic and volumetric efficiencies. The internal isentropic and overall isentropic efficiencies of the compressor at different pressure ratios is shown in Figure 3. Overall isentropic efficiency at T_{source} = 60 °C and 1500 RPM was 73.4%. Higher

isentropic efficiencies were obtained between 1500 and 2000 rpm, with a slightly decreasing trend as the speed increased.

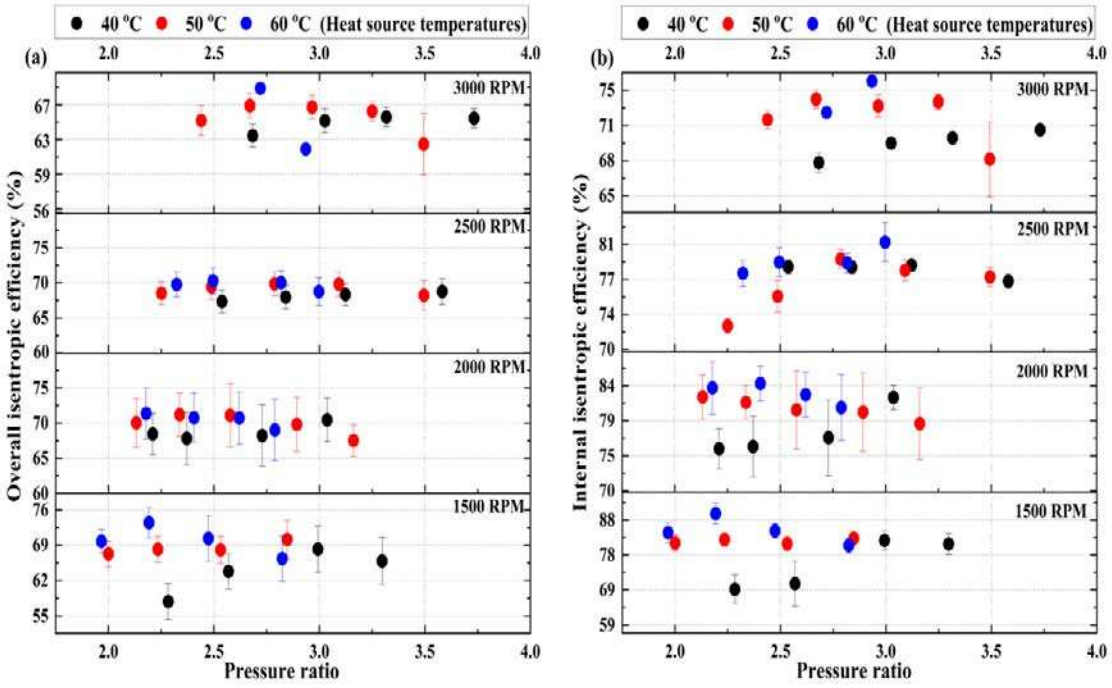

Figure 3: (a) Overall isentropic and (b) internal isentropic efficiencies of the scroll compressor with respect to operating pressure ratio.

386

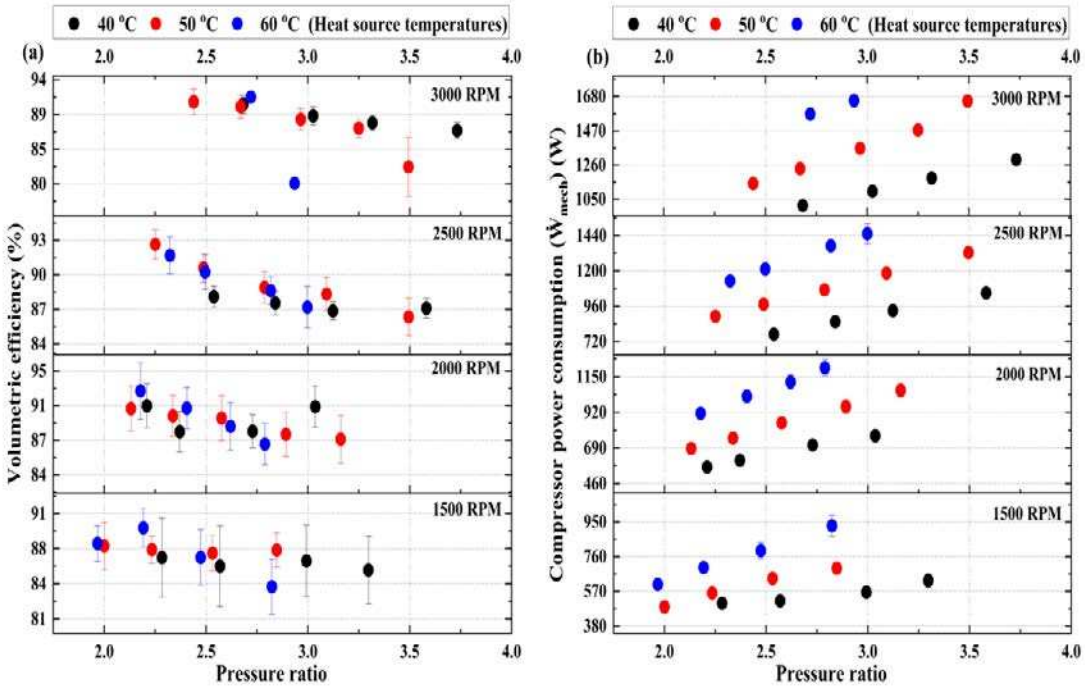

Figure 4: (a) Volumetric efficiency of the scroll compressor and (b) power consumption with respect to operating pressure ratio.

As shown in Figure 4, The volumetric efficiency of the compressor was close to unity (less internal leakages) at lower pressure ratios and decreases with increasing pressure ratio (indicating internal leakages in the compressor) across the range of compressor speeds and source temperatures. The compressor speed also have an impact on the volumetric efficiency. Higher volumetric efficiencies were observed in the 2000 – 2500 RPM range. Volumetric efficiencies showed a slightly decreasing trend in the 2500 – 3000 RPM range. The mechanical power consumption ($\dot{W}_{mech}$) of the compressor varied between 0.48 kW (Ncp: 1500 RPM, rp: 2) and 1.65 kW (Ncp: 3000 RPM, rp: 2.93). The compressor power increased with respect to increase in pressure ratio, compressor speed as well as with respect to rise in source temperature.

The COPs of the system for different temperature lifts (absolute temperature difference between source inlet and sink outlet temperatures) are shown in Figure 5. COP decreases with increase in temperature lift. For a temperature lift of 30 K, maximum COP_{el} and COP_{mech} values of 4.6 (T_{source} = 50 °C, at 1500 RPM) and 5.5 (T_{source} = 60 °C, at 1500 RPM) respectively were obtained.

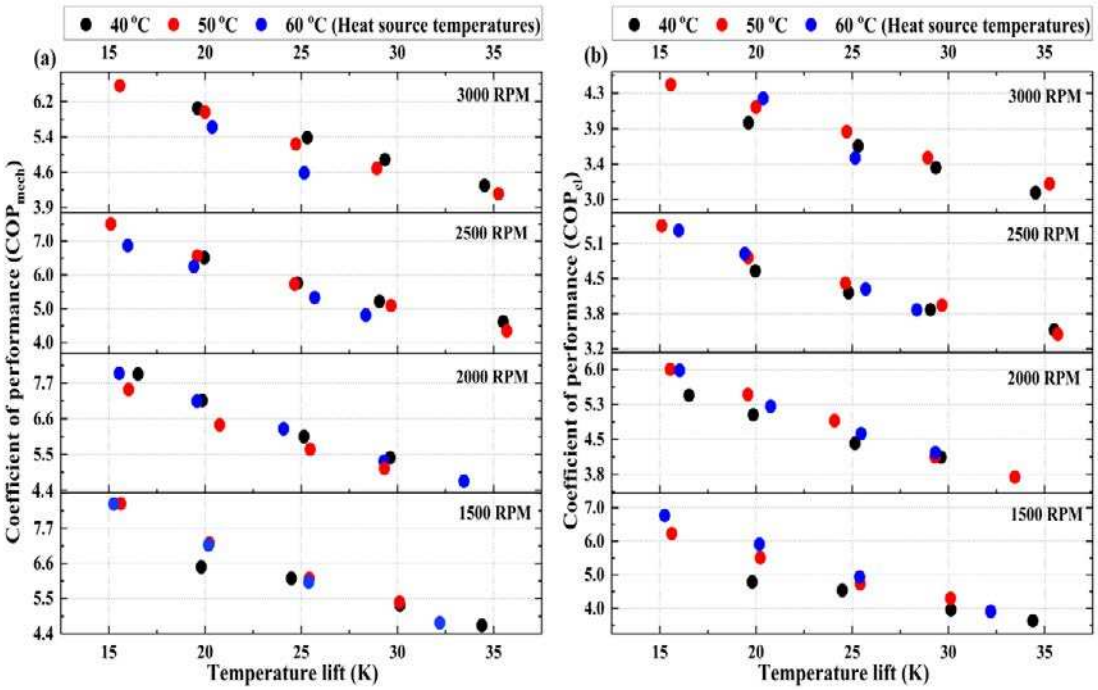

Figure 5: HTHP system performance (a) (COP_{mech}) and (b) (COP_{el}) for various temperature lifts.

5.2 Organic Rankine cycle mode

The internal and overall isentropic efficiencies of the scroll expander is shown in Figure 6. For the operating conditions, the overall isentropic efficiency increases as the mass flow rate increases (filling factor (ϕ_{ff}) reduces at higher mass flow rates indicating less internal leakage and better overall performance of the expander). Maximum isentropic efficiency of 43 % was obtained at a source temperature of 75 °C. The highest value for internal isentropic efficiency was found to be 69 %.

The thermal and overall cycle efficiencies of the system in ORC mode are shown in Figure 7. At a source temperature of 75 °C (pressure ratio, r_p: 2.13), maximum thermal and overall cycle efficiencies of 3.8% and 2.1%, respectively, were achieved. The expander performance in terms of filling factor is shown in Figure 8(a). The filling factor (ϕ_{ff}) decreased as the refrigerant mass flow rate increased. Higher filling factor values up to 2 at T_{source} = 65 °C were observed at lower mass flow rates indicating higher internal leakages in the scroll expander as the working chamber is overfilled. Throughout the experimental campaign under the mentioned operating conditions, filling factor was always found to be

above unity. The gross mechanical power generated by the expander increased with mass flow rate and source temperature (Figure 8(b)) and reached a maximum of 307 W (T_{source}: 75 °C).

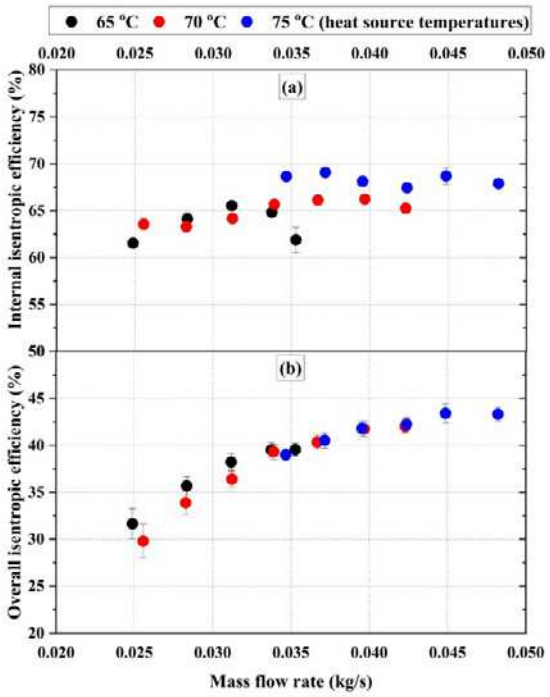

Figure 6: (a) Internal and (b) overall isentropic efficiencies of the expander with respect to mass flow rate.

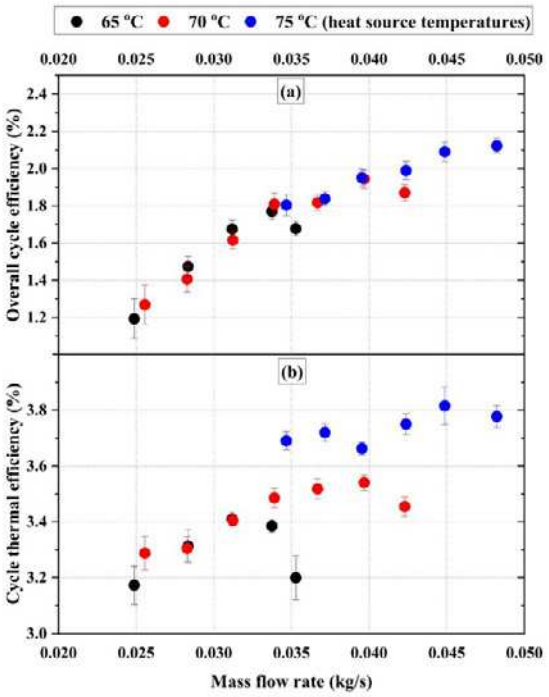

Figure 7: (a) Thermal and (b) overall efficiencies of the system in ORC mode.

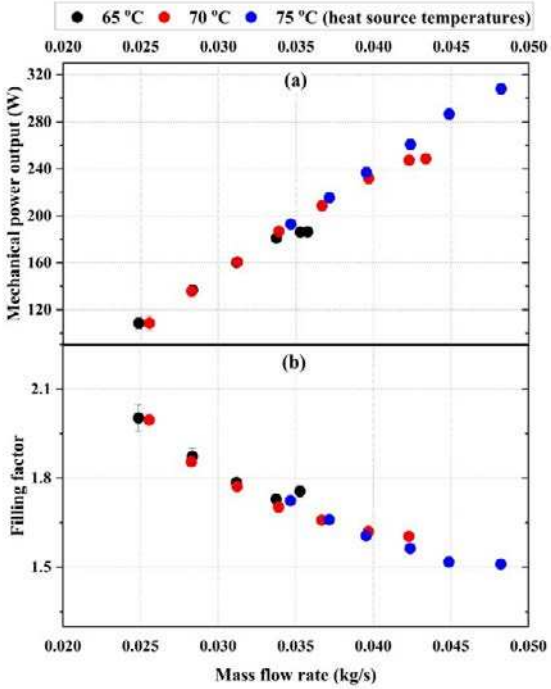

Figure 8: (a) Mechanical power generated and (b) filling factor of the expander with respect to mass flow rate.

6 CONCLUSION

The paper presents the experimental study of a reversible HTHP-ORC system. The performance of the system and the scroll machine in both operating modes were investigated. The scroll machine had better isentropic efficiency values in the compressor role when compared to that of the expander. Maximum overall isentropic efficiencies were 73.4% and 43% respectively in compressor and expander roles. In terms of system performance, a maximum COP_{el} of 4.6 in HTHP mode and a maximum overall cycle efficiency of 2.1% (T_{source}: 75 °C, r_p: 2.13) was obtained in ORC mode. Future experiments in ORC mode will focus on heat source temperatures of 80, 85 and 90 °C.

NOMENCLATURE

$\dot{m}$	Mass flow rate (kg/s)	ff	filling factor
N	Speed (RPM)	int	internal
h	specific enthalpy (J/kg)	is	isentropic
$\dot{Q}$	heat transfer (kW)	lift	lift
$\dot{W}$	power (kW)	mech	mechanical
		overall	overall
Subscript		pp	pump
cd	condenser	r	refrigerant
cp	compressor	sf	secondary fluid
dis	discharge	su	suction
ev	evaporator	therm	thermal
exp	expander	v	volume
el	electrical	vol	volumetric

REFERENCE

Cuevas, C., Declaye, S. and Lemort, V. (2019) 'Experimental characterization of a reversible heat pump for hybrid and electric vehicles', *Advances in Mechanical Engineering*, 11(4), pp. 1–13. Available at: https://doi.org/10.1177/1687814019845806.

Dumont, O., Quoilin, S. and Lemort, V. (2015) 'Experimental investigation of a reversible heat pump/organic Rankine cycle unit designed to be coupled with a passive house to get a Net Zero Energy Building', *International Journal of Refrigeration*, 54, pp. 190–203. Available at: https://doi.org/10.1016/j.ijrefrig.2015.03.008.

Eppinger, B., Steger, D., Regensburger, C., Karl, J., Schlücker, E. and Will, S. (2021) 'Carnot battery : Simulation and design of a reversible heat pump-organic Rankine cycle pilot plant', *Applied Energy*, 288(February), p. 116650. Available at: https://doi.org/10.1016/j.apenergy.2021.116650.

European Commission (2021) 'Fit for 55 - Delivering the EU's 2030 climate target on the way to climate neutrality', *European Commission*, (550 final), p. 15. Available at: https://eur-lex.europa.eu/legal-content/EN/TXT/?uri=CELEX:52021DC0550.

IPCC (2022) *Climate Change 2022 - Mitigation of Climate Change - Full Report*, *Cambridge University Press*.

Kosmadakis, G. and Neofytou, P. (2022) 'Reversible high-temperature heat pump / ORC for waste heat recovery in various ships : A techno-economic assessment', *Energy*, 256, p. 124634. Available at: https://doi.org/10.1016/j.energy.2022.124634.

Palomba, V., Borri, E., Charalampidis, A., Frazzica, A., Cabeza, L.F. and Karellas, S. (2020) 'Implementation of a solar-biomass system for multi-family houses: Towards 100% renewable energy utilization', *Renewable Energy*, 166, pp. 190–209. Available at: https://doi.org/10.1016/j.renene.2020.11.126.

Ravindran, R.V., Huang, M.J. and Hewitt, N. (2023) 'Design and modelling of a small-scale reversible high temperature heat pump – organic Rankine cycle system for industrial waste heat recovery', *International Journal of Low-Carbon Technologies* [Preprint]. Available at: https://doi.org/10.1093/IJLCT/CTAD038.

WMO (World Meteorological Organization), Scientific Assessment of Ozone Depletion: 2018, Global Ozone Research and Monitoring Project–Report No. 58, 588 pp., Geneva, Switzerland, 2018.

ACKNOWLEDGMENT

This research work is funded under LOTNET programme by EPSRC/UKRI under grant agreement EP/R045496/1.

ORC SEVILLE 2023
7th International Seminar on O.R.C. Power Systems

© 2024 Editorial Universidad de Sevilla. Este es un artículo de acceso abierto distribuido bajo los términos de la licencia de uso y distribución Creative Commons (BY-NC-ND 4.0)

DOI: https://dx.doi.org/10.12795/9788447227457_64

TECHNICAL COMPARISON AND EVALUATION OF A PUMPED THERMAL ENERGY STORAGE WITH TWO DIFFERENT DESIGNS

Márcio Santos[1,*], Jorge André[1], Ricardo Mendes[1], José B. Ribeiro[1]

[1] *University of Coimbra, ADAI-LAETA, Coimbra, Portugal*

*Corresponding Author: marcio.santos@dem.uc.pt

ABSTRACT

Increased worldwide demand for energy (especially electricity), rising energy costs, and heightened environmental concerns are factors that continually press for the adoption of technologies to exploit renewable energy sources (RES). In order to adopt these systems, large-scale energy storage systems are needed to ensure the security of supply in energy systems due to the increasing share of renewable energy sources in the energy mix. The paper proposes a new form of energy storage technology that utilizes a combination of a heat pump and an organic Rankine cycle, referred to as Carnot Batteries (CB), which can store thermal energy for several hours to a few days and transform it back to electrical energy. Two different configurations of Carnot Batteries were tested using models created in Matlab programming software, with six working fluids used for technical optimization. The second, more complex configuration increased the roundtrip efficiency mainly due to the better performance of the two-stage heat pump.

1 INTRODUCTION

Rising fossil fuel prices and environmental concerns have led to a growing interest in exploiting renewable energy sources. However, their intermittent nature presents a challenge to the stability and security of power systems and grids. Energy storage systems have emerged as a feasible solution to address this issue, and over the years, various energy storage processes have been developed and implemented (Jafari et al., 2022). Despite their gains, existing energy storage systems such as pumped hydro storage and compressed air storage technologies are limited by geographical features, while battery-based storage systems face limitations such as short lifespan and high economic cost (Gallo et al., 2016).

In recent years, Carnot battery energy storage, which is based on the Carnot cycle, has emerged as a promising approach to overcome the limitations of existing energy storage systems (Nadeem et al., 2019). The Carnot cycle is a thermodynamic cycle that has been used in the field of energy conversion for over a century. Various types of Carnot batteries exist based on the type of thermodynamic cycle used in the charge and discharge phases. Rankine, Brayton, transcritical CO2, and other cycles are examples of thermodynamic cycles employed in Carnot batteries (Dumont et al., 2020). Furthermore, Carnot batteries can achieve greater versatility by utilizing various thermodynamic cycles for upstream and downstream cycles and employing different heat storage methods. One of the most commonly used and well-known Carnot batteries is a system based on an organic Rankine cycle (ORC) process, a thermal energy storage (TES), and a variable heat pump (VHP) (Weiss & Zinn, 2016).

There are several advantages to using CBs. They have a low cost per stored kWh, are long-lasting, and can be utilized for applications ranging from 100 kW to 100+ MW. Additionally, some types of CBs can be powered by both electric energy and heat, which is particularly important. The heat required can be obtained from renewable sources, such as solar or geothermal energy, or from waste heat recovery. This feature allows the technology to function as a hybrid between a storage unit and a power production system, with the added benefit of utilizing low-temperature heat ($T \leq 100$ °C). (Frate et al., 2020).

In this work, we will provide an in-depth analysis of Carnot Batteries, including their working principles, comparing different types of Carnot Batteries, highlighting the advantages and disadvantages of each. The aim of this paper is to examine and compare two different layouts of a Carnot battery based on ORC and VHP technologies for charge phase for discharging phase, respectively.

2 CARNOT BATTERIES

Carnot Batteries work by establishing a thermal gradient between a high temperature reservoir (HTR) and a low temperature reservoir (LTR). Electric energy is used to charge the system by forcing heat flow against the natural gradient, thus storing thermal exergy. In the discharge phase, the heat flows from the hot environment to the cold one, and this flow is used to produce work in a heat engine.
According to O. Dumont et al. (Dumont et al., 2020), a Carnot Battery (CB) is defined as an electrical energy storage (EES) technology where there is always an electric input, and an electric output. A thermal input (waste heat, geothermal water, concentrated solar power, …) may be used to improve the performance of the CB; however, its primary purpose remains the storage of electric energy. Similarly, the battery may output useful thermal energy, but the electric output must be comparable with the electric input. In practice, the reservoirs may be physical ones, such as water tanks or solid materials, or their role may be taken up by the environment (for example, the ambient air). Similarly, electric heat pumps or resistance heaters may be used for charging, and any heat engine (Rankine, Brayton, others) or even a thermoelectric generator may be used for discharging.
The roundtrip efficiency of a PTES is the common parameter for evaluation the performance and calculated, generally, as the product of the COP of the heat pump with the heat engine efficiency (if thermal storage efficiency is not considered). Carnot Batteries offer roundtrip efficiencies (ε_{rt}) in a wide range depending on their boundary conditions (Dumont et al., 2020), (Dumont & Lemort, 2020; Steinmann et al., 2019; Weitzer et al., 2022), low energy costs (Jafari et al., 2022)(Dumont et al., 2020), and high lifetimes (Dumont et al., 2020). These systems are mostly competitive for electricity storage on the scale of several hours, in situations that demand low Power/Capacity (kW/kWh) ratios, with values of 1/4 h-1 and lower. They have a very low environmental impact, and no dependence on geographical conditions (Jafari et al., 2022), making them a suitable competitor to PHS and CAES, whose geographical constraints pose a considerable limit to their exploitability on a large scale. For local, small-scale implementations, Carnot Batteries may also present an adequate replacement for chemical batteries, which are often expensive and environmentally unsafe.
Additionally, an important advantage of Carnot Batteries is the ability to integrate additional thermal reservoirs (such as industrial waste heat), which act as additional exergy sources (Dumont et al., 2020). This thermal integration increases the ε_{rt} of the system, potentially to values greater than unity (>100%), by decreasing the work input or increasing the work output. In Table 1 a brief summary is given of the technical characteristics of some different Carnot battery technologies.

392

Table 1: Technical summary of Carnot Battery technologies (adapted from (Dumont et al., 2020)).

Cycle	Brayton Cycle	Electrical heater and Rankine Cycle	Heat Pump and Rankine Cycle
Power [MW]	Up to 100	Up to 100	Up to 10*
Energy [MWh]	Up to 400	Up to 400	Up to 40*
Temp [°C]	[-70:1000]	Up to 750	Up to 150
Compactness [kW/m^3]	25	~4	[0.05–1.72]
Compactness [kWh/m3]	200	~36	[0.2–207]
Self-discharge	medium	Very low	[30–73]
ε_{rt} [%]	[60-70]	[12-55]	[70-150]**
Price [$/kW]	[395-875]	~376	[272–468]
Price [$/kWh]	[55–198]	~94	[68–117]

Estimated TRL	5	9	7
Typical fluids	Argon, Air	Water	R1233zd(E), CO_2, NH_3, water

* Possible to extend by association in series ** Thermally integrated

If a heat pump is used to charge the thermal storage, the system is designated Pumped Thermal Electrical Storage. These systems may use Brayton heat pumps (HP) with Brayton heat engines (HE), Vapor Compression Heat Pumps (VCHP) in conjunction with Rankine Cycles (RC), or Brayton heat pumps with Rankine Cycles (Frate et al., 2020). The presence of a heat pump for the charge cycle is advantageous if the Coefficient of Performance (COP) is higher than one. This thermal integration allows an increase in efficiency without complex modifications to the thermodynamic cycles and makes the PTES more flexible, as it may now receive two inputs (electric and thermal) instead of just one – in this sense, Thermally Integrated PTES (TI-PTES) may be seen as a hybrid energy storage and waste heat power plant.

Brayton PTES is usually comprised of a Brayton heat pump, based on the inverse Brayton cycle, and a Brayton heat engine, typically working between two sensible reservoirs (Dumont et al., 2020). The typical layout contains two thermal reservoirs and four machines (two compressors and two expanders), however in a reversible system this number could reduce to two. In a Brayton cycle, the working gas is compressed, heated and expanded, and then cooled before the next compression. As the work produced by expansion is greater than the work used in compression, the expander drives the compressor with a net positive work output (as with any heat engine, the driving force is a temperature gradient between the two reservoirs) – this is the cycle followed in the discharge process. For charging, the inverse process occurs – the gas is heated and compressed, drawing heat from the LT reservoir, and then cooled, storing heat in the HT reservoir, followed by expansion (Dumont et al., 2020).

HP/RC systems combine Vapor Compression Heat Pumps with Rankine Cycles, where the VCHP charges the reservoirs with thermal exergy, and the Rankine Cycle produces work by harnessing the temperature difference between HT and LT reservoirs. By comparison with Brayton systems, Rankine-based PTES offers the advantages of high energy density and low temperature operation – these features allow for more compact storage, lower self-discharge, and potentially more efficient integration of waste heat. One of the advantages of HP/ORC systems is the use of commercially available equipment (pumps, compressors, expanders, heat exchangers, valves), which facilitates their construction (Dumont et al., 2020), (Frate et al., 2020), (Eppinger et al., 2021).

3 THERMODYNAMIC MODELLING

3.1 Roundtrip efficiency of the CB

For the study of Carnot Battery systems, the HP/ORC architecture was chosen due to its simplicity and practical feasibility, as well as its low temperatures that facilitate thermal integration; this is also one of the most widely studied types of Carnot Battery, so reference values are readily available.

To study the performance of HP/ORC PTES, each thermodynamic cycle was modelled in MATLAB, with resort to the REFPROP database to calculate fluid properties. The effectiveness of the Carnot battery process is evaluated through the roundtrip efficiency. The value of this variable is affected by the behaviors of the two sub-cycles of vapor compression heat pump (COP) and the organic Rankine cycle (η), and is expressed by:

$$\varepsilon_{rt} = \mathrm{COP} \times \eta \quad (1)$$

In this work, two different configurations of Carnot battery are proposed and identified in Figure 1. The first is a single stage heat pump and a simple organic Rankine cycle (left). The second, placed at right is a two-stage heat pump system for the charging process and a regenerative ORC for the discharge process. Figure 2 depict the thermodynamic cycle diagrams of the proposed configurations of the heat pump and organic Rankine cycle.

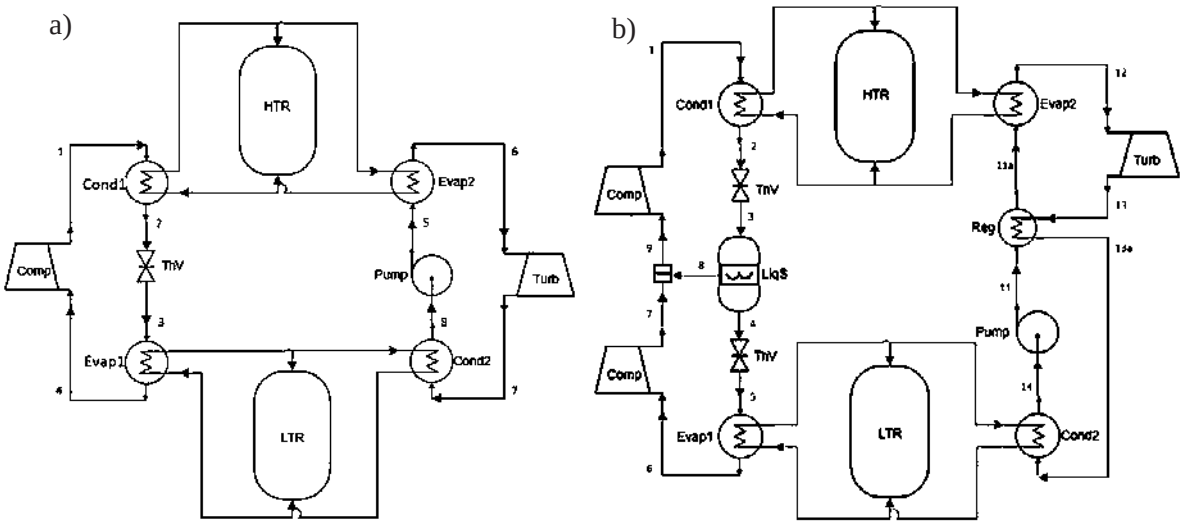

Figure. 1. Proposed Carnot battery, (a) single VCHP and ORC, (b) multi-stage VCHP and regenerative ORC.

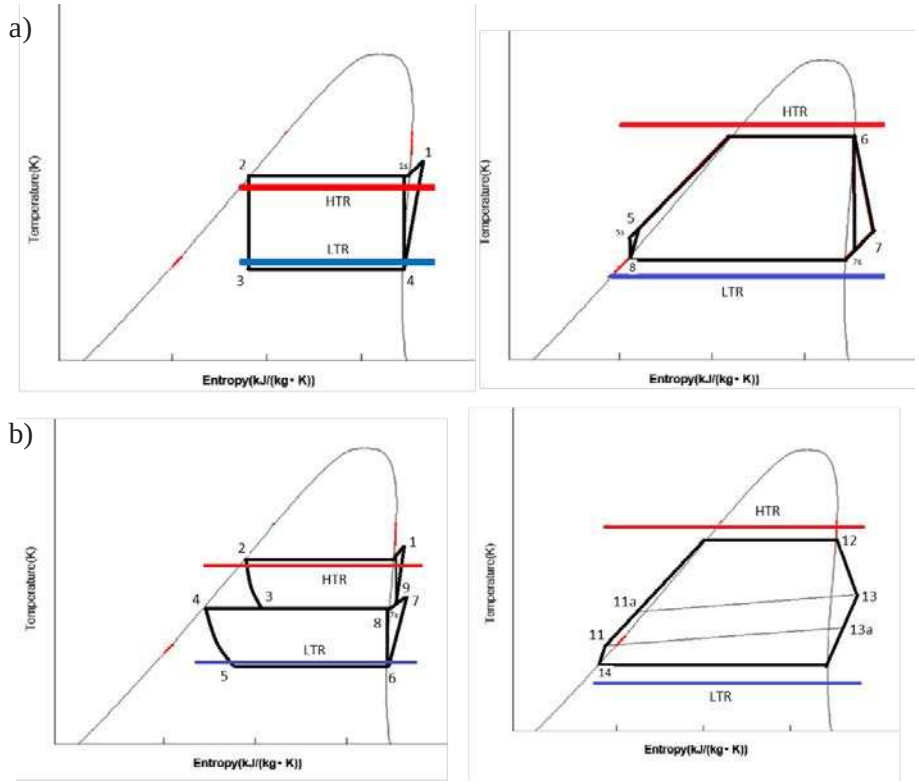

Figure. 2. T-s diagram of the proposed thermodynamic cycles, (a) single VCHP and ORC, (b) multi-stage VCHP and regenerative ORC.

3.2 Vapor Compression Heat Pump (VCHP)

The standard VCHP cycle is shown in Figure 3 In this cycle, almost all processes involve changes in enthalpy in which case, by definition, heat and/or mechanical work (associated with pressure and volume changes) are being exchanged, neglecting changes in kinetic and potential energy of the fluid. From points 4 to 1, the enthalpy of the vapor is increased through compression, and the specific work performed on the system is equal to the enthalpy variation:

$$\dot{W}_{comp} = \dot{m}_f(h_1 - h_4) \quad (2)$$

Between 3 and 4, the fluid cools and condenses in a condenser, releasing heat into the HT reservoir at the condensation temperature:

$$\dot{Q}_{cond1} = \dot{m}_f(h_2 - h_1) \quad (3)$$

Between 3 and 4, the liquid is expanded into the two-phase region. If this happens in a throttling valve, the process is isenthalpic as heat exchanges can be neglected, and no work is performed on the surroundings. This process is highly irreversible, so it can never be isentropic.

$$h_3 = h_2 \quad (4)$$

Finally, the two-phase mixture receives energy in the evaporator and the fluid returns to a gas state, removing heat from the LT reservoir at the evaporation temperature:

$$\dot{Q}_{evap1} = \dot{m}_f(h_3 - h_4) \quad (5)$$

The COP of the heat pump in heating mode is given by the ratio between the heat released from the condenser and the energy consumed in compression. This value is generally greater than unity.

$$COP = \frac{\dot{Q}_{cond1}}{\dot{W}_{comp}} \quad (6)$$

In reality, compression may be non-isentropic and there may be superheating of the vapor at point 1, as well as subcooling of the liquid at point 3. When the compression process is non-isentropic, which is the case with all real compression processes, the specific entropy of the fluid increases from 1 to 2 – this translates into higher compression work for the non-isentropic process. The isentropic efficiency of a compressor $\eta_{s,c}$ can thus be defined as the ratio between the specific work of the compressor in the isentropic scenario and that of the real scenario:

$$\eta_{s,comp} = \frac{(h_{4,s} - h_1)}{(h_4 - h_1)} \quad (7)$$

3.3 Organic Rankine Cycle (ORC)

In the ORC, all processes involve enthalpy changes, as heat and/or mechanical work are exchanged at every step. Between 1 and 2, the vapor is expanded, generating mechanical work – the enthalpy variation is equal to the specific work produced by expansion:

$$\dot{W}_{Turb} = \dot{m}_f(h_7 - h_8), \quad (8)$$

From 2 to 3, the working fluid is condensed, rejecting heat to the LT reservoir:

$$\dot{Q}_{cond2} = \dot{m}_f(h_8 - h_5) \quad (9)$$

Subsequently, the liquid is pumped to the high-pressure level. The enthalpy variation is equal to the specific work performed by the pump; however, this value is very low as the entire process happens in the liquid phase.

$$\dot{W}_{pump} = \dot{m}_f(h_6 - h_5), \quad (10)$$

Finally, the pressurized liquid is heated and vaporized in the evaporator, drawing heat from the HT reservoir and returning to the state of point 1.

$$\dot{Q}_{evap2} = \dot{m}_f(h_7 - h_6) \quad (11)$$

The efficiency of the ORC is given by the ratio between the net energy output, and the heat input at the evaporator:

$$\eta = \frac{\dot{W}_{turb} - \dot{W}_{pump}}{\dot{Q}_{evap2}} \quad (12)$$

As with the vapor compression cycle, the real Rankine cycle involves irreversibilities, some of the most significant being the non-isentropic behavior of the expander and the pump. The isentropic efficiencies of these machines are defined the same way as with the compressor – a ratio between an ideal and a non-ideal amount of work between two states:

$$\eta_{s,turb} = \frac{(h_7 - h_8)}{(h_7 - h_{8,s})} \quad (13)$$

$$\eta_{s,pump} = \frac{(h_{6,s} - h_5)}{(h_6 - h_5)} \quad (14)$$

3.4 Multi-stage VCHP

The two-stage heat pump can be seen as a double loop with two stages of compression and expansion where the top loop considers all working fluid and the bottom loop only partially, as described next

$$\dot{m}_4 = \dot{m}_3 - \dot{m}_8 \quad (15)$$

In the two-stage heat pump it is considered that the pressure ratio in both expanders is equal. The intermediate pressure is then easily calculated by the expression 16 knowing the higher and lower pressures of the cycle.

$$p_3 = \sqrt{(p_1 \cdot p_6)} \tag{16}$$

After the first expansion in the throttle valve, a liquid separator are included to assure that only liquid flows to the second throttle valve while the vapor merges with the working fluid from the bottom loop between the two compressors. The energy balance in the liquid separator is given by:

$$\dot{m}_8(h_3 - h_8) = \dot{m}_4(h_4 - h_3) \tag{17}$$

Similarly, the mixture chamber between the two compressor joins the working fluid from the bottom loop and the saturated vapor after the first expansion.

$$\dot{m}_9 \cdot h_9 = \dot{m}_8 \cdot h_8 + \dot{m}_7 \cdot h_7 \tag{18}$$

The COP of this configuration can be calculated by expression 19.

$$COP = \frac{(h_1 - h_2)}{(h_1 - h_9) + (\dot{m}_4/\dot{m}_3)(h_7 - h_6)} \tag{19}$$

3.5 Regenerative ORC

The inclusion of the intermediate heat exchanger (regenerator), requires to include the energy balance equation in the regenerator, which adds points 11a and 13a.

$$\dot{m}_f(h_{11a} - h_{11}) = \dot{m}_f(h_{13} - h_{13a}) \tag{20}$$

396

3.6 Thermodynamic models

The steady-state models were developed in MATLAB software to compare the system performance of the different cycles. The calculations are based on energy and mass conservation with the following assumptions:

- Pressure drops and heat losses in piping and heat exchangers are neglected, as they are much lower compared with the pressure variation of the cycle.
- Heat exchangers are ideal with a zero-approach temperature difference (pinch = 0°C).
- The evaporation and condensation temperatures of the refrigerant are the same as the temperatures of the heat source (HTR) and sink (LTR), meaning that no superheating and subcooling are used.
- All expansion valves operate adiabatically and provide isenthalpic expansion processes.
- All compressors operate adiabatically with a specific isentropic efficiency of $\eta_{comp} = 0.8$.
- The turbines operate adiabatically with a specific isentropic efficiency of $\eta_{turb} = 0.7$, typical value for volumetric expanders in ORC systems.
- The pumps operate adiabatically with a specific isentropic efficiency of $\eta_{pump} = 0.5$.
- The separators have perfect separation efficiencies and the fluid outlets are saturated vapors and liquids.
- The higher and low temperature reservoir are assumed as latent heat storage type and the temperature remains constant in charging and discharging processes

4 RESULTS AND DISCUSSION

The model exploration started by doing a parametric exploration varying the LTR temperature from 20°C and HTR temperature from the LTR up to the critical temperature of each working fluid tested with a 2°C step. Figure 3 present the results for the working fluid Isopentane, for the COP of the heat pump, the η of the organic Rankine cycle and the last for the roundtrip efficiency for the single VCHP and ORC (left) and multi-stage VCHP and regenerative ORC (right).

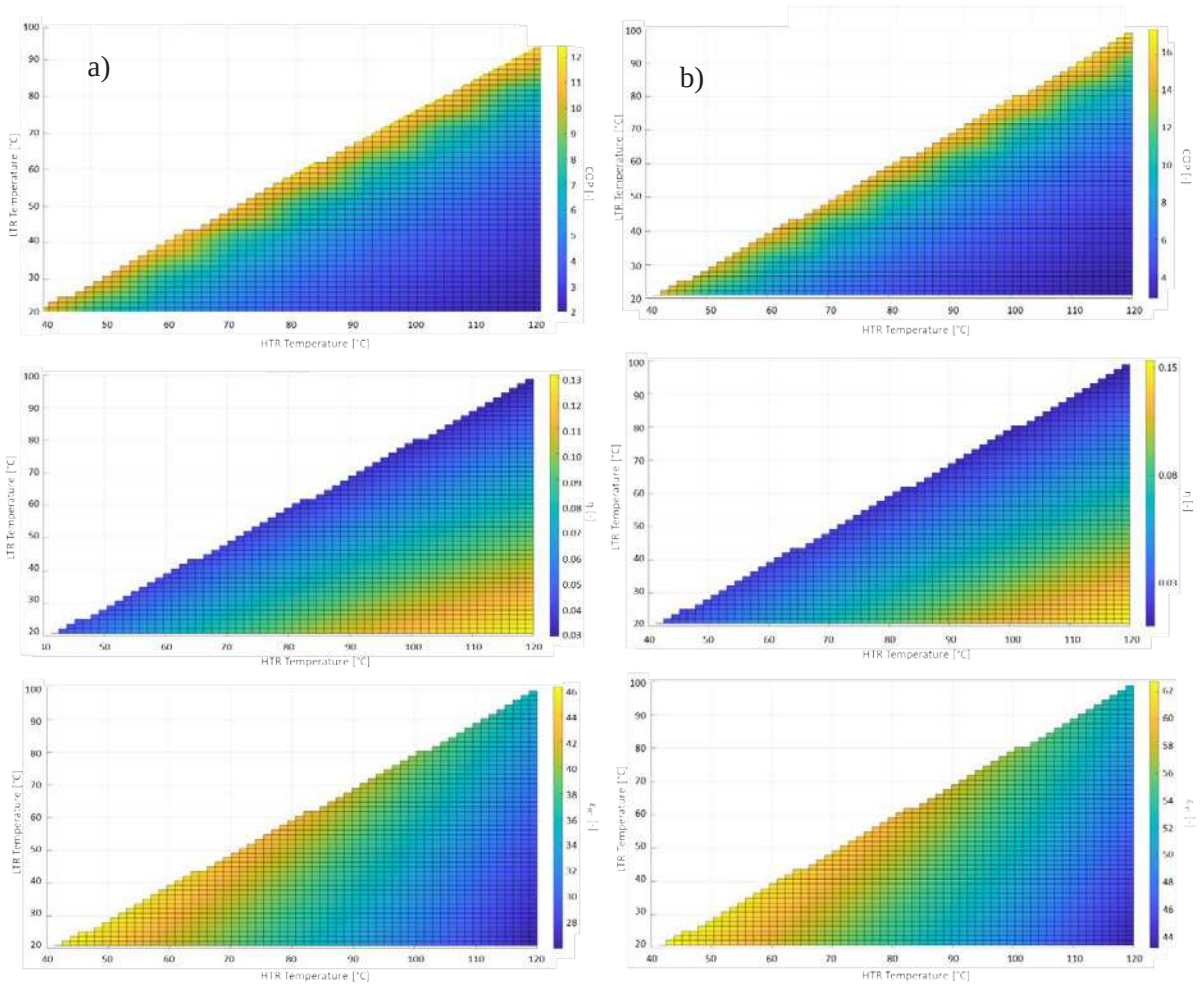

Figure. 3. Exploration results for COP, η_{ORC} and ε_{RT} with several temperatures combinations of HTR and LTR for configuration (a) single VCHP and ORC, (b) multi-stage VCHP and regenerative ORC.

Figure 3 indicates that the COP of the heat pump increases as the temperature difference between the two reservoirs decreases. Specifically, when the hot reservoir temperature is 120 °C and the cold reservoir temperature is 100 °C, the heat pump achieves its highest COP. Conversely, the efficiency of the Organic Rankine cycle is greater when there is a larger gap between the cold and hot reservoir temperatures. The maximum P2P is achieved at lower temperatures and a smaller temperature difference due to the interplay between the COP of the heat pump and the efficiency of the organic Rankine cycle. This relationship is linked to the specific enthalpy variation with temperature, which affects the compression and expansion of the cycles.

The improvement between the previous simple model and the sophisticated model, is notorious, the COP rises from values of 13 to values around 17 which indicates that the multi-stage heat pump can be an addition for this system. The addition of a regenerator in the organic Rankine cycle it is proved to be an improvement to the cycle efficiency, increasing the efficiency from 0,13 to 0,15. The biggest improvement is on the roundtrip efficiency where the increment is 15%.

Finally, a minimum temperature condition of 20°C was added between the two reservoirs and the condition that maximized the roundtrip efficiency of the cycle was obtained. The results for the 6 working fluids considered in this work are showed in Table 2.

Table 2: Best case scenario of roundtrip efficiency for both configurations.

			single VCHP and ORC			multi-stage VCHP and regenerative ORC		
Fluids	T_{HTR} [°C]	T_{LTR} [°C]	**COP [-]**	η_{ORC} [%]	ε_{RT} [%]	**COP [-]**	η_{ORC} [%]	ε_{RT} [%]
R1233zd	40	20	11,15	4.15	46,35	14,87	4,17	62,14
R1234yf	40	20	10,39	3.80	39,43	14,03	3,76	52,86
R11	40	20	11,36	4,23	48,09	15,05	4,20	63,35
R236ea	40	20	10,89	4,06	44,18	14,64	4,11	60,32
R245fa	40	20	11,07	4,13	45,77	14,80	4,15	61,50
Isopentane	40	20	11,14	4,16	46,30	14,90	4,22	62,92

The most favorable outcome is obtained using R11, which yields a roundtrip efficiency of 48% and 63% when the hot reservoir temperature is at 40 degrees and the cold reservoir temperature is at 20 degrees for configurations a) and b), respectively. However, due to its prohibition from use, R11 has only been tested for research purposes. Therefore, the optimal choice of working fluid is either Isopentane or R1233zd, with the main distinction being that the former is flammable.
It is very interesting that the maximum roundtrip efficiency is obtained for the lowest temperature lift allowed. It can be concluded that the COP of the heat pump has more influence than the Rankine cycle efficiency on this parameter. Moreover, this result should be even more noticeable if the heat losses in the reservoirs and temperature differences in the heat exchangers were included in the model as the losses increase with higher temperature differences for the ambient which would further decrease the overall efficiency for the higher temperatures of the reservoirs and be minimal for the temperatures obtained in this optimization.

398

5 CONCLUSIONS

In this study, a preliminary assessment of a Carnot batteries as an innovative electrical energy storage system was made. The study converged in several points with the bibliography already made and presented an interesting new perspective for future studies.
The main conclusions reached in this assessment were:

- The best working fluid (excluding R11) for CBs configurations a) and b) is R1233zd and the isopentane, respectively;
- The addiction of a new stage to the heat pump increased the COP by 22%;
- The ORC efficiency slightly improved with the addiction of the regenerator by 3%;
- The second proposed CB configuration got an improvement on the roundtrip efficiency of 26%.

The COP of the heat pump increases as the temperatures of the thermal reservoirs are closer while the ORC efficiency increases for larger spread of the reservoir's temperatures. Moreover, in all fluids and both configurations the COP of the heat pump surpasses the importance of the ORC efficiency as the highest roundtrip efficiency obtained coincides with the highest COP condition.
Future work will be to sophisticate this model to include temperature differences between the exchangers and reservoirs, taking into account the pitch point, model the components with variable efficiencies instead of assuming constant efficiencies, and include the temperature change in the reservoirs over time at charging and discharging, thus making the model transient.

NOMENCLATURE

CAES	Compressed Air Energy Storage	
CB	Carnot battery	
COP	coefficient of performance	(-)
EES	Electrical Energy Storage	

Subscript

cond	condenser
comp	compressor
evap	evaporator

h	specific enthalpy (kJ/kg)	f	working fluid
HTR	high temperature reservoir	pump	pump
HE	Heat Engines	s	isentropic
LTR	Low temperature reservoir	turb	turbine
$\dot{m}$	mass flow rate (kg/s)		
ORC	Organic Rankine Cycle		
PHS	Pumped Hydro Storage		
Q	Heat flux (kW)		
RES	Renewable energy source		
RT	Roundtrip		
TES	Thermal Energy Storage		
VCHP	Variable Capacity Heat Pump		
W	Work (kW)		
η	ORC efficiency		
ε	RT efficiency		

REFERENCES

Dumont, O., Frate, G. F., Pillai, A., Lecompte, S., De paepe, M., & Lemort, V. (2020). Carnot battery technology: A state-of-the-art review. *Journal of Energy Storage*, *32*. https://doi.org/10.1016/j.est.2020.101756

Dumont, O., & Lemort, V. (2020). Mapping of performance of pumped thermal energy storage (Carnot battery) using waste heat recovery. *Energy*, *211*. https://doi.org/10.1016/j.energy.2020.118963

Eppinger, B., Steger, D., Regensburger, C., Karl, J., Schlücker, E., & Will, S. (2021). Carnot battery: Simulation and design of a reversible heat pump-organic Rankine cycle pilot plant. *Applied Energy*, *288*. https://doi.org/10.1016/j.apenergy.2021.116650

Frate, G. F., Ferrari, L., & Desideri, U. (2020). Rankine carnot batteries with the integration of thermal energy sources: A review. In *Energies* (Vol. 13, Issue 18). MDPI AG. https://doi.org/10.3390/en13184766

Gallo, A. B., Simões-Moreira, J. R., Costa, H. K. M., Santos, M. M., & Moutinho dos Santos, E. (2016). Energy storage in the energy transition context: A technology review. In *Renewable and Sustainable Energy Reviews* (Vol. 65, pp. 800–822). Elsevier Ltd. https://doi.org/10.1016/j.rser.2016.07.028

Jafari, M., Botterud, A., & Sakti, A. (2022). Decarbonizing power systems: A critical review of the role of energy storage. In *Renewable and Sustainable Energy Reviews* (Vol. 158). Elsevier Ltd. https://doi.org/10.1016/j.rser.2022.112077

Nadeem, F., Hussain, S. M. S., Tiwari, P. K., Goswami, A. K., & Ustun, T. S. (2019). Comparative review of energy storage systems, their roles, and impacts on future power systems. In *IEEE Access* (Vol. 7, pp. 4555–4585). Institute of Electrical and Electronics Engineers Inc. https://doi.org/10.1109/ACCESS.2018.2888497

Steinmann, W. D., Bauer, D., Jockenhöfer, H., & Johnson, M. (2019). Pumped thermal energy storage (PTES) as smart sector-coupling technology for heat and electricity. *Energy*, *183*, 185–190. https://doi.org/10.1016/j.energy.2019.06.058

Weiss, A. P., & Zinn, G. (2016). Micro Turbine Generators For Waste Heat Recovery And Compressed Air Energy Storage. *15th Conference on Power System Engineering, Thermodynamics & Fluid Flow - ES 2016*, 1–9.

Weitzer, M., Müller, D., Steger, D., Charalampidis, A., Karellas, S., & Karl, J. (2022). Organic flash cycles in Rankine-based Carnot batteries with large storage temperature spreads. *Energy Conversion and Management*, *255*. https://doi.org/10.1016/j.enconman.2022.115323

ACKNOWLEDGEMENT

This work is funded by National Funds through the FCT - Fundação para a Ciência e Tecnologia, I.P., under the scope of the project 2022.05282.PTDC.

ORC SEVILLE 2023
7th International Seminar on O.R.C. Power Systems

© 2024 Editorial Universidad de Sevilla. Este es un artículo de acceso abierto distribuido bajo los términos de la licencia de uso y distribución Creative Commons (BY-NC-ND 4.0)

DOI: https://dx.doi.org/10.12795/9788447227457_68

The potential of CO_2-Plume Geothermal (CPG) Systems for CO_2 component manufacturers: opportunities and development needs

Christopher Schifflechner[1,*], Jasper de Reus[2], Hartmut Spliethoff[1], Martin O. Saar[2,3], Sebastian Schuster[4], Dieter Brillert[4]

[1] *Chair of Energy Systems, School of Engineering and Design, Technical University of Munich, Garching, Bavaria, Germany*
[2] *Chair of Geothermal Energy and Geofluids, Department of Earth Sciences, ETH Zurich, Sonneggstrasse 5, 8092 Zurich, Switzerland*
[3] *Department of Earth and Environmental Sciences, 116 Church Street SE, Minneapolis, MN 55455, USA*
[4] *Chair of Turbomachinery, University of Duisburg-Essen, 47057 Duisburg, Germany*

*Corresponding Author: c.schifflechner@tum.de

ABSTRACT

Subsurface reservoirs play an important role in decarbonizing the energy sector, be it through geothermal energy production or carbon capture and storage (CCS). In recent years, there has been an increasing interest in CO_2-Plume Geothermal (CPG) systems, which combine CCS with geothermal, using CO_2 instead of water as a subsurface heat and pressure energy carrier. As explained later in the paper, applying CO_2 as a subsurface working fluid can be more efficient than water as it has a higher mobility (inverse kinematic viscosity) and as its large thermal expansion coefficient results in a thermosiphon effect that reduces the pumping power required. CO_2 can also directly be utilized in a turbine for power generation. Furthermore, since CPG systems are added to full-scale CO_2 Capture and Sequestration operations, all of the initially injected CO_2 is ultimately stored. CPG therefore constitutes of both CO_2 Capture Utilization as well as Storage.
This paper assesses the huge technical potential of the CPG technology, identifying a potentially highly relevant market for CO_2 equipment manufacturers and discusses the current research demand, based on the current state of the art of CO_2 equipment. Both temperature and pressure levels are significantly lower than CO_2 turbine designs investigated and proposed so far for other applications, such as waste heat recovery. Together with CPG-specific requirements, due to produced fluid impurities, it becomes evident that significant further development efforts are still necessary regarding future commercial CPG CO_2 turbines.

1 INTRODUCTION AND SCOPE OF THIS PAPER

A fundamental and rapid transformation of the global energy system is necessary to limit global warming to 1.5°C or at least 2.0°C. This includes a major expansion of various renewable energy sources such as solar, wind and geothermal. At the same time, almost all of the IPCC transformation pathways to limit global warming to 1.5°C require the future use of large-scale carbon capture and storage (CCS) technologies (Greig and Uden, 2021). Although the expansion of renewable energies and the development of a CCS infrastructure can, of course, happen separately, a technology that can combine both necessary aspects into one concept would be of great benefit. Such a true CO_2 Capture Utilization and Storage (CCUS) concept can enhance the economic performance of CCS projects since it provides energy in the form of electricity and/or heat to achieve revenues. CO_2-Plume Geothermal (CPG) systems, which will be explained in more detail in the following chapter, can combine both aspects of a true CCUS system: large-scale and ultimately long-term to permanent sequestration of all of the initially injected CO_2 and utilization of the CO_2 in form of electricity generation with a CO_2 turbine (Randolph and Saar, 2011). Applying CO_2 as an energy carrier for geothermal systems has various advantages as discussed in Chapter 2.

400

Parallel to the increasing interest in the use of CO_2 as an energy carrier in geothermal systems, it is also strongly investigated as an attractive working fluid for closed-loop power plant processes, for example, for industrial waste heat utilization (White et al., 2021). The growing interest can also be seen in the increasing number of large-scale experimental activities for CO_2 compressors (Hacks et al., 2018) and turbines (Moore et al., 2018). Therefore, on the one hand, a strong commercialization drive exists for both CO_2 turbines and CO_2 compressors (for both sCO_2 power plant cycles and CO_2 injection projects). On the other hand, especially under the operation conditions of CO_2 turbines, strong deviations between the temperature and pressure levels at the turbine inlet and outlet exist. Both pressure and temperature at the turbine inlet are significantly lower than for the standard sCO_2 system (e.g. for waste heat recovery) and the CO_2 within the open CPG system will contain impurities, for example, in the form of liquid water. Thus, while the CO_2 turbines currently being developed and tested provide a suitable starting point, they may not be directly applicable to potential future CPG power plants without further development.

This paper addresses several aspects: First, we provide a compact overview of the CPG technology and the resulting operational conditions for CO_2 turbines. Second, we assess the technical potential of the CPG technology, identifying a potentially highly relevant market for CO_2 equipment manufacturers. Finally, we discuss the current research demand, based on the current state of the art of CO_2 equipment, considering the significantly different operational characteristics within a CPG system, compared, for example, with an industrial waste heat recovery sCO_2 power plant. Thus, we present, for the first time, a compact overview about CPG's market potential and future research demand, with a focus on the CPG surface equipment. Although no direct new numerical results are presented here, this work contributes to science and industry by pointing at avenues for potential future research activities and economic developments concerning the entire CO_2 equipment market.

2 WORKING PRINCIPLE OF CPG

The basic principle of the CPG technology is shown in Figure 1. Similar as in CCS, CO_2 is injected in a naturally permeable reservoir at e.g. 2 to 5 km depth. However, in case of CPG the geothermally heated CO_2 is then back-produced, expanded through a turbine, cooled, and re-injected into the original CO_2 storage reservoir so that all CO_2 is ultimately permanently stored underground (Randolph and Saar, 2011). The primary advantage of using CO_2, compared to water, is its favorable mobility (the inverse of kinematic viscosity), enabling higher mass flows through the reservoir than for liquid water, all else being equal. This mobility effect dominates over the reduced specific heat capacity of sCO_2 compared to H_2O at relevant reservoir pressures and temperatures, thereby increasing the geothermal energy extracted from the subsurface. Favorably, even at relatively shallow reservoir depths, CPG power generation can take place directly in a turbine, while a conventional water/brine geothermal system would require an Organic Rankine Cycle (ORC) as a binary cycle. Another benefit from using CO_2 is the thermosiphon effect (Adams et al., 2014), due to the large difference in density of cold CO_2 in the injection well as opposed to the hot CO_2 in the production well. This results in a difference in gravitational head that contributes to the pressure differential in the reservoir required to make the CO_2 flow, leading to reduced pumping requirements to circulate the CO_2. The lower fluid densities and gas-like properties in the production well lead to higher wellhead pressures compared to H_2O. After the expansion in the CO_2 turbine, the CO_2 is cooled and (depending on the pressure level) condensed for re-injection into the original reservoir, so that ultimately all CO_2 is permanently stored. Figure 2 visualizes the general temperature-entropy and temperature-density diagram of a CPG system. As the CO_2 produced from the reservoir is directly expanded in the CO_2 turbine, liquid water and other fluids are likely to enter the turbine along with the CO_2. While such liquid water in a sCO_2 turbine constitutes a potential problem, it is not unsurmountable, as the density of liquid water of about 1000 kg/m^3 is only about a factor of 2.5 higher than the typical density of sCO_2 of about 400 kg/m^3 when produced from typical reservoirs considered for CPG (Fleming et al., 2020). As the fluid flowrate through the turbine should be maximized, the water is ideally not removed before the turbine. Thus, a goal of sCO_2 turbine development for CPG power plants is to develop turbines that can tolerate significant amount of liquid water, together with mostly sCO_2. The free-phase liquid water can stem from two sources, namely 1)

401

from flow from the reservoir into the production well and 2) from exsolution of water from the sCO_2 in the production well, as the sCO_2 rises in the production well and as pressure and temperature decline, decreasing the water solubility index in the sCO_2. This water exsolution is an exothermic reaction, providing up to 41% additional power to CPG power plants under the conditions investigated by Fleming et al. (2020). In summary, CPG power plants yield increased thermal (and thus electric) power, compared to groundwater-based geothermal power plants due to 1) the higher mobility of sCO_2, compared to water, under typical CPG-reservoir conditions, more than making up for the reduced specific heat capacity of sCO_2 compared to water under those conditions, 2) the thermosiphon effect and 3) exothermic water exsolution from sCO_2 in the production well during the ascent of sCO_2 that has water dissolved in it, as is typically the case when water-bearing geologic reservoirs are used for CCS and CPG operations.

Since most of the current publications focus on the conceptual investigation of the overall system and the impact of the subsurface conditions (permeability, etc.), detailed investigations and designs regarding the surface component have not been carried out. E.g. regarding the isentropic turbine efficiency, most recent studies assume a value of 78 % (e.g. Adams et al. (2021b) and Ezekiel et al. (2020)), which was initially introduced in one of the first CPG-specific publications by Adams and Kuehn (2012). Gladysz et al. (2020) assume a turbine efficiency of 85 %. For the CO_2 cooler/condenser, an approach temperature of 7 K is one of the most commonly used assumptions (Adams et al., 2015). The actual extracted heat from the geothermal reservoir depends mainly on the number of wells and the corresponding CO_2 mass flow rate (cf. Section 3). However, several studies report the expected thermal efficiency of CPG systems. E.g. Hansper et al. (2019) and Schifflechner et al. (2022) report thermal efficiencies between 5 and 8 %, indicating the ratio between the achievable net power output and extracted heat from the geothermal reservoir.

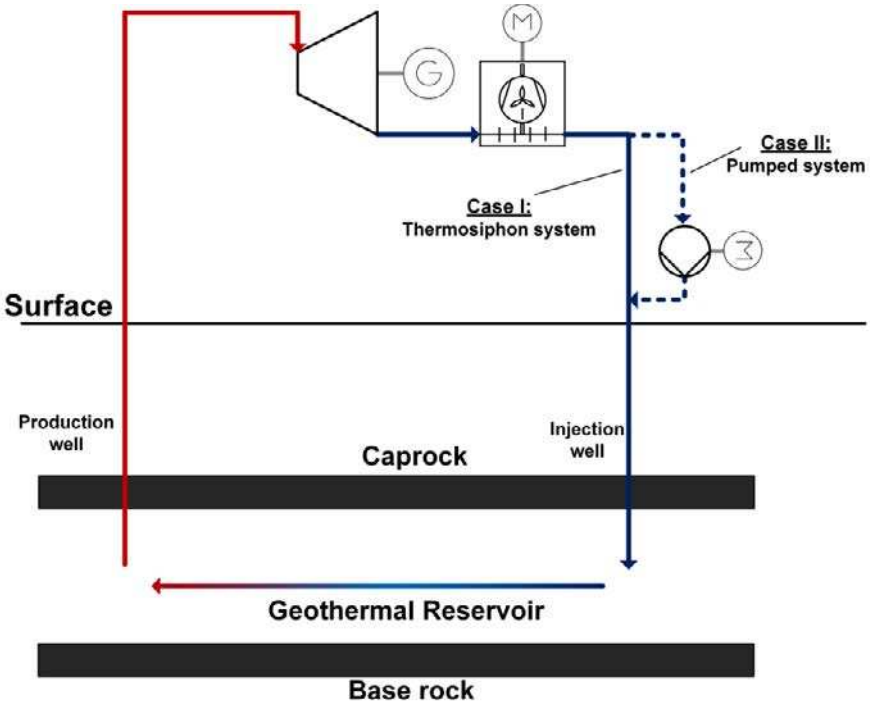

Figure 1: General working principle of a CPG system

402

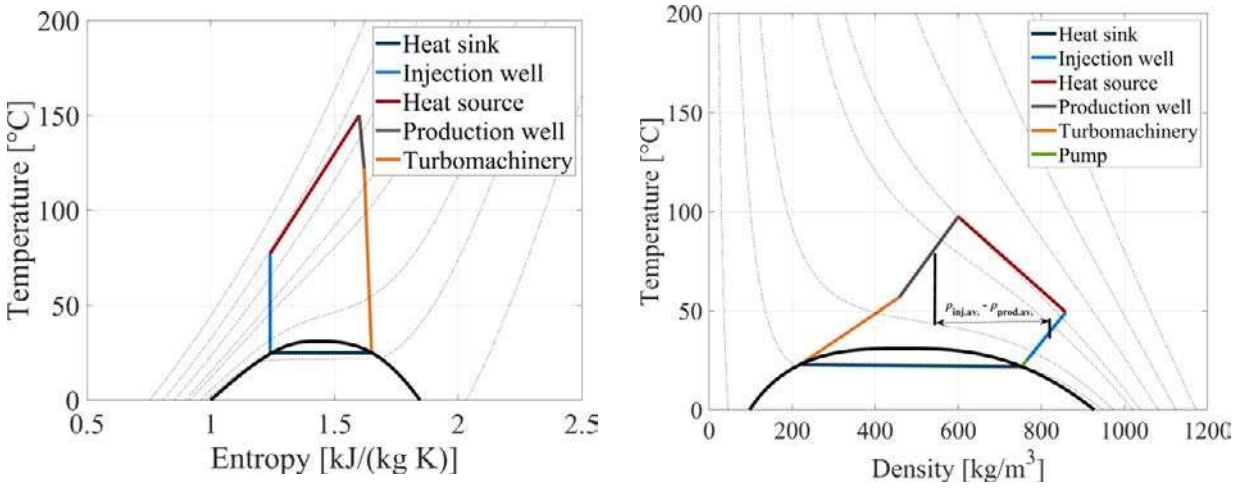

(a) (b)

Figure 2: General (a) temperature-entropy of a thermosiphon system and (b) temperature-density diagram of a pumped CPG system

3 THE POTENTIAL OF CPG

CPG is applicable in a broad range of geologic reservoirs where geologic CO_2 storage is considered, ranging from depleted oil and gas fields (both on- and offshore) to, in particular, deep saline formations. (Adams et al., 2021a) demonstrate that using CO_2 as a subsurface heat extraction fluid, compared to water, decreases the cost of geothermal electricity across most geologic conditions. The reservoir temperature and transmissivity, which is the product of reservoir permeability and thickness, are the most sensitive parameters that drive the performance of CPG. The CPG sensitivity analysis by Ezekiel et al. (2021) for CPG operations after enhanced gas recovery (EGR) also shows that, as expected, high reservoir temperatures are critical for geothermal power generation. However, they also show that the next most sensitive CPG parameters after temperature are the well diameter, followed by the ambient air heat rejection temperature, the permeability anisotropy, the horizontal permeability and finally the relative permeability of the geologic reservoir.

403

Comparing the levelized cost of electricity (LCOE) for both energy carriers (sCO_2 versus water) at different reservoir depths (and thus different hydrostatic fluid pressures) and reservoir transmissivities reveals that the favorability of CO_2 depends on several factors, such as depth (Adams et al., 2021a). At shallower reservoir depths (i.e. lower reservoir temperatures and pressures) and a given transmissivity, the LCOE of CPG is lower than that of H_2O. At greater reservoir depths (i.e. higher reservoir temperatures and pressures), the difference reduces, but overall more power is produced, while the LCOE reduces further. While a single well pattern produces a power output of a few MW_e (Adams et al., 2015), a larger field development, combining numerous such well patterns, results in a much larger combined power output in the range of several dozen MW_e or more (Hansper et al., 2019). The power is produced by multiple smaller CO_2 turbines distributed over the areal extent of the field (which is multiple square kilometers) or from a large-scale CO_2 turbine at a central power plant. The optimal mass flow rate of the CPG system depends also on several factors, such as reservoir transmissivity, reservoir depth or well diameters. As shown exemplary for one well pair in Figure 3, there is one optimal CO_2 mass flow rate resulting in the highest possible net power output. While higher mass flow rates increase on the one hand the power generation potential, the available turbine pressure differential decreases and the power demand for the cooling system increases. Thus, high mass flow rates are not necessarily providing the highest possible power output.

Regarding the thermo-economic performance of CPG systems, the LCOE can only be estimated with high uncertainties since a first real-world large-scale CPG demonstrator is still missing. Furthermore, due to the significant amounts of CO_2 required for such systems, the transportation and potential

purchase costs or achievable revenues by storing the CO_2 will have a pivotal impact on the economic performance. Due to high uncertainties regarding future CO_2 prices, these costs are currently neglected in most papers (e.g. Hansper et al., 2019). Wang et al. (2022) present a thermo-economic optimization of a large-scale direct supercritical CO_2 electric power generation system, while not calling it directly CPG. Their findings for a depth of 2500 m indicate achievable LCOE between 190 and 170 $/MWh_e$, depending on the plant capacity. Their economic models suggest rather similar investment costs for both the surface plant capital and geothermal wells. For a sCO_2-EGS system, Gladysz et al. (2020) present a detailed thermo-economic evaluation. Depending on the particular scenario, the share of the surface equipment on the overall investment costs is between 20 and 55 %. Langenfeld and Bielicki (2017) investigate aquifers in Wyoming (United States) for their thermo-economic potential for CPG application. They identified more than 80 promising aquifers with achievable LCOEs between 200 and 250 $/MWh_e$. McDonnell et al. (2020) evaluate the potential performance of a CPG site in a sandstone reservoir in the West of Germany. For the base case scenario they report achievable LCOE of 60 $/MWh_e$ while considering also potential supporting grants by the government and additional revenues due to the CO_2 storage. Hansper et al. (2019) report achievable LCOE of a CPG brownfield system between 120 and 200 170 $/MWh_e$. Sudhoff et al. (2019) evaluate the achievable LCOE for different numbers of wells and reservoir types. The results indicate a quite large range between 36 and 194 $/MWh_e$ with minimal achievable LCOE of 36 $/MWh_e$.

A study of the saline formations in the United States suggests an economic potential of 200 GW_e considering greenfield projects (no existing infrastructure assumed) and LCOE below 100 $/MWh_e$ (Adams et al., 2021a). Considering that the currently installed worldwide ORC capacity is around 4 GW_e (Wieland et al., 2023), CPG has the potential to be a highly relevant market for manufacturers of sCO_2 turbines, compressors and other relevant equipment such as heat exchangers or cooling/condensing towers.

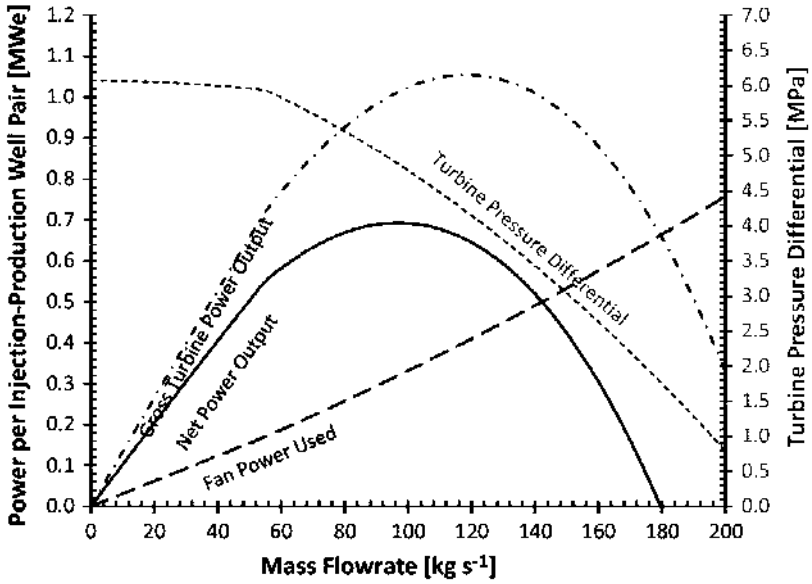

Figure 3: Exemplary power output of a direct CO_2 thermosiphon (un-pumped) system for one injection–production well pair (figure taken from Adams et al. (2015))

4 OPERATIONAL CHARACTERISTICS AND RESEARCH DEMAND OF SURFACE EQUIPMENT FOR COMMERCIAL CPG SYSTEMS

The recent review by White et al. (2021) provides a detailed overview of the current general trends and research demands for sCO_2 power systems. However, the review is not addressing CPG and its individual requirements and challenges. Considering the limited space for the work here, the following section focuses on the operational characteristics and research demands for CPG-specific surface power plant equipment.

The sCO_2 turbine for the CPG process needs to be designed for the thermal conditions at the design point, has to cope with load point variations throughout the year and with the composition of the fluid produced from the well, depending on the level of processing upstream of the turbine, as discussed briefly at the end of Section 2. The design point of the turbine in terms of pressure and temperature varies with the reservoir depth with wellhead exit pressures between 100 bar to 230 bar and wellhead exit temperatures between 45°C to 130°C (see Figure 4). The condenser determines the back-pressure, which is normally around 57 bar to 62 bar, depending also on the approach temperature of the cooling/condensing tower system. For a reservoir depth of 5 km, the sCO_2 expansion process results in an isentropic enthalpy drop of 56 kJ/kg. A typical radial turbine design can convert this enthalpy difference into mechanical work within one stage, with a circumferential velocity of around 240 m/s. The associated centrifugal force induces a mechanical strain well below typical steel yield strengths.
The circumferential Mach number gives a good indication for aerodynamic design aspects. In this case, the circumferential Mach number is close to unity (Ma = 0.96) at the impeller inlet, thus, requiring a careful aerodynamic design. A two-stage design might be desirable to achieve higher flexibility, such as to cope with decreasing condenser pressures.

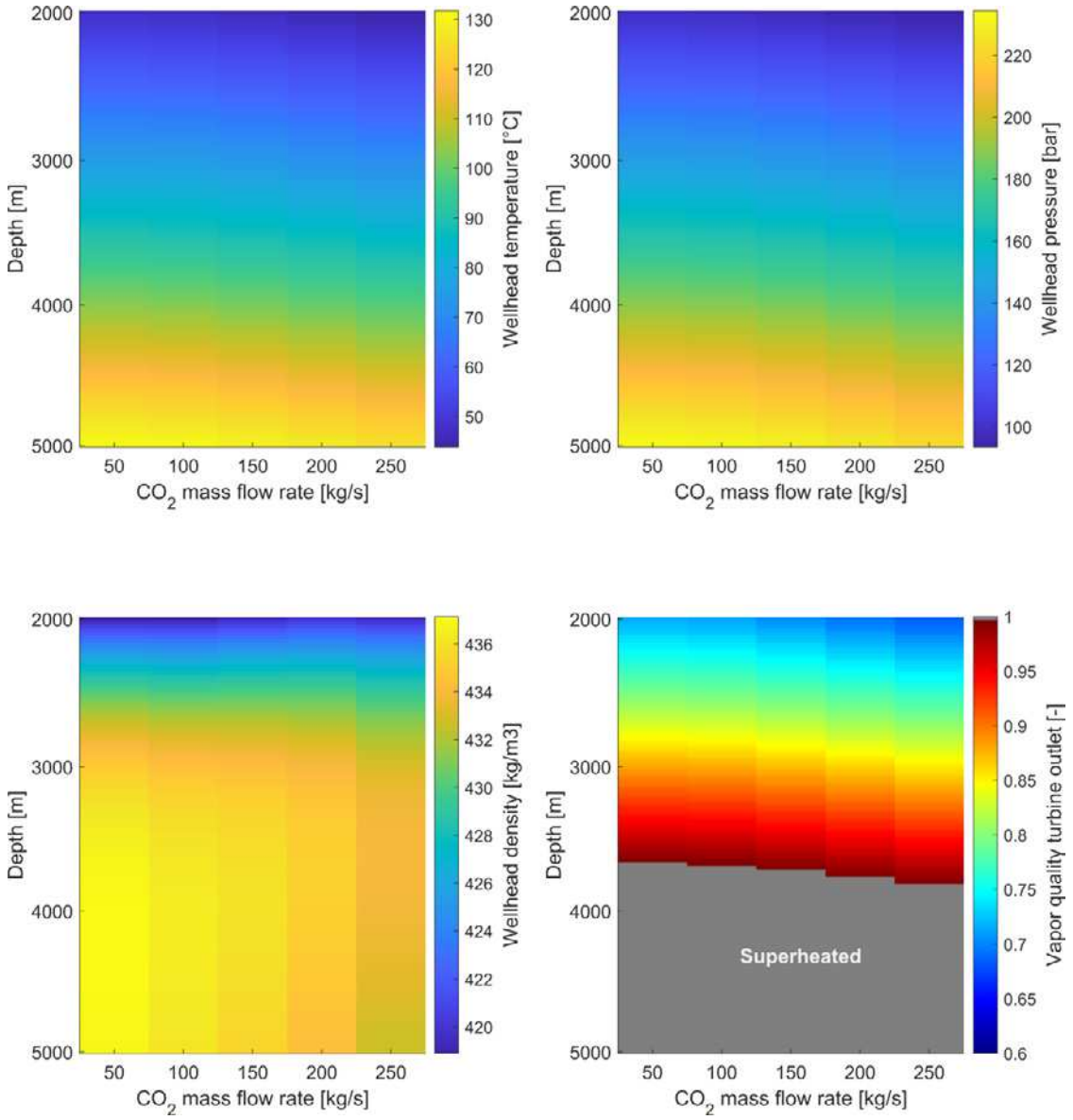

Figure 4: Summary of the turbine operating conditions, considering the turbine inlet temperature, turbine inlet pressure, turbine inlet density and turbine outlet conditions.

With the given mass flowrate, an initial design can be computed, exemplarily for a potential typical mass flowrate of 150 kg/s (cf. Adams et al. (2015)) and for a reservoir depth of 5 km for the design of an sCO_2 turbine. For this case, a typical one-stage radial turbine design has a rotational speed of 23'000 rpm to 42'000 rpm and an impeller diameter between 96 mm to 155 mm, meaning that the design has certain degrees of freedom. Both the turbine rotational speed and its size are feasible and the margins to rotodynamic, structural dynamics and manufacturing limits are large enough to cope with the lowest and largest assumed mass flowrates. A multi-stage axial turbine is also possible. The volume flowrate changes marginally for reservoirs at shallower depths, however, the enthalpy differences during expansion in the turbine decrease from 56 kJ/kg to 11 kJ/kg (cf. Schifflechner et al. (2023)). This results in a lower rotational speed of around 10'000 rpm. Next to the inlet pressure conditions, the turbine inlet temperature can also strongly impact the achievable mass-specific power output. Considering the same in- and outlet pressures of a turbine, a higher inlet temperature results in a significantly higher turbine outlet power.

As outlined later in the paragraph, the load point in terms of mass flowrate and/or turbine back pressure can change through the year and over the years as reservoir temperatures and pressures decline due to energy extraction. Using a wet-bulb cooling tower might ensure a condensation of the CO_2 over the whole year, however, this may come with a water demand that could be economically and environmentally challenging in dry areas. Thus, while air-cooled coolers/condensers, often employed by geothermal power plants, have no water consumption, they can only cool but not condense the CO_2 during certain periods in the summer, depending also on the climate at a given geographic power plant location, affecting not only the turbine outlet conditions but also the performance characteristic of the overall CPG system itself. Therefore, to extract a maximum of available work with the turbine, measures to adjust the turbine for seasonally changing heat rejection temperature conditions must be taken. A combination of speed control and adjustable guide vanes gives flexibility but comes with investment cost, especially for the speed control. Current research suggests that system design codes with integrated turbomachinery models allow determining the required control interventions and help to determine the trade-off between investment for control measures and increased work output. When considering turbine costs it is also critical to keep in mind that turbine components (e.g. blades) may degrade relatively quickly in open power loop systems (i.e. CPG), where impurities (e.g. liquid water, but potentially also H_2S) are produced from the geologic reservoir along with the CO_2. While these impurities (which have to be removed before CO_2-reinjection to maintain a high injectivity index of the CO_2 injection well) could be removed upstream of the turbine, this comes with power generation penalties (see also end of Section 2).

Other aspects to consider are the possibilities and challenges associated with an expansion into the two-phase CO_2 flow region as well as the composition of the fluid leaving the well and eventually entering the turbine. Expanding into the two-phase flow region gives the system designer more freedom during the design phase. Expanding into the two-phase flow region can also allow higher enthalpy drops in the turbine. For example, for the 2 km deep reservoir case, already 35 % of the CO_2 is condensed at the turbine outlet. Another possible scenario can be decreasing ambient temperatures, which lower the condenser back pressure accordingly. As shown in Figure 4, the vapor quality of the CO_2 at the turbine outlet increases with higher reservoir depths and is superheated for deep CPG systems. Thus, the two-phase expansion and its potential impact on the turbine design is mainly relevant for rather shallow CPG systems.

A certain expansion into the two-phase flow region - commonly quantified with the subcooling - can be allowed without any harmful concomitants. A further reduction of the outlet pressure results in the formation of droplets accompanying the expansion into the two-phase region. These droplets might lead to liquid film formation on the rotor and the formation of so-called secondary droplets that lead to droplet impingement erosion. Little knowledge is available for condensation at high expansion rates as typical for turbines at high pressures, even less for CO_2 and only a few studies exist for radial turbines. Research is required on this process that eventually leads to design guidelines. Such design guidelines might limit the allowed subcooling or provide measures to prevent droplet erosion, e.g., hardening of

the steel in certain areas where droplet impact is to be expected. The impact of liquid in any form in the fluid leaving the well on the turbines must be treated carefully. At the current state of research, the liquid needs to be separated before the fluid enters the turbine, reducing the turbine mass flowrate and thus power output (see also end of Section 2). The separation process is associated with an inevitable pressure loss which can be avoided if the turbine withstands the liquid. Research suggests that distinct regions with droplet erosion can be identified in which steel hardening might reduce the erosion process to an acceptable value (Wittmann et al., 2022). Thus, while the presence of e.g. natural water increases the CPG surface power plant complexity, its exothermic exsolution in the production well can result in significantly higher wellhead temperatures and pressures, increasing the achievable power output of the system (Fleming et al., 2020). Non-condensable gases, such as methane, potentially produced (in small quantities) during CPG operations after enhanced gas recovery (EGR) in the fluid are not harmful to the turbine but change the enthalpy drop for the given pressure ratio. Such variations in the fluid composition can be mitigated with the control interventions.

The previous section provides a summary of the special operating conditions of potential CPG specific turbines. Considering the stated existing CO_2 turbine designs, summarized in the recent review by White et al. (2021), highlights that the CPG application is characterized by significantly lower turbine temperatures and pressures than those addressed in the literature so far. Thus, while the current research activities on CO_2 turbines for other applications, such as waste heat recovery, provide a profound basis for the development of CPG-specific CO_2 turbines, future research activities are required, as the existing designs and activities cannot be directly applied to a CPG system due to the different operational conditions and the likely impurities within the CO_2 stream.

5 CONCLUSION & OUTLOOK

This work presents a compact overview of the working principle of the CPG technology and its technical potential. The operational conditions, resulting requirements, and research demand for CPG-suitable CO_2 turbines in particular, are discussed. The main findings are:

- CPG can combine both aspects of a true CCUS system: large-scale storage of all CO_2 and utilization of the CO_2 in the form of electricity generation with a CO_2 turbine.
- CPG can be applied in a wide range of subsurface settings, ranging from saline formations to depleted oil and gas fields. Techno-economic analyses indicate a large potential application field for this technology (estimated at several hundred GW_e), translating to a sizable market for CO_2 equipment.
- The design point of the turbine in terms of pressure and temperature varies with the reservoir depth with wellhead exit pressures between 100 bar to 230 bar and with wellhead exit temperatures between 45°C to 130°C.
- Both temperature and pressure levels are significantly lower than CO_2 turbine designs investigated and proposed so far for other applications, such as waste heat recovery. Together with CPG-specific requirements, due to produced fluid impurities, it becomes evident that significant further development efforts are still necessary regarding future commercial CPG CO_2 turbines.

First, large-scale demonstration projects are necessary regarding the potential future market uptake of CPG. Recently, a proof of concept of a stable circulation due to the CO_2 thermosiphon in a former oil and gas field was reported (Böhmer et al., 2022). Over 25 days a stable pressure difference of 14 bar between production and reinjection well was achieved. While this step is an important first milestone for a future commercial, large-scale CPG projects, a larger field demonstration is the next step in de-risking commercial CPG operations. A joint industry-academic CPG consortium has been initiated by the ETH Zurich for this purpose.
Next to reliable base load power generation, CPG power plants can also be applied for combined heat and power generation (Schifflechner et al., 2022) or to provide flexible power generation (Fleming et al., 2022), thereby also supporting only intermittently available energy resources, such as wind and

solar power (van Brummen et al., 2022). Therefore, especially considering CPG systems in Central Europe, these advanced conceptual aspects should be addressed in more detail within future studies.

ACKNOWLEDGEMENT

Regarding the contribution of the Technical University of Munich, funding from the Bavarian State Ministry of Science and the Arts in the framework of the Project Geothermal-Alliance Bavaria is gratefully acknowledged.

REFERENCES

Adams, B., Ogland-Hand, J., M. Bielicki, J., Schädle, P., Saar, M., 2021a. Estimating the Geothermal Electricity Generation Potential of Sedimentary Basins Using genGEO (The Generalizable GEOthermal Techno-Economic Simulator).

Adams, B.M., Kuehn, T.H., 2012. The Complementary Nature of CO2-Plume Geothermal (CPG) Energy Production and Electrical Power Demand, in: Volume 6: Energy, Parts A and B. ASME 2012 International Mechanical Engineering Congress and Exposition, Houston, Texas, USA. 09.11.2012 - 15.11.2012. American Society of Mechanical Engineers, pp. 1791–1798.

Adams, B.M., Kuehn, T.H., Bielicki, J.M., Randolph, J.B., Saar, M.O., 2014. On the importance of the thermosiphon effect in CPG (CO2 plume geothermal) power systems. Energy 69, 409–418. https://doi.org/10.1016/j.energy.2014.03.032.

Adams, B.M., Kuehn, T.H., Bielicki, J.M., Randolph, J.B., Saar, M.O., 2015. A comparison of electric power output of CO2 Plume Geothermal (CPG) and brine geothermal systems for varying reservoir conditions. Applied Energy 140, 365–377. https://doi.org/10.1016/j.apenergy.2014.11.043.

Adams, B.M., Vogler, D., Kuehn, T.H., Bielicki, J.M., Garapati, N., Saar, M.O., 2021b. Heat depletion in sedimentary basins and its effect on the design and electric power output of CO2 Plume Geothermal (CPG) systems. Renewable Energy 172, 1393–1403. https://doi.org/10.1016/j.renene.2020.11.145.

Böhmer, F., Schäfer, D., Wechsung, M., Szelenyi, J., 2022. NextGen Geothermal Power (NGP) - A new sCO2 based geothermal concept, in: Proceedings of the European Geothermal Congress 2022, Berlin.

Ezekiel, J., Ebigbo, A., Adams, B.M., Saar, M.O., 2020. Combining natural gas recovery and CO2-based geothermal energy extraction for electric power generation. Applied Energy 269, 115012. https://doi.org/10.1016/j.apenergy.2020.115012.

Ezekiel, J., Kumbhat, D., Ebigbo, A., Adams, B.M., Saar, M.O., 2021. Sensitivity of Reservoir and Operational Parameters on the Energy Extraction Performance of Combined CO2-EGR–CPG Systems. Energies 14, 6122. https://doi.org/10.3390/en14196122.

Fleming, M.R., Adams, B.M., Kuehn, T.H., Bielicki, J.M., Saar, M.O., 2020. Increased Power Generation due to Exothermic Water Exsolution in CO2 Plume Geothermal (CPG) Power Plants. Geothermics 88, 101865. https://doi.org/10.1016/j.geothermics.2020.101865.

Fleming, M.R., Adams, B.M., Ogland-Hand, J.D., Bielicki, J.M., Kuehn, T.H., Saar, M.O., 2022. Flexible CO2-plume geothermal (CPG-F): Using geologically stored CO2 to provide dispatchable power and energy storage. Energy Conversion and Management 253, 115082. https://doi.org/10.1016/j.enconman.2021.115082.

Gladysz, P., Sowiżdżał, A., Miecznik, M., Pajak, L., 2020. Carbon dioxide-enhanced geothermal systems for heat and electricity production: Energy and economic analyses for central Poland. Energy Conversion and Management 220, 113142. https://doi.org/10.1016/j.enconman.2020.113142.

Greig, C., Uden, S., 2021. The value of CCUS in transitions to net-zero emissions. The Electricity Journal 34, 107004. https://doi.org/10.1016/j.tej.2021.107004.

Hacks, A.J., Vojacek, A., Dohmen, H.J., Brillert, D., Vojacek, A., others, 2018. Experimental investigation of the sCO2-HeRo compressor, in: 2nd European supercritical CO2 Conference, Essen, Germany, pp. 30–31.

Hansper, J., Grotkamp, S., Langer, M., Wechsung, M., Adams, B.M., Saar, M.O., 2019. Assessment of Performance and Costs of CO2 Plume Geothermal (CPG) Systems, in: European Geothermal Congress.

Langenfeld, J.K., Bielicki, J.M., 2017. Assessment of Sites for CO2 Storage and CO2 Capture, Utilization, and Storage Systems in Geothermal Reservoirs. Energy Procedia 114, 7009–7017. https://doi.org/10.1016/j.egypro.2017.03.1842.

McDonnell, K., Molnár, L., Harty, M., Murphy, F., 2020. Feasibility Study of Carbon Dioxide Plume Geothermal Systems in Germany−Utilising Carbon Dioxide for Energy. Energies 13, 2416. https://doi.org/10.3390/en13102416.

Moore, J., Day, M., Cich, S., Hofer, D., others, 2018. Testing of a 10 MWe supercritical CO2 turbine, in: Proceedings of the 47th Turbomachinery Symposium.

Randolph, J.B., Saar, M.O., 2011. Combining geothermal energy capture with geologic carbon dioxide sequestration. Geophys. Res. Lett. 38, n/a-n/a. https://doi.org/10.1029/2011GL047265.

Schifflechner, C., Wieland, C., Spliethoff, H., 2022. CO2 Plume Geothermal (CPG) Systems for Combined Heat and Power Production: an Evaluation of Various Plant Configurations. J. Therm. Sci. https://doi.org/10.1007/s11630-022-1694-6.

Schifflechner, C., Wieland, C., Spliethoff, H., Saar, M.O., 2023. CO2 Plume Geothermal (CPG) Systems for Combined Heat and Power: Opportunities and Challenges, in: 48th Workshop on Geothermal Reservoir Engineering.

Sudhoff, R., Glos, S., Wechsung, M., Adams, B., Saar, M.O., 2019. Next Level Geothermal Power Generation (NGP) – A new sCO2-based geothermal concept, in: German Geothermal Congress / Der Geothermie Kongress (DGK 2019), Munich, Germany, November 19-21, 2019.

van Brummen, A.C., Adams, B.M., Wu, R., Ogland-Hand, J.D., Saar, M.O., 2022. Using CO2 -Plume geothermal (CPG) energy technologies to support wind and solar power in renewable-heavy electricity systems. Renewable and Sustainable Energy Transition 2, 100026. https://doi.org/10.1016/j.rset.2022.100026.

Wang, X., Pan, C., Romero, C.E., Qiao, Z., Banerjee, A., Rubio-Maya, C., Pan, L., 2022. Thermo-economic analysis of a direct supercritical CO2 electric power generation system using geothermal heat. Front. Energy 16, 246–262. https://doi.org/10.1007/s11708-021-0749-9.

White, M.T., Bianchi, G., Chai, L., Tassou, S.A., Sayma, A.I., 2021. Review of supercritical CO 2 technologies and systems for power generation. Applied Thermal Engineering 185, 116447. https://doi.org/10.1016/j.applthermaleng.2020.116447.

Wieland, C., Schifflechner, C., Dawo, F., Astolfi, M., 2023. The Organic Rankine Cycle Power Systems Market: Recent Developments and Future Perspectives. Applied Thermal Engineering, 119980. https://doi.org/10.1016/j.applthermaleng.2023.119980.

Wittmann, T., Lück, S., Bode, C., Friedrichs, J., 2022. On the Impact of Condensation and Liquid Water on the Radial Turbine of a Fuel Cell Turbocharger. Machines 10, 1053. https://doi.org/10.3390/machines10111053.

ORC SEVILLE 2023
7th International Seminar on O.R.C. Power Systems

© 2024 Editorial Universidad de Sevilla. Este es un artículo de acceso abierto distribuido bajo los términos de la licencia de uso y distribución Creative Commons (BY-NC-ND 4.0)

DOI: https://dx.doi.org/10.12795/9788447227457_69

DEVELOPMENT OF A GENERALISED LOW-ORDER MODEL FOR TWIN-SCREW COMPRESSORS

Florian Kaufmann[1,*], Ludwig Irrgang[1], Christopher Schifflechner[1], Hartmut Spliethoff[1]

[1] *Technical University of Munich, Chair of Energy Systems, Boltzmannstraße 15, Garching, Germany*

*Corresponding Author: florian.k.kaufmann@tum.de

ABSTRACT

Twin-screw compressors (TSC) are commonly used in heat pump processes due to their robustness and flexibility. They exhibit two core properties, i.e. the swept volume and the built-in volume ratio (BVR), which heavily influence their capacity limits and off-design efficiency. Several models of vastly different computational costs have been proposed in literature to calculate the performance of TSCs. For applications that rely on large amounts of simulation runs, the computational cost of the compressor model becomes an essential factor. This work presents a new low-order model, which can accurately predict a TSC's behaviour. First, a semi-empirical model from literature is slightly adapted and used to generate performance data for a large operational field. Then a polynomial model with a linearisation for high pressure ratios is fitted to this data. The model uses the external pressure ratio and volumetric compressor inlet flow to calculate isentropic efficiency and compressor speed. Both input parameters are normalised with a reference flowrate (calculated from the swept volume) and the BVR, respectively. This results in a generalised model of low numerical cost, which can be used for explorative studies independent of the specific machine size and BVR. A gain in computational speed by a factor of roughly 375 is achieved compared to a semi-empirical reference model. The model displays good predictive accuracy when used to predict the performance of machines with similar BVRs, but different sizes. When there is a difference in size and BVR, the prediction accuracy is still reasonable but significantly declines for small pressure ratios. Nevertheless, the proposed new approach extends the state-of-the-art by introducing a low-order model, which combines the advantages of low computational cost, good accuracy, physically correct predictions over a wide operational range and scalability to different machine capacities and BVRs.

1 INTRODUCTION

With an increasing demand for efficient and sustainable heating and cooling, vapour compression heat pumps have become the cornerstone of many industrial and residential chilling and heating applications. The key component of these heat pumps is often a volumetric compressor such as a lubricated twin-screw compressor (TSC) or scroll compressor, which are also used in other applications such as air and process gas compression. These machines are widely acknowledged for their robustness and flexibility (Liu *et al.*, 2012). The design, evaluation and control of facilities using TSCs require component models that can accurately predict the machine performance during full- and part-load operation. Hence, different modelling approaches for volumetric compressors have been proposed in literature, which can roughly be divided into empirical, semi-empirical and geometrical models (Byrne *et al.*, 2014). In this context, models originally developed for scroll machines are often adapted for TSCs due to the shared basic working principles of both machines. The accuracy and extrapolation capability but also the computational cost increases from empirical over semi-empirical to geometrical models. For applications that require low computational cost, empirical and semi-empirical models are favourable. Empirical models are usually based on a set of polynomials that are fitted to the operational data of a specific machine requiring no knowledge of the machine geometry and working principle. Their advantage of low computational cost is opposed by a very limited extrapolation capability. In addition,

operational ranges not covered by the fitting data can result in significant inaccuracies (Cuevas *et al.*, 2010). Kosmadakis and Neofytou (2022) propose an empirical model for a small-scale TSC used in annual simulations of a reversible Organic Rankine cycle. Moreover, Navarro-Peris *et al.* (2013) present an interesting approach to correlate the non-dimensional mass flow rate and power consumption of different volumetric compressors to only five empirically determined parameters. Semi-empirical models employ physics equations to describe the thermodynamic and mechanical processes inside the machine as well as empirical parameter equations, which are fitted to operational data. This requires more extensive knowledge on the specific machine and often needs iterative solvers leading to higher computational costs. Giuffrida (2016) proposed a simple semi-empirical model for TSCs with good accuracy based on six experimentally determined parameters. Furthermore, Salts *et al.* (2019) present a detailed semi-empirical modelling framework for oil-injected twin-screw compressors, accounting for a large variety of internal thermo-physical processes inside a TSC. For an insight into higher-order models for TSCs (i.e. CFD models), which are less relevant to this work, the interested reader is referred to the work of Basha *et al.* (2019) and Andres *et al.* (2018).

Two constructional parameters, i.e. the swept volume and the built-in volume ratio (BVR), heavily influence the capacity limits and part-load efficiency of TSCs. At the same time, these parameters are used in most (semi-)empiric models to describe the machine performance making it impossible to use the models for any other machine than the one the model was fitted on. This work presents a new low-order model that accurately predicts the behaviour of a TSC with a broad scope of validity. In the first step, a semi-empirical model is used to generate performance data for a large operational field. Then a polynomial model with linearisation for high pressure ratios is fitted to this data. The model uses the external pressure ratio and volumetric compressor inlet flow to calculate isentropic efficiency and compressor speed. Both input parameters are normalised with a reference flowrate and the BVR, respectively. This results in a generalised model of low numerical cost, which can be used for explorative studies independent of the specific machine size and BVR. The novelty of the model is defined by two key features, that separate it from previously proposed models. On one hand, the linearisation enables the model to give physically meaningful predictions outside of the operational range used in the fitting procedure, which is not the case for most published polynomial models. On the other hand, it accurately predicts part-load efficiency for different machine capacities, which is also not possible with most published low-order models.

411

2 BASE MODEL AND DATA GENERATION

Due to limitations in available operational data, the performance data that is used to fit and validate the novel model is generated from a semi-empirical TSC model. The semi-empirical model used in this work is a modified version of the one proposed by Giuffrida (2016). This section first gives a brief explanation of the model and the operational data it is based on. Afterwards, the data set generation for fitting the novel model is described. The model implementation and solving are conducted in MATLAB 2021a (The MathWorks Inc., 2021) with the fluid properties being calculated from REFPROP 10 (Lemmon *et al.*, 2018).

2.1 Semi-empirical model

The semi-empirical base model, which was adapted for data generation, is depicted in Figure 1 and considers the most relevant characteristics of a TSC. This includes mechanical losses in the compressor (P_{loss}) as well as internal leakage ($\dot{m}_{\mathrm{leak}}$), suction heat transfer between the incoming working fluid and the compressor housing ($\dot{Q}_{\mathrm{su}}$) and heat losses to the surrounding ($\dot{Q}_{\mathrm{amb}}$). In contrast to the original model, heat transfer between the pressurised gas and the housing ($\dot{Q}_{\mathrm{ex}}$) is neglected in this work. This assumption was validated in pre-studies, which also accounted for the respective heat flow but returned very small values for the according internal heat transfer coefficient. In order to account for the effect of over- and under-compression related to the BVR, the base model applies an isentropic compression (3→4) followed by an isochoric compression (4→5). For the sake of brevity, the interested reader is referred to the original publication of Giuffrida (2016) for a detailed model description.

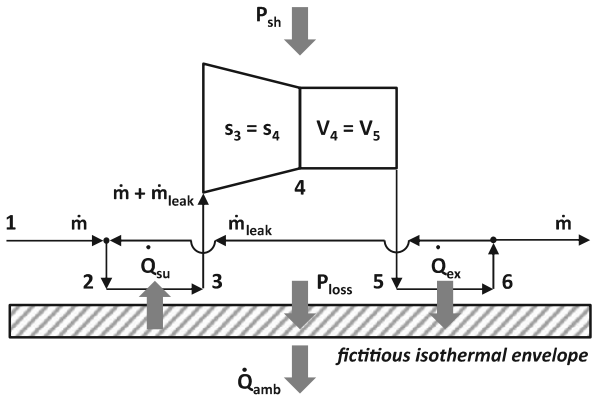

Figure 1: Semi-empirical model structure proposed by Giuffrida (2016)

The model requires the mass flow of the incoming working fluid ($\dot{m}$), its thermodynamic state and the applied external pressure ratio in order to calculate the required mechanical shaft power (P_{sh}), the compressor speed n and the fluid's outlet enthalpy (or temperature). The adapted model is fully described by a set of seven parameters: The leakage area A_{leak} in m², the nominal suction heat transfer coefficient $UA_{su,nom}$ in W/K, the external heat transfer coefficient b_{hl} in W*K$^{-5/4}$, the dimensionless torque loss coefficients $a_{tl,1}$ and $a_{tl,2}$, the machine's swept volume V_s in L and finally its BVR. The first five of the previously mentioned parameters need to be determined by a fitting procedure based on operational data. The last two parameters are constructional and hence determined by the machine.

The compressor model is fitted and validated using catalogue data provided by the manufacturer Bitzer Kühlmaschinenbau GmbH (2023) for the open-drive twin-screw compressor OSKA8591 using the refrigerant R134a as working fluid. The machine exhibits a BVR of 3.1 and a swept volume of 3.075 L per shaft rotation. In order to provide a good database for the fitting and validation procedure, seventy data points are generated with a software tool, which is provided by the manufacturer based on experimental data. For given evaporation and condensation temperatures (corresponding to the inlet and outlet pressure) and a specified compressor speed, the software calculates the necessary shaft power, the gas outlet temperature and the mass flow through the compressor. Thirty-five data points are created for compressor speeds of 2900 rpm and 3500 rpm each, with an inlet superheating of 10 °C. Figure 2a) shows the corresponding temperatures in the data set used for fitting and validation of the semi-empirical model. A total number of twelve data points (six per speed level) are used to fit the model and determine its parameters. The data points used for fitting are evenly distributed among the operational range as indicated in Figure 2a). Using more data points for the fitting procedure only drives up the required time without improving the model accuracy.

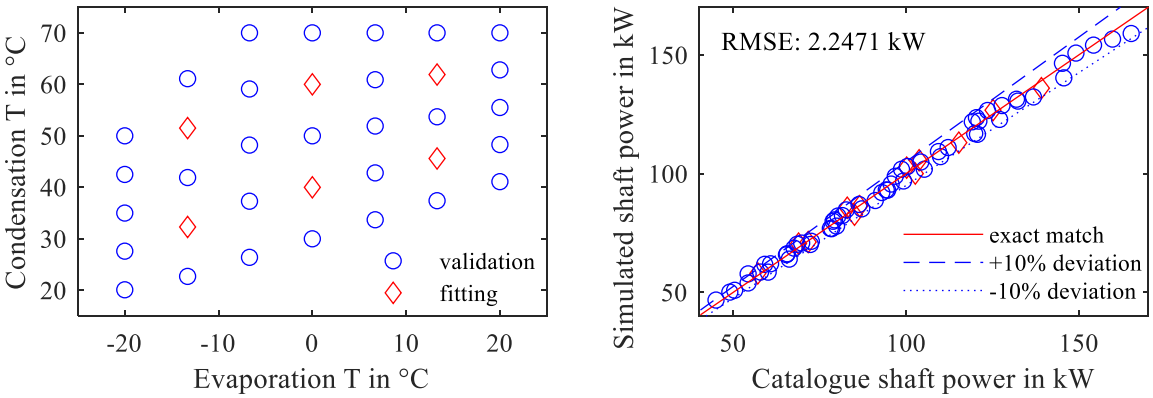

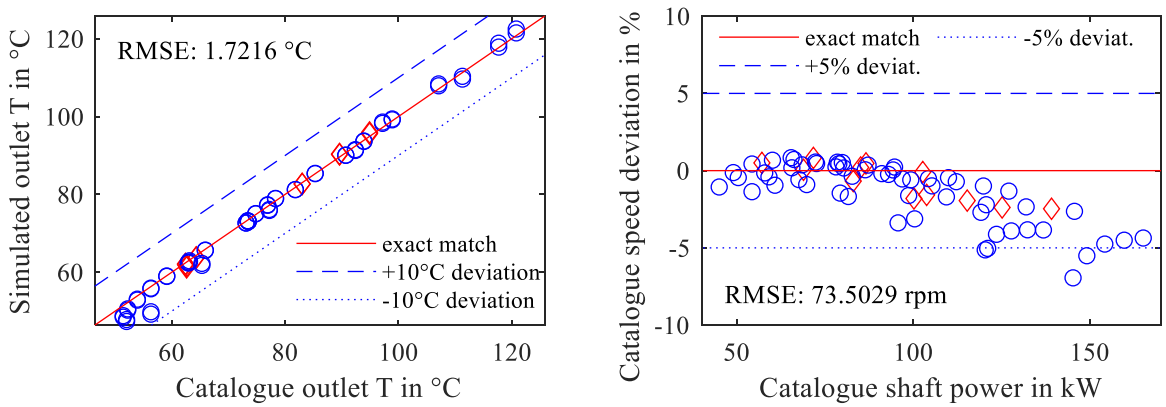

c) d)

Figure 2: Fitting data distribution (a) as well as fitting results and validation (b-d) for the semi-empiric model (fitting data: red diamonds, validation data: blue circles)

The subfigures Figure 2b) and c) show the validation of the fitting procedure in the form of parity plots for the shaft power and outlet temperature. Both parameters are predicted with a high accuracy and show small values for the root mean square error (RMSE) calculated from the validation data points. Figure 2d) shows the relative deviation of the calculated compressor speed from the catalogue speed over the corresponding catalogue shaft power. Due to the limitation on only two catalogue speed levels, a parity plot like in subfigure b) and c) makes no sense for the compressor speed. Since the compressor speed deviation is also reasonably low, the model is deemed suitable for further use. The final model parameters determined in the fitting procedure are summarized in Table 1.

Table 1: Model parameters of the semi-empirical model used for data generation

Parameter	A_{leak} [m²]	b_{hl} [W*K$^{-5/4}$]	$UA_{su,nom}$ [W/K]	$a_{tl,1}$ [-]	$a_{tl,2}$ [-]
Value	13.0556	3.6021	40.3935	0.2065	66.5177

413

2.2 Data set generation

The model described in the previous section is used to generate a set of performance data distributed over a wide operational range with respect to flowrates (translating into compressor speeds) and pressure ratios. To determine the operational limits regarding the flowrate, a minimum and maximum speed of 500 rpm and 4500 rpm respectively are assumed, which is roughly the machine's speed range proposed by the manufacturer. In this context, the volumetric suction flowrate can be determined as the product of compressor speed and the compressor's swept volume, neglecting internal leakages for simplicity reasons. A range between 1.5 and 8 is used for the applied external pressure ratio. With the boundary values for flowrate and pressure ratio at hand, a mesh grid of 1600 (40 x 40) evenly distributed operational points is created. With a constant compressor inlet pressure of 1 bar, the inlet temperature is calculated using a superheating of 10 °C for the suction stream. The inlet mass flow is calculated based on the volumetric suction flow and the inlet density.

Figure 3 shows the isentropic (η_{is}) and volumetric (η_{vol}) efficiencies calculated from the semi-empirical model over the previously described operating range. Both efficiencies display the typical behaviour as it is reported for TSCs in literature. The isentropic efficiency drops sharply for small pressure ratios due to over-compression losses while the decline in efficiency for larger pressure ratios (due to under-compression) is less pronounced. The location of the maximum efficiency with respect to the pressure ratio can be accounted to the machine's BVR of 3.1.

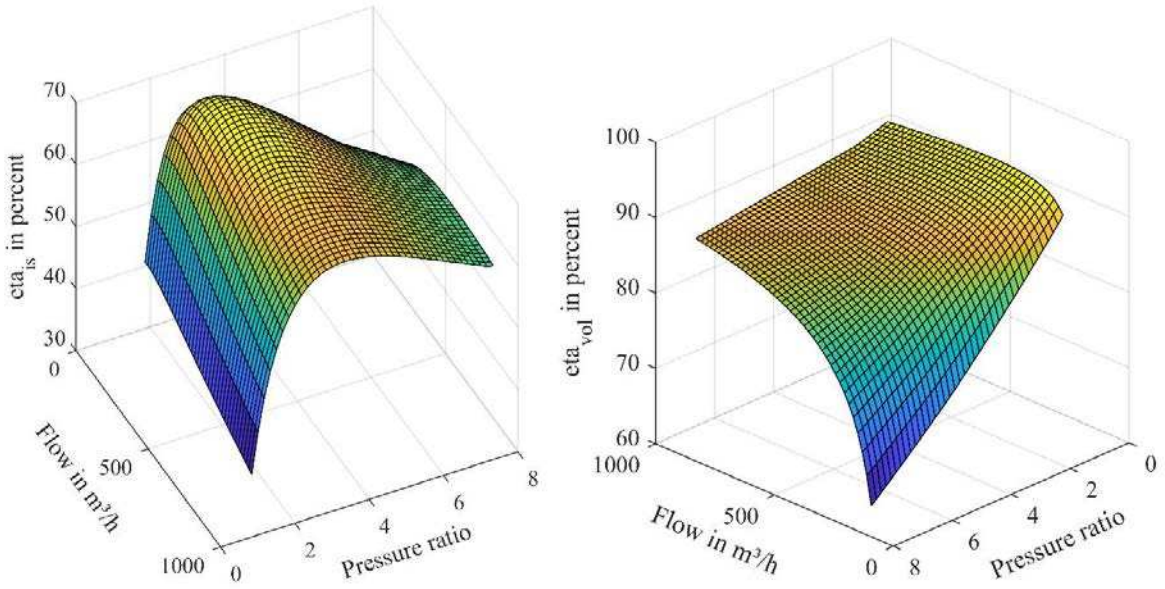

a) b)

Figure 3: Isentropic (a) and volumetric (b) efficiency of the semi-empiric model

As expected, the volumetric efficiency drops significantly for larger pressure ratios, since the driving force for internal leakages between the individual compression chambers increases. Moreover, an increasing flowrate (and hence increasing speed) leads to higher volumetric efficiency as the compressor "outruns" the internal leakages. This is due to the effect that leakage is only proportional to the pressure differential while the total suction flowrate also depends on the compressor speed. The maximum isentropic efficiency obtained over the considered operational range is 70%.

414

3 POLYNOMIAL MODEL DEVELOPMENT

In the next step, the data generated as described in the previous section is used to develop a generalized low-order model based on polynomials.

3.1 Model equations

A normalisation of the volumetric suction flowrate $\dot{V}_{\mathrm{suc}}$ and the applied external pressure ratio r_{p} with a reference flowrate and the machine's BVR aims at providing a generalised model capable to predict realistic machine performance independent from the specific machine size and BVR. The normalized suction flowrate $\dot{V}_{\mathrm{suc,N}}$ and external pressure ratio $r_{\mathrm{p,N}}$ are defined as

$$\dot{V}_{\mathrm{suc,N}} = \dot{V}_{\mathrm{suc}}/(V_s \cdot n_{\mathrm{ref}}) \quad \text{and} \tag{1}$$

$$r_{\mathrm{p,N}} = r_{\mathrm{p}}/\mathrm{BVR}\,. \tag{2}$$

Based on the usual design speed of refrigeration compressors, the reference compressor speed n_{ref} is set to 50 Hz (equal to 3000 rpm) in this work. In order to account for over- and under-compression losses, the applied volume ratio and its relation to the machine's BVR are of major importance. However, only the applied pressure ratio is known a priori, while the specific volume at the compressor outlet depends on the outlet temperature and is hence depending on the initially unknown machine efficiency. This usually requires iterative solving strategies, which should be avoided for low-order models. Consequently, a first polynomial correlating the ratio ($\mathrm{r_{v,p}}$) of the applied volume ratio r_{v} to the applied pressure ratio r_{p} is fitted to the generated data. A polynomial of the general form

$$z = c_1 + c_2 x + c_3 y + c_4 x^2 + c_5 xy + c_6 y^2 + c_7 x^3 + c_8 x^2 y + c_9 xy^2 + c_{10} y^3 + c_{11} x^4 + c_{12} x^3 y + c_{13} x^2 y^2 + c_{14} xy^3 + c_{15} y^4 + c_{16} x^5 + c_{17} x^4 y + c_{18} x^3 y^2 + c_{19} x^2 y^3 + c_{20} xy^4 \quad (3)$$

is used, where x, y and z need to be substituted by $\dot{V}_{\mathrm{suc,N}}$, $r_{\mathrm{p,N}}$ and $r_{\mathrm{p,v}}$, respectively. The applied volume ratio r_{v} is then obtained from $r_{\mathrm{v}} = r_{\mathrm{v,p}} \cdot r_{\mathrm{p}}$. The obtained polynomial coefficients c_{i} of the fitting procedure are summarized for all relevant polynomials in Table 2.

A similar approach is taken to calculate the volumetric efficiency. Here, a polynomial according to Equation 3 (using $\dot{V}_{\mathrm{suc,N}}$, r_{p} and η_{vol} for x, y and z respectively) is fitted to the generated dataset. It returns a value between zero and one. Since the driving force for internal leakages, the applied pressure ratio r_{p}, is independent from the BVR, only the suction flowrate is normalized for this polynomial.

Subsequently, a polynomial for the compressor's isentropic efficiency is fitted based on a polynomial of the from

$$\eta_{\mathrm{is}} = c_1 + c_2 x + c_3 y + c_4 x^2 + c_5 xy + c_6 y^2 + c_7 x^2 y + c_8 xy^2 + c_9 y^3 + c_{10} x^2 y^2 + c_{11} xy^3 + c_{12} y^4 \quad (4)$$

using $\dot{V}_{\mathrm{suc,N}}$ and $r_{\mathrm{v,N}}$ for x and y respectively. The normalised applied volume ratio $r_{\mathrm{v,N}}$ is obtained from r_{v} by dividing it by the BVR analogously to Equation 2.

In order to account for the rather small and approximately linear decline of η_{is} for larger pressure ratios (cf. Figure 3a), the polynomial is blended over into a linearization in the direction of $r_{\mathrm{v,N}}$ at a certain threshold value $r'_{\mathrm{v,N}}$. This allows to accurately match the machine behaviour at small pressure ratios while avoiding unphysical behaviour due to the fourth-order nature of the polynomial at larger pressure ratios. Effectively, Equation 4 is used to calculate η_{is} for all $r_{\mathrm{v,N}} \leq r'_{\mathrm{v,N}}$, while a linear function of the form

$$\eta_{\mathrm{is,lin}} = \eta_{\mathrm{is}}\left(\dot{V}_{\mathrm{suc,N}}, r'_{\mathrm{v,N}}\right) + \frac{d\eta_{\mathrm{is}}}{dr_{\mathrm{v,N}}}\left(\dot{V}_{\mathrm{suc,N}}, r'_{\mathrm{v,N}}\right) \cdot \left(r'_{\mathrm{v,N}} - r_{\mathrm{v,N}}\right) \quad (5)$$

is used for $r_{\mathrm{v,N}} > r'_{\mathrm{v,N}}$. Both Equations 4 and 5 return the isentropic efficiency as a percentage value. The final compressor outputs (speed n, shaft power P_{sh} and specific outlet enthalpy h_{out}) are ultimately calculated based on the Equations 6 to 8:

$$n = \dot{V}_{\mathrm{suc}} / (V_s \cdot \eta_{\mathrm{vol}}) \quad (6)$$

$$h_{\mathrm{out}} = \left(h_{\mathrm{out,is}} - h_{\mathrm{in}}\right) / (\eta_{\mathrm{is}}/100) + h_{\mathrm{in}} \quad (7)$$

$$P_{\mathrm{sh}} = \dot{m} \cdot \left(h_{\mathrm{out}} - h_{\mathrm{in}}\right) \quad (8)$$

In these Equations, h_{in} is the specific enthalpy at compressor inlet while $h_{\mathrm{out,is}}$ is the specific enthalpy after isentropic compression.

The different orders of the previously presented polynomials result from the model development strategy. The lowest possible order resulting in a good fit to the fitting data was chosen. The overarching goal behind this strategy was to reduce the number of polynomial coefficients while simultaneously reducing the risk of abrupt changes in the polynomial's behaviour outside the fitting range.

3.2 Fitting results and validation

The polynomial parameters for $r_{v,p}$ and η_{vol} according to Equation 3 are obtained using MATLAB's curve fitting toolbox. The parameters of Equation 4 and the optimal value for $r'_{v,N}$ are determined by a custom regression, minimizing the mean square error of the polynomial model's isentropic efficiency (defined by Equations 4 and 5) with respect to the efficiency data generated from the semi-empiric model. Table 2 provides the polynomial coefficients obtained for the respective parameters. The threshold value $r'_{v,N}$ is determined to be 1.4052.

Table 2: Polynomial coefficients of the novel low-order model

Parameter	$r_{v,p}$	η_{vol}	η_{is}	Parameter	$r_{v,p}$	η_{vol}	η_{is}
c_1	0.960925	0.942699	-87.0197	c_{11}	-0.200004	-1.149907	-7.9718
c_2	-0.013509	0.420138	-8.0743	c_{12}	0.192685	0.165919	-61.8783
c_3	-0.104981	-0.080470	526.8947	c_{13}	0.016224	0.016782	
c_4	-0.123739	-1.366392	1.4691	c_{14}	0.008725	0.001135	
c_5	0.179216	0.238714	-9.7311	c_{15}	0.001527	0.000009	
c_6	-0.004152	0.003863	-631.6492	c_{16}	0.053729	0.264339	
c_7	0.258855	1.863387	-5.2525	c_{17}	-0.049696	-0.034458	
c_8	-0.291103	-0.306518	30.6287	c_{18}	0.001403	-0.003301	
c_9	-0.012447	-0.017731	321.2015	c_{19}	-0.006167	-0.000684	
c_{10}	-0.005425	-0.000280	-1.8387	c_{20}	-0.000470	-0.000016	

The deviation between the novel low-order model and the semi-empirical model is again visualised in the form of parity plots depicted in Figure 4. The Figure and the RMSE values provided in each subfigure indicate a very good fit between the novel low-order model and the data generated from the base model.

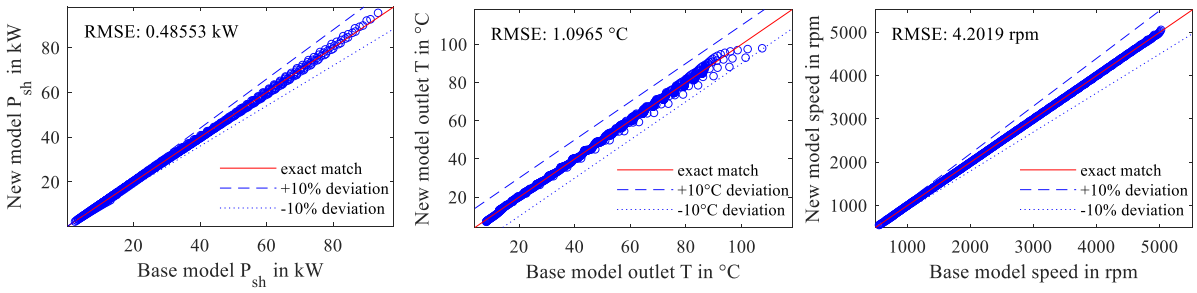

a) b) c)

Figure 4: Parity plots for comparison between base model and novel low-order model

3.3 Numerical cost comparison

A gain in computational speed is one major motivation in the previously described model development. Hence, the computational cost of the semi-empirical base model described in Section 2.1 and the novel polynomial model is subsequently compared. For comparison, the data set generation procedure described in Section 2.2 was repeated with a 20x20 grid, resulting in a total of 400 operational points calculated by the semi-empirical model. The same input data was fed to the polynomial model which also calculated the 400 operational points. In order to account for the varying load on the host machine's CPU caused by the operating system, this procedure was repeated six times. The results are given in Table 3. It can be seen that the required computational times differ depending on the momentary CPU load. However, the mean ratio between the required computation times *t* is on average 375.2, meaning that the polynomial model only requires 0.26 % of the semi-empirical model's solving time. This massive reduction in computational cost for the polynomial model has the potential to drastically reduce the computational time of complex cycle and system simulations such as annual simulations with cycle optimisation.

Table 3: Computational time requirements of the semi-empirical and polynomial compressor models for 400 operational points and ratio of both

$t_{\text{semi-empirical}}$ [s]	333.1	273.1	268.2	268.4	272.5	274.8
$t_{\text{polynomial}}$ [s]	0.8345	0.7148	0.7776	0.6964	0.7886	0.6974
Ratio [-]	399.2	382.1	344.9	385.3	345.6	394.0

4 MODEL TRANSFERABILITY TESTING

In order to evaluate the predictive capabilities of the novel model, it needs to be tested with machine sizes and BVR values different from the ones used during the model development. For this purpose, operational data for two smaller machines with a swept volume of 0.678 L is used. The respective machines are the models OSK5361-K (BVR of 3.1) and OSN5361-K (BVR of 4.7) from the same manufacturer Bitzer. For both machines, a semi-empirical model is fitted according to the procedure described in Section 2.1, which is then used to create the same operational data set described in Section 2.2. In order to account for the size-dependent maximum efficiency of the respective machine, an offset value is introduced into the novel model. It is the difference in maximum efficiency determined from the semi-empirical model within the observed operational area. Figure 5 shows the validation for the OSK5361-K with an efficiency offset of +4.7% using the same working fluid R134a. This offset is determined based on the difference in maximum efficiency calculated from the semi-empirical models for both machines over the observed operational range.

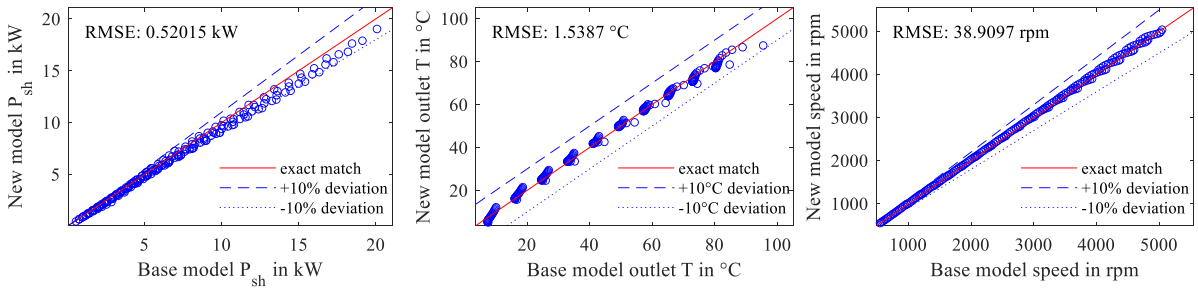

a) b) c)

Figure 5: Model transferability validation for the OSK5361-K with smaller V_s & same BVR

The parity plots for the OSK5361-K confirm very good model accuracy even at a significantly different swept volume when the BVR of the machine remains at the value used for the initial model development. Figure 6 shows the parity plots for the model OSN5361-K with an efficiency offset of - 6.4% and the working fluid R407A, which is a mixture consisting of 40% R134a, 40% R125 (very similar to R134a) and 20% R32.

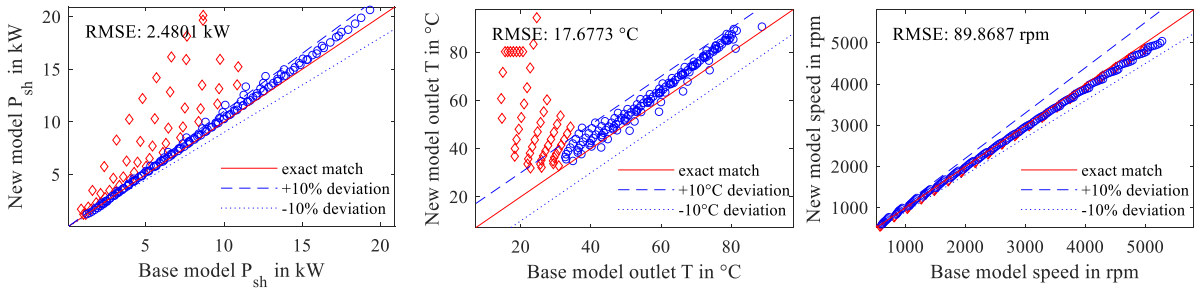

a) b) c)

Figure 6: Model transferability validation for the OSN5361-K with different V_s & BVR (red diamonds: $r_p < 2.9$, blue circles: $r_p > 2.9$)

Unfortunately, no operational data with only R134a was available for this machine. Consequently, with R407A the most similar fluid with data available was chosen. While the general predictive quality for

a combination of differing swept volume and BVR is still quite good, larger deviations from the semi-empirical model can be observed for smaller pressure ratios. This is highlighted by the use of the red diamond markers in Figure 6 for all operating points with an external pressure ratio smaller than 2.9. For these pressure ratios, the novel model significantly underestimates the compressor efficiency, leading to higher shaft power consumption and higher outlet temperatures.

This deviation can be explained by looking at the operational behaviour of two machines with the same swept volume but different BVR values. Figure 7a) shows the isentropic efficiency predicted by the semi-empirical models for the machines OSK5361-K (BVR of 3.1) and OSN5361-K (BVR of 4.7) over the normalised pressure ratio. The values for all flowrates at each normalised pressure ratio were averaged to obtain a 2D graph. Moreover, an efficiency offset of +10% was added to the efficiency of the OSN5361-K to obtain the same maximum efficiency and enable a fair comparison. The figure shows that the efficiency begins to drop sharper for decreasing normalised pressure ratios for the OSK5361-K, which shows very similar behaviour to the OSKA8591 used in the polynomial model development. This leads to a significant difference in efficiency between the machines with different BVRs for smaller normalised pressure ratios. For normalised pressure ratios larger than one, there is also a difference but it is less pronounced. This is also reflected in Figure 7b), which shows the difference in isentropic efficiency for the range of overlapping curves in Figure 7a). Here, the stronger increase in efficiency deviation for smaller normalised pressure ratios compared to larger ones becomes apparent. It can be concluded that major differences in BVR are a limitation of the proposed model in its current form.

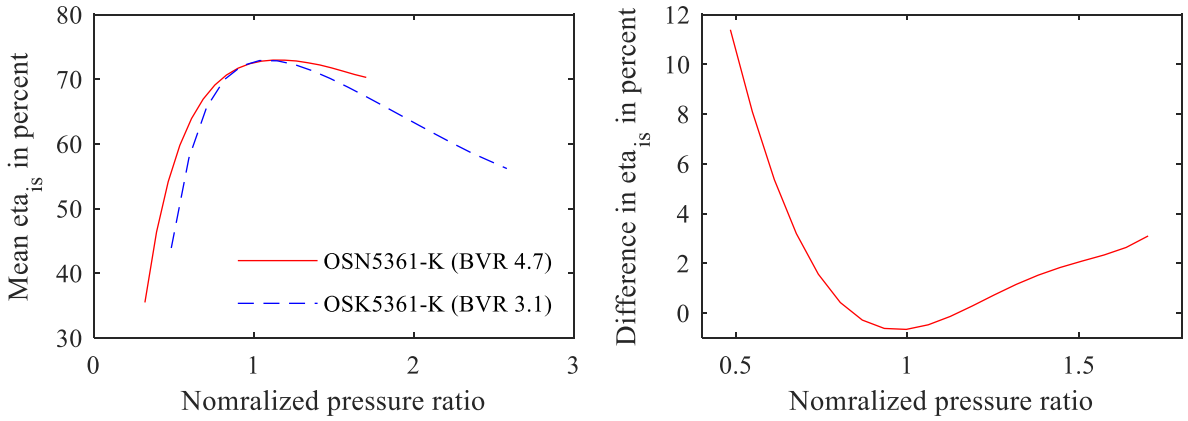

a) b)

Figure 7: Mean isentropic efficiency predicted by the semi-empirical models (a) and difference in predicted efficiency (b) over the normalized external pressure ratio of two machines with the same swept volume but different BVR

5 CONCLUSIONS

This work presents a novel low-order model for twin-screw compressors yielding mostly accurate machine performance predictions independent from the specific machine size and built-in volume ratio. The model is developed in two steps. First, an accurate semi-empirical model from literature is slightly adapted and used to generate performance data for a large operational field. In the next step, a polynomial model with a linearisation for high pressure ratios is fitted to this data. The linearisation allows to accurately simulate the characteristic machine behaviour at small and medium pressure ratios with a fourth-order polynomial while avoiding unphysical behaviour caused by the mathematical properties of a fourth-order polynomial at larger pressure ratios. The model uses the external pressure ratio and volumetric compressor suction flow to calculate isentropic efficiency and compressor speed. Both input parameters are normalised with a reference flowrate (calculated from the swept volume) and the BVR respectively. This results in a generalised model of low numerical cost, which can be used for explorative studies independent of the specific machine size and BVR. When used to predict the performance of machines with similar BVR (3.1 for model development) but different sizes, the model

displays good predictive accuracy. However, when there is a difference in size and BVR, the prediction accuracy is still reasonable but significantly declines for small pressure ratios.

Nevertheless, the presented methodology for accurate and time-efficient models might be of high interest to the heat pump and ORC community enabling the integration of more precise models in computationally intensive simulation and optimization routines. The comparison of the computational cost between the semi-empirical base model and the novel polynomial model shows a drastic reduction in required computational time. The polynomial model on average only requires 0.26 % of the time the semi-empirical model needs to be solved.

Given the availability of enough suitable constructional and operational data, a larger number of TSCs should be used in the future to further validate the model transferability and refine its structure if necessary. Finally, the proposed model could be transferred to similar volumetric compressors such as scroll machines, since they share key working principles and loss mechanisms of TSCs.

REFERENCES

Andres, R., J. Hesse, F. Hetze, and D. Low, 2018, Cfd simulation of a two stage twin screw compressor including leakage flows and comparison with experimental data, *IOP Conf. Ser.: Mater. Sci. Eng*., 425, 12018.

Basha, N., A. Kovacevic, and S. Rane, 2019, Analysis of Oil-Injected Twin-Screw Compressor with Multiphase Flow Models, *Designs* 3, 54.

Bitzer Kühlmaschinenbau GmbH, 2023, *BITZER Software*.

Byrne, P., R. Ghoubali, and J. Miriel, 2014, Scroll compressor modelling for heat pumps using hydrocarbons as refrigerants, *International Journal of Refrigeration* 41, 1.

Cuevas, C., J. Lebrun, V. Lemort, and E. Winandy, 2010, Characterization of a scroll compressor under extended operating conditions, *Applied Thermal Engineering* 30, 605.

Giuffrida, A., 2016, A semi-empirical method for assessing the performance of an open-drive screw refrigeration compressor, *Applied Thermal Engineering* 93, 813.

Kosmadakis, G., and P. Neofytou, 2022, Reversible high-temperature heat pump/ORC for waste heat recovery in various ships: A techno-economic assessment, *Energy* 256, 124634.

Lemmon, E. W., I. H. Bell, M. L. Huber, and M. O. McLinden, 2018, *NIST Standard Reference Database 23: Reference Fluid Thermodynamic and Transport Properties-REFPROP. Standard Reference Data Program* (National Institute of Standards and Technology, Gaithersburg, United States).

Liu, J., Q. Li, F. Wang, and L. Zhou, 2012, A new model of screw compressor for refrigeration system simulation, *International Journal of Refrigeration* 35, 861.

Navarro-Peris, E., J. M. Corberán, L. Falco, and I. O. Martínez-Galván, 2013, New non-dimensional performance parameters for the characterization of refrigeration compressors, *International Journal of Refrigeration* 36, 1951.

Salts, N., D. Ziviani, and E. A. Groll, 2019, Application of a generalized compressor modeling framework for simulating an oil-injected twin-screw compressor, *IOP Conf. Ser.: Mater. Sci. Eng.* 604, 12009.

The MathWorks Inc., 2021, *MATLAB* (Natick, Massachusetts, United States).

ACKNOWLEDGEMENT

Funding from the Bavarian State Ministry of Education, Science and the Arts in the framework of the project Geothermal-Alliance Bavaria is gratefully acknowledged.

ORC SEVILLE 2023
7th International Seminar on O.R.C. Power Systems

© 2024 Editorial Universidad de Sevilla. Este es un artículo de acceso abierto distribuido bajo los términos de la licencia de uso y distribución Creative Commons (BY-NC-ND 4.0)

DOI: https://dx.doi.org/10.12795/9788447227457_71

DECISION-MAKING MATRIX FOR THE SELECTION OF MIXTURE IN ORC APPLICATION

William Combaluzier[1,*], Nicolas Tauveron[1], Michel Beaughon[2], Aldo Serafino[2]

[1] *Université Grenoble Alpes, CEA, LITEN, LCST, F-38054 Grenoble, France*
[2] *Enertime, 1 Rue du Moulin Des Bruyères, 92400 Courbevoie, France*

*Corresponding Author: william.combaluzier@cea.fr

ABSTRACT

ORC is an established and affordable technology to convert efficiently low/medium grade thermal energy to power. The choice of the working fluid is critical to the performance of the ORC. The use of zeotropic mixtures as a cycle working fluid could lead to an efficiency enhancement, thanks to the non-isothermal phase change occurring at both the condenser and the evaporator. Therefore, there has been a growing interest for mixtures, which are often studied by the means of optimization algorithms or thermodynamic calculations that lead to interesting results (Bederna *et al.*, 2021, Lecompte *et al.*, 2014). This work proposes an alternative approach. A selection methodology is used to conduct a preliminary screening to optimize the mixture choice in accordance with the targeted objectives. This methodology is applied to study cyclopentane-based mixtures. For this purpose, a large list of criteria is considered to achieve improved safety, maximized performances, ORC using more environmentally friendly fluids and respecting heat exchangers sizing while following specific technical constraints. Among these criteria, the temperature glide should be carefully taken into account: indeed, it is directly linked to the fractionating risk, which must be prevented for the good functioning of the cycle. Performing this study prior to the classical energetic analysis reduces the risk of exploring mixtures of incompatible or irrelevant fluids. This whole analysis yields a decision-making matrix, gathering selection criteria, relevant properties, and cycle performances. By adapting the different threshold of these criteria, this methodology is adaptable to large-scale ORC applications.

1 INTRODUCTION

Nowadays, energy is a major concern. Industry sector is one of the most energy consuming. The various crises currently experienced are raising prices to new heights and pushing the industry to re-evaluate their relationship to energy. In this context, the reduction of energy consumption and industrial waste heat recovery have become critical. The Organic Rankine Cycle (ORC) is a mature technology that allows harvesting industrial waste heat by converting thermal energy to electrical power. In order to optimize its efficiency according to the application, the components need to be properly sized and the working fluid must be well selected. Since ORC is a well-known classic thermodynamic cycle, a large range of fluids have already been tested and validated. However, there is still a great interest in the use of different pure fluids and zeotropic mixtures. For the latter, considering that the two fluids of such mixture have different condensation and boiling temperatures, the phase changes occurring within the cycle are not isothermal. Using an adapted mixture, the working fluid temperature can better follow the hot and cold source profile along the heat exchangers, thus improve the cycle performances. Moreover, mixtures are considered to potentially improve the cleanliness and safety of working fluids.
In the framework of the DECAGONE project (Horizon Europe), cyclopentane is chosen as the main component of the working fluid mixtures (Vescovo, 2019). A bibliographical study on mixtures commercially available and/or those studied in scientific literature is first conducted. Most cyclopentane-based mixtures commercially available consist of other similar alkanes (pentane, isopentane), or fluorinated gases (CFC, HFC). In the scientific literature, articles are mostly analyses

and numerical studies. Most papers elaborate mixtures discussing thermodynamic performances calculated using simulations (Wang *et al.*, 2022). In chemical engineering, computer-aided molecular design (CAMD) is used to design molecules and select optimum pure working fluid and mixtures (Papadopoulos *et al.*, 2013). Even if thermodynamic properties are considered in these studies, they are mainly used as performances indicators. It is rarely verified that the proposed mixtures are actually relevant with fluid compatibility studies or even experimental results. In this work, a different methodology is proposed. This methodology is based on the prior selection of one fluid of interest that is planned to be mixed with another specie. In order to ensure technical relevance of suggested mixtures, criteria selection are firstly defined to ensure their compatibility, before considering other thermodynamic properties of interest, energetic results and experimental data as tools of the mixture selection choice.

2 LIST OF CRITERIA

The NIST (National Institute of Standards and Technology) database is used to provide thermodynamic data for around 150 fluids, as a basis for a first fluid screening. In the database, four different data cases can be encountered concerning the mixtures properties calculations. In the best case, the exact mixture is present in the database. Then, a mixture with one actual fluid of the couple and one similar to the second fluid can be present, or a mixture with two similar fluids. Finally, in the worst case an estimation of the mixture properties is used. The values calculated later with a software using Refprop database should be used with caution, as their accuracy is uncertain.
The selection of relevant discriminating criteria is crucial, as they are the backbone of the methodology. They need to ensure that the fluids validating the thresholds required enable the good functioning of the process and the safety of the installation. These criteria are split into two classes depending on their criticality: some of them are strict criteria, which means that no variation of the values set are accepted; the other ones are adjustable, so the initial thresholds are open to discussion. This flexibility allows obtaining a greater number of candidates if needed after the screening. Hereafter are listed the criteria with their class and for some of them thresholds.

421

2.1 Auto-ignition Temperature

This first parameter is of great importance as it is a safety guarantor. The minimum required value is strict and depends on the highest temperature possibly reached by the working fluid in the cycle. It is relevant to allow for a safety margin by using a threshold greater than this temperature. Cyclopentane auto-ignition temperature is obtained from a safety data sheet (Carl Roth, 2022).

2.2 Mixing

The fluids studied must be miscible with the preselected working fluid. Only two fluids were identified as non-miscible until then. The miscibility is a criterion that will be checked experimentally for the reduced list of fluids remaining after the selection.

2.3 GWP, ODP, Toxicity

This criterion includes three indicators concerning environment and safety. First, the GWP (Global Warming Potential) value is limited to ensure that the selected fluids have a reduced carbon footprint. Then, the ODP (Ozone Depletion Potential) is considered in order to discard the targeted fluids by Montreal protocol from the considered fluids (CFC, HCFC). More generally, these environment criteria also eliminate HFC and PFC of the list of fluids. Finally, a toxicity criterion is considered. In this application, the American NFPA (National Fire Protection Association) standard 704 is used, as it can be found in safety data sheet of a wide range of fluids. Four indicators are taken into account: health hazard, fire hazard, reactivity, specific hazard. The limits to set for these toxicity indicators should be chosen accordingly to the considered standards and regulations. For this application, the focus is put on health hazard indicator that should not be above two (chosen as limit value). As other standards and regulations exist such as CLP (Classification, Labelling, Packaging) and HAP (Hazardous Air Pollutants) for example, it is relevant to search for more information concerning the fluids after the first selection process.

2.4 Fractionating risk

This criterion is essential. The fractionating phenomenon can occur during a phase change, when the vapour phase consists of one of the components, and the liquid phase consists of the other one. This separation of the mixture could lead to important issues in the cycle. It was observed that a limitation to a 15 K temperature glide (temperature difference of the mixture components during a phase change) should help avoiding this risk (Heberle *et al.*, 2012). In order to keep fluids for which a significant quantity can be mixed with the first fluid, the temperature glide of the mixtures is limited to a maximum of 15 K for a given minimum mass fraction of additive.

2.5 Flammability

Two values characterize the flammability range of a fluid: its lower flammability limit (Lfl) and its upper flammability limit (Ufl). In some cases, mixtures are studied to improve the safety of the cycle, so increasing the Lfl can be of great importance. Many pure fluids flammability limits and a quantitative model used to estimate mixtures lower flammability limits are provided in ISO (International Organization for Standardization) standard (ISO 10156, 2017). With a view to improving safety, the minimum value accepted during the selection process should be the lower flammability limit of the first fluid composing the mixture.

2.6 Liquid phase

The selected fluids must have a melting point lower than the cold source minimum temperature. Actually, the melting point must also be lower that the potential colder temperatures occurring in the geographical area of the ORC installation to prevent any risk of solidification of the working fluids. Moreover, they need to be able to condense at room temperature and low pressure, and have a reasonable vapour pressure.

2.7 Properties definition

Finally, the definition of the properties concerns the NIST Refprop database (Lemmon *et al.*, 2022). In fact, after the first screening, energetic calculations provide performance element to refine the selection; thus, the thermodynamic properties need to be defined at least up to the highest temperatures reached by the cycle for the calculation. As it does not involve safety issue this is an adjustable criterion.

422

Table 1: Criteria values for DECAGONE project

Criterion	Class	Threshold in DECAGONE project
Auto-ignition temperature	Strict	≥ 550 K
Mixing	Strict	Miscible with cyclopentane
GWP, ODP & toxicity	Strict	Low GWP (< 100), ODP ~ 0 NFPA health rating ≤ 2
Solidification temperature	Strict	≤ 250 K
Fractionating risk	Adjustable	Volume fraction minimum of 5 %, 10 % is preferred, of 2nd fluid can be added without exceeding the temperature glide limit of 15 K
Flammability	Adjustable	LFL ≥ 0.5 %, 1.1 % is preferred
Liquid phase	Adjustable	Can condense at room temperature & low pressure, vapour pressure not too low
Properties definition	Adjustable	Thermodynamic properties defined at least up to 525 K, 550 K is preferred

The fractionating risk criterion was the last one applied. Thus, it has been possible to observe how the list of selected fluids would change if the threshold was modified. In this case, all the preferred criteria are kept. As an example, lowering the value to 10 K or increasing the value to 20 K would not change the list of selected fluids. The impact would be observed on the mass fraction allowed that would either decrease or increase.

It highlights that the selection with the criterion chosen is relevant, and that the exact temperature glide value is not critical for the fluids selection: more than 80 % of the fluids of the initial database are discarded by the other criteria.

2.8 First screening

Applying these criteria, a reduced number of candidates are highlighted. This list can be increased with the adjustable parameters. To be more specific, fluids with the least amount of unmet criteria are preferred. Logically, isomers and fluids of the same specie as the first one are represented. However, it is noted that some fluids may have grey areas. Various references found may sometimes give contradictory values concerning certain points, and some values may not be available. Moreover, information that could have a different impact on the fluid selection are provided by other means, such as different standards concerning toxicity for example.

Table 2: Selected fluids

Main Fluid	**Cyclopentane**
Fluid n°1	Acetone
Fluid n°2	Butane
Fluid n°3	Isobutene
Fluid n°4	Isopentane
Fluid n°5	Isobutane
Fluid n°6	2,2-Dimethylbutane
Fluid n°7	2,3-Dimethylbutane
Fluid n°8	Isooctane
Fluid n°9	Hexamethyldisiloxane
Fluid n°10	Butene
Fluid n°11	Cis-butene
Fluid n°12	Trans-Butene

423

Once candidates fulfilling the requirements are identified, the screening progresses in two directions. Based on this short-list, different analyses are performed. On the one hand, there is a great interest in performing experimental tests. Material compatibility tests between the working fluid candidates and the ORC components are important to prove their suitability; also, thermodynamic properties oriented tests (checking database values, confirming that the estimation of mixtures flammability is correct, etc…) aim to confirm that the selection is relevant. On the other hand, energetic calculations add a performance aspect to the selection that helps classifying the previously selected fluids.

3 ADVANCED SELECTION

Once the first selection based on criteria is done, other parameters are used in order to refine the candidates list. Reviewing performances of a certain number of mixtures helps identifying thermodynamic properties of interest.

Whether zeotropic mixtures being studied with a performance or a safety objective, energy results are taken into account in the final choice of working fluid. For this reason, calculations are relevant, even with a simplified model. In fact, if the Refprop database is used, results are only estimations, so the point is to have qualitative results, overall behaviours. In order to do that, a large range of parameters of interest should be monitored as a function of the fluids mixed and their respective mass fractions.

3.1 Cycle operability

First, the temperature glides must be checked because in such calculations the consideration of the thermodynamic cycle and the changes that can occur, such as pressure drops in various components for example, can influence it. As it is one of the most important selection criteria, a second verification of the glide is relevant. Mixing a pure fluid with one of the additive from the fluid short list can induce a modification of the ORC cycle.

Then, temperature pinch points at the various heat exchangers (minimum temperature difference between the cold fluid and the hot fluid at the condenser, evaporator, and recuperator if used) need to be verified to ensure that the phase changes and heat exchanges are consistent. Temperatures and pressures in the whole cycle are also looked at with the same objective of good operability.

3.2 Cycle performances

Classic results are compared to the ones obtained with a pure fluid. The turbine power and cycle efficiency are calculated for the mixtures with varying mass fraction of the additive. Due to the use of zeotropic mixtures, the turbine work and the cycle efficiency can reach a maximum for a specific mass fraction of a mixture. They behave independently; these two maximum are generally reached for different mass fractions. When such behaviour was observed, it is interesting to note that these performance peaks do not necessarily correspond to the highest temperature glide. Moreover, as the fluids considered have been selected in the basis of their compatibility and not their potential performance enhancement, the performances maximum can correspond in some cases to the initial pure fluid instead of a mixture.

Additionally, some input parameters, such as turbine inlet temperature or pump pressure, can be modified to observe if the cycle behaves as expected.

Finally, mixing a pure fluid with an additive can require modifying the size of the ORC components, for a given performance. Two sizing parameters provide a better comprehension of how using a mixture instead of a pure fluid influences the ORC components. On the one hand, the heat exchangers are characterized with the Logarithmic Mean Temperature Difference (LMTD) as listed in equation (1):

424

$$\Phi = U * A * F * LMTD \quad (1)$$

With Φ the thermal power (W), U the heat transfer coefficient ($W.m^{-1}.K^{-1}$), A the surface exchange area (m^2) and F a corrective factor (–).

The pure fluid coefficient (product of heat transfer coefficient by the surface area of the heat exchanger) and the mixture ones are compared and a rough model is used to approximate the ratios of heat transfer coefficients, as observed by Zühlsdorf *et al.* (2019). A similar result has recently been measured by Blondel (2021). In the end, the ratio of the heat exchangers sizing for the various mixtures by the heat exchanger sizing of the pure cyclopentane cycle is obtained.

On the other hand, the turbine size is also a valuable parameter. It is related to the coefficient SP (Invernizzi and Ahmed Sheikh, 2018), for Size Parameter, listed in (2):

$$SP = \frac{\sqrt{\dot{V}}}{(h_{in} - h_{out})^{0.25}} \quad (2)$$

With SP the size parameter (m), $\dot{V}$ the isentropic volume flow ($m^3.s^{-1}$) and h the specific enthalpy (J/kg) at turbine inlet and outlet.

In terms of both footprint and cost, the size of ORC components is an important parameter to consider.

Table 3: Energetic results obtained for the fluid selected

		Mixtures energetic results			
Property / Fluid	Mass fraction considered for mixtures	Wt variation (%)	Efficiency variation	Amix/Acyclo	SPmix/SPcyclo
Main Fluid	100%	0	(20,54) +0%	1,000	1,000
Fluid n°1	50%	0,41	-2,29%	1,31	0,950
Fluid n°2	20%	0,87	-0,87%	1,25	0,950
Fluid n°3	10%	1,32	-0,51%	1,30	0,976
Fluid n°4	50%	-4,51	-1,32%	1,20	0,933
Fluid n°5	10%	1,23	-0,48%	1,29	0,977
Fluid n°6	50%	-7,29	-0,31%	1,20	1,022
Fluid n°7	50%	-6,33	0,12%	1,24	1,064
Fluid n°8	15%	4,01	1,81%	1,43	1,169
Fluid n°9	20%	2,96	1,44%	1,41	1,181
Fluid n°10	10%	1,82	-0,51%	1,30	0,977
Fluid n°11	20%	1,50	-0,96%	1,27	0,950
Fluid n°12	20%	1,41	-0,97%	1,27	0,950

425

3.3 Parameters of interest

In fact, some of them could directly affect the results: condensation and evaporation pressures, critical temperature and pressure (Wang *et al.*, 2022). Even though they are not selection criteria, these parameters are to be considered as they could affect the fluid choice for performance and operability. Moreover, in order to ensure the operability of the ORC loop, additional thermodynamic parameters are evaluated: vapour pressure, viscosity, and fluid behaviour. Vapour pressure is an important parameter regarding the mixture crossing the heat exchangers. Viscosity is linked to the good pumpability of the fluid mixture throughout the hydraulic circuit, and affects heat exchange. Critical temperature and pressure are directly related to the state of the mixture and must be chosen to avoid supercritical state during the cycle. Finally, the behaviour (wet, isentropic or dry) has influence on the thermodynamic cycle. Dry fluids are usually preferred over wet fluids as overheating the fluid is not necessary before the expansion.

In practice, performing experimental tests on various points regarding mixture properties as well as obtaining data from fluid suppliers would bring significant information on fluids and compatibility. Indeed, mixtures properties such as thermal stability, auto-ignition temperature, flammability, but also classic thermodynamic properties, are estimated or based on rough model. Compatibility tests are finally conducted to verify the compatibility of studied mixtures with ORC components materials.

Finally, another parameter must be considered in the very last steps of the selection process. When selecting a pure fluid and especially the supplier, the impurities rate is critical. In fact, depending on the impurities nature and level, the impact on performances could be significant. A few percent of another specie could affect thermodynamic parameters such as condensation and evaporation pressures, resulting in a reduction of the performances. At the very end, the price may also affect the choice between the remaining promising fluids.

4 DECISION-MAKING MATRIX

The working fluid selection process is based on all the elements previously presented: the first selection criteria, the typical thermodynamic properties, the energetic results and the experimental tests. As they all are important to a certain degree, creating a table resuming all of these properties and performances gives a global overview of each fluid potential. Thus, this decision-making matrix enables optimizing the choice of the fluid mixture.

As presented above, seven main criteria are used to select the most compatible fluids: auto-ignition temperature, GWP and ODP, thermal range for properties, lower flammability limit, maximum mass fraction of fluid respecting the temperature glide criterion, solidification temperature, and NFPA rating. However, if they are essential to the screening, some of them will not be taken into account in the final decision. In fact, the auto-ignition temperature, for example, has no further impact: fluids must meet the criterion ($T > 550$ K), but it is not of high importance if their auto-ignition temperature is of 600 or 700 K. Only four of the seven parameters are actually kept in the matrix: lower flammability limit (for the mixtures), thermal range for properties, NFPA rating and environment.

Then, several pure fluids thermodynamic properties are involved in the selection as explained earlier: vapour pressure, viscosity, critical pressure, critical temperature and fluid behaviour (dry, isentropic or wet).

Afterwards, ORC simulation results give performance-oriented results. This information is estimated and needs to be considered as qualitative result to compare to pure fluid cycle. Many values must be monitored with different mass fractions of the fluids: turbine power, efficiency, ratio of SP coefficient of a mixture cycle and of a pure cyclopentane cycle, ratio of evaporator surface of a mixture cycle and of a pure cyclopentane cycle. In addition to that, some thermodynamic properties mentioned are calculated: working fluid viscosity at the pump outlet, and critical pressure and temperature of the mixtures.

Finally, an evaluation of the level of uncertainties is added. It considers the estimations of mixtures properties calculations (flammability, performances), contradictory references found (NFPA rating, GWP and ODP values, flammability limits) and any unknown or not found values. Thus, the complete decision-making matrix is formed so the second fluid composing the mixture can be selected in accordance with the objectives. The next table is an example of matrix, filled with signs (+, o or -), indicating if the parameter is interesting compared to pure cyclopentane. The concentrations indicated for the mass fractions considered for mixtures were estimated using Refprop, being the maximum allowable fraction so that mixtures respect the maximum 15 K glide criterion. A 50% mass fraction means (for the fluid considered here) that the threshold is not reached for any concentration.

Fluids can be classified regarding their relevancy from the matrix, by weighting the various criteria based on their importance for the considered application: for example, with a safety-driven approach flammability and NFPA rating could be prioritized. Thus, doing this for all matrix criteria the best candidates can be identified. The results may differ from CAMD and thermo-economic methods. Indeed, the NIST database was used for this study, so it does not take into account all existing fluids and molecules; moreover, economic impact specific to each fluid is not studied.

The matrix allows a global theoretical global view of the most critical properties of the fluids identified ; however as explained before this is a tool dedicated to pre-selection, and experimental work is necessary to confirm the good behaviour of the mixtures and to reduce the uncertainties due to the estimations made with the various models used.

Table 4a: Example of qualitative decision-making matrix (restrictive criteria)

	Property / Fluid	Main fluid	Fluid n°1	Fluid n°2	Fluid n°3	Fluid n°4	Fluid n°5
	Mass fraction considered for mixtures	100%	50%	20%	10%	50%	10%
2 - Selection criteria	Thermal range for properties (pure fluid)	+	+	+	+	+	+
	NFPA (pure fluid)	o	o	o	-	o	+
	Environment (pure fluid)	o	+	o	o	o	o
	Lower Flammability Limit (mixture)	o	++	+	+	+	+
3.2 - Mixtures energetic results	Wt variation	o	+	+	+	-	+
	Efficiency variation	o	--	-	-	-	-
	Amix/Acyclo	o	-	-	-	-	-
	SPmix/SPcyclo	o	+	+	+	+	+
3.3 - Thermodynamic properties	Fluid behavior (pure fluid)	+	-	+	+	+	+
	Vapor pressure at 25°C (pure fluid)	o	o	o	o	o	o
	Viscosity pump outlet (mixture)	o	+	+	o	+	-
	Critical pressure (mixture)	o	o	o	o	-	o
	Critical temperature (mixture)	o	o	-	o	-	o
General	Thermodynamic model uncertainties	o	-	--	--	-	-
	All uncertainties	o	-	--	--	-	-

Table 4b: Example of qualitative decision-making matrix (adjustable criteria)

	Property / Fluid	Main fluid	Fluid n°6	Fluid n°7	Fluid n°8	Fluid n°9	Fluid n°10	Fluid n°11	Fluid n°12
	Mass fraction considered for mixtures	100%	50%	50%	15%	20%	10%	20%	20%
2 - Selection criteria	Thermal range for properties (pure fluid)	+	+	+	+	+	-	-	-
	NFPA (pure fluid)	o	-	o	?	?	o	o	o
	Environment (pure fluid)	o	?	?	?	?	?	-	?
	Lower Flammability Limit (mixture)	o	?	-	-	--	+	+	++
3.2 - Mixtures energetic results	Wt variation	o	-	-	+	+	+	+	+
	Efficiency variation	o	-	+	+	+	-	-	-
	Amix/Acyclo	o	-	-	-	-	-	-	-
	SPmix/SPcyclo	o	-	-	--	--	+	+	+
3.3 - Thermodynamic properties	Fluid behavior (pure fluid)	+	+	+	+	+	-	+	+
	Vapor pressure at 25°C (pure fluid)	o	o	o	-	-	o	o	o
	Viscosity pump outlet (mixture)	o	+	+	-	-	o	+	+
	Critical pressure (mixture)	o	-	o	o	o	o	o	o
	Critical temperature (mixture)	o	o	o	o	o	o	o	-
General	Thermodynamic model uncertainties	o	--	--	--	---	--	--	--
	All uncertainties	o	----	---	----	-----	---	--	---

427

Table 5: Example of values rating

	Criterion	Value	Sign
2 - Selection criteria	Thermal range for properties (K)	≥ 550	+
		525 < x < 550	-
	NFPA health rating	0	+
		1	o
		2	-
	Environment	GWP < 1	+
		1 < GWP < 10	o
		10 < GWP < 100	-
	LFL (Vol. %)	Lfl > 1.2	++
		1.2 > Lfl > 1.1	+
		Lfl = 1.1	o
		1 < Lfl < 1.1	-
		Lfl < 1	--
3.2 - Mixtures energetic results	Wt variation	0 % < x < 10 %	+
		- 10 % < x < 0 %	-
	Efficiency variation	0 % < x < + 2 %	+
		- 2 % < x < 0 %	-
		< - 2 %	--
	Amix/Acyclo	> 1	-
	SPmix/SPcyclo	- 10 % < x < 0 %	+
		0 < x < + 10 %	-
		> + 10 %	--
3.3 - Thermodynamic properties	Fluid behavior	Dry	+
		Wet	-
	Vapor pressure (Pa)	< 1E+04 or > 5E+05	-
	Viscosity pump outlet (Pa.s)	< 3.70E-04	+
		> 3.80E-04	-
	Critical pressure (bar)	< 40	-
	Critical temperature (K)	< 493	-
General	Thermodynamic uncertainties	1 similar fluid used	-
		2 similar fluids used	--
		Estimation	---
	Other uncertainties	?	-

5 CONCLUSIONS

This paper presents a methodology for the selection of fluids composing a zeotropic mixture for ORC applications. This method is aiming to prevent performing long and expensive mixtures experimental studies on a wide variety of potential fluids. By selecting promising candidates, time and resources may be saved. Starting with a predefined main fluid, a first list of discriminating criteria is used to filter a fluid database and obtain a reduced quantity of compatible fluids. Then, thermodynamic properties and energy results are reviewed and included in a decision-making matrix. Finally, other parameters, resulting of laboratory tests or given by suppliers, can complete the screening, confirming the choices and refining the list of promising fluids. These tests are the best mean to validate the assumptions and estimations that have been made. The remaining candidates can then be classified according not only to their compatibility but also to the performances of the mixtures they are a part. The filling of the decision-making matrix, adaptable to the specificities and the main objectives of the project, is the last step of the optimized selection process.

This detailed method is supposed to facilitate the selection and ensure that the mixtures formed demonstrate great compatibility. The selection criteria are adaptable to the ORC configurations, and the

428

discussion is open about their relevance and other usable parameters for the choice of the fluids. It would be interesting to apply this matrix to fluid selections performed in literature, and to observe if the identified fluids are similar or not to the ones selected with other methods.
Regarding the DECAGONE project, additional experimental work, focusing on mixture properties and material compatibility, follows this mixture study to lead to the final mixture choice.

NOMENCLATURE

Φ	thermal power	(W)
A	heat exchange surface	(m²)
F	corrective factor	(–)
SP	size parameter	(m)
U	heat transfer coefficient	$(\mathrm{W.m^{-1}.K^{-1}})$
V̇	isentropic volume flow	$(\mathrm{m^3.s^{-1}})$
h	specific enthalpy	(J/kg)

Subscript

in	turbine inlet
out	turbine outlet

REFERENCES

Bederna, B.G.; Barta, R.B.; Hesse, U. 2021, Composition optimization of zeotropic mixtures for ORC systems considering constraints, *6th International Seminar on ORC Power Systems*.

Blondel, Q. 2021, Etude et optimisation énergétique des mélanges zéotropes pour les cycles thermodynamiques de Rankine. *PhD Thesis.* University of Grenoble Alpes.

Heberle, F; Preißinger, M; Brüggemann, D. 2012, Zeotropic mixtures as working fluids in organic Rankine cycles for low-enthalpy geothermal resources. *Renew Energy.* 37(1), p. 364-370.

Invernizzi, C.M.; Ahmed Sheikh, N. 2018, High-efficiency small-scale combined heat and power organic binary Rankine cycles. *Energies*, vol.11, 994.

Lecompte, S.; Ameel, B.; Ziviani, D. ; van Den Broek, M. ; de Paepe, M. 2014, Exergy analysis of zeotropic mixtures as working fluids in Organic Rankine Cycles, *Energy Convers. Manag.*, vol. 85, p. 727-739.

Lemmon, E. W.; Bell, I. H.; Huber, M. L.; McLinden, M. O. 2022, *NIST Standard Reference Database 23, NIST Reference Fluid Thermodynamic and Transport Properties, version 10.0*; Standard Reference Data Program, National Institute of Standards and Technology.

Papadopoulos, A. I.; Stijepovic, M.; Linke, P.; Seferlis, P.; Voutetakis, S. 2013, Toward Optimum Working Fluid Mixtures for Organic Rankine Cycles using Molecular Design and Sensitivity Analysis, *Ind. Eng. Chem. Res.* 52(34), p. 12116-12133.

Vescovo R. 2019, High temperature organic rankine cycle (HT-ORC) for cogeneration of steam and power, *AIP Conference Proceedings* 2191, 020153

Wang, E.; Zhang, M.; Meng, F.; Zhang, H. 2022, Zeotropic working fluid selection for an organic Rankine cycle bottoming with a marine engine. *Energy.* vol. 243, article 123097.

Zühlsdorf, B.; Jensen, J.; Elmegaard, B. Heat pump working fluid selection—economic and thermodynamic comparison of criteria and boundary conditions, *Int. J. Refrig.*, vol.98, p. 500-513.

Cyclopentane, Safety Data Sheet No. 2191, Carl Roth

ISO 10156:2017, *Gas cylinders – Gases and gas mixtures – Determination of fire potential and oxidizing ability for the selection of cylinder valve outlets.*

ACKNOWLEDGEMENT

This work was supported by the DECAGONE project funded under the European Union's Horizon Europe research and innovation programme under the grant agreement No 101069740.

ORC SEVILLE 2023
7th International Seminar on O.R.C. Power Systems

© 2024 Editorial Universidad de Sevilla. Este es un artículo de acceso abierto distribuido bajo los términos de la licencia de uso y distribución Creative Commons (BY-NC-ND 4.0)

DOI: https://dx.doi.org/10.12795/9788447227457_72

REVERSIBLE HEAT PUMP-ORC PILOT PLANT – EXPERIMENTAL RESULTS AND FLUID CHARGE OPTIMIZATION

Maximilian Weitzer*, Sebastian Kolb, Dominik Müller, Jürgen Karl

Chair of Energy Process Engineering
Friedrich-Alexander-Universität Erlangen-Nürnberg (FAU)
Fürther Straße 244f, 90429 Nürnberg, Germany

*corresponding author: maximilian.weitzer@fau.de

ABSTRACT

The reversible operation of the heat pump process and the organic Rankine cycle as a Carnot battery has gained attraction of the scientific community in recent years. Despite numerous publications investigating the potential of such systems as a new energy storage technology, experimental results are scarce. The present work presents the outcomes on process level of a first experimental characterization of a reversible heat pump – organic Rankine cycle (HP-ORC) pilot plant designed for a maximum charging capacity of 15 kW_{el} in heat pump mode and discharging capacity of 9 kW_{el} in ORC mode. The experimental campaign comprised 150 stationary operating points. The plant yielded a maximum COP of 9.5 and a maximum ORC net efficiency of 4.4% for the defined boundary conditions of this experimental campaign. While the heat pump favors low temperature lifts for a high COP, high temperature gradients are favorable for ORC operation. Moreover, limitations on component and system level were determined. The challenging aspect of a proper fluid management of such reversible systems was identified as a crucial factor. Finally, the impact of fluid charge on ORC operation was experimentally evaluated and revealed significant optimization potential by means of an adequate fluid management.

1 INTRODUCTION

Balancing the fluctuating production of renewable energies with the demand is a key challenge in today's energy systems and requires large energy storage capacities. Carnot batteries are an emerging energy storage technology that potentially provides large capacities for several days up to few weeks. Surplus electrical energy charges a thermal energy storage, preferably by means of a heat pump process (HP) together with low-grade waste heat (Figure 1). For discharging, the thermal energy is transferred back to electrical energy by a power cycle, e.g. an organic Rankine cycle (ORC).

Carnot batteries in terms of heat pump – ORC systems rely on technically mature components (Vecchi et al., 2022). Moreover, such system allow a straightforward heat source integration and the storage capacity is scalable and low-cost as simple hot water storages can be used for typical operating temperatures up to 200°C (Frate et al., 2020; Weitzer et al., 2022b). Although the primary purpose of Carnot batteries is electrical energy storage (Dumont et al., 2020), several authors proposed heat pump – ORC systems as cogeneration units, e.g. in geothermal applications (Kaufmann et al., 2021; Weitzer et al., 2022a) or in building energy systems (Dumont et al., 2015; Palomba et al., 2021). The idea of reversible HP-ORC systems was initially proposed for building energy systems in combination with a solar roof and geothermal heat (Quoilin, Sylvain and Lemort, 2013). Although numerous simulative studies investigated different configurations of this concept, only few prototypes have been realized so far. Recently, a review paper comprehensively summarized current commercial developments in the

field of Carnot batteries where most of the projects are in concept stage or pilot operation while few commercial installations exist (Novotny et al., 2022).

Combining a heat pump process and an ORC in a reversible configuration significantly reduces the machinery costs as both processes share major components. However, the design of a reversible configuration is not trivial and must pay particular attention to an appropriate choice of components, lubrication concept and fluid selection amongst others (Eppinger et al., 2021; Steger et al., 2020).

The present work presents the findings of a first experimental characterization of a reversible heat pump – ORC pilot plant at FAU Erlangen-Nürnberg. Additionally, the challenging aspect of fluid management in reversible systems is presented in terms of experimentally evaluating the impact of fluid charge on system operation. As experimental results of such systems are still scarce in literature, the outcomes of this work bridge the gap between simulative modelling and experimental validation of reversible heat pump – ORC systems.

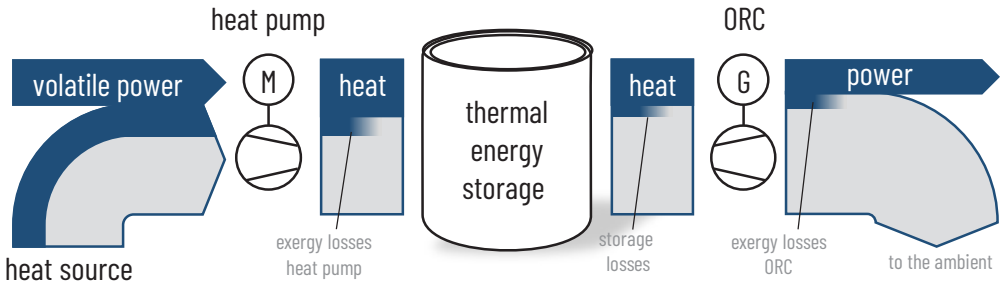

Figure 1: Working principle of a Carnot battery system based on heat pump and ORC.

2 EXPERIMENTAL SETUP AND METHODOLOGY

2.1 Carnot battery pilot plant

The detailed design process as well as the proof of concept and first launch of the reversible heat pump – ORC pilot plant were presented in previous studies (Steger et al., 2020, 2021). The prototype is designed for up to 15 kW_{el} in HP mode and up to 9 kW_{el} in ORC mode with two hot water storages with a storage capacity of 270 kWh_{th}. The pilot plant includes a screw machine that can be operated reversibly and an additional piston compressor that is not investigated in the present study. As shown in the simplified P&ID in Figure 2, the pilot plant is a fully reversible configuration, thus heat pump and ORC share all major components and pipes, beside pump and throttling valve. The brazed plate heat exchangers HEX 1 (state points 3↔4) and HEX 3 (1↔6) serve as condenser and evaporator in heat pump mode and vice versa in ORC mode. Another heat exchanger HEX 2 recuperates heat in both modes (2↔3 and 5↔6). A reversible screw machine is utilized as compressor and expander (4↔5), respectively. In both modes, a reversible oil separator at the high pressure vapor side extracts lubricant oil from the cycle and injects it into the screw machine. Moreover, a liquid receiver is included before the throttling valve (pneumatic needle valve) (2→1). A centrifugal pump circulates the working fluid in the ORC (1→2). Pneumatic valves allow switching between heat pump and ORC mode. The refrigerant R1233zd(E) is used in the experiments. Auxiliary water cycles allow heating or cooling through the heat exchangers, depending on the operating mode. Basic PID control loops for the auxiliary cycles are set up in the programmable logic controller (PLC) to ensure comparable heating and cooling boundary conditions. Furthermore, the PLC logs the data of temperature, pressure and flow sensors in an interval of 2 seconds.

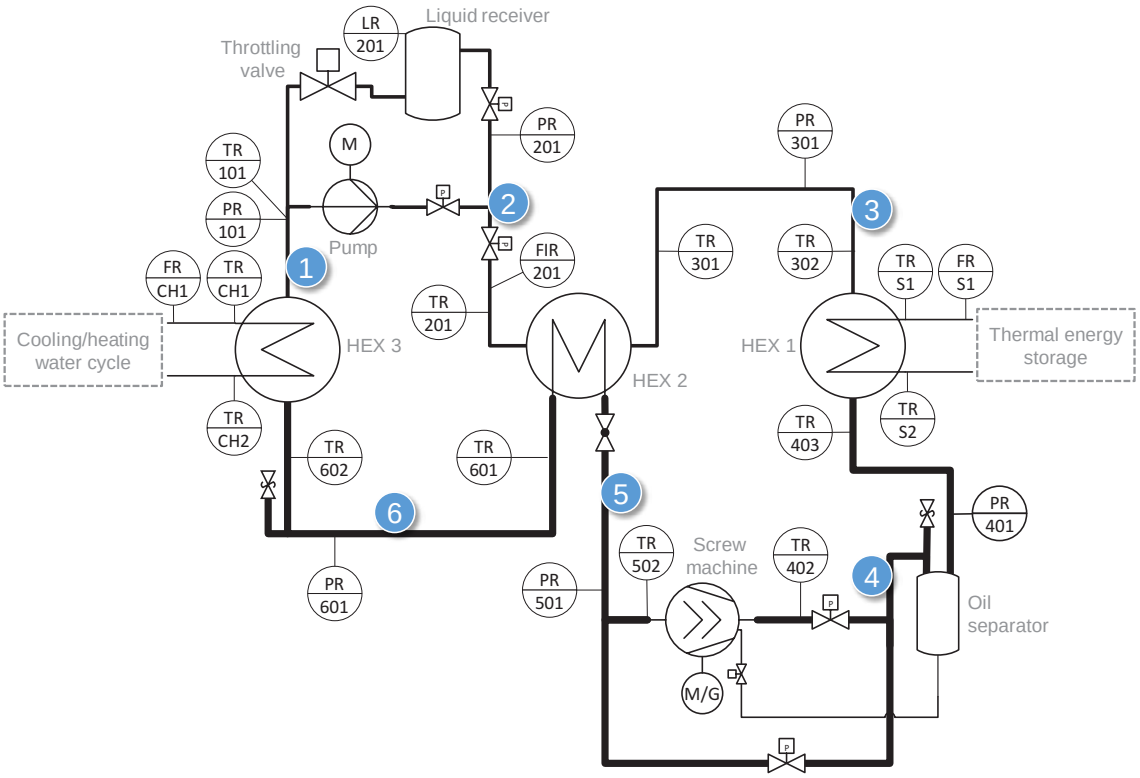

Figure 2: Simplified P&ID of the reversible HP-ORC pilot plant.

2.2 Methodology

In this experimental campaign, 150 stationary operating points were recorded in total, 92 in ORC mode and 58 in heat pump mode. Defined stationary criteria that compare the current 30-second mean values with those from 15 minutes ago ensure equal stationary conditions. The maximum deviation of these mean values is defined at 0.5 K for temperatures and 2% for pressures and flows. 15-minute mean values of the measured data were calculated at stationary conditions for all operating points. An auxiliary water cycle substituted the thermal energy storage.

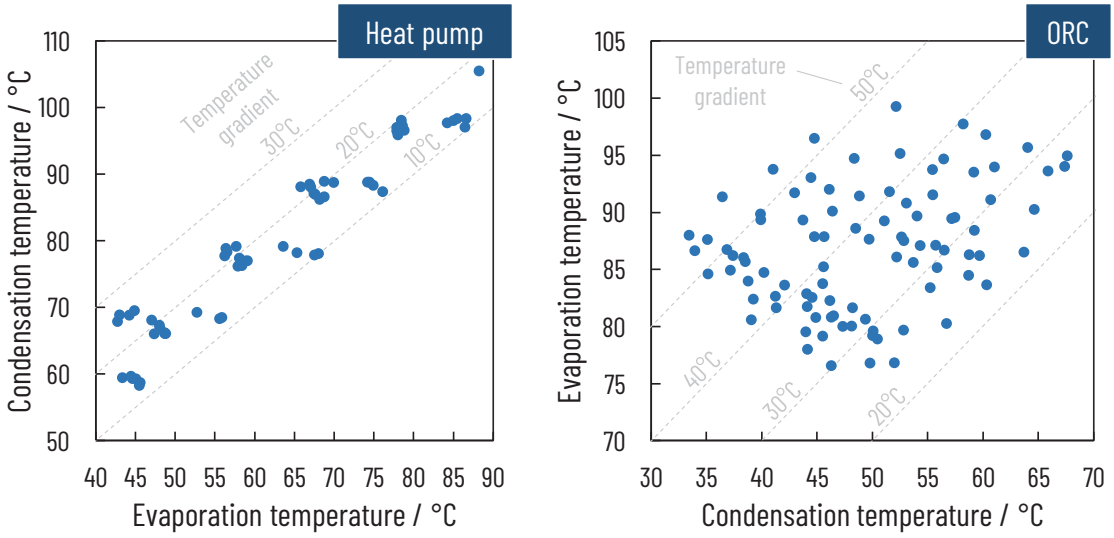

Figure 3: Phase change temperatures of all operating points for heat pump and ORC mode.

In heat pump mode, heat source temperatures from 50°C to 90°C were investigated in steps of 10 K, with upper storage temperatures between 60°C and 110°C and storage temperature glide of 10 K or 20 K. As the motor/generator unit was originally designed for ORC mode, the maximum motor torque limited the temperature lift of the heat pump process which barely exceeds 25 K (Figure 3). Thus, in case of a required high temperature lift, several consecutive heat pump runs might be necessary to reach a certain storage temperature. Moreover, the maximum temperature of the water cooling cycle did not allow exceeding a storage temperature of 110°C. For each heat source temperature, the compressor speed was increased stepwise until the maximum torque was reached. The opening of the throttling valve was adjusted to ensure slightly superheated conditions at the compressor inlet.

A similar methodology was applied for the ORC mode. As illustrated in Figure 3, the ORC reached a broader range of operation compared to the heat pump. Hot storage water with a temperature between 100°C and 120°C and a storage temperature glide of 10 K or 20 K supplied heat to the evaporator. For each heat source temperature, pump speed and expander speed were varied within the component and system limits. Table 1 summarizes the main set and controlled parameters of the experiments.

Table 1: Ranges of set and controlled parameters of the experiments.

HP parameter	Operating range	ORC parameter	Operating range
Heat source temperature	50…90°C	Upper storage temperature	100…120°C
Storage temperature glide	10…20 K	Storage temperature glide	10…20 K
Heat source volume flow	73 l/min	Storage volume flow	20…82 l/min
Upper storage temperature	60…110°C	Cooling water temperature	15…25°C
Storage volume flow	6…42 l/min	Cooling water volume flow	44…51 l/min
Mass flow working fluid	0.05…0.36 kg/s	Mass flow working fluid	0.14…0.36 kg/s
Throttling valve opening	59…99 %	Pump speed	2000…2800 rpm
Compressor speed	600…1800 rpm	Expander speed	1000…3100 rpm

3 EXPERIMENTAL RESULTS

3.1 Heat pump mode

The main performance indicator to assess the cycle efficiency of a heat pump process is the coefficient of performance (COP) defined in equation 1.

$$COP = \frac{\dot{Q}_{storage}}{P_{el,compressor}} = \frac{\dot{m}_{S1} \cdot (h_{S1} - h_{S2})}{P_{el,compressor}} \quad (1)$$

Figure 4 shows the electrical power consumed by the compressor and the COP plotted against the temperature gradient. The temperature gradient describes the difference between condensation and evaporation temperature (see Figure 3). Generally, an increasing power consumption and decreasing COP were observed for an increasing rotational speed of the compressor and a corresponding higher temperature gradient. As the motor/generator was originally selected for ORC operation, the maximum motor torque limited the rotational speed and power of the compressor. Due to that limitation, the temperature gradient did not exceed 25 K. Two sets of experiments were performed. For the upper left group of operating points, the storage water temperature was 10°C higher than the heat source temperature, thus the water temperature lift (i.e. external temperature lift) was around 10 K. These conditions resulted in a COP between 4.9 and 9.5. For the group of operating points at the lower right side, the storage temperature was 20°C above the heat source temperature, leading to a COP between 1.4 and 6.4. Thus, an increasing water temperature lift generally yields lower COP values. However, the COP also depends on the absolute temperature level and the rotational speed leading to scattered values within the two groups of operating points.

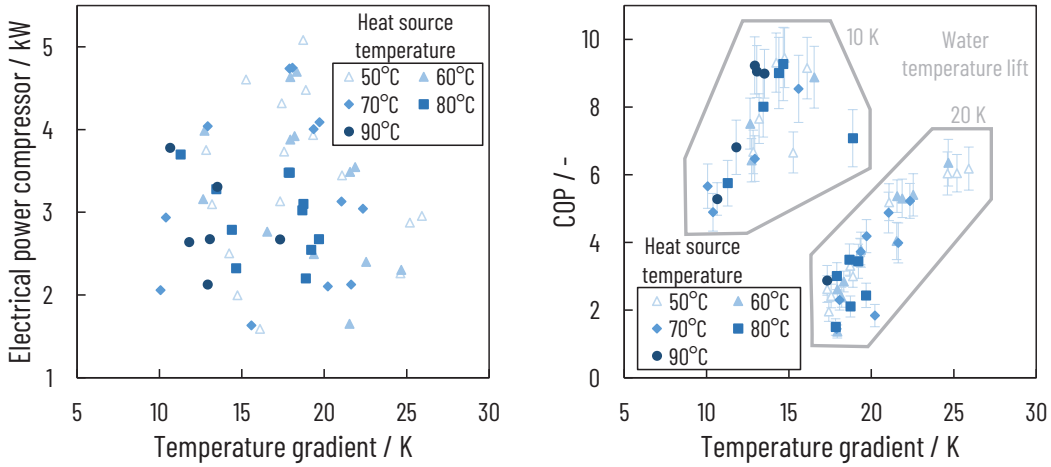

Figure 4: Electrical power consumption of the compressor and COP plotted against the temperature gradient for all heat pump operating points.

Table 2 summarizes the resulting process conditions for heat pump mode. An exemplary T-s diagram with a heat source temperature of 80°C is illustrated in Figure 5. It shows that phase change in condenser and evaporator were often not finished at the heat exchanger outlet. Thus, phase change partly occurred in the recuperator. Experimental tests with another compressor and motor are envisaged to overcome the limited temperature gradient of the current setup.

Table 2: Range of process conditions during the experimental campaign.

HP parameter	Operating range	ORC parameter	Operating range
Storage thermal power	4…31 kW	Storage thermal power	24…67 kW
El. power compressor	1.6…5.1 kW	El. power expander	0.3…3.7 kW
Condensation pressure	58…106°C	Evaporation pressure	6.0…10.3 bar
Evaporation pressure	43…88°C	Condensation pressure	1.7…4.8 bar
Max. COP	9.5	Max. net efficiency	4.4 %

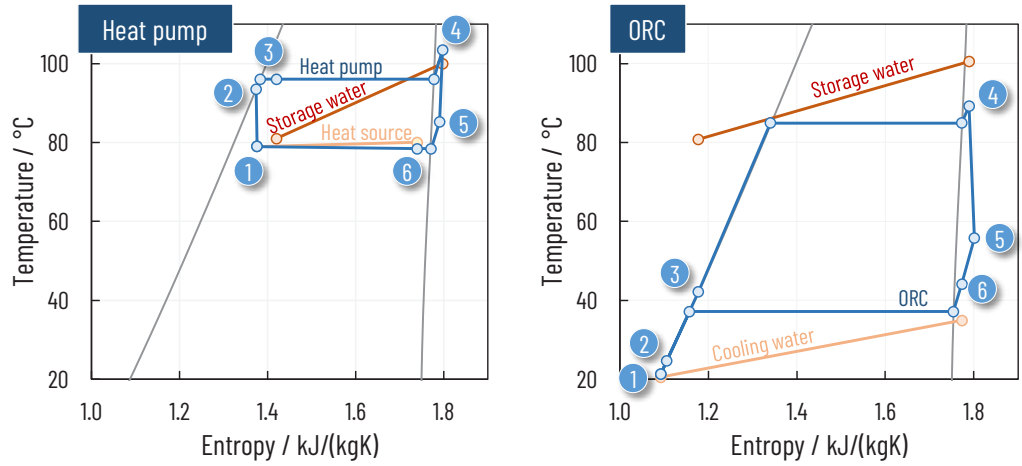

Figure 5: T-s diagram of heat pump and ORC process for upper and lower storage temperature of 100°C and 80°C respectively (state point numbers refer to the P&ID in Figure 2).

3.2 ORC mode

The global efficiency of the ORC is evaluated in terms of the net electrical efficiency as described in equation 2.

$$\eta_{el,net,orc} = \frac{P_{el,net}}{\dot{Q}_{storage}} = \frac{P_{el,expander} - P_{el,pump}}{\dot{m}_{S1} \cdot (h_{S2} - h_{S1})} \quad (2)$$

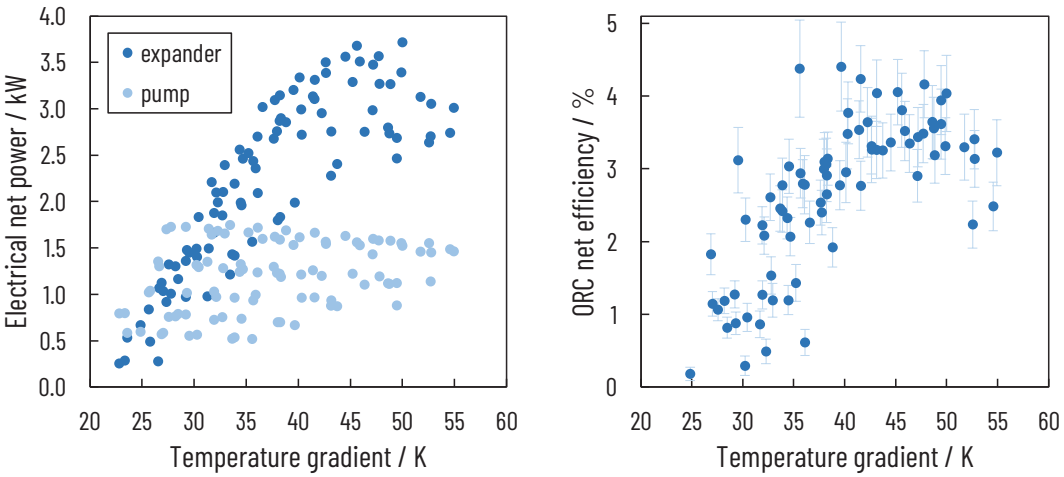

Figure 6: Electrical power of expander and pump and ORC net efficiency plotted against the temperature gradient for all ORC operating points.

Figure 6 shows the electrical power generated by the expander and consumed by the pump as well as the ORC net efficiency against the temperature gradient. For some operating points with low temperature gradients, the pump consumption exceeds the generated power of the expander. This results from a comparably low efficiency of the axial centrifugal pump and could be solved by replacing it with a volumetric pump. The generated power increases with increasing temperature lift. In contrast to the heat pump, a high temperature gradient is beneficial for the ORC efficiency.

Altogether, the ORC yielded a maximum net efficiency of 4.4%. Again, Table 2 summarizes the process conditions and Figure 5 exemplarily illustrates a T-s plot at upper and lower storage temperatures of 100°C and 80°C. A comparatively high degree of subcooling of around 20 K across all operating points indicates that the fluid charge of the ORC was too high. Further potential is thus expected from a fluid charge optimization. The generated power did not reach design conditions due to a limited pump performance, limited cooling capacity of the cooling water grid and refrigerant excess in the condenser. The impact of the latter aspect is investigated in the following section.

4 FLUID CHARGE OPTIMIZATION

4.1 Concepts of reversible fluid management

A challenging aspect in the design of reversible HP-ORC systems is an adequate fluid management in order to supply both processes with the required amount of working fluid at all operating conditions. Excess fluid typically accumulates in the condenser, increases the condensation pressure and reduces the power output in ORCs while too low fluid charges lead to pump cavitation (Dickes et al., 2020). A recent experimental study varied the fluid charge of a 1 kW_{el} reversible HP-ORC test rig and concluded that the fluid charge has a significant impact on overall efficiency, reversible machine performance, system stability and obtainable operation points (Tassenoy et al., 2022). A common measure is the integration of a liquid receiver before the throttling valve in heat pumps and before the pump in ORCs. However, for reversible systems there are several concepts for the integration of liquid receivers (Figure 7). In the first option (a), the liquid receiver is bypassed in both processes. Thus, the fluid charge can only be adapted between operating times or the liquid valve can permanently remain open to the

process. The fluid charge and lower system pressure can be actively controlled by adding a membrane charged with inert gas or a piston in the receiver vessel. In option (b) at least one receiver is directly integrated in the process. Receiver A corresponds to the current setup of the pilot plant. If only one receiver is integrated, the receiver is bypassed in the other operating mode. A reversible utilization of the receiver (c) allows integrating the same receiver in both modes.

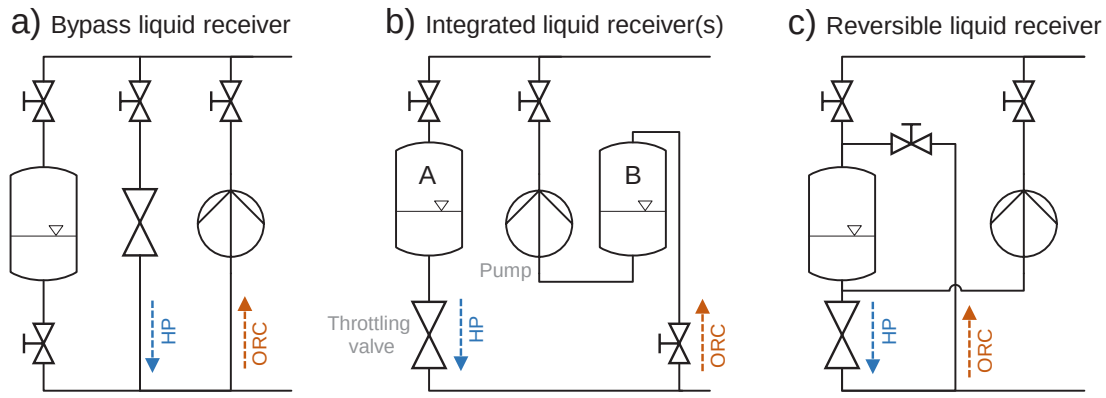

Figure 7: Different configurations of liquid receiver integration in reversible HP- ORC systems.

4.2 Experimental fluid charge evaluation

In the current experimental setup (Figure 2), a liquid receiver is integrated in the heat pump process before the throttling valve. During operation, the integrated liquid receiver stores surplus working fluid and ensures that the process is supplied with the suitable amount of fluid. This principle works as long as the vessel is neither flooded nor emptied. Therefore, a careful selection of proper liquid receiver volume is crucial. Figure 8 shows the balancing role of the liquid receiver during an experimental day with different compressor speeds and throttling valve openings.

436

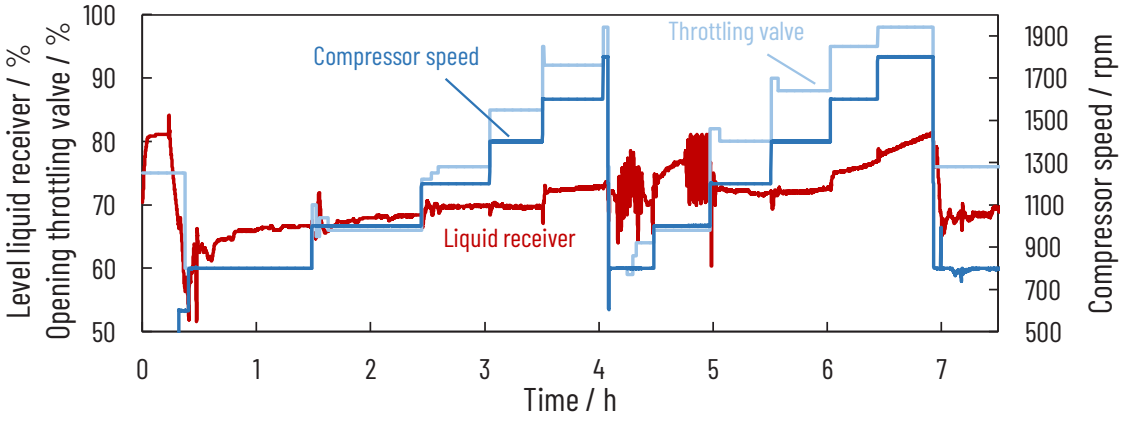

Figure 8: Self-regulating fluid charge due to the liquid receiver in heat pump mode.

In ORC mode, the liquid receiver is bypassed and thus cannot balance the fluid inventory in the cycle. In order to determine the impact of the fluid charge on ORC operation, a separate experimental campaign was started. An excerpt of the results is shown in Figure 9. On the left side, the T-s diagram for eight different ORC fluid charges between 16.3 kg and 22.7 kg at constant operating conditions (mass flow 0.25 kg/s, evaporation temperature 90°C) is given. The results show that the fluid charge mainly affects the condensation temperature. Surplus liquid working fluid accumulates in the condenser and occupies the heat exchange area. This results in high condensation temperatures and a high degree of subcooling. Due to the lower pressure gradient, less power can be generated in the expander (Figure 9 right). The lowest condensation temperature and highest power generation was observed for the lowest

fluid charge. However, even lower fluid charges were not possible due to pump cavitation that prevented a proper ORC operation.

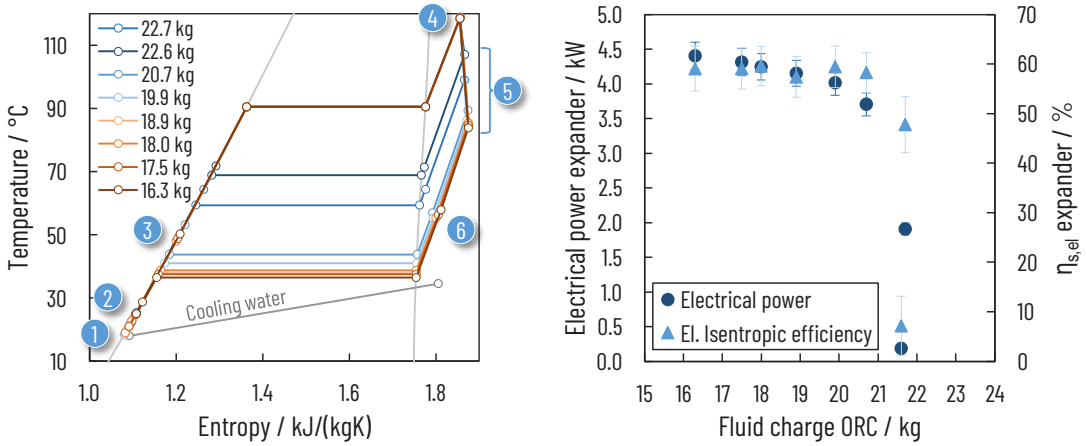

Figure 9: T-s diagram (left) and performance indicators (right) for various ORC fluid charges.

5 CONCLUSION AND OUTLOOK

The first experimental characterization of a reversible heat pump – ORC pilot plant comprised 150 stationary operating points. The pilot plant reached a maximum COP of 9.5 and a maximum ORC net efficiency of 4.4% for the defined boundary conditions of this experimental campaign. While the heat pump favors low temperature lifts for a high COP, high temperature gradients are favorable for ORC operation. The maximal motor torque mainly restricted the operating range of the heat pump. Therefore, experiments with another compressor and motor are envisaged. In ORC operation, the comparatively high consumption and maximum capacity of the centrifugal pump limited the net efficiency. Despite those limitations, the reversible operation of the components worked well and disclosed optimization potential on component and system level. The fluid management of reversible systems was identified as a crucial optimization lever to improve efficiency. Different configurations to optimize the fluid charge for both operating modes were presented. In this context, the liquid receiver in the heat pump process proved its function to balance the working fluid charge. As no liquid receiver is included in the ORC, the ORC efficiency is highly sensitive to the fluid charge in this setup.

Upcoming work will further analyze the experimental results on component and system level in order to identify further optimization potential. Moreover, the optimal fluid charge and optimal fluid properties will be studied in detail and taken into account for upcoming experiments, including different working fluids and fluid mixtures. The results will feed a simulation model of the plant that will also consider fluid charge sensitivity.

NOMENCLATURE

COP	Coefficient of performance	-
h	Specific enthalpy	kJ/kg
HP	Heat pump	
m	mass	kg
ORC	Organic Rankine Cycle	
P	Electrial power	kW
Q	Thermal energy	kJ
s	Specific entropy	kJ/(kg K)
t	Temperature	°C
η	Efficiency	%

Subscript

el	electric
th	thermal

REFERENCES

Dickes, R., Dumont, O., and Lemort, V. 2020. Experimental assessment of the fluid charge distribution in an organic Rankine cycle (ORC) power system, *Applied Thermal Engineering*, vol. 179, 115689

Dumont, O., Frate, G. F., Pillai, A., Lecompte, S., De paepe, M., and Lemort, V. 2020. Carnot battery technology: A state-of-the-art review, *Journal of Energy Storage*, vol. 32, no. July

Dumont, O., Quoilin, S., and Lemort, V. 2015. Experimental investigation of a reversible heat pump/organic Rankine cycle unit designed to be coupled with a passive house to get a Net Zero Energy Building, *International Journal of Refrigeration*, vol. 54, 190–203

Eppinger, B., Steger, D., Regensburger, C., Karl, J., Schlücker, E., and Will, S. 2021. Carnot battery : Simulation and design of a reversible heat pump-organic Rankine cycle pilot plant, *Applied Energy*, vol. 288, no. February, 116650

Frate, G. F., Ferrari, L., and Desideri, U. 2020. Rankine carnot batteries with the integration of thermal energy sources: A review, *Energies*, vol. 13, no. 18

Kaufmann, F., Schifflechner, C., Dawo, F., Wieland, C., and Spliethoff, H. 2021. Evaluation of Reversible Screw Compressors with an Adaptable Built-In Volume Ratio in Reversible Heat Pumps, *6th International Seminar on ORC power systems*, 1–10

Novotny, V., Basta, V., Smola, P., and Spale, J. 2022. Review of Carnot Battery Technology Commercial Development, *Energies*, vol. 15, no. 2

Palomba, V., Borri, E., Charalampidis, A., Frazzica, A., Karellas, S., and Cabeza, L. F. 2021. An Innovative Solar-Biomass Energy System to Increase the Share of Renewables in Office Buildings, *Energies*, vol. 14, no. 4, 914

Quoilin, Sylvain, O. D. and Lemort, V. 2013. Design, Modeling and Performance Optimisation of a Reversible Hp-Orc Prototype, in *2nd International Seminar on ORC Power Systems*

Steger, D., Karl, J., and Schlücker, E. 2021. Launch and First Experimental Results of a Reversible Heat Pump-Orc Pilot Plant As Carnot Battery, *6th International Seminar on ORC Power Systems*, no. 2018, 1–9

Steger, D., Regensburger, C., Eppinger, B., Will, S., Karl, J., and Schlücker, E. 2020. Design aspects of a reversible heat pump - Organic rankine cycle pilot plant for energy storage, *Energy*, vol. 208, 118216

Tassenoy, R., Dumont, O., Lemort, V., De Paepe, M., and Lecompte, S. 2022. Experimental investigation of a thermally integrated carnot battery using a reversible heat pump/ organic rankine cycle: Influence of system charge on performance of the reversible scroll compressor/expander and global performance, *19th International Refrigeration and Air Conditioning Conference Proceedings*, Advance Access published 2022

Vecchi, A., Knobloch, K., Liang, T., Kildahl, H., Sciacovelli, A., Engelbrecht, K., Li, Y., and Ding, Y. 2022. Carnot Battery development: A review on system performance, applications and commercial state-of-the-art, *Journal of Energy Storage*, vol. 55, no. PD, 105782

Weitzer, M., Müller, D., and Karl, J. 2022a. Two-phase expansion processes in heat pump – ORC systems (Carnot batteries) with volumetric machines for enhanced off-design efficiency, *Renewable Energy*, vol. 199, no. February, 720–32

Weitzer, M., Müller, D., Steger, D., Charalampidis, A., Karellas, S., and Karl, J. 2022b. Organic flash cycles in Rankine-based Carnot batteries with large storage temperature spreads, *Energy Conversion and Management*, vol. 255, no. December 2021, 115323

438

ACKNOWLEDGEMENT

This project has received funding from the European Union's Horizon 2020 research and innovation program under grant agreement no. 814945 – SolBio-Rev.

ORC SEVILLE 2023
7th International Seminar on O.R.C. Power Systems

© 2024 Editorial Universidad de Sevilla. Este es un artículo de acceso abierto distribuido bajo los términos de la licencia de uso y distribución Creative Commons (BY-NC-ND 4.0)

DOI: https://dx.doi.org/10.12795/9788447227457_73

PERFORMANCE OF ORGANIC RANKINE CYCLE SYSTEM IN COMBINATION WITH RESIDUAL MUNICIPAL SOLID WASTE GASIFICATION: A SIMULATION ANALYSIS

Luca Cioccolanti[1,*], Giovanni Biancini[1], Ramin Moradi[2], Luca Del Zotto[1], Matteo Moglie[1]

[1] *University eCampus, Research Center for Energy, Environment and Landscape, Via Isimbardi 10, 22060 – Novedrate (CO) Italy*
[2] *Department of Mechanical and Aerospace Engineering, University of Strathclyde, Glasgow, UK*

*Corresponding Author: luca.cioccolanti@uniecampus.it

ABSTRACT

Despite recycling is largely adopted in Europe, the amount of disposed municipal solid waste (MSW) from mechanical-biological treatment is increasing. At the same time, more environmentally friendly waste-to-energy (WtE) solutions are needed to promote sustainable management of residual MSW (RMSW) compared to incineration, which is the most common process to valorise MSW.
Among the waste-to-energy solutions, gasification is considered a promising option and nowadays attention is paid to the use of residual MSW as feedstock. In addition, organic Rankine cycle (ORC) systems are one of the most suitable technologies to produce electricity from low-grade energy sources such as that obtained from the gasification of residual MSW.
Therefore, in this work, a RMSW air gasifier in combination with an ORC unit are investigated using Aspen Plus for combined heat and power (CHP) applications. The simulation analysis is performed considering the potential syngas production from RMSW of a real composting facility in Italy. Three different working fluids are investigated to assess the energy performance of the integrated system for CHP production in district heating networks. The analysis reports an overall conversion efficiency of the integrated system in the range 38.4% - 48.5% and a maximum power production of the ORC unit of 2.14 MW_e with the use of toluene. Therefore, the present study shows that the gasification of RMSW and the exploitation of its energy content in an ORC system is a viable option to reduce the environmental burden in compositing facilities by extending the lifetime of the landfills.

1 INTRODUCTION

The sustainable management of municipal solid waste (MSW) is one of the pillars of the circular economy paradigm and a key action towards a more secure and competitive energy system in the EU. Despite recycling is considered the best solution in waste management, in some cases other methods are adopted for the valorisation of organic fraction of MSW and residual MSW (RMSW). The RMSW is mainly composed of a heterogeneous mixture of unrecycled materials that can be valorised by cold processes like mechanical-biological treatment (MBT) or consolidated waste incineration. As regards the latter, there are yet many operational plants in combination with organic Rankine cycle (ORC) units and it is also largely investigated in the literature. For example, Tozglu et al. (Tozlu et al., 2021) investigated different scenarios for the valorisation of MSW incineration for power production and district heating potential in Turkey finding that gas turbine power plants can increase the power generation capacity of MSW plants for each province by about 20%. Ustaoglu et al. (Ustaoglu et al., 2022), instead, conducted energy and exergy analysis of an ORC cogeneration system powered by MSW incineration for different working fluids finding that R141b performs the best among the selected fluids. However, incineration of MSW comes at the cost of high environmental impact which made other waste-to-energy (WtE) methods of interest. Indeed, MSW can be valorised also by pyrolysis and gasification technologies (Ruiz et al., 2013), which have lower environmental impacts compared to

incineration (Moradi et al., 2023). In the pyrolysis process, the feed material is thermally decomposed into oil, gas, and solid residues through a lean oxidation process while in the gasification the organic and carbon content of the input material process is converted into carbon monoxide, methane, hydrogen, and carbon dioxide with a controlled amount of the oxidant agent at high temperatures (>700°C).
The gasification of biomass feedstocks has been extensively studied in the literature, while co-gasification of mixture of biomass and other materials has not been explored much. For example, Mastellone et al. (Mastellone et al., 2010) investigated a more diverse composition represented by different mixtures of coal, waste plastic, and wood in a bubbling fluidized bed reactor demonstrating the feasibility of gasification of heterogeneous materials. Win et al. (Win et al., 2019) used an air fluidized bed gasifier for syngas production from residual paper, plastic, and wood pellets obtaining a low heating value (LHV) of the produced syngas in the range of 3.4-5.9 MJ/Nm^3 with varying equivalence ratio (ER) and feedstock type. In this context, residue-derived fuel (RDF) which is a pellet-like secondary fuel obtained downstream MBT process is attracting attention thus reducing its landfilling and the environmental burden of its disposal.
However, while the syngas produced from wood biomass gasification can be straightforwardly used in internal combustion engines (ICEs) and gas turbines, the exploitation of that from plastic gasification is more challenging. The high tar content and low ash melting point of the latter, indeed, may limit its use in external combustion power cycles. Among these power plants, ORC systems are one of the most efficient and competitive technologies and prove to perform even better than traditional Rankine cycles (Vankeirsbilck et al., 2011) for this kind of application. In turn, the chemical stability of the working fluids in ORCs usually limits the maximum operating temperature to around 300°C as also reported by Vescovo and Spagnoli (Vescovo & Spagnoli, 2017). For this reason, there are several works in literature (Li et al., 2018; Moradi et al., 2020) dealing with the integration of ORC systems as bottoming units in combined cooling heating and power or combined heating and power plants based on biomass gasification; yet addressing the use of ORC systems in combination with RMSW gasification is relatively scarce. Nevertheless, recent EU directives are supporting more environmentally friendly alternatives to RMSW incineration and therefore in this work the direct combination of RMSW gasification with ORC power plant is investigated. In particular, the general model of a fluidized bed air gasifier developed in a recent paper by the authors (Biancini et al., 2023) to estimate the syngas characteristics from RMSW of a real composting facility is here integrated with the model of a subcritical ORC system. The final aim is to estimate the RMSW overall potential for the provision of combined heat and power (CHP) in district networks in the perspective of more efficient and environmentally friendly management of the RMSW from composting facilities.

2 MATERIALS & METHODS

In this section, the composting facility under investigation is initially described and then the integrated model of the fluidized bed air gasifier and the ORC system is presented.

2.1 The compositing facility under investigation

The composting facility operates in the centre of Italy, and it mainly consists of: i) a section for the treatment of the organic fraction of the MSW which includes the anaerobic digesters and a 700 kW_e/400 kW_t CHP unit; ii) a MBT unit for the shredding, sorting, and recovery of the RMSW produced in the nearby municipalities; iii) a sanitary landfill for the disposal of the RMSW, and iv) a biogas-fuelled 250 kW_e ICE unit. It is worth noting that the CHP unit above works at part load conditions as a consequence of the biogas production from the digesters and that almost all the electricity produced is self-consumed in the air treatment process which represents the most energy-intensive process in the site. Further details about the composting facility can be found in Biancini et al. (Biancini et al., 2022).
In total, almost 80 ktons/year of RMSW are landfilled and about 20 ktons/year of residues are locally produced at the MBT unit. The latter is mainly composed of residual plastic and paper with an overall LHV of about 21 MJ/kg. Since during the operation this composition may be subjected to changes, its variation is accounted in this work by considering data from the literature. In particular, the following two additional compositions are assumed: plastic 68% + paper 32% (defined as “S2”) and plastic 54% + paper 46% (defined as “S6”) according to Bourtsalas and Themelis ((Thanos) Bourtsalas & Themelis,

2022). These mixtures bring to the minimum and maximum syngas LHV of (4526 kJ/Nm^3, with ER=0.33) and (6585 kJ/Nm^3, with ER=0.25) respectively. At the same time, the volumetric flow rate of the obtained syngas is higher in S2 than in S6 being equal to 6788 Nm^3/h and 4290 Nm^3/h respectively. Further details on the compositions and the obtained syngas characteristics are presented in (Biancini et al., 2023).

Therefore, in the present study the configuration of the real composting facility is modified by accounting for the RMSW gasification section and the ORC power generation unit downstream of the gasifier as reported in Figure 1. In particular, the syngas is burnt in an external combustion chamber because of its high tar content and the thermal energy of the flue gas is transferred to the ORC unit using diathermic oil (Therminol VP-1). The proposed scheme of the power cycle is similar to those commercially provided by Turboden and Ormat (Tartière & Astolfi, 2017).

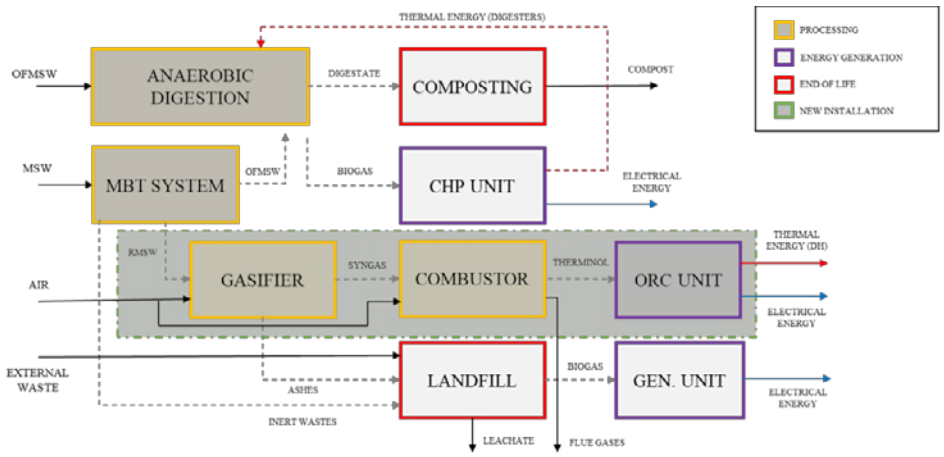

Figure 1: Conceptual scheme of the waste treatment facility. The green colour highlights the proposed gasifier + ORC section integrated into the current composting facility.

441

Hence, concerning the current situation, the proposed configuration would reduce the load on the landfill by limiting the disposal to inert materials and ashes only while increasing the energy valorisation of the MSW. Regarding the working fluids, toluene performs well among cycloalkanes, whereas super-dry fluids like MM and MDM are optimal for regenerative setups (Zhang & Li, 2023). Therefore, these fluids have been selected for the subsequent thermodynamic analyses.

2.2 The model

The thermochemical model of the fluidized bed gasifier was derived from a previous model of a fluidized bed steam gasifier developed by some of the authors of the present paper (Moradi et al., 2020) and adapted to the use of air as the gasifying agent and different feedstock compositions in (Biancini et al., 2023). In the latter, the model was previously validated against experimental data reported in the literature and then its use was extended to RMSW input material. The entire thermochemical process is divided into four main blocks according to an updraft configuration: i) the heater block for the biomass drying; ii) the RYIELD block to emulate the fast pyrolysis process of the input material; iii) the RGIBBS reactor which represents the combustion process providing heat; iv) the RGIBBS reactor to model the gasification process. Further details about the thermochemical model are presented in (Biancini et al., 2023). Then, the produced syngas is burned in an external combustion chamber and the energy content of the exhausts indirectly exploited by the bottoming ORC unit using a diathermic oil loop. A regenerative ORC cycle is considered as shown in Figure 2 to increase the conversion efficiency in accordance with Braimakis and Karellas (Braimakis & Karellas, 2018). The air mass flow rate, $\dot{m}_{air}$ [kg/h], for the syngas combustion, is evaluated from the stoichiometric combustion of the C_nH_mO compounds and considering a certain excess of air, e, to assure its complete combustion. Hence, the air mass flow rate is calculated according to Equations (1-4):

$$\dot{m}_{C_nH_m,st} = \dot{m}_{C_nH_m} \times 32 \frac{(n + m/4)}{(12n + m)} \quad (1)$$

$$\dot{m}_{CO,st} = \dot{m}_{CO} \times \frac{16}{12+26} = 0.571 \times \dot{m}_{CO} \quad (2)$$

$$\dot{m}_{air,st} = \dot{m}_{C_nH_m,st} + \sum \dot{m}_{C_nH_m,st} \quad (3)$$

$$\dot{m}_{air} = \dot{m}_{air,st} \times (1 + e) \quad (4)$$

where $\dot{m}_{air,st}$ is the stoichiometric air mass flow rate [kg/h], $\dot{m}_{C_nH_m,st}$ and $\dot{m}_{CO,st}$ are the stoichiometric air mass flow rates [kg/h] for the complete combustion of both the hydrocarbon gases C_nH_m and CO. The diathermic oil recovers the heat of the exhausts in the heat exchanger HX1 and transfers it to the ORC evaporator heat exchanger HX2. The regenerator is the heat exchanger HX3 and HX4 is the ORC condenser which is water-cooled. The performance of the heat exchangers is estimated using the ε-NTU method after a preliminary geometry characterization of the heat exchangers (Cavallini, 2017): cross-flow type heat exchangers with unmixed gas sides for HX1 and HX3, Shell & Tube (ST) with two shell passages for HX2, and single shell passage ST for HX4.

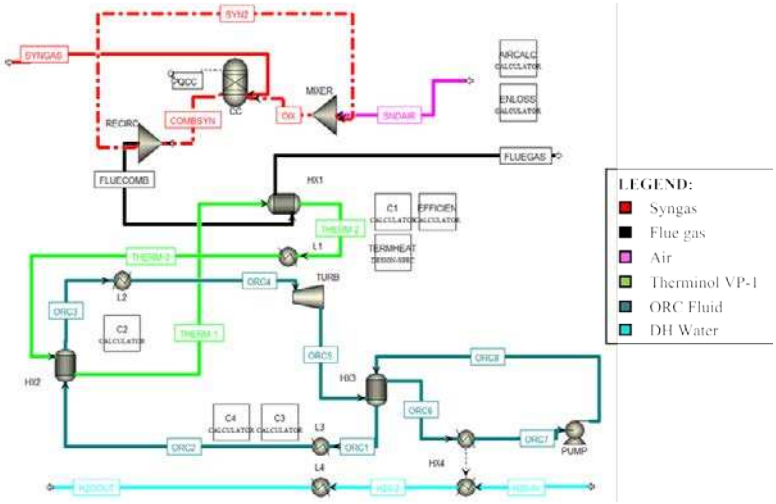

Figure 2: The integrated plant layout of the model developed in Aspen Plus.

The characteristics of the thermodynamical model are summarised in the following:

- The Peng-Robinson with Boston-Mathias modification is used as the equation of state for the calculation of the properties of the fluids. Water properties (light blue in Figure 2) are defined according to IAPWS-95 (Industrial Formulation for the Thermodynamic Properties of Water and Steam).
- The combustor (RGIBBS block) works with a fixed flue gas recirculation ratio of 20% and excess air of 150%. The combustion efficiency is considered 95%. Flue gas temperature after HX1 is fixed to 260°C since lower temperatures may lead to the formation of corrosive substances on the chimney wall, while higher ones may result in failures of the gas cleaning equipment and lower energy recovery rates. Inlet conditions of diathermic oil at HX1 are 180 °C and 10 bar.
- The NTU of each heat exchanger is in the range of 0.2<NTU<5 to avoid unfeasible area design. In such conditions, ε is lower than 95%.
- Thermal losses are accounted for in heat exchangers as follows: 10% for HX1 and HX4, 5% for HX2 and HX3. Such heat losses are modelled using 4 additional heat exchangers (L1 to L4) that have a negative thermal load defined by four calculator blocks (C1 to C4)
- The isentropic efficiency of the three-stage turbine is evaluated through the mathematical correlation proposed by Macchi and Astolfi (Macchi & Astolfi, 2017) for multistage axial turbines. The maximum allowable values for Size Parameter (SP) and Volume Ratio (VR) are

1 and 400 respectively. On the contrary, a constant isentropic efficiency of 75% is assumed for the pump due to its limited influence on the cycle performance. The electrical and mechanical efficiencies are assumed to be 0.97 and 0.95 respectively for the turbine and pump.

- The district heating (DH) network is a third-fourth generation (Yuan et al., 2021). This means that the hot-side water temperatures (T_{DH}) range from 55°C to 95°C with a 20°C step. At the condenser, the temperature difference at the cold side is considered fixed at 30°C, and a sub-cooling degree (ΔT_{SC}) of 5 °C is assumed.
- The maximum pressure of the ORC working fluid is assumed 80% of its critical pressure, and a superheating degree of the working fluid (ΔT_{SH}) of 10°C is assumed at the HX2 outlet.
- The minimum temperature difference of the hot fluid at the recuperator (ΔT_{REG}) is assumed 30°C.

3 RESULTS AND DISCUSSIONS

The quality of the RMSW in terms of its composition, and the ER in the fluidized bed gasifier strongly affects the thermal power input to the bottoming ORC system. Due to the variability of the RMSW, such input cannot be fixed and easily defined at priori. Nevertheless, for the sake of this study three different RMSW compositions and gasifier operating conditions are considered: i) the present composition of the RMSW provided by the composting facility under investigation (Baseline scenario) with ER = 0.3; ii) the S2 composition with ER = 0.33; and iii) the S6 composition with ER = 0.25. Further details of the selected RMSW properties can be found in the authors' previous work (Biancini et al., 2023)

3.1 Energy production from baseline RMSW

The most significant properties of the identified working fluids for the ORC system are reported in Table 1.

Table 1: The properties of the working fluids considered for the ORC system (Lai et al., 2011; Vescovo & Spagnoli, 2017).

Working Fluid	Chemical Formula	Molecular Weight [g/mol]	T_{crit} [°C]	P_{crit} [bar]	T_{min} [°C]	T_{max} [°C]
Toluene	C_7H_8	92.14	318.6	41.1	85	350
MM	$C_6H_{18}OSi_2$	162.38	245.9	19.2	30	290
MDM	$C_8H_{24}O_2Si_3$	236.53	291.3	14.6	80	290

Figure 3 shows the T-s diagrams of the three working fluids and their maximum and minimum operating pressures considering the heat input from the combustion of the syngas from the gasification of the RMSW in the Baseline scenario.

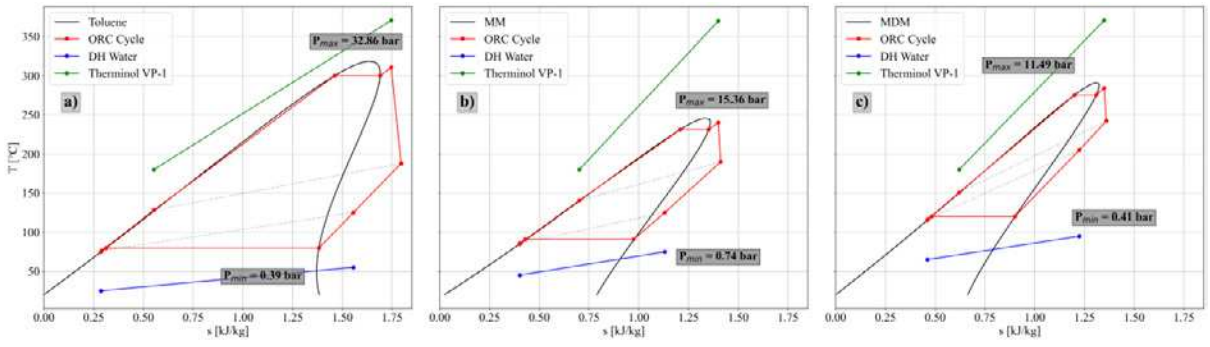

Figure 3: T-s diagram of the selected working fluids: a) toluene; b) MM; and c) MDM.

For a given heat input, the operating conditions of the fluids are strongly influenced by the saturation curves of the fluids. Being fixed the inlet and outlet conditions of the heating and cooling fluids, namely oil and water respectively, and in accordance with the assumptions described above, the model calculates the working fluid mass flow rate iteratively.
MDM has the lowest condensing pressure for a given temperature among the fluids under investigation. At a condensing temperature of 120° C, the corresponding pressure is 0.41 bar. As a consequence, the electric efficiency of the cycle is not affected by the supplying temperature of the hot fluid in the DH network since it is not recommended to operate at lower condensing temperatures. In the case of toluene, instead, the condensing temperature can be reduced to 80°C thus taking benefit of lower hot fluid temperatures in the DH network. Therefore, the minimum T_{DH} of 55°C is considered in the case of toluene. Eventually, MM is in between these two cases with a minimum condensing temperature of 90°C and a corresponding minimum T_{DH} of 75°C. Based on the thermodynamic conditions described before, the model calculates the mass flow rates of the working fluids (34.706 kg/h for Toluene, 63.639 kg/h for MM, and 57.964 kg/h for MDM) resulting in the power generation and conversion efficiencies, with respect to the evaporator (HX2), flue gas (HX1) and gasifier thermal power input, reported in Table 2.

Table 2: Performance of ORC system for the Baseline scenario.

Working Fluid	Q_{cond} [MW]	W_{turb} [MW]	HX2		HX1		Q_{GASIF} = 13.5 MW	
			η_t [%]	η_{el} [%]	η_t [%]	η_{el} [%]	η_t [%]	η_{el} [%]
Toluene	3.92	1.40	63.4	21.7	57.1	19.6	29.1	10.0
MM	4.26	0.97	69.2	15.0	62.3	13.5	31.6	6.8
MDM	4.55	0.74	73.5	11.3	66.2	10.2	33.7	5.2

The highest power production is obtained with toluene whereas the highest thermal output is achieved with MDM. From the conversion efficiencies point of view, toluene has the highest electrical and overall conversion efficiencies of 10% and 39.1% (with respect to the LHV of the RMSW), followed by MDM and MM having a total conversion efficiency of 38.4% and 38.9% respectively.

444

3.2 Energy production from S2 and S6

The performance of the ORC system in S2 and S6 scenarios is reported in Table 3 for all the considered working fluids. The produced electrical and thermal powers are significantly higher for S2 compared to S6 due to the greater syngas yield achieved from the former (mass flow rate of 6800 Nm^3/h and 4300 Nm^3/h for S2 and S6 respectively) despite the lower LHV (4500 kJ/Nm^3 and 6600 kJ/Nm^3 for S2 and S6 respectively). Figure 4 reports the T-s diagrams of the three working fluids for these scenarios.

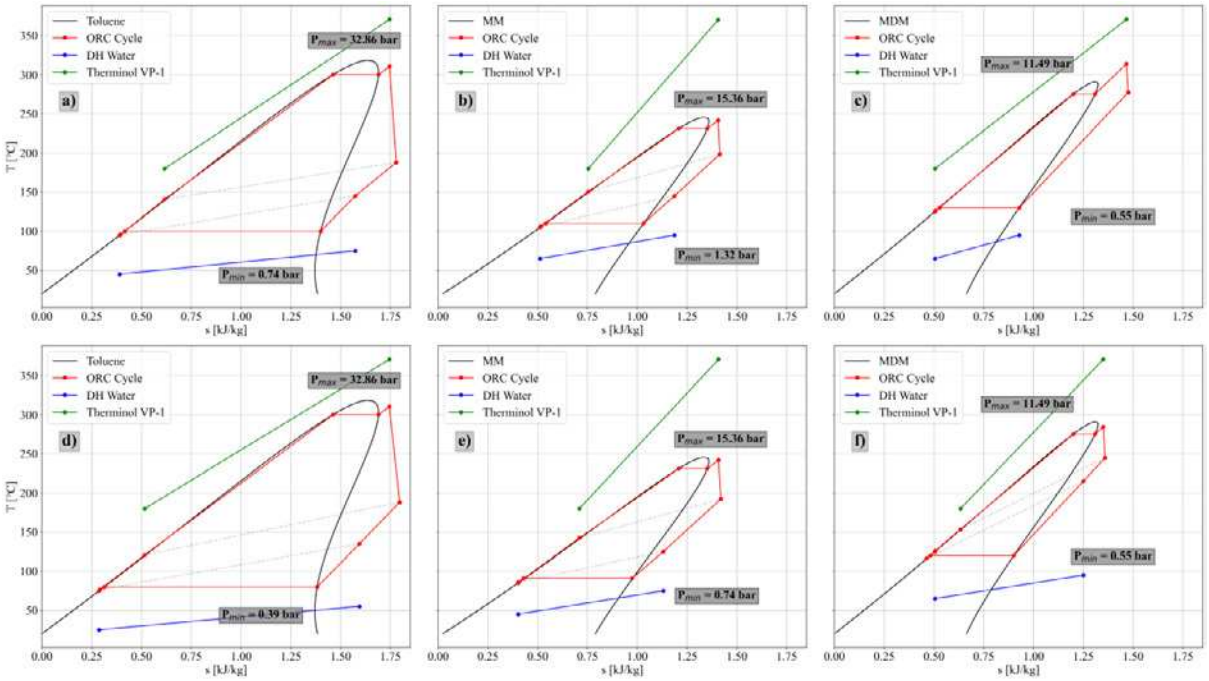

Figure 4: T-s diagram of the three working fluids for S2 (a,b,c) and S6 (d,e,f) scenarios.

Comparing T-s diagrams in Figure 3 with those in Figure 4, it can be noted that the ORC using toluene is not subjected to significant changes in its operation with RMSW composition. On the contrary, regeneration cannot be applied in S2 scenario due to SP > 1 or unfeasible heat exchangers NTU when MDM is considered as depicted in Figure 4c. In this case, higher condensation pressures and lower ΔT_{RIG} at HX3 are required to counterbalance these results. Nevertheless, the SP of MDM is inevitably higher due to the small enthalpy difference in the turbine despite an incremented turbine inlet temperature of 315°C and a superheating degree of 40°C which is far from the optimum operating conditions.

445

Table 3 reports the overall performance of the ORC power unit for S2 and S6 scenarios.

Table 3: Performance of ORC system in S2 and S6 scenarios with different working fluids.

Working Fluid	Q_{cond} [MW]	W_{turb} [MW]	HX2		HX1		Q_{GASIF_S2} = 18.6 MW Q_{GASIF_S6} = 13.8 MW	
			η_t [%]	η_{el} [%]	η_t [%]	η_{el} [%]	η_t [%]	η_{el} [%]
Toluene S2	6.72	2.14	65.3	19.9	58.8	17.9	36.2	11.0
Toluene S6	5.03	1.73	64.1	21.1	57.7	19.0	36.5	12.0
MM S2	7.34	1.38	71.7	12.6	64.5	11.3	39.5	6.9
MM S6	5.40	1.23	69.2	15.0	62.3	13.5	39.1	8.5
MDM S2	7.94	0.94	77.0	8.7	69.3	7.8	42.7	4.8
MDM S6	5.84	0.86	74.6	10.4	67.1	9.4	42.4	5.9

Like the Baseline scenario, the use of toluene leads to the highest electrical efficiency. The thermal recovery, instead, is enhanced with the siloxane fluids i.e. MM and MDM. Therefore, toluene is the best to obtain the maximum power output or overall conversion efficiencies, while siloxanes are suggested for DH application.

3.3 Sensitivity analysis with fluid temperatures in DH network

The analysis in sub-section 3.1 reveals that among the considered working fluids, only toluene can change its condensing pressure in accordance with the entire span of fluid temperatures in the DH network. Hence, a sensitivity analysis with fluid temperatures in DH network is conducted to assess the

variation of ORC performance using toluene as the working fluid. For the sake of this analysis, the discharge pressure of the ORC turbine is iteratively varied to reach a fixed pinch point of 10 °C at HX4 whereas the outlet temperature of the hot fluid after regeneration (HX3) is the minimum one fulfilling the NTU and SP constraints above. The results of this sensitivity analysis are reported in Table 4.

Table 4: Performance of ORC system using toluene with fluid temperature in DH network.

	Discharge Pressure [bar]	**Q_{cond} [MW]**	**W_{turb} [MW]**	**HX2**		**HX1**		**Q_{GASIF} = 13.5 MW** **Q_{GASIF_S2} = 18.6 MW** **Q_{GASIF_S6} = 13.8 MW**	
				η_t [%]	**η_{el} [%]**	**η_t [%]**	**η_{el} [%]**	**η_t [%]**	**η_{el} [%]**
Base 55°C	0.28	3.92	1.36	63.3	21.9	57.0	19.7	29.0	10.0
Base 75°C	0.40	3.94	1.33	63.7	21.5	57.3	19.3	29.2	9.8
Base 95°C	0.91	4.00	1.26	64.8	20.3	58.3	18.3	29.7	9.3
S2 55°C	0.57	6.63	2.14	64.3	20.8	57.9	18.7	35.6	11.5
S2 75°C	0.58	6.60	2.14	64.1	20.8	57.7	18.7	35.5	11.5
S2 95°C	0.91	6.69	2.07	65.0	20.1	58.5	18.1	36.0	11.1
S6 55°C	0.34	4.92	1.77	62.7	22.6	56.4	20.3	35.6	12.8
S6 75°C	0.40	5.01	1.68	63.8	21.4	57.4	19.2	36.3	12.2
S6 95°C	0.90	5.09	1.59	64.9	20.2	58.4	18.2	36.9	11.5

As expected, the electric efficiency increases when the turbine backpressure is decreased while the thermal efficiency has an opposite trend although with minor variations. However, in the case of S2 scenario the turbine power remains the same for hot fluid temperatures in DH network of 55°C and 75°C due to the limits of the working fluid for the fixed constraints. Independently from fluid temperature, the overall efficiency referred to the flue gas (HX1) is around 76% while if reference is made to the LHV of the RMSW a broader variation is obtained, ranging from 39% in the worst case (Baseline) to almost 49% in the best case (S6). Despite this variation, the analysis of each scenario leads to a common conclusion. The best exploitation of the waste material is pursued with a 4th generation of DH network (55 °C), since the electric production is increased and thermal losses in the network are reduced.

446

4 CONCLUSIONS

Gasification of RMSW is a promising WtE solution that can positively valorise the end-of-life of the disposed of material. In this work, the coupling of a fluidized bed gasifier having RMSW as input material with a regenerative ORC power unit for CHP applications is presented and discussed. Three different scenarios, which correspond to different feedstock materials and syngas flow rates, are evaluated with varying working fluids. Despite it is worth mentioning that the investigated operating conditions do not correspond to the optimum ones for each working fluid, the analysis shows that the maximum electrical power production of 2.14 MW_e can be obtained with the use of toluene, while a maximum thermal power output of 7.94 MW_t can be recovered at the condenser when MDM siloxane is selected. However, if technological aspects are considered use of MM instead of MDM is suggested due to the lower condensing temperature for DH applications. Eventually, the results of the sensitivity analysis of ORC performance with DH network temperature with toluene as the working fluid reveal that electric efficiency is more sensitive to the DH network temperature than the thermal efficiency.
In conclusion the analysis shows that the combination of RMSW gasification with an ORC system is a viable alternative to incineration thus improving the environmental performance of composting facilities.

NOMENCLATURE

CHP	combined heat and power
DH	district heating

e	air excess	(-)
ER	equivalence ratio	(-)
HX	heat exchanger	
ICE	internal combustion engine	
LHV (RMSW)	lower heating value	(kJ/kg)
LHV (syngas)	lower heating value	(kJ/Nm^3)
ER	equivalence ratio	(-)
$\dot{m}_{air}$	air mass flow rate	(kg/h)
MBT	mechanical-biological treatment	
MSW	municipal solid waste	
NTU	number of thermal units	
OFMSW	organic fraction of municipal solid waste	
ORC	organic Rankine cycle	
P	pressure	(bar)
Q	thermal power	(kW)
RDF	residue-derived fuel	
RMSW	residual municipal solid waste	
s	entropy	(kJ/kg)
SP	size parameter	
ST	shell and tube	
T	temperature	(°C)
Vr	volume ratio	(-)
W	electric power	(kW)
WtE	waste to energy	
ε	heat exchanger effectiveness	(-)
η	efficiency	(-)

Subscript

air,s	stoichiometric air
cond	condenser
e	electrical
GASIF	gasifier
REG	regeneration
s	saturation
st	stoichiometric
SC	subcooling
SH	superheat
t	thermal
turb	turbine

REFERENCES

Biancini, G., Marchetti, B., Cioccolanti, L., & Moglie, M. (2022). Comprehensive Life Cycle Assessment Analysis of an Italian Composting Facility concerning Environmental Footprint Minimization and Renewable Energy Integration. *Sustainability*, *14*(22), 14961. https://doi.org/10.3390/su142214961

Biancini, G., Moradi, R., Cioccolanti, L., Marchetti, B., Moglie, M., & Del Zotto, L. (2023). A general model for air gasification of heterogenous municipal solid waste. *Energy Conversion and Management*, *278*, 116749. https://doi.org/10.1016/j.enconman.2023.116749

Braimakis, K., & Karellas, S. (2018). Energetic optimization of regenerative Organic Rankine Cycle (ORC) configurations. *Energy Conversion and Management*, *159*, 353–370. https://doi.org/10.1016/j.enconman.2017.12.093

Cavallini, A. (2017). Heat transfer and heat exchangers. In *Organic Rankine Cycle (ORC) Power Systems* (pp. 397–470). Elsevier. https://doi.org/10.1016/B978-0-08-100510-1.00013-2

Lai, N. A., Wendland, M., & Fischer, J. (2011). Working fluids for high-temperature organic Rankine cycles. *Energy*, *36*(1), 199–211. https://doi.org/10.1016/j.energy.2010.10.051

Li, C. Y., Deethayat, T., Wu, J. Y., Kiatsiriroat, T., & Wang, R. Z. (2018). Simulation and evaluation of a biomass gasification-based combined cooling, heating, and power system integrated with an organic Rankine cycle. Energy, 158, 238–255. https://doi.org/10.1016/j.energy.2018.05.206

Macchi, E., & Astolfi, M. (2017). Axial flow turbines for Organic Rankine Cycle applications. In *Organic Rankine Cycle (ORC) Power Systems* (pp. 299–319). Elsevier. https://doi.org/10.1016/B978-0-08-100510-1.00009-0

Mastellone, M. L., Zaccariello, L., & Arena, U. (2010). Co-gasification of coal, plastic waste and wood in a bubbling fluidized bed reactor. *Fuel*, *89*(10), 2991–3000. https://doi.org/10.1016/j.fuel.2010.05.019

Moradi, R., Cioccolanti, L., Del Zotto, L., & Renzi, M. (2023). Comparative sensitivity analysis of micro-scale gas turbine and supercritical CO2 systems with bottoming organic Rankine cycles fed by the biomass gasification for decentralized trigeneration. *Energy*, *266*, 126491. https://doi.org/10.1016/j.energy.2022.126491

Moradi, R., Marcantonio, V., Cioccolanti, L., & Bocci, E. (2020). Integrating biomass gasification with a steam-injected micro gas turbine and an Organic Rankine Cycle unit for combined heat and power production. *Energy Conversion and Management*, *205*, 112464. https://doi.org/10.1016/j.enconman.2019.112464

Ruiz, J. A., Juárez, M. C., Morales, M. P., Muñoz, P., & Mendívil, M. A. (2013). Biomass gasification for electricity generation: Review of current technology barriers. *Renewable and Sustainable Energy Reviews*, *18*, 174–183. https://doi.org/10.1016/j.rser.2012.10.021

Tartière, T., & Astolfi, M. (2017). A World Overview of the Organic Rankine Cycle Market. *Energy Procedia*, *129*, 2–9. https://doi.org/10.1016/j.egypro.2017.09.159

(Thanos) Bourtsalas, A. C., & Themelis, N. J. (2022). Materials and energy recovery at six European MBT plants. *Waste Management*, *141*, 79–91. https://doi.org/10.1016/j.wasman.2022.01.024

Tozlu, A., Abusoglu, A., Ozahi, E., & Anvari-Moghaddam, A. (2021). Municipal solid waste-based district heating and electricity production: A case study. Journal of Cleaner Production, 297, 126495. https://doi.org/10.1016/j.jclepro.2021.126495

Ustaoglu, A., Torlaklı, H., Ergün, A., Erdoğmuş, E., & Emin Akay, M. (2022). Advanced exergy analysis of an integrated solid waste fueled cogeneration system based on organic Rankine Cycle for different working fluids. Energy Conversion and Management, 270, 116294. https://doi.org/10.1016/j.enconman.2022.116294

Vankeirsbilck, I., Vanslambrouck, B., Gusev, S., & De Paepe, M. (2011). Organic Rankine cycle as efficient alternative to steam cycle for small scale power generation. *HEFAT 2011*.

Vescovo, R., & Spagnoli, E. (2017). High Temperature ORC Systems. *Energy Procedia*, *129*, 82–89. https://doi.org/10.1016/j.egypro.2017.09.160

Win, M. M., Asari, M., Hayakawa, R., Hosoda, H., Yano, J., & Sakai, S. (2019). Characteristics of gas from the fluidized bed gasification of refuse paper and plastic fuel (RPF) and wood biomass. *Waste Management*, *87*, 173–182. https://doi.org/10.1016/j.wasman.2019.02.002

Yuan, M., Thellufsen, J. Z., Sorknæs, P., Lund, H., & Liang, Y. (2021). District heating in 100% renewable energy systems: Combining industrial excess heat and heat pumps. *Energy Conversion and Management*, *244*, 114527. https://doi.org/10.1016/j.enconman.2021.114527

Zhang, X., & Li, Y. (2023). An examination of super dry working fluids used in regenerative organic Rankine cycles. *Energy*, *263*, 125931. https://doi.org/10.1016/j.energy.2022.125931

ORC SEVILLE 2023
7th International Seminar on O.R.C. Power Systems

© 2024 Editorial Universidad de Sevilla. Este es un artículo de acceso abierto distribuido bajo los términos de la licencia de uso y distribución Creative Commons (BY-NC-ND 4.0)

DOI: https://dx.doi.org/10.12795/9788447227457_74

ENHANCING KNOWLEDGE OF ENGINEERING STUDENTS AT ALL LEVELS ON ORGANIC RANKINE CYCLE SYSTEMS FOR THEIR APPLICATION IN THE BUILT ENVIRONMENT

Luca Cioccolanti[1,*], Ramin Moradi[1], Ermira Abdullah[2], Syamimi Saadon[2], Mohamad Yusof Idroas[3], Teoh Yew Heng[3], Kwanchai Kraitong[4]

[1]*University eCampus, Research Center for Energy, Environment and Landscape, Via Isimbardi 10, 22060 – Novedrate (CO) Italy.*
[2]*Universiti Putra Malaysia, Faculty of Engineering, 43400 Selangor Darul Ehsan, Malaysia.*
[3]*Universiti Sains Malaysia, School of Mechanical Engineering, 14300 Nibong Tebal, Penang, Malaysia.*
[4]*Naresuan University, Department of Mechanical Engineering, Phitsanulok 65000, Thailand.*

*Corresponding Author: luca.cioccolanti@uniecampus.it

ABSTRACT

According to International Energy Agency (IEA), the global energy crisis is accelerating the use of renewable energy in the next five years. Furthermore, the building sector which accounts for about 30% of the final energy consumption, has a significant room for improvement in curbing its share of energy consumption and integrating renewable energy technologies. Hence, the 'Skybelt' project, co-funded by the EU under the framework of the Erasmus+ programme and coordinated by eCampus University - Italy, aims at enhancing the skills of engineering students at all levels for application of sustainable renewable energy solutions to be integrated into the built environment in several Asian and European universities.
The market analyses conducted in the initial stage of the project have revealed that combined heating and power (CHP) and combined cooling, heating, and power (CCHP) are the most interesting applications of knowledge for future employees on renewable energy. Among the potential CHP and CCHP technologies, Organic Rankine cycle (ORC) systems are interesting for the building energy sector thanks to their capability to be combined with solar and biomass sources.
Therefore, Universiti Putra Malaysia (UPM), Universiti Sains Malaysia (USM) and Naresuan University (NU) opted to be equipped with non-regenerative ORC test benches for training of engineering students at different levels. In particular, bachelor students at UPM will work on the development of different control approaches on small-scale ORC units within the modernised module of 'Control System Analysis', and students at USM and NU will be trained on the operating performance of these systems to be combined with different renewable energy sources. Hence, the project has given the opportunity to foster knowledge about the ORC systems for engineering students at all levels with the perspective of adopting them in buildings.

1 INTRODUCTION

Buildings are the single largest energy consumer in EU accounting for approximately 40% of the EU energy consumption and 36% of greenhouse gas emissions (European Commission, 2021). In particular, 27% of final energy consumption in 2020 was accounted for households according to Eurostat (2022), of which 62.8% for space heating, 15% for water heating and 0.4% for space cooling that is increasing steadily. Despite these numbers may differ in other regions of the world, the high impact of the building sector in the energy consumption is also significant in Asia and South East.

Furthermore, in the transition towards a more secure and sustainable energy supply, renewable power additions must triple (825 GW of renewables each year until 2050) to reach the average milestones set by the IEA's Net Zero scenario by 2050, and by the World Energy Transitions Outlook scenarios from the IRENA (REN21, 2022).

Such a challenging commitment requires a competent workforce of practitioners and professionals with strong knowledge in renewable energy technologies (RETs). In recent years, the labour market has been pulled by an increasing demand of employment linked to RETs. Fragkos and Paroussos (2018) by investigating the net employment impacts of the EU energy sector transformation towards a renewable energy one, found that this low-carbon transition would reallocate about 1.3% of the EU's workforce across sectors by 2050. Hence, educational curricula incorporating themes related to renewable energy and sustainable livelihood required to be considered in the academic education to deliver trained alumni for such transition. Educating green collar workers to develop and promote renewable energy technologies with technical, professional, and managerial abilities for renewable and sustainable energy sector is among the missions of many university programmes worldwide and is strongly promoted by the EU. In this context, the 'Skybelt' project (2020), co-funded by EU under the framework of the European Union's Erasmus + programme and coordinated by the University eCampus - Italy, aims at enhancing the skills of engineering students at all levels for application of sustainable renewable energy solutions to be integrated into the built environment in several Asian and European universities. All these universities are experiencing an increasing interest in offering up to date and advanced courses on RETs with special focus on those to be integrated in the building energy sector. Furthermore, energy efficiency is another pillar to pursue sustainable development. In the building sector, combined heating and power (CHP) and combined cooling, heating, and power (CCHP) may play a crucial role in curbing CO_2 emissions. Among the possible CHP and CCHP technologies, organic Rankine cycle (ORC) systems have attracted attention thanks to their capability to be combined with geothermal, solar and biomass sources.

In the literature, the use of solar ORC in building sector has been investigated by several authors. For example, Freeman et al. (Freeman et al., 2015) compared different solar technologies in combination with an ORC unit using positive-displacement expander for domestic applications in a typical UK home obtaining 80% of hot water demand coverage and total electrical energy production of 776 kWh/year at best. Rodriguez-Pastor et al. (Rodriguez-Pastor et al., 2023) evaluated the potential of integrating ORC units in existing residential solar thermal installations with findings demonstrating positive economic performances for Mediterranean climate area. Arteconi et al. (Arteconi et al., 2019) investigated the integration of a micro solar ORC plant in residential buildings reporting that the operational strategy and the dynamic energy demand of the building was contributed by 26% from the ORC electricity production. Finally, the use of ORC systems as bottoming units of biomass-based micro-CCHP plants for decentralised trigeneration in buildings has been investigated by a few of the authors of the present paper (Moradi et al., 2023). Therefore, in the context of the 'Skybelt' project, three Asian universities opted to equip their laboratories with non-regenerative ORC test benches for training of their engineering students at different levels with the final aim of promoting the use of ORC systems in buildings.

450

2 THE SKYBELT PROJECT

The Skybelt project is a cooperation between 3 EU universities in Italy, United Kingdom, and Turkey, and 6 Asian universities in China, Malaysia, and Thailand. More precisely, eCampus University, Northumbria University and Cukurova University from EU countries, Beijing University of Technology, and Lanzhou Jiaotong University from China, Universiti Putra Malaysia (UPM), Universiti of Sains Malaysia (USM) from Malaysia, and Chiang Mai University and Naresuan University (NU) from Thailand.

The modernised teaching methods and contents to be implemented in the 'Skybelt' project were designed based on a student-centred approach having at its focus the satisfaction of the current and future market needs. In this perspective, relevant stakeholders and organisations were interviewed in the early stage of the project to provide feedbacks on the kind of knowledge and expertise the future

engineers should have. More than 120 organisations were identified in Partner Countries of the project and about 110 interviewed. The most relevant results of this survey can be summarised as follows:

- efficiency improvements and reliability and durability of RETs are considered the main challenges to be faced.
- solar energy and heat pumps are considered the main required topics of knowledge of future employees on RETs;
- great interests were expressed for CHP and CCHP systems;
- 11.4% of the interviewed organisations considered ORC technology of interest;
- control and automation, data analysis, and predictive control are the most demanded expertise for future employees.

Further details on the results of this analysis can be found in (Cioccolanti et al., 2021).
Therefore, the outcomes of this survey have driven the selection of modules to be modernised or introduced in Partner Countries universities, as well as the teaching content and methods. Since ORC technology and CHP/CCHP applications are of interest for many stakeholders, UPM, USM, and NU have decided to include the study of ORC systems in the content of some modules and equip their laboratories with a test bench to train their students in this field.

3 THE ORC TEST BENCHES AND THEIR USE

In this section, the driving aspects in the design of the required ORC system test benches and their use at different Asian universities are discussed. In general, the design of these test benches has been based on the experience gained by colleagues at eCampus University in the test of micro-scale ORC systems for waste heat recovery applications (Moradi et al., 2021a). In this case, a 1 kW_{el} non-regenerative ORC unit charged with R134a was developed, making use of the commercial scroll compressor SANDEN TRS090F as expander. Heat is supplied by five electrical heaters (total power input of 22.5 kWe) and provided through silicone oil Texatherm HT22. A chiller that is able to cool the water temperature down to 8°C was used as the heat sink and plate heat exchangers have been selected. Additionally, an oversized piston pump was installed to accommodate testing of different working fluids and types of expanders. Further details can be found in (Moradi et al., 2021b).

Therefore, considering the target applications and the budget constraints, for all three universities, subcritical and non-regenerative ORC configuration was identified as the most appropriate.
With regards to the expansion device, a scroll compressor converted to expander was selected as the common device in many micro-scale ORC systems. Heat is provided using diathermic oil circuit heated by electrical heaters to replicate low temperature applications such as in the case of traditional solar thermal technologies (solar panels and evacuated tubes). Water is used as cooling medium and its heat discharged to the ambient using a chiller.
The main characteristics of the ORC test benches in each Asian university are reported in the following sub-sections together with the analysis to be performed by students within the modernised curricula.

3.1 Universiti Putra Malaysia

At Universiti Putra Malaysia, the test bench has been installed at the premises of the Department of Aerospace Engineering as shown in Figure 1. It consists of the following main components: (i) 500 W scroll expander; (ii) 10 kW electric heater; (iii) plate heat exchanger evaporator and condenser; (iv) 370 W pump. Silicone oil is used to transfer heat generated by the electric heaters to the working fluid (R134a).
The system has been designed to operate with a nominal evaporation temperature of the working fluid equal to 80°C with a maximum superheating temperature up to 100°C. The condenser temperature for the ORC operation is 20-50°C using the cooling water circuit.

Figure 1: Experimental test rig at the premises of Universiti Putra Malaysia

The students are required to demonstrate the operation of the ORC and analyse the amount of electric power produced by the ORC unit with varying heat source temperature. At the end of the experiment, students are able to correlate the performance of the ORC system in terms of expander power output with the heat source temperature and thermal power input. The procedure for this experiment is as follows:

1. Turn on the chiller and set the cooling water temperature at 20°C;
2. Set the oil inlet temperature to evaporator to at least 40°C;
3. Set the oil pump frequency to 40 Hz and turn on the pump;
4. Set the working fluid pump frequency to 50 Hz;
5. Wait for the stabilization of the operating conditions (i.e., the expander inlet temperature and pressure, working fluid mass flow rate);
6. Check if the outlet temperature of the working fluid from the evaporator is higher than the evaporation temperature;
7. Increase the temperature of the heater slowly with a step of 5°C until it reaches 90°C;
8. The ORC starts to operate when all the critical setting of parameters (Step 1 to 7) are fulfilled. The scroll expander starts rotating and the power output is measured at the load bank.

Within the modernised module of 'Control System Analysis', bachelor students at UPM will develop real time measurement system for the pressure and temperature of the working fluid at the inlet and outlet of the main components. In particular, the LabVIEW software and NI Compact DAQ 9174 chassis will be used to monitor these parameters. The NI 9203 analogue input module will be used to measure the input current from the pressure transducers and the NI 9211 temperature input module will be used to measure the temperature from the thermocouples. The hardware is shown in Figure 2a. For the pressure measurements, students will use LabVIEW software to convert the measured current to pressure such as shown in Figure 2b.

Based on the measured pressures and temperatures the values of the working fluid thermodynamics properties will be calculated using the open-source library Coolprop and the performance of the main components assessed. In particular, students will be able to evaluate the pump and expander performance in terms of power and isentropic conversion efficiency.

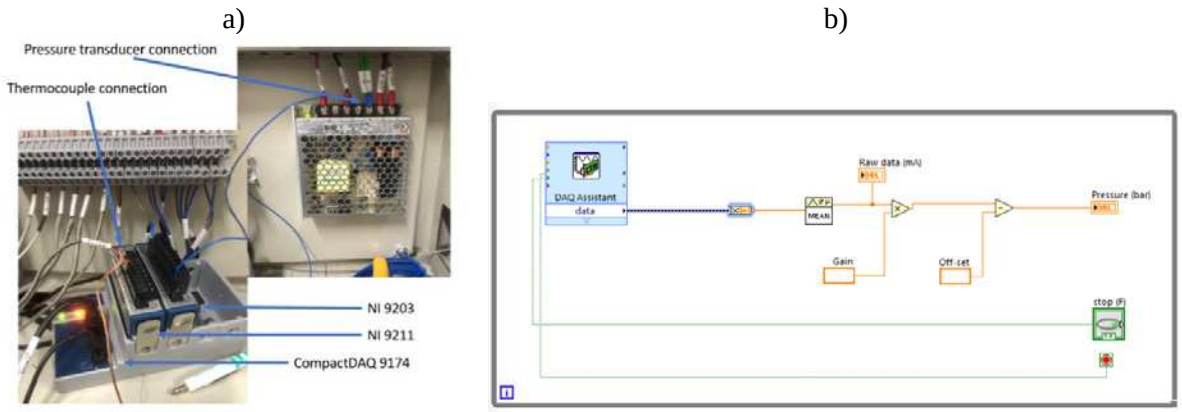

Figure 2: a) Hardware for the data measurement system; b) LabVIEW program for converting current signal to pressure measurement

Furthermore, a more complex experiment will be proposed for the final year project by expanding the function of the data acquisition system. Students will be able to perform a parametric study by changing the variables affecting the outputs of the ORC and design a controller for the ORC system to obtain optimal control of the expander power output. This activity will serve as preliminary study to further improve the present test bench in case additional funds will be available in the future for its upgrade.

3.2 Universiti Sains Malaysia

At Universiti Sains Malaysia, the ORC test bench is installed at the Advanced Renewable Energy Laboratory of the Science and Engineering Research Centre (SERC) as shown in Figure 3. The characteristics of the test bench are the same as the one installed at UPM.

The performance of the ORC unit is assessed in terms of power produced by the expander by changing the electrical load. During the experiments, students will analyse the critical operating parameters such as the evaporation temperature and pressure and the condensing temperature with varying heat source power input and temperature. Furthermore, students will test different working fluids and analyse their impact on the overall system performance.

a) b)

Note:

1. Water Cooler Chiller
2. Condenser
3. Working fluid Pump
4. Expander
5. Generator
6. Liquid Receiver
7. Evaporator
8. Finned Tube Heat Exchanger Tank
9. Control Panel Box
10. Oil Pump
11. Indicators of Temperature and Pressure
12. Control Panel with Switches

454

Figure 3: Experimental test rig at the premises of Universiti Sains Malaysia (a) ORC piping and connection, (b) Control panel with switches and indicators of temperature and pressure.

The experimental procedure, according to which students at Universiti Sains Malaysia will be trained, is very similar to the one previously discussed for the Universiti Putra Malaysia. However, in this case the laboratory equipment will be used by students attending the selected modernised modules of Internal Combustion Engine and Open-ended laboratory. At Universiti Sains Malaysia, besides renewable energy technologies such as solar thermal panels, the focus is also on the biomass-fuelled internal combustion engines (ICEs) as micro-CCHP units in residential buildings. Hence, the students will be trained on improving the overall energy conversion efficiency of ICEs by recovering the heat of the exhausts in ORC units. Then, the gained expertise could be transferred to other sectors such as industrial applications or transport in which waste heat recovery could improve the primary energy use and reduce the related environmental impact. Therefore, it is expected that students at USM will conduct experiments of ORC operation with different working fluids to investigate its performance for a wide range of low-temperature applications.

3.3 Naresuan University

At Naresuan University, the proof of how low-grade heat can be recovered into useful electric power using Organic Rankine Cycle is performed through the test bench installed at the Department of Mechanical Engineering, Faculty of Engineering. The apparatus is designed to support the teaching on ORC systems at different levels as follows: i) undergraduate students in mechanical engineering will be trained on the operating characteristics of ORC systems; ii) postgraduate students in mechanical engineering will understand the capability of ORC systems in exploiting low-temperature renewable heat sources such as solar by attending some elective modernised modules; and iii) PhD students will conduct experimental investigations using the comprehensive measurement devices and data logging systems. Also in this case, R134a is considered as working fluid and a 500 W scroll compressor is converted to operate as expander. The hermetic scroll expander is connected to a brushless generator

with permanent magnets having a maximum DC power of 1500 W at 6000 rpm, high voltage from 200 to 350 V and DC low voltage from 9 to 16 V. Both scroll expander and generator are inside a sealed casing with shell strength of 8.3 MPa on the high-pressure side and 5.2 MPa on the low-pressure side. Compared to the test benches at UPM and USM, this test bench utilises coil heat exchangers for the evaporator and the condenser, and a canned motor centrifugal pump, instead of plate heat exchangers and volumetric-type pump. The low-temperature heat from renewable source is simulated by 12 kW electric heaters and heat is supplied by means of diathermic oil. Water is used as cooling medium at the condenser which, in turn, is cooled down by a dry cooler. The system is designed to operate with nominal evaporating and condensing temperatures of 80°C and 46°C respectively. Figure 4 shows the ORC test rig installed at the Department of Mechanical Engineering of NU.

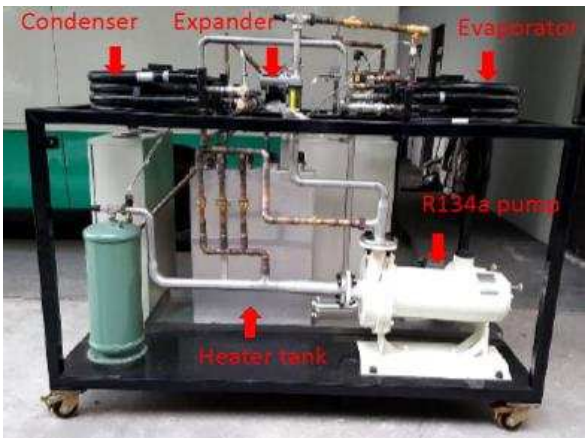

Figure 4: ORC test rig installed at Naresuan University

Pressure transducers having an operating range of 0-40 bar and safety pressure switch are installed at the evaporator inlet and outlet points. Pressure sensors having an operating range of 0-25 bar are installed at condenser inlet and outlet points. Eight thermocouples for measuring the temperature of working fluid, oil, and water are placed at inlet and outlets of condenser and evaporator. A PLC data acquisition and control with LCD touch screen displays real-time operating parameters namely pressure, temperature and flow rate of the fluids together with the power output of the expander.

The data acquisition software is written in LabVIEW and all user inputs and acquired data are monitored. Real time display of temperatures and pressures are available in chart form as shown in Figure 5. This facilitates different training activities such as the recording of the vapor-pressure curve of the cycle, the expander isentropic efficiency and power output, the determination of the heat input and the overall energy conversion efficiency of the system.

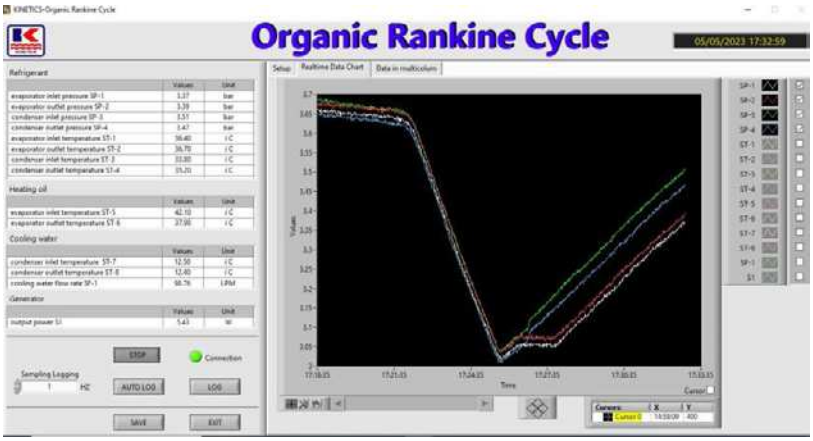

Figure 5: Real-time display of temperatures and pressures by the data acquisition software written in LabVIEW

Students will be trained to operate the ORC system according to the following procedure:

1. Run the oil gear pump which circulates oil between the heater tank and evaporator;
2. Switch on the electric heaters immersed in the heater tank;
3. Switch on the dry cooler;
4. As soon as oil temperature reaches 80°C, switch on the R134a pump. Generator load relays are to be on off-state;
5. When the evaporation pressure of the working fluid reaches 15 bar, open the solenoid valve at the expander inlet;
6. Monitor the superheating degree and subcooling degree and the pressure at evaporator inlet and outlet points;
7. Monitor the shaft speed of the expander;
8. Adjust the generator electrical load as follows: (i) both R1 and R2 relays off (ii) R1 relay on and R2 relay off, and (iii) both R1 and R2 relays on.
9. Adjust heat input by acting on the n°4 electric heaters.

In case of failures, the implemented safety procedure switches off the R134a pump to stop R134a flowing into the evaporator and opens the solenoid valve to release pressure in the evaporator side.

At Naresuan University this laboratory equipment will be used by master students attending the modernised module of Renewable Energy Resources where solar thermal energy is the subject of other modules included in the overall modernisation. In this module, students will simulate the combination of traditional solar thermal panels and evacuated tubes with ORC system for the provision of heating and power to domestic users. The final aim is to assess the performance of such technology with varying ambient conditions and users' needs.

4 CONCLUSIONS

Within the context of 'Skybelt' project, co-funded by the EU under the framework of the Erasmus+ programme and coordinated by eCampus University - Italy, three Asian universities equipped their laboratories with ORC test benches to train their students at different levels on the topic of ORC systems. These universities are Universiti Putra Malaysia, Universiti Sains Malaysia, and Naresuan University.

All the ORC test benches are based on subcritical and non-regenerative ORC units using converted scroll compressor as the expander following the experience gained at eCampus University. Electrical heaters are used to supply heat using a diathermic oil circuit and chilled water is used as cooling medium. The ORC systems have been designed to exploit low-temperature heat sources as renewables sources like solar thermal to promote their integration in building for CHP and CCHP applications.

Students will use the test benches in different modules at Partner Countries Universities with the aim of fostering knowledge and providing expertise in the control and operation of such systems for applications in buildings.

REFERENCES

Arteconi, A., Del Zotto, L., Tascioni, R., & Cioccolanti, L. (2019). Modelling system integration of a micro solar Organic Rankine Cycle plant into a residential building. Applied Energy, 251. https://doi.org/10.1016/j.apenergy.2019.113408

Cioccolanti, L., Moglie, M., Mahkamov, K., Paksoy, H., Chen, C., Lin, J., Li, C., Guan, Y., Zhou, W., Abdullah, E., Mohd Radzi, M.A., Shafie, S., Alimuddin, Z., Yusof I., Mohamad, Yew Heng, T., Azmier Ahmad, M., Azman Miskam, M., Kraitong, K., Wongsapai, W., Chaichana, C., Damronsak, D., 2021, Analysis of labour market needs for engineers with enhanced knowledge in sustainable renewable energy solutions in the built environment in some Asian countries, 2020 Applied Energy Symposium (ICAE), 100RES 2020, E3S WEB OF CONFERENCES, vol. 238: 07004.

Enhancement of engineering skills of students of all levels for application of evidence based sustainable renewable energy solutions in the built environment, 'Skybelt', 2019-2023, www.skybelt.eu.

European Commission-Energy-Energy performance of buildings directive 2021, https://energy.ec.europa.eu/topics/energy-efficiency/energy-efficient-buildings/energy-performance-buildings-directive_en#energy-performance-of-buildings-standards.

Energy consumption in households - statistics Explained, 2022, ,https://ec.europa.eu/eurostat/statistics-explained/index.php?title=Energy_consumption_in_households.

Fragkos, P., Paroussos, L., Employment creation in EU related to renewables expansion, 2018, *Applied Energy*, 230: 935-945.

Freeman, J., Hellgardt, K., & Markides, C. N. (2015). An assessment of solar-powered organic Rankine cycle systems for combined heating and power in UK domestic applications. Applied Energy, 138, 605–620. https://doi.org/10.1016/j.apenergy.2014.10.035

Moradi, R., Cioccolanti, L., Del Zotto, L., & Renzi, M. (2023). Comparative sensitivity analysis of micro-scale gas turbine and supercritical CO2 systems with bottoming organic Rankine cycles fed by the biomass gasification for decentralized trigeneration. *Energy*, *266*, 126491. https://doi.org/10.1016/j.energy.2022.126491

Moradi, R., Villarini, M., & Cioccolanti, L. (2021a). Experimental modeling of a lubricated, open drive scroll expander for micro-scale organic Rankine cycle systems. Applied Thermal Engineering, 190, 116784. https://doi.org/10.1016/j.applthermaleng.2021.116784

Moradi, R., Habib, E., Bocci, E., & Cioccolanti, L. (2021b). Component-Oriented Modeling of a Micro-Scale Organic Rankine Cycle System for Waste Heat Recovery Applications. Applied Sciences, 11(5), 1984. https://doi.org/10.3390/app11051984

Rodriguez-Pastor, D. A., Becerra, J. A., & Chacartegui, R. (2023). Adaptation of residential solar systems for domestic hot water (DHW) to hybrid organic Rankine Cycle (ORC) distributed generation. *Energy*, *263*, 125901. https://doi.org/10.1016/j.energy.2022.125901

REN21. 2022, Renewables 2022 Global Status Report, ISBN 978-3-948393-04-5.

ORC SEVILLE 2023
7th International Seminar on O.R.C. Power Systems

© 2024 Editorial Universidad de Sevilla. Este es un artículo de acceso abierto distribuido bajo los términos de la licencia de uso y distribución Creative Commons (BY-NC-ND 4.0)

DOI: https://dx.doi.org/10.12795/9788447227457_75

STUDYING CARBON DIOXIDE AND ACETONE MIXTURES IN A SINGLE-STAGE ABSORPTION-COMPRESSION CYCLE FOR HEATING AND COOLING APPLICATIONS

Jesús Gómez-Hernández[1]*, Alhi Kholghi[2], Mercedes de Vega[1], Javier Villa Briongos[1], Ronan Grimes[2]

[1] *Energy Systems Engineering Group (ISE), Department of Thermal and Fluid Engineering, Universidad Carlos III de Madrid, Av. Universidad, 30, 28911, Leganés, Madrid, Spain*
[2] *Stokes Laboratories, Bernal Institute, School of Engineering, University of Limerick, Ireland*

*Corresponding Author: jegomez@ing.uc3m.es

ABSTRACT

This communication analyzes the performance of a zeotropic fluid, composed by the mixture of carbon dioxide and acetone, in a vapor compression cycle with a solution circuit. The working fluid is characterized by a high temperature glide that depends on the mixture composition. The high critical temperature of the acetone and the good thermal properties of carbon dioxide makes this mixture a promising heat transfer fluid for industrial heat pumps that need to supply energy for heating and cooling processes. The heat pump analyzed has these components: evaporator, compressor, condenser, two internal heat exchangers and an expansion valve. In addition, a second liquid line with a solution pump is used to circulate the liquid from the gas-liquid separator to an internal heat exchanger, and then, to the condenser. In this way, the gas-liquid separator allows the fluid to leave the evaporator as a vapor-liquid mixture. This heat pump configuration working with the CO_2/acetone mixture could provide the energy needs of an industry that requires both heating and cooling. Depending on the binary mixture composition, the source and sink temperatures change as well as the coefficient of performance. For instance, an 55% CO_2/45% acetone in mass fraction, can provide heat to the sink at an average thermodynamic temperature of 110ºC, and refrigeration at an average thermodynamic temperature of 0ºC, showing a total COP of 2.55. This configuration would work at a high pressure of 40 bar and a low pressure of 10 bar.

1 INTRODUCTION

Decarbonizing process heating and process cooling in industry is key to meet the EU climate goals. Indeed, The EU's heating and cooling needs in 2020 accounted for half of its total gross final energy consumption (Eurostat, 2022). Heating in industrial processes accounted for approximately 25% of global energy consumption in 2021 (Thiel, 2021). In this sense, fossil fuels provided most of this heat. Only 13% of process heat in the EU is provided by renewable sources, 11% of this being provided by biomass, while electricity provides 12% of the EU' s process heat – some of this may be renewable, depending on the local power generation mix (Elsand et al., 2017).

However, the decarbonization of industry is a difficult task because of the inhomogeneous array of processes and temperature requirements (Arpagaus et al., 2018). For instance, steel and cement production may require temperature far beyond 1000°C, while some food industry processes may need only 40-80°C for processes like homogenization or pasteurization. Heat pump technology is emerging as a flexible approach to decarbonizing heating and cooling for medium temperatures. Regarding the heating applications, there are industrial heat pumps available that can provide industrial process heat at temperatures up to 150ºC with high coefficient of performance (Olsson and Schipfer, 2021).

Regarding the simultaneous heating and cooling, an ammonia-based compression heat pump is studied by (Ayou et al., 2022) to provide simultaneous heating at 72ºC and cooling at 4ºC for milk pasteurization.

There is a great interest in exploring new heat pump refrigerants with low Global Warming Potential that can help in the decarbonization of industry with low environmental impact. The binary mixture of carbon dioxide and acetone has been proposed as a good candidate for such a task. Previous studies have experimentally characterized the zeotropic phase change of this refrigerant, which shows high temperature glides that depend on the mixture composition (Höhler et al., 2018) (Ramírez-Ramos et al., 2021). In the same way, a recent paper of the authors explored the use of this mixture for high temperature heat pumps in the range of 150 - 220ºC (Gómez-Hernández et al., 2023).

A zeotropic refrigerant with high temperature glide may present some drawbacks. For instance, when comparing a pure fluid with a zeotropic refrigerant, the phase change process includes a new thermal resistance that reduces the heat transfer coefficient (Huang et al., 2022). In the same way, the compressor may reduce its efficiency due to the inhomogeneous behavior of the mixture during the compression process (Roskosch et al., 2021). However, the potential application of this low GWP refrigerant is mandatory before addressing the aforementioned challenges.

This communication analyzes a single-stage compression-absorption cycle using a binary mixture of carbon dioxide and acetone as refrigerant. This heat pump layout uses a gas-liquid separator to reduce the power consumption of the compressor by changing the refrigerant composition. To the best author knowledge, this study is the first attempt to study the binary mixture of carbon dioxide and acetone to supply simultaneously both heating and refrigeration at milk pasteurization temperatures. Partial phase change processes are considered in both evaporator and condenser in order to supply heat at heating temperatures above 80ºC and cooling at temperatures below 0ºC. The results show the influence of the operating conditions of the gas-liquid separator on the heat sink temperature and on the coefficient of performance for different refrigerant compositions.

2 METHODS

This section describes the heat pump layout, the main thermodynamic properties of the refrigerant and the main assumptions used to calculate the performance indicators.

2.1 Heat pump layout

Figure 1 shows the proposed heat pump layout considered in this study. This single-stage absorption-compression cycle is composed by a gas-liquid separator, a compressor, a pump, two internal heat exchangers, the condenser and the evaporator. The key element is the gas-liquid separator, which is assumed to be at equilibrium for the desired pressure and temperature. The gas-liquid separator divides the flow into a vapor, which flows into the compressor, and a liquid, that is pumped up to the compressor pressure discharge. The vapor has a high content of the most volatile component, CO_2 in this study, while the liquid has a high content of acetone. The liquid is preheated in an internal heat exchanger (IHX1). Then, the compressed vapor stream and the preheated liquid is adiabatically mixed, flowing into the condenser at state 3.

Heat is transferred to the sink during the partial phase-change process that is produced in the condenser. The outlet condenser temperature (state 4) is an input data. The condensation process is completely achieved transferring heat to the acetone high liquid in IHX1, and preheating the refrigerant in the second internal heat exchanger (IHX2). Finally, the refrigerant is at saturated liquid conditions, and then, expanded in the isenthalpic valve up to the evaporator pressure. Such pressure determines the heat received from the source at low temperature. The cycle is closed with the IHX2, that heats up the refrigerant up to the inlet conditions at the gas-liquid separator.

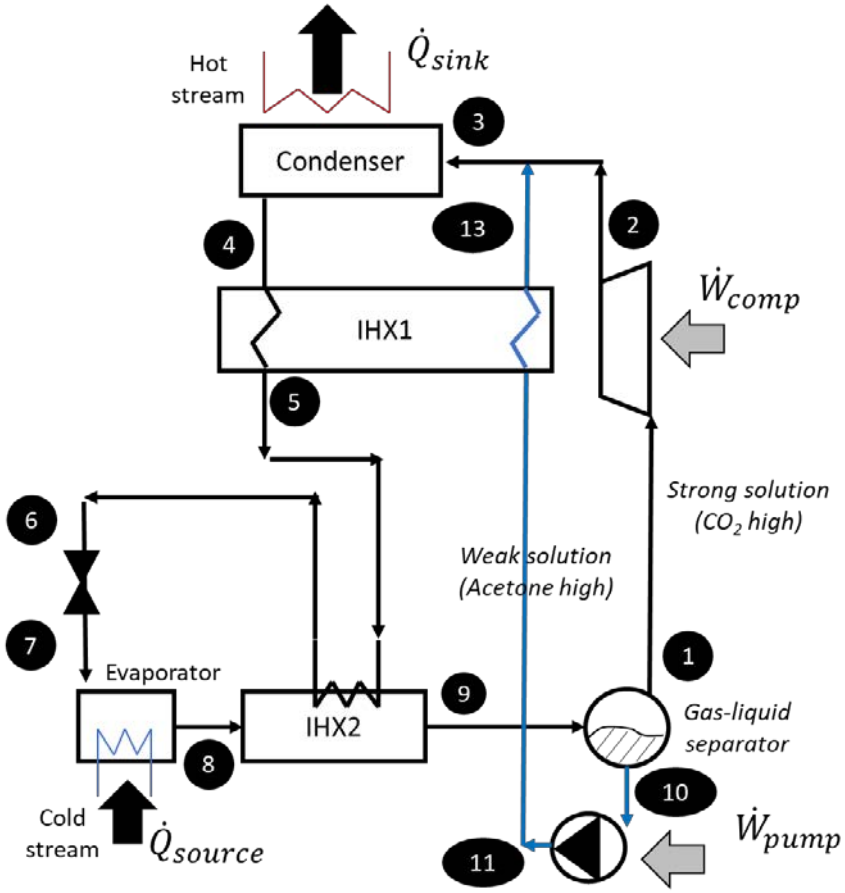

Figure 1: Single-stage absorption-compression cycle.

460

2.2 Refrigerant properties

The binary mixture of carbon dioxide and acetone shows a zeotropic behavior during phase change. Table 1 shows the properties of both pure fluids. Temperature glides up to 120 K can be obtained depending on the mixture composition and the operating pressure (Gómez-Hernández et al., 2023). This work analyzes the performance of the single-stage absorption-compression cycle for an evaporator pressure of 10 bar and for a condenser pressure of 40 bar. Therefore, the temperature evolution as a function of the mixture quality for both pressures is presented in Figures 2 and 3.

Table 1: Pure fluid properties.

Refrigerant	T_{crit} [°C]	P_{crit} [bar]	NBP [°C]	GWP100 [-]	ODP [-]
Acetone	234.95	46.92	56.07	0.5	0
Carbon dioxide	30.98	73.77	-78.46[a]	1	0

[a] Normal Sublimation Point

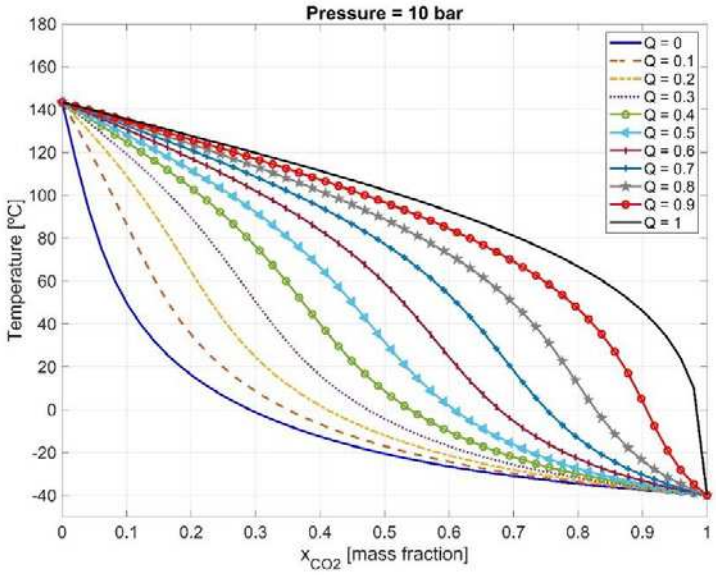

Figure 2: Temperature evolution as a function of the CO_2 content and the mixture quality for a pressure of 10 bar.

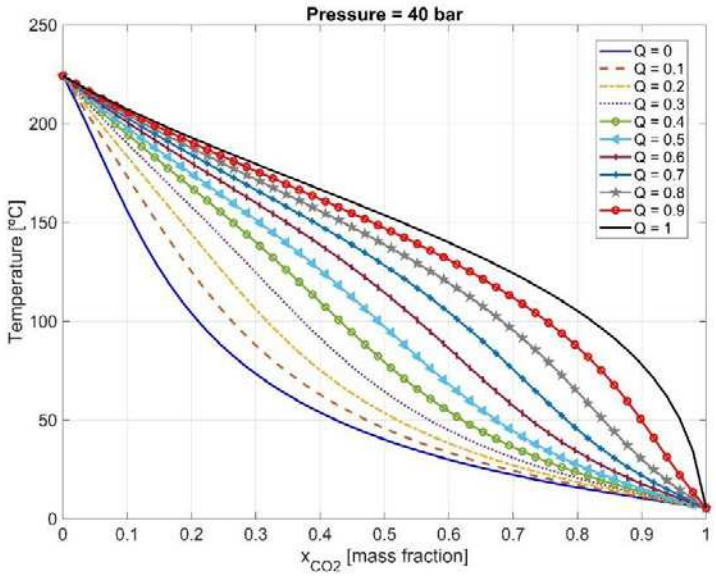

Figure 3: Temperature evolution as a function of the CO_2 content and the mixture quality for a pressure of 40 bar.

Both figures show that the mixture temperature decreases as the CO_2 content increases due to the low critical temperature of this fluid. Figure 2 shows the temperature profiles for the evaporator pressure (10 bar). The low temperatures achieved for binary mixtures with a CO_2 content ranging from 0.3 to 0.9 makes the study of refrigeration applications interesting. Figure 3 shows the temperature profiles when working at 40 bar in the condenser. In this case, the saturated vapor temperatures may help choosing the temperature of the heat sink, and thus, the CO_2 content in the refrigerant.

2.3 Thermodynamic analysis

The heat pump cycle studied in this communication is modeled following these assumptions:

- Steady state conditions.
- All components are adiabatic.

- Isobaric heat exchangers.
- Isentropic compressor efficiency of 70%.
- Isentropic pump efficiency of 80%.
- Internal heat exchanger efficiency of 80%.
- Isenthalpic valve expansion.
- Refprop software (Lemmon et al., 2018) is employed to obtain the thermodynamic properties of the CO_2/acetone mixture.
- Gas liquid separation process modeled following the Vapor-Liquid Equilibrium results experimentally obtained in (Ramírez-Ramos et al., 2021). This allows the calculation of the mass flow rates and the refrigerant composition for both vapor and liquid, which have, respectively, high and low CO_2 content.

The input parameters to the model are:

- High and low pressures (P_{cond} and P_{ev}).
- Gas-liquid separator temperature ($T_9 = T_{10} = T_{11}$).
- Refrigerant composition at the inlet of the gas-liquid separator, $(x_{CO2})_9$ and $(x_{acetone})_9$.
- Outlet condenser temperature (T_4), which is calculated as $T_4 = T_9 + 15$. This condition also sets the refrigerant quality (Q_4) due to the zeotropic behavior of the refrigerant.
- Saturated liquid conditions at the valve inlet ($Q_6 = 0$).

Therefore, the evaporation and condensation operating conditions change as a function of the refrigerant composition. In order to consider also the high temperature glide of the refrigerant, the average thermodynamic temperature is used to calculate the average sink and source temperatures, equation 1:

$$\bar{T} = \frac{\Delta h}{\Delta s} \tag{1}$$

The coefficient of performance (COP) is calculated for both hot and cold applications as:

$$COP = \frac{\dot{Q}}{\dot{W}_{comp} + \dot{W}_{pump}} \tag{2}$$

Being the total COP of the heat pump:

$$COP_{total} = \frac{\dot{Q}_{sink} + \dot{Q}_{source}}{\dot{W}_{comp} + \dot{W}_{pump}} \tag{3}$$

3 RESULTS

This section first describes the evolution of the outlet valve temperature (T_7) as a function of the refrigerant composition. Then, the main outcomes of the single-stage absorption-compression cycle are presented.

Figure 4 shows the decrease in temperature at the outlet valve as the CO_2 content increases in the binary mixture. CO_2 mass fractions above 45% may be interesting for refrigeration applications. Very low temperatures are obtained for CO_2 contents above 60%.

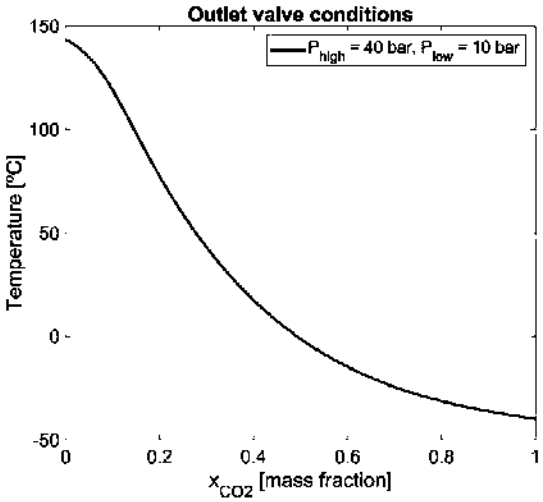

Figure 4. Outlet temperature of the isenthalpic valve for a pressure difference of 40 to 10 bar.

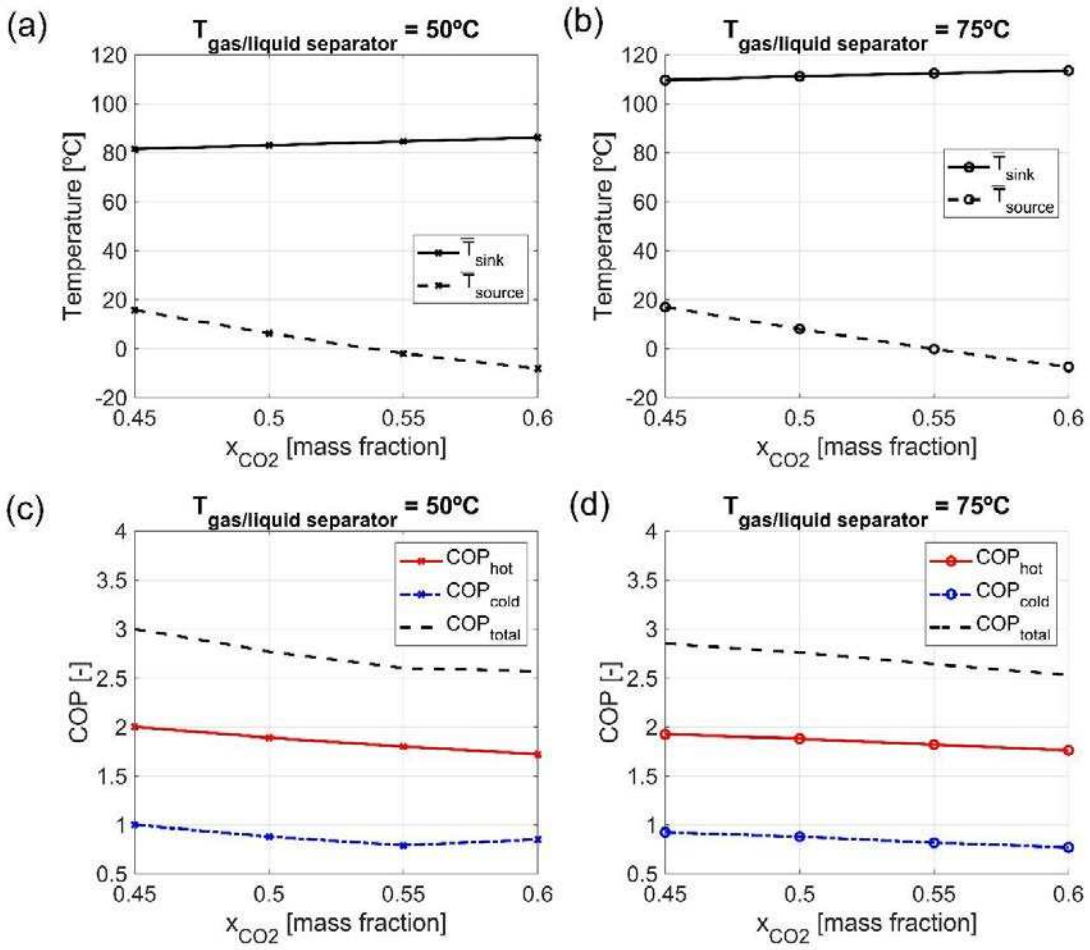

Figure 5. Main performance indicators as a function of the refrigerant composition: (a) average thermodynamic temperatures and (c) COP for a gas-liquid separator at 50ºC, (b) average thermodynamic temperatures and (d) COP for a gas-liquid separator at 75ºC.

Figure 5 explores the average thermodynamic temperature and the COP for CO_2 contents of 45-60% for two temperatures in the gas-liquid separator. In the case of T_9 = 50ºC, the thermodynamic average temperature of the heat sink is around 80ºC (Fig. 5-a), while the heat source presents a wider

temperature range. CO_2 mass fractions above 55% achieve average temperatures below 0ºC. COP values decrease with the increase of CO_2 due to the higher temperature difference between the sink and the source (Fig. 5-c). In the case of T_9 = 75ºC, the heat sink temperature increases about 30ºC (Fig. 5-b), while the heat source temperature remains constant compared to the previous case. The higher gas-liquid separator temperature increases the acetone content in the vapor that flows into the compressor, and thus, modifies the thermal properties of the refrigerant during the compression. However, the COP remains constant (Fig. 5-d).

4 CONCLUSIONS

This communication explores the use of mixtures of carbon dioxide and acetone as refrigerant of a single-stage absorption-compression cycle for both cooling and heating applications. The conclusions can be summarized as follows:

- The mixture presents a high temperature glide, which likely disadvantageous effect on the heat transfer process during phase change has been neglected in this study.
- Binary mixtures of 45 – 60% in mass fractions of CO_2 could supply the heating and cooling demands of many industrial processes. The target temperatures are above 80ºC for the heat sink, and below 0ºC for the heat source.
- A COP of 2.55 is obtained for a mass fraction of 55% CO_2 for an average thermodynamic temperature of 110ºC in the condenser, and an average thermodynamic temperature of 0ºC in the evaporator when the gas-liquid separator temperature is 75ºC.
- The operating conditions of the gas-liquid separator significantly influence the heat sink temperature, while keeping fairly constant the heat source temperatures and the COP.

NOMENCLATURE

COP	coefficient of performance (-)
GWP	global warming potential (-)
IHX	internal heat exchanger
NBP	normal boiling point (ºC)
ODP	ozone depletion potential (-)
P	pressure (bar)
Q	quality (-)
T	temperature (ºC)
$\bar{T}$	average thermodynamic temperature (ºC)
x	mass fraction (-)

Subscript

cond	condenser
crit	critical
ev	evaporator

REFERENCES

Arpagaus C, Bless F, Uhlmann M, Schiffmann J, Bertsch SS, 2018. High temperature heat pumps: market overview, state of the art, research status, refrigerants, and application potentials. Energy; 152:985 – 1010.

Ayou DS, Hargiyanto R, Coronas A, 2022. Ammonia-based compression heat pumps for simultaneous heating and cooling applications in milk pasteurization processes: Performance evaluation, Applied Thermal Engineering, Volume 217, 119168.

Elsand R, Fleiter T, Jakob M, Reiter U, Harmsen R, Mines P, Rivière P, Dittmann F, 2017. Heat Roadmap Europe. Heating and cooling: facts and figures, the transformation towards a low-carbon heating and cooling sector.

Eurostat, 2022. Communication from the Commission to the European Parliament, the European Council, the Council, the European Economic and Social Committee and the Committee of the Regions 'REPowerEU plan' (COM (2022) 230 final).

Gómez-Hernández J, Grimes R, Briongos JV, Marugán-Cruz C, Santana D, 2023. Carbon dioxide and acetone mixtures as refrigerants for industry heat pumps to supply temperature in the range 150–220ºC, Energy, Volume 269, 126821.

Höhler F, Deschermeier R, Rehfeldt S, Klein H, 2018. Gas solubilities of carbon dioxide in methanol, acetone, mixtures of methanol and water, and mixtures of methanol and acetone. Fluid Phase Equil; 459:186 – 95.

Huang X, Zhang J, Haglind F, 2022. Experimental analysis of condensation of zeotropic mixtures from 70 ◦ C to 90 ◦ C in a plate heat exchanger. Int J Refrig.

Lemmon EW, Bell IH, Huber ML, McLinden MO, 2018. NIST standard reference database 23: reference fluid thermodynamic and transport properties-REFPROP, version 10.0. Gaithersburg: National Institute of Standards and Technology, Standard

Reference Data Program; 2018.

Olsson O, Schipfer F, 2021. Decarbonizing industrial process heat: the role of biomass. IEA Bioenergy.

Ramírez-Ramos GE, Zgar Y, Salavera D, Coulier Y, Ballerat-Busserolles K, Coronas A, 2021. Vapor-liquid equilibrium, liquid density and excess enthalpy of the carbon dioxide+acetone mixture: Experimental measurements and correlations, Fluid Phase Equilibria, Volume 532, 112915.

Roskosch D, Venzik V, Schilling J, Bardow A, Atakan B, 2021. Beyond Temperature Glide: The Compressor is Key to Realizing Benefits of Zeotropic Mixtures in Heat Pumps. Energy Technology, 2000955.

Thiel GP, Stark AK, 2021. To decarbonize industry, we must decarbonize heat. Joule; 5:531 – 50.

ORC SEVILLE 2023
7th International Seminar on O.R.C. Power Systems

© 2024 Editorial Universidad de Sevilla. Este es un artículo de acceso abierto distribuido bajo los términos de la licencia de uso y distribución Creative Commons (BY-NC-ND 4.0)

DOI: https://dx.doi.org/10.12795/9788447227457_77

VALORISING THERMAL RECYCLING PROCESSES OF FIBRE-REINFORCED COMPOSITES USING ORGANIC RANKINE CYCLES FOR COMBINED HEAT AND POWER APPLICATIONS

Ramin Moradi*, Liu Yang

Department of Mechanical and Aerospace Engineering, University of Strathclyde, Glasgow, UK.

*Corresponding Author: *ramin.moradi@strath.ac.uk*

ABSTRACT

Recycling is one of the most challenging issues in many different sectors, which can bring both significant economic and environmental benefits. Hence, recycling is one of the few domains in that economic interests are in line with diminishing environmental concerns. Among the feasible and profitable recyclable materials, fibre-reinforced polymers (FRPs) are at the early stages of technology readiness with end-of-life FRP material projected to increase significantly in the coming years. Therefore, the economic and environmental impacts of FRP recycling plants should be investigated to develop a reliable business case to support the development of a circular economy for these materials. To this end, the recycling process should be robustly designed, optimised, and integrated with energy systems to maximise economic and energy-saving benefits. In this work, an FRP thermal recycling plant coupled with a 30 kW_{el}/175 kW_{th} organic Rankine cycle (ORC) system for combined heat and power (CHP) is studied. The environmental benefits of this integrated recycling-energy system are presented in terms of net CO_2 and operational costs. Results show that the integration with at least 50 residential apartments can significantly improve the economic and environmental indicators compared to the separate recycling plant and buildings being supplied by the electricity and natural gas (NG) grids. These indicators are identified by comparing the direct and indirect CO_2 emission and operational costs of the recycling plant coupled with the ORC-CHP system with those generated by stand-alone systems producing virgin fibres, supplying domestic electric demand using the electric grid, and domestic space heating using the NG grid.

1 INTRODUCTION

Wind energy is one of the most promising and fast-developing renewable energy sources that can replace a significant share of fossil fuels in producing electricity leading to the mitigation of the global warming issue (Liu et al., 2022). Wind turbine (WT) blades are made of glass fibre-reinforced polymers (GFRPs) mainly constituted of thermosetting resins and glass fibres (GFs). Therefore, manufacturing WTs require large energy consumption and CO_2 emissions, which should be considered in the blades' life cycle to correctly calculate the environmental impacts of wind energy power systems. The strong structure of the blade and the properties of the thermosets that they cannot turn to the liquid phase by heating, make their recycling difficult (Krauklis et al., 2021). On the other hand, the volume, and the growth rate of the WT blades to be decommissioned in coming years are huge: an estimated 789000 tonnes in 2021 and a total of 43 million tonnes by 2050 (Liu & Barlow, 2017). Therefore, a thermal recycling process of GFRPs having WT end-of-life (WT EoL) scraps as the main material is proposed within the project (*PRoGrESS, 2022*, n.d.) to build the first pilot-scale plant of this process in the UK. Since the recycling process (*PRoGrESS, 2022*, n.d.) requires electric and thermal energy, its carbon emissions and operational costs are included in the overall evaluation of the recycling of the GFs. To assess the potential for valorizing this system, a waste heat recovery (WHR) system using organic Rankine cycle (ORC) systems is investigated in this work. The ORC system is coupled with residential

buildings to supply their electric and thermal demands for a year in Aberdeen, Scotland, which makes a combined heat and power (CHP) system.
Indeed, WHR has great potential to improve the efficiency of industrial plants thus reducing their fossil fuel consumption and related carbon emissions (Moradi, Habib, et al., 2021). Organic Rankine cycle (ORC) systems have attracted particular attention in recent years due to their reliability, flexibility, safety, and applicability for low-temperature power generation (Li et al., 2018). ORC systems are one of the most promising technologies to valorize low-grade heat into electricity (Mahmoudi et al., 2018). In addition, the building sector is considered as the application since it is accounted for approximately 40% of the EU energy consumption and 36% of the greenhouse gas emissions (*European Commission-Energy-Energy Performance of Buildings Directive*, 2021). In particular, 27% of final energy consumption accounted for households in 2020 (*Eurostat, 2022*, n.d.), out of which 62.8% for space heating, 15.1% for water heating, and 0.4% for space cooling. Therefore, the annual performance of an innovative GFRP recycling unit coupled with an ORC-CHP system is investigated in this work for the first time to assess the benefits of such integration for similar thermal FRP recycling processes.

2 Modelling of the integrated CHP plant

The integrated CHP system consists of five main units: I) the GFRP recycling unit; II) the ORC system; III) the water heating/cooling unit, IV) the electricity grid, and V) the residential buildings. The waste heat from the GFRP recycling plant is exploited by a small-scale ORC unit to generate electricity and heat. The generated electricity supplies the users' electric demand, and the excess electricity is sent to the grid, while users may use the grid if the on-site production is not adequate. The produced heat at the condenser of the ORC system is sent to the water tank and passes through an internal spiral tube heat exchanger (HE) unless the tank temperature has reached its pre-set maximum resulting in the cooling water being redirected to the dry cooler (DC). The hot water (HW) and service water for space heating (SH) are modelled using thermal energy taken from the water mass in the tank at each time step without modelling the heat transfer process. If the tank temperature is below the pre-set threshold, the required thermal energy is supplied by the boiler and the tank is charged by the hot water from the condenser.
Therefore, the tank temperature is calculated at each timestep using the energy balance constituted of the output thermal energies of HW, SH, the thermal losses, and the input thermal energy coming from the ORC unit. The latter is modelled using a fixed overall heat transfer coefficient (OHTC) of the HE. The schematic of the integrated system is shown in **Figure 1**. The models of the main units and their components are presented in the following sub-sections in detail.

2.1 The GFRP recycling unit

The GFRP recycling unit is considered with the capacity, thermal process, and configuration as in the developing pilot-scale plant within the (*PRoGrESS, 2022*, n.d.). The considered GFRP is the WT blade scraps downsized to the suitable range for the recycling process. Nonetheless, the recycling plant can handle other types of GFRP materials manufactured with thermoset plastics. In addition, the designed process can be used to recycle carbon FRP (CFRP) materials with some considerations in the component design and adjustments in the process and operating conditions. Hence, the product will be recycled carbon fibre (rCF), which replaces virgin CFs (vCFs) having significantly higher manufacturing cost and carbon footprint compared to vGFs. However, only WT EoL materials are considered in this work based on the scopes of (*PRoGrESS, 2022*, n.d.).
The design adopted in this work is the most conservative one presented in (*PRoGrESS, 2022*, n.d.) for being a scaling-up mission from a lab-scale rig to a pilot-scale plant. In addition, the capacity of the pilot-scale plant is the first intermediate step on the commercialisation route. Hence, it is more energy intensive with higher operational costs and carbon emissions than the prospective commercial plant. Furthermore, additional economic benefits from charging the FRP scrap owners for carrying the recycling task and avoiding landfilling are not considered in the model which can be a game-changing factor in real commercial cases. Yet, the results of the pilot plant can be used to have an overview of the economic and environmental impacts of the integration with a CHP unit.

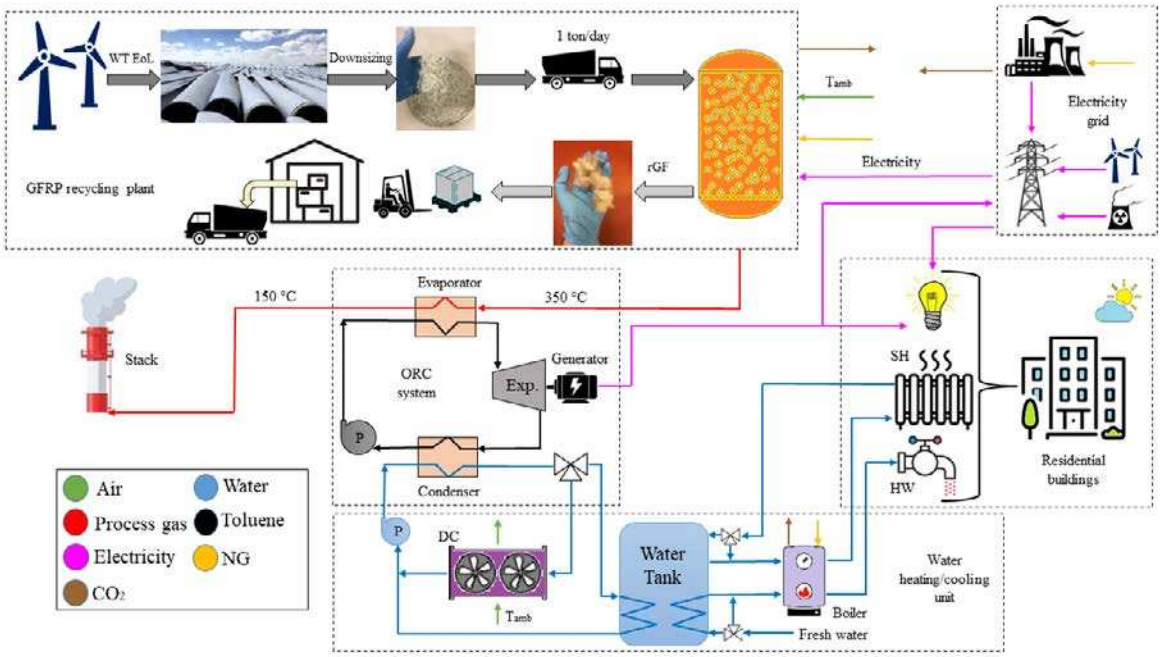

Figure 1: The scheme of the integrated GFRP recycling-ORC-CHP plant.

The recycling process and its models and parameters are not presented in this paper due to the non-disclosure agreements within the project. Nevertheless, the main energy, economic, and environmental parameters of the plant model used in the net calculations of the integrated system are presented in **Table 1**.

The CO_2 production of the plant is based on the direct emissions due to the decomposition of the WT blades in the recycling process and NG consumption on site, and the indirect emissions due to the electricity consumption at the site calculated using the Scottish grid performance in 2020 (*Scottish Energy Statistics Hub*, n.d.). It is noteworthy that 57% of the Scottish grid is supplied by renewable sources (mostly wind energy) and 29.8% by nuclear energy in 2021 (*Scottish Energy Statistics Hub*, n.d.). Hence, its equivalent emission is significantly lower compared to typical values like the English grid with 152.1 g CO_2/kWh_{el} in 2020 (*Scottish Energy Statistics Hub*, n.d.). Furthermore, the considered rates for buying and selling energy vary by time and the energy company; hence, typical values in the UK market are considered without any incentives.

468

Table 1: The economic and environmental parameters and results of the pilot-scale WT blade recycling plant and the energy and cost parameters adopted in the model.

Model inputs				Model outputs	
p/kWh_{th}	10.3	MJ_{th}/kg vGF	48.33	rGF [t/y]	243.7
p/day_{th}	28.0	kg CO_2/kg vGF	2.04	MJ_{th}/kg rGF	16.38
p/kWh_{el}	34.0	£/kg vGF	1.77	MJ_{el}/kg rGF	20.14
p/day_{el}	46.0	GF landfill [p/kg]	5.0	kg CO_2/kg rGF	2.45
p/$kWh_{el,ex}$[1]	7.5	g CO_2/kWh_{el}[2]	33.6	£/kg rGF	2.37

[1]Selling electricity to the grid.
[2]For the Scottish grid

2.2 The ORC system

The ORC system is a non-regenerative, small-scale unit producing electrical and thermal power. The working fluid is toluene based on the recommendations for the design temperature of the waste stream (Moradi, 2021; Rahbar et al., 2017) and its good environmental indexes. The ORC system is modelled using the characteristics and assumptions presented in **Table 2**. Box models are adopted for the heat

exchangers using the fixed temperature difference and maintaining a minimum temperature pinch, which gives the high and low pressures of the system. The other two assumptions for the system boundary identification are fixed superheating and subcooling degrees in the evaporator and condenser respectively.

In particular, the high and low pressures of the ORC system are identified using the temperature difference between the inlet of the hot fluid and the saturation temperature of the working fluid in the evaporator, and the inlet temperature of the cold fluid and the condensation temperature of the working fluid in the condenser. Considering the scope of this work, a reasonable temperature difference of 60 K is taken for the evaporator corresponding to the evaporation temperature of 290°C for toluene, which has a critical temperature of about 319°C. Hence, 60 K is a reasonable value for having gas in the hot stream and keeping toluene in a subcritical state. The high and low pressures of the system are 28.84 and 0.39 bar respectively using the design temperature differences reported in **Table 2**. The temperature pinch in the HEs is maintained by adjusting the design values of the temperature differences reported in **Table 2**. In addition, the mass flow rate of the hot fluid is calculated from the GFRP recycling plant model. The mass flow rate of the cooling water in the condenser is calculated assuming the net electric efficiency of the ORC system of 10% and cooling water temperature equal to the initial temperature of the tank (60°C) and 20 K temperature increment at the condenser outlet. The design values of the hot and cold fluid mass flow rates are 0.83 kg/s and 1.85 kg/s respectively. The mass flow rate of the working fluid is calculated to maintain the design superheating degree in the evaporator.

The pump and turbine are presented using single-coefficient models. The combination of the single-coefficient models for the machines and the box models for the heat exchangers with the fixed temperature differences for system pressures are suitable for such analysis when the monthly and annual performances of the system are of interest (Moradi et al., 2021). It is a good compromise between the computational time and modelling efforts and the accuracy of the calculated monthly or annual electric and thermal powers.

The varying heating demand affects the water tank temperature and may bring the boiler and the dry cooler to the service. This affects the low pressure of the ORC system resulting in changes in the expander pressure ratio and the mass flow rate of the working fluid. Hence, the ORC system mostly operates in off-design conditions, and it is considered in the model by the changes in the expander's pressure ratio and the mass flow rate of the working fluid. These affect the produced electric and thermal power of the system.

Table 2: The characteristics of the ORC main components and the model assumptions.

Turbine isentropic efficiency	0.80	Superheating degree	10 K
Pump isentropic efficiency	0.60	Subcooling degree	5 K
Pump & turbine mechanical efficiency	0.95	$dT_{ev,des}$	60 K
Generator efficiency	0.95	$dT_{cd,des}$	20 K
Working fluid	toluene	Temperature pinch	5 K

2.3 The residential users

A five-floor building having a 100 m^2 floor area with walls directed toward the four cardinal directions is modelled using TRNBuild® considering the indoor comfort temperature of 20-24°C. Since the model is performed for weather conditions of Aberdeen in Scotland, the cooling demand is found negligible and disregarded. The demand for HW is calculated in a separate TRNSYS simulation according to the European standard UNI EN15316-3 (Technical Committee CEN/TC 228, 2006). Both SH and HW demands have been considered with a unitary contemporaneity factor.

The hourly electrical demand is taken from the results for the working days in a survey study on seasonal variations of the electrical demand of dwellings in the UK based on electrical appliances only (Fazeli & Gillott, 2013). The different seasonal demands are attributed to the active occupancy that is higher in winter compared to summer and the difference between seasonal daytime, which grows in higher latitudes. For the sake of the present analysis, the same pattern of hourly electrical demand is considered

for each season. The data were reported for 1000 two-person dwellings; hence, a coincidence factor is introduced to estimate the electric demand of one dwelling. The coincidence factor considers the asynchronous effect in the total demand from all the users in a network. For *n* apartments, it is defined as the following:

$$c = \frac{W(n)}{n \cdot W_i} \tag{1}$$

where c is the coincidence factor, $W(n)$ is the power demand of the network of n users, and W_i is the power demand of each user. The coincidence factor is estimated using a model based on empirical studies (Nickel & Braunstein, 1981):

$$c = 0.5\left(1 + \frac{5}{2n+3}\right) \tag{2}$$

The coincidence factor is then applied to the calculations of the electrical demand of any arbitrary number of dwellings considered for the simulation.
The daily sum of the thermal energy demand of one building (five apartments) and the average daily ambient temperature of Aberdeen are shown in **Figure 2** for a year. In addition, the hourly electrical demand in each season is shown in **Figure 2** for a two-person dwelling considering the calculated coincidence factor.

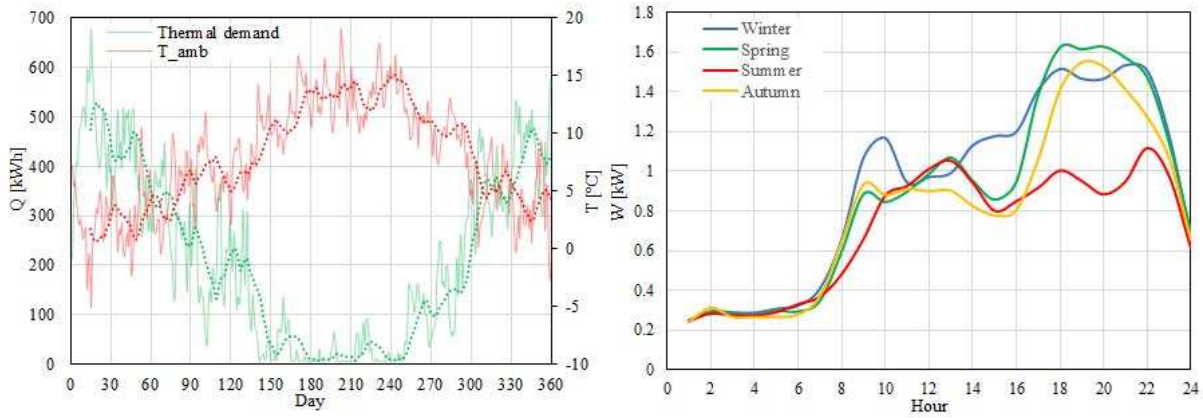

Figure 2: The daily thermal energy demand of one building and the average daily temperature of Aberdeen, Scotland, (left), and the seasonal hourly electrical power demand of a two-person dwelling according to (Fazeli & Gillott, 2013) and calculated coincidence factor (right).

2.4 The water heating/cooling unit

The water heating/cooling unit consists of the water tank, the DC, the boiler, the water pump, and three control valves to adjust the circuit. These are needed to control the water tank temperature, provide HW and SH comfortably and reliably, and maintain the heat sink for the operation of the ORC system. The characteristics of the main components of the water heating/cooling unit adopted in the model are reported in **Table 3**. The DC and boiler are modelled using a constant capacity ratio and thermal efficiency respectively. The DC capacity ratio is adopted from the average seasonal value reported in the German standard to calculate the energy consumption of buildings (Fugmann et al., 2015).
In addition, the water outlet temperature of the DC is assumed 5 K higher than the ambient temperature taken from the specifications of commercial dry coolers. A constant OHTC is assumed to calculate the thermal losses of the water tank to the ambient, and heat transfer between the cooling water and the water in the tank using the internal spiral tube HE. The geometry of the spiral tube needed to calculate its heat transfer area is reported in **Table 3**. The heat transfer between the cooling water and the water in the tank is modelled using the finite volume method to consider the temperature profile of the water at the height of the spiral tube. This 1D model leads to a more accurate calculation of the cooling water outlet temperature compared to the uniform tank model.

Table 3: The characteristics of the main components of the water heating/cooling unit.

DC capacity ratio	0.045 [kWel/kWth]	OHTC of tank losses	1 [$W.m^{-2}.K^{-1}$]
Tank diameter	2.5 [m]	OHTC of the spiral tube HE	700 [$W.m^{-2}.K^{-1}$]
Water tank volume	700 [litre/apartment]	Diameter of the spiral tube	0.8×tank diameter
Boiler thermal efficiency	0.95	Height of the spiral tube	Tank height/3
Water pump isentropic efficiency	0.75	The pitch of the spiral tube	4.1 [cm]
$T_{ex,water,DC} - T_{amb}$	5 K	Spiral tube diameter	30 [cm]

The control logic of the water heating/cooling unit is reported in **Table 4**. The control logic consists of 5 rules to control the status of the boiler, the DC, and the control valves depending on the tank temperature at the new timestep and the status of the boiler and the DC in the previous timestep. A hysteresis of 5 K is considered in the controller to avoid frequent on-off commands in short intervals. The minimum and maximum tank temperatures are considered 50°C and 95°C respectively suitable for the users' comfort and to avoid boiling the water in the tank.

Table 4: The control logic of the water heating/cooling unit.

Rule	Conditions	Actions
1	$T_{tk,min} < T_{tk} < T_{tk,max}$ AND Boiler and DC are off	ORC cooling water passes through the tank Keep/turn the boiler and DC off
2	$T_{tk} \leq T_{tk,min}$	ORC cooling water passes through the tank Turn the boiler on
3	$T_{tk} \geq T_{tk,max}$	ORC cooling water passes through the DC Turn the DC on
4	$T_{tk} \leq T_{tk,min}$+5 AND Boiler is on	ORC cooling water passes through the tank Keep the boiler on
5	$T_{tk} \geq T_{tk,max}$-5 AND DC is on	ORC cooling water passes through the DC Keep the DC on

3 Results and discussion

The integrated system is modelled for one year with a timestep of 5 minutes considering the weather conditions of Aberdeen, Scotland, assuming a 24/7 operation of the GFRP recycling plant at the design throughput and operating conditions. The ORC unit is a 30 kW_{el}/175 kW_{th} system having a heat source with a constant mass flow rate and temperature. The ORC system operates in off-design conditions though due to variations of the heat sink conditions as the tank temperature changes, or the cooling water circuit that may change if the tank temperature reaches its pre-set maximum temperature. In this case, the cooling water bypasses the tank and goes through the DC resulting in a sudden drop in its temperature entering the condenser of the ORC system.

The system performances are presented using the net electric energy production of the ORC system, the net electric efficiency of the ORC system, and the net CHP efficiency of the ORC-CHP system as in Equation (3-5) respectively.

$$W_{net,ORC} = W_t - W_{p,ORC} - W_{DC} - W_{p,water} \quad (3)$$

$$\eta_{net} = \frac{W_{net.ORC}}{Q_{in,HF}} \quad (4)$$

$$\eta_{CHP} = \frac{W_{net,ORC} + Q_{delivered}}{Q_{in,HF}} \quad (5)$$

where $Q_{in,HF}$ is the thermal energy transferred to the ORC system calculated in the hot stream of the evaporator, and $Q_{delivered}$ is the thermal energy transferred to the users from the water tank. The net CO_2 emissions (E) and the operational costs of the integrated system are calculated using Equations (6 and 7). The sources and sinks of the CO_2 emissions and costs are associated with the rGF production in the GFRP recycling plant, replacing the production of vGF with rGF, avoiding landfilling of WT EoL, and users' thermal and electrical energy supply using the boiler and the interaction with the electricity grid (buying from it (-), and selling to it (+)).

$$E_{net} = \left(E_{th} + E_{el,eq}\right)_{rGF} + \left(E_{boiler} + E_{el,eq,grid-} - E_{el,eq,grid+}\right)_{users} - E_{vGF} \quad (6)$$

$$£_{net} = (£_{th} + £_{el})_{rGF} + \left(£_{boiler} + £_{el,grid-} - £_{el,grid+}\right)_{users} - £_{vGF} - £_{landfill} \quad (7)$$

The first step in assessing the impact of the integration of the GFRP recycling plant and the ORC-CHP unit is finding a suitable number of users. Therefore, the system is modelled with a different number of apartments coupled with the same ORC unit. As indicated in **Table 3**, the water tank volume varies with the number of apartments, the total thermal demand at each timestep changes linearly with the number of apartments, and the electrical demand alters considering the coincidence factor.

Various factors from different perspectives can be considered to identify the suitable number of users such as minimum use of fossil fuels (NG) by the users, the lowest net CO_2 emissions considering the users, the local power system and energy source, and the energy grid, or similar terms for operational costs. In this work, the conformity between the users' thermal energy demand and the system's thermal production in a year is taken as the indicator for choosing the suitable number of users (Moradi et al., 2023). The considered thermal conformity indicator (TCI) is a technical parameter that prioritises the conformity between thermal production and demand patterns. Hence, it may not minimise the emission nor the operational costs, but it compromises them to have more users.

472

To this end, the nominal day of each month is found, in which the average daily temperature is the closest to the average monthly temperature. Then, the absolute difference between the produced thermal energy and users' thermal demand is calculated for each nominal day. These values are summed for the twelve nominal days to calculate the TCI. In addition, the total annual CO_2 emission of the integrated system is calculated considering the direct emission due to NG combustion and indirect emissions of electric energy consumption considering the characteristics of the Scottish grid emissions and specific emissions of vGF production reported in **Table 1**. Similarly, the operational costs of the integrated system are calculated considering the NG and electricity rates and the specific costs of producing vGFs plus their landfilling as reported in **Table 1**.

These calculations are conducted for residential users with and without the ORC-CHP system. Furthermore, the net emissions and costs are calculated for the integrated GFRP recycling-ORC-CHP plant, and for the case of vGF production and the buildings supplied with the electricity and NG grids. These parameters are presented in **Figure 3** for a different number of apartments. The integration with the CHP significantly reduces the net emissions and costs and valorises the GFRP recycling substantially.

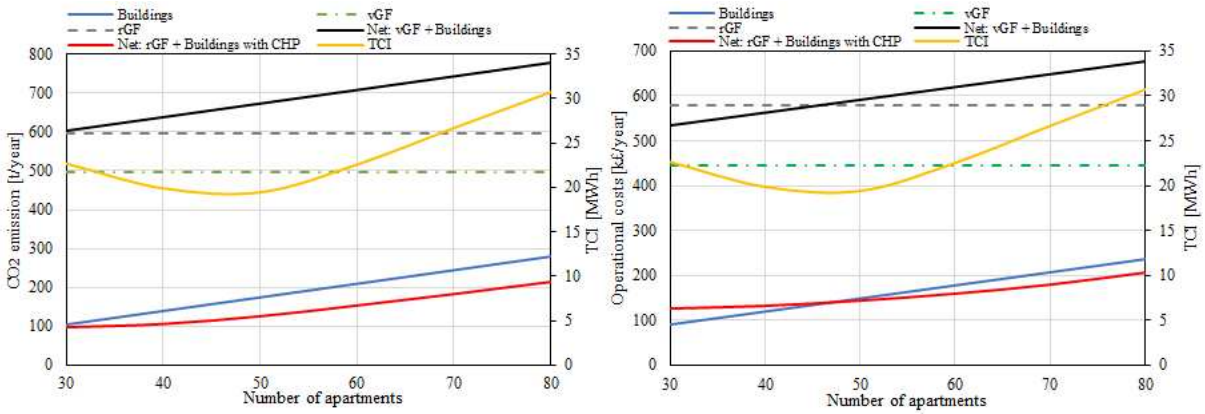

Figure 3: The annual emissions (left) and the annual operational costs (right) of the systems with different levels of integrity. TCI is presented in both figures.

The suitable number of apartments is considered 50 (10 five-floor buildings as in the model) for this system, which gives a TCI close to the minimum. It is a compromise between good thermal and electrical coverage and relatively low annual emissions and operational costs. It is also worth pointing out that the costs of the integrated system become lower than the buildings coupled with the energy grids, and the difference between the emission of the buildings coupled with the energy grids and the integrated system has increased and does not grow further significantly.
The thermal energy provided by the boiler, the excess electrical energy sent to the grid, and the electrical energy consumption of the DC are determining factors in the annual emissions and costs of the ORC-CHP system. The latter indicates the excess thermal energy produced by the ORC system that cannot be delivered to the users. These parameters are shown in **Figure 4** versus the number of apartments.

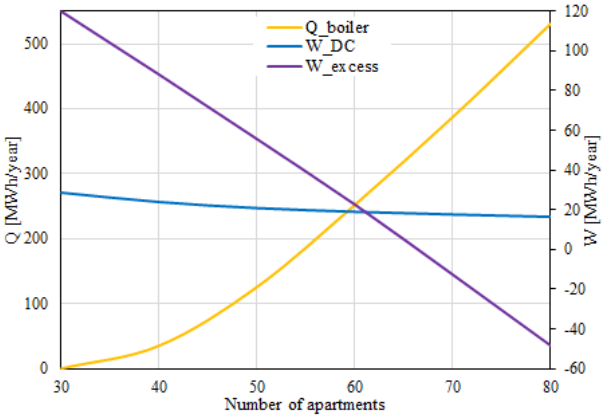

Figure 4: The annual thermal energy consumption by the boiler, excess electrical energy sent to the grid, and the electrical energy consumption of the DC for the different number of apartments.

The monthly thermal and electrical performances of the integrated GFRP recycling-ORC-CHP system are presented in **Figure 5** for 50 apartments in Aberdeen. The boiler is required in cold months to supply the users' demand, while the DC turns on in summer and mid-season to dissipate the thermal energy produced by the ORC system. The users' thermal demand profile varies significantly by season especially due to having negligible cooling demand in Aberdeen as shown in **Figure 2**. Both the boiler and DC are at service in mid-season, in which the thermal demand and production get close to each other resulting in steeper daily variations of the water tank temperature compared to the other months. The net produced electrical energy calculated based on Equation (3) is always higher than the electrical demand resulting in excess electricity being sent to the grid in all months. Finally, the net electric efficiency of the ORC system does not change significantly, while the CHP efficiency drops

considerably in the summertime due to low thermal demand resulting in the produced heat being rejected to the ambient through the DC.

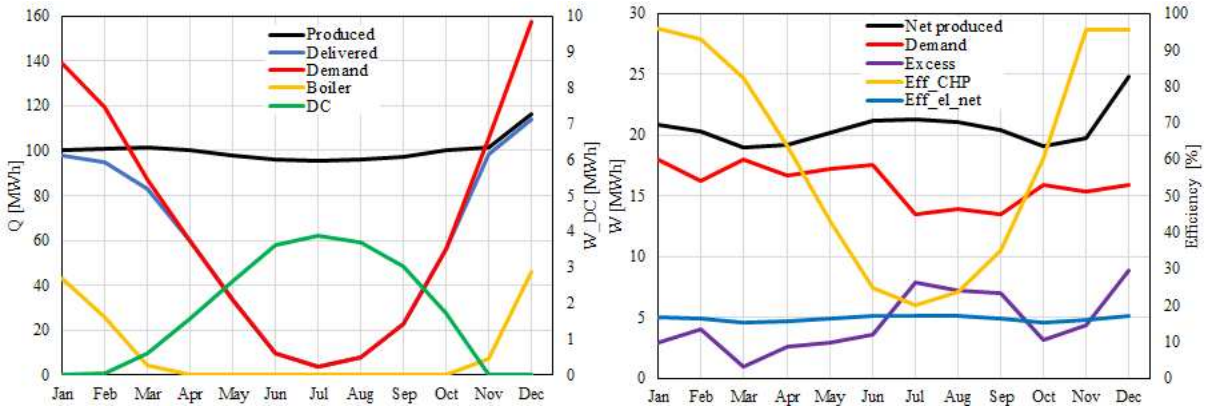

Figure 5: The monthly thermal (left) and electrical (right) performances of the ORC-CHP system for 50 apartments.

4 CONCLUSIONS

A pilot-scale GFRP thermal recycling plant is modelled according to the design conducted within (*PRoGrESS, 2022*, n.d.). The main end goal of the project is to devise a commercial solution for recycling the WT EoL aiming to replace vGFs with rGFs in less-demanding applications compared to WTs resulting in a sustainable way to dispose of the WT EoL. The sustainability is in terms of I) recycling WT EoL without allocating lands to it; II) reducing the CO_2 emissions of GFRP materials by replacing vGFs with rGFs; III) reducing the cost of the GFRP materials by replacing vGFs with rGFs. To further encourage the sustainability of the GFRP recycling plant, its integration with the residential users using an ORC-CHP system is studied in this work. A 30 kW_{el}/175 kW_{th} ORC system is adopted as a WHR unit to generate electricity and heat. The generated heat is managed using the water heating/cooling unit to deliver to the users, partially stored in the water tank, or wasted to the ambient. The results show that the pilot plant can supply at least 10 buildings constituting 50 apartments with a 100 m^2 floor area located in Aberdeen, Scotland. The integration not only reduces the emissions and costs of the separate recycling plant and the buildings supplied by the electricity and NG grid significantly but also the much lower than vGF production stats.

474

Furthermore, the presented results and conclusions are for the pilot-scale plant with a conservative design and weather conditions of Aberdeen with no cooling demand. Hence, the benefits can be elevated in the case of commercial GFRP thermal recycling plants coupled with buildings with cooling demand in summer which can take more electric and thermal energy produced by the system in a year. Finally, the recycling process can be adopted for CFRP, which has significantly higher production costs and carbon footprint compared to GFRPs. Hence, the economic and environmental impacts of integration would increase a lot with CFRPs. However, the volume of WT EoL coming to the market encourage focusing on them to subside the associated environmental and sustainability issues in decomposing them.

REFERENCES

European Commission-Energy-Energy performance of buildings directive. (2021). https://ec.europa.eu/energy/topics/energy-efficiency/energy-efficient-buildings/energy-performance-buildings-directive_en#energy-performance-of-buildings-standards

Eurostat, 2022. (n.d.). Retrieved September 22, 2022, from https://ec.europa.eu/eurostat/statistics-explained/index.php?title=Energy_consumption_in_households

Fazeli, A., & Gillott, M. (2013). Analysing the effects of seasonal variation on occupancy in an electricity demand model. *International Journal of Low-Carbon Technologies*, *8*(4), 282–288. https://doi.org/10.1093/ijlct/cts032

Fugmann, H., Nienborg, B., Trommler, G., Dalibard, A., & Schnabel, L. (2015). Performance Evaluation of Air-Based Heat Rejection Systems. *Energies 2015, Vol. 8, Pages 714-741*, *8*(2), 714–741. https://doi.org/10.3390/EN8020714

Krauklis, A. E., Karl, C. W., Gagani, A. I., Jørgensen, J. K., Krauklis, C. :, Karl, A. E. ;, Gagani, C. W. ;, & Jørgensen, A. I. ; (2021). Composite Material Recycling Technology—State-of-the-Art and Sustainable Development for the 2020s. *Journal of Composites Science 2021, Vol. 5, Page 28*, *5*(1), 28. https://doi.org/10.3390/JCS5010028

Li, J., Ge, Z., Duan, Y., Yang, Z., & Liu, Q. (2018). Parametric optimization and thermodynamic performance comparison of single-pressure and dual-pressure evaporation organic Rankine cycles. *Applied Energy*, *217*, 409–421. https://doi.org/10.1016/j.apenergy.2018.02.096

Liu, P., & Barlow, C. Y. (2017). Wind turbine blade waste in 2050. *Waste Management*, *62*, 229–240. https://doi.org/10.1016/J.WASMAN.2017.02.007

Liu, P., Meng, F., & Barlow, C. Y. (2022). Wind turbine blade end-of-life options: An economic comparison. *Resources, Conservation and Recycling*, *180*. https://doi.org/10.1016/J.RESCONREC.2022.106202

Mahmoudi, A., Fazli, M., & Morad, M. R. (2018). A recent review of waste heat recovery by Organic Rankine Cycle. In *Applied Thermal Engineering*. https://doi.org/10.1016/j.applthermaleng.2018.07.136

Moradi, R. (2021). *Object-oriented modeling of micro-ORC systems for low-grade waste heat recovery applications* [Doctroal thesis, Doctroal thesis, Sapienza University of Rome]. https://doi.org/http://hdl.handle.net/11573/1549644

Moradi, R., Campana, P. E., Tascioni, R., & Cioccolanti, L. (2021). Thermodynamic analysis of the off-design performance of a micro solar organic Rankine cycle trigeneration system. *6th International Seminar on ORC Power Systems*. https://www.researchgate.net/publication/355668644_THERMODYNAMIC_ANALYSIS_OF_THE_OFF-DESIGN_PERFORMANCE_OF_A_MICRO_SOLAR_ORGANIC_RANKINE_CYCLE_TRIGENERATION_SYSTEM

Moradi, R., Cioccolanti, L., Del Zotto, L., & Renzi, M. (2023). Comparative sensitivity analysis of micro-scale gas turbine and supercritical CO2 systems with bottoming organic Rankine cycles fed by the biomass gasification for decentralized trigeneration. *Energy*, *266*, 126491. https://doi.org/10.1016/J.ENERGY.2022.126491

Moradi, R., Habib, E., Villarini, M., & Cioccolanti, L. (2021). Assumption-free modeling of a micro-scale organic Rankine cycle system based on a mass-sensitive method. *Energy Conversion and Management*, *245*, 114554. https://doi.org/10.1016/j.enconman.2021.114554

Nickel, D. L., & Braunstein, H. R. (1981). Distribution transformer loss evaluation: II — Load characteristics and system cost parameters. *IEEE Transactions on Power Apparatus and Systems*, *PAS-100*(2), 798–811. https://doi.org/10.1109/TPAS.1981.316932

PRoGrESS, 2022. (n.d.). Retrieved March 27, 2023, from https://www.strath.ac.uk/whystrathclyde/news/2021/2milllionpilottodevelopuksfirstwindturbinebladerecyclingprojectgetsgo-ahead/

Rahbar, K., Mahmoud, S., Al-Dadah, R. K., Moazami, N., & Mirhadizadeh, S. A. (2017). Review of organic Rankine cycle for small-scale applications. In *Energy Conversion and Management* (Vol. 134, pp. 135–155). Elsevier Ltd. https://doi.org/10.1016/j.enconman.2016.12.023

Scottish Energy Statistics Hub. (n.d.). Retrieved March 27, 2023, from https://scotland.shinyapps.io/sg-scottish-energy-statistics/?Section=RenLowCarbon&Subsection=RenElec&Chart=GridEmissions

Technical Committee CEN/TC 228. (2006). *Heating systems in buildings — Method for calculation of system energy requirements and system efficiencies — Part 3-1 Domestic hot water systems, characterisation of needs (tapping requirements)*.

ORC SEVILLE 2023
7th International Seminar on O.R.C. Power Systems

© 2024 Editorial Universidad de Sevilla. Este es un artículo de acceso abierto distribuido bajo los términos de la licencia de uso y distribución Creative Commons (BY-NC-ND 4.0)

DOI: https://dx.doi.org/10.12795/9788447227457_80

Prediction of the ideal maximum operational temperature of hydrocarbon and HFCs as working fluids of organic Rankine cycle power plants based on transition state theory

Wei Yu[1], Chao Liu[1]*, Xijie Ban[1], Zhirong Li[1], Tianlong Yan[1]
[1]*Key laboratory of low-grade Energy Utilization Technologies and Systems, Ministry of Education, School of Energy and Power Engineering, Chongqing University, Chongqing, 400030, China,*
*Corresponding author: liuchao@cqu.edu.cn

ABSTRACT

The use of organic working fluids in organic Rankine cycle (ORC) power plants may lead to thermal decomposition, which can negatively impact system performance and safety. Therefore, it is essential to determine the safe operating temperature range of the working fluids. In this paper, a simplified theoretical method based on the transition state theory is proposed to predict the ideal maximum operational temperature of working fluids. This method involves considering the initial decomposition reaction of the working fluids and calculating the total reaction rate of the initial decomposition using the transition state theory. By setting an acceptable decomposition rate, the ideal maximum operational temperature of the working fluid can be determined. Using this method, the total reaction rate constants of several typical hydrocarbon and hydrofluorocarbon working fluids, including n-butane, isobutane, n-pentane, isopentane, neopentane, n-hexane, HFC-245fa, HFC-134a, HFC-125, HFC-236fa, HFC-227ea, HFC-143a, and HFC-152a, were obtained in the temperature range of 300~700K. The predicted maximum operational temperatures were in good agreement with most experimental results. Furthermore, by analyzing the branch ratio of each initial decomposition path of these working fluids, it was found that C-C bond cleavage contributed mainly to the decomposition of hydrocarbons, while the removal of HF and C-C bond cleavage contributed mainly to the decomposition of HFCs. As the C-C bond breakage paths and HF removal reaction paths have high branching ratios (>99%), only considering these reactions in the reaction rate calculation can greatly reduce the calculation cost without significantly impacting the prediction accuracy.

1 INTRODUCTION

When organic Rankine cycle (ORC) system is applied to medium-high temperature heat sources, the organic working fluids will face the risk of thermal decomposition, which results in performance loss and many important operation problems (Niggemann, 1969; Koplow et al., 1984). Therefore, in the practical application of ORC systems, the thermal stability of organic working fluids is vital important. Obtaining the maximum safe use temperature is the focus of the research on the thermal stability of working fluids.

At present, the most effective method is to obtain the decomposition rate data of the working fluids at relatively high temperature by experiment, and obtain the correlation between the decomposition rate

and temperature by fitting the decomposition rate at different temperatures. By analyzing the impact of the pyrolysis of working fluids on the system performance and determining the acceptable decomposition rate threshold of working medium in the life cycle of ORC, the maximum safe operation temperature of working fluids can be determined (Pereira et al., 2022).

(Dai et al., 2016a) obtained the decomposition kinetics correlation of n-pentane through experiments. Under the condition of 1% threshold of acceptable decomposition rate within the life of ORC, the evaluated upper limit operation temperature of n-pentane in ORC systems is 280 ℃~300 ℃. Although this method is very effective, it requires a high cost to determine the kinetics correlation. (Dai et al., 2016b) further proposed a fast pyrolysis experiment method to determine the pyrolysis temperature of hydrocarbon. By this method, the decomposition temperature of n-pentane, n-hexane, isopentane, cyclopentane, n-butane and isobutane are obtained. Using the same method, (Dai et al., 2018) measured the pyrolysis temperatures of HFC-245fa, HFC-152a, HFC-134a, HFC-236fa and HCFC-123. Compared with the experimental results of (Calderazzi and di Paliano, 1997) and (Angelino and Invernizzi, 2003), the pyrolysis temperature measured by (Dai et al., 2018) is relatively low. This is due to differences in experimental conditions and judgment indicators. (Dai et al., 2016a, 2018) also carried out an analysis of the influence of pressure on the decomposition rate of n-pentane and HFC-245fa. The results showed that at 340 ℃, pressure has little effect on the decomposition rate of n-pentane, and the correlation equation for fitting the reaction rates measured in the experiment conforms to the first-order reaction kinetics; At 320 ℃, the pressure has little effect on the decomposition of HFC-245fa. This indicate that under these temperatures, the second order reaction has little effect on the decomposition of these working fluids. Therefore, the pyrolysis can be reasonably described by first-order reaction kinetic model.

477

Since the working fluids are usually operating in a high-pressure environment greater than atmospheric pressure in ORC systems, the rate constants of each decomposition reaction path can be reasonably evaluated by the high-pressure limit transition state theory (TST) (Eyring, 1935; Nikitin, 1974) which is established based on statistical thermodynamics and quantum mechanics. By considering the structure and energy of the reactants at the transition state, as well as the vibrational frequencies between the reactants and the transition state, the prediction and interpretation of chemical reaction rates can be made. In present work, we carried out high-precision quantum chemical calculations on the initial pyrolysis reaction paths of several hydrocarbon working fluids and HFCs working fluids commonly used in ORC systems (Wang et al., 2022). Based on the first-order reaction kinetic model and the transition state reaction rate calculation, the decomposition kinetic correlations of these working fluids in temperature range of 300~700 K were obtained. The contribution of different reaction paths in the decomposition process is further analyzed, and the main contribution path is determined. This work provides a novel method for determining the thermal stability temperature of working fluids under ideal conditions (without considering the impact of impurities and contact materials on thermal stability).

2 COMPUTATIONAL DETAILS

2.1 Quantum chemical calculation

The geometry optimization, frequency calculations and transition state searches have been carried out at the density functional theory (DFT), M062x/def2-TZVP level (Weigend and Ahlrichs, 2005; Zhao

and Truhlar, 2008) with ZPE scale factor of 0.971 (Alecu et al., 2010), and single point energy calculations were carried out at CCSD(T)/cc-PVTZ level. All the DFT calculations were accomplished using Gaussian-16 software package (Frisch et al.) at temperature of 298.15K and at pressure of 0.1MPa. In the frequency analysis, all the molecular and radical optimized structures have no imaginary frequency, while the transition state structure has only one imaginary frequency. For the transition state structure, the correctness is further guaranteed by the calculation of intrinsic reaction coordinates (IRC). The thermodynamic parameters at different temperatures are calculated using Shermo software package (Lu and Chen, 2021).

2.2 Reaction rate constant calculation

The reaction rate constants were calculated by using the high-pressure limit transition state theory (TST) (Eyring, 1935; Nikitin, 1974). The TST calculation can be expressed as follows (Al-Otaibi et al., 2021),

$$k^{TST}(T) = \sigma \frac{k_B T}{h} \left(\frac{RT}{P^0} \right)^{\Delta n} e^{\frac{-\Delta^{\neq} G^0(T)}{k_B T}} \tag{1}$$

where, σ is degeneracy of the reaction path; k_B, h, R and T are the Boltzmann constant, Planck constant and general gas constant, temperature in Kelvin, respectively; P^0 is the standard pressure; $\Delta^{\neq} G^0(T)$ is the Gibbs free energy barrier of the reaction path at a given temperature and standard atmospheric pressure; For monomolecular decomposition reaction, $\Delta n = 0$.

Due to the study of the reaction rate at relative low temperatures, the quantum tunneling effect correction is carried out for the reaction path containing transition states, the Wigner correction method (Wigner, 1937) was used to calculate the tunneling correction factor (κ),

$$\kappa = 1 + \frac{1}{24} \left(\frac{h\nu^{\neq}}{k_B T} \right)^2 \tag{2}$$

where, $\nu^{\neq}$ is the imaginary frequency of transition state. Then, the reaction rate considering tunneling correction can be expressed as:

$$k^{TST,\kappa}(T) = \kappa k^{TST}(T) \tag{3}$$

After obtaining the reaction rate of each path, the total reaction rate of the initial decomposition reaction can be obtained as follows,

$$k_{total}^{TST,\kappa}(T) = \sum_i^n k_i^{TST,\kappa}(T) \tag{4}$$

The reaction branching ratio is used to measure the contribution of each reaction path to decomposition. The branching ratio is calculated as follows,

$$BR(i)\% = \frac{k_i^{TST,\kappa}(T)}{k_{total}^{TST,\kappa}(T)} \times 100 \tag{5}$$

3 RESULTS AND DISCUSSION

3.1 Decomposition kinetics of six hydrocarbon working fluids

Six common hydrocarbon working fluids including n-butane, isobutane, n-pentane, isopentane, neopentane and n-hexane were used as research objects. In the initial stage of decomposition, the weaker chemical bond in the molecule breaks, resulting in the initial decomposition of molecule. For these

hydrocarbons, mainly considers two types of initial decomposition reactions (Xin et al., 2020): C-H bond cleavage reactions and C-C bond cleavage reactions. Taking n-pentane as example, the initial reaction paths and degeneracy of reaction paths (σ) are shown in Table 1.

Table 1: Initial reaction paths of n-pentane.

Reaction path	Reaction	σ
RP1	$n-C_5H_{12} \rightarrow CH_3\bullet + C_4H_9\bullet$	2
RP2	$n-C_5H_{12} \rightarrow C_2H_5\bullet + C_3H_7\bullet$	2
RP3	$n-C_5H_{12} \rightarrow H\bullet + \bullet CH_2(CH_2)_3CH_3$	6
RP4	$n-C_5H_{12} \rightarrow H\bullet + CH_3\bullet CH(CH_2)_2CH_3$	4
RP5	$n-C_5H_{12} \rightarrow H\bullet + CH_3CH_2\bullet CHCH_2CH_3$	2

The branching ratio reflects the contribution of each reaction path to the total reaction rate, which is shown in Fig.1. As shown in Fig.1a, the reaction rate of each path follows the following order: deethylation reaction rate (RP2) > demethylation reaction rate (RP1) >> C-H bond cleavage reaction rate (RP3, RP4 and RP5). As shown in Fig. 1b. In the temperature range of 300K~700K, the branching ratio of the reaction path for the deethylation reaction (RP2) is about 99.5%, the branching ratio of the demethylation reaction (RP1) is about 0.5%~0.4%, and the branching ratio of the reaction paths for the C-H bond cleavage (RP3, RP4 and RP5) is less than 0.1%.

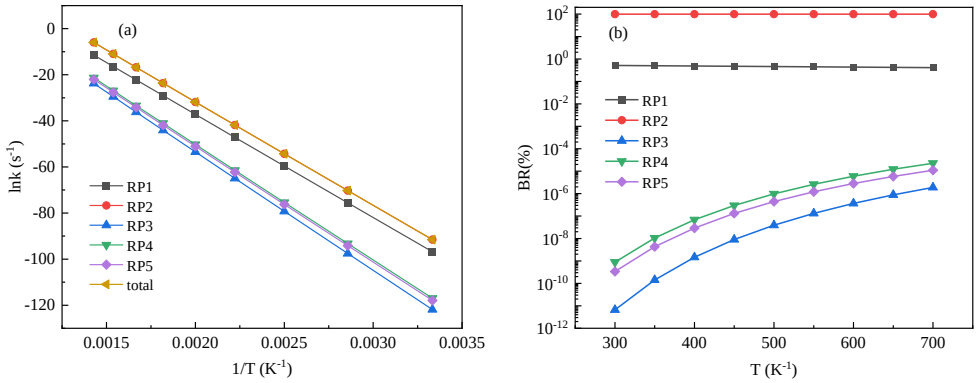

Figure 1: Reaction rate (a) and branching ratio (b) of each reaction path of n-pentane.

The total reaction rate fitting correlations of six hydrocarbon working fluids are shown in Fig. 2. In order to evaluate the accuracy of these fitting correlation equations in predicting the decomposition reaction rates, a comparison was made with experimental data from existing literature, and the results are shown in Table 2. As shown in Table 2, for n-pentane, compared with experimental data, the correlation equation overestimates the reaction rate at 603.15 K and below, while it underestimates the reaction rate above 603.15 K; at temperature of 588.15 K, the correlation equation overestimates the reaction rate of isopentane, while show excellent prediction accuracy of neopentane. Overall, the obtained correlation shows good prediction accuracy. Further, with 1% annual decomposition as the threshold, the ideal maximum operational temperatures of six hydrocarbon working fluids are predicted by using the obtained kinetic correlations, and compared with the ideal maximum operational temperatures recommended in the literature (Dai et al., 2016b), which was obtained through rapid pyrolysis experiments. The lower limit of the range corresponds to the highest temperature at which no

decomposition products are detected after 24 hours of heating, while the upper limit corresponds to the lowest temperature at which decomposition products are detected after 24 hours of heating, with a temperature interval of 20 K. The results are shown in Table 3. For n-butane, isobutane and isopentane, the predicted temperature is within the ideal maximum operational temperature range recommended by the experiment; for isobutane and n-hexane, there are deviations of -3.27 K and 32.5 K. On the whole, the obtained kinetic expressions have good performance in predicting the ideal maximum operational temperature of hydrocarbon working fluids. Moreover, it is worth mentioning that due to the high branching ratio of RP1 and RP2, the contribution of RP3, RP4 and RP5 can be ignored when fitting the kinetic correlation, which has little impact on the prediction of ideal maximum operational temperature.

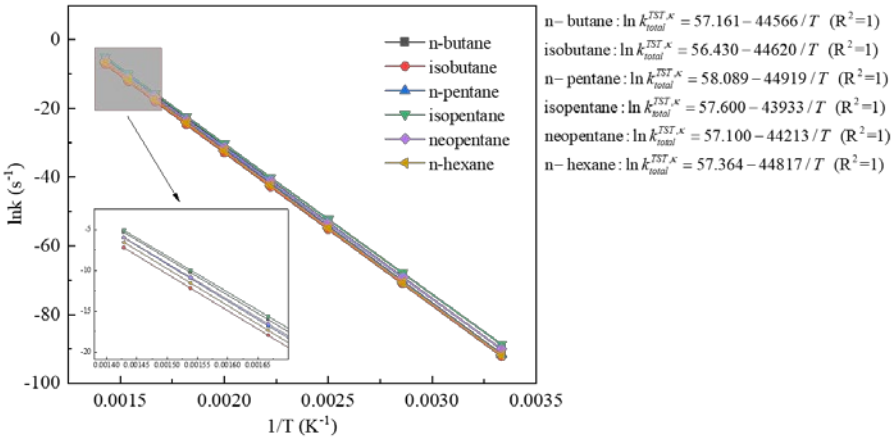

Figure 2: Total reaction rate of six hydrocarbon working fluids.

480

Table 2: Comparison of reaction rate predicted by correlation equation with experimental data.

Working fluid	Temperature (K)	Reaction rate predicted by correlation equation (s^{-1})	Reaction rate obtained by experiment (s^{-1})
n-pentane	588.15	1.15×10^{-8}	$(4.07\pm0.70)\times10^{-9}$ (Andersen and Bruno, 2005)
	603.15	7.67×10^{-8}	$(3.2998\pm0.1971)\times10^{-8}$ (Dai et al., 2016a)
	613.15	1.15×10^{-8}	$(1.4246\pm0.1176)\times10^{-8}$(Dai et al., 2016a)
	623.15	2.58×10^{-7}	$(6.1062\pm0.4748)\times10^{-7}$(Dai et al., 2016a)
isopentane	588.15	3.76×10^{-8}	$(7.9\pm1.6)\times10^{-9}$(Andersen and Bruno, 2005)
neopentane	588.15	1.48×10^{-8}	$(1.5\pm0.3)\times10^{-8}$((Andersen and Bruno, 2005)

Table 3: Ideal maximum operational temperature predicted by obtained kinetics correlations.

Working fluid	Predicted T_{max} (K)	Recommended T_{max} by experiment (K) (Dai et al., 2016b)
n-butane	563.93	573.15~593.15
isobutane	569.88	573.15~593.15
n-pentane	561.79	553.15~573.15
isopentane	552.85	533.15~553.15

neopentane	559.60	-
n-hexane	565.65	533.15~553.15

3.2 Thermodynamic and kinetics of decomposition of seven HFCs working fluids

In this part, seven HFCs working fluids (HFC-245fa, HFC-134a, HFC-227ea, HFC-236fa, HFC-143a, HFC-152a, HFC-125) commonly used in ORC were selected as research objects. For HFCs, the initial pyrolysis has the following reaction paths: C-C bond cleavage, C-H bond cleavage, C-F bond cleavage and HF removal. Taking HFC-245fa as an example, the initial reaction paths and degeneracy of reaction paths are shown in Table 3.

Table 4: Initial reaction paths of HFC-245fa.

Reaction path	Reaction	σ
RP1	$CF_3CH_2CF_2H \rightarrow \bullet CF_3 + \bullet CH_2CF_2H$	1
RP2	$CF_3CH_2CF_2H \rightarrow CF_3CH_2\bullet + \bullet CF_2H$	1
RP3	$CF_3CH_2CF_2H \rightarrow H\bullet + CF_3CH\bullet CF_2H$	2
RP4	$CF_3CH_2CF_2H \rightarrow H\bullet + CF_3CH_2CF_2\bullet$	1
RP5	$CF_3CH_2CF_2H \rightarrow F\bullet + \bullet CF_2CH_2CF_2H$	3
RP6	$CF_3CH_2CF_2H \rightarrow F\bullet + CF_3CH_2CFH\bullet$	2
RP7	$CF_3CH_2CF_2H \rightarrow CF_3CH_2CF_2H(TS_1) \rightarrow HF + CF_2=CHCF_2H$	6
RP8	$CF_3CH_2CF_2H \rightarrow CF_3CH_2CF_2H(TS_2) \rightarrow HF + CF_3CH=CFH$	4

Fig. 5 shows the reaction rate and branching ratio of each reaction path. As shown in Fig.5a, In the temperature range of 300~500 K, the reaction rate of each path follows the following order: HF removal (RP7 and RP8) > C-C bond cleavage (RP1 and RP2) > C-H bond cleavage (RP3 and RP4) > C-F bond cleavage (RP5 and RP6). However, because the reaction rate of C-C bond cleavage increases faster with temperature, when the temperature is higher than 500 K, the reaction rate of C-C bond cleavage gradually exceeds that of HF removal. As shown in Fig. 5b, in the temperature range of 300~550 K, the branching ratio of the HF removal reactions is nearly 100%. In the temperature range of 550~700 K, the branching ratio of the HF removal reactions decrease, and that of C-C bond cleavage reactions increase. When the temperature exceeds 650 K, the branching ratio of C-C bond cleavage reaction exceeds HF removal reaction, the cleavage of the C-C bond will become the dominant reaction for the initial decomposition of HFC-245fa. In the temperature range of 300~700 K, the branching ratio of C-F bond and C-H bond cleavage reaction are close to 0, which is difficult to occur.

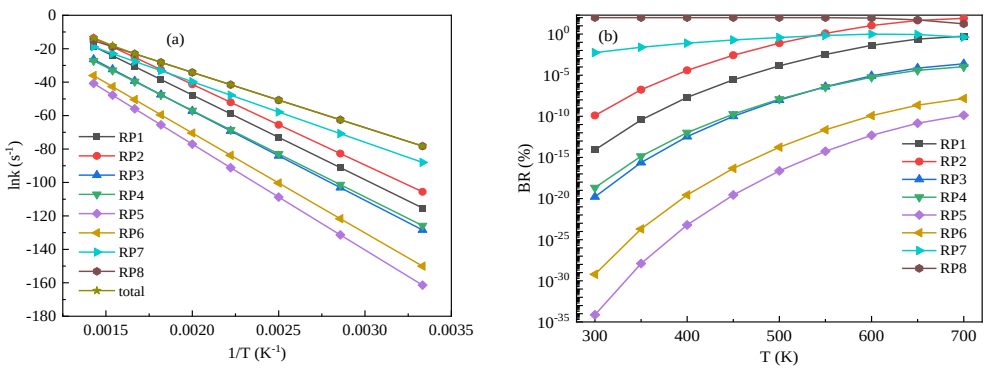

Figure 5: Reaction rate (a) and branching ratio (b) of each reaction path of HFC-245fa.

The total reaction rate fitting correlations of seven HFCs working fluids are shown in Fig. 6. As shown in Fig. 6, the decomposition rate of each working fluids varies greatly with temperatures. Further analysis shows that in the temperature range of 300~700 K, the decomposition of the seven working fluids is almost all contributed by HF removal and C-C bond, as shown in Fig. 7. Therefore, for HFCs, the reaction of C-H bond and C-F bond breaking can be ignored when calculating the decomposition rate. To evaluate the accuracy of the obtained kinetic correlations, the ideal maximum safe operational temperatures of seven HFCs working fluids are calculated with the annual decomposition amount of 1% as the threshold, and compared with the literatures. The results are shown in Table 5. For the temperature range given in the literature, the lower limit value was used as the ideal maximum operational temperature for comparison. According to Table 5, except for HFC-152a, HFC-227ea and HFC-134a, which have large deviations from the experimental results, 179.29 K, 91.56 K and 58.46 K, respectively, the other four working fluids are in good agreement with the experimental values, and the deviations are within 35 K. In addition to the inherent error in calculating energy using DFT, the deviation between the predicted values and the experimental ones may be caused by the following reasons: (1) The experimental values are determined by the fluoride ion concentration (Dai et al., 2018) or pressure deviation (Angelino and Invernizzi, 2003) after the thermal stress experiment, which is somewhat different from the decomposition rate of the reactant; (2) The metal surface under experimental conditions have a certain catalytic effect on the decomposition of HFCs (Dai et al., 2017; Huo et al., 2019). Due to the high branching ratio of the C-C bond cleavage reaction paths and HF removal reaction paths, the contribution of the C-H bond and C-F bond cleavage can be ignored when fitting the kinetic correlation, which has little impact on the prediction of ideal maximum operational temperature.

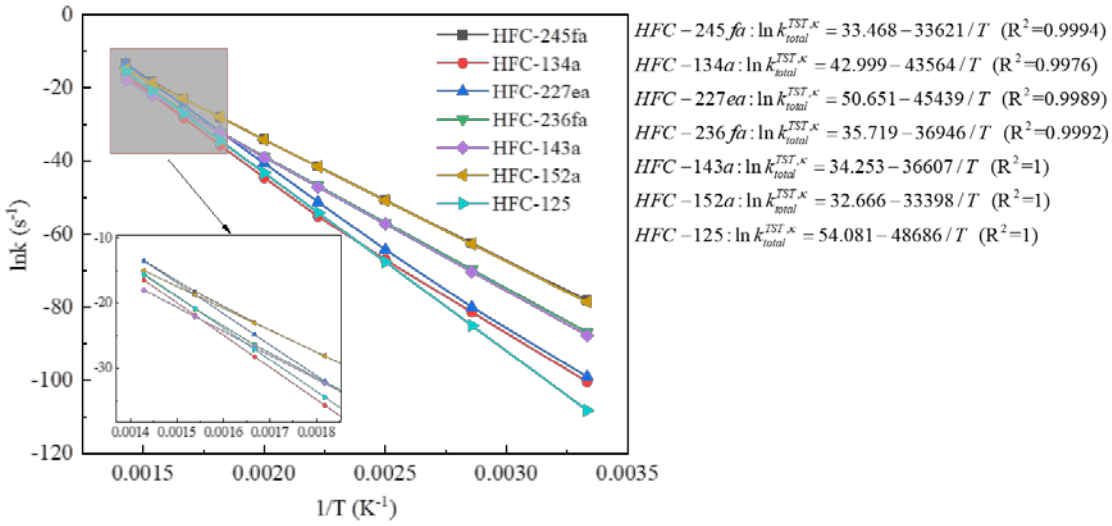

Figure 6: Total reaction rate of seven HFCs working fluids.

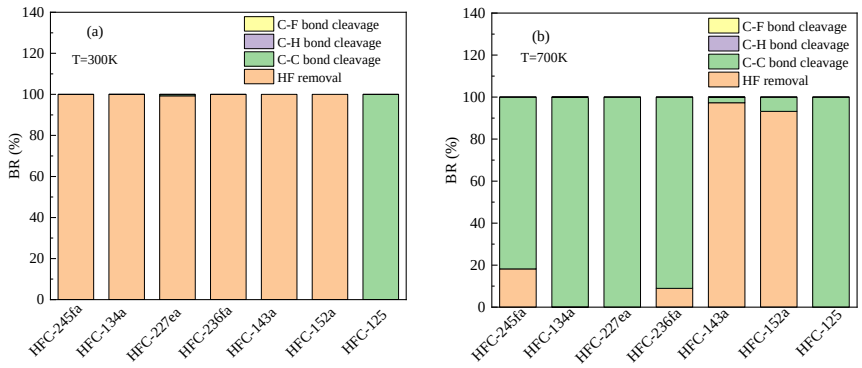

Figure 7: Reaction path branching ratios at different temperatures: (a) 300K; (b) 700K.

Table 5: Ideal maximum operational temperature predicted by obtained kinetics correlations.

Working fluid	Predicted T_{max} (K)	Recommended T_{max} by experiment (K)
HFC-245fa	606.59	573.15~593.15 (Dai et al., 2018)
HFC-134a	671.60	613.15~633.15 (Dai et al., 2018)
HFC-227ea	626.59	698.15 (Angelino and Invernizzi, 2003)
HFC-236fa	641.58	673.15 (Angelino and Invernizzi, 2003)
HFC-143a	652.30	623.15 (Calderazzi and di Paliano, 1997)
HFC-152a	612.44	433.15~453.15 (Dai et al., 2018)
HFC-125	641.05	669.15 (Calderazzi and di Paliano, 1997)

483

4 CONCLUSIONS

In present work, combining high-precision quantum chemical calculations and transition state theory, a simplified method for predicting the ideal maximum operational temperatures of hydrocarbon and HFCs working fluids in ORC power plants was proposed, and its prediction effect was evaluated. The main conclusions are drawn as follows:

- For the decomposition of hydrocarbon working fluids, using the obtained decomposition kinetics correlations, accurate ideal maximum operational temperature prediction can be achieved. The ideal maximum operational temperature of n-butane, isobutane, n-pentane, isopentane, neopentane, and n-hexane predicted with the annual decomposition rate of 1% as the threshold value is 563.93 K, 569.88 K, 561.79 K, 552.8 K, 559.60 K and 565.65 K, respectively.
- For the decomposition of HFCs working fluids, the ideal maximum operational temperatures of HFC-245fa, HFC-134a, HFC-227ea, HFC-236fa, HFC-143a, HFC-152a and HFC-125 predicted by the obtained decomposition kinetics correlations are 606.59 K, 671.60 K, 626.59 K, 641.58 K, 652.30 K, 612.44 K and 641.05 K, respectively.
- For hydrocarbon working fluids, the initial decomposition is mainly contributed by the C-C bond cleavage reaction paths, while for HFCs working fluids, the initial decomposition is mainly contributed by the C-C bond cleavage and HF removal reaction paths.

NOMENCLATURE

BR	branching ratio	(%)
DFT	density functional theory	(-)
HFCs	hydrofluorocarbons	(-)
h	Planck constant	(J·s)
k_B	Boltzmann constant	($J \cdot K^{-1}$)
k	reaction rate constant	(s^{-1})
ORC	organic Rankine cycle	(-)
R	general gas constant	($J \cdot mol^{-1} \cdot K^{-1}$)
RP	reaction path	(-)
R^2	mean square error	(-)
T	temperature	(K)
TST	transition state theory	(-)
σ	degeneracy of the reaction path	(-)

Subscript

max	Ideal maximum operational temperature

REFERENCES

Al-Otaibi, J.S., Abdel-Rahman, M.A., Almuqrin, A.H., El-Gogary, T.M., Mahmoud, M.A., El-Nahas, A.M., 2021. Thermo-kinetic theoretical studies on pyrolysis of dimethoxymethane fuel additive. Fuel 290, 119970.

Alecu, I., Zheng, J., Zhao, Y., Truhlar, D.G., 2010. Computational thermochemistry: scale factor databases and scale factors for vibrational frequencies obtained from electronic model chemistries. Journal of chemical theory and computation 6, 2872-2887.

Andersen, W.C., Bruno, T.J., 2005. Rapid screening of fluids for chemical stability in organic Rankine cycle applications. Industrial & Engineering Chemistry Research 44, 5560-5566.

Angelino, G., Invernizzi, C., 2003. Experimental investigation on the thermal stability of some new zero ODP refrigerants. International Journal of Refrigeration 26, 51-58.

Calderazzi, L., di Paliano, P.C., 1997. Thermal stability of R-134a, R-141b, R-13I1, R-7146, R-125 associated with stainless steel as a containing material. International journal of refrigeration 20, 381-389.

Dai, X., Shi, L., An, Q., Qian, W., 2016a. Chemical kinetics method for evaluating the thermal stability of Organic Rankine Cycle working fluids. Applied Thermal Engineering 100, 708-713.

Dai, X., Shi, L., An, Q., Qian, W., 2016b. Screening of hydrocarbons as supercritical ORCs working fluids by thermal stability. Energy Conversion and Management 126, 632-637.

Dai, X., Shi, L., An, Q., Qian, W., 2017. Screening of working fluids and metal materials for high temperature organic Rankine cycles by compatibility. Journal of Renewable and Sustainable Energy 9.

Dai, X., Shi, L., An, Q., Qian, W., 2018. Thermal stability of some hydrofluorocarbons as supercritical ORCs working fluids. Applied Thermal Engineering 128, 1095-1101.

Eyring, H., 1935. The activated complex in chemical reactions. The Journal of Chemical Physics 3, 107-115.

Frisch, M., Trucks, G., Schlegel, H., Scuseria, G., Robb, M., Cheeseman, J., Scalmani, G., Barone, V., Petersson, G., Nakatsuji, H., Gaussian 16, revision B. 01; Wallingford, CT, 2016. Google Scholar There is no corresponding record for this reference.

Huo, E., Liu, C., Xu, X., Liu, L., Wang, S., 2019. Dissociation mechanism of HFC-245fa on Cu(1 1 1) surfaces with and without oxygen-covered: A density functional theory study. Applied Surface Science 480, 487-496.

Koplow, M., Di Nanno, L., Di Bella, F., 1984. Status report for an RC-1 organic rankine bottoming cycle for an adiabatic diesel engine, Proceedings of the 21st Automotive Technology Development Contractors' Coordination Meeting, Dearborn, MI, October, pp. 21-24.

Lu, T., Chen, Q., 2021. Shermo: A general code for calculating molecular thermochemistry properties. Computational and Theoretical Chemistry 1200, 113249.

Niggemann, R., 1969. ORGANIC RANKINE CYCLE TECHNOLOGY PROGRAM. Quarterly Progress Report No. 12, January 1, 1969--April 1, 1969. Sundstrand Aviation-Rockford, Ill.

Nikitin, E.E.e., 1974. Theory of elementary atomic and molecular processes in gases(Book). Oxford, Clarendon Press.

Pereira, J.S., Santos, M., Mendes, R., André, J.C., Ribeiro, J.B., 2022. Thermal degradation assessment study of a direct vaporization ORC based micro-CHP system under close-to-real operating conditions. Applied Thermal Engineering 214, 118878.

Wang, S., Liu, C., Zhang, S., Li, Q., Huo, E., 2022. Multi-objective optimization and fluid selection of organic Rankine cycle (ORC) system based on economic-environmental-sustainable analysis. Energy Conversion and Management 254, 115238.

Weigend, F., Ahlrichs, R., 2005. Balanced basis sets of split valence, triple zeta valence and quadruple zeta valence quality for H to Rn: Design and assessment of accuracy. Physical Chemistry Chemical Physics 7, 3297-3305.

Wigner, E., 1937. Calculation of the rate of elementary association reactions. The Journal of Chemical Physics 5, 720-725.

Xin, L., Liu, C., Liu, Y., Huo, E., Li, Q., Wang, X., Cheng, Q., 2020. Thermal decomposition mechanism of some hydrocarbons by ReaxFF-based molecular dynamics and density functional theory study. Fuel 275, 117885.

Zhao, Y., Truhlar, D.G., 2008. The M06 suite of density functionals for main group thermochemistry, thermochemical kinetics, noncovalent interactions, excited states, and transition elements: two new functionals and systematic testing of four M06-class functionals and 12 other functionals. Theoretical chemistry accounts 120, 215-241.

ACKNOWLEDGEMENT

This work was financially supported by the National Natural Science Foundation of China (No. 52076018) and the Chongqing Graduate Research and Innovation Project (No. CYB22020).

ORC SEVILLE 2023
7th International Seminar on O.R.C. Power Systems

© 2024 Editorial Universidad de Sevilla. Este es un artículo de acceso abierto distribuido bajo los términos de la licencia de uso y distribución Creative Commons (BY-NC-ND 4.0)

DOI: https://dx.doi.org/10.12795/9788447227457_82

Comparison of Different Evaporator Topologies for Industrial Heat Pumps

Sanjay Vermani [1*], Nitish Anand [1], Johan Van Bael [1], Evgueni Touliankine [2], Aldo Serafino [2], Carlo De Servi [1,3]

[1] Thermal Energy Systems Group, Energy Technology Unit, Flemish Institute for Technological Research (VITO), Mol, Belgium.

[2] Enertime Courbevoie, France

[3] Propulsion & Power Group, Faculty of Aerospace Engineering, Delft University of Technology, Delft, The Netherlands.

* Corresponding Author: sanjay.vermani@vito.be

ABSTRACT

Reducing the energy consumption associated with industrial process heating is one of the crucial steps toward building a green and climate-neutral Europe, as the thermal energy demand of industry accounts for a significant portion of the total primary energy consumption and carbon emissions of this sector. In this regard, waste heat utilization using high-temperature heat pump systems is one of the most promising solutions to increase industrial energy efficiency. To efficiently recover and convert the available waste heat, the performance of the individual heat pump components, in particular the heat exchangers, is key. This paper reports a comparison between two different evaporator concepts considered for high-temperature heat pump systems, namely the shell and tube and the falling film evaporator. Four key characteristics of the two evaporator concepts are analyzed and compared: the overall heat transfer coefficient, the induced pressure losses, the footprint, and the required refrigerant charge. The results indicate that the falling film evaporator features a higher overall heat transfer coefficient and enables approximately a 77% reduction of the required working fluid charge with respect to the shell and tube evaporator.

1. INTRODUCTION

A critical milestone toward attaining climate neutrality is the decarbonization of the energy demand in industry. Currently, process heating accounts for a significant proportion of the total energy demand of the industrial sector. For example, in 2019, the share associated with process heating alone was approximately 53% (Robert et al., 2020). One of the solutions to offset this energy demand consists in recovering waste thermal energy from industrial processes.

In such a context, the exploitation of waste heat through high-temperature heat pump (HTHP) systems is recognized as one of the main options to enhance industrial energy efficiency (Kosmadakis, 2019; Arpagaus et al., 2018). However, despite the potential of the technology, the deployment of high-temperature heat pumps in industrial processes is still marginal. The reason thereof is related to several technical limitations, e.g., low thermal efficiencies, relative large footprint, and other installation requirements, which hamper the integration of new heat pump systems in existing factories (Jiang et al., 2022).

Heat exchangers are key components of this technology, as their design affect the thermodynamic, and economic performance of the heat pump. A conventional vapour compression cycle-based heat pump comprises at least two heat exchangers, namely an evaporator and a condenser. As far as the evaporator is concerned, such a component enables the heat transfer between the waste heat source and the working fluid. In large-scale industrial heat pump systems, the evaporator is often of the shell and tube type with a kettle configuration (Reay, 2002; Zohuri, 2022). The simplicity of the design and operation is obtained at the cost of a large working fluid inventory and installation footprint. A potential alternative to kettle boilers, or more in general pool-boiling heat exchangers, is the falling film evaporator with horizontal tubes. This solution offers several advantages, like reduced installation footprint and operating costs (Höfler, 2019). Those benefits arise from the higher heat transfer coefficient on the working fluid side of the heat exchanger, and the reduced amount of working fluid charge needed (Roques and Thome, 2007a). In recent years, horizontal falling film evaporators have seen successful applications in various industrial sectors, such as petrochemicals, seawater desalination and refrigeration systems (Fernández-Seara and Pardiñas, 2014).

This article reports a comparative study between a shell and tube pool-boiling type evaporator and a falling film evaporator for an industrial high-temperature heat pump. The comparison is drawn at design point conditions, with respect to key performance quantities, such as the overall heat transfer coefficient, pressure losses, installation footprint, and the required refrigerant charge. Furthermore, an off-design performance analysis was performed for the falling film evaporator. The performance of the falling film evaporator was simulated by means of a 1D steady-state model, while the commercial design software `ASPEN` was utilized to simulate the shell and tube evaporator (Aspentech, 2022).

2. METHODOLOGY

This section describes the modelling approach adopted for the the falling film and shell and tube evaporator models.

2.1 Falling Film Evaporator (FF)

To simulate the falling film evaporator, a steady-state lumped parameter model was developed, whose system boundaries are shown in Figure 1. The hot fluid enters the tubes from the top inlet, while the cold refrigerant is sprayed onto the tube bundle. To simplify the model, the following assumptions are made:

1. The shell-side pressure is constant.
2. Thermal losses to the environment are negligible.
3. Flow maldistribution effects due to non-uniform liquid film distribution over the tubes are neglected.

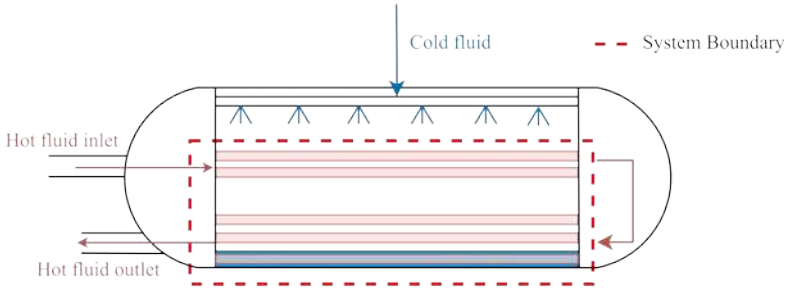

Figure 1: System boundaries of the falling film evaporator model.

To capture the variation of the mass flow rate of the liquid film from the top to the bottom rows, a tube row-wise discretization of the evaporator is implemented, as shown in Figure 2, where the index "i" and "j" refer to a given tube row and pass, respectively.

The energy balance and heat transfer rate across a tube can be expressed as

$$\dot{m}_{\mathrm{hot,\,i}} c_{P,\mathrm{hot,\,i}} \left(\mathrm{T}_{\mathrm{hot\ in,\,i}} - \mathrm{T}_{\mathrm{hot\ out,\,i}}\right) = \pi \mathrm{d}_{\mathrm{inner}}\, L_{\mathrm{tube}}\, h_{\mathrm{hot,\,i}} \left(\mathrm{T}_{\mathrm{hot\ mean,\,i}} - \mathrm{T}_{\mathrm{wall\ inner,\,i}}\right), \tag{1}$$

$$\dot{m}_{\mathrm{evap,\,i}}\, \Delta H_{\mathrm{vap}} = \pi \mathrm{d}_{\mathrm{outer}}\, L_{\mathrm{tube}}\, h_{\mathrm{film,\,i}} \left(\mathrm{T}_{\mathrm{wall\ outer,\,i}} - \mathrm{T}_{\mathrm{film}}\right), \tag{2}$$

$$\dot{m}_{\mathrm{hot,\,i}} c_{P,\mathrm{hot,\,i}} \left(\mathrm{T}_{\mathrm{hot\ in,\,i}} - \mathrm{T}_{\mathrm{hot\ out,\,i}}\right) = \frac{2\pi\, \lambda_{\mathrm{wall}}\, L_{\mathrm{tube}} \left(T_{\mathrm{wall\ inner,\,i}} - T_{\mathrm{wall\ outer,\,i}}\right)}{\ln\left(d_{\mathrm{outer}}/d_{\mathrm{inner}}\right)}, \tag{3}$$

where Equation (1) and Equation (2) express the energy balance and heat transfer rate for the hot fluid inside the tubes and the cold fluid film respectively, while Equation (3) refers to the tube wall.

Here, $\dot{m}$ is the fluid mass flow rate, c_P the specific heat capacity, T the temperature, λ the thermal conductivity, and h the heat transfer coefficient. The parameters d_{outer}, d_{inner} and L indicate the tube's outer

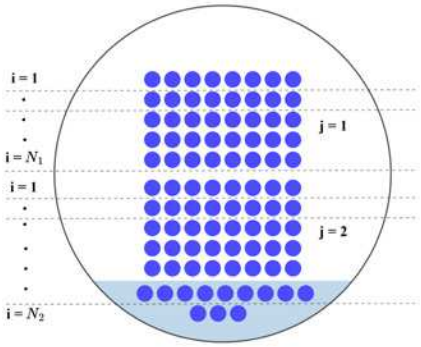

Figure 2: Discretization scheme used for the falling film evaporator model.

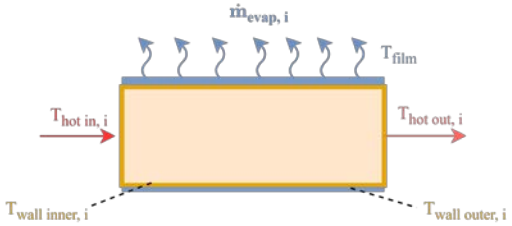

Figure 3: Schematic of the elementary volume of the discretization scheme adopted in the falling film evaporator model.

diameter, inner diameter, and length. The subscripts 'out' and 'in' refers to the inlet and outlet of an individual tube.

To estimate the convective heat transfer coefficient of the hot fluid inside the tubes (h_{hot}), the correlation proposed by Bell and Muller (2001) is used. This correlation accounts for the fluid properties and the tube characteristics and reads

$$h_{\mathrm{hot}} = \frac{C\,\lambda_{\mathrm{hot}}}{d_{\mathrm{inner}}}\,\mathrm{Re}^{0.8}\,\mathrm{Pr}^{1/3}\left(\frac{\mu_{\mathrm{hot}}}{\mu_{\mathrm{wall,\,inner}}}\right)^{0.14}, \tag{4}$$

where Re and Pr represent the Reynolds number and Prandlt number. Besides, μ represents the dynamic viscosity of the fluid and C is a constant that varies depending on the tube type (plain or finned). In the current study, plain tubes are considered. The corresponding value of C is 0.021.

Concerning the liquid film, three main flow modes have been described in the literature, namely, droplet, column/jet, and sheet mode (Mitrovic, 1986), that may influence heat transfer. In addition, two intermediate flow modes can establish in the falling film: column-sheet and droplet-sheet, as reported by Hu and Jacobi (1996). The dependency of the heat transfer coefficient as a function of the flow mode is, to a first approximation, limited, and, at the same time, quite complex to model, as mentioned in (Roques and Thome, 2007b). Thus, in engineering practice, the heat transfer correlations account only for the onset of dryout (Yang and Wang, 2011).

Different methods have been proposed in the literature (Zhao et al., 2022; Thome, 2016) to predict the onset of dryout and the corresponding heat transfer coefficient as a function of film Reynolds number and heat flux. However, since the majority of these methods have been developed for specific fluids and are only valid for a specific range of Reynolds number and heat flux, their applicability to the evaporator of the heat pump system under investigation in this study is arguable. Therefore, three different correlations for the film heat transfer coefficient were assessed. The predictions of these correlations were compared with literature data to identify the most suitable one for the design of a falling film evaporator for the considered heat pump system (see Section 4.1).

The first method is the one developed by Shah (2021) for plain tubes, which can be, in principle, used with arbitrary fluids. Such a method is an extension of the superposition method reported by Rohsenow (1952). The other two procedures evaluated for the film heat transfer coefficient estimation were those developed by Roques and Thome (2007b) and Jin et al. (2019). As that of Shah (2021) was eventually selected for the falling film evaporator model, only this method is reported here in detail.

According to Shah (2021), the overall heat transfer coefficient during boiling in forced convection can be expressed as a linear combination of the heat transfer due to nucleate boiling and that due to forced convection. Moreover, when nucleate boiling occurs, the stirring action of the bubbles makes the tran-

sition from laminar to turbulent flow occur at low Reynolds numbers. Then, the two-phase heat transfer coefficient for the falling film can be written as

$$h_{\mathrm{film}} = \max\left[h_{\mathrm{c,lam}}, \left(h_{\mathrm{nb}} + h_{\mathrm{c,turb}}\right)\right], \tag{5}$$

where h_{nb} represents the heat transfer coefficient for the nucleate boiling regime, while $h_{\mathrm{c,lam}}$ and $h_{\mathrm{c,turb}}$ represent the laminar and the turbulent forced convection heat transfer coefficient, respectively.

To compute the forced convection heat transfer coefficients, the method of Shah relies on the correlations developed by Lorenz and Yung (1979) for the laminar and turbulent flow regime, which read

$$h_{\mathrm{c,lam}} = 0.821 \left(\frac{\nu_{\mathrm{film}}^2}{g\lambda_{\mathrm{film}}^3}\right)^{-1/3} \mathrm{Re}_{\mathrm{film}}^{-0.22}, \tag{6}$$

$$h_{\mathrm{c,turb}} = 0.0038 \left(\frac{\nu_{\mathrm{film}}^2}{g\lambda_{\mathrm{film}}^3}\right)^{-1/3} \mathrm{Re}_{\mathrm{film}}^{0.4} \left(\frac{\nu_{\mathrm{film}}}{\alpha_{\mathrm{film}}}\right)^{0.65}. \tag{7}$$

In Equation (6) and Equation (7), ν and α are the kinematic viscosity and the thermal diffusivity of the fluid, respectively. Besides, $\mathrm{Re}_{\mathrm{film}}$ is defined as $\mathrm{Re}_{\mathrm{film}} = 4\Gamma/\mu_{\mathrm{film}}$, where Γ is the film mass flow rate per unit length on one side of the tube.

In Equation (5), h_{nb} is estimated using the correlations developed by Mostinski (1963) and Cooper (1984). Shah (2021) recommends Mostinski's correlation for hydrocarbons and Cooper's correlation for all the other fluids. For completeness, the two correlations are reported below

$$h_{\mathrm{nb}} = \begin{cases} Mostinski: \ 0.00417\, q^{0.7} p_{\mathrm{c}}^{0.69} \left(1.8 p_{\mathrm{r}}^{0.17} + 4 p_{\mathrm{r}}^{1.2} + 10 p_{\mathrm{r}}^{10}\right), \\ Cooper: \ 55\, q^{0.67} M^{-0.5} p_{\mathrm{r}}^{(0.12-0.087 \ln f)} \left(-0.4343 \ln p_{\mathrm{r}}\right)^{-0.55}. \end{cases} \tag{8}$$

In Equation (8), q represents the heat flux, M refers to the molecular weight of the refrigerant and p refers to the fluid pressure, whereas the subscripts "r" and "c" indicate the reduced and critical pressure respectively.

In the vapour superheating region of the falling film evaporator, the main heat transfer mechanism is that of forced convection. The corresponding heat transfer coefficient and friction factor are predicted with the correlations recommended in (Verein deutscher Ingenieure, 2010, Chapter G7 and M1), assuming that the tube bundle features low-finned tubes.

Once the various heat transfer coefficients are known, the overall thermal resistance (U) across a tube wall can be computed as

$$\frac{1}{U} = \frac{1}{h_{\mathrm{int}}} \left(\frac{d_{\mathrm{out}}}{d_{\mathrm{in}}}\right) + \frac{d_{\mathrm{out}}}{2\lambda_{\mathrm{wall}}} \left(\ln \frac{d_{\mathrm{out}}}{d_{\mathrm{in}}}\right) + \frac{1}{h_{\mathrm{film}}} + \mathrm{R}_{\mathrm{foul}} \left(\frac{d_{\mathrm{out}}}{d_{\mathrm{in}}}\right), \tag{9}$$

where the reference area is the external one of the tubes. The heat flux over each tube row is evaluated assuming the log-mean temperature difference (LMTD) as the effective temperature difference between the hot and the cold fluid, namely

$$q = U \cdot \mathrm{LMTD} = U \, \frac{\left(T_{\mathrm{hot\ in,\,i}} - T_{\mathrm{hot\ out,\,i}}\right)}{\ln\left(\frac{T_{\mathrm{hot\ in,\,i}} - T_{\mathrm{film}}}{T_{\mathrm{hot\ out,\,i}} - T_{\mathrm{film}}}\right)}. \tag{10}$$

Finally, the total thermal energy exchange in the evaporator is computed as

$$Q_{\mathrm{total}} = \sum_{j=1}^{N_{\mathrm{pass}}} \sum_{i=1}^{N_{\mathrm{j}}} q_{(\mathrm{j,\,i})} \, A_{\mathrm{tube}}, \tag{11}$$

where A_{tube} refers to the outer surface area of a single tube.

The complete procedure used to design the falling film evaporator is illustrated in Figure 4. Given the process conditions, the evaporation region is designed first. Next, the number of tubes required for the vapour superheating is computed, and finally, the required shell geometry is obtained. The whole model is linked to an optimizer, as also shown in the same figure.

The target of the optimization is the minimization of the net volume of the evaporator while satisfying various design constraints, namely, the overall thermal duty and the minimum evaporated mass flow rate. The design variables are the tube length, the number of tubes in the first and second pass of the tube bundle where the evaporation occurs, as well as the number of tubes per row. All the other geometric characteristics, such as tube diameter and fin dimensions, are prescribed inputs.

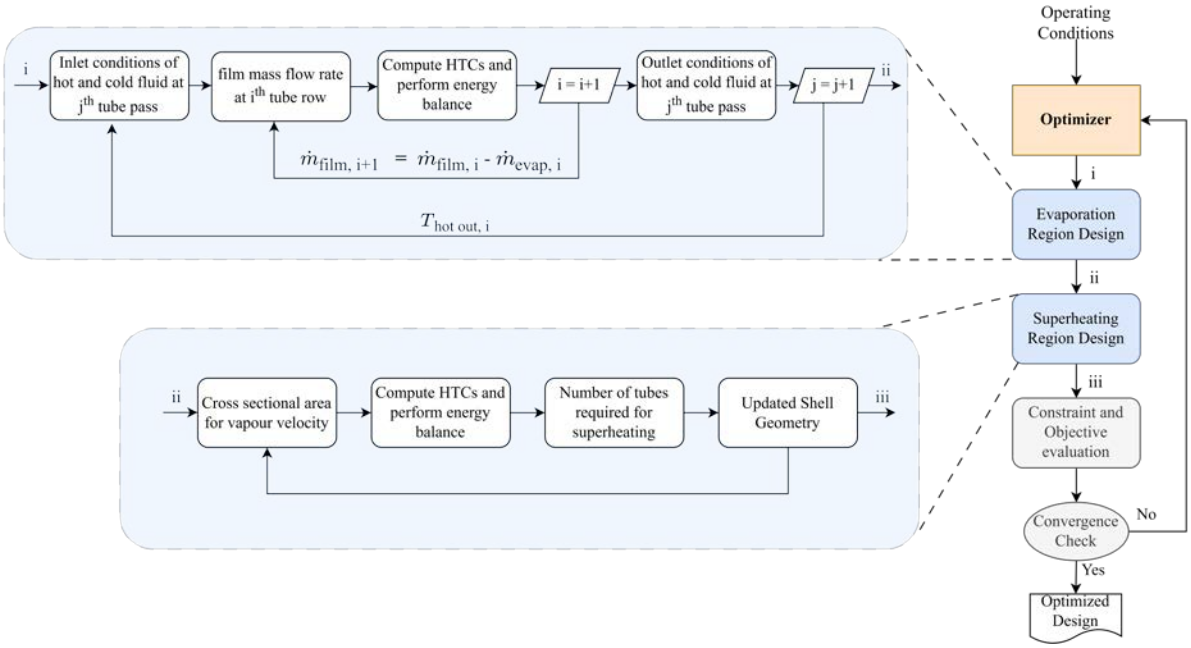

Figure 4: Falling film evaporator model structure.

All the fluid properties are evaluated using `REFPROP-10.0` (Lemmon et al., 2018). The Single Objective Genetic Algorithm (SOGA) is used as the optimization method, while the Latin hypercube sampling (LHS) algorithm is adopted to obtain an initial population of the solutions of SOGA, with 10 samples per design variable (Blank and Deb, 2020).

2.2 Shell and Tube Evaporator (ST)

The commercial software package `ASPEN` (Aspentech, 2022) is used to model the shell and tube pool-boiling type evaporator. This features an unbaffled tube bundle with 4 passes on the tube side and a single one on the shell side (TEMA Type: NXN).

3. CASE STUDY

The application of interest is a vapour compression cycle-based industrial high-temperature heat pump (HTHP). Figure 5 shows the schematic of the selected heat pump and Table 1 presents the associated design specifications of the evaporator. As mentioned earlier, the total shell volume was selected as the design objective to be minimized. The bounds of the design variables included in the optimization are shown in Table A1.

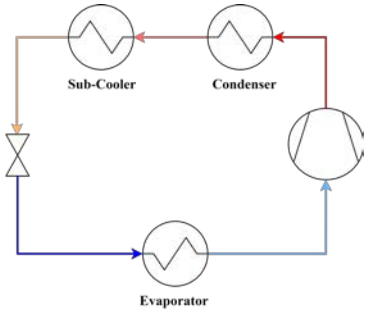

Figure 5: Selected heat pump process flow diagram.

Table 1: Evaporator design specifications for the selected heat pump test case.

	Refrigerant (R1233zdE)		Hot Source (H_2O)	
	In	Out	In	Out
Temperature [K]	340.15	355.15	365.15	345.15
Mass flow rate [kg s^{-1}]	15.44	15.44	25.0	25.0
Vapor Quality [-]	0.2715	1.0	0.0	0.0
Pressure [10^5 Pa]	4.73	-	4.0	-

4. RESULTS AND DISCUSSION

This section reports first the verification study of the developed falling film evaporator model. Subsequently, the comparison between the falling film and the shell and tube evaporator design is reported for the heat pump case under consideration.

4.1 Falling Film (FF) Model Verification

To verify the falling film evaporator model, the numerical results reported by Höfler (2019) were used as a benchmark. The author documented a 2D model of a falling film evaporator for an ORC application, though the adopted film heat transfer coefficient correlation was not mentioned. As discussed previously, the model developed in this work can make use of three different correlations to this purpose, more precisely those proposed by Roques and Thome (2007b), Jin et al. (2019), and Shah (2021).

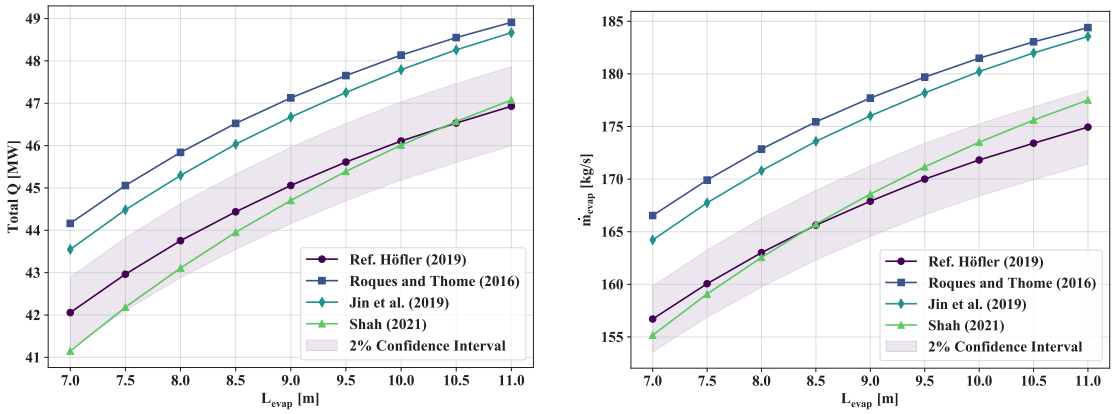

(a) Total thermal energy exchange. **(b) Evaporated fluid mass flow rate.**

Figure 6: Falling Film evaporator model verification with the data provided in Höfler (2019).

Figure 6a and Figure 6b show the comparison between the results reported by Höfler (2019) and those obtained from the model developed in this study. Notably, the overall thermal duty and the evaporated fluid mass flow rate are compared for the three different film heat transfer correlations considered in this work. It can be observed that the correlation developed by Roques and Thome (2007b) and that of Jin et al. (2019) result in a relative deviation of about ~5% with respect to the reference data. Conversely, the correlation developed by Shah (2021) show a maximum difference of ~2%. Note that the correlations of Jin et al. (2019) and Shah (2021) were derived by considering experimental data for falling films of different fluids. However, Jin et al. (2019) only considered 5 fluids and reported a high discrepancy between the predictions of the correlations and the experimental data (+/- 30%), whereas Shah (2021) considered 11 different fluids and reported a higher accuracy of the developed correlation (+/- 20% of deviation with respect to the experimental data). Based on this consideration and the better match with

491

the data in Höfler (2019), the correlation of Shah (2021) was, thus, selected for the design of the falling film evaporator in this study.

4.2 On-design Results

Both the falling film (FF) and the shell and tube (ST) evaporator were designed for the process specifications reported in Table 1. Table 2 compares the corresponding characteristics of the two heat exchangers, where ϵ represents the relative difference of a specific design characteristic (x) with respect to the shell and tube evaporator design. The FF evaporator features plain tubes in the evaporating region and finned tubes in the superheating part. For the ST evaporator, finned tubes were considered for the whole tube bundle. The main geometric parameters of the considered plain and finned tubes are presented in Table A2.

Table 2: Main characteristics of the falling film and shell and tube evaporators at design conditions.

Parameter	Unit	Shell and Tube	Falling Film	ϵ [%]
Total Cold Fluid Evaporated	$\mathrm{kg\ s^{-1}}$	11.25	11.25	0.0
No. of Tubes for Evaporation	-	305	120	−60.7
No. of Tubes for Superheating	-	202	148	−26.7
Tube Length	m	5.9	5.79	−1.9
Shell Outer Diameter	m	0.65	0.61	−6.2
Total Shell Volume	$\mathrm{m^3}$	1.97	1.67	−15.2
Average U	$\mathrm{W\ m^{-2}\ K^{-1}}$	555.1	1455.8	162.3
Liquid Refrigerant Inventory	kg	1590.7	361	−77.3
Pressure Drop Hot Fluid	kPa	67.1	21.5	−67.9

The overall heat transfer coefficient for the FF evaporator is 2.6 times higher than that of the ST evaporator. As a result, the heat transfer area required is smaller for the FF heat exchanger, and the number of tubes in the evaporating region is more than halved as compared to the ST evaporator. The latter features four tube passes, whereas the FF evaporator three tube passes, one for superheating and two for evaporation. This difference in the pass configuration, in combination with shorter tubes, results in a three-time lower pressure drop in the hot fluid inside the tubes in the case of the FF evaporator as compared to the ST one.

492

Another significant difference between the two heat exchanger types is the required cold fluid inventory in operation. This quantity was estimated by evaluating the liquid level in the shell, given the number of submerged tubes, and the corresponding volume. Notice that there is no accumulation of working fluid in the FF evaporator during operation. This heat exchanger has a limited number of fully submerged tubes, whereas in the ST evaporator 60 % of the tubes are fully submerged. Therefore, the required liquid refrigerant mass in the FF heat exchanger during operation is ~77% lower than in the ST evaporator.

Figure 7a and Figure 7b shows the cross-sectional view of the ST and FF evaporators, respectively. In the case of the FF evaporator (see Figure 7b), a qualitative representation of the film liquid distributor over the tubes is also included. Due to the high degree of superheating targeted in the design, a large number of tubes are required in both evaporators to reach this vapour condition. In addition, a different tube arrangement is adopted in the main two zones of the FF evaporator: the tube bundle where the vapour is superheated features a staggered arrangement, while that where the fluid evaporates an inline configuration with a much lower number of tubes per unit volume. Thus, a more compact tube arrangement is achieved in the ST evaporator. It results that the shell diameter of the two heat exchangers is similar, in spite of the lower required heat transfer area in the case of the FF topology.

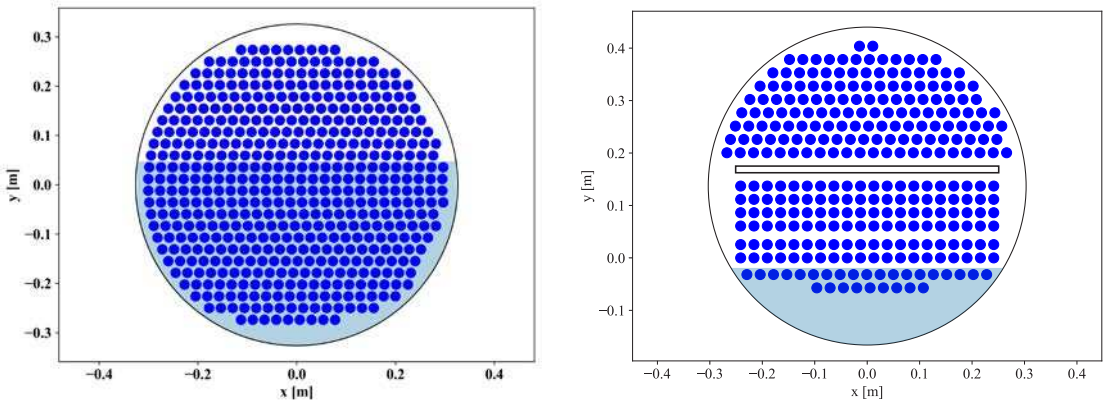

(a) Shell and Tube (b) Falling Film

Figure 7: Cross-sectional view of the tube bundle for the two evaporator types.

4.3 Falling Film Evaporator Off-design Performance

This section describes how the thermal performance of the FF evaporator, with the geometry specified in Table 2, varies as a function of the injected working fluid mass flow rate. In particular, Figure 8 shows the corresponding trend in the evaporator thermal duty and the non-evaporated fluid mass flow rate: the higher the injected mass flow rate, the greater the thermal duty and the amount of evaporated working fluid. The increase is, however, limited. The thermal duty augments by less than 1% with respect to the nominal conditions. At the same time, the difference between the injected mass flow rate and the evaporated one increases, leading to a rise in the liquid level in the shell over time. System operation becomes thus feasible only if the evaporator is equipped with a recirculation pump. It is worth also noting that these trends pertain to an optimal FF evaporator design obtained assuming no fluid recirculation. A better peformance may be achieved if the evaporator design is optimized for larger film flows than the targeted evaporating mass flow rate.

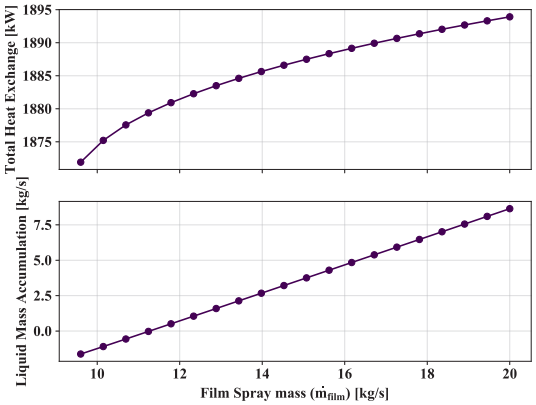

Figure 8: Falling film evaporator performance with film spray mass flow rate (top: thermal duty, bottom: liquid accumulation).

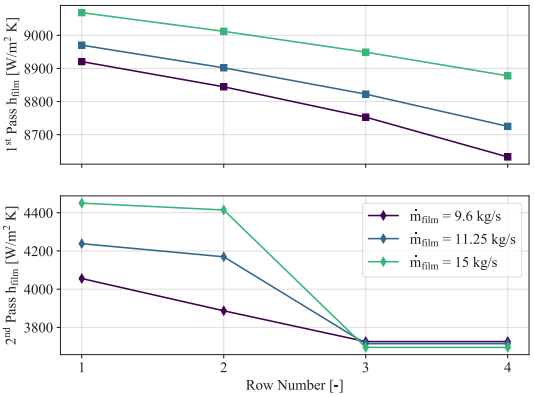

Figure 9: Row-wise heat transfer coefficient variation with film spray mass flow rate (top: first tube pass, bottom: second tube pass).

Figure 9 illustrates the variation of the film heat transfer coefficient along the tube rows of the two passes in the evaporation region as a function of the film mass flow rate. The heat transfer coefficient in the second pass is consistently lower than that in the first pass, regardless of the sprayed mass flow rate. This phenomenon can be attributed to the decrease in the total liquid mass from the top to the bottom of the evaporator. Additionally, the temperature of the hot fluid inside the tubes decreases as it moves downwards. Thus, a higher temperature difference is established at the top of the heat exchanger than at the bottom. Notice also that the last two rows of the second pass are fully submerged by the liquid.

If the local film mass flow rate on the tube surface is insufficient and the corresponding tube wall temperature is high enough, a local dryout may occur. This results in a smaller effective wetted area on the tube, leading to a lower effective heat transfer coefficient. This effect becomes more prominent at low film mass flow rates. One potential strategy to prevent these conditions is to implement a control loop over the working fluid feed pump, thereby ensuring a proper wetting of the tubes. However, this strategy, again, entails the use of a recirculation pump to maintain a constant liquid level in the shell (Höfler, 2019).

5. CONCLUSIONS

This study compares two evaporator concepts, namely the falling film and the shell and tube, for an industrial high-temperature heat pump application. A 1D model of the falling film evaporator was developed and verified by comparing its predictions against reference data reported in the literature for a test case similar to that investigated in this paper. The shell and tube evaporator is of the pool-boiling type, features a tube bundle with four passes on the hot side, and its design was performed using the commercial tool `ASPEN`. Based on the results of this study, the following conclusions can be drawn

1. The falling film evaporator features a 2.6 times higher overall heat transfer coefficient with respect to the shell and tube heat exchanger.
2. A fluid inventory reduction of around 77% is achieved by means of the falling film evaporator due to the lower number of submerged tubes. In addition, the falling film evaporator allows for about a 15% reduction in total component volume, as compared to the standard shell and tube evaporator.
3. For high degrees of superheating, the required number of tubes tends to be large, dictating the overall shell size for the case of the falling film evaporator. Therefore, it is expected that the smaller the degree of superheating, the more compact the falling film evaporator.
4. The heat transfer in the the falling film evaporator can be further enhanced increasing the injected liquid mass flow rate. This can be especially useful to prevent the occurrence of dryout in the tube rows at the bottom of the evaporator. This solution entails a higher system complexity, as a recirculation pump would be necessary to maintain a constant liquid level in the evaporator.

494

Future work will focus on comparying additional heat exchanger types, such as plate and shell-and-plate evaporators, to identify the most suitable heat exchanger topologies for high-temperature heat pumps.

ACKNOWLEDGEMENTS

This work was conducted within the PUSH2HEAT project, which received funding from the European Union's Horizon Europe research and innovation programme under grant agreement No.101069689.

REFERENCES

Arpagaus, C., Bless, F., Uhlmann, M., Schiffmann, J., and Bertsch, S. (2018). High Temperature Heat Pumps: Market Overview, State of the Art, Research Status, Refrigerants, and Application Potentials. *Energy*, 152:985–1010.

Aspentech (2022). Aspen v14. `https://www.aspentech.com/en`.

Bell, K. J. and Muller, A. C. (2001). *Wolverine Engineering Data Book II*. Wolverine Tube Inc.

Blank, J. and Deb, K. (2020). pymoo: Multi-objective Optimization in Python. *IEEE Access*, 8:89497–89509.

Cooper, M. G. (1984). Heat Flow Rates in Saturated Nucleate Pool Boiling - A Wide-Ranging Examination Using Reduced Properties. *Advances in Heat Transfer*, 16:157–239.

Fernández-Seara, J. and Pardiñas, A. A. (2014). Refrigerant Falling Film Evaporation Review: Description, Fluid Dynamics and Heat Transfer. *Applied Thermal Engineering*, 64(1):155–171.

Hu, X. and Jacobi, A. M. (1996). The Intertube Falling Film, Part 1: Flow Characteristics, Mode Transitions and Hysteresis. *Journal of Heat Transfer*, 118:616–625.

Höfler, M. (2019). *Theoretical Evaluation of Falling Film Evaporation for Organic Rankine Cycle Process*. PhD thesis, Institude of Heat and Mass Transfer RWTH Aachen, Aachen.

Jiang, J., Hu, B., Wang, R., Deng, N., Cao, F., and Wang, C.-C. (2022). A Review and Perspective on Industry High-Temperature Heat Pumps. *Renewable and Sustainable Energy Reviews*, 161:112106.

Jin, P. H., Zhang, Z., Mostafa, I., Zhao, C. Y., Ji, W. T., and Tao, W. Q. (2019). Heat Transfer Correlations of Refrigerant Falling Film Evaporation on a Single Horizontal Smooth Tube. *International Journal of Heat and Mass Transfer*, 133:96–106.

Kosmadakis, G. (2019). Estimating the Potential of Industrial (High-Temperature) Heat Pumps for Exploiting Waste Heat in EU Industries. *Applied Thermal Engineering*, 156:287–298.

Lemmon, E. W., Bell, I. H., Huber, M. L., and McLinden, M. O. (2018). NIST Standard Reference Database 23: Reference Fluid Thermodynamic and Transport Properties-REFPROP, Version 10.0, National Institute of Standards and Technology.

Lorenz, J. J. and Yung, D. (1979). A Note on Combined Boiling and Evaporation of Liquid Films on Horizontal Tubes. *Journal of Heat Transfer*, 101:178–180.

Mitrovic, J. (1986). Influence of Tube Spacing and Flow Rate on Heat Transfer from a Horizontal Tube to a Falling Liquid Film. *Proceedings of the Eighth International Heat Transfer Conference*, 4:1949–1956.

Mostinski, I. L. (1963). Application of the Rule of Corresponding States for Calculation of Heat Transfer and Critical Heat Flux. *Teploenergetika*, 4:66–71.

Reay, D. A. (2002). Compact Heat Exchangers, Enhancement and Heat Pumps. *International Journal of Refrigeration*, 25(4):460–470.

Robert, d. B., Marina, A., Zühlsdorf, B., Arpagaus, C., Bantle, M., Wilk, V., Elmegaard, B., Corberán, J., and Benson, J. (2020). Strengthening industrial heat pump innovation: Decarbonizing industrial heat.

Rohsenow, W. M. (1952). A Method of Correlating Heat-Transfer Data for Surface Boiling of Liquids. *Trans. ASME*, 74:969–975.

Roques, J. F. and Thome, J. R. (2007a). Falling Films on Arrays of Horizontal Tubes with R-134a, Part I: Boiling Heat Transfer Results for Four Types of Tubes. *Heat Transfer Engineering*, 28(5):398–414.

Roques, J. F. and Thome, J. R. (2007b). Falling Films on Arrays of Horizontal Tubes with R-134a, Part II: Flow Visualization, Onset of Dryout, and Heat Transfer Predictions. *Heat Transfer Engineering*, 28:415–434.

Shah, M. M. (2021). A General Correlation for Heat Transfer during Evaporation of Falling Films on Single Horizontal Plain Tubes. *International Journal of Refrigeration*, 130:424–433.

Thome, J. R. (2016). *The Heat Transfer Data Book III: Enhanced Heat Transfer Design Methods for Tubular Heat Exchangers*. Publico Publications.

Verein deutscher Ingenieure (2010). *VDI Heat Atlas*. Springer.

Yang, L. and Wang, W. (2011). The Heat Transfer Performance of Horizontal Tube Bundles in Large Falling Film Evaporators. *International Journal of Refrigeration*, 34:303–316.

Zhao, C.-Y., Qi, D., Ji, W.-T., Jin, P.-H., and Tao, W.-Q. (2022). A Comprehensive Review on Computational Studies of Falling Film Hydrodynamics and Heat Transfer on the Horizontal Tube and Tube Bundle. *Applied Thermal Engineering*, 202:117869.

Zohuri, B. (2022). *Compact Heat Exchangers*. Springer.

A. APPENDIX

Table A1: Bounds considered for the design variables of the falling film evaporator

Design Variable	Bounds
Number of tube rows (1st pass)	[2, 25]
Number of tube rows (2nd pass)	[2, 25]
Number of tubes per row	[2, 20]
Length of tube	[0.5, 6.0]

Table A2: Geometric characteristics of the tubes.

Parameter	Unit	Plain Tube	Finned Tube
d_{outer}	mm	19.05	19.05
d_{inner}	mm	17.78	12.58
d_{root}	mm	-	15.88
Fin height	mm	-	1.588
Fin thickness	mm	-	0.4
Fin pitch	mm	-	0.9775

ORC SEVILLE 2023
7th International Seminar on O.R.C. Power Systems

© 2024 Editorial Universidad de Sevilla. Este es un artículo de acceso abierto distribuido bajo los términos de la licencia de uso y distribución Creative Commons (BY-NC-ND 4.0)

DOI: https://dx.doi.org/10.12795/9788447227457_83

On the plant improvement of Solar-driven ORC-based power unit for domestic micro-cogeneration

Fabio Fatigati*, Marco Di Bartolomeo, Arianna Coletta, Diego Vittorini, Davide Di Battista, Giammarco Di Giovine, Roberto Cipollone

University of L'Aquila, Department of Industrial and Information engineering and economics, P.zzle Ernesto Pontieri, L'Aquila, 67100, Italy

*Corresponding Author: fabio.fatigati@univaq.it

ABSTRACT

The integration of flat solar thermal collectors and ORC-based power units ensures the simultaneous production of heat and electric power in domestic applications (CHP). Thus, such micro-cogenerative solutions ensure to reduce the use of fossil fuels and CO_2 in a sector that accounted for about 30% of global energy-related CO_2 emissions in 2021, considering both residential and commercial buildings. The significant variability of solar power during the day and domestic hot water (DHW) demand pushes the unit to work in off-design and transient conditions frequently. Therefore, to maximize the energy recovery of the unit, the design phase and the components selection assume a crucial role. The critical component is the expander and, generally, volumetric machines are adopted for their operating flexibility and robustness when working with highly variable hot sources. Among the volumetric expanders adopted for this kind of application, scroll machines present higher performance and reliability than other positive displacement technologies. Nevertheless, similarly to the other volumetric expanders, such devices still have room for improvement. Indeed, in many applications, they are obtained by reversing scroll compressors. Hence, to participate in the improvement of these machines, a comprehensive model was developed following an integrated zero and mono-dimensional (0-1D) thermo-fluid-dynamic approach. The model was validated through experimental data measures during a comprehensive testing campaign performed on a fully instrumented solar-driven ORC-based power unit which employs a 1 kW scroll expander as mechanical power at design. Once the scroll expander model was validated, it was theoretically optimized in terms of working fluid flow rate aspiration (volumetric efficiency), indicated performances and mechanical power produced. Subsequently, the benefits of the optimized machine to the recovery unit performances have been estimated.

1 INTRODUCTION

Among the various sources of renewable energy existing – wind, tidal, and geothermal energy (Ardeh *et al.*, 2019) – solar energy is one of the most promising because it is available in large quantities and can be converted easily into electric or thermal energy (H. Chen *et al.*, 2022). On the other hand, solar energy fluctuates and becomes intermittent and very diffuse, so a proper thermal storage system is required (Altayib and Dincer, 2022), and solar-driven systems have higher costs and lower efficiency compared to conventional plants (Algieri *et al.*, 2022). Solar radiation can be converted directly into electricity using photovoltaic technology or thermal energy through solar thermal collectors (Y. Chen et al., 2022). In the second case, the heat obtained from solar radiation is transformed into electric power in downstream recovery units based on an Organic Rankine Cycle - ORC- (Gupta *et al.*, 2022), a conversion cycle suitable from medium-low grade temperature heat sources (Alvi *et al.*, 2020). Solar-ORC-based plants employed as cogeneration units are a promising solution for reducing GHG emissions in the residential sector since they can meet both the needs for electricity and domestic hot water (Jaubert *et al.*, 2021; Bagherian and Mehranzamir, 2020); Martinez *et al.*, 2021). Solar ORC units allow for reducing losses associated with energy transport and distribution (Pereira *et al.*, 2018), but their economic convenience depends on the scenario in which they operate (Arteconi *et al.*, 2019). The most common layout modification consists of changing the

basic cycle architecture by inserting a recovery heat exchanger after the pressurization of the working fluid fed by when it leaves the expander to increase the cycle efficiency. Ochoa *et al.* (2022) compared the performance of two different configurations (base and regenerative) from energy, exergy, and thermo- economic perspective, considering the average solar radiation data of six areas and concluding that the regenerative configuration is not convenient under the examined operating conditions. A thermal recovery before the main one prevents part of the primary recovery inside the Heat Recovery Steam Generator (HRSG), reducing the hot source exploitation. Javed and Tiwari (2023) carried out a comparative analysis of the energy and economic performances of three layouts (base, recuperative and regenerative) for four different working fluids. The best performances are obtained through the recuperative configuration with a power increase of +36.6% compared to the basic layout; A similar result is also assessed by Nondy *et al. (*2021), who found that the layout with the best performance is the recuperative-regenerative one, which shows net power and exergy efficiency 16.19% and 15.33% higher than the basic configuration. Concerning the components, the expander behavior affects the plant's performance and cost-effectiveness (Imran *et al.*, 2016). Scroll expander is one of the most adopted machines thanks to its reliability and high efficiency. Zhang *et al.* (2023) conducted experiments on an ORC-based recovery unit using three scroll expanders (two hermetic and one open-drive) with different built-in volume ratios. Ziviani *et al. (*2018) integrated an open-drive and oil-free scroll expander into an ORC-based plant. The low maturity level of the scroll expander technology requires design and technological improvements supported by theoretical and experimental studies. In fact, basic studies can be supported by models, but real performances necessarily require experimental data (Fatigati *et al.*, 2022a, Kolasinski *et al.*, 2017). This paper proposes a thermo-fluid-dynamic model of a scroll expander developed with a mono and zero-dimensional approach subsequently validated with experimental data on a test bench in which an ORC-based solar-driven recovery unit is operated. The model of the expander was modified to consider the effects of geometrical modifications to improve volumetric, indicated and mechanical efficiencies. The effects on the performances of the whole ORC-based solar-driven recovery unit have been investigated.

497

2 MATERIALS AND METHODS

The test bench developed in Fatigati *et al. (*2022a) was adopted to provide the experimental characterization of the ORC-based power unit. The ORC-based power unit (Figure 1) was built to be integrated with 15 m^2 of flat plate solar thermal collectors mounted on a rooftop located in central Italy. The rated power of the unit is 500 W. The solar power is simulated through the modulation of two electric resistances of 12 kW each (a), heating the hot water (HW) stored in a 135 L tank pressurized with air to avoid its evaporation (b). In this way, modulating the heat delivered by the electrical resistances, the effect of the solar source was simulated. Hot water is circulated by a dedicated electric motor-driven pump (c), and its mass flow rate is regulated through a valve (d) to reproduce the variations in the thermal load on the evaporator caused by the fluctuating availability of solar radiation. In the plate heat exchanger Heat Recovery Vapor Generator (HRVG) (e), the hot water heats the working fluid (WF) (R245fa), which enters a scroll expander (Figure 2) (f) as a superheated vapor. The lubrication was provided with an ISOVG 68 POE oil mixed with the working fluid (R245fa). The amount of oil was set at 5 % of the total charge (3kg). The mechanical power produced by the expander is converted into electrical power through a generator and dissipated on a rheostat-adjustable electric load (g). Hence, the rotation speed of the scroll expander is not externally imposed, but it is defined by the dynamic equilibrium of the positive torque produced by the expander and of the negative torque produced by the electric generator, which feeds a variable electric load. In other words, being the electrical generator not connected to the grid, the speed of rotation cannot be actively controlled. It was observed as it grows linearly with the mass flow rate, thus helping keep the expander pressure ratio close to the design value. The plant adopts a recuperative configuration, according to previous literature results showing the potential benefits of this configuration (Nondy *et al.,* 2021). The working fluid enters the internal heat exchanger after evolving in the expander (h) and before entering the condenser (i). This way, the working fluid exiting the pump is pre-heated before entering the HRVG, increasing the unit efficiency and reducing the thermal load in the condenser. In the condenser, fed by tap water on the cold side, the working fluid is brought back into a subcooled liquid state and then gathered by a 3 L tank (l) working as a fluctuation damper. It also behaves as a working fluid reservoir when a sudden flow rate increase is requested by the pump, avoiding a

potential lack of fluid at the pump intake. The working fluid is finally recirculated by a diaphragm pump with a 6.3 cm3 volume displacement (m), driven by an asynchronous electric motor with an inverter that allows the flow rate to be adjusted according to the operating requirements of the system. The instrumentation includes temperature and pressure sensors upstream and downstream of each component (n), a Coriolis (o) and two magnetic flowmeters (p) for reading respectively the flow rates of working fluid and water at the evaporator and condenser, a wattmeter for measuring the expander and pump power (q), and an optical probe inside the scroll casing that provides the measurement of the rotational speed and transmits the signal to an oscilloscope. The experimental data allows the validation of a dedicated expander model. Subsequently, an operating map was provided by the expander model and introduced inside a comprehensive model of the whole ORC-based power unit. The scroll theoretical model was obtained by updating the one developed by the authors in Fatigati *et al.* (2022b) for the application at hand. The considered scroll is reported in Figure 2, where the fixed (a) and orbiting (b) scroll can be observed. The fixed and orbiting scrolls define six chambers (Figure 3). During the intake phase, the machine chambers are in 1a and 1b positions and they are axially filled. The intake phase ends after a complete rotation of the shaft. After the intake phase, the chambers branch off and are in positions 2a and 2b. As the expansion continues, the chambers proceed toward positions 3a and 3b in correspondence to which the discharge phase occurs. Therefore, such behavior suggests a symmetric structure for the model, where the chambers are symmetrically represented, reproducing the chamber expansion from position 1 to 3.

Figure 1: Solar ORC-based power unit

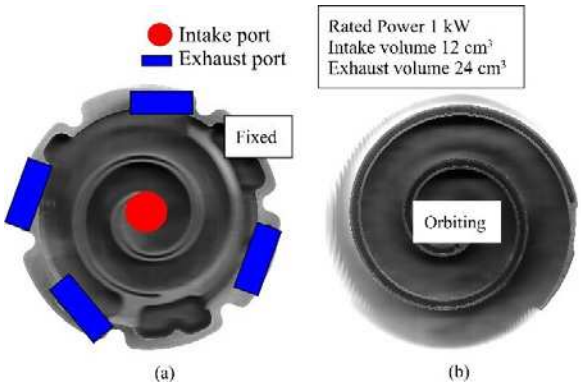

Figure 2: Scroll geometrical model

The model of the scroll was developed in the GT-Suite™ environment following an integrated mono (1D) and zero (0D) thermo-fluid-dynamic approach. The 1D approach was adopted to represent the dynamic phenomena taking place in the connecting pipes during the intake and discharge phases. The intake and discharge pipes were discretized and the Navier-Stokes Equations were solved through an explicit integration method for each subsystem. Concerning the 0-D analysis, it was used to represent the volumetric losses modeled through the Poiseuille-Couette equations and mainly caused by flank and radial leakages represented in Figure 3 as RL and FL components. Leakages not only affect the volumetric efficiency but play a significant effect also from an energetic point of view. Indeed, they influence the trend of the pressure inside the chamber as a function of its volume over time, i.e., the indicated power. The net power delivered by the expander can be determined by subtracting the mechanical losses due to friction from the indicated power. Concerning the model of the mechanical losses, it was considered according to a map of the mechanical efficiency following the approach of Fatigati et al. (2022b). Once validated, the expander model was used as a software platform to optimize its performance. Subsequently, an operating map can be provided for a wide operating range and introduced in the comprehensive model of the ORC-based power unit developed following the approach of Marchionni et al. (2022). Compared to the cited model, the main novelty is the introduction of a recuperative stage. Moreover, the present recovery unit presents a lower size than the one just cited, which was designed to recover thermal energy from the exhaust gases of an Internal Combustion Engine. The model of the ORC-based power plant developed here is reported in Figure 4. The pump (a) was modeled through a look-up table preliminary derived for simplicity. The recuperator (b), the Heat Recovery Vapor Generator (HRVG) (c), and the condenser (e) can be modeled through physical models which consider the geometry of the heat exchangers and the different heat transfer coefficients during different heat exchanges. The correlations of Dittus and Boelter (1985) are used for the single-phase and supercritical case as it is recommended for turbulent flow in smooth pipes for heating or

cooling application. For the two-phase case, the correlation developed by Yan et al. (1999) was used for the condensation, whereas the evaporation was represented through the correlation developed by Kandlikar (1990). These correlations are recommended for the plate heat exchanger to represent the two-phase condensation and evaporation, respectively. Through element (f), the 3 L plenum upstream of the pump can be modeled, while element (n) allows considering the working fluid mass charge and the initial conditions. The flow rate of the hot water of the reservoir (set by the pump speed (g)) and its temperature were input data (h) at the HRVG from one side. Knowing the working fluid flow rate and its inlet temperature at the other side of the HRVG, the conditions of the two fluids at their respective outlets can be calculated, as well as the thermal power absorbed by the ORC-based recovery unit. At the condenser side, the temperature of the tap water sets the condensation pressure of the working fluid. Flow rate and tap temperature (m) entering the condenser fix the conditions at one side of the condenser, while the flow rate of the working fluid and its temperature (from the expander outlet) fix the conditions at the other side. It is worth noting that for the considered plant architecture, the expander speed is not externally imposed but depends on the equilibrium realized on the shaft. A linear dependence of the speed (ranging from 4073 RPM up to 5458 RPM) with the working fluid mass flow rate and, consequently, the pump speed was observed and implemented inside the model. Although the model was used for steady-state analysis in this work, it can also be used to evaluate the transient behavior of the unit.

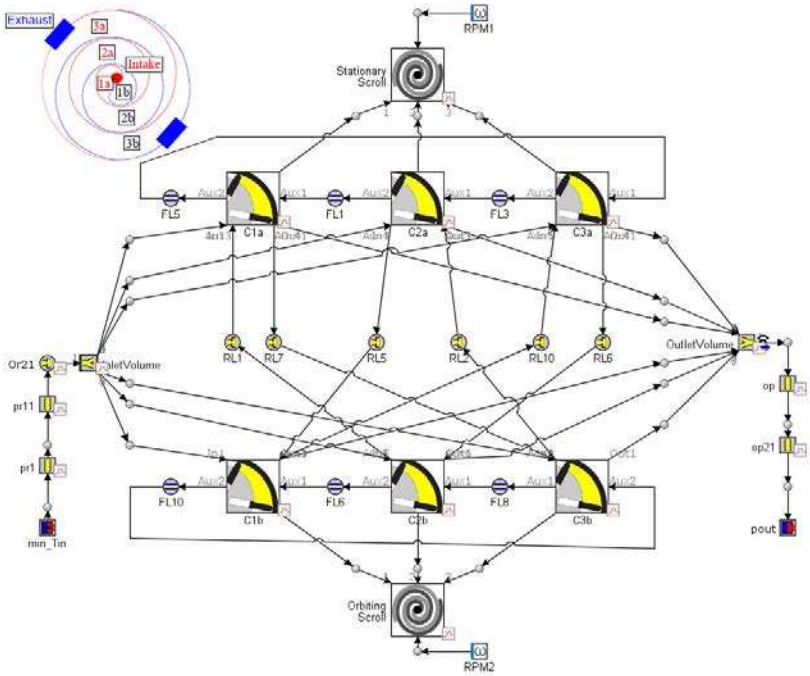

Figure 3: GT-Suite scroll numerical model

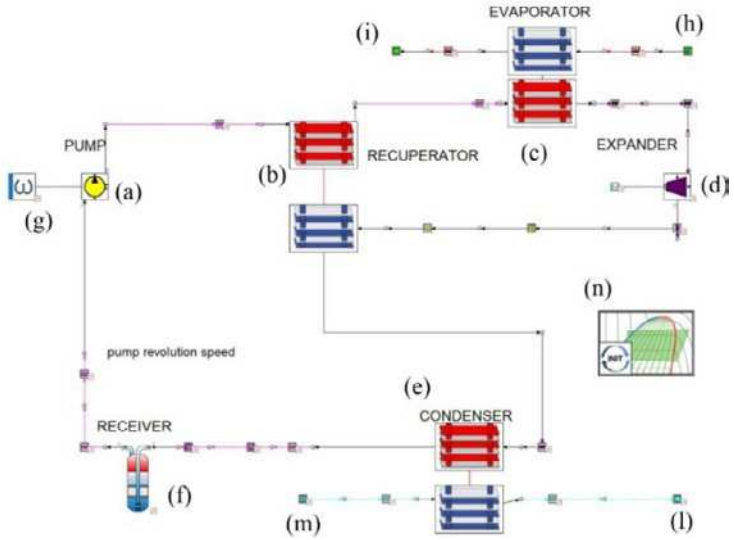

Figure 4: ORC-based power unit model

Thanks to the broad experimental data set, expander and ORC unit models were validated to demonstrate their accuracy. A satisfactory agreement was obtained by comparing the theoretical results of the expander model with the experimental data reported in Table 1. In particular, the Root Mean Square Errors (RMSE) in terms of expander intake pressure, power and efficiency are equal to 4%, 2 % and 4% respectively. The model also presents a good prediction regarding the discharge temperature of the working fluid with an average absolute error of -2 K. Therefore, the model reproduces the real expander behavior. Once validated, an operating map was developed and introduced inside the ORC-based recovery unit software platform. The accurate model of the expander contributes to a good prediction of the performances of the whole recovery unit. Indeed, in Table 2, the differences between theoretical and experimental data are reported. Concerning the working fluid mass flow rate, the maximum error was equal to -1.8%, whereas for maximum and minimum pressures, maximum errors were equal to -2.7% and 10.5%, respectively. It is worth noticing that maximum pressure and temperature were measured at the evaporator outlet, whereas minimum pressure and temperature were at the pump inlet. Regarding the greatest and lowest temperatures, the maximum errors were equal to -5 K and 9.6 K, respectively. The maximum errors on the hot side inlet and outlet temperatures at the regenerator are equal to 5.7 K and 4.5 K. On the other hand, the cold side outlet temperature differs by 6.1 K from the experimental value. Maximum deviations between modeling and experimental results of power and efficiency of the recovery unit are -14.7 % and 10.7%, respectively. Hence, the model accuracy can be considered satisfactory given the wide operating range analyzed. Indeed, the 6 points chosen represent a significant variation in the mass flow rate of the working fluid (from 17 g/s up to 50 g/s) compared to the design value (40 g/s). Indeed, in Marchionni et al. (2022), the proposed model approach accurately reproduces an ORC-based unit with more extended operating conditions.

Table 1: Experimental quantities

Experimental quantities	**Units**	**1**	**2**	**3**	**4**	**5**	**6**
mass flow rate	g/s	50.7	45.9	41.4	49.3	17.8	23.0
Maximum pressure	bar	10.4	9.7	9.0	10.1	5.0	5.9
Maximum temperature	K	381	377	379	377	365	364
Minimum pressure	bar	1.5	1.5	1.4	1.5	1.2	1.3
Minimum temperature	K	293	293	291	296	288	287
Expander speed	RPM	5458	5256	5066	5399	4073	4292
Expander power	W	583	565	546	563	271	347
Expander efficiency	%	39	42	45	40	58	55
Power	W	360	386	404	354	256	314

Table 2: Errors between experimental and theoretical data

errors	**1**	**2**	**3**	**4**	**5**	**6**
mass flow rate [%]	-1.0	-0.9	-1.3	-0.4	-1.6	-1.8
ORC maximum pressure [%]	-1.9	-0.1	-0.2	-2.7	-2.1	-1.8
ORC maximum temperature [K]	-1.6	2.5	1.6	-5.0	0.8	0.7
ORC minimum pressure [%]	1.5	-1.2	0.6	-4.9	9.3	10.5
ORC minimum temperature [K]	5.3	4.5	6.6	2.1	8.2	9.6
Expander electrical power [%]	-0.6	-1.3	-1.1	-0.4	-10.8	-7.6
Expander efficiency [%]	1.1	1.4	1.0	0.6	11.9	2.8
ORC unit electrical power [%]	-5.4	-3.8	-10.0	-11.7	-12.7	-14.7
ORC efficiency [%]	4.4	2.5	9.2	11.4	9.0	10.7

3 RESULTS

Once verified the effectiveness of the model for both the expander and the whole recovery unit, it has been used as a software platform to assess the impact of some expander technological improvements on the recovery unit performances. Hence, the first step was to analyze the improvement on the expander produced by different clearance flank gap values ranging from 10 to 30 μm, being 20 μm the value considered as a reference. The performance of the ORC unit in a wide range of operating

conditions was assessed through the model. The variation of ORC unit power and performance as a function of the working fluid mass flow rate and the hot water temperature inside the tank is reported. The hot water inside the tank represents the hot source of the recovery unit; it feeds the Heat Recovery Vapor Generator favoring the vaporization and the superheating of the working fluid. The analysis refers to a fixed hot water flow rate of 8 L/min. As Figure 5 reports, the reduction of the clearance gaps provides an improvement in the machine performance according to the expectations. Indeed, it can be seen how the power produced by the expander grows as the clearance gap decreases. Considering, for instance, the case in which the mass flow rate is equal to 70 g/s, the power grows from 853 W up to 985 W reducing the clearance from 30 μm to 10 μm. This reduction can be achieved from a technological point of view and the effect on power produced is significant (+15% power increase). Such improvement is due to the increase in volumetric efficiency, which is the ratio between the theoretical working fluid mass flow rate entering the chambers and the measured one.

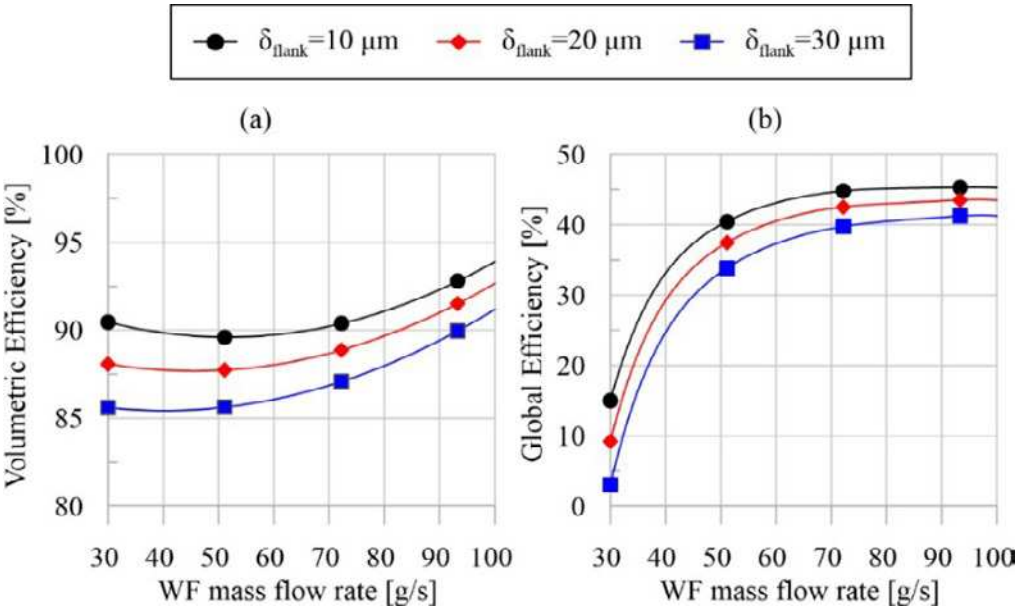

Figure 5: Expander volumetric (a) and global efficiency (a) as a function of WF mass flow rate for different values of clearance flank gap.

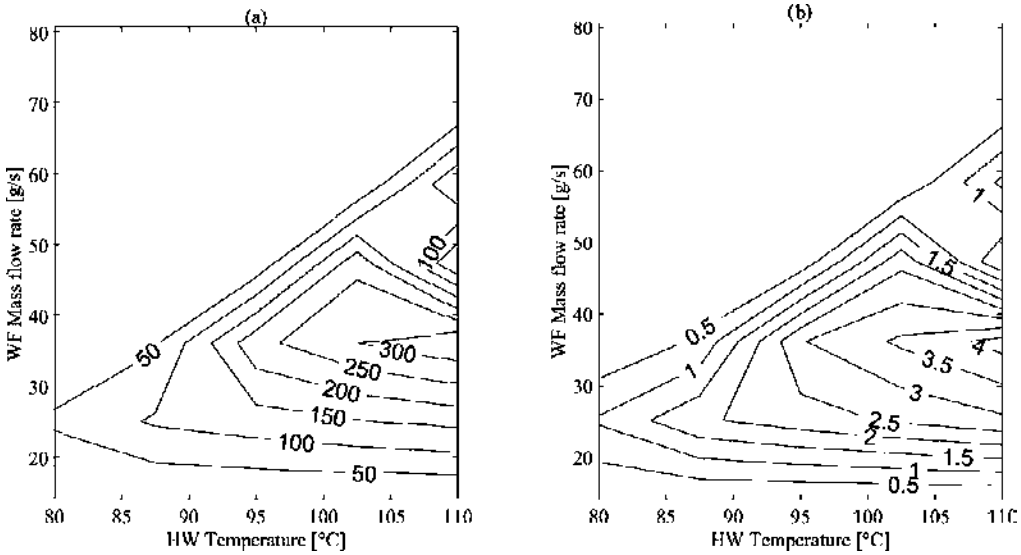

Figure 6: Iso-power [W] (a) and efficiency [%] (b) as a function of WF mass flow rate and hot water temperature for a HW flow rate of 8 L/min.

The clearance reduction reduces leakages and the immediate effect is an intake pressure increase, which produces a benefit in terms of power and expander global efficiency -Figure 5(b)- defined as

the ratio between the measured electric expander power and the one referred to an adiabatic isentropic transformation.Therefore, a minimum clearance gap equal to 10 μm was fixed and the new performances of the whole recovery unit were calculated for a working fluid (WF) mass flow rate and hot water (HW) temperature ranging from 20 g/s up to 80 g/s and from 110 °C (383 K) up to 80 °C (353 K), respectively. A reference value of 8 L/min was chosen for the hot water flow rate. In Figure 6, the power of the recovery unit (a) and efficiency (b) are reported. The efficiency was evaluated as the ratio of the net power produced by the unit and the thermal power provided by the hot water. It can be seen that if the hot water temperature decreases (reservoir whose temperature inside is decreasing), the range of working fluid mass flow rate that produces a useful power decreases, thus limiting the recovery into mechanical energy when the reservoir is discharging. At 110 °C (383 K), the WF mass flow rates range between 14 g/s and 75 g/s, whereas when the temperature decreases to 80 °C (353 K), this range is sensibly reduced (14 g/s - 27 g/s). The maximum power stands at 300 W for a mass flow rate between 30 g/s and 40 g/s and a hot water temperature of 110 °C (383 K). These results agree with the theoretical expectations since the maximum power is expected to be reached when the hot source assumes the maximum temperature. The efficiency of the ORC unit is reported in Figure 6(b), assuming similar isolines distribution when the clearance is reduced. The maximum efficiency stands at 4 %, in good agreement with the literature results of those applications involving the introduction of a recuperative heat exchanger (Ancona *et al*.(2022), Eyerer *et al*. (2020)). Analogies also exist for the expander behavior as an efficiency ranging from 30% up to 60% is observed in Eyerer *et al.* (2020) and Unamba *et al.* (2019)). The results shown in the iso-lines are also interesting in terms of operating range definition and performance of the unit in off-design conditions. As a matter of fact, an “activation line” can be seen observing Figure 6. This line delimits a region of WF mass flow fate and HW temperature, ensuring the plant activation; the “activation line” could be inserted into a model-based strategy of the unit and orient its management according to the temperature inside the reservoir. The data refer to a specific hot water flow rate equal to 8 L/min; a broader analysis for different flow rates gives a working condition map which could be the base of a model-based control. The maps reported in Figure 6 also demonstrate how wide is the region of the off-design performance of the unit. In particular, for a fixed hot water temperature of 110 °C (383 K), in correspondence to a reduction of the WF mass flow rate, the power and efficiency decrease, but the isolines are farther than in the case in which the WF mass flow rate is increased. This means that the power and efficiency reduction presents a lower slope when the WF mass flow rate is decreased from the design point compared to the case according to which WF mass flow rate increases.

CONCLUSIONS

In the present paper, the influence of the expander clearance gap reduction on the performance of a micro-cogenerative solar-driven ORC-based power unit was experimentally and theoretically analyzed. The results show that by reducing the clearance gap from 30 μm up to 10 μm, the power and efficiency of the expander grow. The improvement of the volumetric efficiency significantly reduces the leakages and realizes a better filling of the chambers, producing more expansion work. This effect can be achieved not only by reducing the geometrical tolerances but also improving the lubrication of the machine. Thus, to assess the effects of such improvement on the whole behavior of the recovery unit, the operating map of the expander with the lower clearance was obtained and introduced into the whole model of the recovery unit. Results show that the reduction of clearance gaps produces an enhancement of 10.5% and 12% of the ORC unit power and efficiency, respectively. Consequently, the electrical energy produced daily by the unit increases by 11%. Moreover, the map of the expander integrated inside the model of the unit identifies an “activation line”, which can be transformed into a model-based-control strategy. Indeed, for a given temperature of the water inside the reservoir which represents the hot source of the unit, the WF mass flow rate range that ensures the activation of the ORC plant is reported as a function of the hot water temperature.

REFERENCES

Algieri A., Morrone P., 2022, Thermo-economic investigation of solar-biomass hybrid cogeneration systems based on small-scale transcritical organic Rankine cycles, Appl. Therm. Eng., vol. 210.

Altayib K., Dincer I., 2022, Development of a geothermal-flash organic Rankine cycle-based combined

system with solar heat upgrade, Energy Convers. Manage., vol. 252.
Alvi J., Feng Y., Wang Q., Imran M., Alvi J., 2020, Modelling, simulation and comparison of phase change material storage based direct and indirect solar organic Rankine cycle systems, Appl. Therm. Eng., vol. 170.
Ancona, M., A., Bianchi, M., Branchini, L., De Pascale, A., Melino, F., Peretto, A., Poletto, C., Torricelli, N., 2022, Solar driven micro-ORC system assessment for residential application, Renewable Energy, Volume 195, , Pages 167-181, ISSN 0960-1481,
Ardeh, E., Loni, R., Najafi, G., Ghobadian, B., Bellos, E., Wen D., 2019, Exergy and economic assessments of solar organic Rankine cycle system with linear V-Shape cavity, Energy Convers. Manage., vol. 199.
Bagherian M., Mehranzamir K., 2020, A comprehensive review on renewable energy integration for combined heat and power production, Energy Convers. Manage., vol. 224.
Chen, H., Zhao L., Cong H., Li X., 2022, Synthesis of waste heat recovery using solar organic Rankine cycle in the separation of benzene/toluene/p-xylene process, Energy, vol. 255.
Chen Y., Feng L., Mansir I., Taghavi M., Sharma K., 2022, Generation and storing of electrical energy, Sustain. Cities Soc., vol. 81.
Dittus, F.W.; Boelter, L.M. 1985, Heat transfer in automobile radiators of the tubular type. Int. ommun. Heat Mass Transf., 12, 3–22.
Eyerer, S., Dawo, F., Wieland, C., Spliethoff, H., 2020, Advanced ORC architecture for geothermal combined heat and power generation, Energy, 205, 117967, ISSN 0360-5442
Fatigati F., Vittorini D., Di Bartolomeo M., Cipollone R., 2022, Experimental characterization of a small-scale solar Organic Rankine Cycle (ORC) based unit for domestic microcogeneration, Energy Convers. Manage., vol. 258.
Fatigati, F., Di Giovine, G., Cipollone, R., 2022, Feasibility Assessment of a Dual Intake-Port Scroll Expander Operating in an ORC-Based Power Unit, Energies, vol. 15.
Gupta P., Tiwari A., Zafar S., 2022, Solar organic Rankine cycle and its poly-generation applications – A review, Sustain. Energy Technol. Assess., vol. 49.
Imran M., Usman M., Park B., Lee D., 2016, Volumetric expanders for low grade heat and waste heat recovery applications, Renew. Sustain. Energy Rev., vol. 57, p. 1090-1109.
Jaubert H., Borel P., Guichardon P., Portha J., Jaubert J., Coniglio L., 2021, Assessment of organic Rankine cycle configurations for solar polygeneration orientated to electricity production and desalination, Appl. Therm. Eng., vol. 195.
Javed S., Tiwari A., 2023, Performance assessment of different Organic Rankine Cycle (ORC) configurations driven by solar energy, Process Saf. Environ. Prot., vol. 171.
Kandlikar, S.G., 1990 A General Correlation for Saturated Two-Phase Flow Boiling Heat Transfer Inside Horizontal and Vertical Tubes. J. Heat Transf., 112, 219–228.
Kolasinski P., Blasiak P., Rak J., 2017, Experimental investigation on multi-vane expander operating conditions in domestic CHP ORC system, *IV International Seminar on ORC Power Systems*.
Marchionni, M., Fatigati, F., Di Bartolomeo, M., Di Battista, D., Petrollese, M., 2022, Experimental and Numerical Dynamic Investigation of an ORC System for Waste Heat Recovery Applications in Transportation Sector, Energies, vol. 15.
Martinez S., Michaux G., Bouvier J., Salagnac P., 2021, Numerical investigation of the energy performance of a solar micro-CHP unit, Energy Convers. Manage., vol. 243.
Nondy J., Gogoi T.K., 2021, Exergoeconomic investigation and multi-objective optimization of different ORC configurations for waste heat recovery: A comparative study, Energy Convers. Manage., vol. 245.
Ochoa G., Chamorro M., Silvera O., 2022, Thermo-economic and sustainability assessment of two solar organic Rankine cycles in the United States, Sustain. Energy Technol. Assess., vol. 50.
Unamba, C.K.; Sapin, P.; Li, X.; Song, J.; Wang, K.; Shu, G.; Tian, H.; Markides, C.N., 2019, Operational Optimisation of a Non-Recuperative 1-kWe Organic Rankine Cycle Engine Prototype. *Appl. Sci.* , *9*, 3024.
Yan, Y.Y., Lio, H., Lin, T, 1999 Condensation heat transfer and pressure drop of refrigerant R-134a in a plate heat exchanger, International Journal of Heat and Mass Transfer, 42, 6, 993-1006, ISSN 0017-9310.
Zhang H., Zhang Y., Feng Y., Chang J., Chang C., Xi H., Gong L., Hung T., Li M., 2023, The parametric analysis on the system behaviors with scroll expanders employed in the ORC system: An experimental comparison, Energy, vol. 268.

Ziviani D., James N., Accorsi F., Braun J., Groll E., 2018, Experimental and numerical analyses of a 5 kWe oil-free open-drive scroll expander for small-scale organic Rankine cycle (ORC) applications, Appl. Energy, vol. 230, p. 1140-1156.

ACKNOWLEDGEMENT

The authors are grateful to SIVAM S.p.A for the support given in this activity. New subroutines employed in the Scroll model were developed in the framework of the PRIN H2-ICE (Project of Relevant National Interest), funded by the Italian Minister of University and Research.

ORC SEVILLE 2023
7th International Seminar on O.R.C. Power Systems

© 2024 Editorial Universidad de Sevilla. Este es un artículo de acceso abierto distribuido bajo los términos de la licencia de uso y distribución Creative Commons (BY-NC-ND 4.0)

DOI: https://dx.doi.org/10.12795/9788447227457_84

MAPPING THE TECHNO-ECONOMIC POTENTIAL OF NEXT-GENERATION CSP PLANTS RUNNING ON TRANSCRITICAL CO_2-BASED POWER CYCLES

Pablo Rodríguez-deArriba[1,*], Francesco Crespi[1], Sara Pace[2], David Sánchez[1]

[1] *University of Seville, Department of Energy Engineering, Camino de los descubrimientos s/n, 41092, Seville, Spain*
[2] *Politecnico di Milano, Department of Energy, Via Lambruschini 4, 20156, Milan, Italy*

[*]Corresponding Author: prdearriba@us.es

ABSTRACT

Although the thermodynamic potential of transcritical/supercritical CO_2-based power cycles for next generation Concentrated Solar Power plants has been already confirmed in literature, further investigation to assess the actual feasibility of this technology from a techno-economic standpoint is needed. In fact, large uncertainty is found when it comes to the estimation of the CAPEX and OPEX of the power block, and the same can be said for the solar subsystem when high Turbine Inlet Temperatures are considered (>700 ºC).

Bearing this in mind, this paper presents a methodology to map the techno-economic potential of next-generation Concentrated Solar Power plants running on CO_2-based mixtures, with the final aim to identify the threshold (breakeven) costs of the main subsystems enabling a clear gain in terms of Levelised Cost of Electricity with respect to state-of-the-art steam-based CSP.

Two different systems are studied which differ in the composition and peak temperature of the Heat Transfer Media: a SoA molten salts system operating at a TIT of 550 ºC (Gen I) and a solid particle system with TIT=700 ºC (Gen II). An integrated platform able to simulate all CSP plant subsystems and perform hourly calculations is built in Matlab employing Artificial Neural Networks to simulate the solar field, ensuring extremely high computational speed.

To overcome the high uncertainty in terms of cost estimation, a two-step analysis is developed: firstly, the CAPEX of the entire plant is calculated assuming correlations from literature, except for the power block, whose estimate brings about the largest uncertainty. As a result, the minimum power block cost allowing a LCoE lower than a certain target is identified. Secondly, an inverse methodology is applied, setting the power block cost and assessing the minimum CAPEX of the solar subsystem. As a result, a map is obtained showing the target CAPEX to be accomplished by sCO_2+CSP if a clear reduction of the LCoE of this technology is to be achieved.

1 INTRODUCTION

Concentrated Solar Power (CSP) plants combined with supercritical carbon dioxide (sCO_2) power cycles are widely believed to be a key-enabler of the complete decarbonisation of the power generation sector. This is due to the combination of various outstanding features of this technology, such as the high thermal efficiency, low footprint and high operational flexibility -notable features attributed to sCO_2 power cycles- as well as high dispatchability, brought by the use of Thermal Energy Storage (TES). This last feature stems as a major advantage over variable renewable energy sources such as photovoltaics and wind. Nevertheless, the cost-effectiveness of CSP+sCO_2 is still unclear, and further investigation is needed to reduce the Levelised Cost of Electricity (LCoE) of this technology in order to make it truly competitive in the energy market. In this regard, the SCARABEUS project aims to reduce the LCoE of CSP plants located in areas with high solar resource and high annually-averaged

ambient temperature. To achieve this, the project investigates the use of innovative power cycles based on CO_2 mixtures that can attain higher thermal efficiency than supercritical CO_2 and steam cycles (Crespi *et al.*, 2022 (b)).

Bearing this in mind, two CO_2-based CSP plants at two different Turbine Inlet Temperature (TIT) levels, 550 ºC (Gen I) and 700 ºC (Gen II), are compared. Gen I uses conventional solar subsystem technology based on Solar Salt as Heat Transfer Media (HTM) coupled with two-tank TES, whereas Gen II is based on free-falling particle receivers (FFPR). A Matlab-based computational platform is developed to calculate the annual electricity production for different Solar Multiple (SM) and TES capacities. A two-step analysis is employed to overcome the high uncertainty in cost estimation: i) in the first step, the CAPEX of the entire plant is calculated using correlations taken from literature for all subsystems except the power block, which is the section of the plant with larges uncertainty. The minimum cost of the power block necessary to achieve the target LCoE (100 $/MWh) -an arbitrary upper limit set according to the objectives of the SCARABEUS project (Binotti *et al.*, 2020)- is then identified for each case; ii) in the second step, an inverse methodology is used to set the cost of the power block and to assess the minimum CAPEX of the solar subsystem accordingly, with the final aim of mapping the target CAPEX that needs to be achieved by sCO_2+CSP to reduce LCoE below state-of-the-art (SoA) technologies based on steam turbines.

2 COMPUTATIONAL ENVIRONMENT

A Matlab-based computational platform has been developed to perform annual plant simulations. The platform comprises four main modules: solar field, solar receiver, TES and power block. Additionally, certain assumptions are made for the calculation of auxiliary loads (i.e., heliostat tracking, heliostat start-up and HTM conveyance). It is worth noting that the technology and models used are specific to each generation considered (Gen I or Gen II), each of which blocks will be further detailed in the following subsections. The hourly calculation flowchart has been adapted from González-Portillo *et al.* (2021). Calculations apply to a plant located in Seville (Spain), with design Direct Normal Irradiance and ambient temperature corresponding to the 95th percentile of the annual distribution: 840 W/m^2 and 36 ºC. The annual direct irradiance is 1773 kWh/m^2·year.

506

2.1 Solar field

The SolarPILOT software is employed to simulate the solar field (Wagner and Wendelin, 2018). For Gen I, the solar field is a circular surrounding field with an external cylindrical receiver atop the central tower. For Gen II, free-falling, cavity-type particle receivers (FFPR) are used, making it not feasible to employ surrounding fields; North-fields are used instead. This approach, however, poses a significant challenge for utility-scale plants (≥100 MW) in terms of land utilisation and, moreover, inefficient optical performance, inasmuch as heliostats that are further from the tower perform poorly from an optical standpoint. As a solution, multi-receiver designs, with more than one receiver in the same tower, are studied. In this work, a design with three FFPRs -facing North, East and West- is considered, as proposed in (Mills *et al.*, 2022); the particular specifications to simulate the multi-FFPR design in SolarPILOT can be retrieved from the works by González-Portillo *et al.* (2021) and Mills *et al.* (2022). With the objective of simplifying the integration of SolarPILOT within the integrated platform and of significantly increasing the computational speed when studying different solar field configurations, a surrogate model based on Artificial Neural Networks was created using Matlab's Deep Learning Toolbox. First, a training dataset of 1000 elements was generated, where each sample represents a feasible design of the solar field -randomly generated by varying the design degrees of freedom- whose performance is evaluated for a random position of the sun selected from a set of equally spaced positions based on declination angle (Wagner, 2008). The Levenberg-Marquardt algorithm was used to train the neural networks, and a sensitivity analysis was conducted on the number of neurons in the hidden layer. As a result, an Artificial Neural Network capable of estimating the solar field's optical efficiency for a given design (specified by the number of heliostats, tower height, and receiver area) and operating conditions (determined by Direct Normal Irradiance and sun position) was created. For multi-receiver designs, the ANN also provides the fraction of thermal power incident on each of the three receivers. The estimation of optical efficiency yields a Root Mean Square Error of 0.82 and 2.3 percentage points,

respectively, indicating the higher computational complexity of the second system compared to the former. Future research should concentrate on thoroughly examining and enhancing the training process, reducing training errors, and investigating the impact of uncertainty on the final results.

2.2 Solar receiver

External receivers similar to those employed in SoA CSP plants are used for Gen I, where Solar Salt (60%$NaNO_3$-40%KNO_3) is the HTM used in the receiver and TES. Molten salts are heated up from 387.9 ºC to 565 ºC in the receiver, whose thermal performance is simulated with the System Advisor Model (SAM). The design of the receiver includes size, number of panels, number of tubes, and thickness and is assumed constant throughout the study for the sake of simplicity.

In the multi-receiver design of Gen II, particles fall through the receiver by gravity and are heated directly by the solar radiation that enters the cavity (Ho *et al.*, 2016). *CARBO Accucast ID50* particles with a diameter of 350 μm are considered, and the thermophysical properties are taken from the work by Ho *et al.* (2017). Particles enter the receiver at 600 ºC and are heated up to 800 ºC. As a further simplification, all three receivers are assumed to have an aspect ratio of 1 and the same aperture area, and the aperture and curtain areas are considered to be equivalent (Mills *et al.*, 2022). The performance of the FFPR is estimated with the model proposed by González-Portillo *et al.* (2021). As a result of a preliminary analysis, it is decided to employ a constant FFPR particle curtain size of 18x18 m.

2.3 TES

A ground-based Thermal Energy Storage system (TES) composed of two cylindrical tanks is considered for both Gen I and Gen II, employing molten salts in the former and solid particles in the latter. The height-to-diameter ratio is set to 0.5 and 2 for molten salts in Gen I and for particles in Gen II, respectively. A dead volume of 20 % is assumed for both systems. The thermal losses are calculated assuming a thermal resistance of 4 m^2K/W, taken from González-Portillo *et al.* (2021).

2.4 Power subsystem

507

The power subsystem includes three modules: power cycle, heat rejection unit and primary heat exchanger (PHX). The power cycle used in this system is a transcritical cycle running on a binary mixture of 80%CO_2-20%SO_2 (molar basis), whose detailed description can be found in previous publications by the authors (Crespi *et al.*, 2022 (a), Crespi *et al.*, 2022 (b), Rodríguez-deArriba *et al.*, 2022). A modular air-cooled heat exchanger with induced-draft axial fans is used to condense the mixture, thus minimising water consumption of the plant. The final design uses multiple units equipped with three axial fans each, two of them with single-speed drives and the other one with a variable frequency drive. This choice is considered a promising trade-off between enhanced performance and moderate capital cost increase (more info in Rodríguez-deArriba *et al.*, 2023b). Further research is needed to determine the optimal number of VFDs though. The primary heat exchangers in Gen I and Gen II are different. For Gen I, a shell-and-tube heat exchanger with molten salts on the shell side and the working fluid flowing inside the tubes is employed. For Gen II, a particle-to-working fluid moving packed-bed shell-and-tube heat exchanger is used; for a detailed description of this component and a comparison with other existing technologies, the readers may refer to the work by Ho *et al.* (2019).

The power cycle is modelled in Thermoflex environment, modified with a series of user-defined modules to enable the simulation of SCARABEUS-specific components. The air-cooled heat exchanger is modelled in Matlab, as explained in past works by partners of the consortium (Illýes *et al.*, 2022, Rodríguez-deArriba *et al.*, 2023a), while a numerical code for the particle-to-working fluid shell-and-tube heat exchanger is also specifically developed in the same environment to design and simulate this component. To calculate the total conductance UA, the heat exchanger has been modelled as a cross-flow heat exchanger. The heat transfer coefficient on the CO_2 side has been determined using Gnielinski's correlation whereas that on the (dominating) particle side is implemented following the simplified heat transfer model presented in Hertfel and Zunft (2022). Table 1 compares the main design parameters for the power subsystem of Gen I and Gen II. In this regard, cycle thermal efficiency refers to the ratio from gross power output to heat input to the cycle. On the other hand, net efficiency refers to the ratio from net power output of the power block to total heat input into the PHX. When calculating

net power output, several factors are considered, including losses in the electric motor and generator, auxiliary power consumption of the air-cooled condenser, and power consumed by the HTM conveyance system from the hot tank to the cold tank through the PHX.

Table 1. Power subsystem design parameters for Gen I and Gen II

Parameter	Gen I	Gen II
Turbine inlet temperature [ºC]	550	700
Minimum cycle temperature [ºC]	50	50
Gross power output [MW]	100	100
Cycle thermal efficiency [%]	44.1	51.05
Air-cooled condenser fan power [kWe]	1181	885.0
PHX power consumption [kWe]	239.7	116.6
Net power output [MWe]	90.96	92.43
Net efficiency [%]	40.1	47.1

The CSP plant is assumed to operate in base load, thus keeping net power output as close to the rated value as possible. Accordingly, the effect of part-load operation is disregarded in this work, which accounts for the impact of variable ambient temperature only. Figure 1 shows the net output (a) and net efficiency (b) of the power subsystem as a function of ambient temperature for Gen I and Gen II. For ambient temperatures lower than design, the power block operates at its design point with reduced auxiliary power consumption of the air-cooled condenser; this results in a slightly higher net power output and efficiency. For ambient temperatures higher than the rated value, the air-cooled heat exchanger is not able to condense the working fluid at the rated condensation pressure, and this pressure must be increased, resulting in a higher minimum cycle temperature. However, doing so also requires decreasing TIT to keep the return temperature of HTM (i.e., temperature at the outlet from the PHX) equal to its design value. All this results in a drastic drop in both net power and efficiency.

508

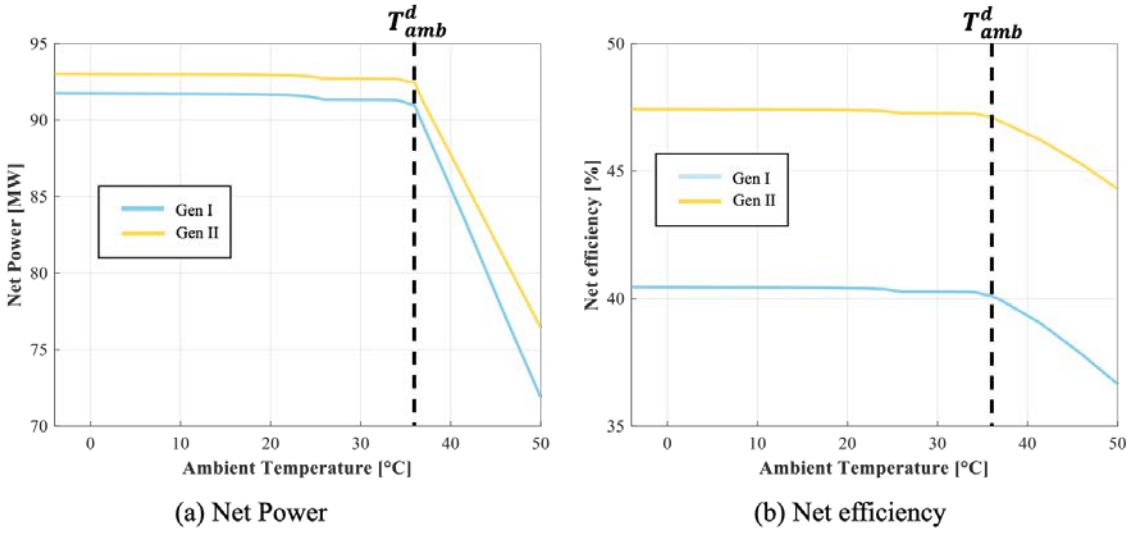

Figure 1. Power subsystem: (a) net power and (b) net efficiency as a function of ambient temperature

2.5 Cost models

Two scenarios are considered for the solar field and site preparation costs: 140 $/m^2, representative of SoA plants (Manzolini *et al.*, 2021), and 60 $/m^2, corresponding to future projections taken from the work by Murphy *et al.* (2019). The costs of the tower and receiver in Gen I are taken from Manzolini *et al.* (2021). The latter cost is then replaced by the costs reported by González-Portillo *et al.* (2021), for the FFPR, particle lifts and particle-based TES system in a Gen II plant. The TES based on Solar Salt is calculated using an in-house tool adapted from past work by some of the authors (Rodríguez *et al.*, 2016), resulting in a specific cost of 38.2 $/kWh. All cost estimates refer to 2020$.

It is to note that, given the lack of reliable cost correlations for the components of a power block running on CO_2 mixtures, the direct calculation of the power block cost is not addressed in this paper. Rather, this cost is reverse-calculated in order to attain the target cost of energy. The additional parameters necessary for the economic assessment are presented in Table 2, taken from González-Portillo *et al.* (2021).

Table 2. Assumptions of the economic assessment

Parameter	Value
Plant lifetime	30 year
Discount rate	7 %
Inflation	2.5 %
Contingency Cost	10 %
Construction Cost	9 %
Land cost	2.47 $/m^2
Fixed O&M Cost	40 $/kW·year
Variable O&M Cost	0.003 $/kWh

3 RESULTS

3.1 Annual Energy Production and reference case

The computational platform described in earlier sections is used to calculate the annual yield of both Gen I and Gen II power plants. A sensitivity analysis is also conducted, varying the number of heliostats (through Solar Multiple, SM) and energy storage capacity (equivalent hours of storage, h_{TES}). The results are shown in Figure 2. It is observed that, for the same number of heliostats and h_{TES}, the Gen I system is able to produce slightly more electricity than the Gen II system. This is because, for the same number of heliostats (i.e., same total reflective area), the surrounding field in Gen I attains higher optical efficiency than the multi-receiver field in Gen II. This data is used to create a spline-fitting surface in Matlab, which is used in the next sections to interpolate the annual production of energy for any intermediate values of SM and h_{TES}.

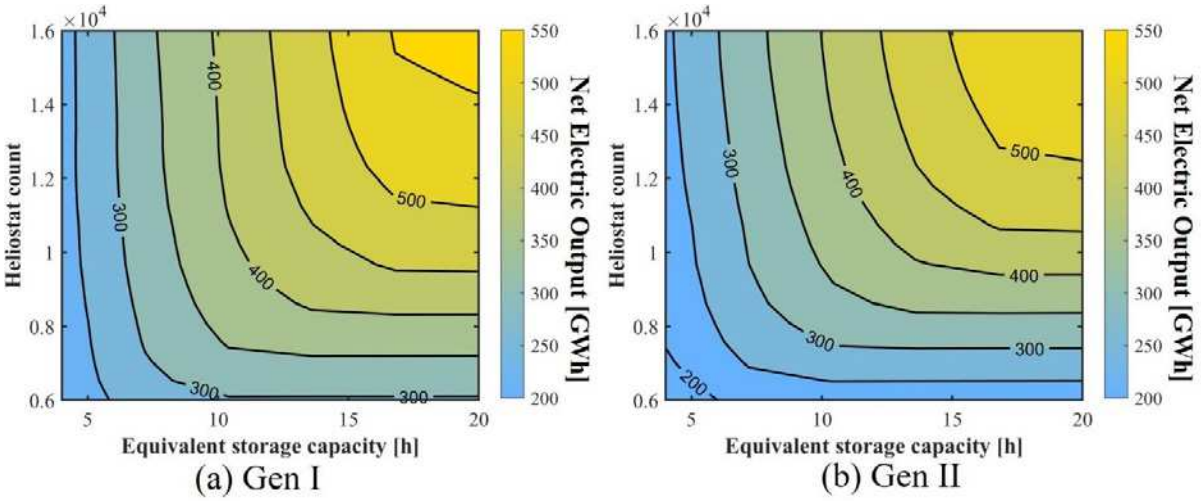

Figure 2. Net electric output as a function of number of heliostats and TES capacity for (a) Gen I and (b) Gen II

For each generation, a reference case is selected, assuming optimised values for the number of heliostats and storage capacity: 11070 heliostats (SM 3.26) and 17 hours for Gen I, 11800 (SM 3.42) and 18.2 hours for Gen II. Interestingly, in spite of the worse optical and thermal performances of the solar field and receiver in Gen II, the corresponding optimum number of heliostats is very similar to that of Gen I. This is because this lower performance is compensated for by the higher net efficiency of the

power block of Gen II in terms of global efficiency. As a consequence, the cost of the solar field is similar in both systems, as observed from a breakdown of specific costs provided in Figure 3.

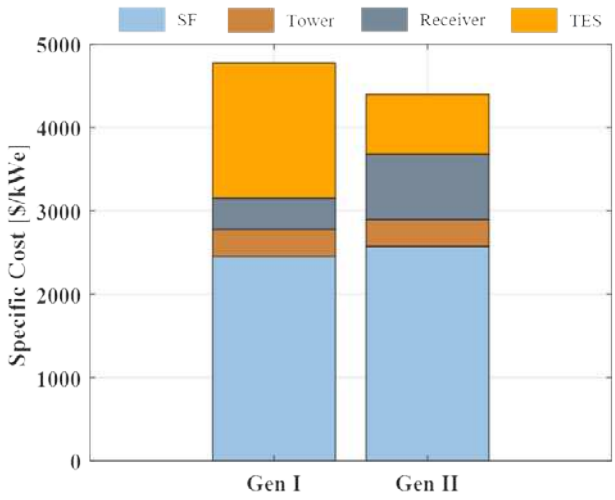

Figure 3. Cost breakdown of the solar subsystem for Gen I and Gen II cases.

The tower costs are identical in both cases, since both make use of a 218 m tower (Gasa *et al.*, 2022). Nevertheless, the multi-receiver system using FFPRs is twice as expensive as the external receiver system in Gen I. In addition to the fact that three receivers are needed in the particle-based solar subsystem, this is also due to the need for a costly particle-elevator system (González-Portillo *et al.*, 2022). Finally, a higher than 50 % cost reduction of the TES system is observed when switching from molten salt storage (Gen I) to particle storage (Gen II). This result is noteworthy since it addresses one of the primary challenges highlighted in literature with regards to the integration of CO_2-based systems with conventional TES based on molten salts: the important increase in cost with respect to the TES employed in SoA steam turbine-based CSP plants, owing to the lower temperature difference between hot and cold tanks.

510

3.2 Optimization of power subsystem cost

In this section, the impact of the power subsystem cost is assessed by means of a sensitivity analysis to its specific cost. For each point of the sensitivity analysis, the solar multiple and the storage capacity are optimised in order to minimise LCoE, using the cost functions for the solar subsystem elements described in the previous section.

Results for both Gen I and Gen II are presented in Figure 4, for the current and future solar field cost scenarios. Firstly, it is worth noting that, regardless of the generation and solar field cost considered, both Gen I and Gen II achieve significantly lower LCoE than 167 $/MWh, a value representative of a CSP plant based on steam turbine and two-tank molten salt TES located in Seville (Manzolini *et al.*, 2021). This highlights the potential of the SCARABEUS concept to reduce the cost of CSP technology. Moreover, it is observed that, considering current SF cost values, the LCoE target of 100 $/MWh (see introduction) can be achieved by any of the two generations of SCARABEUS if the specific capital cost of the power block is below 1700-1800 $/kWe.

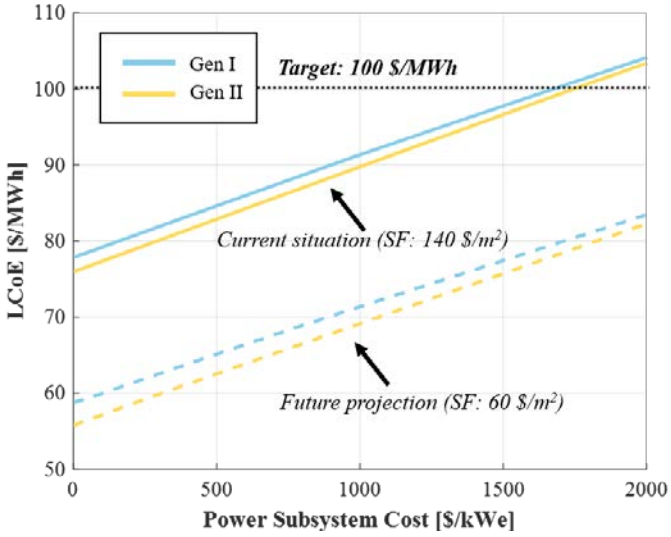

Figure 4. Minimum LCoE [$/MWh] achievable as a function of Power Subsystem Cost [$/kWe]

The results in the foregoing paragraph set an upper limit that the SCARABEUS technology must not exceed in order to yield an LCoE lower than 100 $/MWh. This threshold seems to be achievable in practice, considering that the specific cost of the power block of a SoA steam-based CSP plant is around 1400 $/kWe (Manzolini *et al.*, 2021), and the cost of a supercritical CO_2 recompression cycle is estimated at ~1000 $/kWe (Ho *et al.*, 2016). Assuming that the cost of the technology studied here is similar to that using pure sCO_2, an LCoE~90 $/MWh is to be expected.

Interestingly, Gen I and Gen II perform rather similarly in terms of LCoE, with differences in the range of 0.5-3.5 $/MWh. Thus, even if this result can be affected by the large uncertainty in cost estimation for Gen II, brought about by the very low TRL of this technology, this might suggest that the best path to develop a next-generation CSP is not achieving extremely high TIT (>700 ºC) but, rather, optimising the cycles for intermediate (moderately high) TITs, for which TES based on molten salts are still feasible (≃600 ºC).

Finally, it is worth highlighting that, even if the cost of the power subsystem were zero, there exists a minimum LCoE of around 75-80 $/MWh that the technology cannot exceed, whose exact value depends on the selected location. Regarding the two scenarios of solar field costs, it is observed that if the future projection is met, LCoE would be reduced by 20 $/MWh regardless of the power subsystem cost.

3.3 Minimum solar subsystem cost

Calculating the cost of the solar subsystem is subject to a significant uncertainty as well. Figure 5 presents a mapping of the technology based on the specific cost of the solar and power subsystems, along with iso-lines of constant LCoE. This map allows to set target costs for the SCARABEUS technology based on the desired LCoE or, equivalently, to determine the resulting LCoE for given costs of both subsystems. The figure was generated assuming the reference values of SM and h_{TES} for each generation and for contemporary solar field costs. The total capital cost for a specific LCOE can be calculated by adding the power subsystem cost (x-axis) and solar subsystem cost (y-axis). This value is constant along any iso-LCoE line. Furthermore, the total capital cost evolves linearly with the LCOE. For instance, to achieve a reduction in LCOE from $120/MWh to $60/MWh, the total capital cost should decrease from 7899 $/kWe to 3424 $/kWe for Gen I, and from 7596 $/kWe to 3235 $/kWe for Gen II.

Two grey bands are added, estimating the cost of the solar subsystem according to the correlations from literature. The upper band represents the current costs of the solar field (120 $/m^2) whereas the lower band applies to future projections (60 $/m^2). For each band, the upper boundary corresponds to the solar subsystem cost of Gen I while the lower boundary corresponds to Gen II. Interestingly, an increase in

the solar subsystem cost for higher costs of the power subsystem are observed (i.e., the bands become wider for higher power block costs). This is explained by the larger size of both the solar field and thermal energy storage system that aims to increase the annual yield of the plant in order to compensate for the higher cost of the power subsystem. Also, it is observed that this phenomenon is more pronounced for Gen I (upper limit of the bands) due to the higher specific cost of the molten salt storage system.

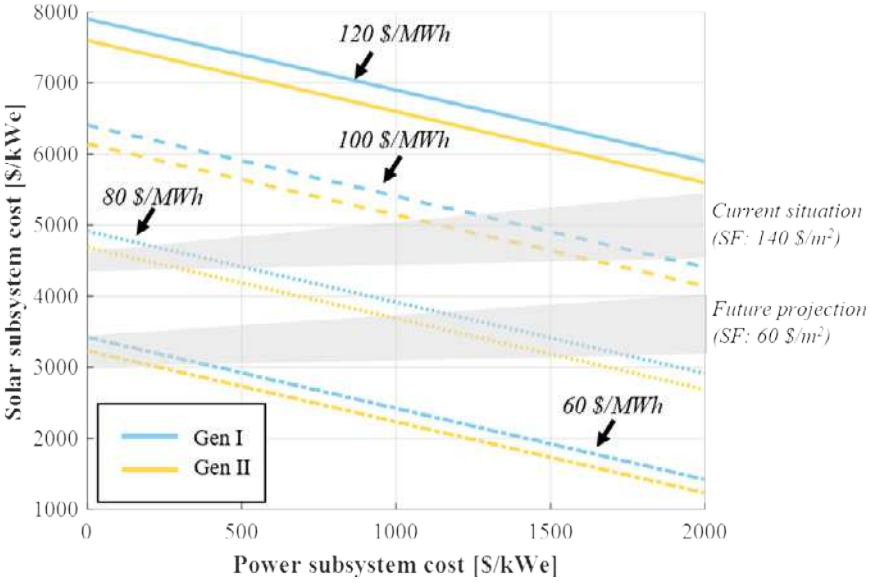

Figure 5. Constant-LCoE lines for different combinations of solar and power subsystem costs (blue for Gen I and yellow for Gen II). Labels report LCoE associated to each line set [$/kWe]

512

The graphical results presented in this section confirm the tight link between the cost of the power and solar subsystems, and the dominant effect of the latter over the former (moderate slope of the constant LCoE lines). From a practical standpoint, the results also confirm that achieving a much lower LCoE than SoA CSP plants based on steam turbines is within reach of the SCARABEUS technology, either with contemporary CO_2-mixture technology (Gen I) or with more advanced components (Gen II). There is of course uncertainty inherent to this analysis but the fact that the methodology adopted works upstream to determine breakeven costs from the target LCoE rather than downstream from the estimated values of different subsystems reduces this uncertainty to a large extent.

4 CONCLUSIONS

In this study, the utilisation of transcritical power cycles based on CO_2 mixtures in CSP plants has been evaluated from a techno-economic standpoint. Two CSP plant schemes using different receiver technology have been compared: conventional molten salt receivers with a maximum temperature of 565 ºC (Gen I) and solid particle receivers with a maximum temperature of 800 ºC (Gen II).

It is concluded that:

- Both systems can potentially achieve LCoE's lower than 100 $/MWh for a reference plant in Seville, as long as the cost of the power subsystem is not higher than 1700 $/kWe. The specific cost of the power subsystem is expected to be lower than that of SoA CSP plants based on steam turbines (1400 $/kWe) due to the lower footprint.
- The resulting LCoE for Gen I and Gen II is very similar, slightly lower for Gen II thanks to the significant cost reduction of the TES system.
- If the specific cost of the solar field were to decrease according to projections from literature, LCoE's in the area of ~70 €/MWh would be within reach for the SCARABEUS concept for a reasonably good location (not necessarily optimum).

However, it must be highlighted that cost estimates for the receiver technology used in Gen II are subject to higher uncertainty. Therefore, future work should address the estimation of the cost of the power block technology, as well as study the uncertainty in cost estimates, especially for the technology used in Gen II. Moreover, the economic performance could be further improved through a simultaneous, joint optimisation of the power cycle and solar subsystem. These efforts will allow for a more robust and accurate evaluation of the potential of SCARABEUS technology in the future power generation sector.

NOMENCLATURE

CAPEX	Capital Expenditure	LCoE	Levelised Cost of Electricity
CSP	Concentrated Solar Power	PHX	Primary Heat Exchanger
FFPR	Free-falling particle receiver	SM	Solar Multiple
Gen	Generation of CSP plant	SoA	State-of-the-art
h_{TES}	Equivalent hours of storage	TES	Thermal Energy Storage
HTM	Heat Transfer Media	TIT	Turbine Inlet Temperature

REFERENCES

Binotti, M. et al. (2020) 'SCARABEUS: Supercritical carbon dioxide/alternative fluid blends for efficiency upgrade of solar power plants', in. *SOLARPACES 2019: International Conference on Concentrating Solar Power and Chemical Energy Systems*, Daegu, South Korea, p. 130002. Available at: https://doi.org/10.1063/5.0028799.

(a) Crespi, F. *et al.* (2022) 'Preliminary investigation on the adoption of CO 2 -SO 2 working mixtures in a transcritical Recompression cycle', *Applied Thermal Engineering*, 211, p. 118384. Available at: https://doi.org/10.1016/j.applthermaleng.2022.118384.

(b) Crespi, F. *et al.* (2022) 'Thermal efficiency gains enabled by using CO2 mixtures in supercritical power cycles', *Energy*, 238, p. 121899. Available at: https://doi.org/10.1016/j.energy.2021.121899.

Gasa, G. *et al.* (2022) 'Life cycle assessment (LCA) of a concentrating solar power (CSP) plant in tower configuration with different storage capacity in molten salts', *Journal of Energy Storage*, 53, p. 105219. Available at: https://doi.org/10.1016/j.est.2022.105219.

González-Portillo, L.F., Albrecht, K. and Ho, C.K. (2021) 'Techno-Economic Optimization of CSP Plants with Free-Falling Particle Receivers', *Entropy*, 23(1), p. 76. Available at: https://doi.org/10.3390/e23010076.

González-Portillo *et al.* (2022). Sensitivity Analysis of the Levelized Cost of Electricity for a Particle-Based Concentrating Solar Power System. *Journal of Solar Energy Engineering*, 144(3), 030902. Available at https://doi.org/10.1115/1.4053167.

Hertel, J.D. and Zunft, S. (2022) 'Experimental validation of a continuum model for local heat transfer in shell-and-tube moving-bed heat exchangers', Applied Thermal Engineering, 206 p. 118092. Available at: https://doi.org/10.1016/j.applthermaleng.2022.118092.

Ho, C.K. *et al.* (2016) 'Technoeconomic Analysis of Alternative Solarized s-CO2 Brayton Cycle Configurations', *Journal of Solar Energy Engineering*, 138(5), p. 051008. Available at: https://doi.org/10.1115/1.4033573.

Ho, C.K. *et al.* (2017) 'Characterization of Particle Flow in a Free-Falling Solar Particle Receiver', *Journal of Solar Energy Engineering*, 139(2), p. 021011. Available at: https://doi.org/10.1115/1.4035258.

Ho, C.K. *et al.* (2019) 'Evaluation of Alternative Designs for a High Temperature Particle-to-sCO2 Heat Exchanger', *Journal of Solar Energy Engineering*, 141(2), p. 021001. Available at: https://doi.org/10.1115/1.4042225.

Illyés, V. *et al.* (2022) 'Design of an Air-Cooled Condenser for CO2-Based Mixtures: Model Development, Validation and Heat Exchange Gain with Internal Microfins', in *Volume 9:*

Supercritical CO2. ASME Turbo Expo 2022: Turbomachinery Technical Conference and Exposition, Rotterdam, Netherlands: American Society of Mechanical Engineers, p. V009T28A016. Available at: https://doi.org/10.1115/GT2022-82438.

Manzolini, G. *et al.* (2021) 'A two-step procedure for the selection of innovative high temperature heat transfer fluids in solar tower power plants', *Renewable Energy*, 177, pp. 807–822. Available at: https://doi.org/10.1016/j.renene.2021.05.153.

Mills, B. *et al.* (2022) *Technoeconomics of Particle-based CSP Featuring Falling Particle Receivers with and without Active Heliostat Control*. SAND2022-13437, 1890267, 710418, pp. SAND2022-13437, 1890267, 710418. Available at: https://doi.org/10.2172/1890267.

Murphy, C., et al. (2019). The potential role of concentrating solar power within the context of DOE's 20230 solar cost targets. Retrieved from https://www.osti.gov/servlets/purl/1506623

Rodríguez, J.M. *et al.* (2016) 'Techno-economic assessment of thermal energy storage solutions for a 1 MWe CSP-ORC power plant', *Solar Energy*, 140, pp. 206–218. Available at: https://doi.org/10.1016/j.solener.2016.11.007.

Rodríguez-deArriba, P. *et al.* (2022) 'The potential of transcritical cycles based on CO2 mixtures: An exergy-based analysis', *Renewable Energy*, 199, pp. 1606–1628. Available at: https://doi.org/10.1016/j.renene.2022.09.041.

(a) Rodríguez-deArriba, P. *et al.* (2023). 'A methodology to design air-cooled condensers for supercritical power cycles using carbon dioxide and carbon dioxide mixtures'. In: *Proceedings of the 5th European sCO_2 Conference for Energy Systems*. Available at: https://doi.org/10.17185/duepublico/77329.

(b) Rodríguez-deArriba, P. *et al.* (2023). 'Assessment of part-load operation strategies of supercritical power cycles using carbon dioxide mixtures in CSP plants, including air-cooled condenser optimisation', in: *Proceedings of ASME Turbo Expo 2023,* Boston, USA.

Wagner, M.J. (2008) 'Simulation and predictive performance modeling of utility-scale central receiver system power plants'. (Doctoral dissertation). University of Wisconsin, Madison. Retrieved from http://digital.library.wisc.edu/1793/45001

Wagner, M.J. and Wendelin, T. (2018) 'SolarPILOT: A power tower solar field layout and characterization tool', *Solar Energy*, 171, pp. 185–196. Available at: https://doi.org/10.1016/j.solener.2018.06.063.

514

ACKNOWLEDGEMENTS

The SCARABEUS project has received funding from the European Union's Horizon 2020 research and innovation programme under grant agreement Nº814985.

The Spanish Ministry of Universities is gratefully acknowledged for sponsoring the contract of Pablo Rodríguez de Arriba via FPU (Formación de Profesorado Universitario). Grant reference FPU21/04892.

ORC SEVILLE 2023
7th International Seminar on O.R.C. Power Systems

© 2024 Editorial Universidad de Sevilla. Este es un artículo de acceso abierto distribuido bajo los términos de la licencia de uso y distribución Creative Commons (BY-NC-ND 4.0)

DOI: https://dx.doi.org/10.12795/9788447227457_86

ACHIEVING 45% MICRO GAS TURBINE EFFICIENCY THROUGH HYBRIDIZATION WITH ORGANIC RANKINE CYCLES

Antonio Escamilla[1,*], David Sánchez Martínez[1], Lourdes García-Rodríguez[1]
[1] *University of Seville, Camino de los Descubrimientos, s/n, 41092, Seville (Spain)*
*Corresponding Author: a.escamilla@us.es

ABSTRACT

The demand for affordable, secure, and sustainable energy storage solutions has grown significantly with the increasing focus on decarbonization and the adoption of renewable energy sources (RES). Power-to-Power (P2P) energy storage systems (ESS) have emerged as a promising solution, utilizing excess electricity from RES to produce hydrogen for future power generation. This document presents a study on increasing the round-trip efficiency of P2P ESS by improving the electric efficiency of micro gas turbines (mGT) and integrating waste heat to power (WHP) technology. The research investigates the potential of mGTs as prime movers in P2P ESS, aiming to break the 45% electric efficiency barrier that would make them competitive with other alternatives like internal combustion engines (ICE) and fuel cells (FC). Increasing the nominal electric efficiency of mGTs would lead to significant reductions in hydrogen consumption, system footprint, and overall capital expenditure. Thus, this research focuses on increasing the electrical efficiency of the mGT by proposing a hybridization between the recuperative Brayton cycle and bottoming organic Rankine cycles, reaching higher than 45% electrical efficiencies in a hybrid configuration. An exhaustive comparison of the main ORC systems hybridized with the recuperative Brayton cycles is presented. The results reveal that hybridizing an intercooling-recuperative Brayton cycle with a simple recuperated ORC has the potential to increase electrical efficiency to 46%. The work also presents a sensitivity analysis to assess how the design parameters influence the performance of the hybrid thermodynamic cycle.

1 INTRODUCTION

In the recent past, storing large amounts of energy was impossible and, even today, it poses many technical challenges. However, with the growing penetration of renewable energy sources (RES) and the push for decarbonization due to new regulations and societal concerns, finding affordable, secure, and sustainable energy storage solutions is crucial. Power-to-Power (P2P) energy storage systems (ESS) have gained significant attention recently, particularly in relation to national plans for developing hydrogen and other decarbonized fuel alternatives (FCH, 2019), (FCHEA, 2020). Additionally, governments are expediting the adoption of RES and energy storage options to ensure the security of supply whilst still in compliance with the Green Deal vision, given the significant uncertainty and volatility of the energy market. The European Commission has introduced the "Fit for 55" legislative package (EU, 2022), aiming to update and implement the regulatory framework necessary to achieve the decarbonization targets for 2030 and 2050.

A Power-to-Hydrogen-to-Power (P2P-ESS in the context of this paper) makes use of excess electricity generated from RES to power an electrolyzer, which breaks water into hydrogen and oxygen. The hydrogen generated is then stored to be used later to run a power generation system. This process enables utilizing initially non-dispatchable renewable electricity, effectively aligning production and consumption of electricity, thus ensuring that the power demand is met at any time. From a practical standpoint, the hydrogen stored can be used to operate fuel cells, gas turbines or other heat engines, although the former two are the main technologies proposed for power generation from hydrogen. Recently, the authors have extensively researched this concept, placing particular emphasis on decentralized and off-grid applications, and employing a micro-gas turbine (mGT) as the primary mechanism for power generation utilizing hydrogen (H2) (Escamilla, 2022) (Escamilla, 2023).

Past work by the authors on P2P-mGT concepts shows that the cost-effectiveness of these systems is compromised by the low efficiency of the prime mover (mGT). In particular, making use of the most efficient micro gas turbines in the market today (26.9% LHV efficiency for 30 kWe rated output) yields

a very low round-trip efficiency of 15.5% only, which is not high enough to compensate for the high capital cost required to implement this solution (Escamilla, 2023). This highlights that the incorporation of much more efficient power generation devices into these P2P-EES systems is the most critical route towards the development of cost-effective, small-scale P2P-EES solutions based on green hydrogen.

Micro gas turbines have power outputs below 500 kWe, typically, a range where the main competing technologies are Internal Combustion Engines (ICE) and Fuel Cells (FC), technologies featuring higher efficiency than mGTs and, for ICEs, also lower capital cost (CapEx). Therefore, despite the visible advantages of mGTs (low NOx, high-grade heat, flexibility, fast-response capability), this does not suffice to emerge as a more interesting prime mover. It is hence essential for mGTs to increase their electric efficiency in order to gain market share in a future energy system transitioning towards decentralized energy solutions (Tilocca, 2023). The Aurelia A400 engine features the highest electric efficiency of all mGTs in the market: 40.2% (LHV) (Aurelia, 2023) (Escamilla, 2022). This efficiency is comparable to ICEs and FCs of similar power output but cannot be sustained at smaller outputs because of the need to adopt simpler cycles or due to the impact of scale effects on component efficiency.

In the foregoing context, the current study aims to increase the efficiency of mGTs for a wider output range in order to enable their utilization in P2P-mGT ESS. To this end, past work by the authors concluded that the efficiency of the power conversion unit must be, at least, 45% since this boosts the round-trip efficiency of the resulting solution to 26% (in lieu of 15.5% for an mGT with 26.9% efficiency). The consequence of this is an almost 45% reduction in hydrogen consumption of the mGT, which translates into a footprint reduction of all systems involved in a P2P-mGT ESS, largely reducing the CapEx of the overall system. Two options to enable such efficiency increase are considered: higher efficiency mGTs and combined mGT + waste heat to power bottoming system. In the latter case, the exhaust gas from the mGT is used to drive a thermomechanical energy conversion system to produce additional electric power from the mGT waste heat. The two options are typically considered for WHP: Steam Rankine Cycle (SRC) and Organic Rankine Cycle (ORC). Amongst the two, steam is not cost-effective at a small scale, given the very low performance and high cost of steam turbines of a few hundred kilowatts (Vanslambrouck, 2012). Therefore, this research investigates the thermodynamic feasibility of integrating ORCs with different recuperative Brayton Cycle layouts, used by microturbines, to boost the power-to-heat ratio, and thus, the electric efficiency. A short literature review on the topic is presented below.

Bao et al. (Bao, 2013) presented a review of organic working fluid and expander options for ORC systems, screening the most prominent Key Performance Indicators for the selection of these two elements. Bonolo de Campos et al. (Bonolo de Campos, 2019) presented a review of the combination of micro gas turbines and ORC systems, concluding that the efficiency of a 100 kWe mGT could increase from 30% to 35% when combined with an ORC system, even if at the expense of 48% higher capital cost; it is to note that the work cited is a review and does not rely on calculations by the authors. Mago et al. (Mago, 2013) examined the potential of using the exhaust gas from microturbines in ORC systems, considering microturbines with different power outputs and different fluids in the ORC system, and basing the analysis on electric and exergy efficiencies. For this, the authors considered a set isentropic efficiency for both the ORC turbine and pump, and also a fixed electric efficiency for the mGT (ranging from 25% to 31%, depending on power output). The work gives a good understanding of which fluids might perform better whereas the present paper goes into more detail about the assessment of potential configurations of Brayton cycles and ORC systems that could help raise global efficiency, and therefore, the round-trip efficiency of the P2P-mGT ESS that the authors have previously investigated. This is of course not a new concept, as the forecited works have studied it already, but the integration of the mGT within a P2P ESS with the objective to break the 45% efficiency barrier and the improvements that are needed are innovative, as deduced from the literature review carried out by the authors. For that, systems forming both cycles will need to be dealt with in detail in the forthcoming sections.

Furthermore, it is recognized that the input data and specifications of the cycle and components, especially for the turbomachinery parts, are strongly influenced by scale even though this is mostly not considered in the literature reviewed. Thus, to assess the relevance of this common assumption, the first part of this paper provides an analysis of the impact of scale effects on the performance of compressors and turbines, which is then used to set the appropriate input data to run simulations. This is aimed at ensuring the credibility of the results. Moreover, the study incorporates diverse configurations of the Brayton cycle and varying power outputs to encompass the entire design range of micro-gas turbines, spanning from 1 kW to 500 kW that could be integrated into the P2P ESS. It is worth noting that the primary fuel utilized in this study is natural gas.

The authors acknowledge that increasing the system's complexity will inevitably lead to higher CapEx and operational expenditures (OpEx) for the mGT. However, if the overall context is considered, integration of a mGT within a P2P ESS, the increase in CapEx and OpEx of the mGT will be hardly noted as the main source of CapEx and OpEx are the PV solar, electrolyser and H_2 storage systems.

The study is organized as follows: 1) introduction to the concepts of P2P-mGT ESSs and waste-heat-to-power applications and literature review of hybrid micro gas turbines and ORC systems. 2) description of the hybridization layouts considered. 3) discussion of the design parameters used for each mGT layout and ORC system, as well as of the list of organic fluids used in the simulations. 4) a discussion of the results from a sensitivity analysis assessing the impact of varying the evaporator pinch-point and the maximum pressure of the ORC system, 5) the presentation of the main conclusions and next steps.

2 HYBRIDIZATION OF THE BRAYTON CYCLE WITH A BOTTOMING ORGANIC RANKINE CYCLE

Gas turbines operate according to a Brayton cycle, comprised of gas compression, heating, expansion and (virtual) cooling; in a practical engine, this latter process involved direct heat and mass transfer between the engine and the environment. Organic Rankine cycles are Rankine cycles where the working fluid is organic, typically with high molar mass and molecular complexity, whose evaporation temperature is lower than that of steam at the usual operating pressures. Heavy-duty combined cycle power plants make use of use of a topping Brayton Cycle and a bottoming steam Rankine Cycle harvesting the available heat at the exhaust from the former. Gas turbines in these systems feature very high turbine inlet temperatures and pressure ratios of around 25:1. When micro gas turbines are used, the turbine inlet temperature is low (limited by the material melting point since blade cooling cannot be used) and so is the associated pressure ratio accomplished by radial turbomachinery. Therefore, these engines rely on recuperative Brayton cycles to increase gas turbine performance, which implies lower exhaust gas temperatures, typically not higher than 250 ºC. For this temperature level, ORCs are better suited than steam Rankine cycles.

Brayton cycles can adopt multiple configurations to increase either thermal efficiency, specific power, or both. Nevertheless, as thermal efficiency increases, the number of components and the complexity of system integration also increase. In the next sections, the different Brayton cycle layouts are discussed – a recuperative Brayton cycle and an intercooled-recuperative Brayton cycle –, the latter in a twin-spool arrangement. Though the added number of components and the complexity of the cycle becomes very visible, adopting the latter layout boosts thermal efficiency by 10 percentage points compared to the single spool recuperative Brayton cycle. Both configurations will be used in the current research.

The implementation of Brayton cycles in gas turbines renders an open-cycle engine (except on very rare occasions) whilst ORC power systems are closed-cycle systems incorporating a condenser for heat rejection. Figure 1 shows the configuration of the reference mGT-ORC system used in this research. The mGT module will adopt different configurations that will be introduced in the following section. The exhaust gases from the mGT are redirected to the evaporator where the organic fluid discharged from the pump undergoes heating and phase change. The resulting saturated vapour is then expanded

across the turbine and then cooled down and condensed; these processes are then carried out cyclically. It is to note that, even though recuperative heat exchangers are typically used in other applications of ORC systems to use the available sensible heat at turbine exhaust to preheat the liquid working fluid upstream of the vapour generator.

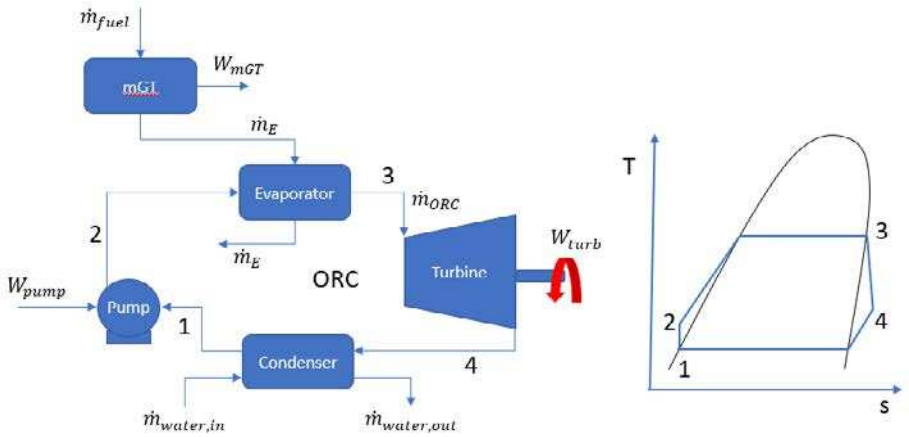

Figure 1. Hybridization of an mGT with a bottoming Organic Rankine Cycle system. The overall layout and T-s diagram of the bottoming cycle.

The selection of thermodynamic parameters for each system as well as the selection of the working fluid for the ORC will be discussed in the following sections.

3 SIMULATION OF BASECASE SCENARIO

3.1 Selection of thermodynamic cycle parameters and simulation

The hybridisation of the three layouts presented in figures 2, 3 and 4 with the bottoming ORC system in Figure 1 has been analysed using a simulation platform built in the Thermoflex environment (Thermoflex, 2022). 518

Out of all the equipment involved, the systems which are affected by scale effects the most are the compressor and turbine in the micro gas turbine, due to the aerodynamic and secondary loss effects; therefore, while carrying out the simulation, it is important to consider the power output (i.e, size) of the system under consideration. Three micro gas turbine options are assessed, combining system layout and power output: R-MGT for 5 and 100 kWe, and ICR-MGT for 400 kWe. The polytropic efficiencies given in Table 1 have been selected for each case, based on the considerations given in the work by Galanti *et al.* (Galanti, 2011). Table 1 presents the remaining boundary conditions and specifications of components.

Figures 2, 3, and 4 show the heat and mass balance of each simulation whilst the corresponding global performance parameters are presented in Table 2. Tables 1 and 2 along with figures 2, 3 and 4 show the validation of the model and allow for the reproduction of the results.

Electric efficiency for each base-case scenario is 26.5%, 29.2% and 40.2%. The electric efficiency increase comes from three different sources: upscale of turbomachinery, turbine inlet temperature, and thermodynamic cycle layout enhancement. Interestingly, each of these cases is intended to replicate existing commercial micro-gas turbines – MTT-EnerTwin (EnerTwin, 2023), Ansaldo-AE-T100 (Ansaldo, 2023), and Aurelia-A400 (Aurelia, 2023) -, even if the specifications reported in Table 1 deviate from the commercial specs announced by the Original Equipment Manufacturers.

Table 1. Input parameters for the simulation of the Brayton cycle for different layouts.

Parameter	Unit	Value		
		R-MGT-1	**R-MGT-2**	**ICR-MGT**
Ambient temperature and pressure	ºC / bar	15 / 1.013	15 / 1.013	15 / 1.013
Working fluid	-	Air	Air	Air
Fuel	-	Natural Gas	Natural Gas	Natural Gas
Exhaust gas flow	kg/s	0.0569	1.018	1.872
Gross Electric power	kW	5.08	101.5	401.0
Turbine inlet temperature	ºC	850	850	1005
Total pressure ratio	-	2.5	2.5	5.8
HP compressor polytropic efficiency	%	-	-	80.2
HP turbine polytropic efficiency	%	-	-	85.2
LP compressor polytropic efficiency	%	76.5	80.5	81.0
LP turbine polytropic efficiency	%	83.8	85.2	85.8
HE thermal effectiveness	%	85.0	85.0	90.5
Combustor efficiency	%	96.0	96.0	98.0
Compressor inlet pressure loss	%	1.0	1.0	1.0
HE pressure loss	%	1.0	1.0	1.0
Combustor pressure loss	%	2.0	2.0	2.0
Mechanical efficiency	%	98.5	98.5	98.5
Generator efficiency	%	96.0	96.0	96.0

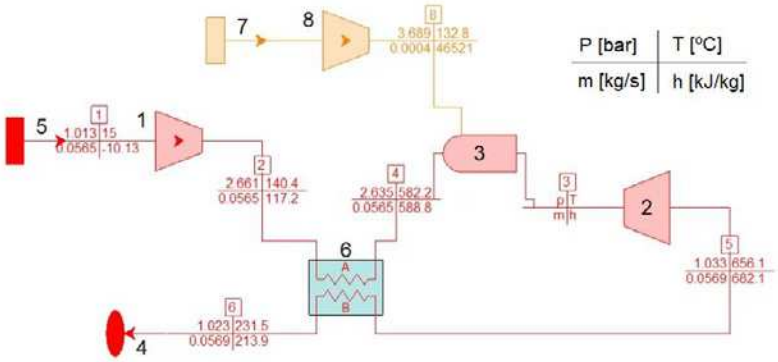

Figure 2. Simulation of R-MGT-1.

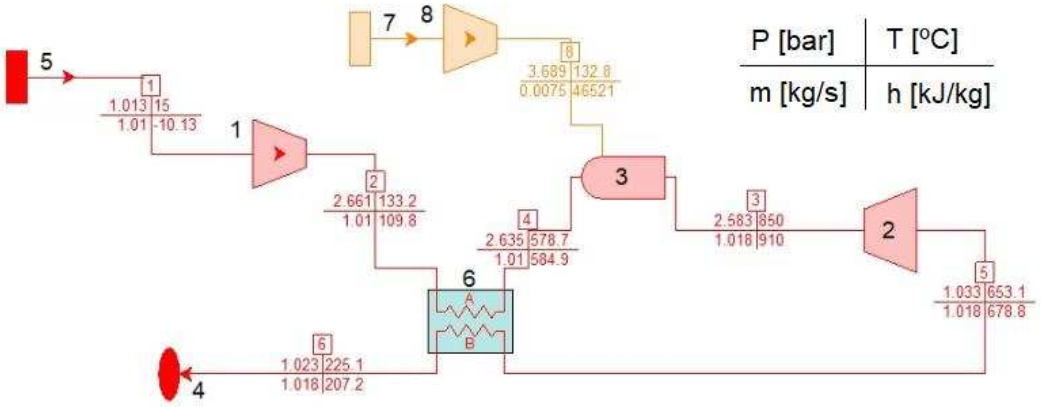

Figure 3. Simulation of R-MGT-2

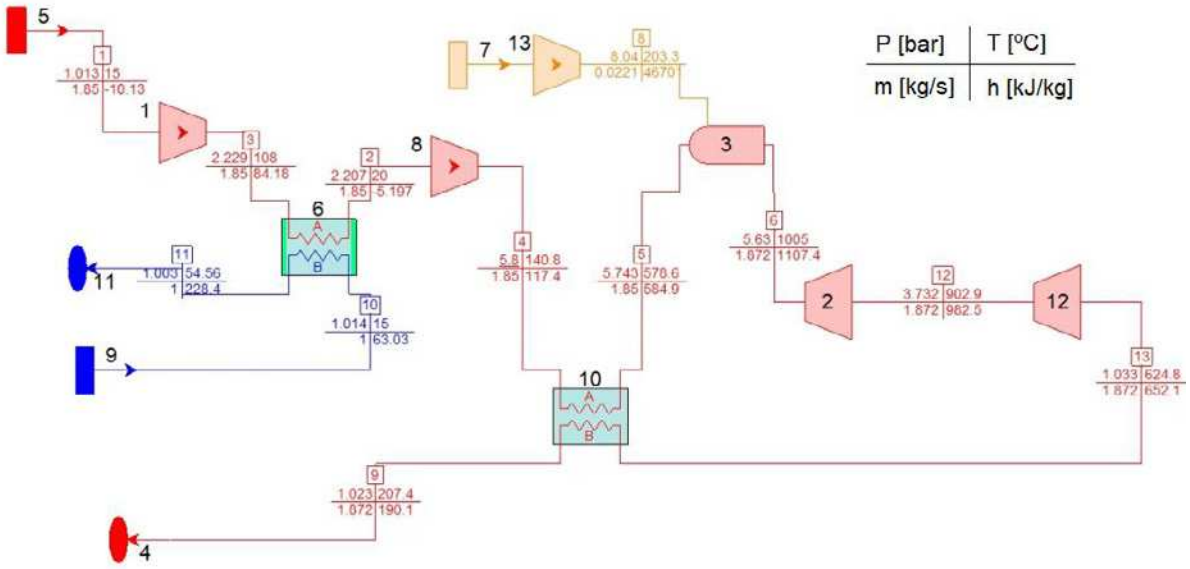

Figure 4. Simulation of ICR-MGT.

Table 2. Main output parameters of the simulated Brayton cycles. Input parameters are displayed in Table 1.

Parameter		Unit	Value		
			R-MGT-1	R-MGT-2	ICR-MGT
Thermal efficiency (LHV)		%	29.4	32.2	43.4
Electric efficiency (LHV)		%	26.5	29.2	40.3
Net electric output		kW	5.08	101.5	401.0
Exhaust gas temperature		ºC	231.5	225.1	204.5
Fuel Input (LHV)		kW	19.2	347.4	995.7
Exhaust gas flow		kg/s	0.0569	1.018	1.872
Exhaust Gas Composition	O_2	% mole	18.08	18.046	16.555
	CO_2	% mole	1.261	1.276	1.967
	H_2O	% mole	3.352	3.382	4.697
	AR	% mole	0.919	0.919	0.913
	N_2	% mole	76.387	76.376	75.868

520

3.2 Selection of organic working fluid and parameters of the ORC system

There is a wide range of organic fluids whose utilisation in ORC systems has been assessed. This selection of the working fluid is not only critical from a thermodynamic standpoint but also in terms of health and safety requirements and capital cost. Furthermore, the working fluid of choice must be tailored to the type and quality of heat available to drive the cycle, which adds another degree of freedom to the optimisation problem. Guoquan Qiu proposed a methodology, based on check steps, to decide which organic fluids could be suitable for certain applications (Qiu, 2012). The methodology is applied in this work, narrowing down the portfolio of organic fluids to be studied, and it is also complemented with information from similar works looking for the most suitable organic fluids for the application considered in this study: waste heat from small gas turbines (Bao, 2013) (Mago, 2012) (Clemente, 2013).

Table 3 shows the fluids and associated thermodynamic properties considered in the analysis whilst Table 4 lists other parameters needed for the simulation of the organic Rankine cycle whose layout was presented in Figure 1. It is worth noting that condenser pressure is different for each fluid as this comes determined by the saturation temperature at the condenser, which depends itself on ambient temperature (same for all cases). In practice, this translates into condenser pressures equal to 0.91 bar, 1.48, and 4.99

bar for R123, R245fa, and R1234ze, respectively. One of the noteworthy features of using organic fluids in the Rankine cycle is the avoidance of vacuum conditions in the condenser. This has several advantages, the most salient of which being that deaeration is no longer needed given that the entire system operates under pressure. This reduces the cost of the system and increases the useful life of components, thanks to the corrosion triggered by oxygen leaking into the system. Additional benefits related to the mechanical design of components. Based on this, and to avoid vacuum conditions in the condenser, it is decided to set the following condenser pressures for the three fluids considered: 1.25 bar, 1.5 bar, and 5 bar, respectively.

Table 3. Properties of the different organic fluids considered.

Parameter [Coolprop]	Unit	Fluid		
		R123	R245fa	R1234ze
Critical pressure	MPa	3.66	3.64	3.64
Critical temperature	ºC	183.7	157.5	109.4
Boiling temperature*1	ºC	27.8	15.3	-18.95
Molar mass	g/mol	153	134	114
GWP (AR5)	-	79.0	858.0	1.00
*1: at 1 bar.				

Table 4. Input parameters for the ORC layouts considered.

Parameter	Unit	Value		
		R-MGT-1	R-MGT-2	ICR-MGT
Condenser temperature	ºC	25	25	25
Pump isentropic efficiency	%	85.0	85.0	85.0
Pump motor efficiency	%	88.0	88.0	88.0
Turbine isentropic efficiency	%	83.8	85.2	85.8
Evaporator thermal effectiveness	%	85.0	85.0	85.0
Evaporator pinch point	ºC	5	5	5
Mechanical efficiency	%	98.5	98.5	98.5
Generator efficiency	%	96.0	96.0	96.0

521

4 HYBRIDIZATION OF MGT AND ORC SYSTEM

Once the base case scenarios have been set, this section explores the benefits of using the exhaust gases from the different mGT layouts to drive an ORC system, considering several organic fluids. The analysis aims to understand how the global electric efficiency of the power generation system is impacted by the hybridization proposed, calculated as follows:

$$\eta_t(\mathrm{LHV}) = \frac{\text{useful power ouput}}{\text{energy input}} = \frac{P_{\mathrm{e,GEN1}} - \mathrm{P}_{\mathrm{e,FUEL}} + P_{\mathrm{e,GEN2}} - P_{\mathrm{e,PUMP}}}{\text{Fuel Input (LHV)}} \quad (1)$$

Where P_e stands for electric power. Generator 1 (GEN1) refers to the generator of the mGT (electric output at generator terminals) whilst Generator 2 is driven by the expander of the ORC system. FUEL and PUMP refer to the electric motor driving the fuel compressor of the Brayton cycle and pump in the ORC unit. There is only one fuel input source: the fuel added in the combustor of the mGT.

The bottoming ORC system is coupled with the stream of exhaust gases from each mGT considered (Table 2) as shown in Figure 5, where stream 2 is the hot gas coming from the turbine. For each mGT layout, three different organic fluids used in the ORC are considered, yielding nine cases in total. In the first part of the study the bottoming system is designed considering a minimum evaporator's pinch point and a maximum pressure of 20 bar. Next, a sensitivity analysis on the maximum pressure of ORC system is carried out to understand the maximum potential of the ORC system to boost the total electric

efficiency of the system. The upper limit of the maximum cycle pressure is set by the critical pressure of each organic fluid (Table 3).

Table 5 shows the results of the first analysis, considering a 5ºC minimum pinch point in the Heat Recovery Vapour Generator and a maximum pressure of the ORC system of 20 bar. The results are highly influenced by the condensation temperature of 25ºC since this directly affects the pressure ratio through modifications of condenser pressure from one case to another. This is reflected in the electric efficiency of the ORC unit, revealing that achieving 45% global efficiency is only possible if the ICR-MGT gas turbine layout is combined with an ORC system running on R245fa. Additionally, there is a clear trend in the contribution of the ORC unit to total power output. This is measured through the ORC Power ratio, (ORC System Power Output)/(Total Power Output), which decreases as the electric efficiency of the mGT increases, given the lower energy content of the exhaust gases from the turbine; i.e., the lower turbine exhaust temperature reduces the efficiency of the Heat Recovery Vapour Generator, meaning that a lower amount of heat is recovered from the turbine exhaust.

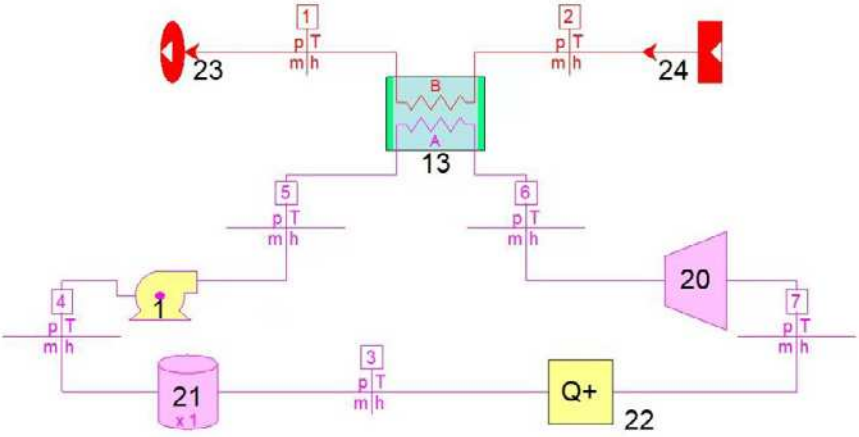

Figure 5. The layout of the ORC (3-4-5-6-7-3) coupled with the exhaust gas stream of an mGT (1 – 2).

Table 5. Results of the hybridized system (Brayton + ORC) considering a maximum pressure of 20 bar. Input parameters are in Table 4.

Parameter	**Unit**	**Value (R-MGT-1/R-MGT-2/ICR-MGT)**								
		R123			**R245fa**			**R1234ze**		
ORC pressure ratio	-	16			13.3			4		
Total electric efficiency	%	35.8	37.9	44.3	35.7	38.2	45.5	32.9	35.5	43.9
ORC system efficiency	%	16.0	16.2	16.3	15.0	15.3	15.4	10.5	10.7	10.7
Total gross electric power	kW	6.88	131.6	441.3	6.85	132.8	453.1	6.32	123.3	437.4
ORC power ratio	-	0.26	0.23	0.09	0.26	0.24	0.12	0.20	0.18	0.08

The effect of maximum cycle pressure is studied next, assuming a pinch point of 5ºC in the vapour generator and a condensation temperature of 25ºC. Figure 6 shows how total electric efficiency is affected by the pressure ratio. The only configuration that achieves the 45% total electric efficiency target is the ICR-MGT with the R245fa organic fluid. In general, for the upper limit of the pressure ratio, it becomes clear that R245fa outperforms R123. For the lower limit of pressure ratio, on the contrary, R1234ze outperforms the other two fluids considered, regardless of the mGT configuration considered. It is worth noting that, due to the constraints set for condensation temperature, the maximum efficiency attainable by R1234ze is limited to 43.5%, corresponding to the ICR-MGT configuration.

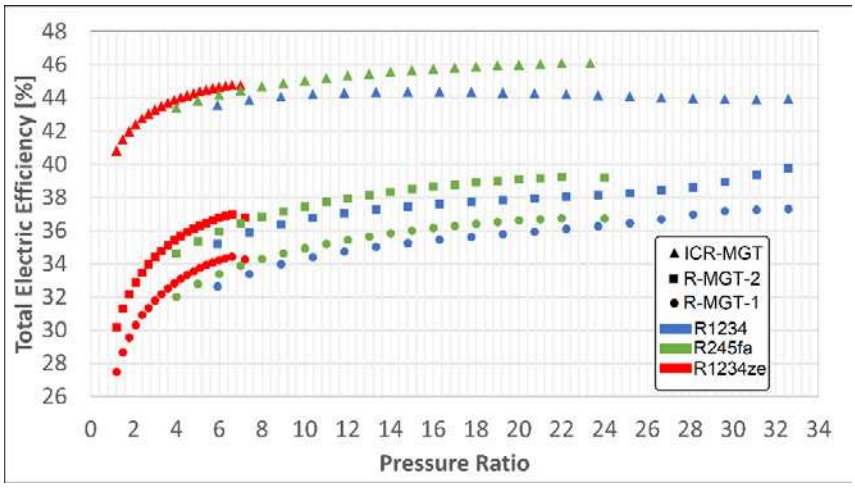

Figure 6. Total electric efficiency when varying the pressure ratio of the ORC system for the 3 mGT configurations and 3 organic fluids.

The results presented reveal that the utilization of a bottoming ORC unit running on R245fa enables achieving the target total electric efficiency of 45%, for a pressure ratio of 10. However, this comes at an environmental cost since, out of the three organic fluids, R245fa has the highest GWP (Table 3), whereas R1234ze presents the lowest value of this index.

Based on these latter results, the authors have conducted a sensitivity analysis to identify the conditions that would enable using an ICR-MGT engine bottomed by an ORC unit running on the least harmful working fluid (R1234ze), still attaining 45% global electric efficiency. The assessment is based on calculating the break-even condensation temperature that would yield 45% total electric efficiency for maximum bottoming cycle pressure of 20 bar and 35 bar. The results obtained suggest that the break-even pressure ratio is 5.8 for the former case (20 bar), for a condensation temperature of 13.3ºC, and these figures increase to a pressure ratio of 7.7 and condensation temperature of 22ºC in the latter case. Therefore, the adoption of R1234ze instead of R245fa in the bottoming system would enable 45% total electric efficiency if the condensation temperature could be reduced.

523

5 CONCLUSIONS

The rationale behind this study is to develop combined (hybrid) mGT-ORC systems that would help to increase the round-trip efficiency of hydrogen-based power-to-power energy storage systems. The authors estimate that breaking the 45% electric efficiency would make the mGT much more competitive and a more solid candidate against the internal combustion engine and fuel cells (Escamilla, 2022) (Escamilla, 2023). To this end, the study focused on three mGT layouts, including the regenerative Brayton cycle (R-MGT) and intercooling-regenerative Brayton cycle (ICR-MGT), and a bottoming ORC system with the simplest layout possible (evaporator, turbine, condenser, pump).

The results of the paper show that the 45% electric efficiency target can be achieved if the ICR-MGT layout is adopted. In particular, the total efficiency could theoretically be as high as 46.1%, with the bottoming ORC system adding 58 kWe to the 400 kWe produced by the mGT. The latter is achieved when the R245fa organic fluid is adopted for a pressure ratio of 10 and a condensation temperature of 25ºC. The 45% electric efficiency barrier can also be surpassed when using the organic fluid R1234ze, which has the lowest GWP value, but with a lower condensation temperature, 22ºC with a pressure ratio of 7.7.

The next steps of this research will look into the correction factors (<1) introduced by scaling effects in turbomachinery and into the economics of the system, in particular as a function of maximum ORC pressure. However, it is to highlight that the additional cost of adopting such a solution would not oppose any major concern as the solution would be integrated into a hydrogen-based power-to-power energy storage system that would dilute the additional cost.

REFERENCES

AE-T100, Ansaldo Energia, [Online]. Available: https://www.ansaldoenergia.com/offering/equipment/turbomachinery/microturbines/ae-t-100. [Accessed 16 04 2023].

Aurelia A400 Turbine, Aurelia, [Online]. Available: https://aureliaturbines.com/aurelia-a400. [Accessed 16 04 2023].

Bao, J., Zhao, L., 2013, A review of working fluid and expander selections for organic Rankine cycle, Renewable and Sustainable Energy Reviews, Elsevier, vol. 24(C), pages 325-342.

Bonolo de Campos, G., Bringhenti, C., Traverso, A., Tomita, J., 2019, A Review on Combining Micro Gas Turbines with Organic Rankine Cycles, SUPEHR19 SUstainable PolyEnergy generation and HaRvesting, E3S Web of Conferences, vol. 113, 03007.

Clemente, S., Micheli, D., Reini, M. Taccani, R., 2013, Bottoming organic Rankine cycle for a small scale gas turbine: A comparison of different solutions, Applied Energy, vol. 106, pp. 355-364.

EnerTwin, MTT, [Online]. Available: https://enertwin.com/. [Accessed 16 04 2023].

Escamilla, A., Sánchez-Martinez, D., García-Rodrgíguez, L., 2022, Assessment of power-to-power renewable energy storage based on the smart integration of hydrogen and micro gas turbine technologies, International Journal of Hydrogen Energy, vol. 47, no. 40, pp. 17505-17525.

Escamilla, A., Sánchez-Martinez, D., García-Rodrgíguez, L., 2023, Techno-economic study of Power-to-Power renewable energy storage based on the smart integration of battery, hydrogen, and micro gas turbine technologies, Energy Conversion and Management: X, vol. 18, p. 100368.

Fuel Cells and Hydrogen Joint Undertaking, 2019, Hydrogen roadmap Europe: A sustainable pathway for the European energy transition, *EU Comission.*

Fuel Cells and Hydrogen Energy Association, 2020, Road map to a US Hydrogen Economy.

Galanti, L., Massardo, A.F., 2011, Micro gas turbine thermodynamic and economic analysis up to 500kWe size, Applied Energy, vol. 88, issue 12, pp. 4795-4802.

Giuseppe, T., Sánchez, D., Torres-García, M., 2023, Applications of the Theory of constraints to unveil the root causes of the limited market penetration of micro gas turbine systems, Energy, vol. 278, pp. 127717.

Mago, P.J., Luck, R., 2013, Energetic and exergetic analysis of waste heat recovery from a microturbine using organic Rankine cycles. International Journal Energy Research, vol. 37, pp. 888-898.

Qiu, G., 2012, Selection of working fluids for micro-CHP systems with ORC, Renewable Energy, vol. 48, pp. 565-570.

Thermoflex, Thermoflow, Version 30, 2022 [Online]. Available: https://www.thermoflow.com/products_generalpurpose.html. [Accessed 16 04 2023].

U.S. Department of Energy's (DOE's) Advanced Manufacturing Office, 2022, 2022 Combined Heat and Power & District Energy System Portfolio Meeting, [Online]. Available: https://www.energy.gov/eere/amo/events/2022-combined-heat-and-power-district-energy-system-portfolio-meeting. [Accessed 31 03 2022].

Vanslambrouck, B., Vankeirsbilck, I., van den Broek, M., Gusev, S., & De Paepe, M., 2012, Efficiency comparison between the steam cycle and the organic rankine cycle for small scale power generation, Renewable Energy World Conference and Expo North America, Proceedings. Presented at the Renewable Energy World Conference & Expo North America, Long Beach, CA, USA.

ACKNOWLEDGEMENT

This work has been developed in the frame of the Next Generation of Micro Gas Turbines for High Efficiency, Low Emissions and Fuel Flexibility, NextMGT, which has received funding from the European Union's Horizon 2020 research and innovation programme under Marie Sklodowska-Curie grant agreement No 861079.

ORC SEVILLE 2023
7th International Seminar on O.R.C. Power Systems

© 2024 Editorial Universidad de Sevilla. Este es un artículo de acceso abierto distribuido bajo los términos de la licencia de uso y distribución Creative Commons (BY-NC-ND 4.0)

DOI: https://dx.doi.org/10.12795/9788447227457_88

OPERATIONAL OPTIMISATION OF THE MAIN HEAT REJECTION UNIT OF CSP PLANTS BASED ON CARBON DIOXIDE MIXTURES

Francesco Crespi*, Pablo Rodríguez-deArriba, David Sánchez, Lourdes García-Rodríguez

University of Seville, Department of Energy Engineering,
Camino de los descubrimientos s/n, 41092, Seville, Spain

*Corresponding Author: crespi@us.es

ABSTRACT

This research, developed in the framework of the SCARABEUS project, studies the off-design performance of transcritical power cycles running on CO_2-SO_2 mixtures in Concentrated Solar Power applications. The objective of this work is to identify optimum operational strategies that maximise net energy production when exposed to variable ambient temperature, with special focus on the operation of the Heat Rejection Unit (Air-Cooled Condenser). The power cycle is simulated in Thermoflex, modified with user-defined scripts to account for the specific off-design performance characteristics of key components. The Air-Cooled Condenser is modelled by means of an in-house Matlab tool, already validated in previous publications, able to accurately simulate the heat transfer process between working fluid and cooling medium (air) and to calculate auxiliary power consumption.

Four different strategies are identified, depending on ambient temperature: variable or constant condensation pressure for ambient temperatures lower than the design value, and constant turbine inlet temperature or constant return temperature of the heat transfer fluid for ambient temperature higher than design value. The results show that a combination of variable and constant minimum cycle pressure is the best alternative for low ambient temperatures, enabling net system efficiencies higher than 41%. On the other hand, constant turbine inlet temperature enables higher net performance than constant return temperature of the heat transfer fluid, even if at the expense of a reduction in energy storage capacity for the same inventory of molten salts.

525

1 INTRODUCTION

Supercritical Carbon Dioxide (sCO_2) power cycles are widely considered as one of the most promising alternatives to enhance the performance of next-generation (higher-temperature) Concentrated Solar Power (CSP) plants, with the final aim of increasing the cost-effectiveness of this technology, thus making it more competitive in the energy market. This is due to some outstanding features of sCO_2 power cycles such as their high thermal efficiency and low footprint, which are in turn enabled by the fact that the compression process is undertaken at high density in the proximity of the critical point (31ºC). Unfortunately, this operating temperature is difficult to achieve in CSP sites, with high Direct Normal Irradiance and ambient temperatures (T_{amb}), resulting in a clear drop in cycle thermal efficiency (Crespi *et al.*, 2022b). This is aggravated by the need to adopt dry-cooling systems in order to reduce water consumption of the power plant, what brings about two harmful effects on cycle efficiency: higher compressor work (lower thermal efficiency) and higher auxiliary power consumption (lower net efficiency). Several authors have investigated different cooling options (Moisseytsev *et al.*, 2017; Pidaparti *et al.*, 2020) and operational strategies to optimise the off-design performance of sCO_2 power

cycles (Alfani *et al.*, 2020; Neises, 2020). Nevertheless, none of these solutions is really able to effectively tackle the detrimental effect of increased T_{amb} on cycle performance.

An alternative solution to this problem is proposed by the SCARABEUS project: increasing the critical temperature of the working fluid (WF) thanks to the addition of certain dopants to the raw CO_2, thus allowing condensation of the working fluid at high T_{amb}. This restores thermal efficiency to the very high values that are achieved at lower ambient temperature when pure CO_2 is used. The thermodynamic potential of this concept has already been demonstrated extensively in previous publications (Crespi *et al.*, 2022a; Crespi *et al.*, 2022b). Building upon that, and in order to take a further step towards the commercialisation of this technology, it is necessary to evaluate possible operational strategies in off-design conditions, especially taking into account the different nature of the SCARABEUS cycles (transcritical instead of supercritical). In this regard, the behaviour of the working fluid during condensation becomes very relevant (more information in Section 3).

Bearing all this in mind, this paper presents the principles of the operational optimisation of CSP plants based on CO_2 mixtures. Firstly, the computational environment and the reference power plant are presented. Secondly, the possible operating strategies are discussed, together with the specific constraints posed by the use of a condensing cycle; this calls for a focus on the operation of the Air Cooled Condenser unit (ACC). Finally, the results of a sensitivity analysis to ambient conditions are presented and discussed, identifying the operation strategy yielding the best off-design performance of the SCARABEUS system.

2 COMPUTATIONAL ENVIRONMENT

This article presents an in-depth analysis of a central receiver CSP plant with a two-tank molten-salt TES system and a transcritical recompression cycle operating on a mixture of 80%CO_2-20%SO_2 in the power block (PB), see Figure 1 (left). This is an adaption of the recompression cycle using pure CO_2 that has been widely studied in literature for next-generation CSP applications (Neises, 2020; Alfani *et al.*, 2022). The PB has been modelled using the Thermoflex v30 with specific performance models for various of the components added via LUA scripts. The thermophysical properties of the working fluid have been incorporated via look-up tables using the 'user-defined refrigerant fluid'. This approach has been adopted in order to obtain a robust calculation platform, while overcoming the lack of specific performance models for equipment running on CO_2 mixtures in Thermoflex. The complete set of specifications is provided in Table 1. The reference location is Seville, Spain, for which meteorological data have been obtained from a public database (EnergyPlus). The design temperature is estimated at 36°C, corresponding to the 95th percentile; according to the available data, the annual ambient temperature in Seville ranges from -2°C to 43°C. To assess the performance of the system under extreme conditions, a range of interest from 0°C to 50°C has been assumed (a conservative assumption, considering that temperatures exceeding 47ºC have never been recorded in the area).

Table 1: Design specifications of the power block

Parameter	Value	Parameter	Value	Parameter	Value
W_{Gross} [MW]	100	TIT [ºC]	550	TOT [ºC]	412.2
T_{min} [ºC]	50	$T_{HTF,in}$ [ºC]	565	$T_{HTF,out}$ [ºC]	387.2
P_{max} [bar]	250	P_{min} [bar]	79.1	η_{th} [%]	44.1

The Heat Rejection Unit of the power block is a modular air-cooled condenser (ACC), capable of condensing the working fluid even in warm operating conditions. The technology employed is a horizontal, direct air-cooled heat exchanger, with axial induced-draft fans (see Figure 1, right), following the indications of the industrial partner of the SCARABEUS consortium. The authors have developed a Matlab-based design and simulation tool of the ACC, built upon preliminary work of Illyés *et al.* (2022) and first presented in (Rodríguez-de Arriba, 2023a). Three different types of bays are studied in (Rodríguez-de Arriba, 2023b): bay with 3 single-speed (i.e., on/off) fans (called *Bay1*), bay

with 2 single-speed and 1 Variable Frequency Drive (VFD) fan (*Bay2*) and bay with 3 VFD fans (*Bay3*). These three scenarios provide an opportunity to evaluate tradeoffs between capital and operational expenses of the ACC. Increasing the number of VFD fans reduces the fan power consumption but also raises installation costs (fans equipped with VFD are ~60% costlier than single-speed fans).

The Primary Heat Exchanger (PHX) is a shell-and-tube heat exchanger with the working fluid in the tubes and molten salts on the shell side. Thermoflex is used to produce a design of the PHX whereas off-design performance is evaluated using the Conductance Ratio Method through a Matlab routine (Crespi *et al.*, 2017).

For further information about the assumptions underlying the aforementioned simulation platform, interested readers may refer to (Rodríguez-de Arriba *et al.*, 2023b).

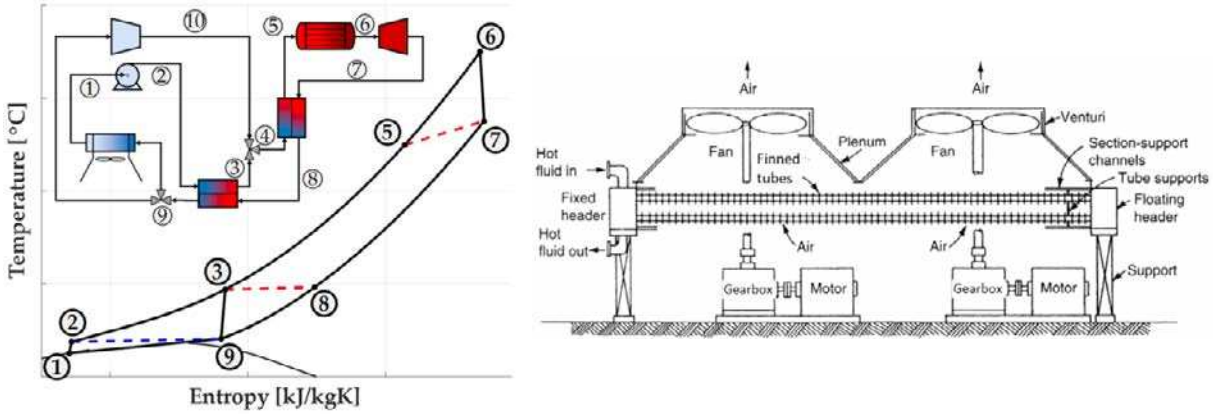

Figure 1: Left: Transcritical Recompression Cycle running on 80%CO_2-20%SO_2 mixture: layout and temperature-entropy diagram – **Right:** General scheme of an induced draft ACHE (Adapted from Serth & Lestina, 2014)

527

3 OPERATING STRATEGIES AND CONSTRAINTS

This study aims to investigate the operation of the subsystem composed by the PB-ACC-PHX in off-design conditions, a topic already assessed by the authors in (Rodríguez-de Arriba *et al.*, 2023b). The objective is to define an operating strategy that yields the best performance of the subsystem while satisfying the operational constraints. The system is assumed to operate base load, and the objective is maximise the annual yield of the power plant. This means that circulating mass flow rate in the system remains somewhat constant, modified by the need to compensate for the variable ambient conditions.

The following operational constraints set by the safe operation of the system are considered:

- Maximum cycle pressure (P_{max}) cannot exceed the design value (250 bar) by more than 5%;
- The turbine operates in sliding pressure;
- Turbine inlet temperature cannot exceed the design value (550ºC), in order to maintain a 15ºC temperature difference with the hot molten salts ($T_{HTF,in}$ fixed at 565ºC).
- Turbine outlet temperature should not exceed 450ºC, a threshold value set by the industrial partners of the project with the aim to avoid the installation of a specific cooling system in the turbine exhaust duct.
- The power consumption of the fans cannot exceed its rated value by more than 5%.
- Turbomachinery (recompressor and turbine) must operate within the safe and stable limits of their respective performance maps.

Regarding the last bullet point, it is of utmost importance to carefully consider the operation of the recompressor, owing to its close proximity to the two-phase region of the phase diagram. This applies

to the operating conditions in the inducer in particular, where cooling arises due to local acceleration. The numerical quantification of this effect can be implemented through a similarity parameter (C) defined by Romei *et al.* (2021), which is a generalisation of the cavitation parameter (see Eq. 8 in the reference). In this work, C^* is defined as the ratio from the actual value of C for a given set of operating conditions to the rated value of such parameter. Bearing this in mind, $C^*>1$ denotes a safer operation than in the design point, $C^*=0$ indicates that the inlet to the recompressor falls inside the condensation dome, and $0<C^*<1$ indicates operating conditions in between the former two (the higher C^*, the safer the operation). Similarly, the flow coefficient of the recompressor and the turbine is evaluated by normalising it to its design value.

Special attention is paid to the operation of the ACC, for which an approach similar to that presented in a previous study by the authors (Rodríguez-deArriba, 2023b) is adopted. In this previous work, component count (i.e., the installation of several units in parallel) was studied as a means to minimise auxiliary power consumption at reduced mass flow rates by independently controlling the mass flow rate flowing through each bay. However, since all bays must operate under the same conditions as long as mass flow rate takes the rated value, this is less relevant in this study. Therefore, the results obtained for one bay are extrapolated to the entire set of bays in this work.

The performance of the ACC is studied at the rated condensation pressure (P_{min}=79.1 bar, corresponding to T_{bub} of 50ºC). Figure 2 illustrates the influence of ambient temperature on the minimum temperature of the working fluid (T_{min}, Figure 2a) and on relative fan power consumption ($W_{ACC,norm}$, Figure 2b) for various combinations of fans in operation and/or reduced fan speeds. Different ACC operation modes are represented (coloured lines) and labelled according to the rotational speed of the VFD fans (ω_i) relative to its rated value: ω_i=1 means fan operating at rated speed, ω_i=0 means fan not in operation, $0<\omega_i<1$ means a VFD fan operating at reduced speed (more information in Rodríguez-de Arriba, 2023b). Any point of the map exhibiting a T_{min} below the bubble temperature (50ºC) represents an operating point where the working fluid is subcooled. The operation of the ACC according to the type of bay under consideration (*Bay1, Bay2* or *Bay3*) can be plotted on this figure.

Avoiding subcooling of the working fluid is not possible if all cells use single-speed fans (*Bay1*), and this has a negative impact on cycle efficiency since the best thermal performance is obtained when the condenser yields saturated fluid at pump inlet ($T_{min}=T_{bub}$); unfortunately, this is possible only if -at least- one fan in each bay incorporates VFD (*Bay2* and/or *Bay3*). It is also observed that, at T_{amb}<27ºC, one of the three fans of *Bay1* can be turned off (ACC operation changes from [1,1,1] to [0,1,1]), hence reducing the fan power consumption to around 67% of the design value. However, it is not possible to shut down a second fan within the temperature range studied (>0ºC), and this yields a higher W_{ACC} for the *Bay1* case than for *Bay2* and *Bay3*. This applies to *Bay2* also but, for this case, the fan with VFD facilitates the transition from the design point (36ºC) to 27ºC, thus reducing fan power consumption. Moreover, a significant reduction in power consumption with respect to *Bay1* is also noticeable below 27ºC, with fan power consumption reaching 35% the rated value. As expected, *Bay3* offers the largest reduction of fan power at part load, reaching 80% when ambient temperature drops from 36ºC to just 30ºC; this is at the expense of a 8% higher capital cost (more info in Rodríguez-de Arriba, 2023b).

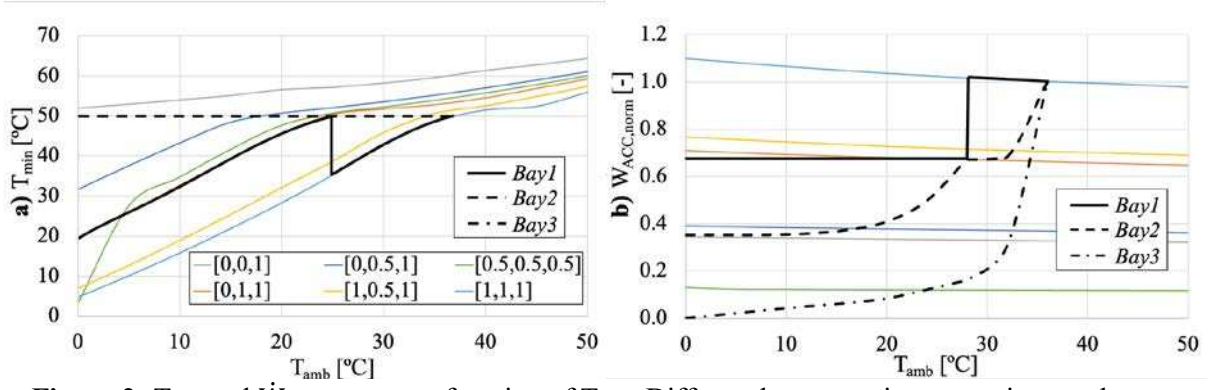

Figure 2: T_{min} and $\dot{W}_{ACC,norm}$ as a function of T_{amb}. Different bay operating strategies are shown.

The previous considerations have been made for constant P_{min}, equal to the design value and corresponding to T_{bub}=50ºC. Nevertheless, the same methodology can be applied to other condensation pressures (hence, different T_{bub}), to create an operational map of the ACC for operation at variable pressure. This is presented in Figure 3, where ACC power consumption is shown as a function of T_{amb} for different T_{bub} and considering T_{min}=T_{bub} (no subcooling at condenser outlet). The blue line represents the running line of the condenser when the fans operate at rated speed (thus, maximum condenser capacity). This operation strategy results in variable P_{min}; also, since subcooling of the working fluid is not allowed (T_{min}=T_{bub}), a lower T_{amb} brings about lower T_{min} (thus, T_{bub}) and P_{min}; in other words, T_{min} always reaches the minimum value achievable by the heat rejection capacity of the ACC. For instance, T_{min} can be reduced from 50ºC to 45ºC when T_{amb} decreases from 36ºC to 30ºC though this is partly offset by the effect of a higher density on power consumption.

The black line in Figure 3 represents operation at constant P_{min}, same case as the dashed line in Figure 2b. It is to note that Figure 3 is based on an ACC with the *Bay2* architecture, a choice aimed at balancing operational and investment costs; a similar study could have been undertaken also considering *Bay1* and *Bay3*, but this is not reported here due to length limitations.

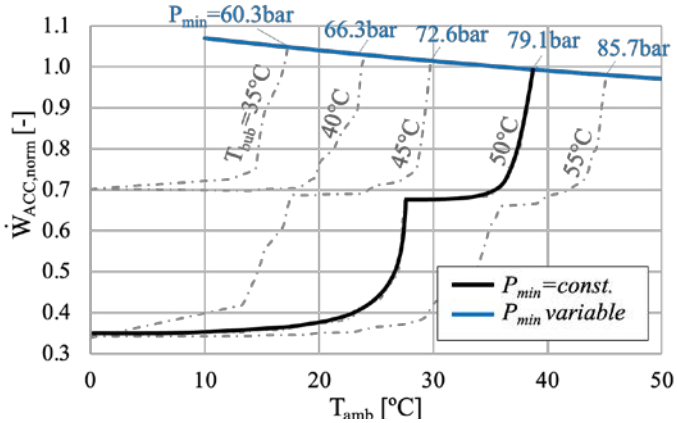

Figure 3: Operational map of the ACC at different T_{amb}

From the foregoing results, the following two strategies for operation at variable ambient temperature are identified:

1. *Constant condensation pressure*: the condenser is oversized for the required cooling capacity at reduced ambient temperature. Therefore, it is possible to reduce fan speed or even shutdown some of them whilst the power block remains unaffected, hence with constant gross efficiency. Net efficiency, on the contrary, increases due to the lower power consumption of the ACC fans.
2. *Variable condensation pressure*: condensation pressure is reduced as much as allowed by the condenser; by doing so, it is possible to achieve lower minimum cycle temperature, potentially increasing cycle efficiency. The fans run at their nominal speed and, hence, fan power remains at the rated value approximately. As a drawback, this strategy poses several challenges to system control, as discussed in the next section.

A final remark regarding operation at higher than rated ambient temperature is also needed. In such conditions, the ACC would not be able to condense the nominal flow rate of working fluid at P_{min} and without violating the restriction not to exceed the rated power of the fans. Thus, the only viable option is to increase condensation pressure, keeping all the fans running at full speed. However, the increase in P_{min} comes with a higher minimum cycle temperature and, thus, with a lower thermal efficiency of the cycle. As a consequence, net system efficiency should be expected to drop significantly; moreover, it has been observed that the return temperature of the HTF in the Primary Heat Exchanger ($T_{HTF,out}$) increases with respect to the design value in these cases, what has a potentially detrimental effect on the energy storage capacity of the TES (Neises, 2020). To overcome this issue, an active control of TIT has

already been presented in previous work by the authors (Rodríguez-deArriba, 2023b), and it is investigated in the next section.

4 RESULTS

4.1 Variable condensation pressure strategy: benefits and limitations

This section explores the performance of the power block when condensation pressure is varied through variations of the minimum cycle temperature. The objective of this study is to get a better understanding of how the different operational constraints evolve under different minimum cycle temperature, both below and above the design point, and to estimate the gross performance of the system (η_{th}). The results are presented in Figure 4. Nine figure of merits are reported: (a) η_{th}, (b) P_{max}, (c) TIT, (d) TOT, (e) $T_{HTF,out}$, (f) C^*, (g) m_{HTF}, (h) flow coefficient of the recompressor ($\Phi_{RECOMPR}$) and (i) flow coefficient of the turbine (Φ_{TURB}). The design point is indicated with a black marker and corresponds to the boundary conditions provided in Table 1. It is to note that, if constant condensation pressure operation is adopted, the system always runs at this point.

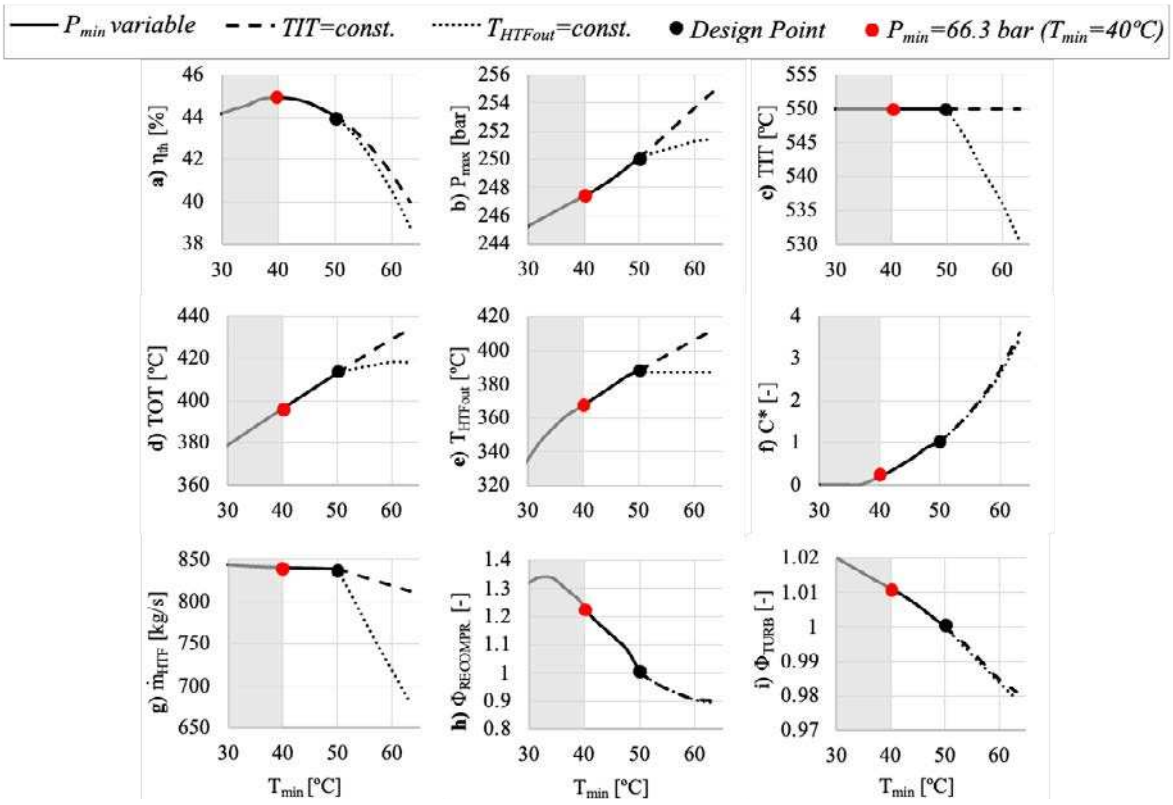

Figure 4: System performance adopting variable P_{min} strategy as a function of T_{min} (various parameters). Sub-figure captions are provided in the y-axis.

Operating conditions for minimum cycle temperature lower than the design value are represented with a solid black line. Thermal efficiency peaks at T_{min}~40ºC, owing to the lower recuperative potential of the system at lower P_{min}, as a consequence of the lower turbine exhaust temperature (TOT). Regarding turbomachinery, the turbine flow coefficient increases slightly due to changes in the speed of sound caused by the fluctuations of P_{max}. However, the most critical situation arises in the recompressor since its inlet temperature decreases as P_{min} decreases, getting closer to the dew point and reducing the safety margin C^*. When T_{min} falls below 40ºC, the inlet to the recompressor falls inside the condensation dome, meaning that the system cannot be operated at variable P_{min} for T_{min}<40ºC (corresponding to T_{amb}~24ºC, see Figure 3, intersection between variable P_{min} and T_{bub}=40ºC). This condition is graphically represented by the grey areas in Figure 4.

A possible solution to extend the operational range of the system to lower ambient temperatures is to employ a hybrid solution: variable P_{min} down to T_{min}=40ºC followed by constant P_{min}, where P_{min} is kept at a constant value of 66.3 bar (corresponding to T_{min}=40ºC). In this second range, the thermal efficiency of the power block remains unchanged, and this is represented by a red marker in Figure 4. It is worth noting that the selection of P_{min}=66.3 bar (corresponding to T_{min}=40ºC) is an arbitrary choice, driven by the fact that such conditions maximise η_{th} (see Figure 4a). Nevertheless, such value could still be problematic for the safe operation of the recompressor (C^* close to 0). In this regard, future works will investigate different values of P_{min} in order to find the best compromise between thermal performance and operability of the cycle.

It is interesting to observe that the temperature of the Heat Transfer Fluid (molten salts) at the outlet from the Primary Heat Exchanger ($T_{HTF,out}$) decreases for operation at variable P_{min}. One approach to control this temperature would be to reduce the mass flow rate circulating through the system. However, this would also reduce the electric output of the plant and, accordingly, the performance gains in comparison with the operation at constant pressure. Furthermore, as demonstrated by Rodríguez-de Arriba (2023b), reducing the mass flow rate when operating at part load shifts hte inlet conditions to the recompressor towards the dew line, thus reducing C^* even further. Another approach would be increasing turbine inlet temperature above its design value, which has been ruled out in this study in order to maintain a minimum temperature difference of 15ºC between the working fluid and the Heat Transfer Fluid.

The operation at very high minimum cycle temperatures (T_{min}>50ºC) does, on the contrary, not pose any particular challenges to the safe operation of the system. Two operating strategies are investigated for this case, the first one of which relies on operating the system at constant TIT (dashed lines in Figure 4). As mentioned in the previous section, increasing minimum cycle pressure (P_{min}) results in lower gross (thermal) efficiency, around 2 percentage points (p.p) when T_{min} increases from 50ºC to 60ºC. This also translates into maximum cycle pressures (P_{max}) shifting to values slightly above the design value (<5 bar) given that the system operates in sliding pressure; these higher pressures are, nevertheless, not foreseen to incur substantially higher mechanical stresses on the component.

Turbine outlet temperature also increases but it always remains below the aforementioned 450ºC threshold, thus avoiding the need for a specific duct cooling system. The flow coefficients of both the recompressor and turbine decrease slightly, well within the limits of the performance map. C^* experiences a large increase, from 1 (design) to 3 at 60ºC, meaning that the recompressor operates with a larger safety margin than in design conditions. Unfortunately, the temperature of the HTF at the outlet from the Primary Heat Exchanger ($T_{HTF,out}$) increases significantly and this reduces the thermal energy storage capacity of the TES for the same inventory of molten salts. In order to avoid this, a new control strategy based on reducing turbine inlet temperature with the aim to operate at constant $T_{HTF,out}$ is considered. This strategy is represented by the dotted lines in Figure 4, where it is observed that TIT is reduced by 15ºC when minimum cycle temperature (T_{min}) increases 10ºC above the design point. This operation brings about lower thermal efficiency than when turbine inlet temperature is kept constant. As a minor benefit though, the increase in turbine inlet pressure when running at high minimum cycle pressure is halved, also with respect to constant TIT operation (1.3 bar *vs.* 3.6 bar). Furthermore, the mass flow rate of HTF is largely reduced, driven by the larger temperature drop of this fluid across the Primary Heat Exchanger. This brings about a lower HTF pumping power (lower auxiliary power consumption) that is beneficial in terms of net cycle efficiency of the plant.

4.2 Comparison between different operational strategies

In this last section, the operational strategies discussed previously are compared in terms of net system efficiency; in the following, net power output (W^*_{net}) and net efficiency (η^*_{net}) account for the contribution of the auxiliary power consumption of the ACC as well as the mechanical losses caused by the electric motors coupled to pump and recompressor, losses in the electric generator and HTF pumping power to enable the flow of molten salts from hot to cold tank through the PHX. A complete description of all the assumptions is provided in Rodríguez-de Arriba (2023b).

The results are presented in Figure 5. Two different strategies are considered at ambient temperature below the design point (T_{amb}<36ºC). First, the operation at constant minimum cycle pressure (P_{min}) (dashed-and-dotted lines) considers that the power block operates at the design point continuously (see marker in Figure 4) and the improvement in W^*_{net} and η^*_{net} is caused by the lower fan power consumption in the ACC, following the map presented in Figure 2b. A smooth transition is observed at ~27ºC, where one single-speed fan of the ACC is shut down.

The operation at variable minimum cycle pressure (P_{min}) is presented in black solid lines in Figure 5. Using this operational strategy, P_{min} is reduced with ambient temperature (T_{amb}) following the blue line in Figure 3 until the minimum cycle temperature (T_{min}=40ºC) is reached, what happens at T_{amb}~24ºC. Beyond this point, minimum cycle temperature cannot be reduced further as, otherwise, the inlet to the recompressor would fall within the two-phase region (see previous section). Consequently, for T_{amb}<24ºC, the system operates at a constant T_{min}=40ºC (red solid lines) with the ACC following the corresponding line in Figure 3; this reduces fan power consumption of the ACC at low T_{amb} (such drop in W_{ACC} being the cause of the smooth increase in W^*_{net} and η^*_{net} when moving from 24ºC to 20ºC). This hybrid strategy achieves an increase in η^*_{net} of ~1 p.p. with respect to constant P_{min} and ~12 MW_e higher electric output (roughly 13% higher W^*_{net}). It is worth noting that this significant gain in W^*_{net} is due not only to the higher η_{th} but also to the fact that more thermal energy is being extracted from the same m_{HTF} (because of the lower $T_{HTF,out}$ enabled in the hybrid strategy than in the constant P_{min} strategy: 360ºC *vs.* 380ºC). This suggests the idea that operating the system at variable minimum cycle pressure (P_{min}) can potentially increase the annual yield of the plant, though it also presents a more complex operation given the potential condensation of the working fluid at the inlet to the recompressor. Further research on this topic is thus required to investigate the actual feasibility of this operational strategy.

For operation at high ambient temperature (higher than the design value), operation at constant TIT or at constant $T_{HTF,out}$ are possible. The resulting trends of η^*_{net} are very similar to those observed in Figure 4a for η_{th}. For operation at constant TIT, a 3 p.p. drop in η^*_{net} is observed when ambient temperature increases from 36ºC to 50ºC. In terms of net power output, this means ~16 MWe. If operation at constant $T_{HTF,out}$ is adopted, the system suffers an additional reduction in η^*_{net} and W^*_{net} of around 0.75 p.p. and 4 MWe, respectively. These results suggest that operating at constant TIT leads to higher net performance of the cycle. Nevertheless, the detrimental effect on thermal energy storage capacity, hence CAPEX (see previous section), must be borne in mind and its impact on the overall economics of the plant must be assessed before a final recommendation can be made. This is currently being explored by the authors in the context of the SCARABEUS project.

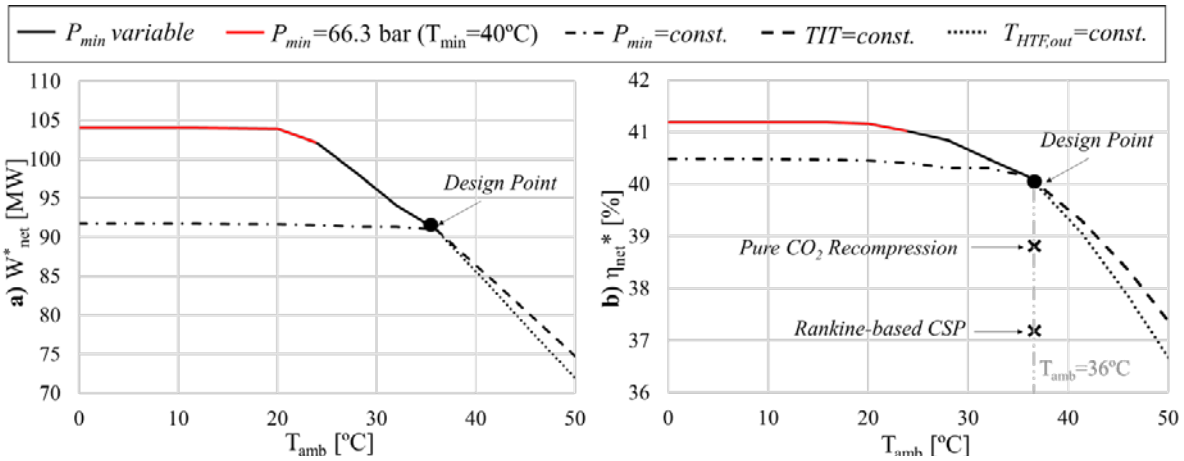

Figure 5: Net power (a) and net efficiency (b) as a function of ambient temperature for various operating strategies

This final part of the paper provides a quick comparison of the SCARABEUS system against the alternative technologies for CSP, either established or under development: steam turbines and pure sCO_2 power systems. To this aim, the net efficiency of the system η^*_{net} is compared for all three cases,

considering similar boundary conditions. The results are presented in Figure 5b, where a reference net efficiency of 37.1% is assigned to a state-of-the-art steam-based CSP plant operating at 574ºC (molten salts temperature). This value corresponds to a gross efficiency of 41.2%, corrected with a gross-to-net conversion efficiency of 0.9, according to the recommendations in (NREL, 2022). The net efficiency of a recompression sCO_2 cycle is, on the other hand, calculated with the in-house platform used to estimate the performance of the SCARABEUS system, using the same boundary conditions specified in Table 1. Comparing the rated performance of these three technologies, the large potential of the SCARABEUS concept is confirmed inasmuch as the utilisation of CO_2 mixtures enables 1 p.p. and 2.4 p.p. net efficiency gains with respect to using pure sCO_2 systems and steam turbines, respectively. Future works by the authors will address a detailed techno-economic comparison of these technologies, based on LCoE and annual yield.

5 CONCLUSIONS

This study has discussed different operating strategies of CSP plants based on supercritical power cycles running on CO_2 mixtures in off-design conditions, with special focus on the operation of the Air-Cooled Condenser. The power block is a transcritical (condensing) recompression cycle operating on 80%CO_2-20%SO_2 is considered. Four different strategies are identified, depending on ambient temperature: variable or constant condensation pressure (P_{min}) for ambient temperature lower than the design point, and constant Turbine Inlet Temperature (TIT) or constant HTF return temperature ($T_{HTF,out}$) for ambient temperature higher than the design value.

The following conclusions are drawn:

- Operation at variable minimum cycle pressure (P_{min}) leads to potentially higher net efficiency and net power output than operation at constant P_{min}. As a drawback, this strategy poses the need for a specific control of the inlet conditions to the recompressor, which experience an important excursion towards the dew line.
- In this regard, the plant cannot be operated at variable minimum cycle pressure T_{min}<40ºC (T_{amb}<24ºC), since the recompressor inlet would experience condensation (assuming thermodynamic equilibrium). To overcome this issue, a hybrid strategy combining variable P_{min} down to T_{min}=40ºC and constant P_{min} for T_{min}<40ºC is explored. This hybrid strategy achieves significantly better performance than the operation at constant P_{min}.
- For ambient temperatures higher than the design value, operating at constant TIT brings about better performance than operating at constant $T_{HTF,out}$. Nevertheless, this comes at the expense of a higher CAPEX for the same storage capacity due to the need for a larger inventory of molten salts.
- In order to identify the best operational strategy, maximising the annual yield and minising LCoE, further investigations are needed. Yet, the present study sets the grounds for this further analysis.

NOMENCLATURE

ACC	Air-cooled condenser	T_{bub}	Bubble temperature [ºC]
C^*	Normalised two-phase parameter	$T_{HTF,out}$	HTF return temperature [ºC]
CSP	Concentrated Solar Power	TIT	Turbine Inlet Temperature [ºC]
HTF	Heat Transfer Fluid	T_{min}	Minimum cycle temperature [ºC]
m_{HTF}	HTF mass flow rate [kg/s]	TOT	Turbine Outlet Temperature [ºC]
PB	Power Block	VFD	Variable Frequency Drive
PHX	Primary Heat Exchanger	WF	Working fluid
P_{max}	Maximum cycle pressure [bar]	W	Power [MW]
P_{min}	Minimum cycle pressure [bar]	η	Efficiency [%]
p.p	Percentage points	ϕ	Flow coefficient
T_{amb}	Ambient temperature [ºC]		

REFERENCES

Alfani, D. *et al.* (2020) 'Off-design performance of CSP plant based on supercritical CO_2 cycles', in. *SOLARPACES 2019: International Conference on CSP and Chemical Energy Systems*, Daegu, South Korea. Available at: https://doi.org/10.1063/5.0029801.

Alfani, D. *et al.* (2022) 'Techno-economic analysis of CSP incorporating sCO_2 brayton power cycles: Trade-off between cost and performance', in. *SOLARPACES 2020: 26th International Conference on Concentrating Solar Power and Chemical Energy Systems*, Freiburg, Germany. Available at: https://doi.org/10.1063/5.0086353.

Crespi, F. *et al.* (2017) 'The Conductance Ratio Method for Off-Design Heat Exchanger Modeling and its Impact on an sCO_2 Recompression Cycle', in *Proceedings of ASME Turbo Expo 2017*, Charlotte, North Carolina, USA. Available at: https://doi.org/10.1115/GT2017-64908.

(a) Crespi, F. *et al.* (2022) 'Preliminary investigation on the adoption of CO_2 -SO_2 working mixtures in a transcritical Recompression cycle', *Applied Thermal Engineering*, 211. Available at: https://doi.org/10.1016/j.applthermaleng.2022.118384.

(b) Crespi, F. *et al.* (2022) 'Thermal efficiency gains enabled by using CO_2 mixtures in supercritical power cycles', *Energy*, 238. Available at: https://doi.org/10.1016/j.energy.2021.121899.

EnergyPlus Weather Data Base. Available online: https://energyplus.net/weather

Illyés, V. *et al.* (2022) 'Design of an Air-Cooled Condenser for CO_2-based Mixtures: Model Development, Validation and Heat Exchange Gain with Internal Microfins', in *Proceeding of ASME Turbo Expo 2022*, Rotterdam, Netherlands. Available at: https://doi.org/10.1115/GT2022-82438.

Moisseytsev, A., Lv, Q. and Sienicki, J.J. (2017) 'Heat Exchanger Options for Dry Air Cooling for the sCO2 Brayton Cycle', in *Proceedings of ASME Turbo Expo 2017*, Charlotte, North Carolina, USA. Available at: https://doi.org/10.1115/GT2017-63187.

Neises, T. (2020) 'Steady-state off-design modeling of the supercritical carbon dioxide recompression cycle for concentrating solar power applications with two-tank sensible-heat storage', *Solar Energy*, 212. Available at: https://doi.org/10.1016/j.solener.2020.10.041.

NREL (2022) "2022 Annual Technology Baseline." National Renewable Energy Laboratory. Golden, CO. Available at: https://atb.nrel.gov/.

Pidaparti, S., White, C.W, Weiland, N.T. (2020). 'Cooling system cost and performance models to minimize cost of electricity of direct sCO_2 power plants', in *Proceedings of the 7th International Supercritical CO_2 Power Cycles Symposium*, San Antonio, Texas.

Rodríguez-deArriba, P. *et al.* (2022) 'The potential of transcritical cycles based on CO_2 mixtures: An exergy-based analysis', *Renewable Energy*, 199. Available at: https://doi.org/10.1016/j.renene.2022.09.041.

(a) Rodríguez-deArriba, P. *et al.* (2023). 'A methodology to design air-cooled condensers for supercritical power cycles using carbon dioxide and carbon dioxide mixtures'. In: *Proceedings of the 5th European sCO_2 Conference for Energy Systems*, Prague, Czech Republic.

(b) Rodríguez-deArriba, P. *et al.* (2023). 'Assessment of part-load operation strategies of supercritical power cycles using carbon dioxide mixtures in CSP plants, including air-cooled condenser optimisation', in: *Proceedings of ASME Turbo Expo 2023,* Boston, USA.

Romei, A., Gaetani, P. and Persico, G. (2021) 'On sCO_2 Compressor Performance Maps at Variable Intake Thermodynamic Conditions', in *Proceedings of ASME Turbo Expo 2021*, Virtual, Online. Available at: https://doi.org/10.1115/GT2021-60252.

Serth, R. W., & Lestina, T. (2014). *Process heat transfer: Principles, applications and rules of thumb*. Academic press.

ACKNOWLEDGEMENT

The SCARABEUS project has received funding from the European Union's Horizon 2020 research and innovation programme under grant agreement Nº814985. The Spanish Ministry of Universities is gratefully acknowledged for sponsoring the contract of Pablo Rodríguez de Arriba via FPU (Formación de Profesorado Universitario). Grant reference FPU21/04892.

ORC SEVILLE 2023
7th International Seminar on O.R.C. Power Systems

© 2024 Editorial Universidad de Sevilla. Este es un artículo de acceso abierto distribuido bajo los términos de la licencia de uso y distribución Creative Commons (BY-NC-ND 4.0)

DOI: https://dx.doi.org/10.12795/9788447227457_89

Mechanical Design and Rotor-dynamic Analysis of the ORCHID Turbine

Matteo Majer[1], Steven Chatterton[2], Ludovico Dassi[2], Alessio Secchiaroli[1], Edoardo Gheller[2], Carlo De Servi[1], Paolo Pennacchi[2], Piero Colonna[1], Matteo Pini[1,*]

[1] *Propulsion and Power, Delft University of Technology, Delft, The Netherlands*
[2] *Department of Mechanical Engineering, Politecnico di Milano, Milano, Italy*

*Corresponding Author: m.pini@tudelft.nl

ABSTRACT

The ORCHID turbine is a 10 kW, high-speed (~100 krpm) radial-inflow organic Rankine cycle (ORC) turbine, under realization in the Propulsion and Power laboratory of Delft University of Technology. The turbine will be installed and tested in the Organic Rankine Cycle Hybrid Integrated Device (ORCHID) facility, the setup for fundamental and applied studies on ORC technology currently in operation in the same lab. Experimental data from future measurement campaigns will be employed to validate numerical tools and develop best practices for designing and operating these unconventional machines.

This work documents the recent design efforts to define the functional requirements, the necessary components, and the mechanical assessment of the turbine test bed. In particular, the detailed design of the rotor assembly, carried out in cooperation with the Rotor-dynamic research group of Politecnico di Milano, is described with emphasis on three main aspects. First, the derivation of the damping characteristics of a squeeze-film-damper cartridge for turbochargers, which has been selected as support bearing for the turbine shaft. Secondly, the estimation of the stiffness and damping coefficients of a labyrinth gas seal with swirl breakers, using 3D CFD simulations of the flow path. Finally, linear elastic rotordynamic simulations were performed on a finite beam element model of the resulting turbine shaft. The bearing stiffness, initially estimated using Hertz contact theory, was varied to investigate the sensitivity of the rotor critical speeds to it.

1 INTRODUCTION

The high-speed, supersonic radial-inflow turbine (sRIT) is the core component of high-temperature organic Rankine cycle (ORC) turbogenerators of power capacity in the 5-100 kW range. These energy conversion systems can be utilized for recovering discharged thermal energy from airborne systems (Perullo, et al., 2013), propulsive engines (Glensvig, et al., 2016), gas turbines for stationary power generation (Cerza, et al., 2022), and flow streams of industrial processes (Wieland, et al., 2023). Several past works (De Servi, et al., 2019), (Cappiello & Tuccillo, 2021) , (Cappiello, et al., 2022) document best practices for the optimal design of sRIT and show that comparatively high fluid-dynamic efficiency (~80-85%) can be attained. An experimental verification of their performance is however lacking and, accordingly, a validation of the methods and tools used for their design has not been performed yet.

The ORCHID turbine is a 10 kW, high-speed (~100 krpm) radial-inflow organic Rankine cycle (ORC) turbine, operating with siloxane MM. This machine will be installed and employed for experimental research in the organic Rankine cycle hybrid integrated device (ORCHID) (Head, 2021), in operation at the aerospace propulsion and power laboratory (APP-lab) of Delft University of Technology. Data derived from future measurement campaigns will serve to i) demonstrate that the high fluid-dynamic performance of RIT predicted by theoretical and numerical studies (De Servi, et al., 2019) are achievable in practice ii) validate the numerical tools employed for the design of these highly unconventional turbines, and iii) develop experience and best practices for their optimal operation, including the thermal management of the bearings system.

Experimentally characterizing the fluid-dynamic performance of small-scale ORC turbines requires a setup that can, most importantly, enable stable and safe operation of the machine from start-up up to nominal design point, and at off-design conditions. A few test benches for small-scale ORC turbines

are currently operational throughout Europe. In 2017, the TFD institute at Leibniz University in Hannover (Seume, et al., 2017) has developed a facility for testing a small-scale, 10kW axial flow impulse turbine operating with ethanol and featuring partial admission nozzles. The rotational velocity at the design point is 100 krpm, while the maximum stage pressure ratio of ~50 was achieved in the half admission operation. The rotor is supported on custom, high precision ball bearings and forms a single turbine-generator unit. More recently, LUT University (Uusitalo, et al., 2020) has commissioned a test facility resembling an organic Rankine cycle turbogenerator and featuring a ~12 kW radial inflow turbine operating with siloxane MDM as expander. The turbine stage was designed to operate at 31500 rpm, with a total-to-static pressure ratio of ~112. The rotor is supported on hydrodynamic bearings operating with MDM in liquid phase and is equipped with a permanent magnet generator for shaft to grid power conversion. Finally, the Laboratory of Applied Mechanical Design of EPFL (Rosset, et al., 2021) successfully designed, constructed, and operated a R245fa radial-inflow turbine at the nominal speed of 100 krpm, measuring a power output of 2.3 kW. The rotor is supported on custom designed gas-lubricated bearings, allowing smaller drag torque compared to liquid lubricated bearings, and offering an efficient oil-free solution for the low power range. Other facilities include (Kang, 2016), (Weiß, et al., 2018), (Klonowicz, et al., 2014), showcasing the increasing interest for small-scale ORC applications throughout Europe and beyond.

Given the notable advantages offered by gas lubricated bearings compared to systems relying on oil lubrication, most importantly the avoidance of working fluid contamination and complexity/weight reduction of the turbine assembly, their adoption to support rotors of sRIT is arguably the best option. However, for machines in which the flow conditions lead to an axial thrust of the order of 100 N, like in the case of the ORCHID turbine, their design still represents a challenge. To reduce the risks associated to the development of a high-speed rotor based on gas dynamic bearings, the first prototype of the ORCHID turbine rotor integrates more conventional rolling element bearings, a choice which also enables the use of off-the-shelf components.

In this paper, the layout of ORCHID turbine rotor and the mathematical modeling of the various parts of the assembly for the rotordynamic analysis are described. A pocket damper gas seal was designed for secondary flows management and, to support the powertrain over the operating envelope, an off-the-shelf rolling element bearings (REB) cartridge with a squeeze-film-damper (SFD) was characterized. Finally, the sensitivity of the dynamic stability characteristics of the turbine rotor to some of the design parameters was investigated, using the results of a rotordynamic calculation performed with a computer program developed in-house by Politecnico di Milano.

536

2 MECHANICAL DESIGN

2.1 Preliminary design

Fundamental requirements for a rotating test rig for academic research include the possibility to test at different speeds and thermodynamic conditions, and tear-down / mounting easiness of the assembly to speed-up the test campaign preparation and execution. Such characteristics result from careful and informed choices on the mechanical design and components employed in the facility.

Three main technical aspects were considered a-priori in the conceptual design phase:

1. The turbine arrangement (straddled or overhung rotor)
2. The type of bearings (gas-dynamic, rolling element or active magnetic bearings)
3. The sealing strategy, intimately linked to the bearings type and turbine arrangement

Figure 1a shows the straddled rotor configuration, in which the turbine wheel is placed within two bearings. Figure 1 b instead shows an example of overhung impeller configuration, with the wheel mounted outboard on the right-hand side. Straddled rotors are arguably more robust and lead to smaller shaft deflections, but the presence of bearings on each side of the wheel calls for a more complex assembly. Conversely, overhung impellers result in a less complex and easier to access assembly, though the rotordynamic design is typically more challenging.

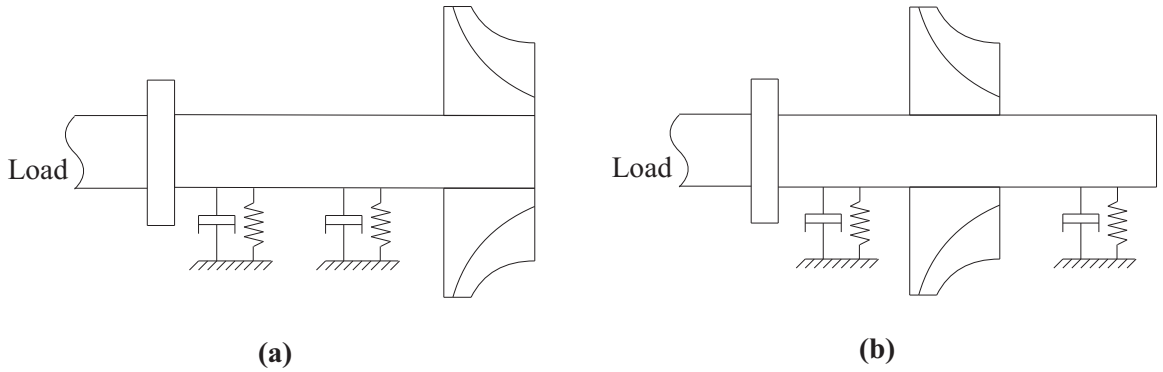

Figure 1 Rotor configuration concepts. a) Straddled impeller, and b) overhung impeller configuration.

The use of ceramic ball bearings for a concept turbine of this type has two main advantages over competing technologies. Firstly, they can handle substantially higher loads than gas lubricated bearings, offering a robust solution in a wide range of working conditions. Secondly, thanks to the widespread use of REB in a plethora of applications, they are available off-the-shelf and can be readily implemented within a new design. Recent trends in turbocharger systems show that rolling element bearings can be used in compact, mobile systems such as automotive turbo-chargers (Schweitzer & Adleff, 2006), offering long term durability with comparable lubrication and mechanical losses with respect to non-contact bearings at high speeds (Nguyen-Schäfer, 2012).

Albeit the use of REB simplifies the assembly design, the presence of lubricant in the system poses additional challenges compared to gas bearings. The cross contamination of the main working fluid and the lubricant can severely impact the performance and integrity of the entire rig. Lubricant contamination of the working fluid loop could lead to poor turbine efficiency and mechanical damage of the rotating components due to erosion. Moreover, leaked oil could accumulate and form hot spots in the closed-loop, increasing the risk of thermal decomposition of siloxane MM. On the other hand, the leakage of MM vapour within the machine casing can cause overheating and poor reliability of the bearings. Therefore, the choice of a proper sealing technology is key to ensure safe and reliable operation.

To seal the machine from oil leaks towards the working fluid loop, a common strategy adopted for large steam power plants is to use a dry-gas seal system (Forsthoffer, 2011), employing an inert gas as a barrier between the two flows to be sealed. As an alternative, contact seals are commonly employed in automotive and guarantee perfect oil sealing. The advantage of the dry-gas solution is the absence of contact parts between the stationary and the rotating components, but this comes at the cost of a more complex rotor design. In fact, the presence of the dry-gas requires more components (for sealing the different flows) and more complex control strategies. Conversely, the contact seal solution leads to a simpler and more compact assembly. Thanks to comparatively lower rotational speed and maximum operating temperatures of ORC turbines, with respect to similar size gas turbines, off-the-shelf lip seals can theoretically be used. Advancements in low friction materials development and temperature resistant coatings enable state-of-art contact seals to operate at peripheral speeds up to 100 m/s in combination with temperatures in excess of 200°. Therefore, PTFE based lip seals were deemed appropriate for this application upon verification with a manufacturer.

The conceptual layout obtained in the initial design phase resulted, after several design iterations, in the rotor configuration shown in Figure 2. The rotor includes a shaft (A), a turbocharger cartridge (B), a turbine wheel (C), and a coupling flange (D). A lock-nut on the left side of the bearing inner raceway (E) is used to regulate the mounted-end-play (MEP) of the rolling elements by adjusting the preload. The cartridge pries axially against a stainless steel thin-disk (F), with the function of moving the oil outwards to the oil drain lines machined in the casing (not visible in figure).

Stationary parts include two off-the-shelf lip seals (G and H) to contain the oil within the turbine casing, and an in-house developed gas seal (J) to limit the leakage of siloxane vapour from the turbine flow-path.

2.2 Characterization of the dynamic response of an SFD

The bearing cartridge has the main function of supporting the powertrain and transfer all loads to the structure. A three-dimensional representation of the bearing cartridge is shown in Figure 3. The cartridge inner ring is fitted to the turbine shaft, while the outer ring has a clearance fit with the casing. Two rows of rolling elements are interposed between the two rings. The outer ring is axially locked in the casing using a snap-ring (K in Figure 2), while a rectangular slot and pin system (L in Figure 2) is used to lock it circumferentially.

The two regions highlighted in red in Figure 3 act as squeeze-film-dampers (SFD's). The clearance fit of 50 μm between the outer ring and the casing ensures that, as a result of lateral motion of the powertrain, the outer ring squeezes the oil film in the gap, resulting in film pressurization.

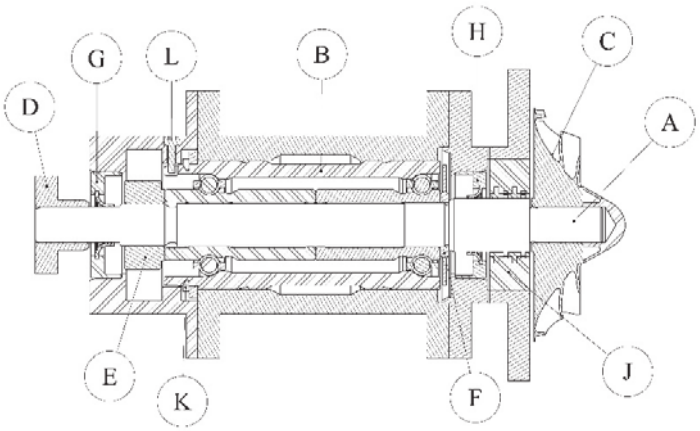

Figure 2 ORCHID turbine cross-section

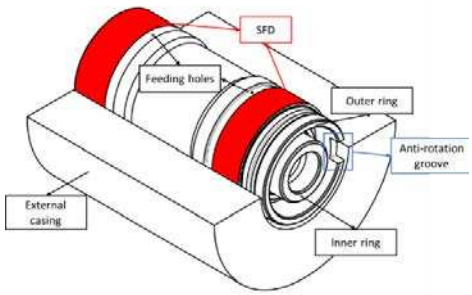

Figure 3 Detail of the REB cartridge

Such pressure introduces damping in the system and can be modelled according to the Reynolds equation **(1)**.

538

$$\frac{\partial}{R\partial\theta}\left(\frac{\rho h^3}{12\mu}\frac{\partial P}{R\partial\theta}\right)+\frac{\partial}{\partial z}\left(\frac{\rho h^3}{12\mu}\frac{\partial P}{\partial z}\right)=\frac{\partial}{\partial t}(\rho h)+\frac{\rho h^2}{12\mu}\frac{\partial^2 \rho h}{\partial t^2} \qquad (1)$$

Where ρ and μ are the oil density and dynamic viscosity, θ and z are the tangential and axial coordinates, while h is the oil film thickness, and P is the oil pressure.

The last term on the right-hand side of Equation (1) represents the temporal inertia contribution. This term has a significant effect on the pressure distribution if the oil film Reynolds number $Re_s = \frac{\rho\omega g^2}{\mu} > 1$, where ω is the whirling frequency and g is the clearance of the SFD gap (Delgado & San Andres, 2010). In the present case, assuming ISO VG 32 as lubricant we obtain $Re_s < 1$ throughout the operating range of the machine. Therefore, the temporal inertia term contribution is neglected in the SFD analysis.

The motion of the outer ring is modeled as a circular centered orbit. Equation (2) describes the oil film thickness distribution.

$$h(\theta,t) = \mathrm{g} - (e\cos\omega t)\cos\theta - (e\sin\omega t)\sin\theta \qquad (2)$$

where e is the radius of the orbit described by the SFD in the plane orthogonal to its axis, and ω its whirling frequency. The orbit can either be a circular or elliptical path resulting from lateral vibrations of the cartridge, originating from the rotor unbalance. Thus, the whirling frequency corresponds – for this particular case – to the shaft rotational frequency.

Due to the high operating speed of the turbine, and the small radial gap of the SFD, oil cavitation may occur (Zeidan & Vance, 1990). Thus, equations (1) and (2) are complemented with a model to predict cavitation as proposed by (Almqvist, et al., 2014), imposing ambient pressure at the two sides of each SFD as a boundary condition.

The pressure distribution is calculated for several shaft positions within a circular orbit and the orbit-based dynamic damping coefficient C is calculated as in (San Andres & Jeung, 2016). The evolution of the dynamic damping coefficients with respect to the speed and the orbit radius $e_r = e/g$ relative to the SFD gap is shown in Figure 4.

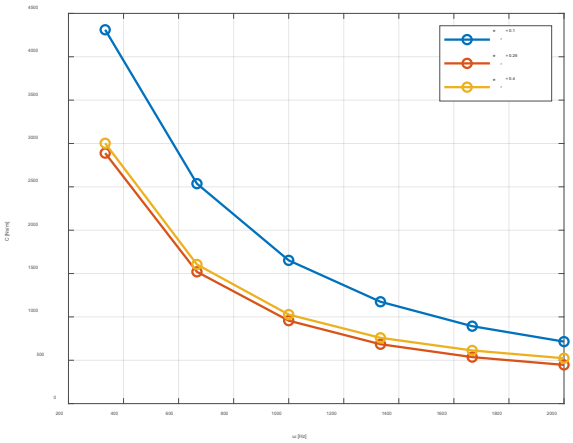

Figure 4 SFD damping coefficient as function of the orbit frequency and the eccentricity.

The damping coefficient of the SFD decreases as a function of the orbit frequency. This trend is to be expected, due to the increasingly higher amount of evaporated oil within the film at higher rotational speed. Previous study on oil cavitation in SFD (Zeidan & Vance, 1990) showed that once the so called "bubbly region" is reached, oil pressure and thus damping characteristics stabilize even with further increase of the rotational speed. Moreover, larger SFD vibrations (thus larger orbits) cause larger pressure differences within the oil film (San Andres & Jeung, 2016), causing larger portions of the film to cavitate. Nevertheless, once the maximum cavitation limit is reached (Zeidan & Vance, 1990), oil pressure and damping characteristics are less sensitive to further increases in eccentricity. This is the reason why the curves for $e_r = 0.25$ and 0.4 in Figure 4 are almost superimposed despite the increasing orbit radius.

To conclude, a progressive degradation of system stability at high speed is expected as a result of enhanced oil cavitation rate in the SFD.

539

2.3 Design and characterization of a pocket-damper gas seal

A pocket damper gas seal was developed to prevent excessive leak of siloxane MM from the ORCHID closed-loop and provide additional damping to the rotor system. Figure 5 a shows the geometry of the seal. The part was designed as a single body, hollow disk made of stainless steel with four rows of pockets acting as labyrinths. Adjacent rows of pockets were shifted relatively to each other to avoid preferential paths for the leaking gas. The pockets extend 50° circumferentially and 1 mm axially to guarantee feasibility with additive manufacturing methods.

RANS simulations of the flow within the gas seal were carried out using ANSYS Fluent on the computational domain of Figure 5 b. The domain was extended at the inlet and outlet of the clearance gap between the seal inner surface and the shaft surface to avoid boundary conditions influencing the flow solution. Table 1 reports the boundary conditions of pressure and temperature imposed. The domain was discretized with 5.1 M cells based on the results of a mesh independence study. The hybrid mesh included a structured layer of 10 cells to resolve the boundary layer on the no-slip walls of shaft and gas seal inner surface. The SST k-ω model was used for turbulence closure, while look-up tables generated using REFPROP were employed to model the fluid properties.

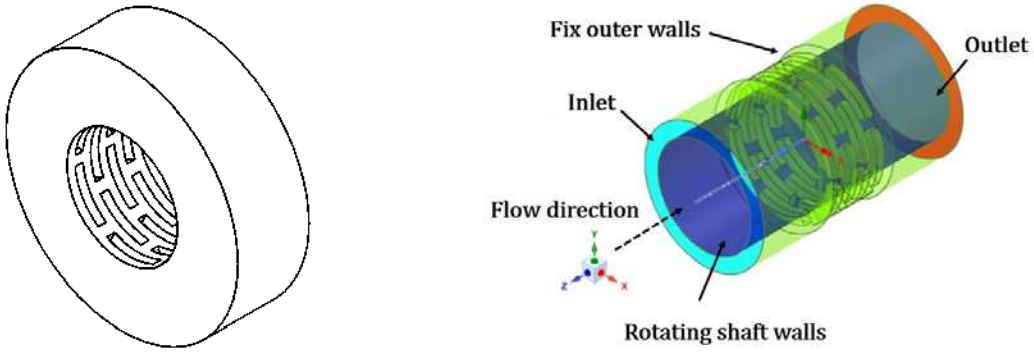

Figure 5 Pocket damper seal. On the left, seal design and main dimensions. On the right, computational domain for CFD simulations and boundary conditions.

Table 1 Boundary conditions for gas seal CFD simulations

Quantity	Inlet	Outlet
Pt	1.73 bar	
Tt	534 K	
P		1.013 bar

Lateral shaft displacement and displacement rates (Δx and $\Delta \dot{x}$) of the rotating shaft wall were imposed. The magnitude of these was determined by means of a convergence study, where their value was varied until the stiffness and damping coefficients stabilized.

Simulations at shaft rotational speed going from 20 to 100 krpm were carried out to investigate the impact of the gas seal on system stability at different speeds.

A nominal radial gap between the inner seal and the shaft outer surface of 50 μm was chosen, that is the same allowed by the SFD. The leakage mass-flow rate of siloxane MM computed from CFD was ~1 g/s, and it was verified to vary linearly as a function of the radial clearance.

The resulting forces in the horizontal and vertical directions F_x and F_y were calculated by integration of the pressure field on the shaft outer surface. The direct and cross-term stiffness and damping coefficients were calculated according to their definitions, as follows:

$$k_{xx} = \frac{Fx - Fx_0}{\Delta x} \; ; \; k_{yx} = \frac{Fy - Fy_0}{\Delta x} \; ; \; c_{xx} = \frac{Fx - Fx_0}{\Delta \dot{x}} \; ; \; c_{yx} = \frac{Fy - Fy_0}{\Delta \dot{x}}$$

where the denominators are the imposed displacement and displacement rate previously introduced. F_{x_0} and F_{y_0} are the aerodynamic forces with null shaft displacement.

Figure 6 shows the computed stiffness and damping coefficients at varying rotational speed of the rotor shaft. Direct terms show a weak dependence on the rotational speed, while cross-terms increase linearly. From a rotordynamic standpoint, the system stability will be negatively affected by the presence of the gas seal as the speed is increased, due to the increasing cross-terms of the stiffness matrix. Cross-coupled stiffness has an important effect only when its magnitude is comparable to the direct terms. In this case, the cross-coupled terms of the gas seal stiffness matrix are relevant at the design speed, as shown by the left-hand graph of Figure 6, and will therefore be accounted for in the rotordynamic analysis.

Cross-coupled damping terms are instead significantly lower than the direct ones, suggesting that their influence on system stability will be rather low. Nevertheless, since their value has a comparable order of magnitude than that of the direct terms, they must be included in the rotordynamic analysis.

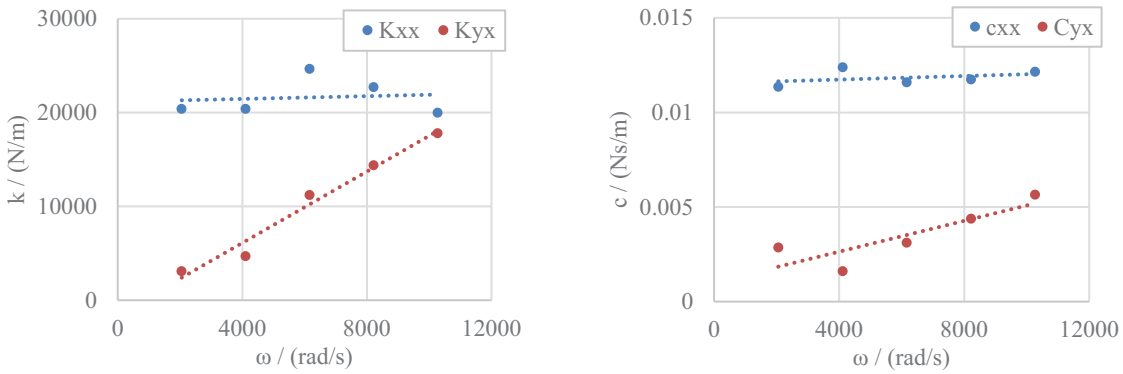

Figure 6 Stiffness (left) and damping (right) coefficients from CFD simulations. Dotted lines represent the linear fit used as input for the rotordynamic analysis.

3 ROTORDYNAMIC ANALYSIS

The dynamic behavior of the machine has been investigated by means of a rotordynamic model of the machine-train. The model includes the finite beam element model of the shaft train, that of the REB cartridge and its SFD characteristics, the gas seal and the cross-coupled aerodynamic forcing of the turbine wheel (San Andres, 2023). The resulting finite element representation of the machine is shown in Figure 7, together with the non-rotating cartridge outer ring. The rotating parts include the coupling hub flange, the bearing lock-nut, the cartridge inner ring, the impeller and the ogive. The effect of the coupling shaft mass and inertia is introduced as a lumped mass on the second node from the left in Figure 7.

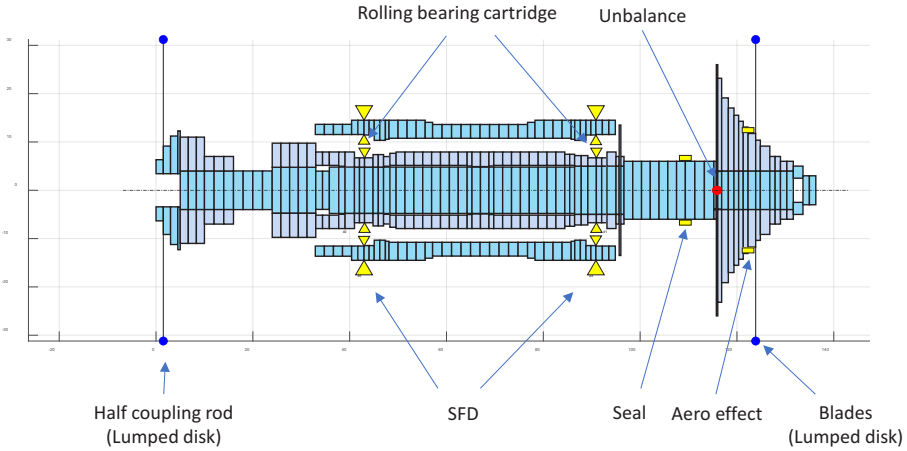

Figure 7 Rotordynamic model showing the mass distribution of the rotor discretized using disks.

The equation of motion of the structure is described by Equation (3):

$$[M]\ddot{\boldsymbol{x}} + ([C] + \Omega[G])\dot{\boldsymbol{x}} + [K]\boldsymbol{x} = \boldsymbol{F} \qquad (3)$$

Where [M], [C] , [G] and [K] are respectively the mass, damping, gyroscopic, and the stiffness matrix, while $\boldsymbol{F}$ is the array of unbalance forces.
The dynamic behaviour of the REB is represented by linearized coefficients using the classical stiffness and damping matrices.

$$[K]^{REB} = \begin{bmatrix} k_{xx}^{REB} & 0 \\ 0 & k_{xx}^{REB} \end{bmatrix};\ [C]^{REB} = \begin{bmatrix} c_{xx}^{REB} & 0 \\ 0 & c_{xx}^{REB} \end{bmatrix};\ [K]^{aero} = \begin{bmatrix} 0 & k_{xy}^{aero} \\ -k_{xy}^{aero} & 0 \end{bmatrix}$$

$[K]^{REB}$ and $[C]^{REB}$ are diagonal matrices because the stiffness and damping cross-terms are negligible for such bearings. The stiffness coefficients used in this study were provided by the bearing manufacturer, computed by means of Hertz contact theory, expressed as a function of the load acting on the bearing. The load depends on the radial and thrust aerodynamic forces, changing with the

rotational speed. $[K]^{aero}$ is the matrix of the aerodynamic forces brought in by the impeller, with non-zero cross-terms and negligible direct terms. The destabilizing cross-term $k_{xy}^{aero} = 633.75e3$ N/m was determined using Wachel's formula, according to a level I analysis as per the API 617 norm for radial expander-compressor systems (API 617, 2014).
The effect of the squeeze-film-damper is considered through a damping matrix with equal direct terms, in which the direct damping coefficient is evaluated by means of the Reynolds model described earlier. Instead, the effect of the seal is included using a stiffness and a damping matrix, both with equal direct terms and opposite cross-terms, estimated by means of CFD simulations for several rotational speeds.

$$[C]^{SFD} = \begin{bmatrix} c_{xx}^{SFD} & 0 \\ 0 & c_{xx}^{SFD} \end{bmatrix} ; \; [K]^{seal} = \begin{bmatrix} k_{xx}^{seal} & k_{xy}^{seal} \\ -k_{xy}^{seal} & k_{xx}^{seal} \end{bmatrix} ; \; [C_{seal}] = \begin{bmatrix} c_{xx}^{seal} & c_{xy}^{seal} \\ -c_{xy}^{seal} & c_{xx}^{seal} \end{bmatrix},$$

The result of the eigenfrequency analysis as a function of the rotational speed is reported in the Campbell diagram of Figure 8. The critical speeds for excitations up to the 2X component, along with the corresponding damping factors in the range from 20krpm to 120krpm are listed in Table 2.
The first 4 mode shapes are mainly rigid modes of the shaft and cartridge relative movement, whereas modes 5 to 8 include the bending of the shaft.

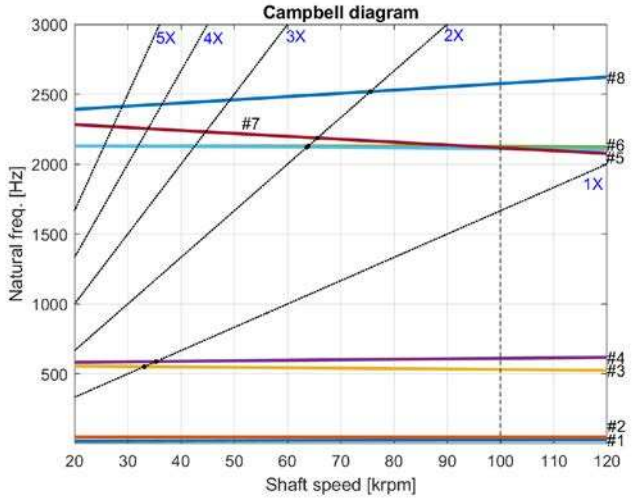

Figure 8 Campbell diagram of the ORCHID turbine rotor

Table 2 Critical speed and damping ratio of mode 3 to mode 8 when crossing the 1X and 2X shaft frequency excitation

Mode #	Critical speed [krpm]	Damping ratio
3	33.1	0.093
4	35.3	0.377
5	63.8	0.584
6	63.6	0.599
7	65.6	0.134
8	75.5	0.181

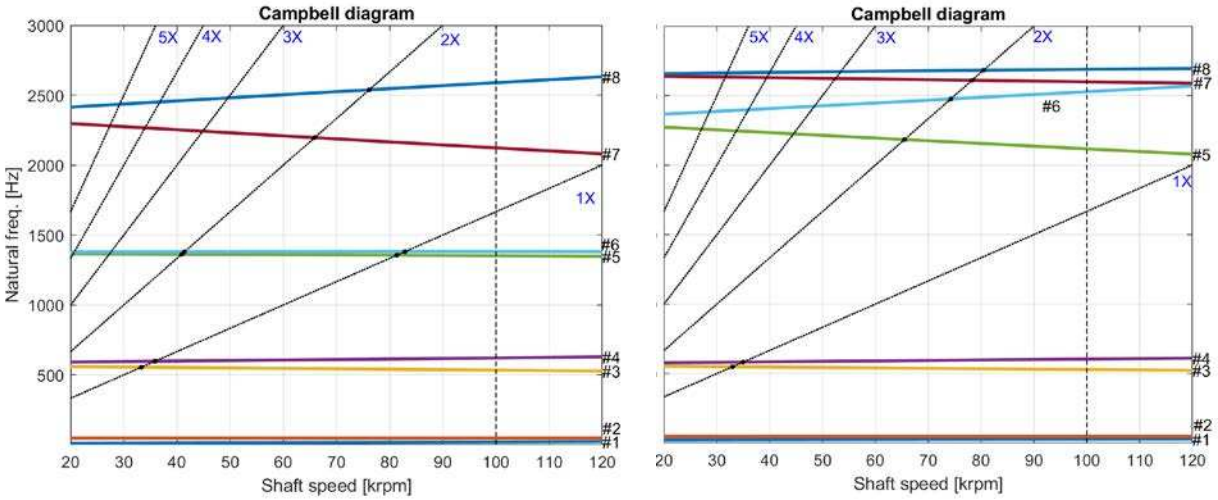

Figure 9 Campbell diagrams of rotor dynamic response using -30% (left) and +30% (right) of the bearing stiffness calculated through Hertzian contact theory

The Campbell diagrams for the change of the stiffness coefficient of the rolling element bearing cartridge, varied in the range +/- 30% with respect to the nominal values, is shown in Figure 9.
The eigenfrequencies of the first 4 rigid modes remain unchanged, whereas those of modes 5 to 8 increase with the increase of the bearing stiffness. Modes 5 and 6 are critical because critical speeds can arise within the operating range of the machine, which is the region going from 80 to 120 krpm.
The response to the unbalance at the design rotational speed of 100 krpm has an amplitude < 1 μm, almost 2 orders of magnitude lower than the gas seal and SFD radial clearances.
The stability of the shaft train has been verified by progressively increasing the stiffness cross-terms of the aerodynamic forcing matrix $[K]^{aero}$. Mode #3 becomes unstable ($h < 0$) even with low values of k_{xy}^{aero} but, since it is a rigid backward mode between the shaft and the REB cartridge, it is not critical.

4 CONCLUSIONS

The current work documents the preliminary design and rotordynamic analysis of the high-speed rotor of the ORCHID turbine. The damping coefficient of a cartridge for turbochargers, featuring a 50 μm squeeze-film-damper, has been characterized throughout the entire rotational speed envelope. The stiffness and damping coefficients of a pocket damper gas seal designed in-house were calculated using CFD simulations, showing that the cross-coupled stiffness coefficients have a non-negligible effect on the rotordynamics. The frequency analysis of the first 8 mode shapes highlighted the presence of 4 rigid modes (1 to 4) and 4 flexible modes (5 to 8). Rotordynamic analyses of the assembly, including the stiffness of the bearings coefficients according to Hertz theory, shows a large sensitivity of the first two flexible shaft modes (mode 5 and 6) to bearing stiffness variations in the range ±30%. In particular, mode 5th leads to a potentially critical frequency in the operating range of the machine, depending on the actual bearing stiffness coefficient. At present time, a conclusive analysis of the dynamic performance of the machine designed in this work is still lacking. Given that the modeling assumptions have significant impact on the results of the present investigation, a comprehensive sensitivity study is envisaged as future work to eventually determine the optimal powertrain design. Finally, future real life balancing and testing will provide the necessary level of confidence on the results here described.

543

NOMENCLATURE

C	Damping coefficient	(Ns/m)	T	Temperature	(K)
E	eccentricity	(μm)	Tt	Total Temperature	(K)
F	Force	(N)	x	Displacement	(m)
g	SFD gap	(μm)	$\dot{x}$	Velocity	(m/s)
K	Stiffness coefficient	(N/m)	$\ddot{x}$	Acceleration	(m/s^2)
$\dot{m}$	Mass-flow rate	(g/s)	θ	Angular coordinate	(rad)
M	Mass	(kg)	μ	Dynamic viscosity	(Pa s)
P	Pressure	(Pa)	ρ	Density	(kg/m^3)
Pt	Total Pressure	(Pa)	ω	Angular velocity	(rad/s)
t	Time	(s)	Ω	Rotational velocity	(rpm)

REFERENCES

Almqvist, A., Fabricius, J., Larsson, R. & Wall, P., 2014. A New Approach for Studying Cavitation in Lubrication. *Journal of Tribology,* Volume 136.

API 617, 2014. *Axial and Centrifugal Compressors and Expander-Compressors for Petroleum, Chemical and Gas Industry.* s.l.:s.n.

Cappiello, A., Majer, M., Tuccillo, R. & Pini, M., 2022. *On the Influence of Stator-Rotor Radial Gap Size on the Fluid-Dynamic Performance of Mini-ORC Supersonic Turbines.* s.l., ASME, p. 15.

Cappiello, A. & Tuccillo, R., 2021. Design Parameter Influence on Losses and Downstream Flow Field Uniformity in Supersonic ORC Radial-Inflow Turbine Stators. *Int. J. Turbomach. Propuls. Power.*

Cerza, M., Meinster, B. & Blair, C. S., 2022. *Implementation of a Waste Heat Recovery Combined Cycle System Employing the Organic Rankine Cycle for a Gas Turbine.* s.l., AIAA.

De Servi, C. M. et al., 2017. *Exploratory Assessment of a Combined Cycle Engine Concept for Aircraft Propulsion.* Zurich, s.n.

De Servi, C. M., Burigana, M., Pini, M. & Colonna, P., 2019. Design Method and Performance Prediction for Radial-Inflow Turbines of High-Temperature Mini-Organic Rankine Cycle Power Systems. *J. Eng. Gas Turbines Power,* 141(9), p. 12.

Delgado, A. & San Andres, L. A., 2010. Model for Improved Prediction of Force Coefficients in Grooved Squeeze-film-dampers and Oil Seal Rings. *Journal of Tribology,* Volume 132, pp. 1-12.

Forsthoffer, W. E., 2011. Dry Gas Seal Best Practices. In: *Forsthoffer's Best Practice Handbook for Rotating Machinery.* s.l.:Elsevier, pp. 501-524.

Glensvig, M., Schreier, H., Tizianel, M. & Theissl, H., 2016. Testing of a Long-Haul Demonstrator Vehicle with a Waste Heat Recovery System on Public Road. *SAE Technical Paper,* pp. 1-9.

Head, A. J., 2021. *Novel Experiments for the Investigation of Non-Ideal Compressible Fluid Dynamics.* Delft(South-Holland): TU Delft.

Kang, S. H., 2016. Design and preliminary tests of ORC (organic Rankine cycle) with two-stage radial turbine. *Energy,* Volume 96, pp. 142-154.

Klonowicz, P. et al., 2014. Design and performance measurements of an organic vapour turbine. *Applied Thermal Engineering,* 63(1), pp. 297-303.

Nguyen-Schäfer, H., 2012. *Rotordynamics of Automotive Turbochargers.* Berlin: Springer Berlin, Heidelberg.

Perullo, C., Mavris, D. & Fonseca, E., 2013. *An Integrated Assessment of an Organic Rankine Cycle Concept for Use in Onboard Aircraft Power Generation.* San Antonio, ASME.

Rosset, K., Pajot, O. & Schiffmann, J., 2021. Experimental Investigation of a Small-Scale Organic Rankine Cycle Turbo-Generator Supported on Gas-Lubricated Bearings. *J. Eng. Gas Turbines Power,* 143(5), p. 14.

San Andres, L., 2023. A Review of Turbine and Compressor Aerodynamic Forces in Turbomachinery. *Lubricants,* p. 22.

San Andres, L. & Jeung, S. H., 2016. Orbit-Model Force Coefficients for Fluid Film Bearings: A Step beyond Linearization. *Journal of Engineering for Gas Turbines and Power,* Volume 138.

Schweitzer, F. & Adleff, K., 2006. Rolling bearings in turbocharger applications. *MTZ worldwide*, Volume 67, pp. 16-19.

Seume, J. R., Peters, M. & Kunte, H., 2017. *Design and test of a 10kW ORC supersonic turbine generator.* s.l., IOP Publishing Ltd, p. 10.

Uusitalo, A., Turunen-Saaresti, T., Honkatukia, J. & Dhanasegaran, R., 2020. Experimental study of small scale and high expansion ratio ORC for recovering high temperature waste heat. *Energy,* Volume 208.

Weiß, A. et al., 2018. Experimental characterization and comparison of an axial and a cantilever micro-turbine for small-scale Organic Rankine Cycle. *Applied Thermal Engineering,* Volume 140, pp. 235-244.

Wieland, C., Schifflechner, C., Dawo, F. & Astolfi, M., 2023. Tho organic Rankine cycle power systems market: Recent development and future perspectives. *Applied Thermal Engineering ,* Volume 224.

Zeidan, F. Y. & Vance, J. M., 1990. Cavitation Regimes in Squeeze-film-dampers and Their Effect on the Pressure Distribution. *Tribology Transactions,* 33(3), pp. 447-453.

ACKNOWLEDGEMENT

The authors would like to acknowledge NWO and the industrial partners of the ARENA project, whose funding grant made this research possible. Moreover, the data and expertise the cartridge manufacturer (and all industrial partners) contributed with was fundamental for the design and modeling presented.

ORC SEVILLE 2023
7th International Seminar on O.R.C. Power Systems

© 2024 Editorial Universidad de Sevilla. Este es un artículo de acceso abierto distribuido bajo los términos de la licencia de uso y distribución Creative Commons (BY-NC-ND 4.0)

DOI: https://dx.doi.org/10.12795/9788447227457_91

THERMODYNAMIC FEASIBILITY OF A PUMPED THERMAL ENERGY STORAGE DRIVEN BY OCEAN TEMPERATURE GRADIENT

Alessandra Ghilardi, Andrea Baccioli*, Guido Francesco Frate, Lorenzo Ferrari

Department of Energy, Systems, Territory and Constructions Engineering (DESTeC), University of Pisa, Pisa, Italy.

*Corresponding Author: andrea.baccioli@unipi.it

ABSTRACT

The significant future penetration of variable renewable energy, necessary to decarbonize power production, will require energy storage to stabilize the electric grids. Electrochemical batteries may not be the best solution for all energy storage needs due to their limited lifetimes, performance degradation and use of critical raw materials. Pumped thermal energy storage (PTES) is an attractive solution since it does not suffer from the abovementioned limitations and might be preferable for long-duration applications. Particularly Thermally Integrated-PTES (TI-PTES), exploiting an external heat source during the charging or discharging phase, represents a significant improvement of this technology regarding the round-trip efficiency . Several TI-PTES systems have been proposed using solar and geothermal energy or industrial waste heat. This paper introduces a novel TI-PTES concept exploiting the temperature difference between the surface and deep oceanic Water in tropical areas. The system comprises a vapour compression chiller, a phase change material (PCM) cold storage, and an organic Rankine cycle. During the charging phase, the chiller operates between the cold seawater and the thermal storage, converting electric energy into a cooling effect. In these conditions, the chiller Energy efficiency ratio (EER) is in the range of 4.6 - 9.0 due to the deep seawater's low temperature. During the discharge phase, the organic Rankine cycle operates between the hot surface and the storage to produce electricity. Results show that the round-trip efficiency ranges from 0.30 to 0.52 depending on the fluids adopted in chiller and ORC and PCM storage temperature, making the investigated technology a promising alternative to other long-duration storage technologies.

1 INTRODUCTION

Recently, the extensive utilization of Renewable Energy Sources (RES) has resulted in substantial emission reduction. However, due to the RES variable generation, the power grids are encountering operational challenges and the mismatch between power generation and demand.
Energy Storage Systems (ESS) may support RES' integration by shifting large amounts of energy in time. Pumped Hydro Energy Storage (PHES) is the most widely utilized technology for this task (Argyrou et al., 2018). However, most energy grids have limited suitable locations for new PHES plants. Li-ion battery energy storage, which dominates the new large-scale storage projects (Killer et al., 2020), may represent a suitable alternative to PHES for short and medium-term applications (4 – 6 hours of charge and discharge). Their cost per installed kWh limits their competitiveness for larger durations (8 – 10+ hours), and their use of critical raw materials poses environmental and geopolitical concerns (Killer et al., 2020).
To overcome these issues, a large group of storage technologies based on thermo-mechanical operating principles have been proposed (Olympios et al., 2021). In the paper, Pumped Thermal Energy Storage (PTES), which stores electric energy as thermal exergy, is considered among the many technologies available. PTES use Heat Pumps (HP) for charging, as they move the heat from a Low Temperature (LT) reservoir to a High Temperature (HT) one, converting power into thermal exergy (Benato and Stoppato, 2018). During the discharge, the stored thermal exergy is converted back into power using a Heat Engine (HE), typically a Brayton or Organic Rankine Cycle (ORC). One thermal reservoir may be eliminated when external thermal exergy sources are available. In this case, the so-called Thermally

Integrated PTES (TI-PTES) is realized (Frate et al., 2020), which may achieve very high electric roundtrip efficiencies, thanks to the exergy contribution of the external sources (Frate et al., 2017).
TI-PTES are categorized as hot and cold according to whether the thermal exergy is stored at temperatures higher or lower than the environment (Dumont and Lemort, 2020). Thermodynamically, hot TI-PTES tend to be more efficient and, for this, has been more often analyzed in the literature in conjunction with solar, geothermal or waste heat sources (Hu et al., 2021). Despite the thermodynamic advantage, the performance of TI-PTES depends on its operating temperatures, and for some configurations of these, hot and cold TI-PTES may achieve similar performance (Frate et al., 2020). Furthermore, cold TI-PTES may have an economic advantage, using standard vapour compression chillers as charging devices (Frate et al., 2023) and storing the thermal exergy at temperatures slightly below ambient, using cheap and durable phase change materials, such as ethylene glycol (Peterson, 2011), the eutectic mixture of NaCl and water or pure water ice (Henchoz et al., 2012). Hot and cold TI-PTES operating in a small-size residential energy district were compared from the thermodynamic and economic points of view in (Frate et al., 2023), finding that, even though the hot configurations achieved slightly better performance, the annualized cost of the cold one was up to 50% lower, when both storage operation and capital cost were considered.
Hot and cold TI-PTES are usually studied with geothermal, solar or industrial waste heat sources. However, an alternative thermal exergy source could be the ocean thermal gradient, which may provide thermal exergy at a temperature lower than the environment. In tropical regions, where the surface water temperature is nearly constant over the year, and the bathymetry is adequate (Langer et al., 2021), a temperature difference of 20 – 25 °C exists between the surface and the deep seawater. Currently, to exploit this temperature difference to produce power, Ocean Thermal Energy Conversion (OTEC) systems have been proposed (Masutani and Takahashi, 2001), but they could be integrated with TI-PTES. The coupling of OTEC with energy storage has rarely been investigated. For example, in (Khosravi et al., 2019), the authors combine an OTEC with RES and hydrogen production and storage, finding that the OTEC may reduce the cost of power produced by the hybrid system.
To the best of the authors' knowledge, the paper's novel contribution is to combine and analyze a cold TI-PTES with an OTEC for the first time in the literature. As is shown in the paper, coupling TI-PTES and OTEC systems increases the PTES efficiency, achieving promising roundtrip efficiencies in line with what was previously achieved in the literature by integrating other thermal exergy sources.
Finally, the provided analysis may improve OTEC flexibility, enabling it to manage RES generation or variable electric demand, thus contributing to power production decarbonization in tropical regions, where fossil fuel-based power generation is still massively used.

546

2 METHODOLOGY

2.1 Analyzed configuration

The system configuration analyzed in the paper is reported in **Figure 1**. The ORC operates between the surface seawater at T_{env}, which provides the heat to evaporate the working fluid, and the cold reservoir, the storage tank where the thermal exergy is stored at T_s, with $T_{env} \geq T_s$, acting as the heat sink absorbing the condensation heat from the ORC fluid.
The chiller is realized with a vapour compression refrigeration cycle and operates between the thermal exergy storage at a temperature T_s and the cold deep seawater at a temperature T_l, with $T_l \geq T_s$.
As for the TI-PTES system, the chiller charges the storage, converting power into thermal exergy at a temperature T_s, while the ORC discharges the storage, converting the thermal exergy into power. For simplicity, the thermal exergy is assumed to be stored in the tank for the desired time without thermal losses. In the analysis, the thermal exergy storage is assumed to operate at a constant temperature with pure water ice as the phase change material.

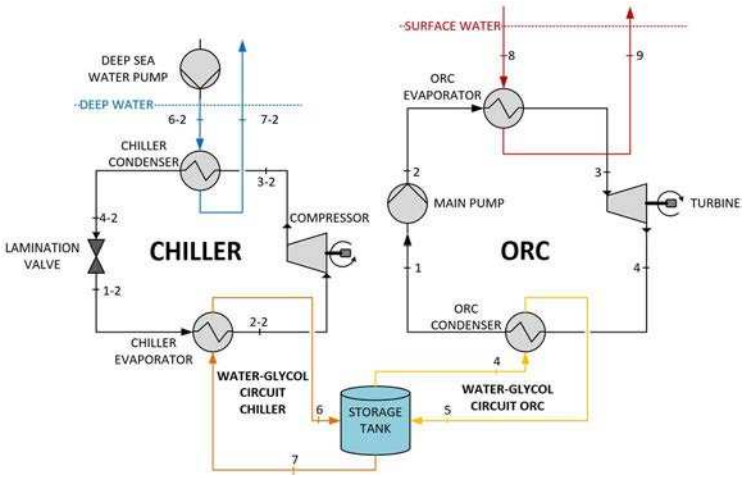

Figure 1: Schematic system representation realized by a cold TI-PTES and an OTEC.

2.2 Performance indicators

The analysis considers two performance indicators to evaluate the storage performance: the round-trip efficiency and the storage tank volume. The first is the objective function to be maximized by the system design, while the second is parameter monitored a posteriori for the investigated designs. The round-trip efficiency ε_{rt} is defined as the ratio between the discharging phase net electric output from the OTEC and the charging phase gross electric input in the chiller (Eq. 1):

$$\varepsilon_{rt} = \frac{E_{dis}}{E_{ch}} = \frac{\dot{W}_{dis} \cdot \tau_{dis}}{\dot{W}_{ch} \cdot \tau_{ch}} = \frac{(\dot{W}_t - \dot{W}_p) \cdot \tau_{dis}}{(\dot{W}_c + \dot{W}_d) \cdot \tau_{ch}} \quad (1)$$

where τ_{dis}, $\dot{W}_{dis}$, τ_{ch}, and $\dot{W}_{ch}$ are the discharging and charging durations in hours and the power output and input in kW, respectively. The ORC net electric power output $\dot{W}_{dis}$ is calculated as the difference between the electric power generated by the turbine $\dot{W}_t$ and the cycle circulating pump consumption W_p. The chiller gross power input is calculated as the sum of the consumption of the chiller compressor $\dot{W}_c$ and the deep seawater pump $\dot{W}_d$, which can be significant in OTEC plants because the cold water is drawn out at depths of around 800-1000 m. $\dot{W}_d$ is expressed as the pumping power necessary to counterbalance the pressure drop in the deep seawater pipe (Eq. 2):

$$\dot{W}_d = \frac{\dot{m}_w}{\eta_d} L \frac{v^2}{2D} \cdot f = \frac{\dot{m}_w}{\eta_d} L \frac{v^2}{2D} \cdot \left[-2log\left(\frac{\varepsilon}{3.72D}\right)\right]^{-2} \quad (2)$$

where L is the pipe length in *m*, $\dot{m}_w$ the seawater mass flow rate per pipe in *kg/s*, v = 2 the velocity inside the pipe in *m/s*, D the pipe diameter in *m*, f the friction factor, and η_d the pump efficiency. f is calculated from the Colebrook equation, in the form valid for very high Reynolds numbers, with ε = 0.05 as the pipe surface roughness in *m*. The pipe diameter is calculated as $D = \sqrt{4\dot{m}_w/(\rho_w v \pi)}$, which must be lower than four meters, D_{max} = 4, for structural reasons. When $D \geq D_{max}$, the mass flow rate is split into multiple pipes of equal diameter, $\dot{m}_w$ in Eq. 2 is recalculated, and the pumping losses are multiplied by the number of used pipes. Additional losses due to the pumping of secondary fluids and the pressure drop on the refrigerant side of heat exchangers have been neglected since previous analyses suggested that their respective impact is negligible compared to the deep sea water pump consumption (Liponi et al., 2022; Vera et al., 2020).

The storage volume V_s is evaluated from the amount of water ice required to absorb the condensation heat produced by the ORC for τ_{dis} hours (Eq. 3):

$$V_s = \frac{\dot{W}_{dis} \cdot \tau_{dis} (1/\eta_{otec} - 1)}{\rho_{ice} \Delta h_{ice}} \quad (3)$$

where η_{otec} is the OTEC thermal efficiency, ρ_{ice} = 917 kg/m^3 is the ice density and Δh_{ice} = 334 kJ/kg is the ice's latent heat.

Finally, the TEC and chiller performance are measured with η_{otec} and the Energy Efficiency Ratio (EER), respectively, defined as (Eq. 4 and 5):

$$\eta_{otec} = \frac{\dot{W}_{dis}}{\dot{Q}_{otec}} \quad (4)$$

547

$$EER = \frac{\dot{Q}_{chill}}{\dot{W}_c} \quad (5)$$

where $\dot{Q}_{otec}$ and $\dot{Q}_{chill}$, in kW, are the heat flow rates absorbed at the ORC and chiller evaporators, respectively.

2.3 Round-trip efficiency optimization

The system is modelled and simulated with the software Aspen Hysys V10. The system's design is optimized with the BOX algorithm embedded in Aspen Hysys, a sequential search algorithm suitable for highly non-linear problems (Giwa and Giwa, 2013).

RefProp (Lemmon et al., 2018) was used in the simulations to evaluate the chiller and OTEC fluids' thermophysical properties. Instead, the Electrolyte NRTL equation of state was used for the seawater, considered a mixture of water and NaCl with a molar fraction of 0.004 (Liponi et al., 2022).

The optimization's objective function f_{obj} is the round trip efficiency η_{rt} maximisation (Equation 4):

$$f_{obj} = \max_{\boldsymbol{x} \subseteq \Phi \subseteq \mathbb{R}^n} \varepsilon_{rt} \quad (4)$$

The optimization variables $\boldsymbol{x}$ can be found in **Table 1**, while the primary constraints, defining the feasible region Φ, can be summarised as:

- Pinch point in ORC heat exchangers $\Delta T_{pp,otec} \geq 2$ K;
- Pinch point in the chiller heat exchangers $\Delta T_{pp,chill} \geq 3$ K;
- ORC super-heating at the turbine inlet $\Delta T_{sh,otec} \geq 2$ K;
- ORC net output power $\dot{W}_{dis}$ = 10 MW.

Table 1: Optimization variable for the hybrid systems composed by the OTEC and the cold TI-PTES

Description	Symbol	Units
Depth from which the seawater is pumped	z_p	(m)
Heat transfer loop temperature at the chiller evaporator inlet	T_7	(K)
Heat transfer loop temperature at the OTEC condenser outlet	T_5	(K)
Surface seawater temperature at the OTEC evaporator outlet	T_9	(K)
OTEC fluid temperature at the turbine inlet	T_3	(K)
OTEC fluid pressure at the turbine outlet	p_4	(bar)
OTEC turbine power output	$\dot{W}_t$	(kW)
Chiller fluid pressure at the compressor discharge	p_{3-2}	(bar)
Chiller fluid temperature at the evaporator inlet	T_{1-2}	(K)

548

2.4 Simulated configurations

For the analysis, the bathymetric profile (T of seawater versus the depth) of the San Blas archipelago in Panama (9°34'N, 78°49'O) was selected. The surface water temperature T_{env} = 28 °C and bathymetry profile data are based on the data reported in (Vera et al., 2020).

In the analysis, the nominal ORC power output is set at 10 MW; the nominal discharging duration τ_{dis} is set to 2 hours, while the nominal charging duration τ_{ch} is 8 hours. For the chiller compressor, the ORC expander and the various pumps in the system, isentropic efficiencies of 0.80, 0.83 and 0.75 were assumed, respectively.

For the ORC and the chiller, the same fluids were investigated. According to (Vera et al., 2020), the following fluids were investigated: ammonia, R152a, R1234yf, and R1234ze. These fluids are suited to operate in the studied temperature range, are commercially available, relatively cheap, non-flammable, and non-toxic except for ammonia (Vera et al., 2020).

The analysis considered two cold storage configurations: one with a constant storage temperature at 0°C and one with a storage temperature below 0°C. For the first configuration, the analysis refers to pure water as a thermal storage material for calculating storage volumes and cost. For the second configuration, the storage temperature was varied to investigate the sensitivity of the system thermodynamic performance to such parameter. To do this, a fictitious material with the appropriate melting temperature was assumed to be available for each investigated temperature value.

3 RESULTS

Two cold storage configurations were considered: one with a constant storage temperature at 0°C and one with a storage temperature below 0°C. Results for the main parameters of interest were obtained for both configurations and are presented in the following sections. The electric round-trip efficiency (η_{rt}), chiller energy efficiency ratio (EER), first principle efficiency of the ORC (η_{ORC}), and depth of seawater withdrawal (z_p) will be analyzed.

3.1 Sensitivity to storage temperature

Sensitivity analysis for the cold storage configuration with a constant temperature of 0°C was conducted by varying the chiller working fluid in order to explore their applicability. The values obtained for ε_{rt} are presented in the histogram in **Figure 2**.

The results show that the use of ammonia leads to significantly better performance, achieving an ε_{rt} of 52%; in the other cases, ε_{rt} never exceeds 40%. Ammonia allows for a higher round trip efficiency value, as the EER of the chiller is significantly greater than that of the other cases. This performance coefficient reaches a value just below 10, as this fluid requires a pressure difference across the compressor of 3.5 bar, compared to the 4.5 – 5 bar required by the other fluids. Moreover, due to its high latent heat, with the ammonia, the plant requires a refrigerant flow rate approximately an order of magnitude lower than that required by the other fluids, resulting in a significant COP increment. Regarding the ORC efficiency, all the fluids achieve similar values, around 5 – 6% (**Figure 2**).

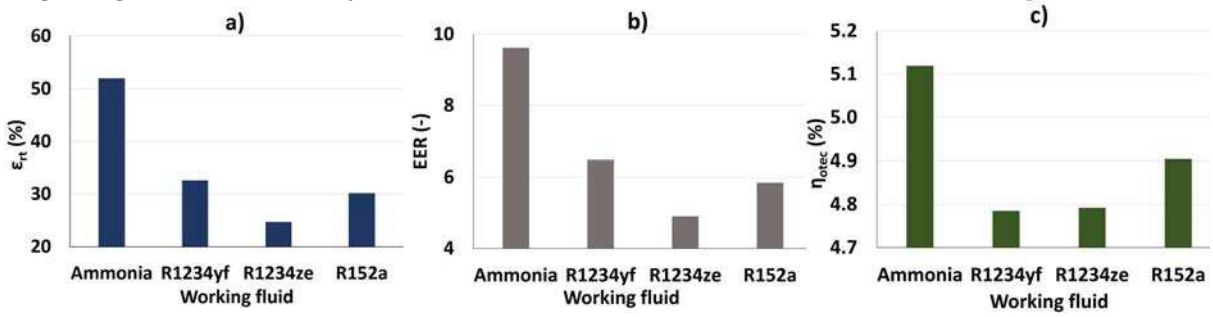

Figure 2. Efficiencies for different ORC and chiller working fluids. a) round-trip efficiency ; b) Chiller Energy Efficiency Ratio; c) ORC efficiency

3.2 Storage volume

The storage system relative to the configuration with constant temperature ice at 0°C is interesting since the system utilizes the solid-liquid state change. This way, the volumes involved can be much smaller than those with sensible storage. **Figure 3** shows the storage volumes for each working fluid.

The histogram shows that the required ice volume is around 4500-5000 m^3. Such a volume can be easily installed by adopting a small-size end-of-life cargo ship to be placed nearby the installation. The ice storage can be easily placed by suitably fitting the ship's cargo holds, thus increasing the ship's life and mitigating the shipbreaking issue, a process currently posing a significant environmental and safety problem.

Once again, ammonia is the fluid that performs best, requiring a storage volume approximately 300 m^3 smaller than the 4850 m^3 required by R1234yf. In reality, the difference between the storage volumes required by the various fluids is small and limited to 300 m^3, so all proposed fluids are equally competitive, considering the ship's potential cargo capacity for storage.

3.3 Deepwater intake

The depth of the deep water intake is reported in **Figure 3** for various fluids. Ammonia, which demonstrated the best performance in terms of ε_{rt} and V_s, has a greater intake depth than all other fluids. This is because the flow rates involved are small, and thus the condenser of the heat pump requires less cooling water; in this way, with reduced pumping losses, water is drawn from deeper depths achieving lower temperatures and, therefore, a higher EER. Shorter intake pipes are desired as they help limit the plant's costs. In this regard, the most advantageous is R1234ze, with an intake depth of around 800 m.

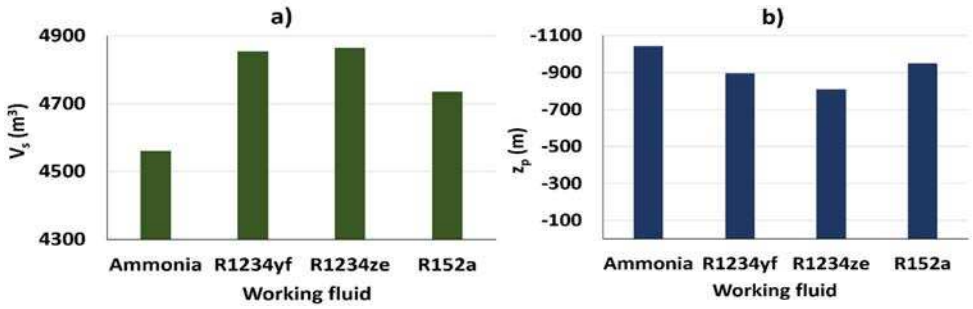

Figure 3: Storage volume (a) and deepwater intake draught (b) for the various working fluids.

3.4 Sensitivity to the storage temperature

The results presented above refer to pure water ice storage, considered one of the best PCMs for its chemical stability and high latent heat. In order to investigate the system performance for temperatures below 0 °C, values down to -7 °C have been investigated. Values above 0 °C were not considered due to the small lift at which the chiller would operate, considering constraints given by pinch points in the heat exchangers and the low isentropic efficiency of the compressor. In the simulations presented in this section, the OTEC operating fluid is ammonia. As already introduced in Section 2.4, a fictitious storage material is used for the calculations reported in this section. The purpose of this is to investigate the sensitivity of the system thermodynamic performance and understand if materials alternative to pure water ice are worth investigating for the proposed applications.

Figure 4 shows that ε_{rt} increases with the temperature, reaching the maximum value of 43% at T_s equal to -4 °C. Although there is an almost linear upward trend, the variation of ε_{rt} between -7 °C and -4 °C is only three percentage points, which make ε_{rt} robust against small storage temperature variations. The increase in the T_s determines a reduction in the chiller operating temperature lift, thus increasing its EER (**Figure 4**). At the same time, as T_s increases, the difference between ORC evaporation and condensation temperatures is reduced, along with η_{otec}. However, the increase in EER is more marked than the decrease suffered by OTEC efficiency, so the ε_{rt} increases as the storage operating temperature approaches 0 °C. This is confirmed by the ε_{rt} values achieved for the previous configuration, which were over 50% for ammonia. Theoretically, the round-trip efficiency increases as long as the difference between the storage and deep sea water temperatures is reduced. However, there are practical limitations to this thermodynamic effect. Firstly, the heat transfer from the storage to the deep sea water through the chiller requires small but finite temperature differences between the chiller operating fluids, the storage materials and the cold water from the sea bottom, which limits the minimum chiller operating temperature difference in practice. Secondly, the chiller compressor is characterized by a minimum practical pressure ratio under which it operates with low performances, limiting the minimum temperature difference between the chiller condenser and evaporator. The value of this minimum pressure ratio depends on the chiller compressor technology.

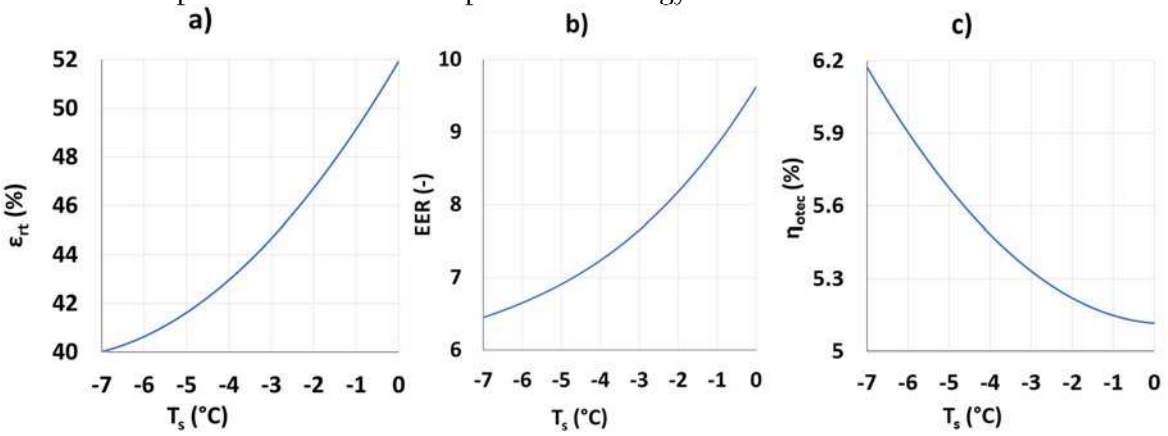

Figure 4: Efficiencies in function of the storage temperature. a) round-trip efficiency b) Chiller EER; c) ORC efficiency

4 LIMITS OF THE PRESENTED TECHNOLOGY

Integrating OTEC and PTES is an innovative solution for large-scale electricity storage, showing great potential for future development. However, like any pioneering technology, the associated costs of development, and infrastructure can be significant. By scaling OTEC costs from previous studies (Liponi et al., 2022), and considering an end-life cargo ship for storage (Ship Brokers, 2023), and the chiller, the total system cost amounts to 31 M€. Consequently, the specific cost of the Carnot battery stands at around 1600 €/kWh, surpassing the current and projected costs of electrochemical batteries. This is attributed to the high costs of marine environmental construction and the relatively lower efficiency of OTEC. To address these challenges, alternative TI-PTES layouts are being explored in future works to mitigate costs and enhance system efficiency. The innovative nature of PTES and OTEC holds significant promise for advancing sustainable energy. Despite the substantial costs involved, their potential to enhance energy generation and storage should not be disregarded.

5 CONCLUSIONS

The study examined a TI-PTES and OTEC system, optimizing its design and round-trip efficiency through an Aspen Hysys model. Various fluids for the OTEC and chiller were compared, yielding the following outcomes:

- The round-trip efficiency peaks at approximately 50% for ammonia with a 0 °C storage temperature (pure ice storage) and decreases with lower storage temperature and increased chiller operating temperature difference.
- Ammonia is the working fluid of the chiller and ORC that maximizes the round-trip efficiency of the system;
- Latent heat enables compact storage, achievable in the sea, e.g., via a repurposed cargo ship.
- The system shows promise for tropical energy storage, leveraging bathymetric gradients for significant temperature differences between ocean surface and bottom.

551

NOMENCLATURE

Acronyms
EER, Energy Efficiency Ratio
ORC, Organic Rankine Cycle
OTEC, Ocean Thermal Energy Conversion
PHES, Pumped Hydro Energy Storage
PTES, Pumped Thermal Energy Storage
RES, Renewable Energy Sources
TI-PTES, Thermally Integrated Pumped Thermal Energy Storage

Symbols
D, Diameter, (m)
ε, round-trip efficiency, (-)
η, Efficiency, (-)
ρ, Density, (kg/m3)
L, Length, (m)
v, Velocity, (m/s)
$\dot{m}$, Mass flow rate, (kg/s)
$\dot{W}$, Power, (kW)
p, Pressure, (bar)
T, Temperature, (K)
τ, Time duration, (hours)

Subscripts
c, compressor
ch, Charge
d, seawater pump
chill, chiller
dis, Discharge
otec, OTEC
p, OTEC pump
rt, Roundtrip
s, Storage
w, Water

REFERENCES

Argyrou MC, Christodoulides P, Kalogirou SA. Energy storage for electricity generation and related processes: Technologies appraisal and grid scale applications. Renew Sustain Energy Rev 2018;94:804–21. https://doi.org/10.1016/j.rser.2018.06.044.

Benato A, Stoppato A. Pumped Thermal Electricity Storage: A technology overview. Therm Sci Eng Prog 2018;6:301–15. https://doi.org/https://doi.org/10.1016/j.tsep.2018.01.017.

Dumont O, Lemort V. Mapping of performance of pumped thermal energy storage ({C}arnot battery) using waste heat recovery. Energy 2020;211:118963. https://doi.org/https://doi.org/10.1016/j.energy.2020.118963.

Frate GF, Antonelli M, Desideri U. A novel Pumped Thermal Electricity Storage (PTES) system with thermal integration. Appl Therm Eng 2017;121:1051–8. https://doi.org/10.1016/j.applthermaleng.2017.04.127.

Frate GF, Ferrari L, Desideri U. Rankine Carnot Batteries with the Integration of Thermal Energy Sources : A Review. Energies 2020;13:4766. https://doi.org/10.3390/en13184766.

Frate GF, Ferrari L, Sdringola P, Desideri U, Sciacovelli A. Thermally integrated pumped thermal energy storage for multi-energy districts: Integrated modelling, assessment and comparison with batteries. J Energy Storage 2023;61:106734. https://doi.org/10.1016/j.est.2023.106734.

Giwa A, Giwa SO. Estimating the optimum operating parameters of olefin metathesis reactive distillation process. ARPN J Eng Appl Sci 2013;8:614–24.

Henchoz S, Buchter F, Favrat D, Morandin M, Mercangöz M. Thermoeconomic analysis of a solar enhanced energy storage concept based on thermodynamic cycles. Energy 2012;45:358–65. https://doi.org/10.1016/j.energy.2012.02.010.

Hu S, Yang Z, Li J, Duan Y. Thermo-economic analysis of the pumped thermal energy storage with thermal integration in different application scenarios. Energy Convers Manag 2021;236:114072. https://doi.org/10.1016/j.enconman.2021.114072.

Khosravi A, Syri S, Assad MEH, Malekan M. Thermodynamic and economic analysis of a hybrid ocean thermal energy conversion/photovoltaic system with hydrogen-based energy storage system. Energy 2019;172:304–19. https://doi.org/10.1016/j.energy.2019.01.100.

Killer M, Farrokhseresht M, Paterakis NG. Implementation of large-scale Li-ion battery energy storage systems within the EMEA region. Appl Energy 2020;260:114166. https://doi.org/10.1016/j.apenergy.2019.114166.

Langer J, Cahyaningwidi AA, Chalkiadakis C, Quist J, Hoes O, Blok K. Plant siting and economic potential of ocean thermal energy conversion in Indonesia a novel GIS-based methodology. Energy 2021;224:120121. https://doi.org/10.1016/j.energy.2021.120121.

Liponi A, Baccioli A, Vera D, Ferrari L. Seawater desalination through reverse osmosis driven by ocean thermal energy conversion plant: Thermodynamic and economic feasibility. Appl Therm Eng 2022;213:118694. https://doi.org/10.1016/j.applthermaleng.2022.118694.

Masutani SM, Takahashi PK. Ocean Thermal Energy Conversion (otec). In: Steele JH, editor. Encycl. Ocean Sci., Oxford: Elsevier; 2001, p. 1993–9. https://doi.org/10.1006/rwos.2001.0031.

Olympios A V, McTigue JD, Farres-Antunez P, Tafone A, Romagnoli A, Li Y, et al. Progress and prospects of thermo-mechanical energy storage—a critical review. Prog Energy 2021;3:022001. https://doi.org/10.1088/2516-1083/abdbba.

Peterson RB. A concept for storing utility-scale electrical energy in the form of latent heat. Energy 2011;36:6098–109. https://doi.org/10.1016/j.energy.2011.08.003.

Ship Brokers. 91m Tanker 1998 – UK Built – 5028 CBM – DWT 4765 2023. https://horizonship.com/ship/91m-tanker-1998-uk-built-5028-cbm-dwt-4765/ (accessed May 31, 2023).

Vera D, Baccioli A, Jurado F, Desideri U. Modeling and optimization of an ocean thermal energy conversion system for remote islands electrification. Renew Energy 2020;162:1399–414. https://doi.org/10.1016/j.renene.2020.07.074.

ACKNOWLEDGEMENT

Funder: Project funded under the National Recovery and Resilience Plan (NRRP), Mission 4 Component 2 Investment 1.3 - Call for tender No. 1561 of 11.10.2022 of Ministero dell'Università e della Ricerca (MUR); funded by the European Union – NextGenerationEU

Dr. Guido Francesco Frate acknowledges the financial contribution of the Italian Operative National Plan (Piano Operativo Nazionale, PON) and the project Ricerca e Innovazione 2014–2020 (PON R&I) (Azione IV.6 "Contratti di ricerca su tematiche Green").

ORC SEVILLE 2023
7th International Seminar on O.R.C. Power Systems

© 2024 Editorial Universidad de Sevilla. Este es un artículo de acceso abierto distribuido bajo los términos de la licencia de uso y distribución Creative Commons (BY-NC-ND 4.0)

DOI: https://dx.doi.org/10.12795/9788447227457_92

EXERGY-BASED METHODS FOR HEAT PUMPS

Mathias Hofmann[1,*], Jonas Freißmann[2,3], Malte Fritz[2,3], Jeremias H. Alexe[1], Francesco Witte[4], George Tsatsaronis[1]

[1]*TU Berlin, Institute for Energy Engineering, Marchstraße 18, 10587 Berlin, Germany*
[2]*Hochschule Flensburg, University of Applied Sciences, Kanzleistraße 91-93, 24943 Flensburg, Germany*
[3]*Center for Sustainable Energy Systems (ZNES), Europa-Universität & Hochschule Flensburg, Munktetoft 3b, 24937 Flensburg, Germany*
[4]*German Aerospace Center (DLR), Institute of Networked Energy Systems, Carl-von-Ossietzky-Straße 15, 26129 Oldenburg, Germany*

*Corresponding Author: hofmann@iet.tu-berlin.de

ABSTRACT

Heat pumps are undoubtedly a relevant technology option for decarbonizing the residential sector's heating supply and providing process steam in the industry. Nevertheless, thermodynamic analysis and evaluation of heat pumps needs to be more accurate.

Exergy analysis provides a method that detects the real thermodynamic inefficiencies of the components and the overall process. Determining the exergetic efficiency also provides a statement about the process quality and the maximum possible potential for process optimization. In addition, heat pump concepts with different inputs (compression heat pumps, absorption heat pumps) can be consistently compared with each other. The exergoeconomic analysis enables the identification of the cost-generation process and the determination of the heat production costs.

Thermal Engineering Systems in Python (TESPy) is a free and open-source software for the simulation and analysis of energy conversion systems like gas turbines, steam power plants, heat pumps, or refrigerators. Exergy balances are solved in postprocessing for all predefined components, and exergetic efficiencies are determined.

Simulation results and comparative exergy analyses are presented for different heat pump concepts. The paper is intended to establish the exergy-based methods for heat pump analysis. The results show which concepts and components are suitable for providing indoor heat and process steam from renewable energy sources.

1 INTRODUCTION

Why are we dealing with heat pumps in general? Reversing the heat engine process makes it possible to bring the thermal energy of a low-temperature level to a higher temperature level by using work. If we use renewable energy sources to provide the necessary power, it is possible to decarbonize a significant part of the final energy use (space heating, industrial process heat, district heating).

At present, technical developments can be observed, especially for high-temperature heat pumps. Within the framework of IEA Annex 58, an overview of manufacturers and product configurations can be viewed online [1]. Currently, heat pumps with a maximum thermal output in the upper tens of MW range can be purchased. According to the manufacturers, temperatures above 200 °C can already be achieved. However, ambitious projects with large temperature spreads or high temperatures often do not reach TRL 9, are demonstrators or custom-made products, and are frequently financed with public funding.

There are numerous contributions on heat pumps. At this point, only a selection of current publications, which deal with comparative thermodynamic analyses of heat pumps, is given. Adamsen et al. [2] and Jiang et al. [3] present comprehensive overviews for heat pump configuration for high-temperature applications and comparatively benchmark them. Arpagaus et al. [4] give a market overview for high-temperature heat pumps, present potential analyses, and coefficient of performance (COP) correlations depending on different process parameters. Schlosser et al. [5] focus on industrial applications, i.e., large-scale heat pumps, and present COP correlations. For a survey of exergy analyses for heat pumps, see Peng et al. [6] and Liu et al. [7].

To date, there is no consistent exergy-based consideration for heat pumps in an open-source framework with complete data availability. The paper aims to present and establish the conventional exergy analysis as an evaluation method for heat pumps. Analyses of different heat pump concepts show the influence of different process parameters and designs on the exergetic efficiency of individual components and the overall process.

The next section presents the Thermal Engineering Systems in Python (TESPy) library, a free and open source software for simulation and analysis of energy conversion systems. The basics of the exergy analysis for heat pumps are presented in Section 3 followed by an example for a simple heat pump. Section 5 is dedicated to the comparative exergy-based analysis of different heat pump concepts. The findings and further steps are summarized in Section 6.

2 THERMAL ENGINEERING SYSTEMS IN PYTHON

The open-source software Thermal Engineering Systems in Python (TESPy) [8] is used for the component-based simulation of the considered energy conversion processes. The software is developed as part of the open energy modeling framework (oemof) in the scientific field and by industrial users.[1] The library is written in Python and its structure is depicted in Fig. 1. The user can build up arbitrary thermodynamic processes from single predefined components like heat exchangers, compressors, valves, or turbines. In addition to heat pumps, geothermal or solar thermal power plants, heat networks, or chillers can also be mapped. The software accesses the likewise open-source substance properties database CoolProp [9]. Detailed documentation with more examples and tutorials is available for the software.[2]

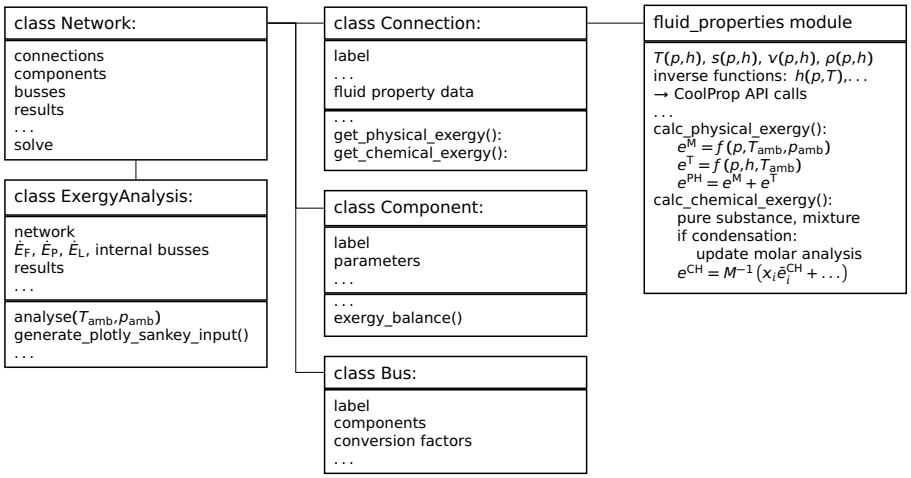

Figure 1: Simplified structure of TESPy

Following process simulation and design, exergy analysis can be used to identify sources of thermodynamic losses. The exergy analysis is performed automatically. Only the exergetic fuel, product, and loss of the overall process have to be passed to the tool [10, 11]. Furthermore, the simulation models can be combined with optimization methods [12].

1 https://oemof.org
2 https://tespy.rtfd.io

3 EXERGY ANALYSIS FOR HEAT PUMPS

A conventional thermodynamic analysis based on the evaluation of mass and energy balances fails in determining the real thermodynamic losses of a system. Consequently, the efficient use of energy sources is not guaranteed.

The misjudgment based on the coefficient of performance (COP) is not only that the impression is given that more energy is supplied than required. Moreover, the theoretical improvement potential of a thermodynamic optimization can not be calculated due to the lack of an inherent upper limit. With the help of the COP itself, no statement can be made about how far the chosen process configuration is from the thermodynamic optimum. An additional performance indicator, e.g. Lorentz COP [13], has to be calculated. In the case of the exergetic efficiency with the limits 0 and 1, this already contains the information sought.

In addition, exergy-based analysis enables the correct evaluation and comparison of processes with more than one product or fuel streams. With reference to heat pumps, Franzke [14] states that only on the basis of exergy a "flawless comparison" of compression heat pumps and absorption heat pumps is possible. In the same way, the correct consideration of the products in a cogeneration process for the simultaneous provision of electricity and heat succeeds only based on exergy [15, 16].

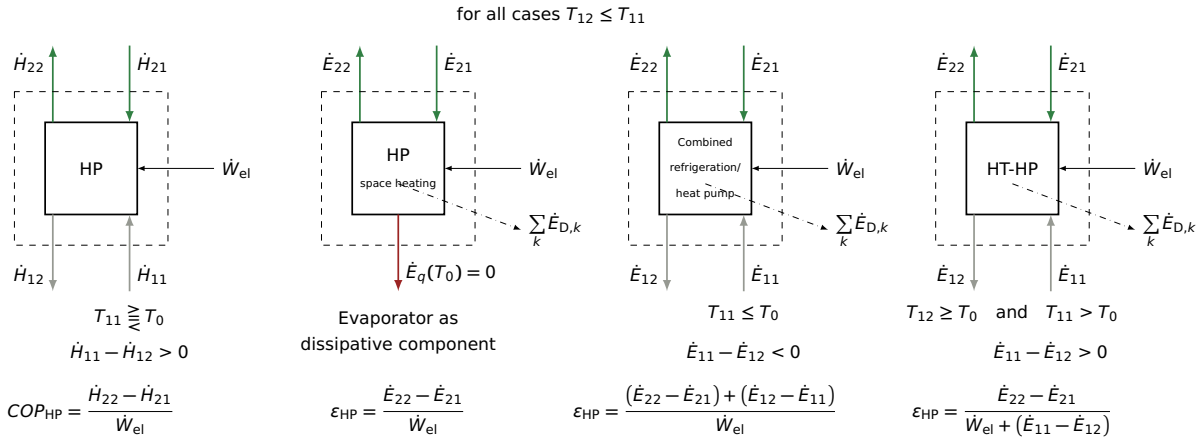

Figure 2: Steady-state energy balance and exergy balances of the heat pump. The different use cases must be distinguished to define the exergetic efficiency consistently. For space heating, the heat pump usually emits the exergy flow rate associated with the supplied heat at T_0.

Figure 2 contrasts the steady-state energy balance with the exergy balance. Following the definition of exergy (zero point at ambient conditions), evaluating the balance must consider whether the process takes place entirely above or partially below the ambient temperature. A heat rate is supplied to the heat pump at the lower temperature level. The enthalpy difference of the streams 11 and 12 is therefore always greater than 0, independent of T_{11}. The exergy difference of streams 11 and 12 is negative for the case T_{11} is lower than or equal to the ambient temperature. This means that a heat rate is energetically supplied to the overall process, but exergetically the exergy rate associated with the heat rate is transferred to the environment or is used as additional exergetic product; the heat pump thus acts like a refrigerating machine at the same time.

In addition to the electrical power required for the motor, the exergetic efficiency of the heat pump also includes the thermal power supplied to the process at the lower temperature level. It must be addressed and is essential, for example, when integrating industrial waste heat for high-temperature heat pumps. It also results in the advantage that the exergetic efficiency has an inherent upper limit compared to the coefficient of performance. It has a maximum value of 1.

555

4 SIMPLE HEAT PUMP EXERGY ANALYSIS

4.1 Thermodynamic Model

A simple thermodynamic model of a heat pump is used to demonstrate the exergy-based analysis. The flow diagram of the process can be found in Fig. 3. The heat pump is used to supply a heating circuit and is characterized by the parameters listed in Table 1. In addition, we assume that the process is steady-state, all components are adiabatic, there are no pressure losses in the heat exchangers, and changes in kinetic and potential energies can be neglected.

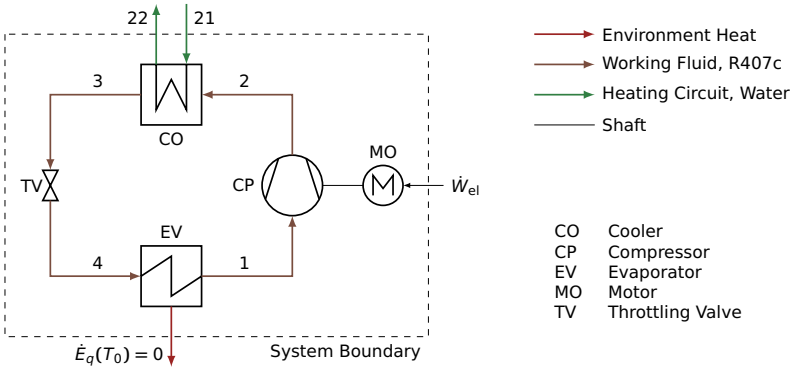

Figure 3: Thermodynamic model of a heat pump for the supply of a heating circuit

Table 1: Process parameters of the heat pump and ambient conditions

Parameter	Symbol	Unit	Value
Heat rate	$\dot{H}_{22} - \dot{H}_{21}$	kW	20
Lower pressure level	p_1	bar	5
Upper pressure level	p_2	bar	20
Superheating at the evaporator outlet	T_1	°C	$T_{sat}(p_1) + 2\,K$
Cooler outlet temperature	T_3	°C	40
Isentropic efficiency of compressor	η_s	%	75
Electric-mechanical efficiency of motor	$\eta_{el,mech}$	%	95
Ambient temperature	T_0	°C	15
Ambient pressure	p_0	bar	1.013

The mass and energy balances are solved for the selected process parameters using TESPy, see Section 2. The model, input data, and all results can be found in a git repository.[3] The exergy values can be calculated for all material and energy flows. Using the exergy balance, the exergy destruction of the components is determined. The definitions of the exergetic efficiencies of the components are noted in Eqs. (1) to (5).

4.2 Exergy Analysis of Components

Electricity is supplied to the motor via the system boundary to provide mechanical power. The latter consequently represents the exergetic product of the component.

$$\varepsilon_{MO} = \frac{\dot{W}_{mech}}{\dot{W}_{el}} \tag{1}$$

Mechanical power is used to compress from state 1 to 2. However, stream 1 is supplied at a temperature below the ambient temperature. Thus, to define the exergetic efficiency, it is necessary to divide the exergy rates into the thermal and mechanical parts [17]. The thermal part of the physical exergy of stream 1 must

3 https://github.com/tub-hofmann/heat-pumps-tespy

be considered as an exergetic fuel in addition to the necessary mechanical power. The increase of the mechanical part of the physical exergy and the thermal part of the physical exergy of stream 2 represents the exergetic product of the compressor.

$$\varepsilon_{\mathrm{CP}} = \frac{\dot{E}_2^{\mathrm{T}} + \left(\dot{E}_2^{\mathrm{M}} - \dot{E}_1^{\mathrm{M}}\right)}{\dot{W}_{\mathrm{mech}} + \dot{E}_1^{\mathrm{T}}} \tag{2}$$

The cooler connects the process with the heating circuit. If the heat capacity flows of the hot and cold sides are not exactly superimposed (infinitely large heat exchanger), any heat transfer is associated with exergy destruction. The exergetic product is the temperature rise in the heating circuit. The exergetic fuel is the exergy difference on the hot side of the heat exchanger.

$$\varepsilon_{\mathrm{CO}} = \frac{\dot{E}_{22} - \dot{E}_{21}}{\dot{E}_2 - \dot{E}_3} \tag{3}$$

If the throttling valve operates entirely above the ambient temperature T_0, it can be considered as a dissipative component. In the present case, T_0 is surpassed during expansion. It is necessary to divide the exergy flows into the thermal and mechanical parts. The thermal part of the physical exergy below ambient temperature represents the exergetic product of the throttling valve [10]. The pressure loss, i.e., the change of the mechanical part of the physical exergy and the thermal part of the physical exergy above the ambient temperature, is considered as exergetic fuel.

$$\varepsilon_{\mathrm{TV}} = \frac{\dot{E}_4^{\mathrm{T}}}{\dot{E}_3^{\mathrm{T}} + \left(\dot{E}_3^{\mathrm{M}} - \dot{E}_4^{\mathrm{M}}\right)} \tag{4}$$

In the example presented here, the evaporator operates completely below the ambient temperature T_0. If we assume that the exergy flow rate $\dot{E}_{\mathrm{q}}$ associated with the heat flow supplied from the environment surpasses the system boundary at T_0, $\dot{E}_{\mathrm{q}}$ results in zero. Consequently, no exergetic product can be defined for the evaporator. The evaporator must be considered as a dissipative component.

$$\varepsilon_{\mathrm{EV}} = \text{n/a} \tag{5}$$

4.3 Exergy Analysis of Overall Process

For the exergy analysis of the overall process, the steady-state exergy balance can be used. Simultaneously, the resulting information of the exergy destruction of the overall process can be compared with the sum of the exergy destruction within the components. Thus, it is easy to ensure that the analysis has been performed correctly.

$$\dot{E}_{\mathrm{D}}^{\mathrm{TOT}} = \sum_k \dot{E}_{\mathrm{D},k} = \dot{W}_{\mathrm{el}} + \dot{E}_{21} - \dot{E}_{22} \qquad \text{with} \quad \dot{E}_{\mathrm{q}} = 0 \tag{6}$$

4.4 Results

Table 2 summarizes the results of the exergy analysis for the components and the overall process. For the components the exergy destruction ratio can be calculated.

$$y_{\mathrm{D},k} = \frac{\dot{E}_{\mathrm{D},k}}{\dot{E}_{\mathrm{F,tot}}} \tag{7}$$

The highest exergy destruction occurs in the compressor. It is followed by the evaporator, the cooler, and the throttling valve. The exergetic efficiency of the overall process illustrates that the predominant part of the electrical power is required to overcome the thermodynamic inefficiencies of the components.

Table 2: Exergy-based analysis, overall process and component results

	R407c, $\dot{m}_1 = 0.101\,\mathrm{kg/s}$ $\dot{E}_\mathrm{D}^\mathrm{TOT} = 3.1\,\mathrm{kW}$	
Component k	ε_k [%]	$y_{\mathrm{D},k}$ [%]
Compressor, CP	79.1	19.9
Cooler, CO	80.6	12.1
Throttling valve, TV	60.9	8.6
Evaporator, EV	diss.	18.4
Heat pump, HP	35.9	

5 COMPARATIVE EXERGY-BASED ASSESSMENT OF HEAT PUMPS

This section analyzes different heat pump process designs, particularly for district heating and industrial process steam use cases. Figure 4 shows the various schematics: (a) simple cycle, (b) cycle with internal heat exchanger (IHX), (c) cycle with IHX and parallel compression (PC), and (d) cycle with IHX and compressor with intercooler (IC). For all heat pump designs the parameters are taken from Table 3. In addition, we assume that the processes are steady-state, all components are adiabatic, there are no pressure losses in the heat exchangers, and changes in kinetic and potential energies can be neglected. The different topologies are analyzed with the application of two natural and two synthetic working fluids: R600, R601, R1233zd(E), and R1336mzz(Z). Unfortunately, the CoolProp implementation of R1336mzz(Z) is lacking and bugs occur in the usage of R601 and R1233zd(E)[4], which makes the utilization of the closed source fluid property database REFPROP [18] necessary. The model, input data, and all results can be found in a git repository[5]. The results of the process simulations are analyzed according to the method shown above.

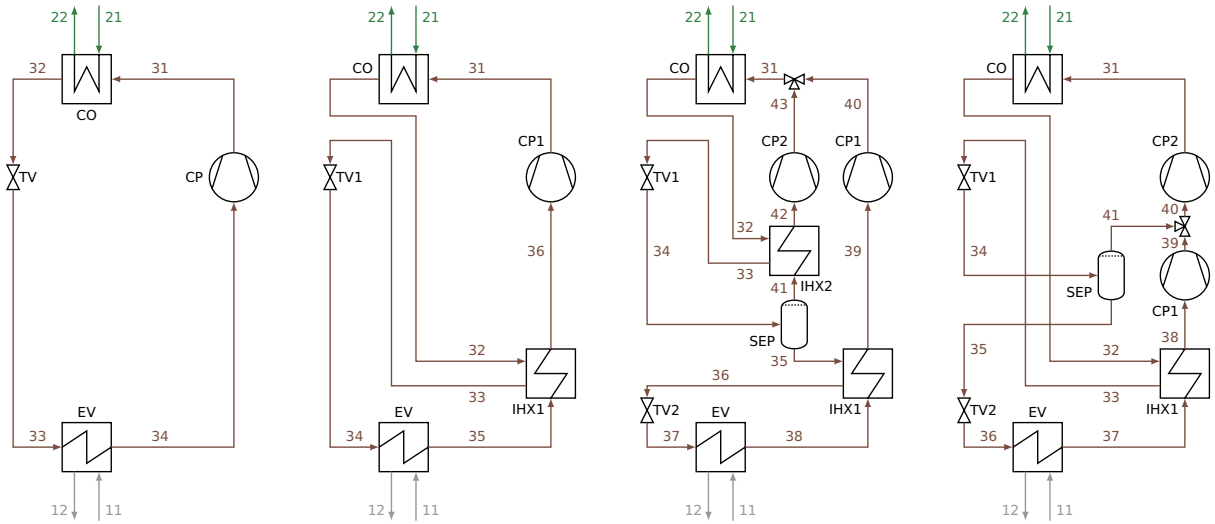

(a) Simple cycle **(b)** With IHX **(c)** With IHX and PC **(d)** With IHX and IC

Figure 4: Heat pump process designs

According to the contributions of Sulzgruber et al. [19, 20], the optimal high pressure of the different processes is identified. With the application of the exergy-based method, we extend their evaluation. The results of the energy analysis and the exergy analysis are compared.

The results are shown in Fig. 5a for the topology with IHX for all working fluids. The shapes of the R600, R1233zd(E), and R1336mz(Z) curves are similar to those of Sulzgruber et al., with a slight deviation of

4 https://github.com/CoolProp/CoolProp/issues/2070
5 https://github.com/tub-hofmann/heat-pumps-tespy

Table 3: Process parameters of the heat pumps and ambient conditions

Parameter	Symbol	Unit	Value
Heat rate	$\dot{H}_{22} - \dot{H}_{21}$	MW	1
Heat sink temperatures	$T_{21}; T_{22}$	°C	160; 200
Heat sink pressure	p_{21}	bar	20
Heat source temperatures	$T_{11}; T_{12}$	°C	95; 90
Heat source pressure	p_{11}	bar	5
Lower terminal temperature difference of cooler	$\Delta T_{\mathrm{l,CO}}$	K	10
Lower terminal temperature difference of evaporator	$\Delta T_{\mathrm{l,EV}}$	K	5
Upper terminal temperature difference of IHX	$\Delta T_{\mathrm{u,IHX}}$	K	15
Isentropic efficiency of compressor	η_s	%	76
Electric-mechanical efficiency of motor	$\eta_{\mathrm{el,mech}}$	%	95
Ambient temperature	T_0	°C	15
Ambient pressure	p_0	bar	1.013

COP depending on working fluid. The models used by Sulzgruber et al. are private. Therefore, parameters, assumptions, and used property functions cannot be fully reproduced. Consequently, deviations due to different input data cannot be excluded. In contrast to Sulzgruber et al., the results plot for R601 shows no local maximum. The absent maximum at decreasing high pressure is likely due to partial subcritical cooling and heat exchanger modeling.

As can be seen from Fig. 5a, the qualitative characteristics of energetic and exergetic analysis are identical. But the exergy analysis can reveal thermodynamic improvement potential more easily. From the maximum value of the exergetic efficiency, 68.7%, of the IHX cycle using R600, it can be concluded directly that 31.3% must be used to overcome the thermodynamic inefficiencies of the components, and represent the quantitative improvement potential of the process.

Figure 5b shows the results for different topologies using the working fluid R600. The values for COP and exergetic efficiency of the simple cycle are lower than for all other process designs by a discernible margin and not depicted in the diagram. The underlying reason for the low values is the low enthalpy difference in the cooler of the simple cycle, as the isentropes shift inwards towards the critical point close to the saturated vapor line. Therefore, any topology improvement leading to superheating after the evaporator will almost double the exergetic efficiency. The highest efficiency is achieved with IHX and PC, see Fig. 4c, followed by the process with IHX, see Fig. 4b and finally, the design with IHX and IC, see Fig. 4d. Generally, lower high-pressure performance maxima correspond with a higher absolute COP and exergetic efficiency, analogous to the results in Fig. 5a.

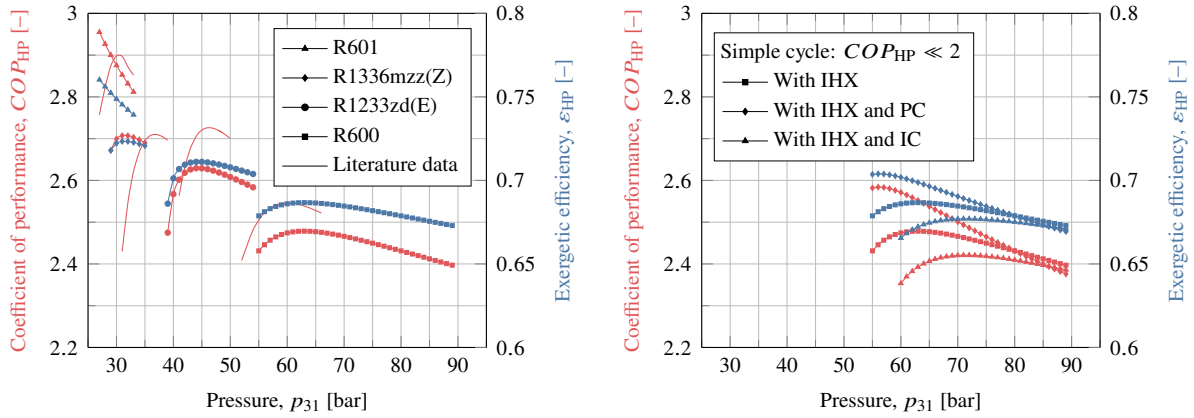

(a) IHX with each working fluid

(b) R600 with each topology

Figure 5: Coefficient of performance and exergetic efficiency for varying high pressure. For Fig. 5a in comparison with literature data from Sulzgruber et al. [19, 20]

The exergy analysis is featured by the possibility of a component-specific assessment. The results are shown in Fig. 6 for the analysis of the process design with IHX using R600 as working fluid. The exergy destruction ratio of each component, defined in Eq. (7), is calculated and plotted for varying high pressure within the cooler. The evaporator, valve, and compressor do not show a significant change in their respective exergy destruction ratio, with only a slight decrease visible in the quantitative results. On the other hand, the exergy destruction rate of the cooler increases with rising high pressure. The reason for this is the rising exit temperature of the compressor with higher pressure which in consequence increases the mean logarithmic temperature. In contrast, the exergy destruction ratio of the internal heat exchanger decreases with higher pressure. The combination of these considerable influences results in the minimum exergy destruction ratio occurring at 63 bar.

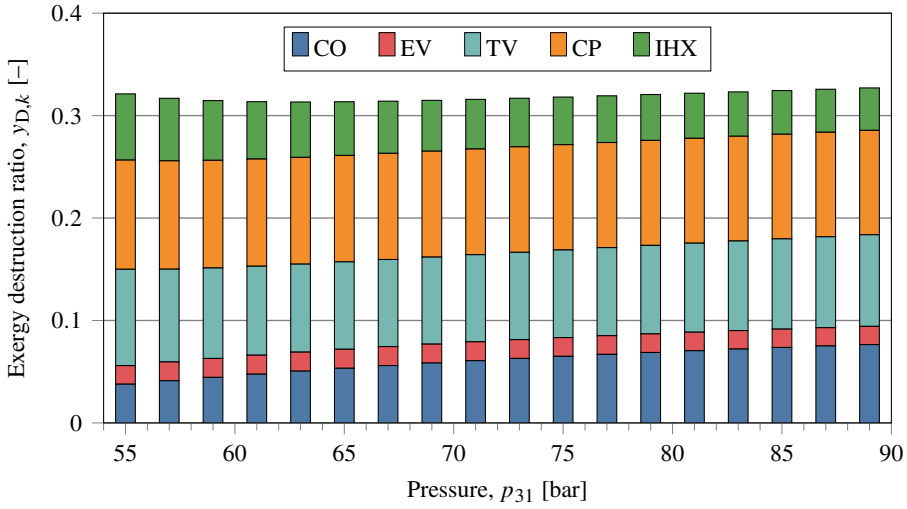

Figure 6: Exergy destruction ratios of the components in IHX with R600

560

6 CONCLUSION

Exergy analysis detects the real thermodynamic inefficiencies of the components and the overall process, which makes it advantageous compared to energy-based evaluation for evaluating and optimizing thermodynamic processes such as heat pumps. Exergy-based methods, especially for heat pumps, are presented within the framework of this contribution. The analysis results have shown that different operating optima are derived from different working fluids and topologies. The influences of the individual system components are presented.

A generic heat pump model would be suitable for a broader analysis of topologies, which requires stable simulations for different working fluids with different process parameters and boundary conditions. For this reason, the co-authors Malte Fritz and Jonas Freißmann are currently developing a framework with a graphical user interface, which will be extended in cooperation with Technische Universität Berlin.

As academic research flourishes with cooperation and knowledge exchange, it is regrettable that using closed-source fluid property databases is necessary for some working fluids or cases. Future research should consider this point as a precondition.

CREDIT AUTHOR STATEMENT

Mathias Hofmann: Conceptualization, Methodology, Software, Validation, Formal analysis, Investigation, Resources, Data Curation, Writing - Original Draft, Writing - Review & Editing, Visualization, Supervision **Jonas Freißmann, Malte Fritz (both equally):** Software, Validation, Formal analysis, Data Curation, Writing - Original Draft, Writing - Review & Editing, Visualization **Jeremias H. Alexe:** Software, Validation, Formal analysis **Francesco Witte:** Conceptualization, Methodology, Software, Validation, Formal analysis, Data Curation, Writing - Review & Editing **George Tsatsaronis:** Review & Editing, Supervision

NOMENCLATURE

Abbreviations

CO	Cooler
CP	Compressor
EV	Evaporator
HP	Heat pump
IHX	Internal heat exchanger
MO	Motor
SEP	Separator
TV	Throttling valve

Latin Symbols

e	Mass specific exergy, J/kg
$\bar{e}$	Molar specific exergy, mol/kg
$\dot{E}$	Exergy rate, W
h	Specific enthalpy, J/kg
$\dot{H}$	Enthalpy rate, W
$\dot{m}$	Mass flow rate, kg/s
M	Molar mass, kg/mol
p	Pressure, bar
$\dot{Q}$	Heat rate, W
s	Specific entropy, J/kg K
T	Temperature, °C
$\dot{W}$	Work rate, W
x_i	Molar fraction, –
y	Exergy ratio, –

Greek Symbols

Δ	Difference, –
ε	Exergetic efficiency, –
η	Energetic efficiency, –

Superscripts and Subscripts

0	At ambient state
amb	At ambient state
CH	Chemical
D	Destruction
el	Electric
F	Fuel
i	Stream
in	At inlet
k	Component
KN	Kinetic
L	Loss
mech	Mechanic
M	Mechanical
out	At outlet
P	Product
PH	Physical
PT	Potential
s	Isentropic
tot	Total
T	Thermal

REFERENCES

1. INTERNATIONAL ENERGY AGENCY (IEA). *Annex 58 about HTHP, Task 1: Technologies – State of the art and ongoing developments for systems and components*. 2022. Available also from: https://heatpumpingtechnologies.org/annex58/task1/#supplier-technology.
2. ADAMSON, K.-M. et al. High-temperature and transcritical heat pump cycles and advancements: A review. *Renew. Sustain. Energy Rev.* 2022, vol. 167, p. 112798. Available from DOI: 10.1016/j.rser.2022.112798.
3. JIANG, J. et al. A review and perspective on industry high-temperature heat pumps. *Renew. Sustain. Energy Rev.* 2022, vol. 161, p. 112106. Available from DOI: 10.1016/j.rser.2022.112106.
4. ARPAGAUS, C. et al. High temperature heat pumps: Market overview, state of the art, research status, refrigerants, and application potentials. *Energy*. 2018, vol. 152, pp. 985–1010. Available from DOI: 10.1016/j.energy.2018.03.166.
5. SCHLOSSER, F. et al. Large-scale heat pumps: Applications, performance, economic feasibility and industrial integration. *Renew. Sustain. Energy Rev.* 2020, vol. 133, p. 110219. Available from DOI: 10.1016/j.rser.2020.110219.
6. PENG, Z.-R. et al. Thermodynamic analysis of novel heat pump cycles for drying process with large temperature lift. *Int. J. Energy Res.* 2019, vol. 43, pp. 3201–3222. Available from DOI: 10.1002/er.4394.
7. LIU, R. et al. A comprehensive and updated review on the exergy analysis of ground source heat pumps. *Sustain. Energy Technol. Assess.* 2023, vol. 55, p. 102906. Available from DOI: 10.1016/j.seta.2022.102906.
8. WITTE, F.; TUSCHY, I. TESPy: Thermal Engineering Systems in Python. *J. Open Source Softw.* 2020, vol. 5, p. 2178. Available from DOI: 10.21105/joss.02178.
9. BELL, I. H. et al. Pure and Pseudo-pure Fluid Thermophysical Property Evaluation and the Open-Source Thermophysical Property Library CoolProp. *Ind. Eng. Chem. Res.* 2014, vol. 53, pp. 2498–2508. Available from DOI: 10.1021/ie4033999.
10. WITTE, F. et al. Generic and Open-Source Exergy Analysis—Extending the Simulation Framework TESPy. *Energies*. 2022, vol. 15, p. 4087. Available from DOI: 10.3390/en15114087.
11. HOFMANN, M. et al. Thermal Engineering Systems in Python (TESPy): The implementation and validation of the chemical exergy. In: *Proceedings of ECOS 2022*. Copenhagen, Denmark, 2022.
12. BISCANI, F.; IZZO, D. A parallel global multiobjective framework for optimization: pagmo. *J. Open Source Softw.* 2020, vol. 5, p. 2338. Available from DOI: 10.21105/joss.02338.
13. JENSEN, J. K. et al. Heat pump COP, part 2: Generalized COP estimation of heat pump processes. In: *13th IIR Gustav Lorentzen Conference on Natural Refrigerants*. Valencia, Spain, 2018, pp. 1136–1145. Available from DOI: 10.18462/iir.gl.2018.1386.
14. FRANZKE, H. H. Vergleich verschiedener Wärmepumpen anhand der Exergie. In: *Tagungsbericht des 3. Internationalen Sonnenforums*. Hamburg, 1980, pp. 791–798. in German.
15. HOFMANN, M. et al. Free and Open-Source Teaching: Understanding Exergy using Thermal Engineering Systems in Python (TESPy). In: *Proceedings of ECOS 2023*. Las Palmas de Gran Canaria, Spain, 2023.
16. PENKUHN, M. et al. Prozessbewertung und Exergieanalyse für ein Heizkraftwerk. In: *Kraftwerkstechnisches Kolloquium*. Dresden, Germany, 2021, pp. 1–12. Available from DOI: 10.14279/depositonce-15966. in German.
17. MOROSUK, T.; TSATSARONIS, G. Splitting physical exergy: Theory and application. *Energy*. 2019, vol. 167, pp. 698–707. Available from DOI: 10.1016/j.energy.2018.10.090.
18. LEMMON, E. W. et al. *NIST Standard Reference Database 23: Reference Fluid Thermodynamic and Transport Properties-REFPROP, Version 10.0, National Institute of Standards and Technology*. 2018. Available from DOI: 10.18434/T4/1502528.
19. SULZGRUBER, V. et al. Concept study for industrial heat pumps up to 250 °C heat sink temperature using radial turbo compressors. In: *13. Internationale Energiewirtschaftstagung an der TU Wien*. Wien, 2023.
20. RIEDL, J. et al. Hochtemperaturwärmepumpen bis 250 °C: Ergebnisse einer thermodynamischen Machbarkeitsanalyse. In: *DKV-Tagung*. Magdeburg, 2022. in German.

ORC SEVILLE 2023
7th International Seminar on O.R.C. Power Systems

© 2024 Editorial Universidad de Sevilla. Este es un artículo de acceso abierto distribuido bajo los términos de la licencia de uso y distribución Creative Commons (BY-NC-ND 4.0)

DOI: https://dx.doi.org/10.12795/9788447227457_93

REDUCED ORDER MODELLING OF OPTIMIZED HEAT EXCHANGERS FOR MAXIMUM MASS-SPECIFIC PERFORMANCE OF AIRBORNE ORC WASTE HEAT RECOVERY UNITS

Fabio Beltrame[1]*, Dabo Krempus[1], Piero Colonna[1], Carlo De Servi[1,2]

[1] *Delft University of Technology, Propulsion and Power, Aerospace Engineering, Delft, The Netherlands*
[2] *VITO, Thermal Energy Systems, Mol, Belgium*

*Corresponding Author: f.beltrame@tudelft.nl

ABSTRACT

Waste heat recovery (WHR) from aeroengines via compact organic Rankine cycle (ORC) units may increase the fuel efficiency of air transportation. Heat exchangers are arguably the key components of ORC systems for aeronautical applications and their design must be optimized to guarantee the best trade-off between fluid pressure drop, weight and induced aircraft drag. At present, no heat exchangers design guidelines are available for waste heat recovery systems aboard aircraft. This study, thus, contributes to defining a proper design methodology for ORC systems of such applications. The chosen test case is a supercritical ORC system with cyclopentane as the working fluid, which recovers waste heat from the auxiliary power unit of an aircraft. The exhaust gas temperature and mass flow rate of the power unit are known and kept constant in the analysis, and so are the ambient conditions, which define the cold sink of the ORC turbogenerator. Three design strategies targeting minimum mass and maximum net power output of the ORC unit have been assessed. In the first one, the multi-objective optimization is performed by prescribing a priori the geometry and frontal area of the heat exchangers. Thus, only the cycle parameters are optimized. The second method tackles, instead, the simultaneous optimization of the geometric parameters of the condenser and the cycle parameters. It was found that the integrated design allows for system mass reduction by 10 - 12% for a given ORC power output, highlighting the importance of performing the simultaneous optimization of the thermodynamic process and the heat exchanger geometry. Finally, the third method addresses the same optimal design problem by leveraging a reduced-order model of the condenser to predict the optimal design space of this component. The generated Pareto front obtained with this method is very similar to that found by optimizing simultaneously the complete condenser geometry and the cycle parameters. The mean deviation is about 2%. With just one heat exchanger surrogate model, the Pareto front was generated in one fourth of the computational time. This is due to the lower number of optimization variables and the faster objective function evaluation.

1 INTRODUCTION

Research on design of compact heat exchangers (HXs) for aerospace applications has been gaining momentum, being HXs key components of the new technical solutions currently under evaluation to improve the efficiency and sustainability of aircraft propulsion systems. Waste heat recovery (WHR) from aeroengines via compact organic Rankine cycle (ORC) units is, for instance, one of these solutions. The preliminary design of HXs of stationary ORC systems is generally performed once the optimization of the thermodynamic cycle configuration is completed, as the optimal range for the main design specifications of these components, i.e. minimum temperature difference and allowable pressure drops, are known based on a consolidated design practice. In case of mobile systems and especially of aerospace applications, the selection of an appropriate HX topology and the related optimal geometry cannot be decoupled from the design of the thermodynamic cycle, as the fuel savings depend not only on conversion efficiency, which is strongly related to the HXs effectiveness and pressure drops, but also on the overall system weight and limitations on the available space. A consequence thereof is that, currently, there are no specific HX design guidelines for such applications. At present, only a few

studies have documented the integrated design of these components and the thermodynamic process. For instance, Lecompte et al. (2014) optimized the HX geometry together with the ORC WHR system for stationary applications, and highlighted how important it is to optimize these components and choose the right topology to maximize cycle efficiency and minimize costs. Similarly, Chatzopoulu et al. (2019) investigated the off-design performance of a medium power capacity ORC unit recovering heat from stationary internal combustion engines. The subcritical non-recuperated ORC cycle was optimized to maximize net power output during both nominal and off design operations for given characteristics of the HXs and the expander. Two different HX topologies were compared based on the off-design performance map of the various system solutions. In these studies, weight or size constraints were not considered.

Recent research works have also demonstrated that HX optimization is key for the optimum design of aerospace thermal systems. For example, Yu et al. (2016) showed that the optimization of the precooler of an air breathing engine flying at high Mach numbers is needed, not only to achieve system performance improvements, but also to enable the operational feasibility of the engine itself. Ascione et al. (2021) optimized the preliminary design of a vapour compression cycle and its components simultaneously. The results show that the optimum HX dimensions depend on the selected thermodynamic conditions, working fluid, as well as the targeted figure of merit in the design.

In this context, the aim of the present work is to contribute to the development of a computationally efficient methodology to predict the mass-specific performance of optimal HX designs in the early design phase of aerospace thermal systems. Notably, the study explores the development and use of a reduced order model of the HXs to replace the conventional preliminary sizing procedure of these components, and to reduce the degrees of freedom associated to their geometry in the optimization. The selected test case to demonstrate the proposed methodology is a supercritical ORC waste heat recovery unit recovering waste heat from an aircraft auxiliary power unit.

2 TEST CASE

The WHR unit studied in this work consists of an organic Rankine cycle turbogenerator serving as bottoming unit of the auxiliary power unit of an Airbus A320. The process flow diagram of this combined cycle system, named CC-APU, is reported in Figure 1. Cyclopentane is chosen as the working fluid as a previous study indicated that such a fluid is especially suited to gas turbine WHR applications (Krempus et al., 2021). A supercritical ORC configuration is adopted to maximize thermodynamic cycle efficiency. Additionally, for the chosen working fluid and HX materials, the supercritical operating conditions lead to HX designs with wall thicknesses close to the minimum value from a manufacturability standpoint, thus mass savings are arguably limited for lower pressures. The APU characteristics are fixed, together with the ambient pressure and temperature, which corresponds to ISA +25 at 0 m MSL. Only the ORC system design is addressed in this study. The exhaust gases are discharged from the APU at 847.15 K and 1.02 bar with a mass flow rate of 0.87 kg/s.

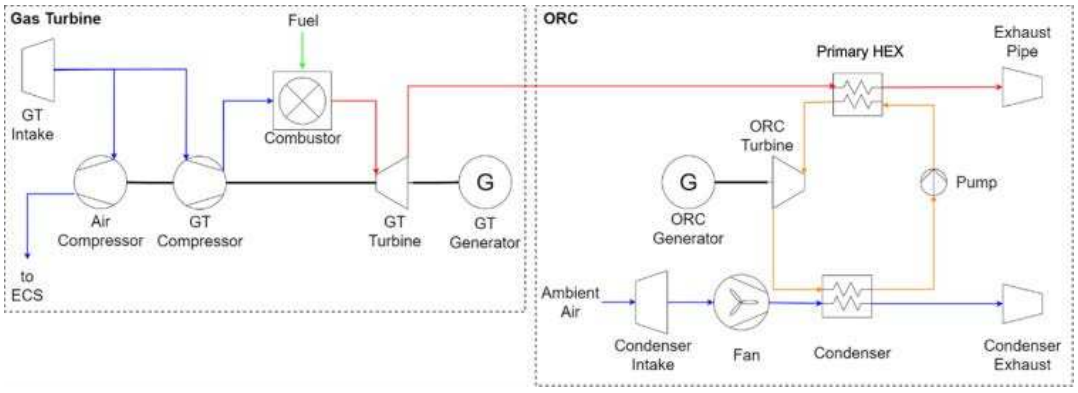

Figure 1: Process flow diagram of the CC-APU system.

3 METHODOLOGY

3.1 ORC system modelling

The performance of the ORC unit is modeled using an in-house tool for on-design thermodynamic cycle calculations. The Helmoltz-energy explicit equation of state (HEOS) implemented in CoolProp (Bell et al., 2014) is used for thermodynamic property modeling of the ORC working fluid. The ideal gas model is, instead, adopted for the APU exhaust gases, whose composition is fixed and assumed to be 74% N2, 15.9% O2, 6.4% CO2, 2.5% H2O, 1.2% Ar (Siebel et al. 2018). Regarding the ORC components, the geometrical characteristics of the primary HX are fixed, while those of the condenser are optimized.

The chosen topology for the primary HX consists in a multi-pass staggered bare-tube bundle where the working fluid circulates inside the tubes, in a counter-crossflow arrangement with respect to the exhaust gases. A nickel-based alloy, HastelloyX, is chosen as the material of the primary HX given the maximum exhaust gas temperature as suggested by Grieb (2004). The tube outer diameter is 1.8 mm, while the tube thickness is calculated given the pressure difference between the working fluid and the exhaust gases. The transverse and longitudinal pitches between the tubes are set to 3 and 1.25 outer diameters, respectively, to minimize the pressure drop and maximize the compactness of the HX, while the number of passes is set to 10. The frontal area is fixed and corresponds to a square of 0.28 x 0.28 meters. These dimensions were chosen considering the size of the APU exhaust duct.

For the ORC condenser, a flat tube microchannel heat exchanger geometry with louvered or offset strip fins is considered. The fin and flat tube thicknesses are set to 0.11 mm and 0.2 mm, respectively, while the height of the microchannels h_{mc} is set to 1.6 mm. The louver fin length L_l was fixed to 85% of the fin height. These values were chosen based on manufacturability considerations. The other geometric parameters highlighted in Table 3 are optimized. The chosen material for the condenser is an aluminum alloy of the 3000 series, as suggested in the technical report by Kaltra Gmbh (2020).

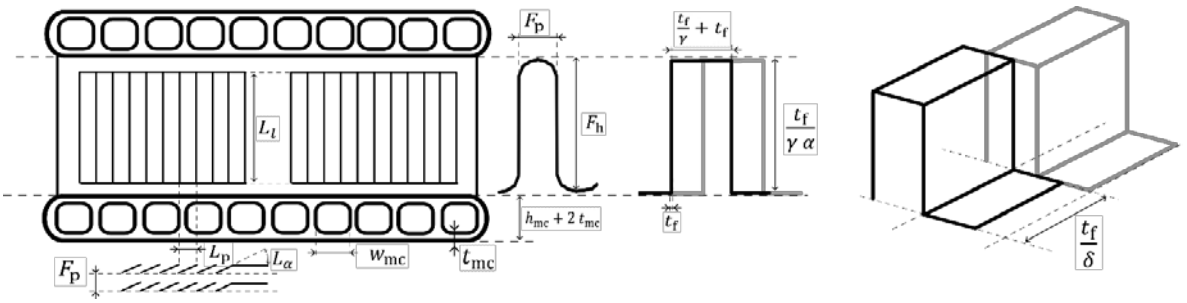

Figure 2: Sketch of the flat tube microchannel with louver or offset strip fins geometry.

The turbine power output $\dot{W}_{\mathrm{turb}}$ is calculated assuming a constant isentropic efficiency of 0.94, a mechanical efficiency of 0.99, and a generator efficiency of 0.97. The working fluid is pressurized by a centrifugal pump, while an electrically driven fan provides the necessary air mass flow rate $\dot{m}_{\mathrm{air}}$ to the condenser. The net power output of the WHR unit is thus calculated by subtracting the fan and pump power consumptions to the turbine power, see Equation (2). The isentropic fan and pump efficiencies are assumed equal to $\eta_{\mathrm{is,f}} = 0.6$ and $\eta_{\mathrm{is,p}} = 0.65$, respectively, while the mechanical and conversion efficiencies are fixed to $\eta_{\mathrm{m,f}} = \eta_{\mathrm{m,p}} = 0.98$.

$$\dot{W}_{\mathrm{net}} = \dot{W}_{\mathrm{turb}} - \frac{\dot{m}_{\mathrm{air}} \Delta P_{\mathrm{air}}}{\rho_{\mathrm{air}} \eta_{\mathrm{is,f}}\, \eta_{\mathrm{m,f}}} - \frac{\dot{m}_{\mathrm{wf}}\, \Delta H_{\mathrm{p}}}{\eta_{\mathrm{is,p}}\ \eta_{\mathrm{m,p}}} \tag{1}$$

The ORC system mass M_{ORC} is estimated as the sum of the mass of the main ORC system components (pump, turbogenerator, condenser, primary HX, fan), of the working fluid, and of the balance-of-plant. The HX mass is an outcome of the respective sizing models, see the following section. Assuming that the primary HX is fully flooded at the start-up, the working fluid mass is estimated as the primary HX cold side volume augmented by 20% to account for system piping, times the fluid density at standard ambient conditions. The turbo-generator mass is estimated assuming a specific power of around 5.5 kW/kg, based on the results in Geest et al. (2015). The same approach is adopted for the centrifugal pump, whose specific power is assumed to be 4 kW/kg as reported by Kwak et al. (2018). The mass of

the fan including its motor and that of the balance-of-plant are assumed to contribute 10% to the overall system mass. Note also that the sizing of the equipment and the weight estimation are performed once the thermodynamic cycle calculations are completed.

3.2 Heat exchanger sizing

The required size of the HX varies depending on the cycle specifications. The HX models thus consist of a sizing procedure aimed at finding the heat transfer area A_{ht} that satisfies the required heat duty given the inlet temperature, pressure, and mass flow rate of the hot and cold streams. For this task, in-house tools have been developed in python and verified using the software EchTherm. The output of the sizing procedure includes the HX dimensions, mass, and pressure drops on the cold and hot sides. For both the heat exchangers of the ORC unit, the height *Y* and width *X* on the gas side, which determine the frontal area, are an input to the design routine. The heat exchanger depth Z is instead calculated to meet the design specifications. In the case of the condenser, this corresponds to determining the number of microchannels n_{mc} of width w_{mc} within the flat tubes, while for the primary HXs the dependent variable is the number of streamwise tubes per pass n_{z}. As fluid properties can change significantly on the working fluid side, in both the condenser and the primary HX models, the geometry is discretized in several control volumes, or cells, in which mean properties are estimated. As the primary HX features multiple fluid passes, the number of cells is set conveniently equal to the number of passes, which is an input of the design problem. For the condenser, the number of cells, or control volumes, is set equal to three, one for each thermodynamic region involved in the condensation process of the fluid (superheated vapour, two-phase fluid, and subcooled liquid). These control volumes encompass a portion of the flow path of both the working fluid and of the air or exhaust gas streams, but they differ in size, due to the different enthalpy drop $\Delta H_{\mathrm{H}}^{i}$ associated with the thermodynamic state. This quantity as well as the pressure drops are estimated by implementing different empirical correlations, depending on the geometry and fluid phase. The heat transfer correlations are formulated in terms of Colburn factor or Nusselt number, while the pressure drop calculation is based on the estimate of the friction factor or the pressure gradient dP/dz. Table 1 lists the set of correlations implemented in the HXs models. The code solves the equations of the model by determining iteratively the heat transfer area A_{ht}^{i} of each control volume or cell i as

$$A_{\mathrm{ht}}^{i} = \frac{\dot{m}\,\Delta H^{\mathrm{i}}}{F^{i}\,\Delta T_{\mathrm{ml}}^{i}\,U^{i}}, \tag{2}$$

where U^{i} is the local overall heat transfer coefficient, $\Delta T_{\mathrm{ml}}^{i}$ is the local mean logarithmic temperature difference, and F^{i} is its correction factor, which is lower than unity for non-constant temperature heat transfer and any flow arrangement different from pure counterflow. The design routine stops when the relative difference in the estimated overall heat transfer area between two consecutive iterations is smaller than 1%.

Table 1: List of correlation used in the heat exchanger models.

HX	Fluid	Property	Reference
Primary HX	Exhaust gas (Tube bundle)	Nu f	Leveque analogy, Shah (2003) VDI (2010, Ch. L1)
Condenser	Air (Louvered fins)	j f	Chang and Wang (1997) Chang et al. (2000)
Condenser	Air (Offset strip fins)	j, f	Manglik and Bergles (1995)
Condenser / Primary HX	WF – single phase	Nu f	Taler (2017) Colebrook-White (VDI, Ch. L1, 2010)
Condenser / Primary HX	WF – two-phase (Condensation)	$\mathrm{d}P/\mathrm{d}Z$ h_c	Müller-Steinhagen and Heck (1986) Shah (2019)

3.3 ORC system design strategies

Three strategies are investigated in this work to design the ORC WHR unit. In the first one, only the thermodynamic cycle parameters are optimized. The degrees of freedom associated with the ORC configuration are the maximum and minimum working fluid temperatures, the maximum cycle pressure, as well as the evaporator and the condenser pinch point temperature differences. Table 2 lists for these variables the considered bounds in the optimization. The second design strategy deals with the simultaneous optimization of the thermodynamic cycle parameters and the condenser geometry. The design variables associated with this component vary depending on the selected fin topology, which can be of the offset strip or louvered type. In both cases, the width of the microchannels within the flat tubes, w_{mc} , is one of the degrees of freedom of the design problem. The total number of design variables is 9 in the case the condenser features offset strip fins, and 10 in the case of louvered fins. Table 3 reports the lower and upper bounds of all the optimization variables related to the condenser geometry. For more details about the parametrization of the fin shapes, the reader is referred to Chang and Wang (1997) for the louvered fins, and to Manglik and Bergles (1995) for the offset strip fins.

Table 2: ORC WHR design parameters and corresponding bounds in the optimization

Parameter	$T_{min,ORC}$ [K]	$T_{max,ORC}$ [K]	$P_{max,ORC}$ [bar]	$\Delta T_{pp,evap}$ [K]	$\Delta T_{pp,cond}$ [K]
Min	367	517.12	47.4	10	10
Max	378	547.84	67.7	50	50

Table 3: Bounds of the optimization variables related to the condenser geometry.

Geometry	Channels	Louvered fins				Offset strip fins		
Parameter	w_{mc} (mm)	F_{h}(mm)	F_{p}(mm)	L_{α} (°)	L_{p}(mm)	α (-)	δ (-)	γ (-)
Min	1	6	0.9	10	0.9	0.1	0.012	0.038
Max	2.5	16	3	30	3	1	0.037	0.122

The third design strategy relies on a reduced-order model of the condenser. This is calibrated by first optimizing the condenser geometry, either featuring offset-strip or louvered fins, for a set of process conditions, by using the same model used for the sizing. The optimization results are then exploited to define a surrogate model representing the optimal design space of the condenser, which is then used to replace the original condenser model when solving the optimal design problem of the ORC unit. The advantage is a drastic reduction in the computational cost of the system optimization. Notably, the number of design variables reduces from 9 or 10, depending on the condenser geometry, to 6.

As for the optimization algorithm, the NSGA-II routine (Deb et al., 2002) is used. Notably, the objective functions considered in the ORC WHR unit preliminary design are the minimization of the system mass M_{ORC} and the maximization of the net power output $\dot{W}_{\mathrm{net}}$. The manipulated variables are the cycle parameters in Table 2 and the condenser design variables in Table 3, depending on the selected fin geometry. If the surrogate model is adopted, the optimization variables associated to the condenser geometry reduces to only one, as explained in Section 3.4. The optimization problem related to the preliminary design of the ORC unit can thus be stated as follows:

$$\begin{aligned} &\text{Minimize:} && M_{ORC}\,, -W_{\mathrm{net}} \\ &\text{Subject to:} && Z_{\mathrm{min}} \leq Z_{HX} \leq Z_{\mathrm{max}} \\ & && \Delta P_{wf} \leq 3\%\ \mathrm{P_{wf,in}}. \end{aligned}$$

3.4 Reduced order model for the optimal condenser design

The proposed reducer-order modeling strategy for the ORC condenser begins with the generation of a dataset of optimal condenser solutions for a set of process conditions. Notably, for a given fin topology, the condenser geometry is optimized with respect to two objective functions, which are the minimization of the HX mass and the air pressure drop. The NSGA-II is again employed to optimize the two objectives simultaneously, by varying the geometry degrees of freedom while satisfying specific

constraints on the size of the HX and the working fluid side pressure drop. The output of the multi-objective optimization is a set of Pareto-optimal solutions for each process condition. The optimization problem can thus be stated as follows:

Minimize: $M_{\mathrm{HX}}\,, \Delta P_{\mathrm{air}}$
Subject to: $Z_{\min} \leq Z_{\mathrm{HX}} \leq Z_{\max}$
$\Delta P_{\mathrm{wf}} \leq 3\%\ \mathrm{P}_{\mathrm{wf,in}}$.

Four process conditions fully specify the design point of the condenser, namely the cooling air and fluid mass flow rates ($\dot{m}_{\mathrm{air}}, \dot{m}_{\mathrm{wf}}$), the condensation pressure p_{cnd} and de-superheating degree, which is defined as $\Delta T_{\mathrm{dsh}} = T_{\mathrm{wf,in}} - T_{\mathrm{cnd}}$. To extend the reduced order model validity, the air inlet temperature $T_{\mathrm{air,in}}$ is also varied. The range considered for these variables, which determine the validity range of the reduced order model, are reported in Table 4. The corresponding condenser heat duty varies from 256 to 388 kW. The upper and lower bounds of Table 4 are defined by analyzing the solutions resulting from the simultaneous optimization of the thermodynamic cycle specifications and the condenser geometry, indicated as optimization strategy #1 in Section 3.3.

Table 4: Range of process conditions for the generation of the condenser optimal design dataset.

	$\dot{m}_{air}$	$\dot{m}_{wf}$	p_{cnd}	ΔT_{dsh}	$T_{air,in}$
Min	7.25 kg/s	0.68 kg/s	3.58 bar	10 K	305.6 K
max	9.25 kg/s	0.85 kg/s	4.76 bar	60 K	316.0 K

The next step of the procedure in the definition of the reduced-order model is data reduction. Let a specific Pareto front be represented by a basis function shared by the whole dataset. This basis function is defined by a small set of coefficients that need to be calculated for each curve, and a validity interval. By nondimensionalizing the heat exchanger mass and pressure drop as $\widetilde{M}_{\mathrm{HX}} = M_{\mathrm{HX}}/(A_{\mathrm{fr}}\,\rho_{\mathrm{mat}}\,l_{\mathrm{ref}})$ and $\widetilde{\Delta P}_{\mathrm{air}} = \Delta P_{\mathrm{air}}\ A_{\mathrm{fr}}^2\,\rho_{\mathrm{air,in}}\,\dot{m}_{\mathrm{air}}^{-2}$, where l_{ref} is the flat tube height, $\rho_{\mathrm{air,in}}$ is the density of the cold air before entering the core, ρ_{mat} is the material density of the HX and A_{fr} is its frontal area, the basis function

$$\phi(x) = w_0 + \left(\frac{x}{w_1}\right)^{w_2} \tag{3}$$

with the Pareto front-specific fit coefficients w_0, w_1, w_2 can reliably and accurately fit the whole database. The fit coefficients $w^* = [w_0, w_1, w_2]$ for each Pareto front are the result of a gradient based optimization that minimizes the coefficient of determination R^2 of equation (3) with respect to the points on the Pareto front. The optimization is performed using the ***minimize*** function of the ***Scipy*** pacakage with the SLSQP solver (Kraft, 1988). The mean standard uncertainties on the three fit coefficients for the whole dataset are 2.3%, 0.9% and 3.7%.

The next step is to determine the range of validity of each Pareto front representation. The nondimensional pressure drop $\widetilde{\Delta P}_{\mathrm{air}}$ is the Euler number with respect to the inlet conditions of the cooling air. The minimum Euler number Eu_m, which is the first point of the Pareto front, proves to be an optimal choice as the predictor for the validity range. The reason thereof is that Eu_{m} follows a quasi-linear trend with respect to the five process variables varied to generate the database. These linear trends can, then, be superimposed to predict the minimum Euler number as

$$Eu_{\mathrm{m}} = Eu_{\mathrm{m}_0} + \frac{\partial Eu_{\mathrm{m}}}{\partial\,\dot{m}_{\mathrm{air}}}\Delta\,\dot{m}_{\mathrm{air}} + \frac{\partial Eu_{\mathrm{m}}}{\partial\,\dot{m}_{\mathrm{wf}}}\Delta\,\dot{m}_{\mathrm{wf}} + \frac{\partial Eu_{\mathrm{m}}}{\partial\,T_{\mathrm{cnd}}}\Delta\,T_{\mathrm{cnd}} + \frac{\partial Eu_{\mathrm{m}}}{\partial\,\Delta T_{\mathrm{dsh}}}\Delta\,\Delta T_{\mathrm{dsh}} + \frac{\partial Eu_{\mathrm{m}}}{\partial\,T_{\mathrm{c,in,cond}}}\Delta\,T_{\mathrm{c,in,cond}}\,, \tag{4}$$

where Δ expresses the difference between the value of a given process variable and the corresponding lower bound in Table (4). The derivatives of the minimum Euler number with respect to each thermodynamic variable v^i are numerically calculated over the dataset as

$$\frac{\partial Eu_{\mathrm{m}}}{\partial\,v^i} = \frac{1}{N_{TC}}\sum_{j=0}^{N_{TC}}\frac{1}{N_{step}^j}\sum_{k=0}^{N_{step}^j}\left(\frac{\Delta Eu_{\mathrm{m}}(j,k)}{\Delta v^i(j,k)}\right). \tag{5}$$

The mean relative error and its standard deviation on the whole database between the predicted value f Eu_{m} using equation (4), and the original values of the Pareto fronts is 3.8% and 8.1 % for the louvered fins, and 3.1% and 10% for the offset strip fins. Figure 3 compares the fitted basis-function predictions with the Pareto front solutions for five exemplary process variable sets. Notice that the curves start from the predicted minimum Euler number, which is highlighted as a red star in the figure.

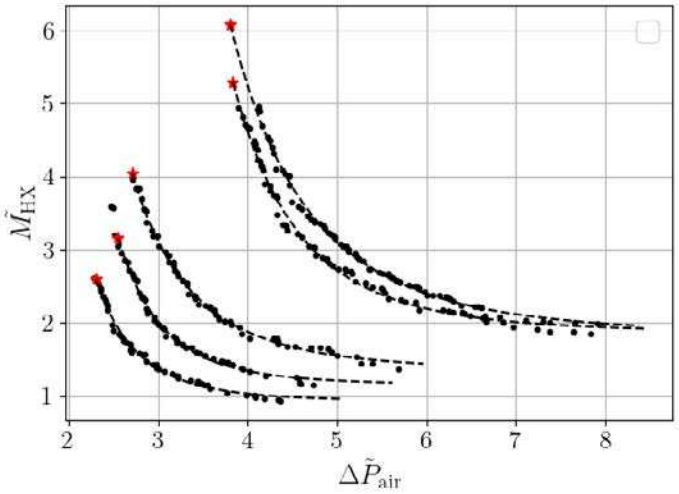

Figure 3: Pareto front fits for five different process conditions - Louvered fin condenser.

The final step of the calibration of the reduced order model is the prediction of the coefficients w^* as a function of the process conditions. A multi-output linear regression model is chosen for this task. The range of the process variables, as well as of the calculated coefficients w^*, is rescaled to (0,1) to properly train the regression model, whose weights are estimated using an ordinary least squares algorithm (Lawson, 1987).

569

The reduced order model of the condenser consists of a function implemented in python language which uses the linear regression model and the coefficients of equation (4) determined for each HX topology to predict the coefficients w^* of ϕ and the minimum Euler number of the Pareto front, given as input the process variables of interest, the heat exchanger frontal area, and material density. By means of the reduced-order model, the degrees of freedom associated to the condenser design reduce to only one: the ratio of the Euler number over the minimum Euler number $Eu^* = Eu/Eu_m$ of the reconstructed basis function. As the range of variation of Eu^* is almost the same for all the Pareto curves of the database, Eu^* can be used as optimization variable. The fact that the maximum value of Eu^* of the Pareto curves varies between 1.8 and 2.5, does not pose a problem to the optimization, as all the curves tend to flatten out in correspondence of their maximum value of Euler number, and this asymptotic trend is captured by the basis-functions.

Thus, the input of the reduced-order model during a system optimization consist of a set of process variables, the Eu^* and the choice of the fin topology. The output, instead, includes the air side pressure drop and the minimum mass of the optimal HX. Note that the working fluid side pressure drop is not predicted by the reduced order model, and it is then assumed constant when estimating the ORC unit performance. Notably, its value is taken equal to upper bound considered for this quantity in the generation of the dataset of optimal condenser geometries, see Section 3.4. This introduces a small error in the system optimization since the working fluid pressure drop does not vary significantly over the optimal design space of the condenser. If during the system optimization the input process conditions exceed the bounds defined in the training dataset, see Table 4, the surrogate model returns a warning, and its prediction can be discarded.

4 RESULTS

The developed simulation and optimization infrastructure has been used i) to investigate for an ORC WHR unit aboard an aircraft the design improvements achievable by optimizing simultaneously the HX geometry and thermodynamic cycle characteristics, ii) to compare, for the same application, two ORC

condenser topologies, namely the flat tube microchannel with either louvered or offset strip fins, in terms of minimum weight and air pressure drop, and iii) to demonstrate the effectiveness of the proposed reduced-order modelling technique for the preliminary design of HXs of aerospace thermal systems.

4.1 Simultaneous optimization of thermodynamic cycle and heat exchanger geometry

To estimate the improvements achievable through the simultaneous optimization of the thermodynamic cycle and heat exchanger preliminary design for the application at hand, the results found via the proposed methodology are compared with those obtained when only thermodynamic cycle optimization is performed, see Figure 4. In this second case, the condenser geometry is fixed by randomly choosing one of the Pareto fronts of the dataset generated for the calibration of the condenser reduced-order model. The geometry is then taken equal to that of the solution located at the center of the chosen Pareto front and kept constant throughout the system optimization.

Several conclusions can be drawn. First, less solutions are found if the condenser geometry is kept constant, regardless of the chosen thermodynamic cycle specifications. This is to be expected, as the geometry cannot be adapted to comply with the different design conditions. Second, the overall system weight decreases by about 12% for the offset strip fins and 10% for the louvered fins for a given net power output of the ORC unit when the thermodynamic cycle specifications and condenser geometry are optimized simultaneously. Third, the condenser with offset strip fins tends to be lighter if low pressure drops are targeted, thus allowing for higher net power outputs. However, the solutions with the louvered fins can yield lighter designs at the costs of larger pressure drops. It follows that depending on the chosen net power output of the ORC system, the optimal HX topology changes, as the two Pareto curves cross each other. In the case of fixed condenser geometry, this crossing point is located at a net power output of 71 kW. If the condenser geometry is optimized together with the thermodynamic cycle, the crossing point shifts to 64 kW, showing that for the chosen test case, the offset strip fins have a larger range of applicability with respect to the louvered fins. The gains in terms of power density achieved by tuning the condenser geometry are significant: if the geometry is kept fixed, the ORC WHR power density ranges from 1.13 to 1.57 kW/kg in the case of offset strip fins, and from 1.09 to 1.67 kW/kg in the case of louvered fins. When the geometry is optimized together with the thermodynamic cycle conditions, the power density range is extended to 1.01 - 1.78 kW/kg for the offset strip fins, and to 1.02 - 1.84 kW/kg for the louvered fins. These results show that the optimization of HX geometry together with the cycle parameters, although computationally more expensive, yields significant performance improvements with respect to fixing a priori the geometry.

570

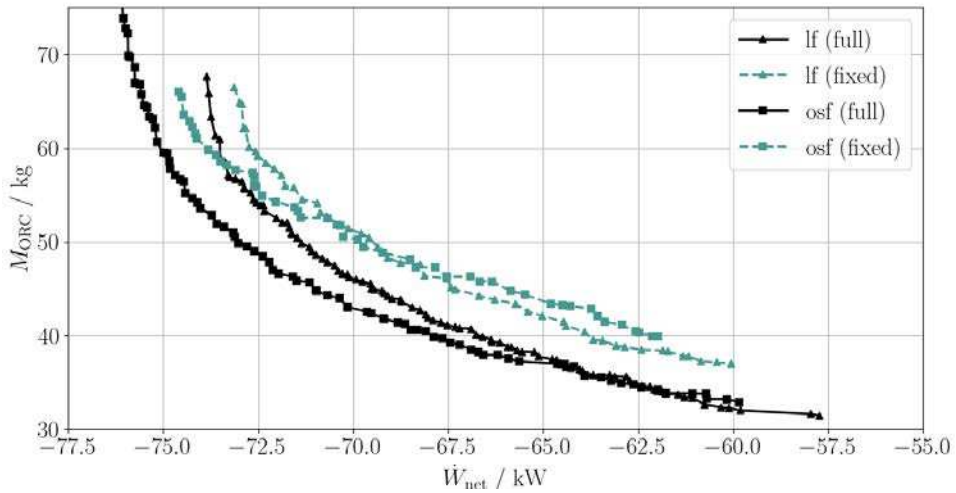

Figure 4: Pareto front of the optimal ORC WHR unit design when the condenser geometry is optimized (full) or when is fixed regardless of the thermodynamic cycle specifications (fixed).

4.2 System design optimization with the optimal HX reduced order model

Figure 5 compares the results of the system optimization obtained using the condenser reduced order model (ROM) with those corresponding to the simultaneous optimization of the thermodynamic cycle

specifications and of the full condenser geometry, for both the louvered fin (a) and offset strip fin (b) cases. The results of the optimization with the condenser ROM match reasonably well those obtained with the original system model for both fin types. Taking the solution of the original system model as reference, the mean relative error between the two set of results is 1.9% for the louvered fin HX (Figure 5a) with a standard deviation of 1.2%, while is 2.4% for the offset strip fin case (Figure 5b) with a standard deviation of 1.4%. Though the Pareto fronts predicted with the two methods are similar, the maximum net power output resulting from the optimization with the condenser ROM tends to be smaller. This can be attributed to i) the limited set of process conditions considered while generating the database used to fit the ROM, and ii) to an underestimation of the minimum Euler number, as high net power outputs are predicted in correspondence of low pressure drops across the condenser. The method adopted to predict the minimum Euler number must then be improved, as the assumption of a linear variation of this quantity with the individual process variables only holds for relatively small variations of the process conditions.

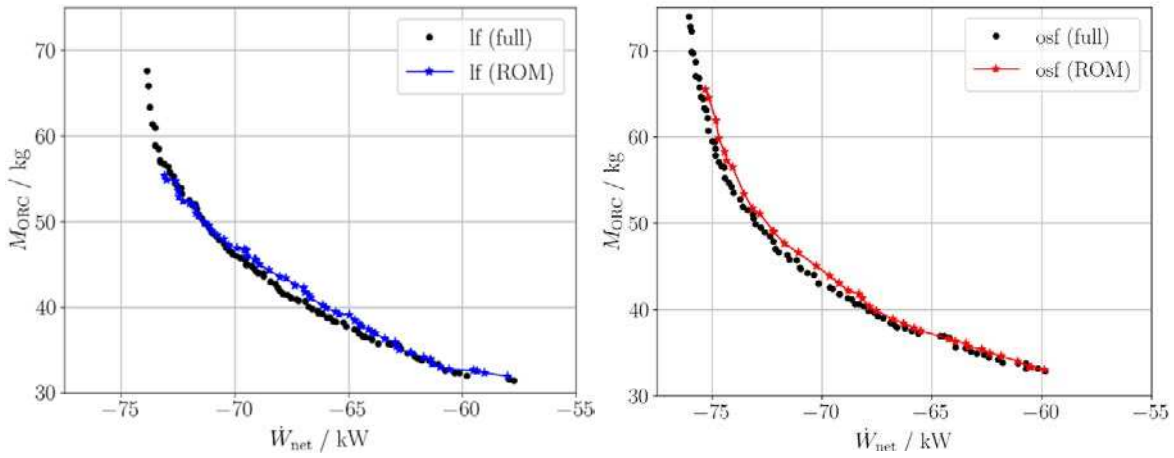

Figure 5: Pareto fronts of the ORC WHR unit optimal designs determined by using the condenser reduced order model (ROM) and by optimizing the HX geometry (full), for both the louvered fin (a) and offset strip fin (b) topologies.

Table 5 compares the computational costs[1] of the three optimization strategies described in Section 3.3. The first one tackles the optimization of the sole thermodynamic cycle design variables, while the HX geometry is fixed. The second and third strategies deal with the simultaneous optimization of both the cycle and condenser design, using the HX sizing procedure of Section 3.2 (strategy #2), or the condenser reduced-order model (strategy #3).

Table 5: Computational performance of the three design optimization strategies

Optimization strategies	Time (min)	pop X gen	Time per iteration
#1	13-14	50 x 50	0.34 s
#2	58-60	96 x 100	0.38 s
#3	15-16	60 x 56	0.29 s

The reduction in computational cost of the system optimization using the ROM is significant, even though this replaces only one HX model. There are two main factors contributing to the reduction of computational time. First and foremost, the optimization problem dimensionality is reduced: the number of optimization variables decreases, together with the population size and number of generations of the genetic algorithm to reach convergence (Pareto optimal solutions invariant for more than 5 generations). The number of function evaluations goes from 9600 to 3360. Secondly, the time per objective function evaluation decreases, as the ROM is about 200 times faster than the condenser sizing model. As a result,

[1] Optimizations were performed on 8 cores, with an AMD Ryzen 4000 series processor.

the average computational time for objective function evaluation using the ROM is reduced by about 25%.

5 CONCLUSIONS

The present work contributes to the development of a design methodology for airborne ORC systems, whose performance is highly dependent on the preliminary design of HXs, as demonstrated in Section 4.1. The following conclusions are drawn from the study:

I) To identify the optimal design of an aerospace ORC unit in terms of efficiency and weight, the optimization of the thermodynamic cycle and the preliminary design of the HXs must be integrated. The performance gains achievable with the integrated optimization vary depending on the HX topology. The microchannel condenser equipped with offset strip fins features a lower weight than in the case of louvered fins, though the latter allows for lighter designs if higher pressure drops are accepted.

II) The outlined methodology to construct a surrogate model of the optimal design space of a HX has proven to be valid: the Pareto front of the optimal solutions for the ORC application at hand predicted when the condenser ROM is used differ from that obtained with the original system model by less than 2%. The accuracy of the reduced order model depends on the size and resolution of the dataset used to fit the model, as well as on the method adopted for the prediction of the minimum Euler number.

III) The use of a ROM for HXs preliminary design significantly reduces the computational cost associated with the integrated optimization of a thermodynamic cycle and its components, at the expense of a small margin of uncertainty. Anyhow, this margin of error is smaller than the benefit achievable with integrated cycle and HX optimization. As the ROM methodology is applied to more HXs, the computational time is expected to decrease significantly.

NOMENCLATURE

A_{fr}	frontal area	(m^2)
A_{ht}	HX heat transfer area	(m^2)
ΔP	pressure drop across the HX	(Pa)
Eu	Euler number	(-)
f	friction factor	(-)
F	correction factor	(-)
F_{h}	fin height	(mm)
F_{p}	fin pitch	(mm)
H	Enthalpy	(J/kg)
j	Colburn factor	(-)
L_α	louver fin angle	(°)
L_{p}	louver pitch	()
M	mass	(kg)
$\dot{m}$	mass flow rate	(kg/s)
n_{mc}	number of microchannels	(-)
n_z	number of streamwise tubes	(-)
p	pressure	(bar)
T	temperature	(K)
t_{f}	fin thickness	(mm)
t_{mc}	microchannel thickness	(mm)
U	global heat transfer coefficient	(W/(m^2 K))
$\dot{W}$	mechanical power	(W)
w_{mc}	microchannel width	(mm)
X	HX width	(m)
Y	HX height	(m)
Z	HX depth	(m)

Greek symbols

α	fin width over height	(-)
γ	fin thickness over depth	(-)
δ	fin thickness over width	(-)
η	efficiency	(-)
ρ	density	(kg/m^3)
ϕ	basis function	(-)

Subscript

air	cold air side
cond	condenser
cnd	condensation conditions
evap	evaporator
f	fan
in	HX inlet conditions
is	isentropic
p	pump
pp	pinch point
wf	working fluid side

572

REFERENCES

Ascione, F., De Servi, C.M, Colonna, P., 2021, 'Assessment of an inverse organic rankine cycle system for the ECS of a large rotorcraft adopting a high-speed centrifugal compressor and a low GWP refrigerant', ORC Conference, id 110.

Bell, I. H., Wronski, J., Quoilin, S. and Lemort, V., 2014, 'Pure and pseudo-pure fluid thermophysical property evaluation and the open-source thermophysical property library Coolprop', Industrial & Engineering Chemistry Research 53(6), 2498–2508.

Chang, Y., Hsu, K., Lin, Y. and Wang, C., 2000, 'A generalized friction correlation for louver fin geometry', International Journal of Heat and Mass Transfer.

Chang, Y. and Wang, C., 1997, 'A generalized heat transfer correlation for louver fin geometry', International Journal of Heat and Mass Transfer.

Chatzopoulou, M.A., Lecompte, S., De Paepe, M., Markides, C. N., 2019, 'Off-design optimisation of organic Rankine cycle (ORC) engines with different heat exchangers and volumetric expanders in waste heat recovery applications', Applied Energy, Vol 253.

Colonna, P. and van der Stelt, T., 2019, 'Fluidprop (version 3.1): A program for the estimation of thermophysical properties of fluids'.

Deb, K., Pratap, A., Agarwal, S., and Meyarivan, T., 2002, "A Fast and Elitist Multi-Objective Genetic Algorithm: NSGA-II," IEEE Transactions on Evolutionary Computation, Vol. 6, No. 2.

Grieb, H., 2004, "Projektierung von Turboflugtriebwerken", Birkhäuser Basel.

Kaltra GmbH (2020), Microchannel condensers: heat exchangers for condenser applications, technical report, URL https://www.kaltra.com/wp-content/uploads/2020/04/TM_Microchannel-Condensers_Ver.3.0_EN.pdf

Krempus, D., Bahamonde, S., Stelt, T. V. D., De Servi, C. M., Klink, W. and Colonna, P.,2021, 'On Mixtures as Working Fluids for Air-cooled ORC Bottoming Power Plants of Gas Turbines', ORC Conference, id 68.

Kraft, D., 1988, "A software package for sequential quadratic programming", Tech. Rep. DFVLR-FB 88-28, DLR German Aerospace Center – Institute for Flight Mechanics, Koln, Germany.

Kwak, H. D., Kwon, S. and Choi, C. H. (2018), 'Performance Assessment of Electrically Driven Pump-fed LOX/Kerosene Cycle Rocket Engine: Comparison with Gas Generator Cycle', Aerospace Science and Technology 77, 67–82.

Lawson C., Hanson R.J., 1987, 'Solving Least Squares Problems', SIAM

Lecompte, S., Van den Broek, M., De Paepe, M., 2014, "Optimal selection and sizing of heat exchangers for organic rankine cycles (ORC) based on thermo-economics" Proceedings of the 15th International heat Transfer Conference, 7381-7394.

Manglik, R. M. and Bergles, A. E., 1995, "Heat Transfer and Pressure Drop Correlations for the Rectangular Offset Strip Fin Compact Heat Exchanger," Experimental Thermal and Fluid Science, Vol. 10, No. 2, pp. 171-180.

Müller-Steinhagen, H. and Heck, K., 1986, 'A simple friction pressure drop correlation for two-phase flow in pipes', Chem. Eng. Process Intensification 20(6), 297–308.

Shah, R. Sekulic, D. (2003), Fundamentals of heat exchanger design, John Wiley and Sons.

Shah, M., 2019, 'Improved Correlation for Heat Transfer during Condensation in Conventional and mini/micro-channels', Int. Journal of Refrigeration.

Siebel, T., Zanger, j., Huber, A., Aigner, M., Knobloch, K., Bake, f:, 2018, 'Experimental Investigation of Cycle Properties Noise and Air Pollutant Emissions of an APS3200 Auxiliary Power Unit', Journal of Engineering for Gas Turbines and Power, ASME.

Yu, S., Jones, S., Ogawa, H., Karwa, N., 2016, 'Multi-Objective Design Optimization of Precoolers for Hypersonic Airbreathing Propulsion', Journal of Thermophysics and Heat Transfer, 31, 1-13.

VDI e. V. (2010), VDI Heat Atlas, 2nd edition, Springer.

ORC SEVILLE 2023
7th International Seminar on O.R.C. Power Systems

© 2024 Editorial Universidad de Sevilla. Este es un artículo de acceso abierto distribuido bajo los términos de la licencia de uso y distribución Creative Commons (BY-NC-ND 4.0)

DOI: https://dx.doi.org/10.12795/9788447227457_97

Basic design of an ORC demonstrator system for implementation in an Iron & Steel plant through the DECAGONE project

Magnus Windfeldt[1], Han Deng[1], Trond Andresen[1,*], Christopher Schifflechner[2]

[1] *SINTEF Energy Research, Trondheim, Norway*
[2] *Technical University of Munich, Munich, Germany*

*Corresponding Author: trond.andresen@sintef.no

ABSTRACT

Waste heat recovery (WHR) technologies offer great opportunities for improving energy efficiency and reducing CO_2 emissions for energy intensive industrial processes. The DECAGONE project is developing an innovative ORC-based WHR system to be demonstrated in an iron & steel plant located in the Czech Republic. The design of the ORC system considers the practical site-specific conditions and limitations, such as variations in heat source conditions, heat sink availability, and size and space limitations for the ORC components. Various cycle configurations are compared with a thermodynamic optimization model for maximizing the net power output subject to the process constraints, including (1) recuperative vs. non-recuperative designs, (2) air vs. water as heat sink and (3) direct vs. indirect evaporation. The recuperative cycle with indirect evaporation and direct air condensation is deemed the most suitable solution for the project site conditions. The results provide recommendations for performance improvement and indications for performance subject to practical plant operating conditions, such as large range of temperature and flow rate of waste heat source. Analyses in this work provide the basis for detailed component design and decision processes towards finalizing the design of the demonstrator.

1 INTRODUCTION

As energy availability decreases and incentives for reducing energy consumption and greenhouse gas emissions increases, energy efficiency measures become increasingly interesting for energy intensive industries. IEA reports (IEA, 2021) that rapid implementation of waste heat recovery solutions in this sector is critical for reaching net zero emissions by 2050, and a recovery potential approaching 300 TWh/year from industrial thermal processes in the EU has been estimated (Bianchi *et al.*, 2019).

The DECAGONE project (Demonstrator of industrial carbon-free power generation from ORC-based waste-heat-to-energy-systems, https://decagone.eu/), funded by Horizon Europe, is developing an innovative ORC-based WHR system to be constructed, integrated, and demonstrated in Třinec Iron and Steel Works in the Czech Republic. Outcomes of the demonstration will be evaluated in terms of potential market and transposability at the European scale for other significant industrial sectors. The overarching goals of this project is to make ORC systems more efficient, more cost-effective, and more adaptable to various industrial sectors in order to increase their rate of implementation.

In the current work, a basic optimization of operating conditions is performed of the entire system comprising the ORC cycle and heat recovery loop, based on measured conditions and practical limitations at the demonstration site. This will provide the first realistic estimate of system performance at the chosen nominal operation point, and will serve as the basis for performance specification and design of all main system components. Thus, some design choices have been made prior to the present work, such as working fluid and cycle layout, while some assumptions are made regarding component performance that will be subject of further study in following work. In addition to the chosen cycle

layout, other design options are explored for their impact on system performance and requirements. This includes solutions deemed unfeasible at the demonstration site, but that could be interesting in other industrial applications.

2 METHODOLOGY

2.1 Problem description

The goal of this work is to compare the performance impact of design choices and alternatives for an ORC recovering waste heat from an iron & steel plant, and for each alternative identify optimized operating conditions while satisfying specific and practical plant conditions. Historic site data from 1.5 years of operation have shown that the flue gas temperature ranges from 400 °C to 500 °C and the volume flow rate ranges from 40 000 Nm^3/h to 80 000 Nm^3/h. Values of 465 °C and 71 000 Nm^3/h are chosen as the design point based on a preceding data analysis, which identified these as the most representative operating conditions.

Collected site data covering one year shows that the ambient temperature ranges from −5 °C in winter to 30 °C in summer. A nominal value of 12.5 °C is chosen for the design point, to be used as the heat sink temperature and as a reference for exergy calculations. Apart from the heat source and sink, the ORC systems will be optimized for maximum power output against other practical constraints, which will be detailed later.

2.2 ORC layout basis

The ORC configuration used as basis for the system modelling and comparison of various design options is illustrated in Figure 1. This configuration includes four fluid circuits: The heat source stream, the indirect fluid loop, the working fluid loop, and the heat sink stream. Therminol66, a commercially available thermal oil, is used as the indirect fluid to extract the heat from the source via the waste heat recovery heat exchanger (WHR HX), and supply the heat for the working fluid loop via the evaporator. Additionally, a bypass of the heated indirect fluid will go to the thermal energy storage (TES) to store the energy when the recovered heat from WHR HX exceeds the heat supplied to the working fluid loop. Cyclopentane is selected as the working fluid which is heated in the evaporator and expand in the turbine to generate power. While the choice of working fluid is beyond the scope of the present work, the use of cyclopentane is justified in the larger project context based on its high suitability for high-temperature ORC applications (Lai *et al*,. 2011), both as a pure fluid and in a zeotropic mixture (Braimakis *et al*., 2015). It has an Ozone Depletion Potential of zero and a Global Warming Potential below 25 (EPA, 2013), and is already commercially applied in existing ORC systems (Lecompte *et al*., 2015).

The layout in Figure 1 is a recuperative design, in which a recuperator is used to recover the heat from the hot turbine outlet and heat up the cold working fluid after it is cooled in the condenser and pumped. The pressure drop for the heat source and heat sink inside the heat exchangers is compensated with the flue gas pump and air fan, so that the pressure of heat source and heat sink out from the system is the same as that into the system.

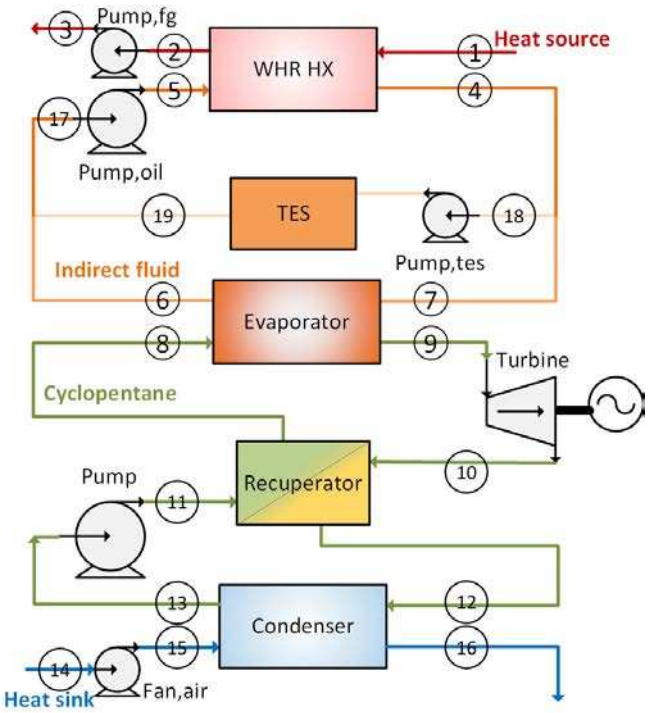

Figure 1: ORC layout for modelling the base case

2.3 System optimization model

The system optimization model combines a steady-state thermodynamic model simulating the system and component performance with an optimization algorithm to find the optimum solution for the given objective function. The model is developed using an in-house framework described in detail in previous work (Deng *et al.* 2020, Hagen *et al.* 2020, Deng *et al.* 2022). The steady-state thermodynamic model is built based on the layout shown in Figure 1, but is flexible to be adapted to other configurations. For example, a non-recuperative cycle can be represented by simply redefining state points 10 and 12 to be equal, and similarly for state points 11 and 13.

576

The steady-state thermodynamic model is built by connecting different sub-models specific for each component. The turbine is modelled based on an isentropic expansion process corrected by an isentropic efficiency, and the power generated is further corrected by a mechanical efficiency. Similarly, an isentropic or isochoric compression process with the efficiency correction is used for the calculation of the pumps and fans, and the power consumption is corrected by a mechanical efficiency. Constant values are used for all efficiencies, which assumes that for each resulting set of operating conditions in explored cases, the relevant components can be individually designed to reach or surpass the defined efficiency. This work does not consider off-design performance.

The heat exchangers are calculated based on the heat balance between the cold and hot side, assuming a counter-current flow. The local temperature differences across each heat exchanger is found by discretizing the heat exchanger into the certain number of sections with equal heat duty and pressure drop, and the UA value of the heat exchanger is then also found as the sum of the local UA values calculated for each section. Sufficient discretization of the heat exchanger can ensure accurate temperature profiles and UA values also for heat exchangers where phase change of a fluid occurs.

For simplicity, the inlet and outlet conditions of the indirect fluid on the thermal energy storage bypass (points 18 and 19) are assumed to be the same as in and out of the evaporator (points 7 and 6). The mass flow rate for the bypass is calculated from a specified TES duty and the enthalpy difference between the inlet and outlet. Then, the mass flow rate of the indirect fluid in the WHR HX is the sum of its mass flow rate through the TES and the evaporator.

For the thermodynamic properties, the flue gas, the working fluid cyclopentane, and the heat sink are calculated using the REFPROP 9.1 library (Bell 2013). The properties of Therminol66 are fitted to the distributor's data sheet and validated using the open-source library CoolProp (Bell *et al.* 2014).

The optimization problem is solved by the gradient-based constrained optimization solver NLPQL (Schittkowski 1986) in a framework which allows for flexibility in the definition of variables, constraints, and objection function. The net power W_{net} is to be maximized as

$$W_{net} = W_{turbine} - W_{fan,fg} - W_{pump,oil} - W_{pump,wf} - W_{fan,air} \quad (1)$$

with W_i being the electrical power produced or consumed by the indicated component. The variables and constraints are set as shown in Table 1, together with other fixed parameters. Some practical limitations are set as the boundary of the variables instead of constraints, such as the minimum allowable flue gas outlet temperature being constrained by the lower limit of the variable. Please note that the specified variable range does not represent the variation in resulting values, it is simply the allowed range provided to the solver. For given values of input variables, the system and components performance are calculated with the models described in the above section. Then the partial derivatives of the objective and constraint functions to the variables are estimated, and the gradient information is used by the NLPQL solver to propose new values for the free variables for the next iteration. The problem is solved when the maximum value of the objective function is found and all the constraints are satisfied.

Table 1: Optimization setup: Variables, constraints, and fixed parameters with their set input values or allowable min-max ranges.

Variables	**State point (symbols)**	**Range/Value**
Flue gas outlet temperature	T_2	150 – 300 °C
Indirect fluid evaporator outlet temperature	T_6	50 – 200 °C
Indirect fluid evaporator temperature change	ΔT_{7-6}	110 – 250 K
Turbine inlet pressure	P_9	15 – 38 bar
Turbine inlet temperature	T_9	50 – 275 °C
Working fluid condenser outlet pressure	P_{13}	0.3 – 2.5 bar
Heat sink temperature increase	ΔT_{16-15}	10 – 15 K
Recuperator effectiveness	η_{recup}: $(h_{10} - h_{12})/(h_{10} - h_{11})$	0.05 – 0.95
Constraints		
Min. pinch point temperature difference	$\Delta T_{\min,WHRHX}/\Delta T_{\min,recup}$	40 / 20 K
Min. temperature difference at bubble point	$\Delta T_{\min,evap}$	20 K
Min. temperature difference at the cold end	$\Delta T_{\min,cond}$	24 K
Max. indirect fluid temperature	$T_{\max,4}$	310 °C
Max. working fluid pressure	$P_{\max,11}$	38 bar
Fixed parameters		
Isentropic efficiencies	$\eta_{pump,fg}/\eta_{pump,wf}/\eta_{turbine}$	0.7 / 0.7 / 0.8
Isochoric efficiencies	$\eta_{fan,air}/\eta_{pump,oil}$	0.63 / 0.7
Motor/generator efficiencies	$\mathrm{H}_{pump,fg}/\mathrm{H}_{pump,wf}/\mathrm{H}_{turbine}$ / $\mathrm{H}_{fan,air}/\mathrm{H}_{pump,oil}$	0.9 / 0.9 / 0.97/ 0.9 / 0.9
Pressure drop of the cold sides in the HXs	$\Delta P_{WHRHX}/\Delta P_{evap}/$ $\Delta P_{recup}/\Delta P_{cond}$	100 / 100 / 50 / 0.15 kPa
Pressure drop of the hot sides in the HXs	$\Delta P_{WHRHX}/\Delta P_{evap}/$ $\Delta P_{recup}/\Delta P_{cond}$	0.5 / 100 / 6 / 12 kPa

577

2.4 Alternative cycle layouts

Apart from the base case layout shown in Figure 1, other common design options with layouts as shown in Figure 2, have been optimized under the same conditions in order to quantify the impact of design alternatives.

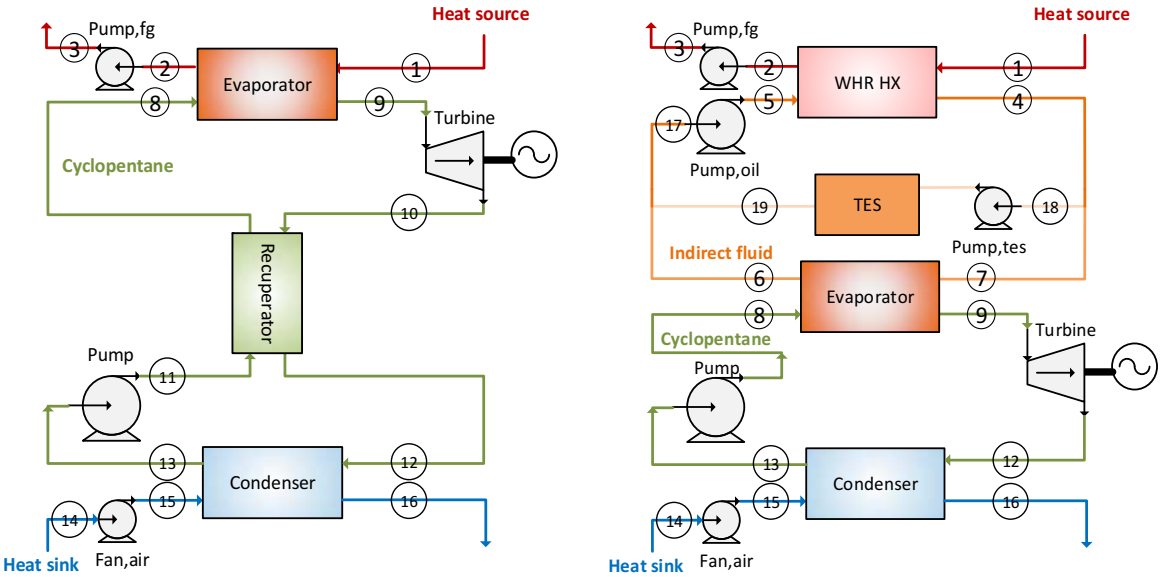

(a) Direct evaporation design (b) Non-recuperative design

Figure 2: Other ORC configurations with (a) direct evaporation (b) non-recuperative design

The direct evaporation design in Figure 2(a) removes the indirect fluid circuit and the thermal energy storage. It enables recovering heat from the flue gas in slightly larger quantities or at higher temperatures, and saves both space and costs of components in the indirect fluid circuit. However, direct heat recovery using the flammable cyclopentane in this application is considered unfeasible for several reasons, such as direct exposure to high temperatures, high fluid charge in contact with the flue gas flow, and poor provisions for buffering of the variable heat source energy. The direct evaporation case is still included to indicate the overall performance difference compared to the chosen indirect system. The non-recuperative design in Figure 2(b), compared with the recuperative design in Figure 1, saves cost, space and pressure drop for the recuperator and pipelines. However, it shifts more cooling duty to the condenser and heating duty to the evaporator which will require these to be larger. The optimization of the non-recuperative design uses the same settings as the recuperative design, where the recuperator is deactivated by setting both the recuperative efficiency and fluid pressure drops to value of 0.

The condenser is expected to be the largest component in the ORC system if using direct air cooling. As the available site space is limited, three additional condensation options are investigated as illustrated in Figure 3, for potential solutions for this specific site and also future applications with different site conditions. These options are (a) direct water condensation, (b) indirect condensation with water in a closed loop and ambient air as heat sink, and (c) spray cooled air condensation. The rest of the system is kept the same as in Figure 1.

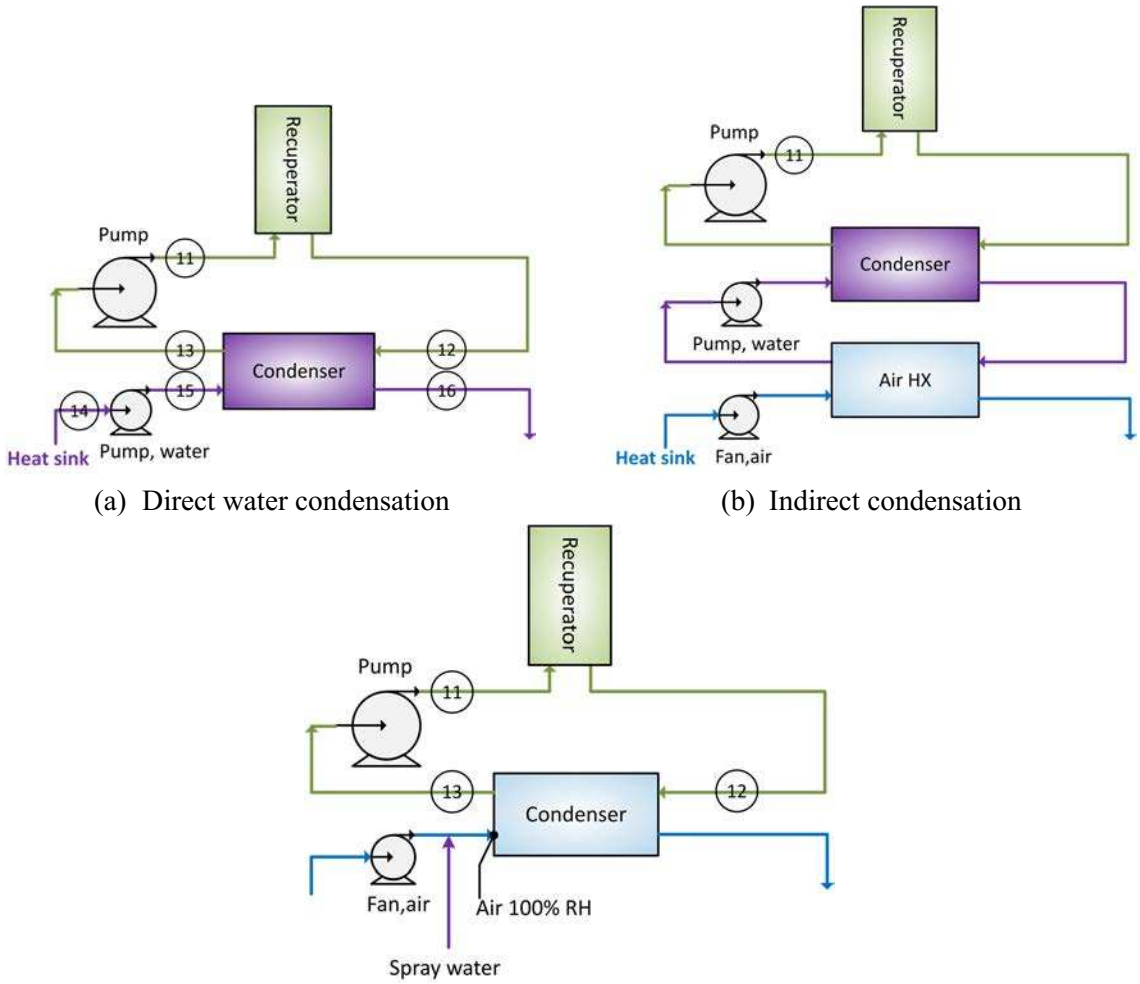

(a) Direct water condensation (b) Indirect condensation

(c) Spray cooled air

Figure 3: Design options for air- and water-cooled condensation

With the direct water solution, the ambient air heat sink is replaced with water, using the same inlet temperature and a reduced temperature lift of 10 K. The temperature difference constraint is also lowered from 24 K to 10 K. The indirect condensation solution also uses water with the same specifications in the condenser, but in a closed air-cooled loop. The benefits of this would be a reduction in working fluid inventory and more freedom in choosing location of the heat sink. However, some performance reduction must be expected due to the additional heat exchange, and more space would be required for the additional heat exchanger and piping. The inlet temperature of the water was increased from 12.5 °C to 32.7 °C, based on an assumption that the water/air heat exchanger is similar in performance to the air-cooled condenser in the base case. This increases the condensation pressure of the cycle. The additional pump and fan work required for this is estimated using isentropic and isochoric efficiencies equal to the pumps and fans in the base case.

Using a spray tower to cool the air used in a direct air condenser would allow for a combination of more compact condenser and reduced condensation pressure. This configuration would require more space and water, both of which are restricted at the demonstration site. For this simulation, it is assumed that temperature of the spray-cooled air is equivalent to dry air cooled to its wet bulb temperature. A relative humidity value of 50 % has been considered, giving air at 12.5 °C a wet bulb temperature of 7.25 °C. Thus, compared to the base case, only the inlet air temperature was changed for the simulation. Any power required for additional auxiliaries with this solution is not included in this consideration.

3 RESULTS AND DISCUSSIONS

3.1 Cycle optimization results

With the boundary conditions described in section 2.1 and the parameter specifications in Table 1, a cycle with the layout as illustrated in Figure 1 achieves an optimized net power output of 1986 kW. The gross power output from the generator is 2252 kW, with the power consumption of the pumps and fans summing to 266 kW, of which the majority is needed for the heat sink fan and working fluid pump. All constraints listed in Table 1 are met. In addition, the variables *flue gas outlet temperature* and *heat sink temperature increase* are at their minimum allowed value and maximum allowed value respectively. Further details on the optimal solution for the base layout are shown in comparison with alternative layouts in Table 2 and Table 3.

3.2 Alternative cycle layouts

The comparison of the different configurations is summarized in Table 2. The thermal efficiency is calculated using the heat recovered from the off-gas as basis, while the exergy efficiency uses the exergy in this heat as well as the electrical input to the cycle.

Table 2: Comparison of system performances of the different configurations

		Base case: Recuperative, Indirect evaporation	**Non-recuperative, Indirect evaporation**	**Recuperative, Direct evaporation**
Net power	[kW_{el}]	1986	1657	2080
WHR HX duty	[kW]	9242	9242	-
Evaporator duty	[kW]	9248	9247	9242
Recuperator duty	[kW]	1928	-	2383
Condenser duty	[kW]	7047	7385	6954
WHR HX UA-value	[kW/K]	113	88	-
Evaporator UA-value	[kW/K]	564	404	106
Condenser UA-value	[kW/K]	370	303	365
Recuperator UA-value	[kW/K]	68	-	79
Thermal efficiency	[%]	21.5	17.9	22.5
Exergy efficiency	[%]	40.9	34.3	42.9

580

It can be seen that using a recuperator is highly beneficial in terms of power output, but at the cost of increased UA values for the other heat exchangers. This is due to a reduction in temperature difference in these heat exchangers, and indicates that a recuperative cycle will require more space and more costly components. Conversely, using an indirect cycle to recover the heat instead of direct evaporation has only a small cost in terms of power output at this nominal operation point, due to the working fluid reaching its maximum temperature in both cases. This loss would be further reduced if the increased uptime afforded by a thermal energy storage, which the indirect cycle enables, could be accounted for.

3.3 Alternative condensation options

The three alternative condensation options are compared with the direct air condensation in Table 3. For the direct water solution, water consumption is equal to water flowrate and is reported as such. Some make-up water would be required to cover leaks in the indirect solution, but this is not accounted for. For the spray cooling, it is assumed that liquid water can be recycled, so that only water that evaporates in the cooling tower is consumed. UA-values are also included as they can be used to indicate component size. However, they are not suited for direct comparison when using different fluids.

Table 3: Key results for various condenser options

		Base case: Direct with air	Direct with water	Indirect	Spray-cooled
Net power	[kW]	1986	2211	1838	2050
Condenser UA	[kW/K]	370	580	551	360
Water consumption	[kg/s]	-	165	-	1.083
Condensation pressure	[bar]	0.66	0.44	0.998	0.544
Condensation temperature	[°C]	36.7	25.9	48.7	31.4

3.4 Exergy analysis

In Figure 4 below, an overview of the exergy losses in the various cycle layouts are shown. In this figure, each column sums to the total exergy input to its respective cycle. This includes both the thermal exergy extracted from the off-gas, which is equal in all cases, and the electrical power supplied to the pumps and fans, which varies. The destruction of exergy in each component, either from temperature/pressure loss or from inefficiencies in conversion to/from electric power, is then subtracted from the total. Removing the exergy leaving the cycle in the heat sink leaves only the gross power output of the generator, which then finally gives the net power by subtracting the total power consumption. Exergy leaving the cycle unused in the off-gas, which is equal in all cases, is not included for readability.

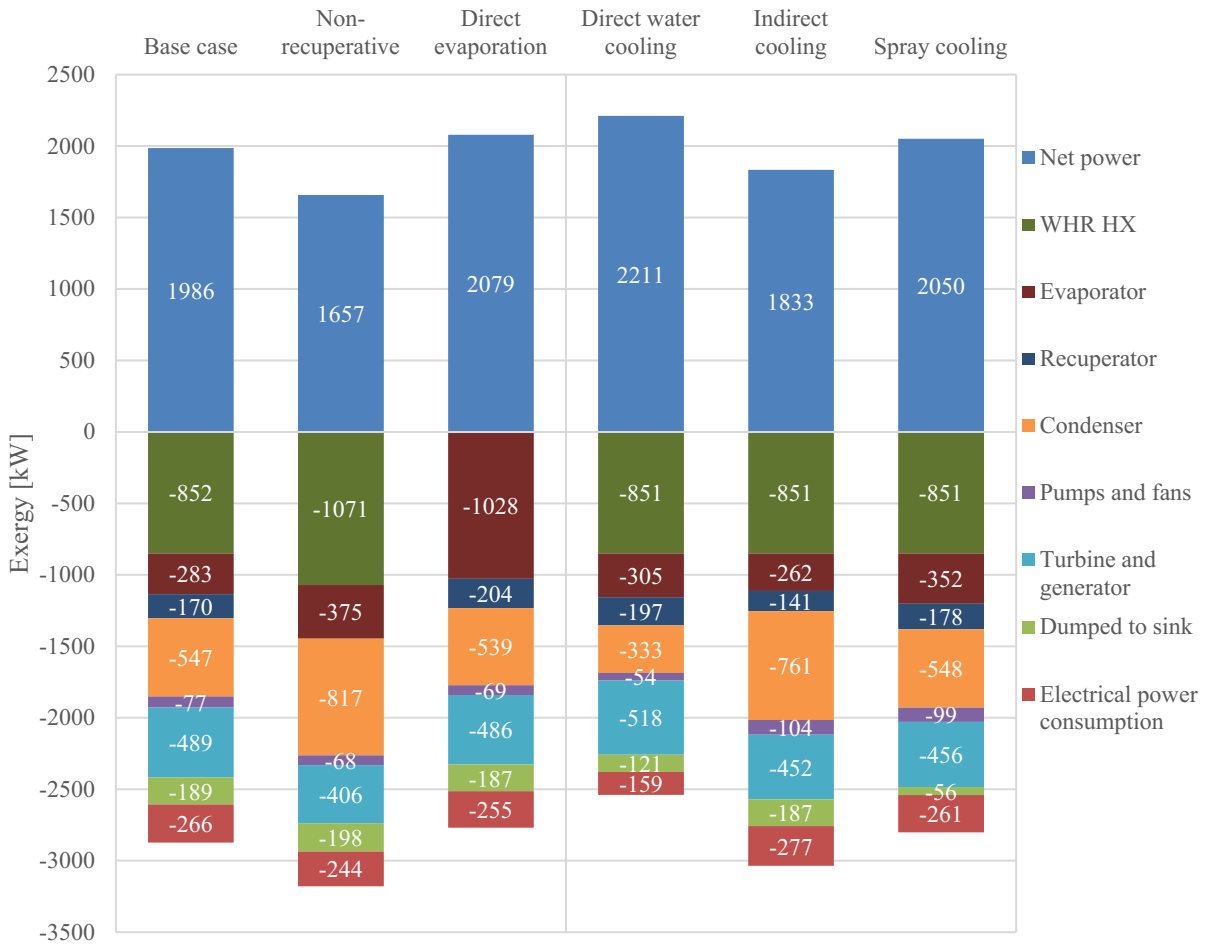

Figure 4: Comparison of exergy losses and resulting power output when optimizing the cycle with various design options, with cycle layouts on the left and condenser options on the right.

To the right in Figure 4, the losses in the entire cycle using the various condenser options are shown. In sites with water available for direct cooling a potential net power increase of 11 % is indicated, compared to the base case using an air-cooled condenser. The amount of exergy dumped to the sink is significantly lowered with the spray-cooled solution, and could be investigated for sites with more space available. Lastly, if an indirect cooling loop has to be used, a net power loss of 8 % can be expected, mainly from the additional temperature loss driving the condensation system.

SUMMARY

In this work, a comparison of designs with optimized operating conditions of an ORC for a future demonstration pilot in an iron & steel plant located in Czech Republic is presented. A system optimization model is developed to maximize the net power output, while satisfying practical limitations, for a heat source design point determined from historical site data. A configuration using indirect heat recovery with an oil loop, recuperative working fluid cycle, and direct air condensation, is used for the base design as it is considered the most suitable to cope with variations of the heat source conditions and the availability of the heat sink. This configuration is optimized against the practical constraints and provides a net power output of 1986 kW with 21.5% and 40.9% in the thermal and exergy efficiency, respectively.

To investigate other potential solutions for this site and expand the applicability of the design for future ORC implementation, alternative designs are also evaluated and compared with the base configuration. The non-recuperative working fluid cycle significantly reduces the net power output by 16%, but may require less space. The direct heat recovery design has a similar level of power output thus is less attractive for the scenario with large variation in heat source. Additionally, several condenser options (direct air; indirect and direct with water; spray-cooled air) are assessed and compared. The direct condensation with water gives the largest power output while the indirect water condensation with a closed air-cooled loop gives the smallest. For the current site conditions, direct air condensation is the most reasonable solution, while the other options have their own advantages and should be considered based on the practical requirements. Exergy analyses for the alternative designs are performed to illustrate the performance losses in the various components and to give insights for future improvement of the design. The results and analyses of the system design will serve as the basis for performance specification and detailed design of all main system components towards finalizing the design of the demonstrator. Also, it provides references to future waste heat recovery applications and ORC implementations.

REFERENCES

Bianchi, G., Panayiotou, G.P., Aresti, L., Kalogirou S.A., Florides G.A., Tsamos K., Tassou S.A., Christodoulides P., 2019, Estimating the waste heat recovery in the European Union Industry. *Energ. Ecol. Environ.* vol. 4: p. 211-221.

Bell, I., 2013, NIST Reference Fluid Thermodynamic and Transport Properties Database (REFPROP) Version 9 - SRD 23, *National Institute of Standards and Technology*.

Bell, I., Wronski, J., Quoilin, S., Lemort, V., 2014, Pure and Pseudo-pure Fluid Thermophysical Property Evaluation and the Open-Source Thermophysical Property Library CoolProp. *Ind. Eng. Chem. Res*. vol. 53, no. 6: p. 2498-2508.

Braimakis, K., Preißinger, M., Brüggemann, D., Karellas, S., Panopoulos, K., 2015, Low grade waste heat recovery with subcritical and supercritical Organic Rankine Cycle based on natural refrigerants and their binary mixtures, *Energy*, vol. 88: p. 80-92.

Deng, H., Hagen, B., Nikolaisen, M., Andresen, T., 2020, Comparing three methods for design analyses of rankine cycle for waste heat recovery from natural gas compression. *Refrigeration Science and Technology*. vol. 2020-July: p. 249-256.

Deng H., Andresen T., Skaugen G., Gladysz P., Pajak L., Sowizdzal A., Miecznik M., 2022. Topside cycles for enhanced geothermal systems with CO_2 and hydrocarbons as working fluids. *15th IIR-Gustav Lorentzen Conference on Natural Refrigerants*. Trondheim, Norway, June 13-15th 2022.

EPA, 2013, Transitioning to Low-GWP Alternatives in Building and Construction Foams. EPA, Washington, D.C.

Hagen, B.A.L., Nikolaisen, M., Andresen, T., 2020. A novel methodology for Rankine cycle analysis with generic heat exchanger models. *Appl. Therm. Eng.* vol. 165: 114566.

IEA, 2021, Net Zero by 2050. IEA, Paris.

Lai, N.A., Wendland, M., Fischer, J., 2011, Working fluids for high-temperature organic Rankine cycles, *Energy*, vol 36, no. 1: p. 199-211.

Lecompte, S., van den Broek, M., & De Paepe, M., 2015, Performance potential of ORC architectures for waste heat recovery taking into account design and environmental constraints, *3rd International Seminar on ORC Power Systems*. Brussels, Belgium October 12-14th 2015.

Schittkowski, K., 1986, NLPQL: A fortran subroutine solving constrained nonlinear programming problems. *Ann. Oper. Res*. vol. 5: p. 485-500.

ACKNOWLEDGEMENT

This work has been part of the DECAGONE project, funded by the European Union's Horizon Europe research and innovation programme under grant agreement No 101069740.

ORC SEVILLE 2023
7th International Seminar on O.R.C. Power Systems

© 2024 Editorial Universidad de Sevilla. Este es un artículo de acceso abierto distribuido bajo los términos de la licencia de uso y distribución Creative Commons (BY-NC-ND 4.0)

DOI: https://dx.doi.org/10.12795/9788447227457_98

Analytical estimation of the presence of non-condensable gases in the condensate tank of an Organic Rankine Cycle

Radheesh Dhanasegaran[1,2*], Antti Uusitalo[1], Juha Honkatukia[1], Teemu Turunen-Saaresti[1]

[1] *LUT University, School of Energy Systems, Yliopistonkatu 34, P.O. Box 20, 53851, Lappeenranta, Finland*

[2] *Sulzer Pumps Finland Oy, P.O. Box 66, FI-48601, Kotka, Finland*

* Corresponding Author: radheesh.dhanasegaran@lut.fi or radheesh.dhanasegaran@sulzer.com

ABSTRACT

The presence of non-condensable gases (NCGs) can have a negative impact on the ORC performance due to the reduced expansion ratio over the expander. The presence of NCGs can reduce the turbine expansion ratio significantly, especially in such systems in where siloxanes or high molecular weight hydrocarbons are used, requiring condensing pressures well below the atmospheric pressure. The ORC facility that uses siloxane MDM as the working fluid at LUT University has been considered in the present study. Experimental and simulation data of the facility from the previously published studies suggest that defining the working fluid state in the condenser and condensate tank suffers from significant uncertainty due to the existence of NCGs. Therefore, an attempt has been made to analytically estimate the quantities of NCGs present in the condensate tank of the ORC system using 1-D calculations based on ideal gas assumptions. It was assumed, that air is the NCG that is present inside the condensate tank for simplifications. Since the compressibility factor of MDM vapor is close to 1 at such low condensing temperatures, its behavior is close to ideal gas and hence, the assumption of ideal conditions seems viable. Data from three different experimental measurements with varying temperatures have been tested using the proposed analytical method and the corresponding quantities of the MDM-air mixture during the system operation have been estimated. The results showed that the presence of the NCG was dominant, especially in the case of measurement data with lower temperatures, and was reduced for higher condensate tank temperatures.

1. INTRODUCTION

In power cycles involving condensation, the presence of non-condensable gases (NCGs) will be detrimental to the overall cycle performance and at the component level by affecting the heat transfer performance due to the increased resistance in heat exchanger components. In principle, in addition to the primary working fluid vapor the NCGs present are usually impure gases that cannot be condensed. Also, the presence of non-condensable gases in the condenser of an ORC system can have a significant effect on the cycle performance and on the turbine expansion ratio, especially when high molecular complex fluids entailing low condensing pressures, such as when siloxanes or heavy hydrocarbons are used. Gökçen Akkurt and Yildirim (2008) found that even if there is a small amount of the NCGs in an ORC cycle, it decreases the energy and exergy of the working fluid to avail its potential in extracting power through an expander. Experimental studies have been performed by Leonard (1984) to determine the magnitude of NCG concentration. It was observed that the presence of NCGs significantly affected thepressure response of the test vessel and also reduced the wall heat transfer.
Various studies can be found in the literature that evaluated the effects of non-condensable gases on steam condensation both numerically and experimentally, revealing that the presence of NCGs significantly increased the heat transfer resistance thereby decreasing the heat transfer performance [Dehbi (1991), Huhtiniemi and Corradini (1993), Jackson et al. (2000), Al-Shammari et al. (2004), and Nagae et al. (2007)]. Also, the following studies (Jeong et al. (2010), Li et al. (2011), Punetha and Khandekar

(2017), Donkers et al. (2020) and Zhang et al. (2020)) were conducted by modeling the condensation in the presence of NCGs to accurately predict the heat and mass transfer characteristics of mixtures containing different proportions of working fluid and non-condensable gases. One of their major findings was that the system performance is associated with the amount of NCG at the condensation surface. An extensive review of vapor condensation in the presence of non-condensable gases has been presented by Huang et al. (2015) giving a special emphasis to the Film Wise Condensation (FWC) and found that the parameters such as condensate film thickness, surface waves, interfacial shear strength, and suction effect play an important role in the FWC heat transfer in the presence of NCGs.

The existence of NCGs, e.g. air or the possible decomposition products of the working fluid in power cycles like ORCs is inevitable due to various reasons such as infiltration due to long-term operation or high temperatures that require periodical maintenance or replacement of its components. A recent study on the thermal degradation of linear siloxanes (MM, MDM, and MM/MDM equimolar mixture) through enhanced chemical analysis by Gallarini et al. (2023) revealed that especially for the case of MDM vapor, the decomposition products were mostly hydrocarbons such as methane, ethane, and ethylene. Also, traces of carbon dioxide and carbon monoxide were detected indicating the presence of a small amount of air in the sample, which was inevitable due to the lower vapor pressure of MDM. In such power cycles involving low vapor pressures, the existence of NCGs can have a huge impact on the accuracy of parameters that are measured experimentally, hence intensive care for the removal of the NCGs should be given before starting the experiments (Keulen (2018)). However, a small mass fraction of NCGs might be still present due to poor sealing or leakage in the components. Also, it is extremely challenging to attain a full vacuum while filling the system, hence it is always possible that there is a very small amount of air in the system. Li et al. (2018) studied the impacts of NCGs in a small-scale ORC system and found that the increase of condenser outlet pressure is more obvious for higher NCG concentrations which had a significant effect on the electricity output compared to that of lower NCG concentrations. Therefore, approximating their quantity is crucial to accurately predict the net work output of the cycle.

In recent years, there have been attempts in estimating the amount of the NCGs in the scientific community through experimentation and computations, however, it has been a challenging task. Kopinga and Doornmalen (2013) presented a physical model that describes the behavior of an instrument (Electronic Test System (ETS)) that predicts the presence of residual NCGs. The model predictions had good agreements with the experimental measurements by the ETS despite many simplifications suggesting its wide applications where NCGs are encountered. Also, Hu and Yuill (2022) built an experimental apparatus to improve the understanding of the interaction of non-condensable gases with the refrigerant and presented a comparison between the theoretical and experimental calculations to quantify the uncertainties from NCGs in refrigeration applications. Their results revealed that the theoretical model using ideal assumptions overpredicted the NCG quantity however their trends were consistent. But no studies were focused on a static component like a condensate tank of a power cycle, especially ORCs where the condensed liquid will be collected. Due to improper sealing of the system, the non-condensable (mostly air) from the atmosphere will accumulate on the low-pressure side of the cycle, namely in the condensate tank (Uusitalo et al. (2017)). The NCGs in such a tank will have a detrimental effect on the accuracy of physical measurements such as pressures and temperatures and for defining the fluid thermophysical properties at the low-pressure side of the cycle, as well as can have a significant negative impact on the ORC turbine performance. Therefore estimating the quantity of the non-condensable becomes important to quantify the uncertainties in the measurements and in defining fluid properties, and to be able to improve the cycle thermodynamic models as well as in improving the performance of ORC systems.

Based on the literature review, there are not many studies investigating the effect of non-condensable gases on the performance of ORCs, especially with such fluids requiring condensing pressures well below atmospheric pressure. In the present study, a condensate tank of an ORC facility at LUT University is investigated. In the previous experimental studies, it has been found that the measured condensate tank temperature and pressure deviate significantly from those of pure MDM vapor at the saturated state, which has been estimated to be caused mainly by the presence of NCGs. Approximately, two-thirds of the condensate tank volume is occupied by gases, whereas approximately one-third is filled with liquid

585

Table 1: Information of the measurement sensors and their accuracies.

	Manufacturer	Type	Accuracy
Pressure	Gems	TR2200, [0-1,0-16 bar(abs)]	± 0.25% full scale
Temperature	Aplisens	CT-GN1	± 0.35 K (at 100 ^{o}C temperature)

MDM during the operation of the cycle. The locations where the measurements are taken, especially the pressure sensor, are located in the volume that is occupied by the mixture of MDM vapor and non-condensable gases, whereas the condensate tank temperature sensor is measuring the liquid temperature. The corresponding information about the uncertainties has been reported in the previous studies by the authors Uusitalo et al. (2020) and Dhanasegaran et al. (2020) however, its quantification was left as future scope. In this study, an analytical procedure has been proposed to estimate the amount of the NCGs present in the condensate tank during the system operation. Three different cases have been considered from the experimental measurements and their corresponding NCG quantities have been estimated based on the analytical method proposed in this study. This paper has been oriented as follows. Section 2 gives the overview of the existing measurements and uncertainties in the measurements of the condensate tank of the ORC facility. A 1-D analytical procedure used in the current study to evaluate the quantity of the NCGs is also presented in this section. Section 3 presents the obtained results from the analytical estimations and a sensitivity study. Finally, section 4 presents concluding remarks and the scope for future work.

2. ANALYTICAL METHODOLOGY

2.1 Problem Description

A simplified model of the condensate tank used in an ORC system has been considered in the present study. The tank is located downstream of a condenser and collects the working fluid (MDM) that is condensed in the condenser. Due to the requirement of a high degree of vacuum on the low-pressure side of the process, there can be leakages through the process sealings. Hence the air from the atmosphere penetrates inside the system and is accumulated in the low-pressure side of the cycle, namely in the condensate tank. There is a vacuum pump installed in the system, that has been used for removing NCGs from the cycle before the test runs. However, despite the efforts to remove all the NCGs from the system, there is a small amount of air remaining in the system. Therefore the pressure measurement that measures the pressure of the MDM-air mixture suffers from uncertainties and represents higher values when compared to the saturated pressure of pure MDM with the respective measured temperature level. This leads to significant deviations in defining the fluid state at the low-pressure side of the cycle when compared to the theoretical values predicted by the 1-D cycle model developed by Uusitalo (2014) and the dynamic simulations developed by Dhanasegaran et al. (2020) which assumes the low-pressure side of the cycle containing pure MDM. In addition, it is unclear how much air is remaining in the system during the experiments. A simplified process diagram showing the locations of its measurement sensors, the T-s diagram, the schematic representation of the condensate tank, and the zoomed view of the experimental facility have been presented in Figure 1. Also, the information regarding the measurement equipment and sensors has been summarized in Table 1.

2.2 Analytical Procedure

The 1-D analytical procedure is developed based on the ideal gas assumptions since the compressibility factor of MDM is close to 1 at low (condensing) temperatures making the validity of the assumptions for this problem. Air is assumed to be the only NCG that is present in the tank for problem simplification. However, it is worth noting that there can be also small amounts of other types of NCGs, such as decomposition products of MDM affecting the condensate tank pressure. The pressure and density of the MDM vapor in the mixture can be first calculated from the measured temperature value assuming saturated conditions. The temperature sensor measures the temperature of the MDM liquid, which can be considered to be close to the average temperature level in the tank. However, it is worth noting

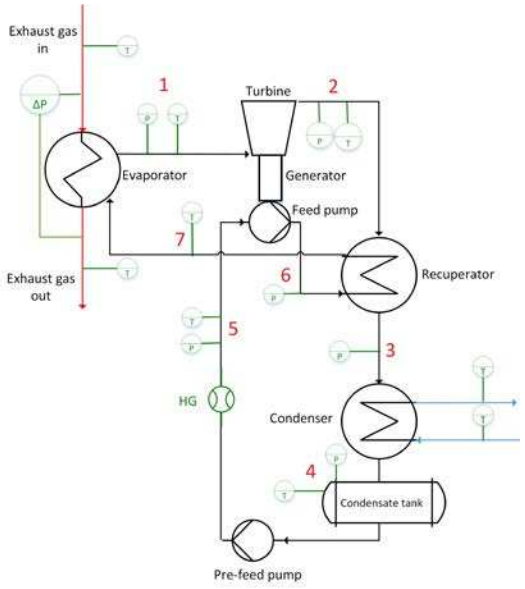

(a) A simplified process diagram of the ORC experimental facility.

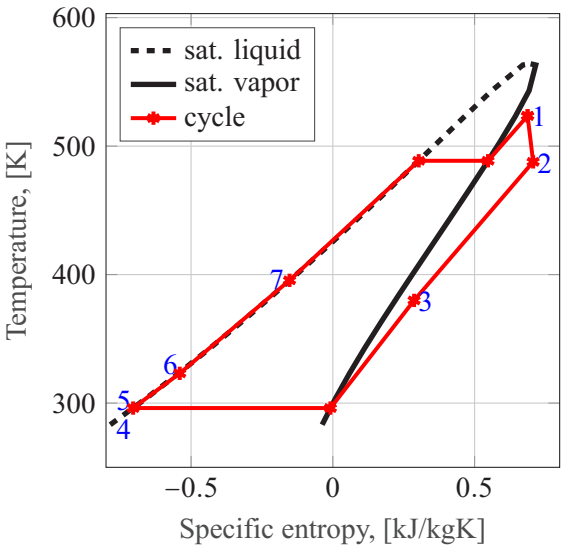

(b) T-s Diagram.

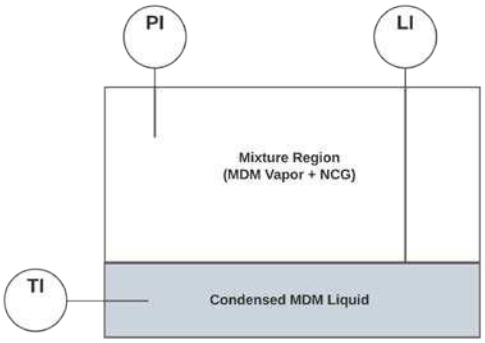

(c) Simplified schematic diagram of the pressure, temperature, and liquid level measurements in the condensate tank of the ORC system.

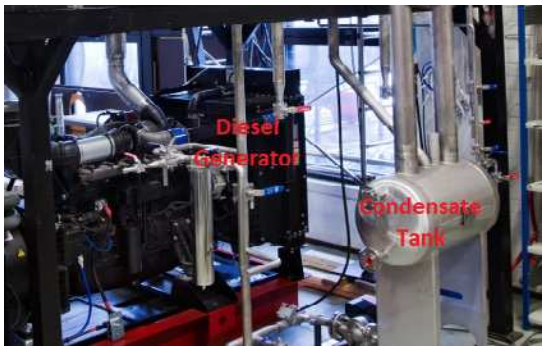

(d) Zoomed view of the ORC experimental facility at LUT University showing the diesel generator and the condensate tank.

Figure 1: Process and schematic diagrams of the ORC facility and the condensate tank at LUT University.

that the temperature distribution inside the tank might not be complete even as the tank is located near the diesel generator producing heat. That heat is expected to accumulate in the condensate tank during the system operation. After solving the pressure and density, the corresponding molar fractions of the MDM vapor and the NCG are calculated. Using the molar fractions and the apparent molar mass of the mixture, the mass fraction values of the mixture components can be determined again from which the volume fractions can be calculated. Individual component pressures can also be ascertained using the computed partial pressures based on Dalton's law. It is to be noted that the 100% relative humidity analogy has been assumed for air, considering that there is a maximum amount of MDM vapor mixed with it. Finally, the mass of the NCG and MDM vapor can be calculated using the mixture volume and density. This procedure has been described in detail through the equations 1-13.

Let the temperature of the mixture (air + MDM vapor) be T_m and let the total volume of the condensate tank be V_t. If we assume V_l to be the volume of the condensed MDM liquid available inside the tank then the volume occupied by the mixture of MDM vapor and non-condensable gases is

$$V_m = V_t - V_l. \tag{1}$$

By applying the ideal gas law for the mixture components, it becomes

$$p_m = \rho_m R_m T_m, \quad p_a = \rho_a R_a T_a, \quad and \quad p_v = \rho_v R_v T_v \tag{2}$$

where

$$T_a = T_v = T_m \tag{3}$$

The vapor temperature of the MDM is considered to be the same as the measured liquid MDM temperature assuming saturated conditions for the vapor.

$$T_{v_{MDM}} = T_{l_{MDM}} \tag{4}$$

The properties of the MDM vapor such as gas constant and molar mass and the saturated pressure based on the measured temperature can be estimated using REFPROP (Lemmon et al. (2018)) or CoolProp (Bell et al. (2014)) and the molar fractions of the vapor and air can be calculated as follows:

$$x_v = \frac{p_v}{p_m} \tag{5}$$

$$x_a = 1 - x_v \tag{6}$$

Then the apparent molar mass of the mixture is

$$M_m = M_v x_v + M_a x_a \tag{7}$$

Using Eqs. 5 - 7, the mass fraction of the mixture components can be calculated as

$$w_v = \frac{x_v M_v}{M_m} \tag{8}$$

$$w_a = 1 - w_v \tag{9}$$

The saturated pressure of MDM vapor, p_v can also be calculated using Dalton's law of partial pressure, and similarly, the partial pressure of air can be calculated.

$$\begin{aligned} p_v &= x_v p_m \\ p_a &= x_a p_m \end{aligned} \tag{10}$$

It is assumed that the volume fraction is equal to the molar fraction, hence

$$\begin{aligned} \varphi_v &= x_v \\ \varphi_a &= x_a \end{aligned} \tag{11}$$

Now, the volume occupied by the mixture components can be computed as

$$\begin{aligned} V_v &= x_v V_m \\ V_a &= x_a V_m \end{aligned} \tag{12}$$

Finally, the mass of the MDM vapor and the NCG can be calculated as described by Lampinen (2015) as follows:

$$m_v = \rho_v V_m$$
$$m_a = \rho_a V_m \tag{13}$$

The measured temperature can be corrected for pure MDM assumptions using the temperature residual equation developed by Li and Braun (2007) based on the Clapeyron Equation described in their theoretical model as

$$\Delta T = \frac{x_a p_v v_{fg_{MDM}}}{h_{fg_{MDM}}} T_{MDM_{exp}} \tag{14}$$

where $v_{fg_{MDM}}$ and $h_{fg_{MDM}}$ are the specific volume and specific enthalpy changes of vaporization for MDM. This residual temperature can be subtracted from the theoretically calculated temperature defined in the model developed by Dhanasegaran et al. (2020) which assumes pure fluid to correct the uncertainty between the experimental and simulation values.

$$T_{MDM_{corr}} = T_{MDM_{sim}} - \Delta T \tag{15}$$

3. RESULTS AND DISCUSSIONS

Three different data from the experimental measurements recorded for different time periods have been utilized to perform the analytical estimation of the NCG quantity. Each case had different ranges for the measured condensate tank temperature to test the varying proportions of the NCG in the mixture region. The measured temperature varied from 290-330 K in the considered experimental data. Also, the saturated temperature values calculated from the measured pressure are also plotted along with the measured temperature as shown in Figure 2 to show the possible higher temperature value for the case of pure MDM liquid with no presence of NCG. The obtained results have been explained with the plots of pressures, mass fractions, and mass of the MDM vapor and NCG (air) through Figures 3-5.

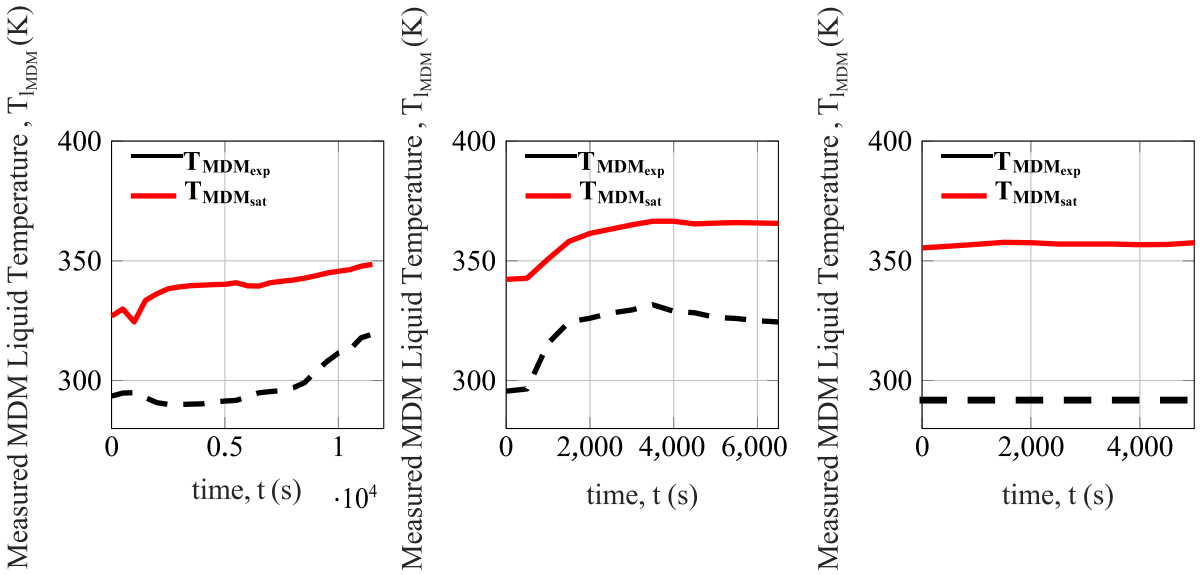

(a) Case 1 **(b)** Case 2 **(c)** Case 3

Figure 2: Variation of the measured and saturated temperatures of MDM over time.

In case 1, the measured temperature varied from a low temperature to a high-temperature value (290K-320K), hence the corresponding saturation pressure also increased proportionally which can be seen in Figure 3a. The mass fraction of the MDM vapor equaled that of air when the measured temperature

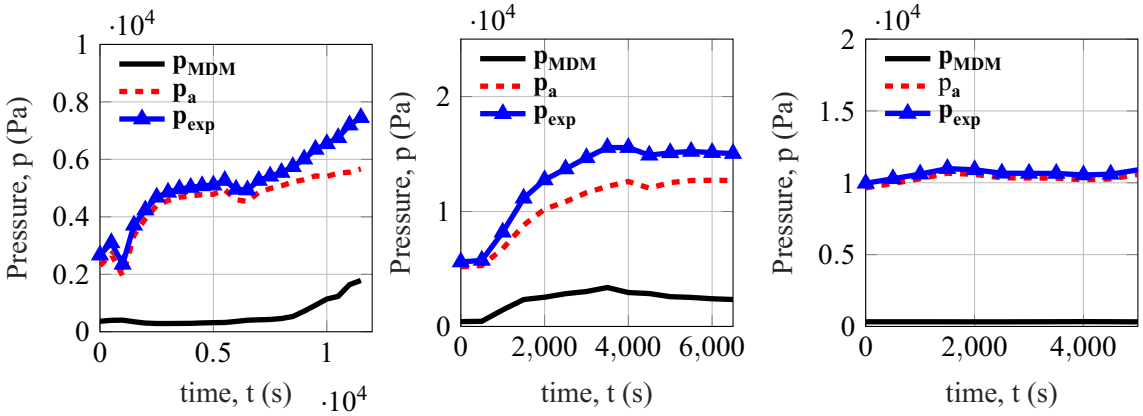

(a) Case 1 **(b)** Case 2 **(c)** Case 3

Figure 3: Variation of the measured and saturated pressures of MDM and air over time.

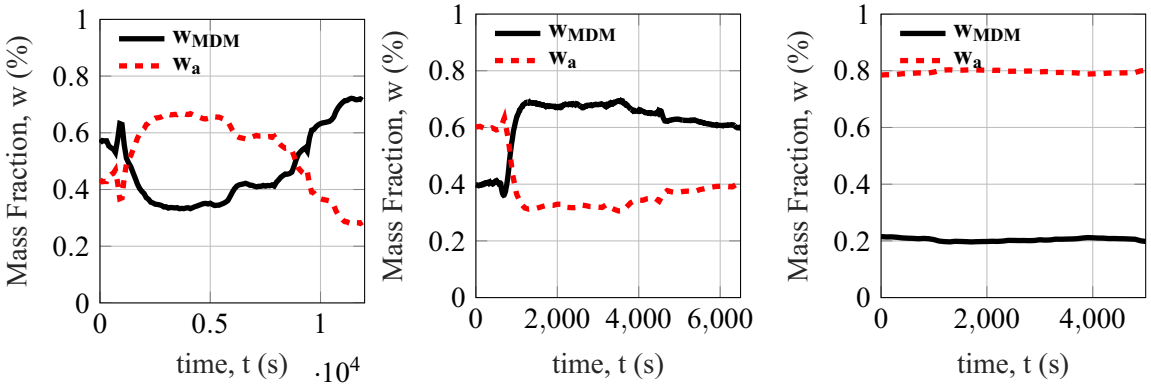

(a) Case 1 **(b)** Case 2 **(c)** Case 3

Figure 4: Variation of the estimated mass fractions of MDM vapor and air over time.

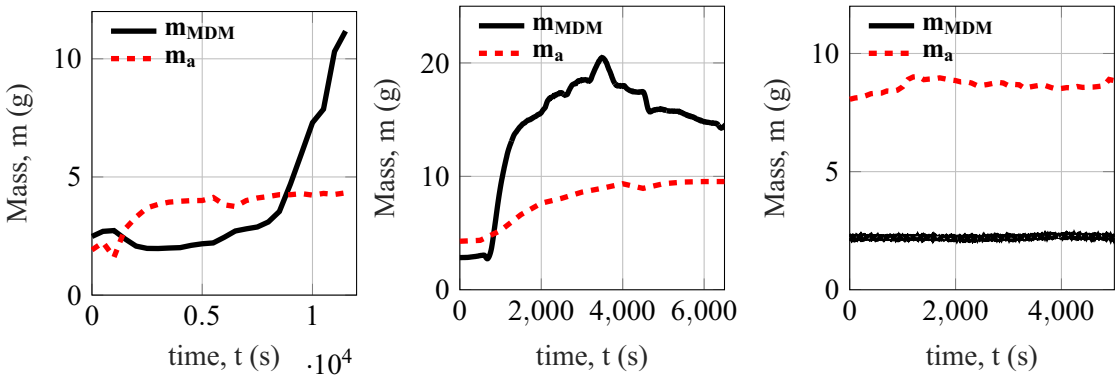

(a) Case 1 **(b)** Case 2 **(c)** Case 3

Figure 5: Variation of the estimated mass of MDM vapor and air over time.

was about 300 K and dominated toward the end when the measured temperature was greater than 300 K implying that the relative amount of NCG reduced with the increasing measured temperature.
In case 2, the measured temperature indicated higher values between 320K and 330K most of the time which resulted in significantly higher vapor pressure for MDM. Here the mass fraction presented in 4b for the MDM vapor dominated the mixture region compared to that of air. On average, the mass fraction of MDM vapor was approximately 60%.

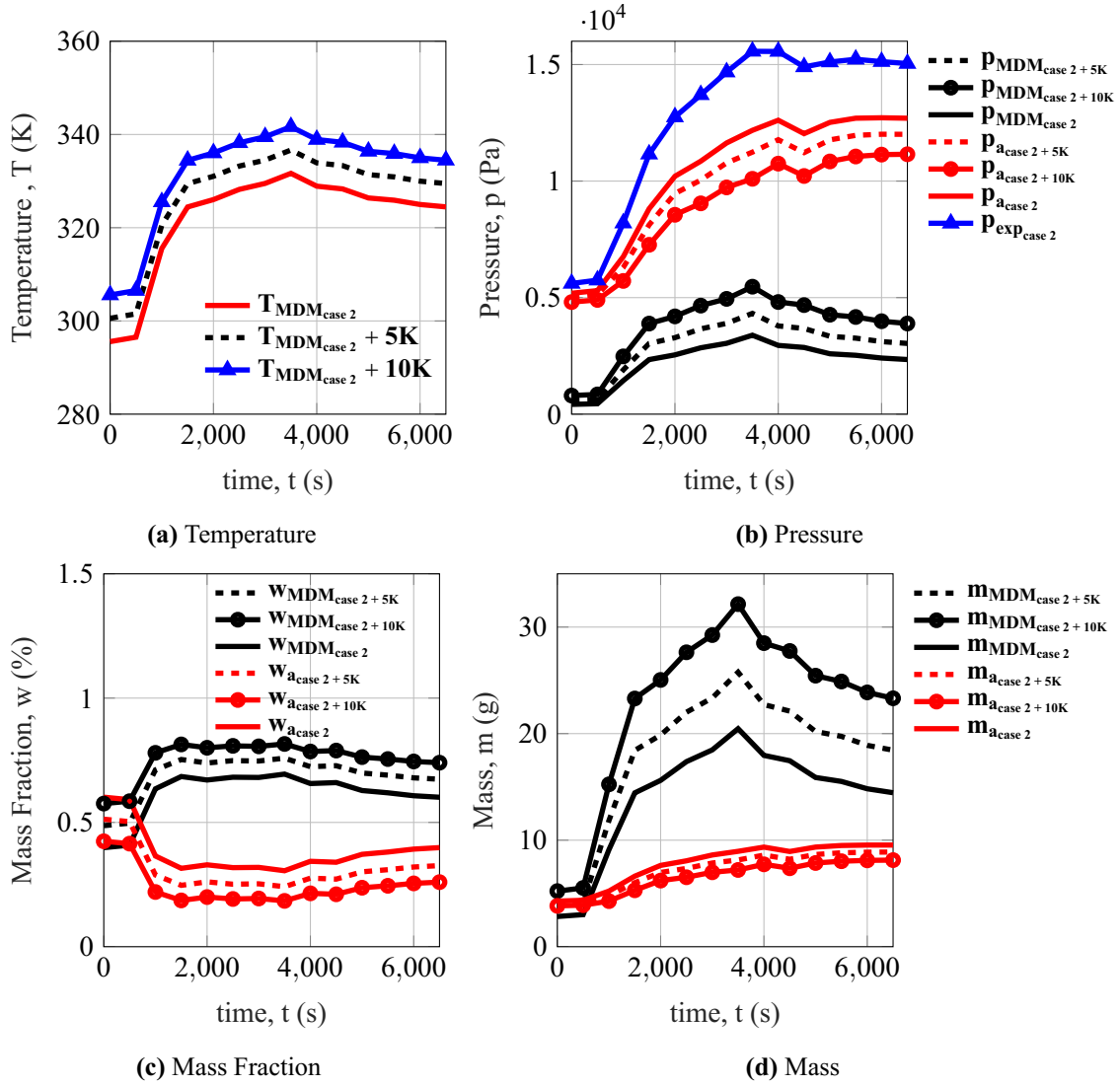

(a) Temperature **(b)** Pressure

(c) Mass Fraction **(d)** Mass

Figure 6: Sensitivity studies performed for case 2 by increasing the measured temperatures by 5 and 10 K.

In case 3, the measured temperature value shown in Figure 2c was really low around 290K compared to the previous cases, and remained almost constant during the experiment, hence the corresponding calculated MDM vapor pressure value was also lower resulting in the lowest mass fractions of MDM vapor compared to that of air which can be seen from the Figures 3c and 4c.

The partial pressure of air remained very close to the measured pressure except in case 2 (see Figure 3b) and their values were higher than the corresponding partial pressures of the MDM vapor for all the cases. This is mainly because in case 2, the measured temperature value was greater than 320K for the majority of the time period whereas, in the rest of the cases, the measured temperature was less than 300K. One of the major reasons for the increase in temperature in case 2 is that the heat coming from the diesel engine located nearby could have heated the tank.

From the plots of the estimated mass variation of MDM vapor and air presented in Figure 5, it can be observed that the variation of the mass corresponded similarly to the trend of the mass fraction as described in Figure 4. The mass of air was initially dominating the mixture region for the first 9000 s in case 1, after which the mass of MDM superseded for the remaining time period. In case 2, the mass of MDM vapor was greater than that of air for most of the time period. On average the mass of MDM was 1.5-2 times higher than the mass of air. In case 3, the mass of air was significantly higher than the mass of MDM, around three times greater, and remained constant throughout the experiments. Despite hav-

ing a lower amount of air (around 10 g) in case 2 compared to the amount of MDM, the corresponding measured pressure had large contributions from the partial pressure of air implying that the presence of NCGs greatly affects the measurements.
Finally, a sensitivity test has been performed by taking case 2 and increasing the temperature by 5 and 10 K, and calculating the pressures, mass fraction, and mass for MDM vapor and air. This sensitivity analysis was carried out since it is expected that the temperature of the vapor mixture in the condensate tank can be slightly higher than the measured temperature of the MDM liquid. It can be observed from the results presented in Figure 6 that the above-mentioned parameters increase with the increase in temperature for MDM and vice versa for the case of air. Especially, the mass of the MDM vapor surpassed that of air in all the cases and the dominance tripled for a 10 K increase in the measured temperature. This reveals that the NCG quantity decreases for higher measured temperature cases. Overall, it was observed that despite the fact that the MDM-air mixture occupies a volume of about 70 l, only a very small amount of air (several g) can significantly increase the pressure level in the condensate tank when compared to the saturated pressure of MDM at the respective temperature levels.

4. CONCLUSIONS

A 1-D analytical model has been developed in the current study using ideal gas assumptions to estimate the amount of the non-condensable gases present in the condensate tank of an ORC system. Air was considered to be the only non-condensable in the tank for problem simplification. Three different data having a wide range of temperature variation from the experimental measurements have been utilized to assess the NCG quantity. The following conclusions can be made from the obtained results of the analytical calculations.

- It was observed that even a small amount of air (a few g) in the condensate tank increases significantly the pressure level of the condensate tank when compared to the pressure level with pure MDM at the measured temperature.
- The mass fraction of the NCG vapor in the mixture region was dominant for the case of lower temperature and vice versa for the higher temperature case.
- In all the cases, the high measured pressure values from the experiments corresponded to the high mass of air which is the NCG considered in the current study.
- The sensitivity studies revealed that if the measured temperature was increased by 5 or 10 degrees then the corresponding NCG quantity subsided. This sensitivity analysis was carried out as it was expected that the temperature level of the vapor mixture can be slightly higher than the measured liquid temperature.

The results from the study provide a preliminary and empirical estimation of the quantities of the NCGs present inside a condensate tank of an ORC system despite the simplifications made. However, its applicability lies within the scope of the present work where the considered NCG is only air and the working fluid behavior is close to an ideal gas at such low temperatures marking its limitations. Using the estimated values of the masses and mass fractions, one can decide about the operation of the vacuum pump depending upon the estimates of the amount of the NCG. The study also revealed the importance of removing NCGs from the system before the experiments, as the presence of air will reduce the cycle expansion ratio significantly. Also, the values of the working fluid state such as pressures and temperatures can be corrected in the dynamic simulations that assume pure MDM using the equations 14 and 15. This information will be very much helpful in synchronizing the data from the experiments and the dynamic simulations considering the goal of building a Digital Twin of the ORC facility in future studies. In addition, it is worth highlighting that the presence of NCGs in ORC systems having low condensing pressures should be taken into account in the design of turboexpanders, as the presence of NCGs will significantly reduce the expansion ratio compared to the prediction of thermodynamic models based on the assumption of using pure fluid properties.

NOMENCLATURE

m	Mass	g
M	Molar mass	$\frac{g}{mol}$
p	Pressure	Pa
R	Gas constant	$\frac{J}{kgK}$
T	Temperature	K
t	Time	s
V	Volume	m^3 or l
w	Mass fraction	%
x	Molar fraction	%

Abbreviations

LI	Liquid indicator
MDM	Octamethyltrisiloxane
NCG	Non-Condensable gas
PI	Pressure sensor
TI	Temperature sensor

Greek

φ	Volume fraction	
ρ	Density	$\frac{kg}{m^3}$

Subscripts

a	Air
corr	Corrected value assuming pure fluid
exp	Experimentally measured
l	MDM liquid
m	Mixture
sat	Saturation-state
sim	Simulations from dynamic modeling
t	Tank
v	MDM vapor

REFERENCES

Al-Shammari, S., Webb, D., and Heggs, P. (2004). Condensation of steam with and without the presence of non-condensable gases in a vertical tube. *Desalination*, 169(2):151–160.

Bell, I. H., Wronski, J., Quoilin, S., and Lemort, V. (2014). Pure and pseudo-pure fluid thermophysical property evaluation and the open-source thermophysical property library coolprop. *Industrial & Engineering Chemistry Research*, 53(6):2498–2508.

Dehbi, A. A. (1991). The effects of noncondensable gases on steam condensation under turbulent natural convection conditions.

Dhanasegaran, R., Uusitalo, A., and Turunen-Saaresti, T. (2020). Dynamic modelling of small scale and high temperature orc system using simulink and coolprop.

Donkers, P., Gao, K., Houben, J., Huinink, H., Erich, B., and Adan, O. (2020). Effect of non-condensable gasses on the performance of a vacuum thermochemical reactor. *Energies*, 13(2).

Gallarini, S., Spinelli, A., Lietti, L., and Guardone, A. (2023). Thermal stability of linear siloxanes and their mixtures. *Energy*, 278:127687.

Gökçen Akkurt, G. and Yildirim, N. (2008). Effect of non-condensable gases on geothermal power plant performance. case study: Kizildere geothermal power plant-turkey. *International Journal of Exergy - INT J EXERGY*, 5.

Hu, Y. and Yuill, D. P. (2022). Non-condensable gas in the refrigerant of air-source heat pumps: interactions between detection features, charge level, and temperature. *International Journal of Refrigeration*.

Huang, J., Zhang, J., and Wang, L. (2015). Review of vapor condensation heat and mass transfer in the presence of non-condensable gas. *Applied Thermal Engineering*, 89:469–484.

Huhtiniemi, I. K. and Corradini, M. L. (1993). Condensation in the presence of noncondensable gases. *Nuclear Engineering and Design*, 141(3):429–446.

Jackson, J., An, P., R. A., and Ahmadinejad, M. (2000). Effects of non-condensable gas on the condensation of steam. *International Atomic Energy Agency, Vienna (Austria)*, 31(27):53–81.

Jeong, K., Kessen, M. J., Bilirgen, H., and Levy, E. K. (2010). Analytical modeling of water condensation in condensing heat exchanger. *International Journal of Heat and Mass Transfer*, 53(11):2361–2368.

Keulen, L. (2018). Non-ideal compressible fluid thermodynamics of mixtures: measurements and modeling.

Kopinga, K. and Doornmalen, van, J. P. C. M. (2013). Measuring non-condensable gases in steam. *The Review of scientific instruments*, 84:115106–1/8.

Lampinen, M. J. (2015). Thermodynamics of humid air. *Dep. Energy Technol. Ene-39.4027-Mass Transf. P.*, 23:2015–2019.

Lemmon, E. W., Bell, I. H., Huber, M. L., and McLinden, M. O. (2018). NIST Standard Reference Database 23: Reference Fluid Thermodynamic and Transport Properties-REFPROP, Version 10.0, National Institute of Standards and Technology.

Leonard, M. T. (1984). The effects of a non-condensable gas on pressurizer insurge transients.

Li, H. and Braun, J. E. (2007). Decoupling features and virtual sensors for diagnosis of faults in vapor compression air conditioners. *International Journal of Refrigeration*, 30(3):546–564.

Li, J., Gao, G., Li, P., Pei, G., Huang, H., Su, Y., and Ji, J. (2018). Experimental study of organic rankine cycle in the presence of non-condensable gases. *Energy*, 142:739–753.

Li, J.-D., Saraireh, M., and Thorpe, G. (2011). Condensation of vapor in the presence of non-condensable gas in condensers. *International Journal of Heat and Mass Transfer*, 54(17):4078–4089.

Nagae, T., Chikusa, T., Murase, M., and Minami, N. (2007). Analysis of noncondensable gas recirculation flow in steam generator u-tubes during reflux condensation using relap5. *Journal of Nuclear Science and Technology*, 44(11):1395–1406.

Punetha, M. and Khandekar, S. (2017). A cfd based modelling approach for predicting steam condensation in the presence of non-condensable gases. *Nuclear Engineering and Design*, 324:280–296.

Uusitalo, A. (2014). Working fluid selection and design of small-scale waste heat recovery systems based on organic rankine cycles.

Uusitalo, A., Honkatukia, J., and Turunen-Saaresti, T. (2017). Evaluation of a small-scale waste heat recovery organic rankine cycle. *Applied Energy*, 192:146–158.

Uusitalo, A., Turunen-Saaresti, T., Honkatukia, J., and Dhanasegaran, R. (2020). Experimental study of small scale and high expansion ratio orc for recovering high temperature waste heat. *Energy*, 208:118321.

Zhang, W., Wang, S., and Lianbo, M. (2020). Analytical Modeling for Vapor Condensation in the Presence of Noncondensable Gas and Experimental Validation. *Journal of Heat Transfer*, 143(1). 011601.

ORC SEVILLE 2023
7th International Seminar on O.R.C. Power Systems

© 2024 Editorial Universidad de Sevilla. Este es un artículo de acceso abierto distribuido bajo los términos de la licencia de uso y distribución Creative Commons (BY-NC-ND 4.0)

DOI: https://dx.doi.org/10.12795/9788447227457_101

Advanced control of compressor inlet temperature in supercritical CO_2 Brayton cycle

Rui Wang[1], Xuan Wang[1,*], Hua Tian[1], Gequn Shu[1,2]

[1] *State Key Laboratory of Engines, Tianjin University, 300072, China*
[2] *Department of Thermal Science and Energy Engineering, University of Science and Technology of China, Hefei 230027, China*

*Xuan Wang: wangxuanwx@tju.edu.cn

ABSTRACT

The supercritical CO_2 (sCO_2) Brayton cycle has gained much interest because of its flexibility, compactness and high efficiency. The sCO_2 at the inlet of compressor should work near the critical point to obtain high system efficiency, while the physical properties of sCO_2 near the critical point change dramatically, which brings great challenges to the control of the compressor inlet temperature. At present, cooling far from the critical point and adjusting the cooling water flow rate with Proportion-Integration-Differentiation (PID) controller is the commonly used method, but it loses system efficiency and may be out of control sometimes. Therefore, in this study Linear Model Predictive Control (LMPC) and Deep reinforcement learning (DRL) are used to control the compressor inlet temperature and compared with PID. A dynamic model of a recompression sCO_2 Brayton cycle is established, and the cooler model is carefully validated against experiment data. The results indicate that both the LMPC and DRL can control the sCO_2 temperature near the critical temperature much better than the PID. LMPC works the best because the cold end parameters fluctuate slightly and the cooler model can be regarded as approximately linear, thus LMPC can find almost the global optimal solution. Nevertheless, DRL control exhibits the fastest real-time computation ability and proves good extrapolation ability.

1 INTRODUCTION

The supercritical carbon dioxide (sCO_2) Brayton cycle has gained more and more interesting due to its advantages of high thermal efficiency, compactness of components, wide temperature range application (Açıkkalp *et al*.,2017) and so on. It has been regarded as the potential power conversion equipment for next generation in numerous applications, including nuclear, solar, fossil fuel and waste heat recovery (Gao *et al*.,2021; Liang *et al*.,2020; Battista *et al*., 2019). These advantages benefit greatly from the high density and low compressibility of CO_2 near its critical point (304.1 K, 7.38 MPa) at the inlet of compressor (Dostal *et al*.,2004).

However, the physical properties of sCO_2 near the critical point change dramatically, which brings significant challenges to the control of the compressor inlet temperature of sCO_2 (Hacks *et al*., 2019). The closer this temperature is to the critical temperature, the smaller the compressor power consumption and the higher the system efficiency, but it is more difficult to control at a stable value, and sometimes it is easy to fall into a trans-critical state, resulting in compressor damage. Therefore, the compressor inlet temperature of sCO_2 in many studies are far from the critical point to ensure the safety operation with the expense of reducing thermal efficiency. Zhang *et al*. (2022) established the dynamic model of Brayton cycle with the compressor inlet temperature of sCO_2 of 35 ℃ and the cycle efficiency is 20.616%. Clementoni *et al*. (2017) also analyzed the transient power operation of a sCO_2 Brayton cycle with the compressor inlet temperature of sCO_2 of 35.5℃, the cycle efficiency under 35% load is 7.4%. Zhou et al. (2021) found that when the compressor inlet temperature of sCO_2 increase from 306 K to 312 K, the system efficiency decreased by two percentage points.

The compressor inlet temperature of sCO_2 is usually controlled at the set value in most studies to ensure the safe operation of the system. At present, this temperature is usually controlled by the cooling water mass flow rate with a Proportion-Integration-Differentiation (PID) controller. For example, Olumayegun and Wang (2019) used the PID controller to keep the compressor inlet temperature of

sCO_2 at the set value. Moisseytsev *et al*. (2011) included a cooler bypass PID control to maintain the compressor inlet temperature, the results demonstrate that the single cooler bypass valve is out of operation when the temperature is expected to decrease much, and it has to cooperate with cold source mass flow rate control. Besides, the PID may fail sometimes.

From the above review, it can be found that the current commonly used control method for compressor inlet temperature of sCO_2, that is, far from the critical point combined with PID controller, not only loses the system efficiency, but also may be out of control in some conditions. Therefore, it is necessary to study more advanced control method to control the temperature more stably near the critical temperature, so as to improve system safety and efficiency.

To this end, the linear model predictive control (LMPC) and deep reinforcement learning (DRL) control are proposed to control the compressor inlet temperature of sCO_2, which have not been applied in sCO_2 Brayton cycle, while exhibited good performance in other control problem such as energy management and unmanned vehicles. For this purpose, the dynamic model of a recompression sCO_2 Brayton cycle with the compressor inlet temperature of sCO_2 near the critical point is established in Simulink/Matlab to ensure the high system efficiency, and the component model of cooler is carefully validated against experiment data. Based on these, the performance of the two control methods is compared with the traditional PID controller.

2 MODELLING DESCRIPTION

Extensive research has been conducted on system configurations and layouts of the sCO_2 Brayton cycle such as reheating, recuperation, intercooling, and recompression. The recompression Brayton cycle stands out owing to its simple layout simplicity and high cycle efficiency. Many sCO_2 experiment system are the recompression cycle, such as Sandia's system. The object of this study is also a recompression sCO_2 Brayton cycle (RCBC) system, the configuration is showed in Figure 1. The main components include a heater, high-temperature recuperator (HTR), low-temperature recuperator (LTR), cooler, main compressor (MC), recompressor (RC), high-pressure turbine (HT), low-pressure turbine (LT), pipes, and valves. The HT is coaxial with MC and is called turbine-and-compressor1 (TAC1); similarly, the LT coaxial with RC is named TAC2. The system design parameters are showed in Figure 1 and Table 1. It should be noticed that the design parameters are not only optimized with system thermodynamic models, but also limited by the actual equipment manufacturing capacity, because the system experiment bench is being built according to the design parameters. For example, although the higher the turbine inlet temperature brings the higher cycle efficiency, but it is hard for manufacturing the boiler and turbine, so the turbine inlet temperature is designed at 550 ℃.

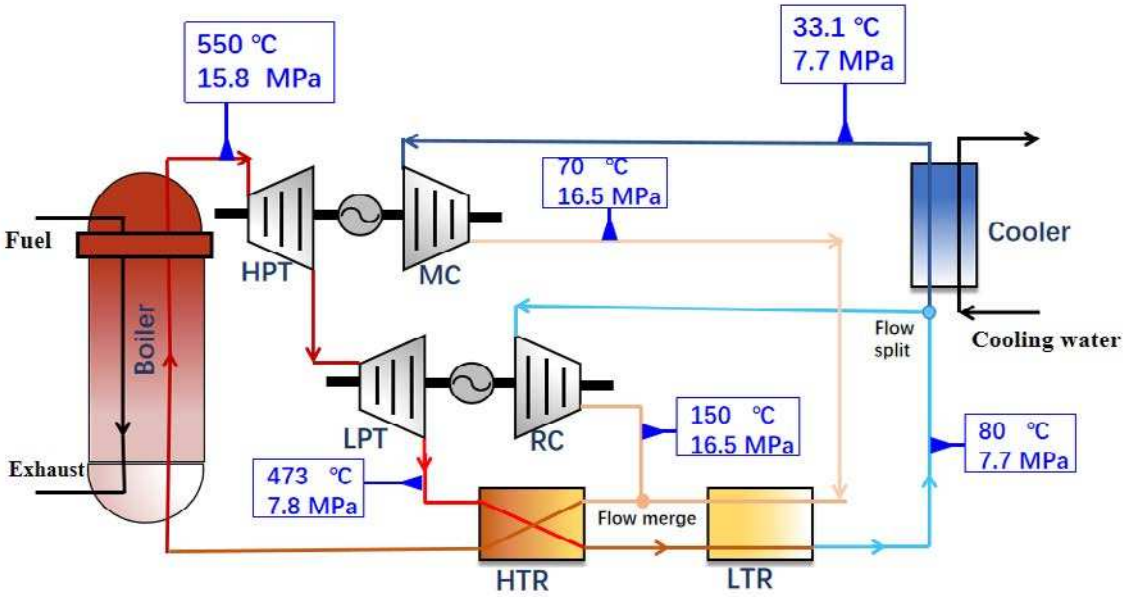

Figure 1: Schematic layout of the system

Table 1: Design parameters of the RCBC dynamic model

Process variable	Unit	Value
Net Power	kW	455.5
Cycle Efficiency	%	34.2
Cycle Flow of sCO_2	kg/s	9.76
Split ratio	/	0.38
MC/RC Isentropic Efficiency	%	68/68
HT/LT Isentropic Efficiency	%	83/77
HTR/LTR Regenerative Rate	%	95/89
Rotation Speed of MC	rpm	71670
Rotation Speed of RC	rpm	109055
Cooling Water Flow	kg/s	13.97
Cooling Water Temperature	℃	25

2.1 Dynamic modelling

The dynamic model of the system is developed by connecting the component models according to the thermodynamic relationship. The modelling process is briefly described in Figure 2 and below content, and more detailed description is available in our previous work (Wang *et al*., 2022).

The dynamic model of the RCBC system is established in the MATLAB/Simulink environment based on the boundary condition provided in Figure1 and Table 1. The properties of CO_2 are obtained by Refprop 9.0. All heat exchangers including a reheater, a HTR, a LTR and a cooler are modeled using Finite Volume method, because no phase change exists in supercritical station. The heat exchanger is discretized into N control units, and each control unit is modeled based on the mass and energy conservations. The heat transfer coefficient of heat source in the boiler is gained from Horst *et al*. (2013), which has been provided suitable for high temperature gas outside the tube heat exchangers. The Ptukhov-Krasnoshchekov-Protopopov correlation from Pitla *et al*. (1998) is applied to CO_2 which are in supercritical phase and has no phase change. The coolant working fluid in the cooler is non-phase change cooling water, so the Petukhov-Kirillov correlation from Gelbe *et al*. (2010) is adopted. These heat transfer coefficients are listed in Table 2.

The zero-dimensional static model is adopted for turbomachinery for its faster response speed compared with heat exchangers. The performance maps from Sandia (Wright *et al*., 2010) are used for accurately predicting the performance of the compressor under off-design conditions. Two dimensionless parameters, including flow and ideal head coefficients, are introduced to describe the performance of the compressors, and the turbine is simplified as an unchoked nozzle model (Bian *et al*., 2022).

Additional pipes and valves are installed among adjacent components. The linear valve model is adopted in this study, the pipe is modeled based on the conservation of mass and energy, as well as the pressure drop equation.

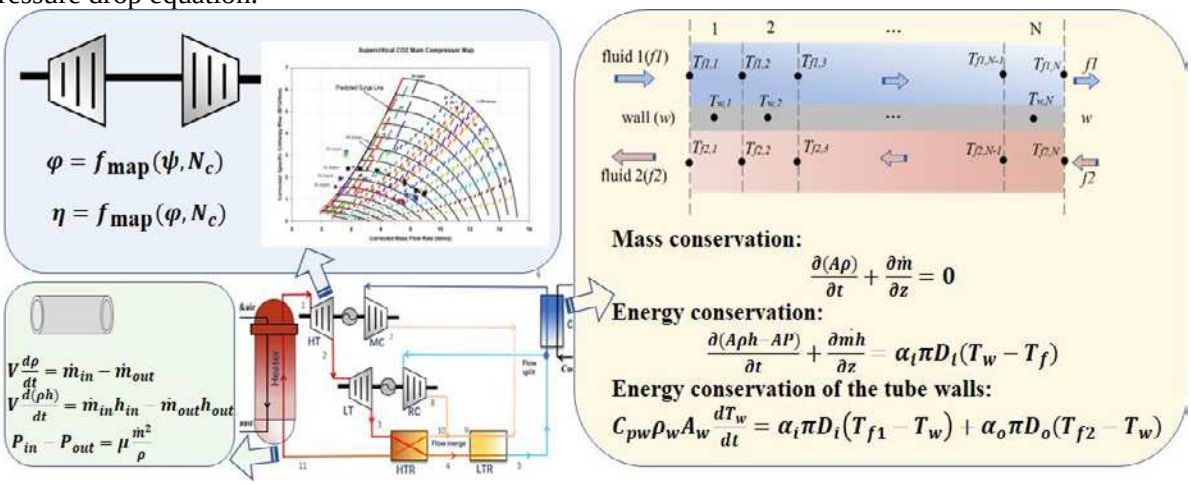

Figure 2: System modelling process

Table 2 Heat transfer correlations

Parts	fluids	Heat Transfer Correlations
Boiler/HTR/LTR/Cooler	sCO_2	$Nu = \frac{(f/8)\cdot Re\cdot Pr}{12.7(f/8)^{0.5}(Pr^{2/3}-1)+1.07}(\frac{\overline{C_p}}{C_{pb}})^{0.35}(\frac{k_b}{k_w})^{-0.33}(\frac{\mu_b}{\mu_w})^{0.11}$
Boiler	Heat source	$\alpha_o = 1.72\frac{\lambda}{d_o^{0.4}}(\frac{d_e w_n \rho}{\mu})^{0.6}(\frac{C_p\mu}{\lambda})^{\frac{1}{3}}(\frac{\mu}{\mu_w})^{0.14}$
Cooler	Water	$Nu = \frac{(f/8)RePr}{12.7(f/8)^{0.5}(Pr^{2/3}-1)+1.07}$

2.2 Model validation

As mentioned in the start of Section 2, the system experiment bench is being built according to the design parameters in Figure 1 and Table 1. The entire system has not been finished, but the compressor test bench with a cooler has been completed. Therefore, the dynamic model of the cooler which is focused in this study can be validated against the corresponding component experimental data.

By changing the experimental boundary conditions, including inlet temperature and flow rate on both the hot and cold sides, these parameters are taken as input parameters of the cooler model. The outlet temperatures on both of the hot and cold sides, and the cooler pressure are taken as output parameters. The input parameters are shown in Figures. 3(a) and (b). The validation results shown in Figures. 3(c) and (d) are the outlet temperature and pressure of CO_2, which demonstrates that the accuracy of the model is sufficient for further simulation.

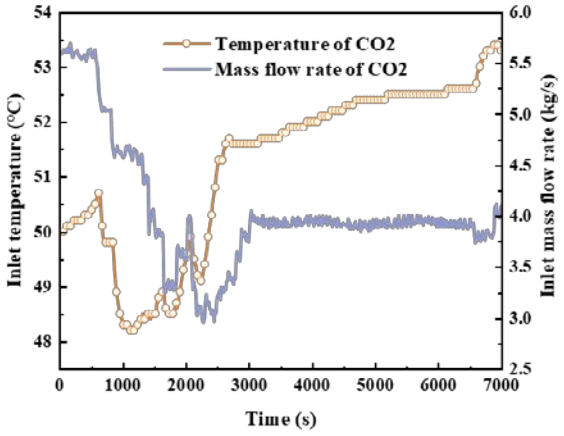

(a) Inlet temperature and flow rate of CO_2

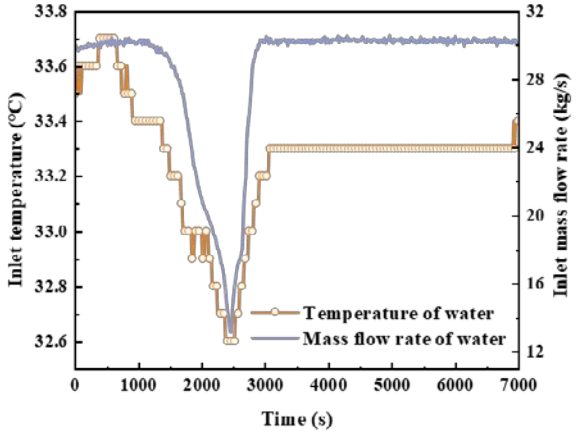

(b) Inlet temperature and flow rate of water

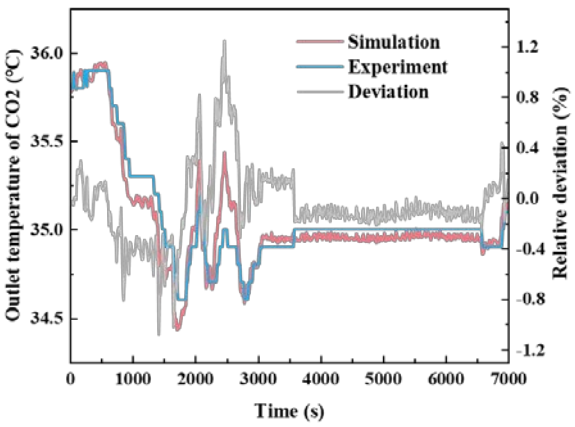

(c) Outlet temperature of CO_2

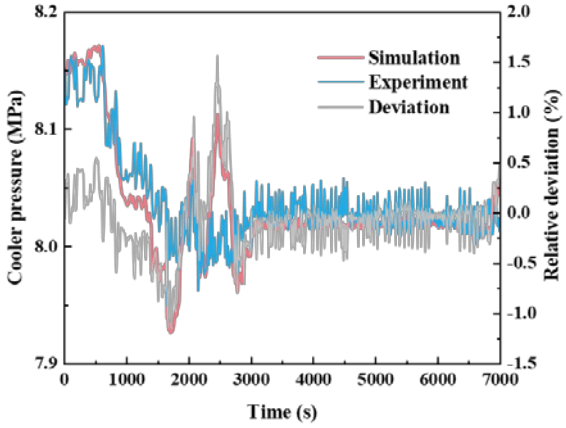

(d) CO_2 pressure

Figure 3: Model validation results of the cooler

3 CONTROL DEVELOPMENT

The compressor inlet temperature of sCO_2 is usually controlled by the mass flow rate of cooling water which can be adjusted by the water valve or the water pump speed. In this section, three control methods of LMPC, DRL, and PID are used to control the temperature all by adjusting the cooling water mass flow rate. The description of each control method is as follows.

3.1 PID control

At present, the PID control is the most widely used, owing to its simplicity and technical maturity. The schematic of PID control is shown in Figure 4. The sCO_2 temperature at the outlet of cooler (the compressor inlet temperature of sCO_2) is compared to the reference temperature and generate the tracking error inputted to the PID controller, in which the action signal is calculated and sent to the actuator such as cooling water valve. The PID parameters are tuned by linearizing the cooler model at the design condition, and they are -0.498 (P), -0.083 (I) and 15.706 (D), respectively.

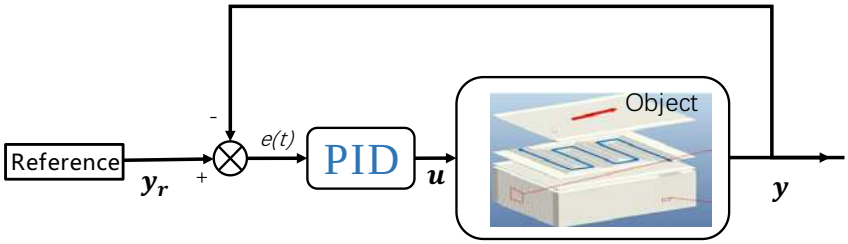

Figure 4: Schematic of PID control method

3.2 LMPC control

As mentioned in the introduction, the PID controller works well under small and slow transient operations, while it may have difficulties in fast and violent transient conditions, owing to the nonlinearity of the cooling process, and the PID is not an optimized control method.

Model predictive control (MPC) is a kind of optimized control method and has been proved to be effective in parameter tracking control in other applications, such as tracking the temperature of a biochemical reactor for yeast fermentation (Lawrynczuk *et al.*, 2008a). Therefore, in this work MPC is applied to control the compressor inlet temperature of sCO_2. To achieve real-time optimized control during system operation, the prediction models used in MPC methods must not be overly complex. Owing to the nonlinearity and complexity of the cooler model, in this work a linearized cooler model under the design condition is used for MPC optimization with a quadratic program solver. The model mismatch generated by the linearization was corrected using feedback. The schematic of the LMPC control method is showed in Figure 5.

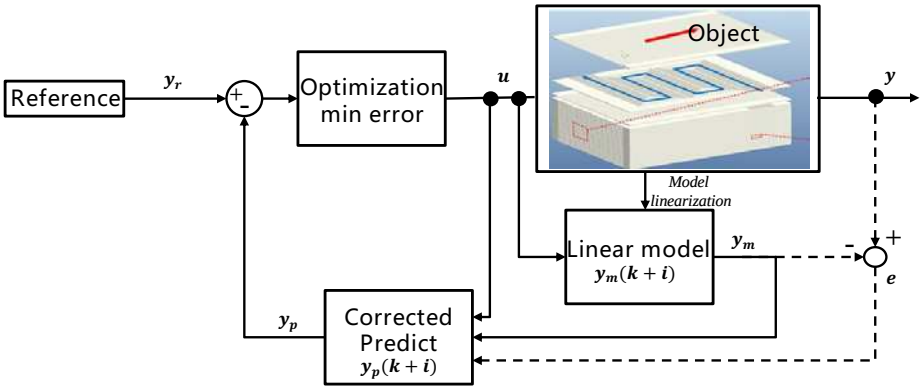

Figure 5: Schematic of LMPC control method

3.3 DRL control

Reinforcement learning (RL) algorithms mimic the learning mechanism of human brain. An RL agent observes and interacts with the environment to learn how to take optimal actions. DRL is the combination of deep learning and RL, possessing the strong nonlinear mapping capability of the former

and the decision-making ability of the latter. Therefore, DRL can solve complex control problems and it has been proved to be effective for the temperature control in Organic Rankine Cycle (Wang *et al*., 2022b).

Compared to the LMPC, DRL can make the optimization offline with complex mechanism model which can reflect the nonlinear process more accurately through repeated training and guarantee real-time decision making. The key elements in the DRL are the agent (a deep neural network), environment (the cooler model), observation (key state parameters), action (cooling water valve opening), and reward. During the training process, the agent learns how to take actions under each observed state to obtain the maximum reward by constantly interacting with the environment.

A DRL control of the compressor inlet temperature of sCO_2 is proposed in this work as illustrated in Figure 6. Therein, the agent is the controller of a deep neural network; the environment is the cooler model; the observation variables are the arithmetic average temperature and pressure of the sCO_2 in the cooler, their change rates, and the tracking and accumulative errors, six variables in total; the action is the cooling water valve opening; the reward means the control performance, that is the less temperature tracking error, the larger reward, and the reward function is shown as Equation (1). The training method used in this work is deep deterministic policy gradient (Lillicrap *et al*., 2016a).

$$r = 8(|e|<0.05)+5(|e|<0.1\&\&|e|\geq 0.05)+3(|e|<0.3\&\&|e|\geq 0.1)+(|e|<0.5\&\&|e|\geq 0.3)$$
$$-(|e|\geq 0.5)-5(\frac{da_t}{dt}\bullet\frac{da_{t+1}}{dt}<0)-100(T<\min T\,||\,T>\max T) \quad (1)$$

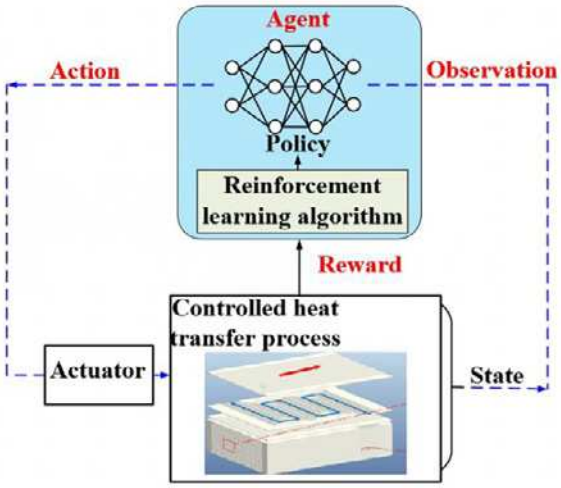

Figure 6: Schematic of DRL control method

During the training process, only the mass flow rate of the sCO_2 changes as shown in Figure 7(a), and other boundary conditions of the cooler are constant. After 1700 episodes of training, the result is converged as shown in Figure 7 (b).

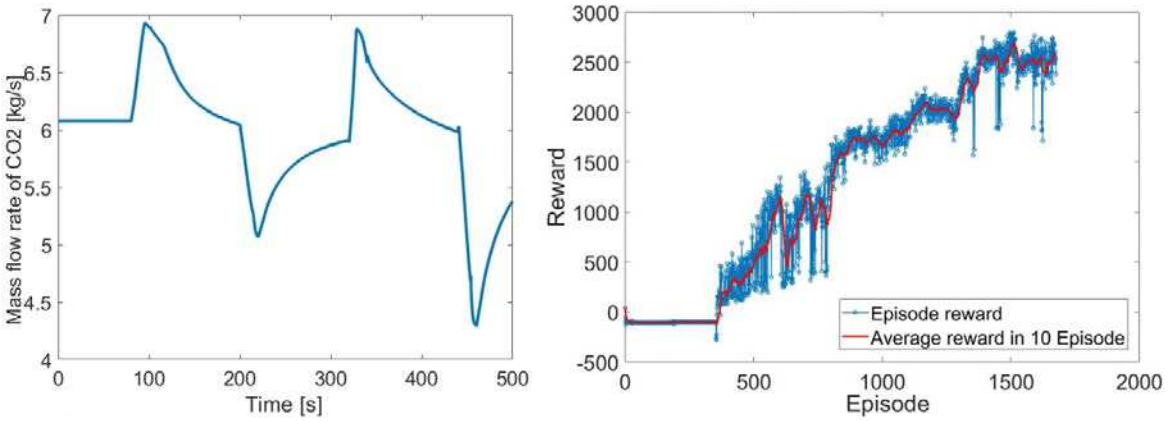

(a) Varying boundary condition during training (b) Training process

Figure 7: Training of the DRL controller

4 RESULT AND DISCUSSION

When the main compressor speed changes as shown in Figure 8(a), the LMPC, PID and DRL controllers for the compressor inlet temperature of sCO_2 are simulated in the entire system model to evaluate the control performance as shown in Figure 8(b). It should be noted that the varying mass flow rate of the sCO_2 in the cooler in this section is not the same as that in the DRL control training process, aiming at testing the extrapolation ability of the DRL control.

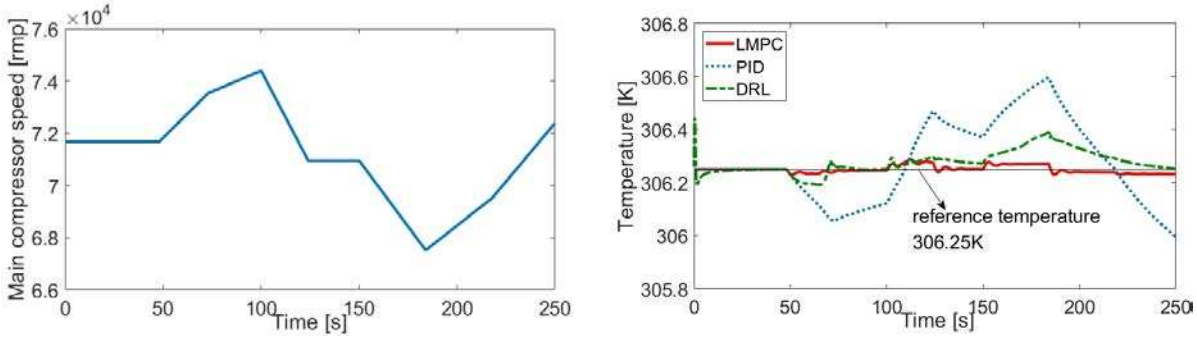

(a) Transient signal of the main compressor speed (b) Temperature control results

Figure 8: Temperature control results for various controller under transient main compressor speed

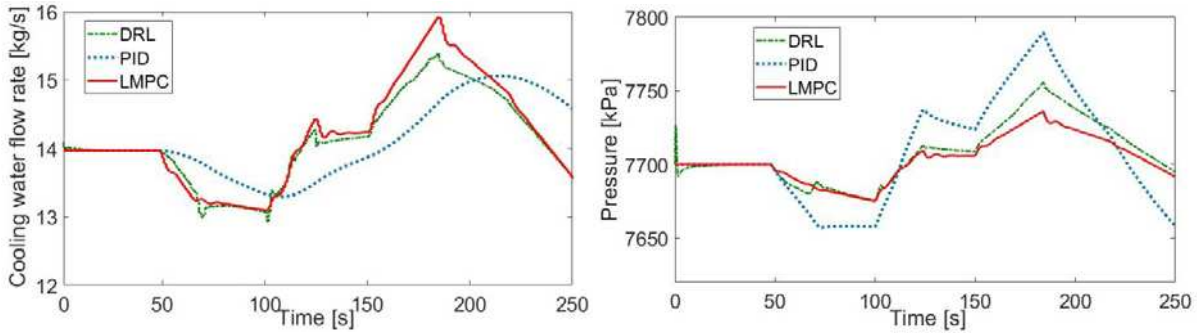

(a) Variation in the pressure in cooler (b) Variation in the mass flow of cooling water

Figure 9: Temperature control results for various controller under transient sCO_2 mass flow rate

It can be found that the compressor inlet temperature of sCO_2 can be controlled within ± 0.35K around the reference temperature under PID control, while that is ± 0.05K under LMPC control and almost ± 0.15K under DRL control. PID does not belong to optimal control, so its control effect is naturally inferior to the other two optimal control methods. LMPC can control the temperature fluctuation of sCO_2 in a very small range. In this range, the model of the cooler can be considered as a linear model, and the global optimal control trajectory can be found for the linear model. Therefore, it can be said that the control trajectory of LMPC is almost the global optimal. However, the convergence result of DRL optimization algorithm may be a local optimum, and it is not easy to judge whether the convergence result is a global optimum. Therefore, DRL does not have obvious advantages over LMPC when the model can be approximately linear in such a small range of state fluctuations.

As can be seen from the Figure 9, more accurate and stable temperature control leads to smaller fluctuation of the pressure in the cooler, which is conducive to maintaining the safe operation of the main compressor. However, the fluctuation of the cooling water mass flow rate of MPC is the largest to get the most accurate temperature control.

Nevertheless, DRL control still exhibits the fastest real-time computation ability during the simulation process, because its optimization calculation is carried out offline, and online it only needs to take the best action according to the trained rules. By contrast, the LMPC needs to be optimized online. For the controller, real-time is a very important performance index. On the other hand, as shown in the simulation results, DRL control proves good extrapolation ability. If the training sample can be enlarged

602

and the training parameters can be optimized, DRL may obtain better control effect.

5 CONCLUSIONS

A dynamic model of the recompression sCO_2 Brayton cycle system is designed near the critical point to obtain high thermal efficiency, and the cooler model is carefully validated. LMPC and DRL control are used to control the compressor inlet temperature of sCO_2 and compared with traditional PID. The conclusions are as follows:

The performance of PID controller with constant parameters is not satisfactory under transient dynamic conditions. The LMPC controller is able to remain the smallest tracking error, because the cooler model is almost linear in such a small range of state fluctuations, and the LMPC can almost find the global optimal solution. By contrast, DRL controller is easy to fall into a local optimal solution, so the control effect is inferior to the LMPC, but much better than the PID. Nevertheless, DRL control still exhibits the fastest real-time computation ability during the simulation process, because its optimization calculation is carried out offline, which is a very important performance index for the controller. Besides, DRL control proves good extrapolation ability. It is believed that the DRL may have more advanced than MPC for more complex nonlinear problem and under the conditions with large uncertain disturbance.

NOMENCLATURE

RCBC	Recompression supercritical CO_2 Brayton Cycle
HTR	High-temperature recuperator
LTR	Low-temperature recuperator
HPT	High-pressure turbine
LPT	Low-pressure turbine
MC	Main compressor
RC	Recompressor
LMPC	Linear Model predictive control
MPC	Model predictive control
DRL	Deep reinforcement learning

REFERENCES

Açıkkalp., Emin., 2017, Ecologic and sustainable objective thermodynamic evaluation of molten carbonate fuel cell–supercritical CO2 Brayton cycle hybrid system, *International Journal of Hydrogen Energy*, vol. 42: p.72-80.

Bian X., Wang X., Wang R., 2022, Optimal selection of supercritical CO2 Brayton cycle layouts based on part-load performance, *Energy*, 256,124691.

Battista D., Fatigati F., Carapellucci R., 2019, Inverted Brayton Cycle for waste heat recovery in reciprocating internal combustion engines, *Applied Energy*, 253.

Clementoni E., Cox T., King M., 2017, Transient Power Operation of a Supercritical Carbon Dioxide Brayton Cycle, *Turbomachinery Technical Conference & Exposition*.

Dostal V., Driscoll MJ., Hejzlar P. 2004, In: A supercritical carbon dioxide cycle for next generation nuclear reactors.

Gao C., Wu P., Liu W., 2021, Development of a bypass control strategy for supercritical CO2 Brayton cycle cooled reactor system under load-following operation, *Annals of Nuclear Energy*, 151,107917.

Gelbe H., Ziada S., 2010, O2 vibration of tube bundles in heat exchangers, Springer Berlin Heidelberg.

Hacks A., Schuster S., Brillert D., 2019, Stabilizing Effects of Supercritical CO2 Fluid Properties on Compressor Operation, *International Journal of Turbomachinery Propulsion and Power*, vol. 4, no.3: p.20.

Horst TA., Rottengruber HS., Seifert M., 2013, Dynamic heat exchanger model for performance prediction and control system design of automotive waste heat recovery systems, Applied Energy ,105:293-303.

Lillicrap T., Hunt J., Pritzel A., 2016, Continuous control with deep reinforcement learning, *International Conference on Learning Representations*, 2016.

Liang Y., Chen J., Luo X., 2020, Simultaneous optimization of combined supercritical CO2 Brayton cycle and organic Rankine cycle integrated with concentrated solar power system, *Journal of Cleaner Production*, 2121927.

Lawrynczuk M.,2008, Modelling and nonlinear predictive control of a yeast fermentation biochemical reactor using neural networks , *Chemical Engineering Journal*, vol.145(2): p.290-307.

Moisseytsev A., Sienicki J., 2011, Investigation of plant control strategies for the supercritical CO2 Brayton cycle for a sodium-cooled fast reactor using the plant dynamics code, *Office of Scientific & Technical Information Technical Reports*.

Olumayegun O., Wang M.,2019, Dynamic modelling and control of supercritical CO2 power cycle using waste heat from industrial processes, *Fuel*, no:249:P.89-102.

Pitla SS., Robinson DM., 1998, Groll EA., Ramadhyani S. Heat transfer from supercritical carbon dioxide in tube flow: a critical review. 4:281-301.

Wright S A., Radel R F., Vernon M E., 2010, Operation and analysis of a supercritical CO2 Brayton cycle.

Wang R., Wang X., Shu G., 2022, Comparison of different load-following control strategies of a sCO2 Brayton cycle under full load range, *Energy*, 246,123378.

Wang, X., Wang, R., Jin, M., et al., 2020b. Control of superheat of organic rankine cycle under transient heat source based on deep reinforcement learning, *Applied Energy*, 278, 115637.

Zhang Y., Li H., Li K., 2022, Dynamic characteristics and control strategies of the supercritical CO2 Brayton cycle tailored for the new generation concentrating solar power, *Applied Energy*, 328,120190.

ACKNOWLEDGEMENT

This work was supported by the National Key R&D Program of China (2022YFE0100100).

ORC SEVILLE 2023
7th International Seminar on O.R.C. Power Systems

© 2024 Editorial Universidad de Sevilla. Este es un artículo de acceso abierto distribuido bajo los términos de la licencia de uso y distribución Creative Commons (BY-NC-ND 4.0)

DOI: https://dx.doi.org/10.12795/9788447227457_103

Potential for surplus-heat-to-power conversion in current and future aluminium production process with off-gas recycling

Jonas Bueie[1,*], Magnus Windfeldt[1], Trond Andresen[1]

[1] *SINTEF Energy Research, Sem Saelands Vei 11, 7034 Trondheim, Norway*

*Corresponding Author: jonas.bueie@sintef.no

ABSTRACT

Increased utilization of industrial surplus heat can make significant contributions towards reaching energy efficiency and emissions reduction goals. The off-gas from metal production smelters can contain large amounts of thermal energy, and conversion to electric power often appears an enticing prospect. However, the practical potential for exploitation can be significantly reduced from plant processes that are designed considering surplus heat as a waste product to get rid of. This typically makes the heat accessible only at reduced temperatures.

The HighEFF research centre for industrial energy efficiency has studied technologies, applications, and cases for surplus heat utilization since its start in 2016. Heat-to-power conversion has been explored in several cases provided by the partner industries from – among others – Norwegian aluminium manufacturers. Centre research activities also include novel production processes and modifications, which has side effects providing very different conditions and constraints for energy recovery. One such process modification is off-gas recirculation, mainly developed to increase concentration of CO_2 in the off-gas to improve conditions for CO_2 capture in the future, but which also will alter off-gas temperature and recoverable heat as a side effect. This could improve the potential for energy recovery.

In this work, the potential for energy recovery is evaluated and compared in four cases – one representing a current aluminium process, and three future process scenarios with flue gas recycling. The simulated heat-to-power conversion is done by applying an organic Rankine cycle (ORC) optimization model to each case. The results indicate significant benefits to energy recovery in the recycling cases. In the case with the highest recycling rate and flue gas temperature, the potential for electric power production increases by 270 % compared to the present-day case. In addition, the reduced work of the main exhaust fans in the recycling cases brings further energy savings on the system level equivalent to 25–50 % of the ORC power output, further increasing overall energy efficiency. From this, some potential synergies between process design, heat-to-power, and thermal integration of other technologies such as CO_2-capture are discussed.

1 INTRODUCTION

Waste heat recovery from industry processes has the potential to save vast amounts of energy globally. Primary metal production industries are promising targets for such heat recovery, as they create large amounts of high-temperature off-gas among other waste heat sources. However, this off-gas is commonly not easily managed, and is usually treated purely as a waste product. In Norway, aluminium production makes up the largest part of the metal industry, certainly in terms of energy use and waste heat. The largest plants can reject around one TWh/y of waste heat through the off-gas alone, which is so far not utilized to any significant extent. One problem is the relatively low temperature. Despite the electrolysis process operating at around 1000 °C, excessive draft air into the cell dilutes the produced off-gas to a temperature in the range of 150 °C, which considerably reduces thermodynamic potential and usability. The gas also contains various components and contaminants, and it can likely be cooled

down to 80-90 °C without causing issues with condensation or downstream gas treatment. So not only is the temperature fairly low, only parts of the thermal energy in the off-gas is recoverable.

HighEFF is a Norwegian Centre for Environment-friendly Energy Research (FME), on the topic of industrial energy efficiency. Norwegian metal production consumes around 25% of the national electric power production, and with strong interest in process improvements and efficiency, the largest industrial companies are all partners in HighEFF. The research of HighEFF has explored both incremental improvements of current and existing processes, as well as evaluation of new, alternative processes. Several measures are needed to take metal production into the low-emission future. One potential step on this way is to recycle flue gas, replacing draft air going into the smelter process. Off-gas recycling promises to increase both energy efficiency and CO_2 concentration to improve conditions for CO_2 capture. This is relevant for several different smelting processes. One off-gas recycling concept for aluminium plants has been patented by GE (Wedde, 2011), and is currently being deployed in an industrial demonstrator. HighEFF research (Solheim and Senanu, 2020) studied the relations between recirculation and draft air rates on gas composition, energy balance, and other important aspects connected to such a concept.

The recycled off-gas must be cooled down before re-entry to the electrolysis cell, to control the heat balance. This cooling could be used for a waste heat recovery system rather than a plain heat sink, and since the latter would be needed anyways, the additional cost to the off-gas recycling loop may not be excessive. Solheim and Senanu (2020) predicted that off-gas recycling can increase the temperature of the off-gas, potentially improving the conditions for heat recovery for power production. In this paper, we study how the potential for surplus heat to power conversion may change as the core process evolve, when the process has been adapted for CO_2 capture by implementation of flue gas recycling.

The organic Rankine cycle is an attractive heat-to-power conversion method in waste heat recovery, due to its relatively low temperature requirement, and to its high efficiency and mature technology. Natural working fluids such as hydrocarbons are attractive to consider for several reasons, such as environmentally safety, long-term predictability, performance, and cost.

606

Several approaches to heat recovery in aluminium electrolysis have been studied previously. Li et al. (2023) have performed a review on different types of waste generated by this process, including surplus heat. Barzi et al. (2018) have designed an ORC system recovering heat from the side walls of the cell, rather than the off-gas. Here, the temperature is higher, but the amount of heat is lower than in the off-gas (Li et al., 2023). Zhao et al. (2016) have performed a detailed exergy analysis of the aluminium production, mapping out the size of exergy losses throughout the process. The study highlights several potential targets for increasing the energy efficiency of aluminium production, not only in the electrolysis. However, the electrolysis process is the most energy intensive, and from this process the off-gas is the main sink for surplus heat.

Power generation from surplus heat in aluminium electrolysis smelters has been studied extensively (Ladam et al., 2016; Nosek et al., 2017). Yet, to the best of our knowledge, previous heat-to-power studies do not consider how core process improvements may affect the off-gas as a heat source. The potential changes in chemical and thermodynamical off-gas conditions have been studied, however, for the introduction of off-gas recycling. Senanu et al. (2022) have studied the amount of CO, HF and SO_2 in recycled aluminium off-gas. The off-gas composition is important to engineering, both for health, safety, and environment reasons, as well as for equipment wear. For example, SO_2 can form sulphuric acid which harms machinery. Therefore, Solheim (2022) has estimated the sulfuric acid dew point in aluminium off-gas. This imposes a lower threshold on the off-gas temperature, which is crucial for heat recovery applications.

Given this background, the scope of this current work is to estimate the potential energy savings from surplus heat-to-power in aluminium production with off-gas recycling. Heat source conditions are calculated from the off-gas properties identified by Solheim and Senanu (2020). Based on these heat

source conditions and component constraints, two different ORC layouts are optimized for maximum power production.

2 METHOD

The simulations performed in the scope of this work consist of two steps: First, the boundary conditions for the waste heat recovery (WHR) system are determined. This is done for all three cases representing potential future off-gas recycling scenarios. Then, an organic Rankine cycle is optimized for each case, considering selected cycle layout and working fluid options.

2.1 Determination of boundary conditions

The model of the recirculation loop consists of two main components: The aluminium electrolysis cell and the WHR heat exchanger. This heat exchanger is connected downstream of the cell, so that all the off-gas from the cell is fed through it. Then, most of the off-gas is routed in a loop back into the cell, while a small portion is sent out of the loop to the gas treatment center (GTC) for filtration.

In practice, fresh air is drawn passively into the cell due to underpressure. The flow rate is mainly determined by how air-tight the cell can be constructed. In our model, we assume that draft air is drawn into the cell at a rate that gives a fixed CO_2 concentration of 10 % in the off-gas, by volume. The baseline case has a CO_2 concentration of 1 %, as given by Solheim and Senanu (2020).

After heat recovery, a small portion of the extracted off-gas is diverted to gas treatment while the rest is reintroduced to the cell. The flow rate going to gas treatment corresponds to the flow rate of draft air, plus the gas that is generated from the electrolysis process. The concept is sketched in Figure 1.

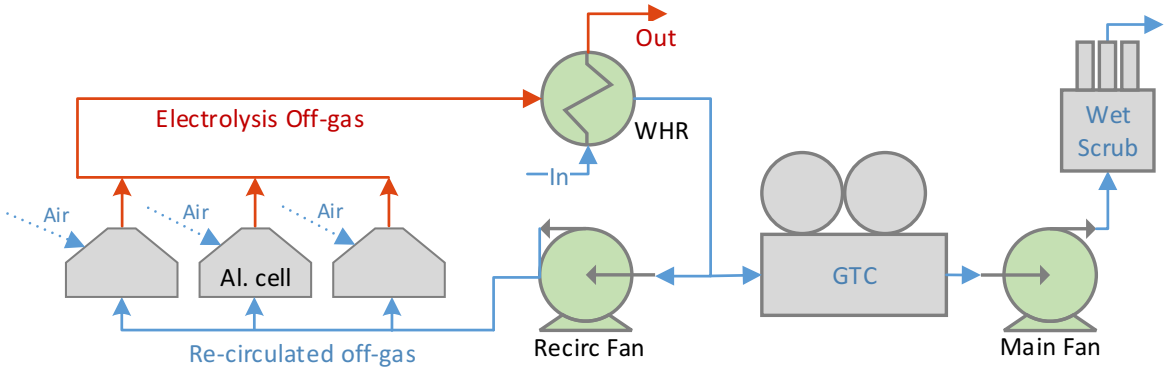

Figure 1: An illustration of the production cycle, including the off-gas recycling loop, the waste heat recovery heat exchanger and the gas treatment centre.

The case conditions are calculated based on a generic and simplified aluminium production gas system, representing a cluster of modern Hall-Héroult (Haupin and Frank, 1981) electrolysis cells, with conditions as described by Solheim and Senanu (2020). In the base case (no recirculation), the system uses 100 000 Nm^3/h draft air, and produces off-gas at 150 °C and a volumetric CO_2 content of 1 %. Other gaseous compounds produced in the cell are not considered. The baseline case is calculated for these conditions, and assuming the gas is cooled to 80 °C in the WHR before gas treatment. The case specifications that are used to compute the ORC boundary conditions are presented in Table 1.

In the cases with recirculation, the gas flowing into the cell is a mixture of the cooled off-gas at 80 °C and fresh draft air at 10 °C. The gases are assumed to be perfectly mixed, so that the temperature and composition are homogeneous inside the cell. The temperature of the off-gas going into the WHR heat exchanger is directly linked to the recirculation flow rate through the heat balance. This again determines the ratio between air and off-gas at the cell inlet. We assume further that the heat transferred to the off-gas from the cell is proportional to the temperature difference between the gas mixture in the

cell and the cell bath temperature. The cell bath is assumed to hold 975 °C. In the case definitions, we specify the off-gas temperature as it leaves the cell. From this, the total flow rate is then determined.

The total off-gas pressure loss from the cell to the stack (including GTC and wet scrubber), is assumed to be 5000 Pa, independent of flow rate. In other words, the pressure loss remains unchanged also in recycling cases with very reduced gas flow in this part of the system, and calculated fan work savings could therefore be considered conservative estimates. Note that the electrolysis cell produces aluminium and CO_2 at a constant rate. Hence, since the concentration of CO_2 is fixed at 10 %, the mass flow to the GTC must be the same in all recycled cases. Thus, the saved fan work at the GTC will be identical for these cases.

Table 1: Case specifications for the off-gas.

Case name	**Baseline** *150-80*	**Recirc 1** *150-80*	**Recirc 2** *200-80*	**Recirc 3** *250-80*	**Unit**
T_{in}	150.0	150.0	200.0	250.0	°C
T_{out}	80.0	80.0	80.0	80.0	°C
Total pressure drop	5.0	5.0	5.0	5.0	kPa
CO_2 content	1	10	10	10	%

2.2 Cycle optimization

Consider now the ORC cycle. A generic organic Rankine cycle is defined within a simulation and optimization framework for thermodynamic cycles, previously described by Skaugen et al. (2015). Here, the gradient-based optimization algorithm NLPQL (Schittkowski, 1986) is used to identify the optimal operating conditions for the ORC. The objective function of the optimizer is maximum net power, defined as the electrical power output of the turbine generator, when the pump and fan power demand are subtracted. Two cycle configurations are considered, one with an internal recuperator and one without. These are illustrated in Figure 2. Note that the evaporators in these cycles are same as the WHR heat exchanger from Figure 1.

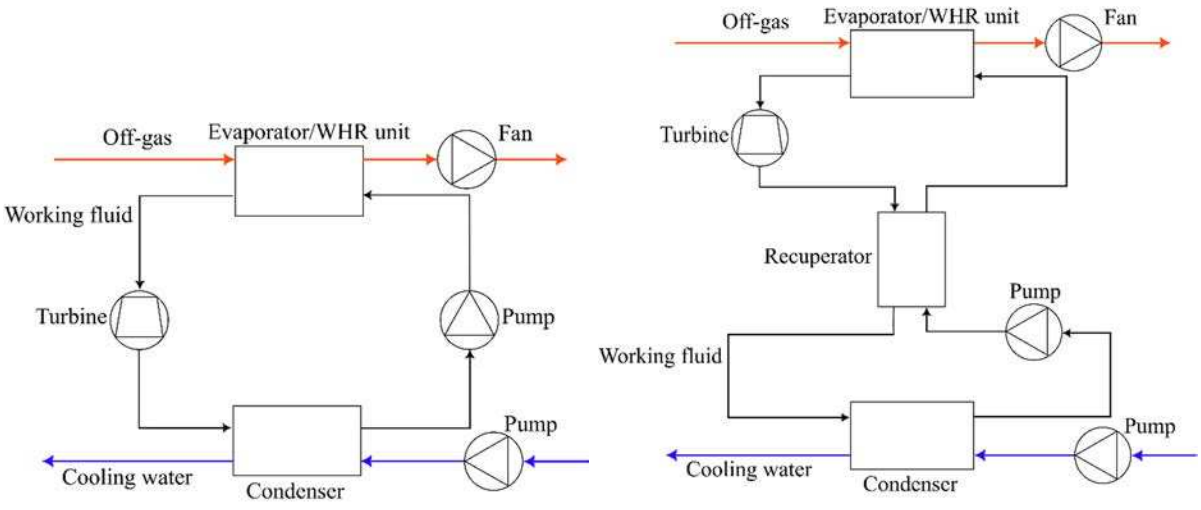

Figure 2: The modelled cycle configurations, with the simple cycle on the left and the recuperated cycle on the right.

The operating conditions of the cycle are defined by the flow rates of each fluid, as well as their pressure and temperature levels between each component. Each case definition fully specifies these for the off-gas. For the heat sink, constant temperatures and ambient inlet pressure is assumed. This leaves four degrees of freedom for the optimizer in the recuperated cycle, and three in the simple cycle. The

remaining variables follow from component specifications. Table 2 shows these variables for the heat exchangers, along with an overview of specified or calculated temperatures. In addition to these specifications, the pressure level at the expander inlet is limited to a maximum of 50 bar.

Table 2: Specifications for the heat exchangers in the model.

Specification	Evaporator	Recuperator	Condenser	Unit
Cold fluid pressure drop	100	50	100	kPa
Hot fluid pressure drop	1	7.5	1	kPa
Cold fluid inlet temperature	*calc*	*calc*	10	°C
Cold fluid outlet temperature	*calc*	*calc*	20	°C
Hot fluid inlet temperature	150-250	*calc*	*calc*	°C
Hot fluid outlet temperature	80	*calc*	*calc*	°C
Minimum temperature difference	20	10	5	K

The heat exchangers are modelled with a lower limit on the minimum temperature difference between its two fluids. This temperature difference is estimated by discretizing over the transferred heat, assuming a linear pressure drop distribution. Both pumps, as well as the off-gas fan and the expander are modelled assuming isentropic processes corrected by an isentropic efficiency, set to 0.85 for the expander and 0.75 for the rest. The power consumption or production of these components is calculated using a motor/generator efficiency of 0.95.

We assume constant pressure losses over the heat exchangers in the optimization model. This is less realistic than a detailed pressure drop model over each individual component but preferred to ignoring pressure drop entirely. The efficiency of working fluids with low operating pressures could be severely overestimated if pressure drop is fully neglected.

609

For the working fluid, several hydrocarbons are considered, based on working fluid screenings for ORCs with similar temperature conditions (Bahrami et al., 2022; Yu et al., 2016). Previous work by Andresen and Hagen (2022) suggests that natural and artificial working fluids perform equally well for waste heat-to-power applications. Therefore, and because the exploration of natural working fluids is a focus of the HighEFF research centre, only natural working fluids have been included. To further narrow down the list, fluid performance in Agromayor and Nord's (2017) study on a comparable but general heat source has been considered. In the end, five working fluids were used in the ORC simulation, spanning critical temperatures from 91.1 to 152.0 °C, as listed in Table 3. While exploring five working fluids is preferable to one, this work is not intended to be an exhaustive working fluid screening. The thermophysical library REFPROP (Lemmon et al., 2013) is used to obtain the properties of these fluids, as well as for the cooling water, and for each component of the off-gas.

Table 3: The working fluids included in this study, with their critical temperature, pressure, and condensation pressure at minimum cycle temperature (15 °C).

Fluid	T_{crit} [°C]	P_{crit} [bar]	P_{cond} [bar]
Propylene	91.1	45.6	10.17
Propane	96.7	42.5	8.36
Isobutane	134.7	36.3	3.02
Butene	146.1	40.1	2.55
Butane	152.0	38.0	2.08

3 RESULTS

The two parts of this work – determining boundary conditions for the off-gas loop and optimizing the ORC under these boundary conditions – are presented in turn in this section.

3.1 Gas flow and heat source calculations

As described in section 2, four aluminium production off-gas scenarios have been defined. One represents the current production processes, and three represent possible future processes with off-gas recycling implemented. In this section, we describe each of the cases, with the cycle boundary conditions computed from the work of Solheim and Senanu (2020).

The baseline case, corresponding to the current state of aluminium manufacturing, is defined with the conditions presented in section 2.1, with the off-gas cooled to 80 °C before the GTC. For the three future cases, a CO_2 concentration of 10 % is assumed, along with off-gas temperatures of 150 °C, 200 °C, and 250 °C. As described, the mass flows follow from these assumptions. Table 4 shows the specifications for each case, together with resulting off-gas flow rate, the recoverable heat, the exergy content in this heat, and the estimated reduction in fan work for the GTC. Recycling the off-gas significantly increases the amount of heat available for recovery, while higher off-gas temperatures increase the exergy content of this heat while reducing the flow rate.

Table 4: Specification of conditions for the heat recovery heat exchanger, including temperatures (T), mass flows, available heat (Q) and exergy (E) for capture, as well as the impact on system fan work compared to the baseline case.

Case name	**Baseline** *150-80*	**Recirc 1** *150-80*	**Recirc 2** *200-80*	**Recirc 3** *250-80*	**Unit**
Mass flow rate	35.76	65.47	36.97	25.23	kg/s
Q_{WHR}	2534.8	4591.6	4471.7	4350.1	kW
E_{WHR}	680.7	1233.0	1385.2	1502.8	kW
Relative E_{WHR}	0.269	0.269	0.31	0.345	-
Diff. fan work (GTC)	0	-202.8	-202.8	-202.8	kW

3.2 Cycle optimization

This section presents the result of the second part of the study, namely the ORC optimization. Using the ORC model with input from the case specifications above, the cases and the working fluids have been compared. This section presents the performance of the ORC, for each case and working fluid.

Figure 3 shows the net power performance of the ORC for each case and fluid. The performance is the electrical power output of the turbine generator, subtracted the power consumption of working fluid and cooling water pumps and recirculation fan, as illustrated in Figure 2. Similarly, Figure 4 below shows the thermal efficiency of the cycles for each working fluid and case, taken as the net power production of the ORC cycle divided by the available recoverable heat in the off-gas in each case.

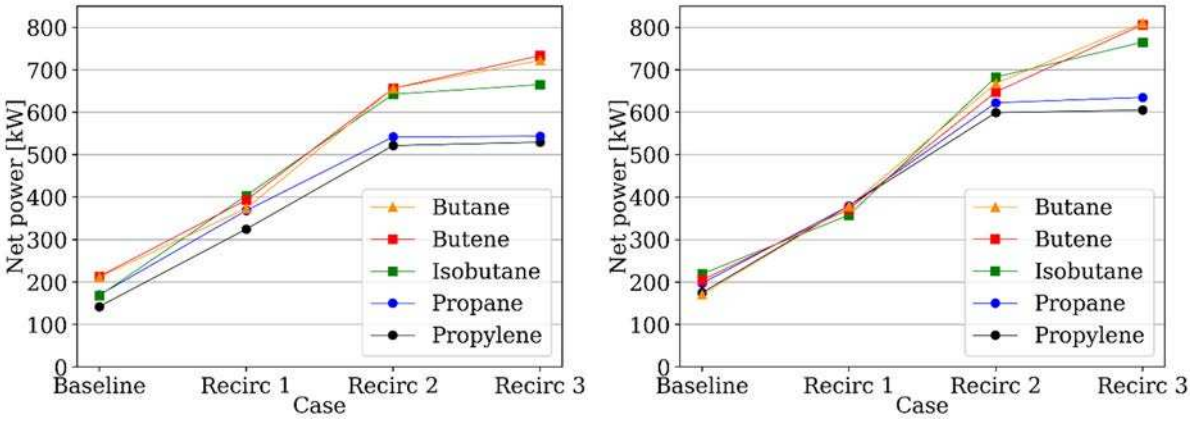

Figure 3: The net power produced by the WHR unit, for each of the four cases. The left figure shows the simple cycle, and the rightmost figure shows the recuperated cycle.

The cycle simulations indicate a significant increase in potential power output of an ORC with off-gas recycling implemented. This is as expected, as both the temperature and available energy in the off-gas is shown to increase. The simulations of the high-temperature off-gas recycling cases can reach more than three times the net power output of the baseline case.

Working fluid choice has significant impact, but mainly in the highest temperature cases. In the recirc 3 case, the maximum turbine pressure of 50 bar limits the power output for all fluids. This occurs for propane and propylene also in the recirc 2 case, which is why there is little change between the two cases for these. In the lower temperature cases, the differences are smaller – especially in the recuperated cycle. Recuperated cycles generally perform better for the explored fluids, with the exception of case Recirc 1. Here, the non-recuperated cycle with Isobutane performs slightly better. This is likely due to a very small benefit from recuperation at the lowest heat source temperature being overcome by the negative effect of additional pressure drops reducing turbine power. For a practical implementation of waste heat-to-power with an ORC in any of these cases, a full working fluid screening would be required.

611

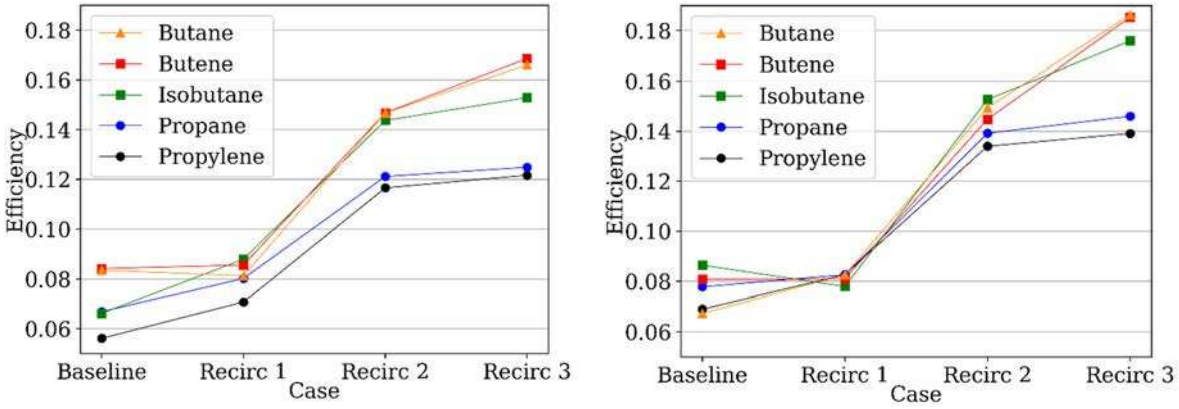

Figure 4: Thermal efficiency of the WHR unit, for each of the four cases. The left figure shows the simple cycle, and the rightmost figure shows the recuperated cycle.

Due to the severely reduced downstream (GTC) flow rates, as well as a high baseline pressure drop, the additional benefit of reduced fan work is considerable compared to the ORC net power. Note that this improvement comes in addition to the indicated threefold increase in power output potential from the

present-day case to the recycling cases. This effect is independent of heat-to-power production but is another significant energy efficiency benefit of this concept.

Table 5 compares the best performing cycle ORC for each case. System power savings are included, taken as the net power production of the ORC with the difference in fan work in the GTC from Table 4 included. Each result uses the working fluid and layout with the highest net power output for each case. There are two main contributors to the increased power potential: The increased amount of recoverable heat caused by the off-gas recirculation, and the increased thermal efficiency when the off-gas temperature (and exergy content) increases.

Solheim and Senanu (2020) have also indicated an energy consumption for the electrolysis cell. Using these numbers, we can compare the ORC power output with the overall "plant" consumption. At 400 kA, and 4.05 V per 10 000 Nm^3/h draught air, the production system in this study consumes 16 200 kW electric energy for the electrolysis. The ORC recovers 6.3 % of this consumed energy in the best case, compared to 1.4 % in the baseline case, which is significant considering the huge scale of energy consumption required for aluminium production.

The respective impact of these contributions can be seen in the bottom part of Table 5, where their values relative to the base case are shown. It can be observed that the relative net power is a product of the relative values of recoverable heat and ORC thermal efficiency. Therefore, these values indicate the relative contribution of difference in heat quantity (Q_{WHR}) and heat quality (resulting in higher cycle thermal efficiency) to the relative net power for the different cases.

Table 5: Breakdown of cycle performance for each case.

	Base	**Recirc 1**	**Recirc 2**	**Recirc 3**	**Unit**
Best performing cycle option	Isobutane Recuperated	Isobutane Simple	Isobutane Recuperated	Butane Recuperated	-
Gross power output	297.8	540.7	862.9	961.7	kW
Recirculation fan work	-50.4[1]	-88.2	-49.8	-34.0	kW
Working fluid pump work	-21.0	-35.3	-118.4	-106.0	kW
Cooling water pump work	-7.4	-13.3	-12.1	-11.3	kW
Net power output	219.0	403.9	682.6	810.4	kW
Recoverable heat (Q_{WHR})	2534.8	4591.6	4471.7	4350.1	kW
ORC thermal efficiency	0.086	0.088	0.153	0.186	-
Reduction in main fan work	0	202.8	202.8	202.8	kW
System power savings	219	606.7	885.4	1013.2	kW
System power savings relative to electrolysis process	1.4	3.7	5.5	6.3	%
Relative to base case					
Net power	1	1.84	3.12	3.70	-
Recoverable heat (Q_{WHR})	1	1.81	1.76	1.72	-
ORC thermal efficiency	1	1.02	1.77	2.16	-
System power savings	1	2.77	4.04	4.63	-

[1] For the base case, this value indicates additional *main* fan work incurred by pressure drop in the WHR

4 CONCLUSIONS

Building on previous work on off-gas recycling in aluminium production cells, boundary conditions for a heat-to-power system using the off-gas as a heat source have been defined. Then, an organic Rankine cycle has been optimized for these boundary conditions. A total of four cases were explored – one baseline case corresponding to the current standard aluminium production processes, and three cases with flue gas recycling. An ORC with and without a recuperator has been optimized for each case, and five different working fluids have been explored.

The results show a very significant increase in potential power output for off-gas recycling cases. For the cases with highest recirculation rates and heat source temperatures, the calculated power output increases more than threefold. Additionally, with off-gas recycling, power is saved due to a lower off-gas flow rate to gas treatment, and thus a reduced need for fan work. This reduction in main extraction fan work was equivalent to 25–50 % of the ORC net power, in other words a significant contribution to the overall system benefit. This strongly indicates that future aluminium production processes could have conditions that enable high-performance and competitive ORC integrations, even though heat-to-power is not the main motivation for implementing off-gas recycling in such processes.

This study leaves some possible paths for future work. An extension of this study to other processes where flue gas recycling is considered could provide further insight into the future of heat-to-power as a method of increasing energy efficiency – both in Norwegian and international metallurgical industry. Also, this work highlights that further research and industrial endeavours to implement off-gas recycling in aluminium production is useful also in terms of energy efficiency. Techno-economical assessments may also help refine optimal boundary conditions and system specifications.

REFERENCES

Agromayor, R., Nord, L.O., 2017, Fluid selection and thermodynamic optimization of organic Rankine cycles for waste heat recovery applications, *Energy Procedia* 129, 527–534.

Andresen, T., Hagen, B.A., 2022, Natural working fluids in cycles for surplus heat-to-power conversion – Perspectives and history from Trondheim. [WWW Document], *15th IIR-Gustav Lorentzen Conference on Natural Refrigerants (GL2022). Proceedings. Trondheim, Norway, June 13-15th 2022.* URL https://iifiir.org/fr/fridoc/fluides-actifs-naturels-dans-les-cycles-de-conversion-de-la-chaleur-145452 (accessed 4.15.23).

Bahrami, M., Pourfayaz, F., Kasaeian, A., 2022, Low global warming potential (GWP) working fluids (WFs) for Organic Rankine Cycle (ORC) applications, *Energy Reports* 8, 2976–2988.

Barzi, Y.M., Assadi, M., Parham, K., 2018, A waste heat recovery system development and analysis using ORC for the energy efficiency improvement in aluminium electrolysis cells, *International Journal of Energy Research* 42, 1511–1523.

Haupin, W.E., Frank, W.B., 1981, Electrometallurgy of Aluminum, *Bockris, J.O., Conway, B.E., Yeager, E., White, R.E. (Eds.), Comprehensive Treatise of Electrochemistry: Electrochemical Processing, Comprehensive Treatise of Electrochemistry*. Springer US, Boston, MA, pp. 301–325.

Ladam, Y., Solheim, A., Segatz, M., Lorentsen, O.-A., 2016, Heat Recovery from Aluminium Reduction Cells, *Lindsay, S.J. (Ed.), Light Metals 2011*. Springer International Publishing, Cham, pp. 393–398.

Lemmon, E.W., Huber, M.L., McLinden, M.O., 2013, NIST Standard Reference Database 23: Reference Fluid Thermodynamic and Transport Properties-REFPROP, Version 9.1, *National Institute of Standards and Technology, Gaithersburg, MD*.

Li, X., Liu, Y., Zhang, T., 2023, A comprehensive review of aluminium electrolysis and the waste generated by it, *Waste Manag Res* 0734242X231164321.

Nosek, R., Gavlas, S., Lenhard, R., Malcho, M., Sedlak, V., Teie, S., 2017, Utilization of waste heat from aluminium electrolytic cell, *AIP Conference Proceedings* 1917, 030001.

Schittkowski, K., 1986, NLPQL: A fortran subroutine solving constrained nonlinear programming problems, *Ann Oper Res* 5, 485–500.

Senanu, S., Solheim, A., Lødeng, R., 2022, Gas Recycling and Energy Recovery. Future Handling of Flue Gas from Aluminium Electrolysis Cells, *Eskin, D. (Ed.), Light Metals 2022, The Minerals, Metals & Materials Series*. Springer International Publishing, Cham, pp. 1004–1010.

Skaugen, G., Hammer, M., Wahl, P.E., Wilhelmsen, Ø., 2015, Constrained non-linear optimisation of a process for liquefaction of natural gas including a geometrical and thermo-hydraulic model of a compact heat exchanger, *Computers & Chemical Engineering* 73, 102–115.

Solheim, A., 2022, An Attempt to Estimate the Sulfuric Acid Dew Point in the Flue Gas from Aluminium Electrolysis Cells, *Eskin, D. (Ed.), Light Metals 2022, The Minerals, Metals & Materials Series*. Springer International Publishing, Cham, pp. 520–527.

Solheim, A., Senanu, S., 2020, Recycling of the Flue Gas from Aluminium Electrolysis Cells, *Tomsett, A. (Ed.), Light Metals 2020, The Minerals, Metals & Materials Series*. Springer International Publishing, Cham, pp. 803–810.

Wedde, G., 2011, A method of ventilating an aluminium production electrolytic cell, . WO2011089497A1.

Yu, H., Feng, X., Wang, Y., 2016, Working Fluid Selection for Organic Rankine Cycle (ORC) Considering the Characteristics of Waste Heat Sources, *Ind. Eng. Chem. Res.* 55, 1309–1321.

Zhao, R., Nowicki, C., Gosselin, L., Duchesne, C., 2016, Energy and exergy inventory in aluminum smelter from a thermal integration point-of-view, *International Journal of Energy Research* 40, 1321–1338.

ACKNOWLEDGEMENT

This work has been funded by the HighEFF – "Centre for an Energy Efficient and Competitive Industry for the Future", an 8-years' Research Centre under the FME-scheme (Centre for Environment-friendly Energy Research, Grant no. 257632). The authors gratefully acknowledge the financial support from the Research Council of Norway and user partners of HighEFF.

614

ORC SEVILLE 2023
7th International Seminar on O.R.C. Power Systems

© 2024 Editorial Universidad de Sevilla. Este es un artículo de acceso abierto distribuido bajo los términos de la licencia de uso y distribución Creative Commons (BY-NC-ND 4.0)

DOI: https://dx.doi.org/10.12795/9788447227457_104

Investigating the application range of ORC power plants for the exploitation of two-phase geothermal resources

Tristan Merbecks[1,2,*], Claudio Pietra[3], Paola Bombarda[1], Martin O. Saar[3], Paolo Silva[1], Dario Alfani[1]

[1] *Politecnico di Milano, Dipartimento di Energia, Via Lambruschini 4, 20157 Milano, Italy*
[2] *ETH Zurich, Department of Earth Sciences Soneggstrasse 5, 8092 Zurich, Switzerland*
[3] *Turboden s.P.a, Via Cernaia 10, 25124, Brescia, Italy*

*Corresponding Author: tristanleonard.merbecks@polimi.it or tmerbecks@ethz.ch

ABSTRACT

The design of a geothermal power plant exploiting a two-phase geothermal resource is a demanding task, due to the fact that different technologies and plant configurations must be considered, as well as the lack of flexible and reliable models for computing the thermophysical properties of geofluids, whose composition and chemistry is highly site-specific.

This study presents a novel thermophysical property modelling framework aimed at modelling any arbitrary single- or two-phase geothermal brine. Recognising the potential synergy of two historically separate fields of research, fluid partition and property modelling, existing partitioning simulators, like Reaktoro, are coupled with high-accuracy thermophysical fluid property computation engines, like CoolProp and ThermoFun. The resultant Python-based framework, GeoProp, is validated against a range of primary and secondary data and will be made available to the public.
Considering a two-phase geothermal resource, the design of direct steam cycles with flash as well as binary geothermal power plants is investigated from a thermodynamic perspective. A parametric study on geofluid composition, i.e. mineral and non-condensable gases (NCG) content, and inlet conditions, i.e. temperature and steam quality, is used to compare the performance and define the application envelope of these two technologies.

1 INTRODUCTION

Geothermal energy is proving to be an attractive and versatile option for grid-scale renewable and dispatchable electricity and heat. Direct steam cycles with flash currently represent the majority of geothermal electricity generation capacity, however binary organic Rankine cycles (ORCs) have allowed the industry to exploit lower enthalpy and otherwise uneconomical geothermal resources.

Binary ORCs have several operational advantages over direct steam cycles (e.g. smaller, cheaper and more durable turbines, closed loop), and in this respect, extending their application envelope is not only of commercial interest but also has the potential to accelerate the adoption of geothermal energy utilization.

While the design, optimisation and operation of ORCs is well understood, the phase behaviour and thermophysical properties of the geothermal fluids represent a key uncertainty for their design, and in particular of the primary heat exchanger, with open-source tools like CoolProp, Reaktoro and ThermoFun only partially providing the required properties. Moreover, the surface handling/reinjection of non-condensable gas (NCG), primarily composed of CO_2, needs to be factored into the techno-economic comparison of direct steam cycles and binary ORCs.

1.1 Objectives

It is in this context that this study aims to:

- present a novel thermophysical property modelling framework for geothermal brines of arbitrary composition, covering a wide range of specific enthalpies and pressures of interest for geothermal applications as well as allowing for the coexistence of aqueous, gaseous, liquid and mineral phases.
- refine the application range of direct steam cycles with flash and binary ORC geothermal power plants for two-phase sources, which are currently predominantly exploited via direct steam cycles.

2 THERMOPHYSICAL PROPERTY MODELLING

A geothermal brine can be regarded as a chemically active system. The constituent species may partition into different phases (e.g. vapour, aqueous, or solid), with some species co-existing in multiple phases (e.g. H_2O[aq] and H_2O[g]), dissociating as they transition into a different phase (e.g. NaCl[s] into Na^+[aq] and Cl^-[aq]), or reacting with each other (e.g. CO_3^{2-}[aq] and H^+[aq] react to HCO_3^-[aq]).

2.1 Theoretical Background

For a system of chemical species (e.g. H_2O[l], Na^+[aq], Cl^-[aq], CO_2[g]), the stable equilibrium state at a pressure, P, and a temperature, T, is the one of minimum Gibbs free energy (e.g. Gyftopoulos & Beretta, 2005). The Gibbs free energy for a given state can be calculated via (1), where G is the Gibbs free energy, $\boldsymbol{n}$ is the vector of species amounts, N is the number of species, n_i is the amount of species i, μ_i is the chemical potential of species i and $\boldsymbol{y}$ is the vector of species mole fractions.

$$G(P,T,\boldsymbol{n}) = \sum_{i}^{N} n_i \mu_i(P,T,\boldsymbol{y}) \tag{1}$$

For a mixture, the chemical potential for each species can be calculated from the species' pure component chemical potential and correcting for interactions with the other species in the system, see (2), where R is the universal gas constant, a_i is the activity of species i and $P°$ and $\boldsymbol{y}°$ refer to the reference pressure and composition, respectively. Conveniently, the partial molar properties of interest, enthalpy, entropy and volume (or density) can be calculated from the chemical potential, see (3) to (5) (Gyftopoulos & Beretta, 2005).

$$\mu_i(P,T,\boldsymbol{y}) = \mu_i^{\circ}\left(T,P^{\circ},\boldsymbol{y}^{\circ}\right) + RT\ln a_i(T,P,\boldsymbol{y}) \tag{2}$$

$$h_i(T,P,\boldsymbol{y}) = \frac{d(\mu_i(T,P,\boldsymbol{y})/T)}{d(1/T)}_{P,\boldsymbol{y}} \tag{3}$$

$$s_i(T,P,\boldsymbol{y}) = -\frac{d(\mu_i(T,P,\boldsymbol{y}))}{d(T)}_{P,\boldsymbol{y}} \tag{4}$$

$$v_i(T,P,\boldsymbol{y}) = \frac{d(\mu_i(T,P,\boldsymbol{y}))}{d(P)}_{T,\boldsymbol{y}} \tag{5}$$

2.2 Existing Models

Although the partitioning and property modelling should be in principle the two faces of the same coin, in practice they are treated as two different disciplines in the academic literature and open-source computing frameworks.

For example, partition models (e.g. (Duan & Sun, 2003; Spycher et al., 2003; Spycher & Pruess, 2010) generally focus on the partition of brines and CO_2 mixtures, but do not include thermophysical properties. This is understandable since these models are primarily developed in the context of carbon capture and storage, where the key question is whether the injected CO_2 will dissolve into the brine at

in-situ conditions. Similarly, the open-source library CoolProp (Bell et al., 2014) implements a number of equations of state (EOS), which can be used for evaluating the thermophysical properties of pure fluids (e.g. water, carbon dioxide and many hydrocarbons and refrigerants), mixtures of pure fluids and some pseudo-pure/binary fluids (e.g. MITSW for seawater (Sharqawy et al., 2010) or LiBr for lithium bromide (Pátek & Klomfar, 2006) etc.). However, more complex fluids, such as mixtures of pure and pseudo-pure fluids (e.g. seawater with CO_2) or mixtures of pseudo-pure fluids (e.g. seawater and lithium bromide), can currently not be captured.

Reaktoro (Leal, 2015), a unified open-source framework for modelling chemically active systems, pairs many open-source thermodynamic databases, like SUPCRT98 or SUPCRTBL, and activity models with powerful and scalable optimisation algorithms. Although the thermophysical property predictions are generally accurate for aqueous systems, they lack accuracy for vapour-liquid systems, see Figure 1 and Figure 2. The observed deviations can be attributed to the underlying databases prescribing non-standard EOS to be used for important vapour species like H_2O[g] and CO_2[g].

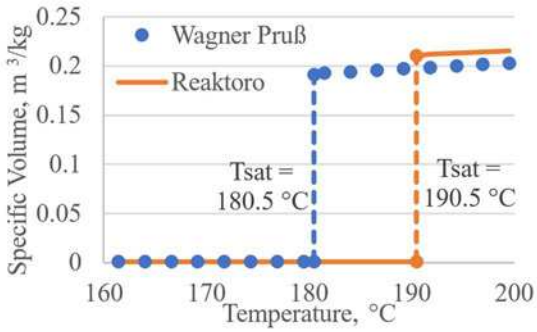

Figure 1: The specific volume of a system consisting of H_2O[aq] and H_2O[g] at a pressure of 10 bar as a function of temperature. The dashed lines indicate the saturation temperatures.

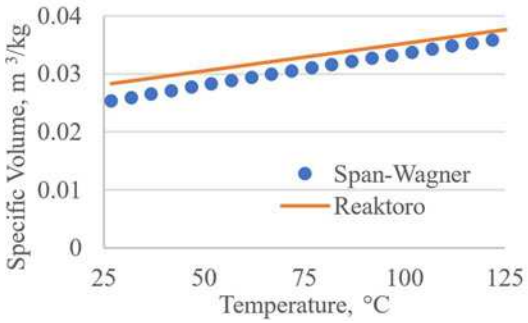

Figure 2: The specific volume of a chemically active system consisting of CO_2[aq] at a pressure of 20 bar as a function of temperature.

3 GeoProp

Leveraging the strengths of the aforementioned tools, a modularised approach was chosen, see Figure 3, – the resultant model, GeoProp, can model geofluids with arbitrary composition over a wide range of conditions.

After defining the main geofluid constituents, the selected partition model, by default Reaktoro, equilibrates the fluid at the specified temperature and pressure. GeoProp then sorts the equilibrium species into the corresponding phases (i.e. aqueous, gaseous and mineral) and passes them to CoolProp and ThermoFun (Miron et al., 2021), whichever is more appropriate, for estimating the thermophysical properties. GeoProp then aggregates the thermophysical properties of the individual phases using a simple mass-based mixing rule. GeoProp is implemented in Python and will available to the public.

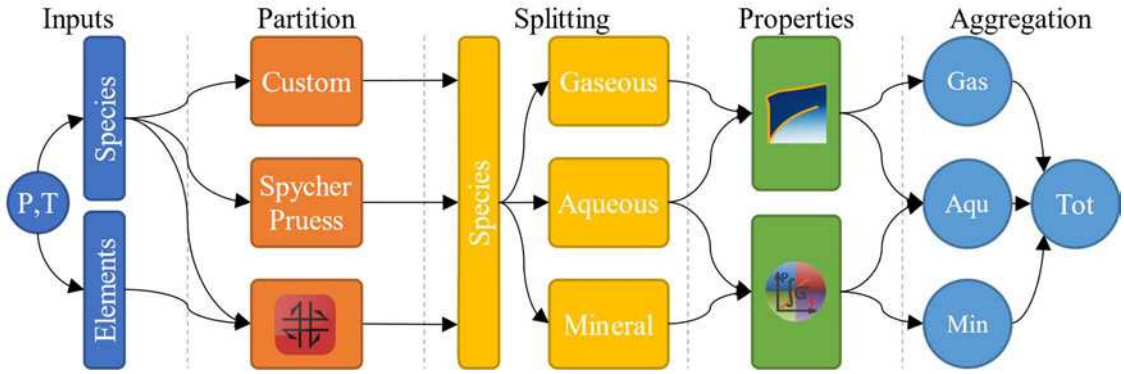

Figure 3: The architecture of the thermophysical property model for brines and NCG.

GeoProp was validated using the MITSW and LiBr models, for seawater and lithium bromide solution, respectively, implemented in CoolProp, as well as published data for three fluids from a geothermal field near Makhackala, Russia, (Abdulagatov et al., 2016). The fluids were recreated in GeoProp, partitioned, to determine the equilibrium compositions, and the thermophysical properties evaluated. GeoProp reproduced the density of the different fluids to within 3 %, slightly outperforming the prediction by Aspen Plus V11's ELECNRTL model, see Figure 4. All models predicted the specific enthalpy to within 1 %, see Figure 5.

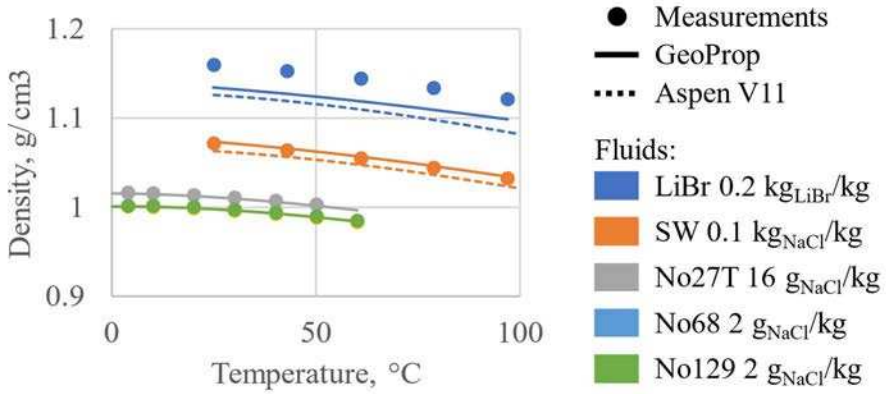

Figure 4: The density of various brines as a function of temperature at 1 bar pressure. Dots represent "measured" data and lines represent property models.

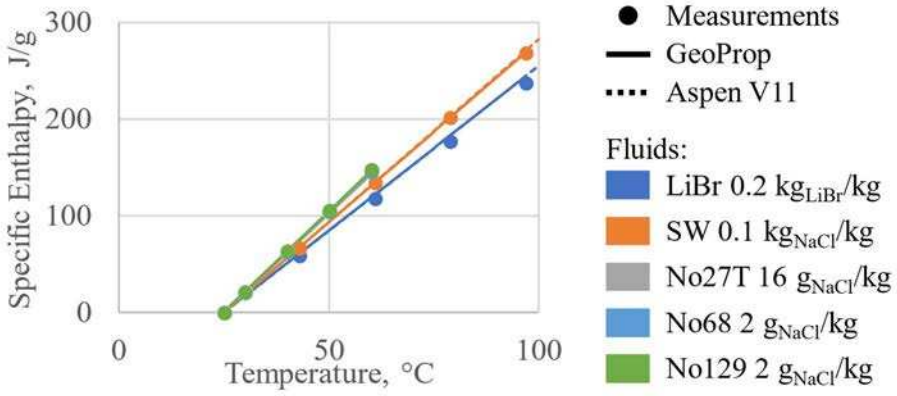

Figure 5: The specific enthalpy of various brines as a function of temperature at 1 bar pressure. The reference temperature is 25 °C. Dots represent "measured" data and lines represent property models.

4 TECHNOLOGY MAP

4.1 Geothermal Sources

Primarily two-phase geothermal sources were considered, with wellhead temperatures ranging between 100 °C and 200 °C and steam quality, defined in (6), ranging between 0 to 0.5. Heat losses between the wellhead and the plant inlet were assumed to be insignificant and therefore neglected. The brine salinities, defined in (7) as NaCl, and NCG content, defined in (8) as CO_2, range between 0 to 0.3 kg_{NaCl}/kg_{H2O} and 0 to 0.03 kg_{CO2}/kg_{H2O} respectively.

$$x = \frac{\dot{m}^V_{H_2O}}{\dot{m}^L_{H_2O} + \dot{m}^V_{H_2O}} \tag{6}$$

$$sal = \frac{\dot{m}_{Salts}}{\dot{m}^L_{H_2O} + \dot{m}^V_{H_2O}} \tag{7}$$

$$NCG = \frac{\dot{m}_{NCG}}{\dot{m}^L_{H_2O} + \dot{m}^V_{H_2O}} \tag{8}$$

While a unit geofluid mass rate could be considered for the power plant simulations, this has the undesirable effect of artificially reducing the power plants' performance as the effective inlet heat rate is lower due to the lower specific heat capacities of salinity and NCG compared to water. Instead, a unit combined mass rate of liquid water and steam is assumed for all cases to which the mass rates of salinity and NCG are added, see (9).

$$\dot{m} = \dot{m}^L_{H_2O} + \dot{m}^V_{H_2O} + \dot{m}_{Salts} + \dot{m}_{NCG} \qquad \text{where, } \dot{m}^L_{H_2O} + \dot{m}^V_{H_2O} = 1 \text{ kg/s} \tag{9}$$

619

4.2 Power Plant Configurations

Two power plant configurations are considered, 1) a direct single flash steam cycle and 2) a binary ORC. In a direct steam cycle only the vapour portion of the geofluid is utilised and subsequently expanded in a turbine, see Figure 6. On the other hand, in a binary ORC the geofluid merely serves as a heat source to vaporise a secondary fluid, which is then expanded in a turbine similarly to the direct steam cycle, see Figure 7. This allows exploiting the heat contained within both the vapour as well as the liquid phase.

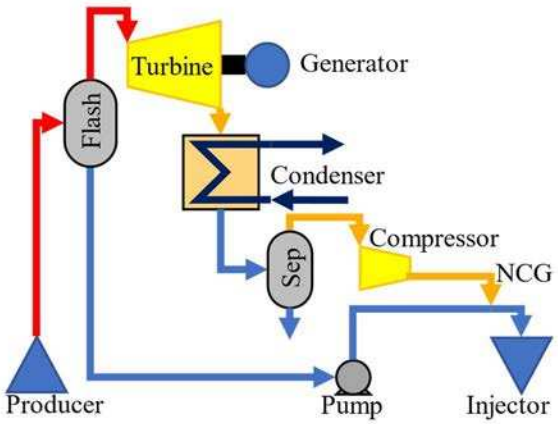

Figure 6: Direct steam cycle geothermal power plant.

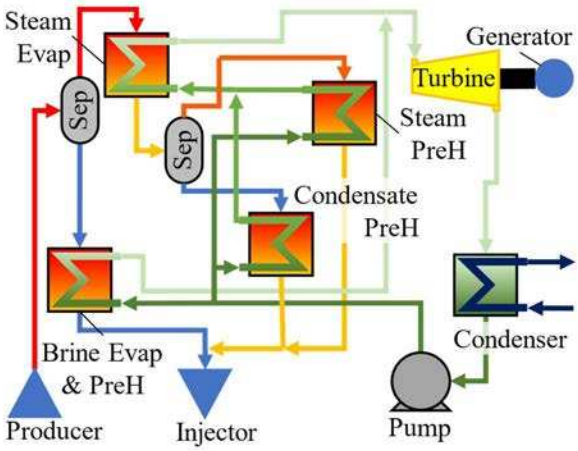

Figure 7: Binary ORC geothermal power plant.

Both power plants are subject to the same boundary conditions:

- Geofluid composition, inlet temperature, pressure and steam quality
- Heat is rejected into the surrounding environment at a temperature of 25 °C
- Geofluid enters and exits the power plant at the same pressure – this is to penalise for NCG handling to ensure that it is not released into the atmosphere but instead reinjected into the formation.
- Geofluid re-injection temperature is not constraint, as scaling is assumed to be negligible.

The specific net power output from the power plant, defined in (10), will be used to judge which performs better for a set of boundary condition.

$$\dot{w}_{net} = \frac{\dot{W}_{turbine} - \dot{W}_{pump} - \dot{W}_{repressurisation}}{\dot{m}^{L}_{H_2O} + \dot{m}^{V}_{H_2O}} \tag{10}$$

4.3 Model Description

For the direct steam cycle:

- The net power is optimised by adjusting the flash temperature/pressure, increasing the vapour mass rate while sacrificing specific enthalpy drop across the turbine; the pressure of the liquid fraction is consequently also decreased by the flash process.
- The stream exiting the turbine is then cooled to 30 °C and then separated into a liquid stream and a NCG stream. All outlet streams, i.e. the liquid stream from the flash chamber, the condensate stream and the NCG stream, must then be repressurised to the inlet pressure so that they can be reinjected into the reservoir.
- Given the bell-shaped vapour dome of water in the T-s (temperature-specific entropy) diagram, the turbine efficiency is corrected for liquid drop out using the empirical Baumann Rule, see (11), where $\eta^{wet}_{turbine}$ is the turbine wet efficiency, $\eta^{dry}_{turbine}$ is the turbine dry efficiency, assumed to be 85 % (DiPippo, 2016), and x_{in} and x_{out} are the mole-based vapour fraction at the turbine inlet and outlet respectively.

$$\eta^{wet}_{turbine} = \eta^{dry}_{turbine} \frac{(x_{in} + x_{out})}{2} \tag{11}$$

For the binary ORC:

- The incoming geofluid is split into a liquid and vapour stream with each stream being used to pre-heat and evaporate the cycle working fluid. The vapour stream is further split into a vapour and condensate following the vapour powered evaporator.
- The net power is optimised by adjusting evaporation and condensation temperature/pressure and the working fluid mass flow rates, while ensuring that the minimum approach temperatures do not fall below 5 °C in liquid dominated and 10 °C in vapour dominated heat exchangers. Moreover, the vapour quality at the vapour evaporator outlet should be above 0.75.
- Iso-butane, n-butane, iso-pentane, n-pentane and cyclopentane were considered as ORC working fluids.
- The simulations were run in Aspen Plus V11.

4.4 Case 1: Pure Water

To establish a base case, the two power plants were simulated in Aspen Plus V11 for a geofluid modelled as pure water for inlet temperatures and steam quality ranging between 100 °C to 200 °C and 0 to 0.5 respectively. The results are shown in Figure 8, Figure 9 and Figure 10. The key observations are:

- The investigated ORC configurations thermodynamically outperform the direct steam cycles at any temperature for saturated liquid sources. For inlet temperatures above 150 °C, the ORC configurations begin to outperform the direct steam cycles at increasingly higher steam quality.

- All ORC working fluids perform similarly poorly at lower temperatures (up to 150 °C), which can likely be attributed to the critical temperatures of the selected working fluids being too high. Isobutane and n-butane appear the most favourable working fluids for the conditions studied.
- Cross-over of isobutane and n-butane in Figure 9 can be attributed to the vapour heated branch becoming vapour fraction constraint (i.e. the vapour quality in the vapour evaporator outlet reaches the limit of 0.75), limiting the amount of working fluid that can be evaporated.

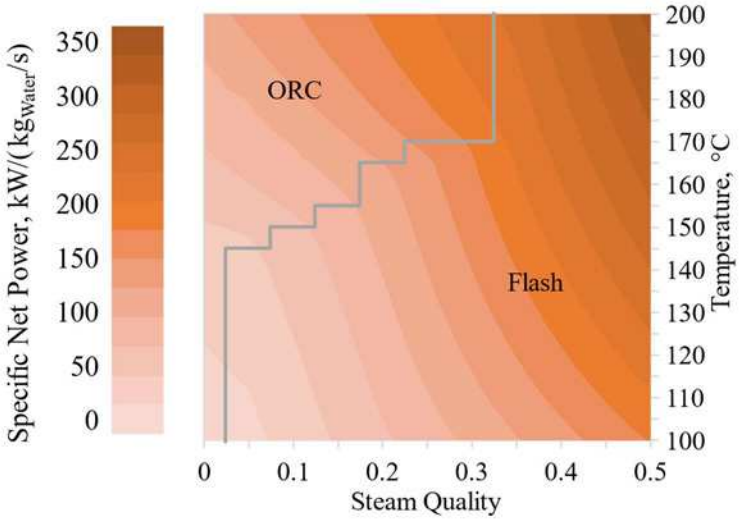

Figure 8: Maximum specific net power from a geofluid of pure water as a function of inlet temperature and steam quality. The grey line indicates the performance boundary between binary ORC and direct steam cycles.

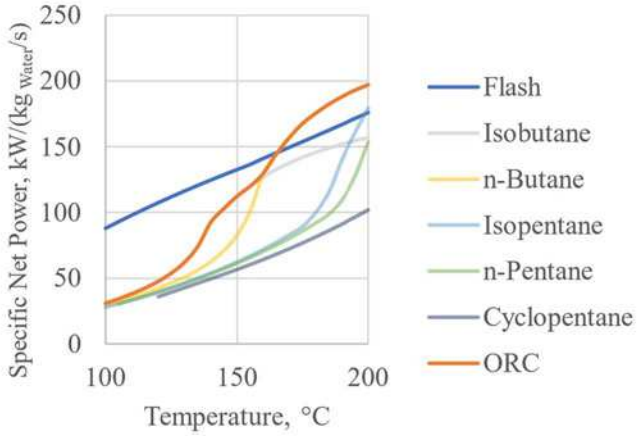

Figure 9 Specific net power from a geofluid of pure water as a function of inlet temperature and a steam quality of 0.25 for a direct steam cycle and binary ORC plant using various working fluids.

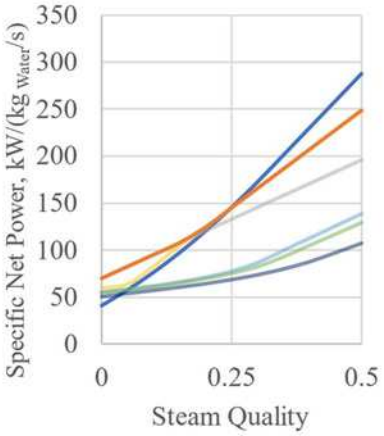

Figure 10 Specific net power from a geofluid of pure water as a function of steam quality and an inlet temperature 165°C for a direct steam cycle and binary ORC plant using various working fluids.

4.5 Salinity and NCG

In reality geofluids are not only comprised of pure water, but may also carry dissolved minerals and NCG. The presence of such impurities alters the geofluid's phase behaviour and thermophysical properties compared to pure water, the magnitude of deviations being strongly related to the effective salinity, see (12), and effective NCG content, see (13), and has implications for the performance of direct steam and binary ORC power plants.

$$sal_{eff} = \dot{m}_{NaCl} \Big/ \dot{m}^{L}_{H_2O} \quad (12)$$

$$NCG_{eff} = \dot{m}_{NCG} \Big/ \dot{m}^{V}_{H_2O} \quad (13)$$

Perhaps most consequential is their effect on the geofluid saturation pressure. Considering a geofluid comprised of H_2O[aq], Na^+[aq], Cl^-[aq] and H_2O[g], the presence of the Na^+[aq], Cl^-[aq] causes a reduction in chemical potential of the H_2O[aq], meaning that mixture prefers to be in the liquid state and thus the saturation pressure is reduced, see Figure 11. Similarly, for a geofluid comprised of H_2O[aq], H_2O[g] and CO_2[g], the fluid prefers to be in the gaseous state and hence the saturation pressure increases.

The change in saturation pressure is particularly important for direct steam cycles, as, for example in the case of high salinity, impedes the ability to optimise flash temperature/pressure and reduces net power. Specifically, a geofluid with an effective salinity of 0.3 kg_{NaCl}/kg_{H2O}, the saturation pressure is reduced from 10 bar to 8 bar.

Salinity and NCG also affect the geofluid's thermophysical properties, such as the specific enthalpy or specific heat capacity. Changes can primarily be attributed to both salts and NCG having far lower heat capacity than pure water and to a smaller extent to the reduction in species chemical potential, although this is more significant for higher concentrations of salts and NCG. That being said, the heat flow is relatively unchanged compared to pure water, see Figure 12. This suggests that, assuming the total mass rate scales with the mass rate of impurities, the performance of the binary ORC is only weakly affected.

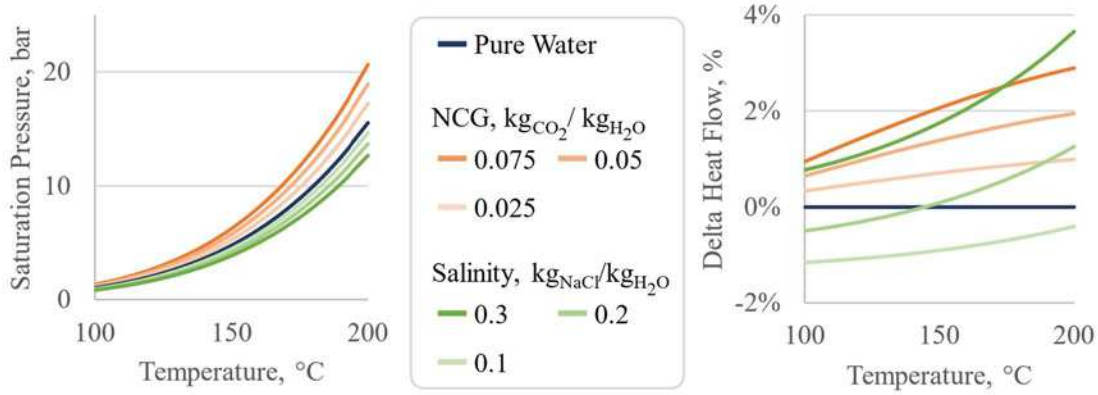

Figure 11: Geofluid saturation pressure as a function of temperature for a range of effective salinity and NCG content.

Figure 12: Deviation of liquid and vapour heat flow from pure water/steam for a range of effective salinity and NCG content, at a steam quality of 0.1, as a function of temperature. The reference conditions are 25 °C and 1 bar.

4.6 Case 2: Salinity and NCG

To investigate the effect of impurities, the two power plants were simulated in Aspen Plus V11 for an inlet temperature of 150 °C and steam quality of 0.1 for geofluid with salinity and NCG content ranging between 0 to 0.2 kg_{NaCl}/kg_{H2O} and 0 to 0.03 kg_{CO2}/kg_{H2O} respectively, see Figure 13 and Figure 14. The key observations were:

- Salinity does not significantly affect the performance of direct steam cycles or ORCs.
- NCG content primarily impacts the performance of direct steam cycles due to the additional compression requirements to reinject the NCG.
- ORCs begin to thermodynamically outperform direct steam cycles at about 0.015 kg_{CO2}/kg_{H2O} for any salinity studied.

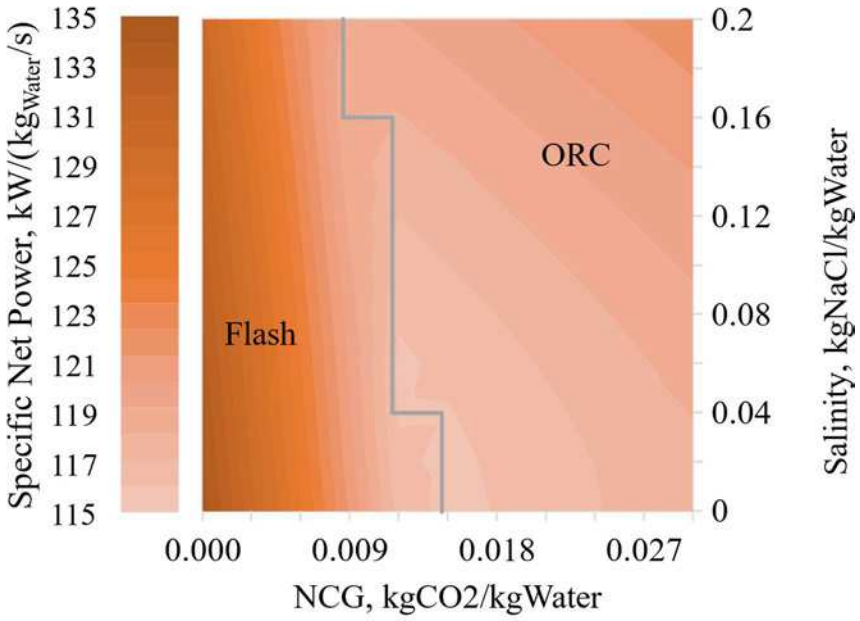

Figure 13: Maximum specific net power from a direct steam cycle or a binary ORC as a function of salinity and NCG content. Inlet temperature is 150 °C and a steam quality of 0.25

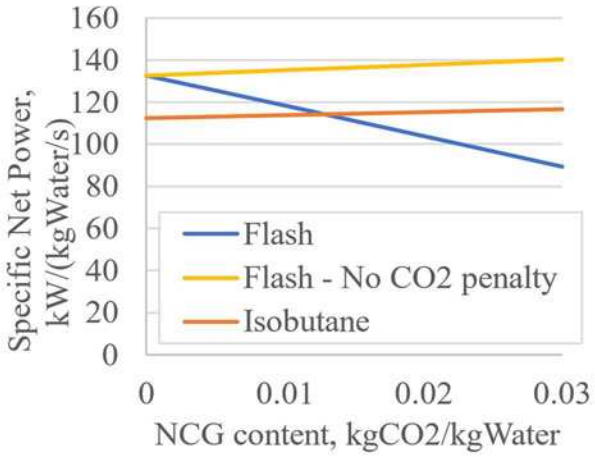

Figure 14: Specific net power as a function of NCG content. Inlet temperature is 150 °C, steam quality is 0.25 and salinity is 0.0 kg_{NaCl}/kg_{H2O}.

5 Conclusions

The thermophysical property modelling framework couples existing partitioning and property models, and while the current capabilities for single phase brines are promising, further work is required for handling two-phase geofluids to the same degree. The Python-based framework will in time be made available to the public.

Simulations of geothermal power plants showed that ORCs can thermodynamically outperform direct steam cycles for inlet steam quality as high as 0.3, provided an appropriate working fluid has been selected - isobutane and n-butane were found to be thermodynamically promising working fluids.
The presence of impurities in the geofluid such as salts and NCG does not significantly affect the heat flow entering the power plant, and in turn the turbine power. That being said, NCG compression for reinjection reduced the net power of direct steam cycles significantly, rendering binary ORCs thermodynamically favourable for NCG content as low as 0.01 kg_{CO2}/kg_{H2O}.

6 References

Abdulagatov, I. M., Akhmedova-Azizova, L. A., Aliev, R. M., & Badavov, G. B. (2016). Measurements of the density, speed of sound, viscosity and derived thermodynamic properties of geothermal fluids from south Russia Geothermal Field. Part II. *Applied Geochemistry*, *69*, 28–41. https://doi.org/10.1016/j.apgeochem.2016.04.003

Bell, I. H., Wronski, J., Quoilin, S., & Lemort, V. (2014). Pure and Pseudo-pure Fluid Thermophysical Property Evaluation and the Open-Source Thermophysical Property Library CoolProp. *Industrial & Engineering Chemistry Research*, *53*(6), 2498–2508. https://doi.org/10.1021/ie4033999

DiPippo, R. (2016). *Geothermal Power Plants* (4th ed.). Butterworth-Heinemann. https://doi.org/10.1016/C2014-0-02885-7

Duan, Z., & Sun, R. (2003). An improved model calculating CO2 solubility in pure water and aqueous NaCl solutions from 273 to 533 K and from 0 to 2000 bar. *Chemical Geology*, *193*(3–4), 257–271. https://doi.org/10.1016/S0009-2541(02)00263-2

Gyftopoulos, E. P., & Beretta, G. P. (2005). *Thermodynamics: Foundations and Applications*. Dover Publications.

Leal, A. M. M. (2015). *Reaktoro: An open-source unified framework for modeling chemically reactive systems.* (No. V2). https://reaktoro.org

Miron, G. D., Kulik, D., Leal, A., & Dmytrieva, S. (2021). ThermoFun: C++/Python code to fetch standard thermodynamic data from ThermoHub database. *Goldschmidt2021 Abstracts*. https://doi.org/10.7185/gold2021.4489

Pátek, J., & Klomfar, J. (2006). A computationally effective formulation of the thermodynamic properties of LiBr–H2O solutions from 273 to 500K over full composition range. *International Journal of Refrigeration*, *29*(4), 566–578. https://doi.org/10.1016/j.ijrefrig.2005.10.007

Sharqawy, M. H., Lienhard, J. H., & Zubair, S. M. (2010). Thermophysical properties of seawater: a review of existing correlations and data. *Desalination and Water Treatment*, *16*(1–3), 354–380. https://doi.org/10.5004/dwt.2010.1079

Spycher, N., & Pruess, K. (2010). A Phase-Partitioning Model for CO2–Brine Mixtures at Elevated Temperatures and Pressures: Application to CO2-Enhanced Geothermal Systems. *Transport in Porous Media*, *82*(1), 173–196. https://doi.org/10.1007/s11242-009-9425-y

Spycher, N., Pruess, K., & Ennis-King, J. (2003). CO2-H2O mixtures in the geological sequestration of CO2. I. Assessment and calculation of mutual solubilities from 12 to 100°C and up to 600 bar. *Geochimica et Cosmochimica Acta*, *67*(16), 3015–3031. https://doi.org/10.1016/S0016-7037(03)00273-4

7 ACKNOWLEDGEMENTS

This project has received funding from the European Union's Horizon 2020 research and innovation programme under the Marie Skłodowska-Curie grant agreement No 956965.

8 NOMENCLATURE

a	Activity	$(-)$	$\dot{w}$	specific work rate	(kW s/kg)
G	Gibbs free energy	(kJ)	x	steam quality	$(-)$
h	specific enthalpy	(kJ/mol)	y	mol fraction	$(-)$
$\dot{m}$	mass rate	(kg/s)	μ	chemical potential	(kJ/mol)
n	amount	(mol)	η	efficiency	$(-)$
NCG	NCG content	(kg_{CO2}/kg_{H2O})			
P	Pressure	(Pa)		**Subscript**	
s	specific entropy	(kJ/mol/K)	i	species index	
sal	salinity	(kg_{NaCl}/kg_{H2O})			
T	Temperature	(K)		**Superscript**	
v	specific volume	(m^3/mol)	L	liquid phase	
$\dot{W}$	Work rate	(kW)	V	vapour phase	

9 Appendix A

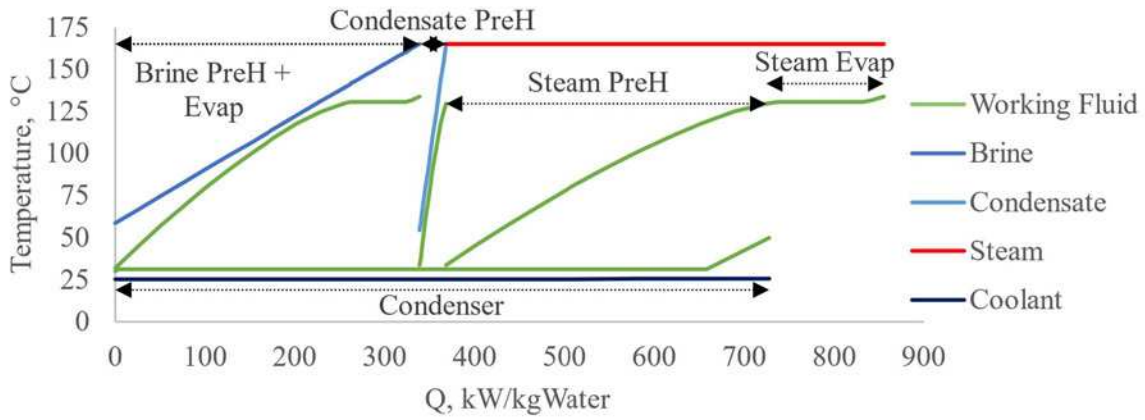

Figure 15 T-Q diagram of the binary ORC plant operating under an inlet temperature of 165 °C and a steam quality of 0.25.

10 Appendix B

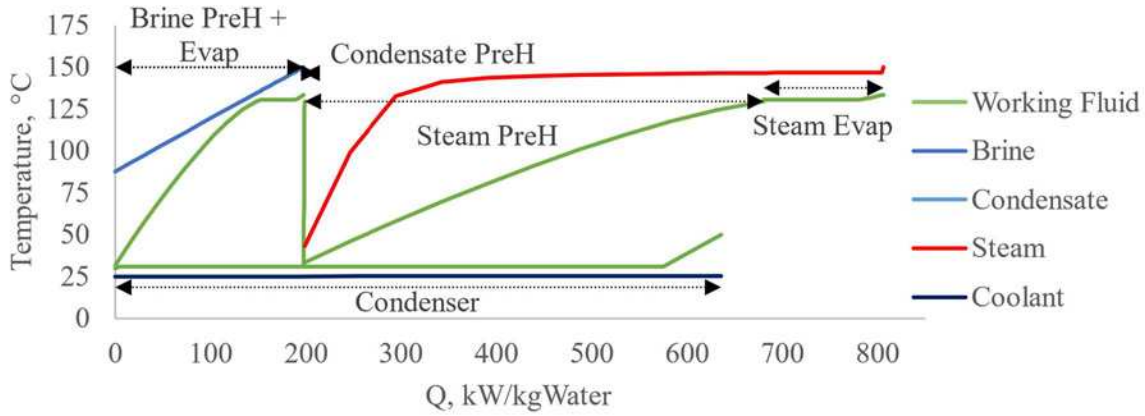

Figure 16 T-Q diagram of the binary ORC plant operating under an inlet temperature of 150 °C, a steam quality of 0.25, salinity of 0.1 kg_{NaCl}/kg_{Water} and NCG of 0.015 kg_{CO2}/kg_{Water}.

625

ORC SEVILLE 2023
7th International Seminar on O.R.C. Power Systems

© 2024 Editorial Universidad de Sevilla. Este es un artículo de acceso abierto distribuido bajo los términos de la licencia de uso y distribución Creative Commons (BY-NC-ND 4.0)

DOI: https://dx.doi.org/10.12795/9788447227457_109

COLD ENERGY RECOVERY IN LNG PLANTS WITH ORGANIC RANKINE CYCLE

Gabriele Marchiori[1,*], Marta Giudici[1], Giorgia Ruffato[1], Marco Astolfi[2]

[1] *Exergy International S.r.l., Olgiate Olona, Italy*
[2] *Politecnico di Milano, Milano, Italy*

*Corresponding Author: g.marchiori@exergy.it

ABSTRACT

During the production phase, natural gas (NG) is compressed and chilled to liquid state (liquified natural gas, LNG) for sake of volume reduction, hence to ease transportation. Approximately, 500 kWh of electricity or mechanical power per ton of LNG is needed for LNG compression and refrigeration during the production phase, which makes cold energy exploitation interesting from a thermodynamics point of view. An effective way to harness the cold energy contained in LNG is through an Organic Rankine Cycle system. A Cold Energy Plant (CEP) is an efficient system based on ORC technology which regasifies liquified natural gas and converts the heat absorbed from sea water into electricity by recovering the valuable exergy content of LNG. This solution allows to produce electrical power on-site without any additional external fuel consumption and no emissions at stacks. The CEP is a low-maintenance and cost-effective solution that can be efficiently applied in the LNG industry to increase energy efficiency and sustainability of operations. The CEP system designed by Exergy achieves high efficiency thanks to the use of the proprietary Exergy Radial Outflow Turbine combined with the Multilevel Condensation Cycle, maximizing the revenue from electricity production. This paper will outline the technical features of a CEP power plant and will present a case study based on a Liquified Natural Gas regassification system engineered to produce Nominal 4 MWe (4000 kWe) net electric power while simultaneously fulfilling the regasification of 180 ton/h (~1 MTPA) of LNG.

1 INTRODUCTION

Among fossil fuels, Natural Gas (NG) is the one having the lowest pollutant content, the highest calorific value and the lower specific CO_2 emission. Moreover, its production is spread among all continents making it a fundamental asset during the energy transition towards renewables. Liquefied Natural Gas (LNG) is gaining more and more attention thanks to the growth in interest from importing countries, mainly Europe and Japan, which aims to increase energy security through suppliers diversification: Natural gas, in its liquefied form, has a density of 430-470 kg/m^3, and can be easily transported worldwide by sea, from many different producing countries, with great geographical & market flexibility. The global LNG trade in 2020-2021 was around 28billion of cubic meters (IEA, 2022). During the production phase, natural gas (NG) is liquefied by cooling at cryogenic temperature, roughly -160 °C, at 1 atm pressure, for sake of volume reduction and ease of transportation and storage. Natural gas refrigeration is an energy intensive process: energy consumption for liquefaction is on average 500 kWh of electricity consumed per ton of LNG produced (Agarwal R., 2017) which correspond to roughly 3.6% of the natural gas LHV.

LNG transportation occurs in insulated cryogenic ship tanks at atmospheric pressure. Before being provided to a transportation and distribution network, LNG must be pressurized, usually at 80 to 120 barg (Mokhatab, 2014), and returned to gaseous state. The latter is performed at LNG import terminals in vaporizers. Conventional vaporizers are submerged combustion (SCV), open-rack (ORV) and intermediate-fluid (IFV) type. For the latter two the heat source is seawater, while in SCV a fraction of NG is combusted and the flue gases heat a pool of water which later provides heat to LNG. In ORV sea

water is flowing in counterflow outside LNG tubes, while the IFV consists in a shell and tube heat exchanger in which an intermediate fluid, in the shell, absorbs heat by vaporizing in contact with sea water and then condenses releasing latent heat to LNG, both LNG and sea water flows in the tubes. In all these vaporization processes a considerable amount of the energy used in the liquefaction phase (around 28%) is wasted to the environment and, additionally, they require the consumption of electrical energy (for LNG pumps and water pumps in ORV) and/or regasified gas in case of SCV.

1.1 Harvesting the Cold Energy Potential

An interesting use of cryogenic LNG, to increase the efficiency of regasification terminals, is electric power generation through the introduction of a power cycle between the environment and the vaporization process. In fact, a thermal engine can convert any meaningful temperature difference into mechanical energy and then into electrical energy in a turbogenerator. Power can be produced in a thermodynamic cycle in which LNG acts as the cold heat sink, and the ambient (e.g. seawater) at higher temperature as hot resource. Generated electrical power becomes a valuable "sub-product" of regasification and can be used for internal LNG terminal consumption and the excess fed to national grid. LNG contains an enormous potential for power generation, the "cold energy potential". The available heat is about 725 kJ_{th}/kg_{LNG} (from -160°C to 15°C @ 80 bara), and the available mechanical exergy from the gasification process alone about 348 kJ_{ex}/kg (Invernizzi M. C., 2016).

The ORC technology is an efficient and market-available way to harness the cold energy potential from LNG and will be the object of this paper. It has been developed since 1980, particularly in Japan by Osaka Gas, but few and sparse information about the pilot plants are available (Astolfi M., 2017). Referring to the schematic in **Figure 1**, in analogy with IFV, in ORC seawater is fed into a series of heat exchanger and vaporizes a low-boiling working fluid. In ORC the high pressure fluid vapor expands in the turbine and is then discharged in the condensers, where the heat is released to LNG to vaporize it until is returned in gaseous form. Similar to traditional IFV, the LNG is vaporized through an intermediate fluid, but with ORC the cold energy potential is not wasted, is converted in a turbo-expander. As a strategy for even higher cold energy conversion efficiency, ORC can be integrated with other technologies, as Direct Expansion (DE) in combined cycle cold energy plants (Invernizzi M. C., 2016) (Sugiyama). Currently, cold energy utilization accounts for less than 1% of its total potential, although around 12 GWe could be produced from its exploitation, which could be further boosted by climate change policies (Agarwal R., 2017). The aim of this paper is to present Exergy International's studies and patented Cold Energy Plant (CEP) for efficient utilization of cold energy potential through internally developed ORC technology and proprietary turbine design.

627

2 COLD ENERGY ORC PLANT

2.1 Exergy International Patented Multi-Level Condensation ORC

Conventional ORC systems are characterized by a single level of condensation and the use of propane, R13, R22 or R23 as working fluid. The typical size ranges from few hundreds kWs to 5 MW (Astolfi M., 2017). The Temperature-Heat Exchanged diagram for the working fluid condensation process (**Figure 5**) demonstrates that this single-condensation plant configuration is characterized by a condensation curve which does not match the LNG vaporization and strongly limits the turbine expansion, thus the ORC plant power production.

To overcome single level ORC performance limitation Exergy International S.r.l. developed and patented (Patent No. EP 3 642 458 B1, 2021) a multi-level condensation ORC CEP, with the final aim to utilize at its maximum the LNG heat sink along the vaporization curve, increase the cycle efficiency thus maximizing the electrical power production at requested regasification rate. The patent allows up to four levels of condensation, with the use of a single feed pump in ORC circuit and Exergy's radial outflow turbine. The advantages of Exergy's multi-level condensation with single feed pump are:

- Higher cycle efficiency, Higher specific power production (SPP), and higher cold-energy-recovery factor than single level: see performance parameter definition in section 2.2.1 and comparison of single vs. two-pressure condensation level-based ORC plants in section 2.2.2.

- Single pump configuration is enabled by the use of a throttling valve at high pressure condensers outlet. At valve outlet the fluid will be de-pressurized and in two-phase, liquid and vapor. The two-phase flow is routed to the lower-pressure condensers where the liquid mixes with the low pressure condensate and the vapor is condensed along with the low-pressure vapor from turbine discharge. Single, low suction pressure, pump means: lower ORC plant complexity and lower plant CAPEX, lower number of critical equipment exposed to cryogenic temperatures, expected lower stops for maintenance and higher plant annual availability.
- Integration with Exergy International's patented high efficiency ROT (Radial Outflow Turbine), see section 3 below, which naturally allow spillages between stages. High pressure and low-pressure expansion both in a single turbomachine unit.
- Suitable for the use of propane as working fluid, which is indicated by literature as one of best performing among hydrocarbons (Astolfi M., 2017) and has high market availability at low cost: in fact propane has already been successfully employed in conventional IFV and many cryogenic applications. Other advantages of propane are: low Global Warming Potential (GWP < 10), moderate vacuum in low pressure condenser (> 0.1 bara)

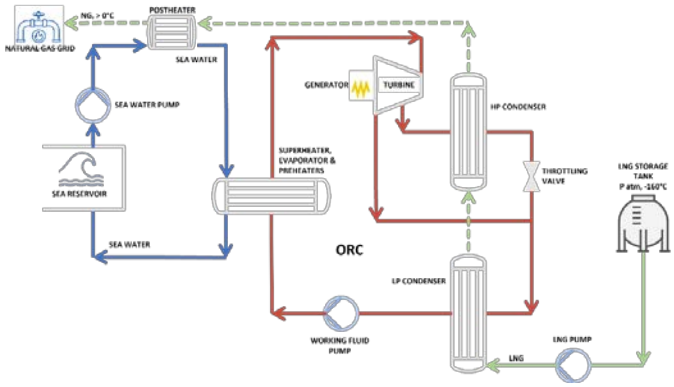

Figure 1 Exergy's Multi-Level Condensation ORC CEP in two-pressure level configuration

628

The schematic above (**Figure 1**) shows the patented multiple condensation levels ORC plant in two-condensation pressure levels configuration. The main ORC equipment are: preheaters, evaporator and superheater, exchanging heat with sea-water, ROT turbine and generator, high pressure (HP) and low pressure (LP) condensers, exchanging heat and achieving the regasification of LNG, single feed pump, condensate throttling valve at HP condenser outlet (ORC side). A LNG post-heater is designed in order to heat up LNG from HP condenser outlet with seawater: the final aim is to guarantee the NG temperature is always higher than the minimum required by NG distribution network.

Even though the patent allows up to four levels of condensation, the two-pressure levels configuration has been selected as the object of this paper and its performance improvements with respect to conventional single-level ORC will be further discussed in next sections. Currently, two-levels of condensation has resulted, by Exergy's internal analysis, as an optimum compromise among efficiency, plant complexity and overall CAPEX.

2.2 Comparison Two-Level Vs. Single-Level Condensation Plants

2.2.1 Performance Parameters, Definitions, Case Description: First law efficiency as usually defined as net power output over heat input is not a suitable parameter for cold energy plants comparison, since it does not directly show the efficiency in utilizing the cold energy potential from LNG. Thermal efficiency could be more effectively defined considering the total heat output, which is discharged at ORC condenser for LNG vaporization:

$$\eta_{Th,net}\,[\%] = \frac{W_{e,net}}{Q_{cond}} \qquad (1)$$

Where: $Q_{cond} = \sum_{i=1}^{N} Q_{cond,i}$ with N = total number of condensation steps.

The capability to utilize at its maximum the available heat sink provided by LNG regasification process from cryogenic temperature (about -160°C) up to the required temperature at interface outlet (generally ≥ 0°C), is shown by the cold-energy recovery factor value, as defined below:

$$f_{CE,REC}\ [\%] = \frac{Q_{cond}}{Q_{LNG}} = \frac{Q_{cond}}{\dot{m}_{LNG}\cdot(h_{NG,out} - h_{LNG,in})} \quad (2)$$

Multiplying the recovery factor with the thermal efficiency, the result is the net cold energy efficiency, representing the net electrical power output per unit of heat that could theoretically be transferred to LNG:

$$\eta_{CE,net}\ [\%] = \frac{W_{e,net}}{Q_{cond}} \cdot f_{CE,REC} = \frac{W_{e,net}}{Q_{LNG}} \quad (3)$$

Literature (Invernizzi M. C., 2016) indicates the SPP (Specific Power Production) parameter as the best index for performance evaluation. SPP is defined as ORC plant net electrical energy production per unit mass of LNG vaporized:

$$SPP\ \left[\frac{MJ_e}{kg_{LNG}}\right] = \frac{EE_{net}}{M_{LNG}} \quad (4)$$

SPP allows to compare perforce of different cold energy recovery technologies in different configurations and correctly represent the effectiveness in generating electrical energy from the required LNG regasification process.

Table 1 Case Description: Input & Design Data, Constraints

LNG regasification plant size	**1 MTPA**	**NG temperature @ Post-heater Outlet**	**10°C**
(Peak) LNG flow to ORC	180 t/h	**Sea Water Temperature**	18°C
LNG pressure @ ORC inlet	94 bara	**Sea Water Allowed ΔT**	4°C
LNG temperature @ ORC inlet	-157 °C	**ORC Working Fluid (WF)**	Propane
ΔP ORC Vapor Phase (Evaporator, Superheater, Turbine inlet line)	0.60 bar	**ΔP ORC Condensers (WF side) HP / LP**	0.05 bar / 0.05 bar
ΔP ORC Turbine Discharge Line	0.02 bar	**ΔP ORC Condensers (LNG side) HP / LP**	0.25 bar / 0.25 bar
ΔP ORC Liquid Phase (Preheater, Liquid Lines)	0.80 bar	**ORC Auxiliaries Consumption (other than WF Pump)**	67 kW
$\eta_{T,el-mec}$	97.5%	$\eta_{P,hyd}$	65%
$\eta_{T,is}$	89%	$\eta_{P,el-mec}$	93%
ΔT_{pp} in ORC Condensers	5°C	**ΔT_{pp} in ORC Evaporator**	≥ 3°C
ΔT_{sc} @ ORC Condensers Outlet	1°C	**ΔT_{pp} in ORC Superheater**	≥ 3°C
Turbine Discharge Vapor ΔT Superheating	≥ 2°C	**Fluid Properties Database**	NIST REFPROP 9

Reported in sections below are the results from the energy balances and sensitivity analysis for the two cold energy ORC configurations: single level and two-level condensation pressure. In **Table 1** the main input data and constraints for the calculations are collected. The cycle constraints are on pinch-point temperature differences in heat exchangers and on turbine outlet temperature, the latter shall always be above saturation to guarantee dry expansion and no liquid droplets in last turbine stages. Simulations have been performed in internally developed Microsoft Excel + VBA code environment with thermodynamic fluid properties from NIST REFROP V9.1 (Lemmon, 2013) database. The optimization algorithm uses the Generalized Reduced Gradient (GRG) non linear code, built-in Excel solver tool (Leon S. Lasdon, 1975). The ORC optimization target, both in single and in two-pressure level configuration, is to maximize the SPP parameter by acting on the following variables: turbine spillage flow rate, ORC evaporation pressure, ORC condensation pressure (both HP and LP for two-pressure levels cycle), degrees of superheating at turbine inlet.

2.2.2 Thermodynamic Results: Reported in **Figure 2** below is the comparison between two and one-pressure level for all the performance parameters defined above. The plot has on the horizontal axis the

LNG temperature at post-heater inlet, i.e. at ORC condensers outlet, which is the HP Condenser outlet for the two pressure levels cycle. This temperature is an indication of the cold energy utilization in the ORC system. Higher LNG post-heater inlet temperature always means higher cold energy recovery for both single and two pressure level configurations. Lower LNG inlet temperatures are associated with lower condensation pressure and therefore to higher ORC thermal efficiency, as defined above by equation (1). There is, therefore, a trade-off between achievable thermal efficiency and cold energy utilization. The optimum SPP and cold energy efficiency are in an intermediate LNG outlet temperature region, where the recovery factor is still adequate and the cycle thermal efficiency is not excessively limited by the LNG condenser outlet temperature, which directly affect the turbine discharge pressure. It can be observed from **Table 2** that the single pressure level cycle optimum SPP point is located at lower temperatures than the two pressure level cycle (-55°C vs -44°C).

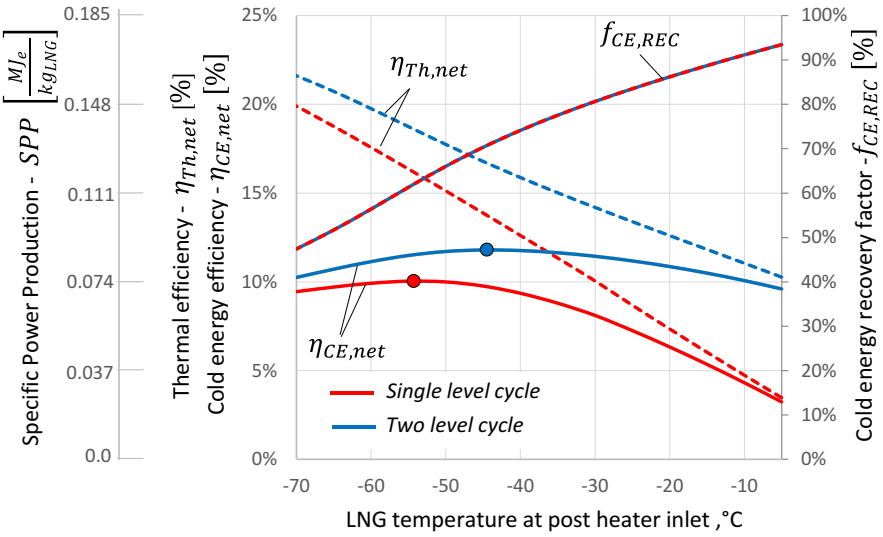

630

Figure 2 Comparison of performance parameters for single and two-condensation pressure level configurations as function of NG temperature at ORC condenser outlet (post-heater inlet).

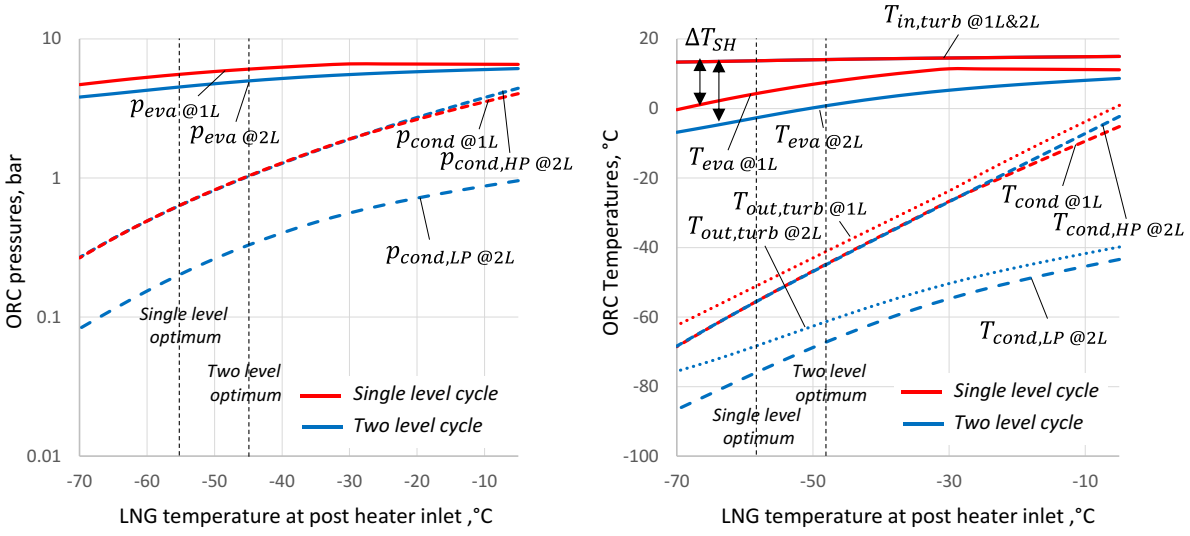

Figure 3 Optimization Variables as function of LNG post-heater inlet temperature

The optimization variables trends are shown in **Figure 3**, again as a function of LNG temperature at post-heater inlet. The power output optimization algorithm slightly increases the evaporation pressure and decreases the superheating as the LNG temperature increases, for both single and two-pressure level cycles, while satisfying the constraint on turbine outlet minimum 2°C superheating to guarantee dry expansion. The superheater pinch point temperature difference is always kept by the algorithm at the

minimum allowed value of 3°C. For single level cycle the trend changes at LNG post-heater inlet temperature greater than -30°C: above this temperature the cycle performance limiting factor shifts from the limitation due to mandatory dry turbine expansion to minimum pinch-point temperature difference inside the ORC evaporator, and the optimization algorithm starts decreasing the evaporation pressure while increasing again the turbine inlet superheating to satisfy the requirement: this behavior is expected since in low temperature region the propane vapor saturation curve is slightly bell-shaped, see Ts-diagram in **Figure 5**, while from -30°C the curve becomes almost vertical, or "isentropic".

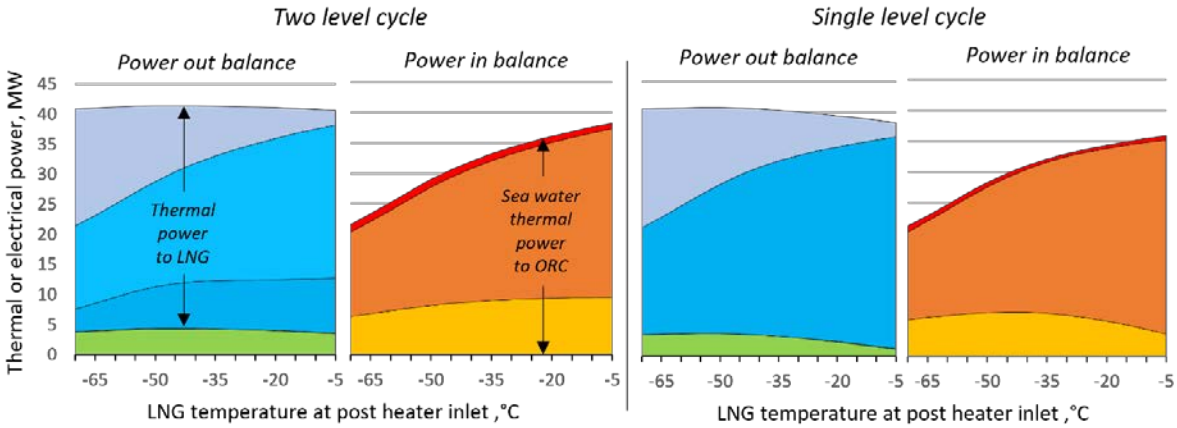

Figure 4 First Law Energy Balance as function of LNG temperature at post-heater inlet. Legend: LNG post-heater; LP condenser in two level cycle; HP condenser in two level cycle / condenser in single level cycle; Energy Losses; Electrical Power output; Superheater; Evaporator; Preheater

The first law balances results are presented in **Figure 4**. It is evident that the higher the LNG temperature at post-heater inlet, the higher the seawater thermal power required entering the ORC. Most of the thermal duty on seawater-propane side is processed by evaporator, while superheater thermal power is relatively small, hinting on the possibility of integration of these two units in a single exchanger for possible capital cost reduction. Superheater duty in two level cycle is higher than in single level, showing the necessity to increase more the turbine inlet temperature in the first configuration. On LNG side the majority of ORC wasted heat to LNG is discharged by low pressure condenser in the two-level cycle. In both configurations post-heater duty, and therefore necessary exchanger area and costs, increases as the LNG temperature at its inlet decreases.

631

Table 2 Best SPP Point Comparison: Two-level vs. Single Level

Case:	Two Level	Single Level
LNG Temperature @ Post-Heater Inlet	-44°C	-55°C
Propane Temperature @ ORC Turbine Outlet	-59°C	-48°C
Evaporation Pressure	5.0 bara	5.6 bara
Turbine Inlet Superheating	12.5°C	8.4°C
Condensation Pressure (HP / LP)	1.0 / 0.3 bara	0.6 bara
Net Electric Power	4.3 MWe	3.7 MWe
SPP [MJ/kg] (4)	0.087	0.074
Recovery Factor [-] (2)	70.3%	61.3%
Thermal Efficiency [-] (1)	16.8%	16.4%
Cold Energy ORC Efficiency [-] (3)	11.8%	10.0%

The two best SPP operating points have been selected for both cycles and the major results from the calculations are reported in **Table 2**. The two-pressure level cycle configuration alone allows an increase in SPP of around +18% and achieve the optimum performance at +9°C LNG temperature at

condenser outlet, or post-heater inlet, thus at less critical cryogenic temperatures (above -50°C), this is thanks to the much higher cold energy recovery factor.

In **Figure 5**, for the two best SPP cases, the temperature-heat exchanged diagram and temperature-entropy diagram are plotted. The advantage of more than one single condensation pressure is evident: in two level case the condensation curve better match the LNG heating and regasification process, while achieving lower turbine discharge pressure and therefore higher electrical power production. In temperature-entropy diagram for the two-level cycle is shown the spillage from an intermediate turbine stage. The spilled flow is routed to the HP condenser for full condensation (marked points x-y), then the HP condensate is throttled by a valve (y-y') down to LP condenser pressure. The low pressure condensate is, in both cases, pressurized and sent to primary heat exchangers by a single feed pump.

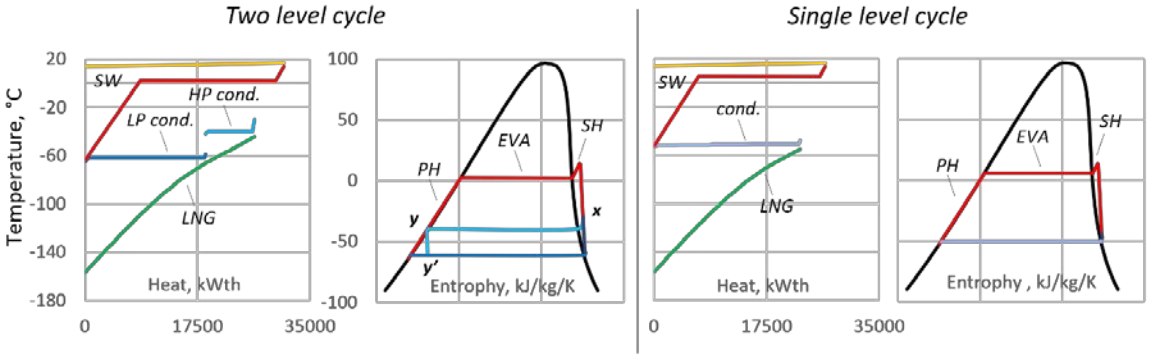

Figure 5 Temperature-Heat Exchanged diagrams and Temperature-Entropy Diagrams for the two configurations in best SPP point. Note: Thermal duty in LNG post-heater is not here represented.

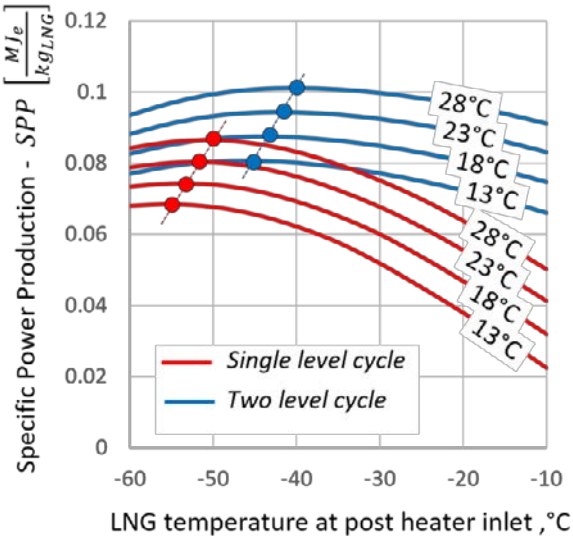

Figure 6 Effects of Sea Water temperature on ORC SPP performance parameter. For all the cases the maximum allowed water cooling is 4°C

2.2.3 Effect of Sea Water Temperature: Seawater temperatures vary during the year and by geographical region, and the above study has been performed at an average seawater temperature of 18°C. Nevertheless, the maximum seawater temperatures are between 21.5 ◦C and 29.1 ◦C and are consistent across the globe, while the minimum mean seawater temperature range between 8.1°C and 24.1°C, reaching below 5°C only in few countries during winter (Agarwal R., 2017). A dependency study highlights the effect of seawater temperature on the ORC performance. In **Figure 6** are reported the results for seawater temperature ranging from 13°C to 28°C, which is a representative interval, both for two and single-pressure level cycle configuration. As expected, ORC always benefits from an increase in seawater temperature: higher temperature means higher ORC evaporator pressure, thus higher power production and SPP. The optimum SPP point shifts at higher post heater inlet temperature, meaning

higher recovery factor is achieved. For the two level cycle optimum SPP increases +25% passing from 13 to 28°C.

2.3 ORC Configuration: Effects on Turbomachinery

The selection and design of the ORC turboexpander is clearly affected by the thermodynamic properties at its inlet and outlet interfaces and, in the case of multi-pressure condensation cycles, also at the intermediate spillage point.

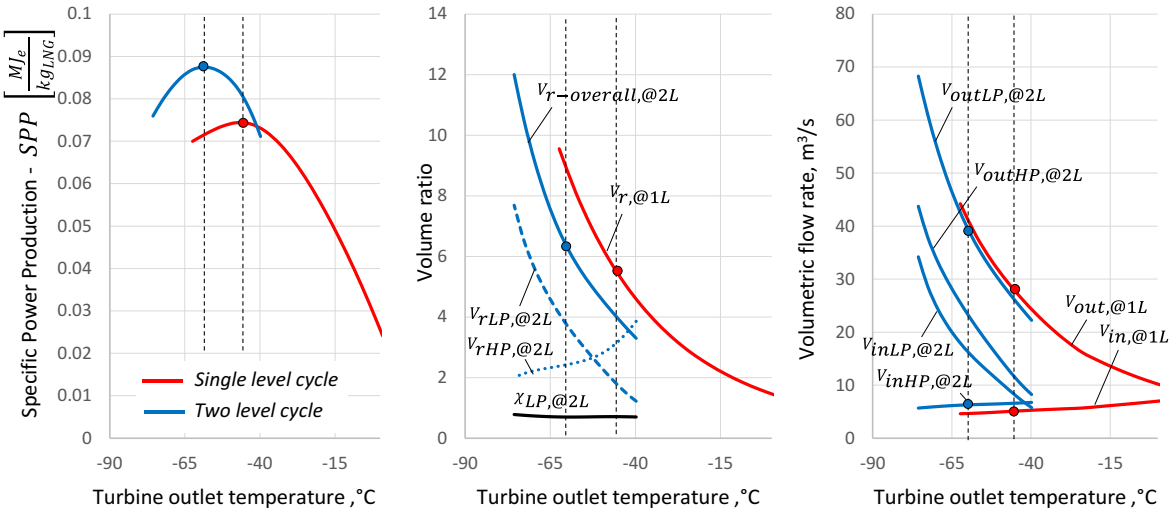

Figure 7 ORC Results for Turbomachinery: SPP vs. turbine outlet temperature, volume ratio and volume flow rate for two and single pressure level cycles.

The main parameters that give the first direction to be taken for the turbomachinery design, and which roughly determine the overall dimensions (outside diameter, stages radius) and the total number of stages, are the volume ratio and outlet volume flow rate. For cold energy applications, the turbine outlet temperature also has a major impact: as cryogenic it determines the proper material selection. For this reason, the plots presented in this section (**Figure 7**) are as function of turbine outlet temperature (LP turbine outlet for multi-level cycle). The optimum SPP point for two level cycle is located at lower temperature, thus pressure, than for the single-level cycle. The lower pressure results in a higher volumetric flow rate at turbine discharge than in the single-pressure case, but the two level is not excessively higher (approximately 40 m^3/s vs. slightly under 30). Nevertheless, the volume ratio processed by the machines, at the optimum SPP points, is close to 6 for both configurations. All of the above indicates that the two turbo-machines for the two optimal SPP cycles will be very similar in terms of sizing, and therefore it can be reasonably predicted that a two-pressure level turbine will have a comparable manufacturing cost of a single-pressure level turbine for cold energy applications. A precise cost analysis and comparison may be the object of future study.

633

3 RADIAL OUTFLOW TURBINE FOR COLD ENERGY PLANT

The patented multi-level condensation CEP, as described in the previous section, involves the use of the Radial Outflow Turbine (ROT) as turbo-expander. Radial Outflow Turbine architecture can process high volumetric flow ratio and important enthalpy drops, typical of organic working fluid, while achieving very high efficiency: this thanks to the possibility to have multiple stages, limiting the load on each stage and, therefore, subsonic flows (Spadacini C., 2015).

The ROT has been conceptualized and produced by Exergy based on Ljungstrom turbine and launched in the market in 2009. In this particular application the ROT, keeping the standard single rotor disk architecture, is conceptually re-designed to meet the Multi-level Condensation Cycle needs:

- Both turbine sections, high pressure and low-pressure level, have been optimized using an internally developed Excel-based simulation tool, which output is the preliminary 1D turbine

sizing. Then, the geometry is designed tridimensionally with Ansys CFX, and several geometric parameters are tuned to extract the best possible performance.

- The ROT mechanical group have been designed to be extracted for easy maintenance, minimizing service effort. Bearing and shaft of the turbine are located in the non-cryogenic process area (see **Figure 8**), far from the low temperature discharge of the working fluid: mechanical group is never exposed to cryogenic temperatures minimizing the use of valuable materials, making possible to employ well-known and robust technology and reducing the overall thermal effects on the machine.
- The CEP ROT presents nitrogen seal system with double mechanical arrangement that allows the sealing of the turbine shaft thus minimizing propane leakages to the environment. In normal operating conditions, may happen that the sealing fluid leaks from both side, atmospheric and process side. The use of nitrogen (instead of seal oil) as barrier fluid prevents the problem of solidification of mineral oil in cryogenic conditions due to leakage on the process side.
- The control unit comprises dedicated fin fan coolers as well as a vacuum pump to guarantee turbine sealing even in case of failures, hence enhancing the turbine lifetime.

The Radial Outflow Turbine ensures different advantages in cryogenic applications compared to other solutions. The isentropic efficiency is high both in on and off-design conditions thanks to: optimization of velocity triangles, multiple reaction and action stages, the natural radial increase of passage area, that allows to expand high volumetric flow ratio. The ROT configuration naturally allows spillages between stages in single-disc turbine, therefore can enable the multi-level condensation pressure level ORC in a single machine: no need for multiple turbines at different pressure levels. The ROT shaft length, unlike the axial turbines, does not need to be increased to make room for the spillages point clearance, avoiding several rotor dynamic problems for overhung configuration. In addition, the low rotational speed makes possible the direct drive avoiding the need for additional gearbox.

Table 3 Turbine sizing for the two level ORC CEP at best SPP point (see Section 2, Table 2); "R out" is the outer radius for the last stage for each pressure level. Selected rotational speed is 1500 rpm.

		HP	LP
N°stages	[-]	3	2
R out	[mm]	751	897

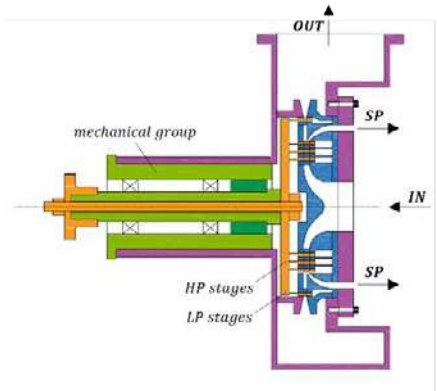

Figure 8 ROT sectional drawing for two-pressure level CEP. IN = Working fluid inlet; SP = Spillage point, to HP condenser; OUT = Turbine discharge, working fluid outlet to LP condenser.

4 CONCLUSIONS

Cold Energy Plant (CEP) based on Exergy International's patented multi-level condensation, single pump, and ROT turbine ORC is a market-available solution for the cold energy recovery from the LNG vaporization process. The calculations and the results demonstrated that the single-pump two-pressure level cycle has better performance than conventional single-level cycle, about +18% in net Specific Power Production (SPP). Performance is, in both cases, strongly dependent on seawater temperature:

ORC efficiency in power production from LNG strongly benefits from warm climates. The analysis on the process parameters for turbine sizing demonstrated that no significant differences in size and cost compared to a single pressure level turbine are to be expected. The multi-level ORC patent involves the use of Radial Outflow Turbine (ROT), which enables the multi-level CEP since naturally allows spillages between stages and accommodates the large volumetric expansion while achieving high efficiency. Furthermore, the ROT mechanical group is located far from turbine cryogenic region.

NOMENCLATURE

Nomenclature and Acronyms

LNG	Liquefied Natural Gas
LHV	Lower Heating Value (MJ/kg)
SCV	Submerged Combustion Vaporizer
ORV	Open Rack Vaporizer
IFV	Intermediate Fluid Vaporizer
DE	Direct Expansion
ORC	Orgnic Rankine Cycle
CEP	Cold Energy Plant
ROT	Radial Outflow Turbine
GWP	Global Warming Potential
HP	High Pressure
LP	Low Pressure
η	Efficiency (%)
f	Recovery Factor (%)
SPP	Specific Power Production (MJe/kg-LNG)
EE	Electric Energy (MJe)
M	Mass (kg of LNG)
MTPA	Million Tons Per Annum of LNG (1000 kg LNG/year)
WF	Working (Organic) Fluid
SW	Seawater
T	Temperature (°C)
P	Pressure (bara)
PH	Preheater or Economizer
EVA	Evaporator, Evaporation
SH	Superheater
COND	Condenser, Condensation
V	Volume
L	Levels, of condensation pressure
R	Radius (mm)

Subscripts

th	Thermal
e, el	Electrical
CE	Cold Energy
REC	Recovery
net	Net
T, turb	Turbine
P	Pump
is	Isentropic
el-mec	Electro-mechanical
hyd	Hydraulic
pp	Pinch Point
SH	Superheating
r	Ratio

635

REFERENCES

Agarwal R., R. T. (2017). LNG Regasification Terminals: The role of Geography and Meteorology on Technology Choices. *Energies*.

Astolfi M., F. A. (2017). Cryogenic ORC To Enhance The Efficiency of LNG Regasification Terminals. In *Energy Procedia 129* (pp. 42-49).

Egashir, S. (2013). LNG Vaporizer For LNG Re-gasification Terminal. *KOBELCO TECHNOLOGY REVIEW NO.32*.

EXERGY INTERNATIONAL SRL. (2021, 05 26). *Patent No. EP 3 642 458 B1*.

IEA. (2022, October 26). *Global LNG balance, year-on-year change, 2021-2022*. Retrieved from https://www.iea.org/data-and-statistics/charts/global-lng-balance-year-on-year-change-2021-2022

Invernizzi M. C., I. P. (2016). The Exploitation of the Physical Exergy of Liquid Natural Gas by Closed Power Thermodynamic Cycles. An Overview. In *Energy, Volume 105* (pp. 2-15).

Lemmon, E. H. (2013). NIST Standard Reference Database 23: Reference Fluid Thermodynamic and Transport Properties-REFPROP, Version 9.1. Gaithersburg: National Institute of Standards and Technology, Standard Reference Data Program.

Leon S. Lasdon, A. D. (1975, March). Design and testing of a generalized reduced gradient code for nonlinear optimization.

Mokhatab, S. (2014). *Handbook of Liquefied Natural Gas.* Gulf Professional Publishing.

Spadacini C., C. L. (2015, October 12-14). Fluid-Dynamics of the Radial Outflow Turbine. *3rdInternational Seminar on ORC Power Systems.* Brussels.

Sugiyama, M. (n.d.). The Utilization of LNG Cryogenic Energy. In *EIT No.32.*

ORC SEVILLE 2023
7th International Seminar on O.R.C. Power Systems

© 2024 Editorial Universidad de Sevilla. Este es un artículo de acceso abierto distribuido bajo los términos de la licencia de uso y distribución Creative Commons (BY-NC-ND 4.0)

DOI: https://dx.doi.org/10.12795/9788447227457_110

NUMERICAL INVESTIGATION OF ORGANIC VAPOR FLOW EFFECTS ON A MICRO-SCALE RADIAL TURBOCOMPRESSOR

Andrés Sebastián*, Rubén Abbas, Manuel Valdés

Universidad Politécnica de Madrid (UPM), José Gutiérrez Abascal 2, 28006 Madrid, Spain
*Corresponding Author: andres.sebastian@upm.es

ABSTRACT

Radial turbocompressor-based heat pump-like systems are currently being studied for novel environmentally friendly energy applications. Hence, the development of small centrifugal compressors using different organic vapors is in the spotlight. This work proposes some upgrades to a previously developed similarity-based and generalized flow turbomachinery scaling methodology for organic vapors. The main objective is to conduct a numerical study of the non-ideal effects on micro-scale radial turbocompressor working at different operating conditions using two organic fluids (propane and isobutene). Results show a good degree of agreement between the analytical predictions and the numerical simulation. Furthermore, the use of new similarity parameters is discussed in the range of the operating conditions of the study. The findings of this work set out that some intrinsic vapor effects are well predicted by the proposed methodology, which allows the micro-turbocompressors scaling from ideal gas to vapor flow conditions.

1 INTRODUCTION

Research and development of novel sustainable technologies is required to accomplish the necessary transition towards a low-carbon global energy model. There is a wide range of potential technologies such as increased-efficiency heat pumps (Schiffmann and Favrat, 2010), polygeneration systems (Sebastián *et al*., 2021a), or different proposals of thermal energy storage systems (Steger *et al.*, 2020), where the use of downsized radial turbocompressors might be proposed using working fluids other than air, such as organic vapors. Radial micro-turbocompressors, also referred to as micro centrifugal compressors, are classified according to Casey et al. (2013) for having impeller outer diameters less than 30 mm and rotational speeds greater than 200 $kmin^{-1}$. Due to the increased interest in turbomachinery for organic Rankine cycles, there has been intense research work during the last decades devoted to the analysis, design, experimentation and manufacturing of organic axial and radial-flow turbines (Macchi and Astolfi, 2017). Hence, there is ongoing research on the characterization of non-ideal compressible flows on turbines performance (Romei *et al* 2020, Baumgärtner *et al* 2021). Indeed, recent studies concerning the extension of the dimensional analysis for turbomachinery operating with dense vapor flows have been published, such as Giuffre and Pini (2021). However, according to aus der Wische and Reinker (2022), there are still gaps in the general comprehension of turbomachinery beyond typical perfect gas assumptions such as the dimensional analysis and performance laws using organic vapor flows.

Research efforts are required as a consequence of the rising trend of studying organic vapor compressions, instead of expansions, for further applications as those environmentally friendly energy systems. Indeed, the influence of the isentropic exponent on similarity conditions and proposed corrections on compressor performance indicators have been discussed by Van den Braembussche (2019) and Casey and Robinson (2021). In addition, novel similarity methods and corrections were proposed for different working media apart from organic vapors, such as supercritical conditions (Jeong *et al*., 2020) or noble gases (Zou and Ding, 2018). The theoretical framework for the analysis of one-dimensional flows of perfect gases is currently extended to the case of non-ideal compressible flows through different studies such as Tosto *et al*., (2021), where the molecular complexity and dense-vapor effects are analyzed in compressible internal flows. Giuffre *et al* (2022) conducted a numerical

investigation on the effect of working fluid on high-speed centrifugal compressors and provided further evidence that efficient designs operating with organic may feature pressure ratios up to five at off-design, are feasible from the dynamic standpoint. All these efforts lead to the concept presented by aus der Wische and Reinker (2022) for generalized performance laws for organic vapor flow turbomachinery, being specifically tested for radial turbocompressors.

This work aims to conduct a numerical study based on computational fluid dynamics applied to a small-scale radial turbocompressor assessing its performance using air as well as two different organic fluids (isobutane and propane) at different operating points keeping dynamical similitude conditions. The novelty in this work lies in the assessment and improvement of the abovementioned generalized performance laws for organic vapors, evaluating its adequacy when using new similarity numbers better suited to turbocompressors operating in vapor conditions. The structure of the manuscript is as follows: after establishing the scope and the grounds of the paper in the introduction section, Section 2 presents the analytical and numerical methodology together with the operating points selection and the definition of the reference machine; Section 3 shows the obtained results and the numerical comparison among the selected set of working conditions. Finally, the main conclusions are drawn in Section 4.

2 METHODOLOGY

This section describes the methods and actions developed to carry out the numerical investigation proposed. First, a generalized dimensional analysis is set for organic vapor turbomachinery which will be used to generate operating points keeping dynamic similarity conditions, also named homologous points. Then, the numerical modelling approach is explained along with the definition of the micro-scale radial turbocompressor geometry. Finally, the selection of the working fluids and the operating points to be analytically and numerically studied is discussed.

2.1 Dimensional analysis for organic vapor turbomachinery

Generalized flow scaling laws are required when dealing with compressible flow turbomachinery using fluids other than air. As introduced in the previous section, aus der Wische and Reinker (2022) developed a novel formulation for the dimensional analysis of turbomachinery working with non-ideal fluids, which intends to be valid also for complex fluids (fluids with a behavior far from the ideal) such as organic vapors. This functional relationship based on Buckingham's Π-theorem goes beyond the conventional approach of perfect gas and is expressed in Equation 1. Total-to-total pressure ratio and efficiency are chosen as key performance indicators. Then, blade Mach number (Π_n), dimensionless mass flow rate ($\Pi_{\dot{m}}$) and Reynolds number (*Re*) are formulated as usually found in literature. Now, two new similarity dimensionless groups are raised. The first one is called modified Eckert number ($Ec^{*1/2}$), which can be replaced by γ-similarity in case of a perfect gas and should be understood as a representation of dissipation effects. Finally, another new similarity number is proposed, called the Traupel number (*Tr*), which takes into account the non-perfectness of the fluid through the partial derivative of the compressibility factor along an isentropic compression/expansion process instead of simply the compressibility factor (*Z*). For a perfect gas (or vapor), *Tr*=0 holds.

$$\frac{p_{02}}{p_{01}}, \eta = f\left(\frac{nD}{a_{01}}, \frac{\dot{m}\sqrt{RT_{01}}}{p_{01}D^2}, \frac{\rho n D^2}{\mu}, \frac{nD}{(RT_{01})^{1/2}}, \rho n^2 D^2 \frac{\partial Z}{\partial p}\bigg|_s\right) \tag{1}$$

On this innovative basis, some modifications are proposed for the sake of a major generalization following Sebastián *et al.* (2021b), as Equation 2 holds. First, inlet stagnation properties are set to all the fluid properties considered in the analysis. Then, the use of stagnation inlet speed of sound is proposed in the dimensionless mass flow rate in order to not consider any perfect gas assumption. Finally, isentropic stage loading or head coefficient ($\Delta h_s/a_{01}^2$) is proposed instead of the direct use of total-to-total pressure ratio. This may improve the characterization of the compression/expansion dynamical similarity preservation since isentropic enthalpy rise can be kept as a function of media speed of sound without any kind of perfect gas assumption. One may note that neither the ideal adiabatic

specific heat ratio ($\gamma=c_p/c_v$) nor the real isentropic pressure-volume exponent (γ_{pv}), see Equation 3, are taken as independent dimensionless numbers.

$$\frac{\Delta h_{0s}}{a_{01}^2}, \eta = f\left(\frac{nD}{a_{01}}, \frac{\dot{m}}{\rho_{01} a_{01} D^2}, \frac{\rho_{01} n D^2}{\mu}, \frac{nD}{(RT_{01})^{1/2}}, \rho_{01} n^2 D^2 \frac{\partial Z}{\partial p}\bigg|_s\right) \tag{2}$$

$$\gamma_{pv} = -\frac{v}{p}\frac{\partial p}{\partial v}\bigg|_s = -\gamma \frac{v}{p}\frac{\partial p}{\partial v}\bigg|_T \tag{3}$$

Once the functional relationship is set, one must choose which dimensionless numbers are required to be kept to provide any other operating points when varying boundary conditions or working fluid. Through the two first dimensionless groups, the calculation of homologous rotational speed and mass flow rate is straightforward. The third group influence may be omitted if Reynolds number is large enough not to fall below the critical threshold under which viscous friction on the boundary layer becomes dominant. Finally, the modified Eckert and the Traupel numbers are selected as the degree of freedom of the system. Hence, their value will be analyzed and compared to seek the method's potential deviations. Considering that dynamical similarity is preserved, efficiency and dimensionless isentropic enthalpy rise must be kept. Total-to-total pressure ratio can be then analytically calculated through real gas data properties taken from REFPROP database.

The proposed analytical methodology will be used for a reference geometry of a small-scale turbocompressor to generate a set of operating points at different working conditions. This variation includes the change of working fluid from air to two organic vapors. Hence, the novel formulation presented above will generate the required boundary conditions for the numerical simulation, which will be then compared to the scaling laws to check the prevalence of dynamical similarity conditions.

2.2 Numerical modelling and reference turbocompressor

The numerical model used for this analysis is an upgraded version of the micro-scale radial compressor model developed in Sebastián *et al.* (2021b) using ANSYS-CFX. It is a one-stage air centrifugal compressor consisting of a 20 mm impeller with seven blades and seven splitter blades rotating at 220 $kmin^{-1}$ at design conditions and a vaneless diffuser. At the design point, the micro-compressor with air as working fluid provides an overall total-to-total pressure ratio around 1.4 consuming 330 W. Further technical data can be also found in Sebastián *et al.* (2023).

The stage modeled is formed by a seventh part of the straight inlet duct, the impeller and the vaneless diffuser passage of the reference micro-scale radial turbocompressor, providing a reference mesh of 4.8 million cells, with an average cell size of 0.043 mm. The Grid Convergence Index (GCI) proposed by Celik *et al* (2008) is obtained to determine the error band on the convergence solution (discretization error). Two additional meshes have been studied following the Celik's method: a coarse mesh (2.2 million cells, 0.055 mm average cell size) and a fine mesh (10.9 million cells, 0.032 mm average cell size). The GCI value from the fine grid to the intermediate (GCI_{12}) based on the total-to-total pressure ratio is 0.09%, well below 0.54% of the GCI from the intermediate to the coarse mesh (GCI_{23}). Hence, these very low values allow the use of the reference mesh for this numerical problem ensuring stable and grid-insensitive results. The inlet condition is specified in terms of the total temperature and pressure of the fluid; the outlet sets the mass flow rate. This inlet-outlet configuration is the one that provides the best numerical stability. The lateral faces of the fluid domain are defined as rotational periodic boundaries to simulate the full stage as Figure 1 shows. Stationary-rotating interfaces were solved by means of the mixing plane approach. Working fluid real properties are characterized using the Aungier-Redlich-Kwong model and $\kappa-\omega$ shear stress transport is the turbulence model selected. Regarding the solver control parameters, both high-resolution advection schemes and turbulence numerics have been applied. The convergence criterion of the root mean square residuals is set to 10^{-5} while ensuring convergence of total-to-total pressure ratio and polytropic efficiency.

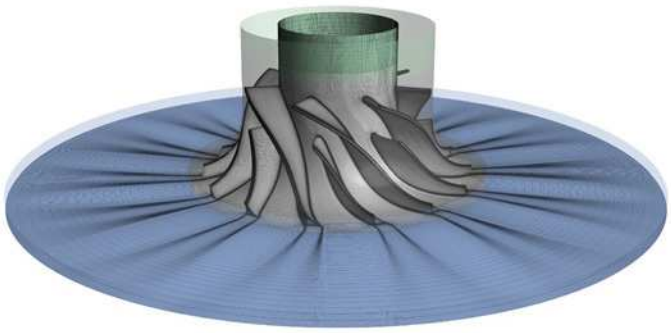

Figure 1: Meshed view of the numerical model solid parts (inlet, impeller and diffuser) of the reference micro-scale centrifugal compressor geometry.

As mentioned above, the design working fluid of the reference geometry is air at inlet design operating point conditions 1 bar and 20 ºC. At these conditions, the chord-based Reynolds number falls in the range of 10^4-10^5, resulting in a viscous sublayer thickening where viscous effects increase. This may affect the velocity flow field and Reynolds number corrections must be used if dynamical similarity is sought. In order to provide a reference operating point at a turbulent enough flow regime, new reference conditions of inlet air at 5 bar and 20 ºC are established applying the methodology proposed by Sebastián *et al.* (2021b), which is analytically and numerically validated. Hence, these conditions are the reference for keeping dynamical similarity through the method proposed in previous Equation 2. This allows to generate homologous operating points using organic vapor at any conditions, obtaining the new rotational speed, mass flow rate and inlet pressure/temperature, which are used as inputs for the numerical simulations. The next section will deal with the selection of the boundary conditions of these new sets using organic fluids.

2.3 Organic vapors and operating points selection

Two low global warming potential and zero ozone depletion potential non-toxic organic compounds have been selected for this analysis: propane and isobutane. These working fluids have been proposed for different environmentally-friendly small-scale turbo-heat-pump-based energy systems, such as Sebastián *et al.* (2021a). Figure 2 collects in an enthalpy-entropy diagram the selected operating points for both propane and isobutane working fluids, where also temperature contour levels can be observed. A set of homologous points are calculated at 1 bar and 25 ºC inlet conditions for both media. These corresponding polytropic compression lines are represented far from the saturation line at increased specific entropy values, but still in the vapor region. Then, three operating points are fixed in the pursuit of simulating a near-saturation line compression, similar to those compressions for heat pump-like systems. Inlet pressure has been selected in relation to the saturation pressure at 5 ºC, 25 ºC and 45 ºC considering a compressor suction superheat control of 5 K. These boundary condition temperature levels have been selected to represent evaporating lines for heat pumps providing cooling, air heating and heat upgrading, respectively. These eight homologous operating points will be the object of numerical analysis in the next Section.

These dense vapor compression processes entail a non-perfect thermodynamic behavior. Figure 3a shows the compressibility factor evolution at isentropic compressions lines for the studied compressors operating points. While the perfect gas behavior can be noted using air, propane and isobutane operating points provide significant variation of $Z \neq f(s)$. This means that the selected conditions are closer to a non-perfect gas than to a perfect vapor behavior. Meanwhile, Figure 3b represents the variation in the speed of sound at the selected compression lines where its decrease along the compression features non-ideal effects. These operating points, Pr. #2-4 and Ib. #2-4, feature a fundamental derivative Γ below 1 (in the range of 0.88-0.98). One may also note a lower variation using the organic vapors than using air, which may ease the dynamical similitude behavior preservation.

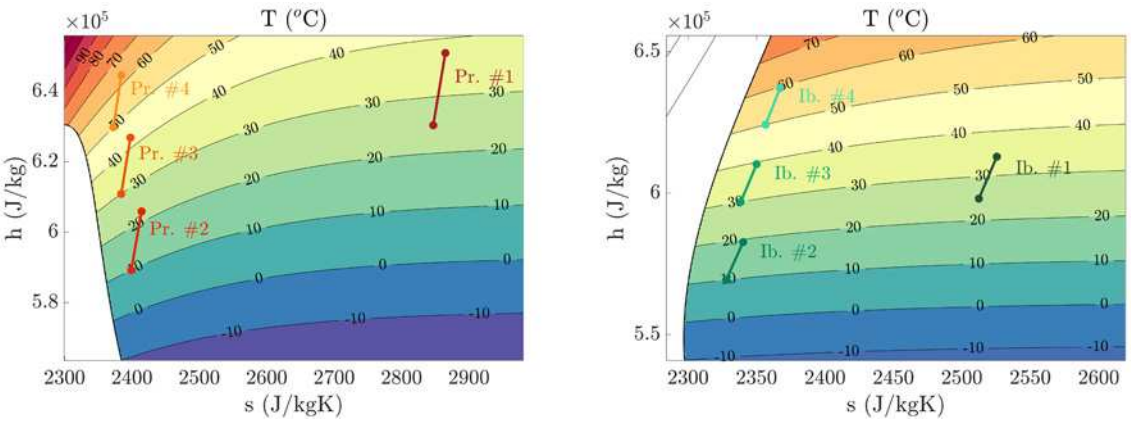

a) Propane b) Isobutane

Figure 2: Temperature contours on an enthalpy-entropy diagram for both organic fluids. The resultant compression lines for the set of studied operating points are marked and labelled. Pr. and Ib. stands for propane and isobutene, respectively.

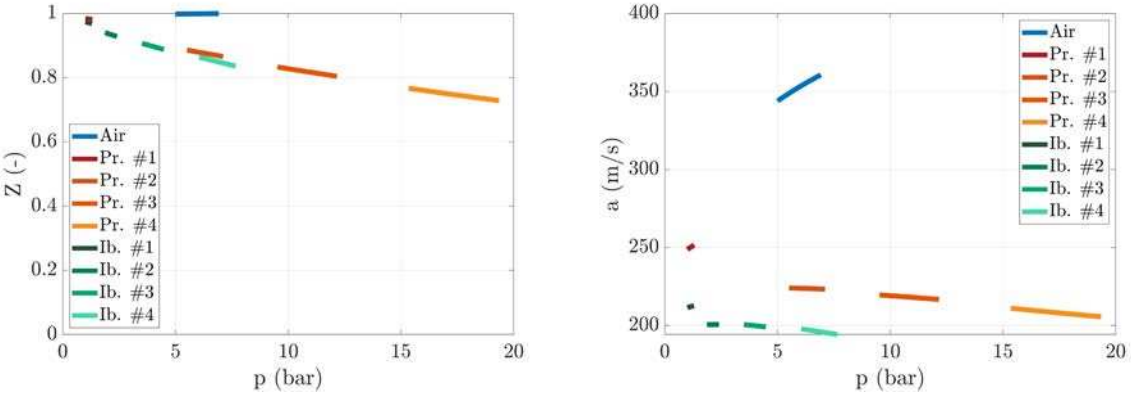

a) b)

Figure 3: Compressibility factor (a) and speed of sound (b) evolution at the studied isentropic compression lines for the set of new operating points to be numerically simulated.

640

3 RESULTS

The results section is structured as follows: first, the analytical results obtained through the proposed generalized similarity-based methodology for the selected organic fluids and operating conditions set in the previous section; next, numerical results are shown to confirm dynamical similarity preservation; finally, averaged numerical key indicators are compared with analytical indicators to understand the source of deviations when scaling to organic fluids.

3.1 Analytically-obtained similitude for the selected organic operating points

Table 1 collects the results of applying the similarity-based methodology to the set of points selected for this analysis. One may note that keeping dynamical similitude while varying the working fluids and pressure/temperature conditions leads to a blade Mach number (Π_n), a dimensionless mass flow rate ($\Pi_{\dot{m}}$) and the isentropic stage loading coefficient ($\Delta h_s/a_{01}^2$) constant. *Re* values are all above 10^5 which allows neglecting the influence of this number on key performance indicators assuming a fully developed turbulent flow regime. Regarding $Ec^{*0.5}$, small deviations are observed for both propane and isobutene. These deviations increase following the rise in compressor inlet pressure, leading to an $Ec^{*0.5}$ study range of 0.183-0.253. Meanwhile, near-zero *Tr* values are obtained with negative values due to the negative compressibility factor slope along the previously shown organic compressions. It is

interesting to highlight that despite these notable slopes shown in previous Figure 3a, the factor composed of rotational speed, density and characteristic dimensions is not large enough to obtain a non-zero *Tr*. For instance, the first factor of *Tr* in Pr. #3 operating point is $4.4 \cdot 10^4$, while its compressibility factor slope is $-1.1 \cdot 10^{-7}$. A doubled rotational speed and five times the inlet density would be needed to obtain a *Tr* around -0.1. This means that at present subsonic Mach conditions (<0.6) using the proposed organic vapors, non-ideal flow can be assumed as perfect vapor behavior. Finally, resultant variations of the total-to-total pressure ratio (β_{TT}) are shown.

Table 1: Resultant dimensionless numbers calculated using the proposed scaling laws for the selected operating points. Pr. and Ib. stands for propane and isobutene, respectively.

	Air (ref)	Pr. #1	Pr. #2	Pr. #3	Pr. #4	Ib. #1	Ib. #2	Ib. #3	Ib. #4
p_{01} (bar)	1.0	1.0	5.5	9.5	15.3	1.0	1.9	3.5	6.0
T_{01} (ºC)	20	25	10	30	50	25	10	30	50
Π_n (-)					0.214				
$\Pi_{\dot{m}}$ (-)					0.043				
Re (-)	$4.8\ 10^5$	$2.4\ 10^5$	$1.4\ 10^6$	$2.2\ 10^6$	$3.2\ 10^6$	$2.9\ 10^5$	$5.9\ 10^5$	$1.0\ 10^6$	$1.6\ 10^6$
$Ec^{*1/2}$ (-)	0.253	0.222	0.207	0.196	0.183	0.217	0.213	0.206	0.196
Tr (-)	0	-0.001	-0.003	-0.005	-0.006	-0.001	-0.002	-0.003	-0.005
$\Delta h_s/a_{01}^2$ (-)					0.242				
β_{TT} (-)	1.384	1.306	1.290	1.277	1.261	1.294	1.289	1.280	1.268

3.2 Numerical validation of velocity flow field similarity

This subsection aims to prove and validate that dynamical similarity is achieved in numerical simulations through the inputs generated by the proposed generalized scaling laws. Mass flow averaged absolute (*Ma*) and relative (Ma_w) Mach numbers are shown in Figure 4a at different stations along the compressor stage. Reference air design point is plotted together with the eight selected operating conditions using propane and isobutane. Their relative differences with the reference case are shown in Figure 4b. One may note that an average ±2.5% of discrepancy is found. In addition, there is a reasonably good Mach agreement among the operating points using organic vapor flows, especially across the impeller. This confirms that homologous conditions provided by the analytical scaling entails that dynamical similarity conserves the dominant flow Mach numbers.

641

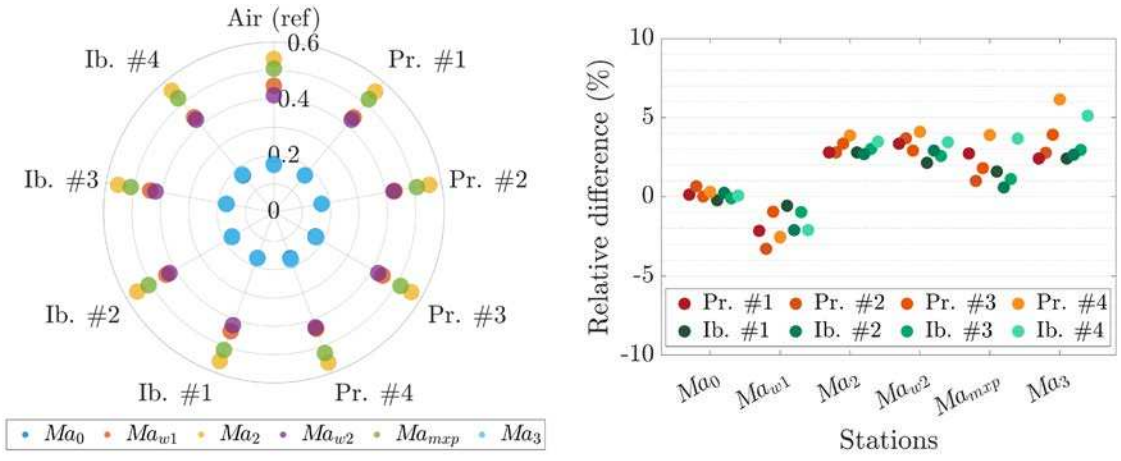

a) b)

Figure 4: Absolute (*Ma*) and relative (Ma_w) mass flow averaged Mach number at different stations: a) values and b) relative difference vs air. (0: inlet, 1: near impeller leading edge, 2: near impeller leading edge, *mxp*: mixing plane, 3: diffuser outlet) for all the operating points set selected.

Two organic operating points using propane at the highest pressure (Pr. #4) and isobutane at the lowest (#Ib. 1) are selected to verify that not only averaged Mach numbers are preserved but also the velocity flow fields. Figures 5a and 5b show both absolute and relative Mach number contours on a compressor blade-to-blade view at half span location to perform a qualitative comparison One may observe the similar main flow structure, the similar incidence at leading edge, and the same tip-leakage-induced bubble at the trailing edge suction side. Therefore, it can be confirmed that homologous working conditions on an organic micro-scale turbocompressor are achieved.

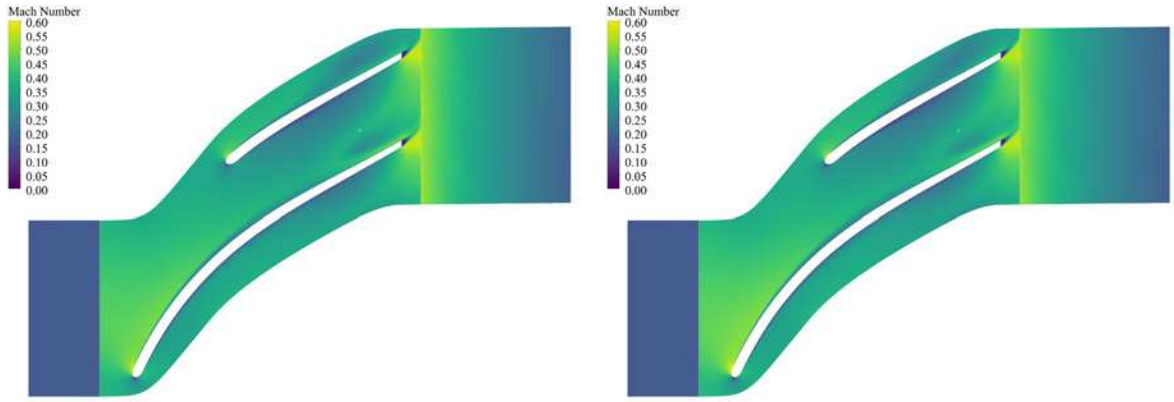

a) Pr. #4 b) Ib. #1

Figure 5: Mid-span blade-to-blade view of stationary and relative Mach number for two selected operating points at organic vapor conditions.

3.3 Numerical-analytical comparison

642

Once similitude is numerically proven for the selected organic vapors conditions, it is interesting to analyze the analytical-numerical deviations on key performance indicators and the emerging trends between different thermodynamic properties. It is shown the relationship between the total-to-total pressure ratio and the compressibility factor (Figure 6a) and also between the real isentropic pressure-volume exponent (Figure 6b) through the proposed analytical dynamic similitude method (DS) and using the numerical model (CFD) for all the simulated operating points. One may remark that pressure ratio trend is properly predicted despite Z and γ_{pv} are not explicitly considered as independent dimensionless groups scaling the organic fluid through the DS method. The relationship between the isentropic loading coefficient and the mentioned thermodynamic properties can be shown in Figure 6d-6e. Deviations between analytical and numerical results do not form an identifiable pattern as expressed in the mentioned plots. This means that the key performance indicator is not exactly kept and its deviations could not be followed by Z and γ_{pv}, which are two of the main non-ideal gas thermophysical properties. In other words, isentropic loading coefficient deviations are not caused by the organic vapor non-perfectness itself since good matches can be found at high and low γ_{pv}.

As explained in Subsection 3.1, variations on Traupel number cannot be responsible for these variations since their values were in the range -0.006 up to 0 in the selected conditions set. Hence, alterations on the second new dimensionless number (the modified Eckert number) are studied. Figure 6c shows the impact of these variations on the relative static impeller outlet temperature. A substantial change when moving to organic vapors can be appreciated and then is kept among the different data points. Nevertheless, Figure 6f does not show a clear pattern between both parameters. Hence, it cannot be stated that the variations on this new dimensionless number in the range of 0.183-0.253 convey an effect on the chosen similitude key performance indicator. Overall, one may find a notable good agreement between CFD and DS method on the resultant total-to-total pressure ratio, thus the scaling analysis works.

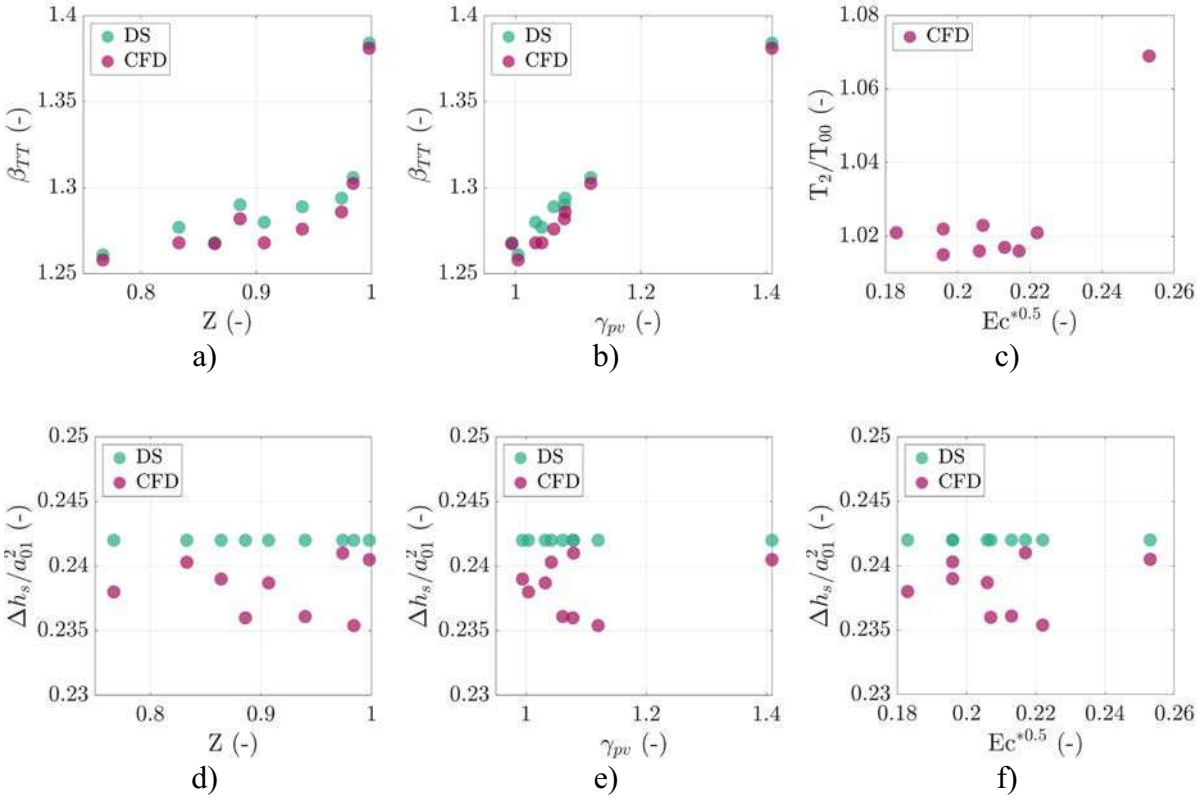

Figure 6: Scatter plots among selected variables for the whole set of operating points comparing dynamical similitude (DS) calculations versus numerically obtained (CFD) results.

643

4 CONCLUSIONS

The present study investigates the non-ideal effects on a small radial turbocompressor when similitude is sought for two organic fluids at different operating conditions near the saturation line, where heat pump-like systems work. In light of the results of this paper, the following findings can be drawn:

- The upgraded version of the generalized flow turbomachinery dynamic similarity method proposed in this work is able to capture non-ideal effects and provides an accurate pressure ratio prediction including implicit variations on compressibility factor and real isentropic pressure-volume exponent. These trends have been numerically validated. Hence, the scaling analysis can be performed without taking compressibility factor and real isentropic pressure-volume exponent as independent dimensionless groups.
- Dynamical similarity conditions are numerically checked through averaged Mach numbers across the stage but also along the velocity flow fields. This means that analytically-generated input conditions to the CFD model are well computed.
- The set of operating points at different conditions and organic vapors (propane and isobutane) working with the reference micro-scale turbocompressor provide Traupel number values close to zero. Therefore, perfect vapor behavior is expected as Traupel number does not imply a substantial effect. Regarding the modified Eckert number, small variations are detected without a clear trend related to the isentropic loading coefficient.
- Radial micro-turbocompressors scaling from ideal gas to perfect vapor conditions is allowed under the conditions of this study for the pressure ratio prediction.

This study has confirmed the suitability of the scaling method for high-speed radial micro-turbocompressor operating in a thermodynamic area where heat-pump-like systems usually work when using propane and isobutane. Despite the high rotational speed, the near-zero Traupel number leads one to assume perfect vapor behavior. One may wonder when these assumptions cannot be extended. On this basis, the next step will be to study micro-compressors providing higher pressure ratios per stage, to fulfil more closely the requirements of heat pump-based applications. Furthermore, the notable focus on high-temperature heat pumps makes it also interesting to study scaling methods when more relevant non-ideal flow effects dominate.

REFERENCES

aus der Wiesche, S. and Reinker, F., 2022, Dimensional analysis and performance laws for organic vapor flow turbomachinery, Energy, 257, 124635.

Baumgärtner, D., Otter, J. J. and Wheeler, A. P. S., The effect of compressibility factor on turbine performance, Proceedings of the ASME Turbo Expo 2021: Turbomachinery Technical Conference and Exposition, Volume 4, V004T06A020.

Casey, M., Krähenbuhl, D., Zwyssig, C., 2013, The Design of Ultra-High-Speed Miniature Centrifugal Compressors, Proceedings of 10th European Conference on Turbomachinery Fluid dynamics & Thermodynamics, ETC10-004, Lappeenranta, Finland.

Casey, M. and Robinson, C., 2021, Radial Flow Turbocompressors, Cambridge University Press.

Celik, I. B., Ghia, U., Roache, P. J., Freitas, C. J., Coleman, H., and Raad, P. E., 2008, Procedure for estimation and reporting of uncertainty due to discretization in CFD applications. Journal of fluids Engineering-Transactions of the ASME, 130(7):078001–078001–4.

Giuffre, A. and Pini, M., 2021, Design guidelines for axial turbines operating with non-ideal compressible flows, Journal of Engineering for Gas Turbines and Power 143.1: 011004.

Giuffre, A., Colonna, P. and Pini, M., 2022, The effect of size and working fluid on the multi-objective design of high-speed centrifugal compressors, International Journal of Refrigeration, 143, 43-56.

Jeong, Y., Son, S., Cho, S. K., Baik, S., Lee, J. I., 2020, Evaluation of supercritical CO2 compressor off-design performance prediction methods, Energy, 213, 119071.

Macchi, E. and Astolfi, M., 2017, Organic Rankine Cycle (ORC) Power Systems, Woodhead Publishing Series in Energy, Elsevier.

Romei, A., Vimercati, D., Persico, G. and Guardone, A., 2020, Non-ideal compressible flows in supersonic turbine cascades, Journal of Fluid Mechanics, 882, A12.

Schiffmann, J. and Favrat, D., 2010, Design, experimental investigation and multi-objective optimization of a small-scale radial compressor for heat pump applications, Energy, 35, 436–450.

Sebastián, A., Abbas, R., Valdés, M., Rovira, A., 2021, Modular micro-trigeneration system for a novel rotatory solar Fresnel collector: A design space analysis, Energy Conversion and Management, 227, 113599.

Sebastián, A., Abbas, R., Valdés, M., 2021, Analytical prediction of Reynolds-number effects on miniaturized centrifugal compressors under off-design conditions, Energy, 227, 120477.

Sebastián, A., Abbas, R., Valdés, M., 2023, Experimental investigation of key aerothermal phenomena in micro-scale radial turbocompressors, Thermal Science and Engineering Progress, 39, 101748.

Steger, D., Regensburger, C., Eppinger, B., Will, S., Karl, J., Schlucker, E., 2020, Design aspects of a reversible heat pump - organic rankine cycle pilot plant for energy storage. Energy, 208, 118216.

Tosto, F., Lettieri, C., Pini, M., Colonna, P., 2021, Dense-vapor effects in compressible internal flows, Phys. Fluids, 33, 086110.

Van den Braembussche, R., 2019, Design and analysis of centrifugal compressors, JohnWiley&Sons.

Zou, Z. and Ding, C., 2018, A new similarity method for turbomachinery with different working media, Applied Thermal Engineering, 133, 170–178.

ACKNOWLEDGEMENT

This research has been supported by the Spanish *Ministerio de Ciencia e Innovación* under the project of reference number PID2019-110283RB-C32. The authors also would like to thank the reviewers for their valuable feedback and insightful comments.

ORC SEVILLE 2023
7th International Seminar on O.R.C. Power Systems

© 2024 Editorial Universidad de Sevilla. Este es un artículo de acceso abierto distribuido bajo los términos de la licencia de uso y distribución Creative Commons (BY-NC-ND 4.0)

DOI: https://dx.doi.org/10.12795/9788447227457_112

DESIGN, MODELING AND SIMULATION OF AN EXPERIMENTAL RANKINE PTES SYSTEM

Mario Petrollese[1,*], Giorgio Cau[1], Matteo Marchionni[1], Marcello Lorenzo Marroccu[1], Rosa Merchán[2]

[1] *Department of Mechanical, Chemical and Materials Engineering, University of Cagliari, Via Marengo, 2 09123 Cagliari, Italy*
[2] *Department of Applied Physics and Institute of Fundamental Physics and Mathematics (IUFFYM), University of Salamanca, 37008 Salamanca, Spain*

*Corresponding Author: mario.petrollese@unica.it

ABSTRACT

Pumped Thermal Energy Storage (PTES) is a promising technology for the long-term storage of electrical energy by using thermal energy reservoirs. PTES can be mainly classified into system configuration employing Joule-Brayton cycles and systems using Rankine cycles. With respect to Rankine cycles, the coupling between a high-temperature heat pump with an ORC power system is attracting increasing interest. In this framework, an experimental Rankine PTES system based on the coupling between a kW-scale ORC system with a high temperature heat pump is going to be developed and commissioned. In this paper, the procedure followed for the design of such experimental facility is presented and discussed. Four main configurations are proposed and compared in terms of achievable system roundtrip efficiency and minimization of the exergy destruction rate. Results demonstrate that roundtrip efficiencies lower than 40% are reached with the use of out-of-shelf devices, while by a proper system configuration and the customized design of the heat engine and heat pump, roundtrip efficiencies higher than 60% can be achieved.

1 INTRODUCTION

Long-term energy storage is currently considered as a key technology to increase the penetration of renewables in the energy mix, and thus accelerate the transition towards a decarbonized economy. Among the possible technologies, Pumped Thermal Energy Storage (PTES) emerges as a promising solution (Tian & Xi, 2022). During charging phase, surplus electricity feeds a Heat Pump (HP), which transfers heat from a cold reservoir to a hot one. The electrical energy is therefore stored in the form of heat in a Thermal energy storage (TES) system. During the discharging phase, a heat engine uses the heat stored at the hot reservoir to convert it back to electrical energy. Main advantages of PTES systems include low costs, high scalability, flexible operation, long operating life, small footprint and low self-discharge rate (Benato & Stoppato, 2018). Usually heat engines employed within PTES architecture are based on two main thermodynamic cycles: Joule-Brayton and Rankine. Brayton PTES systems can operate at higher temperatures with consequent higher efficiencies. Nevertheless, PTES systems based on Rankine technology, especially Organic Rankine Cycles (ORC), are more compact, their components are technically mature and can convert heat available at lower temperatures, which facilitates thermal integration with the TES and heat pump system and in turn reduces costs (Dumont & Lemort, 2022). A typical Rankine PTES system is composed by a heat pump, two or more thermal reservoirs and an ORC unit. The heat pump, in its simplest configuration, embeds a compressor, a condenser, an expansion valve and an evaporator. More complex layouts include a recuperator or a second compressor to improve performance. The implementation of trans-critical thermodynamic cycles is also considered a promising way to improve heat pumps efficiency (Dumont & Lemort, 2022). On the other hand, an ORC engine in its more basic form presents an evaporator, a turbine, a condenser and a pump. Possible ways of improving performance also in this case include the introduction of a

recuperator, the heat recovery stage occurring above the working fluid critical pressure, the use of flash or triangular cycles as well as the adoption of zeotropic mixtures (Dumont & Lemort, 2022). In the literature, some works explored these possible alternatives, for instance (Tian & Xi, 2022) compared four Organic Flash Cycles with a basic ORC and found that the latter presents better economic metrics, higher roundtrip efficiency and increased exergy efficiency. The analysis also revealed that improving the roundtrip efficiency and the economic viability of Rankine PTES systems is critical to accelerate the path towards commercialization. Concerning the working fluid, several studies identify the R1233zd(E) as an optimal solution (Eppinger et al., 2021,), with R1234ze(Z), R245fa and pentane showing similar performance (Frate et al., 2020). In general, the heat pump compressor represents the largest cost item in such systems and, while Rankine PTES are currently not cost-competitive compared to other storage solutions, they are expected to become bankable in the future due to forecasted cost reductions (Tillmanns et al., 2022).

Despite the research available on this technology, few works have been devoted to the experimental investigation of Rankine PTES systems. Among them, CHESTER project (*CHESTER Project*, 2018) employs a high-temperature HP and an ORC unit and stores both sensible and latent heat. Both units employ R1233zd(E) as working fluid (Hassan et al., 2022).This pilot plant has already been launched and first experimental tests are being conducted (Steger et al., 2021). However, the availability of experimental data is still scarce, and more research is required also at a theoretical level to assess the techno-economic feasibility of such technology (Dumont & Lemort, 2022).

For this reason, an experimental PTES plant composed by a high temperature HP, two thermal reservoirs and a kW-scale ORC is going to be developed and commissioned with the objective of advancing the Technology Readiness Level (TRL) of Rankine PTES systems. The experimental activity will allow to characterize the performance of the storage system during nominal, off-design and transient operating conditions, with the possibility of identifying the most critical parameters affecting the system performance during charge and discharge operations. In this paper, the methodology followed during the preliminary design phase of the experimental set-up is presented. Four different system configurations will be considered and compared. The basic one starts from considering commercially available units, while the remaining three explore more complex layouts tailored for the application. The improvement of the latter configurations compared to the basic one will be measured in terms of increasing the roundtrip efficiency of the overall energy storage system and minimizing the exergy destruction rates at a component level. The system performance has been also investigated for different operating conditions of the heat pump, mainly varying the inlet temperature at the heat pump evaporator.

646

2 SYSTEM CONFIGURATION

As shown in Figure 1, the experimental facility includes a heat pump and an ORC system integrated with each other through a TES subsystem. The latter consists of two storage tanks at different temperature levels (hot tank and cold tank) and two pumps. These pumps enable the circulation of a heat transfer fluid (based on the expected working temperatures a thermal oil is chosen) to transfer the thermal power supplied by the heat pump to the ORC engine. During the charging phase, a high-temperature heat pump based on a reverse Rankine cycle (subsystem on the left) is used to raise the temperature of the heat transfer fluid, which is subsequently stored in the hot tank. The compressor (COMP.HP) and the thermal oil pump (PUMP2.TES) are coupled with inverter-driven electrical motors. An electric heater is included at the evaporator inlet side to simulate various inlet temperature conditions. This allows testing the performance of the heat pump under different operating conditions, representing real-life scenarios where the system is powered by a PV system as the electricity supplier and a solar thermal system as the heat source. During the discharge phase, the heat transfer fluid stored in the hot tank is used as a heat source for the ORC system (subsystem on the right). Similarly, the pumps are coupled to inverter-controlled electric motors. The thermal oil pump (PUMP1.TES) is controlled to meet the desired electrical power, while the organic fluid pump (PUMP.ORC) is operated to adjust the ORC evaporating pressure according to the controller logic.

Based on preliminary evaluations, the design temperature of the hot tank has been set at 140°C, and an ORC unit with a net power output of approximately 15 kW has been considered. Currently, in this preliminary phase of the study, four alternative configurations for the heat pump and the ORC system are being examined:

- *Configuration A*: both HP and ORC are based on products already available on the market.
- *Configuration B*: a commercial ORC system is considered while the design of the heat pump is optimized for the application considered.
- *Configuration C*: both the heat pump and the ORC system expressly conceived for this application are designed. Specifically, the introduction of an intermediate TES system and the introduction of subcooling sections downstream of the COND.HP and upstream of the EVAP.ORC is considered.
- *Configuration D:* same heat pump design as configuration B and the ORC system equipped with an additional heat exchanger and volumetric machine able to expand the working fluid under two-phase conditions to implement an additional triangular cycle.

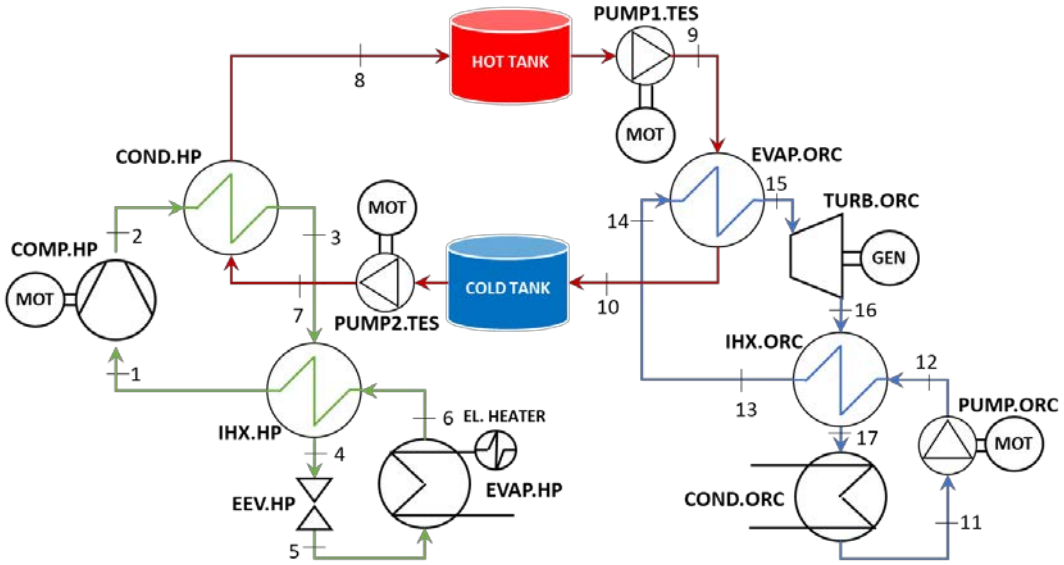

Figure 1: System configuration of the experimental Rankine PTES system.

3 METHODOLOGY

A model of the system has been developed in MATLAB software to evaluate the performance of the heat pump, TES section and ORC unit under design conditions. Thermophysical properties for water and organic fluids have been obtained through CoolProp (Bell et al., 2014) while the thermal oil has been characterized by data provided by the manufacturer (Eastman, n.d.). For both HP and ORC models, temperature, pressure, entropy and enthalpy of each point have been calculated by establishing flow mass and enthalpy balances and taking into account compressor and turbine isentropic efficiencies and pump efficiency (the assumed values are reported in Table 1), while pressure drops within components have been neglected. Based on recommendations provided by (Hassan et al., 2020), the maximum temperature reached at the outlet side of COMP.HP has been limited to 160°C.
The exergy of each subsystem has been also computed in order to analyze the exergy efficiency and the exergy losses at component level. The classical exergy rate balance equation at steady state has been implemented for each component, as follows:

$$\sum \dot{m}_i e_i + \dot{Q}\left(1 - \frac{T_a}{T_c}\right) = \sum \dot{m}_o e_o + \dot{W} + \dot{E}_D \qquad (1)$$

where $\dot{m}$ is mass flow rate of the stream substance, $\dot{Q}$ is heat flow through component boundary, T_a is the ambient temperature, T_c is the temperature at component boundary, at which heat is exchanged with the environment, e is the specific exergy of the stream (based on the system configuration only the physical exergy defines the total specific exergy of such streams), $\dot{W}$ is work rate of the component, and $\dot{E}_D$ is the exergy destruction in the component due to irreversibility. Subscripts i and o represent inlet and outlet to and from the component, respectively.

Table 1: Main assumed efficiencies in the model.

TURB.ORC isentropic efficiency	Pump efficiency	ORC Organic efficiency	COMP.HP isentropic efficiency	COMP.HP electro-mechanical efficiency	TES efficiency
0.7	0.6	0.9	0.8	0.95	0.98

The roundtrip efficiencies expressed in energy and exergy terms have been used as main performance indexes of the PTES system. Specifically, the roundtrip efficiency expressed in energy terms (η_{RT}) is defined as the ratio between the electrical energy produced by the ORC (W_{ORC}) during a complete discharge phase and that absorbed by the heat pump (W_{HP}) during a fully charging phase. By assuming that the heat pump and ORC always operates at nominal conditions, η_{RT} can be also computed as the multiplication of the Coefficient of Performance of the Heat Pump (COP_{HP}) by the efficiency of the ORC (η_{ORC}) and by the efficiency of the TES system (η_{TES}):

$$\eta_{RT} = \frac{W_{ORC}}{W_{HP}} = \frac{\dot{W}_{ORC} \cdot t_{DIS}}{\dot{Q}_{EVAP.ORC} \cdot t_{DIS}} \cdot \frac{\dot{Q}_{EVAP.ORC} \cdot t_{DIS}}{\dot{Q}_{COND.HP} \cdot t_{CH}} \cdot \frac{\dot{Q}_{COND.HP} \cdot t_{CH}}{\dot{W}_{COMP.HP} \cdot t_{CH}} = \eta_{ORC} \cdot \eta_{TES} \cdot COP_{HP} \quad (2)$$

where t_{DIS} and t_{CH} are the discharging and charging times, respectively. Instead, the exergy roundtrip efficiency is defined as the ratio of the overall exergy produced by ORC (which corresponds to electrical energy) and the overall exergy introduced in the HP, that is, the sum of the electrical energy absorbed by the compressor and the exergy introduced in the evaporator of the heat pump ($\dot{E}_{EVAP.HP}$):

$$\eta_{EX,RT} = \frac{\dot{W}_{ORC}}{\dot{E}_{EVAP.ORC}} \cdot \frac{\dot{E}_{EVAP.ORC} \cdot t_{DIS}}{\dot{E}_{COND.HP} \cdot t_{CH}} \cdot \frac{\dot{E}_{COND.HP}}{\dot{W}_{COMP.HP} + \dot{E}_{EVAP.HP}} \quad (3)$$

4 RESULTS

4.1 Configuration A

The first configuration analyzed concerns the use of an off-the-shelf high temperature HP and a commercial ORC unit. To evaluate the expected performance of this configuration, the technical data reported in the datasheets of the commercial units produced by Rank (Rank, n.d.) have been used as a reference. The declared nominal efficiency of the ORC unit is about 10% while the heat pump COP achieved with a temperature lift of 40°C (which means an inlet water temperature at EVAP.HP of 100°C) is about 4. Consequently, the roundtrip efficiency of this PTES system should be lower than 40%. With the aim of identifying the main exergy losses and introducing some improvements on the system configuration, an exergy analysis has been carried out. As a first step, the thermodynamic cycles of the two subsystems have been defined. The refrigerant R1233zd(E) has been assumed as working fluids for both the ORC system and the HP, since it is a fluid with a very low greenhouse effect, non-flammable and with no impact on ozone depletion. Other assumptions are a minimum temperature difference in the heat exchangers of 10°C and a subcooling of the working fluid at COND.HP of 5°C.
Figure 2 shows the T-s diagram of the ORC cycle and of the heat pump expected at design conditions with a water inlet temperature at the heat pump evaporator of 100°C. The calculated performance resembles the data declared by the manufacturer. In this configuration, the electrical power absorbed by the HP is about 30 kW while the thermal power required by the ORC unit is 15% greater than the amount provided by the HP, meaning that the system shows a reduced duration in the discharge phase.

The exergy analysis of this PTES system (Figure 3(a)) highlights that the main irreversibility occurs in the machines (TURB.ORC and COMP.HP). However, reducing these endogenous exergy destructions is hindered by the current technological state-of-art. Significant irreversibility occurs also in the heat exchangers, especially in the EVAP.ORC. These losses can be reduced by decreasing the minimum allowed temperature (with a consequent increase in the heat transfer area) but since they are mainly exogenous, its minimization can be reached only reducing the mean temperature difference. By assuming a water inlet temperature at the EVAP.HP of 100°C, an energy and exergy roundtrip efficiency of about 41% and 27%, respectively, are expected. Decreasing the water inlet temperature at EVAP.HP results in an increase in the temperature lift provided by the heat pump. Consequently, as shown in Figure 3(b), this leads to increased exergy losses and degradation of the overall PTES performance, with a drop in the roundtrip efficiencies up to 20% and a decrease in the thermal power produced by heat pump.

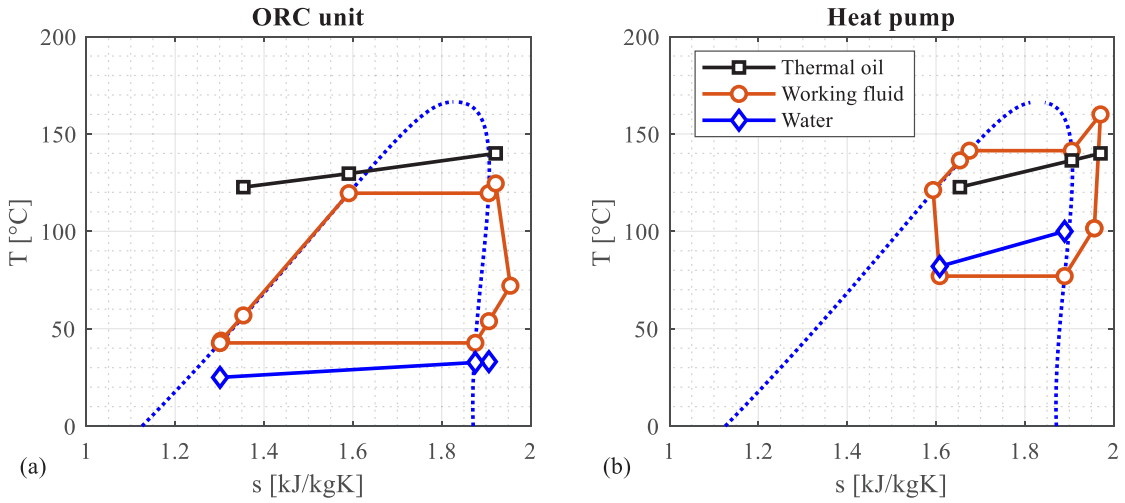

649

Figure 2: Thermodynamic cycle of (a) ORC unit and (b) heat pump for the configuration A.

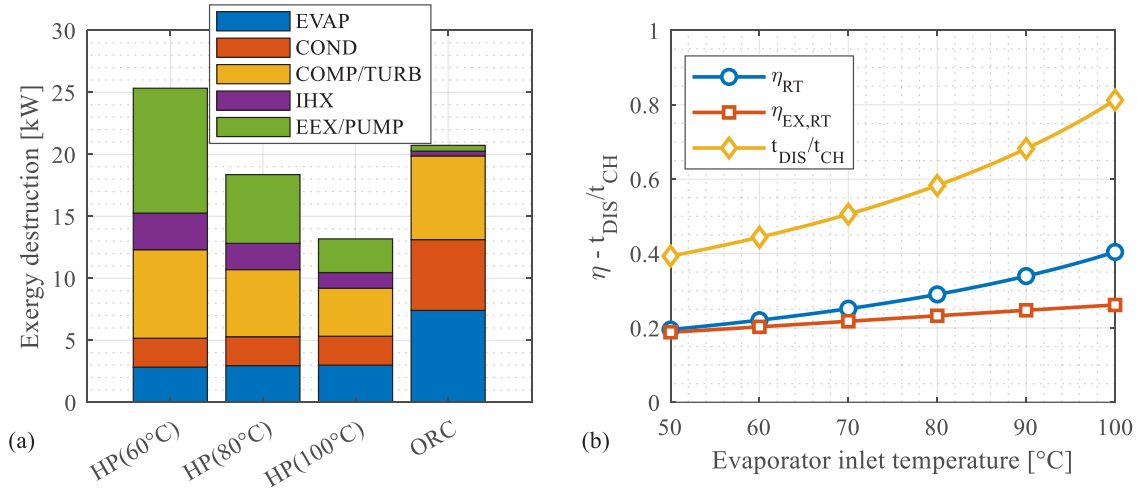

Figure 3: (a) Exergy destruction in the heat pump and ORC and (b) expected performance indexes as a function of the evaporator inlet temperature for configuration A.

4.2 Configuration B

An alternative configuration features a commercial ORC engine and a custom HP through the addition of a sub-cooler downstream of the condenser. Moreover, different types of working fluid of the heat pump are analyzed to identify the solution that allows to maximize the HP performance. In a preliminary

screening step, the selection space has been reduced to a group of organic fluids considering criteria as critical temperatures falling within the range of 150-245 ºC, low flammability, as well as Ozone Depletion Potential (ODP) and Global Warming Potential (GWP) lower than 5. Afterwards, a parametric analysis aimed at maximizing the COP by varying the inlet water temperature at the EVAP.HP has allowed to further reduce the list of suitable candidates. Figure 4(a) shows the ones with the highest potential to maximize the roundtrip efficiency of the system. In general, the fluids selected show better performance compared to the fluid used in the commercial heat pump (R1233zd(E)), with an increase of 10-15% in the energy roundtrip efficiency. At higher evaporating temperature (above 60°C), n-hexane leads to the highest energy roundtrip efficiency (53%), while slightly lower performance is achieved by acetone and cyclopentane. On the other hand, acetone should be preferred below these temperatures although the performance improvement over that obtained by using n-hexane is marginal (less than 1 percentage point). To better understand the effect of the chosen working fluid on PTES performance, Figure 4(b) compares the exergy destruction between acetone and n-hexane for temperatures at the HP evaporator inlet of 60ºC and 100ºC. Compared to the previous configuration, the main advantages come from the reduction of the exergy losses in the EEX and IHX. This is mainly due to the introduction of a sub-cooler downstream of the condenser, which decreases both the average temperature difference in the IHX and the fluid cooling occurring in the EEX. At 60°C no Internal Heat Exchanger (IHX) is considered for acetone since it is a wet fluid. A reduction in exergy destruction can be observed with higher evaporating temperatures, which allow to reduce the exergy losses in the compressor, internal heat exchanger and electronic expansion valve. At an evaporator temperature of 100ºC, the exergy destruction for the n-hexane case is about 8% lower than that of acetone thanks to the lower irreversibility introduced in the EEX.

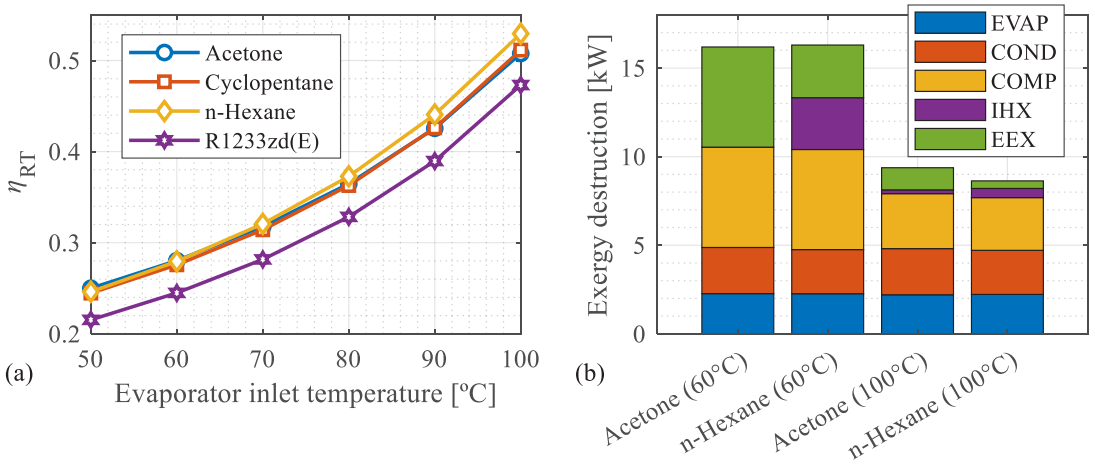

Figure 4: (a) Roundtrip efficiency and (b) exergy destruction in the heat pump at two evaporator inlet temperatures for configuration B.

4.3 Configuration C

In this third configuration, in addition to the design of a custom heat pump, the design of the ORC unit is also optimized with the aim of maximizing the roundtrip efficiency of the PTES system. The exergy analysis of the first configuration highlighted the important exergy destruction occurred in the ORC heat exchangers. To reduce it, the minimum temperature difference at the EVAP.ORC and COND.ORC is lowered to 5°C by increasing their heat transfer area. Furthermore, since the main irreversibility in the EVAP.ORC occurs in the liquid-to-liquid heat transfer stage, a preheater is introduced into the ORC layout together with an intermediate TES tank. The new arrangement allows to lower the thermal oil mass flow rate circulating in the preheater with respect to that circulating in the evaporator. The better match between the flow streams allows then to improve the heat transfer and decrease the exergy destroyed in the heat exchangers. The T-s diagram of the thermodynamic cycle realized by such a configuration is shown in Figure 5(a). Obviously, a proper modification of the HP layout with the

introduction of a sub-cooler downstream of the condenser is also required. This change allows to keep the same temperature level at the intermediate TES and to operate with a ratio between mass flow rate circulating in the HP sub-cooler ($\dot{m}_{SC.HP}$) and that circulating in the condenser ($\dot{m}_{COND.HP}$) equal to the ratio between the flow rate circulating in the ORC preheater ($\dot{m}_{PHX.ORC}$) and in the subsequent evaporator ($\dot{m}_{EVAP.ORC}$). The improvements on the performance of the PTES system consequent to the layout proposed in configuration C are shown in Figure 6. A further increase in the energy roundtrip efficiency of about 8-10 percentage points is achieved compared to configuration B reaching values higher than 60% for inlet water temperature at EVAP.HP of 100°C and minimum allowed ratio between thermal oil circulating in ORC preheater and evaporator. In fact, as can be observed in Figure 6(a), the lower the ratio of the mass flow rates is, the greater the increase in the PTES roundtrip efficiency (at the same time, this also requires the introduction of a larger intermediate TES). This is mainly due to the increasingly reduction of the average temperature difference between cold and hot flow during the preheating phase of the ORC working fluid, with a consequent decrease in the exergy losses in this component. This is confirmed by Figure 6(b), where an important reduction in the exergy destroyed in the EVAP.ORC can be observed compared to previous configurations (about 2 kW instead of 7 kW obtained in the configuration A). It should be noted that there is minimum value of the ratio $\dot{m}_{PHX.ORC}/\dot{m}_{EVAP.ORC}$, which occurs when the temperature difference at the ORC preheater between the incoming organic fluid and the outgoing heat transfer fluid reaches the minimum value (5°C).

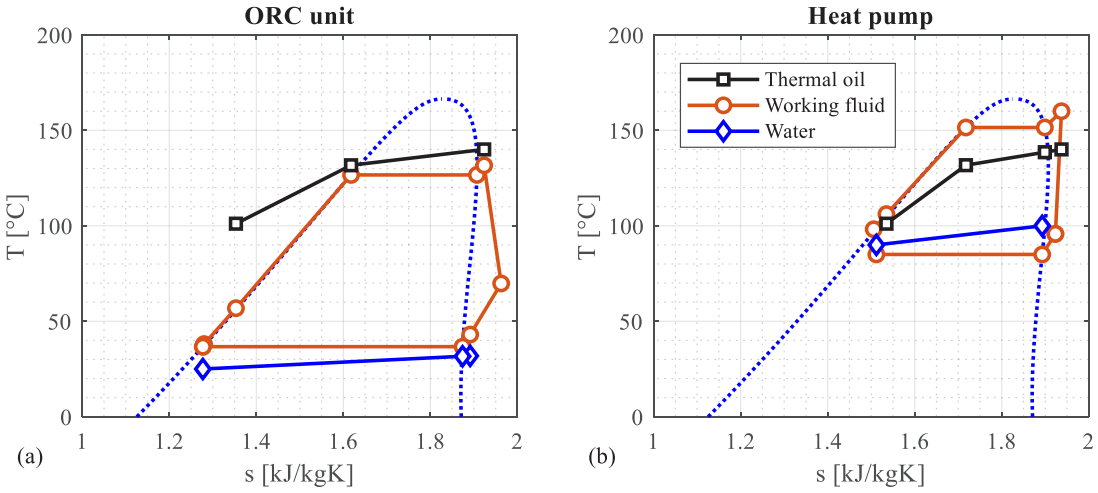

Figure 5: Thermodynamic cycle of (a) ORC unit and (b) heat pump for the configuration C.

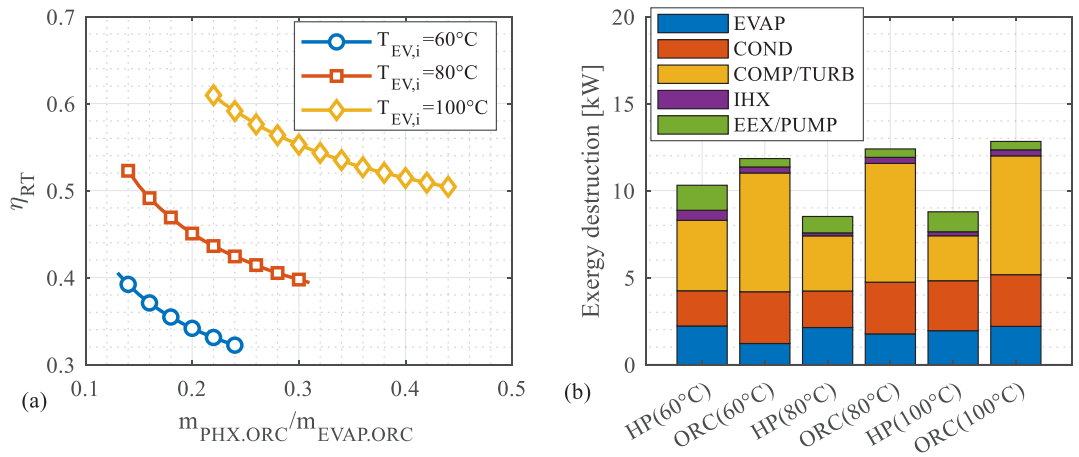

Figure 6: (a) Performance indexes as a function of the evaporator inlet temperature and (b) exergy destruction in the heat pump and ORC for configuration C.

4.4 Configuration D

In the last configuration the layout of the TES system is kept in its simplest form, with just two thermal storage tanks, but with the inclusion of a volumetric expander and preheater (PHX.ORC) in the ORC subsystem. This allows to realize an additional Trilateral Flash Cycle (TFC) by processing more mass flow rate in the circuit. In particular, the refrigerant mass flow rate is heated up in the ORC preheater and after split in two streams, one undergoing a two-phase expansion in a volumetric expander and the other one vaporizing and then expanding in the turbine. The T-s diagram in Figure 7(a) shows the thermodynamic cycle realized by this configuration. The advantage of such ORC layout relies in its operational flexibility. The addition of a TFC leads indeed to increase the utilization rate of the ORC, which from one side can exploit heat streams at lower temperatures and thus can be operated in off-design conditions, and from the other side can eventually provide larger quantities of electrical power by utilizing more heat from the TES. Figure 7(b) shows the exergy destruction for the different components of configuration D as well as the irreversibility occurring in the heat pump for different water temperature at the EVAP.HP. It can be seen that the total exergy destruction in the ORC unit is about 15 kW, which is still lower than the 21 kW occurring in the commercial configuration A (Figure **3**(a)), but higher than configuration C (13 kW, Figure 6(b)). This is due to the introduction of the trilateral flash cycle, which being able to generate a lower power per unit of thermal energy provided, reduces the overall efficiency of the power generation. At a component level an advantage of this configuration is the lower exergy destruction rate at the COND.ORC, which however is balanced by a higher exergy loss in the evaporator and the preheater, due to the higher amount of fluid processed.

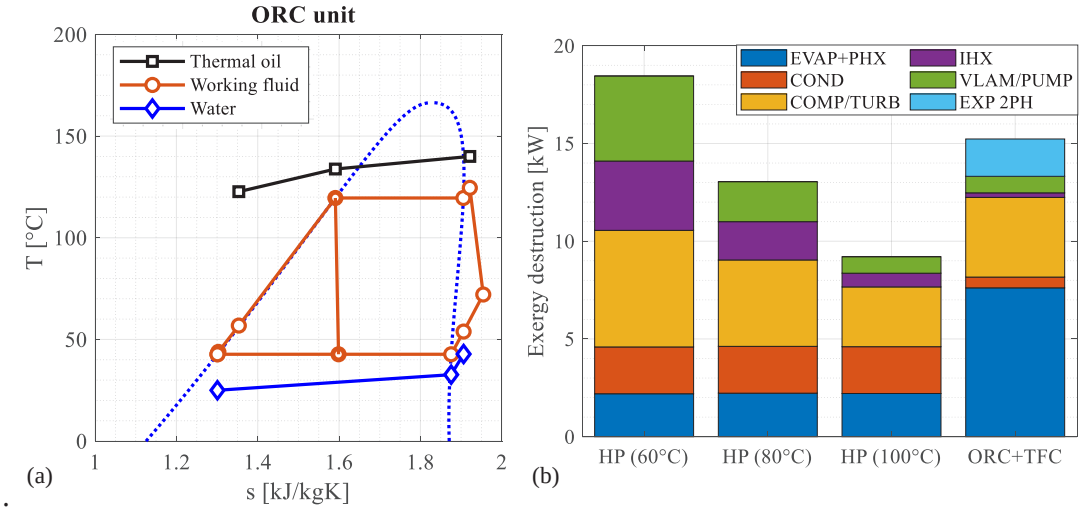

Figure 7: (a) Thermodynamic cycle of ORC unit equipped with a bi-phase expander and (b) exergy destruction in the heat pump and ORC for configuration D.

5 CONCLUSIONS

This paper discussed an experimental Rankine PTES system that is going to be developed and commissioned at University of Cagliari. The design of the facility has been investigated and multiple configurations have been proposed. Three different layouts have been compared to a more conventional solution composed by a commercial ORC and heat pump units integrated with a TES system. It has been demonstrated that by adopting a heat pump and an ORC unit available on the market, important exogenous exergy destructions should occur and expected roundtrip efficiencies lower than 40% should be achieved also with high temperatures at the evaporator inlet side of the heat pump. The three modified configurations allow to reduce the exergy destruction compared to the fully commercial one and so, to improve roundtrip efficiency. When optimizing the heat pump, n-hexane is found to be the optimal working fluid that allows to reach both the highest energy and exergy roundtrip efficiencies (up to 53%) when the inlet water temperature at the evaporator exceeds 60°C, while for lower temperature

652

a wet working fluid as acetone should be preferred. A roundtrip efficiency higher than 60% could be achieved by optimizing the heat transfer between the TES and the ORC system. This has been done by adding a TES tank at intermediate temperature and a dedicated preheater introduced in the ORC layout. The last configuration analyzed, obtained by adding a two-phase expander and a pre-heater upstream the evaporator, leads to slightly lower roundtrip efficiency, 55%, but allows to have a higher operational flexibility in off-design conditions as well as during the power discharge phase. All the obtained results are based on data declared by manufacturer that will be validated during the experimental activities. Moreover, the obtained energy and exergy roundtrip efficiencies are based on the assumption that both the heat pump and the ORC unit always operate under nominal conditions. Obviously, as energy storage, the PTES system will frequently operate under off-design conditions. Therefore, the analysis of the performance under these operating conditions will be numerically and experimentally investigated in the future works.

NOMENCLATURE

Regular symbols

$\dot{E}$	exergy rate	(kW)
$\dot{E}_D$	exergy destruction rate	(kW)
$\dot{m}$	mass flow rate	(kg/s)
$\dot{Q}$	heat flow	(kW)
T	temperature	(ºC)
W	electrical energy	(kJ)
$\dot{W}$	electrical power	(kW)
e	specific exergy	(kJ/kg)
s	specific entropy	(kJ/kgK)
t	time	(h)

Subscripts

CH	charge
DIS	discharge
EX	exergy
RT	roundtrip
a	ambient
c	component boundary
i	inlet
o	outlet

Abbreviations

COMP	Compressor
COND	Condenser
COP	Coefficient of Performance
EEX	Electronic Expansion Valve
EVAP	Evaporator
GWP	Global Warming Potential
HP	Heat Pump
IHX	Internal Heat Exchanger
ODP	Ozone Depletion Potential
ORC	Organic Rankine Cycle
PHX	Pre-heater
PTES	Pumped Thermal Energy Storage
PV	Photovoltaic
SC	Sub-cooler
TES	Thermal Energy Storage
TFC	Triangular Flash Cycle
TURB	Turbine

Greek symbols

η	efficiency	(-)

REFERENCES

Bell, I. H., Wronski, J., Quoilin, S., & Lemort, V. (2014). Pure and Pseudo-pure Fluid Thermophysical Property Evaluation and the Open-Source Thermophysical Property Library CoolProp. *Industrial & Engineering Chemistry Research*, *53*(6), 2498–2508. https://doi.org/10.1021/ie4033999

Benato, A., & Stoppato, A. (2018). Pumped Thermal Electricity Storage: A technology overview. *Thermal Science and Engineering Progress*, *6*, 301–315. https://doi.org/10.1016/J.TSEP.2018.01.017

CHESTER Project. (2018). https://www.chester-project.eu/

Dumont, O., & Lemort, V. (2022). Pumped Thermal Energy Storage Based on ORC. In *Encyclopedia of Energy Storage* (pp. 68–78). Elsevier. https://doi.org/10.1016/b978-0-12-819723-3.00087-1

Eastman. (n.d.). *Therminol SP Heat Transfer Fluid | Therminol | Eastman*. Retrieved April 19, 2023, from https://www.therminol.com/product/71093454?pn=Therminol-SP-Heat-Transfer-Fluid

Eppinger, B., Steger, D., Regensburger, C., Karl, J., Schlücker, E., & Will, S. (2021). Carnot battery: Simulation and design of a reversible heat pump-organic Rankine cycle pilot plant. *Applied Energy*, *288*. https://doi.org/10.1016/J.APENERGY.2021.116650

Frate, G. F., Ferrari, L., & Desideri, U. (2020). Rankine Carnot Batteries with the Integration of Thermal Energy Sources: A Review. *Energies 2020, Vol. 13, Page 4766*, *13*(18), 4766. https://doi.org/10.3390/EN13184766

Hassan, A. H., Corberán, J. M., Ramirez, M., Trebilcock-Kelly, F., & Payá, J. (2022). A high-temperature heat pump for compressed heat energy storage applications: Design, modeling, and performance. *Energy Reports*, *8*, 10833–10848. https://doi.org/10.1016/J.EGYR.2022.08.201

Hassan, A. H., O'Donoghue, L., Sánchez-Canales, V., Corberán, J. M., Payá, J., & Jockenhöfer, H. (2020). Thermodynamic analysis of high-temperature pumped thermal energy storage systems: Refrigerant selection, performance and limitations. *Energy Reports*, *6*, 147–159. https://doi.org/10.1016/J.EGYR.2020.05.010

Rank. (n.d.). *Rank® Organic Rankine Cycle equipment, modules and systems*. Retrieved April 19, 2023, from https://www.rank-orc.com/es/

Steger, D., Karl, J., & Schlücker, E. (2021, October). Launch and first experimental results of a reversible Heat Pump-ORC pilot plant as Carnot Battery. *6 Th International Seminar on ORC Power Systems*. https://mediatum.ub.tum.de/doc/1633021/1633021.pdf

Tian, W., & Xi, H. (2022). Comparative analysis and optimization of pumped thermal energy storage systems based on different power cycles. *Energy Conversion and Management*, *259*, 115581. https://doi.org/10.1016/J.ENCONMAN.2022.115581

Tillmanns, D., Pell, D., Schilling, J., & Bardow, A. (2022). The Thermo-Economic Potential of ORC-Based Pumped-Thermal Electricity Storage: Insights from the Integrated Design of Processes and Working Fluids. *Energy Technology*, *10*(7). https://doi.org/10.1002/ENTE.202200182

ORC SEVILLE 2023
7th International Seminar on O.R.C. Power Systems

© 2024 Editorial Universidad de Sevilla. Este es un artículo de acceso abierto distribuido bajo los términos de la licencia de uso y distribución Creative Commons (BY-NC-ND 4.0)

DOI: https://dx.doi.org/10.12795/9788447227457_113

SMALL-SCALE TURBOPUMPS FOR WASTE HEAT RECOVERY APPLICATIONS BASED ON AN ORGANIC RANKINE CYCLE, MODELING, ANALYTICAL AND EXPERIMENTAL INVESTIGATIONS.

Sajjad Zakeralhoseini*
Ecole Polytechnique Fédérale de Lausanne (EPFL)
Laboratory for Applied Mechanical Design
CH-1015 Lausanne, Switzerland
sajjad.zakeralhoseini@epfl.ch

Jürg Schiffmann
Ecole Polytechnique Fédérale de Lausanne (EPFL)
Laboratory for Applied Mechanical Design
CH-1015 Lausanne, Switzerland
jurg.schiffmann@epfl.ch

*Corresponding Author

ABSTRACT

The organic Rankine cycle (ORC) system is considered a promising technology to exploit thermodynamic potential of waste heat. The weight and size of standard pumps can penalize the benefits of installing an ORC system on vehicles. Small-scale ORC applications would greatly benefit from more compact and efficient pumps. This paper presents the results of numerical and experimental analyses of small-scale turbopumps for ORC systems. A parameterized design tool is developed, allowing the rapid generation of numerous turbopump geometries and their fluid domains. The design tool creates a dataset of numerous turbopumps with different geometrical parameters. The turbopumps are investigated with CFD analysis, and the accomplished results are analyzed to characterize the influence of tip clearance and splitter blades on the performance (slip factor and head rise) of small-scale ORC turbopumps. The numerical results are employed to infer dimensionless maps (specific speed-specific diameter) and 1D models, which enable the capturing of the influence of down-scaling in the early design process of such machines. In the next step, two turbopumps are designed using the new design tool and then tested experimentally to validate the numerical procedure. The good agreement between experimental performance characteristics and developed models validates the computational results and reduced-order models. Following the experimental validation, the performance of an ORC system designed for the waste heat recovery of truck engines is estimated using the performance characteristics of the experimental turbopumps instead of a commercial multi-stage centrifugal pump. The developed turbopumps are one order of magnitude more compact compared to commercial systems. Further, the comparison suggests that the designed turbopumps improve the targeted ORC's thermal efficiency by 0.51% and reduce its back-work ratio by 42% and 67%.

Keywords: small-scale turbopump, organic Rankine cycle, computational fluid dynamics, experimental investigation, pre-design diagrams, 1D models

1. INTRODUCTION

Organic Rankine cycle (ORC) systems are thermodynamic power cycles that can generate electricity from waste heat such as from exhaust gases of internal combustion engines. Pumps that circulate the working fluid through the cycle are an essential component of an ORC system. Organic fluids have a lower latent heat compared to water, which means that a higher mass flow rate is required to generate the same power levels (Bao & Zhao, 2013). Thus, the size and power consumption of the pumping stage increase significantly (Meng et al., 2017). Small-scale systems, however, ease the retrofitting of vehicles, minimizing the need for major engine modifications or extensive reengineering. The compact size also allows for installing waste heat recovery systems in a variety of vehicle types and sizes (Xu et al., 2019). Additionally, the reduced material requirements result in cost savings during the manufacturing and fabrication processes. Hence, there is a need for smaller and more efficient pumps in innovative waste heat recovery systems. Different types of commercial pumps were studied for ORC systems, such as multi-stage centrifugal pumps (Meng et al., 2017; Yang et al., 2019), reciprocating pumps (Landelle et al., 2017),

sliding vane pumps (Bianchi et al., 2017), Roto-Jet pumps (Lei et al., 2016), and diaphragm pumps (Xu et al., 2017). Previous research showed that the choice of pump affects the ORC's efficiency and that some pumps are more suitable for certain conditions than others. For instance, Yang et al. (2019) suggested using pumps with very low specific speeds to achieve a higher thermal efficiency of the ORC system. Meanwhile, Yang et al. (2018) recommended that the thermal efficiency of the ORC system studied by Meng et al. (2017) can be improved if a hydraulic diaphragm metering pump is employed in place of the original multi-stage pump. In summary, there is disagreement on the ideal pumping technology for ORC systems, and a lack of investigation on small-scale pumps suitable for mobile ORC systems.

Pre-design maps and 1D models: Pre-design diagrams for turbopumps (i.e., Balje, 1962; 1981) are useful tools in designing a pump, allowing engineers to quickly select the rotational speed and impeller outlet diameter for a given set of operating conditions. These maps show the relationship between specific speed (Eq. 1), specific diameter (Eq. 2), and efficiency.

$$n_q = \frac{505.158 n Q^{1/2}}{(gH)^{3/4}} \tag{1}$$

$$d_s = d\frac{(gH)^{1/4}}{Q^{1/2}} \tag{2}$$

The maps proposed by Balje (1962), (1981) are based on experimental data from large-scale pumps and are only applicable to pumps operating at high Reynolds numbers (>10^8). Hence, these maps neglect the effects of Reynolds number and relative roughness. However, for small-scale turbopumps typical Reynolds numbers range from 10^5 to 10^6, and predictions from classical Balje maps may entail significant errors.

Once the main parameters are calculated using pre-design maps, 1D models (e.g., Gülich, 2010; Japikse et al., 2006) can be used for selecting other parameters. The advantage of 1D models is that they are computationally efficient and can be used to explore a variety of design alternatives quickly. The 1D models available in the literature (e.g., Gülich, 2010) are developed based on large-scale turbopumps. The influence of down-scaling, which may lead to an imperfect similarity between models and small-scale machines due to variations in Reynolds number, tip clearance ratio, and relative surface roughness, remains unaddressed. The slip factor and head rise coefficient are crucial performance indicators that can be influenced by such variations. Much has been investigated regarding the slip factor, as evidenced by Gülich (2010) and von Backström (2006). However, a slip factor model applicable to unshrouded impellers is still lacking, and the impact of critical factors, such as tip clearance and splitter blades, on these performance indicators remains poorly understood. Recent work by Zakeralhoseini & Schiffmann (2022)a, (2023)b has shown that the slip factor exhibits variation under off-design conditions and both the slip factor and head rise coefficient can be influenced by splitter blades. Consequently, state-of-the-art reduced-order models fall short of accurately characterizing small-scale unshrouded turbopumps.

This study presents updated n_q–d_s diagrams, efficiency estimations, and 1D models that account for the effects of tip clearance and splitter blades in small-scale high-speed turbopumps designed for ORC applications. The models are developed through extensive CFD calculations and can be used for the preliminary design and optimization of such pumps. Two small-scale turbopumps are then designed and tested to highlight the application of the proposed models in designing ORC turbopumps efficiently. These validated design guidelines and n_q–d_s diagrams can aid in the initial design of centrifugal pumps for ORC systems.

2. NUMERICAL PROCEDURE

To establish reliable models, a wide array of training and validation data is required. Therefore, a parametric design tool, which can rapidly create a turbopump geometry is developed and coupled to numerical 3D computations to generate training data on an extensive range of geometries to infer new pre-design tools and 1D models. The methodology implemented for this work is summarized in **Figure 1**. The design tool creates a dataset of 2500 possible geometries for a study of pre-design maps, 576 geometries for a study of tip clearance, and 1620 geometries for a study of the splitter blades within the ranges specified in **Table 1**.

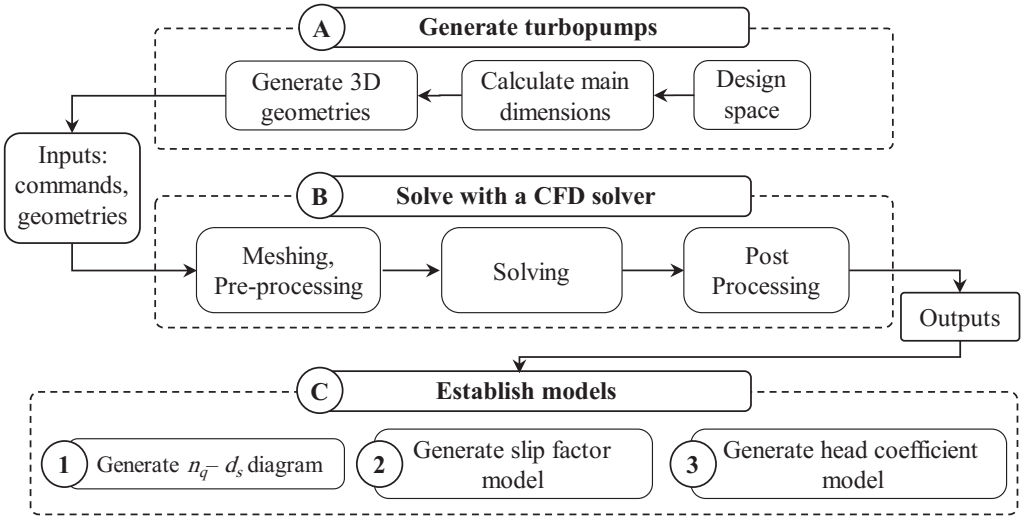

Figure 1 – Methodology flowchart

Table 1 – The parameter ranges of turbopumps for CFD computations

Model	Parameter	Symbol	Unit	Range
Pre-design map	Rotational speed	n	*krpm*	15 – 100
	Mass flow rate	$\dot{m}$	*kg/s*	0.1 – 0.4
	Pressure rise	Δp	*bar*	10 – 25
	Blade outlet angle	β_{2B}	°	18 – 90
1D model: tip clearance	Blade outlet angle	β_{2B}	°	15, 22.5, 27.5, 32, 50, 90
	No. of blades	Z	–	5, 6, 7
	Tip ratio	*c/b*	–	0.05, 0.1, 0.15, 0.2, 0.3, 0.4, 0.6
	Rotational speed	n	*krpm*	40, 50, 63.5, 75
1D model: splitter blade	Blade outlet angle	β_B	°	22.5, 50, 90
	No. blades	Z	–	4, 5, 6
	Tip clearance ratio	*c/b*	%	shrouded, 0.05, 0.1
	Rotational speed	n	*krpm*	40, 50, 75
	Pitch of splitters	φ_{sp}	%	25, 37, 50, 62, 75
	Meridional location of splitters	$m'_{le,sp}$	%	25, 37, 50, 62

For each set of parameters given in **Table 1**, the design tool generates a turbopump geometry by incorporating the equations given in section 2-1 (**Figure 1**, step A).

2-1. Turbopump design and numerical methods

The turbopump design starts by establishing the main parameters of the impeller, followed by the design of a volute to efficiently collect the flow discharged from the impeller.

Impeller. The equations determining the impellers' parameters are summarized in **Table 2**. A hub ratio (υ) of 0.35 and a suction-specific speed (n_{ss}) of 220 are considered to size the inlet diameter. The meridional profiles are shaped systematically for a given medial axis (see Figure 2) and have a linear distribution of the impeller's cross-section areas according to Zakeralhoseini & Schiffmann (2022)a. The blade is shaped 3D and elliptically at the leading edge and narrows to a 2D shape at the trailing edge. The blade angles are determined by two parabolic curves that meet at a common tangent and have the same length, satisfying $\beta_{le} = \beta_{1\mathrm{B}}$ and $\beta_{te} = \beta_{2\mathrm{B}}$.

Volute. The width of the volute is the same as the impeller's outlet width, and the cutwater is positioned at a 17° circumferential angle in the impeller's rotation direction. The volutes are designed with elliptical or circular cross-sections, and the throat area follows the recommendations of Gülich (2010). To establish the

volute cross-sections, the method of conservation of angular momentum (Pfleiderer, 2013) is used. A script is developed to create the 3D geometry of the volute and outlet pipe, utilizing the ANSYS Design Modeler engine to loft the volute profiles.

Table 2 – Impeller's equations

Parameter	Equation	
Head coefficient (Gülich (2010))	$\psi_{opt} = 1.21\, e^{-7.71266\times10^{-3} n_q}$	(3)
Impeller outlet diameter	$d_2 = 60/\pi n \sqrt{2gH/\psi}$	(4)
Inlet diameter	$d_{1,s} = 2.9\left(\frac{Q_{imp}}{n\,(1-\upsilon^2)\tan\beta_{1d}} \times \left(1+\frac{\tan\beta_{1d}}{\tan\alpha_1}\right)\right)^{1/3}$	(5)
Flow angle at the inlet	$\tan\beta_{1d} = (1-\upsilon^2)^{1.1}\,(125/n_{ss})^{2.2}\,\left(n_q/27\right)^{0.418}$	(6)
Leading edge angle	$\beta_{1B} = 0.975\tan^{-1}\beta_1$	(7)
Inlet width	$b_1 = (1-\upsilon)d_1$	(8)
Outlet width	$b_2 = \left[0.017 + 2.62\left(\frac{n_q}{1000}\right) - 8\left(\frac{n_q}{1000}\right)^2 + 9.3\left(\frac{n_q}{1000}\right)^3\right] d_2$	(9)

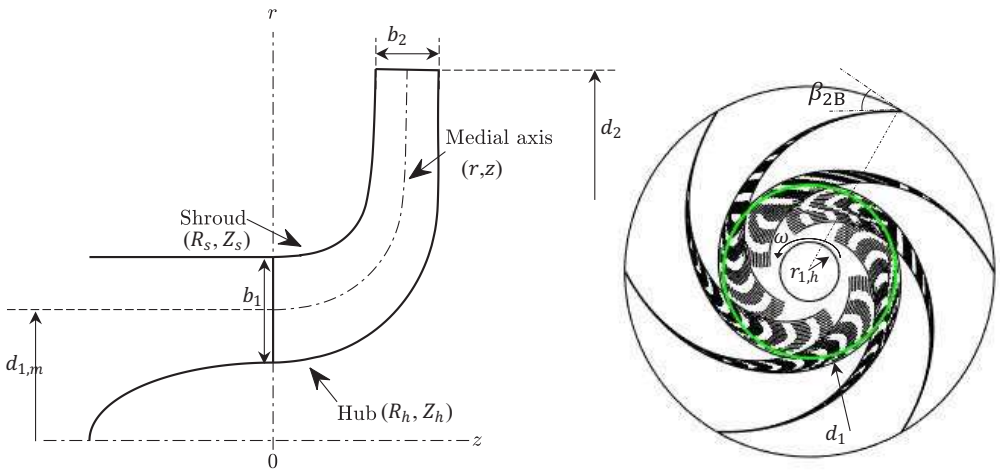

Figure 2 – Impeller's parameters and meridional curves

On average, the time required for generating each geometry is 6.3 seconds. Once a turbopump geometry is generated, the design tool prepares the geometry and initiates the CFD solver (**Figure 1**, step B). The solver is then given a set of appropriate commands to solve the flow passing through the pump. The analysis is conducted with ANSYS CFX.

CFD analysis: The impeller and inlet pipe are meshed using a structured grid, while an unstructured mesh is used for the volute. The near-wall elements are carefully adjusted to ensure y^+ values fall within the turbulence model's validity range. A dense mesh comprising over 45 layers is employed for the tip clearance gap, with an end ratio ranging from 30 to 43. The impeller is set as a relative flow domain, rotating at the pump's speed. The steady-state CFD analysis is carried out on R245fa in a liquid state with a density of 1311.9 kg.m^{-3} and a dynamic viscosity of 3.525×10^{-4} Pa.s. The boundary conditions of total pressure and mass flow rate are set for the inlet and outlet of the pump, respectively. The SST model (Menter et al., 2003) is used to model turbulence.

3. PRE-DESIGN MAPS AND 1D MODELS

The CFD results are then used to infer pre-design maps and 1D models considering the effects of tip clearance and splitter blades (**Figure 1**, step C).

3-1. Pre-design maps

The non-dimensional parameters of specific speeds (n_q), specific diameters (d_s) and internal efficiency (η_i) are calculated and plotted on Cordier diagrams providing updated pre-design maps for the preliminary sizing of turbopumps suitable for small-scale ORC applications. **Figure 3** presents the obtained $n_q - d_s$ diagram for shrouded and unshrouded turbopumps with a 5% tip clearance ratio. The figure suggests that the feasible design region becomes narrower with decreasing specific speeds, as observed in the original Balje (1962) diagrams. Centrifugal pumps with a low specific speed suffer from high leakage losses, disk friction, and secondary flows (Olimstad et al., 2018), leading to a narrower range of feasible designs at low specific speeds. The figure suggests that the internal efficiency decreases with the increase of the specific diameter for a given specific speed, leading to a pattern of efficiency variations with the changes of n_q and d_s. Efficiency contours are plotted using MATLAB's built-in contour function. The function needs gridded data, so the efficiencies are interpolated for the gridded n_q and d_s data. The data suggest that unshrouded pumps can experience an efficiency decrease of up to 56% (relative) depending on the tip clearance ratio and geometric parameters compared to shrouded machines.

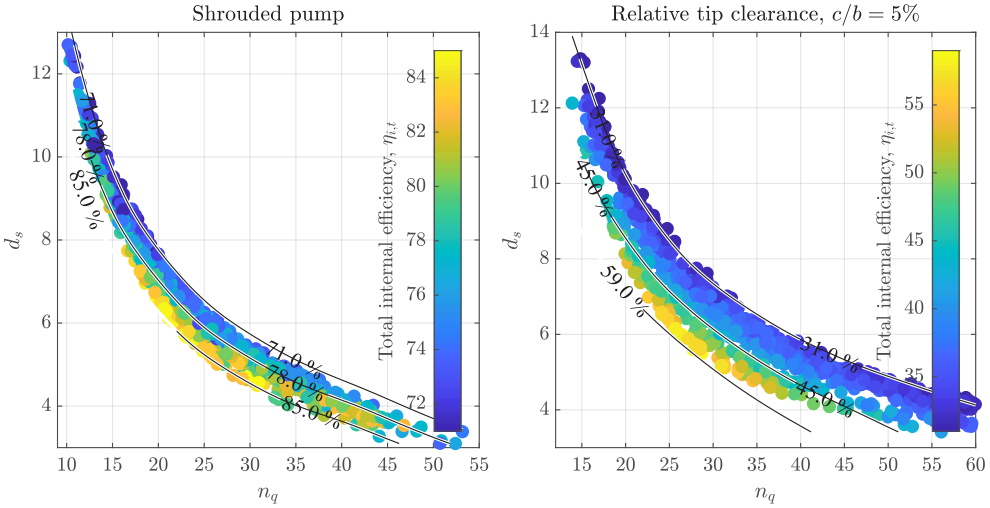

Figure 3 – Efficiency distribution in the $n_q - d_s$ diagram for shrouded and unshrouded pumps

The regression models for shrouded (Eq. 10) and unshrouded pumps (Eq. 12) were developed to predict the pump efficiency based on n_q and d_s using efficiency contour coordinates rather than CFD data. Eq. (11) and Eq. (13) can be used to estimate the impeller outlet diameter in the early design steps of the ORC pump.

Table 3 – Pre-design correlations

Geometry	Correlation	
Shrouded ($10<n_q<55$)	$\eta_{i,t} = 227.7091 + 0.4423d_s^2 + 0.1043n_q^2 - 4.882n_q - 13.4851d_s - 0.1008n_q d_s - 0.0009n_q^3$	(10)
	$d_s = 9.8564e^{-0.0269n_q} + 20.1711e^{-0.0.1503n_q}$	(11)
Unshrouded ($13<n_q<60$)	$\eta_{i,t} = 265.1359 + 0.7301d_s^2 + 0.0733n_q^2 - 0.037\frac{n_q^2}{d_s} - 5.5275n_q - 22.077d_s - 0.0003n_q^3$	(12)
	$d_s = 17.455e^{-0.0413n_q} + 8.8408e^{-0.1333n_q}$	(13)

3-2. The 1D modeling with Neural networks

Zakeralhoseini & Schiffmann (2022)a, (2023)b showed that the validity of current models for the effects of tip clearance is questionable for small-scale turbopumps and proposed neural network (NN)-based surrogate models to account for the influence of tip clearance and splitters on the slip factor and head loss coefficient of turbopumps. These models are trained on a wide range of design parameters using the CFD

results. The parameters of the NN are available in a data repository published by Zakeralhoseini & Schiffmann (2022)b. **Figure 4** shows the neural network architecture. The NN predictions can be achieved by computing consecutively the neuron values on each layer using Eq. **(**14**)**:

$$Z_i = W^{(i)}\left(\sigma(Z_{i-1})\right) + b^{(i)} = W^{(i)}h_{i-1} + b^{(i)} \quad (14)$$

where σ and h are the activation functions applied to the previous layer and its output, respectively.

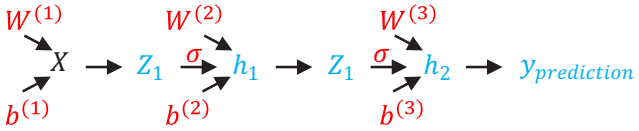

Figure 4 – General neural network architecture

The slip factor model takes the tip clearance ratio, the number of blades, β_{2B}, and the flow coefficient as input parameters. The head coefficient model takes β_1, d_1/d_2, and n_q in addition to the input parameters of the slip model. When splitter blades are considered, the models will also need the splitters' pitch and relative meridional length. The slip factor model predicts the slip of both shrouded and unshrouded impellers. In contrast, the head coefficient model estimates the relative head loss of an unshrouded impeller compared to the same shrouded impeller.

4. EXPERIMENTAL TURBOPUMPS AND VALIDATION

Two turbopumps, sized for specific speeds of 8.9 and 28.5, are designed for experimental investigation with the developed tool. **Table 4** presents the specifications and dimensions of experimental turbopumps working with R134a.

Table 4 – Main dimensions and operating conditions of the experimental turbopump

Item	Parameter	Symbol	Unit	Turbopump 1	Turbopump 2
Experimental characteristics (post-calculated)	Specific speed	n_q	–	28.5	8.9
	Pressure rise at the design point	Δp	*bar*	6.169	18.4
	Mass flow rate	$\dot{m}_r$	*kg s*$^{-1}$	0.140	0.280
	Rotational speed	n	*rpm*	50,000	25,000
Impeller	Blade trailing edge angle	β_{2B}	°	27.5	90
	Number of blades	Z	–	6	8
	Outlet diameter	d_2	*mm*	12.93	37.75
	Outlet width	b_2	*mm*	1.235	1.442
Volute	The base shape of cross-sections	–	–	Elliptic/Circular	Rectangular
	Cutwater diameter	d_{cw}	*mm*	13.62	42.0

4-1. Experimental analysis

The test rig is a simulative ORC (Zakeralhoseini & Schiffmann, 2023a) with an expansion valve replacing the turbine (see **Figure 5**). It consists of a pump test section, a condenser, a sub-cooler, and an evaporator. Instruments measuring the mass flow rate, temperature, and pressure are connected to a data acquisition system. The test conditions are controlled by heating and cooling loads applied to the heat exchangers. The rotor speed is controlled by the spindle drive control unit. The electric spindle drives the hermetic turbopump through a magnetic coupling. Preloaded ball bearings support the rotor and are lubricated with the working fluid.

4-2. Data reduction method

The LabVIEW interface utilizes REFPROP (Lemmon et al., 2018) to assess the working fluid's thermodynamic properties and post-process sensor data, with post-processing relations given in **Table 5**.

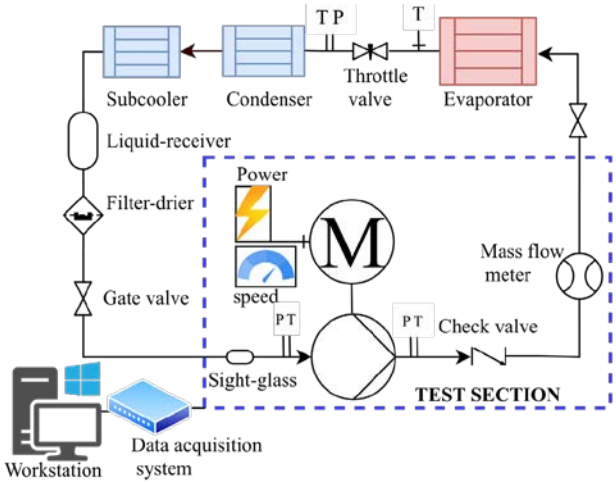

Figure 5 – The flow diagram of the test rig

Table 5 – Post-processing equations of experimental data

Parameter	Equation	
Useful power given to the flow	$\dot{W}_{us} = (p_o - p_{in})Q$	(15)
Total power given to the flow	$\dot{W}_t = \dot{m}(h_o - h_{in})$	(16)
Internal efficiency	$\eta_{i,t} = \dot{W}_{us}/\dot{W}_t$	(17)
Head coefficient	$\psi = gH/u_2^2$	(18)
Back-work ratio	$BWR = \dot{W}_P/\dot{W}_T$	(19)
Thermal efficiency	$\eta_{th} = (\dot{W}_T - \dot{W}_P)/\dot{Q}_{EV}$	(20)

4-3. Application of proposed models in the design of ORC turbopumps

Table 4 presents the experimental pressure rise of the pump at the design flow rate. In this section, the accuracy of the developed 0D and 1D models in correctly predicting the impeller diameter is assessed and compared with previous models. Using a reverse approach, the models are employed to estimate the impeller diameter necessary to achieve the experimental pressure increase. **Figure 6** shows the estimated diameter deviations using pre-design maps and 1D models. The labels on the y-axis represent the maps, or 0D models (first item) and 1D models (second item).

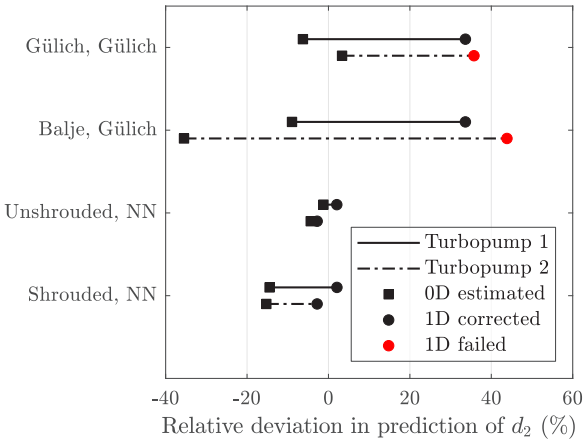

Figure 6 – Deviation of d_2 predicted with correlations from experimental turbopumps

The initial impeller diameter is estimated through the utilization of the pre-design map (square symbol). Subsequently, the impeller diameter is modified through an iterative process using a one-dimensional model

(black circle symbol) while maintaining a constant blade outlet angle to achieve the desired pressure rise. The figure suggests that, for both turbopumps, the unshrouded pre-design map achieved in this study provides the most accurate estimate of the impeller diameter, followed by the Gülich (2010) model (Eq. 3). The Balje (1981) diagram underpredicts the impeller diameter by 8.9% for turbopump 1, while the error is 35.5% for turbopump 2. When using NN models (Zakeralhoseini & Schiffmann, 2022a, 2023) for slip factor and tip clearance to correct the impeller diameter, the estimation deviation is only 3%. However, when using the models from Gülich (2010) for turbopump 1, the deviation is around 33.7%. For turbopump 2 (red circle symbol), the correction of impeller diameter does not converge when using the models from Gülich (2010). Utilizing the models developed in this study significantly reduces the design time of a turbopump. The impeller diameter necessary to meet the required pressure rise can be attained through a mere two iterations. In contrast, the Gülich (2010) models exhibit an impeller diameter deviation of over 33% and fail to converge for turbopump 2. Such imprecise estimation extends the number of design iterations in the CFD analysis stage. Notably, each CFD iteration takes several hours on today's powerful computers, while the 1D calculations are executed in a fraction of a second, highlighting the benefit of the updated pre-design maps and improved 1D models.

4-4. Characteristic curves of experimental turbopumps

Figure 7 presents characteristic curves of the small-scale turbopump at different rotational speeds and a tip clearance of 100 µm. The CFD analysis and experimental results exhibit a maximum deviation of only 3.51% for the head coefficient, demonstrating the high reliability of the CFD analysis. Turbopump 2 with a β_{2B} of 90° shows little variation in the head coefficient with capacity, which agrees with the Euler equation. In contrast, turbopump 1 with a β_{2B} of 27.5° exhibits a significant decrease in head coefficient with increasing capacity. The figure also suggests that similarity laws apply to the unshrouded pump, as the results for different rotor speeds collapse onto the same curves.

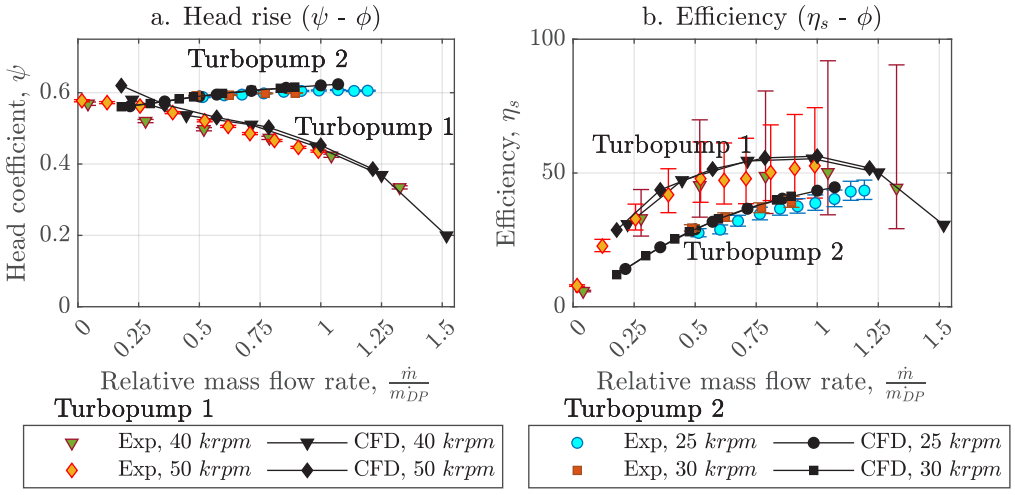

Figure 7 – Experimental and numerical performance characteristics of turbopumps

4-5. ORC performance characteristics

An existing ORC system is used as a baseline to investigate the influence of the developed turbopumps on its performance. The system incorporates a small-scale radial inflow turbine developed and tested by Rosset et al. (2021). Designed for waste heat recovery on truck engines, the system achieves a net output power of 8 kW. Originally, the ORC system was driven by a 27-stage GRUNDFOS (CRNE 1-27) centrifugal pump with a maximum rotational speed of 3000 rpm to achieve the required pressures. **Figure 8** compares the performance of the ORC system using small-scale turbopumps with the original multi-stage centrifugal pump. The results suggest that the BWR of the system decreases up to 11.6% and 6.8% of the generator's output power and is 67% and 42% lower for turbopumps 1 and 2, respectively, compared to the commercial

pump. Moreover, the figure suggests that using small-scale turbopumps can lead to a mean increase of 0.51% points in thermal efficiency.

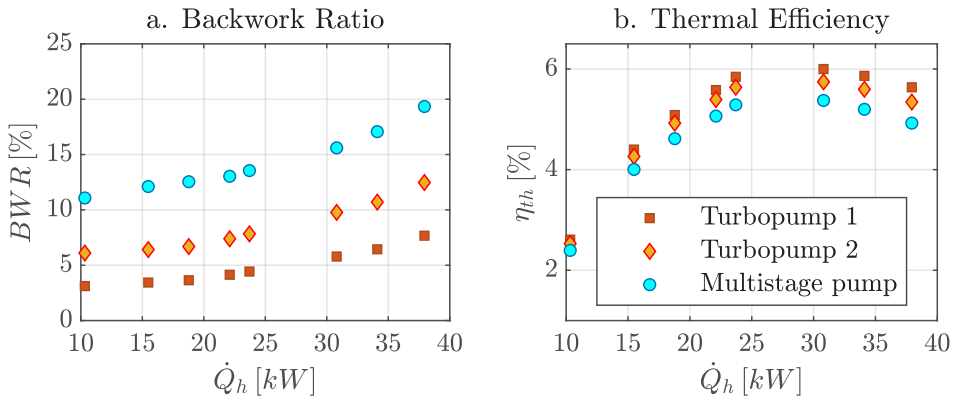

Figure 8 – Comparison of performance characteristics for the targeted ORC system

5. CONCLUSIONS

Small-scale single-stage turbopumps offer cost reduction in materials, simplified mechanical design, space efficiency, and fuel savings for driving ORC systems. The pump design is an iterative process to ensure that the pump is efficient and reliable for its application. A parameterized design model that allows for the automated design and CFD evaluation of turbopump geometries is developed to characterize the performance of numerous turbopump geometries for small-scale ORC applications. Pre-design maps and 1D models, which have proven to be effective tools for designing pumps, are developed for small-scale ORC applications. The presented models can reduce the time and cost associated with the iterative design process. The models' validity is verified through experiments on small-scale turbopumps. The very small deviations observed between the CFD analyses and experimental results validate the numerical and CFD analysis conducted on the small-scale turbopumps for ORC systems. The small-scale turbopumps designed in this study are expected to improve the thermal efficiency of the ORC by 0.51% and decrease the BWR by 67% compared to a 27-stage commercial pump. This study represents a significant step in developing compact and efficient turbopumps for ORC systems, which opens exciting avenues for future research. The updated $n_q - d_s$ diagrams and the new 1D models obtained through data-driven approaches are validated against two experimental turbopumps with specific speeds of 8.9 and 28.5. Further experimental investigations are needed to explore additional small-scale turbopumps with different geometric features, to extend the validation of the pre-design maps at various specific speeds.

NOMENCLATURE

b	channel width, m	Z	number of blades	*h*	hub
c	tip clearance, m		**Greek letters**	*o*	outlet
d	diameter, m	α	absolute flow angle, °	*s*	shroud
d_s	specific diameter	β_B	blade angle, °	*th*	thermal
H	head, m	β	flow angle, °	*t*	total
h	enthalpy, J	ρ	density, kg m^{-3}	*us*	useful
$\dot{m}$	mass flow rates, kg s^{-1}	η	efficiency	*1*	impeller inlet
n	rotational speed, rpm	ψ	head coefficient	*2*	impeller outlet
n_q	specific speed		**Subscripts**		**Abbreviations**
n_{ss}	suction specific speed	*cw*	cutwater	BWR	back-work ratio
p	total pressure, Pa	*DP*	design point	CFD	computational fluid dynamics
Q	flow rate, m^3 s^{-1}	*i*	internal	ORC	organic Rankine cycle
u	peripheral velocity, m s^{-1}	*in*	inlet	1D	one dimensional
$\dot{W}$	power, W	*EV*	Evaporator	3D	three dimensional

REFERENCES

Balje, O. E. (1962). A Study on Design Criteria and Matching of Turbomachines: Part B—Compressor and Pump Performance and Matching of Turbocomponents. *Journal of Engineering for Power*, *84*(1), 103–114.

Balje, O. E. (1981). *Turbomachines-A guide to design, selection, and theory* (Issue BOOK). John Wiley & Sons.

Bao, J., & Zhao, L. (2013). A review of working fluid and expander selections for organic Rankine cycle. *Renewable and Sustainable Energy Reviews*, *24*, 325–342.

Bianchi, G., Fatigati, F., Murgia, S., & Cipollone, R. (2017). Design and analysis of a sliding vane pump for waste heat to power conversion systems using organic fluids. *Applied Thermal Engineering*, *124*, 1038–1048.

Gülich, J. (2010). *Centrifugal pumps*. Springer.

Japikse, D., Marscher, W., & Furst, R. (2006). *Centrifugal pump design and performance*. White River Junction, Vermont: Concepts NREC.

Landelle, A., Tauveron, N., Revellin, R., Haberschill, P., Colasson, S., & Roussel, V. (2017). Performance investigation of reciprocating pump running with organic fluid for organic Rankine cycle. *Applied Thermal Engineering*, *113*, 962–969.

Lei, B., Wang, J. F., Wu, Y. T., Ma, C. F., Wang, W., Zhang, L., & Li, J. Y. (2016). Experimental study and theoretical analysis of a Roto-Jet pump in small scale organic Rankine cycles. *Energy Conversion and Management*, *111*, 198–204.

Lemmon, E. W., Bell, I. H., Huber, M. L., & McLinden, M. O. (2018). NIST Standard Reference Database 23: Reference Fluid Thermodynamic and Transport Properties-REFPROP, Version 10.0, National Institute of Standards and Technology. *Standard Reference Data Program, Gaithersburg*.

Meng, F., Zhang, H., Yang, F., Hou, X., Lei, B., Zhang, L., Wu, Y., Wang, J., & Shi, Z. (2017). Study of efficiency of a multistage centrifugal pump used in engine waste heat recovery application. *Applied Thermal Engineering*, *110*, 779–786.

Menter, F., Kuntz, M., & Langtry, R. B. (2003). Ten years of industrial experience with the SST turbulence model. *Heat and Mass Transfer*, *4*.

Olimstad, G., Osvoll, M., & Finstad, P. H. E. (2018). Very Low Specific Speed Centrifugal Pump—Hydraulic Design and Physical Limitations. *Journal of Fluids Engineering*, *140*(7).

Pfleiderer, C. (2013). *Die Kreiselpumpen für Flüssigkeiten und Gase: Wasserpumpen, Ventilatoren, Turbogebläse Turbokompressoren*. Springer-Verlag.

Rosset, K., Pajot, O., & Schiffmann, J. (2021). Experimental Investigation of a Small-Scale Organic Rankine Cycle Turbo-Generator Supported on Gas-Lubricated Bearings. *Journal of Engineering for Gas Turbines and Power*, *143*(5), 1-14,51015.

von Backström, T. (2006). A Unified Correlation for Slip Factor in Centrifugal Impellers. *Journal of Turbomachinery-Transactions of The Asme - J TURBOMACH-T ASME*, *128*.

Xu, B., Rathod, D., Yebi, A., Filipi, Z., Onori, S., & Hoffman, M. (2019). A comprehensive review of organic rankine cycle waste heat recovery systems in heavy-duty diesel engine applications. *Renewable and Sustainable Energy Reviews*, *107*, 145–170.

Xu, W., Zhang, J., Zhao, L., Deng, S., & Zhang, Y. (2017). Novel experimental research on the compression process in organic Rankine cycle (ORC). *Energy Conversion and Management*, *137*, 1–11.

Yang, Y., Zhang, H., Tian, G., Xu, Y., Wang, C., & Gao, J. (2019). Performance Analysis of a Multistage Centrifugal Pump Used in an Organic Rankine Cycle (ORC) System under Various Condensation Conditions. *Journal of Thermal Science 2019 28:4*, *28*(4), 621–634.

Yang, Y., Zhang, H., Xu, Y., Zhao, R., Hou, X., & Liu, Y. (2018). Experimental study and performance analysis of a hydraulic diaphragm metering pump used in organic Rankine cycle system. *Applied Thermal Engineering*, *132*, 605–612.

Zakeralhoseini, S., & Schiffmann, J. (2022a). Analysis and modeling of the tip leakage flow on the performance of small-scale turbopumps for ORC applications. *Applied Thermal Engineering*, 119160.

Zakeralhoseini, S., & Schiffmann, J. (2022b). *Neural network models for centrifugal pumps* (No. 2). Mendely Data.

Zakeralhoseini, S., & Schiffmann, J. (2023a). Design, computational and experimental investigation of a small-scale turbopump for organic Rankine cycle systems. *Energy Conversion and Management*, *287*, 117073.

Zakeralhoseini, S., & Schiffmann, J. (2023b). The influence of splitter blades and meridional profiles on the performance of small-scale turbopumps for ORC applications; analysis, neural network modeling and optimization. *Thermal Science and Engineering Progress*, *39*, 101734.

ORC SEVILLE 2023
7th International Seminar on O.R.C. Power Systems

© 2024 Editorial Universidad de Sevilla. Este es un artículo de acceso abierto distribuido bajo los términos de la licencia de uso y distribución Creative Commons (BY-NC-ND 4.0)

DOI: https://dx.doi.org/10.12795/9788447227457_116

DOUBLE-STAGE ORC SYSTEM BASED ON VARIOUS TEMPERATURE WASTE HEAT SOURCES OF THE NEGATIVE CO_2 POWER PLANT

Kamil Stasiak*, Paweł Ziółkowski, Dariusz Mikielewicz

Gdańsk University of Technology, Faculty of Mechanical Engineering and Ship Technology, Institute of Energy, 11/12 Gabriela Narutowicza Street, 80-233 Gdańsk, Poland

*Corresponding Author: kamil.stasiak@pg.edu.pl

ABSTRACT

Analysed is the modification of the thermodynamic cycle with the negative CO_2 power plant concept by its combination with the organic Rankine cycle. The analysed power plant operates on a gas produced from the gasification of sewage sludge. The negative emission term comes from the aggregated CO_2 balance resulting from the capture of the CO_2, while the sewage sludge is one of the inevitable environmental sources of CO_2 to be avoided. In short, the principle of this power plant is to produce electrical power by converting sewage sludge fuel as the substrate to CO_2 as a product, which is an intricate process in-between, with many opportunities for waste heat recovery. There are four main sources of waste heat in such a system. One is the drying process of the producer gas, which must be properly cooled from the high temperature after gasification to the temperature at which no moisture is present in the gas. In the wet combustion chamber, the syngas is oxy-combusted under high temperatures with water injection to control the combustion temperature. This mixture is then expanded in the gas turbine. The mixture leaving the turbine is a major source of heat supply for the ORC. The second heat source is a mixture of steam and gas – a major supply of heat source for ORC. Next, the mixture is undergoing separation process in a cyclone separator and then the CO_2 (with a small content of moisture) is directed to carbon capture unit. The CO_2 is then compressed in a system that requires intercooling. Due to the wide range of temperatures of the listed waste heat sources, the double ORC combination is investigated. The combined ORC cycle is connected by a cascade heat exchanger. The ORC fluid parameters are selected computationally to match the temperature distribution lines. The power plant processes are simulated in the steady-state process simulator using the most accurate equations of state from the literature. Optimum operating conditions of the ORC integrated power plant are obtained through optimization techniques.

1 INTRODUCTION

The increasing demand for sustainable energy solutions has stimulated research into innovative ways of using waste heat to generate electricity. One such approach is the use of Organic Rankine Cycle (ORC) technology in conjunction with waste heat recovery from gasification or gas scrubbing processes in bioenergy with carbon capture and storage (BECCS) systems. This study deals with the modification of the thermodynamic cycle combining the negative CO_2 power plant concept with ORC. The investigated power plant operates with gas produced from the gasification of sewage sludge, where the negative emission term results from the aggregated CO_2 balance resulting from CO_2 capture. The introduction of ORC technology enables the utilisation of waste heat, ultimately increasing the overall efficiency of the power plant. In addition, research into multi-stage ORC combinations is addressing the wide range of temperatures associated with waste heat sources, paving the way for more advanced and efficient waste heat recovery systems.

Relevant literature includes work focusing on the integration of ORC technology and waste heat recovery in various applications. Mikielewicz et al., (2016) utilise waste heat from a power plant by employing a double-stage ORC system with bleed steam as heat source and an additional waste heat source from flue gas, thereby further improving energy efficiency. Moradi et al., (2020) investigate the feasibility of integrating biomass gasification with a steam-injected micro gas turbine and an ORC unit revealing that the ORC combination and steam injection into the combustion chamber results in higher net electrical power. Johansson et al., (2023) authors proposed a model that predicts convective and condensation heat recovery in a centrifugal scrubber, which may be applicable to gas scrubbing processes within BECCS systems. Brachi et al., (2022) explore the integration of waste heat recovery or ORC systems with sewage sludge gasification for combined heat and power (CHP) production in wastewater treatment plants, demonstrating improved energy efficiency and reduced environmental impact. Wang et al., (2021) investigate the integration of waste heat recovery using ORC technology with a counterflow direct contact scrubber for coal-fired flue gas treatment, demonstrating the simultaneous cleaning of the flue gas by removal of harmful pollutants and the recovery of waste heat for additional power generation through the ORC.

The process flow diagram (PFD) of negative emission CO_2 gas power plant (nCO_2PP) is shown in Figure 1 (Ziółkowski et al., 2023). In this configuration, the GT^{bap} turbine is used for the low pressure expansion. The novelty in the nCO_2PP reference case presented in Ziółkowski et al., (2021) is the use of the Spray-Ejector Condenser (SEC) to condense the steam in a direct condensation process, separate the CO_2 and create the vacuum required by GT^{bap}. There is also HE1, which cools the flue gases upstream of the SEC by regeneratively heating high pressure water fed to the Wet Combustion Chamber (WCC) (Ziółkowski et al., 2023).

The PFD, where ORC has been introduced instead of low pressure expansion, is shown in Figure 2. In this modification, the heat exchanger HE1 is located in the same place, but it receives energy from flue gases with a pressure of 1 bar and a significantly higher temperature. From an efficiency point of view, it is preferable that HE1 exchanges as much heat as possible. After HE1, an ORC cycle is incorporated to utilise the remaining heat that could not otherwise be used by HE1 but would be lost in the condenser. A second ORC stage is added to match the water condensation from the producer gas in the gas scrubber, where the temperature from the gasification unit is 760 ºC. The flow from the first stage is also diverted for superheating to the temperature source, which is the main waste heat source of the second stage, this is done because the first stage has a higher pressure and therefore efficiency.

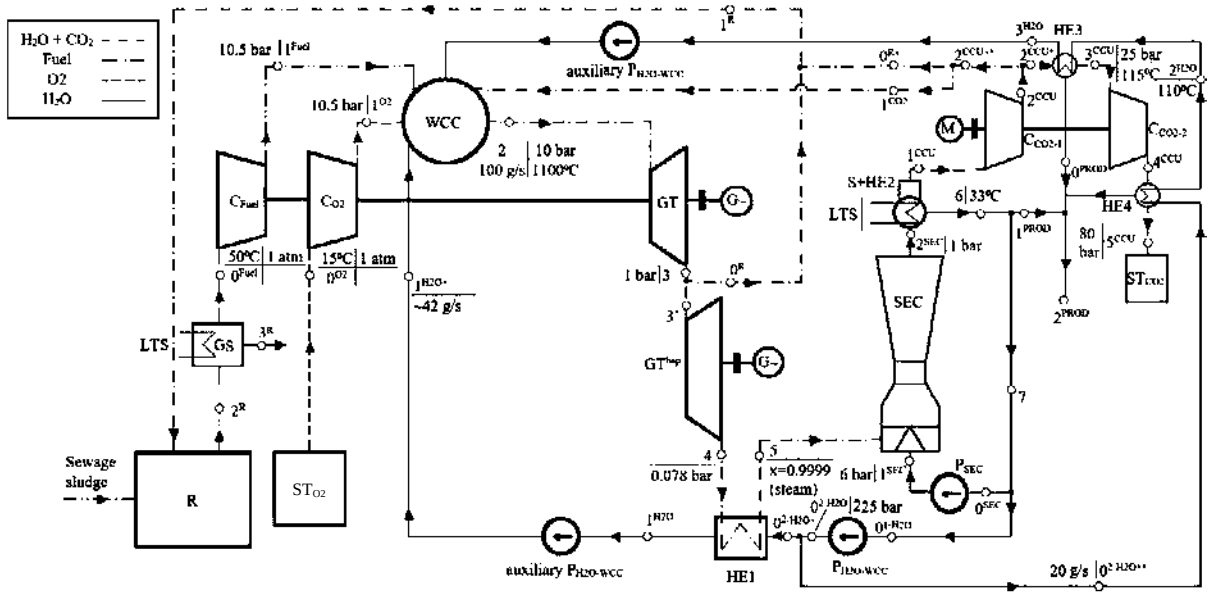

Figure 1: Process flow diagram of the negative CO_2 power plant reference case (Ziółkowski et al., 2023).

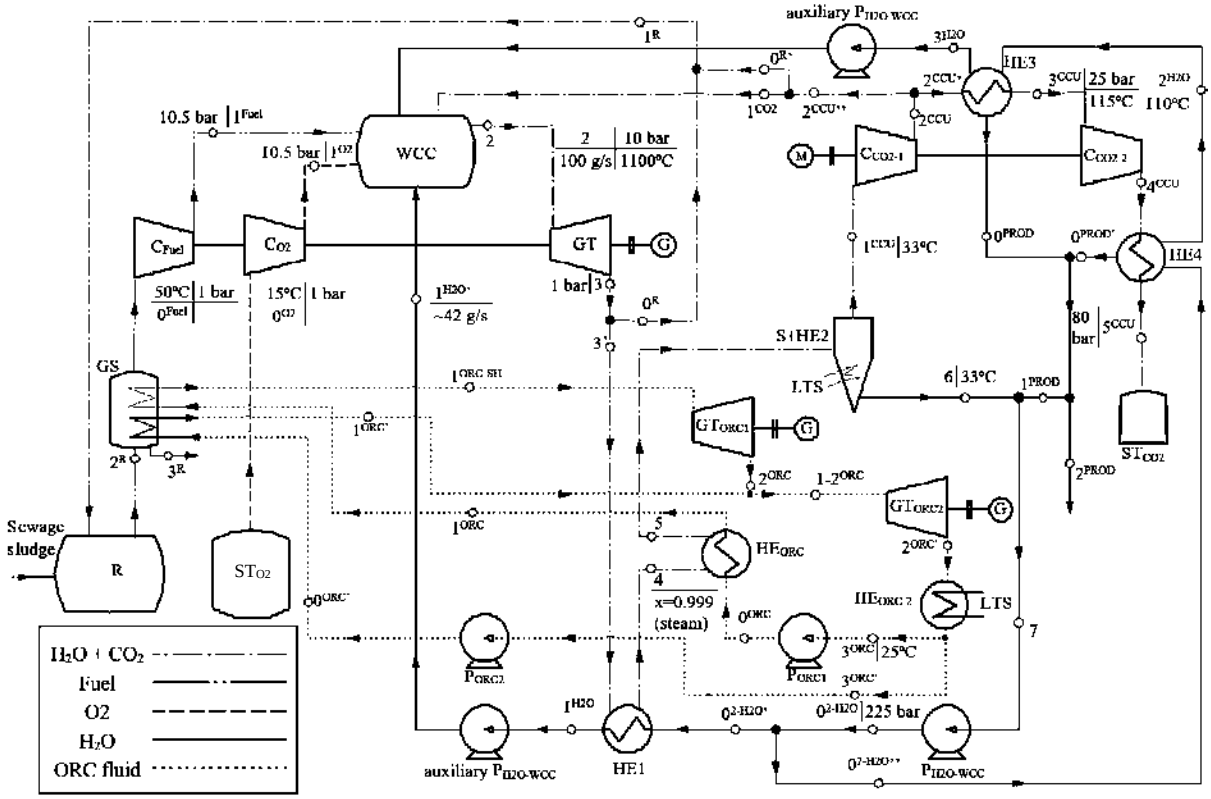

Figure 2: Process flow diagram of the negative CO_2 power plant with double stage ORC.

2 METHODOLOGY

The simulation software used in this study is Aspen Plus, which uses the REFPROP equations of state package, providing highly accurate calculations.
The ORC working fluid used in the simulation is R1233zd(E), which is a new promising candidate for industrial use in heat transfer applications due to its excellent thermodynamic properties, low price and low environmental impact (Pysz et al., 2023). Previously, the authors in Stasiak et al., (2022) conducted analyses of several ORC fluids and found R1233zd(E) to be the most favourable among them. In addition, R1233zd(E) is available for turbo chillers. This ORC fluid can be an alternative to R245fa and is therefore expected to be used for ORC.
For this study, the reference case nCO_2PP (without ORC) is compared with its combination with one-stage ORC and with double-stage ORC.
The composition of sewage sludge digested in the gasification unit, was assumed as mass fractions 27.9% C, 6.7% H, 28.9% O, 4.4% N, 32.2% Ash, with an LHV of 9.8 MJ/kg (cf. Table 1) (Ziółkowski, Badur, et al., 2022). The efficiency of the gasifying reactor is η_{R_H}=0.71 and HHV = 15.70 MJ/kg. The proximate and ultimate composition were taken from the work of Ziółkowski, Badur, et al., (2022).

The producer gas produced by gasification in a steam atmosphere at 760 °C and, after cleaning in the gas scrubber, has a volumetric composition of 9.3% CO, 46.8% H_2, 13.9% CH_4, 26.4% CO_2 and 3.5% C_3H_8. Assumptions for gas turbine equipment such as compressors, combustion chamber and expanders are given in Table 2. Among the most relevant parameters are the temperature of 1100 ºC after the combustion chamber and the pressure of 10 bar. This work analysis was carried out for a commercial scale plant with a capacity of 10,000 tonnes of dried sewage sludge mass flow per year (see Table 2). The internal efficiencies of the GT/GT^{bap} expanders, water pumps and compressors were assumed to be relatively high, but this was done to refer to previous work analysing the nCO_2PP cycle (Ertesvåg et al., 2023; Stasiak et al., 2023; Ziółkowski, Głuch, et al., 2022). These values help to establish a reference value for two modifications of the system with ORC cycles.

Table 1. Proximate and ultimate analysis of sewage sludge for reactor (Ziółkowski, Badur, et al., 2022).

Specification	Unit	Value
Fixed Carbon	$\%_{dry}$	9.40
Volatile Matter	$\%_{dry}$	58.10
Ash	$\%_{dry}$	32.50
Moisture content *	$\%_{wb}$	2.00
C	$\%_{dry}$	27.89
H	$\%_{dry}$	6.67
N	$\%_{dry}$	4.36
S	$\%_{dry}$	0.29
O **	$\%_{dry}$	28.29

* – assumed value, after drying of sewage sludge; ** – determined by difference

Table 2. Assumptions for the gas turbine cycle

Parameter	Symbol	Unit	Value
Temperature exhaust after WCC (before GT)	t_2	ºC	1100
Mass flow of the dried sewage sludge mass flow annually	$\dot{m}_{ss}$	t/yr	10 000
Exhaust pressure after WCC	p_2	bar	10
Oxygen-fuel excess ratio in WCC	λ	-	1
Initial syngas temperature, after gas scrubber	t_{fuel}	ºC	50
Initial oxygen temperature	t_{O2}	ºC	15
Syngas fuel pressure before C_{fuel} compressor	p_{0-fuel}	bar	1
Oxygen pressure before C_{O2} compressor	p_{0-O2}	bar	1
Fuel to WCC pressure loss factor	δ_{fuel}	-	0.05
Oxygen to WCC pressure loss factor	δ_{O2}	-	0.05
Regenerative water pressure to WCC	p_{1-H2O}	bar	225
Turbine GT, internal efficiency (η_i)	η_{iGT}	-	0.89
Turbine GT^{bap}, η_i	$\eta_{iGT-bap}$	-	0.89
Fuel compressor C_{fuel}, η_i	$\eta_{iC-fuel}$	-	0.87
Oxygen compressor C_{O2}, η_i	η_{iC-O2}	-	0.87
WCC water pump $P_{H2O\text{-}WCC}$, η_i	$\eta_{iP-H2O-WCC}$	-	0.8
Mechanical efficiency for all devices	η_m	-	0.99

The useful product in the GT/GT^{bap} section is electricity. On the other hand, in the CCS unit with a set of compressors, the other desired product is the clean CO_2 obtained after the exhaust gas separation and subsequent compression. The assumptions for these units are given in Table 3.

Table 4 refers to the ORC cycle, where the useful product is electricity, but at the same time it is possible to compensate for the loss of waste heat energy to the environment. The basic assumptions for this new part of the system are the efficiencies of the pump, the expanders and the upper and lower temperatures in the evaporator and condenser. The internal efficiencies of the ORC turbines and the ORC pump were set at a high level for this type of equipment, namely 0.8 and 0.89 for the pump and the expanders, respectively (Micheli et al., 2013; Mikielewicz & Mikielewicz, 2010, 2014; Pan et al., 2020; Wajs et al., 2016). This is as reasonable as possible, given the potential of using hybrid algorithms to optimise flow systems (Delgado-Torres & García-Rodríguez, 2010; Witanowski, Klonowicz, et al., 2023; Witanowski, Ziółkowski, et al., 2023; Zheng et al., 2023; Ziviani et al., 2014).

Table 3. Assumptions for CO_2 separation and CCS system.

Parameter	Symbol	Unit	Value
Exhaust vapor quality after HE1	x_5	-	0.999
Exhaust temperature after HE1, before SEC	t_5	ºC	33
CO_2 pressure after compressor C_{CCU1}	p_{2-CCU}	bar	25
CO_2 pressure after compressor C_{CCU2}	p_{4-CCU}	bar	80
H_2O temperature after HE4	t_{2-H_2O}	ºC	110
CO_2 temperature after HE3	t_{3-CCU}	ºC	115
Water vapor from Separator in 1^{CCU} mixed with CO_2 vapor	-	%	100% humid
Temperature after SEC	t_6	ºC	35
SEC water pump P_{SEC}, η_i	η_{iP-SEC}	-	0.8
CO_2 compressor $C_{CO2\text{-}1}$, η_i	$\eta_{iC-CO2-1}$	-	0.87
CO_2 compressor $C_{CO2\text{-}2}$, η_i	$\eta_{iC-CO2-2}$	-	0.87
Sewage sludge treated as renewable energy source by Polish law (MINISTERSTWO ŚRODOWISKA, 2016)	R	-	-0.9

Table 4. Assumptions for incorporation ORC

Parameter	Symbol	Unit	Value
Pressure after GT^{bap}, without ORC	p_4	bar	0.078
Pressure after GT, when ORC is incorporated	p_3	bar	1
ORC lower temperature source	t_{3-ORC}	ºC	25
ORC pump P_{ORC}, η_i	η_{iP-ORC}	-	0.8
Turbine ORC-1, internal efficiency (η_i)	$\eta_{iT-ORC1}$	-	0.89
Turbine ORC-2, η_i	$\eta_{iT-ORC2}$	-	0.89

669

In addition, a paper Maksiuta et al., (2017) presents a selection of examples of radial inflow and radial outflow ORC turbines with efficiencies of around 90% and outputs of the order of 3 MW. A paper Lampart et al., (2018) reports several ORC turbines with efficiencies as high as 89.6% at an inlet medium temperature of 175 ºC. In another study available in the literature Zaniewski et al., (2019), one can find design and CFD calculations of turbines with proven efficiencies of 89-90% by both methods. These values refer to the radial inflow reaction turbine with a turbine inlet temperature of 210 ºC. This type of design already has an established methodology in the world literature by experts in the field (Fiaschi et al., 2012).

Furthermore, in order to obtain optimal configurations of the flue gas heat recovery system, the thermodynamic cycles analysed in the literature start from a temperature difference of 3 K (Jankowski & Borsukiewicz, 2019). It is worth mentioning that the authors Jankowski & Borsukiewicz, (2019), as a result of comparing the two optimisation methods, obtained a similar optimal evaporation temperature in the evaporator for the refrigerant R1234yf, namely 85 ºC. Similar values for the minimum temperature difference (namely 4 K) for an evaporator with an evaporation temperature of 140 ºC were obtained by the authors Quoilin et al., (2011). On the other hand, in the context of heat recovery systems from low-temperature sources such as geothermal, the temperature difference in the exchanger is assumed to be 3-20 K (Liu et al., 2017). The authors Jankowski et al., (2020) carried out an optimisation for evaporation temperatures below 120 ºC in ORC systems, achieving a minimum temperature difference of 5 K in the evaporator.

The economic analysis was carried out for a commercial scale plant with a capacity of 10,000 tonnes of dried sewage sludge mass flow per year (see Table 5), which could correspond to the capacity of a wastewater treatment plant. This scale plant is designed on the basis of commercial components (such as pumps, oxygen generation station, heat exchangers, etc.) and their operational reliability is high (they are guaranteed by their manufacturers). GT and GT^{bap} with WCC and SEC, the sludge drying system and the gasifier with plasmatron are still prototypes, but will first be tested on a smaller scale.

Table 5. Assumptions for economic analysis

Parameter	Unit	Value
Two gas turbines with a combustor for nCO_2PP reference case	EUR	-9 000 000
One gas turbine with a combustor for nCO_2PP with ORC case	EUR	-6 000 000
Spray-ejector condenser, for nCO_2PP reference case	EUR	-330 000
Spray-ejector condenser, for nCO_2PP with ORC case	EUR	0
ORC one stage (1304 EUR per kW)	EUR	-796 265
ORC double stage (1304 EUR per kW)	EUR	-859 966
Auxiliary devices (Pumps, heat exchangers, CO_2 compressors)	EUR	-94 000
Plasma gasifier+ gas cleaning	EUR	-910 000
Pre-treatment (drying)	EUR	-980 000
Yearly cost of oxygen	EUR/yr	-1 369 236
Yearly cost of GT/GT^{bap} servicing for nCO_2PP reference case	EUR/yr	-900 000
Yearly cost of GT/GT^{bap} servicing for nCO_2PP with ORC case	EUR/yr	-600 000
Discount rate	%	6.9
Sewage sludge disposal price	EUR/t	53
Electricity price	EUR/MWh	311.2
Avoided CO_2 price	EUR/t	70

It is worth noting that the authors did not find an increase in efficiency but a decrease when using the additional heat source for ORC from the WCC. The decrease in efficiency of the whole system can be explained by the fact that a heat exchanger has to be used between the flue gas and the low boiling medium. Thus, the ORC medium entering the ORC cycle turbine is at least several degrees lower in temperature than the exhaust gas going directly from the WCC to the GT (see Figure 1). In addition, considering the present problem in terms of exergetic analysis, the addition of an exchanger instead of direct transfer of the medium to the expander results in entropy production and exergy destruction. Finally, in the methodology of this work it has been assumed that only waste heat (whereas in WCC it would not be waste heat), or improved heat management, is used for the ORC cycle, leaving the GT high pressure part as in the reference nCO_2PP concept.

670

To illustrate the optimum choice of ORC parameters, Figure 3 shows a temperature distribution approach on a logarithmic scale for heat exchangers exchanging heat between the producer gas, the exhaust gas temperature lines and the ORC cooling fluid and pressurised water directed to the WCC temperature lines. This graph in Figure 3 is for one-stage ORC only, but this stage is the same as part of the double-stage ORC configuration, except for the superheat. The exhaust gas temperature is shown as a solid line, the ORC fluid as a dashed line and the pressurised water regeneratively heated by the hot waste heat exhaust gas before being fed to the WCC as a dotted line. In addition, the graph is divided into two segments, described at the top of the graph, where 'ORC' is the heat exchange taking place in the HE-ORC evaporator and 'HE1' corresponds to the heat exchange in the regenerative heat exchanger 'HE1' between the exhaust gas and the pressurised water fed to the WCC.

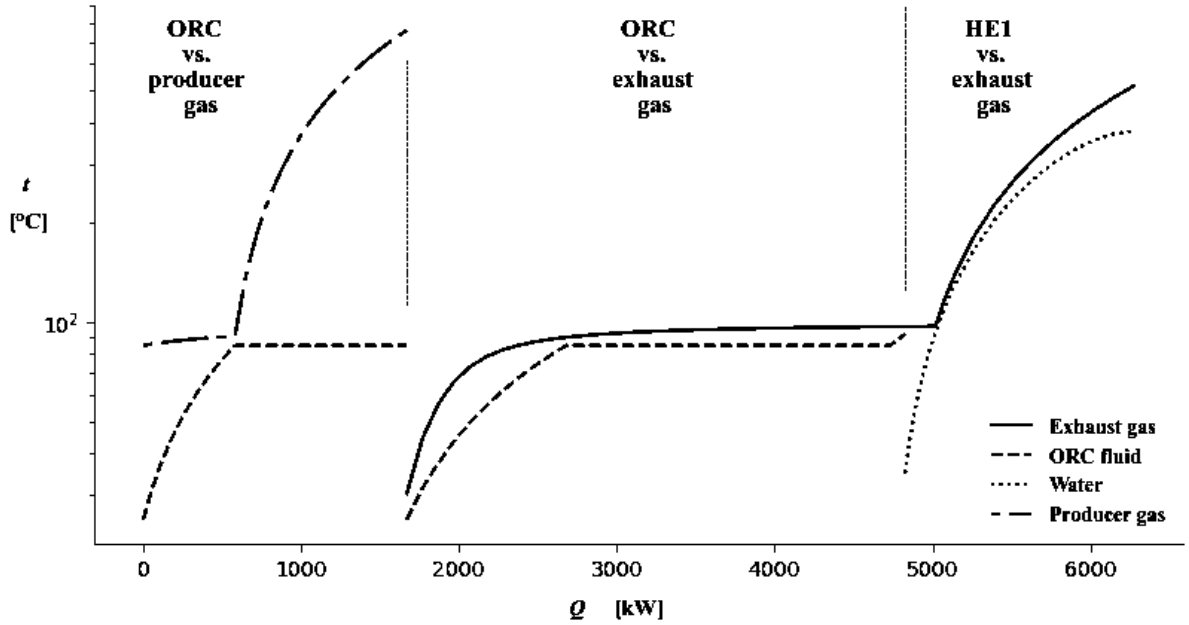

Figure 3: Logarithmic scale temperature distribution as ORC fluid in HE_{ORC} and HE1 heat exchangers

2.1 Equations formulated

The net power (work rate):

$$\dot{W}_{net} = \dot{W}_t - \dot{W}_{cp} + \dot{W}_{t-ORC-1} + \dot{W}_{t-ORC-2} \quad (1)$$

671

where: $\dot{W}_t$ is the power of the GT/GT^{bap} gas turbines, $\dot{W}_{cp}$ is the sum of the power consumption of the compressors and pumps, $\dot{W}_{t-ORC-1}$ and $\dot{W}_{t-ORC-2}$ are the power of the ORC turbines.

$$\dot{W}_{cp} = \dot{W}_{C-Fuel} + \dot{W}_{C-O2} + \dot{W}_{C-CO2-1} + \dot{W}_{C-CO2-2} + \dot{W}_{P-H2O} + \dot{W}_{P-SEC} + \dot{W}_{P-ORC-1} + \dot{W}_{P-ORC-2} \quad (2)$$

Where: $\dot{W}_{C-Fuel}$, $\dot{W}_{C-O2}$, $\dot{W}_{C-CO2-1}$, $\dot{W}_{C-CO2-2}$ are compressor power consumption for fuel, oxygen, and carbon dioxide respectively, while $\dot{W}_{P-H2O}$, $\dot{W}_{P-SEC}$ and $\dot{W}_{P-ORC-1}$, $\dot{W}_{P-ORC-2}$ are pump power consumption for WCC water supply, SEC water supply and ORC fluid drive, respectively.

The overall cumulative power plant efficiency:

$$\eta_{cum} = \eta_{R_H} \cdot \frac{\dot{W}_{net}}{LHV_{syngas} \cdot \dot{m}_{0-fuel}} \quad (3)$$

Where η_{R_H} is the hot gas efficiency of the gasifying reactor, LHV_{syngas} is the Lower Heating Value of the syngas and $\dot{m}_{0-fuel}$ is the mass flow of the syngas.

The authors decided no to use the term net efficiency, which can be found in other works of the authors Ziółkowski et al., (2023), because it includes the efficiency of the gasification reactor, which is multiplied with the net efficiency of the whole nCO_2PP system to form the cumulative efficiency and is therefore not called net efficiency, in order not to confuse both efficiency measures in their works. The CO_2 emissivity of the whole system is defined as follows:

$$eCO_2 = R\frac{\dot{m}_{2-CO_2}}{\dot{W}_{net}}3600 \quad (4)$$

where $\dot{m}_{2-CO_2}$ is the mass flow rate of CO_2 captured, R is the factor considered only for the power plant with the CO_2 capture, which indicates the fraction of the energy source that is treated as renewable by local law. If the system has CO_2 capture, the emission is zero, but if there is a renewable energy source, the value is negative. The avoided eCO_2 would be the sum of the emissions without CO_2 capture and an absolute value of the negative emissions from the renewable energy source.

The Net Present Value NPV is a widely used technique for the financial evaluation of long-term projects (Ziółkowski, Pawlak-kruczek, et al., 2022). It quantifies the surplus or deficit of cash flows in present value terms, reflecting the time value of money:

$$NPV = \sum_{t=1}^{n}\frac{CF_t}{(1+r)^t} - I_0 \quad (5)$$

where CF_t is the net cash flow in period t, while r is representative of the discount rate, and I_0 stands for the initial investment. The variable t denotes the time at which the cash flow occurs, and n denotes the duration of the project. In addition to NPV, there is another important financial indicator - the internal rate of return (IRR). It is the discount rate that makes the NPV of all projected future cash flows equal to zero and serves as the break-even threshold, therefore it can be derived by finding the value of r in equation (5) that makes the NPV equal to zero.
It should be noted that the IRR assumes that cash flows are reinvested at the same rate, which may not be the reality for a long-term power plant project. Despite this limitation, the IRR remains a valuable measure of the potential profitability of a project.

The Levelized Cost of Electricity $LCOE$ is another economic indicator that calculates the average cost of electricity production over the life of the project and is calculated according to BEIS (UK Department for Business, Energy & Industrial Strategy) (Aldersey-Williams & Rubert, 2019):

$$LCOE = \frac{\sum_{t=1}^{n}\frac{CFout_t}{(1+r)^t}}{\sum_{t=1}^{n}\frac{E_t}{(1+r)^t}} \quad (6)$$

where $CFout_t$ is the capital cost in period t and E_t is the energy generated in period t, both being discounted. The $LCOE$, in this context, represents the net breakeven price per unit of total output (electricity plus other revenue streams per MWh), that a project must receive over its lifetime to cover all costs and break even. Therefore a lower $LCOE$ indicates a more economically competitive project. In addition, the $LCOE$ often decreases as the lifetime of a project increases, as the costs are spread over a larger volume of electricity produced.

672

3 RESULTS AND DISCUSSION

Table 6 shows the main results for the two ORC cycle variants with the pressures of the individual ORC pumps and the upper temperatures. In the one-stage ORC variant the ORC fluid is saturated (84.8 ºC) (see Figure 4), while in the double-stage variant it is superheated (171.7 ºC) (see Figure 5), both at a pressure of 7.38 bar. Also in the double-stage variant, the ORC flow is injected at a lower pressure (5.24 bar) between two turbines with a saturated temperature of 72.6 ºC. Figure 4 shows a temperature distribution plot on a logarithmic scale for heat exchangers in one-stage ORC configuration exchanging heat between the exhaust gas temperature line and the ORC cooling fluid and pressurised water directed to the WCC temperature lines. Figure 5 shows the double-stage variant.

Table 6. Results for the ORC power cycle (both layout) with pressure, temperature, mass flow rate for the relevant cases.

nCO₂PP case	$\dot{m}_{ORC}$, **g/s**	p_{ORC1}, **bar**	p_{ORC2}, **bar**	t_{ORC-SH}, **ºC**	$t_{ORC'}$, **ºC**
one-stage ORC	20,965	7.38	-	84.8	-
double-stage ORC	19,012	7.38	5.24	171.7	72.6

Table 7 shows the results comparing different nCO₂PP cases. First is the reference case nCO₂PP power plant with SEC and no ORC (Ziółkowski et al., 2023), then the hybrid nCO₂PP with one-stage ORC using R1233zd(E) refrigerant as working fluid, and then the double-stage ORC. One-stage ORC differs from double-stage ORC in that only one ORC boiling temperature is used. In addition, each result corresponds to the maximum overall net power plant efficiency obtained by adjusting the optimum ORC parameters, namely ORC boiling temperature and mass flow. For comparison, the CO_2 mass flow in the flue gas, the total mechanical power of the turbines, the power for own consumption, the chemical energy rate from combustion, the cumulative efficiency of the nCO₂PP power plant are shown, the emisivity and the avoided CO_2 emissions are shown.

Table 7: Different configurations results

nCO₂PP case	$\dot{m}_{2-CO2}$, **g/s**	$\dot{W}_T$, **kW**	$\dot{W}_{cp}$, **kW**	$\dot{Q}_{CC}$, **kW**	η_{cum}, **%**	eCO_2, **kgCO₂/MWh**	Avoid eCO_2, **kgCO₂/MWh**
reference (Ziółkowski et al., 2023)	313	2,107	602	3,785	27.9	-672.8	1,420.3
one-stage ORC	313	2,120	376	3,813	32.3	-580	1,224.4
double-stage ORC	313	2,167	374	3,813	33.2	-551.3	1,163.8

673

It can be seen that the cumulative efficiency is increased compared to the reference case. The main reason for this is that in the reference case there is a low pressure expansion obtained by the spray ejector condenser, which is driven by a pump with high electricity consumption to move a large amount of water. The low pressure expansion also allows a higher gas turbine output. In the ORC combination cases, there is no low pressure expansion, but the ORC is treated as a moisture exhaust gas condenser, recovering waste heat from this process, thus increasing the amount of waste heat recovered water that goes to the WCC, further increasing the water content in the exhaust gas. In addition, in ORC variants, water from the producer gas is condensed in the gas scrubber. The first stage operates at a higher boiling point, with a pressure of 7.38 bar and a mass flow of 13,301 g/s (see Figure 5), allowing it to effectively recover heat from the flue gas water condensation. Meanwhile, the second stage is designed to match the producer gas water condensation in the gas scrubber, with the ORC fluid pressure maintained at 5.24 bar and 5,714 g/s mass flow. The higher temperature of the producer gas is used to overheat the working fluid in the first stage, as the increased pressure of the working fluid in this stage results in higher efficiency. For comparison purposes, a one-stage ORC has been configured (see Figure 4), and for this purpose the efficiency of this configuration is the maximum, where the ORC fluid also recovers heat from the producer gas at the gasification temperature of 760 ºC and pressure of 1 bar (which gradually condenses water below 90.6 ºC), but is not able to use all the waste heat because it is a single stage adapted to a different temperature source at 96.8 ºC and 1 bar pressure (which gradually condenses water below this temperature). There are two main reasons for the increased efficiency of the double-stage ORC compared to the one-stage ORC, although in both the one-stage and the double-stage ORC the parameters are optimised for maximum efficiency. The first is that the additional stage fits better to the temperature line of the producer gas during moisture condensation, thus recovering more heat in the lower temperature region, and then, to maximise efficiency, the remaining heat at 760 ºC from the producer gas is used to overheat the higher boiling temperature ORC stage. The secondary small increase from the addition of the second ORC stage is due to the connection of the second stage turbine,

which reduces entropy generation. The main reason for this is that mixing the expanded working fluid with the additional flow effectively lowers the average temperature of the mixture, thereby reducing the entropy generated during the expansion process. When the mixed fluid enters the second turbine, it expands at a lower average temperature and the entropy generated at this stage is also lower than in a one-stage turbine. The emissivity (as well as its avoided variant), which is negative for all nCO_2PP cases, decreases in its absolute values for the ORC cases, which is a positive trend, meaning that less CO_2 would be emitted into the environment if it was not captured. It also means that a higher power output is obtained for the same amount of CO_2 flow in the system.
Table 8 compares the economic results of three scenarios over a decade: a reference case and two ORC variants using either a one-stage or a double-stage ORC. From a financial perspective, the double-stage ORC outperforms the other two, with the highest IRR and NPV, implying the highest profits. In addition, the double-stage ORC gives the lowest LCOE, which means it is the most cost-effective in terms of electricity production (plus other revenue streams per MWh). Therefore, the double-stage ORC scenario appears to be the most economically advantageous.

Table 8: Results for economic analysis for 10 year lifetime

nCO_2PP case	$\dot{m}_{SS}$, **t/yr**	$\dot{m}_{CO_2}$, **t/yr**	E_t, **MWh/yr**	IRR, **%**	NPV, **EUR**	$LCOE$, **EUR/MWh**
reference (Ziółkowski et al., 2023)	10,000	9,854	13,191	27.8	11,876,698	276
one-stage ORC	10,000	9,854	15,277	48.5	20,565,106	200
double-stage ORC	10,000	9,854	15,707	49.7	21,445,389	195

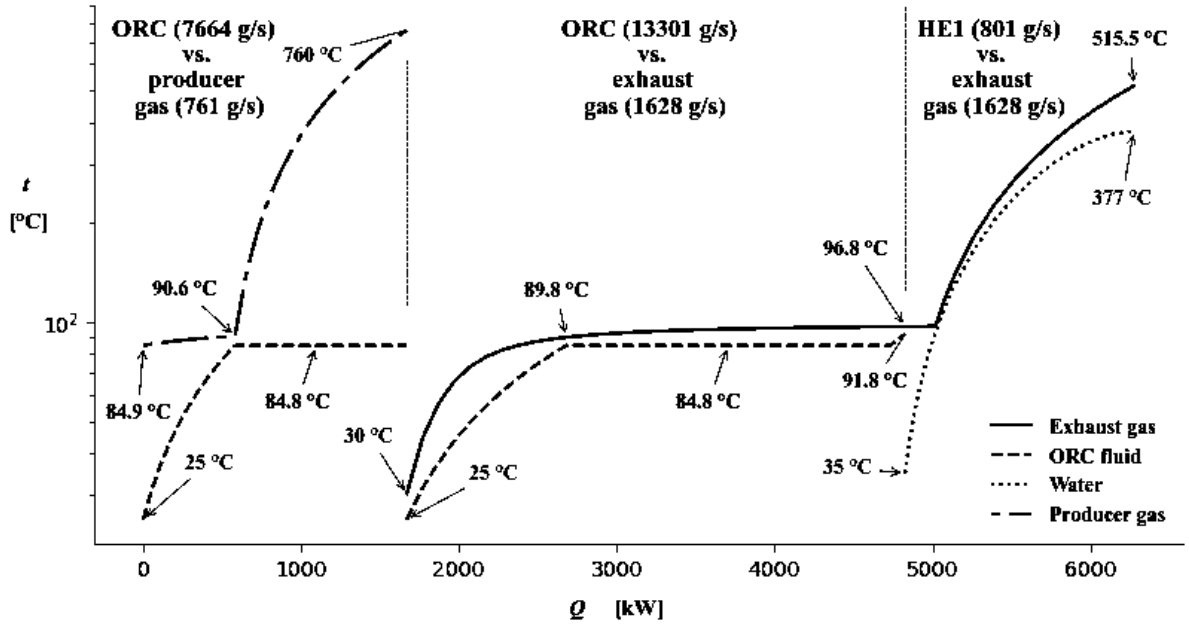

Figure 4: Logarithmic scale temperature distribution with R1233zd(E) as ORC fluid in one-stage HE_{ORC} and HE1 heat exchangers

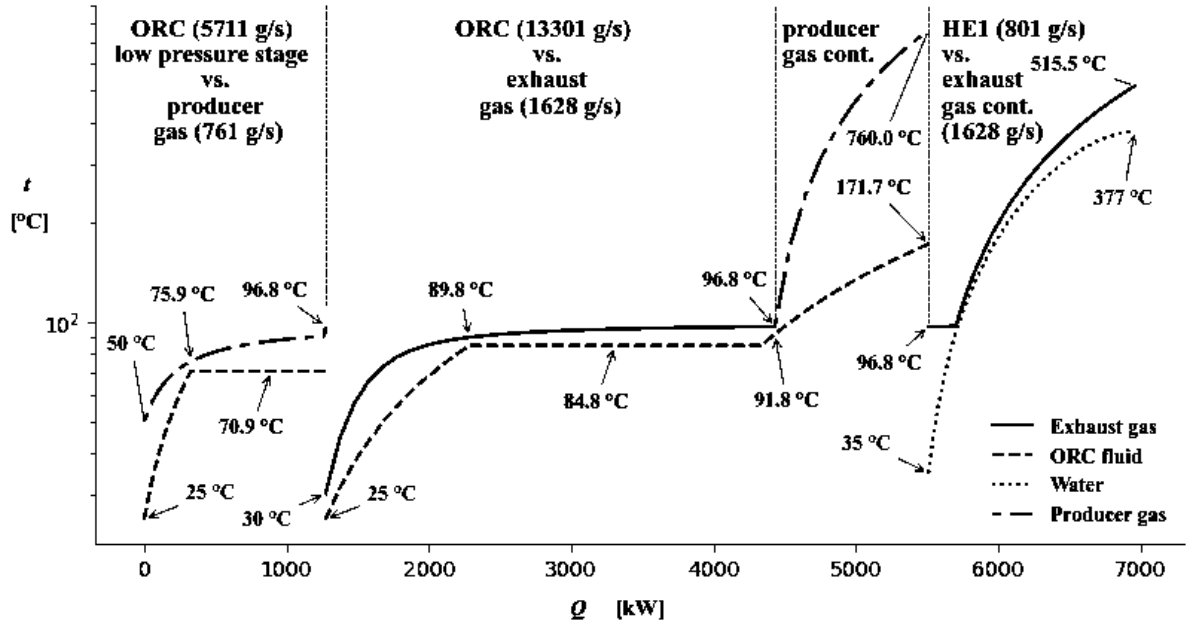

Figure 5: Logarithmic scale temperature distribution with R1233zd(E) as ORC fluid in double-stage HE_{ORC} and HE1 heat exchangers

4 CONCLUSIONS

The integration of a double-stage ORC using R1233zd(E) as the working fluid significantly improves the cumulative efficiency of the nCO_2PP power plant (33.2%) compared to a one-stage ORC (32.3%) or the reference case (27.9%). The ORC integration has an efficiency advantage over the reference case due to the increased heat recovery and the elimination of the high power spray ejector pump. However, the double-stage ORC has an advantage over the one-stage ORC due to better adaptation to the second temperature source. Another reason is the reduction in entropy generation due to the addition of the lower temperature ORC fluid flow to the first stage expanded flow prior to the second turbine expansion. By using an advanced heat recovery process of a double-stage ORC combined with the nCO_2PP power plant and exploiting the special thermodynamic properties of R1233zd(E), this conceptual configuration achieved the highest efficiency.

675

The results suggest that the implementation of ORC in the negative CO_2 emission system outperforms the reference case in terms of energy efficiency, economic return and environmental benefits. The double-stage ORC offers a moderate increase in efficiency and economic return when considering the trade-off in complexity compared to the one-stage ORC variant. Double-stage also offers the lowest CO_2 emissivity in absolute terms, resulting in less CO_2 emissions to mitigate, which is consistent with sustainable and economically sound practices driven by revenue streams.

Nomenclature

eCO_2	emissivity of CO_2, $kgCO_2/MWh$
$\dot{m}$	mass flow rate, g/s
N	power, kW
p	pressure, bar
t	temperature, °C
Greek symbols	
η_{cum}	cumulative efficiency, %
η_i	internal efficiency of devices, %

η_m	mechanical efficiency of devices, %
η_{R_H}	gasifying reactor efficiency, %

Abbreviations

BECCS	bioenergy with carbon capture and storage
C	compressor
CCS	carbon capture and storage
G	generator
GS	gas scrubber
GT	gas turbine
HE	heat exchanger
IRR	internal rate of return
LCOE	levelised cost of electricity
nCO_2PP	negative CO_2 emission gas power plant
NPV	net present value
P	pump
R	gasifier
SEC	spray ejector condenser
WCC	wet combustion chamber

REFERENCES

Aldersey-Williams, J., & Rubert, T. (2019). Levelised cost of energy – A theoretical justification and critical assessment. *Energy Policy*, *124*, 169–179. https://doi.org/10.1016/j.enpol.2018.10.004

Brachi, P., Di Fraia, S., Massarotti, N., & Vanoli, L. (2022). Combined heat and power production based on sewage sludge gasification: An energy-efficient solution for wastewater treatment plants. *Energy Conversion and Management: X*, *13*, 100171. https://doi.org/10.1016/J.ECMX.2021.100171

Delgado-Torres, A. M., & García-Rodríguez, L. (2010). Analysis and optimization of the low-temperature solar organic Rankine cycle (ORC). *Energy Conversion and Management*, *51*(12), 2846–2856. https://doi.org/10.1016/j.enconman.2010.06.022

Ertesvåg, I. S., Madejski, P., Ziółkowski, P., & Mikielewicz, D. (2023). Exergy analysis of a negative CO2 emission gas power plant based on water oxy-combustion of syngas from sewage sludge gasification and CCS. *Energy*, *278*, 127690. https://doi.org/10.1016/J.ENERGY.2023.127690

Fiaschi, D., Manfrida, G., & Maraschiello, F. (2012). Thermo-fluid dynamics preliminary design of turbo-expanders for ORC cycles. *Applied Energy*, *97*, 601–608. https://doi.org/10.1016/j.apenergy.2012.02.033

Jankowski, M., & Borsukiewicz, A. (2019). Multi-objective approach for determination of optimal operating parameters in low-temperature ORC power plant. *Energy Conversion and Management*, *200*, 112075. https://doi.org/10.1016/j.enconman.2019.112075

Jankowski, M., Borsukiewicz, A., Wiśniewski, S., & Hooman, K. (2020). Multi-objective analysis of an influence of a geothermal water salinity on optimal operating parameters in low-temperature ORC power plant. *Energy*, *202*, 117666. https://doi.org/10.1016/j.energy.2020.117666

Johansson, W., Li, J., & Lin, L. (2023). Module-based simulation model for prediction of convective and condensational heat recovery in a centrifugal wet scrubber. *Applied Thermal Engineering*, *219*, 119454. https://doi.org/10.1016/J.APPLTHERMALENG.2022.119454

Lampart, P., Witanowski, Ł., & Klonowicz, P. (2018). Efficiency Optimisation of Blade Shape in Steam and ORC Turbines. *Mechanics and Mechanical Engineering*, *22*(2), 553–564. https://doi.org/10.2478/mme-2018-0044

Liu, X., Zhang, Y., & Shen, J. (2017). System performance optimization of ORC-based geo-plant with R245fa under different geothermal water inlet temperatures. *Geothermics*, *66*, 134–142. https://doi.org/10.1016/j.geothermics.2016.12.004

Maksiuta, D., Moroz, L., Burlaka, M., & Govoruschenko, Y. (2017). Study on applicability of radial-outflow turbine type for 3 MW WHR organic Rankine cycle. *Energy Procedia*, *129*, 293–300. https://doi.org/10.1016/J.EGYPRO.2017.09.156

Micheli, D., Pinamonti, P., Reini, M., & Taccani, R. (2013). Performance Analysis and Working Fluid Optimization of a Cogenerative Organic Rankine Cycle Plant. *Journal of Energy Resources Technology, Transactions of the ASME*, *135*(2). https://doi.org/10.1115/1.4023098/365899

Mikielewicz, D., & Mikielewicz, J. (2010). A thermodynamic criterion for selection of working fluid for subcritical and supercritical domestic micro CHP. *Applied Thermal Engineering*, *30*(16), 2357–2362. https://doi.org/10.1016/j.applthermaleng.2010.05.035

Mikielewicz, D., & Mikielewicz, J. (2014). Analytical method for calculation of heat source temperature drop for the Organic Rankine Cycle application. *Applied Thermal Engineering*, *63*(2), 541–550. https://doi.org/10.1016/j.applthermaleng.2013.11.047

Mikielewicz, D., Wajs, J., Ziółkowski, P., & Mikielewicz, J. (2016). Utilisation of waste heat from the power plant by use of the ORC aided with bleed steam and extra source of heat. *Energy*, *97*, 11–19. https://doi.org/10.1016/j.energy.2015.12.106

MINISTERSTWO ŚRODOWISKA. (2016). *Dziennik ustaw Rozporządzenie Ministra środowiska w sprawie warunków technicznych kwalifikowania części energii odzyskanej z termicznego przekształcania odpadów*. https://isap.sejm.gov.pl/isap.nsf/download.xsp/WDU20160000847/O/D20160847.pdf

Moradi, R., Marcantonio, V., Cioccolanti, L., & Bocci, E. (2020). Integrating biomass gasification with a steam-injected micro gas turbine and an Organic Rankine Cycle unit for combined heat and power production. *Energy Conversion and Management*, *205*, 112464. https://doi.org/10.1016/J.ENCONMAN.2019.112464

Pan, Z., Yan, M., Shang, L., Li, P., Zhang, L., & Liu, J. (2020). Thermoeconomic analysis of a combined natural gas cogeneration system with a supercritical CO2 brayton cycle and an organic rankine cycle. *Journal of Energy Resources Technology, Transactions of the ASME*, *142*(10). https://doi.org/10.1115/1.4047306/1083973

Pysz, M., Głuch, S., & Mikielewicz, D. (2023). Experimental study of flow boiling pressure drop and heat transfer of R1233zd(E) at moderate and high saturation temperatures. *International Journal of Heat and Mass Transfer*, *204*, 123855. https://doi.org/10.1016/J.IJHEATMASSTRANSFER.2023.123855

Quoilin, S., Declaye, S., Tchanche, B. F., & Lemort, V. (2011). Thermo-economic optimization of waste heat recovery Organic Rankine Cycles. *Applied Thermal Engineering*, *31*(14–15), 2885–2893. https://doi.org/10.1016/j.applthermaleng.2011.05.014

Stasiak, K., Ertesvåg, I. S., Ziółkowski, P., & Mikielewicz, D. (2023). Exergetic analysis of the nCO2PP cycle with particular reference to the exergy destruction of sewage sludge due to gasification. *THE 36TH INTERNATIONAL CONFERENCE ON EFFICIENCY, COST, OPTIMIZATION, SIMULATION AND ENVIRONMENTAL IMPACT OF ENERGY SYSTEMS*.

Stasiak, K., Ziółkowski, P., & Mikielewicz, D. (2022). Assessment, optimisation and working fluid comparison of organic Rankine cycle combined with negative CO2 gas power plant system. *7th International Conference on Contemporary Problems of Thermal Engineering*, 357–367. https://www.s-conferences.eu/ftp/cpote/CPOTE_proceedings_19_10.pdf

Wajs, J., Mikielewicz, D., Bajor, M., & Kneba, Z. (2016). Experimental investigation of domestic micro-CHP based on the gas boiler fitted with ORC module. *Archives of Thermodynamics*, *37*(3), 79–93. https://doi.org/10.1515/AOTER-2016-0021

Wang, H., Wu, X., Liu, Z., Granlund, K., Lahdelma, R., Li, J., Teppo, E., Yu, L., Duamu, L., Li, X., & Haavisto, I. (2021). Waste heat recovery mechanism for coal-fired flue gas in a counter-flow direct contact scrubber. *Energy*, *237*, 121531. https://doi.org/10.1016/J.ENERGY.2021.121531

Witanowski, Ł., Klonowicz, P., Lampart, P., & Ziółkowski, P. (2023). Multi-objective optimization of the ORC axial turbine for a waste heat recovery system working in two modes: cogeneration and condensation. *Energy*, *264*, 126187. https://doi.org/10.1016/j.energy.2022.126187

Witanowski, Ł., Ziółkowski, P., Klonowicz, P., & Lampart, P. (2023). A hybrid approach to optimization of radial inflow turbine with principal component analysis. *Energy, 272*, 127064. https://doi.org/10.1016/j.energy.2023.127064

Zaniewski, D., Klimaszewski, P., Witanowski, Ł., Jędrzejewski, Ł., Klonowicz, P., & Lampart, P. (2019). Comparison of an impulse and a reaction turbine stage for an ORC power plant. *Archives of Thermodynamics*.

Zheng, J., Zhong, J., Chen, M., & He, K. (2023). A reinforced hybrid genetic algorithm for the traveling salesman problem. *Computers & Operations Research, 157*, 106249. https://doi.org/10.1016/j.cor.2023.106249

Ziółkowski, P., Badur, J., Pawlak- Kruczek, H., Stasiak, K., Amiri, M., Niedzwiecki, L., Krochmalny, K., Mularski, J., Madejski, P., & Mikielewicz, D. (2022). Mathematical modelling of gasification process of sewage sludge in reactor of negative CO2 emission power plant. *Energy, 244*. https://doi.org/10.1016/j.energy.2021.122601

Ziółkowski, P., Głuch, S., Ziółkowski, P. J., & Badur, J. (2022). Compact High Efficiency and Zero-Emission Gas-Fired Power Plant with Oxy-Combustion and Carbon Capture. *Energies, 15*(7), 2590. https://doi.org/10.3390/en15072590

Ziółkowski, P., Madejski, P., Amiri, M., Kuś, T., Stasiak, K., Subramanian, N., Pawlak-Kruczek, H., Badur, J., Niedźwiecki, Ł., & Mikielewicz, D. (2021). Thermodynamic analysis of negative CO2 emission power plant using aspen plus, aspen Hysys, and ebsilon software. *Energies, 14*(19). https://doi.org/10.3390/en14196304

Ziółkowski, P., Pawlak-kruczek, H., Madejski, P., Bukowski, P., Ochrymiuk, T., Stasiak, K., Amiri, M., Niedzwiecki, L., & Mikielewicz, D. (2022). Thermodynamic, ecological, and economic analysis of negative CO2 emission power plant using gasified sewage sludge. *2nd International Conference on Negative CO2 Emissions*.

Ziółkowski, P., Stasiak, K., Amiri, M., & Mikielewicz, D. (2023). Negative carbon dioxide gas power plant integrated with gasification of sewage sludge. *Energy, 262*, 125496. https://doi.org/10.1016/j.energy.2022.125496

Ziviani, D., Beyene, A., & Venturini, M. (2014). Design, Analysis and Optimization of a Micro-CHP System Based on Organic Rankine Cycle for Ultralow Grade Thermal Energy Recovery. *Journal of Energy Resources Technology, 136*(1). https://doi.org/10.1115/1.4024858

ACKNOWLEDGEMENT

The research leading to these results has been funded by Norway Grants 2014-2021 via the National Centre for Research and Development. This study has been prepared within the project "Negative CO_2 Emission Gas Power Plant" - NOR/POLNORCCS/NEGATIVE-CO_2-PP/0009/2019-00, co-funded by the "Applied Research" Programme under the Norwegian Financial Mechanisms 2014-2021 POLNOR CCS 2019 - Development of CO_2 capture solutions integrated in power and industrial processes.

ORC SEVILLE 2023
7th International Seminar on O.R.C. Power Systems

© 2024 Editorial Universidad de Sevilla. Este es un artículo de acceso abierto distribuido bajo los términos de la licencia de uso y distribución Creative Commons (BY-NC-ND 4.0)

DOI: https://dx.doi.org/10.12795/9788447227457_117

Optimization of organic Rankine cycle using ocean thermal energy based on NSGA-II

Zheng Hu [1], Jiufa Chen [1,2], Bin Guo [3], Chengbin Zhang [1,*]

[1] *Key Laboratory of Energy Thermal Conversion and Control of Ministry of Education, School of Energy and Environment, Southeast University, Nanjing, Jiangsu 210096, P. R. China*
[2] *Nanjing Purple Mountain Institute Ltd, 6 Fengxin Road, Yuhua District, Nanjing, Jiangsu 210096, P. R. China*
[3] *College of Water Conservancy and Civil Engineering, Shandong Agricultural University, Taian, Shandong 271018, P. R. China*
230198429@seu.edu.cn, chen.jiufa@seu.edu.cn, guobin@sdau.edu.cn, cbzhang@seu.edu.cn,
*Corresponding Author

ABSTRACT

The organic Rankine cycle is one of the key methods to utilize ocean thermal energy, which is abundant and continuous renewable energy. In this paper, a non-dominated sorting genetic algorithm-II (NSGA-II) based approach is utilized to optimize an organic Rankine cycle-based ocean thermal energy conversion system. The objective is to maximize the degree of thermal energy utilization and the maximum system power output in. The decision variables considered for optimization include evaporation temperature, condensation temperature, degree of superheating, and working fluid mass flow. The objective functions are defined as thermal efficiency and net power output. The optimization process for the ocean thermal energy conversion Rankine cycle is performed using NSGA-II. The results indicate an inverse relationship between thermal efficiency and power output, meaning that achieving the highest thermal efficiency does not necessarily result in the highest net power output. The utilization of NSGA-II enables the identification of multiple optimal solutions that lie on the Pareto front, representing the best trade-off between thermal efficiency and power output. By considering the investment cost constraint, the most suitable solution for achieving the maximum net power output can be determined.

1 INTRODUCTION

Ocean thermal energy refers to the thermal energy stored within the temperature gradient between surface warm sea water and deep cold seawater. It owns the advantages of stableness, non-fluctuation with temporal and spatial variance. Closed Organic Rankine Cycle (ORC) is the most promising for commercial application of ocean thermal energy conversion (OTEC) since it has the simplest configuration and is easy to miniaturize. However, ocean thermal energy functions within a small temperature gradient (usually ≤23°C) and has low thermal efficiency (usually around 3%). To improve thermal efficiency, many researchers focus on the selection of working fluids, optimization of cycle configuration. Hung *et al*. (2010) found that at low temperature difference conditions, the working fluids with high latent heat of evaporation can achieve higher thermal efficiency. Ganic *et al*. (1980) compares the performance of a closed ORC cycle using inorganic working fluid (ammonia), and organic working fluids (R290, R114). The results show that using ammonia as working fluid can achieve the highest thermal efficiency since its latent heat of evaporation is the highest. In the OTEC process, the temperature fluctuation of warm sea water inside the evaporator will increase the temperature difference between the working fluid outlet of the evaporator and heat source, causing the irreversible loss of heat transfer when using pure working fluid. Therefore, in recent years, researchers are searching for non-zeotropic working fluid to enhance OTEC's efficiency (Araghi *et al*, 2016; Yoon *et al*, 2015). Meanwhile, methods to improve the ORC cycle, such as the introduction of heat recovery heat

exchanger, ejector and multi-stage expansion in the system design, can also enhance the efficiency (Yoon *et al*, 2015).

Both the adoption of non-zeotropic working fluid and the improvement of the ORC cycle add the complexity of the ORC system. Optimizing the design and operation parameters of the ORC cycle can be another solution to enhance the system's performance. Sun *et al*. (2012) selected warm sea water temperature, warm sea water flow rate, evaporation temperature and condensation temperature as decision variables, and ORC net power generation as target variables. The optimal system design parameter is obtained. Wang *et al*. (2019) set evaporation temperature, condensation temperature, warm seawater outlet temperature and cold sea water outlet temperature as optimization variables, and levelized electricity cost and exergy efficiency as objective functions. The normalized Pareto front was obtained using multi-objective particle swarm optimization algorithm. In summary, most researches work on OTEC performance enhancement focus on the selection of working fluids and cycle improvement, while research focusing on optimization of the design and operation parameter are less and only limited to single objective optimization.

To deepen the understanding of the thermal characteristics of OTEC based on closed ORC, this paper established the theoretical static model for the closed ORC cycle. The impact of evaporation temperature, condensation temperature, superheat at turbine inlet and flow rate on the turbine output, cycle thermal efficiency, system investment cost and levelized cost of electricity are calculated and analyzed. Based on this, the generic algorithm is adopted to conduct bi-objective optimization based on the OTEC power plant. In the design optimization, the turbine output power and thermal efficiency are the objective functions, the system investment cost, warm and cold seawater flow rate are the constraints, the evaporation temperature, condensation temperature, turbine inlet overheat and flow rate of working fluids are the optimization variables. Non-dominated Sorting Generic Algorithm is adopted to conduct bi-objective optimization of OTEC and obtain Pareto front of the turbine output power and thermal efficiency to guarantee the maximum thermal efficiency under the designed installed capacity of OTEC.

In summary, this paper demonstrates the use of NSGA-II for optimizing an organic Rankine cycle-based ocean thermal energy conversion system. The methodology considers multiple decision variables and objectives, leading to a set of Pareto-optimal solutions. The study highlights the trade-off between thermal efficiency and power output and provides valuable insights for selecting the optimal design that maximizes net power output within the specified investment cost constraint.

680

2 OTEC MODEL

2.1 System description

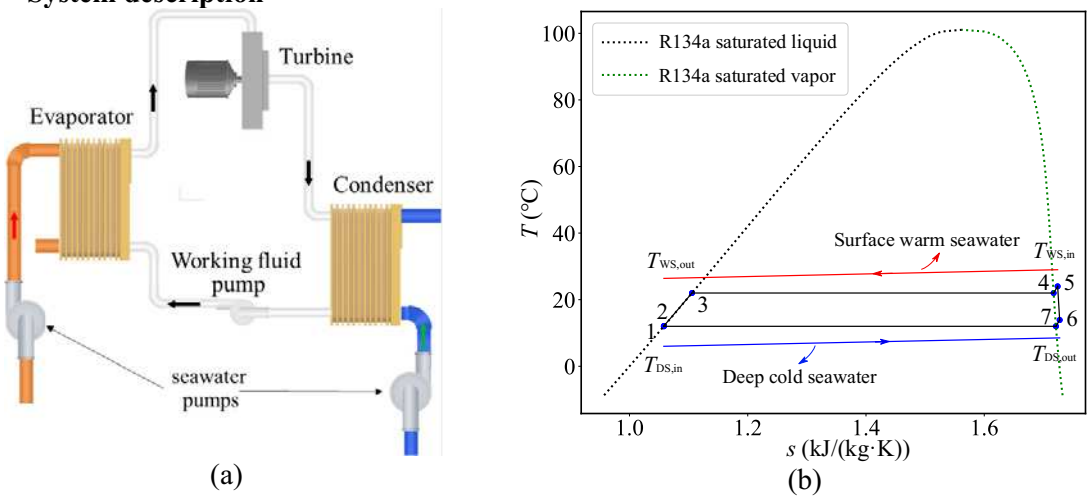

Figure 1: Rankine cycle-based OTEC: (a) working principle, (b) *T-s* diagram.

OTEC system utilizes the temperature gradient between warm surface seawater and cold deep seawater to generate electricity. Figure 1 provides the schematic of Rankine cycle-based OTEC.

Organic fluid R134a is selected as the working fluid. Liquid R134a (state point 1) is pressurized to state point 2 and sent into the evaporator. The working fluid exchange heat with warm surface seawater in the evaporator, which goes through saturated liquid state (point 3), saturated gas state (point 4) and overheat state (point 5). The gas-phase working fluid enters turbine at the evaporator outlet for expansion to generate electricity, while the exhaust gas at the turbine outlet (state point 6) enters the condenser for heat exchange and condenses to state point 1.

2.2 Thermodynamic model

The key to the thermodynamic calculation is to determine the thermodynamic parameters at each point on the *T-s* diagram. Therefore, the thermodynamic model of the cycle is established in Matlab according to the conservation of energy and mass, and the other thermodynamic parameters (including enthalpy and entropy) at each state point are determined by the pressure and temperature parameters, and the physical properties of the work material are calculated using Refprop. The energy equations for each component are listed in Table 1.

Table 1: Energy equations for ORC-based OTEC system

Components	Equations
Working fluid pump	$W_{\mathrm{pump,wf}} = m_{\mathrm{wf}}(h_1 - h_2) = m_{\mathrm{wf}}\left(h_1 - h_{2,\mathrm{is}}\right)\eta_{\mathrm{pump,wf}}$
Evaporator	$m_{\mathrm{WS}} \cdot c_{\mathrm{p,WS}} \cdot \left(T_{\mathrm{WS,in}} - T_{\mathrm{WS,out}}\right) = m_{\mathrm{wf}}(h_5 - h_2)$
Turbine	$W_{\mathrm{tur}} = m_{\mathrm{wf}}(h_5 - h_6) = m_{\mathrm{wf}}\left(h_5 - h_{6,\mathrm{is}}\right)\eta_{\mathrm{tur}}$
Condenser	$m_{\mathrm{DS}} \cdot c_{\mathrm{p,DS}} \cdot \left(T_{\mathrm{DS,in}} - T_{\mathrm{DS,out}}\right) = m_{\mathrm{wf}}(h_6 - h_1)$
Seawater pumps	$W_{\mathrm{pump,SW}} = \dfrac{Q v_{\mathrm{SW}} \Delta P_{\mathrm{t}}}{\eta_{\mathrm{pump,SW}}}$
The subscript pump stands for pump, wf stands for working fluid, η stands for isentropic efficiency of pump; eva and con refer to evaporator and condenser, respectively, WS and DS refer to warm seawater and deep seawater, tur stands for turbine, η_{tur} stands for turbine isentropic expansion efficiency of the turbine, Q_v stands for volume flow rate, ΔP_{t} is the total pressure loss during seawater transportation which can be calculated according to Hu *et al.* (2022).	

Hence, the Net power generation of ORC is obtained by

$$W_{\mathrm{net}} = W_{tur} - W_{\mathrm{pump,wf}} - W_{\mathrm{pump,WS}} - W_{\mathrm{pump,DS}} \quad (1)$$

The net thermal efficiency is given by

$$\eta_{\mathrm{themal}} = \frac{W_{\mathrm{net}}}{Q_{\mathrm{eva}}} \quad (2)$$

The heat transfer areas of the evaporator and condenser can be calculated by

$$Q = UA\Delta T \quad (3)$$

where, U is total heat transfer coefficient, A is the total heat transfer area, ΔT is Logarithmic mean temperature difference (LMTD).

The total heat transfer coefficient is calculated by

$$\frac{1}{U} = \frac{1}{h_{\mathrm{h}}} + \frac{\delta}{\lambda_{\mathrm{p}}} + \frac{1}{h_{\mathrm{c}}} + R_{\mathrm{f}} \quad (4)$$

where, h_h and h_c are the convective heat transfer coefficient on hot and cold sides, respectively, δ is the plate thickness, λp is the thermal conductivity of the plate, R_f is the thermal resistance of dirt.

The LMTD is calculated by

$$\Delta T = \frac{\Delta T_{\max} - \Delta T_{\min}}{\ln\left(\Delta T_{\max}/\Delta T_{\min}\right)} \quad (5)$$

For the evaporator, only a single-phase heat transfer model is established for the warm sea water side. For working fluid in the evaporator, since it goes through subcooling, evaporation and overheat processes. The subcooling and superheat processes are single-phase processes while the

evaporation lies in a two-phase region. Similarly, the working fluid in the condenser goes through two-phase condensation and single-phase subcooling. Therefore, the calculation of evaporation and condenser can be divided into single-phase and two-phase convective heat transfer.

2.2.1 Single-phase convective heat transfer

For single-phase convective heat transfer of plate heat exchanger, Chishom and Wanniarachchi correlations are used to calculate the Nusselt number of warm seawater, cold seawater working fluid in condenser and evaporator in single-phase region (Garcia *et al.*, 2007).

$$Nu_{\mathrm{s}} = 0.724\left(\frac{6\beta}{\pi}\right)^{0.646} Re_{\mathrm{s}}^{0.583} Pr_{\mathrm{s}}^{1/3} \tag{6}$$

where, β is the ripple angle plate, Re and Pr are Reynolds number and Prandtl number, subscript s refers to single-phase. Convective heat transfer hs is calculated by:

$$h_{\mathrm{s}} = \frac{\lambda \cdot Nu_{\mathrm{s}}}{d_{\mathrm{e}}} \tag{7}$$

2.2.2 Two-phase convective heat transfer

In both the condenser and evaporator, two-phase convective heat transfer of the working fluids is calculated by the modified LMTD method. The two-phase region is divided into multiple small sections, in which the thermal and physical properties are considered unchanged. For each section i, the Nusselt number can be calculated using Equation 8 (Wang *et al.* 2013).

$$Nu_{\mathrm{eva,t},i} = 1.926 Pr_{\mathrm{l}}^{1/3} Bo_{\mathrm{eq},i}^{0.3} Re_{\mathrm{eq},i}^{0.5}\left[1 - x_{\mathrm{m},i} + x_{\mathrm{m},i}\left(\frac{\rho_{\mathrm{l}}}{\rho_{\mathrm{s}}}\right)^{0.5}\right] \tag{8}$$

where, subscript t refer to the evaporator and two-phase flow region, Pr_l is the Prandtl number of the saturated liquid state, x_m is the vapor fraction, $Bo_{eq,i}$ and $Re_{eq,i}$ are the equivalent Boiling number and equivalent Reynolds number respectively. Therefore, for the evaporation process, the convective heat transfer coefficient $h_{eva,t}$ of each unit in two-phase region can be calculated using Equation 9.

$$h_{\mathrm{eva,t}} = \frac{\lambda_{\mathrm{l}} \cdot Nu_{\mathrm{eva,t},i}}{d_{\mathrm{e}}} \tag{9}$$

where, λ_l stands for heat conductivity of the liquid.

After the vapor exits from turbine outlet and enters condenser, it flows within the narrow channel between plates at high flow rate and is condensed by the cold seawater. For the two-phase region in the condenser, the liquid film thickness increases gradually along the flow rate direction and heat conductivity gradually decreases. The convective heat transfer coefficient for the two-phase region in the condenser can be calculated using Equation 10-11 (Yan *et al.* 1999).

$$Nu_{\mathrm{con,t}} = 4.118 Re_{eq}^{0.4} Pr_{l}^{1/3} \tag{10}$$

$$\mathrm{h}_{\mathrm{con,t}} = \frac{\lambda_{\mathrm{l}} \cdot Nu_{\mathrm{con,t}}}{d_{\mathrm{e}}} \tag{11}$$

2.3 Thermo-economic model

To evaluate the economic viability of the ocean thermal energy conversion (OTEC) system, a thermal economic model for the system is constructed, using the total investment cost and the levelized cost of energy (LCOE) as economic indicators. The Module Costing Technique (Turton *et al.*, 2018) is utilized for the cost estimation of OTEC systems, which uses the equipment procurement cost C_{P}^{0} under basic conditions (using carbon steel materials at atmospheric pressure) as the base purchase cost for equipment, and employs fitting relationships with the same form for different equipment to calculate equipment costs. The equations for the calculation are as follows:

$$\log_{10} C_{\mathrm{P,e}}^{0} = K_{1,\mathrm{e}} + K_{2,\mathrm{e}} \log_{10}(Y) + K_{3,\mathrm{e}}[\log_{10}(Y)]^2 \tag{12}$$

$$C_{\mathrm{BM,e}} = C_{\mathrm{P,e}}^{0} \cdot \left[Z_{1,\mathrm{e}} + Z_{2,\mathrm{e}} \cdot (F_{\mathrm{M,e}} F_{\mathrm{P,e}})\right] \tag{13}$$

$$C_{\mathrm{BM,tur}} = C_{\mathrm{P,tur}}^{0} \cdot F_{\mathrm{tur}} \tag{14}$$

$$\log_{10} F_{\mathrm{P,e}} = B_{1,\mathrm{e}} + B_{2,\mathrm{e}} \log_{10}(P) + B_{3,\mathrm{e}}[\log_{10}(P)]^2 \tag{15}$$

$$C_{\mathrm{OTEC}} = C_{\mathrm{BM,eva}} + C_{\mathrm{BM,con}} + C_{\mathrm{BM,pump}} + C_{\mathrm{BM,tur}} + C_{\mathrm{BM,ele}} \tag{16}$$

$$C_{\mathrm{OTEC},2019} = C_{\mathrm{OTEC},2001} \cdot \left(\frac{CEPCI_{2019}}{CEPCI_{2001}}\right) \tag{17}$$

$$LCOE = \frac{\frac{i(1+i)^n}{(1+i)^n-1} C_{OTEC,2019} + r_{\mathrm{M}} C_{\mathrm{OTEC},2019}}{W_{\mathrm{net}} \cdot t_{\mathrm{op}}} \tag{18}$$

Here, the subscript e represent the equipment, including plate heat exchanger (PHE), turbine (Tur), pump (Pump), and generator (Gen), i is the annual interest rate selected as 5%, and n is the number of years of operation assumed to be 20 years.

Table 2 Bare model cost parameters

e	Y	K_1	K_2	K_3	Z_1	Z_2	B_1	B_2	B_3	F_M	$F_{P,e}$	F_{tur}
PHE	A/(m^2)	4.6656	-0.1557	0.1547	0.96	1.21	0	0	0	2.4	Eq.(28)	-
Tur	W/(kW)	2.2476	1.4965	-0.1618	-	-	-	-	-	-	-	3.5
Pump	W/(kW)	3.3892	0.0536	0.1538	1.89	1.35	-0.3935	0.3957	-0.00226	2.15	Eq.(28)	-
Gen	P/(kW)	$C_{\mathrm{BM,ele}} = 1850000\left(\frac{P}{11800}\right)^{0.94}$										

2.4 Bi-objective optimization

The installed capacity and cycle thermal efficiency of the ocean thermal energy conversion (OTEC) system are chosen as the objective functions for optimization. The decision variables for optimization are the evaporator temperature (T_{eva}), condenser temperature (T_{con}), turbine inlet steam superheat (T_{sh}), and working fluid mass flow rate (m_{wf}). Under given cold and heat source conditions, the multi-objective optimization problem of the ocean thermal energy conversion system can be described as follows:

$$\begin{cases} Max\{W_{tur} = f_1(T_{\mathrm{eva}}, T_{\mathrm{con}}, T_{\mathrm{sh}}, m_{\mathrm{wf}})\} \\ Max\{\eta_{\mathrm{thermal}} = f_2(T_{\mathrm{eva}}, T_{\mathrm{con}}, T_{\mathrm{sh}}, m_{\mathrm{wf}})\} \end{cases} \tag{19}$$

For the design of ocean thermal energy conversion (OTEC) systems, considering the potential damage to turbine blades caused by liquid droplets in the turbine, there are constraints on the dryness fraction of turbine exhaust during the thermodynamic cycle. Additionally, the heat exchange process in the heat exchangers is limited by the pinch point temperature difference (T_{pp}). Furthermore, the manufacturing cost of the OTEC system is also constrained. Therefore, the constraints for optimizing ocean thermal energy conversion systems are:

$$x_{\mathrm{tur,out}} \geq x_{\mathrm{tur,en}} \tag{20}$$

$$T_{\mathrm{pp,eva}} \geq T_{\mathrm{pp.en}} \tag{21}$$

$$T_{\mathrm{pp,con}} \geq T_{\mathrm{pp,en}} \tag{22}$$

$$C_{\mathrm{OTEC},2019} \leq C_{\mathrm{OTEC,en}} \tag{23}$$

$x_{\mathrm{tur,out}}$ is the dryness fraction of the exhaust at the outlet of the turbine, and to ensure the safety of the system operation, it is required to design the turbine outlet exhaust dryness fraction to be greater than or equal to 0.98. $T_{\mathrm{pp,eva}}$ and $T_{\mathrm{pp,con}}$ are the pinch point temperature differences of the evaporator and condenser, respectively, which are typically located at the saturated liquid point of the working fluid in the evaporator (i.e., state point 3) and the saturated gas point of the working fluid in the condenser (i.e., state point 7). Noted that the improved NSGA-II proposed by Deb *et al.* (2002) is used to solve this multi-objective problem as it offers a robust and effective approach for optimizing ORC system. Its ability to handle multiple objectives, generate Pareto-optimal solutions, maintain convergence and diversity, and efficiently explore the design space makes it a valuable tool for finding optimal designs in ORC-based ocean thermal energy conversion system. Figure 2 depicts the flowchat of the optimization process.

683

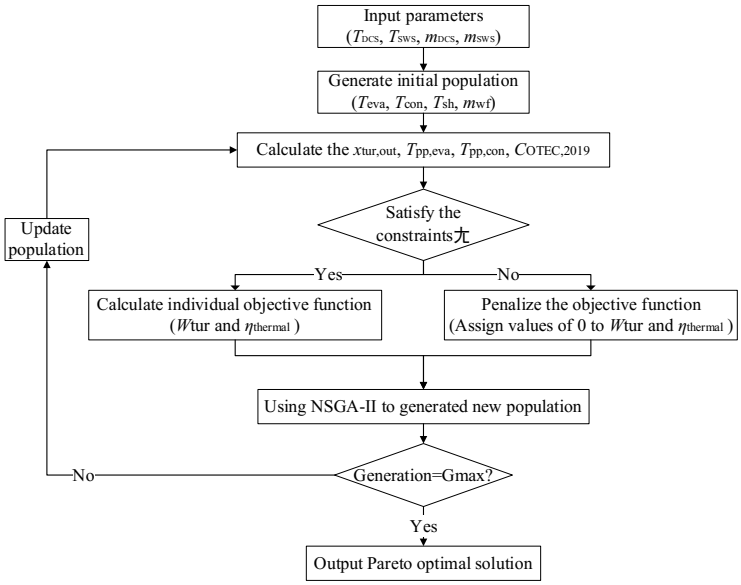

Figure 2: Optimization flowchart.

3 RESULTS AND DISCUSSION

In this section, the decision variables are set as the evaporator temperature, condenser temperature, superheat, and working fluid flow rate, with the system investment cost as a constraint. The turbine output power and cycle thermal efficiency are chosen as objective functions. Genetic algorithm is used to optimize the ocean thermal energy conversion (OTEC) power generation efficiency, and the Pareto front of the bi-objective optimization is obtained. Table 3 gives the input data of the genetic algorithm. Based on the optimization results, the performance of the OTEC system are examined for different installed capacities.

684

Table 3 Input data for genetic algorithm

Items	Values
Population size	200
Number of iterations	200
Crossover rate	0.9
Mutation rate	0.2

Figure 3 shows the Pareto front obtained with sea water mass flow rates as design parameters, where the temperature of the warm and cold seawater is fixed. It can be observed that for the same installed capacity, a larger seawater mass flow rate leads to a higher optimal thermal efficiency of the system. This is mainly because a larger seawater mass flow rate allows for higher evaporator temperature and lower condenser temperature, according to the Carnot cycle principle. Additionally, Figure 4 presents the change in generational distance with evolution generations, showing that the algorithm converges around 100 generations.

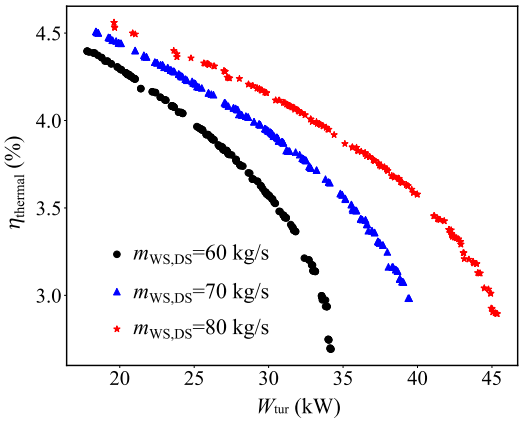

Figure 3: Pareto frontier

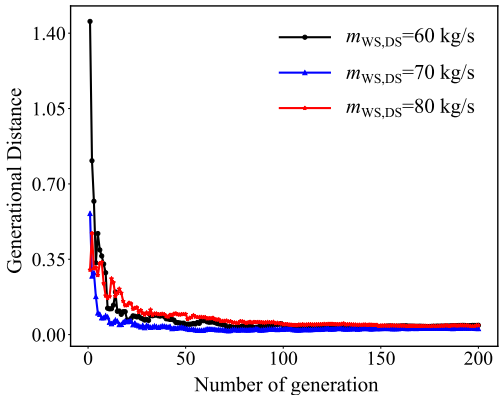

685

Figure 4: Relationship among number of generations and generation distance.

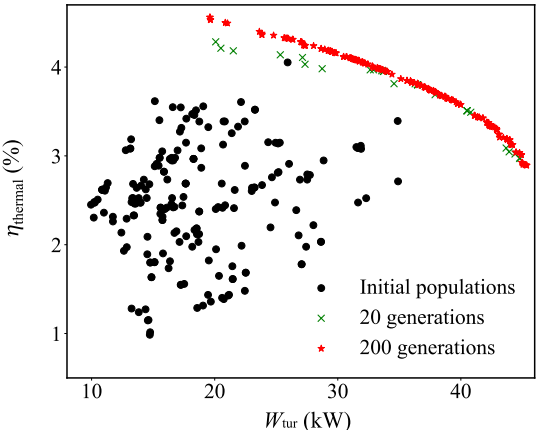

Figure 5: Non-dominated solutions of different generations and initial populations.

To quantify the optimization process and results of the OTEC system's design parameters, with seawater flow rates of hot and cold sides set at 80 kg/s as the design parameters, the system design parameters were optimized. Figure 5 shows the initial population and the non-dominated solution set obtained from the 20th and 200th generations of the optimization process. Figure 6 presents the net power generation capacity, investment cost, and decision variables for some of the Pareto optimal solutions. These solutions represent a trade-off between the two objective functions, and design engineers can choose the best solution for different application conditions. In other words,

each set of solutions ensures the optimal thermal efficiency of the system for a given installed capacity. The solution number in Figure 6 is sorted in ascending order of installed capacity, and from the results, it can be observed that under the given constraints, as the installed capacity increases, the optimal evaporating temperature decreases, the condensing temperature increases, the working fluid mass flow rate increases, which in turn leads to a decrease in the average heat absorption temperature and an increase in the average heat rejection temperature, resulting in lower optimal thermal efficiency, which is in accordance with the Carnot theorem. In other words, increasing the installed capacity of the system comes at the cost of sacrificing the cycle thermal efficiency under the given boundary conditions. Furthermore, as the installed capacity increases, the net output power of the system gradually increases, and the evaporator and condenser areas also increase, as well as the investment cost, but all remain within the given cost constraints.

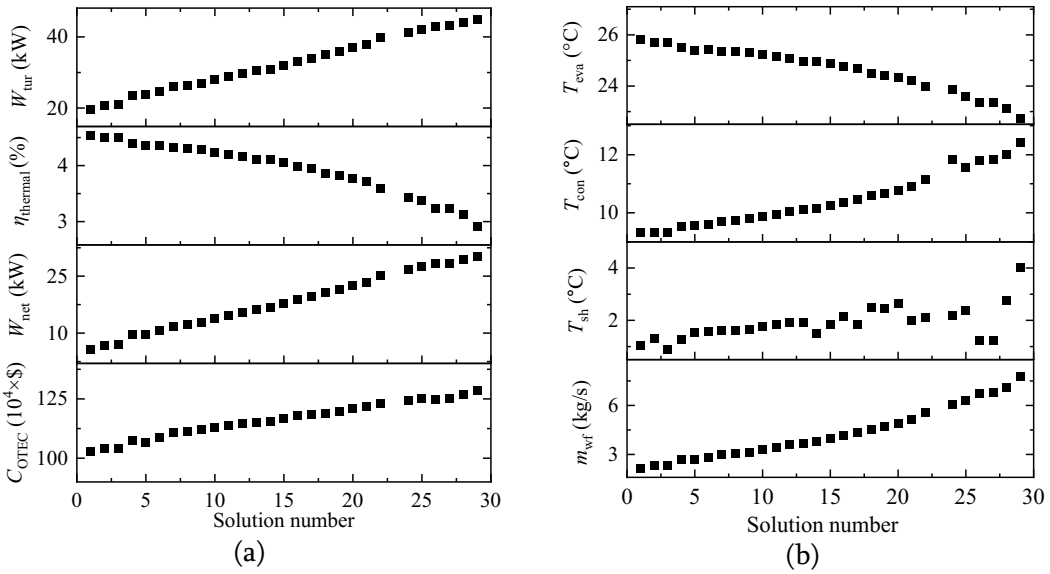

Figure 6: Optimal results of Pareto frontier: (a) objection function, (b) decision variable.

The design parameters of 20kW, 30kW, and 40kW were selected from the optimization results, and the system's other thermodynamic parameters and economic parameters are further obtained, as shown in Table 4. For the oceanic temperature difference closed-cycle power generation system with a capacity of 30kW, using R134a as the organic working fluid, the optimal evaporating temperature is 24.98℃, the condensing temperature is 10.11℃, the superheat is 1.91℃, the mass flow rate of the working fluid is 3.70 kg/s, and the net power generation capacity of the system is 16.17kW. The required evaporator and condenser areas are 122.95 m2 and 57.64 m2, respectively. The total investment cost is 1.1499 million US dollars, and the levelized cost of electricity is 0.86 US dollars/kWh.

Table 5 Performance evaluation of optimized OTEC plants

Item	Unit	20 kW-class	30 kW-class	40 kW-class
W_{tur}	kW	20	30	40
W_{net}	kW	5.70	16.17	25.13
$\eta_{thermal}$	%	4.531	4.116	3.587
T_{eva}	℃	25.83	24.98	23.98
T_{con}	℃	9.33	10.11	11.15
T_{sh}	℃	1.06	1.91	2.13

m_{wf}	kg/s	2.16	3.70	5.58
A_{eva}	m^2	103.02	122.95	135.63
A_{con}	m^2	43.33	57.64	67.46
C_{OTEC}	10^4 \$	102.93	114.99	123.11
LCOE	\$/kWh	2.18	0.86	0.59

4 CONCLUSIONS

To optimize the design parameters prior to the construction of the OTEC power plant, a bi-objective optimization is carried out for the OTEC system, where the evaporator temperature, condenser temperature, turbine inlet superheat, and working fluid mass flow rate are selected as decision variables. Under the constraint of system investment cost and with the objectives of OTEC system installed capacity and cycle thermal efficiency, the thermodynamic cycle parameters were optimized using genetic algorithm to obtain the Pareto optimal solution set. Each design in the solution set maximizes the cycle thermal efficiency for a given installed capacity of the OTEC system. The main findings can be summarized as follows:

(1) Higher evaporation or lower condensation temperatures will result in higher thermal efficiency, but the power output of the system will decrease. This is mainly due to a decrease in the amount of input heat.

(2) OTEC power plants exhibit economies of scale, with larger scale resulting in lower levelized cost of electricity.

(3) For a Rankine cycle-based OTEC system with an installed capacity of 30 kW, the optimal evaporator temperature was found to be 24.98℃, the condenser temperature was 10.11℃, the superheat was 1.91℃, and the working fluid mass flow rate was 3.70 kg/s. The net electricity generation capacity of the system was 16.17 kW, and the required evaporator and condenser areas were 122.95 m2 and 57.64 m2, respectively. The total investment cost of the system was 1.1499 million \$, and the levelized cost of electricity was 0.86 \$/kWh.

REFERENCES

Hung, T.C., Wang, S.K., Kuo, C.H., Pei, B.S., Tsai, K.F., 2010, A study of organic working fluids on system efficiency of an ORC using low-grade energy sources, *Energy*, vol. 35, no. 3:1403-1411.

Ganic, E.N., Wu, J., 1980, On the selection of working fluids for OTEC power plants, *Energy Convers. Manag.*, vol. 20, no. 1:9-22.

Araghi, A.H., Khiadani, M., Hooman, K., 2016, A novel vacuum discharge thermal energy combined desalination and power generation system utilizing R290/R600a, *Energy*, vol. 98, no. 1:215-224.

Yoon, J.I., Soo, C.H., Seol, S.H., Kim, H.U., Ha, S.J., Jung, S.H., Kim, H.J., Lee, H.S., 2015, Performance analysis of OTEC power cycle with a liquid-vapor ejector using R32/R152a, *Int. J. Heat Mass Transf.*, vol. 51, no. 11:1597-1605.

Sun, F., Ikegami, Y., Jia, B., Arima, H., 2012, Optimization design and exergy analysis of organic rankine cycle in ocean thermal energy conversion, *Appl. Ocean Res.*, vol. 35:38-46

Hu, Z., Wan, Y., Zhang, C., Chen, Y., 2022, Compression-assisted absorption refrigeration using ocean thermal energy. *Renew. Energ.*, vol. 186, 755-768.

García-Cascales, J. R., Vera-García, F., Corberán-Salvador, J. M., & Gonzálvez-Maciá, J., 2007, Assessment of boiling and condensation heat transfer correlations in the modelling of plate heat exchangers, *Int. J. Refrig.*, vol. 30 no. 6:1029-1041.

Wang, J., Yan, Z., Wang, M., Li, M., Dai, Y., 2013. Multi-objective optimization of an organic Rankine cycle (ORC) for low grade waste heat recovery using evolutionary algorithm, *Energy Convers. Manag.*, vol. 71:146-158.

Yan, Y. Y., Lio, H. C., Lin, T. F., 1999, Condensation heat transfer and pressure drop of refrigerant R-134a in a plate heat exchanger, *Int. J. Heat Mass Transf.*, vol. 42, no 6:993-1006.

Turton, R., Shaeiwitz, J., Bhattacharyya, D., Whiting, W., 2018, *Analysis, Synthesis and Design of Chemical Processes*, Pearson, New Jersey, 1520 p.

Deb, K., Pratap, A., Agarwal, S., Meyarivan, T.A.M.T., 2022. A fast and elitist multiobjective genetic algorithm: NSGA-II, *IEEE transactions on evolutionary computation*, vol. 6, no. 2:182-197.

ACKNOWLEDGEMENT

This work was supported by the National Key R&D Program of China (2019YFB1504303).

ORC SEVILLE 2023
7th International Seminar on O.R.C. Power Systems

© 2024 Editorial Universidad de Sevilla. Este es un artículo de acceso abierto distribuido bajo los términos de la licencia de uso y distribución Creative Commons (BY-NC-ND 4.0)

DOI: https://dx.doi.org/10.12795/9788447227457_118

TES4TRIG: DEVELOPMENT OF A DEMONSTRATOR FOR THE PRODUCTION OF ELECTRICITY, HEATING AND COOLING BASED ON AN ORGANIC RANKINE CYCLE AND AN EJECTOR COOLING CYCLE DRIVEN BY HIGH-TEMPERATURE PARABOLIC TROUGH COLLECTORS WITH THERMAL ENERGY STORAGE

Konstantinos Braimakis[1,*], Dimitrios Tziritas[2], George M. Stavrakakis[2], Julio Terrón Gutiérrez[3], Siddharth Dutta[4], Christos Xynos[5], Panagiotis Zervas[2], Sotirios Karellas[5]

[1] *Laboratory of Refrigeration, Air Conditioning & Solar Energy*
National Technical University of Athens, Athens, Greece
[2] *MES ENERGY S.A., Athens, Greece*
[3] *CADE Soluciones de Ingeniería, S.L., Parque Científico y Tecnológico de Albacete, Albacete , Spain*
[4] *Protarget A.G., Cologne, Germany*
[5] *Laboratory of Thermal Processes*
National Technical University of Athens, Athens, Greece

*Corresponding Author: mpraim@central.ntua.gr

ABSTRACT

This study presents the development of the TES4Trig demonstrator that will be installed for covering the energy needs of the Administration building of the Lavrio Technological and Cultural Park (LTCP) in Attica, Greece within TES4Trig CSP-ERANET project. The system is driven by high-temperature parabolic trough collectors (PTC) coupled with innovative solid-state thermal energy storage (TES). Heat is supplied to an Organic Rankine Cycle (ORC) – Ejector cooling cycle (ECC) through a heat transfer fluid (HTF). The ORC-ECC is capable of the following operating modes: 1) electricity-only, 2) combined heat and power (CHP) and 3) cooling. The system energy production and consumer demand were considered for the conceptual design and preliminary definition of the operating strategies of the ORC-ECC. The final design of the ORC-ECC system is based on the use of R1233zd(E) as a working fluid, operating at a maximum temperature of 140°C.

1 INTRODUCTION

As of 2023, the vast majority of existing commercial concentrating solar power (CSP) plants (97 out of 105) are based on Steam Rankine Cycle (SRC) and are oriented toward large power capacities above 10 MW_e (IRENA, 2022). Despite the significant development of the technology in the last decades, the economics of CSP is still unfavorable, as it is associated with the highest levelized cost of electricity (LCOE) among other renewable power generation technologies, mainly due to its high capital investment cost (CAPEX).

Two main strategies to increase the cost-effectiveness of CSP plants include the increase of their thermal energy storage (TES) capabilities to improve their capacity factor as well as polygeneration, to produce heating and/or cooling in addition to electrical energy and thus increase their revenue. The latter option is usually infeasible in the case of large CSP plants that are typically located in remote locations (for example in desert areas) far from heating and cooling consumers because of their significant land requirement linked with their low energy density (77 kWh_e/m^2/year) (Lovering et al., 2022). Meanwhile, cost-effective, long-term TES technologies are needed to make CSP plants competitive against utility PV which typically include electrical batteries of limited storage capacity. Considering the above, polygeneration CSP plants at smaller scales that could service building energy consumers combined

with cost-effective TES could have significant market potential and improve the share of CSP in the energy mix.

At smaller scales, the Organic Rankine Cycle (ORC) is more suitable for thermal power generation than SRC, making it attractive for small-scale CSP plants. One of the most typically considered solar collector technology for such plants is parabolic trough collectors (PTCs), which offer good efficiencies at high heat transfer fluid (HTF) temperatures, up to 400°C (Kalogirou, 2023)(Kalogirou, Karellas, Badescu, et al., 2016; Kalogirou, Karellas, Braimakis, et al., 2016). Furthermore, in the last years, the cost of PTCs is declining, presenting opportunities for increasing the cost-competitiveness of the technology (Kurup & Turchi, 2015).

PTC-driven ORC plants for exclusive electricity production or polygeneration based on parabolic trough collectors (PTCs) have been extensively investigated at a theoretical level from a thermodynamic and techno-economic perspective. However, very few examples of experimental prototypes and real-world plants are available, especially considering polygeneration (Kasaeian et al., 2022) Aiming to fill this gap, this study presents the conceptual design and definition of the main operating strategies and main technical specifications of the TES4Trig demonstrator plant (TES4Trig Project, 2023), which will consist of a small-scale, PTC-driven ORC coupled with an ejector cooling cycle (ECC) into a singular ORC-ECC system for the production of electricity, heating and cooling. The demonstrator will also feature an innovative solid-state TES. The demo will service the energy needs of the Administration "Serpieri" Building of Lavrio Technological and Cultural Park (LTCP) in Attica, Greece in the context of a project funded by CSP ERANET (CSP ERANET, 2023).

2 TES4TRIG CONCEPTUAL DESIGN

2.1 Description of the demo site

The TES4Trig demo will be installed to cover the energy needs of the Administration (Admin) "Serpieri" building of the LTCP. The building houses several offices, seminar rooms and library/archive rooms. The area considered for installing the prototype is located at the west of the Admin building, which is sufficiently large for the installation of the solar field of the system. The Admin building was built in 1875 and has high symbolic and architectural value. As a result, great care had to be taken to ensure the harmonious integration of the TES4Trig system with them.

690

2.2 Heating, cooling and electrical energy demands

At present, the building's heating and cooling system consists of a heating oil boiler and a chiller and a hydronic distribution system to deliver hot/chilled water to the building terminal units (fan coil units-FCUs). The boiler has an average capacity of 93.04 kW_{th} and a maximum capacity of 125 kW_{th}. The chiller is a type HRA 0252 model from Climaveneta with a nominal cooling capacity of 61.6 kW_c.

For the needs of the project, the hourly variation of the heating and cooling demand of the building was calculated for 12 characteristic days of the year, each corresponding to a different month. Note that the electricity loads were not a critical factor in the design of the TES4Trig system because its scale is significantly lower than the electricity loads of the building. For the calculation of the heating load, DIN 4701 standard was implemented (DIN, 1995a, 1995b). For the calculation of the cooling load, CLTD/CLF method was implemented (ASHRAE, 1985). The hourly variation of the heating and cooling load of the building for the characteristic day of each month of the heating and cooling periods is illustrated in the diagrams of **Figure 1**.

The maximum heating demand occurs in January at 9:00 am and is about 70 kW_{th}. Generally, the maximum heating demand appears early in the morning, when the building occupants arrive and gradually declines until noon, owing to the solar radiation heat gains. Right after noon, as many of the building areas are not used, the demand abruptly declines, remaining approximately constant until 16:00, at which all users of the building leave.

As far as cooling demand is concerned, its maximum value is around 73 kW_c and occurs near noon in the summer months (July and August). Like the heating demand, the cooling demand abruptly declines after noon. According to calculations, the total annual heating, cooling and electricity demand are equal to 17580 kWh/year, 22720 kWh/year and 11540 kWh/year, respectively.

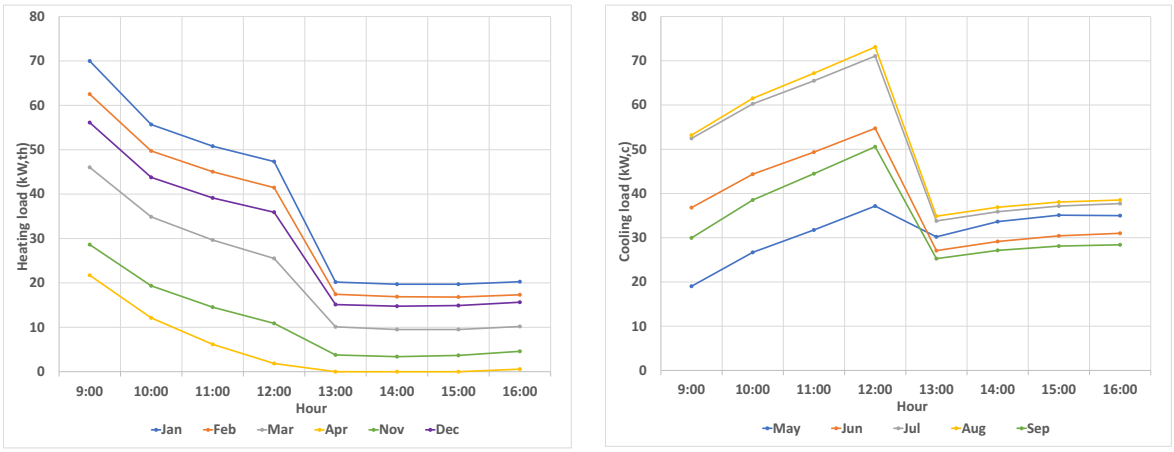

Figure 1: Heating (left) and cooling (right) loads for the characteristic day of each month

2.3 Parabolic trough collectors field

The solar field size was predetermined at the start of the project. It consists of two arrays of a total of 8 modules (4 modules/array) of single-axis tracking PTCs, each having an aperture of about 150 m^2 (total aperture of solar field is about 300 m^2. The PTCs are installed in an approximately N-S orientation, which is preferable for maximizing the annual solar thermal power production based on the available plot of land. The gross land surface occupied by the solar field (considering also necessary spacing of PTC arrays) is about 600 m^2. The peak and average solar thermal power output, as well as the generated energy by the solar field for the two corresponding to maximum (summer) and minimum (winter) solar irradiance throughout the year, are summarized in **Table 1**. The PTC field is capable of a maximum operating HTF temperature of about 400 °C. The project partner responsible for the development and manufacturing and installation of the solar field is the German industrial company Protarget AG (Protarget AG, 2023).

691

Table 1: Solar field main specifications

	Peak power (kW)	**Average power 08:00 – 18:00 (kW_{th})**	**Generated energy (kWh_{th})**
Summer	125	100	1000
Winter	90	51	510

2.4 Thermal energy storage

The TES, developed by project partner CADE Engineered Technologies (CADE Engineered Technologies, 2023) works in parallel with the PTC field and the ORC-ECC (**Figure 2**). Normally, when the solar power produced by the solar field is greater than the thermal demand of the ORC-ECC, the surplus solar power is stored in the TES. On the other hand, when the ORC-ECC thermal demand is higher than the solar power produced by the solar field, thermal energy is supplied from the TES to the ORC-ECC.

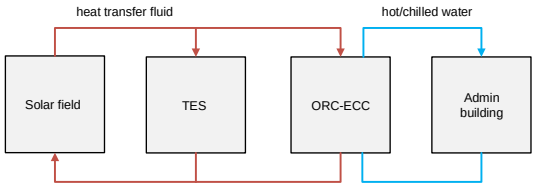

Figure 2: Simplified TES4Trig block diagram

2.5 ORC-ECC

The ORC-ECC system consists of an ORC coupled with an ECC. A recuperative ORC is implemented. The ECC is a thermally-driven cooling cycle, which is applied for the production of cooling through the exploitation of thermal energy and has been widely considered as a solar cooling technology (Braimakis, 2021). It is similar to the conventional vapor compression cycle; however, the mechanical compression of the latter is replaced by a dynamic compression occurring in an ejector device. In the TES4Trig project, an innovative ORC-ECC configuration is designed, which consists of an ORC coupled with an ECC. Both cycles run with the same working fluid and use a common heat exchanger as an ORC evaporator/ECC generator, as well as a common condenser, subcooler and pump.

The ORC-ECC has three operating modes: 1) electricity-only, 2) combined heat and power (CHP), and 3) cooling-only. In the first two modes, only the ORC is operational, while in the third mode, only the ECC is operational. In electricity-only mode, the ORC working fluid is heated in the ORC evaporator, passes through the expander, the recuperator hot-side and subsequently through the condenser and subcooler, exiting it as subcooled liquid which is then discharged by the ORC pump to the recuperator's cold-side. The CHP mode is similar, however, in this mode, the recuperator is bypassed and the condenser pressure/temperature is raised to produce heat at higher temperature. In cooling mode, the working fluid exiting the ORC evaporator is driven to the high-pressure inlet port of the ejector where it is mixed with low-temperature and pressure vapor coming from the ECC (cooling) evaporator that enters the low-pressure port of the ejector. In the ejector, the two streams are mixed and the resulting mixed vapor stream leaves the ejector at an intermediate pressure from its outlet port and is supplied to the condenser and subcooler. The subcooled liquid stream is pressurized in the pump and split into two streams. The first is conveyed to the ORC evaporator and the second to the ECC cooling evaporator.

A simplified schematic of the ORC-ECC configuration for the three different operating modes is shown in **Figure 3**. In each layout, the active sections of the system in each mode are highlighted. Note that the schematics shown in this figure are conceptual and do not represent the actual system. For each mode, the processes occurring are illustrated in temperature-entropy diagrams shown in the same figure.

2.6 -Integration of ORC-ECC with consumer building

692

The ORC-ECC system will be integrated into the existing heating and cooling building infrastructure through an intermediate water-glycol circuit, which is used for the interconnection between the refrigerant circuit (ORC-ECC) and the hydronic distribution network of the building. The water-glycol circuit includes a heating heat exchanger (for the provision of heating), a cooling heat exchanger (for the provision of cooling) and a dry cooler, which is used for rejecting excess heat to the ambient, as shown in **Figure 4**.

As it will be shown next, the cooling produced by the ECC is much smaller than the cooling demand of the building. Therefore, all cooling produced by the ECC is fully utilized. On the other hand, the heating produced by the ORC in CHP mode is comparable to the heating demand of the building. Consequently, because the heating demand of the building fluctuates, the flow rate of the water-glycol being supplied to the heating heat exchanger is adjusted through a three-way valve, while the remaining water-glycol flow is rejected through the dry cooler. At all times, the oil boiler and chiller of the building operate as auxiliary systems.

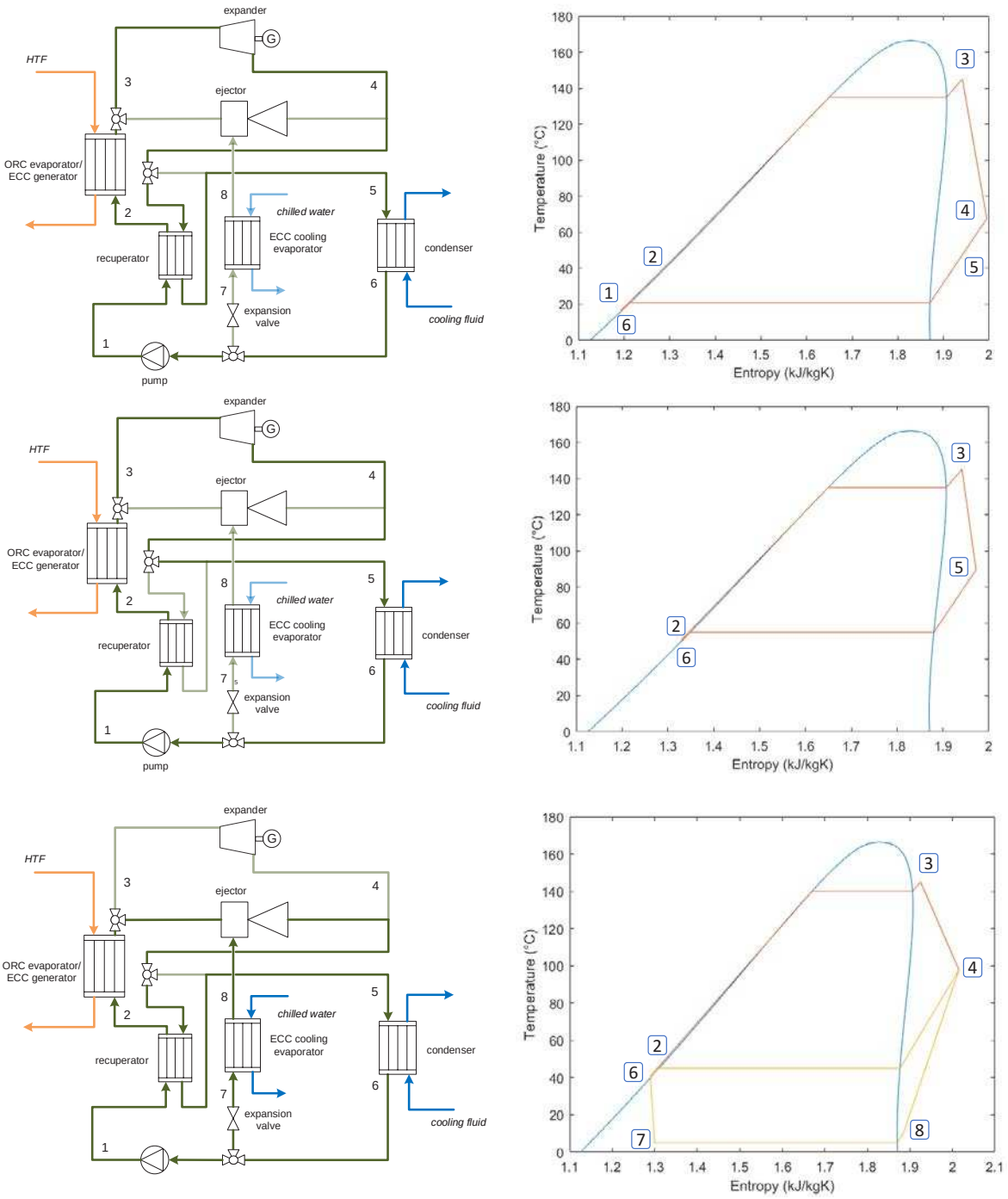

Figure 3: ORC-ECC layout and thermodynamic processes occurring in electricity-only mode (top), CHP mode (middle) and cooling mode (bottom)

693

3 TECHNICAL SPECIFICATIONS AND OPERATING STRATEGIES

3.1 Main technical specifications of ORC-ECC system

For the ORC-ECC, it was decided to use hydrofluoroolefin R1233zd(E) as a working fluid (Honeywell, 2018), as it is non-toxic, non-flammable and environmentally friendly (Braimakis et al., 2017). One of its drawbacks is its relatively lower efficiency for use in ORCs and ECCs because it has a lower critical temperature (167°C) and the fact that its maximum operating temperature is relatively limited to below

150-180°C because of its thermostability (Kim et al., 2018). Notably, the use of the particular low-critical temperature fluid instead of a working fluid of higher critical temperature (such as a hydrocarbon or siloxane) that would result in higher cycle efficiencies in the particular application which is driven by high-temperature PTCs is sub-optimal (Braimakis et al., 2017). Nevertheless, the safety of operation was prioritized over efficiency in the demonstrator because of its special characteristics (non-industrial environment, within a historical site and next to a building that is used as an office by non-trained personnel). Because of the aforementioned limitations, the maximum ORC-ECC cycle temperature was limited to 140°C. The detailed design specifications of the ORC-ECC for the three main operating modes are summarized in **Table 2**. The design specifications were determined by modeling the system in Matlab (*MATLAB - MathWorks*, 2023), using REFPROP (Huber et al., 2022) for the calculation of all thermophysical properties and the 1-D ejector model by Huang et al. (Huang et al., 1999).
Briefly, in the electricity-only and CHP modes, the cycle's maximum temperature is 135 °C and a superheating degree of 10 K is applied, while the condensation temperature is 21/40°C (winter/summer) and 55°C, respectively. Regarding the ECC, the maximum cycle temperature is slightly increased to 140°C and a lower superheating degree is applied (5 K), while a condensation temperature of 45°C is assumed.

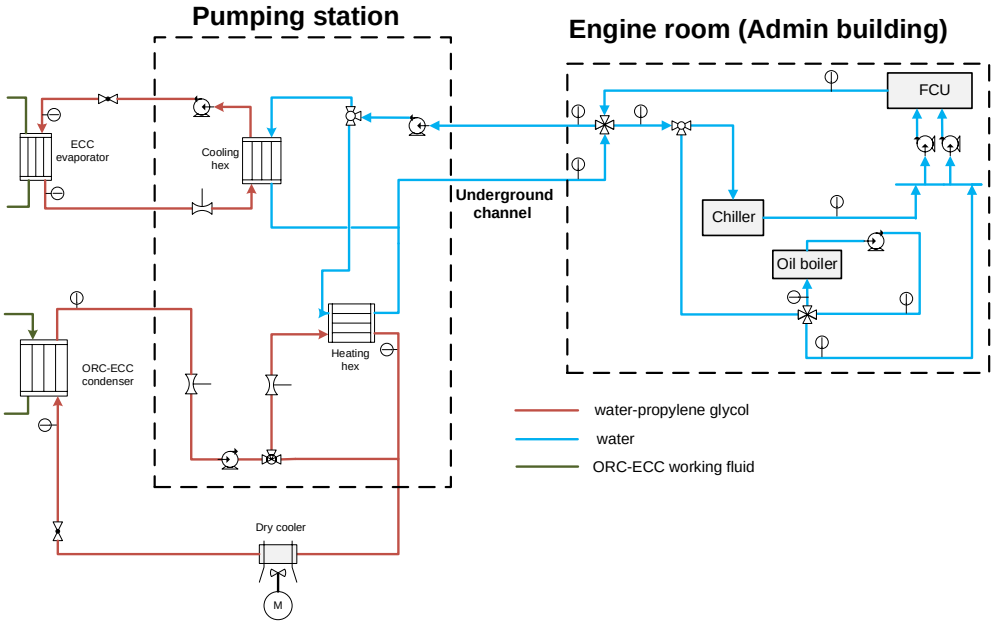

Figure 4: Simple schematic of the integration layout of the ORC-ECC with the building

Critical limitations regarding the ORC upper and lower pressure selection arise because of expander limitations at the targeted power range (about 5-20 kW). In the project, two similar twin-screw expanders with different built-in volume ratios will be used, which are modified commercial compressor models produced by Bitzer. The first is an OSK-5361 model (built-in volume ratio=3.5) that had been used in a past experimental test rig by TUM (Dawo et al., 2021) and the second is an OSN-5361 model (built-in volume ratio 5.6) offered to NTUA by Bitzer (Bitzer, 2023)(TAIRIS AEBE, 2023).
In the following equations, the basic performance indexes are presented based on which the efficiency of the whole system is calculated.
The heat supplied to the ORC-ECC :

$$\dot{Q}_{in} = \dot{m}_{HTF} \cdot \left(h_{HTF}^{in} - h_{HTF}^{out}\right) = \dot{m}_{WF} \cdot (h_2 - h_1) \quad (1)$$

The net electric power produced by the ORC is given by the following equation:

$$P_{e,net} = \dot{m}_{WF} \cdot \left[(h_3 - h_4) \cdot n_{em} - \frac{(h_1 - h_6)}{n_{pump}}\right] \quad (2)$$

The cooling output in the ECC evaporator is given by the following equation:

$$\dot{Q}_c = \dot{m}_{WF} \cdot (h_8 - h_7) \quad (3)$$

The useful heat produced by the condenser in CHP mode is given by the following equation:

$$\dot{Q}_h = \dot{m}_{WF} \cdot (h_5 - h_6) \quad (4)$$

The two main performance indexes of the system are the electric efficiency of the ORC and the thermal coefficient of performance (COP) of the ECC. These are defined according to the following equations:

$$\eta_e = \frac{P_{e,net}}{\dot{Q}_{in}} \quad (5)$$

$$COP_{th} = \frac{\dot{Q}_c}{\dot{Q}_{in}} \quad (6)$$

3.2 Sizing and operating strategies

The starting point for sizing the TES4Trig demonstrator and the definition of its operating strategies was the size of the solar field (determined a priori) and the heating/cooling demand of the building. For the needs of the project, two objectives were prioritized: 1) high annual solar energy utilization, and 2) covering substantial shares of the heating and cooling demand of the building, while also producing as much electrical energy as possible. The following operating strategy was thus defined for the preliminary sizing of the ORC-ECC system:

- Throughout the whole year, the ORC-ECC is operational whenever sufficient thermal power is available either from the solar field or from the TES.
- To ensure the reliability of operation, the ORC operates under a relatively constant thermal input (corresponding to the design thermal input point) with a cut-off threshold of 75% of the design. On the other hand, the ECC operates exclusively at the design point. Meanwhile, the operating mode of the ORC-ECC (and thus the produced useful energy) changes depending on the demand status of the building between electricity-only, CHP and cooling modes.
  - When there is neither heating nor cooling demand, the ORC-ECC produces electricity.
  - When there is heating demand, the ORC-ECC operates in CHP mode. If the produced heat is higher than the heating demand, the excess heat generated in the condenser is rejected to the ambient through the dry cooler. If the produced heat is lower than the heating demand, the ORC-ECC provides all the heat it can to the building and the remaining heat demand is covered by the oil boiler.
  - When there is cooling demand, the ORC-ECC operates in ECC mode. Since the cooling output of the ECC is much lower than the cooling demand, all produced cooling is utilized for covering the cooling demand of the building, while the remaining cooling demand is covered by the chiller of the building.

695

Table 2: ORC-ECC design specifications

Parameter	Electricity-only	CHP	Cooling-only
HTF inlet/outlet temperature (°C)		400/350	
Maximum working fluid temperature (°C)	135		140
Maximum fluid pressure (bar)	17.4		20.9
Working fluid superheating degree at ORC evaporator/ECC generator outlet (K)	10		5
Expander model used	OSN-5361 (winter) OSK-5361 (summer)	OSK-5361	-
Condensation temperature (°C)	21 (winter) 40 (summer)	55	45
Cold stream temperature rise in recuperator (K)	30 (winter) 20 (summer)	0	25
Cooling evaporator saturation temperature (°C)	-		5
Cooling evaporator superheating degree (K)	-		2
Subcooling degree at pump inlet (K)		5	
Expander isentropic efficiency (%)	65		-
Generator electromechanical efficiency (%)	96		
Pump isentropic efficiency (%)		65	
Pump motor electromechanical efficiency		85	
Water-glycol temperature at ECC evaporator inlet/outlet (°C)			13/8
Hot/chilled water return/supply temperature to/from building hydraulic network (°C)	-	47/52(hot water)	18/17.4 (chilled water)
Water-glycol temperature at condenser inlet/outlet (°C)	13/18 (winter) 32/47 (winter)	47/52	37/42
ORC electric efficiency (%)	13.6 (winter) 10.7 (summer)	8.9	-
Heating efficiency (%)	-	87.4	-
ECC ejector entrainment ratio (-)	-		0.13
ECC thermal COP (-)	-		0.10

696

Regarding the thermal input to the ORC-ECC by the solar field and TES, the following operating strategy is applied:

- If there is no sun (no SF solar thermal power - $\dot{Q}_{SF} = 0$) the following cases are distinguished:
  - If the available thermal power from the TES ($\dot{Q}_{TES} = 0$) is lower than the minimum required by the ORC-ECC ($\dot{Q}_{min}$), the TES is idle while the ORC-ECC is not operational (**No operation mode**).
  - If the available thermal power from the TES is higher than the minimum required by the ORC-ECC ($\dot{Q}_{TES} > \dot{Q}_{min}$), the TES drives the ORC-ECC (**TES production and discharge mode**). The following cases are distinguished regarding the ORC-ECC:
    - If the available thermal power from the TES is lower than the nominal required by the ORC-ECC ($\dot{Q}_{nom} > \dot{Q}_{TES} > \dot{Q}_{min}$), the ORC-ECC operates in part-load (**TES production and discharge mode A**).

- If the available thermal power from the TES is higher than the nominal required by the ORC-ECC ($\dot{Q}_{TES} > \dot{Q}_{nom}$), the ORC-ECC operates in full load (**TES production and discharge mode B**).

- If there is sun ($\dot{Q}_{SF} > 0$) the following cases are distinguished:
  - If the SF solar thermal power is lower than the minimum required by the ORC-ECC ($\dot{Q}_{SF} < \dot{Q}_{min}$), the following cases are distinguished:
    - If the sum of the SF solar thermal power and available thermal power from the TES is lower than the minimum required by the ORC-ECC ($\dot{Q}_{SF} + \dot{Q}_{TES} < \dot{Q}_{min}$), the ORC-ECC is not operational and the TES is charged (**Charge mode**).
    - If the sum of the SF solar thermal power and the available thermal power from the TES is higher than the minimum required by the ORC-ECC but lower than the nominal ($\dot{Q}_{nom} > \dot{Q}_{SF} + \dot{Q}_{TES} > \dot{Q}_{min}$), the ORC-ECC operates in part-load and is driven by both the SF and TES **(SF-TES production and discharge mode**).
  - If the SF solar thermal power is higher than the minimum required by the ORC-ECC but lower than the nominal ($\dot{Q}_{nom} > \dot{Q}_{SF} > \dot{Q}_{min}$), the SF solar thermal power is used for driving the ORC-ECC, which operates in part-load. No heat is stored (**SF production mode**).
  - If the SF solar thermal power is higher than the nominal required by the ORC-ECC ($\dot{Q}_{SF} > \dot{Q}_{nom}$), the needed SF solar thermal power is used for driving the ORC-ECC while the surplus solar thermal power ($\dot{Q}_{SF} - \dot{Q}_{nom}$) is stored in the TES (**SF production and charge mode**).

In the flowchart of **Figure 5** the described operation strategy is illustrated.

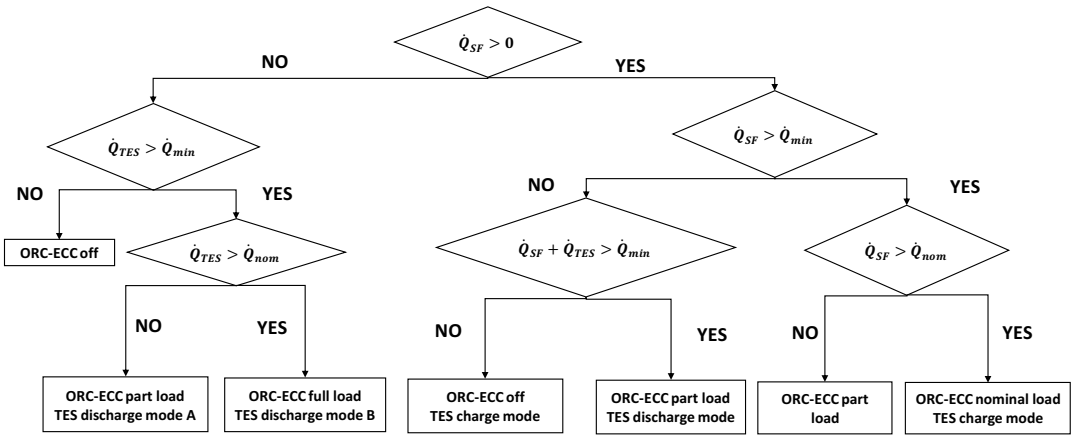

Figure 5: Flowchart of the operating strategy

3.3 TES4Trig demonstrator overall conceptual design and operating strategies

Based on the aforementioned considerations, the ORC-ECC was sized based on a nominal thermal input of 75 kW_{th}, equal to the nominal thermal power capacity of the TES, which will have a total energy storage capacity of 400 kWh_{th}. Based on the specifications shown in **Table 2**, the power, heating and cooling output of the system is presented in **Table 3**.

Table 3: Electric power, heating and cooling output of TES4Trig system (nominal)

Parameter	Electricity-only	CHP	Cooling-only
Electric power output (kW_e)	10.2 (winter) 8.0 (summer)	6.7	-
Heating output (kW_{th})	-	65.6	-
Cooling output (kW_c)	-	-	7.7

3.4 Experimental validation and challenges

The commissioning of the prototype is planned for Q1 2024. Comissioning tests are necessary to fully define the control of each subsystem and the overall prototype. Following commissioning, the prototype will be demonstrated for the following years to evaluate its performance under variable conditions of solar availability for different cases of the building energy demand for all operational modes.

To date, the most challenging aspect of the project is the integration of the prototype into the consumer building. Because of the architectural and historical value of the building, great care had to be taken to minimize aesthetic disruption of the location. This necessitated the development of a very long underground channel to house piping and cables (power supply, automation) since it was not acceptable to carry out any non-reversible interventions on the building itself. Secondly, integration challenges arise because of the sophisticated automation, large number of equipment components (valves, sensors) and complexity of the piping interconnection layout with the existing infrastructure of the building, considering all different operating modes and the need for providing heating and cooling at specific temperatures. An additional challenge is the development of fully automated control, which should orchestrate all different subsystems of the prototype (solar field, thermal energy storage, ORC-ECC) as well as the consumer building itself.

Regarding the ORC-ECC, the major challenge was the difficulty of developing a micro-scale ORC to be driven by a very high-temperature heat source, which was the original scope of the project. This is because of several reasons. First, there is currently very limited (if any) availability of micro-scale expansion machines capable of operating at very high temperatures above 140°C. Secondly, because of the installation of the prototype in a non-industrial site, safety precautions dictated the use of non-flammable working fluids, excluding the use of alkanes which are suitable for high temperatures. As a result, the system was eventually designed for operation at a maximum temperature of 140°C. This decision required the use of a sophisticated, tailor-made evaporator, because of the significantly high-temperature difference between the working fluid and the HTF.

4 CONCLUSIONS

698

In the present work, the conceptual design, operating strategy and sizing of the TES4Trig prototype and its subsystems were described. The system will be installed for covering the energy needs of the Admin building of the Lavrio Technological and Cultural Park (LTCP).

NOMENCLATURE

Abbreviations

CHP	Combined Heat & Power
ECC	Ejector Cooling Cycle
HTF	Heat Tranfer Fluid
LTCP	Lavrio Technological and Cultural Park
ORC	Organic Rankine Cycle
PTC	Paracolic Trough Collectors
SF	Solar Field
TES	Thermal Energy Storage

Variables

COP	Coefficient of performance	(-)
h	specific enthalpy	(kJ/kg)
$\dot{m}$	mass flow rate	(kg/s)
P	power	(kW)
$\dot{Q}$	heat duty	(kW)

Greek letters

η	efficiency	(-)

Subscript

c	cooling
e	electric
em	electromechanical (expander-generator)
h	heating
HTF	heat transfer fluid
in	input, inlet
min	minimum thermal power required for driving the ORC-ECC
n	net
net	net
nom	nominal thermal power required for driving the ORC-ECC
out	outlet
pump	pump
SF	thermal power produced by solar field
TES	thermal power available from thermal energy storage
th	thermal
WF	working fluid

REFERENCES

ASHRAE. (1985). *American Society of Heating, Refrigerating and Air-Conditioning Engineers, 1985 ASHRAE Handbook: Fundamentals, Atlanta: American Society of Heating, Refrigerating and Air-Conditioning Engineers, 1985.*

Bitzer. (2023). *BITZER*. https://www.bitzer.de/gb/en/

Braimakis, K. (2021). Solar ejector cooling systems: A review. *Renewable Energy*, *164*, 566–602. https://doi.org/10.1016/j.renene.2020.09.079

Braimakis, K., C. Roumpedakis, T., Leontaritis, A.-D., & Karellas, S. (2017). Comparison of Environmentally Friendly Working Fluids for Organic Rankine Cycles. *Advances in New Heat Transfer Fluids*, 377–426. https://doi.org/10.1201/9781315368184-13

CADE Engineered Technologies. (2023). *https://cadeengineering.com/*.

CSP ERANET. (2023). *https://csp-eranet.eu/results/thermal-energy-storage-demand-solar-trigeneration-tes4trig*.

Dawo, F., Eyerer, S., Pili, R., Wieland, C., & Spliethoff, H. (2021). Experimental investigation, model validation and application of twin-screw expanders with different built-in volume ratios. *Applied Energy*, *282*, 116139. https://doi.org/10.1016/J.APENERGY.2020.116139

DIN. (1995a). *DIN 4701-1 Rules for calculating the heat load of buildings- Part 1: Basic rules for calculation*.

DIN. (1995b). *DIN 4701-2 Rules for calculating the heat requirement of buildings - Part 2: Tables, pictures, algorithms*.

Honeywell. (2018). *A Better Environment with Next-Generation Solstice® zd Refrigerant Solstice zd: Compliant with Regulations*.

Huang, B. J., Chang, J. M., Wang, C. P., & Petrenko, V. A. (1999). A 1-D analysis of ejector performance. *International Journal of Refrigeration*, *22*(5), 354–364. https://doi.org/10.1016/S0140-7007(99)00004-3

Huber, M. L., Lemmon, E. W., Bell, I. H., & McLinden, M. O. (2022). The NIST REFPROP Database for Highly Accurate Properties of Industrially Important Fluids. *Industrial and Engineering Chemistry Research*, *61*(42), 15449–15472. https://doi.org/10.1021/ACS.IECR.2C01427

IRENA. (2022). *Renewable Power Generation Costs in 2021*.

Kalogirou, S. A. (2023). *SOLAR ENERGY ENGINEERING : processes and systems.*

Kalogirou, S. A., Karellas, S., Badescu, V., & Braimakis, K. (2016). Exergy analysis on solar thermal systems: A better understanding of their sustainability. *Renewable Energy*, *85*, 1328–1333. https://doi.org/10.1016/J.RENENE.2015.05.037

Kalogirou, S. A., Karellas, S., Braimakis, K., Stanciu, C., & Badescu, V. (2016). Exergy analysis of solar thermal collectors and processes. *Progress in Energy and Combustion Science*, *56*, 106–137. https://doi.org/10.1016/J.PECS.2016.05.002

Kasaeian, A., Mirjavadi, K., Pourmoghadam, P., Asgari Sima, F., Amirhaeri, Y., Borhani, S., & Fereidooni, L. (2022). Organic Rankine cycles powered by parabolic trough collectors: An overview. *Sustainable Energy Technologies and Assessments*, *54*, 102847. https://doi.org/10.1016/J.SETA.2022.102847

Kim, S., Rached, W., & Abbas, L. (2018). Performance and Stability of E-1233zd in Energy Recovery Applications. *International Refrigeration and Air Conditioning Conference*. https://docs.lib.purdue.edu/iracc/2053

Kurup, P., & Turchi, C. S. (2015). *Parabolic Trough Collector Cost Update for the System Advisor Model (SAM)*. https://doi.org/10.2172/1227713

Lovering, J., Swain, M., Blomqvist, L., & Hernandez, R. R. (2022). Land-use intensity of electricity production and tomorrow's energy landscape. *PLOS ONE*, *17*(7), e0270155. https://doi.org/10.1371/JOURNAL.PONE.0270155

MATLAB - MathWorks. (2023). https://www.mathworks.com/products/matlab.html

Protarget AG. (2023). *https://protarget-ag.com/*.

TAIRIS AEBE. (2023). *Ταΐρης ΑΕΒΕ – Κορυφαίες λύσεις ψύξης, κλιματισμού & θέρμανσης σε όλους τους κλάδους την βιομηχανίας*. https://www.tairis.gr/en/enhome/

TES4Trig Project. (2023). *Thermal Energy Storage for On-demand Solar Trigeneration (TES4Trig), http://www.solar.demokritos.gr/ERANET/*.

ACKNOWLEDGEMENT

The study has been funded by the TES4Trig project within the CSP ERANET 1st Joint Call.

700

ORC SEVILLE 2023
7th International Seminar on O.R.C. Power Systems

© 2024 Editorial Universidad de Sevilla. Este es un artículo de acceso abierto distribuido bajo los términos de la licencia de uso y distribución Creative Commons (BY-NC-ND 4.0)

DOI: https://dx.doi.org/10.12795/9788447227457_119

Simulation and Operation of a CSP that works with a HRB cycle

Antonio J. Subires[1*], Antonio Rovira[1]

[1]Universidad Nacional de Educación a Distancia (UNED), c/ Juan del Rosal, 12, 28040 Madrid, Spain,
*asubires@ind.uned.es

ABSTRACT

A Hybrid Rankine Brayton power cycle (HRB) is proposed as an alternative to the current technology used in Concentrated Solar Powerplants (CSPs) that work with medium temperatures (<400ºC). Other alternative power cycles that are common in the technical literature are presented in this paper for comparison purposes: a supercritical CO2 recompression Brayton cycle (sCO2-RB), and an Organic Rankine Cycle (ORC). To do this, a parametric analysis is first carried out to compare the efficiencies of the cycles. After that, the HRB power block with the highest efficiency is sized, and a new parametric analysis of the cycles is carried out taking the HRB design as reference. For this, the related parameters to the total area of the heat exchangers of the power block and the area of the solar field are standardized. After that, the designs that maximize the power produced for each cycle are selected. Finally, an annual simulation and a comparison between the annual energy produced for each case is done.

1 INTRODUCTION

1.1 Background

CSPs are a technology that plays a significant role in the electricity production through renewable energy. CSPs allow a dispatchable production, a characteristic that not all the renewable energy technologies have. This allows the decoupling between the availability of the renewable resource and the moment of electricity production. Consequently, production can be adjusted to the supply and demand curves. This is achieved by adding a heat storage system (TES) between the solar field and the power cycle.

The technology used in each of the CSP systems is quite established. For the solar field there are different solutions depending on the radiation concentration factor: Fresnel and parabolic trough collectors (PTC) for low-medium concentration and tower for high concentration. The higher the concentration, the temperature of the hot sink increases, leading to higher power cycle efficiencies. The technology mostly used in TES is the molten salt tanks, which exchange sensible heat with the heat transfer fluid (HTF) that comes from the solar field. For this, a hot and a cold storage tank are used, circulating the salts from one to the other depending on whether energy is stored or released from the system.

The steam Rankine power cycle with superheating, reheating and regenerative preheat is the most widespread choice. Different alternatives of power cycles as well as working fluids have been proposed in the technical literature. One of the main drawbacks of the Rankine steam cycle is the great complexity of the installation, since it includes many heat exchangers as well as steam extractions in the turbine. In the technical literature there are several studies that use subcritical and transcritical ORC alternatives[1], [2]. These cycles simplify the installation but are slightly less efficient than Rankine steam cycles. In ORCs, the steam extractions from the turbine are avoided and the number of recuperators is reduced (generally to just one). In addition, by choosing a suitable fluid, dry expansions are achieved in the last stages of the turbine as well as a high values of power density. ORCs applications are focused on the electricity production of limited power, through biomass, solar, geothermal, and waste heat from industrial processes [3], [4]. The main disadvantage of ORCs is the limitation of the maximum temperature they can reach (usually below 400ºC), so they are useful for medium and low temperature applications.

Another alternative is the sCO2-RB [5]. Although thermodynamic properties of CO2 are less attractive than those of the organic fluids usually used in ORCs, CO2 has no maximum temperature limitation, so it is recommended in high temperature applications (>500ºC). For turbine inlet temperatures higher than 550 °C, the sCO2-RB reaches higher efficiency values than the supercritical steam Rankine cycle [6].

The HRB configuration was presented in [7] . It includes some insights of the sCO2-RB that make it suitable for medium-low temperatures (<400ºC), obtaining higher efficiencies than the ORCs. However, the working fluid must be selected carefully to make it suitable for the cycle.

In this paper, four alternative power cycles (HRB propane, HRB isobutane, ORC toluene and sCO2-RB) are proposed to work in a 100 MW CSP with TES and PTC. The powerplant is located in Sevilla. In Section 1.2, a set of thermodynamic factors that allow to compare the efficiency of the power cycles are showed. In Section 1.3 and Section 1.4, the layout and general considerations of the cycles are described. Section 2 shows the methodology used to carry out the parametric analysis, the sizing of the different systems and the operation and simulation of a typical year. Section 3 shows the results and Section 4 the conclusions and future work.

1.2 Thermodynamic factors

Considering the Carnot efficiency, a set of factors are defined [8] .These factors allow to compare the efficiency of the different power cycles. Equation 1 shows that factors:

$$\eta = 1 - \frac{Q_c}{Q_h} = 1 - \frac{\tilde{T}_c \cdot \Delta s_c}{\tilde{T}_h \cdot \Delta s_h} = 1 - \frac{T_{min}}{T_{max}} \cdot \frac{T_{max}}{\tilde{T}_h} \cdot \frac{\tilde{T}_c}{T_{min}} \cdot \frac{\Delta s_c}{\Delta s_h} = 1 - \frac{1}{CN} \cdot \frac{1}{F_h \cdot F_C \cdot F_s} \quad (1)$$

Where $\tilde{T}_h$ is the mean temperature of heat addition, $\tilde{T}_c$ the mean temperature of heat rejection, Δs_h the entropy increment of heat addition and Δs_c the entropy increment of heat rejection. CN is the Carnot factor, which reduces the efficiency when the maximum and minimum temperatures of the cycle are closer. F_h and F_c are the factors of heat addition and rejection. These factors take the unit value when during the heat addition or rejection the temperature of the fluid is constant. This happens when processes take place through a latent heat exchange. Sensible heat exchanges take values lower than one. On the other side F_s is the entropy generation factor. This parameter considers the irreversibilities in all the processes of the cycle.

1.3 Description of the HRB cycle

In the HRB cycle, a Brayton and a supercritical Rankine cycle take place. Hybridization is achieved by bypassing part of the low-pressure flow that leaves the recuperator through a compressor as it is shown in Figure 1. Most of the main flow follows a supercritical Rankine cycle, while the bypass fraction follows a Brayton cycle.

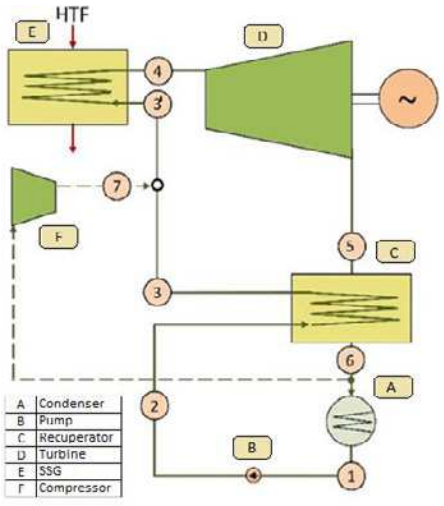

Figure 1: Layout of HRB cycle

F_c is high since the cooling process of the Rankine cycle is a condensing process. F_h is also high because the cycle includes a regenerator. The penalisation of F_s in the efficiency can be reduced selecting a good design: Choosing an optimal compression ratio can move the heat addition process away from the critical point, so the specific heat of the fluid remains constant during all the process. On the other hand, the irreversibility of mixing the bypassing flow and the flow that is heated in the recuperator could be reduced if the thermal properties are similar. Finally, selecting a proper bypassing factor could balance the heat capacity of the vapor and liquid state flows that exchanges energy in the recuperator.

It is important to choose a suitable working fluid. A high cp/R at ideal gas condition implies a lower difference between the specific heat of the vapor and the liquid state, so a lower recompression fraction value to balance the recuperator is needed. This leads to a lower compression work. Besides, it should be noted that a too high cp/R value can lead to wet compression, since the slope of the saturated vapor curve is positive. The proposed fluids, propane and isobutane, meet the above conditions. Figure 2 shows the T-S diagram of propane and isobutane cycles. It can be seen how the slope of the saturated vapor curve in isobutane is higher than that of propane.

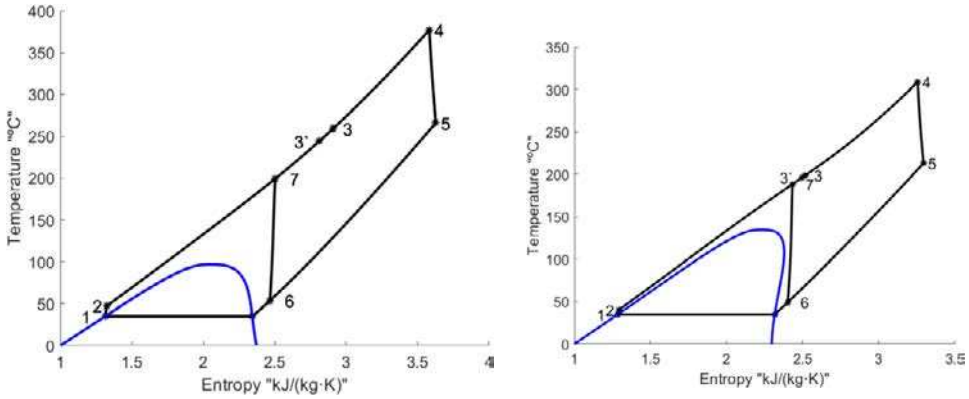

Figure 2: T-S diagram of HRB layout working with propane (left) and isobutane (right)

1.4 Description of sCO2-RB and ORC

sCO2-RB has a similar layout that the HRB but only changing the pump for a compressor, and the condenser for a cooler since the heat rejection is a sensible heat exchange. In this paper, the sCO2-RB showed has only one recuperator since the temperature range is not high. sCO2-RB in high temperature applications has two recuperators. The inlet compressor temperature and pressure is slightly above the critical point. The high specific heat capacity and low compressibility factor near this region, leads to a lower work of the compressor and a lower heat rejection mean temperature that increases the F_s factor. Figure 3 shows the T-S diagram of sCO2-RB cycle.

ORCs have different layouts depending on whether they are subcritical or transcritical. In the transcritical ones, the conventional boiling process is replaced by a sensible heating one that could lead to lower irreversibilities. As the recuperator is not balanced (there is not a bypass fraction), it is interesting select fluids with high heat capacity of the vapor to reduce the F_s. Toluene is a good candidate since it also has a high critical temperature. Figure 4 shows the T-S diagram of a transcritical and subcritical ORC toluene, respectively.

703

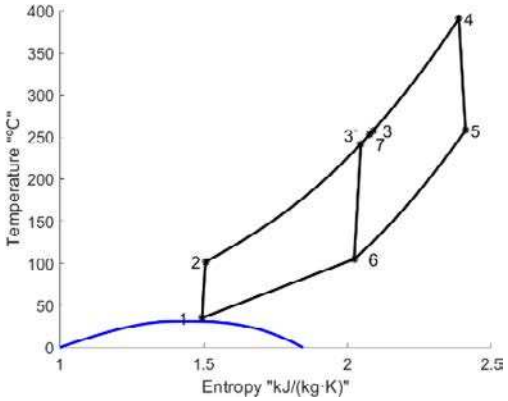

Figure 3: T-S diagram of sCO2-RB

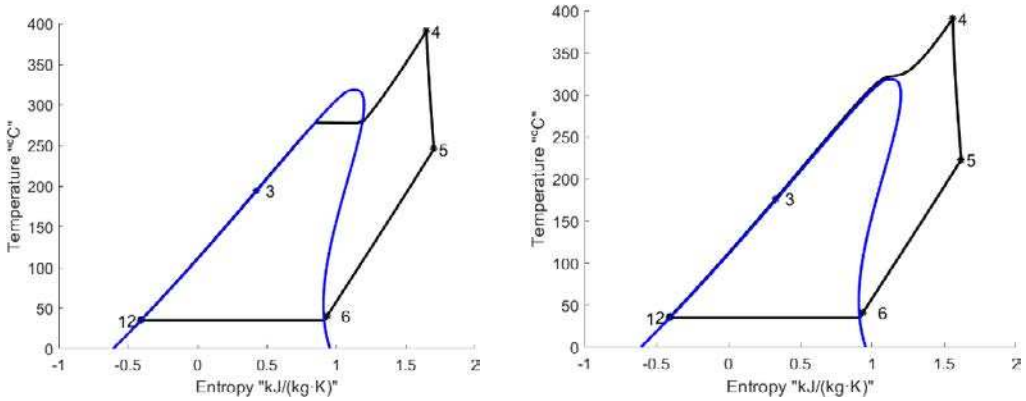

Figure 4: ORC toluene transcritical (left) and subcritical (right)

2 METHODOLOGY

2.1 Non standardized parametric analysis (NSPA)

The NSPA allows to compare the nominal efficiency of the different cycles from a set of fix and variable data. For each cycle, a map of efficiency values is obtained by varying the compression ratio (rc) and the bypass fraction, (x). The maximum rc value is limited by two conditions: A limit value of 300 bar in the high side pressure and a rc limit value of 20:1 for the turbocompressor. Besides**,** the inlet turbine temperature is limited by two conditions: The maximum temperature that the power fluid can reach without degradation (Table 1) and a minimum value of 5º in the SSG (HTF/propane heat exchanger) Pinch Point. The HTF inlet temperature in the SSG is considered equal to the solar field outlet temperature (396ºC).

The nominal dry bulb temperature considered is 25ºC and the temperature difference between the inlet air and the outlet power fluid is 10ºC, so the low temperature of the cycles is 35ºC. The sCO2-RB low pressure has been selected near the critical pressure to increase the density of the fluid at the compressor inlet. These input data are showed in Table 2.

The polytropic efficiency is used to calculate the inlet and outlet states related to the turbomachinery. To apply it, the enthalpy change in each turbomachinery is divided in 25 parts. For the pump and the compressor, Equation 2 is applied to each part. Equation 3 is used for the turbine. The SSG pressure drop corresponds to the high-pressure side and the recuperator SSG pressure drop corresponds to the low-pressure side. The pressure is assumed to decrease linearly.

Table 1: Maximum temperature limit of each fluid

	HRB Isobutane	HRB Propane	ORC Toluene	sCO2-RB
Maximum temperature limit (°C)	308.85	377	426.85	-

Table 2: Input data in the NSPA

	HRB Isobutane	HRB Propane	ORC Toluene	sCO2-RB
Fix data				
T_1(°C)	35	35	35	35
T_4(°C)	308.85	377	391	391
P_{cond} (bar) at 35°C	4.64	12.17	0.06	-
P_1 (bar)	4.64	12.17	0.06	80
SSG pressure drop	2%	2%	2%	2%
Recuperator pressure drop	5%	5%	5%	5%
Turbomachinery polytropic efficiency	0.9	0.9	0.9	0.9
Recuperator Pinch Point	5º	5º	5º	5º
Variable data				
x	0-0.27	0-0.25	-	0-0.29
rc	6-20	6-20	200-900	2.35-2.75

$$\eta_{pB,C} = \frac{dh_s}{dh} \quad (2) \qquad \eta_{pT} = \frac{dh}{dh_s} \quad (3)$$

The specific heat of the propane varies significantly around the critical point, so the Pinch Point in the recuperator can be achieved at the ends or inside it. So, the enthalpy change has been divided into 25 parts. This number is also enough to consider parallel flow heat exchangers without making significant errors. The next steps were taken to calculate the thermodynamic properties related to each part: 1º) T_3 is estimated. 2º) Energy balances are done in each segment, calculating the related temperatures. 3º) Pinch Point is calculated. 4º) A new T_3 is calculated using Newton-Raphson method. The process ends when the convergence is achieved.

705

2.2 HRB propane power block sizing

The power generated by the power block is 100 MW. Compression ratio and bypass fraction values are calculated in the NSPA and leads to the maximum power block efficiency. The nominal inlet and outlet temperature of the solar field are respectively 290ºC and 396ºC. The other fix input values are the same as the NSPA input values. The thermodynamic properties of each state are calculated like in the NSPA. The Recuperator UA factor is calculated by adding the UA factors of each part. The UA factor of each part is calculated from the heat exchanged ($\dot{Q}_i$) and the arithmetic mean temperature difference (AMTD_i) as it is showed in Equation 4. The SSG enthalpy change has been divided in 25 parts too. The SSG UA factor has been calculated with the same expression.

$$UA = \sum_{i=1}^{25} UA_i = \sum_{i=1}^{25} \frac{\dot{Q}_i}{\mathrm{AMTD}_i} \quad (4)$$

2.3 HRB propane cooling system sizing

The cooling system uses air, so the power consumption is significantly. The air mass flow rate ($\dot{m}_a$), can be calculated through the heat rejected ($\dot{Q}$), the specific heat capacity (cp_{air}), the Cooler Initial Temperature difference (ΔT_{ITD}) and the Cooler Approach temperature (AP_{cond}) as it is shown in Equation 5. The cooling UA factor is calculated as the sum of the UA factors associated to the rejection of sensible and latent heat of the cycle. In this case, the UA factors are calculated using the logarithm mean temperature difference (LMTD) since the refrigerator is not divided into smaller parts. The fan

power is calculated as in [9].The fan power is proportional to the enthalpy increase of the air. The outlet fan temperature ($T_{fan,out,s}$) is calculated considering an isentropic compression (Equation 6) using the ideal gas model. The isentropic efficiency allows the calculation of the outlet enthalpy considering the irreversibilities. Finally, the fan power is calculated from the mechanical efficiency, the air mass flow rate, and the enthalpy increase. Table 3 shows the nominal data inputs.

$$\dot{m}_a = \frac{\dot{Q}}{cp_{air} \cdot (\Delta T_{ITD} - AP_{cond})} \quad (5)$$

$$T_{fan,out,s} = T_{db} \cdot rp_F^{\frac{R}{cp_{air}}} \quad (6)$$

Table 3: Cooling system input data

Fan isentropic efficiency	0.8
Fan mechanical efficiency	0.94
Cooler Initial Temperature difference*	10º
Cooler Approach temperature**	3º
Fan pressure ratio	1.0028

*It is defined as the difference between the outlet temperature of the power cycle and the air inlet temperature.
*It is defined as the difference between the condensing temperature of the power cycle and the air outlet temperature

2.4 Standardized parametric analysis (SPA)

The NSPA does not allow an adequate comparison between the cycles as it does not standardize the area of the heat exchangers (recuperator, SSG and refrigerator) nor solar field area. The SPA allows to compare the PB efficiency and the net power of the different cycles taking the sized HRB power block as reference. The calculated total UA factor of the heat exchangers (the sum of recuperator, SSG and refrigerator UA factors), the nominal inlet and outlet solar field temperatures, and the calculated nominal thermal power transmitted to the PB are the input data along with the data of Table 2 (except the recuperator Pinch Point, that is an output data).

706

Each power cycle is sized for each value of compression ratio and bypass fraction. The algorithm follows an iterative process in which each UA factor is initially estimated and then recalculated until convergence is achieved. The calculation of the thermodynamic properties related to the enthalpy change of each heat exchanger is calculated using the Newton Raphson method explained in Section 2.1 but considering the UA factor as a function instead off the Pinch Point.

For the HRB isobutane and ORC toluene cycles, the cooling UA factor is recalculated as it is showed in Section 2.3. In these two cases, the input data used are the same as those shown in Table 3. In the sCO2-RB, the UA factor is calculated by dividing the enthalpy change in 25 parts since the specific heat capacity of the CO2 varies significantly near the critical point. In this case, as the cooling process is a sensible heat exchange process, the outlet temperature of the air can be higher than the outlet temperature of the power fluid. So, in this case we consider that the temperature change value of the air is 20ºC.

2.5 Solar field sizing

The peak optical efficiency is calculated using Equation 7. The mirror reflectance (β), the intercept factor (γ), the envelope transmittance (τ) and the absorber absorptance (α) corresponds to geometrical and optical parameters of the collectors (Eurotrough-150) and the receivers (Schott PTR70).

$$\eta_{opt|_{peak}} = \beta \cdot \gamma \cdot \tau \cdot \alpha|_{\varphi=0º} \quad (7)$$

The incidence angle, φ, is calculated using the equation exposed in [10], [11] considering that the collectors rotation axis coincides with the North-South axis. Equation 8 allows to calculate the incidence angle modifier for an ET-150. This expression includes the cosine effect.

$$K = \cos(\varphi) - 2.859621e-5 \cdot (\varphi)^2 - 5.25097e-4 \cdot \varphi \quad (8)$$

The Equation 9 is used to calculate the heat losses per meter of absorber tube. ΔT is the difference between the average temperature of a collector loop and the dry bulb temperature.

$$\dot{q}_{perd} = 0.00154 \cdot \Delta T^2 + 0.2021 \cdot \Delta T - 24.89 + \left[(0.00036 \cdot \Delta T^2 + 0.2029 \cdot \Delta T + 24.899) \cdot \left(\frac{DNI}{900}\right) \cdot \cos(\varphi)\right] \quad (9)$$

The number of required Solar Collector Assemblies (SCAs) per loop is calculated using an energy balance (Equation 10). This value must be an even number since a collector loop is divided into two halves. Then, the HTF mass flow rate per loop ($\dot{m}_{col}$) is recalculated. h_{sfout} and h_{sfin} are the nominal outlet and inlet solar field enthalpies, A_{SCA} and L_{SCA} are the area and length of each SCA.

$$N_{SCA} = \dot{m}_{col} \cdot \frac{h_{sf_{out}} - h_{sf_{in}}}{DNI \cdot A_{SCA} \cdot \eta_{opt}|_{peak} \cdot K - \dot{q}_{perd} \cdot L_{SCA}} \quad (10)$$

The number of loops should be the upper integer number resulting from dividing the required thermal power by the thermal power of the unitary loop. As the solar multiple value is 2, the required thermal power is twice the thermal power demanded by the power block. The nominal input data is showed as Supplementary data.

2.6 Storage system sizing

Two-tanks system with a storage capacity for 12 hours of nominal power block thermal power requirement have been considered. The nominal temperatures of the hot and cold molten salts tanks are respectively 391ºC and 285ºC. The HTF/molten salts heat exchanger UA factor is calculated by the NTU method (Equation 11).

$$UA = NTU \cdot Cmin = \frac{\epsilon}{1-\epsilon} \cdot \frac{\dot{Q}}{T_{hot_{salt}} - T_{cold_{salt}}}; \quad \epsilon = \frac{T_{hot_{HTF}} - T_{cold_{HTF}}}{T_{hot_{HTF}} - T_{cold_{salt}}} \quad (11)$$

2.7 Off design power cycle/cooler calculation

The methodology assumes the following criteria: 1) The Stodola-Frügel Law is used to describe the behaviour of the steam turbine at partial load [12]. 2) We consider constant volumetric flow in the compressor. 3) The turbomachinery efficiency at off-design conditions is reduced from the nominal value as the capacity moves away from the design value. Equation 12 relates the turbomachinery efficiency to its capacity. Equation 13 describes the turbomachinery capacity from the mass flow rate, the pressure, and the inlet temperature. 4) The recuperator and SSG UA factors decrease as the mass flow rate of the fluid with the highest thermal resistance also does. The SSG UA factor is calculated using the Equation 14. The recuperator UA factor is also calculated using Equation 14 but considering propane instead of the HTF as fluid.

$$\eta_{tb} = \eta_{tb_{dis}} - \left|1 - \frac{\phi_{tb}}{\phi_{tb_{dis}}}\right|/3 \quad (12) \qquad \phi = \dot{m}\frac{\sqrt{T}}{P} \quad (13) \qquad UA_{obj} = UA_{dis} \cdot \left(\frac{\dot{m}_{HTF}}{\dot{m}_{HTF_{dis}}}\right)^{0.8} \quad (14)$$

The off-design power cycle algorithm follows an iterative process in which the data input is the HTF temperature at the SSG inlet, the HTF mass flow rate, the cooling temperature, the inlet turbine temperature, and the low-pressure value. The main results are the thermal power required, the power production and the HTF temperature at the SSG outlet. T_6, P_4 and the bypass fraction are initially estimated and recalculated until they reach the convergence.

The off-design power cooler algorithm follows an iterative process in which the data input is the outlet and inlet cooler temperature at the power fluid side and the inlet temperature of the air. The main result is the power consumed by the fan. The outlet temperature of the air is initially estimated and recalculated until it reaches the convergence. Fan isentropic/mechanical efficiency and fan pressure ratio take the

707

design value. Cooling UA factor is calculated using Equation 14 but considering the air instead of the HTF as fluid.

2.8 Annual simulations

The following operation conditions are considered in all cases: 1) The HTF mass flow rate through the SSG and the outlet temperature of the solar field take the design value; 2) Ambient temperature and inlet SSG temperature at HTF side (in the case that the TES provides thermal energy to the PB) take off-design values; 3) In HRB and the ORC, the low temperature is fixed 10ºC over the dry bulb temperature. 4) In the sCO2-RB, the low temperature is set in 35ºC. If the ambient temperature is higher than the design value, the air mass flow rate increases until a 15% higher than the nominal value.

The CSP follows a dispatch strategy that prioritizes production from energy coming directly from the solar field with only one PB startup per day. The PB startup is constrained by a time duration and a thermal energy fraction. The time duration constrain value is 30 min and the energy constraint value is a 20% of the thermal energy demanded by the PB during 1 hour at nominal conditions. The following premises are considered: 1) Every day after the solar field startup and before the PB startup, the minimum energy necessary to store is calculated so that the PB works uninterruptedly during daylight hours. 2) The PB startup operation only demands energy that comes directly from the solar field so the operation can take a longer time than the time duration constrain. 3) If the power absorbed by the solar field is higher than the maximum power that the cycle can demand, the power excess is derived to the storage system. 4) If the solar power absorbed is lower, the stored energy is transferred to the PB complementing the flow that comes from the solar field. 5) After the sunset, the salts are discharged at the nominal value, so the remaining energy stored is transferred to the PB increasing the production.

For each case we have done hourly simulations. The meteorological data used to calculate the annual simulations, correspond to a database of a typical year for Sevilla provided by METEONORM. It includes the weather station coordinates, as well as values taken hourly of DNI and dry bulb temperature. Row shadowing losses, solar field startup thermal energy and thermal tank losses are also considered. They are explained in [13], [14].

708

3 RESULTS

Figure 5 shows the values of the efficiency for each cycle depending on the bypass fraction and the compression ratio in the NSPA. The highest efficiency value is achieved by the HRB propane cycle as it is showed in Table 4**.** Toluene achieve a slightly lower value. The compression ratio that corresponds with this value leads to a transcritical Rankine cycle. The F_s of ORC with toluene is high considering that the recuperator is not balanced. This occurs because the toluene has a high cp/R, so the vapor flow has a high specific heat. F_c of the sCO2-RB is considerable high although the heat rejected is sensible heat. This is because the inlet compressor flow is close to the critical point.

The HRB that works with isobutane has a higher value of F_s, F_c and F_h than the HRB that works with propane; however, the propane achieves a higher efficiency. This is because the isobutane has a lower maximum temperature, which penalizes the CN factor. sCO2-RB does not achieve high efficiency, which justifies that it works better with higher temperatures.

Table 5 shows the UA factors in case of sizing the cycles standardizing only the solar field. The thermal power required by the PB in each case coincides with that demanded by the HRB propane in the design that achieves the greatest efficiency. Temperature difference at the ends (cold and hot) of each heat exchanger are also showed. The HRB cycles need the highest total UA factor values while the ORC needs the lowest. The main reason is that the recuperator needs a higher UA in the cycles that have a bypass fraction. In these cases, the heat capacity is equalized, so the temperature change in each end of the recuperator is similar. Besides, recuperator UA factor in HRB propane is considerably higher than in the sCO2-RB cycle although the temperature difference at the ends is similar. This is because the specific heat capacity varies a lot inside the recuperator, so the temperature difference in each part of

the recuperator can varies considerably too. This justifies the division of the heat exchanger in smaller segments. Besides, HRB and ORC cycles needs a higher cooler UA factor than in the sCO2-RB although in the latter, the efficiency of the cycle is the lowest. This is because HRB and ORC reject mostly latent heat while the sCO2-RB rejects only sensible heat.

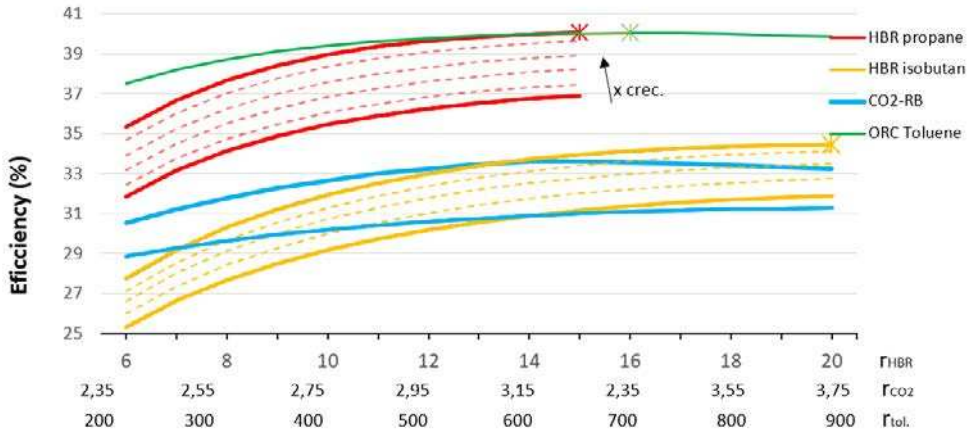

Figure 5: NSP results for each power cycle

Table 4. Maximum efficiency NSPA results for each power cycle

	HRB Isobutane	HRB Propane	ORC Toluene	sCO2-RB
Efficiency (%)	35.12	40.06	40.04	33.62
F_h	0.8956	0.8901	0.8446	0.8806
F_c	0.9989	0.9965	0.9998	0.9411
F_s	0.9123	0.8915	0.9163	0.8434
CN	1.889	2.109	2.155	2.155
x (bypass fraction)	0.25	0.25	-	0.29
rp (compression ratio)	20	15	700	3.15

Table 5: Standardized UA factors

	HRB Isobutane			HRB Propane			ORC Toluene			sCO2-RB		
	UA(MW/K)	ΔT_h	ΔT_c	UA	ΔT_h	ΔT_c	UA	ΔT_h	ΔT_c	UA	ΔT_h	ΔT_c
SSG	2.7	87	93	7.9	19	46	7.1	5	113	14.3	5	36
Recuperator	37.2	12	6	45.8	5.2	6.5	4.5	46	5	28.1	5	5
Cooler	38.2	21	3	22.3	20	3	25	16	3	6.5	73	10
Total	**78.1**	-	-	**75.9**	-	-	**36.6**	-	-	**48.9**	-	-

Table 6 shows the results of the SPA, that also standardizes the total UA factor. The design that maximizes the net power of each cycle is showed. All cycles increase their efficiency with respect to the SPA. ORC toluene produce more net power than the HRB propane as the UA total factor has been increased considerable. sCO2-RB produces more net power than the HRB isobutane although its efficiency is lower. As the cooler rejects only sensible heat in sCO2-RB, the temperature change of the cooler fluid (air) is higher, so the cooler power consumption is lower.

The results of the annual simulation for each power cycle are shown in Table 7. The thermal energy demanded by the PB is the solar thermal energy absorbed minus the solar field and PB startups and minus the heat losses in molten salts tank. In all cycles, these parameters are similar because the size of

the TES and solar field are the same. The variations are due the heat losses by defocusing while the PB is off, and the TES is storing energy. Total net energy production in HRB Propane and ORC toluene are similar. The same happens between the HRB isobutane and sCO2-RB however in this case it is due the lower cooling system power consumption of the sCO2-RB. In all cycles, the average net power produced, and the average efficiency of the power block are slightly lower than the nominal values.

Table 6: Maximum efficiency SPA results for each power cycle

	HRB Isobutane	HRB Propane	ORC Toluene	sCO2 RB
Efficiency (%)	35.34	40.06	40.38	34.44
Power produced (MW)	88.5	100.3	101.1	86.2
Cooler consumption (MW)	7.3	6.8	6.7	2.6
Net Power produced(MW)	81.1	93.5	94.3	83.6
X (bypass fraction)	0.25	0.25	-	0.28
rp (compression ratio)	20	15	700	3.25
P_{max} (bar)	91.9	183	43.7	260
UA_{gv} (MW/K)	2.5	7.9	7.3	14.2
UA_{rc} (MW/K)	47.2	45.7	43.1	49.7
UA_{cond} (MW/K)	26.3	22.3	25.6	12.1

Table 7: Main Annual simulation results

	HRB isobutane	HRB Propane	ORC Toluene	sCO2-RB
Solar thermal energy absorbed (GWh)	1040.5	1039.5	1040	1036.8
Solar field startup thermal energy(GWh)	103.6	103.8	103.8	103.8
PB startup thermal energy(GWh)	16.8	16.8	16.8	16.8
Heat losses in molten salts tanks(GWh)	8.5	8.5	8.5	8.5
Thermal energy demanded by the PB (GWh)	911.5	910.4	910.9	907.6
Total energy production (GWh)	315.8	357.9	362	299.5
Cooling system consumption (GWh)	25.7	24.7	24.6	9.4
Total net energy production (GWh)	290	333.2	337.3	290
Nº hours Power Block	3680	3672	3683	3720
Mean total power produced (MW)	85.8	97.5	98.3	80.5
Mean net power produced (MW)	78.8	90.7	91.6	80
Mean Power Block efficiency (%)	34.64	39.32	39.73	33
Power range (MW)	73.7/92	78.4/118.5	87.8/113.5	58/86.2
Net Power range (MW)	66.6/89	72.4/111.1	81/106	54.8/85
Cooling system power range (MW)	2.9/7.3	6/7.4	6.1/6.8	1.2/3
Power Block efficiency range (%)	31.25/36.07	34.34/42.19	35.61/42.61	25.53/34.44
Lower PB temperature range (ºC)	30/55.5	17.7/53.2	17.7/53.2	35/44.5
Ambient temperature range (ºC)	7.7/43.2	7.7/43.2	7.7/43.2	7.7/43.2

In all cases the net power range is wider than the power range because the cooling system consumes more energy at high ambient temperatures (when the PB efficiency is also lower). In HRB propane, the maximum power value is higher than in the ORC although the maximum efficiency value in the last is higher. This can be an advantage for the HRB when the objective is to produce more energy at the hours of highest sales price. Because of that the number of PB working hours is lower in the HRB propane than in the ORC. However, the minimum efficiency value in the HRB propane is considerably lower than the minimum efficiency value in ORC. This is because compressor and turbine rotate at same speed, so at high ambient temperature the bypass fraction value increases too much, unbalancing the recuperator and increasing the compressor consumption.

In HRB isobutane, the minimum condensing temperature is limited to 30ºC because lower temperatures could lead to wet compression. As a disadvantage, the maximum value of cycle efficiency in low ambient temperatures is also limited. However, the cooling power consumption is reduced. In sCO2-RB the minimum temperature of the cycle has been limited to 35 ºC. For ambient temperatures above

the nominal, the cooling system has been optimized to work up to a maximum air flow of 1.15 the nominal value. With this, it has been possible to reduce the maximum value of the temperature at the compressor inlet to 44.5ºC when the ambient temperature is 43.2 ºC. Despite this, the performance is reduced up to a 25.53%. This is mainly due to the decrease in the density value at the compressor inlet.

4 CONCLUSIONS

Different power cycles have been presented as alternatives to the current technologies used in CSPs. A method that allows to compare the performance of the power cycles without sizing the solar field and the TES has been proposed. To achieve this, the UA factors of the PB and the thermal power demanded have been standardized. Annual simulations have been done to compare the annual energy production. In this case, the same solar field and TES have been sized for all the power cycles studied.

The low consumption of the sCO2-RB aerocondenser is an advantage, but the efficiency is severely penalized when the compressor inlet conditions are far from the critical point. On the other hand, despite the high efficiency developed by the ORC toluene, it has a major drawback: Condensing pressures for common ambient temperatures are very low, in vacuum. So, air can enter in the circuit. This is a risk considering that toluene is very flammable. The HRB propane cycle with a balanced recuperator has proven to develop high performance for medium temperature applications. The critical pressure of propane is not very high, which allows working in the supercritical region without too high pressures. Independent shafts for turbine and compressor could lead to select different bypassing fractions in each off-design condition. So, the performance could be increased considerably at high ambient temperatures.

Supplementary data: AntonioSubires/Supplementary-data-of-Simulation-and-Operation-of-a-CSP-that-works-with-a-HRB-cycle- · GitHub

711

ACKNOWLEDGMENTS

Grant PID2019-110283RB-C31 and PRE2020-094353 funded by MCIN/AEI/ 10.13039/501100011033, by “ESF Investing in your future” and, as appropriate, by “ERDF A way of making Europe”, by the “European Union” or by the “European Union NextGenerationEU/PRTR”.

REFERENCES

[1] H. Singh and R. S. Mishra, “Performance evaluation of the supercritical organic rankine cycle (SORC) integrated with large scale solar parabolic trough collector (SPTC) system: An exergy energy analysis,” *Environ Prog Sustain Energy*, vol. 37, no. 2, pp. 891–899, Mar. 2018, doi: 10.1002/ep.12735.

[2] D. Sánchez, B. M. Brenes, J. M. Muñoz de Escalona, and R. Chacartegui, “Non-conventional combined cycle for intermediate temperature systems,” *Int J Energy Res*, vol. 37, no. 5, pp. 403–411, Apr. 2013, doi: 10.1002/er.2945.

[3] E. Cayer, N. Galanis, and H. Nesreddine, “Parametric study and optimization of a transcritical power cycle using a low temperature source,” *Appl Energy*, vol. 87, no. 4, pp. 1349–1357, 2010, doi: 10.1016/j.apenergy.2009.08.031.

[4] B. F. Tchanche, G. Lambrinos, A. Frangoudakis, and G. Papadakis, “Low-grade heat conversion into power using organic Rankine cycles - A review of various applications,” *Renewable and Sustainable Energy Reviews*, vol. 15, no. 8. Elsevier Ltd, pp. 3963–3979, 2011. doi: 10.1016/j.rser.2011.07.024.

[5] Y. Liu, Y. Wang, and D. Huang, “Supercritical CO2 Brayton cycle: A state-of-the-art review,” *Energy*, vol. 189. Elsevier Ltd, Dec. 15, 2019. doi: 10.1016/j.energy.2019.115900.

[6] J. I. Linares, M. J. Montes, A. Cantizano, and C. Sánchez, “A novel supercritical CO2 recompression Brayton power cycle for power tower concentrating solar plants,” *Appl Energy*, vol. 263, Apr. 2020, doi: 10.1016/j.apenergy.2020.114644.

[7] A. Rovira, M. Muñoz, C. Sánchez, and J. M. Martínez-Val, "Proposal and study of a balanced hybrid Rankine-Brayton cycle for low-to-moderate temperature solar power plants," *Energy*, vol. 89, pp. 305–317, Sep. 2015, doi: 10.1016/j.energy.2015.05.128.
[8] A. Rovira, C. Rubbia, M. Valdés, and J. M. Martínez-Val, "Thermodynamic cycles optimised for medium enthalpy units of concentrating solar power," *Energy*, vol. 67, pp. 176–185, Apr. 2014, doi: 10.1016/j.energy.2014.02.029.
[9] M. J. Wagner and P. Gilman, "Technical Manual for the SAM Physical Trough Model," 2011.
[10] J. A. Duffie and W. A. Beckman, *Solar Engineering of Thermal Processes*, 2nd ed. New York: John Wiley & Sons, 1991.
[11] A. Rabl, *Active solar collectors and their applications*. New York : Oxford University Press, 1985.
[12] A. Rovira, R. Abbas, C. Sánchez, and M. Muñoz, "Proposal and analysis of an integrated solar combined cycle with partial recuperation," *Energy*, vol. 198, 2020, doi: 10.1016/j.energy.2020.117379.
[13] A. J. Subires and A. Rovira, "Economic Optimization of a Thermal Solar Power Plant that Operates with a HRB Cycle by Improving the Operation Schedule," in *SolarPACES 2022 – 26th International Conference on Concentrating Solar Power and Chemical Energy Systems* ,
[14] A. J. Subires and A. Rovira, "Sizing and simulation of a solar thermal power plant that operates with a HRB cycle," in *XII National and III International Conference on Engineering Thermodynamics (CNIT 2022).*, Madrid.

712

ORC SEVILLE 2023
7th International Seminar on O.R.C. Power Systems

© 2024 Editorial Universidad de Sevilla. Este es un artículo de acceso abierto distribuido bajo los términos de la licencia de uso y distribución Creative Commons (BY-NC-ND 4.0)

DOI: https://dx.doi.org/10.12795/9788447227457_123
Paper ID #123, page 1 of 10

Toward a Green Energy Community: Integration of micro-ORCs combined with renewable energy technologies in buildings.

Diego Antonio Rodríguez-Pastor*[,1], Víctor Manuel Soltero Sánchez[2], Elisa Carvajal Trujillo[1], José Antonio Becerra[1], Ricardo Chacartegui[1]

[1] *University of Seville, Escuela Técnica Superior de Ingenieros, Camino de los Descubrimientos s/n, 41092 Seville, Spain*
[2] *University of Seville, Escuela Politécnica Superior, 41011, Seville, Spain*

*Corresponding author: drodriguez4@us.es

ABSTRACT

Distributed microgeneration is an alternative for aggregate energy integration into the electricity grid. Low-temperature heat recovery systems, such as ORCs, are particularly interesting given their compactness and safety for application in the residential sector, operating at moderate pressures and low heat source temperatures. Energy surpluses generated by renewable technologies commonly used in the building sector, such as photovoltaics or micro-wind, can be used to power systems that provide backup and add inertia to the grid. In this study, micro-ORCs (< 2 kWe) were integrated with different heat supply technologies in buildings, including storage with DHW water tanks or sensible heat in bedrock for heating. An overview of possible configurations and techno-economic optimization is provided, offering combined strategies with other installations and additional characterization of energy communities with a larger number of connected neighbors, determining optimized integrations for covering thermal and electrical demands.

1 INTRODUCTION

As global concerns regarding climate change and environmental degradation have increased, there is a growing need to transition to sustainable and renewable energy sources (IEA, 2022). Integrating energy communities in rural areas has emerged as a promising solution for increasing sustainability, promoting the use of renewable energy sources, and reducing carbon emissions (Koirala et al., 2016; Streimikiene et al., 2021). By leveraging local renewable energy resources and fostering cooperation between energy users and producers, energy communities can contribute significantly to achieving a sustainable energy future (Bassam, 2021). Furthermore, the integration of renewable energy technologies into residential buildings is a critical component of this transition (Klein & Coffey, 2016), and the cost-efficient implementation of cogeneration (CHP) systems in single-family homes represents a significant step towards achieving this goal (Ceglia et al., 2022a).

The integration of organic Rankine cycles (ORC) in single-family homes is presented as a promising option for the generation of electricity from residual thermal energy produced by, for example, the time gap between demand and the generation of domestic solar hot water (Ancona et al., 2022; Pereira et al., 2018a). (Rodriguez-Pastor et al., 2023) analysed the optimal sizing of ORCs for solar domestic hot water systems, depending on the demand and solar resources available at the site, and reported improvements in the efficiency of solar collectors owing to a lower fraction of cold-water mixing. (Braimakis et al., 2021) studied centralized scenarios incorporating district heating systems that further enhance the performance and feasibility of ORC systems. Using low-grade waste heat, such as solar domestic hot water systems (Bou Lawz Ksayer, 2011), the ORC system can produce electricity while simultaneously providing heat to the building through the District Heating network.

Energy communities are groups of households, businesses, or other entities collaborating to generate, consume, and share energy locally (Andoura et al., 2010). By leveraging surplus thermal energy from

systems such as domestic hot water with storage for electricity generation, ORC systems can contribute to the development of sustainable and self-sufficient energy communities (Alberto et al., 2022; Ceglia et al., 2022b). They can reduce dependence on the electric grid, promote energy independence, and enhance local resilience to power outages and disruptions (Dóci et al., 2015). They can also optimise the utilisation of surplus thermal energy, which would otherwise go to waste, by converting it into electricity, thus improving energy efficiency and reducing the environmental impact (Baral et al., 2015). Additionally, energy communities can promote social cohesion, participation, and empowerment among their members as they jointly participate in energy production and consumption decisions (Lowitzsch et al., 2020). However, there are also associated challenges and considerations, including regulatory and legal frameworks, technical complexities of power production system installation and operation (Loni et al., 2021; Pereira et al., 2018b), financial aspects such as investment costs and revenue sharing among community members (Busch et al., 2021), and potential disparities in energy demand and supply among different households or entities within the community (Frieden et al., 2020). Addressing these challenges requires careful planning, coordination, and stakeholder engagement (Mishra et al., 2022).

This study aimed to analyze the technical and economic feasibility of integrating ORC systems into single-family homes in southern Spain in decentralized and centralized scenarios. This study focuses on analyzing the potential for the use of waste heat from solar hot water systems to generate electricity and provide heating to buildings. A detailed techno-economic analysis of the ORC system and SDHW was conducted by considering different configurations and operating conditions. These results provide valuable information to policymakers, energy planners, and homeowners regarding the adoption and implementation of ORC systems in the residential sector.

2 SYSTEM DESCRIPTION

In a decentralized system integrating ORCs in the residential sector, each household or residential unit has its own installed micro-ORC, which uses surplus thermal energy from its domestic hot water system with storage to generate electricity (**Figure 1**). This approach involves the installation of smaller capacity micro-ORC systems in each household or residential unit. Each micro-ORC can operate autonomously and generate electricity in individual operation (Physical System). The excess electricity produced can be injected into the grid, allowing the possibility of earning income by selling energy to the grid. This decentralized approach offers advantages in terms of energy autonomy for each residential unit.

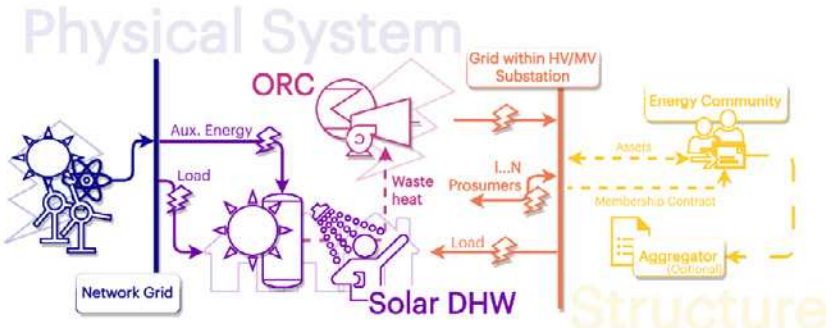

Figure 1. Conceptual diagram of the proposed decentralised ORC-SDHW system

In contrast, in a centralized system integrating ORCs in the residential sector, a higher-capacity ORC is installed in a central location, which can be a community facility or power generation plant (**Figure 2**).

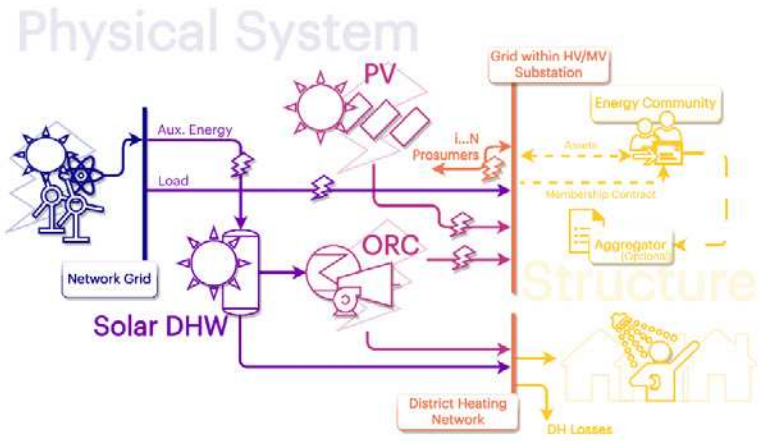

Figure 2. Conceptual diagram of the proposed centralised ORC-SDHW system

For the centralized approach presented, the central ORC system harnesses residual energy from industrial thermal processes or utilizes solar thermal energy for domestic hot water systems during periods of low demand or high solar resource, resulting in a decrease in the flow rate of the cold-water mix and a consequent increase in the performance of solar collectors. The central ORC can operate more efficiently and cost-efficiently because of its economy of scale, with a reduced kilowatt cost and better control and management of electricity generation. The produced electricity can be injected into the grid and distributed to households or residential units in a zone or community. This centralized approach offers advantages in terms of efficiency, economics, and management of electricity generation on a larger scale, as discussed. In a decentralized system, each household or residential unit has its own micro-ORC for local electricity generation, whereas in a centralized system, a higher-capacity ORC is used at a central location to harness surplus thermal energy from multiple households or residential units in a zone or community. Both approaches have advantages and challenges, and the choice between them depends on the specific needs and characteristics of the project or application under consideration, where the management of production/generation is provided by a contractual structure system (Structure).

715

In this study, the R245fa fluid was selected based on the criteria of condensing at atmospheric pressure at temperatures on the order of ambient temperature. This allows for greater flexibility in installation, considering that the facility is applied in a residential environment.

3 SIMULATION

Figure 3 shows the proposed system. This was simulated using the commercial software TRNSYS (S.A Klein, 2017). For this purpose, an ORC type was created that modelled the ORC cycle based on the values of the parameters in **Table 1**.

Table 1. Thermodynamic considerations for power system simulation.

Variable	Value
Heat Exchangers approach temperature	20 K
Isentropic efficiency of pump	50%
Isentropic efficiency of expander	60%
Maximum refrigerant pressure	$0.85 \cdot p_{crit}$
Storage setpoint temperature for ORC start-up.	75 ºC

Refrigerant property calculations are performed through a subroutine that calls Coolprop (Bell et al., 2014), obtaining the associated power production in the expander at each time step. Several articles

have employed this methodology, such as the studies by (Ancona et al., 2022). The following considerations and assumptions have been considered for the calculation of the power system in residential ORC systems with solar hot water systems. i) The minimum water outlet temperature of the ORC evaporator is 60°C to avoid penalizing the demand. ii) The mass flow rate of the refrigerant varied according to the waste heat power of the SDHW system to satisfy the energy balance in each case. iii) The calculations were performed in a quasi-dynamic regime. iv) The temperature of the cold fluid used for condensation is 25°C.

The TRNSYS simulations use Types 4 and 1 to represent the storage tank and collectors, respectively. The system equations will be simplified algebraically within TRNSYS, where the collector efficiency is described by three parameters (a_0, a_1, and a_2) in accordance with ASHRAE, SRCC, and CEN standards.

$$\eta_{coll} = a_0 - a_1 \frac{\Delta T}{I_T} - a_2 \frac{(\Delta T)^2}{I_T} \quad (1)$$

The collector area is determined by the volume/area ratio of 50 l/m^2, where the storage volume is designed to cover 1.5 times the total daily demand (Duffie & Beckman, 1991). The demand will be calculated according to the Spanish regulation standard, which is 28 l/s·person·day at a temperature of 60ºC (Ministerio de Fomento, 2019).

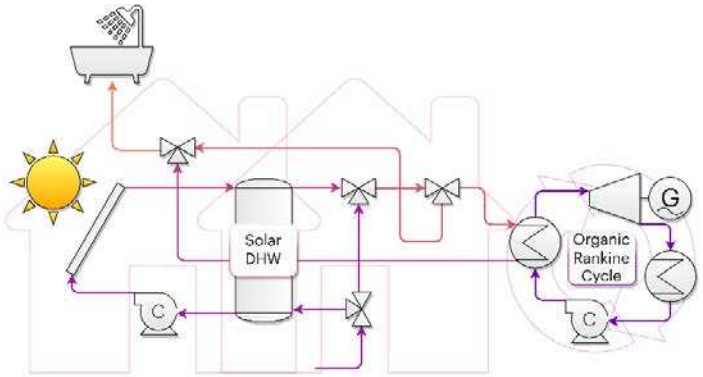

Figure 3. Flow diagram of the proposed SDHW-ORC system

Meteorological data from Seville (-5.9731700º; 37.3828300°) were used, considering the variation in demand associated with the occupancy of the residence in the decentralized case and for several residences of four people in the centralized case. **Table 2** lists the thermodynamic parameters that describe the solar-loop components.

Table 2. Thermodynamic parameters of the solar collectors

Parameter	Value	Units
Fluid specific heat	4.19	*kJ/kg.K*
Tested flow rate	0.011	*kg/s.m*^{2}
Intercept efficiency (a_0)	0.801	-
Efficiency slope (a_1)	3.93	*W/m*^{2}*.K*
Efficiency curvature (a_2)	0.026	*W/m*^{2}*.K*^{2}
1st-order IAM	0.2	-

These values were used to evaluate the technical and economic feasibility of the installation and its integration in an energy community context. No subsidies or grants were considered in the analyses. The objective is to provide correlation coefficients for evaluating the system based on the number of people participating in the energy community, proposing simple expressions that may be valuable for

716

organizations such as governments or municipalities that intend to implement ORC-based energy communities. The expressions have the following forms (Equations 2 and 3):

$$E_{DHW}^{d} = a_{DHW}^{d} + b_{DHW}^{d} \cdot Persons + c_{DHW}^{d} \cdot Persons^{2} \quad (2)$$

Where E_{DHW}^{d} is the annual thermal demand for domestic hot water of the household in kWh.

$$E_{ORC}^{d} = a_{ORC}^{d} + b_{ORC}^{d} \cdot Persons + c_{ORC}^{d} \cdot Persons^{2} \quad (3)$$

And E_{ORC}^{d} is the annual ORC production for the decentralised case in kWh. When forming a community considering a centralized system that supplies several residences, the expressions are as follows (Equations 4 and 5).

$$E_{DHW}^{c} = a_{DHW}^{c} + b_{DHW}^{c} \cdot Households + c_{DHW}^{c} \cdot Households^{2} \quad (4)$$

Being E_{DHW}^{c} is the annual thermal demand for domestic hot water of the households in kWh.

$$E_{ORC}^{c} = a_{ORC}^{c} + b_{ORC}^{c} \cdot Households + c_{ORC}^{c} \cdot Households^{2} \quad (5)$$

And E_{ORC}^{c} is the annual ORC production for the centralised case in kWh. On the other hand, the Internal Rate of Return (IRR) will be evaluated from Equation 6.

$$IRR = r\ when \sum^{n} \frac{CF_k}{(1+r)^k} = 0 \rightarrow IRR^i = a_j^i + b_j^i E_{DHW}^i + c_j^i {E_{DHW}^i}^2 + d_j^i E_{ORC}^i + e_j^i {E_{ORC}^i}^2 \quad (6)$$

For a useful life (n) of the installation of 20 years and a discount rate (r) of 5%. Similarly, to evaluate the cost of energy, the Levelized Cost of Energy (LCOE) is used, as expressed in Equation 7: 717

$$LCOE = \frac{CAPEX + \sum_{k=1}^{n} \frac{OPEX_k}{(1+r)^k}}{\sum_{k=1}^{n} \frac{E_{ORC}^i}{(1+r)^k}} \quad (7)$$

$CAPEX$ being the initial investment cost of the plant, $OPEX_i$ is the annual operation and maintenance cost and E_{ORC} the annual energy produced in the ORC in kWh. Investment and maintenance costs were estimated using CEPCI (Jenkins, 2014) indices. The energy cost is determined by the wholesale price in Spain in 2022 (OMIE, 2022).

4 SUBMISSION OF MANUSCRIPT

4.1 Decentralized systems

In decentralized systems, the trend of irradiance is crucial for the correct operation of the ORC and an increase in production. This variable is directly related to the number of people living in the house, as it requires a larger solar loop size (larger area and storage) to meet the demand. The ORC production for months of high irradiation will practically double (450 kWh) for the case of maximum occupancy (six people), owing to the lack of demand and a higher thermal level than in other cases (**Figure 4, left**). On the right side of **Figure 4**, the points are displaced according to the number of people and associated demand for domestic hot water. This shows that, in many solar DHW systems, there is a significant excess of energy that is not used and is lost when hot water is mixed with cold water from the main source. This was deduced from the amount of energy produced in the ORC from the waste heat in solar DHW systems. For a setpoint temperature of 60 °C, according to the regulations governing these systems, there is a thermal resource at the outlet that can be used in a simple way through the ORC

evaporator, designed such that it does not affect the demand in this case, and that the consumer receives domestic hot water at the temperature that he/she establishes.

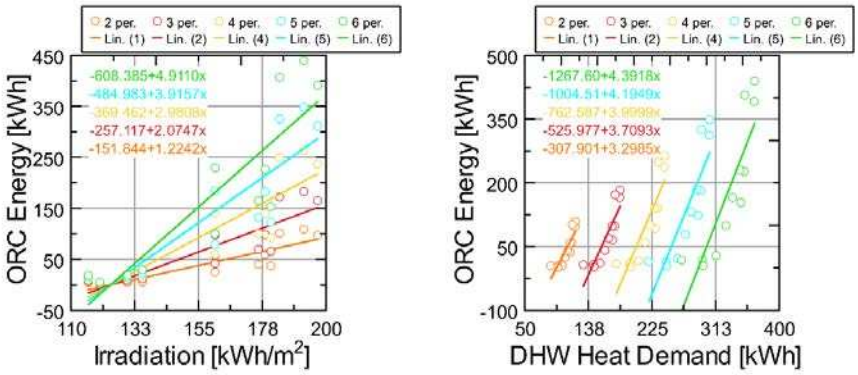

Figure 4. Monthly ORC energy production as a function of the number of people in the household and left: monthly incident irradiation (kWh/m^2) and right: monthly domestic hot water demand (kWh)

From an economic point of view, ORCs still have challenges to be fully competitive on a small scale, with costs of 45 cents/kWh, more than twice that of photovoltaic systems without storage, and even above those with batteries (Lazard, 2023). Cost reductions may occur with a greater number of people to supply and optimised management of the available heat. An increase of 500 kWh in the ORC production per year may decrease the associated LCOE by 10 cents until it stabilizes (**Figure 5, left**). This also applies to the net present value (NPV), which reaches a maximum of five people (2300 €) and then decreases. Therefore, there is a strong correlation between the demand and annual production (**Figure 5, right**), which can take advantage of almost half of the energy applied to the demand in ORC production. As the heat demand increases, the net present value will eventually stabilize, as the sizing of the ORC will have to increase, and the cost correlations will be different from those considered in the micro-ORC field. In this sense, it is of interest to opt for centralized configurations, as discussed in the next section.

718

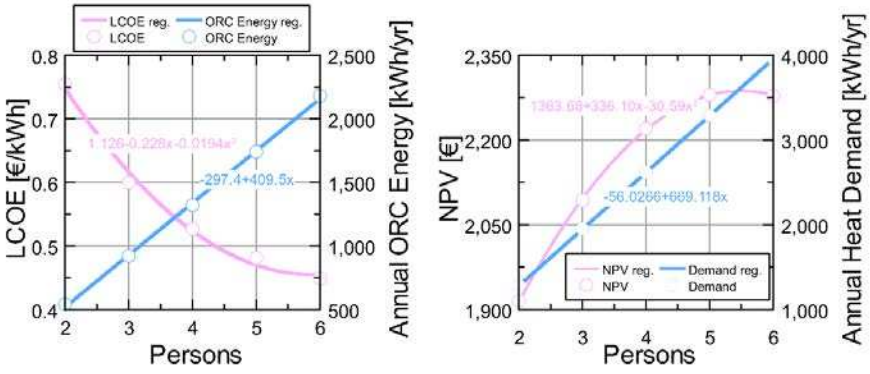

Figure 5. Regressions as a function of the number of people living in the house for the left, LCOE (€/kWh), and annual energy produced by ORC (kWh/yr); and right, net present value (€) and annual heat demand (kWh/yr).

4.2 Centralized systems

For centralized systems, the investment cost associated with the Rankine cycle is lower because of economies of scale as well as the establishment of different energy production strategies and better power cycle efficiencies. Thus, as occupancy increased, the technical and economic feasibility became

more notable (**Figure 6**). Thus, for the centralised case, the LCOE can already be competitive (€0.25/kWh), including both storage and joint production of domestic hot water, with some community photovoltaic installations (€0.18/kWh) provided by (Lazard, 2023). From 10 houses (40 persons) in the energy community, integration became viable from the point of view of IRR>r, where net present values (NPV) became greater than the investment cost (**Figure 6, bottom**).

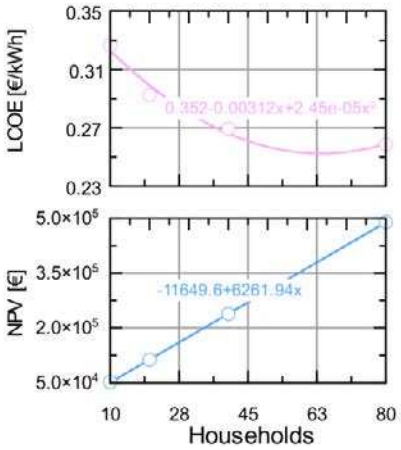

Figure 6. Regression of the LCOE and NPV as a function of the number of households associated with the energy community.

These levelized cost values indicate a great interest in the proposed configuration, as it proposes a system that can be competitive with solar photovoltaic energy communities (<35% difference compared to energy communities based on photovoltaics), where a system with storage (water tank) and a dual use of energy both in thermal form (DHW) and in electrical form through the ORC is also proposed. High cogeneration efficiencies were obtained for the central plant with the solar ORC, reaching their maximum for 66 houses for the studied configuration. Beyond this point, the cost of storage increases exponentially, and its average temperature decreases. Therefore, it is recommended to section the installation into several smaller ones that offer better performance (**Figure 7**). However, the trend of the IRR is linearly upward as more electrical energy is produced and the investment is returned in less time.

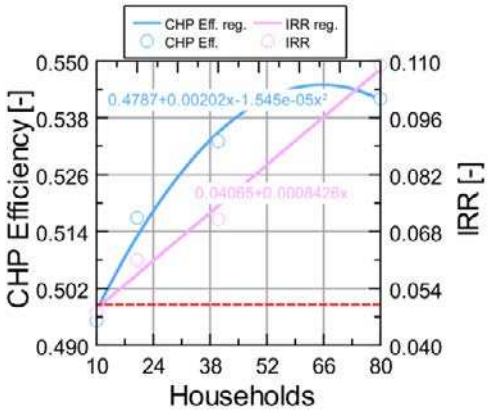

Figure 7. Cogeneration efficiency and internal rate of return as a function of the number of houses in the energy community

It is also noted that for the economic cost-effectiveness baseline (red dotted line in **Figure 7**), where IRR>r, the minimum number of dwellings to be covered by the community energy modality with SDHW-ORC will be at least 10-12 dwellings. In the case of lower associated demand or lower

occupancy in the energy community, smaller ORC equipment and decentralised modular configurations should be chosen.

To establish simple mathematical relationships for the technical-economic evaluation of the configurations studied, statistical correlations with a high coefficient of determination (R^2>90%) have been carried out, which allow different hot water demand scenarios to be adapted to the associated design output in the ORC. The results obtained from the statistical fitting of the simulation are listed in **Table 3**, where they can be implemented according to the building occupancy to be applied in **Table 4** to obtain the economic feasibility of the ORC-SDHW integration. A linear trend of demand with respect to occupancy is observed, mainly given by regulatory norms in Spain and the expression of water consumption used.

Table 3. Regression coefficients for the demand for domestic hot water (kWh) and associated ORC production (kWh) as a function of occupancy in each case.

Variable	a_j^i	b_j^i	c_j^i
E_{DHW}^{dec}	1.36367779E+03	3.36101028E+02	-3.05942581E+01
E_{ORC}^{dec}	-4.15466000E+01	6.60843314E+02	1.03428571E+00
E_{DHW}^{cen}	-2.58935167E+02	2.72777354E+03	6.79019086E-02
E_{ORC}^{cen}	-3.67802467E+03	2.34557525E+03	5.83261022E-01

Table 4. Regression coefficients for obtaining IRR for each case studied.

Variable	a_j^i	b_j^i	c_j^i	d_j^i	e_j^i
IRR^{dec}	9.05291474E+02	-1.59023221E-02	4.68049936E-05	-9.55433309E-02	1.34798619E-05
IRR^{cen}	3.41658317E-02	1.70048237E-06	-	-1.58635444E-06	-

5 CONCLUSIONS

720

This study proposes the integration of an ORC into domestic hot water systems to evaluate its techno-economic viability. It studied a decentralised case with micro-ORC and low annual thermal demand and another case in which a group of houses are grouped into an energy community, thus establishing a central ORC system and production of DHW with solar collectors. Several important conclusions can be drawn from the results and analysis presented in this paper.

- First, it shows that the integration of the ORC in solar domestic hot water systems can be technically and economically viable, especially in centralised systems with higher thermal demand (>40 persons).
- In the decentralised case, it was found that the micro-ORC can be an interesting option for small demands, but economic viability may be limited (IRR<2%). In the centralised case (energy community), it was demonstrated that the integration of the ORC and solar collectors could result in a significant decrease in energy cost (IRR>10%) and an increase in cogeneration efficiency (>51%).
- Competitive LCOE values were obtained compared to energy communities based on photovoltaics with <35% difference, adding to our case a storage system and thermal power generation.
- In addition, the number of homes in an energy community significantly impacts the economic viability of ORC integration, with a minimum of 10 homes necessary for the project to be sufficiently profitable. Domestic hot water demand and ORC production are highly correlated, suggesting that the integration of these systems can be highly efficient because there is a large thermal resource that can be harnessed with ORC (almost half of the thermal demand for domestic hot water) instead of mixing with cold water to reach the 60 °C required by regulations.

NOMENCLATURE

E	energy	(kWh)
CF	cashflow	(€)
η	efficiency	(–)
CHP	combined heat and power	
ORC	organic Rankine cycle	
DHW	domestic hot water	
IRR	internal rate of return	(-)
NPV	net present value	(€)
LCOE	levelized cost of energy	(€/kWh)

Subscript/superscript

cen	centralised
dec	decentralised
coll	collector

REFERENCES

Alberto, C., Ceglia, F., Davide Maria Laudiero, Alessandro, M., Marrasso, E., & Laura, V. (2022). *Energy analysis of a geothermal-based energy community equipped with heating and cooling network coupled to an ORC plant*. *0385*, 1–12. https://iris.unisannio.it/handle/20.500.12070/56499

Ancona, M. A., Bianchi, M., Branchini, L., De Pascale, A., Melino, F., Peretto, A., Poletto, C., & Torricelli, N. (2022). Solar driven micro-ORC system assessment for residential application. *Renewable Energy*, *195*, 167–181. https://doi.org/10.1016/J.RENENE.2022.06.007

Andoura, S., Hancher, L., & Van Der Woude, M. (2010). *Towards a European Energy Community: A Policy Proposal*. http://inis.iaea.org/Search/search.aspx?orig_q=RN:48094830

Baral, S., Kim, D., Yun, E., & Kim, K. C. (2015). Energy, Exergy and Performance Analysis of Small-Scale Organic Rankine Cycle Systems for Electrical Power Generation Applicable in Rural Areas of Developing Countries. *Energies 2015, Vol. 8, Pages 684-713*, *8*(2), 684–713. https://doi.org/10.3390/EN8020684

Bassam, N. El. (2021). Current distributed renewable energy in rural and urban communities. *Distributed Renewable Energies for Off-Grid Communities: Empowering a Sustainable, Competitive, and Secure Twenty-First Century*, 297–326. https://doi.org/10.1016/B978-0-12-821605-7.00024-6

Bell, I. H., Wronski, J., Quoilin, S., & Lemort, V. (2014). Pure and pseudo-pure fluid thermophysical property evaluation and the open-source thermophysical property library coolprop. *Ind. Eng. Chem. Res.*, *53*(6), 2498–2508. https://doi.org/10.1021/ie4033999

Bou Lawz Ksayer, E. (2011). Design of an ORC system operating with solar heat and producing sanitary hot water. *Energy Procedia*, *6*, 389–395. https://doi.org/10.1016/J.EGYPRO.2011.05.045

Braimakis, K., Charalampidis, A., & Karellas, S. (2021). Techno-economic assessment of a small-scale biomass ORC-CHP for district heating. *Energy Conversion and Management*, *247*, 114705. https://doi.org/10.1016/J.ENCONMAN.2021.114705

Busch, H., Ruggiero, S., Isakovic, A., & Hansen, T. (2021). Policy challenges to community energy in the EU: A systematic review of the scientific literature. *Renewable and Sustainable Energy Reviews*, *151*, 111535. https://doi.org/10.1016/J.RSER.2021.111535

Ceglia, F., Marrasso, E., Roselli, C., Sasso, M., Coletta, G., & Pellegrino, L. (2022a). Biomass-Based Renewable Energy Community: Economic Analysis of a Real Case Study. *Energies 2022, Vol. 15, Page 5655*, *15*(15), 5655. https://doi.org/10.3390/EN15155655

Ceglia, F., Marrasso, E., Roselli, C., Sasso, M., Coletta, G., & Pellegrino, L. (2022b). Biomass-Based Renewable Energy Community: Economic Analysis of a Real Case Study. *Energies 2022, Vol. 15, Page 5655*, *15*(15), 5655. https://doi.org/10.3390/EN15155655

Dóci, G., Vasileiadou, E., & Petersen, A. C. (2015). Exploring the transition potential of renewable energy communities. *Futures*, *66*, 85–95. https://doi.org/10.1016/J.FUTURES.2015.01.002

Duffie, J. A., & Beckman, W. A. (1991). *Solar engineering of thermal processes*. 919.

Frieden, D., Tuerk, A., & Neumann, C. (2020). *Collective self-consumption and energy communities: Trends and challenges in the transposition of the EU framework*. https://doi.org/10.13140/RG.2.2.25685.04321

IEA. (2022). *World Energy Outlook 2022*. www.iea.org/t&c/

Jenkins, S. (2014). Construction-cost indices. *Chemical Engineering*, *121*(6), 28–29. https://go.gale.com/ps/i.do?p=AONE&sw=w&issn=00092460&v=2.1&it=r&id=GALE%7CA371192960&sid=googleScholar&linkaccess=fulltext

Klein, S. J. W., & Coffey, S. (2016). Building a sustainable energy future, one community at a time. *Renewable and Sustainable Energy Reviews*, *60*, 867–880. https://doi.org/10.1016/J.RSER.2016.01.129

Koirala, B. P., Koliou, E., Friege, J., Hakvoort, R. A., & Herder, P. M. (2016). Energetic communities for community energy: A review of key issues and trends shaping integrated community energy systems. *Renewable and Sustainable Energy Reviews*, *56*, 722–744. https://doi.org/10.1016/J.RSER.2015.11.080

Lazard. (2023, April). *2023 Levelized Cost Of Energy+ | Lazard*. https://www.lazard.com/research-insights/2023-levelized-cost-of-energyplus/

Loni, R., Mahian, O., Markides, C. N., Bellos, E., le Roux, W. G., Kasaeian, A., Najafi, G., & Rajaee, F. (2021). A review of solar-driven organic Rankine cycles: Recent challenges and future outlook. *Renewable and Sustainable Energy Reviews*, *150*, 111410. https://doi.org/10.1016/J.RSER.2021.111410

Lowitzsch, J., Hoicka, C. E., & van Tulder, F. J. (2020). Renewable energy communities under the 2019 European Clean Energy Package – Governance model for the energy clusters of the future? *Renewable and Sustainable Energy Reviews*, *122*, 109489. https://doi.org/10.1016/J.RSER.2019.109489

Ministerio de Fomento. (2019). Código Técnico de la Edificación. Documento Básico HE Ahorro de Energía. *Código Técnico de La Edificacion*, 1–129. http://www.arquitectura-tecnica.com/hit/Hit2016-2/DBHE.pdf

Mishra, R., Naik, B. K. R., Raut, R. D., & Paul, S. K. (2022). Circular economy principles in community energy initiatives through stakeholder perspectives. *Sustainable Production and Consumption*, *33*, 256–270. https://doi.org/10.1016/J.SPC.2022.07.001

OMIE. (2022). *Market Results*. https://www.omie.es/

Pereira, J. S., Ribeiro, J. B., Mendes, R., Vaz, G. C., & André, J. C. (2018a). ORC based micro-cogeneration systems for residential application – A state of the art review and current challenges. *Renewable and Sustainable Energy Reviews*, *92*, 728–743. https://doi.org/10.1016/J.RSER.2018.04.039

Pereira, J. S., Ribeiro, J. B., Mendes, R., Vaz, G. C., & André, J. C. (2018b). ORC based micro-cogeneration systems for residential application – A state of the art review and current challenges. *Renewable and Sustainable Energy Reviews*, *92*, 728–743. https://doi.org/10.1016/J.RSER.2018.04.039

Rodriguez-Pastor, D. A., Becerra, J. A., & Chacartegui, R. (2023). Adaptation of residential solar systems for domestic hot water (DHW) to hybrid organic Rankine Cycle (ORC) distributed generation. *Energy*, *263*, 125901. https://doi.org/10.1016/J.ENERGY.2022.125901

S.A Klein. (2017). TRNSYS 18: A Transient System Simulation Program. *Solar Energy Laboratory, University of Wisconsin, Madison, USA*. http://sel.me.wisc.edu/trnsys

Streimikiene, D., Baležentis, T., Volkov, A., Morkūnas, M., Žičkienė, A., & Streimikis, J. (2021). Barriers and Drivers of Renewable Energy Penetration in Rural Areas. *Energies 2021, Vol. 14, Page 6452*, *14*(20), 6452. https://doi.org/10.3390/EN14206452

ACKNOWLEDGEMENT

This work was partially funded by ESASUR and VS ENERGY TECH SL, a spin-off company of the University of Seville.

ORC SEVILLE 2023
7th International Seminar on O.R.C. Power Systems

© 2024 Editorial Universidad de Sevilla. Este es un artículo de acceso abierto distribuido bajo los términos de la licencia de uso y distribución Creative Commons (BY-NC-ND 4.0)

DOI: https://dx.doi.org/10.12795/9788447227457_129

ASSESSMENT OF HIGH TEMPERATURE HEAT PUMP LAYOUTS EQUIPPED WITH A BLADELESS TURBOEXPANDER

Matteo Passalacqua[1,*], Simone Maccarini[1], Stefano Barberis[1], Alberto Traverso[1]

[1]*Thermochemical Power Group, University of Genova, Via Montallegro 1, 16145 Genova, Italy*

*Corresponding Author: matteo.passalacqua@edu.unige.it

ABSTRACT

Efficient and resilient reverse cycles at MW-scale are needed in industry and energy communities for pursuing the ambitious targets of electrification of industrial processes and thermal generation via renewable power.
This work evaluates the optimal thermodynamic performance features of heat pump cycles comparing conventional layouts with those adopting a Tesla turboexpander, for recovering pressure drop in high temperature applications. The paper focuses on n-pentane (R601), a natural refrigerant, being a favorable substitute of synthetic refrigerants thanks to its low global warming potential (GWP) and adequate thermophysical properties that could allow to reach high temperature thermal outputs (>150°C), thus, being suitable for some specific industrial processes. Tesla or bladeless turboexpanders are a promising technology for small volumetric flows and two-phase fluids, featuring low sensitivity to downscaling effects, while retaining high rotor efficiency, which is being investigated for energy-harvesting solutions. The benefit of introducing such expansion device in place of a conventional lamination valve is assessed, in different layout configurations. Simulations were conducted using an improved version of WTEMP-EVO modeling tool, proprietary to University of Genoa.
Results show that the use of Tesla expander improves significantly the overall thermal efficiency in terms of coefficient of performance (COP), thanks to power recovered, depending on the cycle layout.

1 INTRODUCTION

The continuous increase of GHG emissions, in particular carbon dioxide that reached a world record in 2022, is encouraging many sectors to adopt new strategies to reduce emissions. Transport, buildings, and industry are the most relevant sectors in terms of final energy consumption, about 2.9 Gtoe each for a total of 60% (IPCC, 2021).
The course of action to abate pollutant substances and GHG emission includes the electrification of heating systems, both industrial and DHNs, which together account for roughly 30% the total emission (IPCC, 2021). However, a benefit from electrification is only obtained if electricity is produced mostly from renewable sources (e.g., solar photovoltaic, concentrated solar power, wind power, hydro, biomass) or carbon-free energy carriers (green hydrogen and green ammonia).
From this point of view, heat pumps are a promising solution. The latest research has focused mainly on three aspects of heat pump plants, namely plant design and machinery optimization, expander introduction, high temperature heat pumps (HTHP) applications and the use of low-GWP natural refrigerants. Recent literature contains numerous studies on heat pumps performance assessment and the replacement of inefficient heating systems with such technology (Adamson et al., 2022) (Chen et al., 2022) (Pan et al., 2021) (Dai et al., 2020) (Jibran et al., 2022).. Working fluids for reverse cycles typically feature high specific heat, high latent heat of vaporization. Halogenated hydrocarbons, such as hydrofluorocarbons (HFCs) and hydrochlorofluorocarbons (HCFCs) are employed at present in many heat pump plants. In accordance with Montreal Protocol (Montreal Protocol, 1987), Kyoto Protocol (Kyoto Protocol, 1997) and the successive Kigali Amendment (Kigali Amendment, 2019) there is an evident need for reducing their usage.

Organic working fluids are a promising alternative to of synthetic refrigerants since they have low GWPs while showing comparable thermophysical properties. Besides, some of them allow to achieve high heat sink temperatures thanks to their high critical temperature, interesting for a variety of different industrial application. The recent scientific research focused on natural and low-GWP refrigerants performance (Meinel, Wieland and Spliethoff, 2014) (Kumar Saini et al., 2021) as well as comparative reviews (Bamigbetan et al., 2017) (Frate, Ferrari and Desideri, 2019). A promising example is n-pentane (R601): in accordance with several literature sources (Arpagaus et al., 2018) (Wu et al., 2020), with the relevant exception of water (R718), it has the highest expected COP in the typical temperature range of HTHPs. Some authors (Arpagaus et al., 2018) perform a widespread analysis on several heat pump working fluids, including n-pentane, to evaluate the most suitable ones for high heat sink temperatures. They found that such hydrocarbon is outperformed in terms of optimal temperature range by water and R1336mzz(Z) only. Their results show that R601 is among the most efficient fluids in the range 130-160°C of heat sink temperatures, topping out at a COP of 3.27 for a temperature lift of 70 K. Other authors (Sulaiman et al., 2022) compare different low-GWP refrigerants for HTHP application, showing that R601 has 4% to 18% lower power consumption compared to R245fa. Besides, TEWI for R601 is around 27% lower. Very little literature is available specifically on n-pentane heat pumps. In an old work (Yamazaki and Kubo, 1985), researchers evaluated a 400 kW R601 layout supplying steam at 130°C from waste heat at 90°C. They obtained a COP of 4.5 for source and sink temperatures of 80°C and 135°C, respectively.

The introduction of a dynamic expander in reverse cycles as an energy harvesting device is covered in literature (Zhang et al., 2013) (Nickl et al., 2005) and the performance improvements are registered between 10% and 30% with respect to the base cycle, depending on the layout characteristics (Murthy et al., 2019). Multidisc bladeless friction turboexpanders, also known as Tesla turbines (Tesla, 1913), represent a promising technology as small-scale machinery due to their low sensitivity to downscaling effects, retaining high rotor efficiency. Some authors performed a systematic loss characterization (Renuke et al, 2022), showing that the largest contributions reside in stator-rotor interaction (40%) and ventilation (15%) losses, followed by leakages. Nowadays, its ability to handle low volumetric flows, including two-phase fluids, may pave the way towards Tesla expander adoption in heat pumps as COP booster. In general, this paper aims to widen the knowledge on such an innovative and effective solution to emissions reduction.

724

2 METHODS

2.1 Layouts analysed

This work assesses different layouts of n-pentane reverse cycles, firstly comparing performance of simple expansion cycle with a novel layout featuring a Tesla turboexpander, and secondly evaluating to what extent two stage compression is beneficial.

Figures 1a-1d describe the investigated layouts: for each of them, models of physical components are created and interfaced with each other to assemble complete cycles.

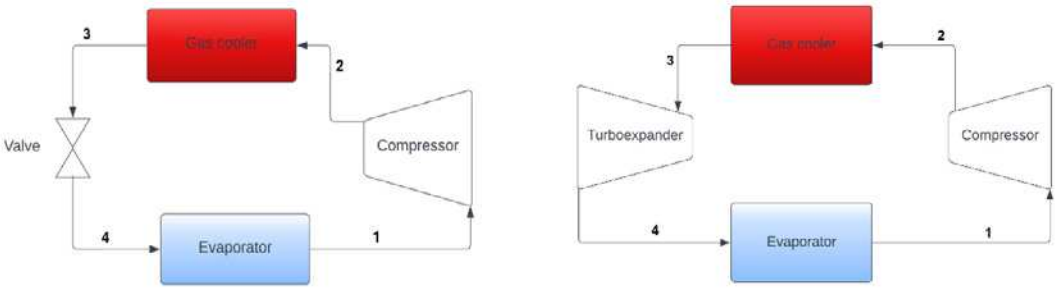

a) **b)**

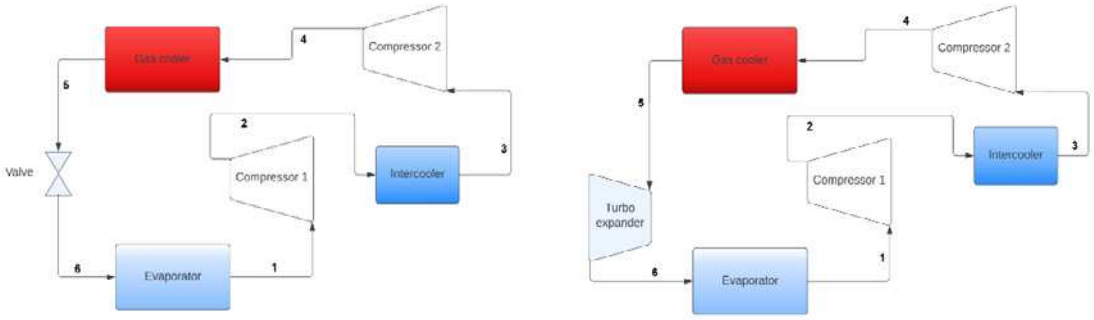

c) **d)**

Figure 1a-1d – Schematics of investigated layouts

2.2 Thermodynamic Modelling

This section describes the underlying principles behind the M physical component models constituting the system. The simulation program WTEMP-EVO has been devised to assess and enhance the techno-economic effectiveness of various cycle arrangements and can evaluate several pure fluids with a two-phase or real-gas nature via the utilization of CoolProp (Bell et al., 2014) thermodynamic libraries. This is, in essence, an expansion of WTEMP (Traverso et al., 2004) retaining its modular approach, implying that every component is depicted by a subroutine that calculates parameters based solely on basic thermal evaluations performed within each component, independently of the other constituents. This numerical approach permits the components to be interlinked to obtain the evaluation of any preferred layout. Most component models are lumped representations of real components, with the exception of heat exchangers, which are modelled as 1D components, discretized in 30 computation sections. All components are adiabatic, thus, heat losses towards the environment are neglected.

The compressor reproduces the real component in the plant configuration. Equation (1) reports the definition of polytropic efficiency used in this work for such component. Here, β is the compression ratio, k is the specific heat ratio ($k = c_p/c_v$) and m the exponent of the polytropic transformation. Equation (2) highlights the link between isentropic efficiency and polytropic exponent.

$$\eta_{pol} = \frac{m}{m-1} \cdot \frac{k-1}{k}, \tag{1}$$

$$\eta_c = \frac{1-\beta^{\frac{k-1}{k}}}{1-\beta^{\frac{m-1}{m}}} \tag{2}$$

$$h_{out,turb} = h_{in,turb} - (h_{in,turb} - h_{out,s,turb}) \cdot \eta_{s,turb} \tag{3}$$

The turboexpander operates an expansion of the working fluid, generating power at the shaft. This component was assessed by means of equation (3).

The modelling of the expansion valve simply considers an isoenthalpic process between inlet and outlet. The heat exchanger model refers to a shell and tube heat exchanger. The modeling is based on a counter-flow rationale, with the user setting a primary temperature or quality and other parameters such as approach, pinch point temperature difference, and pressure losses. The results of the thermodynamic cycle are then used to determine the geometrical characteristics of the heat exchanger, for which inputs include the velocities of the working and source fluids (u_{fluid} and u_{source}), as well as the internal and external diameters of the pipes (D_{int} and D_{ext}). The heat transfer is computed by use of the *ε-NTU* criterion, as suggested by notable works (Incropera et al., 2010).

The heat exchanger is discretized into a number of cells (N=30 for this work) assuming a constant overall heat transfer coefficient for each cell. The convective heat transfer coefficient is calculated for each cell. The product *UA* is then calculated by assessing the effectiveness ε for each cell. This involves

assuming equal thermal power exchange for each cell and comparing the actual enthalpy drop of the fluid to the enthalpy drop experienced by the fluid with the lowest heat capacity. The heat transfer surface area is then determined for each cell and summed up to calculate the total surface area of the heat exchanger. It should be noted that thermal conduction along the axial coordinate within the piping material is disregarded in the analysis.

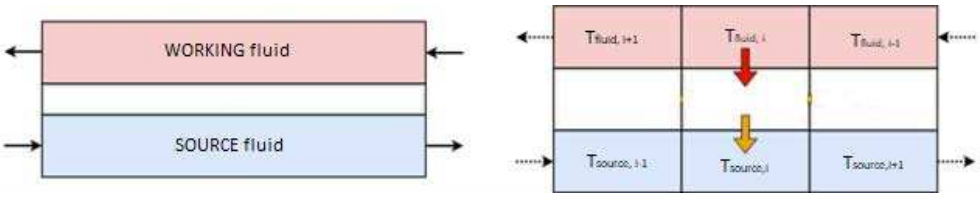

Figure 2: Scheme of counter-flow heat exchanger (cooler)

3 SIMULATION AND RESULTS

3.1 Model Inputs and Constraints

This section describes the model inputs and main constraints. A size of 1 MW_{heat} heating power was chosen as a reference of a sizeable heat pump plant. Table 1 contains the boundary conditions and the general assumptions for each component of the cycle.

Table 1: Boundary conditions and general assumptions

BCs and General Assumptions	
Working fluid	R601
Reference size (Q_{heat})	1 MW_{heat}
Heat exchanger pressure loss	3%
Thermal loss towards ambient	Neglected
Max compressor outlet temperature	180 °C
ΔT superheating (compressor inlet)	50 °C
ΔT subcooling (expander inlet)	30 °C
Condensation pressure (reference)	20 bar
Evaporation pressure (reference)	0.8 bar
Minimum ΔT at HXs	5 K
Mechanical efficiency	0.85
Electrical efficiency	0.9
Compressor polytropic efficiency	0.91
Tesla turbine isentropic efficiency	0.44

It is worth noting that a polytropic compressor efficiency was assumed, according to the assumptions in Table 1. In addition, a maximum temperature of the cycle, that is the compressor outlet temperature, was chosen (Table 1). The justification for this choice is two-fold. On the one hand, high temperatures lead to thermal decomposition of the compressor lubricant, which should be avoided. On the other hand, operation near the critical temperature of R601 (196°C) should be avoided for thermodynamic reasons, such as high variability of the specific heat around the critical point. In addition, such temperature is adequate to ensure sufficient heat transfer even at very high heat sink temperatures. This choice is in line with previous studies (Frate, Ferrari and Desideri, 2019) (Ommen et al., 2015).

3.2 Parametric analysis

The COP is defined as usual for heat pumps, that is, by the following equations:

$$COP_{HP} = \frac{\dot{Q}_{heat}}{\dot{W}_{elect}} \quad (3)$$

A parametric analysis exploring different key parameters was conducted, both for the simple cycle (Figures 3a-3c) and for the Tesla modified cycle (Figures 4a-4c).

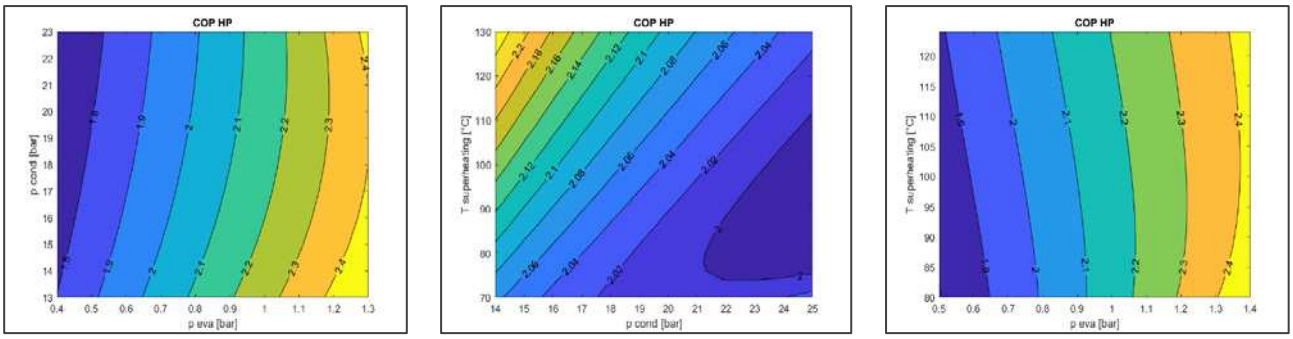

a) **b)** **c)**

Figure 3a-3c: COP sensitivity against a) p_{cond}/p_{eva}, b) T_{sh}/p_{cond} and c) T_{sh}/p_{eva} for simple cycle

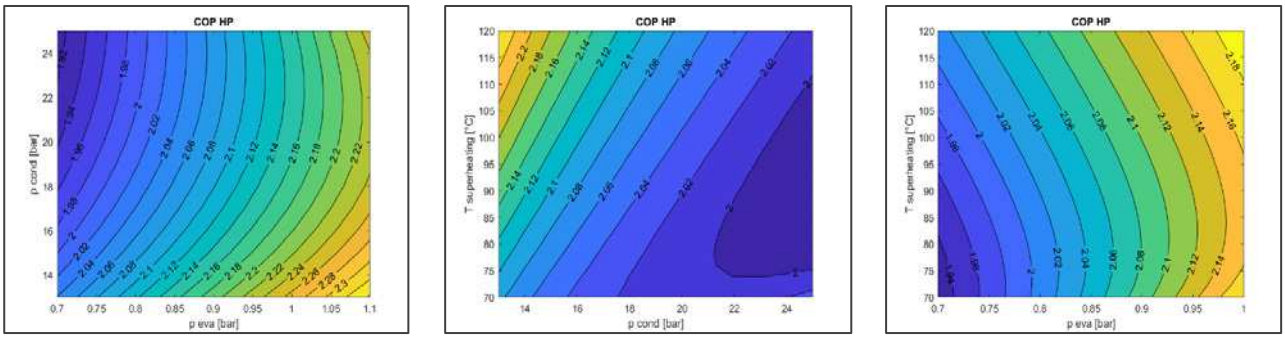

a) **b)** **c)**

Figure 4a-4c: COP sensitivity against a) p_{cond}/p_{eva}, b) T_{sh}/p_{cond} and c) T_{sh}/p_{eva} for Tesla cycle

Figure 3a demonstrates that COP of the heat pump is scarcely sensitive to condensation pressure, while highly depends on evaporation pressure. Figure 3b depicts an increasing heat pump performance with increasing superheating temperature (i.e., compressor inlet temperature) at low condensation pressures, and Figure 3c show that evaporation pressure have a negligible influence on the COP value. For the Tesla modified cycle, trends depicted are similar, with performance values varying less but in accordance with a narrower pressure range on horizontal axis.

It should be noted that the superheating temperatures are consistently higher than the saturation temperatures at evaporating pressures, confirming that dry refrigerants require high degree of superheating before compressor inlet. In addition, dry refrigerant may not benefit from two-stage compression, or the efficiency gain is very marginal, as shown in previous literature (Meinel, Wieland and Spliethoff, 2014).

Figures 5a to 5c display the required compressor thermodynamic power. With reference to equation (4), the trends are in line with the COP plots.

727

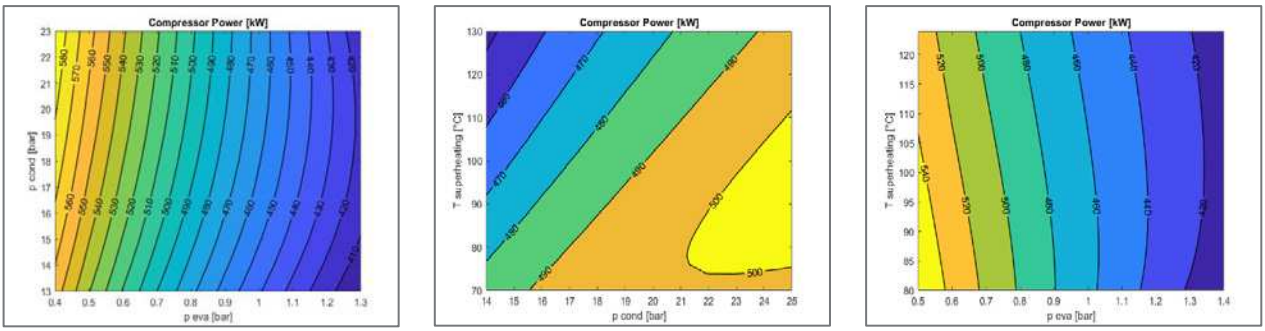

a) **b)** **c)**

Figure 5a-5c: Compressor power against a) p_{cond}/p_{eva}, b) T_{sh}/p_{cond} and c) T_{sh}/p_{eva}

With the purpose of addressing energy harvesting, the available expansion power for the Tesla expander is depicted in Figures 6a-6c. It may be observed that such power is slightly dependent on condensation pressure, while increases with decreasing evaporation pressure and superheating temperature.
Figure 7 highlights the COP improvement for three values of evaporation pressure, assuming constant condensation pressure (20 bar). The percentage difference is defined as the difference between Tesla cycle COP and simple cycle COP, divided by the simple cycle COP. The evaporation pressures reported in Figure 7 correspond to R601 saturation temperatures of 16.8 °C, 29.8 °C and 35.7 °C, respectively.

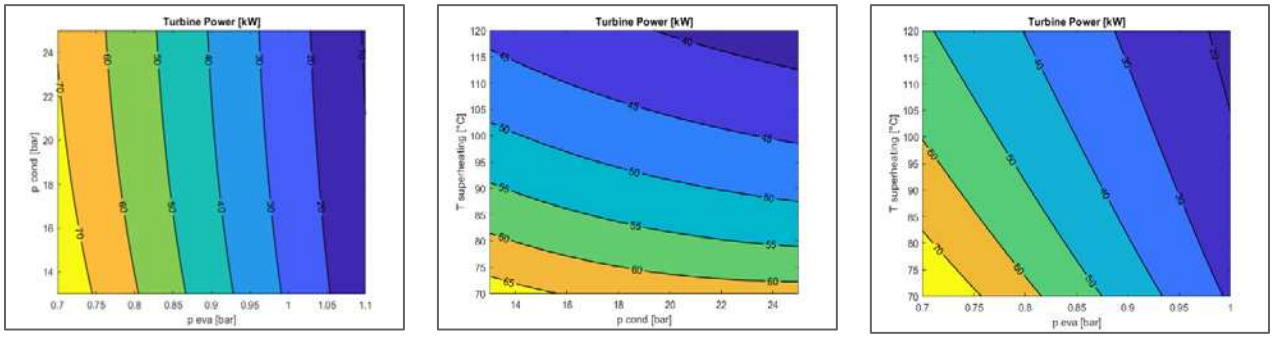

a) **b)** **c)**

Figure 6a-6c: Tesla expander available power against a) p_{cond}/p_{eva}, b) T_{sh}/p_{cond} and c) T_{sh}/p_{eva}

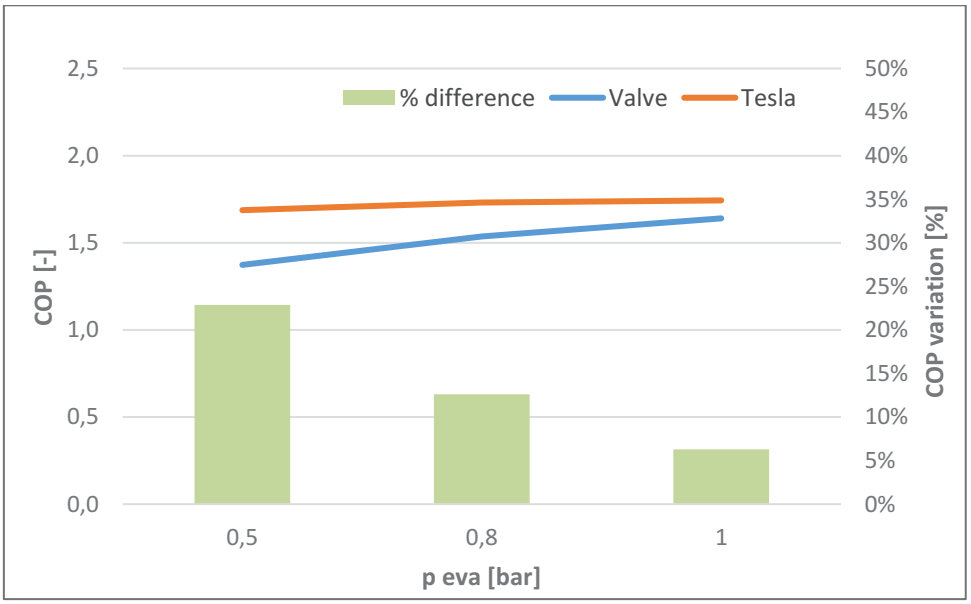

Figure 7: COP comparison between simple and Tesla modified cycle (p_{cond} = 20 bar)

4 PROPOSED CASE STUDY

Despite being a very promising energy recovery option, low-temperature waste heat has major challenges associated with its recovery. Moreover, heat pump performance is always reduced when heat upgrade requires high temperature lifts. To further improve the knowledge of HTHP technology, a real industrial case study is presented below. These results might indicate the suitability of HTHP for various industrial applications and justify further detailed research and experimental activities.

4.1 Case Study Description

A manufacturer of laminate products for the building and furniture industry disposes of a hot water tank from the pressing process, that is to be evaluated as a thermal source for the production of pressurized hot water at 160°C and 20 bar for a different process.
Since a consistent temperature glide is involved (around 100 °C, Table 2), R601 was evaluated due to its favourable properties. Machinery efficiencies are the same reported in Table 1.

Table 2: Boundary conditions for the case study

BCs and General Assumptions	
Source water inlet temperature	≈ 60 °C
Source water outlet temperature	≈ 35 °C
Process water inlet temperature	≈ 120 °C
Process water outlet temperature	160 °C

4.2 Case Study Results

Table 3 delivers briefly the results of the simulation for the aforementioned industrial case study.

Table 3: Performance comparison for R601 HTHP according to the case study

COP comparison	
COP simple cycle	1.54
COP Tesla modified cycle	1.73

As expected, the heat pump performance benefits from the presence of a Tesla expander by matter of 13%, in good accordance with numerous literature sources. To complete the analysis, Figures 8a-8b report p-h charts for the two cases and Figures 9a and 9b show examples of T-Q chart along the discretization coordinate x relative to two relevant heat exchange processes for the case study conditions. Figure 8a refers to the de-superheating process of the refrigerant prior to its condensation.

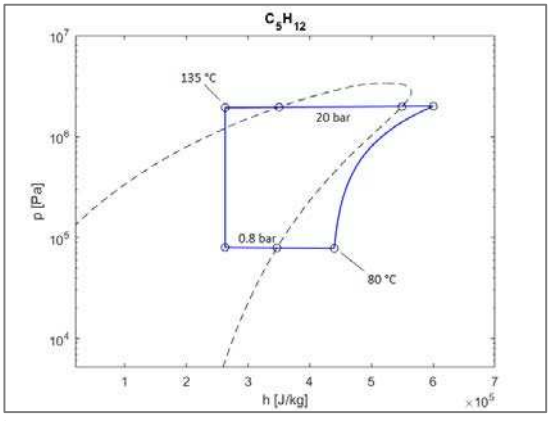

a)

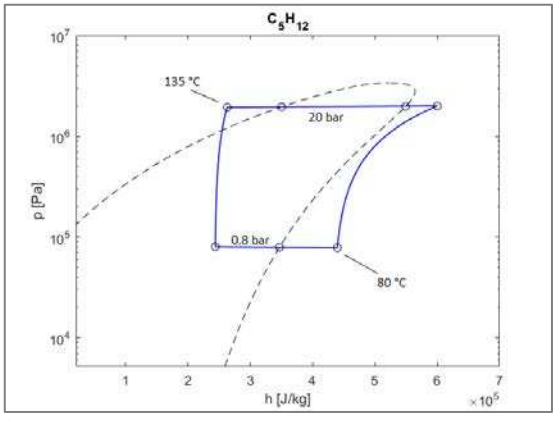

b)

Figure 8a-8b: Semi-logarithmic p-h comparison for R601 HTHP according to the case study

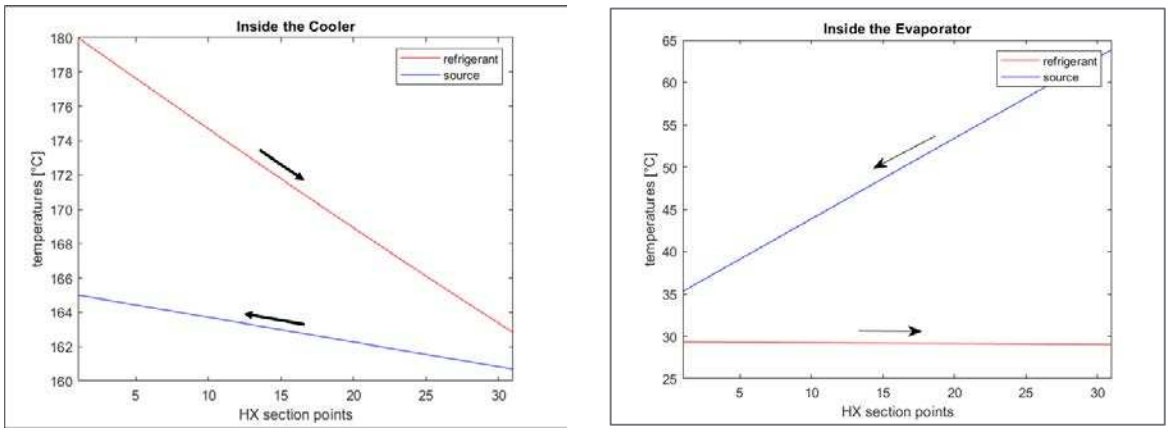

a) **b)**

Figure 9a-9b: T-x chart for the a) de-superheating and b) evaporation according to the case study (x represents the axial coordinate of the external heat transfer fluid)

5 CONCLUSIONS

In this paper, techno performance of n-pentane HTHP have been analysed. A MW-sized plant was investigated as reference for an industrial application. The updated WTEMP-EVO software was adopted to model and simulate the cycle. Performance was assessed under on-design conditions and a sensitivity analysis on relevant parameters was performed.

The results confirm the promising use of expanders to harvest a significant amount of energy and to improve the COP of the cycle. Optimal conditions for turboexpander cycle are obtained in a narrower range of operating conditions. A 13% COP improvement was achieved in the industrial case study simulation. In addition, Tesla turbines have further advantages concerning almost size-independent efficiency and reduced cost with respect to traditional turboexpanders, and potentially can better manage two-phase flows, without the risk of erosion. Dual stage compression cycles were not assessed, since R601 is a dry refrigerant and, having a very sloped saturation curve, compression "follows" that curve quite solidly (Figures 6a-6b), so fluid intercooling may not improve significantly cycle performance, considering also the added plant complexity and costs.

730

NOMENCLATURE

COP	Coefficient of Performance
GHG	Greenhouse Gas
GWP	Global Warming Potential
HP	Heat Pump
HTHP	High Temperature Heat Pump
IPCC	Intergovernmental Panel on Climate Change
NTU	Number of Transfer Units
TEWI	Total Equivalent Warming Impact
UNFCC	United Nations Framework Convention on Climate Change

Symbols

P	Pressure	[bar]
T	Temperature	[°C, K]
h	Enthalpy	[kJ/kg]
s	Entropy	[kJ/kg K]

m	Mass flow	[kg/s]
x	HX discretization coordinate	[-]
ΔT	Temperature gradient	[K]
β	Pressure ratio	[-]
k	Heat capacity ratio	[-]

Subscript

in	Inlet
out	Outlet
int	Internal
ext	External
elect	Electrical
s	Isentropic
pol	Polytropic
cond	condenser
eva	evaporator
sh	Superheating
subc	Subcooling
fluid	Working fluid
source	Source fluid
heat	Heating power

REFERENCES

Adamson, K.M, et al., 2022, "High-temperature and transcritical heat pump cycles and advancements: A review,." *Renewable and Sustainable Energy Reviews*.

Arpagaus, C., Bless, F., Uhlmann, M., Schiffmann, J. and Bertsch, S.,2018, High temperature heat pumps: Market overview, state of the art, research status, refrigerants, and application potentials, *Energy* 152, 985-1010.

Bamigbetan, O., Trygve, M.E., Neska, P., and Bantle, M., 2017, Review of vapour compression heat pumps for high temperature heating using natural working fluid, *International Journal of Refrigeration* 80, 197-211.

Bell, I., Wronski, J., Quoilin, S., and Lemort, V., 2014, Pure and pseudo-pure fluid thermophysical property evaluation and the open-source thermophysical property library CoolProp, *Ind Eng Chem Res* 53, 2498-2508.

Bergman, T.L., Lavine, A., Incropera, F. and DeWitt, D., 2018, *Fundamentals of Heat and Mass Transfer, 8th Edition.* Wiley & Sons.

Chen, Y., Standl, P., Weiker, S., and Gaderer, M., 23022, A general approach to integrating compression heat pumps into biomass heating networks for heat recovery, *Applied Energy* 310.

Dai, B., Qi, H., Dou, W., Liu, S., Zhong, D., Yang, H., Nian, V. and Hao, Y., 2020, Life cycle energy, emissions and cost evaluation of CO2 air source heat pump system to replace traditional heating methods for residential heating in China: System configurations, *Energy Conversion and Management* 218.

European Fluorocarbons Technical Committee, https://www.fluorocarbons.org/environment/climate-change/global-warming-potential/ (accessed November 30, 2022).

Ferrando, M., Renuke, A., Traverso, A. and Sishtla, V., 2021, A new design method for two-phase nozzles in high efficiency heat pumps, *International Journal of Refrigeration*, 148-156.

Frate, G.F, Ferrari, L. and Desideri, U., 2019, Analysis of suitability ranges of high temperature heat pump working fluids, *Applied Thermal Engineering*, 628-640.

IPCC, Sixth Report Assessment (AR6), Geneva (CH), 2021.

Jibran, M., Zuberi, S., Hasanbeigi, A. and Morrow, W., 2022, Bottom-up assessment of industrial heat pump applications in U.S. Food manufacturing, *Energy Conversion and Management* 272.

Kigali Amendment, Kigali, 2019.
Kyoto Protocol, Kyoto, 1997.
Meinel, D, Wieland, C. and Spliethoff, H., 2014, Effect and comparison of different working fluids on a two-stage ORC concept, *Applied Thermal Engineering*, 246-253.
Montreal Protocol, Montreal, 1987.
Murthy, A.A, Subiantoro, A., Norris, S., and Fukuta, A., 2019, A review on expanders and their performance in vapour compression refrigeration systems, *International Journal of Refrigeration* 106, 427-446.
Nickl, J., Will, G., Quack, H., and Kraus, W.E., 2005, Integration of a three-stage expander into a CO2 refrigeration system, *International Journal of Refrigeration* 28, no. 8, 1219-1224.
Ommen, T, Jensen, J.K., Markussen, W.B., Reinholdt, L., and Elmegaard, B., 2015, Technical and economic working domains of industrial heat pumps: Part 1 – Single stage vapour compression heat pumps, *International Journal of Refrigeration*, 168-182.
Pan, M., Zhu, Y., Liang, Y., Lu, F., Zhi, R., and Xiao, G., 2021, Performance assessment of a waste-heat driven CO2-based combined power and refrigeration cycle for dual-temperature refrigerated truck application, *Energy Conversion and Management* 249, no. 114863
Renuke, A., Reggio, F., Traverso, A., and Pascenti, M., 2022, Experimental Characterization of Losses in Bladeless Turbine Prototype, *Journal of Engineering for Gas Turbines and Power*, 144.
Renuke, A., and Traverso, A., 2022, Performance assessment of Tesla expander using Three-Dimensional numerical simulation, *Journal of Engineering for Gas Turbines*, 144, no. 11
Sarbu, I. 2014, A review on substitution strategy of non-ecological refrigerants from vapour compression-based refrigeration, air-conditioning and heat pump systems, *International Journal of Refrigeration* 46, 123-141.
Sulaiman, A., Cotter, D.F., Le, X.K., Huang, M.J., and Hewitt, N.J., 2022, Thermodynamic analysis of subcritical high temperature heat pump using low GWP refrigerants: A theoretical evaluation, *Energy Conversion and Management* 268.
Tesla, N., Turbine. U.S. Patent 1061206, 1913.
Traverso, A. Reverse cycle machine provided with a turbine. Patent WO2018127445A1
Traverso, A., A.F Massardo, Cazzola, W. And Lagorio, G., 2004, WIDGET-TEMP: a novel web-based approach for thermoeconomic analysis and optimization of conventional and innovative cycles, *ASME Turbo Expo 2004: Power for Land, Sea, and Air*, 623-631.
UNFCCC. Paris Agreement, Paris, 2015.
Westphalen, D., and Dieckmann, J., 2004, Scroll Expander for Carbon Dioxide Air Conditioning Cycles, *International Refrigeration and Air Conditioning Conference.* Purdue, IN (US).
Wu, D., B Hu, Wang, R.Z., Fan, H., and Wang, R., 2020, The performance comparison of high temperature heat pump among R718 and other refrigerants, *Renewable Energies*, 715-722.
Yamazaki, T., and Kubo, Y., 1985, Development of a high-temperature heat pump, *IEA Heat Pump Centre Newsletter* 3, no. 4, 18-21.
Zhang, Z., Yitai M., Li, M., and Li Z., 2013, Recent advances of energy recovery expanders in the transcritical CO2 refrigeration cycle, *HVAC&R Research* 19, no. 376-384.

732

ORC SEVILLE 2023
7th International Seminar on O.R.C. Power Systems

© 2024 Editorial Universidad de Sevilla. Este es un artículo de acceso abierto distribuido bajo los términos de la licencia de uso y distribución Creative Commons (BY-NC-ND 4.0)

DOI: https://dx.doi.org/10.12795/9788447227457_133

Selection of The Optimal Working Fluid in an Organic Rankine Cycle for Waste Heat Recovery Through Multi-Objective Optimization and Decision Making

Bipul Krishna Saha[1,] *, El Mouatez Billah Messini [2,3,4], Syed J Haque[1], B Aneesh Bhat[1], Pramod Kumar[1]

[1] *Interdisciplinary Centre for Energy Research, Indian Institute of Science, Bengaluru, 560012*
[2] *LAGE Laboratory, University of Ouargla, 30000 Ouargla, Algeria*
[3] *Electrical Engineering Department, Faculty of Applied Sciences, Ouargla University, Road Ghardaia, 30000 Ouargla, Algeria*
[4] *Sonatrach - Institut Algérien du Pétrole - École de Hassi Messaoud - BP 54 – Hassi Messaoud, 30001, Ouargla, Algeria*
*Corresponding Author: bipulsaha@iisc.ac.in

ABSTRACT

In India, utilising low-temperature waste heat is crucial to improving energy efficiency. The regenerative organic Rankine cycle (ORC) process is a promising waste heat recovery technique in this study. Here, the thermodynamic behaviour of eight working fluids: Butane, Heptane, Hexane, Pentane, Cyclopentane, HexMDiSiloxn (MM), Benzene, and Toluene, was carefully examined. An elite Non-dominated sorting genetic sorting algorithm (NSGA-II) was used in Multi-objective Optimization (MOO) to address the incongruent behaviour of thermodynamic performance (exergy efficiency) and economic performance (levelized energy cost, LEC). Every eight working fluids are the subject of MOO studies, and the resulting Pareto optimal fronts are created. Several advanced Pareto ranking techniques are taken into account to choose one ideal solution from the Pareto optimal front. These include Simple additive weighting (SAW), The technique for order of preference by similarity to deal Solution (TOPSIS), Grey relation analysis (GRA), and Multi-attributive border approximation area comparison (MABAC).
The most economically advantageous working fluid is chosen using an explicit economic performance assessment index called the Static Investment Payback Period (SIPP). The results show that Pentane is the most economically advantageous working fluid with the shortest SIPP and a medium waste heat temperature range. The findings also imply that any working fluid can be used TOPSIS, SAW, GRA, and MABAC with entropy information considered in this study to recover low-temperature waste heat in the ORC.

1 INTRODUCTION

One of today's most talked-about topics is waste heat recovery. There is always enough waste heat in industrial processes to be directly released into the atmosphere, causing environmental pollution. One of the most important concerns for researchers is how to sustainably reuse or recycle waste heat. Increasing energy consumption and lowering carbon dioxide emissions are crucial to addressing energy and environmental issues (García-Afonso et al., 2022). The organic Rankine cycle (ORC) is the most well-established mechanism in the world for converting waste heat into electricity. The simple, stable, and adaptable ORC technology may recover medium-to-low temperature waste heat (100°C–300°C) (Krishna and Basab 2016).
In an ORC system, heat source temperature, working fluid choice, heat sink conditions, cycle configuration, component selection, and process factors all have an impact on ORC performance (van Kleef et al., 2019). Yet, the primary objective of ORC research has been system optimisation, which is essential for achieving optimal system performance, including selecting the optimal system parameters and working fluid based on waste heat. The most useful optimisation criteria include economic factors like payback period and total investment cost and thermodynamic criteria like thermal efficiency, net power output, etc. (Zhang et al. 2018). Multi-objective Optimisation (MOO) is one of the most effective optimisation techniques for handling this problem with many conflicting objectives. MOO offers a number of solutions that all work just as well in terms of the stated goals. These solutions, which are

called Pareto optimal front and nondominated solutions, show how different implementation options and goals affect each other.

In scientific literature, much has been talked about choosing the best solution from a set of nondominated options. Choose one of the non-dominant Pareto-optimal solutions as the next step. There are a number of Pareto-optimal strategies accessible in the literature, with TOPSIS being one of the most popular selection techniques in process engineering. In spite of the fact that finding Pareto-optimal solutions is not yet prevalent in process engineering, there is a great deal of research on the topic. For finding Pareto-optimal solutions, GRA, SAW, CODAS, MEW, MWRA, VIKOR, and MABAC are utilised in addition to TOPSIS (Wang and Rangaiah 2017).

Numerous studies have been conducted based on multi-objective optimisation between optimum thermal efficiency and economic factors. The Levelised Energy Cost with the maximum power output of the ORC system was examined by (Saha et al. 2019). To find the optimal working fluid, they collected waste heat data from five different energy-intensive industries and contrasted maximum exergy efficiency with economical cost using eight different working fluids.

The main goal of this work is to use and compare different ways to find a nondominated solution for applications of regenerative ORC systems. Four methods are chosen for this purpose based on how easy they are to use, how well they can handle goals with different sizes, and how much user input they need. They are implemented using Visual Basic for Applications (VBA) programming in Microsoft Excel.

In addition, a thorough analysis of the thermodynamic analysis and off-design performance of the Regenerative ORC cycle is presented. A Python-based code for thermodynamic cycle simulation has been developed and integrated with the CoolProp fluid properties database. Due to their low global warming potential and ozone depletion potential, eight distinct organic fluids, including Butane, propane, and n-pentane, are considered the working fluids of the Regenerative ORC cycle. Their effect on thermodynamic performance is then evaluated. The most efficient working fluid for cycle configurations is propane.

2 SYSTEM DESCRIPTION

It is imperative to provide a clear and concise account of all materials and methods utilised in the research. This study aims to examine the techniques utilised to enhance the regenerative Organic Rankine Cycle (ORC) efficiency in the context of industrial exhaust gases. Figure 1 below illustrates the schematic depiction of the regenerative ORC. The presented regenerative Organic Rankine Cycle (ORC) is designed to optimise energy recuperation from the available heat sources.

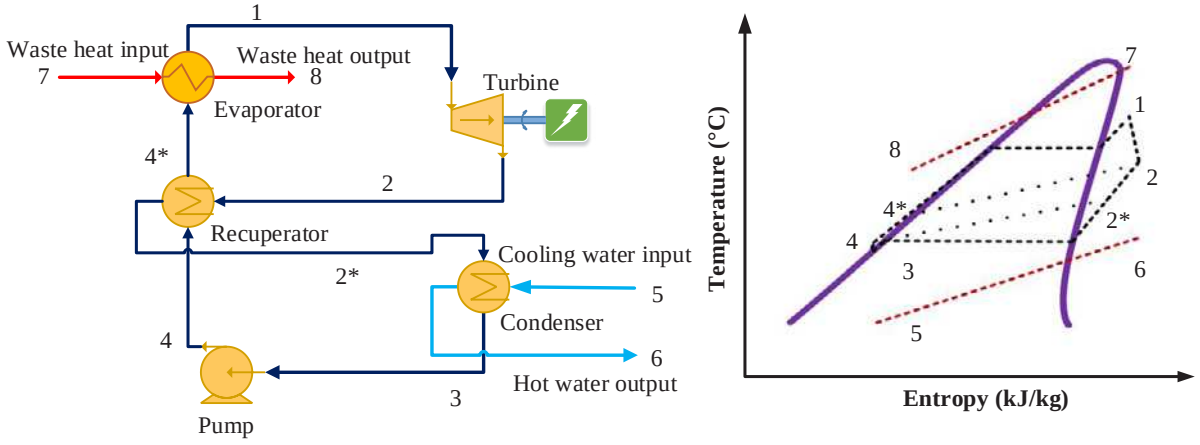

Figure 1: Biaxial machine with the chosen sample geometry

The Regenerative ORC system comprises five distinct equipment components. The components include the evaporator, turbine, recuperator, condenser, and pump. A recuperator is employed in this system to effectively recover the highest amount of thermal energy from the turbine's exhaust. The initial stage of the process involves the utilisation of a pump (process 3-4) to elevate the pressure of the working fluid. Subsequently, the working fluid extracts heat from the recuperator through processes 2-2* and 4-4*. Additionally, the partially heated fluid undergoes a phase change in the evaporator via process 4*-1, utilising waste heat (process 7-8). The fluid characterised by high pressure and temperature undergoes a thermodynamic process (1-2) by entering the turbine and subsequently generating power. The working

fluid that has undergone expansion proceeds towards the condenser (through processes 2*-3 and 5-6) to release heat.

2.1 Working fluid selection.

Two crucial evaluation criteria for the ORC system are the Normal Boiling Point (NBP) temperature and the Critical temperature (T_C) of working fluids. Working fluids must also have a high decomposition temperature and stability to prevent flammability, chemical deterioration, non-explosive nature, and non-toxicity. This study also examines the waste heat temperature ranges for choosing the working fluid (see Table 1). This research exclusively considers hydrocarbon-based working fluids. The authors are aware that fluids containing hydrocarbons are combustible. The amount of oxygen a specific hydrocarbon needs to keep a flame is called the minimum combustion oxygen. When oxygen levels fall below this threshold, but hydrocarbon concentrations remain high, and an ignition source is present, deflagration or fire has not occurred. The minimum oxygen content for hydrocarbon combustion ranges from 8 to 12 % by volume. Inflammable hydrocarbon gas concentrations must fall within a specific range. The lower flammability limit is the lowest point in this flammability range (LFL). The upper limit of the range is determined by the Upper Flammability Limit (UFL) (Haq 2021).

Table 1. Selected working fluid for study (Haq 2021).

Working fluids	Molar mass (gm)	T_c	P_c	Safety data		Environmental data			T_w
		°C	bar	LFL (%)	ASHRAE 34 Safety Group	Atmospheric life (Days)	ODP	GWP 100 year	
Benzene	78.1	289	49.0	-	A2	9.4	0		250-300
Butane	58.12	146.1	40.1	-	-	-	0	-	125-200
Cyclopentane	70.1	238	45.8	-	-	-	0		200-275
Heptane	100.2	267	27.3	-	-	-	0	-	225-300
Hexane	86.17	234.6	30.3	-	-	-	0	-	200-275
HexMDiSiloxn (MM)	162.4	245	19.3	-	-	-	0		200-275
Pentane	72.15	196.6	33.7	1.4	-	0.01	0	~20	200-275
Toluene	91.14	318.6	41.2	-	A2	1.9	0	-	275-300

735

2.2 Description of Thermodynamic Code

To perform a simulation of thermodynamic cycles, an in-house code has been developed to study the impacts of the operating variables. The Python environment has been integrated with the CoolProp database to enable runtime simulation with the available data. The Regenerative ORC cycle has been simulated with a nested iteration of four variables where each single operation parameter has been independently varied over the code execution.

2.3 Mathematical model

The following equation is used to determine the exergy of a stream:

$$\dot{E}x_{mass} = \dot{m}[(h - h_0) - T_0(s - s_0)] \quad (1)$$

The Regenerative ORC cycle's exergy efficiency (EXE) is defined as

$$\eta_{ex} = \left(\frac{W_{net}}{\dot{m}[(h_{W,in} - h_0) - T_0(s_{W,out} - s_0)]}\right) * 100 \quad (2)$$

2.4 Financial Analysis

In this part, the economic model of Regenerative ORC is discussed. The maintenance, operation, and investment costs of Regenerative ORC have been calculated. Also assessed is the projected cost of equipment for the Regenerative ORC. This technique for cost estimation is already discussed in the literature and is acceptable in process engineering. Assume that the heat exchanger, recuperator, and condenser have been constructed from carbon steel and copper. The pump and expander have been constructed from carbon steel (Zhang et al. 2018).

The Bare module cost (C_{BM}) of the Regenerative ORC major component is shown below:

$$C_{BM} = C_{PC}.F_{BM} \quad (3)$$

Here, C_{PC} indicates the purchase cost of the Regenerative ORC component, and the Bare module cost factor of equipment denotes F_{BM}. The Bare module cost factor is dependent on the equipment of the materials.

Purchase equipment cost (C_{PC}) is stated as follows:

$$log_{10}C_{PC} = K_1 + K_2 log_{10}Y + K_3[log_{10}(Y)^2] \quad (4)$$

Where Y is the equipment's capacity or size, the value cost coefficients K_1, K_2, and K_3 are given in Table 2.

The overall amount of capital costs (C_{CC}) is as follows:

$$C_{CC} = \sum \quad C_{BM} \quad (5)$$

The "Chemical Engineering Plant Cost Index (ICEPC)" is added to adjust for inflation-related concerns (Mignard 2014). As reported by equipment manufacturers, the ICEPC values for 2001 and 2022 are 394.3 and 813.0, correspondingly.

All equipment's total capital cost is determined as follows:

$$C_{CC,2022} = \frac{C_{CC}.I_{CEPC,2022}}{I_{CEPC,2001}} \quad (6)$$

The "Capital Recovery Factor (C_{RF})" is computed as follows:

$$C_{RF} = \frac{i(1+i)^n}{(1+i)^n - 1} \quad (7)$$

Where (n) is the lifetime of the Regenerative ORC system, and (i) is the interest rate. Table 3 provides the specification of the economic parameter. The "Levelised Energy Cost (LEC)" is obtained as follows:

$$LEC = \frac{C_{RF}.C_{CC,2022} + C_{OM}}{T_{OM}.W_{net}} \quad (8)$$

Where T_{om} is the number of hours of operation in a year, and C_{OM} is the cost of operation and maintenance, which is calculated as 1.5% of $C_{CC,2022}$.

The definition of the "Static investment payback period (SIPP)" is as follows:

$$SIPP = \frac{C_{cc,2022} + C_{OM}}{I_r} \quad (9)$$

Where I_r revenue per hour from reclaiming waste heat for energy production is expressed as:

$$I_r = \eta_{System}.\dot{m}(h_{Wasteheat.in} - h_{Wasteheat.out}).C_{electricity} \quad (10)$$

The term "$C_{electricity}$" in the equation above stands for the price of electricity, which is assumed to be 0.1512 USD/kWh, and refers to the industrial pricing that the U.S. Energy Information Administration published for the year 2022 (U.S. Energy Information Administration 2022).

Table 2. The coefficient of capital cost estimation model (R. Turton, R.C. Bailie 2013).

Components	Y	K_1	K_2	K_3	F_{BM}	Units, Capacity
Condenser, Evaporator, and Recuperator (Fixed Tube)	$A_{eva}(m)^2$, Heat Transfer area	4.3247	-0.3030	0.1634	2.9	Area, m^2 (100-4000)
Turbine (Radial)	$W_{Turbine}(kW)$, Power capacity	2.476	1.4965	-0.1618	3.5	kW (100-1500)
Pump (Centrifugal)	$W_{pump}(kW)$, Power capacity	3.3892	0.0536	0.1538	2.8	kW (1-300)

2.5 Optimisation outline

The optimisation study using the NSGA II technique was started with four parameters- HT pressure ORC, LT pressure ORC, Massflow of ORC working fluids, and waste heat temperature. The maximum overall efficiency has always been observed at the optimal values (maximum and minimum of the given

range). Throughout the optimisation simulation, it has been ensured that the high-temperature pressure in the turbine inlet is consistently higher than the low-temperature pressure at the turbine outlet. The NSGA-II algorithm is based on Pareto dominance, which evaluates the quality of candidate solutions. NSGA-II generates a collection of Pareto-optimal solutions that reflect the balance between the optimised objectives. This study presents a comparative analysis between the outcomes of NSGA II with other Pareto-optimal solutions methods, namely TOPSIS, GRA, SAW, and MABAC (Wang and Rangaiah 2017) (Wang et al. 2020) (Wang et al. 2021). Table 4 provides the relevant NSGA-II parameters. Table 3 provides the relevant NSGA-II parameters.

Table 3: Specification of the parameters used in economic analysis.

Parameters	Value	Ref.
i	14 %	(Mosaffa et al. 2017)
n	15 Years	(Mosaffa et al. 2017)
Operation and Maintenance Cost	1.5%	(Mosaffa et al. 2017)
Operation hours	7300 h	(Mosaffa et al. 2017)

2.2.1 Objective Function

The regenerative ORC system's multi-objective optimisation (MOO) design problem is formulated. The primary objective of MOO research is to maximise energy efficiency (percentage) while decreasing Levelized energy costs (USD/kWh)$^{-1}$. The MOO optimisation problem is constructed such that the high side pressure of the turbine is always more significant than the low side pressure. In addition to the design space, the working fluid's massflow rate and the waste heat's temperature are included as optimisation parameters. The MOO issue is described as follows:

$$Max = \eta_{ex}, f\left(W_T, P_{in}, P_{out}, m_{ORC,}\right) \quad (11)$$

$$Min = LEC, f\left(W_T, P_{in}, P_{out}, m_{ORC,}\right) \quad (12)$$

Subject to:

$$\left(P_{in} > P_{out} \geq P_0\right)$$

737

There are two types of operational parameters; fixed parameters are constant throughout the study, while variable parameters can be modified within the set limitations to enhance the cycle performance. Referring to the WHR cycle in Figure 1, The general form of the objective function is expressed as follows: where waste heat temperature Input and the output pressure of turbine and massflow of the working fluid.

Table 4: NSGA II parameters used in the present study.

Parameter	Values
Population size	50
Number of generations	70
No. of objectives	2
No. of variables	4
Mutation type	Gaussian
Crossover type	Intermediate
Scale	0.1
Shrink	0.5

2.6 Modelling assumptions

The modelling assumption parameters are displayed in Table 5. Fixed and variable parameters are used in this work, and values for fixed parameters are carefully selected from the literature.

3 RESULTS AND DISCUSSION

According to the waste heat temperature shown in Table 1, the working fluids for this work have been chosen. Also, the waste heat temperature range is being optimised based on the waste heat range of each working fluid. The maximum temperature range for waste heat is 225 °C to 300 °C. This range includes benzene, Toluene, and Heptane. 200 °C to 275 °C is the medium waste heat temperature range. MM,

Cyclopentane, Pentane, and Hexane have been identified in this range. Butane (125 °C to 200 °C) has the lowest temperature range. After that, all the recommended working fluids were tested in the regenerative ORC system's subcritical range of turbine inlet and outlet pressure, where the inlet pressure is always greater than the outlet pressure. The working fluids massflow rate, which varies from 1 to 30 kg/s for each fluid, is another significant variable component. NSGA II is used to identify the most effective working fluid in various waste heat ranges based on these optimisation functions.
The Pareto frontiers for the outcomes of levelized energy costs and energy efficiency optimisation across working fluids using NSGA-II are displayed in Figure 2. For each working fluid, the best compromise solution was found by balancing the maximum energy efficiency and the minimum levelized energy cost. The Pareto frontier consisted of 3500 optimal ideal solutions for all working fluids. The economic weight is not necessarily equal to the thermodynamic weight due to practical requirements and choices. However, for this research, all working fluids have the same weight (0.5) for both objective functions.

Table 5: The accepted nominal parameters for the designed Regenerative ORC.

Operating parameter	Value/range	Unit
Fixed Design Parameter		
Exhaust gas composition	Air	-
Exhaust gas pressure	1	bar
Exhaust gas mass flow rate (Köse et al. 2020)	12	kg/s
Isentropic efficiency of the pump (DiPippo 2015)	85	%
Isentropic efficiency of the turbine (Gopal and Seshadri 2022)	85	%
Isentropic efficiency of the compressor (Hoque and Kumar 2021)	75	%
Pump input temperature	40	°C
Ambient temperature	35	°C
Pipes pressure drops (El Samad et al. 2020)	0	bar
Pinch temperature of condenser, recuperators, and heater (El Samad et al. 2020)	5	°C
Pressure drops in the heat exchanger, recuperators, and condenser (Wang et al. 2014)	1.5	bar
Variable Design Parameter		
Exhaust gas temperature (W_T)	125-300	°C
ORC Turbine inlet pressure (P_{in})	1- 40	bar
ORC Turbine outlet pressure (P_{out})	1- 40	bar
ORC Turbine inlet mass flow rate (m_{ORC})	1-30	kg/s

738

As mentioned, the waste heat's temperature determines which working fluid to use. So, using the multiple criteria decision-making (MCDM) technique with TOPSIS, GRA, and SAW, the best compromise solutions for Butane have been found as ordered pairs of values (exergy efficiency in percentage, LEC) of (34.86, 0.36) and the MABAC (34.39, 0.36) for the lowest temperature range. According to the results, TOPSIS, GRA, and SAW all provided the same value for Butane; therefore, this value is the strongest value accepted for the best compromise solutions.
Cyclopentane, Pentane, MM, and Hexane are chosen for the medium temperature range (200 - 275 °C) investigation. The best compromise solutions for MM, Pentane, and Hexane have been identified as ordered pairs of values (exergy efficiency in %, LEC) of (29.75, 0.43), (34.39, 0.36), and (35.28, 0.34), respectively, using the multiple criteria decision-making (MCDM) technique with TOPSIS, MABAC,

GRA, and SAW. The ordered pairs of values (exergy efficiency in %, LEC) for TOPSIS, MABAC, and SAW that represent the optimum compromise option for Cyclopentane is (28.79, 0.34) and the GRA result is (23.72, 0.41). Considering the findings, the value offered by TOPSIS, GRA, MABAC, and SAW for MM, Pentane, and Hexane is the most substantial value acknowledged for optimum compromise options. TOPSIS, MABAC, and SAW offered the best compromise solutions for Cyclopentane.

A higher waste heat temperature range (225–300 °C) has been used for this study. Heptane, Toluene, and Benzene are the hydrocarbons selected for this temperature range. Using the multiple criteria decision-making (MCDM) technique with TOPSIS, MABAC, GRA, and SAW, the best compromise solutions for Heptane, Toluene, and Benzene have been identified as ordered pairs of values (exergy efficiency in%, LEC) of (41.26, 0.32), (42.75, 0.29), and (41.33, 0.30), respectively. The value provided by TOPSIS, GRA, MABAC, and SAW for Heptane, Toluene, and benzene is the most critical value acknowledged for the best compromise options, according to the findings. Toluene has emerged as the best solution for higher temperatures regarding the best working fluid. Hexane is the best working fluid for medium temperature ranges, and Butane has the best solution for applications with the lowest waste heat temperature range.

Table 6 displays the ranking obtained from the SIPP calculation and the optimal values of the objective functions. The working fluid Butane requires 11650.98 hours of operation and maintenance and covers the capital cost of the Regenerative ORC based on the lowest range of waste heat temperature. Pentane has the shortest recovery time for waste heat temperatures in the middle range, 10837.29 hours. Other medium-range working fluids underperform, including hexane, mm, and cyclohexane. In the higher temperature range, Heptane has the shortest recovery time, 11578.54 hours, to recover the value of operation and maintenance and cover the capital cost, while Benzene and Toluene perform poorly because their SIPP values exceed 19987.7 hours.

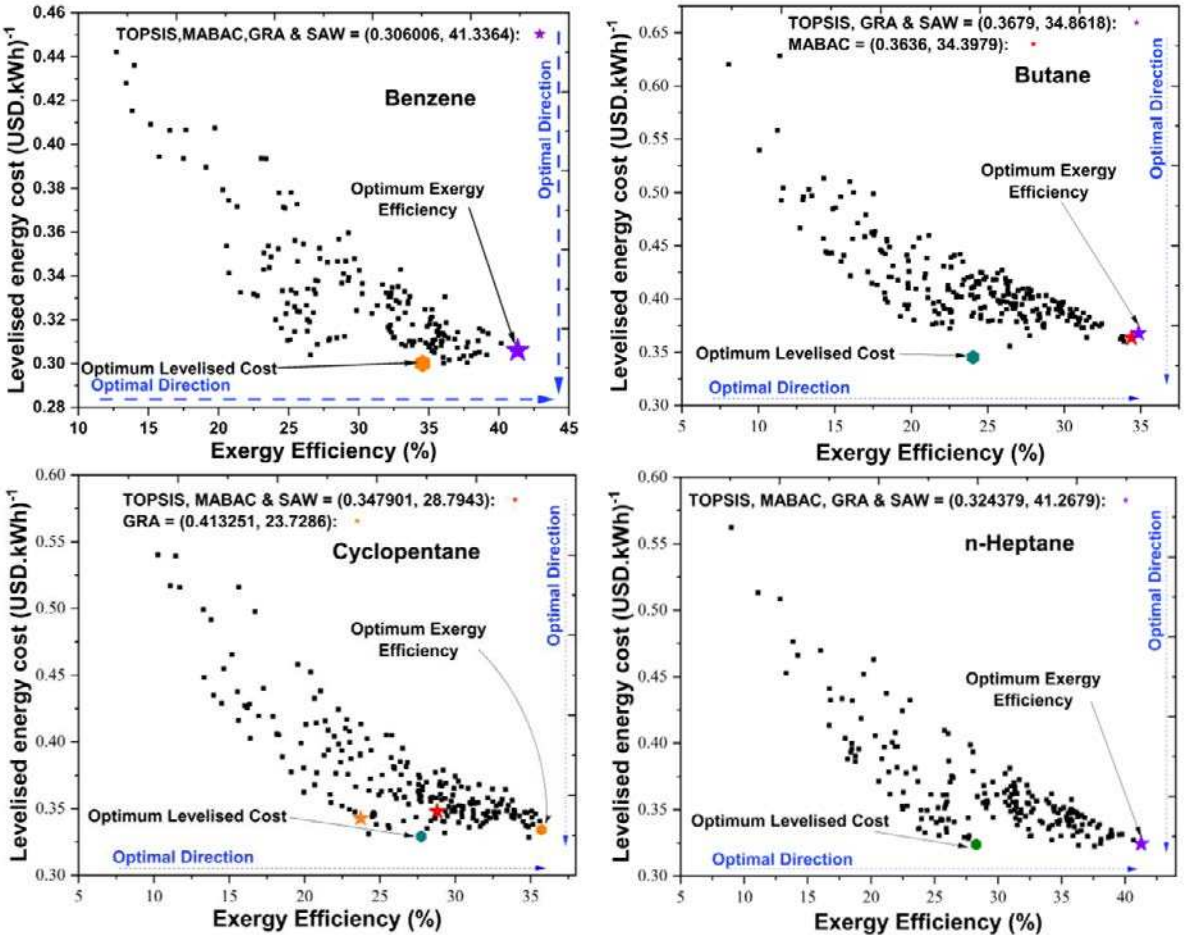

739

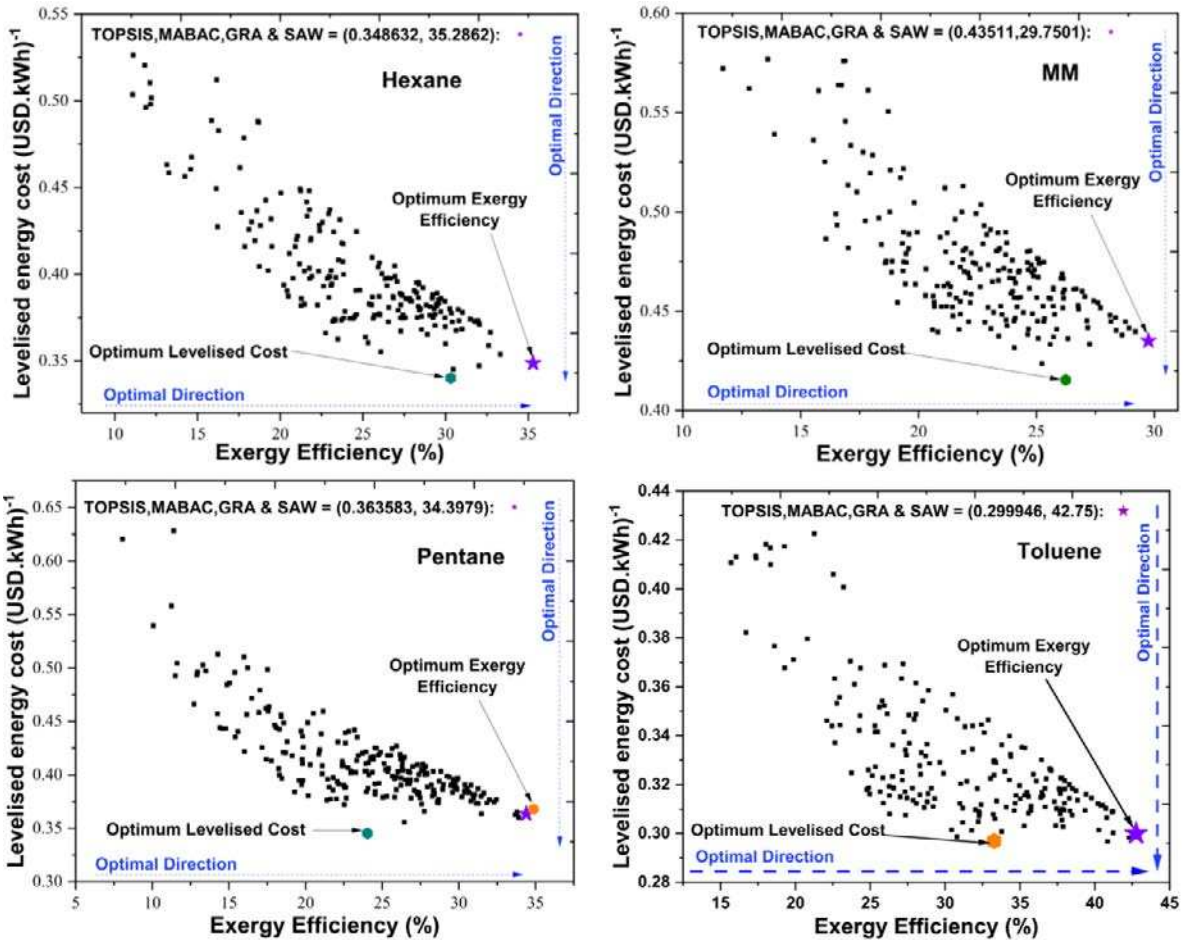

740

Figure 2: Optimal compromise solution on the Pareto frontiers of eight candidates: Benzene, Butane, Cyclopentane, Heptane, Hexane, MM, and Toluene.

Table 6: Optimum values of the objective function and SIPP ranking.

Working Fluid	Waste heat temperature range (T_w)	Waste heat temperature (°C)	Massflow rate (kg/s)	Pressure Turbine inlet (bar)	Pressure Turbine outlet (bar)	SIPP (hrs.)
Benzene	250-300	290.0	0.500	42.66	1.25	20879
Butane	125-200	226.0	0.763	39.66	3.76	11650
Cyclopentane	200-275	298.9	0.644	20.21	1.75	22184
Heptane	225-300	244.0	0.538	22.09	1.12	11578
Hexane	200-275	259.0	0.528	13.35	1.37	11837
HexMDiSiloxn (MM)	200-275	267.5	0.522	16.35	1.61	18250
Pentane	200-275	232.5	0.519	11.70	1.45	10837
Toluene	275-300	298.9	0.514	18.11	1.83	19987

4 CONCLUSIONS

This article examined a regenerative ORC cycle based on the distinctive properties of eight different working fluids. The Pareto frontier for all working fluids contained 3500 optimal ideal solutions using MOO. The best compromise options were found using the MCDM method using TOPSIS, GRA, and SAW. Waste heat temperature ranges are optimised for each working fluid. The maximum waste heat range is 225–300°C. Benzene, Toluene, and Heptane are included in this range. Medium waste heat temperatures are 200–275 °C. This range includes MM, Cyclopentane, Pentane, and Hexane. Butane (125–200°C) has the lowest temperature range. After completing the optimisation process,

Regenerative ORC with Toluene generated the highest exergy efficiency and LEC, 57.5% and 0.31, respectively. Using the multiple criteria decision-making (MCDM) technique with TOPSIS, MABAC, GRA, and SAW, the best compromise solutions for medium temperature range hexane have been identified as ordered pairs of values (exergy efficiency in%, LEC) of 35.28 and 0.34, respectively. Butane was found as values of (exergy efficiency in percentage, LEC) for the lowest temperature range for TOPSIS, GRA, and SAW (34.86, 0.36) and MABAC (34.39, 0.36). In the SIPP index, Pentane has the shortest recovery time for waste heat temperatures in the middle range, 10837.29 hours, compared to all other working fluids.

NOMENCLATURE

$\dot{m}$	mass flow rate	kg/s	s	entropy	kJ/kg K
h	enthalpy	kJ/kg	η	efficiency	
W	work	kW	P	pressure	bar
T	Waste heat	°C			

Subscript

0	reference/ambient	out	output
in	Input		

REFERENCES

DiPippo R (2015) Geothermal Power Plants: Principles, Applications, Case Studies and Environmental Impact: Fourth Edition

El Samad T, Teixeira JA, Oakey J (2020) Investigation of a radial turbine design for a utility-scale supercritical CO2 power cycle. Appl Sci 10:1–26. https://doi.org/10.3390/APP10124168

García-Afonso Ó, Delgado-Torres AM, González-Díaz B (2022) Potential of Organic Rankine Cycle for waste heat recovery from piston engine-based power plants in isolated power systems. Appl Therm Eng 203:117815. https://doi.org/https://doi.org/10.1016/j.applthermaleng.2021.117815

Gopal V V., Seshadri S (2022) Effect of cut-off and compression ratio on the isentropic efficiency during off-design and part-load operations of a Wankel rotary steam expander used for small scale cogeneration. Appl Therm Eng 207:118212. https://doi.org/10.1016/j.applthermaleng.2022.118212

Haq MZ (2021) Optimisation of an organic rankine cycle-based waste heat recovery system using a novel target-temperature-line approach. J Energy Resour Technol Trans ASME 143:1–12. https://doi.org/10.1115/1.4050261

Hoque SJ, Kumar P (2021) Analysis of a Dual Recuperated Dual Expansion Supercritical CO2 Cycle for Waste Heat Recovery Applications. Trans Indian Natl Acad Eng 6:439–459. https://doi.org/10.1007/s41403-021-00211-4

Köse Ö, Koç Y, Yağlı H (2020) Performance improvement of the bottoming steam Rankine cycle (SRC) and organic Rankine cycle (ORC) systems for a triple combined system using gas turbine (GT) as topping cycle. Energy Convers Manag 211:112745. https://doi.org/10.1016/j.enconman.2020.112745

Krishna B, Basab S (2016) Utilisation of low-grade waste heat-to-e.nergy technologies and policy in Indian industrial sector : a review. Clean Technol Environ Policy. https://doi.org/10.1007/s10098-016-1248-2

Mignard D (2014) Correlating the chemical engineering plant cost index with macro-economic indicators. Chem Eng Res Des 92:285–294. https://doi.org/10.1016/j.cherd.2013.07.022

Mosaffa AH, Mokarram NH, Farshi LG (2017) Thermo-economic analysis of combined different ORCs geothermal power plants and LNG cold energy. Geothermics 65:113–125. https://doi.org/10.1016/j.geothermics.2016.09.004

R. Turton, R.C. Bailie WBW and JAS (2013) Analysis, synthesis, and design of chemical processes

Saha BK, Chakraborty B, Pundeer P (2019) Thermodynamic and thermo economic analysis of organic rankine cycle with multi-objective optimisation for working fluid selection with low- temperature waste sources in the Indian industry. 5th Int Semin ORC Power Syst 5–12

U.S. Energy Information Administration (2022) Analysis & Projections. Price summary (historical and forecast). In: U.S. Energy Inf. Adm. https://www.eia.gov/analysis/. Accessed 5 Apr 2023

van Kleef LMT, Oyewunmi OA, Markides CN (2019) Multi-objective thermo-economic Optimisation of organic Rankine cycle (ORC) power systems in waste-heat recovery applications using computer-aided molecular design techniques. Appl Energy 251:112513. https://doi.org/10.1016/j.apenergy.2019.01.071

Wang X, Liu X, Zhang C (2014) Parametric optimisation and range analysis of Organic Rankine Cycle for binary-cycle geothermal plant. Energy Convers Manag 80:256–265. https://doi.org/10.1016/j.enconman.2014.01.026

Wang Z, Parhi SS, Rangaiah GP, Jana AK (2020) Analysis of weighting and selection methods for pareto-optimal solutions of multi-objective optimisation in chemical engineering applications. Ind Eng Chem Res 59:14850–14867. https://doi.org/10.1021/acs.iecr.0c00969

Wang Z, Rangaiah GP (2017) Application and Analysis of Methods for Selecting an Optimal Solution from the Pareto-Optimal Front obtained by Multi-objective Optimization. Ind Eng Chem Res 56:560–574. https://doi.org/10.1021/acs.iecr.6b03453

Wang Z, Rangaiah GP, Wang X (2021) Preference Ranking on the Basis of Ideal-Average Distance Method for Multi-Criteria Decision-Making. Ind Eng Chem Res 60:11216–11230. https://doi.org/10.1021/acs.iecr.1c01413

Zhang Z, Zhang X, Bai H, et al (2018) Multi-objective Optimisation and fast decision-making method for working fluid selection in organic Rankine cycle with low-temperature waste heat source in industry. Energy Convers Manag 172:200–211. https://doi.org/10.1016/j.enconman.2018.07.021

742

ACKNOWLEDGEMENT

The authors acknowledge the Department of Science and Technology, Government of India, for financial support vide sanction order(s): TMD/CERI/CSP/2020/1(G) dated 21–09–2020, and TMD/CERI/Clean Coal/2017/034 (IISc) (G) dated 13–09–2018. The CSR grants for FY-22-23 from Triveni Turbines Limited, Tata Consulting Engineers (TCE), and Ansys Software Pvt. Ltd., Bangalore, and valuable inputs in carrying out this work, are also gratefully acknowledged.

The authors acknowledge the financial support received from the Science and Engineering Research Board, GoI, under The SERB-National Post-Doctoral Fellowship (N-PDF) Fellowship towards support the current research Department of Science and Technology, Government of India for financial support vide sanction order(s): PDF/2021/002268 dated 12–01–2022.

The present piece of work is dedicated to the memory of Sidharth Sankar Parhi, who unfortunately passed away during the Covid pandemic. During the process of conception, he played an active role as a member of this work.

ORC SEVILLE 2023
7th International Seminar on O.R.C. Power Systems

© 2024 Editorial Universidad de Sevilla. Este es un artículo de acceso abierto distribuido bajo los términos de la licencia de uso y distribución Creative Commons (BY-NC-ND 4.0)

DOI: https://dx.doi.org/10.12795/9788447227457_139

DUAL CONDENSING PRESSURE ORC FOR CRYOGENIC ENERGY STORAGE

William M. Conlon, Jr.[1,*], Milton J. Venetos[1]

[1] *Pintail Power LLC. 2330 Bryant Street; Palo Alto, CA 94301 USA*

*Corresponding Author: bill.conlon@pintailpower.com

ABSTRACT

A liquid air combined cycle (LACC) is a hybrid energy storage system that uses cryogenic air as a storage medium. Discharge of stored energy involves the pressurization and re-gasification of the stored liquid air, sensible heating of gaseous air, and expansion of the air through a turbine that discharges to atmosphere. During discharge of stored energy, an Organic Rankine Cycle (ORC) operates as a bottoming cycle drawing low-temperature heat from the gas turbine exhaust and using the cryogenic liquid as a heat sink. The quantity of low-grade heat that can be extracted from gas turbine exhaust is constrained by the amount of heat that must be rejected from the ORC. The overall efficiency of the LACC is the net power output divided by the energy inputs, which are the electricity used to cryogenically liquefy air during charging and the fuel consumed by the gas turbine during discharging. Power output can be increased by maximizing the heat input to the ORC, potentially including the water of combustion. To relieve the constraint imposed by the limited availability of cryogenic liquid air and to maximize the heat input and power output, a novel dual condensing pressure cycle is described. The cycle includes both high and intermediate pressure turbines, with one condenser operating at intermediate pressure and the second operating at a low pressure. A fraction of the ORC working fluid is extracted at intermediate pressure and cooled by heating regasifed air. The remainder of the working fluid expands through the intermediate pressure turbine and condenses at low pressure using the cryogenic liquid air as a low temperature heat sink. The low-pressure liquid is pumped to intermediate pressure and used to directly condense the cooled fraction, whereupon the mixture is recuperated and then heated by gas turbine exhaust.

1 INTRODUCTION

As the world transitions to zero-carbon energy systems, large-scale energy storage is expected to be needed to time-shift renewable energy on daily, weekly, and seasonal timeframes. Long duration energy storage (LDES) will be required to enable grid decarbonization via intermittent renewable resources, such as solar and wind generation. Sepulveda et al. (2021) identified key techno-economic characteristics of LDES for a zero-carbon power grid.

- Systems with storage durations greater than one hundred hours have the greatest impact on electricity cost.
- Energy storage capacity cost must be less than $20/kWh to be cost-effective and must be less than $1/kWh to fully displace other low-carbon technologies, such as hydrogen fueled gas turbines or carbon capture. Energy storage capacity cost reflects the cost of storage medium and container, exclusive of the charging and discharging equipment.
- High discharge efficiency (kWh-discharge per kWh-charge) is equally important.
- The cost of charge and discharge capacity and the charge efficiency play secondary roles.

Pumped Storage Hydro (PSH) represents most of the existing installed base of energy storage on both a power (MW) and energy (MWh) basis. Most PSH systems are designed for diurnal operation coupled with baseload generation, i.e., charging with off-peak power when load is low to later supply on-peak

power, rather than for LDES. Electrochemical batteries (ECB), especially Lithium-based, are increasingly being deployed to provide peaking power and ancillary services, such as frequency regulation. According to Viswanathan et al. (2022), for a 1000MW x 100-hour energy storage system built in 2030, the energy storage capacity cost is $53.0/kWh for a PSH reservoir and in the range between $80.30/kWh and $100.04/kWh for a Lithium-ion DC storage block.

Alternatives to PSH and ECB are needed to meet the techno-economic requirements of LDES identified by Sepulveda et al. (2021). Since it is freely available and can be compressed or liquefied to high energy storage density, air can potentially meet the energy storage capacity cost requirement, depending on the capital cost of the storage reservoir.

Compressed Air Energy Storage (CAES) requires large underground caverns, so like PSH, has geological and geographical limitations. Cavern costs for CAES have been estimated in the range of $2.8/kWh to $13.8/kWh according to Viswanathan et al. (2022). The two commercial CAES projects are both hybrid systems (non-adiabatic), using fuel to provide heat energy for discharge.

Vecchi et al. (2021) undertook a literature search and comparison of Liquid Air Energy Storage (LAES), dividing the technical approaches into:

- Standalone LAES, shown in Figure 1a, wherein the primary energy input and output is electricity, with some waste heat rejection.
- Hybrid LAES, shown in Figure 1b, wherein additional energy supplements the electricity. The supplemental energy input could be used for additional heating of the air, as in the hybrid CAES system, or may be waste cold from an LNG regasification process.

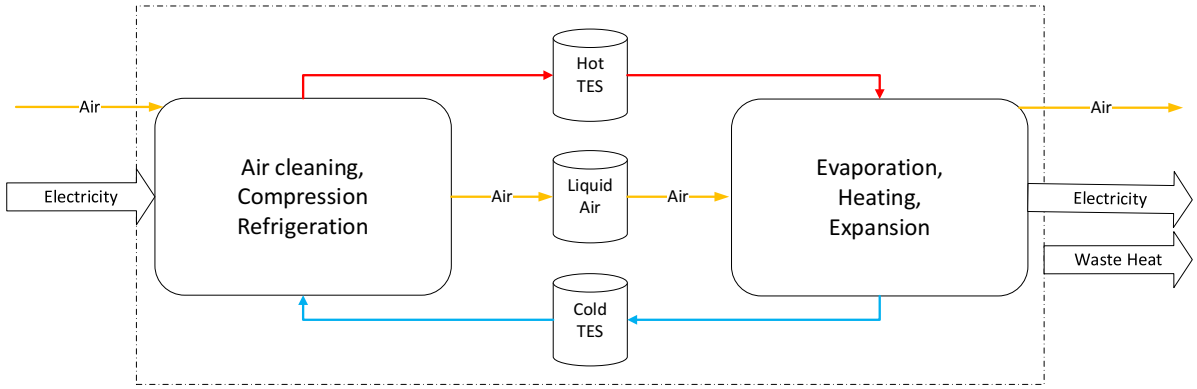

Figure 1a: Standalone LAES process, adapted from Vecchi et al. (2021).

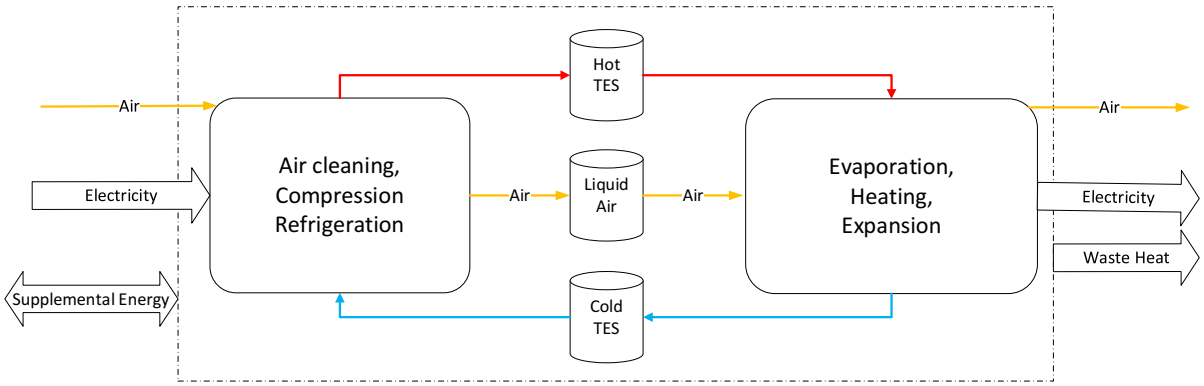

Figure 1b: Hybrid LAES processes adapted from Vecchi et al. (2021).

A notable aspect of these LAES approaches is the use of hot and cold thermal energy storage (TES) units in addition to cryogenic liquid air storage. The hot TES captures heat of compression during charging to be used for air heating during discharging. The cold TES is cooled by the liquid air during

discharge with the cold recycled to the cryogenic refrigerator to reduce the energy intensity of the charging process.

Vecchi et al. (2021) report the liquefaction work ranged from 0.2 to 0.3 kWh/kg using cold recycle to produce liquid air at atmospheric pressure, compared to 0.32 to 0.33 kWh/kg without cold recycle. Liquefaction work could be reduced to 0.163 kWh/kg if the liquid air were pressurized (and stored at higher temperature), but that would lose economy of scale due to the need for multiple smaller diameter pressure vessels compared to a single atmospheric pressure storage tank. Strahan (2013) provide a more conservative estimate for liquefaction work without cold recycle using the best available technology as 0.439 kWh/kg.

Vecchi et al. (2021) also reported the discharge performance of standalone LAES as specific work output in the range of 333 to 552 kJ/kg, which is equivalent to specific discharge air consumption (SDAC) of 10.8 to 6.5 kg/kWh. They report that LAES discharge cycles operating at higher pressure have lower SDAC, but also less cold recycle available to reduce the liquefaction work.

Focusing on atmospheric pressure storage, and associating the higher SDAC with the lower liquefaction work, the ratio of charge to discharge energy is in the range of 2.16 kWh/kWh (0.2 kWh/kg x 10.8 kg/kWh) to 1.95 kWh/kWh (0.3 kWh/kg x 6.5 kg/kWh), which is an electrical round-trip efficiency of 46.3% to 51.3%. Using a charging cost of $0.042/kWh as assumed by Lazard (2021), the marginal cost of discharge electricity would range from $0.091/kWh to $0.082/kWh.

Salazar and Bulte (2022) estimated that a 200,000 m^3 atmospheric pressure cryogenic storage tank would cost $72.3 million. Liquid air density is 878.4 kg/m^3, so a full tank would contain 175.7 million kg of liquid air. Based on the above SDAC, a standalone LAES system could discharge between 16.3 and 27.0 million kWh of electricity, corresponding to an energy storage capacity cost between $4.44/kWh and $2.68/kWh, respectively.

745

The hybrid LAES concepts surveyed by Vecchi et al. (2021) featured coupling to external processes but retained the use of cold recycle. Of pertinent interest are those coupled to upstream combustion, where the specific work output was reported to exceed 900 kJ/kg (SDAC of 4 kg/kWh). The reduction of SDAC increases the energy capacity of the storage tank to 43.9 million kWh with a corresponding reduction of energy storage capacity cost to $1.65/kWh.

Vecchi et al. (2021) also note that the round-trip efficiency of hybrid LAES can exceed 100%. N.B., round trip efficiency is defined as the electrical energy output per electrical energy input and is distinct from the thermodynamic efficiency that accounts for all energy inputs. Efficiency greater than 100% is often confusing, so in its Performance Test Code for Energy Storage Systems (PTC-53), ASME adopted the term primary energy rate, analogous to fuel heat rate, which is the ratio of electrical energy input to electrical energy output, i.e., the inverse of round-trip efficiency.

2 HYBRID LIQUID AIR COMBINED CYCLE

Conlon et al. (2022) described a hybrid LAES system called the Liquid Air Combined Cycle (LACC), illustrated in Figure 2, using gas turbine exhaust heat for driving the discharge process. To reduce complexity and capital cost, the LACC approach eliminates the intermediate cold and hot TES, so only liquid air is used for storage. Without cold recycle, the charging energy consumption is increased, but the SDAC is reduced so the overall charge energy and charge cost is less than systems with cold recycle. Decoupling the charging and discharging processes also simplifies startup and off-design operation, since pre-charging a cold store is not needed to begin producing liquid air.

The LACC uses any type of cryogenic refrigeration process (1) to produce liquid air to charge the liquid air storage tank (2). During discharge, the liquid air is pressurized (3) and heated by the condensing ORC working fluid (4), heated by low-pressure working fluid exhausted by the ORC turbine (5), and further heated by gas turbine exhaust (6). The condensed working fluid is pressurized (11), recuperated (12) and warmed by cooling the gas turbine inlet air (13), and then absorbs gas turbine exhaust heat (14) before expansion (15) to produce power. Fuel powers the gas turbine (9), whose exhaust heat (10) drives the discharge process. Ethane was selected as the working fluid because of its low freezing point, positive pressure at the condensing temperature (about -80°C) to avoid air ingress, and its environmental characteristics in the event of a leak, with nil Ozone Depletion Potential and moderate Global Warming Potential.

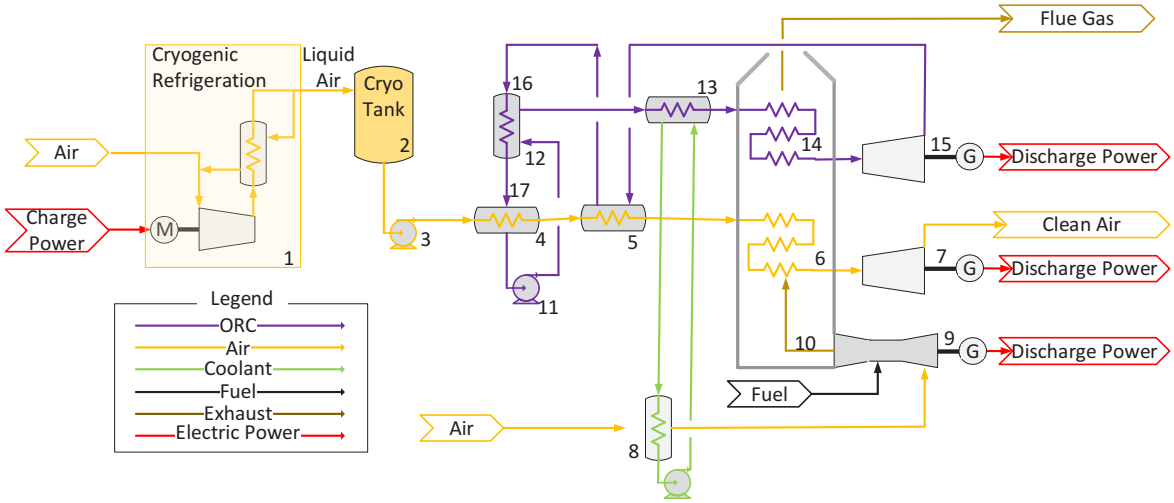

Figure 2: Liquid Air Combined Cycle from Conlon et al. (2022).

746

The discharge performance was modeled using Ebsilon Professional version 15.03. LACC operating conditions were selected based on a techno-economic analysis that included thousands of cases (Rimpel and Conlon 2023). With a Siemens SGT-800 gas turbine, Conlon et al. (2022) reported net power of 116984 kW at an SDAC of 2.32 kg/kWh, which corresponds to 75.7 million kWh of storage in a 200000 m^3 tank, and an energy storage capacity cost of $0.95/kWh. This is below the $1/kWh threshold identified by Sepulveda et al. (2021) for LDES to displace other dispatchable generation.

The relatively high charge energy of LACC without cold recycle is offset by the lower SDAC, so the charge to discharge energy ratio is 1.02 kWh/kWh (0.439[1] kWh/kg x 2.32 kg/kWh), which is approximately 98% round-trip efficiency. By reducing liquid air use, the charging cost is reduced to about $0.043/kWh, substantially less than the systems with cold recycle. On the other hand, the LACC combusts fuel at net heat rate of 5041 kJ/kWh (HHV). Assuming a fuel cost of $7.03/GJ ($1.00/kg of hydrogen, which is the target of the U.S. Department Hydrogen Shot[2]), an additional $0.035/kWh would be added to the cost of discharge energy, bringing the marginal cost of discharge energy to $0.078/kWh, less than the standalone LAES systems with cold recycle.

Except for the ORC, the LACC is largely comprised of commercially available equipment. As shown in Table 1, the ORC operates at significantly lower temperatures and higher pressures than is typical for ORC power cycles. Accordingly, both the pump and the turbine require development.

[1] The more conservative estimate from Strahan (2013) is used.
[2] https://www.energy.gov/eere/fuelcells/hydrogen-shot accessed 25 April 2023

Table 1: ORC turbine conditions for LACC of Figure 2

Parameter	Turbine
Isentropic Efficiency	0.88
Shaft Power	17873 kW
Mass Flow	44.75 kg/s
Inlet Volume Flow (ACMH)	2057 m^3/h
Inlet Pressure	127.4 bar
Inlet Temperature	335°C
Exit Pressure	4.5 bar
Exit Temperature	165°C
Exit Volume Flow (ACMH)	42977 m^3/h
Condensing Temperature	-73.9°C

Pryor et al. (2022) evaluated axial and radial turbomachinery for LACC and concluded that either an axial (8- or 9-stage) or radial (four stages at two shaft speeds) turbine would be capable of handling the pressure ratios. The axial expander is expected to have somewhat higher efficiency and reduced complexity.

3 ORGANIC RANKINE CYCLE

Pryor et al. (2023) describe a development and demonstration program at pilot (about one-tenth) scale, which would be followed by full-scale development and demonstration. This approach would entail the serial development and testing of new turbomachinery at both pilot and full-scale with the attendant expenses, risks, and timelines.

This paper investigates an accelerated commercialization path that foregoes development of custom turbomachinery in favor of commercially available Generator Loaded Expanders (GLX). GLX units couple a radial turbo-expander to a generator, typically via a speed reducing gearbox, are available from a range of manufacturers and are marketed for applications such as Air Separation Units and natural gas liquefaction where they improve efficiency compared to Joule-Kelvin valves. In the LACC application, two GLX units would be operated in series as suggested by Pryor et al. (2022).

One vendor's commercially available radial GLX specifies maximum inlet pressure of 206 bar_g and maximum turbine inlet temperature of 260°C. The maximum volumetric flow rate is 10000 m^3/h for a 10000 kW expander and 16000 m^3/h for a 14000 kW expander. The vendor suggested 80% isentropic efficiency for modeling purposes.

The lower turbine efficiency compared to Table 1 impacts cycle design by reducing power output and increasing the quantity of heat rejected from the ORC to the cryogenic air. To accommodate the lower ORC turbine efficiency in the cycle of Figure 2, liquid air flow rate could be increased to provide more cooling or ORC working fluid flow rate could be reduced. An aftercooler could also be employed to reject heat from the ORC turbine exhaust in order to maintain the heat balance. Each of these approaches would increase SDAC.

Another approach was proposed by Conlon (2022), wherein a fraction of the working fluid is extracted from the exhaust of a high pressure (HP) turbine, used to heat the regasified air and then condensed at an intermediate pressure (IP). The balance of the working fluid continues to an IP turbine to produce additional power and is then condensed at low temperature using the liquid air as the heat sink.

In the arrangement shown in Figure 3, liquid air is pressurized and regasified by absorbing the latent heat of condensation from working fluid exhausted from the IP turbine. The air is then heated by the

coolant used to chill the gas turbine inlet air and by the working fluid fraction extracted between the HP and IP turbines, before being heated by the gas turbine's exhaust.

Turning to the ORC, refer to the corresponding numerals on the simplified process flow diagram of Figure 3 and the Temperature-entropy (Ts) diagram of Figure 4. The low-pressure ORC working fluid is desuperheated, condensed, and subcooled (1) by the liquid air. The fluid is pumped to intermediate pressure (2) and flows to the IP condenser, where it desuperheats and condenses the fraction exiting the IP Cooler (10). Subcooled liquid (3) from the IP Condenser is then pumped to high pressure (4), heated in the recuperator (5), and further heated by exhaust gas (6) to be expanded to intermediate pressure (7) by the HP turbine. Approximately 30% of the working fluid exhausted from the HP turbine is sent to the IP Cooler with the balance expanded to low pressure by the IP turbine (8). This larger fraction of working fluid is cooled (9) in the recuperator and then flows to the LP Condenser, completing the cycle.

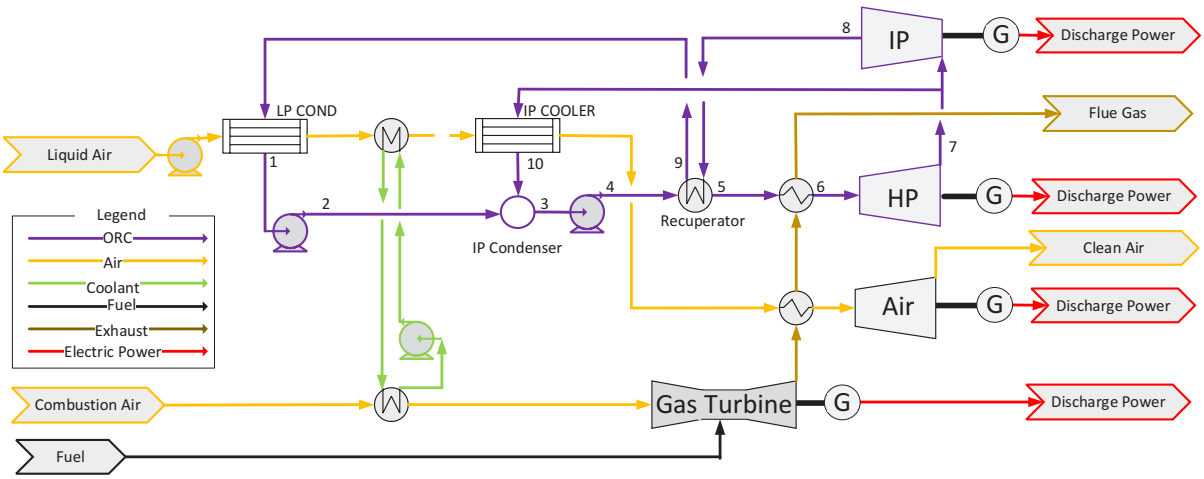

Figure 3: Dual Condensing Pressure ORC for LACC

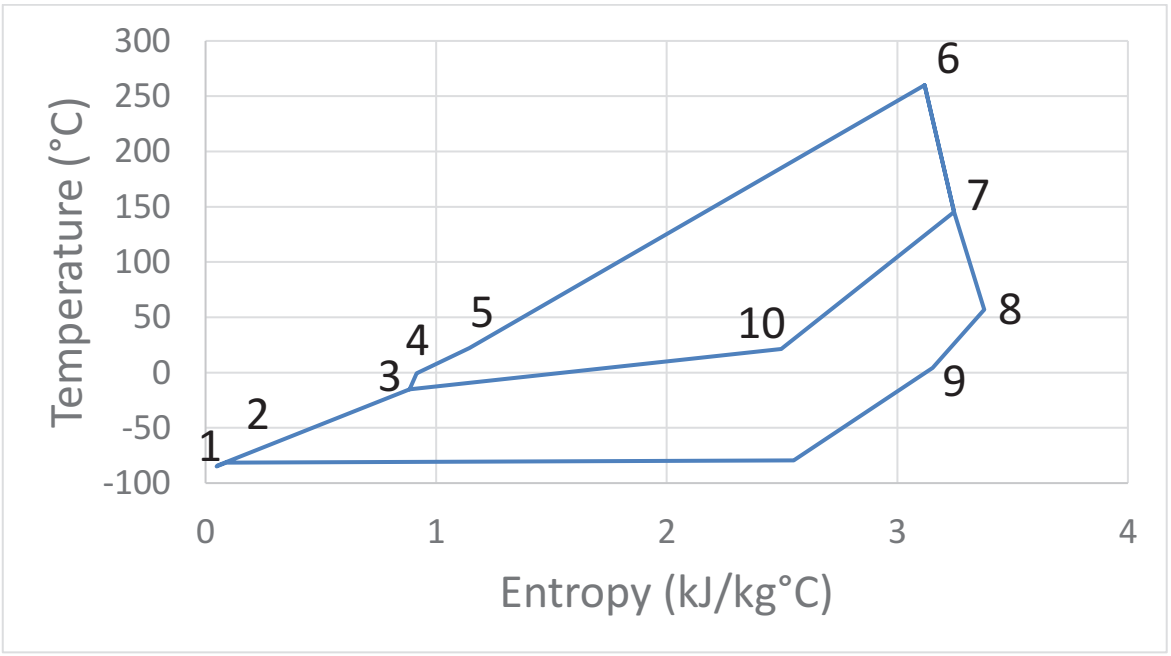

Figure 4: Temperature-entropy diagram for Dual Condensing Pressure ORC

The system was modeled using Ebsilon Professional version 15.03, with similar equipment assumptions as the LACC of Figure 2. However, it was necessary to increase the flue gas exit temperature by about 18°C to reduce the heat input into the ORC and balance the available cooling. On the other hand, the ORC condensing pressure was reduced by moving the air heater to the intermediate pressure loop.

Table 2 compares the performance of the LACC of Figures 2 and 3 at the same ambient, gas turbine, and air turbine conditions. For the dual condensing pressure system of Figure 3, the net power output is about 3.3% less due to lower ORC output, which causes the fuel heat rate to increase by 2.6%, and the SDAC by about 3.4%. The marginal cost of energy, using the same cost assumption, increases 2.6%. Notably, the cycle analyses used the same liquid air flow rate and air turbine inlet conditions, which may not be optimal for the dual condensing pressure cycle.

Table 2: ORC performance comparison Single (Fig. 2) vs. Dual Condensing Pressure (Fig. 3)

Parameter	Single Pressure	Dual Pressure
Net Power (kW)	116984	113148
HHV Net Fuel Heat Rate (kJ/kWh)	5041	5172
SDAC (kg/kWh)	2.32	2.4
Flue gas temperature (°C)	49	67
ORC Condensing Pressure (bar)	2.1	1.58
ORC shaft power (kW)	17919	14819
Marginal cost of energy ($/kWh)	0.078	0.081

The operating conditions for the HP and IP turbines in the dual condensing pressure system of Figure 3 are shown in Table 3. The pressure ratios for the HP and IP turbines were 9.2:1 and 8.6:1, respectively, each with assumed 80% isentropic efficiency. Total shaft power from the two turbines is 14819 kW, 3100 kW less than the higher efficiency turbine in Table 1. Importantly, all parameters were within the range of the vendor's commercially available GTX units.

749

Table 3: ORC turbine conditions for Dual Condensing Pressure LACC of Figure 3

Parameter	HP Turbine	IP Turbine
Isentropic Efficiency	0.80	0.80
Shaft Power	9495 kW	5324 kW
Mass Flow	46 kg/s	32 kg/s
Inlet Volume Flow (ACMH)	1350 m^3/h	7071 m^3/h
Inlet Pressure	165 bar	18 bar
Inlet Temperature	260°C	145°C
Exit Pressure	18 bar	2.1 bar
Exit Temperature	149.8°C	57.0°C
Exit Volume Flow (ACMH)	10165 m^3/h	49202 m^3/h
Condensing Temperature	-12.0	-79.9 °C

4 CONCLUSIONS

This paper has described an alternative Organic Rankine Cycle for use in Liquid Air Combined Cycle energy storage systems. The objective is to avoid the cost, time, and risk of developing custom turbomachinery by employing commercially available Generator Loaded Expanders. To accommodate power, pressure, temperature, and flow rate specifications, and a reduced isentropic efficiency, the ORC

has been modified to extract a working fluid fraction at intermediate pressure, where it is used for heating regasified air prior to condensation by mixing with sub-cooled working fluid.

The overall performance impact is modest (about 3%), despite a substantial (about 17%) reduction in the ORC turbine power output and an 8% reduction in its isentropic efficiency. Cycle optimization may improve performance, but the isentropic efficiency of the ORC turbines is clearly the most important performance factor.

From a commercial perspective, the dual condensing pressure ORC provides a means to employ proven turbomachinery and pumps and thereby increase the Technology Readiness Level of LACC.

REFERENCES

Conlon, W.M., 2022, "Cryogenic Combined Cycle Power Plant," European Patent EP 3566013.

Conlon, WM, Venetos, M, & Rimpel, A., 2022, "Liquid Air Combined Cycle." Proceedings of the ASME Turbo Expo 2022: Turbomachinery Technical Conference and Exposition. Volume 4: Cycle Innovations; Cycle Innovations: Energy Storage. Rotterdam, Netherlands. June 13–17, 2022. V004T07A001. ASME. https://doi.org/10.1115/GT2022-80426

Lazard, 2021, Lazard's Levelized Cost of Storage – v7.0. Page 14. December 2021. https://www.lazard.com/media/42dnsswd/lazards-levelized-cost-of-storage-version-70-vf.pdf

Pryor, O, Rimpel, A, & Conlon, W., 2022 "Organic Rankine Cycle Turbine and Heat Exchanger Sizing for Liquid Air Combined Cycle." Proceedings of the ASME Turbo Expo 2022: Turbomachinery Technical Conference and Exposition. Volume 4: Cycle Innovations; Cycle Innovations: Energy Storage. Rotterdam, Netherlands. June 13–17, 2022. V004T07A005. ASME. https://doi.org/10.1115/GT2022-82263

Pryor, O. M., Conlon, W. M., Rimpel, A. M., Venetos, M. J., 2023, "Design and Modeling of a Demonstration-scale ORC Cycle for the Liquid Air Combined Cycle." 7th International Seminar on ORC Power Systems. Seville, Spain, September 2023.

Rimpel, A., Conlon, W.M., 2023, "Liquid Air Combined Cycle™ for Power and Storage." Final Report U.S. Department of Energy Award No. DE-FE0032002, May 2023.

Salazar, T., Bulte, A, 2022, "Liquid Air Combined Cycle – Air Liquefaction Study Report". Report received from John Wood Group, PLC as part of project DE-FE-0032002, 2022

Sepulveda, N.A., Jenkins, J.D., Edington, A. *et al.* 2021, The design space for long-duration energy storage in decarbonized power systems. *Nat Energy* **6**, 506–516 (2021). https://doi.org/10.1038/s41560-021-00796-8.

Strahan, D. (editor), 2013, "Liquid Air in the Energy and transport systems." The Center for Low Carbon Futures.

Vecchi, A., Li, Y., Ding, Y., Mancarella, P., Sciacovelli, A., 2021, Liquid air energy storage (LAES): A review on technology state-of-the-art, integration pathways and future perspectives, *Advance in Applied Energy*, vol. 3, https://doi.org/10.1016/j.adapen.2021.100047

Viswanathan, V., Mongird, K., Franks, R., Li, X., Sprenkle, V., Baxter, R., "2022 Grid Energy Storage Technology Cost and Performance Assessment." 2022, Technical Report PNNL-33283, August 2022. https://www.pnnl.gov/sites/default/files/media/file/ESGC%20Cost%20Performance%20Report%202022%20PNNL-33283.pdf

ORC SEVILLE 2023
7th International Seminar on O.R.C. Power Systems

© 2024 Editorial Universidad de Sevilla. Este es un artículo de acceso abierto distribuido bajo los términos de la licencia de uso y distribución Creative Commons (BY-NC-ND 4.0)

DOI: https://dx.doi.org/10.12795/9788447227457_141

OPTIMUM COUPLING OF THERMAL ENERGY STORAGE AND POWER CYCLES FOR CARNOT BATTERIES

Salvatore Guccione[1,*], Rafael Guedez[1]

[1] *KTH Royal Institute of Technology, Brinellvägen 68, 100 44, Stockholm, Sweden*

*Corresponding Author: guccione@kth.se

ABSTRACT

To enable the widespread exploitation of intermittent, low-cost, and non-dispatchable renewable energy technologies, energy storage plays a key role in providing the required flexibility. In the spectrum of energy storage systems, one out of a few geographically independent possibilities is the storage of electricity into heat, so-called Carnot batteries. For thermal-to-electricity reconversion, depending on the operating energy storage temperatures, conventional or advanced power cycles can be integrated into the system, yielding different techno-economic performances. This work proposes a methodology that enables decision-making in selecting the adequate power cycle and Thermal Energy Storage (TES) type for a wide range of operating temperatures between 200 and 800 °C. To select the optimum coupling of TES and power block, a techno-economic optimization has been conducted aimed at minimizing the Levelized Cost of Storage (LCOS) for different plant capacities and charging costs. The study explores various power block configurations, including Organic Rankine Cycle (ORC), steam Rankine cycle, and supercritical CO_2 (sCO_2) Brayton cycle. Additionally, it evaluates different TES options such as molten salt, particle, and air packed bed TES. Results highlight that, for a charging cost of 50 EUR/MWh, the most cost-effective combination of TES and power block involves sCO_2 power blocks with recompression and intercooling, along with particle-based TES operating at temperatures between 600 to 800 °C and a temperature difference of 200 °C. ORCs are suitable for low temperatures (up to 350 °C) and high temperature differences, while the steam Rankine cycle is considered optimal between the low-temperature and the sCO_2 preferred regions. Air-packed bed TES is suggested as a viable option when TES represents a large share of the capital cost, with low charging costs, low hot temperatures, or low temperature differences. Molten salt TES is ideal when its design temperatures align with the operating limitations of the salts. Particle-based TES is the most cost-effective choice across a wide range of temperatures, at small (10 MW) and large scales (100 and 200 MW).

1 INTRODUCTION

To address the growing need for flexibility, cost-effectiveness, and efficiency in storing energy from fluctuating renewable sources, the utilization of energy storage systems has become crucial. Among the viable options, Carnot batteries have emerged as a cost-effective solution. During the charging phase, electricity is transformed into thermal energy and stored. Subsequently, during the discharging process, the stored heat is converted back into electricity. This approach enables the balancing of energy supply and demand while ensuring a reliable and secure energy supply (Benato & Stoppato, 2018). Previous studies have examined the technologies and configurations of Carnot batteries, along with performance metrics and experimental prototypes (Vecchi et al., 2022). Studies have examined technical barriers and selection criteria for key components of Carnot batteries for specific applications (Liang et al., 2022). At the system level, several techno-economic studies have been conducted to optimize both round-trip efficiency and financial metrics for two groups of Carnot batteries: Rankine-based (Hu et al., 2021) and Brayton-based (Albert et al., 2022). Rankine-based configurations include water steam Rankine cycles, trans-critical CO2 Rankine cycles (Morandin et al., 2012), and organic Rankine cycles (Frate et al., 2020). Brayton cycles with sCO_2 are considered a promising candidate due to their high thermal efficiency for heat sources above 350 °C, simple and compact physical footprint, and good operational flexibility to deal with uncertain renewable energy source availability (White et al., 2021). The potential of sCO_2 has been confirmed by the increase in research activity and international financial support for technological development over the last decade. Carnot batteries store energy using sensible heat, which can be in the form of liquids (Laughlin, 2017) or solid like molten salts and rocks. However, the working

temperature range of molten salts is limited due to the high melting temperature of 240 °C and the chemical decomposition limit of 580 °C (D'Aguanno et al., 2018), making them challenging to use for high-temperature applications beyond 600 °C, and requiring costly maintenance. Particle-based thermal energy storage technology provides notable advantages over traditional systems, as it can maintain stability even at high temperatures up to 1200 °C, is resistant to corrosion, utilizes low-cost materials, and allows for cycle selection and optimization due to its broad temperature range (Ma, 2020). Packed bed systems store energy by heating and cooling solid particles through a heat transfer fluid that passes through the bed (Hänchen et al., 2011). Air is a promising heat transfer fluid due to its low cost, safety, availability, and direct heat transfer capabilities with the storage material. Alumina Energy has proposed a system that uses low-cost, high-temperature stable particles to store and recover thermal energy up to 1600 °C (Al-Azawii et al., 2021). Despite previous investigations into storage technologies and power cycles at the component and system levels for specific applications, a literature gap still exists in the form of a comprehensive study that compares the various combinations of these technologies. There is a lack of a comprehensive analysis to evaluate which power cycle represents the most cost-effective solution depending on the type of thermal energy storage and system boundary conditions, as noted by the authors. To fill the identified gap, the present study proposes a methodology that enables decision-making for the selection of an appropriate power cycle and TES for a range of operating temperatures that include heat sources from 200 to 800 °C. This study investigates a broad spectrum of power block configurations, including organic Rankine, steam Rankine, and supercritical CO_2, (sCO_2) Bryton cycles. A techno-economic optimization has been conducted to determine the optimum coupling of power cycles and TES technology, including molten salt, particle, and air packed bed TES. In developing quasi-steady state system models, the study considers variable boundary conditions, scale-dependent cost functions, performance correlations, different heat sources and maximum temperature difference that is compatible with various storage technologies. The study investigates the impact of scale and charging cost on the performance of the system through sensitivity analyses.

2 SYSTEM DESCRIPTION

Figure 1 shows the schematic of the introduced energy storage plant. The system uses an electric heater to convert electricity sourced from either the electric grid or a renewable electricity system into thermal energy, which is then stored in the TES. A power block is integrated into the system to enable thermal-to-electricity reconversion. During periods of low-cost electricity or intermittent renewable electricity production, the Electric Heater (EH) is used to charge the TES. Conversely, the thermal energy storage is discharged to produce electricity when the cost of electricity is higher or renewable energy generation is unavailable. The present study considers three distinct types of TES, as shown in Figure 2. The first TES adopted is a two-tank molten salt energy storage (M) with a temperature range of 295 to 580 °C (Turchi et al., 2019). During the charging phase, the cold molten salts flow into the EH and are then stored directly in the hot tank. During the discharge phase, the hot molten salts flow into the primary heater and provide the thermal power to operate the power block. Next, a two-silos setup that employs particles (P) as a storage medium is examined, with a maximum temperature of up to 1200 °C (Ma, 2020). The cold particles that are stored in the cold silo are conveyed via conveyor belts and allowed to free-fall into a direct particle EH. The third storage configuration is characterized by an air-packed bed (A), which can operate at temperatures higher than 1200 °C. During the charging phase of this system, air is passed through an EH and then into the packed bed, where thermal energy is stored in the rocks that serve as the storage medium. This is reversed during the discharge phase.

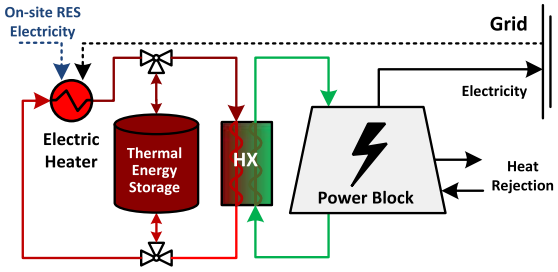

Figure 1: Layout of the energy storage plant

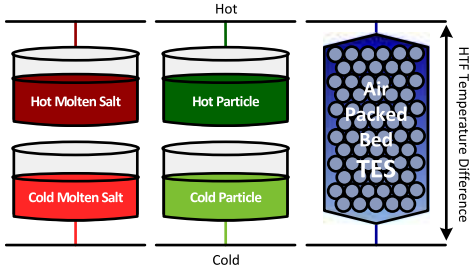

Figure 2: Thermal energy storage layouts

a) PB1: sCO_2 - Simple Recuperated Brayton

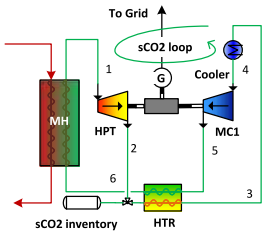

b) PB8: sCO_2 - Recuperated + Reheat + Recompression + Intercooling

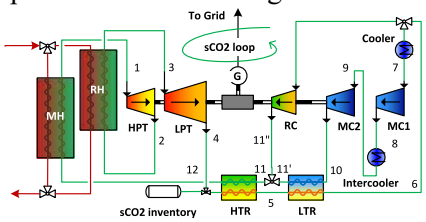

c) PB9: Steam Rankine Cycle

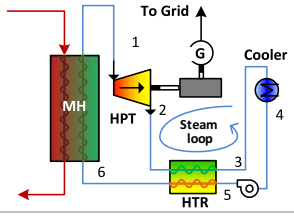

d) PB10: Organic Rankine Cycle

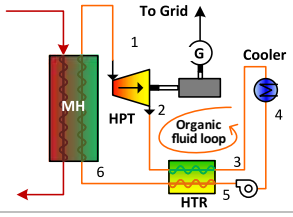

Figure 3: Power block configurations investigated

Table 1: Power block type description

PB1	Simple Recuperated sCO2 Brayton	**PB2**	PB1 + Intercooling
PB3	PB1 + Reheat	**PB4**	PB3 + Intercooling
PB5	PB1 + Recompression	**PB6**	PB5 + Intercooling
PB7	PB1 + Reheat + Recompression	**PB8**	PB7 + Intercooling
PB9	Steam Rankine	**PB10**	Organic Rankine Cycle

The analysis explores all potential combinations of these energy storage types and 10 power block configurations, while considering temperature limits and other boundary conditions. Figure 3 illustrates the power block layouts explored in this study, while Table 1 provides a description of each configuration to enhance clarity. These power blocks are labeled from 1 to 8 for the sCO_2-based layouts, 9 and 10 for the steam Rankine cycle and the organic Rankine cycle respectively. The eight sCO_2 power cycles have been outlined by modifying the simple recuperated Brayton cycle by employing intercooling, reheating, and recompression. All eight configurations are designed with dry cooling and feature turbomachinery on a single shaft, with variable speed gearboxes allowing for operation at different rotational speeds. Figure 3a and Figure 3b show the simplest and most efficient configurations of these layouts. Figure 3c shows the schematic of a recuperated steam Rankine cycle (PB9), while Figure 3d displays a recuperated organic Rankine cycle (PB10). The selection of organic fluids in the ORC cycle depends on the temperature of the heat source. Five distinct fluids have been utilized for this purpose. Isopentane has been employed for heat sources below 275 °C, while pentane is suitable for temperatures up to 325 °C. Cyclo-pentane is selected for temperatures ranging from 325 to 450 °C. Benzene, on the other hand, is considered for higher temperatures, up to 600 °C. The temperature ranges for these different organic fluids have been chosen to align with the limitations of the media and to optimize the thermal cycle efficiency within those ranges (Astolfi et al., 2018).

753

3 METHODOLOGY

The plant's techno-economic performance was evaluated using MoSES (Modeling of Solar Energy Systems), a Python-based tool developed by KTH Royal Institute of Technology. To evaluate the techno-economic indicators, the thermo-economics were coupled with an economic model based on a bottom-up estimation method, as shown in Figure 4. The thermodynamic states of the different media investigated in this study are estimated using CoolProp (Bell et al., 2014) The optimization problem was formulated to minimize the LCOS of the plant, an indicator to assess the relative profitability of the plant. The decision variables for the problem comprise of the thermal energy storage technology options including molten salt (M), particle (P), and air packed bed (A), power block layout, hot HTF temperature, and temperature difference between the hot and cold HTF temperatures in the TES.

$$LCOS = (CAPEX \cdot CRF + OPEX)/AEY \quad (1)$$

$$CRF = r \cdot (1 + r)^N/((1 + r)^N - 1) \quad (2)$$

The LCOS is a function of the investment cost (CAPEX), operational cost (OPEX), and Annual Energy Yield (AEY), as defined in equation (1). The Capital Recovery Factor (CRF), defined in equation (2), is a function of the lifetime (N), and the real discount rate (r).
The plant's operation assumes perfect daily charging and discharging cycles, as well as a constant electricity price. To begin, the energy storage plant is optimized for a capacity of 100 MWe and 12 hours of thermal energy storage, using a charging cost of 50 EUR/MWh, consistent with the average European spot price for the period 2020-2021 (European Network for Transmission System Operators in Electricity, 2023). A map is presented that outlines power block layouts and TES technologies, which minimize the LCOS for different HTF hot temperatures and temperature differences. Next, this study evaluates the impact of charging costs on system optimization and the best selections map by considering electricity costs of 0 and 100 EUR/MWh. The upper bound is selected based on the peaks of the average European spot prices (European Network for Transmission System Operators in Electricity, 2023), whereas the lower bound is used to simulate scenarios where surplus electricity is obtained from either the grid or on-site renewable generators. In the end, the effect of the scale has been investigated adopting capacities of 10 and 200 MWe.

3.1 Thermodynamic model

The amount of energy stored in the thermal energy storage technologies was determined as the product between the hours of storage (TES_h) and the thermal power design of the power block. The energy storage efficiency (η_{TES}) is determined by calculating the ratio of the energy discharged to the energy charged in a full storage cycle and is used to oversize the storage unit by accounting for thermal losses. For the commercial molten salt technology used in this study, an efficiency of 0.97 has been assumed for all combinations of HTF hot temperatures and hot-cold temperature differences (Turchi et al., 2019). In the case of the air packed bed layout, the TES efficiency ranges between 0.83 and 0.9, adopting a model developed by the authors in (Trevisan et al., 2020), which has been scaled with temperatures and validated in (Trevisan et al., 2022). The same approach has been implemented for the particle system, with efficiencies ranging between 0.87 and 0.94. Instead, the electric heater component was modeled using a fixed electric-to-thermal efficiency approach with an assumed efficiency of 0.95 for all the different thermal energy storage technologies. The power block models were implemented by developing and interconnecting thermodynamic models of the main components, with media properties estimated trough integration of CoolProp into the model. The performance of the sCO_2 power cycles have been estimated following the methodology introduced by the authors in (Guccione et al., 2022), including the key assumptions and the correlations to consider the effect of size on isentropic efficiencies. A regression model was developed based on (Hirsch & Khenissi, 2014) to estimate the performance of the Rankine cycle at varying operating temperatures, pressures, and installed capacities. Similarly, a regression model was developed also for the ORC, based on (Astolfi et al., 2018), to estimate varying efficiencies based on the heat source temperature and the specific organic fluid used. Figure 5 displays the maximum temperature boundaries for the storage and power block layouts. The study calculates the return temperature for each power block layout, taking into account thermodynamic assumptions and cycle configurations. Consequently, more efficient sCO_2 cycle layouts are distinguished by higher return temperatures compared to the simple recuperated cycle, as an example.

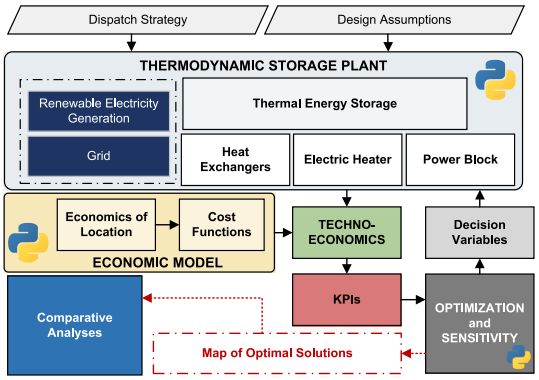

Figure 4: Methodology flowchart

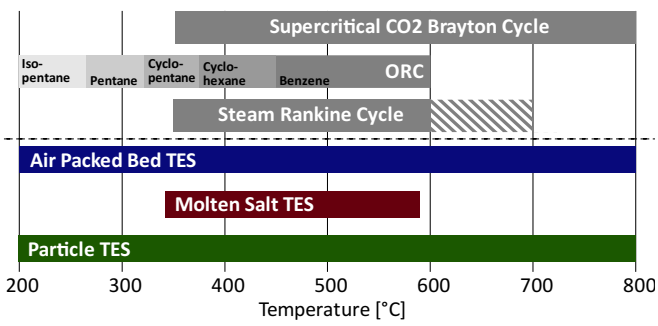

Figure 5: Maximum temperature limits

3.2 Economic model

The economic analysis of the storage plant takes into account two primary indicators, namely capital investment cost (CAPEX) and operational cost (OPEX). The capital investment includes both direct and indirect costs of all the main components involved in the storage plant as shown in equation (3). The operational cost comprises the charging cost and the operation and maintenance expenses of the plant, categorized as production-dependent and capacity-dependent yearly costs, as in equation (4). Table 2, provides a summary of the cost assumptions made for the plant's primary components. The main cost function developed by the authors are included in Appendix. A plant operational lifetime of 30 years was considered for the plant (USA DoE, 2019). The cost assumptions were converted into EUR based on the 2021 average USD-to-EUR exchange rate of 0.84 (European Central Bank, 2021). A nominal discount rate of 7% and an interest rate of 2.5% were adopted (USA DoE, 2019).

$$CAPEX = (C_{\text{site}} + C_{\text{TES}} + C_{\text{BOP}} + C_{\text{EH}} + C_{\text{PB}}) \cdot (1 + f_{\text{CONT}}) \cdot (1 + f_{\text{EPC}}) + C_{\text{land}} \quad (3)$$

$$OPEX = c_{\text{OM,fix}} \cdot P_{\text{net}} + c_{\text{OM,prod}} \cdot AEY + c_{\text{el}} \cdot E_{\text{charging}} \quad (4)$$

Table 2: Cost assumptions for the plant.

Description	Unit	Value	Ref.
Electric heater (electrical)	EUR/kW	15	*
Electric heater (thermal)	EUR/kW	125	*
Temperature factor 1	1/°C	16	*
Temperature factor 2	-	0.2	*
Molten Salt			
Storage	EUR/kWh$_t$	18–23	(Turchi et al., 2019) - (Herrmann et al., 2004)
Particle			
Particle lift	EUR/(m-kg/s)	49	(González-portillo et al., 2021)
Particle silo	EUR/m^2	1033	(González-portillo et al., 2021)
Particle	EUR/kg	0.84	(González-portillo et al., 2021)
Air			
High-T insulation	EUR/m^3	4303	(Trevisan et al., 2020)
Low-T insulation	EUR/m^3	621	(Trevisan et al., 2020)
Tank material	EUR/m^3	42693	(Trevisan et al., 2020)
Rocks	EUR/m^3	67	(Trevisan et al., 2020)
Foundations	EUR/m^2	1220	(Trevisan et al., 2020)
sCO$_2$ Power Block			
Heater(s)	EUR/(W/K) $^{0.8778}$	14.7	(Ho et al., 2015)
sCO$_2$ turbine	kEUR/(MW) $^{0.5561}$	15	(Weiland et al., 2019)
sCO$_2$ compressor	kEUR/(MW) $^{0.3992}$	1033	(Weiland et al., 2019)
sCO$_2$-sCO$_2$ recuperator	EUR/(W/K) $^{0.7544}$	41.5	(Weiland et al., 2019)
sCO$_2$-Air cooler	EUR/(W/K) $^{0.75}$	27.6	(Weiland et al., 2019)
Gearbox	kEUR/(MW) $^{0.2434}$	149	(Weiland et al., 2019)
Generator	kEUR/(MW) $^{0.5463}$	92	(Weiland et al., 2019)
sCO$_2$ piping	%PB cost	15 (20)	(Weiland et al., 2019)
Rankine Cycle			
Steam specific cost	EUR/kW	874	(Turchi et al., 2019)
ORC specific cost	EUR/kW	1000	(Lemmens, 2015)
Reference size	kW	100000	(Turchi et al., 2019)
Scaling exponent	-	0.7	-
Other costs			
Land	EUR/m^2	2.1	(Turchi et al., 2019)
Site Improvement	EUR/m^2	8.4	(Turchi et al., 2019)
Balance of Plant	EUR/kW$_e$	244	(Turchi et al., 2019)
Contingency	%direct costs	7	(Turchi et al., 2019)
EPC	%direct costs	13	(Turchi et al., 2019)
Fixed O&M cost – cap	EUR/kW-yr	34	(Turchi et al., 2019)
Variable O&M cost – gen	EUR/MWh-yr	3	(Turchi et al., 2019)

*based on a real quotation

755

4 RESULTS AND DISCUSSION

Figure 6a shows the map of the TES configurations that minimize the LCOS of the plant considering different HTF hot temperature and temperature difference across the storage. Figure 6b illustrates the corresponding LCOS values associated with various combinations of temperatures, storage, and power block layouts. The changes in LCOS values are depicted through the marked contours, aligning with the colors shown in the color bar. To facilitate comparison, the identical color bar has also been employed for Figure 7b and Figure 7e. Figure 6c depicts the map of optimal power block layouts.

For a 100 MWe plant, the optimal LCOS with 12 hours of storage and an electricity cost of 50 EUR/MWh is achieved by coupling a particle TES with a sCO_2 power block with recompression and intercooling (PB6). The minimum LCOS value of 154.7 EUR/MWh is obtained at a HTF hot temperature ($T_{hot,HTF}$) of 750 °C and a design temperature difference (ΔT_{HTF}) of 200 °C, as marked in Figure 6b. On one hand, reducing the temperature of the hot HTF can reduce costs for EH, TES, and power block, as it enables the use of less expensive materials. This also decreases the efficiency of converting thermal energy to electricity, resulting in higher LCOS. On the other hand, raising the HTF temperature can increase LCOS due to more expensive components, but also improve power block efficiency. Simultaneously, increasing the temperature difference across the TES can make storage more compact and cost-effective, but decrease storage efficiency. The power block layout and installed recuperator capacity determine the return temperature, and higher recuperation increases efficiency but also costs. Figure 6a shows that for most temperature combinations considered, the particle-based TES (P) offers the most cost-effective option. Although this TES has higher specific costs than an air-based TES, its higher efficiency leads to a lower electricity demand for charging compared to the air-based TES, resulting in a lower LCOS. The air-packed (A) TES is the optimal choice for regions characterized by low HTF temperatures and low temperature differences. At low HTF temperatures, the power block and electric heater costs become less significant, and the storage becomes the largest share of capital cost. Similarly, when the temperature difference decreases, the storage cost increases, making air-packed the optimal solution due to its lowest specific cost. The third region identified in Figure 6a is the molten salt TES (M), which is the best option when the design temperatures align with the limitations of the molten salt. The higher TES efficiency results in a significant reduction of charging power, leading to the lowest LCOS despite its higher specific costs compared to air and particle-based solutions. Figure 6c shows the optimal power block layouts for various design temperatures. The region of minimum LCOS is primarily occupied by sCO_2 power blocks with recompression and intercooling (PB6), along with a few configurations with recompression only (PB5). For temperature differences higher than 275 °C, simpler cycles such as sCO_2 simple recuperated (PB1) or simple recuperated with intercooling (PB2) with lower sCO_2 return temperatures should be preferred. The most complicated sCO_2 power block (PB8) is optimal only for low temperature differences and limited hot HTF temperatures, owing to its high efficiency and high return temperature.

In the region of low temperatures (up to 350 °C) and high temperature differences, the organic Rankine cycles (PB10) are the predominant choice. On the other hand, the steam Rankine cycle (PB9) is considered the optimal cycle between the low-temperature region and the region where the sCO_2 cycle is preferred. For high-temperature difference steam Rankine cycle is preferred to the sCO_2 one until the maximum hot temperature bounds for this technology is reached.

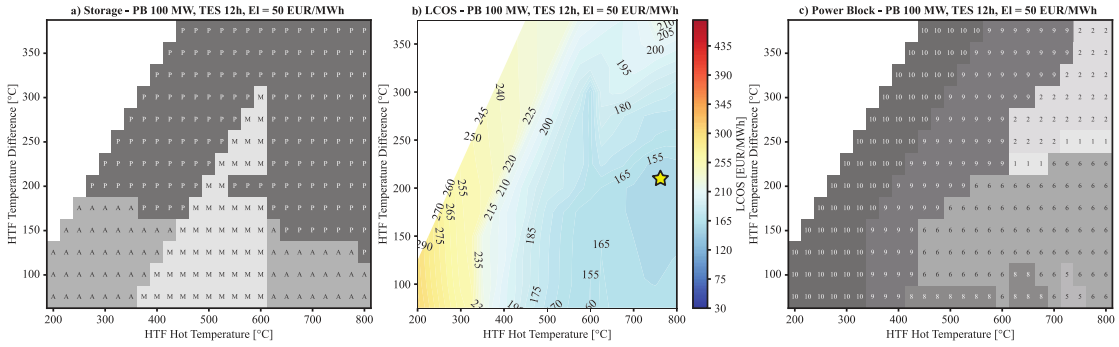

Figure 6: Map of optimal storage and power block layouts as a function of the design temperature across the thermal energy storage (P_{PB} = 100 MW, TES_h = 12 h, c_{el} = 50 EUR/MWh)

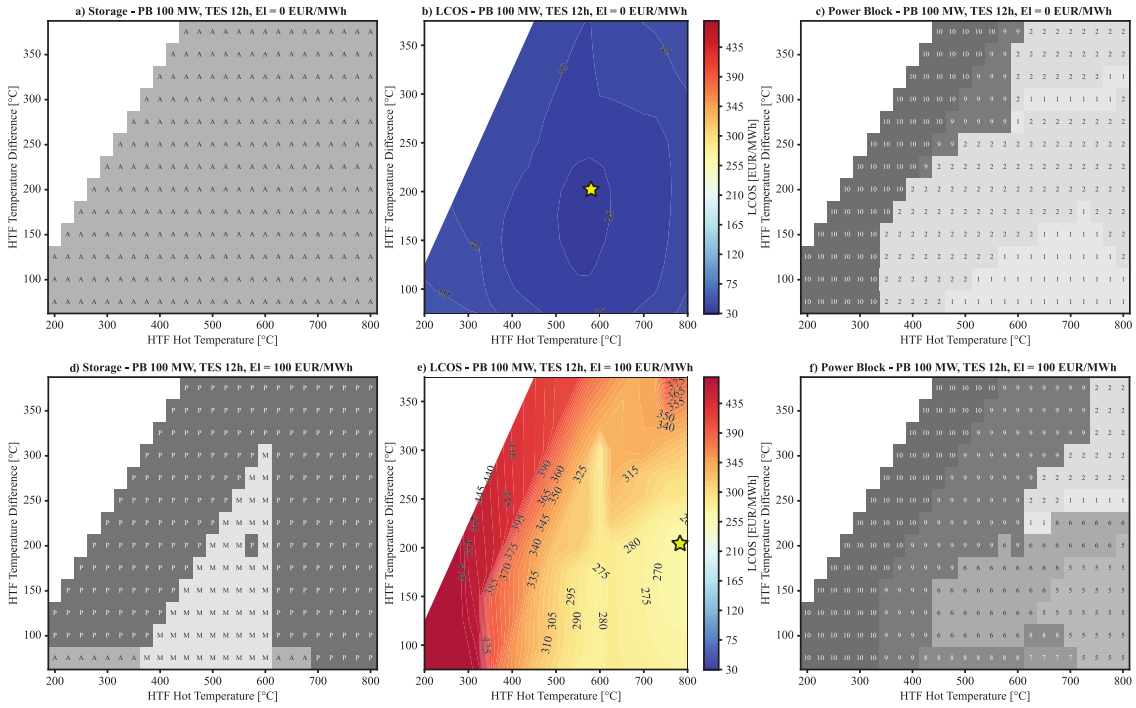

Figure 7: Sensitivity analysis on charging cost (c_{el} = 0 and 100 EUR/MWh) - Maps of optimal storage and power block layouts (P_{PB} = 100 MW, TES_h = 12 h)

4.1 Sensitivity on installed capacity cost

A smaller scale system with a capacity of 10 MW yields a worse LCOS compared to the base-case, due to the lack of economy of scale. The highest HTF temperatures result in a minimum LCOS of 170 EUR/MWh. All optimal designs feature sCO_2 power blocks, which are compact and cost-efficient even at a small scale, unlike steam Rankine cycles. As the scale increases to 200 MW, the LCOS slightly decreases for all possible combinations of temperatures, storage, and power blocks. The storage selection remains relatively consistent with the base-case, while the power block map features more steam Rankine (PB9) configurations. At 200 MW, the minimum LCOS is achieved using a molten salt TES and a conventional steam Rankine cycle with maximum operating temperatures of 580 °C.

757

4.2 Sensitivity on charging cost

The cost breakdown of the LCOS showed that the charging cost is the most significant parameter affecting the maps proposed. Figure 7 presents the sensitivity on the optimal design maps for two charging cost scenarios: 0 and 100 EUR/MWh. In the first case, the optimal configuration is characterized by an air-packed bed TES coupled with a sCO_2 simple recuperated cycle with intercooling (PB2). A minimum LCOS of 30 EUR/MWh was achieved with a hot HTF temperature of 575 °C and a design temperature difference of 200 °C. When the electricity cost is zero, the optimal configuration is characterized by a less expensive TES and sCO_2 power block layout compared to the base-case analysis. Figure 7a indicates that air-packed bed TES is the most suitable option for most temperature combinations when the charging cost is negligible. Air-packed bed solutions are favorable in this scenario because the compressor power required to move air in the system has no impact on system cost. However, molten salt technology may be preferred due to its higher maturity when the temperatures are feasible, as the difference in performance between air and molten salt is less than 10%. Regarding power block selection, investing in more efficient power block cycles does not pay off, and a simple sCO_2 recuperated cycle or a simple cycle with intercooling is recommended.

Figure 7d, 7e, and 7f demonstrate that increasing the charging cost results in an increase in the minimum LCOS to 275 EUR/MWh, which is achieved with a hot temperature of 800 °C and a temperature difference of 200 °C. The optimal power block consists of an sCO_2 power block with recompression or recompression and intercooler (PB5, PB6) coupled with particle-based TES. The trend of optimal TES and power block layouts is like the base-case study, with a smaller region characterized by air-based TES. The sCO_2 power block layouts cover a larger region of the optimal selection map due to their

lower costs and higher efficiencies. As the charging cost increases, the gap between the LCOS observed in the region where ORC layouts with low efficiency (23-30%) are utilized and the area where sCO_2 layouts are employed becomes even wider. Similarly to the base case, the ORCs are selected for the low-temperature region. One of the limitations of these findings is the assumption of a perfect daily cycling pattern with a fixed charging price, which may not reflect the real-world scenario. The optimal dispatch strategy would be influenced by the fluctuations in the charging cost. If there is a seasonal variation in charging cost, this will have a greater impact on the cost. A system like this would be more beneficial for a location with large daily changes in electricity prices.

5 CONCLUSIONS

This work introduced a techno-economic analysis to identify the best pairing of power cycle and thermal energy storage for a wide range of operating temperatures (200-800 °C). Various power block configurations are evaluated and coupled with different types of storage, including molten salt, particle, and air packed bed TES. To identify the most cost-effective combination of power cycle and TES, the study conducted an optimization aimed at minimizing the LCOS of the plant, considering different plant capacities and charging costs. Based on the results presented, the following conclusions can be drawn:

- The most cost-effective solution for a 100 MWe plant with 12 hours of storage and a charging cost of 50 EUR/MWh is the coupling of a sCO_2 power block with recompression and intercooling with a particle TES. The minimum LCOS value of 154.7 EUR/MWh was achieved with a temperature of 750 °C and a design temperature difference of 200 °C.
- When electricity is free, an intercooled sCO_2 power block coupled with an air-packed bed TES represents the most cost effective solution. An LCOS of 30 EUR/MWh can be achieved with a maximum HTF temperature of 575 °C. Air-packed bed TES should be preferred when storage represents a significant portion of the capital cost, especially with low HTF temperatures, low temperature differences, or low charging costs.
- A particle-based energy storage is the most cost-effective selection of TES for the largest region of the temperature combinations investigated, both at small (10 MW) and at larger scales (>100 MW).
- Molten salt is the suggested option for TES as long as the design temperatures fall within the temperature limitations of the salt, which are between 290 and 580 °C.

758

NOMENCLATURE

A	Air	MC (RC)	Main (Re-) Compressor
AEY	Annual Energy Yield	MH	Main Heater
BOP	Balance of Plant	OM	Operation and Maintenance
CAPEX	Capital Expenditure	OPEX	Operational Expenditure
CONT	Contingencies	ORC	Organic Rankine Cycle
EH	Electric Heater	P	Particle
EPC	Engineering, Procurement, Construction	PB	Power Block
H(L)PT	High (Low) Pressure Turbine	R	Reheat
HTF	Heat Transfer Fluid	RH	Re-Heater
H(L)TR	High (Low) Temp. Recuperator	RR	Recompression and Reheat
LCOS	Levelized Cost of Storage	TES	Thermal Energy Storage
M	Molten Salts	TIT	Turbine Inlet Temperature

REFERENCES

Al-Azawii, M. M. S., Alhamdi, S. F. H., Braun, S., Hoffmann, J. F., Calvet, N., & Anderson, R. (2021). Experimental study on packed-bed thermal energy storage using recycled ceramic as filler materials. *Journal of Energy Storage*, *44*(PA), 103375. https://doi.org/10.1016/j.est.2021.103375

Albert, M., Ma, Z., Bao, H., & Roskilly, A. P. (2022). Operation and performance of Brayton Pumped Thermal Energy Storage with additional latent storage. *Applied Energy*, *312*(January), 118700. https://doi.org/10.1016/j.apenergy.2022.118700

Astolfi, M., Alfani, D., Lasala, S., & Macchi, E. (2018). Comparison between ORC and CO2 power systems for the exploitation of low-medium temperature heat sources. *Energy*, *161*, 1250–1261. https://doi.org/10.1016/j.energy.2018.07.099

Bell, I. H., Wronski, J., Quoilin, S., & Lemort, V. (2014). Pure and pseudo-pure fluid thermophysical property evaluation and the open-source thermophysical property library coolprop. *Industrial and Engineering Chemistry Research*, *53*(6), 2498–2508. https://doi.org/10.1021/ie4033999

Benato, A., & Stoppato, A. (2018). Pumped Thermal Electricity Storage: A technology overview. *Thermal Science and Engineering Progress*, *6*, 301–315. https://doi.org/10.1016/j.tsep.2018.01.017

D'Aguanno, B., Karthik, M., Grace, A. N., & Floris, A. (2018). Thermostatic properties of nitrate molten salts and their solar and eutectic mixtures. *Scientific Reports*, *8*(1), 1–15. https://doi.org/10.1038/s41598-018-28641-1

European Central Bank. (2021). *Euro foreign exchange reference rates: average 2021 US dollar excahnge rate*. https://www.ecb.europa.eu/ stats/ policy_and_exchange_rates/ euro_reference_exchange_rates/ html/ eurofxref-graph-usd.en.html

European Network for Transmission System Operators in Electricity. (2023). *ENTSO-E Transparency Platform*. https://transparency.entsoe.eu/

Frate, G. F., Ferrari, L., & Desideri, U. (2020). Multi-Criteria Economic Analysis of a Pumped Thermal Electricity Storage (PTES) With Thermal Integration. *Frontiers in Energy Research*, *8*(April). https://doi.org/10.3389/fenrg.2020.00053

Glatzmaier, G. (2011). Developing a Cost Model and Methodology to Estimate Capital Costs for Thermal Energy Storage. *Nrel/Tp-5500-53066*, *December*, 1–17.

González-portillo, L. F., Albrecht, K., & Ho, C. K. (2021). *Techno-Economic Optimization of CSP Plants with Free-Falling Particle Receivers*. https://doi.org/10.3390/e23010076

Guccione, S., Trevisan, S., Guedez, R., Laumert, B., Maccarini, S., & Traverso, A. (2022, June 13). Techno-Economic Optimization of a Hybrid PV-CSP Plant With Molten Salt Thermal Energy Storage and Supercritical CO2 Brayton Power Cycle. *Proceedings of the ASME Turbo Expo 2022: Turbomachinery Technical Conference and Exposition. Volume 4: Cycle Innovations; Cycle Innovations: Energy Storage.* https://doi.org/10.1115/GT2022-80376

Hänchen, M., Brückner, S., & Steinfeld, A. (2011). High-temperature thermal storage using a packed bed of rocks - Heat transfer analysis and experimental validation. *Applied Thermal Engineering*, *31*, 1798–1806. https://doi.org/10.1016/j.applthermaleng.2010.10.034

Herrmann, U., Kelly, B., & Price, H. (2004). Two-tank molten salt storage for parabolic trough solar power plants. *Energy*, *29*(5–6), 883–893. https://doi.org/10.1016/S0360-5442(03)00193-2

Hirsch, T., & Khenissi, A. (2014). A systematic comparison on power block efficiencies for CSP plants with direct steam generation. *Energy Procedia*, *49*, 1165–1176. https://doi.org/10.1016/j.egypro.2014.03.126

Ho, C. K., Carlson, M., Garg, P., & Kumar, P. (2015). Cost and Performance Tradeoffs of Alternative Solar-Driven s-CO2 Brayton Cycle Configurations. *ASME 2015 9th International Conference on Energy Sustainability Collocated with the ASME 2015 Power Conference*. https://doi.org/10.1115/ES2015-49467

Hu, S., Yang, Z., Li, J., & Duan, Y. (2021). Thermo-economic analysis of the pumped thermal energy storage with thermal integration in different application scenarios. *Energy Conversion and Management*, *236*, 114072. https://doi.org/10.1016/j.enconman.2021.114072

Laughlin, R. B. (2017). Pumped thermal grid storage with heat exchange. *Journal of Renewable and Sustainable Energy*, *9*(4). https://doi.org/10.1063/1.4994054

Lemmens, S. (2015). A Perspective on Costs and Cost Estimation. *Proceedings of the 3rd International Seminar on ORC Power Systems*, *2010*, 1–10.

Liang, T., Vecchi, A., Knobloch, K., Sciacovelli, A., Engelbrecht, K., Li, Y., & Ding, Y. (2022). Key components for Carnot Battery: Technology review, technical barriers and selection criteria. *Renewable and Sustainable Energy Reviews*, *163*(May), 112478. https://doi.org/10.1016/j.rser.2022.112478

Ma, Z. (2020). *Particle Thermal Energy Storage Components for Pumped Thermal Energy Storage*.

Morandin, M., Maréchal, F., Mercangöz, M., & Buchter, F. (2012). Conceptual design of a thermo-electrical energy storage system based on heat integration of thermodynamic cycles - Part A: Methodology and base case. *Energy*, *45*(1), 375–385. https://doi.org/10.1016/j.energy.2012.03.031

Trevisan, S., Guédez, R., & Laumert, B. (2020). Thermo-economic optimization of an air driven supercritical CO2 Brayton power cycle for concentrating solar power plant with packed bed thermal

energy storage. *Solar Energy*, *211*(October), 1373–1391. https://doi.org/10.1016/j.solener.2020.10.069

Trevisan, S., Wang, W., Guedez, R., & Laumert, B. (2022). Experimental evaluation of a high-temperature radial-flow packed bed thermal energy storage under dynamic mass flow rate. *Journal of Energy Storage*, *54*. https://doi.org/https://doi.org/10.1016/j.est.2022.105236

Turchi, C. S., Boyd, M., Kesseli, D., Kurup, P., Mehos, M., Neises, T., Sharan, P., Wagner, M. J., & Wendelin, T. (2019). CSP Systems Analysis - Final Project. *Nrel/TP-5500-72856*, *May*.

USA DoE. (2019). *Gen 3 CSP Topic 1–Phase 3 Test Facility Down-Selection Criteria*.

Vecchi, A., Knobloch, K., Liang, T., Kildahl, H., Sciacovelli, A., Engelbrecht, K., Li, Y., & Ding, Y. (2022). Carnot Battery development: A review on system performance, applications and commercial state-of-the-art. *Journal of Energy Storage*, *55*(PD), 105782. https://doi.org/10.1016/j.est.2022.105782

Weiland, N. T., Lance, B. W., & Pidaparti, S. R. (2019). sCO2 Power Cycle Component Cost Correlations From DOE Data Spanning Multiple Scales and Applications. *ASME Turbo Expo 2019: Turbomachinery Technical Conference and Exposition*, *9*, 1–17. https://doi.org/10.1115/GT2019-90493

White, M. T., Bianchi, G., Chai, L., Tassou, S. A., & Sayma, A. I. (2021). Review of supercritical CO2 technologies and systems for power generation. *Applied Thermal Engineering*, *185*(December 2020). https://doi.org/10.1016/j.applthermaleng.2020.116447

ACKNOWLEDGEMENT

The authors acknowledge the financial support from the European Union's Horizon 2020 research and innovation program, project No. 952953.

APPENDIX

Electric Heater

$$C_{\mathrm{EH}} = c_{\mathrm{EH}} \cdot P_{\mathrm{EH,des}} \quad \text{(a)}$$

$$c_{\mathrm{EH}} = c_{\mathrm{EH,el}} + c_{\mathrm{EH,th}} \cdot f_{\mathrm{T,EH}} \quad \text{(b)}$$

$$f_{\mathrm{T,EH}} = c_1 \cdot \log(T_{\max}\,[^{\circ}C]) - c_2 \quad \text{(c)}$$

Air Packed Bed TES

$$C_{\mathrm{TES}} = c_{\mathrm{rocks}} \cdot V_{\mathrm{rocks}} + \left(c_{\mathrm{HT_{ins}}} \cdot V_{\mathrm{HT_{ins}}} + c_{\mathrm{LT_{ins}}} \cdot V_{\mathrm{LT_{ins}}} + c_{\mathrm{mat}} \cdot V_{\mathrm{mat}} \right) \cdot fT_{\mathrm{TES}} + c_{\mathrm{foundations}} \cdot A_{\mathrm{land_{TES}}} \quad \text{(d)}$$

Molten Salt TES

$$C_{\mathrm{TES}} = c_{\mathrm{TES}} \cdot E_{\mathrm{TES,des}}\,* \quad \text{(e)}$$

*The specific molten salt TES cost model is calculated using the following approach:

$$c_{\mathrm{TES}} = c_{\mathrm{media,TES}}/(1 - \%_{\mathrm{non-media}}) \quad \text{(f)}$$

where $c_{media,TES}$ is the TES specific cost proportional to the medium and $\%_{nonmedia}$ is the complementary share of the TES cost. The specific TES cost ($c_{TES,1}$) has been assumed equal to 23 EUR/kWh for a TES temperature difference between the hot and cold tank ($\Delta T_{TES,1}$) equal to 98 °C (Turchi et al., 2019). For $\Delta T_{TES,1}$, the share of non-media TES can be assumed equal to 0.55 (Turchi et al., 2019). Similarly, for $\Delta T_{TES,2}$ equal to 275 °C, the share of non-media TES can be assumed equal to 0.54 (Glatzmaier, 2011) and the specific cost $c_{TES,2}$ can be assumed equal to 18 EUR/kWh (Turchi et al., 2019). Then, for a given ΔT_{TES}, the $c_{media,TES}$ is calculated as in equation (g). The parameters $a1_{TES}$ is defined in equation (h). The share of non-media is estimated as a function of the ΔT_{TES} as in equation (i), where the parameters $a2_{TES}$ is calculated as in equation (j).

$$c_{\mathrm{media,TES}} = a1_{\mathrm{TES}} \cdot \Delta T_{\mathrm{TES}} + \left(c_{\mathrm{media,TES,1}} - \Delta T_{\mathrm{TES,1}} \cdot a1_{\mathrm{TES}} \right) \quad \text{(g)}$$

$$a1_{\mathrm{TES}} = \frac{c_{\mathrm{media,TES,2}} - c_{\mathrm{media,TES,1}}}{\Delta T_{\mathrm{TES,2}} - \Delta T_{\mathrm{TES,1}}} \quad \text{(h)}$$

$$\%_{\mathrm{non-media}} = a2_{\mathrm{TES}} \cdot \Delta T_{\mathrm{TES}} + \left(\%_{\mathrm{nonmedia,1}} - \Delta T_{\mathrm{TES,1}} \cdot a1_{\mathrm{TES}} \right) \quad \text{(i)}$$

$$a2_{\mathrm{TES}} = \frac{\%_{\mathrm{non-media,2}} - \%_{\mathrm{non-media,1}}}{\Delta T_{\mathrm{TES,2}} - \Delta T_{\mathrm{TES,1}}} \quad \text{(j)}$$

**If reheat is included in the power block, the share of piping cost is equal to 0.2, otherwise 0.15.

ORC SEVILLE 2023
7th International Seminar on O.R.C. Power Systems

© 2024 Editorial Universidad de Sevilla. Este es un artículo de acceso abierto distribuido bajo los términos de la licencia de uso y distribución Creative Commons (BY-NC-ND 4.0)

DOI: https://dx.doi.org/10.12795/9788447227457_142
Paper ID #142, page 1 of 11

AERODYNAMIC DESIGN AND NUMERICAL ANALYSIS OF A COUNTER-ROTATING CENTRIFUGAL COMPRESSOR

Cheikh Brahim ABED*, Arthur LEROUX,

ENOGIA, 19 Av. Paul Héroult, Marseille, France

*Corresponding Author: cheikh-brahim.abed@enogia.com

ABSTRACT

Counter-rotating turbomachines offer more design and control options than conventional machines. While axial counter-rotating turbomachines have been widely studied, few studies have focused on centrifugal ones. This paper presents a detailed numerical study on the benefits of counter-rotating impellers for centrifugal compressors, specifically the impact of speed ratio on performance gain. The study used 0D/1D models and optimization methods to meet design criteria. The aerodynamic performance of the new designs was compared to a baseline configuration consisting of a centrifugal impeller and a vaned wedge diffuser. The new design features a first impeller with perfect axial inlet and mixed flow or a purely radial blade at the impeller exit, and a parametrically designed counter-rotating bladed diffuser with radial or mixed flow inlet and radial outlet. Optimized solutions were determined using validated 0D/1D loss models and analyzed using a 3D CFD solver. The results show that this new configuration can increase efficiency on a wide range compared to the baseline using speed ratio modulation.

1 INTRODUCTION

Counter-rotating CR turbomachines with two rotors were promising for improving performance, such as efficiency, power density, and operating range. However, previous studies have primarily focused on axial machines, which have shown that the most significant advantage of CR machines is the additional degree of freedom, namely the speed ratio ($\theta = N_{FR}/N_{RR}$) compared to single-rotor machines SR. In CR machine, the upstream or front rotor is named FR while the downstream or rear one is called RR and are rotating in opposite direction as shown in Fig.1.

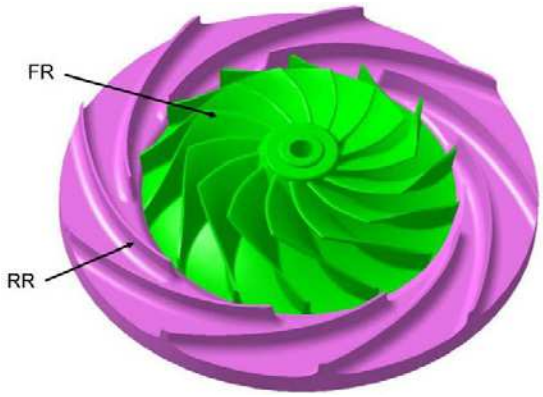

Figure 1: FR and RR rotors for a CR centrifugal compressor

A literature review on CR machines conducted in previous studies (Abed et al., 2020, 2021, 2022) revealed that, for axial CR configurations, adjusting the speed ratio θ of impellers in axial CR compressors enhances pressure rise and stall margin. When rear rotor RR rotating faster than front rotor FR, stall suppression is increased by almost 50%. Boosting the rotational speed of FR improves maximum efficiency, but marginally decreases pressure rise. Conversely, lowering the speed of FR while maintaining RR's speed results in fewer stable operating conditions. Furthermore, it was discovered that RR is more prone to stalling when the speed ratio exceeds 0.9, and its leakage flow

decreases at a lower speed than FR. Similarly, adjusting the speed ratio positively impacts the performance of counter-rotating axial pumps and fans.

Moreover, in radial counter-rotating CR configurations, the previous literature survey has demonstrated that the speed ratio θ plays a significant role in enhancing the overall performance of CR mixed-flow pump. This is attributed to the fact that by determining the optimal rotational speed for FR and RR at each operating point, the power density offered by the CR configuration can be maximized compared to the baseline single rotor SR. This optimization can be achieved by rotating RR at a higher speed than the FR for low flow rates and vice versa. Additionally, the literature survey reveals that blockage tends to occur earlier in CR machines compared to their SR counterparts. Similar observations regarding the impact of the speed ratio between FR and RR on the performance of CR mixed-flow pumps have been made in the context of CR radial fans. (Dejour and Vo, 2018) research on a hybrid configuration, which consists of a mixed-flow impeller as FR and an axial impeller as RR, reveals a substantial increase in pressure rise compared to a single rotor SR. However, this improvement does not coincide with a corresponding increase in efficiency. It is also noteworthy that blockage tends to occur earlier in this CR configuration compared to SR.

Furthermore, the work of (Abed et al., 2020, 2021, 2022) recently carried out extensive research to develop a validated design method for counter-rotating CR centrifugal compressor. This work was driven by the limited information found in the literature concerning the design approach and performance analysis of such machines. The cited studies on CR centrifugal compressor configurations primarily concentrate on the design method, its experimental and numerical validation, and a broad performance comparison with single rotor (SR) configurations. However, these investigations have not specifically explored the influence of the speed ratio on operating conditions and its wider implications, which is one of the main aims in the current work.

In this study, unshrouded impellers are employed for the CR configuration to facilitate comparison with the baseline single rotor SR. The SR configuration here consists of a single centrifugal impeller and a wedge-vaned diffuser, for which limited experimental and geometrical data can be found in Gaetani et al. (2012). The primary objective of this work is to emphasize the performance improvements offered by the CR configuration in comparison to the SR machine.

762

2 DESIGN METHOD

2.1 Velocity triangles

The key to design CR rotors is the correct formulation of its velocity triangles and understanding what implies. FR and SR rotors are similar and so are they're velocity triangles. However, RR is a counter-rotating rotor, so its inlet velocity triangles are distinctive because of its strong inlet counter swirl as shown by Fig. 2. Small gap of $J = 4mm$ is considered between FR and RR and to assume that no change occurs between FR and RR in terms flow properties of velocity triangles:

$$C_2 = C_3, C_{t2} = C_{t3}, C_{m2} = C_{m3} \quad (1)$$

The tangential component of absolute velocity at the outlet of FR, C_{t2}, contributes to increase the tangential component of the relative velocity at the inlet of RR impeller as:

$$W_{t3} = U_3 + C_{t3} \quad (2)$$

Eqn. 2 shows how the relative velocity at the inlet of RR increases by the counter-rotating effect.

This can lead to transonic or sonic inlet conditions and should be considered in the design procedure of CR. To compare the increase of enthalpy provided by CR and SR, RR outlet diameter is assumed equal to the peripheral diameter of SR impeller. Rotational speed of SR impeller and RR are also assumed to be equal, so we have $U_{2SR} = U_{4RR}$. Using the Euler's formula for ideal flow and assuming no pre-swirl at the inlet suction of both configurations, we can write the enthalpy rise of SR using Eqn.3:

$$\Delta h_{SR} = U_{2SR}.C_{t2SR} \quad (3)$$

The enthalpy rise of CR is the sum of each FR and RR enthalpy rise as expressed by Eqn. 4:

$$\Delta h_{CR} = \Delta h_{FR} + \Delta h_{RR} \quad (4)$$

RR rotational direction is considered as the positive one. The enthalpy rise of FR can be expressed using Eqn.5:

$$\Delta h_{FR} = (-U_2).(-C_{t2}) = U_2.C_{t2} \quad (5)$$

And the enthalpy of RR having negative pre-swirl at inlet can be formulated using Eqn. 6:

$$\Delta h_{RR} = U_4.C_{t4} - (U_3).(-C_{t3}) = U_4C_{t4} + U_3C_{t3} \quad (6)$$

Assuming ideal flow and the same outlet blade angle for SR impeller and RR with $U_{2SR} = U_{4RR}$, the increase of enthalpy given by CR compared to SR is in fact $U_3C_{t3} + U_2C_{t2}$.

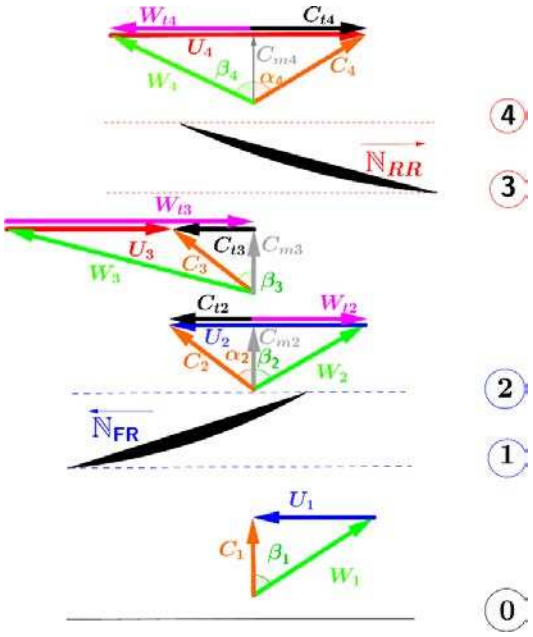

Figure 2: CR centrifugal compressor velocity triangles, (0): inlet station, (1): FR leading edge, (2): FR trailing edge, (3): RR leading edge, (4): RR trailing edge

763

2.2 CR Design approach

In the present work, two additional features have been added to a previous design procedure presented in (Abed et al., 2020, 2021) This approach for CR presented in Fig. 3 is composed of a 0D/1D design method coupled with NSGA-II optimization algorithm. The geometric parametrization of CR including FR and RR is summarized in Fig. 4.

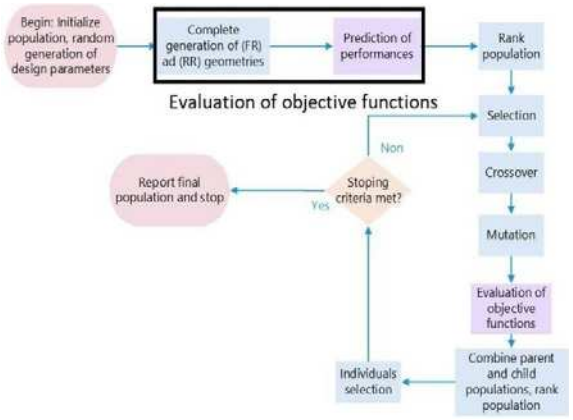

Figure 3: CR centrifugal compressor design flowchart

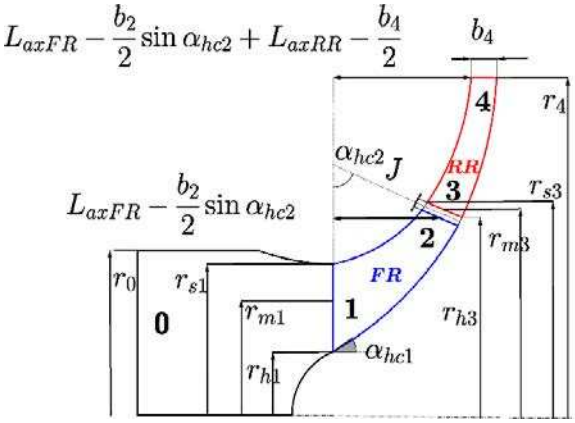

Figure 4: CR centrifugal compressor geometrical design parameters

It was found that the predicted outlet flow of FR is not quite accurate in some design operating conditions, so an additional step in the design of FR is considered by evaluating its performance using an adapted set of loss models developed in the thesis of (Abed 2021) and published in the paper

(Abed et al., 2021) in which an experimental validation of the design method is presented.

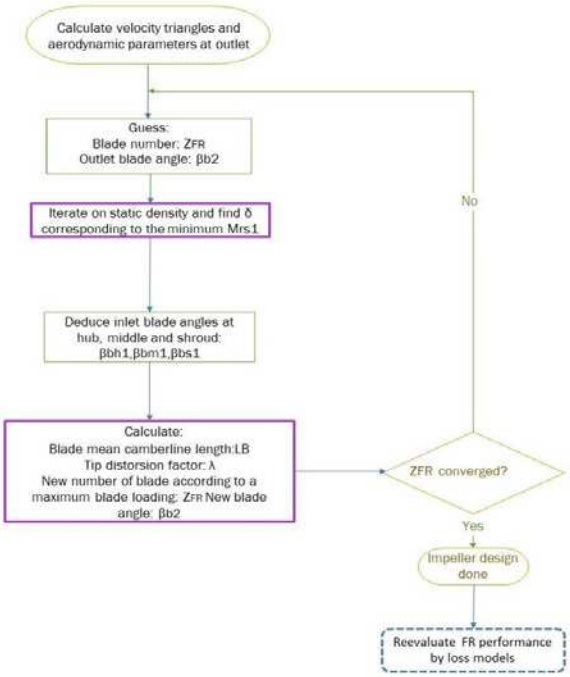

Figure 5: FR design flowchart, updated from (Abed,2020)

3 CASE STUDY

The case study in this paper is a design of CR configurations based on a baseline centrifugal compressor SR selected from literature. The aim is to design a CR configuration having the same outlet diameter of RR as that of SR impeller.

3.1 Reconstruction of SR configuration based on available data

The baseline configuration SR considered in this study is a conventional high specific-speed centrifugal compressor composed of a radial impeller and a wedge vaned diffuser. Geometrical parameters and experimental measurements at three operating conditions in which the impeller rotates at 12.5 kRPM can be found in the work of Gaetani et al. (Gaetani et al. 2012) and summarized in Tabs. (1-2). Some important geometrical parameters of the baseline are not provided such as clearance gap and axial distance. To estimate those values, clearance gap was fixed at 5% of impeller blade width $b2$ and axial distance is calculated iteratively to match the desired pressure ratio of 1.6 of the whole stage. At every value of Lax, the complete geometry of SR impeller and the wedge vaned diffuser is generated, and then the pressure is estimated using the previous validated set of loss models. Fig. 11 shows the flowchart of axial distance calculation. The value obtained for the axial distance of the baseline SR is $L_{ax} = 114.2\ mm$. Figures 12 and 13 show respectively the blade angle distribution from inlet to outlet and the meridional view of the SR impeller. The wedge vaned diffuser is built in the same way as that of SR impeller considering a purely radial meridional variation and constant variation of the blade angle distribution. Figure 14 shows the comparison of total-total pressure ratio obtained from CFD

calculations and experimental data. SM is the CFD simplified model using single passage per component and FM is the full model using all passages.

Table 1: SR main geometrical parameters extracted from (Gaetani et al. 2012)

Radial Impeller				
r_{s1}	r_{s1}	b_2	Z_{SR}	$\boldsymbol{\beta}_{b2}$
131,5 mm	200 mm	17.4 mm	16	-24°
Vanned wedge diffuser				
r_3	r_4	$b_3 = b_4$	Z_{dif}	$\boldsymbol{\beta}_{b2}$
220 mm	382.5 mm	22 mm	25	63°

Table 2: SR operating conditions, extracted from (Gaetani et al. 2012)

	Near stall	**Best efficiency**	**Near choke**
$\dot{m}$ [kg/s]	2.61	3.28	4.7
π_{t4}	1.56	1.605	1.48

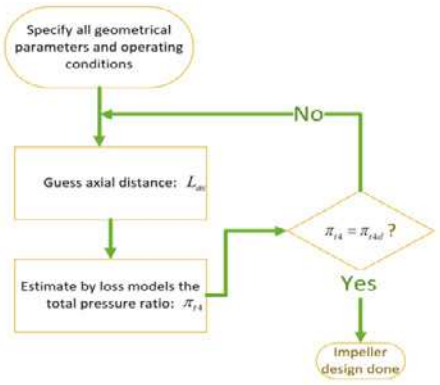

Figure 11: SR axial distance calculation of SR impeller

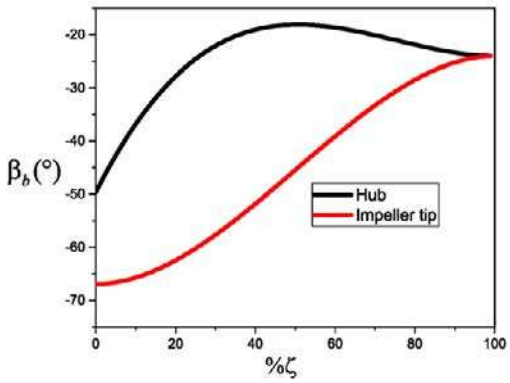

Figure 12: Blade angle distribution pf SR impeller

765

Tab. 4 resumes the errors between CFD calculations for the constructed SR configuration and experimental data of the baseline SR extracted from (Gaetani et al. 2012) at three operating conditions. These errors are small enough to be acceptable. Fig. 15 shows the original baseline and the reconstructed one by the developed tool.

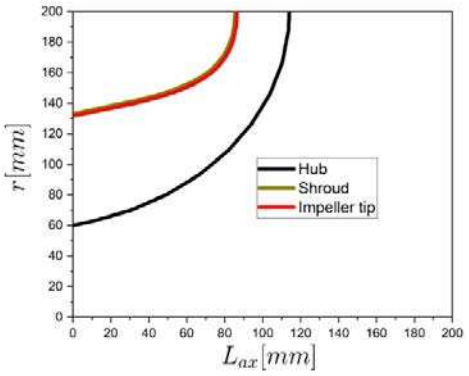

Figure 13: Meridional shape of SR impeller

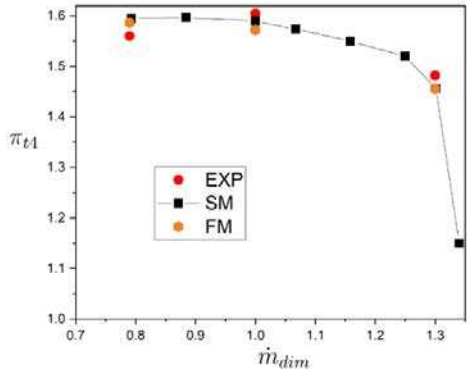

Figure 14: Pressure ration comparison between CFD and experimental of SR

Table 4: Validation of the constructed baseline SR

Pressure ratio	Experimental data	CFD (SM)	Error (%)	CFD (FM)	Error (%)
Near stall	1.56	1.595	2.24	1.585	1.6
Best efficiency	1.605	1.589	0.997	1.572	2.05
Near choke	1.482	1.456	1.754	1.455	1.78

Figure 15: Original SR (left) and constructed SR (right)

3.2 CR design method

The design of CR follows the method specified in [15]. The interface of FR and RR is determined by the factor $\chi_{FR} = r_2/r_4$ which defines indirectly the specific amount of enthalpy increase that FR and RR should give.

For the optimization loop, the set of parameters: $\chi_{FR}, b_5, \beta_{b5}, N_{FR}, N_{RR}$ presents the decision variables while some constraints have been specified such as the relative Mach number at the inlet of RR to avoid choke. The operating mass flow is fixed by the designer and corresponds here to the design mass flow of SR which correspond to the best operating point. Finally, the two objectives of optimization are the maximization of total-total pressure ratio π_{t4} and the corresponding isentropic efficiency η_{t4} of CR. Finally, the range of design parameters are described as following:

$$\dot{m}_d = 3.28 kg/s,$$
$$0.3 \leq \chi_{FR} \leq 0.77,$$
$$10\ kRPM \leq N_{FR} \leq 18\ kRPM,$$
$$10\ kRPM \leq N_{RR} \leq 12.5\ kRPM,$$
$$max(Mr_{thFR}, Mr_{thRR}) \leq 0.9,$$
$$0.1 b_2 \leq b_5 \leq 3 b_2, -90° \leq \beta_{b5} \leq 0°$$

The optimization procedure in the phase of CR design is presented in Fig. 3. In this flowchart, the step framed in black color corresponds to the evaluation of the objective functions according to NSGA-II algorithm in which the design and performances of FR and RR are performed by the in-house code.

4 RESULTS

4.1 Optimization results

The Pareto front obtained from optimization for CR configuration is shown in Fig 16. Pareto front shows a large variation of π_{t4} from 1.84 to 2.4 according to a slight variation η_{t4}. χ_{FR}. The Pareto front obtained from optimization for CR configuration is shown in Fig 16. Pareto front shows a large variation of π_{t4} from 1.84 to 2.4 according to a slight variation η_{t4}. χ_{FR}varies between 0.51 to 0.78 is

while the value of N_{RR} remains between 11.35$kRPM$ to 12.49$kRPM$. The value of N_{FR} is between 16.85 $kRPM$ to 17.89 $kRPM$. 11 prototypes are selected from Pareto front to be analyzed using 3D CFD simulations.

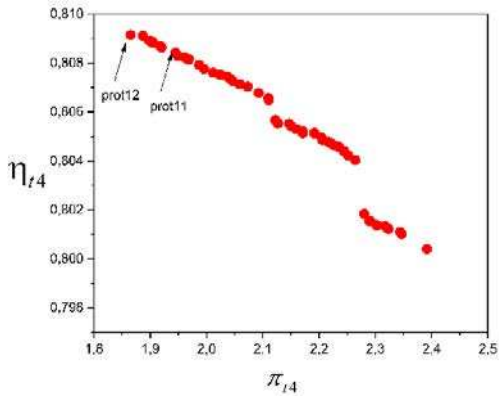

Figure 16: Pareto front obtained from the design optimization of CR configurations

4.2 Numerical method

The numerical calculations were carried out using a commercial CFD software ANSYS 2022R2. Simulations were performed using high resolution for advection scheme and turbulence equations. The $k-\omega$ SST turbulence model is employed. Calculations with mixing-plane interface are carried out to obtain the performance of all CR configurations with SR. For the sake of time and computational cost, a simplified passage model SM with rotational periodicity for component is simulated to generate the performance. Full model simulations are carried out also to assess the SM model. The fluid domain using air ideal gas contains an inlet pipe, two impellers and a vaneless diffuser for CR configurations and one impeller along with a vaned diffuser for SR. Fig. 17 shows the details of computational mesh for SR and a CR configuration. Theses meshes are obtained after a mesh sensitivity study with values about 2.45 millions elements for CR and 3.25 millions elements for SR.

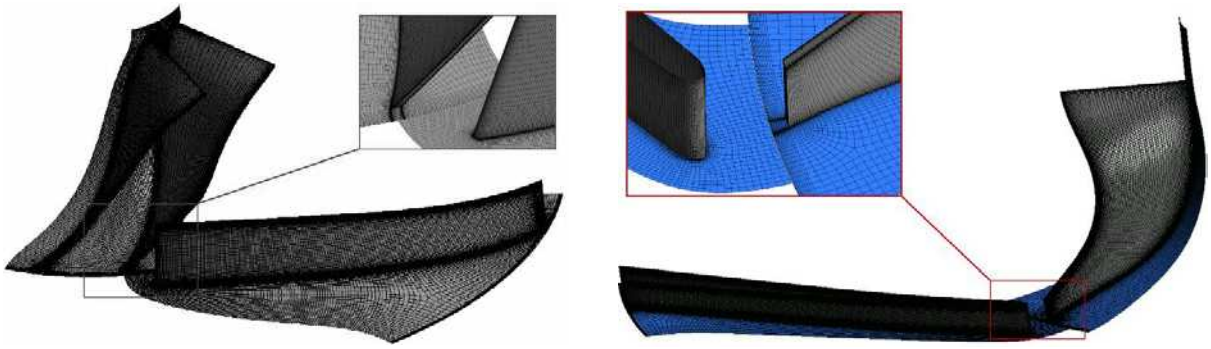

Figure 17: Blade mesh details of CR (left) and SR (right)

4.3 Obtained results

Fig. (18-19) show the performances of 11 simulated configurations of CR (prot1 to prot11) as well as SR. The total-total pressure ratio and the corresponding isentropic efficiency are calculated as:

$$\pi_{t4} = \frac{p_{t4}}{p_{t0}}, \qquad \eta_{t4} = \frac{\dot{m}.C_p.T_{t0}\left(\pi_{t4}^{\frac{\gamma-1}{\gamma}} - 1\right)}{\Gamma_{FR}.\omega_{FR} + \Gamma_{RR}.\omega_{RR}} \tag{12}$$

All parameters are calculated using area-averaged based on a section located at $r = 1.18\, r_{TE}$.

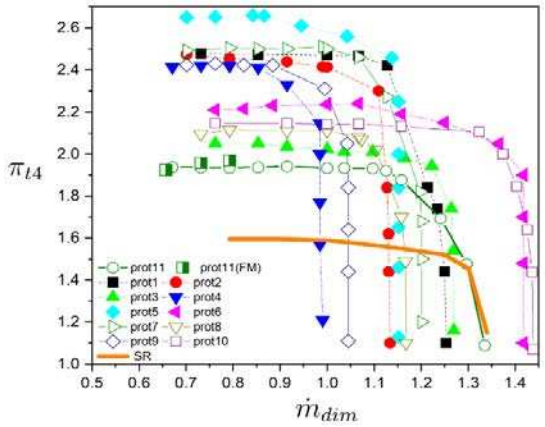

Figure 18: Total-total pressure ratio of 11 CR compressors selected from Pareto front

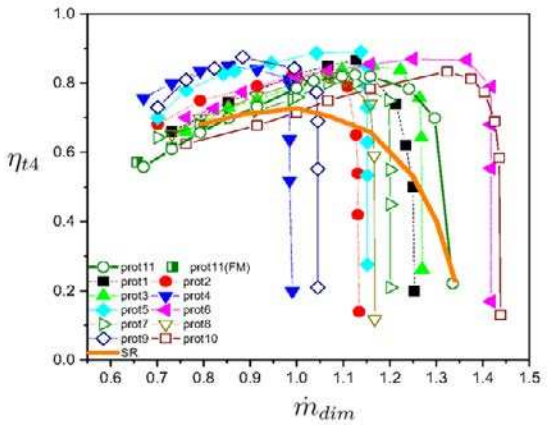

Figure 19: Isentropic efficiency of 11 CR compressors selected from Pareto front

The full model (FM) is also used on prot11 to assess the simplified model with one passage per component at low mass flow and both results are in good agreement. From these figures, one can see that prot10 and prot6 give the largest choking margin with a large efficiency. Prot4 gives the lowest choking margin and prot5 gives the highest pressure rise of the selected CR configurations. prot11 gives the lowest pressure rise, an acceptable choking margin and the largest stall margin. It has the lowest value of $\text{chi}_{\{\text{FR}\}} = 0.51$. Fig. 20 shows a clear comparison between the prot11 and SR. The static pressure is illustrated at the Hub surfaces, while turbulent kinetic energy (TKE) is shown on the blade surfaces. As mentioned before, since the outlet diameter and the rotation speed are identical for prot11 and SR, a fear comparison of the pressure rise between them can be illustrated. Higher static pressure is reached by the prot11 at the outlet. However, the TKE is also higher on the blade surfaces of RR than that of SR because of the high interactions between the FR and RR impellers. All CR configurations deliver higher efficiency and pressure ratio compared to the baseline SR. The total-total and total-static pressure rise coefficients are calculated using Eqn. 14.

768

$$\Psi_4 = \frac{p_4 - p_{t0}}{0.5\rho_{t0}{U_4}^2}, \Psi_{t4} = \frac{p_{t4} - p_{t0}}{0.5\rho_{t0}{U_4}^2} \tag{13}$$

4.4 Effect of the speed ratio on the performance of CR machine: Case of prot12

Prot12 gives the lowest pressure ratio of all selected CR configurations and therefore selected to be further analyzed in terms of pressure rise and efficiency by speed ratio θ modulation while RR rotational speed remains fixed $N_{RR} = 12.5kRPM$.

Fig. 21 shows the evolution of total-total pressure rise and the corresponding isentropic efficiency coefficient according to a variation of θ in which the choke and stall margin are improved drastically. At design conditions $\dot{m}_{dim} = \dot{m}/\dot{m}_d = 1.0$, $\theta = 1.44$, $N_{RR} = 12.5kRPM$, prot12 delivers an increase of pressure rise about 87% and efficiency about 12% compared to SR.

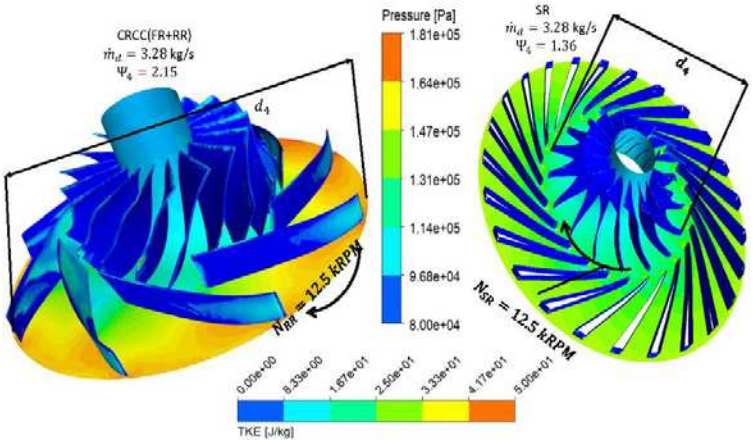

Figure 20: Comparison between the prot11 (left): design mass flow $\dot{m}_d = 3.28kg/s$ and corresponding pressure rise coefficient $\Psi_{t4} = 2.1$, RR speed $\omega_{RR} = 208.3\ Hz$ and conventional SR (impeller and vaned diffuser), (right): $\dot{m}_d = 3.28kg/s$ for pressure rise coefficient of $\Psi_{t4} = 1.4$, $\omega_{SR} = 208.3\ Hz$.

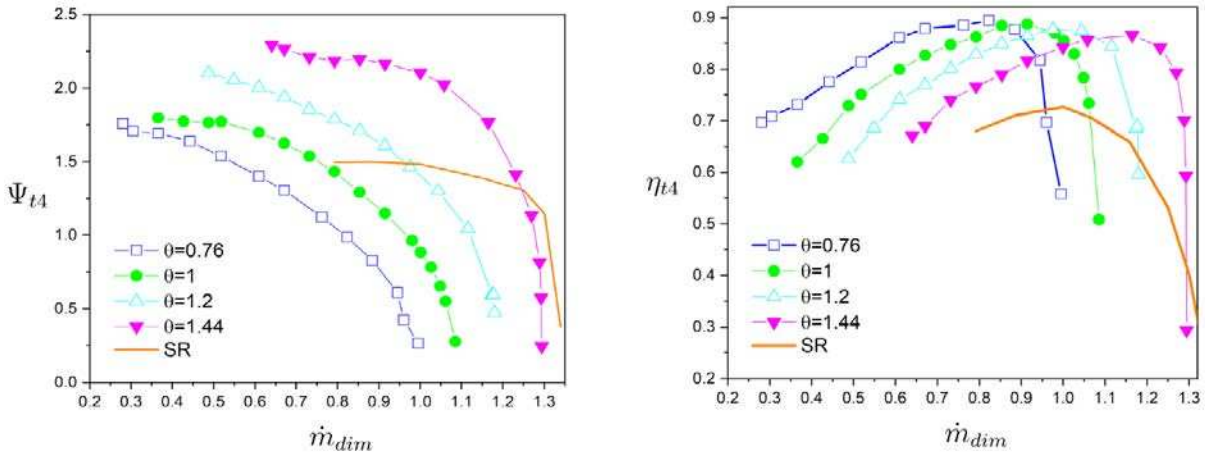

Figure 21: total-total pressure rise coefficient evolution (left) and corresponding isentropic efficiency (right) according to a variation of θ while $N_{RR} = 12.5kRP\mathrm{M}$

Another advantage of the CR configuration is the increase of power density by a factor of 5 compared to SR as shown in Fig. 22 at design condition. The isentropic power density is defined as the power to the size of the machine and calculated by Eqn. 14. SR configuration was designed to produce a total-total pressure ratio of \$1.6\$. By using the CFD data of prot12, it is possible to obtain a maximum totat-total isentropic efficiency for a fixed value of total-total pressure ratio of 1.6 by changing the peripheral speed of both FR and RR impellers as shown in Fig. 23. This figure shows that the nondimensional efficiency area of prot12 is 2.88 times higher than that of SR. This parameter is calculated using Eqn. 15.

$$Power_t = \frac{\dot{m} C_p T_{t0} \left((p_{t4}/p_{t0})^{\frac{\gamma-1}{\gamma}} - 1 \right)}{\pi {r_4}^2 L_{ax} \rho_{t0}} \tag{14}$$

$$S = \int_{\dot{m}_{stall}}^{\dot{m}_{choke}} \frac{\eta_{t4}}{\dot{m}_d} d\dot{m} \tag{15}$$

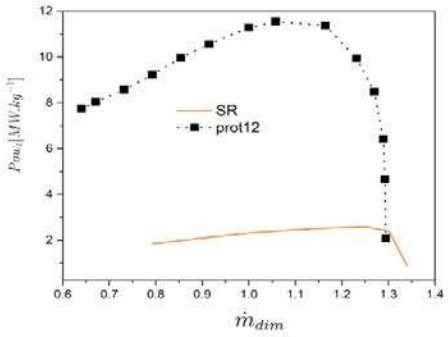

Figure 22: Isentropic power density comparison of prot12 and SR

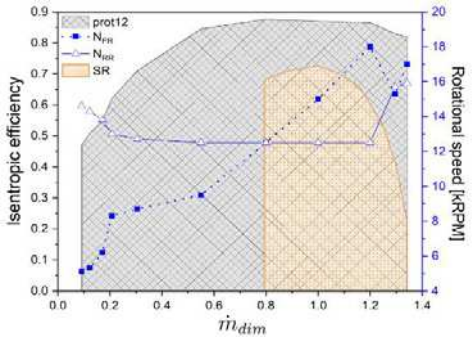

Figure 22: Area of Isentropic power density comparison of prot12 and SR

5 CONCLUSIONS

The objective of this work is to present a detailed design optimization method applied to CR configurations in centrifugal compressor stages and to highlight their advantage compared to standard configuration SR focusing on the effect of speed ratio of CR and its effect on the performance. Thereby, a Meanline approach coupled with optimization techniques is proposed allowing an efficient design of CR. During the design step and because of the compressibility of the flow, specific attention is considered when designing the inlet of RR to obtain an acceptable blockage margin. Furthermore, 12 configurations selected from Pareto front are analyzed by using a 3D CFD solver. The obtained results illustrate global performance improvement with respect to the same outlet radius and peripheral speed of the baseline. By modulating the speed ratio of FR and RR, it's possible to improve the stall and choke margin while increasing the efficiency on a wide range of operating points. The results show that the isentropic total-total power density is increased by a factor of 5 compared to that of SR.

770

Nomenclature

N, ω	Rotational speed	(RPM, rad/s)
θ	Speed radio (-)	
C	Absolute velocity	(m/s)
W	Relative velocity	(m/s)
U	Peripheral speed	(m/s)
Δh	Enthalpy rise	(J/kg)
b	Blade width	(m)
τ	Boundary layer thickness	(m)
T	Temperature	(K)
p	Pressure	(Pa)
β_b	Blade angle	(°)
ρ	Density	($kg.m^{-3}$)
π	Pressure ratio(-)	
η	Isentropic efficiency	
Γ	Torque	(N.m)

Subscript

FR	Front impeller

RR Rear impeller
t Total condition, tangentiel component
m Meridional composent
CR Counter-rotating configuration
SR Baseline
th Throat conditions

REFERENCES

Abed, C.B., Khelladi, S., Deligant, M., El Marjani, Bakir, F., 2020, Preliminary Study of a Centrifugal Compressor With Counter-Rotating Impellers: Design and Performances Study. *Turbo Expo: Power for Land, Sea, and Air. Vol. 84102. American Society of Mechanical Engineers.*

Bourabia, L., Abed, C. B., Cerdoun, M., Khalfallah, S., Deligant, M., Khelladi, S., & Chettibi, T., 2021. Aerodynamic preliminary design optimization of a centrifugal compressor turbocharger based on one-dimensional mean-line model. Engineering Computations, 38(9), 3438-3469.

Abed, C. B., Khelladi, S., Deligant, M., El Marjani, A., Solis, M., & Bakir, F. 2021. Experimental Validation of the Aerodynamic Performance of an Innovative Counter-Rotating Centrifugal Compressor. Energies, 14(9), 2582.

Nguyen, V. T., Abed, C. B., Danlos, A., Ravelet, F., Paridaens, R., Deligant, M., Bakir, F. 2022. Experimental study of a novel centrifugal compressor with two successive and independent rotors. *J. of Engineering for Gas Turbines and Power, 144(1).*

Dejour, Q., Vo, H. D., 2018, Assessment of a novel non-axial counter-rotating compressor concept for aero-engines. *In Turbo Expo: Power for Land, Sea, and Air (Vol. 50992, p. V02AT39A041). American Society of Mechanical Engineers.*

Aungier, R.H., 2000, Centrifugal compressors: A strategy for aerodynamic design and analysis. *American Society of Mechanical Engineers Press: New York, NY, USA.*

Abed, C.B., 2021, Modélisation, Analyse et Contrôle des Compresseurs Centrifuges Contrarotatifs: *Aérodynamique Numérique et Expérimentale, Ph.D Thesis, Arts et Métiers Institute of Technology, ParisTech, France.*

Japikse, D., 1986, Advanced topics in turbomachinery technology, Concepts Eti.

Oh, H. W., Yoon, E. S., & Chung, M. K., 1997, An optimum set of loss models for performance prediction of centrifugal compressors. *Proceedings of the Institution of Mechanical Engineers, Part A: J. of Power and Energy, 211(4), 331-338.*

McKain, T. F., Holbrook, G. J., 1997, Coordinates for a high performance 4: 1 pressure ratio centrifugal compressor, *No. E-10833, NTRS.*

Dolan, F. X., Runstadler Jr, P. W., 1979, Design, development, and test of a laser velocimeter for a small 8: 1 pressure ratio centrifugal compressor, *No. NASA-CR-134781, NTRS.*

Gaetani, P., Persico, G., Mora, A., Dossena, V., and Osnaghi, C., 2012, Impeller-Vaned Diffuser Interaction in a Centrifugal Compressor at Off Design Conditions. ASME. J. Turbomach. November 2012; 134(6): 061034.

771

This book contains the compilation of works contributed to the *7th International Seminar on Organic Rankine Cycle Power Systems* (ORC 2023), held in Seville between the 4th and 6th of September 2023. The event was hosted by Universidad de Sevilla on behalf of the Knowledge Centre on Organic Rankine Cycle Technology (KCORC), incorporated in The Netherlands.

The ORC conference, organized biennially, stems as the only conference that is specific to ORC technology, therefore gathering a diverse community whose affiliation spans across all the interested stakeholders, not only in this particular technology but also and in a broader context, in the energy transition. Original equipment manufacturers, professional associations, end-users, investors, policy makers, academics, scientists feel at home at ORC 2023.

The almost 100 proceedings in this book cover a wide variety of topics, from fundamentals to system integration through component design, accounting for thermodynamic performance as well as component design. In addition to this, and as a new track in 2023, works on heat pump technology were also accepted in order to raise awareness of the strong ties between both technologies, specifically in energy storage applications.

This book provides an excellent overview of the current maturity of power systems based on Organic Rankine Cycle technology for applications as diverse as geothermal and waste heat recovery in industry or downstream of other prime movers (e.g., marine applications). It is also an excellent source of information to understand the current challenges faced by the technology, stemming from a very competitive market and increasingly stringent environmental regulations.

The organizers of ORC 2023 hope that the reader finds this work as exciting as the attendees to the conference and, maybe, make the decision to join the 8th edition to the conference in 2025.

KCORC
KNOWLEDGE CENTER
ORGANIC RANKINE CYCLE

EUS EDITORIAL
UNIVERSIDAD DE SEVILLA